REVIEWS IN MINERALOGY AND GEOCHEMISTRY

Volume 77 2013

Geochemistry of Geologic CO_2 Sequestration

EDITORS

Donald J. DePaolo
Lawrence Berkeley National Laboratory
Berkeley, California

David R. Cole
The Ohio State University
Columbus, Ohio

Alexandra Navrotsky
University of California Davis
Davis, California

Ian C. Bourg
Lawrence Berkeley National Laboratory
Berkeley, California

ON THE FRONT COVER:

The cover figure shows $scCO_2$/brine distribution in a reservoir sandstone during drainage, as imaged using dynamic synchrotron X-ray microtomography at *in situ P/T* conditions. The sample is a micro-core obtained from the Domengine Formation, a potential carbon storage target in the Sacramento Basin; $scCO_2$ is shown in yellow and residual brine is shown in blue. The size of the rendered cube is 5 mm and the underlying image volume has a resolution of 4.43 microns. The dataset was collected at the Advanced Light Source (Beamline 8.3.2) by J.B. Ajo-Franklin and T-H. Kwon and processed/visualized by M. Voltolini.

Series Editor: ***Jodi J. Rosso***

MINERALOGICAL SOCIETY OF AMERICA
GEOCHEMICAL SOCIETY

Reviews in Mineralogy and Geochemistry, Volume 77

Geochemistry of Geologic CO_2 Sequestration

ISSN 1529-6466
ISBN 978-0-939950-92-8

Copyright 2013

The MINERALOGICAL SOCIETY of AMERICA
3635 Concorde Parkway, Suite 500
Chantilly, Virginia, 20151-1125, U.S.A.
www.minsocam.org

The appearance of the code at the bottom of the first page of each chapter in this volume indicates the copyright owner's consent that copies of the article can be made for personal use or internal use or for the personal use or internal use of specific clients, provided the original publication is cited. The consent is given on the condition, however, that the copier pay the stated per-copy fee through the Copyright Clearance Center, Inc. for copying beyond that permitted by Sections 107 or 108 of the U.S. Copyright Law. This consent does not extend to other types of copying for general distribution, for advertising or promotional purposes, for creating new collective works, or for resale. For permission to reprint entire articles in these cases and the like, consult the Administrator of the Mineralogical Society of America as to the royalty due to the Society.

Geochemistry of Geologic CO_2 Sequestration

77 *Reviews in Mineralogy and Geochemistry* **77**

TABLE OF CONTENTS

1 Geochemistry of Geologic Carbon Sequestration: An Overview

Donald J. DePaolo, David R. Cole

INTRODUCTION 1
MINERALIZATION OF CO_2 4
PROPERTIES OF CO_2 AND CO_2-BRINE MIXTURES 5
MINERAL-FLUID REACTIONS 7
MINERAL SURFACE CHEMISTRY 9
LEAKAGE PATHWAYS AND ENGINEERING OPTIONS 10
MONITORING AND VERIFICATION OF CO_2 STORAGE 11
SUMMARY 11
ACKNOWLEDGMENTS 11
REFERENCES 11

2 Natural Analogues

Mike Bickle, Niko Kampman, Max Wigley

INTRODUCTION 15
REVIEW OF NATURAL CO_2 ACCUMULATIONS 17
Petrological studies of subsurface CO_2-reservoirs 17
The Colorado Plateau and southern Rocky Mountains CO_2 province 22
NOBLE GAS STUDIES OF THE COLORADO PLATEAU AND SOUTHERN ROCKY MOUNTAINS CO_2 PROVINCE 26
Noble gases and natural CO_2 reservoirs 26
Noble gas solubility's and Henry's Law 26
Solubility fractionation of gas compositions 28
Terrestrial noble gas reservoirs and sources 29
The Colorado Plateau and southern Rocky Mountains CO_2 fields 31
FLUID-MINERAL REACTIONS AND REACTION RATES 38
The Green River natural analogue 39
SUMMARY AND FURTHER WORK 64
ACKNOWLEDGMENTS 65
REFERENCES 65

3 Thermodynamics of Carbonates

A.V. Radha, A. Navrotsky

INTRODUCTION 73
SEQUENCES OF CARBONATE CRYSTALLIZATION 74
Thermodynamics of prenucleation clusters 75
Thermodynamics of metastable liquid precursors 77
Mesocrystallization 80
Amorphous carbonates: Energetics of the $CaCO_3$-$MgCO_3$-$FeCO_3$-$MnCO_3$ system ... 80
Nanophase carbonates and surface energies 85
CRYSTALLINE DIVALENT CARBONATES 88
Thermodynamics of rhombohedral and orthorhombic carbonates 88
Calcite-aragonite phase transition at high pressure and orientational disordering in calcite at high temperature 89
Vaterite 91
BINARY DIVALENT METAL CARBONATE SYSTEMS 93
$CaCO_3$-$MgCO_3$ 93
$FeCO_3$-$MgCO_3$ 94
$CaCO_3$-$MnCO_3$ 95
$CaCO_3$-$SrCO_3$ 97
Dolomite-type structures and energetics of order-disorder phenomena 97
$CdCO_3$-$MgCO_3$ 98
$CaMg(CO_3)_2$ - $CaFe(CO_3)_2$ solid solution (dolomite - ankerite join) 99
CARBONATE BEARING MULTICOMPONENT PHASES 100
Thermodyanmics of hydrotalcite-type layered double hydroxides (LDH) 100
Dawsonite type compounds $MAl(OH)_2CO_3$ (M = Na, K, NH_4) 102
K_2CO_3-$CaCO_3$ double carbonates 104
Rare earth oxycarbonates 104
Thermodynamics of calcium silicate carbonate minerals 105
A SUMMARY OF THERMODYNAMIC DATA FOR CARBONATE MINERALS 107
CONCLUSIONS AND OUTLOOK 107
ACKNOWLEDGMENTS 107
REFERENCES 114

4 *PVTX* Properties of H_2O-CO_2-"salt" at *PTX* Conditions Applicable to Carbon Sequestration in Saline Formations

Robert J. Bodnar, Matthew Steele-MacInnis, Ryan M. Capobianco, J. Donald Rimstidt, Robert Dilmore, Angela Goodman, George Guthrie

INTRODUCTION 123
SUMMARY OF AVAILABLE *PVTX* DATA AND EOS 125
H_2O 125
CO_2 125
H_2O-"salt" 125
H_2O-CO_2 126

H_2O-CO_2-"salt" 126
Models and EOS to estimate the *PVTX* properties of H_2O-CO_2-"salt" at CCS conditions 128
PROTOCOL TO ESTIMATE FLUID PVTX PROPERTIES AT CCS CONDITIONS 130
PVTX PROPERTIES OF H_2O-CO_2-"SALT" AT CCS CONDITIONS 134
CO_2-rock reactions 137
EFFECT OF TRAPPING MECHANISM ON STORAGE VOLUMES 141
Relationship between storage mechanism and storage security 144
Applications to estimating required formation volumes 144
GAPS IN KNOWLEDGE AND UNDERSTANDING 147
CONCLUDING STATEMENT 147
ACKNOWLEDGMENTS 148
REFERENCES 148

5 Experimental Perspectives of Mineral Dissolution and Precipitation due to Carbon Dioxide-Water-Rock Interactions

John Kaszuba, Bruce Yardley, Muriel Andreani

INTRODUCTION 153
CARBON DIOXIDE IN A FLUID-ROCK SYSTEM 154
Targets for modeling 155
Fluid- and rock-dominated reaction systems 156
Role of co-contaminants 158
EXPERIMENTAL TECHNIQUES 158
Materials for experimental apparatus 158
Specific surface area measurements 159
Batch reactors 161
Mixed flow-through reactors 162
Plug-flow/flow-through reactors 162
pH measurements under GCS conditions 163
CARBON DIOXIDE-WATER-ROCK INTERACTIONS IN RESERVOIR ROCKS AND CAPROCKS: EXPERIMENTAL PERSPECTIVES 164
Olivine and pyroxene 164
Feldspars 168
Phyllosilicates 169
Quartz 173
Carbonates 173
Sulfates 174
Sulfides 176
Iron oxyhydroxides 178
Reservoir and cap rocks 178
SUMMARY AND CONCLUSIONS 179
DIRECTIONS FOR FUTURE WORK 180
ACKNOWLEDGMENTS 181
REFERENCES 181

6 Molecular Simulation of CO_2- and CO_3-Brine-Mineral Systems

Laura M. Hamm, Ian C. Bourg
Adam F. Wallace, Benjamin Rotenberg

INTRODUCTION 189
CO_3-BRINE-MINERAL SYSTEMS 190
- CO_3-brine speciation 190
- Amorphous $M^{(II)}CO_3$ phases 192
- Crystalline carbonate phases 194
- Geochemical kinetics at $M^{(II)}CO_3$-water interfaces 198

CO_2-BRINE-MINERAL SYSTEMS 202
- CO_2-brine two-phase systems 202
- CO_2-brine-mineral systems with a single fluid phase 208
- CO_2-brine-mineral systems with two fluid phases 209
- CO_2 clathrate hydrates 214

FUTURE RESEARCH OPPORTUNITIES 217
ACKNOWLEDGMENTS 217
REFERENCES 218

7 *In situ* Investigations of Carbonate Nucleation on Mineral and Organic Surfaces

James J. De Yoreo, Glenn A. Waychunas,
Young-Shin Jun, Alejandro Fernandez-Martinez

INTRODUCTION 229
THERMODYNAMIC DRIVERS OF NUCLEATION 230
CLASSICAL NUCLEATION THEORY 231
- Homogeneous nucleation 231
- Heterogeneous nucleation 233
- Deviations from a flat energy landscape: Cluster aggregation and size dependent α 235

GISAXS MEASUREMENTS OF INTERFACE PRECIPITATION AND NUCLEATION RATES 238
- GISAXS: from scattered intensity to interfacial energy 242

AFM OBSERVATIONS OF NUCLEATION AND GROWTH OF NEWLY FORMED PRECIPITATES 244
- *Ex situ* AFM observations of GISAXS samples 245

CALCIUM CARBONATE NUCLEATION ON ORGANIC FILMS 247
IMPLICATIONS OF NUCLEATION INFORMATION ON GEOLOGIC CO_2 SEQUESTRATION 252
- Precipitate/mineral interfacial energies 252
- Location and topology of high-density nucleation and subsequent growth 253
- Effects of solution composition on nucleation and growth rates 253

REFERENCES 255

8 Pore Scale Processes Associated with Subsurface CO_2 Injection and Sequestration

Carl I. Steefel, Sergi Molins, David Trebotich

INTRODUCTION 259
Pore scale structure and CO_2 sequestration 260
Pore scale methods 261
Organization of chapter 262
PHYSICS OF SINGLE PHASE FLOW AT THE PORE SCALE 262
PHYSICS OF MULTIPHASE FLOW AT THE PORE SCALE 264
PHYSICS OF MULTICOMPONENT SOLUTE TRANSPORT AT THE PORE SCALE 266
Advection 266
Diffusion 266
Electrochemical migration 267
Péclet number 267
Damköhler numbers 267
Upscaling of flow and transport processes to continuum scale parameters 268
GEOCHEMICAL PROCESSES AT THE PORE SCALE 270
Mineral dissolution and precipitation reaction rates 271
PORE SCALE CHARACTERIZATION AND EXPERIMENTATION 273
2D backscattered electron mapping 274
3D microtomography (XCMT and FIB-SEM) 275
Small Angle Neutron Scattering 278
Nuclear Magnetic Resonance (NMR) and Magnetic Resonance Imaging (MRI) 278
Micromodels 280
INCORPORATING MICROSCOPIC CHARACTERIZATION INTO NUMERICAL PORE SCALE MODELS 280
MODELING APPROACHES FOR THE PORE SCALE 281
Pore network models 284
Lattice Boltzmann method 285
Particle methods: Smooth particle hydrodynamics and moving particle 286
Direct numerical simulation 287
EMERGENT PROCESSES 288
Physical evolution of the pore space 288
Chemical evolution of the pore space: reactive surface area 292
CO_2 invasion 294
NEW DIRECTIONS 296
ACKNOWLEDGMENTS 297
REFERENCES 297

9 Carbon Mineralization: From Natural Analogues to Engineered Systems

Ian M. Power, Anna L. Harrison, Gregory M. Dipple, Siobhan A. Wilson, Peter B. Kelemen, Michael Hitch, Gordon Southam

INTRODUCTION 305
FUNDAMENTAL PROCESSES OF CARBON MINERALIZATION 307
Mineral dissolution 308
CO_2 supply 311
Carbonate mineral precipitation 312
Implications for carbon mineralization 314
NATURAL ANALOGUES 314
High-temperature carbonate alteration of peridotite: listvenite and soapstone 315
Shallow subsurface peridotite weathering and related alkaline springs 315
Hydromagnesite–magnesite playas 318
ENHANCED WEATHERING 320
CARBONATION AT INDUSTRIAL SITES 321
Passive weathering and carbonation 322
Accelerated carbonation 324
BIOLOGICALLY MEDIATED CARBONATION 325
Microbially enhanced mineral dissolution 325
Carbonate biomineralization 326
CARBON MINERALIZATION IN INDUSTRIAL REACTORS 330
Process routes for carbon mineralization in industrial reactors 331
Pre-treatment of minerals 333
IN SITU CARBON MINERALIZATION 335
MONITORING AND STABILITY 336
CAPACITY AND RATES OF CARBON MINERALIZATION STRATEGIES 337
Enhanced weathering 338
Industrial waste carbonation 338
Carbonate biomineralization 344
Carbon mineralization in industrial reactors 344
In situ carbon mineralization 345
SUMMARY 346
ACKNOWLEDGMENTS 347
REFERENCES 347

10 Acid Gases in CO_2-rich Subsurface Geologic Environments

Ariel A. Chialvo, Lukas Vlcek, David R. Cole

INTRODUCTION 361
Background on flue gas sources, composition, and CO_2 - acid gases co-injection ... 361
Consequences of the presence of acid gases on water-rock geochemical reactions . 363

NEED FOR ACCURATE DESCRIPTIONS OF FLUID – FLUID INTERACTIONS.....366
Molecular modeling of CO_2-X phase equilibria at CCUS relevant conditions.....366
Force fields for CO_2-acid gas systems.....368
THE SIGNIFICANT ROLE OF CO_2 FLUID – MINERAL INTERACTIONS.....378
Coexistence of solvation and confinement phenomena.....378
Grand canonical molecular dynamics simulation of mineral confined fluids.....380
Confined fluids behave radically different from their bulk counterparts.....383
THE CRUCIAL ROLE OF (ACID GAS) CO_2 CONTAMINANTS.....384
Contrasting interfacial behavior of CO_2-rich environments containing H_2O, SO_2, H_2S, or NO_x species.....384
SUMMARY OF MOLECULAR-BASED OBSERVATIONS AND THEIR IMPLICATIONS IN MACROSCOPIC MODELING.....389
CONCLUDING REMARKS.....391
ACKNOWLEDGMENTS.....391
REFERENCES.....391

11 Geochemical Monitoring for Potential Environmental Impacts of Geologic Sequestration of CO_2

Yousif K. Kharaka, David R. Cole, James J. Thordsen, Kathleen D. Gans, R. Burt Thomas

INTRODUCTION.....399
FIELD AND LABORATORY METHODS.....401
GEOLOGIC STORAGE OF CO_2.....402
CO_2 trapping mechanisms.....403
CO_2 injection into basalts and ultramafic rocks.....404
Sequestration of CO_2 in sedimentary basins.....404
POTENTIAL IMPACTS AND RISKS OF GEOLOGIC STORAGE OF CO_2.....414
Environmental impacts.....415
Health and safety impacts.....415
GEOCHEMICAL TRACERS OF CO_2 FLOW AND LEAKAGE.....416
Deep subsurface monitoring for early detection: The Frio I Brine test.....418
Near surface monitoring: The ZERT site, Bozeman, Montana.....419
CONCLUDING REMARKS.....422
ACKNOWLEDGMENTS.....423
REFERENCES.....423

12 Multi-scale Imaging and Simulation of Structure, Flow and Reactive Transport for CO_2 Storage and EOR in Carbonate Reservoirs

John P. Crawshaw, Edo S. Boek

INTRODUCTION.....431
MICRO-FLUIDIC EXPERIMENTS OF FLOW IN ETCHED MICRO-MODELS.....433

Drainage and imbibition 433
Fractured media 434
High pressure studies 434
Reactive transport 436
Future research opportunities 436
MULTI-SCALE IMAGING OF STRUCTURE AND FLOW IN CARBONATE ROCKS 437
Macroscopic X-ray CT 438
Confocal Laser Scanning Microscopy (CLSM) 439
micro-CT 440
FIB-SEM 443
Future research opportunities 443
MULTI-SCALE SIMULATION OF FLUID FLOW AND TRANSPORT IN CARBONATE ROCKS 445
Fundamental aspects 447
Pore network models 447
Molecular Dynamics 447
Dissipative Particle Dynamics 448
Stochastic Rotation Dynamics (SRD) 450
Lattice Gas and lattice-Boltzmann models 451
Future research opportunities 455
CONCLUSIONS 455
ACKNOWLEDGMENTS 455
REFERENCES 455

13 Caprock Fracture Dissolution and CO_2 Leakage

Jeffrey P. Fitts, Catherine A. Peters

INTRODUCTION 459
BIG PICTURE PERSPECTIVE OF CAPROCK PERFORMANCE 460
BASELINE ASSESSMENTS OF CAPROCK DISSOLUTION POTENTIAL 463
CAPROCK CHARACTERISITICS 466
FLOW PATHS THROUGH CAPROCKS 466
RELEVANT BRINE ACIDIFICATION PROCESSES 467
PREDICTING THE EVOLUTION OF CAPROCK FLOW PATHS 468
GEOCHEMICALLY-DRIVEN EVOLUTION OF FLOW PATHS 470
CONCLUDING REMARKS 473
ACKNOWLEDGMENT 476
DISCLAIMER 476
REFERENCES 476

14 Capillary Pressure and Mineral Wettability Influences on Reservoir CO_2 Capacity

Tetsu K. Tokunaga, Jiamin Wan

INTRODUCTION 481
$scCO_2$-BRINE INTERFACIAL TENSION 482
CONTACT ANGLE MEASUREMENTS 483
Background 483
Recent measurements 484
WETTING FILMS CONFINED BY CO_2 487
Background 487
A DLVO model for aqueous films on mineral surfaces, confined by $scCO_2$ 488
Experimental measurements of film thicknesses under controlled P_c 492
CAPILLARY PRESSURE-SATURATION RELATIONS 493
Background 493
Recent capillary scaling tests of brine-$scCO_2$ drainage and rewetting in quartz sand 495
SUMMARY AND RESEARCH NEEDS 499
ACKNOWLEDGMENTS 499
REFERENCES 500

15 Geochemistry of Wellbore Integrity in CO_2 Sequestration: Portland Cement-Steel-Brine-CO_2 Interactions

J. William Carey

INTRODUCTION 505
Geochemistry and wellbore integrity in CO_2 sequestration 505
Leakage in wells 506
Other research areas relevant to geochemistry and wellbore integrity 507
CHARACTER OF THE WELLBORE ENVIRONMENT 508
Construction and physical features 508
Physical and chemical conditions at the wellbore 510
Role of coupled processes 510
CEMENT 511
Background on Portland cement 511
Thermodynamic properties of cement and model cement systems 511
Solid solution in C-S-H crystal chemistry 513
Chemical reactions of cement-CO_2 514
Field and experimental observations of cement-CO_2 reactions 515
Reactive transport calculations of cement carbonation 520
STEEL AND STEEL-CEMENT INTERACTIONS 523
Corrosion reactions 523
Role of Portland cement in corrosion 524
Modeling of corrosion reactions 526

COUPLED PROCESSES 527
Flow processes and multiphase behavior 528
Reactive transport in well integrity 529
Coupled geomechanics, flow and reaction 532
Self healing and well integrity 533
CONCLUSIONS AND FUTURE RESEARCH 534
Future research directions 535
ACKNOWLEDGMENTS 535
REFERENCES 536

Reviews in Mineralogy & Geochemistry
Vol. 77 pp. 1-14, 2013
Copyright © Mineralogical Society of America

Geochemistry of Geologic Carbon Sequestration: An Overview

Donald J. DePaolo

Earth Sciences Division
Lawrence Berkeley National Laboratory
Mail Stop 74R316C
Berkeley, California 94720, U.S.A.

djdepaolo@lbl.gov

David R. Cole

School of Earth Sciences
The Ohio State University
125 South Oval Mall
275 Mendenhall Laboratory
Columbus, Ohio 43210, U.S.A.

cole.618@osu.edu

INTRODUCTION

Over the past two decades there has been heightened concern about, and an improving scientific description of, the impacts of increasing carbon dioxide concentrations in Earth's atmosphere. Despite this concern, the global rate of addition of carbon dioxide to the atmosphere by the burning of fossil fuel, now approaching 10 Gton C/yr, continues to increase, and at an accelerating rate (Fig. 1a). Although many still hope and believe that carbon emissions can be arrested at near the current rates, and decreased over the remainder of the 21st century, there is as yet little evidence that this is going to occur.

The driver for carbon emissions is a globally increasing demand for energy, and the fact that energy can be produced relatively inexpensively and with well-developed technology by burning coal, oil and natural gas. Given that the focus on fossil fuel energy is not lessening to an appreciable degree (Fig. 1b), it is not only prudent, but necessary to have the technology to reduce the carbon emissions associated with fossil fuel burning. This reduction can potentially be accomplished with large-scale carbon capture and storage, where carbon dioxide would be captured from the flue gases of electric power generation facilities, purified, compressed, and injected underground as a supercritical fluid into porous geologic rock formations (Oelkers and Cole 2008). To be effective in reducing carbon accumulation in the atmosphere, this injected or "stored" CO_2 must remain underground for thousands of years with only insignificant amounts of leakage back to the surface (Benson and Cook 2005). To date, a significant number of large CO_2 injection demonstrations and more modest pilot tests have been linked to either Enhanced Oil (EOR) or Gas Recovery (EGR) operations such as at the Weyburn EOR site in Canada, the In Salah site in Algeria and the Cranfield EOR in Mississippi, USA (Crawshaw and Boek 2013, this volume).

It is useful when thinking about this problem to recognize that the effect of burning fossil fuels is to take carbon from long-term geologic storage (as buried coal, oil and gas) and release it to the atmosphere. The idea of geologic carbon storage (GCS) is to reverse this process,

1529-6466/13/0077-0001$05.00 http://dx.doi.org/10.2138/rmg.2013.77.1

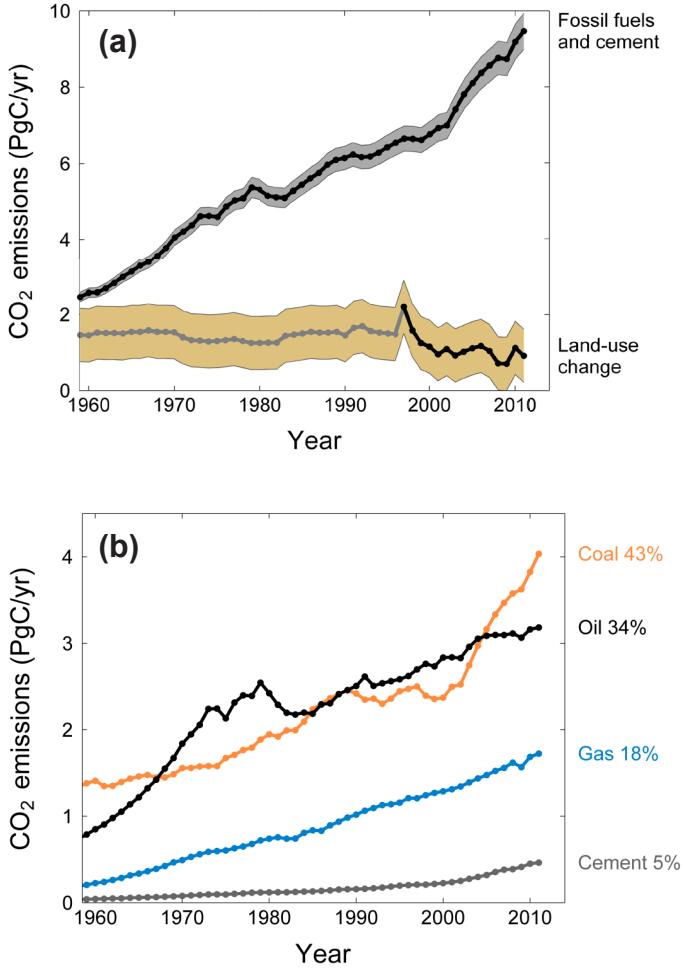

Figure 1. (a) Total carbon emissions to the atmosphere from fossil fuel burning and cement production, and from land use change. Fifty years ago land use change was a large fraction of net emissions, but at present fossil fuel combustion is by far the largest contributor to excess carbon emissions to the atmosphere. (Figure reproduced from *Global Carbon Project (2012)* Carbon budget and trends 2012 released on 3 December 2012. [www.globalcarbonproject.org/carbonbudget]. Data from Le Quéré et al. 2012.) (b) Total global carbon emissions from burning fossil fuel and from cement production, with breakdown by fuel type. Note that the proportion of the emissions coming from coal combustion is increasing rapidly. (Figure reproduced from *Global Carbon Project 2012*, Carbon budget and trends 2012. [www.globalcarbonproject.org/carbonbudget] released on 3 December 2012. Data from Le Quéré et al. 2012.)

returning the released carbon back to geologic storage. The nominal net rate at which C is transferred from geologic storage to the atmosphere by natural processes is about 0.03 Gt/yr (Morner and Etiope 2002). So the 1000 to 5000 GtC that may ultimately be released to the atmosphere over the next 300 years (cf. Archer et al. 2009) represents about 30,000 to 150,000 years of normal transfer. If and when this carbon is returned to geologic storage, it would be advantageous to have it remain stored for a similar amount of time. Consequently, the conversion of supercritical CO_2 to more stable forms (bicarbonate ion dissolved in subsurface brine or carbonate minerals) is highly desirable.

The CO_2 injected underground would be forced under pressure into the pore space of sedimentary rocks, pore space that was initially occupied by saline fluids (brine) (Fig. 2) or possibly brine/hydrocarbon mixtures in the case of EOR. The invasion process is complicated by the contrast in properties between supercritical CO_2 and brine, and the fact that the two fluids are relatively mutually insoluble. In particular, $scCO_2$ has a density that is roughly 50 to 70% of that of typical brines, and a viscosity that is about 15 times lower (Benson and Cole 2008). To first order, CO_2 behaves as a non-wetting fluid phase, which causes it to form bubbles in the pore spaces in contrast to brine, which tends to form thin films on the surfaces of mineral grains (Kim et al. 2012a). The issues that most researchers have focused on reflect the view that the injection process involves (effectively) two inert fluids, and the longer-term behavior is regarded as mostly determined by the difference in density, wetting properties, and the minor amount of mutual solubility (Doughty 2007; Lu et al. 2009; Bodnar et al. 2013, this volume; Tokunaga and Wan 2013, this volume). Injected CO_2 tends to migrate upward within the porous, permeable rock formations into which it is injected, and hence it can only be kept underground if the porous rocks are overlain by impermeable rock layers (Fig. 2). In so far as the footprint of the CO_2 plume injected from a single well could be about 100 km^2 in area, the requirement that the CO_2 be "sealed" underground by impermeable layers is not trivial, but nevertheless appears to be achievable in many known geologic environments in the U.S. and elsewhere (DOE 2012).

The question underlying the contributions in this volume is the degree to which geochemistry can affect the behavior of geologic sequestration systems. There are a number of ways in which chemical reactions between fluids, and between fluids and minerals, can modify expectations that might be derived from a view in which the physical properties of the fluids and medium were the primary controlling factors. Reactions between the fluids and minerals can help to immobilize the CO_2 through mineralization, can change the properties of the rocks by dissolution and precipitation reactions, and can change the wetting properties of $scCO_2$ relative to brine. These interactions can have significant effects on the flow, transport and trapping of CO_2 within rocks, and on the short- and long-term risks associated with escape

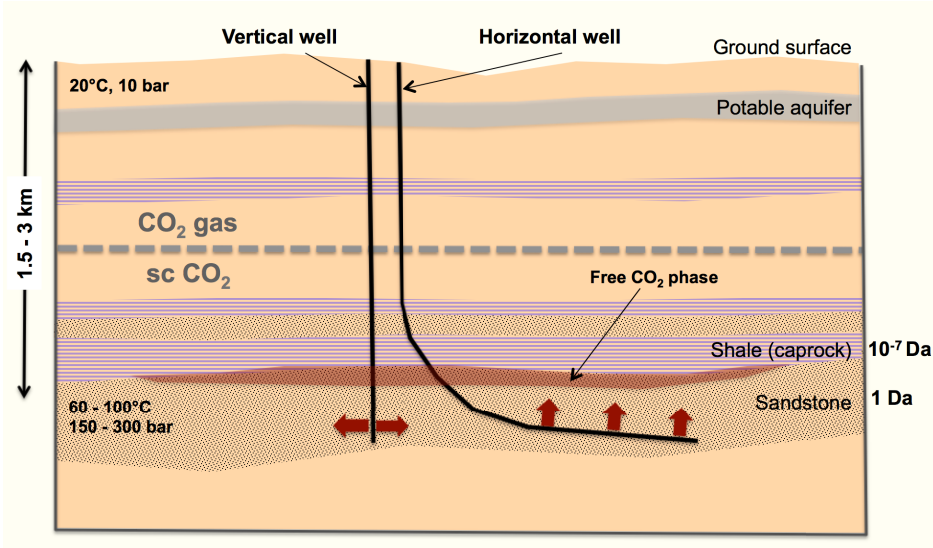

Figure 2. Schematic diagram of a carbon sequestration system shown as geologic cross section and illustrating the typical conditions and rock properties encountered. The transition of gaseous CO_2 to supercritical CO_2 typically occurs at depths of 1-1.5 km.

of CO_2 from the intended storage formations. Understanding the fate of injected CO_2 over the thousands of years required for effective storage amounts to a specialized reactive transport problem, one of a general type that has been recognized as important in many subsurface contexts (e.g., Steefel et al. 2005; Steefel et al. 2013, this volume). A major objective is to predict the transport and fate of the CO_2 over thousands of years, which requires predictive knowledge of the geochemistry, hydrology and geology of the systems.

MINERALIZATION OF CO_2

Supercritical CO_2 at the pressure and temperature conditions typical of subsurface storage is soluble to a limited degree in water and saline brine (Fig. 3). This relatively small amount of dissolved CO_2 transforms the brine into a carbonic acid solution with pH of about 3. The acidification of the brine can be represented as the reaction:

$$CO_2 + H_2O = H^+_{(aq)} + HCO_3^-{}_{(aq)} \quad (1)$$

The acidified brine can react with (dissolve) silicate minerals in the rocks, which will act to neutralize the brine by reactions of the type:

$$H^+_{(aq)} + CaAl_2Si_2O_8 + H_2O = Ca^{2+}_{(aq)} + Al_2Si_2O_5(OH)_4 \quad (2a)$$

In the presence of calcium carbonate there is also potential to remove some of the brine acidity:

$$H^+ + CaCO_3 = Ca^{2+}_{(aq)} + HCO_3^-{}_{(aq)} \quad (2b)$$

If there is sufficient carbonate present in the rocks, Equation (2b) will drive the brine pH to a value of roughly 4.6 to 5, at which point rapid neutralization will cease (e.g., Audigane et al. 2007; Bickle et al. 2013; Kaszuba et al. 2013). Equation (2a) represents a form of silicate rock "weathering," the same process by which weathering at and near the Earth's surface slowly removes CO_2 from the atmosphere (Berner 2003; Power et al. 2013). The second part of the weathering cycle can also occur in underground reservoirs—the recombination of released divalent cations like Ca, Mg and Fe with dissolved CO_2 to form solid carbonate minerals:

$$Ca^{2+}_{(aq)} + HCO_3^- = CaCO_3 + H^+_{(aq)} \quad (3)$$

Summing Equations (1), (2a), and (3) results in the overall weathering reaction:

$$CO_2 + CaAl_2Si_2O_8 + 2H_2O = Al_2Si_2O_5(OH)_4 + CaCO_3 \quad (4)$$

In this example one mole of the silicate mineral anorthite is converted to kaolinite and calcite, and one mole of CO_2 is removed from the atmosphere (or from the injected $scCO_2$ phase) and returned to long-term geologic storage as secondary calcite precipitated in the pore spaces of the host sandstone. The calcite precipitation reaction typically occurs at significant rates only when pH increases to about 8, which should occur in the subsurface once there has been sufficient silicate mineral dissolution (Eqn. 2a).

A key issue is the extent to which the process represented by equation 4 is important for CO_2 storage. The answer depends on the availability of divalent cations contained in silicate minerals and the kinetics of mineral dissolution, both of which depend on many other characteristics of the rocks and of the geometry of invasion of $scCO_2$ into the pore space (Audigane et al. 2007; Gaus et al. 2005; Xu et al. 2005; Kaszuba et al. 2013, this volume). The rate of mineral dissolution is determined by the extent of chemical disequilibrium between the fluids and the minerals, the accessible reactive surface area (RSA) of the minerals, the character of the mineral surfaces and whether those surfaces are affected by the presence of minor chemical constituents including organic material, the spatial distribution of the source of acidity (the $scCO_2$) and the minerals of interest, and transport of reactant and product species in the fluids (cf. Steefel et al. 2005; Molins et al. 2012; Bickle et al. 2013, this volume; Kaszuba et al. 2013, this volume).

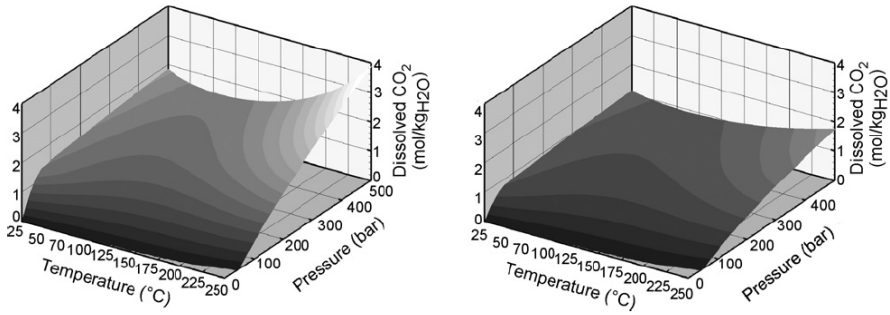

Figure 3. Pressure and temperature dependence of the solubility of CO_2 in in pure water (left) and in a brine with salt concentration of 200 g/l (right). [Used with permission of Elsevier, from Gaus (2010).]

PROPERTIES OF CO_2 AND CO_2-BRINE MIXTURES

An important aspect of the feasibility of CO_2 sequestration is the fact that CO_2 gas transforms to a supercritical liquid with about 2/3 the density of water at relatively modest pressures and temperatures corresponding to depths in the Earth greater than about 1 to 1.5 km (e.g., Benson and Cole 2008; Bodnar et al. 2013, this volume). Potential underground storage reservoirs are relatively easy to reach by drilling, but the relevant geochemistry is at pressures greater than about 10 MPa and temperatures in the range of 40-100 °C. The transformation to a supercritical fluid decreases the volume of the CO_2 by a factor of roughly 600, which is a huge advantage in pumping costs and storage space utilization underground.

The solubility of CO_2 in aqueous fluids is a function of pressure, temperature and fluid salinity. For typical subsurface brines with 10 to 25% salinity, the brine can dissolve up to about 0.5 to 1.5% CO_2 on a molar basis, the smaller amount being associated with the higher salinity (Spycher and Pruess 2003; 2005; Bodnar et al. 2013, this volume). Water is much less soluble in $scCO_2$; typical water contents of $scCO_2$ under relevant conditions are only a few tenths percent (King et al. 1992). Supercritical CO_2, as well as being somewhat less dense than brine, is also much more fluid-like; the viscosity being about 15 times lower than that of pure water (Lemmon et al. 2005).

As CO_2 is injected into brine-filled pore space, the small mutual solubility ensures that there will be two separate phases. The injection of a low-viscosity fluid into a pore network containing a higher viscosity fluid generates channeling and generally a geometrically complicated anastomosing pattern of fingers of CO_2 within the brine on various scales (Saadatpoor et al. 2010; Reeves and Rothman 2012; Ellis and Bazylak 2012). This complication is useful in that it tends to make the surface area of contact between brine and CO_2 large (accelerating dissolution into the brine phase), and during imbibition also allows for some of the CO_2 to be trapped in the pores as discrete, essentially immobilized, residual droplets. This same complication adds some uncertainty into predicting where injected CO_2 will go, because the infiltration pattern is dictated largely by heterogeneity in the rocks, which can be characterized in general, stochastic terms, but is extremely difficult if not impossible to characterize in detail over large length scales. This complication also adds some substantial uncertainty to the application of reservoir flow and transport models, which assume that most properties (like CO_2-to-brine ratio) are uniform over a volume element of the calculation domain of the numerical model, which for typical models could be 10's of cubic meters.

In general it is also the case that water and brine wet (or adhere to) mineral surfaces much more strongly than $scCO_2$ (Espinoza et al. 2010). This property, if it were in fact strictly true,

has two implications. One is that as CO_2 flows through pore networks it does not completely displace the preexisting brine. Instead, thin films of brine are left coating the mineral surfaces (Tokunaga 2012; Kim et al. 2012a; Hamm et al. 2013, this volume). If, as is the case near the injection well, the rock pore space is flushed many times with $scCO_2$, eventually all of the brine will "evaporate" into the CO_2 phase, leaving a salt coating on the mineral grains (Giorgis et al. 2007; Pruess and Miller 2009; Kim et al. 2012c), possibly reducing permeability, a process referred to as "salting". On the other hand, there is evidence that the passage of CO_2 through the system alters the mineral surfaces and hence their wetting properties, and in some cases mineral surfaces may become CO_2-wet (Kim et al. 2012b). Ionic strength and temperature also affect the brine/CO_2/mineral contact angles (Jung and Wan 2012; Fig. 4). The other consequence of the difference in wetting properties and the high CO_2/brine interfacial tension (cf. Nielsen et al. 2012) is that high entry pressures are often required to displace brine during drainage, particularly in the case where pore apertures are small (Fig. 5). This latter effect also determines the extent to which CO_2 droplets can be residually trapped in the pore

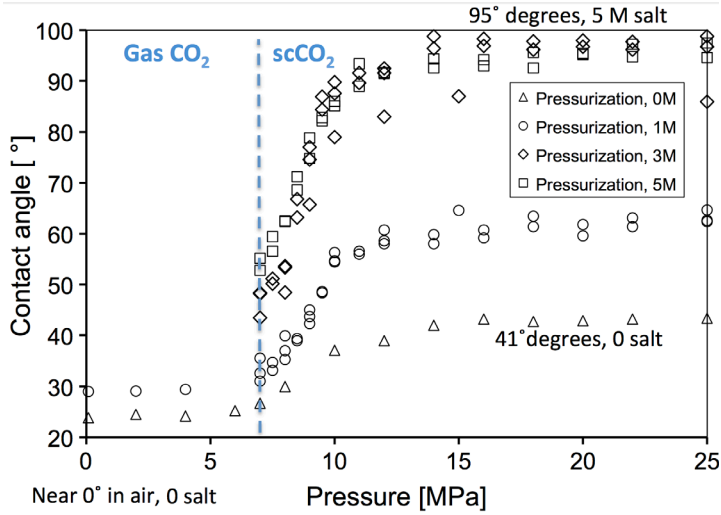

Figure 4. Experimental data showing the effect of salinity and temperature on the wetting angle of CO_2 bubbles in brine on the surface of mica. [Reprinted with permission from Jung and Wan (2012). Copyright 2012 American Chemical Society.]

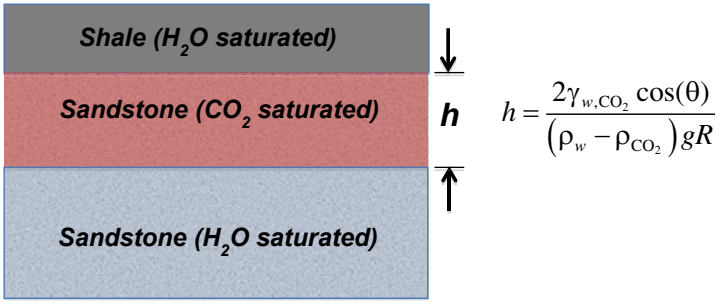

Figure 5. Illustration of the controls on the column height of super critical CO_2 that can be maintained under a shale caprock. The height "*h*" depends on the interfacial tension (γ), the wetting angle (θ), and the pore throat radii (R) as well as on the density contrast between $scCO_2$ and brine.

spaces, and is a key parameter in predicting the storage potential of underground reservoirs (Alkan et al. 2010; Doughty 2007).

MINERAL-FLUID REACTIONS

The contrasts in properties, and the mixing behavior of $scCO_2$ and brine provide unusual conditions for water-rock interaction during CO_2 injection and storage. In general, the rate and extent of mineral dissolution is dependent on the degree of under-saturation of the solution, and the kinetics of reaction. The latter is in turn dependent on the "reactive" surface area (RSA; Landrot et al. 2012) of the mineral grains and on the mechanism(s) of dissolution. The precipitation of secondary minerals, some of which may contain structural CO_3 groups, also depends on solution saturation state, controls on nucleation sites and rates, and the nature of the pore space and mineral surfaces available for nucleation and growth. One special aspect of GCS mineral-fluid reaction is the fact that during the injection phase, brine is largely flushed from the pore space, which becomes filled with a high proportion of $scCO_2$. However, if the brine is a strong wetting phase in comparison with $scCO_2$, the mineral grains will remain coated with a thin brine film even though the pores are filled mostly with CO_2. The brine films are expected to remain quite acidic as the dissolution of silicates (which tends to neutralize the film) will be balanced by diffusion of new CO_2 from the bulk CO_2 into the brine film. Dispersal of the dissolution products may also be retarded by transport within the brine film, so dissolution will be slowed due to higher saturation states maintained in the films.

The amount and kinetics of mineral dissolution are major factors determining whether there will be a significant amount of mineralization of injected CO_2. Modeling studies show a range of results. In some cases only a few percent of injected CO_2 is converted to solid carbonate over 10,000 years (Audigane et al. 2007; Bickle et al. 2013). In other cases, half or more of the CO_2 is converted to solid carbonate in 1000 years (Zhang et al. 2013). The difference in outcome is mainly a function of the sandstone mineralogy. Sands made up predominantly of quartz and K-feldspar, are poor in divalent cations, react slowly, and therefore do not allow for much mineralization. At the other extreme, volcanogenic sands, which contain pyroxenes, amphibole, and mafic-to-intermediate volcanic rock fragments, have an abundance of divalent cations, and the minerals that contain them dissolve more rapidly than quartz and alkali feldspar (Zhang et al. 2013). Intermediate cases include relatively young sandstones with abundant high-Ca plagioclase feldspars (50% > Anorthite); an example is the lower horizon of the regionally extensive Mokelumne River Formation in the Sacramento Basin (Beyer et.al. 2013).

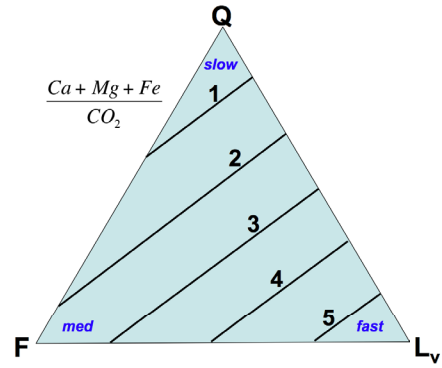

Figure 6. Schematic illustration of the relationship between sandstone mineralogy, the capacity of the sandstone to convert CO_2 to carbonate minerals via the weathering cycle reactions, and the rate at which the conversion occurs. Q = Quartz; F = Feldspar, L = volcanic lithic fragments. The contours are for the molar ratio of divalent cations to CO_2, (Ca+Mg+Fe)/CO_2, for sandstone with 10% by volume capillary-trapped CO_2. In quartz-rich rocks, there is little potential for conversion to solid carbonate, and the process is extremely slow. In rocks with more Ca-feldspar component, and especially in rocks with substantial proportions of andesitic volcanic fragments, there are abundant divalent cations and the weathering reactions are much faster.

The dependence of "reactivity" on sandstone mineralogy is illustrated in Figure 6. For this figure, it is assumed that essentially

all of the mineral dissolution takes place after injection has stopped and after there is re-entry of brine into the pore space until the residual CO_2 saturation is reached. When the flow and imbibition processes are complete there may be 5 to 10% CO_2 by volume in the rocks, or about 30 to 60 kg CO_2/m^3, which is equivalent to 700 to 1400 moles CO_2/m^3. If the rock matrix contains 10-20% of reactive, divalent cation- bearing minerals with typical density, then there are 1000 to 2000 moles of divalent cation available. If the dissolution rate is typical of pyroxene or plagioclase at 75°C, the release rate of cations is about 0.8 mol/m^3/yr, which means that most of the CO_2 could be combined with Ca, Mg and Fe within 1000 years, and perhaps all of it could be mineralized on a longer time scale (Zhang et al. 2013)

The uncertainty in applying the above reasoning is whether the actual values of the dissolution rates can be estimated accurately. The typically used rate values result in a prediction of 10-50% mineralization. If the values are off by a factor of 3 to 10 in either direction, this represents the difference between complete mineralization and almost none. One of the difficulties in accurately estimating rock dissolution rates is in knowing the actual mineral surface area that is involved in the dissolution reactions at any time. There have been recent advances in coupling EM imaging and spectroscopy (e.g., FIB/SEM & EDS) with tomographic characterization of pore networks so that the phase-specific mineral surface area exposed to connected fluids can be accurately determined (Landrot et al. 2012). This analysis can be performed only on small volumes of rock of order 1 mm^3. Dissolution rates may also be affected by coatings on minerals, including organic material, so overall there are still substantial uncertainties.

In general, the precipitation rates of secondary carbonate minerals are substantially faster than the dissolution rates of the silicate minerals that must supply the cations. Growth rates of carbonate minerals at low oversaturations are approximately 10^{-8} mol/m^2/sec (Fig. 7), although at low oversaturations there are kinetic barriers to nucleation (De Yoreo et al. 2013, this volume; Hamm et al. 2013, this volume). Dissolution rates of silicate minerals are on the order of 10^{-10} mol/m^2/sec or slower. However, it is likely that the surface area of dissolving minerals might be two orders of magnitude greater than that of the growing secondary minerals, so that

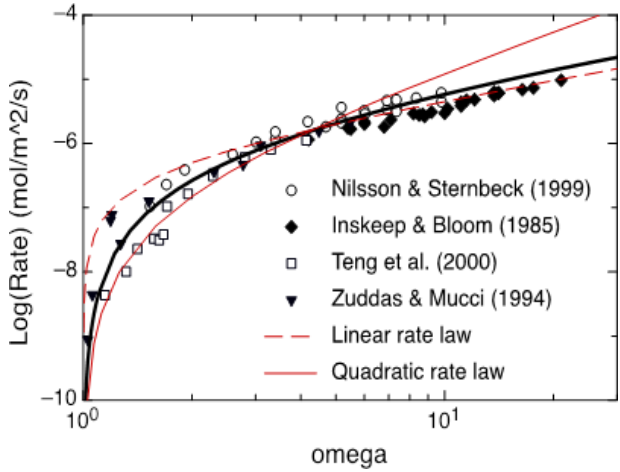

Figure 7. Rate of calcite precipitation versus oversaturation, showing that the rate becomes quite low at very low oversaturations, a feature that is not captured well by reactive transport models that assume first order kinetics for this process. This figure shows curves representing both linear (first order) and quadratic (2^{nd} order) rate laws as well as a mechanistic rate law based on ion-by-ion growth models and presented in Nielsen et al. (2013).

the supply and consumption might be roughly equal. Most modeling studies have assumed that carbonate precipitation is very fast in comparison to silicate dissolution, faster than the time step in the numerical models (cf. Audigane et al. 2007; Xu et al. 2005). This means that the codes typically keep the fluids in equilibrium with respect to carbonate minerals. Although this is a reasonable first guess, there are enough questions concerning carbonate nucleation that this might not be a fully defensible assumption.

The rate of nucleation and growth of secondary minerals might be less important than the location within the pore networks (Steefel et al. 2013, this volume). Secondary mineral growth in large pores probably does not affect the permeability of the rocks substantially, whereas growth in and near pore throats could have a large effect (Chaudhary et al. 2013). There is evidence that calcite nucleation is favored on some mineral surfaces as opposed to others (Fernandez-Martinez et al. 2013), so the relationship between pore-wall mineralogy and pore geometry is of interest. If pore throats are closed down during secondary mineral growth, it could also tend to increase the capillary trapping efficiency of the rocks.

The foundational information that is necessary to understand and predict mineral-fluid interactions is of course the equilibrium thermodynamic properties of the minerals. Solubilities are relatively straightforward for common minerals, but it has been become increasingly evident that there are amorphous and partly crystalline phases in the carbonate system that can play an important role in the formation of secondary minerals (Forbes et al. 2011; De Yoreo et al. 2013, this volume). Sorting out the thermodynamics is an excellent starting point for predicting system evolution (Radha and Navrotsky 2013, this volume). In natural systems, however, no mineral is ever a pure phase, and there is much to be learned still about the effects of minor impurities on both mineral stabilities and kinetics (Nielsen et al. 2013).

MINERAL SURFACE CHEMISTRY

The nature and behavior of mineral surfaces are a major factor in determining the performance of geologic sequestration systems. As noted above, coatings on mineral grains, brine films in contact with mineral surfaces, and wetting properties all contribute to the behavior of CO_2-bearing brines interacting with storage and caprock lithologies. Chemical interactions with $scCO_2$ or acidified brine are likely to change the properties of mineral surfaces during and after CO_2 injection. There is new evidence that wetting properties can change substantially after mineral surfaces are exposed to CO_2-acidified brine (Kim et al. 2012b; Tokunaga and Wan 2013).

Mineral surfaces also come into play in determining the characteristics of fluid phases within pores. New research suggests that adsorption on pore walls can densify the fluid phase to a substantial degree when the pore diameters are 10's of nanometers or smaller (Rother et al. 2012; Cole et al. 2010; Chialvo et al. 2012; Gruszkiewicz et al. 2012; Fig. 8). Indeed, there is general agreement that the collective structure and properties of bulk fluids are altered by confinement between two mineral surfaces or in narrow pores due to the interplay of the intrinsic length scales of the fluid molecular size and the length scale due to confinement (Gelb et al. 1999; Chialvo et al. 2013, this volume; Hamm et al. 2013, this volume). Other research is demonstrating that nanoporosity is a significant fraction of total porosity (Anovitz et al. 2013), and that mineral nucleation rates are modified in nanopores and on mineral surfaces with nanoscale roughness (Hedges and Whitelam 2012).

Minor components of the fluid phases can also change the behavior of mineral surfaces. A small concentration of peptide-like inorganic molecules can accelerate calcite precipitation by more than an order of magnitude at low supersaturations (Chen et al. 2011; De Yoreo et al. 2013, this volume). The presence of other impurities, like Mg for example, markedly slows calcite growth rates as is well documented (cf. Nielsen et al. 2013).

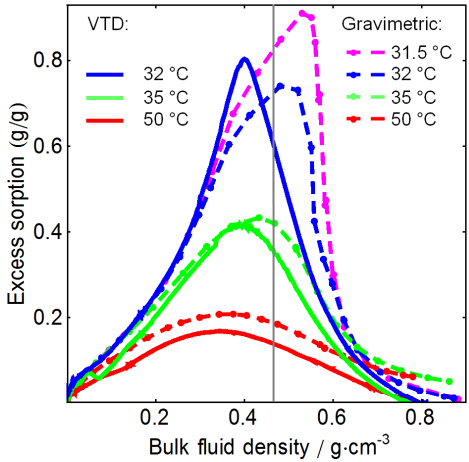

Figure 8. Excess sorption versus bulk fluid density for supercritical CO_2 in silica nanopores. At 35 °C the fluid density is about 40% higher than that of bulk $scCO_2$ due to the presence of a dense absorbed phase on the pore walls. This excess sorption disappears at higher bulk fluid densities but is quite prominent when the density is in the range 0.4 to 0.6 c/cm^3, which is fairly typical of sequestrations conditions. [Used with permission from Gruszkiewicz et al. (2012). American Chemical Society.]

With regard to geologic sequestration, an interesting question is whether mineral surfaces can be made more reactive rather than less, since the release of cations by mineral dissolution is required to mineralize injected CO_2. The presence of small amounts of other acid gas components (like SO_2) could promote changes in wetting and phase behavior in pores (Chialvo et al. 2013, this volume) and variable rates of silicate mineral dissolution (Xu et al. 2007). Secondary gases are often available at capture facilities, particularly in the cases of natural gas separation facilities or post-combustion capture for power generation with high sulfur coal as the fuel stock. Additionally, the presence or absence of oxygen could affect the rates of oxidation-reduction reactions involving Fe-bearing minerals (Palandri and Kharaka 2005).

LEAKAGE PATHWAYS AND ENGINEERING OPTIONS

Although CO_2 storage is generally believed to be safe and secure under many conditions, there is still a need to accurately quantify the possibility that injected gas might return to the surface or enter shallow aquifers used for drinking water. One such scenario is the fracturing of overlying shale caprocks due to the overpressure needed to force CO_2 into the storage formations (e.g., Zoback and Gorelick 2012; see, however, Juanes et al. 2012). Modeling studies have shown that the subsurface volume affected by increased pore pressure is much larger than the volume actually containing injected CO_2 (Zhou and Birkholzer 2011), so it is likely that pore pressure increases could impact a large area, although it also true that this not a long-term problem because pressures return to normal within decades after injection stops. Caprocks or seals can also be heterogeneous with regard to permeability, and contain natural faults and fractures (Fitts and Peters 2013, this volume). Understanding whether these imperfections in the sealing formations are serious concerns involves both hydrology and geochemistry.

One leakage pathway that has received considerable attention is wellbores, both the wells used for injection and existing and potentially unknown abandoned wells (Gasda et al. 2004; Celia et al. 2006; Nordbotten et al. 2009; Carey 2013). Most of the sedimentary basins of the U.S., for example, have hundreds to thousands of wells that were drilled over the last century or more, and not all of them are represented in databases (Zhang et al. 2011). The Ca-silica cement components are soluble in acidified bring so there is some concern that the CO_2 flooded region near the injection wells could lead to enhanced permeability, especially in the annulus around the casing, and particularly at the interface between cement and surrounding rocks (Carroll et al. 2011; Newell and Carey 2012; Jun et al. 2013).

Subsurface pore space in the depth range where CO_2 injection will be targeted contains microbial populations, although in general the nature of those populations is poorly known. Recent work has shown that the presence of microbial biomass, either living or dead, can accelerate the growth of carbonate minerals in oversaturated fluids (Cappuccio et al. 2011). This observation, and the more general observation that some organic molecules accelerate calcite growth (Chen et al. 2011; Hamm et al. 2013, this volume), leads to the idea that microbial populations could be manipulated to mitigate leakage along wellbores and in other circumstances (Armstrong and Ajo-Franklin 2011).

MONITORING AND VERIFICATION OF CO_2 STORAGE

A critical issue in CO_2 storage is in verifying the amount of CO_2 injected and stored, and in monitoring the migration and fate of the CO_2. The emphasis for these issues has been on geophysics (e.g., Daley et al. 2007), but there is also an important role for geochemistry as tracers of fluid-fluid interactions and fluid-rock processes (cf. Clark and Fritz 1997; Kharaka et al. 2013). Kharaka and Cole (2011) provide an excellent review of recent applications of geochemistry to CO_2 injection experiments and specific examples are described by Kharaka et al. (2009). An example is the use of a gas concentration ratio (He/CO_2) that is sensitive to the mutual dissolution of CO_2 and brine (Bickle et al. 2013, this volume). Dissolution of injected CO_2 into brine also results in fractionation of C and O isotopes (Dubacq et al. 2012), and when this occurs during injection there is a possibility of kinetic isotope effects and also effects due to differing relative permeability between fluid phases. Dissolution and precipitation of minerals can also result in isotopic shifts in elements like Ca and Mg, and the isotopic composition of dissolved Sr and trace metal components may help track brine migration. Trace metals in overlying aquifer waters are also expected to be useful as sensitive tracers of upward migration of CO_2 from storage formations, due to the acidification that the CO_2 causes (Apps et al. 2010).

SUMMARY

Geochemistry plays a significant role in many aspects of geologic carbon sequestration, from dissolution and precipitation of minerals in the reservoir and seal rocks, to modification of the properties of mineral surfaces and their effects on fluid flow and capillary trapping. The properties of supercritical CO_2, brines, and their mixtures are also critical to designing, predicting the behavior, and monitoring sequestration systems and sites. In this volume, there are illustrations of many of the important geochemical challenges relating to carbon sequestration. The contributions also showcase modern techniques and approaches that are being employed to advance knowledge of these fluid-rock systems that may be critical to mitigation of carbon emissions.

ACKNOWLEDGMENTS

This material is based upon work supported as part of the Center for Nanoscale Control of Geologic CO_2, an Energy Frontier Research Center funded by the U.S. Department of Energy, Office of Science, Office of Basic Energy Sciences under Award Number DE-AC02-05CH11231.

REFERENCES

Alkan H, Cinar, Y, Ulker EB (2010) Impact of capillary pressure, salinity and in situ conditions on CO_2 injection into saline aquifers. Transp Porous Med 84:799-819

Anovitz LM, Cole DR, Rother G, Allard LF, Jackson AJ, Littrell KC (2013) Diagenetic changes in macro- to nano-scale porosity in the St. Peter Sandstone: An (ultra) small angle neutron scattering and backscattered electron imaging analysis. Geochim Cosmochim Acta 102: 280-305

Apps JA, Zheng L, Zhang Y, Xu T, Birkholzer JT (2010) Evaluation of potential changes in groundwater quality in response to CO_2 leakage from deep geologic storage. Transp Porous Med 82: 215-246

Archer D, Eby M, Brovkin V, Ridgwell A, Cao L, Mikolajewicz U, Caldeira K, Matsumoto K, Munhoven G, Montenegro A, Tokos K. (2009) Atmospheric lifetime of fossil fuel carbon dioxide. Ann Rev Earth Planet Sci 37:117-134

Armstrong R, Ajo-Franklin J (2011) Investigating biomineralization using synchrotron based Xray computed microtomography. Geophys Res Lett 38: L08406,doi:10.1029/2011GL046916

Audigane P, Gaus I, Czernichowski-Lauriol I, Pruess K, Xu TF (2007) Two-dimensional reactive transport modeling of CO_2 injection in a saline Aquifer at the Sleipner site, North Sea. Am J Sci 307:974-1008

Benson SM, Cole DR (2008) CO_2 sequestration in deep sedimentary formations. Elements 4(5):305-310

Benson SM, Cook P (2005) Underground Geological Storage. *In:* Carbon Dioxide Capture and Storage: Special Report of the Intergovernmental Panel on Climate Change (IPCC). Cambridge University Press, Interlachen, Switzerland, p 5-1 to 5-134

Berner RA (2003) The long-term carbon cycle, fossil fuels and atmospheric composition. Nature 426:323-326

Beyer JH, Ajo-Franklin JB, Burton E, Conrad M, Doughty C, Kneafsey T, Nakagawa S, Spycher N, Voltolini M (2013) "Geologic Characterization Based on Deep Core and Fluid Samples from the Sacramento Basin of California - an Update". *CCUS 2013*, Pittsburgh, PA., May

Bickle M, Kampman N, Wigley M (2013) Natural analogues. Rev Mineral Geochem 77:15-71

Bodnar RJ, Steele-MacInnis M, Capobianco RM, Rimstidt JD, Dilmore R, Goodman A, Guthrie G (2013) PVTX Properties of H_2O-CO_2-"salt" at PTX conditions applicable to carbon sequestration in saline formations. Rev Mineral Geochem 77:123-152

Cappuccio JA, Pillar VD, Xiao C, Ajo-Franklin CM (2011) Bacterial acceleration of $CaCO_3$ mineralization. Biophys J 100(3):487a

Carey JW (2013) Geochemistry of wellbore integrity in CO_2 sequestration: Portland cement-steel-brine-CO_2 interactions. Rev Mineral Geochem 77:505-539

Carroll SA, McNab WW, Torres SC (2011) Experimental study of cement - sandstone/shale -brine - CO_2 interactions. Geochem Trans 12:9

Celia MA, Kavetski D, Nordbotten JM, Bachu S, Gasda SE (2006) Implications of abandoned wells for site selection. *In*: CO_2SC 2006 International Symposium on Site Characterization for CO_2 Geological Storage, March 20-22, 2006. Proceedings: Berkeley, CA, Lawrence Berkeley National Laboratory, p 157-159

Chaudhary K, Cardenas MB, Den W, Bennett PC (2013) Pore geometry effects on intra-pore viscous to inertial flows and effective hydraulic parameters. Water Resources Res 49:1149-1162, doi:10.1002/wrcr.20099

Chen C-L, Qi J, Zuckermann RN, De Yoreo JJ (2011) Engineered biomimetic polymers as tunable agents for controlling $CaCO_3$ mineralization. J Am Chem Soc 133:5214-5217

Chialvo AA, Vlcek L, Cole DR (2012) Aqueous CO_2 Solutions at silica surfaces and within nanopore environments: Insights from isobaric-isothermal molecular dynamics. J Phys Chem C 116:13904-13916

Chialvo AA, Vlcek L, Cole DR (2013) Acid gases in CO_2-rich subsurface geologic environments. Rev Mineral Geochem 77:361-398

Clark ID, Fritz P (1997) Environmental Isotopes in Hydrogeology. CRC Press, New York.

Cole DR, Chialvo AA, Rother G, Vlcek L, Cummings PT (2010) Supercritical fluid behavior at nanoscale interfaces: Implications for CO_2 sequestration in geologic formations. Philos Mag Special Issue on Layer Silicate Materials and Clays 90(17-18):339-2363

Crawshaw JP, Boek ES (2013) Multi-scale imaging and simulation of structure, flow and reactive transport for CO_2 storage and EOR in carbonate reservoirs. Rev Mineral Geochem 77:431-458

Daley TM, Solbau RD, Ajo-Franklin JB, Benson SB (2007) Continuous active-source seismic monitoring of CO_2 injection in a brine aquifer. Geophysics 72(5):A57-A61

De Yoreo JJ, Waychunas GA, Jun Y-S, Fernandez-Martinez A (2013) *In situ* investigations of carbonate nucleation on mineral and organic surfaces. Rev Mineral Geochem 77:229-257

DOE (2012) Department of Energy, Office of Fossil Energy, Carbon Utilization and Storage Atlas, The United States 2012, 4th edition

Doughty C (2007) Modeling geologic storage of carbon dioxide: comparison of non-hysteretic and hysteretic characteristic curves. Energy Convers Manage 48:1768-1781

Dubacq B, Bickle MJ, Wigley M, Kampman N, Ballentine CJ, Lollar BS (2012) Noble gas and carbon isotopic evidence for CO_2-driven silicate dissolution in a recent natural CO_2 field. Earth Planet Sci Lett 341-344:10-19

Ellis JS, Bazylak A (2012) Dynamic pore network model of surface heterogeneity in brine-filled porous media for carbon sequestration. Phys Chem Chem Phys 14:8382-8390

Espinoza DN, Santamarina JC (2010) Water-CO_2-mineral systems: Interfacial tension, contact angle, and diffusion-implications to CO_2 geological storage. Water Resour Res 46:W07537; doi: 10.1029/2009WR008634

Fernandez-Martinez A, Hu Y, Lee B, Jun Y-S, Waychunas GA (2013) In situ determination of interfacial energies between heterogeneously nucleated $CaCO_3$ and quartz substrates: thermodynamics of CO_2 mineral trapping. Environ Sci Technol 47(1):102-109

Fitts JP, Peters CA (2013) Caprock fracture dissolution and CO_2 leakage. Rev Mineral Geochem 77:

Forbes TZ, Radha AV, Navrotsky A (2011) The energetics of nanophase calcite. Geochim Cosmochim Acta 75:7893-7905

Gasda S, Bachu S, Celia M (2004) Spatial characterization of the location of potentially leaky wells penetrating a deep saline aquifer in a mature sedimentary basin. Environ Geol 46:707-720

Gaus I (2010) Role and impact of CO_2–rock interactions during CO_2 storage in sedimentary rocks. Int J Greenhouse Gas Control 4:73-89

Gaus I, Azaroual M, Czernichowski-Lauriol I (2005) Reactive transport modeling of the impact of CO_2 injection on the clayey cap rock at Sleipner (North Sea). Chem Geol 217:319-337

Gelb LD, Gubbins KE, Radhakrishnan R, Sliwinska-Bartkowiak M (1999) Phase separation in confined systems. Rep Prog Phys 62:1573-1659

Giorgis T, Carpita M, Battistelli A (2007) Modeling of salt precipitation during the injection of dry CO_2 in a depleted gas reservoir. Energy Convers Manage 48(6):1816-1826

Gruszkiewicz MS, Rother G, Wesolowski DJ, Cole DR, Wallacher D (2012) Direct measurements of pore fluid density by vibrating tube densimetry. Langmuir 28:5070-5078

Hamm LM, Bourg IC, Wallace AF, Rotenberg B (2013) Molecular simulation of CO_2- and CO_3-brine-mineral systems. Rev Mineral Geochem 77:189-228

Hedges LO, Whitelam S (2012) Patterning a surface so as to speed nucleation from solution. Soft Matter 8:8624-8635

Juanes R, Hager BH, Herzog HJ (2012) No geologic evidence that seismicity causes fault leakage that would render large-scale carbon capture and storage unsuccessful. Proc Natl Acad Sci USA 109:E3623

Jun Y-S, Giammar DE, Werth CJ (2013) Impacts of geochemical reactions on geologic carbon sequestration. Envion Sci Technol 47:3-8

Jung JW, Wan J (2012) Supercritical CO_2 and ionic strength effects on wettability of silica surfaces: equilibrium contact angle measurements. Energy Fuels 26(9):6053–6059; doi: 10.1021/ef300913t

Kaszuba J, Yardley B, Andreani M (2013) Experimental perspectives of mineral dissolution and precipitation due to carbon dioxide-water-rock interactions. Rev Mineral Geochem 77:153-188

Kharaka YK, Cole DR (2011) Geochemistry of geologic sequestration of carbon dioxide. *In:* Frontiers in Geochemistry: Contributions of Geochemistry to the Study of the Earth. Harmon RS, Parker A (eds) Blackwell, p 135-174

Kharaka YK, Cole DR, Thordsen JJ, Gans KD, Thomas RB (2013) geochemical monitoring for potential environmental impacts of geologic sequestration of CO_2. Rev Mineral Geochem 77:399-430

Kharaka YK, Thordsen JJ, Hovorka SD, Nance HS, Cole DR, Phelps TJ, Knauss KG (2009) Potential environmental issues of CO_2 storage in deep saline aquifers. Geochemical results from the Frio-I Brine Pilot test, Texas, USA. Appl Geochem 24:1106-1112

Kim T-W, Tokunaga TK, Shuman DB, Sutton SR, Newville M, Lanzirotti A (2012a) Thickness measurements of nanoscale brine films on silica surfaces under geologic CO_2 sequestration conditions using synchrotron X-ray fluorescence. Water Resour Res 48:W09558, doi:10.1029/2012WR012200

Kim Y, Wan J, Kneafsey TJ, Tokunga TK (2012b) Dewetting of silica surfaces upon reactions with supercritical CO_2 and brine: pore-scale studies in micromodels. Environ Sci Technol 46(7):4228-4235

Kim Y, Han WS, Oh J, Kim T, Kim J-C (2012c) Characteristics of salt-precipitation and the associated pressure build-up during CO_2 storage in saline aquifers. Transp Porous Med 92:397-418

King MB, Murbarak A, Kim JD, Bott TR (1992) The mutual solubilities of water with supercritical and liquid carbon dioxide. J Supercrit Fluids 5:296-302

Landrot G, Ajo-Franklin J, Cabrini S, Yang L, Steefel CI (2012) Measurement of accessible reactive surface area in a sandstone, with application to CO_2 mineralization. Chem Geol 318-319:113-125

Lemmon EW, McLinden MO, Friend DG (2005) Thermophysical properties of fluid systems. *In:* Chemistry Web Book. NIST Standard Reference Database Number 69. Linstrom PJ, Mallard WG (eds) National Institute of Standards and Technology.

Le Quéré C, Andres RJ, Boden T, Conway T, Houghton RA, House JI, Marland G, Peters GP, van der Werf G, Ahlström A, Andrew RM, Bopp L, Canadell JG, Ciais P, Doney SC, Enright C, Friedlingstein P, Huntingford C, Jain AK, Jourdain C, Kato E, Keeling RF, Klein Goldewijk K, Levis S, Levy P, Lomas M, Poulter B, Raupach MR, Schwinger J, Sitch S, Stocker BD, Viovy N, Zaehle S, Zeng N (2012) The global carbon budget 1959–2011. Earth Syst Sci Data Discuss 5:1107-1157

Lu C, Han WS, Lee S-Y, McPherson BJ, Lichtner PC (2009) Effects of density and mutual solubility of a CO_2-brine system on CO_2 storage in geological formations: "Warm" vs. "cold" formations. Adv Water Res 32(12):1685-1702

Molins S, Trebotich D, Steefel CI, Shen C (2012) An investigation of the effect of pore scale flow on average geochemical reaction rates using direct numerical simulation. Water Resour Res 48:W03527; doi:10.1029/2011WR011404

Morner N-A, Etiope G (2002) Carbon degassing from the lithosphere. Global Planet Change 33:185-203

Newell DL, Carey JW (2013) Experimental evaluation of wellbore integrity along the cement-rock boundary. Environ Sci Technol 47:276-282

Nielsen LC, Bourg IC, Sposito G (2012) Predicting CO_2-water interfacial tension under pressure and temperature conditions of geologic CO_2 storage. Geochim Cosmochim Acta 81:28-38

Nielsen LC, De Yoreo JJ, DePaolo DJ (2013) General model for calcite growth kinetics in the presence of impurity ions. Geochim Cosmochim Acta 115:100-114

Nordbotten JM, Kavetski D, Celia MA, Bachu S (2009) Model for CO_2 Leakage including multiple geological layers and multiple leaky wells. Environ Sci Technology 43:743-749

Oelkers EH, Cole DR (2008) Carbon dioxide sequestration: A solution to global problem. Elements 4:305-310

Palandri JL, Kharaka YK (2005) Ferric iron-bearing sediments as a mineral trap for CO_2 sequestration: iron reduction using sulfur-bearing waste gas. Chem Geol 217:351-364

Power IM, Harrison AL, Dipple GM, Wilson SA, Kelemen PB, Hitch M, Southam G (2013) Carbon mineralization: from natural analogues to engineered systems. Rev Mineral Geochem 77:305-360

Pruess K, Müller N (2009) Formation dry-out from CO_2 injection into saline aquifers: 1. Effects of solids precipitation and their mitigation. Water Resour Res 45:W03402; doi:10.1029/2008WR007101

Radha AV, Navrotsky A (2013) Thermodynamics of carbonates. Rev Mineral Geochem 77:73-121

Reeves, D, Rothman DH (2012) Impact of structured heterogeneities on reactive two-phase porous flow. Phys Rev E 86: 031120, doi 10.1103/PhysRevE.86.031120

Rother G, Krukowski EG, Wallacher D, Grimm N, Bodnar RJ, Cole DR (2012) Pore size effects on the sorption of supercritical carbon dioxide in mesoporous CPG-10 silica. J Phys Chem C 116:917-922

Saadatpoor E, Bryant SL, Sepehrnoori K (2010) New trapping mechanism in carbon sequestration. Transport Porous Media 82(1):3-17

Spycher N, Pruess K, Ennis-King J (2003) CO_2-H_2O mixtures in geological sequestration of CO_2, I: Assessment and calculation of mutual solubilities from 12 to 100°C and up to 600 bar. Geochim Cosmochim Acta 67:3015-3031

Spycher N, Pruess K (2005) CO_2-H_2O mixtures in the geological sequestration of CO_2. II. Partitioning in chloride brines at 12-100°C and up to 600 bar: Geochim Cosmochim Acta 69: 3309-3320

Steefel CI, Molins S, Trebotich D (2013) Pore scale processes associated with subsurface CO_2 injection and sequestration. Rev Mineral Geochem 77:259-303

Steefel CI, Lichtner PC, DePaolo DJ (2005) Reactive transport modeling: An essential tool and a new research approach for the Earth sciences. Earth Planet Sci Lett 240:539-558

Tokunaga TK (2012) DLVO-based estimates of adsorbed water film thicknesses in geologic CO_2 reservoir. Langmuir 28:8001-8009

Tokunaga TK, Wan J (2013) Capillary pressure and mineral wettability influences on reservoir CO_2 capacity. Rev Mineral Geochem 77:481-503

Zhang M, Bachu S (2011) Review of integrity of existing wells in relation to CO_2 geological storage: What do we know? Int J Greenhouse Gas Control 5:826-840

Zhang S, DePaolo DJ, Xu T, Zheng L (2013) Mineralization of carbon dioxide sequestered in volcanogenic reservoir rocks. Int J Greenhouse Gas Control, in press

Zhou Q, Birlholzer JT (2011) On scale and magnitude of pressure build-up induced by large-scale geologic storage of CO_2. Greenhouse Gases-Sci Tech 1:11-20

Zoback MD, Gorelick SM (2012) Earthquake triggering and large-scale geologic storage of carbon dioxide. Proc Natl Acad Sci 109(26):10164-10168

Xu T, Apps JA, Pruess K (2005) Mineral sequestration of carbon dioxide in a sandstone-shale system. Chem Geol 217: 295-318

Xu T, Apps JA, Pruess K, Yamamoto H (2007) Numerical modeling of injection and mineral trapping of CO_2 with H_2S and SO_2 in a sandstone formation. Chem Geol 242:319-346

Reviews in Mineralogy & Geochemistry
Vol. 77 pp. 15-71, 2013
Copyright © Mineralogical Society of America

Natural Analogues

Mike Bickle, Niko Kampman, Max Wigley

Department of Earth Sciences
University of Cambridge
Cambridge, CB2 3EQ, United Kingdom

mb72@hermes.cam.ac.uk njsk2@cam.ac.uk mmwigley@googlemail.com

INTRODUCTION

Geological carbon storage will require that less than ~0.01% of the mass of CO_2 stored escapes per year if significant climatic impacts are to be avoided (Hepple and Benson 2005). This requires that the geological storage sites retain much of the CO_2 for more than 10,000 years. Predicting the security of CO_2 in storage sites for such time periods raises questions which relate to a number of poorly understood fundamental processes concerning fluid-rock interactions in the near subsurface of the Earth. Because many of these processes are sluggish it is not possible to predict their significance from observations on active injection experiments with durations of, at most, a few tens of years. Nor do these experiments yet sample the full spectrum of potential behavior of CO_2 in storage sites. For these reasons it is useful to study sites where natural CO_2 has been retained in geological strata for periods which range from tens of thousands to millions of years.

Geological storage of CO_2 will be mainly in depleted oil and gas reservoirs or saline aquifers at depths greater than about 800 m (DePaolo and Cole 2013, this volume). Under these conditions the CO_2 will be in the denser supercritical state, but less dense than formation brines. As such it will tend to rise buoyantly and be retained by an impermeable caprock. A key concern is that the CO_2, or CO_2-charged brines will react with and corrode caprocks or faults and allow the CO_2 to migrate upwards. CO_2-rich waters are known to react with minerals but predicting the rates of fluid-mineral reactions at low temperatures is problematic (White and Brantley 2003) and the consequent changes in permeability of the caprocks or fault zones are uncertain (e.g., Gaus et al. 2005). However there are a series of other processes likely to act in CO_2 storage reservoirs and the long-term fate of the CO_2 will be governed by these and their complex interactions. Key processes which might increase the security of CO_2 storage include 1) residual trapping of a fraction of the CO_2 by surface tension as moving CO_2 is replaced by brine, 2) solubility trapping by dissolution of CO_2 in brine, which increases the density of the brine, stabilizing storage of the dissolved CO_2 and 3) reactions between silicate minerals and CO_2-charged brines which cause precipitation of carbonate minerals further stabilizing CO_2 storage. The progress of these processes is represented schematically in Figure 1 (IPCC 2005) but, apart from structural and stratigraphic trapping, the rates and ultimate significance of these processes are poorly constrained.

The uncertainty in the rates of these trapping mechanisms is due, in part, to the complexity of the processes within the storage reservoirs. Residual trapping and solubility trapping will both depend on the flow of the CO_2 in the reservoir. Residual trapping takes place as brine replaces CO_2 and therefore will only occur when the CO_2 plume is mobile. Solubility trapping takes place by diffusion of CO_2 into brines and this sluggish process will therefore be enhanced if the contact area between the CO_2 and brine is increased by fingering of less-viscous CO_2 and by flow in a heterogeneous reservoir, or by convective removal of the denser, CO_2-saturated brine

1529-6466/13/0077-0002$10.00 http://dx.doi.org/10.2138/rmg.2013.77.2

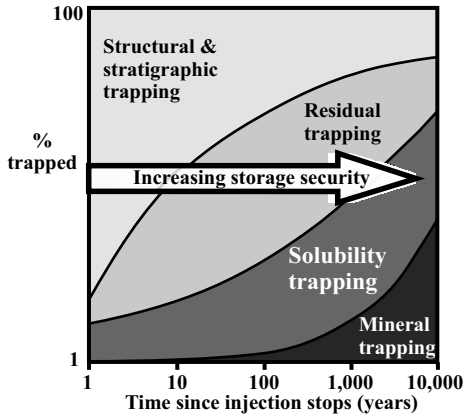

Figure 1. Schematic illustration of the magnitude of trapping mechanisms with time after (IPCC 2005). Note that the rates and ultimate significance of each of these processes, which are additional to structural and stratigraphic trapping, are very poorly constrained.

below a CO_2 cap (e.g., Neufeld et al. 2010). Mineral trapping by precipitation of carbonates will be dependent on the rates at which the CO_2 dissolves in brines and the subsequent flow of the CO_2-charged brines (reactions between supercritical CO_2 and minerals are much less studied). The fluid-mineral reactions may also alter the permeability structure of the reservoir. Dissolution of carbonates and Fe-oxyhydroxides by CO_2-charged brines is rapid with fluid saturation observed to take place in days during injection experiments (e.g., Frio, Salt Creek) and even small changes in porosity may cause large changes in permeability in reservoir rocks. Conversely the more sluggish precipitation of carbonate may reduce permeabilities which might be critical in retarding CO_2 diffusion into caprocks.

Natural CO_2 accumulations allow the operation of these processes to be observed over time periods comparable to those over which the CO_2 needs to be stored. However, recovering useful information from such natural analogues for storage is challenging. Frequently access to samples of rocks or fluids is very limited and even when the CO_2 is exploited—as in the large accumulations in the Colorado Plateau—caprocks and fault zones are generally not cored. Since the rates of most of the geochemical interactions will depend on the flow paths of CO_2 during filling and on the subsequent relative flows of CO_2 and brine in the reservoirs, it is critical to be able to model the hydrology to be able to infer the rates of the processes. Interpretation of many of the geological analogues therefore depends on our ability to infer the nature and rates of past fluid-mineral interactions from the petrology and geochemistry of core samples with limited sampling of the fluid phases. This is a severe test of geologists' ability to infer past processes and particularly the impacts of past fluid-flows from the present record. The continual controversies over the genesis of igneous rocks, fluid flow in metamorphic rocks and chemical weathering reactions in the critical zone attests to the difficulty. However natural CO_2 accumulations are good examples on which to develop a reliable geological toolkit. It is possible to sample recent or even active systems and the economic interest in CO_2 as a resource and in CO_2 storage allows recovery of fluids and drill core from selected natural analogues.

A final caveat is that each potential geological reservoir may exhibit very different geochemical interactions reflecting the differing structure, size, flow paths and particularly lithologies of reservoir and caprock materials. The natural analogues studied also exhibit substantial diversity although it may not be possible to find an analogue for each potential reservoir.

In this chapter we briefly review available natural analogues for CO_2 storage and identify those likely to reward further study. We then review studies of noble gas concentrations and isotopic compositions in natural CO_2 accumulations as these provide compelling evidence for the significance of dissolution of a substantial fraction of CO_2 in formation brines. Finally a

detailed case study of the leaking CO_2 system at Green River Utah is presented as we have worked extensively on this system and it illustrates the richness and variety of the information that can be recovered as well as the complexities and ambiguities in the interpretations.

REVIEW OF NATURAL CO_2 ACCUMULATIONS

Natural accumulations of CO_2 provide important constraints on subsurface fluid flow and the geochemical processes that sequester the gaseous and supercritical CO_2 into fluids and minerals. The important questions that may be answered with observations from natural analogues include the nature, magnitude and rates of geochemical reactions that stabilize the CO_2 in geological reservoirs including: CO_2 dissolution into formation brines; acidity and solute buffering silicate dissolution reactions; and carbonate precipitation. The fluid-fluid and fluid-mineral reactions, and their long-term consequences for reservoirs, caprocks and fault zones can be assessed from petrological observations and from geochemical measurements on reservoir fluids and gases.

Noble gas isotope measurements from reservoir fluids and gases are an important source of information on the fluid-fluid reactions (e.g., Dubacq et al. 2012) and the magnitude of CO_2-dissolution in reservoir brines (e.g., Gilfillan et al. 2009). Spatial and temporal variation in fluid geochemistry preserves information on the rates of the fluid-fluid and fluid-mineral reactions (e.g., Kampman et al. 2009). The rates of the reactions can be constrained where information is available on mineralogy and mineral surface areas, and on groundwater hydrology, or from isotopic constraints on fluid flow rates (e.g., U-series, $^{234}U/^{238}U$; Andrews and Kay 1982). Geochemical, mineralogical and petrophysical profiles through caprocks exposed to CO_2 and CO_2-charged brines can be used to reconstruct the impacts of the CO_2, and when combined with advective-diffusive modeling or isotopic dating, used to constrain the rates of the alteration. Information about the mobilization and immobilization of potentially harmful trace elements (e.g., As, Pb, Cd) may also be gained from studying CO_2-charged fluid geochemistry (e.g., Keating et al. 2010) and from geochemical profiles across fluid-mineral reaction fronts in exhumed CO_2-reservoirs (e.g., Wigely et al. 2013b).

Globally, there are numerous natural accumulations of CO_2 in geological reservoirs, in a variety of geological environments (see reviews in Allis et al. 2001; Haszeldine et al. 2005; Pearce 2004, 2006). However, in most of these, the reservoirs are inadequately sampled, fluid and gas samples maybe unavailable and details of the age and hydrology of the reservoirs are limited. Petrological studies of reservoir rocks from exhumed or cored natural CO_2 reservoirs provide an important basis for examining the long-term mineralogical, geochemical and petrophysical consequences of exposure to CO_2-charged fluids and gases. Many of the early studies of natural CO_2 accumulations focused on hydrocarbon gas reservoirs rich in CO_2, for which core (and fluid samples) were available (e.g., Watson et al. 2004; Wilkinson et al. 2009b). Increasingly, studies have focused on the Colorado Plateau CO_2 province where numerous large accumulations of pure CO_2 (Allis et al. 2001) and exhumed CO_2-reservoirs (Wigley et al. 2012) provide a natural laboratory from which fluid-fluid and fluid-rock interactions in reservoirs, faults and caprocks can be evaluated.

Petrological studies of subsurface CO_2-reservoirs

Reservoir mineralogy and CO_2-fluid-mineral reactions. Petrological studies of natural CO_2 reservoirs reveal a range of degrees of fluid-mineral reaction ranging from minor amounts of silicate (e.g., feldspar), phyllosilicate (e.g., chlorite) and carbonate mineral dissolution to complete dissolution of all reactive silicate mineral phases and the deposition of relatively insoluble Ca-Mg-Fe carbonate minerals, including ankerite, siderite and dolomite (Franks and Forester 1984; Watson et al. 2004; Wilkinson et al. 2009b; Heinemann et al. 2013), and dawsonite (Baker et al. 1995; Moore et al. 2005; Wilkinson et al. 2009b). The petrological

consequences of exposure to CO_2-rich fluids vary between sites as a result of differences in: primary reservoir mineralogy and mineral surface properties; reservoir hydrology; initial formation fluid solute, pH and redox chemistries; CO_2 emplacement mechanism and rates; thermodynamic differences in CO_2 and mineral solubility across the wide range of pressure temperature conditions experienced by natural CO_2 reservoirs; and the slow reaction rates of natural fluids due to transport controlled weathering and the weathering of minerals close to thermodynamic equilibrium. Most studies have observed trapping of CO_2 in carbonate minerals (Watson et al. 2004; Moore et al. 2005); however, the volumes deposited vary between sites and spatially within individual reservoirs due to: heterogeneities in primary reservoir mineralogies; heterogeneous fluid flow and reaction; the coupling of carbonate precipitation to the slow dissolution of silicate minerals close to thermodynamic equilibrium; and transport controls on CO_2 and solute fluxes and mineral reaction rates.

The mineralogy of carbonate cements formed in natural CO_2 reservoirs varies from the relatively soluble pure calcite end-member to more insoluble Fe-Mg-Ca carbonate minerals, including ankerite, siderite and dolomite. The phase stability is governed by the thermodynamic considerations of pressure, temperature and solute chemistry and by the activities of constituent species in the fluid phase (see Radha and Navrotsky 2013, this volume). Calcite cements typically precipitate in reservoir sandstones poor in detrital Fe- and Mn-bearing minerals, or from fluids with high oxygen fugacities. In Fe-rich sediments, such as in red-bed aeolian sandstones, in contact with reducing formation fluids, the high activities of Fe^{2+} and Mn^{2+} in solution can lead to the formation of siderite [$FeCO_3$] and in the presence of Mg^{2+} rich fluids, ankerite [$Ca(Fe,Mg,Mn)(CO_3)_2$] and/or dolomite [$CaMg(CO_3)_2$]. Predicting the stable carbonate phase in CO_2 reservoirs is undermined by the limited experimental data on the kinetic growth, and thermodynamic stability, of the more complex Ca-Mg-Fe carbonate minerals, and such data is critically needed to enable accurate model predictions.

The acid hydrolysis of silicate minerals in natural fluids is largely incongruent being balanced by the precipitation of clay minerals. The low solubilities of Al^{3+} and SiO_2 at the temperatures and pressure conditions relevant to CO_2 storage preclude significant mass transport of these constituents from the site of the dissolving silicate grain. The chemistry and mineralogy of the clay mineral precipitates is highly sensitive to temperature, fluid pH and solute activities. Experimental and model predictions include the growth of illite, illite-smecite and kaolinite minerals (e.g., Credoz et al. 2009; Kohler et al. 2009) and observations from natural accumulations support this (e.g., Moore et al. 2005; Wigley et al. 2012).

The formation of dawsonite [$NaAlCO_3(OH)_2$] is predicted from modeling studies (Hellevang et al. 2005; Xu et al. 2005) but its occurrence in natural CO_2 accumulations is rare (e.g., Moore et al. 2005). The scarcity of natural dawsonite is likely the result of its limited phase stability (Bénézeth et al. 2007) in carbon-rich alkaline fluids, and its subordinate stability to other aluminosilicate minerals (e.g., analcime; Kaszuba et al. 2005).

The contrasting sets of observations gathered from natural CO_2 reservoirs are best illustrated by studies from two CO_2-rich hydrocarbon gas accumulations; the Fizzy accumulation in the southern North Sea and the Ladbroke Grove accumulation in Southern Australia; and from observations from a pure CO_2 accumulation at Springerville–St. Johns Dome, Arizona and a collection of exhumed CO_2-reservoirs in central-eastern Utah. Markedly different degrees of fluid-rock reaction and CO_2 mineralization are observed between these sites, reflecting differences in reaction duration, primary reservoir mineralogy and reservoir hydrology.

Fizzy accumulation, North Sea. Wilkinson et al. (2009a) investigated CO_2-fluid-mineral reactions in aeolian sandstones of the Permian Rotliegend Group from the 2.3 km deep CO_2-rich hydrocarbon gas field of the "Fizzy" accumulation, southern North Sea. Here, hydrocarbon gas contains ~50 mol% CO_2 and the gas occupies ~68% of the pore space, the rest being occupied by brine. The mineralogy was quantified in samples taken from a single core from

both the gas and water legs of the reservoir and compared to core from similar intervals in the nearby, CO_2-poor "Orwell" hydrocarbon gas field. The fields are located >150 km from surface outcrops of the Permian sediments on the surrounding continental margins and can be considered relatively hydrologically inactive. The reservoir rock contains corroded K-feldspar grains and volcanic rock fragments, but no detrital plagioclase or mica is present, limiting the availability of Ca^{2+} and Mg^{2+}. Wilkinson et al. identified small amounts of dolomite and dawsonite (0.4 ± 0.3 vol%) cement that had formed in the 50 Ma since the reservoir was first charged with CO_2. Using sequentially extracted C- and O-isotopic compositions of the dolomite, Heinemann et al. (2013) estimated the amount of secondary dolomite precipitated from the CO_2-charged fluid in that 50 Ma period was up to ~22% of the dolomite present in the reservoir, equating to sequestration of 11% ± 8% of the CO_2 charge as dolomite. The authors concluded that the remaining 70-95% of the CO_2 is present as a free phase, after tens of millions of years, and that mineral trapping is an unimportant process in such reservoirs.

Ladbroke Grove field, Australia. (Watson et al. 2004) describe CO_2-fluid-mineral reactions within the Ladbroke Grove hydrocarbon gas field, Otway Basin, southeastern South Australia. The hydrocarbon gas contains up to 57 mol% CO_2 and significantly elevated HCO_3^- concentrations were observed in fluid samples from the gas leg. The reservoir rock is an early Cretaceous lithic-rich sandstone at a depth of ~3 km, and CO_2 is thought to have migrated into the reservoir between 1 Ma and 4.5 ka ago. No information is available about the reservoir hydrology, but as an onshore reservoir, formation fluid flow rates may be influenced by contemporary groundwater recharge. The impact of the CO_2 on reservoir mineralogy can be evaluated by comparison with samples from the neighbouring Katnook field, which contains low concentrations of CO_2 gas (~1 mol%). In reservoir samples from Ladbroke Grove the CO_2 charged fluids dissolved albite, volcanic rock fragments, chlorite and calcite resulting in an approximate doubling of porosity (from 7.5 to 16 vol%) and permeability (from 28 to 52 mD) relative to reservoir samples from the CO_2-poor Katnook field. The CO_2-charged fluids dissolved primary minerals, producing alkalinity and secondary precipitates via the reactions;

$$2NaAlSi_3O_8 + 3H_2O + 2CO_2 \rightarrow Al_2Si_2O_5(OH)_4 + 4SiO_2 + 2Na^+ + 2HCO_3^- \quad (1)$$

$$[Fe,Mg]_5Al_2Si_3O_{10}(OH)_8 + 5CaCO_3 + 5CO_2 \rightarrow \quad (2)$$
$$5Ca[Fe,Mg](CO_3)_2 + Al_2Si_2O_5(OH)_4 + SiO_2 + 2H_2O$$

Products of the reaction included quartz, kaolinite, siderite and ferroan dolomite, with the ferroan carbonates occupying up to ~15 vol% of the reservoir samples and carbonate precipitation is most abundant close to the gas-water contact. The source of Ca^{2+} and Fe^{2+} for ferroan carbonate precipitation was the dissolution of poikiolitic calcite cement and chlorite. It is notable that the ingress of CO_2 was relatively recent (about 5 ka to 1 Ma), meaning that significant reaction has occurred over relatively short timescales, and is in contrast to the observations of Wilkinson et al. (2009b) for samples from the Fizzy field. Thus, in the presence of a reactive reservoir mineralogy and under active hydrological conditions, significant reaction can occur in just a few thousands of years and can trap CO_2 in a dissolved form and as secondary carbonate phases.

Springerville–St. Johns Dome, USA. Moore et al. (2005) describe CO_2-fluid-mineral reactions within the Springerville–St. Johns Dome CO_2 field in eastern Arizona and western New Mexico, USA. The site is part of the wider Colorado Plateau CO_2 province discussed in detail below (Fig. 2). At Springerville–St. Johns Dome >90% CO_2 gas is trapped at depths <800 m in fine grained sandstone, siltstone and limestone members of the Permian Supai Formation, and the reservoir was filled through normal faults in the local granitic basement.

The site is notable for having extensive surface travertine deposits >33 km^2 that record episodic CO_2-leakage from the reservoir through local normal faults, with volumetric CO_2-

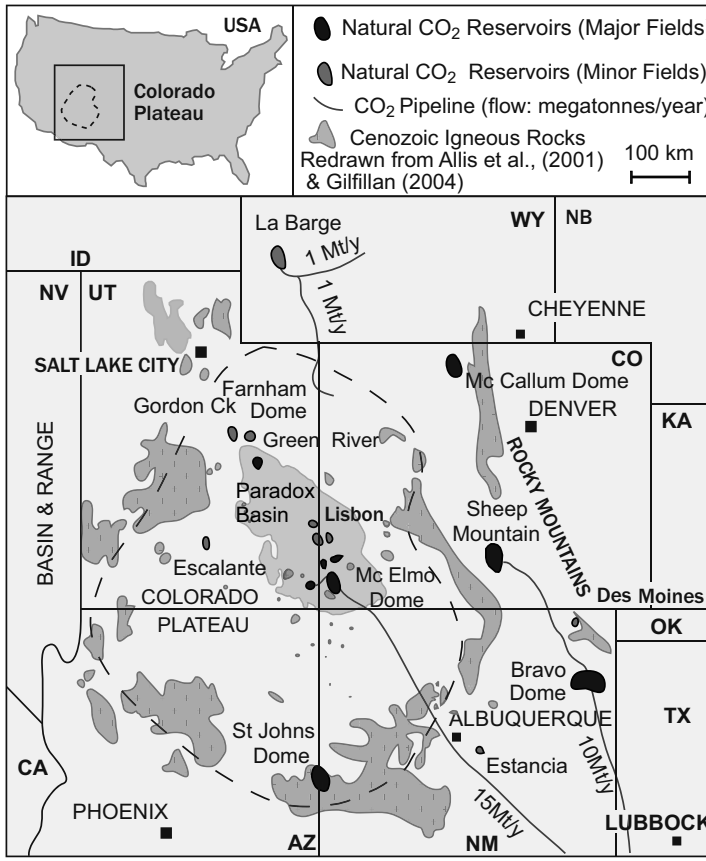

Figure 2. The Colorado Plateau CO_2 Province, is an extensive uplifted region covering portions of Utah, Colorado, Arizona and New Mexico, that contains abundant natural accumulations of CO_2. Some CO_2 fields, notably Bravo Dome (NM), McElmo and Sheep Mountain (CO), Farnham Dome (UT), Springerville (AZ), and Big Piney-LaBarge (WY) have been exploited for commercial purposes, mainly for enhanced oil recovery and dry ice production. The source of the CO_2 is considered to be dominantly volcanogenic, juvenile CO_2 generated from Cenozoic magmatic activity and mantle degassing (Gilfillan et al. 2008; 2009). The gas reservoirs, usually sandstone or dolomite, lie in four way dip closed or anticlinal structures with mudstone or anhydrite top seals. Fault seals are common along the margins of the reservoirs (Allis et al. 2001; Shipton et al. 2004). The gases from the fields can be > 98% CO_2 with trace quantities of N_2 (4%), He (0.1-1%), Ar, and CH_4. Redrawn after Allis et al. (2001).

leakage rates in the geological past that were significantly larger than leakage rates in the present day (Embid and Crossey 2009). U-Th ages of the travertines constrain the time of reservoir filling with CO_2 to prior to 350 ka, from local volcanic activity that ceased at ~308 ka (Embid and Crossey 2009). Successive pulses of CO_2-leakge at 350-300, 280-200, and 100-36 ka are thought to be related to groundwater flushing of the reservoir (Embid and Crossey 2009) and climate driven changes in fault hydraulic properties (see Kampman et al. 2012), highlighting the hydrologically active nature of the CO_2 reservoir.

Moore et al. (2005) describe core samples from the CO_2-bearing siltstone and fine sandstone intervals, which are characterized by the dissolution of authigenic calcite cements (1-2 wt%) and detrital plagioclase (6-13 wt%) and K-feldspar (6-13 wt%) grains and by the forma-

tion of dawsonite and kaolinite in intervals flushed by CO_2-charged fluids. Flushing of these units by low pH CO_2-charged fluids is thought to have dissolved feldspar grains and produced successive generations of dawsonite (5–17 wt%) and kaolinite (2-6 wt%) growth, as the phase stability varied with changing pCO_2 and HCO_3^- concentrations, via the reaction

$$NaAlSi_3O_8 + H_2O + CO_2 \rightarrow NaAlCO_3(OH)_2 + 3SiO_2 \quad (3)$$

Dolomite is a relatively abundant phase (10 to 15 wt%) in the altered reservoir rock, fault conduits in the granitic basement are extensively dolomitized, and the modern CO_2-charged formation fluids are supersaturated with respect to dolomite. However the extent to which dolomite growth is related to the CO_2-charged fluids has not been evaluated directly.

The reservoir lithologies and their petrophysical properties are highly heterogeneous and this is reflected in heterogeneous CO_2-related fluid-rock reaction that likely reflects extensive variability in CO_2 and groundwater flow. This site provides an intermediate case between those of the Fizzy and Ladbroke Grove accumulations. It highlights the important role that geological heterogeneity and fluid flow can have on controlling the fluid-rock reactions and CO_2 mineralization.

Implications for fluid-fluid and fluid-mineral reactions. These studies highlight important questions about the mechanisms that control CO_2 dissolution and carbonate precipitation in natural CO_2 reservoirs. In stagnant gas reservoirs such as the Fizzy field the fluid-mineral reactions may be strongly limited by the transfer of CO_2 from the gas to the fluid phase. What physical processes control the flux of CO_2 entering the reservoir fluid from the gas cap and what are the hydrological processes important for determining the volume of mineral contacted by the CO_2-charged brine? Below the gas cap, a boundary layer will develop whose thickness is controlled by diffusive CO_2 transport in the fluid phase and convective mixing of dense CO_2-saturated fluid with the original brine (e.g., Neufeld et al. 2010). In layered geological reservoirs with high vertical porosity/permeability contrasts, lateral groundwater flow may limit downward propagation of the CO_2 saturated front. This will depend on the ratio of the sinking rate of the CO_2-saturated brines to lateral advection of the groundwaters. Replenishment of the reservoir by recharge with meteoric groundwater may sustain convective circulation of the CO_2 saturated brines beneath the gas cap, or the convective processes may shut down in these old CO_2 reservoirs. Model predictions of these processes are entirely untested. For the Fizzy accumulation little information is available on the 3D hydrology of the reservoir, making the significance of such processes difficult to assess.

In such systems, pure CO_2 (or brine saturated in CO_2) will precipitate carbonate minerals while reacting with silicates until either the silicate minerals are exhausted, or until the activity of CO_2 in the aqueous phase is reduced such that the brine, silicate minerals, and carbonate minerals are all in equilibrium. Given the 50 Ma history of the Fizzy field it is likely that equilibrium, or some close to equilibrium (pseudo) steady state, has been attained. Did the reactions in the "Fizzy" field terminate because suitable silicate minerals were exhausted, or because a reduction in CO_2 activity brought the silicates and dolomite close to equilibrium? Insufficient information is available on the compositions of the silicate minerals in this system and the thermodynamics of fluid-mineral equilibria to properly answer these questions. In these static reservoirs the reactions are likely limited by the availability of reactants, whereas in hydrologically active CO_2 accumulations, and during the buoyant flow of supercritical CO_2 in storage sites, the CO_2-charged fluids are exposed to a large surface area of reacting minerals as they migrate through the reservoir. Observations from such flowing CO_2 accumulations provide the most constraints on fluid-mineral reactions and reaction rates, where fluids and gases can be sampled along flow paths and the rates of fluid transport can be constrained from hydrological models or isotopic constraints. A number of such systems are available for study in the Colorado Plateau and southern Rocky Mountains region of the southwestern USA.

These include the Springerville–St. Johns Dome accumulation in Arizona which is discussed above, and two other important sites; a collection of CO_2 accumulations in the region of the San Rafael Swell, east-central Utah, including the leaking CO_2 accumulation at Green River and the commercially produced Bravo Dome accumulation, north-eastern New Mexico.

The Colorado Plateau and southern Rocky Mountains CO_2 province

In the Colorado Plateau and southern Rocky Mountains region, USA CO_2 produced by Cenozoic magmatic activity has been stored securely in a variety of geological reservoirs for thousands to many millions of years (Fig. 2; Allis et al. 2001; Gilfillan et al. 2008). CO_2 from several of these reservoirs is exploited for use in enhanced oil recovery (Allis et al. 2001) and therefore samples of CO_2 gas and some core are available. Analyzes of surface travertine deposits (Embid and Crossey 2009; Kampman et al. 2012; Burnside et al. 2013) and the noble gas isotopic composition of the CO_2 gas have put important constraints on the age of the accumulations (Ballentine et al. 2001) and CO_2 mobility (Gilfillan et al. 2011) and CO_2-fluid interactions (Gilfillan et al. 2008; Gilfillan et al. 2009; Dubacq et al. 2012; Zhou et al. 2012). However samples of the reservoir, caprocks and waters are not generally available, the exception being the active leaking system at Green River, Utah, where natural CO_2-driven cold water geysers allow sampling at surface (e.g., Kampman et al. 2009) and a 2012 scientific drilling campaign has sampled core and fluids from the active reservoir.

Exhumed CO_2-reservoirs of the Colorado Plateau, USA. Exhumed ancient CO_2 reservoirs provide the best means of mapping large-scale patterns of fluid flow and fluid-rock reaction, where the passage of the CO_2-charged fluids is preserved as mineralogical and geochemical changes in the rock. The Jurassic red-bed Entrada and Navajo sandstones of Utah, south western USA, are bleached over large scales (tens of meters to tens of kilometers) by the passage of volatile rich diagenetic fluids which have dissolved Fe-oxides from the sediment bleaching them from red to white. These exposures allow mapping of the fluid flow pathways, and the assessment of lithologic versus hydrodynamic controls on fluid flow. Where mineralogical and geochemical measurements can be made as profiles across reactions fronts between the bleached and unbleached sediment the mechanisms controlling the fluid-mineral reactions and the propagation of the fronts, and the relative importance of fluid transport versus mineral surface reaction controlled mineral dissolution, can be assessed (Wigley et al. 2013a). The Entrada and Navajo Sandstones, and their regional equivalents, are high porosity/permeability sandstone formations which cover large portions of the Colorado Plateau and they have been identified as important potential target CO_2 storage reservoirs (e.g., Parry et al. 2007).

Iron oxide dissolution during CO_2-injection experiments. The dissolution of Fe^{3+}-bearing oxide and oxy-hydroxide minerals is increasingly appreciated as an important geochemical buffer during the injection of CO_2 into sandstone reservoirs (e.g., Kharaka et al. 2006a; Trautz et al. 2012; Rillard et al. 2013). Elevated concentrations of Fe^{2+} have been observed in fluid samples from the Frio-I (Kharaka et al. 2006a,b) and Frio-II (Daley et al. 2007a,b) CO_2 injection experiments and in numerous CO_2-EOR projects (e.g., Shevalier et al. 2009), within days of the break-through of CO_2 and CO_2-charged fluids at observation wells (see review by Kampman et al. 2013a). Dissolution of Fe-bearing minerals and the corresponding changes in the Fe^{2+} content of the fluid account for much of the early pH buffering and generation of alkalinity in these fluids (Kampman et al. 2013a). The source of much of this Fe^{2+} is thought to be the acid-reductive dissolution of diagenetic Fe-oxyhydroxide grain coatings and disseminated cements (Kharaka et al. 2006a), where mineral dissolution and reduction of insoluble Fe^{3+} to soluble Fe^{2+} is driven by acidity generated from dissolved CO_2 and fluid redox chemistry controlled by reduced species (e.g., CH_4, H_2S) already present in the formation fluids, following a reaction stoichiometry such as

$$4Fe_2O_3 + 15CO_2 + 6H_2O + CH_4 \rightarrow 8Fe^{2+} + 16HCO_3^- \quad (4)$$

Exhumed natural CO_2 reservoirs in red-bed sandstones represent excellent analogues to this process, where the migration of the fluids can be mapped over meter to kilometer scales by mineralogical changes preserved in the rock.

Red-bed sandstone bleaching, Utah. Much of the sandstone bleaching in the Jurassic sediments of Utah and in the wider Colorado Plateau region is localized to the crests of anticlines and this is attributed to the passage of buoyant hydrocarbon and CH_4-rich fluids, which reduce Fe^{3+} present as Fe-oxide grain coatings to soluble Fe^{2+} and dissolves it from the rock (Beitler et al. 2003, 2005). Recently, bleaching in portions of the Jurassic Entrada and Navajo Sandstone in and around the San Rafael Swell, central eastern Utah, has been attributed to reactions driven by CO_2-rich brines, containing quantities of dissolved CH_4 (Loope et al. 2010; Kettler et al. 2011; Wigley et al. 2012, 2013a,b; Potter-McIntyre et al. 2013).

San Rafael Swell CO_2 Province. The San Rafael Swell is comprised of an uplifted region formed by movement on a Laramide age basement fault, above which a ~75 km long monocline of Cambrian to Jurassic sediments was developed (Fig. 3). The Jurassic through to Permian sediments are exposed in the swell. The swell is bounded to the east by a leaking

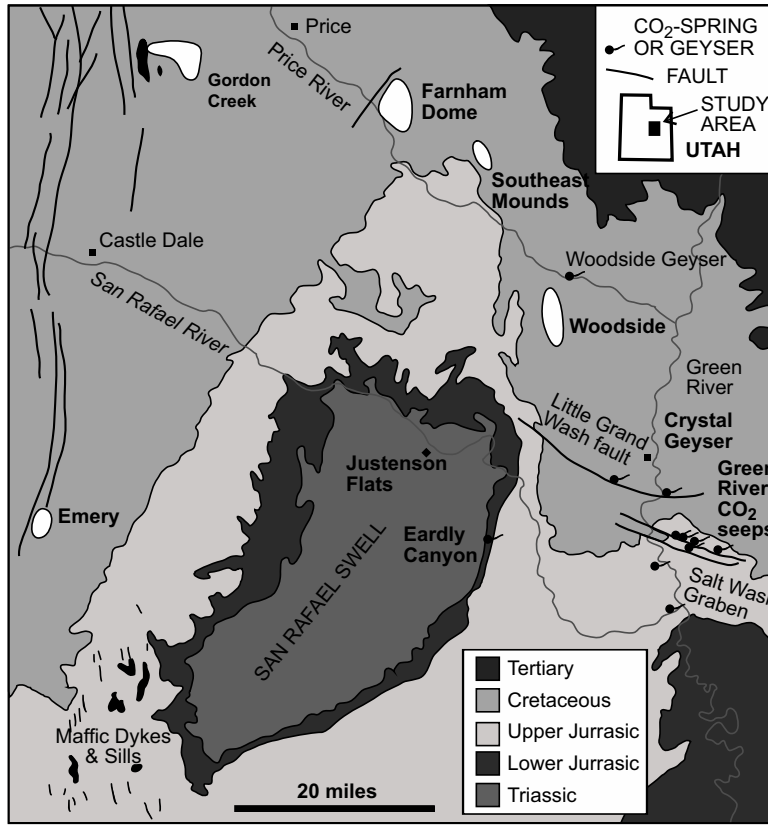

Figure 3. The San Rafael Swell CO_2 province showing the location of the major CO_2 fields and the CO_2 degassing springs and seeps.

CO_2 accumulation at Green River and on all sides by numerous large secure CO_2-reservoirs including the Gordon Creek (Morgan and Chidsey 1991), Farnham Dome (Peterson 1954; Morgan 2007), Woodside (Osmond 1956), Emery (Campbell 1978) and Escalante (Allison et al. 1997) accumulations (Fig. 2). The majority of the reservoirs are located in the Jurassic Entrada and Navajo Sandstones, the Permian White Rim Sandstone and the overlying Kaibab and Moenkopi Formations, and in carbonate strata of the Pennsylvanian and Mississippian (Campbell 1978; Morgan and Chidsey 1991). The high ^3He and N_2 content of these gases has lead several authors to attribute their origin to mantle derived fluids, with inputs of radiogenic crustal-derived gases from the granitic basement rocks. Laterally extensive zones of bleaching are found in the Jurassic Navajo and Entrada sandstones exposed in the swell and along exhumed normal faults bordering the swell at sites like Green River. The region is also notable for its rich uranium reserves, predominantly hosted in Triassic strata of the Chinle Formation, and several authors have hypothesized that CO_2 played a role in their emplacement (Garrels and Richter 1955; Gruner 1956; Morrison and Parry 1988).

Entrada and Navajo Sandstone Bleaching: source fluids, petrology and large-scale fluid flow. Determining the composition of the fluid(s) responsible for these bleaching reactions in these now exhumed reservoirs is only possible by indirect means. The composition of the fluids can be inferred from the mineralogy and isotopic composition of the reaction products or from fluids trapped in these diagenetic minerals.

Beitler et al. (2005) discuss the reaction products and textures found in bleached Navajo Sandstone attributed to buoyant hydrocarbon and CH_4-rich fluids at sites across Utah. The alteration includes; patchy zones of quartz and calcite cement, dissolution of K-feldspar grains to generate grain coating illite and kaolinite, and high secondary porosity. The alteration is typically contained to structural highs and this is interpreted to reflect the passage of buoyant fluids, where the CH_4 content of the brines is sufficient to lower their density through hydrogen bond interactions. The carbonate cements typically contain isotopically light carbon ($\delta^{13}C_{calcite}$ of −3 to −15‰) and this is interpreted to reflect precipitation from fluids containing dissolved organically derived carbon (Beitler et al. 2005; Wigley et al. 2012).

Wigley et al. (2012, 2013a) discuss the reaction products and textures found in bleached Entrada Sandstone associated with CO_2-rich, CH_4-bearing brines at Salt Wash Graben, Utah. The alteration includes; zones of ferroan dolomite and quartz cementation, especially localized to bleached faults and at reaction fronts, and dissolution of K-feldspar grains to generate grain-coating and pore-filling kaolinite and illite, with an overall reduction in porosity. The alteration is typically localized towards the base of the sandstone formations and this is interpreted to reflect the passage of dense CO_2-rich brines. The carbonate cements typically have relatively heavy C-isotope composition ($\delta^{13}C_{dolomite}$ 0 to −3‰) and this is interpreted to reflect precipitation from fluids containing dissolved carbon derived from mantle or crustal derived CO_2.

Wigley et al. (2012) used Raman spectroscopic measurements of vapor bubbles in two-phase water-gas fluid inclusions in diagenetic quartz and gypsum in bleached portions of the Entrada Sandstone at Green River to estimate the volatile composition of the bleaching fluid. Determining vapor bubble compositions in low temperature diagenetic fluid inclusions using Raman spectroscopy is complicated by mineral turbidity, the small size of the fluid inclusions and trapped vapor bubble, Brownian motion of the bubble and proximity to the fluid-gas homogenization temperatures. Wigley et al. (2012) examined >120 fluid inclusions in quartz overgrowths and gypsum veins petrographically linked to the bleaching. The authors determined vapor bubble compositions in eight fluid inclusions; five bubbles contained pure $CO_{2(g)}$ and three contained CO_2-CH_4 mixtures, up to 28 vol% $CH_{4(g)}$. The authors used microthermometry measurements of the ice melting temperatures in these inclusions to show that the trapped fluid was relatively saline (2.5-7.0 wt% NaCl equivalent), being enriched in brines derived from evaporites in the Paradox Formation, deeper in the basin. This is in contrast to

the largely ^{18}O-depleted meteoric fluids associated with hydrocarbon bleaching elsewhere, and this is reflected in the heavy O-isotopic composition of the carbonate cements at Green River.

Potter-McIntyre et al. (2013) examined similar zones of carbonate and Fe-oxide mineralization in an interval of the Navajo Sandstone exhumed in the Justensen Flats of the northern San Rafael Swell, ~40 km to the west of Green River. The authors investigated a 45 m by 5 m, laterally extensive "tongue" of bleached cross-bedded sandstone with an interior relatively depleted in Fe-oxyhydroxide, surrounded by a yellow-brown reaction front of carbonate and Fe-oxide cementation. The alteration and morphology of the bleaching is similar to that described by Wigely et al. (2012, 2013a). The authors attributed the dissolution of grain coating Fe-oxyhydroxide to the passage of CH_4-bearing CO_2-charged fluids. The bleaching was accompanied by K-feldspar dissolution and illite and kaolinite precipitation and the extensive precipitation of Fe-dolomite/ankerite and Fe-oxides at the surrounding reaction front.

Similarly, Loope et al. (2010) examined bleaching and Fe-precipitation within the Navajo Sandstone near the southeast flank of the Escalante anticline, southern Utah, ~50 km south of the San Rafael Swell. The Escalante anticline holds an estimated 1.5 to 4 trillion cubic feet of gas (93%-99% CO_2, 1%-6% N_2, 0.4%-0.7% CH_4; Allison et al. 1997) within a 600-m-thick sequence of Permian strata, including the White Rim Sandstone and Kaibab Limestone, although CO_2 gas shows were also observed in transmissive units in Triassic and Jurassic sediments in the overburden (Campbell 1978). To the southeast of the anticline, over a region extending some ~50 km, the Navajo Sandstone is bleached and Fe-mobilized during the bleaching is redeposited down-dip as pipe-like and spheroidal Fe-concretions and as Fe-rich calcite. Loope et al. (2010) attributed this alteration to the flow of meteoric fluids from recharge zones on the Aquarius Plateau that subsequently dissolved CO_2 and CH_4 in the anticline, becoming dense, and bleached the Navajo Sandstone during their down-dip passage to discharge in the Colorado River. This alteration had previously been attributed to the passage of buoyant CH_4-rich fluids (Beitler et al. 2003, 2005; Chan et al. 2011) and the concretions have been proposed as a potential analogue to hematite concretions (Martian "blueberries") imaged by the Mars rover *Opportunity* (Chan et al. 2004). The concretions have thick, iron oxide–cemented rinds and lightly cemented, iron-poor sandstone cores (Loope et al. 2010). Loope et al. (2010) attribute the formation of both the spheroidal and the pipe-like Fe-concretions to microbially mediated oxidation of precursor siderite-cemented concretions formed during CO_2-CH_4 bleaching of the sediment by flushing of the reservoir with oxygenated meteoric waters during exhumation. Loope et al. (2010) mapped asymmetric spheroidal concretion "comet tails" and groups of near horizontal, sub-parallel pipes and used their orientation to infer the flow direction of the CO_2-charged groundwater, to the southeast. This alteration is similar to those documented at Green River and the San Rafael Swell described above, but the mineralization of the CO_2 here is predominantly thought to be as siderite, as opposed to ferroan dolomite described in the sites above. These differences probably reflect differences in fluid geochemistry and a_{Mg+}, with some sites containing fluids dominated by Mg-rich basinal brines, and others dominated by dilute meteorically derived fluids.

Parry (2011) used modeling to constrain the rates of formation of such concretions to ~2800-3800 $cm^{-1}year^{-1}$, depending on the relative rates of diffusive versus advective-diffusive solute transport. Such deposits provide invaluable evidence on the patterns of large-scale fluid flow, although the origin of the Fe-precipitates is still highly debated (Chan et al. 2011; Kettler et al. 2011). Such studies illustrate the wealth of information available from exhumed reservoirs, but also the inherent complexities in interpreting exhumed systems where the composition of the altering fluids must be inferred by indirect means and were the mineralogy and geochemistry of the reservoir is altered by diagnetic and weathering reactions. This highlights the importance of collection core and subsurface fluid samples from active CO_2 reservoirs, such as those at Green River, where the mineralogy is preserved and measurements

on fluid geochemistry can be used to constrain and interpret the driving geochemical reactions. The discussion below covers recent scientific drilling at the Green River site and how measurements from reservoir rocks and caprocks, and fluid geochemistry, are being used to constrain the fluid-mineral reactions and fluid transport, to decipher their rates and controlling mechanisms.

NOBLE GAS STUDIES OF THE COLORADO PLATEAU AND SOUTHERN ROCKY MOUNTAINS CO_2 PROVINCE

Noble gases and natural CO_2 reservoirs

The five noble gases helium (He), neon (Ne), argon (Ar), krypton (Kr), and xenon (Xe) collectively have twenty-two stable or long half-life isotopes between them. They are chemically inert and due to their volatile nature they have a strong tendency to partition into gas or fluid phases and can be used as tracers for the origin and the transport of fluids. The wider application of noble gases to problems in geological CO_2 storage is reviewed in Holland and Gilfillan (2013).

CO_2 can be produced naturally within the crust from a number of sources including the thermal breakdown of marine carbonates, the diagenetic breakdown of carbonate cements, methanogenesis, microbial hydrocarbon degradation or hydrocarbon oxidation. CO_2 can also be introduced to the crust from the mantle via the degassing of magma bodies or as a mobile supercritical volatile-rich fluid. Microbial activity and alteration of hydrocarbons typically produce gas accumulations that are rich in both CO_2 and hydrocarbon gases such as CH_4. Only the thermal decomposition of carbonate rocks and mantle volatile degassing can produce nearly pure CO_2 accumulations. Distinguishing between these sources is an important aspect of interpreting the origin, age and evolution of natural CO_2 reservoirs.

Noble gas concentrations and isotope ratios in the natural CO_2 reservoirs of the Colorado Plateau and the southern Rocky Mountains have been studied extensively to determine CO_2 and groundwater sources and to constrain the noble gas geochemistry of the mantle CO_2 source. Both element (e.g., $CO_2/^3He$) and isotope ratios (e.g., $^3He/^4He$) have been used to determine the origins of the natural CO_2 and to infer its emplacement mechanism, and to constrain fluid-fluid and fluid-rock interactions that subsequently modify the CO_2 and noble gas budget of the accumulations.

Noble gas solubility's and Henry's Law

Physical processes such as gas dissolution and exsolution can modify the ratio of CO_2 and noble gases in both the gas and water phases. This is because of the large difference in solubility between relatively soluble gases like CO_2 and the highly insoluble noble gases, and the relatively large variation in solubility between the individual noble gases. The solubility contrast is such that upon degassing CO_2-charged fluids quantitatively degas their dissolved light noble gas load, as the noble gases are far more soluble in the contacting gas phase. Conversely, during dissolution of CO_2 from a free gas cap the light noble gases (e.g., He) behave conservatively, being retained in the gas phase as CO_2 is lost to solution. In order to interpret measurements of gas and water CO_2 and noble gas ratios we must first be able to constrain the theoretical solubilities of the dissolved species in each of the respective phases.

The solubility of any gas in solution (e.g., CO_2, He) can be described by Henry's Law:

$$p_i = K_i x_i \tag{5}$$

where p_i is the partial pressure of gas i in equilibrium with a fluid containing x_i mole fraction of i in solution and K_i is the Henry's constant for the species. Henry's coefficients vary with

temperature and water salinity. Limited experimental data is available on the solubility of a pure noble gas phase in water (see review in Ballentine et al. 2002) and there is currently no published experimental data available on noble gas solubilities in gaseous or supercritical CO_2. Such data is critically needed to facilitate the application of noble gases to the study and interrogation of fluid-fluid interactions in CO_2-injection sites and natural CO_2 reservoirs. The limited experimental data sets for pure noble gas solubilities in water provide a first order prediction of noble gas partitioning between geological fluids and gas but the application of noble gas solubilities in water to modeling their partition into supercritical CO_2 is untested. Groundwaters and reservoir brines are moderate to high salinity fluids of variable ionic strength, which span a range of pressures and temperatures in geologic systems. Solubilities deviate from linearity (Eqn. 5) at higher pressures and in concentrated solutions due to intermolecular interactions and may be described by a modified form of Henry's Law that accounts for non- ideality in the liquid and gas phase. The modified equation becomes:

$$\Phi_i p_i = \gamma_i K_i x_i \tag{6}$$

where Φ_i is the gas phase fugacity coefficient and γ_i is the liquid phase activity coefficient. From the virial theorem of statistical mechanics the relation between real molar volume and pressure can be defined as

$$PV_m = \mathrm{R}T\left(1 + \frac{B(T)}{V_m} + \frac{C(T)}{V_m^2} + \frac{D(T)}{V_m^3} + \ldots\right) \tag{7}$$

where P is pressure, T is the temperature, R is the ideal gas constant and V_m the molar volume. B, C and D are first, second and third order empirical virial constants determined for each gas. Most systems can be described by the truncated second order form, with the third order expression required only to describe behavior at high pressures. The truncated gas phase fugacity coefficient can be derived as

$$\ln \phi_i(P,T) = \frac{B(T)}{V_m} + \frac{C(T) + B(T)^2}{2V_m^2} \tag{8}$$

where the virial coefficients can be estimated from P-V-T data and the fugacity coefficients calculated. Non-ideality in the liquid phase is difficult to determine using equations of state because of the complexity of solute/solute and solvent/solute interactions (see for example Dubacq et al. 2013). γ is considered to be independent of pressure and deviation from ideality caused by temperature and electrolyte concentration is assessed from empirically derived data. For charged species in geological fluids this is typically done using chemical speciation codes that calculate activity coefficients in complex aqueous solutions using the law of mass action and experimentally determined equilibrium constants for the speciation reactions (e.g., PHREEQC; Parkhurst and Appelo 1999). Such codes are limited in their ability to model non-ideality in high ionic strength solutions, which is an important issue for geological storage which involves CO_2-fluid interactions in high ionic strength brines. The activity coefficient (γ) of a neutral species, such as a dissolved noble gas, can be assumed to depend linearly on ionic strength such that;

$$\log \gamma_i = k_m I \tag{9}$$

where k_m is a Setschenow coefficient and I is the ionic strength of the solution (mol^{-1}). Setschenow coefficients for the noble gases have been determined empirically (Smith and Kennedy 1983). The solubility of the noble gases decreases with increasing salinity, but this salting out effect decreases with increasing temperature.

The solubilities of the noble gases decrease with increasing temperature, until a minimum solubility is reached, with the gases becoming more soluble at higher temperatures. This

solubility minimum occurs at higher temperatures for individual noble gases as a function of increasing mass, ranging from ~35 °C for He to ~115 °C for Xe. The absolute solubility of individual noble gases also varies as a function of increasing mass, with Xe being ~10× as soluble as He at 25 °C. CO_2 is ~90× more soluble than He at 25 °C and ~8× as soluble as Xe. This wide variation in solubility between the noble gases, and between the noble gases and CO_2 makes solubility fractionation between geological fluids and gas an important indicator of physical processes.

Solubility fractionation of gas compositions

Progressive degassing of a liquid containing dissolved gases will lead to fractionation of the elemental gas ratios in the residual dissolved gas and the in the contacting gas phase due to solubility fractionation effects. As the degassing proceeds the least soluble gases will tend to be enriched in the gas phase (c.f. Holland and Gilfillan 2013). The equilibrium molar concentration of the i^{th} gas in the gas phase ($[i]_g$) is dependent on the gas/liquid volume ratio (V_l/V_g) and the initial molar concentration of gas in the liquid phase ($[i]_{total}$) related by:

$$[\mathrm{i}]_g = \frac{[\mathrm{i}]_{total}}{\frac{V_l}{V_g K_d^i} + 1} \tag{10}$$

such that as $V_l/V_g \rightarrow 0$, $[i]_g \rightarrow [i]_{total}$. For non-ideal gases and Henry's constant in units of molality, Equation (10) becomes;

$$[i]_g = [i]_{total} \frac{22.4 T \rho_l V_l}{273 \frac{\gamma_i}{\phi_i} K_d^i V_g} \tag{11}$$

where ρ_l is the density of the liquid (g cm^{-3}), T is temperature (K), $V_{g,l}$ is the gas or liquid volume (cm^3) and K_d^i is the Henry's constant (kg atm mol^{-1}). If the initial noble gas concentration in the liquid phase is known Equations (10) or (11) can be used to determine the volume of gas with which a liquid has equilibrated, by using only one noble gas concentration in the liquid phase (e.g., Zhou et al. 2005). In practice it is often difficult to assess the initial noble gas concentration in the liquid phase, and the relative fractionation between two different noble gases can be employed to determine the extent of the fractionation, such that;

$$\left[\frac{i}{j}\right]_g = \left[\frac{i}{j}\right]_0 \frac{\left(\frac{V_g}{V_l} + \frac{1}{K_j}\right)}{\left(\frac{V_g}{V_l} + \frac{1}{K_i}\right)} \tag{12}$$

where $[i/j]_0$ is the initial ratio of two noble gases i and j in the groundwater and $[i/j]_g$ is the ratio in the gas phase. For small degrees of degassing the partitioning of the noble gases tends towards the equilibrium fractionation coefficient (α) for the system, which is determined by the Henrys' constants ($K^l_{(i,j)}$), liquid ($\gamma_{i,j}$) and gas ($\phi_{i,j}$) phase activity coefficients for the i^{th} and j^{th} noble gas such that:

$$\frac{V_g}{V_l} \rightarrow 0 \qquad \frac{[i/j]_g}{[i/j]_0} \rightarrow \frac{\frac{\gamma_i}{\phi_i} K_i^l}{\frac{\gamma_j}{\phi_j} K_j^l} = \alpha \tag{13}$$

Progressive degassing of a fluid can lead to preferential striping of the insoluble noble gases from the liquid phase and their enrichment in the gas phase. Such degassing can be

modeled as a Rayleigh type process and the ratio of noble gases $[i/j]_1$ in the depleted reservoir in the groundwater evolves as:

$$\left[\frac{i}{j}\right]_1 = \left[\frac{i}{j}\right]_0 f^{(\alpha-1)} \tag{14}$$

The analogous Rayleigh equation for fractionation of the noble gas ratios during gas dissolution is thus:

$$\left[\frac{i}{j}\right]_1 = \left[\frac{i}{j}\right]_0 f^{\left(\frac{1}{\alpha}-1\right)} \tag{15}$$

Such Rayleigh fractionation during gas dissolution can lead to extreme noble gas ratios during the long-term redissolution of noble gases into groundwaters and this is discussed in detail below.

Terrestrial noble gas reservoirs and sources

The noble gases distributed through the atmosphere, crust and mantle reservoirs on the Earth are derived from two principle sources: those originating during planetary accretion which are commonly known as 'primordial' noble gases (e.g., ^{3}He) and radiogenic noble gases generated by terrestrial radioactive decay processes (e.g., ^{4}He). The production of noble gases by radiogenic and nucleogenic processes in the crust is reviewed in Ballentine and Burnard (2002) and Ballentine et al. (2002) and only a brief discussion of the relevant decay series is included here. The radiogenic noble gases are produced primarily by radioactive decay (^{4}He, ^{40}Ar, ^{86}Kr, ^{131}Xe, ^{132}Xe, ^{134}Xe, ^{136}Xe) and nucleogenic reactions (^{21}Ne, ^{21}Ne, ^{22}Ne, ^{3}He), although minor amounts are also generated in the atmosphere by cosmic ray spallation. The noble primordial gases and noble gases produced within the crust by radiogenic and nucleogenic processes are the most relevant to the study of subsurface systems, with the isotopes of He, Ne, Ar and Kr being the most studied and providing the most constraint on CO_2 behavior in natural reservoirs (Fig. 4).

Atmospheric reservoir. The Earth's atmosphere represents a relatively concentrated reservoir of noble gases. Because of their high volatility much of the primordial noble gas content of the mantle was out-gassed early in Earth's history (Farley and Neroda 1998), with much of the He being subsequently lost to space (Axford 1968). Surface waters derive their noble gas load from equilibration with the concentrated noble gas reservoir in the atmosphere (predominantly Ar and Ne with trace He, Kr and Xe). The absolute concentrations are controlled by the relative gas solubilities and the temperature and pressure of equilibration, and the isotope ratios are derived directly from the atmospheric ratios, with the exception of He-isotopes which are fractionated during dissolution (Benson and Krause 1980). For meteoric or surface derived groundwaters the fluid noble gas elemental and isotopic composition is expected to reflect air saturated water (ASW) (Ozima and Podosek 2002). This initial composition can be subsequently modified by the addition of 'excess air' trapped in soil and shallow sediments, additions of radiogenic and nucleogenic crustal noble gases and variable degrees of heavy noble gas enrichment due to addition of air trapped and adsorbed in/on old sediments (e.g., Torgersen and Kennedy 1999). This is most notable for Xe which is depleted in air by more than an order of magnitude relative to concentrations expected for planetary out-gassing, due to hydrodynamic loss (Porcelli et al. 2001) and sediment stripping of the atmosphere (Podosek et al. 1980).

Ar represents ~1% of the atmosphere, which is dominated by radiogenic ^{40}Ar and comprises almost the entire inventory of ^{36}Ar (Lee et al. 2006). The ^{40}Ar/^{36}Ar ratio of the atmosphere has evolved from the original solar ratio of $<10^{-3}$ to the present ratio of 295.5 by radiogenic production of ^{40}Ar (Sarda et al. 1985).

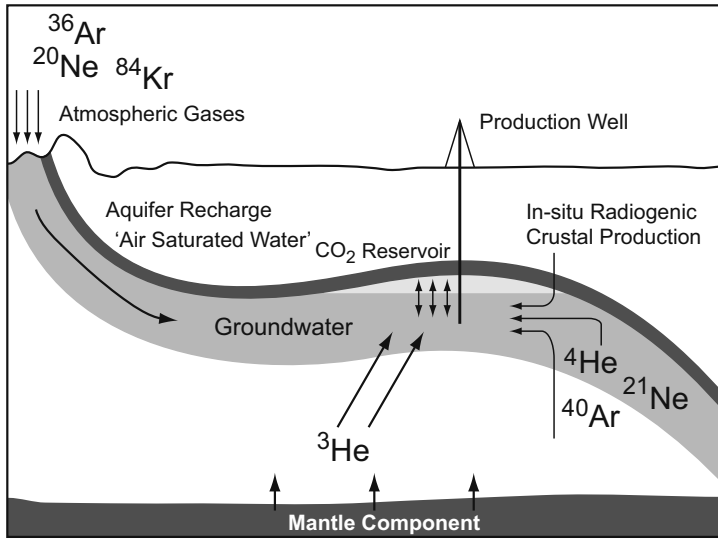

Figure 4. Schematic diagram of a natural CO_2 accumulation, highlighting the three distinct terrestrial noble gas reservoir sources and their characteristic isotopic components. The radiogenic noble gases (e.g., ^{4}He, ^{21}Ne and ^{40}Ar) are produced within the Earth's crust by the radioactive decay of U, Th and K. Atmospheric noble gases (e.g., ^{20}Ne and ^{36}Ar) are input into the gas phase as a result of equilibration with the groundwater at recharge. Within areas of continental extension or magmatic activity mantle derived noble gases (e.g., ^{3}He) may also be present. The distinct elemental and isotopic composition of the noble gases from these three components permits the contribution from each to be quantitatively resolved from any crustal fluid. Redrawn after Ballentine et al. (2002).

The atmosphere is the primary reservoir of ^{20}Ne. The atmosphere and air saturated water have ^{20}Ne/^{22}Ne and ^{21}Ne/^{22}Ne ratios of 9.80 and 0.029, respectively (Kennedy et al. 1990), which have evolved from the initial mantle out-gassed ratios of 9.85 and 0.0284 by hydrodynamic escape of Ne to space (Yatsevich and Honda 1997).

The He inventory of the atmosphere is a combination of material out-gassed from the mantle (which is rich in ^{3}He), material produced in and out-gassed from the crust (which is rich in ^{4}He), cosmogenic material (rich in ^{3}He) and material lost to space (^{3}He is preferentially lost over ^{4}He as it is lighter and more volatile). The atmospheric ^{3}He/^{4}He value is commonly referred to as R_a, where R_a is the ^{3}He/^{4}He ratio of air at 1.4×10^{-6} and He-isotope measurements are generally reported relative to the ratio in air as R/R_a.

Substantial loss of Xe (and other gases) early in Earth's history has produced a relatively depleted atmospheric reservoir with a fractionated noble gas composition (Porcelli et al. 2001). The other significant atmospheric noble gases are ^{20}Ne, ^{84}Kr, ^{129}Xe and ^{132}Xe which have characteristic abundance ratios relative to Ar of ^{20}Ne/^{36}Ar = 0.5237, ^{84}Kr/^{36}Ar = 0.0207 and ^{132}Xe/^{36}Ar = 1.17×10^{-4} (Ozima and Podosek 2002).

Crustal reservoir. Radiogenic noble gas production in the crust further enriches groundwaters in noble gases, although this production is highly heterogeneous, depending on the concentrations of U, Th and K in the contacting rocks, their thermal history and age (Ballentine and Burnard 2002). Crustal production is dominated by ^{4}He and ^{40}Ar, with minor amounts of nucleogenic ^{21}Ne and ^{22}Ne production (Dunai and Porcelli 2002).

Radiogenic ^{4}He is produced from α-decay of ^{238}U, ^{235}U and ^{232}Th, which are concentrated in crustal rocks (Ozima and Podosek 2002). Crustal ^{3}He/^{4}He ratios are typically within the

range of 0.01 – 0.05 R_a (Tolstikhin et al. 1996; Ozima and Podosek 2002). Similarly, ^{40}K is concentrated in crustal rocks and its daughter isotope ^{40}Ar is produced in great abundance. Volume weighted $^4He/^{40}Ar$ production ratios for the continental crust are ~5.7, but vary from ~6.00 in the upper crust to ~3.09 in the lower crust (Ballentine and Burnard 2002). In addition to local production, groundwaters can become strongly enriched in ^4He and ^{40}Ar due to a pervasive flux of He and Ar through the continental crust (Torgersen et al. 1989), although the validity of a bulk crustal flux versus local pervasive fluxes is still widely debated (Ballentine and Burnard 2002; Solomon 2000). Such processes complicate the use of ^4He and ^{40}Ar as direct measures of crustal fluid residence times, although robust estimates can be made in hydrologically well-constrained groundwater systems (e.g., Solomon 2000).

The decay of U and Th in the crust produces α-particles and neutrons that bombard lighter elements and produce noble gases by nucleogenesis. The production of Ne within the crust, including ^{20}Ne, ^{21}Ne and ^{22}Ne, is almost entirely derived from nucleogenic reactions involving O, Mg and F (Ballentine et al. 2002, 2005). The production rates of these isotopes depend on the abundance of radioelement and target element concentration and distribution (Ballentine and Burnard 2002). Crustal production of Ne, predominantly from micas and amphiboles, is dominated by ^{21}Ne and ^{22}Ne and the crust is characterized by well-defined $^{20}Ne/^{22}Ne$ and $^{21}Ne/^{22}Ne$ of 0.3 and 0.52, respectively (Kennedy et al. 1990; Ballentine 1997; Ballentine and Burnard 2002; Kennedy and van Soest 2006). Quantities of fissionogenic ^{86}Kr and ^{136}Xe can be produced in regions rich in ^{244}Pu and ^{238}U (Porcelli et al. 2001).

Mantle reservoir. The loss of primordial gases early in Earth's history impacts the mantle with characteristic noble gas element and isotope ratios. An undegassed mantle reservoir (possibly primitive lower mantle), sampled by oceanic island basalts, is enriched in ^3He with $^3He/^4He$ ratios of between 9 to 32 R_a (Farley and Neroda 1998). The degassed upper mantle, sampled by mid ocean ridge basalts, is depleted in ^3He and exhibits a narrow range of $^3He/^4He$ ratios of ~8.75±2.14 R_a (Graham 2002), although the continental lithospheric mantle may have more variable $^3He/^4He$ ratios of ~4-9 R_a (e.g., Crossey et al. 2009). Loss of primordial ^{36}Ar and radiogenic production of ^{40}Ar imparts the mantle with extreme $^{40}Ar/^{36}Ar$ ratios >30,000 (Burnard et al. 1997). The average upper mantle is characterized by well-defined $^{20}Ne/^{22}Ne$ and $^{21}Ne/^{22}Ne$ of 12.5 and 0.06, respectively (Harrison et al. 1999; Yokochi and Marty 2004; Ballentine et al. 2002, 2005).

The Colorado Plateau and southern Rocky Mountains CO_2 fields

The five major CO_2 accumulations of the Colorado Plateau and southern Rocky Mountains region; Bravo Dome, St Johns Dome, McCallum Dome, Sheep Mountain and McElmo Dome, comprise gas or supercritical fluids (>90% CO_2) hosted in a variety of sedimentary reservoirs.

CO_2 reservoir geology. Bravo Dome is estimated to contain 450 billion m^3 of high-purity CO_2 (99%) gas accumulated over about 2000 km^2 in the Permian Tubb sandstone. The formation has an average thickness of 30 m and varies in depth between 600 m and 700 m (Broadhead 1993). The reservoir lithology varies from well-sorted mature and fine-grained arkose to poorly sorted arkose with abundant detrital clay and silt and is of arid and semi-arid origin. The Springerville-St Johns Dome is estimated to contains 445 billion m^3 of almost pure CO_2 gas (>90%) stored in carbonate, anhydrite and siltstones of the Permian Supai Formation, at depths of 200 m to 700 m (Moore et al. 2005). McCallum Dome contains supercritical CO_2 stored in the Lower Cretaceous Dakota and Lakota sandstones at depths of 1500 m to 1900 m (Gilfillan et al. 2008). Sheep Mountain is estimated to contain 70 billion m^3 of almost pure supercritical CO_2 (> 97%) stored in aeolian and fluvial sandstones of the Cretaceous Dakota and Jurassic Entrada formation at depths of 1400 m to 1800 m (Stevens et al. 2001). McElmo Dome is estimated to contain 476 billion m^3 of supercritical CO_2 within porous dolomite beds of the ~100 m thick Mississippian Leadville limestone at depths of 1800 to 2600 m (Allis et al. 2001; Stevens et al. 2001).

Local volcanism and timing of CO_2 charge. Radiometric dating of surface volcanics surrounding these natural CO_2 accumulations gives an indication of the approximate timing of the reservoir CO_2 charge. Bravo Dome is thought to be the youngest of these accumulations originating from magmatic activity in the nearby Raton-Clayton volcanic field that initiated at ca. 50 ka, with continued volcanic activity as recently as 10 ka and 8 ka (Stroud 1997). Present day soil gas surveys suggest the reservoir is a dynamically filling structure (Baines and Worden 2001). The next youngest event is associated with the Springerville-St. Johns Dome, where volcanic activity from the nearby Springerville Volcanic field dates from 0.3 to 2.1 Ma (Rauzi 1999), and travertine mound ages suggest reservoir filling initiated at ca. 350 ka (Embid and Crossey 2009). The older Sheep Mountain and McCallum Dome CO_2 reservoirs are associated with magmatic centres that were active in the Late Tertiary (Maughan 1989; Woodward 1983). The oldest intrusive igneous rocks are those associated with McElmo Dome, from the nearby Ute Mountain and La Plata Mountain laccoliths which have been dated at 40-72 Ma (Stevens and Tye 2005). The even older JM Brown Basset Field in the Permian Basins of west Texas is believed to have contained CO_2 for some 300 million years (Ballentine et al. 2001).

Mantle CO_2 source. The presence of primordial ^{3}He in the mantle and the low rates of nucleogenic ^{3}He production in the crust and atmosphere impart mantle derived magmas and fluids with characteristic $^3He/^4He$ ratios (~4-9 R/R_a). In addition the large concentration of ^{3}He in mantle derived volatiles, relative to the low concentrations of ^{3}He typical of crustal CO_2 sources (such as thermal decarbonation), has enabled the $CO_2/^3He$ to be used as an indicator of mantle provenance, where mantle $CO_2/^3He$ ratios exhibit a small range compared to other crustal fluids (10^9 to 10^{10}) (Ballentine et al. 2001) (Fig. 5). Systematically decreasing $CO_2/^3He$ ratios in the CO_2 phase of individual CO_2 reservoirs has been interpreted to reflect dissolution of the CO_2 in contacting formation water, where the relatively insoluble ^{3}He is retained in the CO_2 phase as the CO_2 dissolves (e.g., Gilfillan et al. 2009).

Similarly, the characteristic and well-known $^{20}Ne/^{22}Ne$ and $^{21}Ne/^{22}Ne$ ratios of the mantle, crust and atmosphere can be used to determine the origin of crustal fluids and gas, and to quantify the relative proportions of the noble gas budget being derived from each of the terrestrial reservoirs (Ballentine et al. 2002, 2005) (Fig. 6).

The five major CO_2 accumulations of the Colorado Plateau and southern Rocky Mountains region are all characterized by $CO_2/^3He$ within the mantle or magmatic range (Gilfillan et al. 2008) (Fig. 2). The young Bravo Dome accumulation

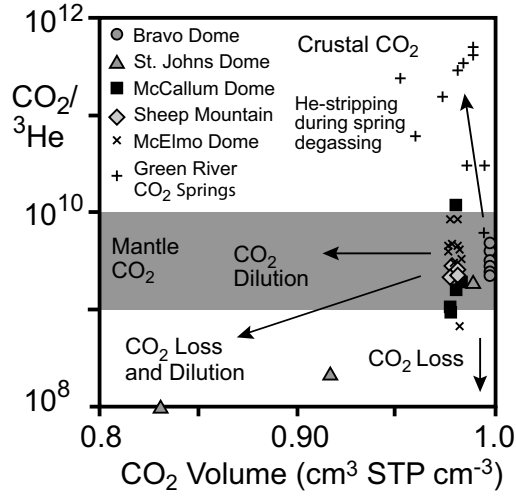

Figure 5. Plot of $CO_2/^3He$ against CO_2 concentration for all of the major CO_2 fields and the CO_2-springs at Green River, Utah. The shaded region highlights the range of $CO_2/^3He$ values measured in pure magmatic samples (MORB). All samples of gas collected from the gas caps of the natural CO_2 fields plot within or below this range, indicating the presence of a significant quantity of magmatic ^{3}He. Samples of exsolved gas collected from the CO_2-degassing springs at Green River plot above this range, and this may reflect an origin by decarbonation reactions in the crust or modification of an originally mantle $CO_2/^3He$ ratio by multiple stages of CO_2 dissolution and exsolution, and solubility fractionation of the ratios. Data from Gilfillan et al. (2008) and Wilkinson et al. (2009b).

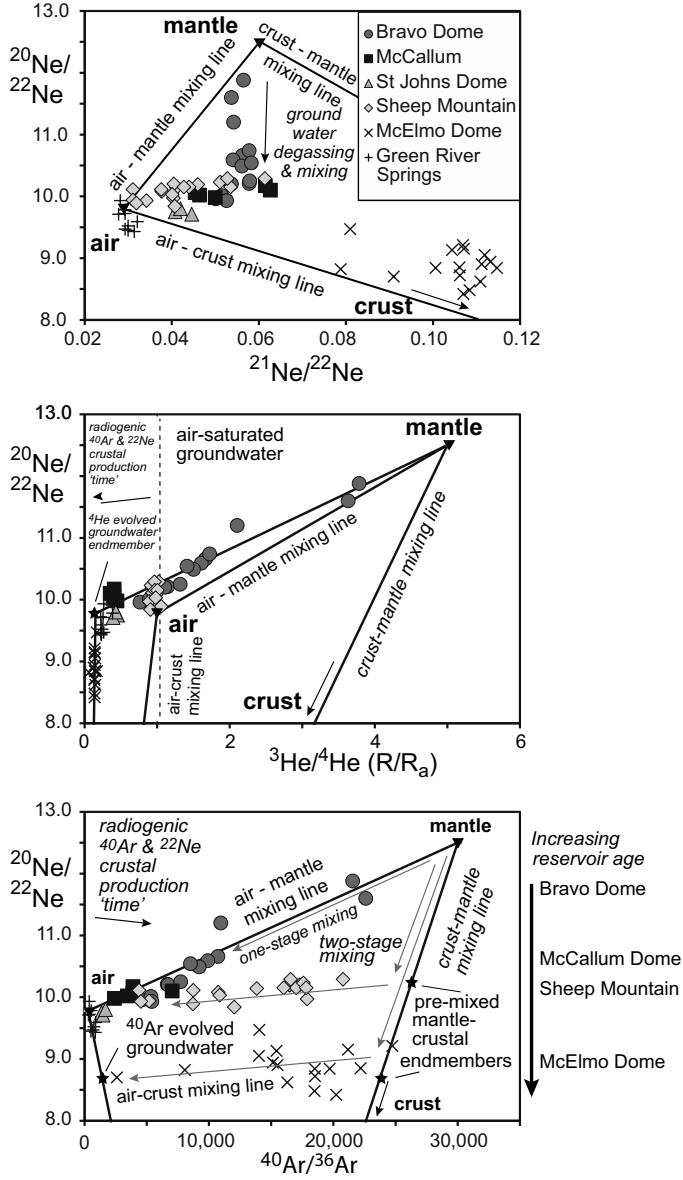

Figure 6. Noble gas data from Colorado CO_2 reservoirs taken from Ballentine et al. (2005), Gilfillan et al. (2008); Holland and Ballentine (2006) and Wilkinson et al. (2009b). A) Plot of $^{20}Ne/^{22}Ne$ ratio against $^{21}Ne/^{22}Ne$ for the major CO_2 fields. Bravo Dome exhibits mixing between a pre-mixed crust/air component and the mantle. St. John's, Sheep Mountain and McCallum highlight mixing between a pre-mixed crust/mantle component and air. The distinct values measured from McElmo Dome show that this field contains the highest proportional contribution from crustal/radiogenic sources. B) Plot of $^{20}Ne/^{22}Ne$ against $^{3}He/^{4}He$ ratio. Bravo Dome is characterized by $^{3}He/^{4}He$ (R/R_a) >1, a mixing trend between a pre-mixed crust/air component and the mantle. The other fields are all characterized by $^{3}He/^{4}He$ (R/R_a) <1 due to radiogenic crustal addition. C) Plot of $^{20}Ne/^{22}Ne$ against $^{40}Ar/^{36}Ar$ ratio. Mixing trends are as before but the very old fields of Sheep Mountain and McElmo Dome are further displaced towards crustal contributions due to addition of radiogenic ^{40}Ar and ^{22}Ne. All end-member compositions are constructed using data from Ballentine et al. (2002) and references therein.

and numerous CO_2-degassing springs (Mayo et al. 1991; Crossey et al. 2009; Karlstrom et al. 2013) in the region have elevated $^3He/^4He$ ratios, indicative of a mantle CO_2 source. Interpretation of the He- and Ne-isotope signature of the older CO_2 accumulations at St Johns Dome, McCallum Dome, Sheep Mountain and McElmo Dome and in CO_2-degassing springs, such as those at Green River, is complicated by a number of factors. The production of radiogenic ^4He, ^{21}Ne and ^{22}Ne in the crust imparts these older, originally mantle derived accumulations, with a crustal He- and Ne-isotope signature. Degassing of groundwater, which contains high concentrations of atmospherically derived noble gases, enriches the contacting CO_2 phase with an atmospheric noble gas signature. Similarly, in CO_2-degassing springs, which contain dissolved mantle derived CO_2, the noble gas composition of the degassing CO_2 is dominated by atmospheric and crustal inputs in the water and the CO_2/noble gas ratios can be strongly fractionated by the degassing processes.

The young CO_2 field: Bravo Dome. CO_2 gases from across the Bravo Dome field have been sampled from producing wells in the CO_2 gas cap (Ballentine 1997; Gilfillan et al. 2008). Some of the CO_2 gas samples are characterized by near mantle noble gas isotopic compositions, which have been used as important constraints on the Ne- and Xe-isotopic budget of the mantle (Ballentine 1997; Ballentine et al. 2005; Holland and Ballentine 2006). Spatial He and Ne-isotopic trends reflect mixing between mantle CO_2 inputs along faults in the south western portions of the field, with progressive addition of noble gases to the north east, from degassing of groundwater into the gas cap (Gilfillan et al. 2008; Dubacq et al. 2012). The groundwater degassing generates "one-stage" noble gas mixing trends between a mantle end-member and a premixed atmospheric-crustal end-member, originating from the groundwater. This is in contrast to the more complex 'two-stage' mixing trends observed in the older CO_2 fields, discussed below.

At Bravo Dome, the groundwater end-member is enriched in ^4He and ^{21}Ne relative to air saturated water, resulting from radiogenic noble gas inputs from the granitic basement underlying the Tubb sandstone (Dubacq et al. 2012). The degassing of the premixed air-crust noble gas signature from the groundwater generates linear mixing trends in $^{40}Ar/^{36}Ar$ versus $^{20}Ne/^{21}Ne$ isotope space between the mantle inputs and the groundwater derived gases. The trends preclude significant input of crust-derived ^{40}Ar from the reservoir sediment. This is consistent with the relatively young age of the field and the slow production of ^{40}Ar in the sediment relative to rapid ^4He production in the granitic basement. Mixing of the mantle and the atmosphere-crust derived noble gases is also preserved in mixing plots of noble gas element ratios such as $^{20}Ne/^{36}Ar$ versus $^{84}Kr/^{36}Ar$ (Fig. 7).

$CO_2/^3He$ ratios and the long-term dissolution of CO_2. In the sampled gases at Bravo Dome, the concentrations of the atmospheric and crustal-derived noble gases ^4He, ^{36}Ar and ^{20}Ne increase simultaneously with decreasing $CO_2/^3He$ ratios (Dubacq et al. 2012) (Fig. 8). During dissolution of the reservoir gas cap, relatively insoluble ^3He remains in the gas phase whilst the CO_2 dissolves and thus the $CO_2/^3He$ can be used as a measure of the degree of CO_2 dissolution (Fig. 8). Increasing concentrations of the noble gases (e.g., ^4He, ^{36}Ar and ^{20}Ne) with decreasing $CO_2/^3He$ reflects both a concentration affect due to removal of the solvent (CO_2) and progressive addition of noble gases from groundwater degassing. Care should be taken when interpreting plots of noble gas concentration versus $CO_2/^3He$ due to concentration affects that result due to removal of the solvent. Similarly, both Ne- and He-isotopes vary systematically with decreasing $CO_2/^3He$ due to progressive addition and mixing of noble gases derived from the simultaneous groundwater degassing and CO_2 dissolution (Dubacq et al. 2012) (Fig. 9).

The amount of CO_2 lost from the gas cap may be estimated from the change in $CO_2/^3He$ relative to the maximum ratio measured for an individual field (Gilfillan et al. 2009). This simple method ignores concentration effects and the addition of ^3He from groundwater degassing, and thus generally over estimates the proportion of CO_2 loss by ~20%. For Bravo

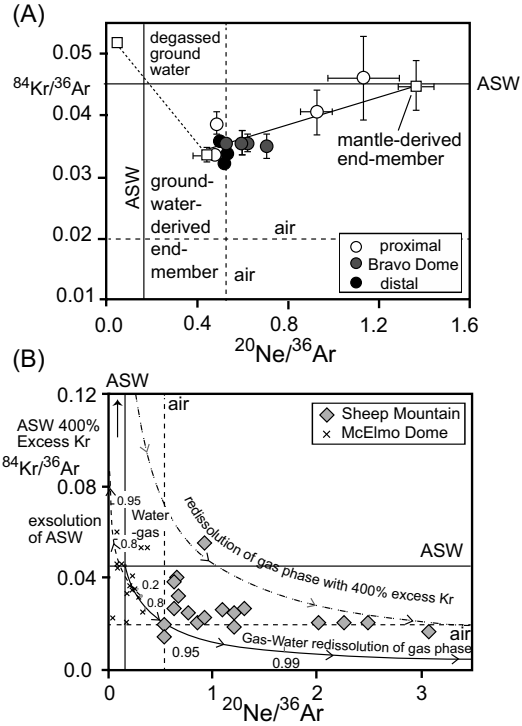

Figure 7. A) $^{84}Kr/^{36}Ar$ plotted against $^{20}Ne/^{36}Ar$ for Bravo Dome samples, compared with air (dotted gray line), air-saturated water (ASW, solid gray line) and the calculated mantle-derived and groundwater end-members, redrawn from Dubacq et al. (2012). The trends in the concentration ratios of the noble gases can be described by a simple mixing model of mantle derived noble gases and atmospheric noble gases derived from degassed groundwater. B) Plot of $^{84}Kr/^{36}Ar$ against $^{20}Ne/^{36}Ar$ for the Sheep Mountain and McElmo Dome fields redrawn from Gilfillan et al. (2008). Also plotted are Rayleigh fractionation curves modeled by Gilfillan et al. (2008), calculated for a gas phase evolving from an ASW groundwater (dashed line) and for a gas with an ASW composition redissolving into degassed water containing no noble gases (solid line). This second model accounts for the observed extreme $^{20}Ne/^{36}Ar$ observed at Sheep Mountain. However, the observed $^{84}Kr/^{36}Ar$ values are up to 4× higher than predicted, possibly as a result of the addition of excess sedimentary Kr.

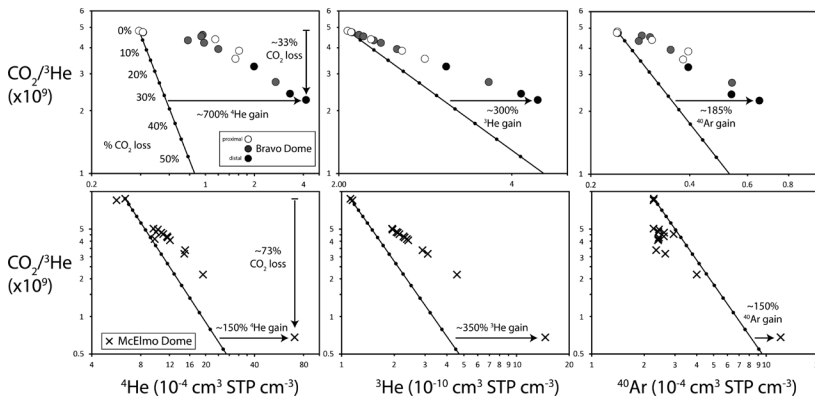

Figure 8. $CO_2/^3He$ ratios versus ^4He, ^3He and ^{40}Ar content of gas samples from the Bravo Dome and McElmo CO_2 fields. Lines model the increase in the concentration of ^4He, ^3He and ^{40}Ar resulting from loss of CO_2 by dissolution, taking the sample with the highest $CO_2/^3He$ value as a starting point. All fields are characterized by an excess of noble gases derived from groundwater degassing and radiogenic ^4He and ^{40}Ar production. Note the use of log–log scales. Calculated using data from Gilfillan et al. (2008).

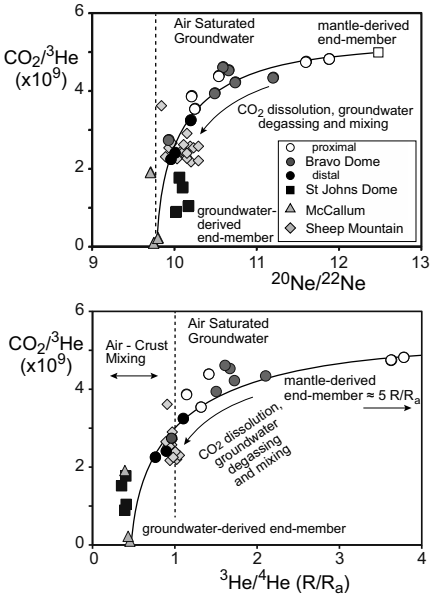

Figure 9. Trends from groundwater degassing mixing with a noble gas-poor mantle-derived end-member at Bravo Dome, St Johns Dome, McCallum and Sheep Mountain. Solid lines are the best fit mixing lines calculated from Dubacq et al. (2012) for Bravo Dome. Variations in $^{20}Ne/^{22}Ne$ and $^{3}He/^{4}He$ during CO_2 dissolution for Bravo Dome samples are driven by mixing of mantle and atmospheric derived noble gas components.

Dome the implied CO_2 loss is ~33% of the CO_2 initially in place, when concentration affects are considered. Many of the older CO_2 fields discussed below show an excess of 70% loss of CO_2 compared to the highest $CO_2/^3He$ ratio measured.

The old CO_2 fields: St Johns Dome, McCallum Dome, Sheep Mountain and McElmo Dome. The older CO_2 fields of St Johns Dome, McCallum Dome, Sheep Mountain and McElmo Dome are all variably enriched in atmospheric and crustally derived noble gases (Fig. 6). These fields are generally characterized by $^{3}He/^{4}He$ <1 due to accumulated inputs of radiogenic crustal ^{4}He and the long residence time of the CO_2 (Fig. 6).

Ne- and Ar-isotope data for these CO_2 fields (Fig. 6) are consistent with two-stage mixing of i) a premixed mantle and crustal derived end-member followed by ii) progressive mixing of this premixed mantle-crustal end-member with noble gases derived from air saturated groundwater degassing. St Johns Dome, McCallum Dome and Sheep Mountain are characterized by linear mixing arrays in $^{21}Ne/^{22}Ne$ versus $^{20}Ne/^{22}Ne$ isotope space between this pre-mixed mantle-crust end-member and progressive inputs of an atmospheric noble gas signature from groundwater degassing. Generally, $^{3}He/^{4}He$ ratios for these fields increase towards the ASW ratio as $CO_2/^3He$ ratios decrease, reflecting increased interaction with, and degassing of groundwater, as CO_2 dissolution proceeds (Fig. 9). St Johns Dome is characterized by near-atmosphere noble gas isotope ratios and this likely reflects the strong influence of interaction with groundwater on the noble gas isotopic composition of the CO_2 phase in this hydrologically active CO_2 field.

Sheep Mountain is also characterized by extreme ratios of air-derived noble gases (e.g., $^{20}Ne/^{36}Ar$) much in excess of ratios expected for equilibrium degassing of air saturated groundwater (Fig. 7). Equilibrium degassing of ASW predicts a maximum enrichment in the $^{20}Ne/^{36}Ar$ of the exsolved gas by a factor of ~2 corresponding to a maximum of 0.304 (Gilfillan et al. 2008). The Sheep Mountain data exhibits $^{20}Ne/^{36}Ar$ values from 0.530 to 2.496 (Gilfillan et al. 2008). This enrichment is thought to result from Rayleigh fractionation during redissolution of the gas phase, which had previously been enriched in air derived noble gases during the initial filling of the reservoir (Gilfillan et al. 2008).

The very old CO_2 reservoir at McElmo Dome has $^{3}He/^{4}He$, $^{21}Ne/^{22}Ne$ and $^{20}Ne/^{22}Ne$ ratios characteristic of the addition of significant crust-derived He and Ne (Fig. 6). This is consistent with the considerable age of the reservoir (>40 Ma), inferred from dating of the nearby volcanic fields. Ne-, He- and Ar- isotope mixing trends are consistent with two-stage mixing of a pre-mixed crust-mantle end-member with noble gases derived from air saturated groundwater that is itself characterized by enrichment in crustally derived gases, suggesting the groundwater itself is also of considerable age. This is consistent with the depth of the field (>2 km), the likely hydrologically isolated nature of the groundwater system and the considerable age of the reservoir.

Stable C-isotopes and CO_2 dissolution mechanism. Using stable carbon isotopes in conjunction with noble gas data it is possible to examine the mechanism by which CO_2 is lost to solution (Gilfillan et al. 2009; Dubacq et al. 2012). The $^{13}C/^{12}C$ isotopic ratio of the $CO_{2(g)}$ ($\delta^{13}C_{CO_2(g)}$) is fractionated as CO_2 dissolves, due to preferential loss of ^{13}C. The magnitude of this fractionation is sensitive to the $CO_{2(aq)}/HCO_3^-$ ratio of the water into which the $CO_{2(g)}$ is dissolving, due to differences in the fractionation between $CO_{2(g)}$ and $CO_{2(aq)}$, and $CO_{2(g)}$ and HCO_3^-. The $CO_2/^{3}He$ ratio and $\delta^{13}C_{CO_2(g)}$ are thus an important measure of CO_2 dissolution processes that stabilize these accumulations over geological timescales and can be used to quantify this process (Fig. 10).

The $CO_{2(aq)}/HCO_3^-$ ratio of the water is sensitive to fluid pH, the formation pressure and the total dissolved CO_2 concentration. As fluid-rock reactions proceed in CO_2-charged groundwaters acidity generated from the dissolved CO_2 is neutralized as HCO_3^- is generated from mineral dissolution. The solubility of CO_2 in formation brine depends on the temperature, pressure and fluid salinity and the competing effects of pressure with temperature and salinity lead to solubility maxima for CO_2 at depths of between 0.7 to 1 km for typical geothermal gradients, pore fluid pressures and basin scale pore salinity profiles. As pressure increases the concentration of CO_2 in equilibrium with a free CO_2 phase will generally increase and thus the $CO_{2(aq)}/HCO_3^-$ ratio will generally increase with increasing pressure.

For the siliclastic reservoirs the trends in $\delta^{13}C_{CO_2(g)}$ versus $CO_2/^{3}He$ space are consistent with the majority of the CO_2 being removed by dissolution into the formation water (Fig. 10). The carbonate dominated reservoirs exhibit very little variation in $\delta^{13}C_{CO_2(g)}$ values compared to the much wider range of values which were exhibited in the silicilastic dominated reservoirs. This narrow range in the carbonate fields is likely due to buffering of the C-isotopic composition of the CO_2 gas by the much larger reservoir of C in the host carbonate.

In the relatively young silicastic reservoir at Bravo Dome the trends in $CO_2/^{3}He$ ratio and $\delta^{13}C_{CO_2(g)}$ imply that CO_2 is dissolving into water with a high HCO_3^- concentration. This is due to significant buffering of the reservoir pH and alkalinity generation due to the dissolution of silicate minerals (Dubacq et al. 2012). This suggests the high rates of groundwater and CO_2 flow in this field results in more extensive fluid-rock reaction, alkalinity production and ionic trapping of the CO_2 (Dubacq et al. 2012), as compared to the other, more stagnant CO_2 reservoirs.

In the deep siliclastic CO_2 fields at Sheep Mountain and McCallum the trends are characterized by CO_2 dissolution into a fluid dominated by $CO_{2(aq)}$. This may reflect the low rates of groundwater flow in these fields and the development of a CO_2-saturated boundary layer beneath the stagnant CO_2 cap, with little fluid-rock reaction, or stripping of all reactive phases from the reservoir.

A final caveat is that C-isotopes can probably only inform on the mechanism controlling CO_2 transport between the gas and fluid phases, and not on subsequent methods of CO_2 removal from the reservoir fluid. This is because the slow rates of fluid and solute transport and the stagnant nature of the formation water in most of these fields precludes the instantaneous isotopic equilibrium between fluid and gas, especially far from their interface, required to

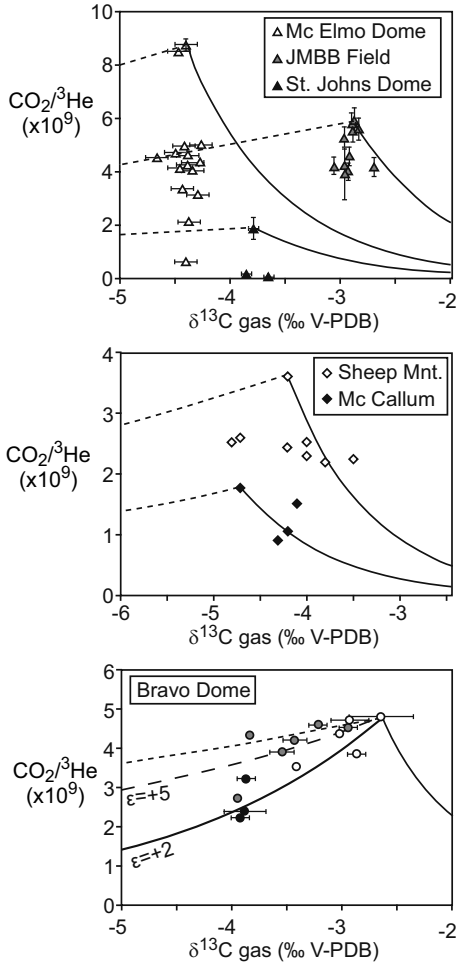

Figure 10. $CO_2/^3He$ versus $\delta^{13}C_{CO2(g)}$ ratios from natural CO_2 accumulations redrawn after Gilfillan et al. (2009) and Dubacq et al. (2012). (a) Carbonate reservoirs, USA, (b) clastic reservoirs of the Sheep Mountain and McCallum fields, USA and (c) the Bravo Dome reservoir, USA. Most natural CO_2 is derived from mantle magmatic sources with $CO_2/^3He$ ratios between 10^9 and 10^{10}. Loss of up to ~70% CO_2 to solution in groundwaters reduces $CO_2/^3He$ ratios. The C-isotopic composition of the CO_2 gas is fractionated by dissolution of CO_2 into the contacting brine, with a fractionation factor ε that varies as a function of the $CO_{2(aq)}/HCO_3^-$ ratio of the contacting formation water. Variation in the $CO_{2(aq)}/HCO_3^-$ depends on pressure temperature and the amount of alkalinity generated by fluid-rock interaction. Solid lines show the expected evolution of $\delta^{13}C$ from Rayleigh distillation of the gas phase induced by CO_2 dissolution in an aqueous fluid assuming all DIC is in the form $CO_{2(aq)}$. The short dashed line shows the evolution of $\delta^{13}C$ following Rayleigh distillation of the gas phase in equilibrium with calcite. For the carbonate HCO_3^- enriched fluid, in reservoirs in (a) the isotopic composition of the gas does not vary as a function of $CO_2/^3He$ due to buffering of the gas and fluid C-isotopic composition by the much larger reservoir of carbon in the host carbonate. For the young (<50 kyrs) CO_2 field at Bravo Dome the important role of fluid-rock interaction in the generation of HCO_3^- is evidenced from the large negative fractionation associated with dissolution of the $CO_{2(g)}$. [Used by permission of Elsevier, redrawn after Dubacq et al. (2012), Fig. 2.]

preserve information on CO_2 removal from the brine phase, and information on carbonate precipitation is unlikely to be preserved in the isotopic composition of the gas cap. Direct observations from core and fluid sampling of the CO_2 reservoirs are required to constrain the fluid-rock reactions in natural CO_2 reservoirs and the efficiency of carbonate precipitation as a long-term trapping mechanism.

FLUID-MINERAL REACTIONS AND REACTION RATES

CO_2-charged fluid-mineral reactions in CO_2 reservoirs may include the relatively rapid dissolution of carbonate and Fe-oxyhydroxide minerals and the more sluggish dissolution of silicate minerals accompanied by the precipitation of carbonate minerals. The nature, rates and consequences of these reactions will be governed by the evolving composition of the fluid phase and the composition and physical conditions of the reservoir. Predicting the nature of the fluid mineral reactions is not straightforward where mineral dissolution and precipitation rates are determined by the inadequately known equilibrium thermodynamics of the minerals and fluids and by the even less well known kinetics of the reactions. Further the kinetics of mineral disso-

lution and precipitation are dependent on their approach to equilibrium making forward modeling of the fluid mineral reactions a complex coupled problem with poorly known uncertainties. The wealth of experimental data on mineral and fluid equilibrium thermodynamics obtained by experiment over the last 50 years is conveniently packaged in accessible thermodynamic databases with computational routines for calculating equilibrium mineral and fluid compositions (e.g., PHREEQC; Parkhurst and Appelo 2013). However the databases do not propagate uncertainties from the experimental determinations, and the quality of the experimental determinations is variable: there are considerable difficulties in reaching fluid-mineral equilibrium at temperatures characteristic of near-surface conditions; data for some fluid species and minerals are estimated, there may be considerable uncertainties in the composition and structure of minerals stable at lower temperatures such as the clay minerals which are important reaction products and high ionic strength fluids and high P_{CO_2} conditions are inadequately modeled.

The kinetics of fluid-mineral reactions is necessarily less well known than their equilibrium thermodynamics, and experimentally or theoretically determining mineral-fluid kinetics is particularly problematic. There is no proven thermodynamic model of the atom-scale processes that control fluid-mineral interactions at the mineral surface. A number of models have been proposed that attempt to model the energy barriers between ions dissolved in fluids and those that make up mineral structures and often these involve intermediate species whose composition and even existence is speculative (e.g., Brantley 2008). The lack of a full underlying theory is compounded by the difficulty of carrying out laboratory experiments on mineral-fluid reaction kinetics. Many of the reactions of interest, particularly those with silicate minerals, are relatively sluggish which makes it difficult to determine reaction rates with any precision, particularly as the reactions slow as they approach equilibrium. Fluids are generally close to equilibrium in many natural rock-dominated systems. The problems are compounded by the difficulties of measuring the appropriate reactive surface areas of natural minerals (Peters 2009; Landrot et al. 2012), the possibility that mineral surfaces undergo time- and reaction-rate dependent changes in composition and structure, the complex porosity and permeability structures in natural rocks which moderate fluid-mineral interactions and the possibility that the other minerals and reaction products might shield reacting minerals from the fluid phase. The multiple controls on fluid compositions, which in most rocks include the kinetics of several competing mineral dissolution and precipitation rates, further complicates the calculations.

For all these reasons it has proved important to compare laboratory determinations of mineral dissolution rates with estimates recovered from natural settings. White and Brantley (2003) summarized the comparisons available then (see Fig. 11) and reviewed the well-known observation that dissolution rates determined in the laboratory are orders-of-magnitude higher than apparent natural dissolution rates. There is now general agreement that much of the discrepancy arises from the marked decrease in reaction rates as minerals approach thermodynamic equilibrium with the fluids (e.g., White and Brantley 2003; Kampman et al. 2009; Maher et al. 2009; Zhu and Lu 2013). However fluid-silicate mineral reaction rates in laboratory experiments at surface conditions and close-to-equilibrium are too sluggish to give useful information and the data used to test models of reaction rates is mostly derived from experiments at higher temperatures (e.g., Hellmann and Tisserand 2006; Lu et al. 2013). Since most data from natural systems is in the close-to-equilibrium region comparison of the natural data with laboratory experiments at surface temperatures depends on how the variation in reaction rate with approach to equilibrium is modeled. Maher et al. (2009) and Moore et al. (2012) have discussed how modeling natural dissolution rates in soil profiles may be used to distinguish between the different models for the variations in reaction rate with approach-to-equilibrium.

The Green River natural analogue

The natural CO_2 system at Green River, Utah, allows a number of approaches to be applied to determine the nature and rates of the fluid-mineral reactions in a CO_2-rich system. At

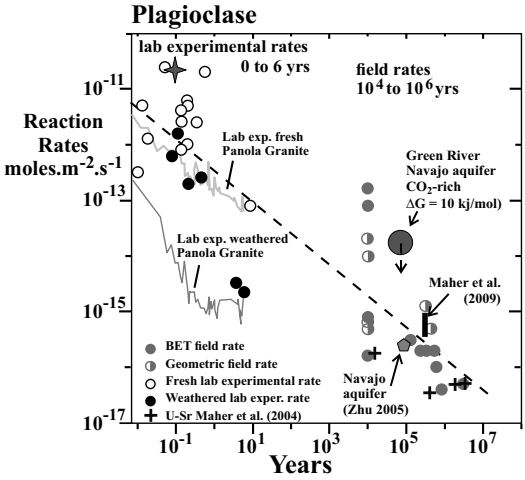

Figure 11. Estimates of plagioclase dissolution rates from experiments and natural settings plotted against estimated duration of dissolution. Note that mineral surface areas have been estimated by both gas absorption (BET) measurements and from mineral geometries and the former gives higher surface area estimates. Diagram replotted using data presented by White and Brantley (2003) with data from Maher et al. (2009), Maher et al. (2004), Zhu (2005) and Kampman et al. (2009) added.

Green River natural CO_2 escapes through a series of natural seeps and springs along the Little Grand Wash and the Salt Wash Graben faults, as well as through abandoned oil and water drill holes (Fig. 12). The geological setting, structure and the evolution of this CO_2 field has been described by Heath (2004), Shipton et al. (2004), Kampman et al. (2009), Dockrill and Shipton (2010), Kampman et al. (2012) and Burnside et al. (2013). The shallow dipping Paleozoic to Cretaceous stratigraphic succession is in the north part of the Paradox Basin and comprises continental fluvial and aeolian sandstones, shales, limestones and evaporites. The succession is exposed by thrusting-related exhumation in the San Rafael Swell about 60 km WNW of Green River, gently folded about a NNW trending anticline at Green River and cut by two east-west striking fault sets, the Little Grand Wash and Salt Wash Graben faults (Fig. 12). The latter are postulated to date between the early Tertiary and the Quaternary (Pevear et al. 1997; Shipton et al. 2004).

The $CO_2/^3He$ ratios of the Green River gasses exceed the mantle range and $^3He/^4He$ ratios are (R/R_a) are <1 (Heath et al. 2009; Wilkinson et al. 2009a) implying that the CO_2 contains quantities of nobles gases derived from long-term residence in the crust. The CO_2 source might be diagenetic decarbonation of marls in the Leadville Limestone at ~ 150 °C during maximum burial at 40 Ma (Nuccio and Condon 1996). Alternatively the CO_2 might be derived from magmatic sources and the $CO_2/^3He$ ratios elevated by multiple interactions between CO_2 and formation waters and $^3He/^4He$ ratios reduced by inputs of crustally derived ^4He. The CO_2, associated with brines from the evaporites of the Paradox Formation which overlie the Leadville Limestone, rises along the main fault sets and escapes at the intersection of these faults with the crest of the Green River Anticline. This is indicated by the location of the natural CO_2 springs and associated travertines (Fig. 12) and the geochemical trends with distance of the spring waters which exhibit significant inflections across the faults (Fig. 13). Spring temperatures and water chemistries imply that the fluids are mainly derived from the Navajo Formation (Fig. 14). Sampling of fluids in the Green River Borehole, drilled through the Entrada and Navajo aquifers north of the Little Grand Wash Fault just west of Crystal Geyser (Fig. 12) in 2012, and from Crystal Geyser, which erupts from a borehole which extends down 800 m to the Permian White Rim Sandstone (Fig. 14) also confirms spring fluid compositions represent mixing between brines and shallow aquifer fluids (Kampman et al. 2013b). In particular a systematic increase in both the CO_2-saturation and brine contents in four samples collected downhole at pressure with depth in the Navajo Formation is consistent with the CO_2 and brines being introduced up the fault zones (Fig. 15).

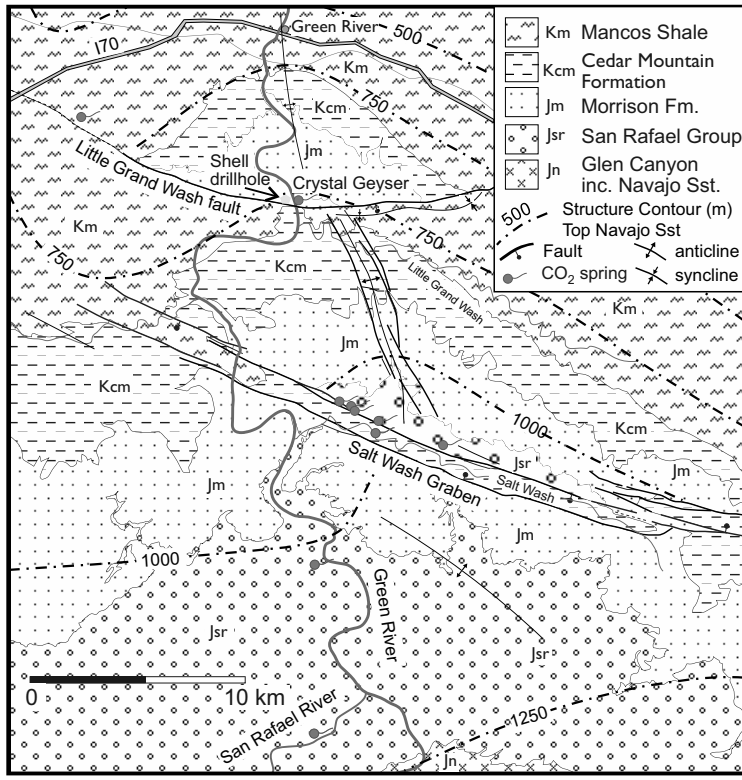

Figure 12. Geology and location of natural and artificial CO_2 springs and geysers in Green River, Utah. The Jurassic and Cretaceous stratigraphy is gently folded about the NNW trending Green River Anticline which is cut by the Little Grand Wash and the Salt Wash Graben faults along which CO_2 has been escaping for > 400 ka. Crystal Geyser and the CO_2 springs located away from faults are exploiting abandoned hydrocarbon exploration or water drill holes. [Used by permission of Elsevier, redrawn after Kampman et al. (2009), Fig. 3.]

A series of travertine mounds around the active springs and geysers close to river level and inactive mounds up to 37 meters above river level (Shipton et al. 2004) reflect the present and past locations of CO_2 springs. U-Th dating of aragonites from these mounds demonstrates that CO_2 has been escaping from this site for at least 400 ka (Burnside et al. 2013). Kampman et al. (2012) argue from secular changes in the aragonite vein chemistries that CO_2 re-charge into the system was episodic and occurred during deglaciation events as the faults responded to rapid crustal unloading and changes in groundwater recharge rates.

The nature of the mineral-fluid reactions and rates of these reactions at Green River are constrained by two approaches. Kampman et al. (2009) used gradients in the chemistry of the springs down the flow direction in the Navajo sandstone to infer the nature and rates of fluid-mineral reactions following a number of other studies on fluid-mineral reactions in aquifers (Zhu 2005; Maher et al. 2006; Singleton et al. 2006). Wigley et al. (2012) examined the petrology of the Entrada sandstone where it is exposed adjacent to the Salt Wash Graben in Green River. Here, at the crest of the Green River anticline, the lower part of the Entrada sandstone is bleached which Wigley et al. (2012) argue is due to CO_2-charged brines escaping from the fault system.

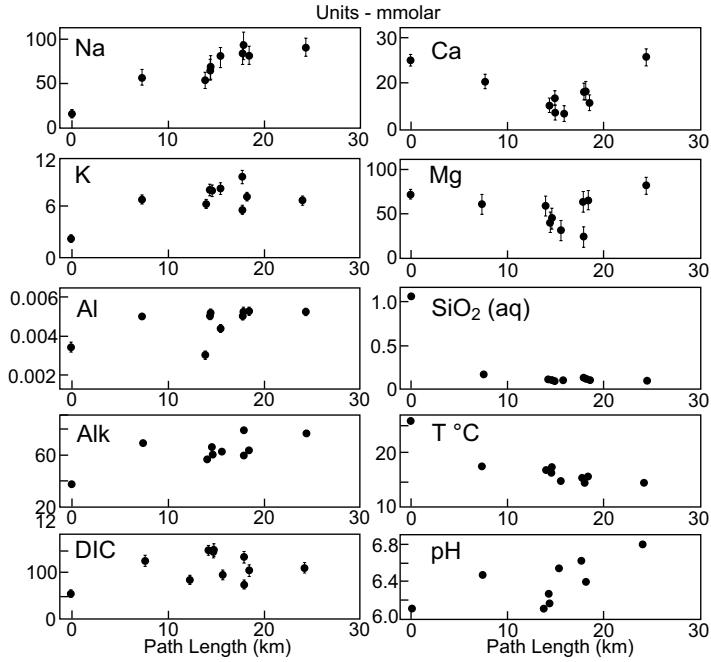

Figure 13. Green River Spring chemistry with brine input subtracted plotted against flow distance downstream of Green River Airport Well. Note inflection in pH at 14 km where additional CO_2 is introduced at the Salt Wash Graben. [Used by permission of Elsevier, redrawn after Kampman et al. (2009), Fig. 5.]

Fluid-mineral reactions in the Navajo aquifer. The stoichiometry of the fluid-mineral reactions is calculated from the changes in water chemistry down the flow direction as sampled by the CO_2 springs (Fig. 13), given the compositions of the participating minerals from the mineralogy of the aquifer. The method is based on mass-balance of the change in dissolved constituents (see discussion of the original work by Garrels and Mackenzie (1967) in Drever 1997). Thus the change in concentration of component k, Δm_k (concentration m_k mol/l), in the water between two points along the flow path is given by:

$$\Delta m_k = \sum_{j=1}^{n} M_j \, b_{j,k} \tag{16}$$

where $b_{j,k}$ is the stoichiometric coefficient of component, k, in mineral phase, j, and M_j is the number of mols of the j^{th} mineral (n minerals in total). Kampman et al. (2009) solved Equation (16) for the components Si, Al, Mg, Ca, Na, K, S, C and alkalinity and the solid phases silica, plagioclase, K-feldspar, calcite, dolomite, gypsum, kaolinite and illite-smectite. Equation (16) is solved for the number of moles of the solid phases and CO_2 consumed or precipitated where the change in water chemistry, Δm_k, is taken between the upstream well, Green River Airport Well, and each of the downstream wells. Examples of the results (Fig. 16) show that there is net consumption of plagioclase, K-feldspar, gypsum, and CO_2 and net precipitation of calcite and silica along the whole flow path. Smectite and gypsum are consumed and dolomite precipitated in the path segments to the upstream wells but this is reversed with net precipitation of smectite and gypsum and consumption of dolomite downstream.

The results of this sort of calculation are subject to a number of systematic uncertainties. The number of solid phases that can be included in the calculation is limited by the number

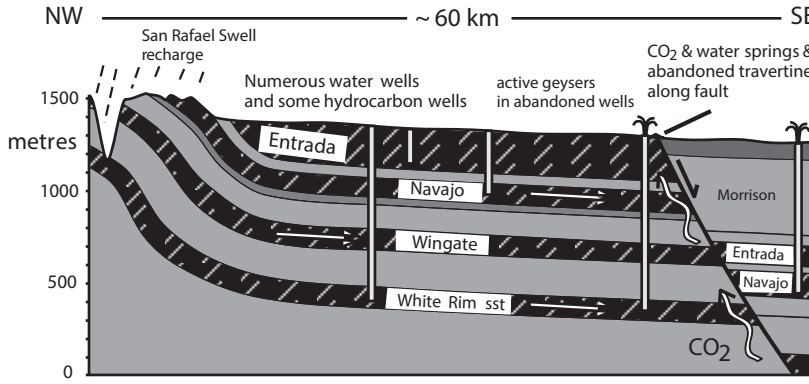

Figure 14. Diagrammatic section through the geology between the San Rafael Swell and Green River. The major aquifers are recharged in the San Rafael Swell and groundwater flow is towards the south-east. CO_2 and brines migrate up the damage zones associated with faults and mix with the meteoric waters and flow SE.

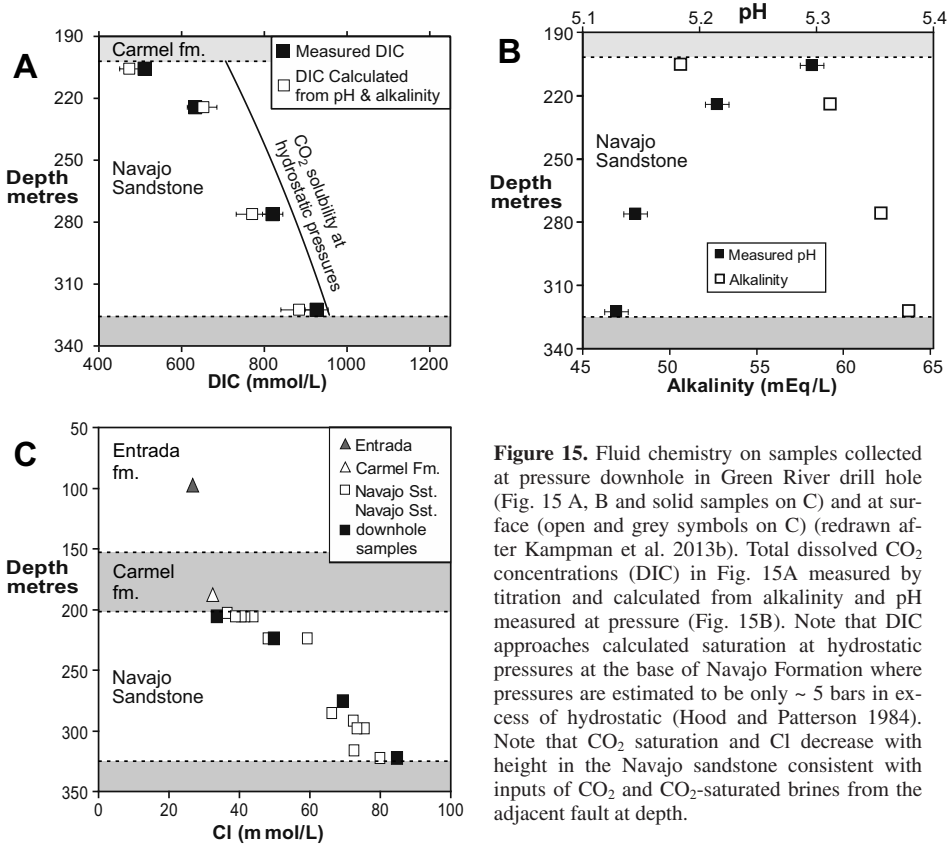

Figure 15. Fluid chemistry on samples collected at pressure downhole in Green River drill hole (Fig. 15 A, B and solid samples on C) and at surface (open and grey symbols on C) (redrawn after Kampman et al. 2013b). Total dissolved CO_2 concentrations (DIC) in Fig. 15A measured by titration and calculated from alkalinity and pH measured at pressure (Fig. 15B). Note that DIC approaches calculated saturation at hydrostatic pressures at the base of Navajo Formation where pressures are estimated to be only ~ 5 bars in excess of hydrostatic (Hood and Patterson 1984). Note that CO_2 saturation and Cl decrease with height in the Navajo sandstone consistent with inputs of CO_2 and CO_2-saturated brines from the adjacent fault at depth.

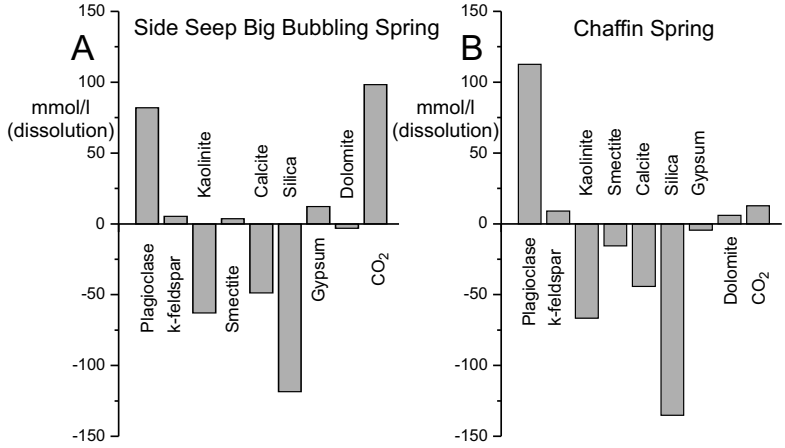

Figure 16. Modal changes in minerals necessary to account for changes in spring water chemistry between the upstream well (Airport Well) and A) Side Seep Big Bubbling Spring and B) Chaffin Spring.

of independent components—which is nine in this study—so that muscovite and other minor phases are ignored. The composition of the solid phases is constrained by limited analyzes on core chips from exploration wells in the Green River area (Kampman et al. 2009) and analyzes of core and outcrop elsewhere in the Paradox Basin (especially by Zhu et al. 2006). Fine-grained illite-smectite is difficult to analyze and the analysis used by Kampman et al. (2009) is derived from electron microprobe analyzes of grain coating clays in the core chips. Petrological observations in the Green River drill hole indicate that the Navajo sandstone contains an earlier diagenetic Fe-poor dolomite and later carbonates are iron-bearing dolomites but little or no calcite. This contrasts with the travertines and associated carbonate veins where calcite and aragonite are abundant. The iron is probably derived from dissolution of the hematite grain coatings as discussed further below. A further complication is that spring waters contain variable fractions of the brine associated with the CO_2 inputs. This has been accounted for by assuming that Cl is brine derived and that the brine composition is that of the brines sampled from the Paradox Formation (Spangler et al. 1996). Exchangeable cations have not been taken into account.

Total dissolved inorganic carbon (DIC) was analyzed in the fluids sampled at the surface springs which will have lost CO_2 by the degassing associated with the cold-water geysering. Assayag et al. (2009) argue that the carbon-isotopic systematics of Crystal Geyser require shallow degassing but the samples collected downhole in the Green River Drillhole (Fig. 15) indicate the fluids are close to CO_2 saturation. The uncertainty in fluid DIC contents maps directly onto the estimates of CO_2 consumed and impacts estimates of the extent of fluid-mineral thermodynamic disequilibrium discussed further below.

Zhu (2000, 2005) made a comparable study of fluid composition gradients in the Navajo sandstone in north-eastern Arizona where there are no deep CO_2 inputs. The results again indicate dissolution of plagioclase and K-feldspar and precipitation of kaolinite, smectite, silica and calcite and variable precipitation/dissolution of gypsum. Zhu (2005) also observed significant input of Na from, and loss of Ca to, exchangeable sites on clay minerals. The rates of mineral dissolution inferred by Zhu are discussed further below.

It is clear that a complete model of the fluid-mineral reactions will require both modeling of changes in fluid chemistry in conjunction with a full understanding of the petrology of the

sandstone aquifer in which it will be essential to distinguish reaction products related to the present phase of alteration from earlier detrital and diagenetic phases.

Fluid-mineral reaction rates in the Navajo Sandstone. Fluid mineral reaction rates can be calculated, given the stoichiometry of the fluid-mineral reactions, if the surface areas of the minerals involved and the flow rate and porosity of the aquifer is known. Estimating mineral surface areas is one of the more problematic aspects of determining mineral dissolution kinetics. White and Brantley (2003) used a compilation of measurements by gas adsorption (BET) and geometric surface areas assuming spherical grains to show that the ratio of BET to geometric estimates of surface areas for most minerals, termed "surface roughness," ranged from ~ 4 to ~ 800 and was a function of the time the minerals were exposed to chemical weathering. Peters (2009) and Landrot et al. (2012), using a range of high resolution imaging techniques, showed that the apparent accessible surface areas of minerals were between 1% and 80% of the mineral surface area. Landrot et al. (2012) also estimated total mineral reactive surface areas as 40% of the area deduced from BET measurements. However the imaging techniques are still limited by their resolution. Kampman et al. (2009) assumed BET mineral surface areas were the same as those measured by Zhu (2005) on whole rock samples of the Navajo sandstone from north-eastern Arizona which had clay minerals removed by ultrasonic washing. These estimates (mean 0.7 ± 0.2 1σ m^2/g) are only ~ a factor of 30 more than the geometric surface area of 0.1 mm grains (Zhu 2005) but the estimates of the plagioclase and K-feldspar surface areas are based on the assumption that the feldspars have similar surface areas to the average of the quartz-dominated mineralogy and that their surfaces areas can then be calculated from their modal proportions in the sandstone. Since the surface areas of unreactive quartz is likely to increase at a much slower rate than the feldspars, the BET estimates of the feldspar surface areas in the Navajo are likely to be minimum values. The correlation between weathering age and surface area from White and Brantley (2003) would indicate surface roughness factors up to ~ 300, an order of magnitude higher than assumed in the feldspar dissolution rate estimates for the Navajo sandstone by Zhu (2005) and Kampman et al. (2009). This potential order-of-magnitude uncertainty in the field reaction rates dominates the uncertainty estimates.

Flow rates in the aquifer are calculated from hydraulic conductivity measurements made on widely distributed core samples of the Navajo sandstones (Hood and Patterson 1984; Weigel 1986; Weiss 1986) and the hydraulic head measurements in the numerous boreholes in the area (Hood and Patterson 1984). Potential sealing along the segments of the Little Grand Wash and Salt Wash Graben faults at maximum throw across the crest of the Green River anticline (Dockrill and Shipton 2010) may divert the flow paths along the faults.

Groundwater flow trajectories for fluid feeding individual springs is estimated from the topology of the potentiometric surface in the Navajo Sandstone, constrained by data from widely distributed groundwater wells, taking into account deflection of the flow paths close to sealing portions of the faults (Hood and Patterson 1984). Complexities in the flow paths of groundwater feeding individual springs, and heterogeneous fluid flow, may result in some uncertainty in the flow path length. However, such certainties are actually small compared to the order of magnitude uncertainties in mineral surface areas.

The increase in the molar fractions of plagioclase and K-feldspar dissolved by the Navajo waters with flow path distance are illustrated in Figure 17. The curves exhibit a monotonic increase in the dissolution of both minerals but with a marked inflection where the flow path intersects the Salt Wash Graben. This reflects inflections at the same point in the cation and pH profiles (Fig. 13) and is interpreted to indicate addition of CO_2 to the Navajo waters at the Salt Wash Graben. The observations at Crystal Geyser and the nearby Green River Drillhole suggest significant CO_2 is also added at the Little Grand Wash Fault but spring density over

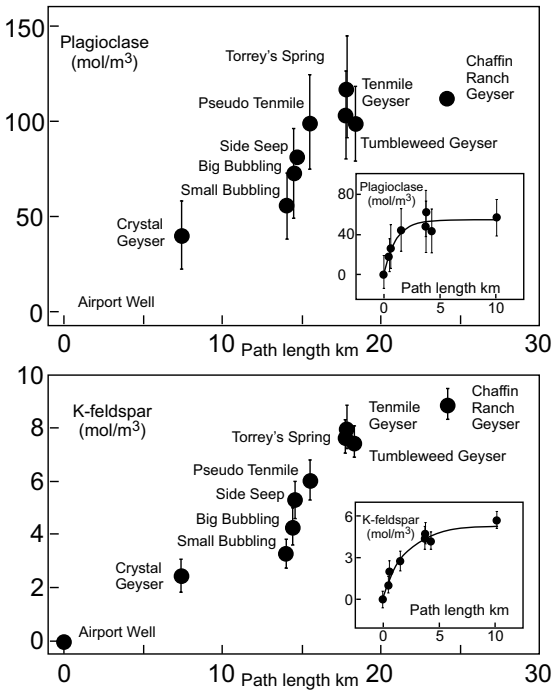

Figure 17. Variation in moles of plagioclase and K-feldspar added to fluids against flow path distance from upstream Airport Well. Note the inflection at 14.8 km where CO_2 is thought to be introduced at the Salt Wash Graben (cf. Fig. 15). Insets show best fit exponential curves (Eqn. 17) to feldspar modes downstream of Small Bubbling spring. [Used by permission of Elsevier, redrawn after Kampman et al. (2009) Fig. 6.]

this upstream section of the flow path is insufficient to properly determine gradients of mineral dissolution rates with distance. Mineral dissolution rates are calculated from the gradient of mineral modes with time where time is estimated from the flow rates and distance. Kampman et al. (2009) fitted empirical exponential curves to the variation of mineral modes with distance of the form

$$M_j = A(1-\exp^{-Bz}) \tag{17}$$

where M_j is the concentration of mineral j (mol/L), z is distance down the flow path from Small Bubbling spring at Salt Wash Graben and A and B are constants defined by the best fits (insets on Fig. 17). Equation (17) can then be differentiated to give the rate of change of the mineral mode with distance, i.e.

$$\frac{\partial M_j}{\partial z} = AB\exp^{-Bz} \tag{18}$$

The differential equation describing how the molar concentration of a component will vary with time in a flowing system may be written

$$\phi\frac{\partial M_j}{\partial t} = R_j S_j - \omega_0 \phi \frac{\partial M_j}{\partial z} \tag{19}$$

where R_j is the reaction rate (mol m^{-2} s^{-1}) and S_j is the surface area (m^2/m^3) for phase j, ϕ is the porosity and ω_0 the fluid velocity. For flow systems where S_j varies slowly with time and reaction rates are sluggish such that the term $\varphi(\partial M_j / \partial t)$ is small compared with the other terms, Equation (19) may be approximated by (the quasi-stationary state approximation, Lichtner 1988),

$$\frac{\partial M_j}{\partial z} = \frac{R_j S_j}{\omega_0 \phi} \tag{20}$$

where $\omega_0\phi$ is the fluid flux calculated from the hydraulic conductivity and hydraulic head. Equation (20) allows calculation of the reaction rate, R_j which for plagioclase and K-feldspar are compared to a range of laboratory and field estimates in Figure 18. This shows that the rates estimated for Green River span the range of estimates for field rates although up to two orders of magnitude faster than rates in the Navajo sandstone in an area where CO_2 is absent (Zhu 2005). The far-from-equilibrium laboratory rates are characteristically two or more orders-of-magnitude faster. The calculated reaction rates in such field settings are subject to a number of uncertainties. The error bars on the Green River results on Figure 19 include the uncertainties on chemical analyzes and estimates of the hydrological petrological parameters used in Equation (20). However the real uncertainties include both these errors and a number of potential systematic uncertainties that are hard to evaluate. In the Green River example these include: 1) The well-known discrepancies in estimates of mineral surface areas between gas adsorption (BET) and geometric measurements discussed above. 2) How well BET-measured surface areas represent the mineral reactive surface areas and how the BET-measured surface areas partition between the different minerals when measured on bulk samples. 3) The uncertainty which propagates from that of the modal proportions of the minerals and porosity

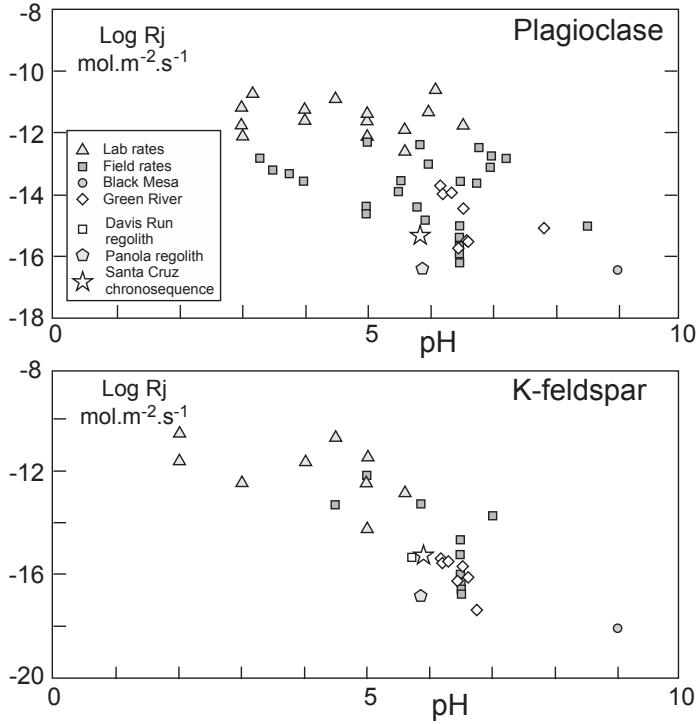

Figure 18. Variation in feldspar dissolution rate versus pH for a compilation of laboratory (White and Brantley, 2003) and *in situ* dissolution rates (Maher et al. 2009; Malmstrom et al. 2000; White and Brantley 2003; White et al. 2001), feldspar dissolution rates in the Navajo Sandstone at Black Mesa (Zhu 2005), and the rates calculated at Green River. [Used by permission of Elsevier, redrawn after Kampman et al. (2009) Fig. 7 with additional data.]

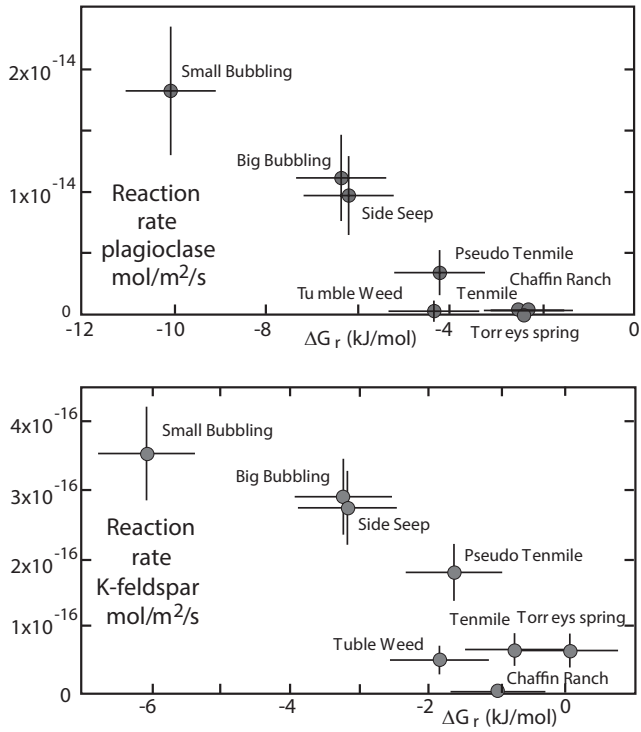

Figure 19. Dissolution rates for plagioclase and K-feldspar from Green River against degree of disequilibrium. Error bars 1σ. [Used by permission of Elsevier, redrawn after Kampman et al. (2009) Fig. 8.]

in the bulk rock. For example Kampman et al. (2009) estimate mineral modal proportions from their measurements of mineral compositions and analyzes of Navajo sandstone whole rock compositions by least-squares solution to the mass balance equations which introduce additional uncertainties arising from both the mineral and whole rock analyzes, and more fundamentally, from the limitation on the number of minerals so modeled to the number of stoichiometric chemical components in the minerals. 4) The estimates of the porosity, permeability and composition and mineralogy of the Navajo sandstone are compiled from measurements on samples taken with a regional distribution. All these parameters are likely to show both regional variations and local heterogeneities. Further information on the Navajo sandstone is now available from core sampled in the 2012 drillhole and the implications of this is discussed further below. 5) The uncertainties on the geometry of the flow path and fluid flux estimated from the regional hydraulic head measurements and with simple treatment of local complexities such as the fault systems.

Reaction rates and approach to equilibrium. It is axiomatic that reaction rates will tend to zero as equilibrium is approached and there are now a number of studies that have made quantitative estimates of the relationship between feldspar dissolution rates and the degree of fluid-mineral thermodynamic disequilibrium under field conditions (e.g., White and Brantley 2003; Kampman et al. 2009; Maher et al. 2009; Moore et al. 2012).

The estimates of the Green River feldspar reaction rates on thermodynamic disequilibrium nicely illustrate this reaction rate dependence. The degree of thermodynamic disequilibrium for a reaction where *a* moles of component A plus *b* moles of B react to give *c* moles of C and

d moles of D, i.e.,

$$aA + bB = cC + dD \tag{21}$$

is calculated as the Gibbs free energy of reaction, ΔG_r (kJ/mol) (see Drever 1997, Ch, 2 for a full discussion), where

$$\Delta G_r = \Delta G_R^0 + RT \ln\left[\frac{a_C^c a_D^d}{a_A^a a_B^b}\right] \tag{22}$$

where ΔG_r is the free-energy of reaction for the components at the adopted standard state, R is the gas constant (kJ K^{-1} mol^{-1}), T is absolute temperature (K) and a_J^j is the activity of component J raised to the power j where the component might be part of a solid phase or in solution in the water phase. The equilibrium constant K_{eq} is defined as the product of activities at *equilibrium*, i.e.

$$K_{eq} = \frac{a_C^c a_D^d}{a_A^a a_B^b} = e^{\frac{-\Delta G_R^0}{RT}} \tag{23}$$

from which it follows that the degree of thermodynamic disequilibrium is given by

$$\Delta G = RT \ln\left[\frac{IAP}{}_{eq}\right] \tag{24}$$

where *IAP* is the ion activity product and log (*IAP/K*) is defined as "*the saturation index*."

For Green River, Kampman et al. (2009) modeled the plagioclase-fluid equilibrium as

$$Na_{0.62}Ca_{0.38}Al_{1.38}Si_{2.62}O_8 + 2.76H^+ + 5.24H_2O = 0.62Na^+ + 0.38Ca^{2+} + 1.38Al(OH)_2^+ + 2.62H_4SiO_4 \tag{25}$$

and the K-feldspar fluid equilibrium as

$$K_{0.95}Na_{0.05}AlSi_3O_8 + 6H_2O + 2H^+ = 0.95K^+ + 0.05Na^+ + Al(OH)_2^+ + 3H_4SiO_4 \tag{26}$$

Kampman et al. (2009) used equilibrium constants calculated from published thermodynamic sources and calculated the distribution of aqueous species and their activities using the computer code and database PHREEQC (Parkhurst and Appelo 1999). Thus the ion activity products are given by

$$IAP_{plag} = \frac{a_{Na^+}^{0.62} a_{Ca^{2+}}^{0.38} a_{Al(OH)_2^+}^{1.38} a_{H_4SiO_4}^{2.62}}{a_{H^+}^{2.76}} \tag{27}$$

$$IAP_{Kspar} = \frac{a_{K^+}^{0.95} a_{Na^+}^{0.05} a_{Al(OH)_2^+}^{1.38} a_{H_4SiO_4}^{3}}{a_{H^+}^{2}} \tag{28}$$

Dissolution rates for plagioclase and K-feldspar are plotted against the degree of disequilibrium in Figure 19 and show the expected decrease in dissolution rate with decrease in degree of disequilibrium and that these waters are close to equilibrium. The observation that feldspar dissolution takes place near to equilibrium reinforces similar observations on dissolution rates in natural settings (Stefansson and Arnorsson 2000; White and Brantley 2003; Maher et al. 2009; Moore et al. 2012). It reinforces the importance of knowing the form of dissolution-rate dependence as a function of degree of disequilibrium in modeling mineral reactions at low temperature.

The Green River data is compatible with laboratory studies which suggest rate laws which exhibit an exponential decrease in the gradient as equilibrium is approached such as the experiments of Hellmann and Tisserand (2006) shown in Figure 20. This contrasts with the predictions of the simplest rate law, the linear transition state theory (TST) rate law in the form originally proposed by Aagaard and Helgeson (1982) as illustrated in Figure 20, which predicts an exponentially increasing rate of decrease in reaction rate as equilibrium is approached. The other field studies which have modeled dissolution rates, most notably Maher et al. (2009), have come to a similar conclusion.

However, there are a number of assumptions in the calculation of the feldspar dissolution rates at Green River by Kampman et al. (2009) which should be questioned. The adoption of hydraulic conductivity measurements, mineral surface area measurements, bulk rock composition and mineral compositions from either elsewhere in the Paradox Basin or from measurements on limited drillcore most likely results in systematic errors in the Green River data. However these errors are unlikely to change the general relationship between degree of disequilibrium and reaction rate. Another potential uncertainty is the significance of the analysis of Al concentrations on waters filtered through 0.2 μm filters. Colloidal and very fine particulates may pass through such filters and the magnitude of the dissolved Al concentrations may have been over estimated. However reducing the activity of $Al(OH)_2^+$ by an order of magnitude only makes ΔG_r of the plagioclase dissolution reaction more negative by about 7 kJ/mol.

A more important assumption is the use of pH measurements made at surface. The presence of geysers shows that CO_2 degassing occurs as the waters rise to the surface which would raise pH dependent on the magnitude of the degassing. The downhole fluid samples taken at pressure in the Green River Drillhole revealed that fluids in the Navajo sandstone near the Little Grand Wash fault were saturated with CO_2 or close to saturation, with pH values a unit less than measured at surface at the Green River drillhole site and at the nearby Crystal Geyser. Substituting a downhole pH of 5.2 into Equation (27), rather than the surface values of between ~ 6.1 to 6.8, makes ΔG_r more negative by about 15 to 20 kJ/mol. It is unlikely that the waters remain saturated in CO_2 away from the faults which introduce the CO_2 and the waters in the Green River drillhole exhibit significant gradients in pH and CO_2 saturation across the ~ 120 m

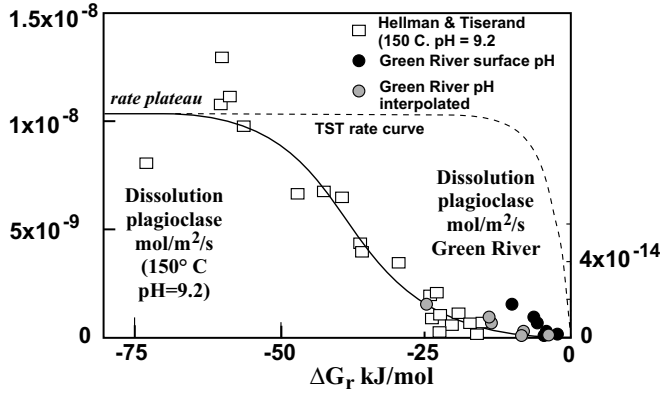

Figure 20. Albite dissolution rates from laboratory experiments by (Hellmann and Tisserand 2006) (left axis) at 150 °C and pH = 9.2 (open squares) compared with rates from Green River (right axis) taking 1) surface pH measurements (filled circles) and 2) assuming CO_2-saturated pH of 5.2 from the Green River drillhole for upstream Small Bubbling spring with linear interpolation to surface pH value for downstream Torrey's spring (grey circles). Broken line shows calculated dissolution rates as a function of ΔG_r from the simplest transition state theory (Hellmann and Tisserand 2006).

thickness of the formation (Fig. 15). Figure 20 illustrates how the ΔG_r estimates would be altered by the extreme assumption that the waters at Small Bubbling spring, the upstream well of the section used to calculate reaction rate, were CO_2 saturated and saturation decreased downstream at a rate proportional to the decrease in ΔG_r so that the most distal spring, Torrey's spring, had a downhole pH equivalent to that measured at the surface. This would stretch the profile, as illustrated in Figure 20, but not change the fundamental observation that reaction rate was dependent on approach to equilibrium and that reaction rate varied relatively slowly with degree of disequilibrium in the close-to-equilibrium region of these natural samples.

The uncertainty in ΔG_r resulting from the pH measurements is of a comparable magnitude to the uncertainty introduced by using laboratory derived feldspar dissolution equilibrium constants to predict the position of thermodynamic equilibrium in natural systems. The wide compositional variability in feldspar (and other silicate mineral) solid solutions (e.g. Ca-Na-K contents and Al-Si ordering) results in a large thermodynamic range in mineral solubility, with the anorthite end-member being orders of magnitude more soluble than that of albite (e.g. Arnorsson and Stefansson 1999). In addition there are multiple complexities inherent in the measurement of silicate mineral equilibrium constants at low temperature that include; the difficulty in attaining equilibrium in the experiments, uncertainty in the presence and role of precursor species on the mineral surface, variation in Al-Si ordering, the complex speciation of Al at low and intermediate pH, and the role of complexing ions and ligands present in natural waters that are not accounted for in the laboratory experiments. Thus, thermodynamic equilibrium constants from different experiments are often applicable only to a very specific range of fluid compositions and conditions, and measurements at comparable thermodynamic conditions frequently do not agree. Further measurements of the silicate mineral thermodynamic constants are critically needed to accurately model fluid-mineral reactions in CO_2 reservoirs.

Several authors have emphasized that clay mineral precipitation rates are important in controlling silicate mineral dissolution rates (e.g., Maher et al. 2009; Zhu and Lu 2013). Since Al solubility is very small, clay mineral precipitation rates must essentially balance feldspar dissolution rates. The dissolved concentrations of Na, Al and Si in conjunction with the other cations will increase to a quasi-steady state at which the thermodynamic overstep of the clay mineral precipitation reactions will drive their precipitation at a rate which balances the thermodynamic understep of the feldspar dissolution reactions. Figure 21 illustrates the estimated rate of kaolinite precipitation as a function of ΔG_r for both the measured pH at surface and the downhole value of 5.2, considered the minimum possible and almost certainly an underestimate for the more downstream sites. There is a general correlation between precipitation rate and ΔG_r although the scatter in ΔG_r probably reflects systematic uncertainties related to estimates of surface areas, mineral modes and fluid CO_2 concentrations.

It is clear that a more robust recovery of dissolution rates from the Green River analogue site would require a series of drill holes to recover core and fluids from the Navajo sandstone along the flow path.

The Green River Drill Hole - revision of inferences from surface sampling. The drilling, coring and fluid recovery from the Green River Drill Hole in 2012 offered an important chance to test some of the inferences made from the surface sampling. This work will allow analysis of fluids sampled at pressure and a set of mineralogical and petrological measurements on core recovered from the Navajo sandstone at Green River, rather than inferring the Navajo sandstone properties from samples collected from more distal sites in the Paradox basin. The hole was drilled west of the Green River just north of the Little Grand Wash Fault and thus close to an inferred source of CO_2. Much of the planned work on the drill core is yet to be completed at the time of writing. However important initial observations include 1) that the fluids are saturated or close to saturation with CO_2 at hydrostatic pressures (Fig. 15, Kampman et al. 2013b) resulting in a maximum uncertainty in ΔG for the plagioclase dissolution reaction

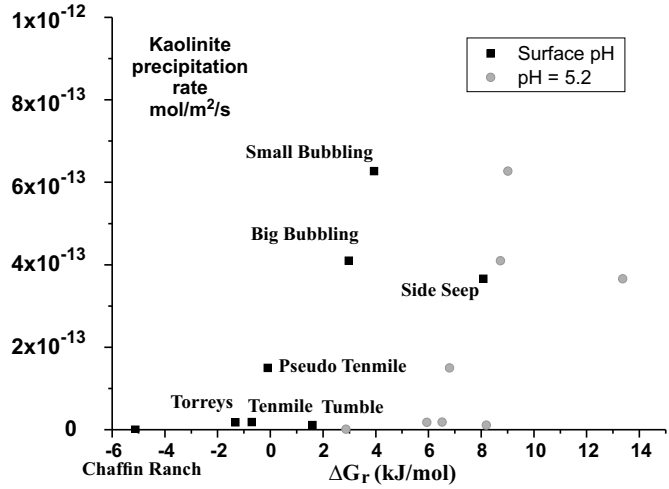

Figure 21. Kaolinite precipitation rate versus degree of over saturation calculated from stoichiometry of sampled fluids at Green River and estimates of clay mineral surface areas in the northern Paradox Basin by Zhu (2005). ΔG_r calculated assuming surface pH measurements (black squares) and pH from Green River Drillhole samples (grey squares). The latter almost certainly underestimates pH especially in the more downstream samples.

of ~ 20 kJ/mol, 2) the carbonate phases encountered in the drill core are predominantly Fe-bearing dolomites rather than the calcites predicted to be precipitated by the modeling of the fluid, and 3) basal Carmel Formation caprock to the Navajo sandstones and intra-formational aquitards in the overlying Entrada sandstone are highly cemented by carbonate inferred to have been precipitated by CO_2-rich fluids reacting with silicate minerals or degassing CO_2 as a consequence of decompression (Kampman et al. 2013a). A further important observation made by Bickle and Kampman (2013) based on the CO_2 contents of the sampled fluids, is that the mass of CO_2 removed by flow along the Navajo sandstone is about 20× the rate of natural leakage at the surface from the fault system estimated by U-Th dating of travertines (Burnside et al. 2013). If similar amounts of CO_2 are removed where the faults intercept the Wingate and White Rim sandstones, major aquifers below the Navajo sandstone, then only ~ 0.01% of the CO_2 introduced at depth leaks at surface. Such a low surface leakage rate should be acceptable from geological storage sites (Hepple and Benson 2005). It should also be noted that the open abandoned drill hole at Crystal Geyser leaks CO_2 at ~ 50× the natural leakage rate along the fault (Burnside et al. 2013).

Surface exposures of bleached sandstones at Green River: a Palaeo-CO_2 reservoir? Occurrences of bleached sandstones in the Paradox Basin where the bleaching fluid is thought to have been caused by CO_2-saturated brines are reviewed in the discussion of specific natural analogue sites above. At Green River the Entrada sandstone, part of the San Rafael Group, is exposed in the northern footwall of the Salt Wash Graben around its intersection with the Green River anticline (Fig. 12). Here the lower part of the Entrada sandstone is bleached white in marked contrast to the normal red sandstone (Fig. 22). The bleaching occurs in a broad domal structure which reaches ~ 20 m thick at the crest of the Green River anticline, extends to the limit of exposure of the Entrada sandstone a few hundred meters west of the anticline and dies out in a series of ~ 30 cm-thick fingers ~ 2 km east of the anticline (Fig. 23B). The bleaching probably also thins and dies out to the north but exposures are limited to short gulleys eroded into the east-west cliffs that expose the Entrada sandstone north of the Salt Wash Graben. The nearly continuously exposed upper contact of the bleached sandstone is sharp and cuts gently

down the stratigraphy to the East (Fig. 22). Near the crest of the anticline a series of closely spaced fractures acted as a fluid pathway allowing the bleaching fluids to escape upwards (Fig. 22) and bleaching also extends laterally away from small vertical fractures which extend up from the main sub-horizontal bleaching front (Fig. 23A).

Wigley et al. (2012, 2013a) argue that the bleaching is due to migration of CO_2-charged brines away from the Salt Wash graben fault as discussed below and in the review on exhumed CO_2 reservoirs above (Fig. 24). This allows us to study the petrography of the fluid mineral reactions in detail, put constraints on the rates of the reactions and examine the mobility of metals which might contaminate potable aquifers.

Wigley et al. (2012) describe the petrological changes across from the red sandstones to the bleached sandstone. The Entrada sandstone is a fine to medium grained aeolian deposit which exhibits large scale cross-bedding. The unaltered sandstone is quartz-rich with ~ 12% K-feldspar, 4.5% plagioclase and carbonates comprising an Fe-poor calcite and dolomite post-dated by a ferroan dolomite. Grain coatings of hematite and goethite give the sandstone its characteristic red color and are coated in turn by illite-smectites, minor kaolinites and euhedral quartz overgrowths. In the bleached samples the iron oxide grain coatings have been removed which is reflected in a drop of total Fe from between 0.9 to 0.8 wt% in the unbleached sandstone to ~0.6 wt% in the bleached sandstone (Fig. 26). The bleached sandstones have less K-feldspar (3% vs. 6%) and more carbonate (10% vs. 5.3%) than the unbleached rock, and mixed Fe-Ti oxides in the unbleached samples have recrystallized to pure Fe or Ti oxides. In the fault zone (Fig. 22), presumed to be more intensely altered, K-feldspar is reduced to 2.7% and carbonates increase to 18%. The faults and fractures also contain narrow gypsum veins, occasional calcite veins and bands of coarse Fe-oxides which occasionally preserve pyrite cores. The continuity of the fracture-associated bleaching with the large scale bleaching and their similar petrological and stable isotopic compositions are consistent with both being caused by the same fluids.

The nature of the fluids which cause bleaching in the Navajo sandstone is disputed. Chan et al. (2000, 2011) and Beitler et al. (2005) have argued for leaching of the Fe-oxide coatings by reduced fluids containing hydrocarbons, methane, organic acids or hydrogen sulfide. Kettler et al. (2011) and Loope et al. (2010) argue that bleaching in some of the localities described by Chan et al. (2000) was by CO_2-charged brines. Of course bleaching is probably caused by different fluids in different places.

Wigley et al. (2012) argue that the fluids responsible for the bleaching of the Entrada at Green River were CO_2-charged for the following reasons:

- The bleaching is adjacent to a fault known to have been associated with CO_2 escape for > 400 ka.
- Bleaching is towards the base of the Entrada sandstone consistent with higher density of a CO_2-charged fluid. It should be noted that in the outcrops reviewed by (Chan et al. 2011) they argue bleaching is by a lower-density fluid.
- Fluid inclusions in the quartz overgrowths and gypsum veins petrographically linked to the bleaching contain CO_2 and some contain minor CH_4.

Calcite cements from the bleached Entrada sandstone have heavy $\delta^{13}C$ and $\delta^{18}O$ isotopic compositions compared with other bleached Jurassic sandstones from the Paradox basin but more comparable with those of the aragonite veins in the travertine mounds formed by the present-day CO_2 geysers.

Reaction stoichiometry and spatial distribution. Iron is soluble in relatively reduced fluids at lower pH values (Fig. 25). Wigley et al. (2012) calculated that a reductant was necessary to maintain relatively reducing conditions as hematite was dissolved, otherwise the fluid would

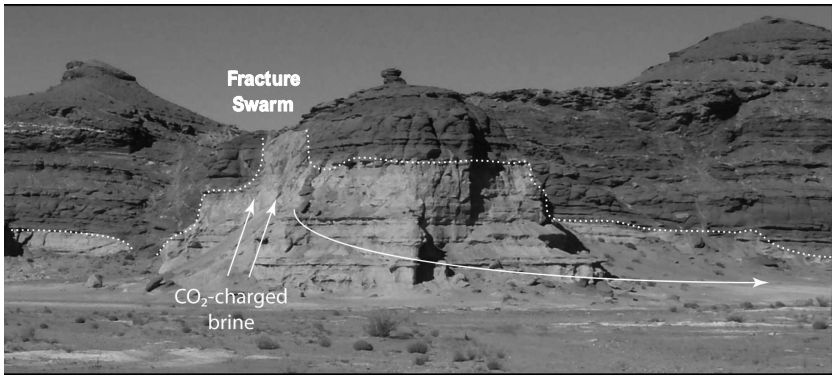

Figure 22. View of large scale bleaching at crest of Green River anticline. Note 1) upwards escape structure associated with numerous fractures, 2) that the bleaching occurs along the base of the Entrada (the top of underlying Carmel Formation is exposed at about the level of the base of the cliff and 3) how the top of the bleached zone (horizontal contact) cuts down across the bedding. [Used by permission of the Geological Society of America from Wigley et al. (2012), Fig. 1B.]

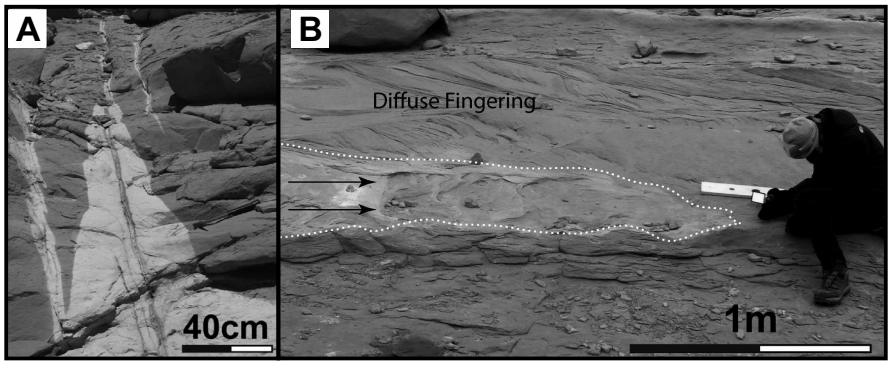

Figure 23. A) vertical aragonite and gypsum vein with bleaching of its wall rock and B) outcrop at Eastern limit where bleaching terminates as a series of bedding-unit confined fingers (outline of finger emphasized by dotted line).

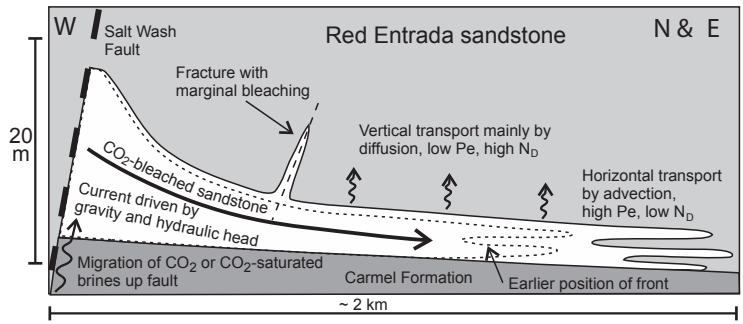

Figure 24. Diagramatic illustration of inferred flow of CO_2-charged brine away from fault at Salt Wash Graben. [Used by permission of Elsevier. Redrawn after Wigley et al. (2013a), Fig. 2A.] Flow is driven north and east by density contrast and regional hydraulic gradient in the Entrada sandstone.

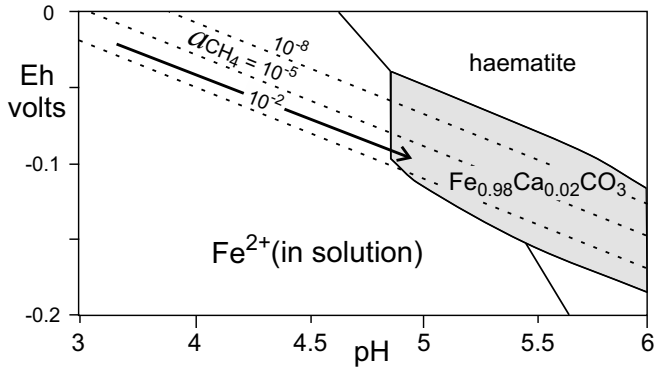

Figure 25. Stabilities of hematite and siderite in Eh-pH space redrawn from calculations using PHREEQC (Parkhurst and Appelo 1999) at a_{Fe} = 0.005, a_{Ca} = 0.01 and total C = 0.1 mol/L. Dotted lines contours of methane activities. Arrow shows path taken by fluid with initial pH = 3.5, Eh = 0.02 reacting with hematite. [Used by permission of the Geological Society of America. Redrawn after Wigley et al. (2012), Fig. 5.]

be rapidly oxidized and minimal hematite dissolution would take place. Since methane was present in the analyzed fluid inclusions this was implicated as the reductant and the calculated reaction trajectory in Figure 25 modeled with the stoichiometry

$$20Fe_2O_3 + 5CH_4 + 64CO_2 + 19H_2O + 11H^+ = 30Fe_2^{+} + 10FeHCO_3^{+} + 59HCO_3^{-} \quad (29)$$

with a_{Ca} fixed at 0.01 and the hematite and siderite phase boundaries calculated for total C = 0.05 mol/L and a_{Fe} = 0.005. If the fluid CO_2 content is reduced below 0.025 mol/L siderite is no longer a potential reaction product and magnetite is stable. The reaction predominantly consumes CO_2 with minor CH_4 consumption despite the trace CH_4 (> 10^{-4} mol/L) being needed to maintain reducing conditions. Sulfur was not included in this modeling as pyrite weathers rapidly in the surface environment. The presence of pyrite and gypsum veining in the cores of veins associated with bleaching, pyrite in the fresh core of the Navajo sandstone from the Green River Drill Hole, and ~ 19 mmolar SO_4 concentrations in the fluids sample in the Navajo sandstone in the Green River Drill Hole (Kampman et al. 2013b) demonstrate that the fluids did contain sulfur and the role of H_2S as a reductant remains to be evaluated. However S-bearing aqueous fluids in equilibrium with pyrite have very low Fe^{2+} concentrations (e.g., Drever 1997, Ch. 7) which would be unable to transport Fe in solution. It is possible that subordinate amounts of sulfur are removed from the fluid by precipitating pyrite.

The petrography and geochemical profiles across the bleaching fronts are consistent with Equation (29) and the phase relations in Figure 25. The horizontal bleaching front exhibits a 1 to 2 cm thick zone of finely intergrown Fe-oxides and carbonate phases precipitated just upstream of the bleached-red contact which is responsible for the spikes in bulk-rock Fe, Ca, Mg and Sr concentrations (Fig. 26). Wigley et al. (2013a) explained these spikes as a consequence of rapid increases in the saturation indices of hematite and carbonate (calculated as calcite) at the front due to the complex interactions between advective transport and diffusive gradients in chemical species.

The equation describing advective and diffusive transport of an aqueous species can be written (Bickle and McKenzie 1987),

$$\phi\frac{\partial C}{\partial t} = D\tau\phi\frac{\partial^2 C}{\partial x^2} - \omega\phi\frac{\partial C}{\partial x} \quad (30)$$

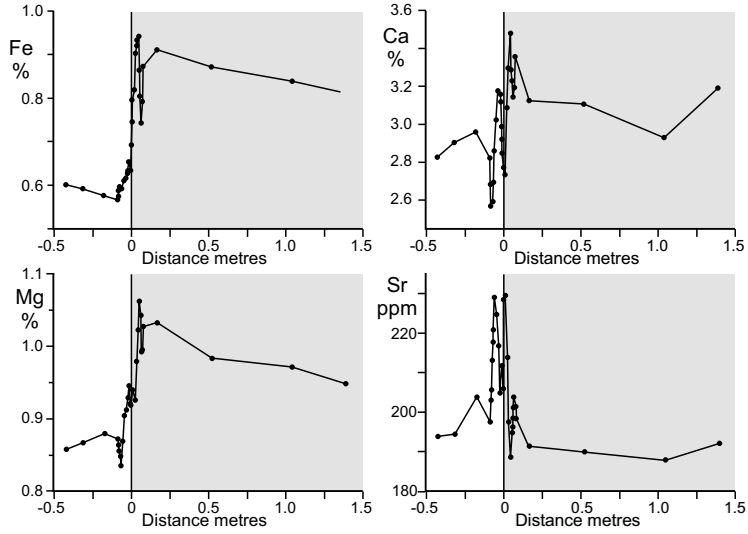

Figure 26. Chemical profiles across the "horizontal" bleached-red transition. Replotted using data from Wigley et al. (2012). Lines join adjacent samples. Note enrichments just downstream of front which reflects precipitation of fine grained Fe-oxides and carbonates. Positive x into red sandstones.

where C is the concentration of the tracer in the fluid phase, t is time, x is distance from the reaction front, D is diffusivity of the aqueous species and τ is tortuosity. Tortuosity arises from the additional path length required for diffusion through a porous medium and has been calculated as $\tau = 0.5$ for cubic packed spheres (Wyllie and Rose 1950) and is likely less than this in natural sandstones where determination of the interconnected pore structure would be necessary for its calculation.

Where the reaction front is moving slowly the term in $\phi(\partial C / \partial t)$ can be ignored and a solution to Equation (30) is of the form

$$C = C_1 + (C_0 - C_1) e^{-\frac{\omega}{D\tau}x} \tag{31}$$

where x is distance from the front, C_0 the concentration on the front and C_1 the concentration as $x \rightarrow \infty$. The pH and Eh downstream of the front will be buffered by the hematite-carbonate assemblage and these signals will diffuse upstream. Assuming a calcite-saturated and Fe-bearing fluid impinge on the front from upstream, Fe and Ca will diffuse downstream. The saturation indices for calcite (or siderite) and hematite can then be calculated from thermodynamic programs and datasets (e.g., PHREEQC). Figure 27 illustrates these showing asymmetric spikes in the saturation states of hematite and calcite. Calculation of mineral modal profiles taking into account mineral dissolution, transport and precipitation with kinetically sluggish reactions requires a numerical solution. Wigley (2013) shows that these predict spikes in Fe-oxides and carbonate and the size and location of these evolve both with time and are sensitive to the physical and thermodynamic parameters controlling transport and reaction.

Transport of trace metals. Figure 28 illustrates trace metal profiles across the horizontal bleached profile after Wigley et al. (2013b). All these metals show one or more distinct spikes in concentration within 10 cm of the red-bleached contact and the spacing of these is thought to be related to their pH adsorption edges at which the metal partitions onto clays and Fe-oxides (Fig. 29). All the metals are soluble at lower pH values (e.g., Benjamin and Leckie 1981) and

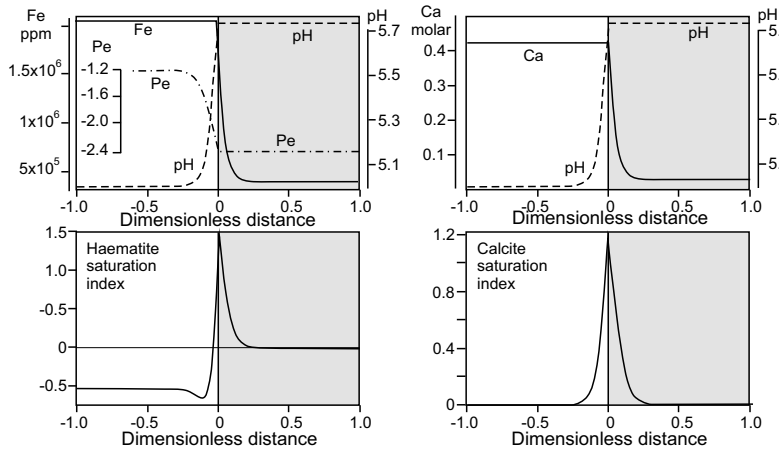

Figure 27. Diffusion model showing fluid compositions (Fe, Ca, pH and oxidation state, Pe) and calculated saturation indices for hematite and calcite. Calculated for a Peclet number = 30 with the length scale taken as 1 meter, that is a fluid velocity of 1 m/yr and diffusivity for components in the fluid of 10^{-9} m^2/s. Positive x into red sandstones.

are presumed to be dissolved from grain coatings at the low pH of the bleaching fluid and redeposited at the front as the pH rises. Wigley et al. (2013b) used leaching experiments to show that the majority of the trace metals in the samples with enriched spikes were associated with the carbonate and Fe-oxide phases. Arsenic (Fig. 28E) is of interest as it is one of the more toxic metals and is sensitive to oxidation state as well as pH.

It is possible to use the enrichment of metals at the contact, combined with the measurements of the relative depletion of the metals in the bleached zone to calculate the thickness of bleached zone from which the metals are removed. The estimates for several metals are shown in Figure 28F and indicate depletion of ~ 25 cm, rather less than the thickness of the bleached zone of 5 to 20 meters. The metals are likely to have also been removed by advective transport parallel to the main horizontal contact.

There is considerable concern that migration of CO_2 into potable aquifers could mobilize these potentially toxic trace metals. There are two critical questions: 1) are the trace metals quantitatively deposited when the pH rises across reaction fronts and 2) do the concentrations in formation waters reach levels above those permitted for drinking waters? The bleaching adjacent to veins where width of rock bleached is known, and advection and diffusion are likely to be predominantly away from the vein, allows quantification of the fraction of the metals deposited at the bleaching fronts. Estimates of this fraction given by Wigley et al. (2013b) range from 0.4 ± 0.3 to 1.8 ± 0.8 (1σ uncertainties) with less-well constrained examples between 2.8 ± 1.7 to 3.4 ± 2.4. The large uncertainties arise from the relatively small differences in background values in bleached and red sandstones coupled with the scatter in these values but in general it appears that the trace metals are quantitatively redeposited. It is also possible to estimate maximum fluid concentrations from the mass of metal deposited at the front and the ratio of the front velocity to the fluid flux. The relative front velocity is calculated from the stoichiometry of the hematite dissolution reaction (Eqn. 29) which gives a retardation factor of ~25 for likely fluid pH, Pe and CO_2 concentrations (Wigley et al. 2013b). The mean concentration in the fluid (C_f) is then given by

$$C_f = \frac{\mathrm{M}}{TIFF} \tag{32}$$

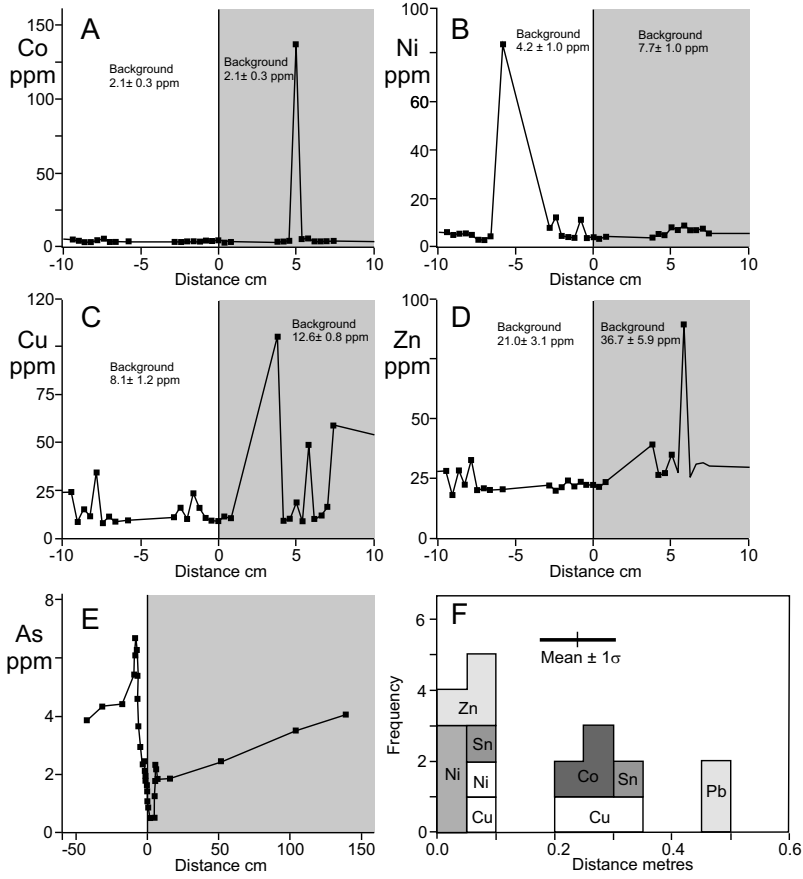

Figure 28. A - E) Trace metal profiles across bleached to red sandstone contact (+ve distance into red sandstone) from transect 1 (redrawn after Wigley 2013). F) Vertical distance moved by the horizontal bleaching front calculated from the difference in background concentration and enrichment of each of the metals at the front averaged over the four transects analyzed.

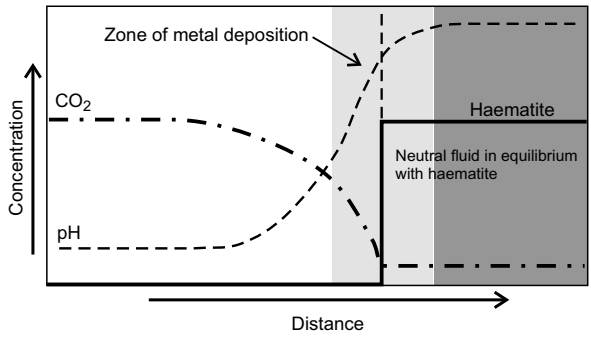

Figure 29. Diagramatic illustration of zone of variable pH in which metals are deposited as pH rises to critical pH adsorption edge for the particular metal.

where M is the mass of metal at the front (mol/m^2) and *TIFF* is the time-integrated fluid flux (m^3/m^2, Bickle and McKenzie 1987) ca1culated from the retardation factor and the distance of the bleaching front from the vein. The calculated concentrations of Cu, Zn and Sn are well below World Health Organization guidelines. Arsenic remains concentrated in vein centers in the profiles across veins. Given the ratio of As enrichment to Cu enrichment on the horizontal contacts (Fig. 28C, E and F) and the estimates of fluid Cu concentration of ~ 0.3 mg/L from Equation (32) by Wigley et al. (2013b), it seems possible that As concentrations would have exceeded the World Health Organization (2011) limits of 10 μg/L at the reaction front. However all the metals are rapidly deposited close to the reaction fronts suggesting their mobility will be limited until aquifers are completely swamped with CO_2.

Hematite and K-feldspar dissolution kinetics. The bleaching reaction fronts in the Entrada sandstone have also been used to put constraints on the mineral dissolution rates (Wigley et al. 2013a). To do this it is necessary to be able to put a constraint on the velocity at which the reaction is progressing as well as estimate the petrological parameters, including the change in mineral mode across the reaction front, the porosity of the rock and the mineral surface area. The reaction front velocities for the horizontal bleaching fronts are estimated from the conclusion that they are predominantly driven by diffusion and knowledge of the diffusion coefficients. The fluid velocities across the fractures are estimated from the asymmetry of the bleached margins to the veins. Full modeling of the coupled reactions and fluid chemistry with the various ions have differing diffusion constants (H^+ diffuses an order-of-magnitude faster than most ions) requires numerical solutions to the equations modeling transport and fluid-mineral reactions and Wigley (2013) has presented such solutions. However it is instructive to use simpler analytical solutions to solve the transport and reaction equations.

The approximate duration of the bleaching event can be estimated to be on the order of 100,000 years from the 2 km width of the bleaching, a fluid flux of ~ 5 m/yr and the reaction stoichiometry of the hematite dissolution reaction (Eqn. 29) which gives a retardation factor of 25. This is consistent with the timescale of the current CO_2 system in the underlying Navajo sandstone which has been leaking CO_2 to surface for at least 400,000 yrs (Burnside et al. 2013). Over such a timescale continued vertical displacement of the horizontal front must be predominantly by diffusion. If advective displacement was significant the vertical displacement would have to be much greater than the 20 m maximum thickness of the bleached layer. The importance of advective relative to diffusive transport is described by the Peclet number, Pe, given by

$$Pe = \frac{\omega_o \phi h}{D_{\text{eff}}} \tag{33}$$

where ω_o is fluid velocity, ϕ porosity, h the length scale and D_{eff} the effective diffusivity ($D_{\text{eff}} = D\phi\tau$ where D is the diffusion coefficient, and τ tortuosity). For advective transport to be significant, *Pe* must be greater than ~ 1 (Bickle and McKenzie 1987). Since the horizontal bleaching fronts have moved at most 20 m vertically and given that the diffusivity of cations in low temperature aqueous fluids is ~ 10^{-9} m^2/s, if the Peclet number was as high as 1, then the fluid flux ($\omega_{o\phi}$) would only be ~ 10^{-11} m/s and the advective displacement of the reaction front 6 m. It is probable that the main advective component was parallel to bedding and much of the thickness of the bleached zone was established early in the event, at least close to the source of the CO_2. The vertical fluid flux would then be rather less than this estimate, and the vertical displacement driven by diffusion could be as little as 25 cm from mass balance of the trace metals (Fig. 28F). At Peclet numbers of 1 or less advection is unimportant and the solutions insensitive to choice of Peclet number (Fig. 30)

Wigley et al. (2013a) estimated fluid fluxes across the bleached veins from the asymmetry of the bleaching (Fig. 31E,G). The differential equation describing advective and diffusive

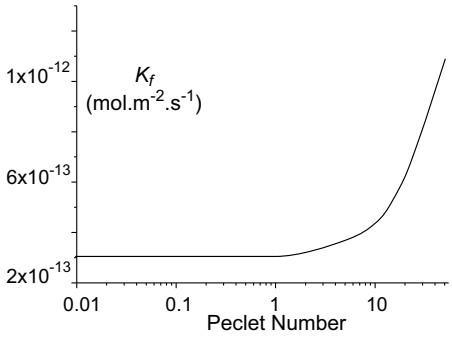

Figure 30. Illustration of insensitivity of calculated mineral dissolution rate to choice of Peclet number when Peclet number is less than one. Calculated for K-feldspar dissolution rate in Transect 1 (see Fig. 31B).

transport of a component, concentration C in the fluid phase may be written (e.g., Skelton et al. 1997)

$$\phi\frac{\partial C}{\partial t}=D\tau\phi\frac{\partial^2 C}{\partial x^2}-\omega_0\phi\frac{\partial C}{\partial x}-\frac{\partial\psi}{\partial t} \tag{34}$$

where ϕ is porosity, t is time, x is distance, D is the diffusivity of the component C in the fluid, τ is tortuosity, ω_0 is fluid pore velocity, and ψ is the concentration of the component in the rock. The reaction (exchange) rate of the component between the fluid and solid near to equilibrium may be approximated by a linear law as (e.g., Lasaga 1981):

$$\frac{\partial\psi}{\partial t}=\begin{cases}K_r\alpha\left(\dfrac{\Delta G}{\mathrm{R}T}\right) & (x\geq l)\\ 0 & (x<l)\end{cases} \tag{35}$$

where K_r is the reaction rate constant (mol·m^{-2}·s^{-1}), α is mineral surface area (m^2/m^3), ΔG is the free energy change per mole of the component dissolving (e.g., hematite), R is the gas constant, T temperature in Kelvin and l is the position of the reaction front. Following Skelton et al. (1997), we assume that the component driving the reaction is CO_2 and the change of CO_2 across the reaction front is small relative to the mole fraction of CO_2 in the fluid. If ΔG is small these assumptions allow ΔG to be approximated by (Walther and Wood 1986)

$$\Delta G=\mathrm{R}T\ln\left(\frac{\Delta C}{C_{\mathrm{eq}}}\right) \tag{36}$$

If ΔC is small compared to C, Equation (35) may be rewritten

$$\frac{\partial\psi}{\partial t}=\left\{\begin{matrix}k_f\alpha C_{\mathrm{eq}}\left(\dfrac{\Delta C}{C_{\mathrm{eq}}}\right)(x\geq l)\\ 0 \qquad\qquad (x<l)\end{matrix}\right\} \tag{37}$$

where in this example ΔC is the change in the molar fraction of CO_2 in the fluid phase across the reaction front and C_{eq} is the mole fraction of CO_2 in the fluid phase at equilibrium and k_fC_{eq} equivalent to K_{r} in Equation (35). Wigley et al. (2013a) show that ΔC is ~ 0.0032 mol/L for the hematite dissolution reactions and $\Delta G/\mathrm{R}T$ is thus 0.15 which is close to equilibrium. It should be noted that Equation (37) imposes a condition that reaction rate varies with a linear dependence on CO_2 concentration. The reaction rates recovered from solutions to Equations (34) and (37) thus decrease from a maximum at the reaction front, the value quoted below, to zero as the fluid tends to equilibrium with the unreacted rock.

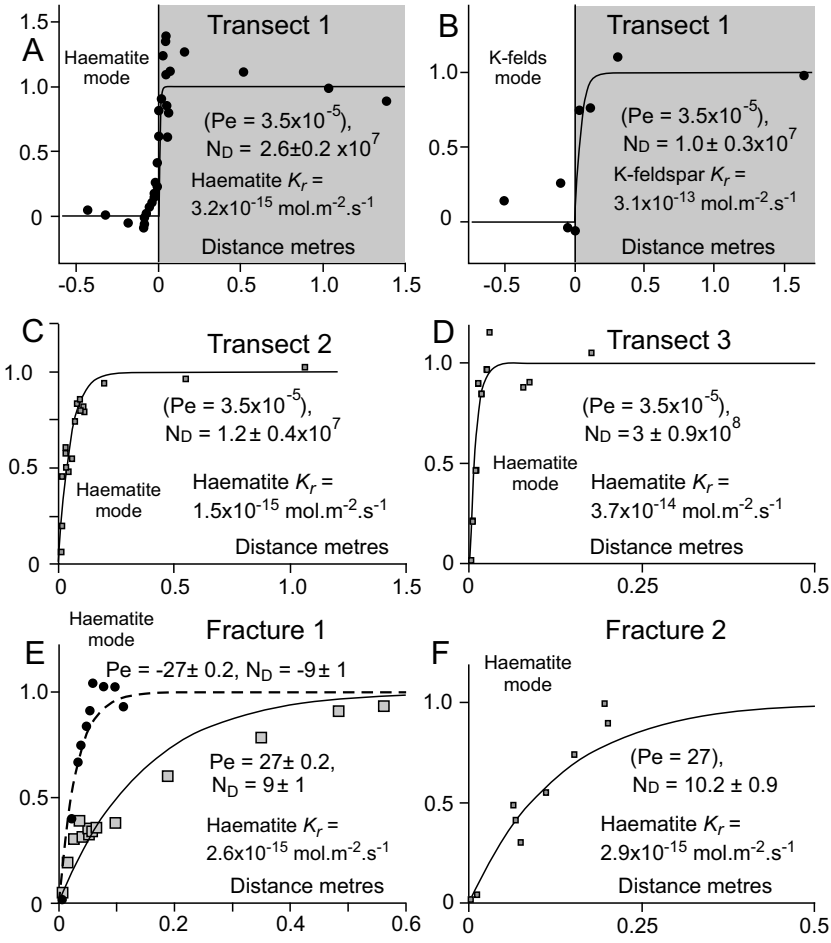

Figure 31. Fits to reaction progress using Equation (42) to A) hematite and B) K-feldspar across horizontal Transect 1 where Pe is fixed at a low value, scaling distance is taken as 1 meter and mineral modes are normalized to zero in bleached and 1 in red sandstones. C) Fits to N_D across horizontal Transect 2 and D) Fits to N_D across horizontal Transect 3 hematite profiles given low Pe. E) Fits to Pe and N_D to asymmetric bleached zone across Fracture 1 using Equations (42) and (43). Solid circles and dashed line fit are to west (upstream F1b) and grey squares and solid line fit to east (downstream F1a). Mineral modes normalized as above and scaling distance is taken as 1 meter. F) Fits to N_D to asymmetric bleached zone downstream in Fracture 2 assuming the Pe calculated from fracture 1. G) Photograph of Fracture 1 prior to sampling showing bleached zone and where F1b is profile upstream to west and F1a is the profile downstream to the east. Recalculated with distance scaling corrected after (Wigley et al. 2013a).

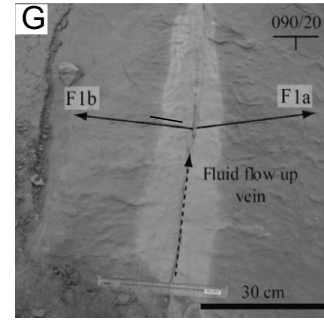

The transformation to dimensionless variables is made by

$$x' = \frac{x}{h} \tag{38}$$

$$t' = \frac{\omega_0 \varphi t}{h}$$

$$C' = \frac{C - C_{eq}}{C_0 - C_{eq}}$$

$$\psi' = \frac{\psi - \psi_{eq}}{\psi_0 - \psi_{eq}}$$

where h is an appropriate length scale, C_0 is the concentration of the component in the infiltrating fluid, C_{eq} is the concentration of the component in the fluid at equilibrium with the solid, ψ_{eq} is the initial concentration of the reaction product in unreacted rock and ψ_0 is the concentration of the reaction product in rock in equilibrium with the infiltrating fluid.

Where the velocity of the reaction *front* is slow compared with that of the fluid, the term $\phi \partial C / \partial t$ is small compared to the other terms in Equation (36) and can be ignored (the quasi-stationary state approximation of Lichtner 1988). Making this assumption and transforming to the dimensionless variables using Equation (38) allows Equations (34) and (37) to be combined as

$$0 = \frac{1}{Pe}\frac{\partial^2 C'}{\partial x'^2} - \frac{\partial C'}{\partial x'} - N_D C' \tag{39}$$

whose solution depends on the two dimensionless numbers, Pe, the Peclet number, the ratio of diffusive time constant to advective time constant and N_D, the Damköhler-I number, the ratio of transport time over the time for reaction. These are given by

$$Pe = \frac{\omega_0 \phi h}{D \varphi \tau} \tag{40}$$

and

$$N_D = \frac{k_f \alpha h}{\omega_0 \phi} \tag{41}$$

The solution to Equation (39) as derived by Lichtner (1988) where $\omega_{0\phi}$ is positive is

$$\psi' = \begin{cases} \exp\left(-\frac{Pe}{2}\left(\sqrt{1 + \frac{4N_D}{Pe}} - 1 \right)\left(x' - l' \right) \right) & \left(x' \geq l' \right) \\ 1 & \left(x' < l' \right) \end{cases} \tag{42}$$

and by Skelton et al. (1997) if $\omega_{0\phi}$ is negative

$$\psi' = \begin{cases} \exp\left(-\frac{Pe}{2}\left(\sqrt{1 + \frac{4N_D}{Pe}} + 1 \right)\left(x' - l' \right) \right) & \left(x' \geq l' \right) \\ 1 & \left(x' < l' \right) \end{cases} \tag{43}$$

where l' is the position of the reaction front.

Wigley et al. (2013a) use the hematite and K-feldspar mineral modes across the reaction fronts to solve Equations (42) and (43) using different assumptions for the horizontal reaction

fronts and the vein-associated fronts. For the horizontal fronts they assume that vertical advection is unimportant and set the Peclet number to a low value so that diffusion will dominate the solution as, with a single reaction front at moderate or large N_D it is impossible to solve for both N_D and Pe independently. The choice of Pe controls the value of N_D but not the reaction rate parameter ($k_{r\alpha}$) inferred from the fits (Fig. 30). This is calculated by multiplying Equations (40) and (41) to give

$$k_f \Delta C = \frac{\Delta C N_D Pe D \phi \tau}{\alpha h^2} \tag{44}$$

where $k_f \Delta C$ is the rate constant in mol·m^{-2}·s^{-1} and ΔC is taken as the maximum, i.e. the change in dissolved total carbon across the reaction front. The rate constant estimated is dependent on the assumption that the reaction front is driven by diffusion and that the appropriate diffusivity is that of CO_2 in the fluid. It should be noted that the average reaction rate will be about half that quoted given the linear dependence on the fluid CO_2 in excess of equilibrium.

The veins with asymmetric bleached margins allow solution for both Pe and N_D. It is assumed that the fluid flux out of the vein into the wall rock is negligible compared with the flux parallel to bedding within the sandstone. The downstream boundary (profile F1a in Fig. 31E,G) is fit with Equation (42) for diffusion and advection in the same direction and simultaneously the upstream boundary (profile F1b in Fig. 31C,D) is fit with Equation (43) for diffusion towards positive x, measured upstream but advection towards negative x. The reaction front ($x = 1$) is taken as the vein boundary where the hematite modes fall to zero (Fig. 31C). The results give $Pe = 27 \pm 0.2$ and $N_D = 9 \pm 1$ with flow to the east (note that there was an error in the scaling distances in Wigley et al. 2013a). Substituting the diffusivity of CO_2 (2×10^{-9} m^2/s), tortuosity = 0.5 and porosity = 10.2% into Equation (40) gives a fluid flux of 0.08 m/yr. This is rather less than estimated for the spread of the CO_2-charged brine but the fracture-related flow may have been active for small fraction of the total CO_2 flooding event and the background flow of CO_2-poor brine in the red sandstone may have been significantly less than the rate of spread of the denser CO_2-charged brine. The solution here implies a duration of only ~ 50 yrs. The reaction rate may be calculated from Equation (44) as above.

The calculated reaction rates are fastest where ΔC is largest at the start of the reaction front, and here are in the range 1.5×10^{-15} to 3.7×10^{-14} mol·m^{-2}·s^{-1} for hematite dissolution and $3.1 \pm 2.0\times10^{-13}$ mol·m^{-2}·s^{-1} for K-feldspar dissolution (see Fig. 31, note scaling error has increased estimated reaction rates for hematite by an order-of-magnitude over those quoted by Wigley et al. 2013a). The rates for hematite range from an-order-of-magnitude lower, to similar to the inferred rates used in reactive transport models (e.g., Xu et al. 2010 at pH = 5) based on coarse-grained hematite. The rates for K-feldspar are 1 to 2 orders-of-magnitude slower than those derived from far-from-equilibrium conditions (e.g., Stillings et al. 1996; Welch and Ullman 1996) but three orders of magnitude faster than those inferred for the present-day reactions in the underlying Navajo sandstone discussed above. This is most likely because the Green River reaction fronts are in the "close to equilibrium" range but less close to equilibrium than in the Navajo sandstone. It is not possible to calculate the degree of disequilibrium without better constraints on fluid compositions.

The discrepancy between the inferred hematite and K-feldspar dissolution rates mostly likely arises because of factors slowing down hematite dissolution. Incongruent Al-silicate mineral dissolution reactions reach a quasi-steady state in which the degree of disequilibrium adjusts so that the dissolution reaction is balanced by the rate of precipitation of the secondary clay minerals as fluid aluminum contents are small (e.g., Maher et al. 2009). Where multiple reactions are taking place all of them may impact fluid compositions. For the Entrada sandstone bleaching reaction Wigley et al. (2013a) note the following dissolution reactions and the kaolinite precipitation reaction probably dominate the controls on fluid chemistry

$$Fe_2O_3 + 6H^+ + 2e^- = 2Fe_2^{+}{}_{(aq)} + 3H_2O \quad (45)$$

$$2KAlSi_3O_8 + 6H_2O + 2H^+ = K^+_{(aq)} + 3H_4SiO_{4(aq)} + Al(OH)_2^{+}{}_{(aq)} \quad (46)$$

$$2H_4SiO_{4(aq)} + 2Al(OH)_{2(aq)} = Al_2Si_2O_5(OH)_4 + H_2O + 2H^+ \quad (47)$$

$$CaCO_3 + H^+ = Ca^{2+}_{(aq)} + HCO_3^-{}_{(aq)} \quad (48)$$

Because carbonate-fluid reactions are rapid, the CO_2-rich brines introduced to the formation along the Salt Wash Graben are carbonate saturated and the acidity of the system would be buffered by CO_2 pressure in equilibrium with carbonate dissolution/precipitation reactions (Eqn. 48). As the fluids drive the hematite and K-feldspar dissolution reactions, acidity and $CO_{2(aq)}$ will be consumed with the fluids becoming more alkaline. The K-feldspar dissolution reaction consumes about 3× the acidity of the hematite dissolution reaction although kaolinite precipitation returns about 50% of the acidity. The K-feldspar reaction will therefore tend to lag the hematite reaction and the hematite reaction rate will therefore be reduced by the reduction in acidity. The two reactions should therefore have similar velocities. The velocity of a reaction front (v_f) is given by the reaction rate times the surface area divided by the molar density of the phase (M, mol/m^3), i.e.,

$$v_f = \frac{k_f \alpha}{M} \quad (49)$$

For the reaction rates and mineral modes estimated above this gives a velocity of 4.5×10^{-10} m/s for the hematite reaction front and 1.3×10^{-10} m/s for the K-feldspar reaction front, values within error given the large uncertainties on the calculations.

Numerical modeling of the system H-C-O-Ca-Fe-K-Si, with the fluid components and phases discussed above, by Wigley (2013) essentially reproduces these results. It also models the enrichment of Fe and carbonate minerals at the front as a time-varying peak which is not reproduced by the simple solutions above and which is a function of the changing activities of the multiple components each moderated by reaction and diffusion.

SUMMARY AND FURTHER WORK

Natural CO_2 systems provide useful analogues for the longer-term processes which might take place in anthropogenic geological storage of CO_2. They are capable of providing information on the extent of dissolution of CO_2 in formation brines, the nature of the fluid-mineral reactions, the kinetics of the fluid-mineral reactions, the behavior of sealing cap rocks exposed to CO_2 or CO_2-charged brines and the consequences of escape of CO_2 or CO_2-charged brines up fault zones. However the natural analogues need to be properly sampled to recover this information. Surface sampling of fluids from active systems and rocks from exhumed systems allows inference of the nature and rates of critical processes but quantification of these processes from such data requires a significant number of assumptions such as the extent of CO_2 degassing from fluids sampled at surface and the nature of paleofluids responsible for alteration of exhumed CO_2 reservoirs. Work on such systems also highlights the need for better data and estimates of uncertainties on the data needed to describe equilibrium thermodynamics of minerals and fluids and the large uncertainties in the correct description of mineral reaction kinetics. Indeed the data recovered from natural CO_2 systems significantly adds to the body of data recovered from natural systems on mineral-fluid reaction rates close to equilibrium where rates are too slow to be measured in laboratory experiments but which characterize most processes in near-surface geological environments.

The important findings from the analogue studies to date include 1) a large fraction of CO_2 in natural reservoirs has dissolved in formation brines, 2) the extent of fluid-mineral

reactions in reservoirs is strongly dependent on reservoir mineralogy, 3) dissolution of iron minerals and precipitation of iron-bearing carbonates is an important process in reservoirs in continental red sandstones and permanently stabilizes CO_2 in solid phases and also fixes potential metal contaminants, 4) the geological reservoirs are rock-dominated and the fluid-mineral reactions will take place in the close-to-equilibrium region. Modeling the reaction kinetics therefore requires that the dependence of reaction rate with degree of disequilibrium needs to be much better understood, and 5) where CO_2 does escape up fault systems through stacked permeable horizons a large fraction of the escaping CO_2 is likely to be trapped by dissolution rather than escape to surface.

The behavior of caprocks subject to long-term exposure to supercritical CO_2 or CO_2-charged fluids is a critical factor in calculating the risks of long-term CO_2 storage. Despite the exploitation of natural CO_2 reservoirs, which have stored CO_2 for hundreds of thousands to millions of years, we know of no good core sections from their caprocks. The few cores through caprocks are either from CO_2-bearing hydrocarbon gas reservoirs and the shallow CO_2-charged fluids from Green River.

Full exploitation of the valuable data on the long-term behavior of CO_2 in geological storage will therefore require that there is significant investment in sampling and studying the natural analogues. This will require the drilling of holes dedicated to recovering core and fluids from the natural reservoirs. Coring and sampling of supercritical CO_2 and associated reservoir brines faces special challenges in drilling into over-pressured formations but this work will cost a small fraction of the ultimate investment in geological carbon storage. It will provide critical information on the long-term storage of carbon dioxide and technical expertise in sampling supercritical CO_2 reservoirs.

ACKNOWLEDGMENTS

The Carbon Research into Underground Storage program (CRIUS) at Cambridge is supported by the UK Department of Energy and Climate Change through the Carbon Capture and Storage research and development program and by the Natural Environment Research Council grant NE/F004699/1. Niko Kampman acknowledges financial support from Shell Global Solutions International. Max Wigley acknowledges PhD support from the Natural Environment Research Council.

REFERENCES

Aagaard P, Helgeson HC (1982) Thermodynamic and kinetic constraints on reaction rates among minerals and aqueous solutions I. Theoretical considerations. Am J Sci 282:237-285

Arnorsson S, Stefansson A (1999) Assessment of feldspar solubility constants in water in the range of 0 to 350 C at vapor saturation pressures. Am J Sci 299:173-209

Allis R, Chidsey T, Gwynn W, Morgan C, White S, Adams M, Moore JC (2001) Natural CO_2 reservoirs on the Colorado Plateau and Southern Rocky Mountains: candidates for CO_2 sequestration DOE/NETL: *In:* Proceedings of the 1st National Conference of Carbon Sequestration; http://www.netl.doe.gov/publications/proceedings/01/carbon_seq/6a2.pdf

Allison L, Blackett RE, Chidsey TC Jr, Tabet DE, Gloyn RW, Bishop MCE (1997) A Preliminary Assessment of Energy and Mineral Resources within the Grand Staircase-Escalante National Monument. Utah Geological Survey Circular 93

Andrews JN, Kay RLF (1982) $^{234}U/^{238}U$ activity ratios of dissolved uranium in groundwaters from a jurassic limestone aquifer in England. Earth Planet Sci Lett 57:139-151

Assayag N, Bickle M, Kampman N, Becker J (2009) Carbon isotopic constraints on CO_2 degassing in cold-water Geysers Green River Utah. Energy Procedia 1:2361-2366

Axford W (1968) The polar wind and the terrestrial helium budget. J Geophys Res 73:6855-6859

Baines S, Worden R (2001) Geological CO_2 disposal: Understanding the long-term fate of CO_2 in naturally occurring accumulations. *In:* Proceedings of Fifth International Conference on Greenhouse Gas Control Technologies, Cairns CSIRO Collingwood, p 311-316

Baker JC, Bai GP, Hamilton PJ, Golding SD, Keene JB (1995) Continental-scale magmatic carbon dioxide seepage recorded by dawsonite in the Bowen-Gunnedah-Sydney basin system eastern Australia. J Sediment Res 65:522-530

Ballentine C (1997) Resolving the mantle He/Ne and crustal $^{21}Ne/^{22}Ne$ in well gases. Earth Planet Sci Lett 152:233-249

Ballentine CJ, Burnard PG (2002) Production release and transport of the noble gases in the continental crust. Rev Mineral Geochem 47:481-538

Ballentine CJ, Schoell M, Coleman D, Cain BA (2001) 300-Myr-old magmatic CO_2 in natural gas reservoirs of the west Texas Permian basin. Nature 409:327-331

Ballentine CJ, Burgess R, Marty B (2002) Tracing fluid origin transport and interaction in the crust. Rev Mineral Geochem 47:539-614

Ballentine CJ, Marty B, Sherwood-Lollar BS, Cassidy M (2005) Neon isotopes constrain convection and volatile origin in the Earth's mantle. Nature 433:33-38

Beitler B, Chan MA, Parry WT (2003) Bleaching of Jurassic Navajo sandstone on Colorado Plateau Laramide highs: Evidence of exhumed hydrocarbon supergiants? Geology 31:1041-1044

Beitler B, Parry W, Chan M (2005) Fingerprints of fluid flow: chemical diagenetic history of the Jurassic Navajo Sandstone southern Utah USA. J Sediment Res 75:547-561

Bénézeth P, Palmer DA, Anovitz LM, Horita J (2007) Dawsonite synthesis and reevaluation of its thermodynamic properties from solubility measurements: Implications for mineral trapping of CO_2. Geochim Cosmochim Acta 71:4438-4455

Benjamin MM, Leckie J (1981) Multiple-site adsorption of Cd Cu Zn and Pb on amorphous iron oxyhydroxide. J Colloid Interface Sci 79:209-221

Benson B, Krause D Jr. (1980) Isotopic fractionation of helium during solution: A probe for the liquid state. J Solution Chem 9:895-909

Bickle M, Kampman N (2013) Lessons in carbon storage from geological analogues. Geology 41:525–526

Bickle MJ, McKenzie D (1987) The transport of heat and matter by fluids during metamorphism. Contrib Mineral Petrol 95: 384-392

Brantley SL (2008) Kinetics of mineral dissolution. *In:* Kinetics of Water-Rock Interaction. Brantley SL, Kubicki JD, White AF (eds) Springer New York, p 151-210

Broadhead RF (1993) Carbon dioxide in northeast New Mexico. West Texas Geological Society Bulletin 32: 5-8

Burnard P, Graham D, Turner G (1997) Vesicle-specific noble gas analyzes of "popping rock": implications for primordial noble gases in earth. Science 276:568-571

Burnside N, Shipton Z, Dockrill B, Ellam RM (2013) Man-made versus natural CO_2 leakage: A 400 k.y. history of an analogue for engineered geological storage of CO_2. Geology, doi: 10.1130/G33738.1

Campbell JA (1978) Carbon Dioxide Resources of Utah. Utah Geological and Mineral Survey Report of Investigation 125: 36

Chan MA, Parry WT, Bowman JR (2000) Diagenetic hematite and manganese oxides and fault-related fluid flow in Jurassic sandstones southeastern Utah. AAPG Bull 84:1281-1310

Chan MA, Beitler B, Parry W, Ormö J, Komatsu G (2004) A possible terrestrial analogue for hematite concretions on Mars. Nature 429:731-734

Chan M, Parry W, Bowen B, Potter S (2011) Follow the water: Connecting a CO_2 reservoir and bleached sandstone to iron-rich concretions in the Navajo Sandstone of south-central Utah USA: COMMENT. Geology 39:e250-e250

Credoz A, Bildstein O, Jullien M, Raynal J, Pétronin J-C, Lillo M, Pozo C, Geniaut G (2009) Experimental and modeling study of geochemical reactivity between clayey caprocks and CO_2 in geological storage conditions. Energy Procedia 1:3445-3452

Crossey LJ, Karlstrom KE, Springer AE, Newell D, Hilton DR, Fischer T (2009) Degassing of mantle-derived CO_2 and He from springs in the southern Colorado Plateau region—Neotectonic connections and implications for groundwater systems. Geol Soc Am Bull 121:1034-1053

Daley T, Freifeld B, Ajo-Franklin JB., Doughty C, Benson SM (2007a) Frio II Brine Pilot: Report on GEOSEQ Activities. Lawrence Berkeley National Lab, *http://www.osti.gov/bridge/servlets/purl/928451-bs4PuK/928451.pdf*

Daley TM, Solbau RD, Ajo-Franklin JB, Benson SM (2007b) Continuous active-source seismic monitoring of injection in a brine aquifer. Geophysics 72:A57-A61

DePaolo DJ, Cole DR (2013) Geochemistry of geologic carbon sequestration: an overview. Rev Mineral Geochem 77:1-14

Dockrill B, Shipton ZK (2010) Structural controls on leakage from a natural CO_2 geologic storage site: Central Utah U.S.A. J Struct Geol 32:1768-1782

Drever JI (1997). The geochemistry of natural waters. Prentice Hall, Upper Saddle River

Dubacq B, Bickle MJ, Wigley M, Kampman N, Ballentine CJ, Sherwood Lollar B (2012) Noble gas and carbon isotopic evidence for CO_2-driven silicate dissolution in a recent natural CO_2 field. Earth Planet Sci Lett 341-344:10-19

Dubacq B, Bickle MJ, Evans KA (2013) An activity model for phase equilibria in the H_2O-CO_2-NaCl system. Geochim Cosmochim Acta 110:229-252

Dunai TJ, Porcelli D (2002) Storage and transport of noble gases in the subcontinental lithosphere. Rev Mineral Geochem 47:371-409

Embid E, Crossey L (2009). U-series dating geochemistry and geomorphic studies of travertines and springs of the Springerville area east-central Arizona and tectonic implications. Masters Thesis, University of New Mexico Albuquerque

Farley K, Neroda E (1998) Noble gases in the earth's mantle. Annu Rev Earth Planet Sci 26:189-218

Franks SG, Forester RW (1984) Relationships among secondary porosity pore-fluid chemistry and carbon dioxide Texas Gulf Coast. Clastic diagenesis: AAPG Memoir 37:63-79

Garrels RM, Mackenzie FT (1967) Origin of the chemical composition of some springs and lakes. *In:* Equilibrium Concepts in natural Water Systems. Advances in Geochemistry. Gould RF (ed) American Chemical Society Washington: 222-242

Garrels RM, Richter DH (1955) Is Carbon dioxide an ore-forming fluid under shallow-earth conditions? Econ Geol 50: 447-458

Gaus I, Azaroual M, Czernichowski-Lauriol I (2005) Reactive transport modeling of the impact of CO_2 injection on the clayey cap rock at Sleipner (North Sea). Chem Geol 217:319-337

Gilfillan S (2004) Deep magmatic degassing and the Colorado Plateau uplift. Ph.D. Thesis, University of Manchester, UK

Gilfillan S, Lollar B, Holland G, Blagburn D, Stevens S, Schoell M, Cassidy M, Ding Z, Zhou Z, Lacrampe-Couloume G (2008) The noble gas geochemistry of natural CO_2 gas reservoirs from the Colorado Plateau and Rocky Mountain provinces USA. Geochim Cosmochim Acta 72:1174-1198

Gilfillan S, Lollar B, Holland G, Blagburn D, Stevens S, Schoell M, Cassidy M, Ding Z, Zhou Z, Lacrampe-Couloume G (2009) Solubility trapping in formation water as dominant CO_2 sink in natural gas fields. Nature 458:614-618

Gilfillan SMV, Wilkinson M, Haszeldine RS, Shipton ZK, Nelson ST, Poreda RJ (2011) He and Ne as tracers of natural CO_2 migration up a fault from a deep reservoir. Int J Greenhouse Gas Control 5:1507-1516

Graham DW (2002) Noble gas isotope geochemistry of mid-ocean ridge and ocean island basalts: Characterization of mantle source reservoirs. Rev Mineral Geochem 47:247-317

Gruner JW (1956) Concentration of uranium in sediments by multiple migration-accretion. Econ Geol 51:495-520

Harrison D, Burnard P, Turner G (1999) Noble gas behavior and composition in the mantle: constraints from the Iceland Plume. Earth Planet Sci Lett 171:199-207

Haszeldine RS, Quinn O, England G, Wilkinson M, Shipton ZK, Evans JP, Heath J, Crossey L, Ballentine CJ, Graham C (2005) Natural geochemical analogues for carbon dioxide storage in deep geological porous reservoirs a United Kingdom perspective. Oil Gas Sci Technol 60:33-49

Heath JE (2004) Hydrogeochemical characterization of CO_2 charged fault zones in east-central Utah. Utah State University Logan: 166

Heath JE, Lachmar TE, Evans JP, Kolesar PT (2009) Hydrogeochemical characterization of leaking carbon dioxide-charged fault zones in east-central Utah with implications for geologic carbon storage. In: McPherson B, Sundquist E (Eds.) Carbon sequestration and its role in the global carbon cycle. American Geophysical Union Monograph. American Geophysical Union Washington DC: 147-158

Heinemann N, Wilkinson M, Haszeldine S, Fallick A, Pickup G (2013) CO_2 sequestration in a UK North Sea analogue for geological carbon storage. Geology 41:411-414

Hellevang H, Aagaard P, Oelkers EH, Kvamme B (2005) Can dawsonite permanently trap CO_2? Environ Sci Technol 39:8281-8287

Hellmann R, Tisserand D (2006) Dissolution kinetics as a function of the Gibbs free energy of reaction: An experimental study based on albite feldspar. Geochim Cosmochim Acta 70:364-383

Hepple R, Benson S (2005) Geologic storage of carbon dioxide as a climate change mitigation strategy: performance requirements and the implications of surface seepage. Environ Geol 47:576-585

Holland G, Ballentine CJ (2006) Seawater subduction controls the heavy noble gas composition of the mantle. Nature 441:186-191

Holland G, Gilfillan S (2013). Application of noble gases to the viability of CO_2 storage. *In:* The Noble Gases as Geochemical Tracers. Burnard P (ed) Springer, p 177-223

Hood J, Patterson D (1984) Bedrock aquifers in the northern San Rafael Swell area. Utah with special emphasis on the Navajo Sandstone. State of Utah Department of Natural Resources Technical Publication 78

IPCC (2005) IPCC Special Report on Carbon Dioxide Capture and Storage. Working Group III of the Intergovernmental Panel on Climate Change. Cambridge University Press New York

Kampman N, Bickle M, Becker J, Assayag N, Chapman H (2009) Feldspar dissolution kinetics and Gibbs free energy dependence in a CO_2-enriched groundwater system Green River Utah. Earth Planet Sci Lett 284:473-488

Kampman N, Burnside NM, Shipton ZK, Chapman HJ, Nicholl JA, Ellam RM, Bickle MJ (2012) Pulses of carbon dioxide emissions from intracrustal faults following climatic warming. Nat Geosci 5:352-358

Kampman N, Bickle M, Wigley M, Dubacq B (2013a) Geochemical processes in geological carbon storage. Chem Geol, in review

Kampman N, Maskell A, Chapman H, Bickle M, Evans J, Purser G, Zhou Z, Schaller M, Dubacq B, Wigley M, Assayag N, Rochelle C, Ballentine C, Busch A (2013b) Downhole fluid sampling of a natural CO_2 reservoir Green River Utah: Implications for fault-hosted fluid flow and cold water CO_2-geysers. Chem Geol, in review

Karlstrom KE, Crossey LJ, Hilton DR, Barry PH (2013) Mantle ^3He and CO_2 degassing in carbonic and geothermal springs of Colorado and implications for neotectonics of the Rocky Mountains. Geology 41:495-498

Kaszuba JP, Janecky DR Snow MG (2005) Experimental evaluation of mixed fluid reactions between supercritical carbon dioxide and NaCl brine: Relevance to the integrity of a geologic carbon repository. Chem Geol 217:277-293

Keating EH, Fessenden J, Kanjorski N, Koning DJ, Pawar R (2010) The impact of CO_2 on shallow groundwater chemistry: observations at a natural analog site and implications for carbon sequestration. Environ Earth Sci 60:521-536

Kennedy BM, van Soest MC (2006) A helium isotope perspective on the Dixie Valley, Nevada, hydrothermal system. Geothermics 35(1):26-43

Kennedy B, Hiyagon H, Reynolds J (1990) Crustal neon: a striking uniformity. Earth Planet Sci Lett 98:277-286

Kettler RM, Loope DB, Weber KA (2011) Follow the water: Connecting a CO_2 reservoir and bleached sandstone to iron-rich concretions in the Navajo Sandstone of south-central Utah USA: REPLY. Geology 39:251-252

Kharaka YK, Cole DR, Hovorka SD, Gunter WD, Knauss KG, Freifeld BM (2006a) Gas-water-rock interactions in Frio Formation following CO_2 injection: Implications for the storage of greenhouse gases in sedimentary basins. Geology 34:577-580

Kharaka YK, Cole DR, Thordsen JJ, Kakouros E, Nance HS (2006b) Gas–water–rock interactions in sedimentary basins: CO_2 sequestration in the Frio Formation Texas USA. J Geochem Explor 89:183-186

Kohler E, Parra T, Vidal O (2009) Clayey cap-rock behavior in H_2O-CO_2 media at low pressure and temperature conditions: an experimental approach. Clays Clay Miner 57:616-637

Landrot G, Ajo-Franklin JB, Yang L, Cabrini S, Steefel CI (2012) Measurement of accessible reactive surface area in a sandstone, with applications to CO_2 mineralization. Chem Geol 318-319:113-125

Lasaga A (1981) Transition state theory. Rev Mineral 8:135-169

Lee J-Y, Marti K, Severinghaus JP, Kawamura K, Yoo H-S, Lee JB, Kim JS (2006) A redetermination of the isotopic abundances of atmospheric Ar. Geochim Cosmochim Acta 70:4507-4512

Lichtner PC (1988) The quasi-stationary state approximation to coupled mass transport and fluid rock interaction in a porous medium. Geochim Cosmochim Acta 52:143-165

Loope DB, Kettler RM, Weber KA (2010) Follow the water: Connecting a CO_2 reservoir and bleached sandstone to iron-rich concretions in the Navajo Sandstone of south-central Utah USA. Geology 38:999-1002

Lu P, Fu Q, Seyfried WS, Hedges SW, Soong Y, Jones K, Zhu C (2013) Coupled alkali feldspar dissolution and secondary mineral precipitation in batch systems – 2: New experiments with supercritical CO_2 and implications for carbon sequestration. Appl Geochem 30:75-90

Maher K, DePaolo DJ, Lin JCF (2004) Rates of silicate dissolution in deep-sea sediment: In situ measurement using U-234/U-238 of pore fluids. Geochim Cosmochim Acta 68:4629-4648

Maher K, DePaolo DJ, Christensen JN (2006) U-Sr isotopic speedometer: Fluid flow and chemical weathering rates in aquifers. Geochim Cosmochim Acta 70:4417-4435

Maher K, Steefel CI, White AF, Stonestrom DA (2009) The role of reaction affinity and secondary minerals in regulating chemical weathering rates at the Santa Cruz Soil Chronosequence California. Geochim Cosmochim Acta 73:2804-2831

Malmstrom ME, Destouni G, Banwart SA, Stromberg BHE (2000) Resolving the scale-dependence of mineral weathering rates. Environ Sci Technol 34:1375-1378

Maughan EK (1989) Geology and Petroleum Potential Colorado Park Basin Province North-Central Colorado. U.S. Geological Survey Open-File Report 88-450 E

Mayo AL, Shrum DB, Chidsey Jr TC (1991) Factors contributing to exsolving carbon dioxide in ground water systems in the Colorado Plateau Utah. Utah Geological Association, p 335-342

Moore J, Adams M, Allis R, Lutz S, Rauzi S (2005) Mineralogical and geochemical consequences of the long-term presence of CO_2 in natural reservoirs: An example from the Springerville–St. Johns Field Arizona and New Mexico USA. Chem Geol 217:365-385

Moore J, Lichtner PC, White AF, Brantley SL (2012) Using a reactive transport model to elucidate differences between laboratory and field dissolution rates in regolith. Geochim Cosmochim Acta 93:235-261

Morgan CD (2007) Structure Reservoir Characterization and Carbon Dioxide Resources of Farnham Dome Field Carbon County Utah. Utah Geological Association, p 297-310

Morgan CD, Chidsey Jr TC (1991) Gordon Creek, Farnham Dome and Woodside fields Carbon and Emery Counties Utah. Utah Geological Association, p 301-310

Morrison SJ, Parry W (1988) Age and formation conditions of alteration associated with a collapse structure Temple Mountain uranium district Utah. Geol Soc Am Bull 100:1069-1077

Neufeld JA, Hesse MA, Riaz A, Hallworth MA, Hamdi A, Tchelepi HA, Huppert HE (2010) Convective dissolution of carbon dioxide in saline aquifers. Geophys Res Lett 37:L22404

Nuccio VF, Condon S M (1996) Burial and thermal history of the Paradox Basin Utah and Colorado and petroleum potential of the middle Pennsylvanian Paradox Formation Evolution of sedimentary basins - Paradox Basin. U.S. Geological Survey Bulletin 2000–O. US. Geological Survey

Osmond JC (1956) Woodside Anticline Emery County Utah. Utah Geological Association: 178-180

Ozima M, Podosek FA (2002). Noble Gas Geochemistry. Cambridge University Press

Parkhurst D, Appelo C (1999) User's guide to PHREEQC (version 2)—a computer program for speciation batch-reaction one-dimensional transport and inverse geochemical calculations. US Geological Survey Water-Resources Investigations Report 99: 310

Parkhurst DL, Appelo CAJ (2013). Description of input and examples for PHREEQC version 3—A computer program for speciation batch-reaction one-dimensional transport and inverse geochemical calculations: Ch. A43. U.S. Geological Survey Techniques and Methods book 6. USGS

Parry WT (2011) Composition nucleation and growth of iron oxide concretions. Sediment Geol 233:53-68

Parry WT, Forster CB, Evans JP, Bowen BB, Chan MA (2007) Geochemistry of CO_2 sequestration in the Jurassic Navajo Sandstone Colorado Plateau Utah. Environ Geosci 14:91-109

Pearce J (2004) Natural analogues for the geological storage of CO_2. Final report of the Nascent project. British Geological Survey Technical Report 122

Pearce J (2006) What can we learn from natural analogues? Advances in the Geological Storage of Carbon Dioxide: 127-139

Peters C (2009) Accessibilities of reactive minerals in consolidated sedimentary rock: an imaging study of three sandstones. Chem Geol 265: 198–208

Peterson V (1954) The Mounds and Farnham Area of the Northern San Rafael Swell: Carbon and Emery Counties Utah. Utah Geological Association: 86-88

Pevear DR, Vrolijk PJ, Longstaffe FJ (1997) Timing of Moab fault displacement and fluid movement integrated with burial history using radiogenic and stable isotopes. *In:* Geofluids II '97. Contributions to the Second International Conference on Fluid Evolution, Migration and Interaction in Sedimentary Basins and Orogenic Belts. Hendry J, Carey P, Parnell J, Ruffel A, Worden R (es) p 42-45

Podosek FA, Honda M, Ozima M (1980) Sedimentary noble gases. Geochim Cosmochim Acta 44:1875-1884

Porcelli D, Woolum D, Cassen P (2001) Deep Earth rare gases: initial inventories capture from the solar nebula and losses during Moon formation. Earth Planet Sci Lett 193:237-251

Potter-McIntyre S, Allen J, Lee S, Han WS, Chan M, McPherson B (2013) Iron precipitation in a natural CO_2 reservoir: Jurassic Navajo Sandstone in the northern San Rafael Swell UT USA. Geofluids 13: 82-92

Radha AV, Navrotsky A (2013) Thermodynamics of carbonates. Rev Mineral Geochem 77:73-121

Rauzi SL (1999). Carbon Dioxide in the St. Johns-Springerville Area Apache County Arizona. Arizona Geological Survey

Rillard J, Gombert P, Toulhoat P, Zuddas P (2013) Kinetic rate of iron release during artificial CO_2 injection in a shallow aquifer: preliminary results. Procedia Earth Planet Sci 7:742-745

Sarda P, Staudacher T, Allègre CJ (1985) $^{40}Ar/^{36}Ar$ in MORB glasses: constraints on atmosphere and mantle evolution. Earth Planet Sci Lett 72:357-375

Shevalier M, Nightingale M, Johnson G, Mayer B, Perkins E, Hutcheon I (2009) Monitoring the reservoir geochemistry of the Pembina Cardium CO_2 monitoring project Drayton Valley Alberta. Energy Procedia 1:2095-2102

Shipton ZK, Evans JP, Kirschner D, Kolesar PT, Williams AP, Heath J (2004) Analysis of CO_2 leakage through 'low-permeability' faults from natural reservoirs in the Colorado Plateau east-central Utah. Geol Soc London Special Pub 233:43-58

Singleton MJ, Maher K, DePaolo DJ, Conrad ME, Dresel PE (2006) Dissolution rates and vadose zone drainage from strontium isotope measurements of groundwater in the Pasco Basin WA unconfined aquifer. J Hydrol 321:39-58

Skelton ADL, Bickle MJ, Graham CM (1997) Fluid-flux and reaction rate from advective-diffusive carbonation of mafic sill margins in the Dalradian southwest Scottish Highlands. Earth Planet Sci Lett 146: 527-539

Smith S, Kennedy B (1983) The solubility of noble gases in water and in NaCl brine. Geochim Cosmochim Acta 47:503-515

Solomon DK (2000) ^{4}He in Groundwater Environmental Tracers in Subsurface Hydrology. Springer pp. 425-439

Spangler LE, Naftz DL, Peterman ZE (1996) Hydrology chemical quality and characterization of salinity in the Navajo aquifer in and near the Greater Aneth oil field San Juan County Utah. U.S. Geol Surv Water-Resour Invest Report 96-4155: 90

Stefansson A, Arnorsson S (2000) Feldspar saturation state in natural waters. Geochim Cosmochim Acta 64:2567-2584

Stevens S, Pearce J, Rigg A, Sydney N (2001) Natural analogs for geologic storage of CO_2: An integrated global research program. In: Proceedings for 1st International Conference on Carbon Sequestration, USDOE National Energy Technology Laboratory, May 15-17, 2001. http://www.netl.doe.gov/publications/proceedings/01/carbon_seq/6a1.pdf

Stevens SH, Tye BS (2005) NACS -- Natural CO_2 analogs for Carbon Sequestration. Final Report for DOE Award # DE-FC26-01NT41150. Advanced Resources Intl Inc, http://www.osti.gov/energycitations/servlets/purl/902517-FcAFPU/902517.pdf

Stillings LL, Drever JI, Brantley SL, Sun Y, Oxburgh R (1996) Rates of feldspar dissolution at pH 3-7 with 0-8 mM oxalic acid. Chem Geol 132: 79-89

Stroud JR (1997) The Geochronology of the Raton-Clayton Volcanic Field with Implications for Volcanic History and Landscape Evolution. New Mexico Institute of Mining and Technology

Tolstikhin I, Lehmann B, Loosli H, Gautschi A (1996) Helium and argon isotopes in rocks minerals and related ground waters: A case study in northern Switzerland. Geochim Cosmochim Acta 60:1497-1514

Torgersen T, Kennedy BM (1999) Air-Xe enrichments in Elk Hills oil field gases: role of water in migration and storage. Earth Planet Sci Lett 167:239-253

Torgersen T, Kennedy BM, Hiyagon H, Chiou KY, Reynolds JH, Clarke WB (1989) Argon accumulation and the crustal degassing flux of 40Ar in the Great Artesian Basin Australia. Earth Planet Sci Lett 92: 43-56

Trautz RC, Pugh JD, Varadharajan C, Zheng L, Bianchi M, Nico PS, Spycher NF, Newell DL, Esposito RA, Wu Y, Dafflon B, Hubbard SS, Birkholzer JT (2012) effect of dissolved CO_2 on a shallow groundwater system: a controlled release field experiment. Environ Sci Technol 47:298-305

Walther JV, Wood BJ (1986) Mineral-Fluid Reaction Rates. *In:* Fluid-Rock Reactions during Metamorphism. Walther JV, Wood BJ (eds) Springer-Verlag Berlin, p 194-211

Watson MN, Zwingmann N, Lemon NM (2004) The Ladbroke Grove–Katnook carbon dioxide natural laboratory: A recent CO_2 accumulation in a lithic sandstone reservoir. Energy 29:1457-1466

Weigel JF (1986) Selected hydrologic and physical properties of Mesozoic formations in the upper Colorado River Basin in Arizona Colorado Utah and Wyoming excluding the San Juan Basin. US Geol Surv Water-Resour Invest Rep 86-4170: 68 pp

Weiss E (1986) Ground-water flow in the Navajo Sandstone in parts of Emery Grand CarbonWayne Garfield and Kane Counties southeast Utah. US Geol Surv Water-Resour Invest Rep 86-4012

Welch SA, Ullman WJ (1996) Feldspar dissolution in acidic and organic solutions: Compositional and pH dependence of dissolution rate. Geochim Cosmochim Acta 60:2939-2948

White AF, Brantley SL (2003) The effect of time of the weathering of silicate minerals: why do weathering rates differ in the laboratory and field? Chem Geol 202:479-506

White AF, Bullen TD, Schulz MS, Blum AE, Huntington TG, Peters NE (2001) Differential rates of feldspar weathering in granitic regoliths. Geochim Cosmochim Acta 65:847-869

Wigley M (2013). Fluid-Mineral Reactions in an Exhumed CO_2-Charged Aquifer Green River Utah USA unpublished PhD Thesis University of Cambridge 266 pp

Wigley M, Kampman N, Dubacq B, Bickle M (2012) Fluid-mineral reactions and trace metal mobilisation in an exhumed natural CO_2 reservoir Green River Utah. Geology 40:555-558

Wigley M, Dubacq B, Kampman N, Bickle M (2013a) Controls of sluggish CO_2-promoted hematite and K-feldspar dissolution kinetics in sandstones. Earth Planet Sci Lett 362:76-87

Wigley M, Kampman N, Chapman H, Dubacq B, Bickle M (2013b) *In situ* re-deposition of trace metals mobilized by CO_2-charged fluids. Geochem Geophys Geosys 14(5):1321-1332

Wilkinson M, Gilfillan SVM, Haszeldine RS, Ballentine CJ (2009a) Plumbing the depths: Testing natural tracers of subsurface CO_2 origin and migration Utah. *In:* Carbon dioxide sequestration in geological media —State of the science. Grobe M, Pashin JC, Dodge RL (eds) AAPG Studies in Geology, p 619-634

Wilkinson M, Haszeldine RS, Fallick AE, Odling N, Stoker SJ, Gatliff RW (2009b) CO_2–mineral reaction in a natural analogue for CO_2 storage—implications for modeling. J Sediment Res 79:486-494

Woodward LA (1983) Geology and hydrocarbon potential of the Raton Basin New Mexico. Four Corners Geological Society, p 789-798

Wyllie RJ, Rose WD (1950) Application of the Kozeny Equation to consolidated porous media. Nature 165: 972, doi: 10.1038/165972a0

Xu T, Apps J, Pruess K (2005) Mineral sequestration of carbon dioxide in a sandstone–shale system. Chem Geol 217:295-318

Xu T, Kharaka YK, Doughty C, Freifeld BM, Daley TM (2010) Reactive transport modeling to study changes in water chemistry induced by CO_2 injection at the Frio-I Brine Pilot. Chem Geol 271:153-164

Yatsevich I, Honda M (1997) Production of nucleogenic neon in the Earth from natural radioactive decay. J Geophys Res Solid Earth 102:10291-10298

Yokochi R, Marty B (2004) A determination of the neon isotopic composition of the deep mantle. Earth Planet Sci Lett 225:77-88

Zhou Z, Ballentine CJ, Kipfer R, Schoell M, Thibodeaux S (2005) Noble gas tracing of groundwater/coalbed methane interaction in the San Juan Basin USA. Geochim Cosmochim Acta 69:5413-5428

Zhou Z, Ballentine CJ, Schoell M, Stevens SH (2012) Identifying and quantifying natural CO_2 sequestration processes over geological timescales: The Jackson Dome CO_2 Deposit USA. Geochim Cosmochim Acta 86:257-275

Zhu C (2000) Estimate of recharge from radiocarbon dating of groundwater ages and numerical flow and transport modeling. Water Resour Res 36:2607-2620

Zhu C (2005) In situ feldspar dissolution rates in an aquifer. Geochim Cosmochim Acta 69:1435-1453

Zhu C, Lu P (2013) The coupling of dissolution and precipitation reactions as the main contributor to the apparent field-lab rate discrepancy. Procedia Earth Planet Sci 7:948-952

Zhu C, Veblen D, Blum A, Chipera S (2006) Naturally weathered feldspar surfaces in the Navajo Sandstone aquifer Black Mesa Arizona: Electron microscopic characterization. Geochim Cosmochim Acta 70:4600-4616

Reviews in Mineralogy & Geochemistry
Vol. 77 pp. 73-121, 2013
Copyright © Mineralogical Society of America

Thermodynamics of Carbonates

A.V. Radha and A. Navrotsky*

Peter A. Rock Thermochemistry Laboratory and
NEAT ORU (Nanomaterials in the Environment, Agriculture,
and Technology Organized Research Unit)
University of California Davis
Davis, California 95616, U.S.A.

ravenkat@ucdavis.edu
*corresponding author: *anavrotsky@ucdavis.edu*

INTRODUCTION

The goal of geologic CO_2 sequestration is not just to pump large volumes of supercritical carbon dioxide into underground repositories but to keep it there for hundreds to thousands of years, preferably in chemically bound form. The permanence of CO_2 storage in geological repositories is important since large leakage rates would diminish the CO_2 abatement achieved with carbon capture and sequestration (CCS). Effective permanent geologic CO_2 storage depends ultimately on the interactions of the supercritical CO_2 with the minerals and fluids present in the host underground repositories and their caprock sealing (Xu et al. 2005; Kharaka et al. 2006, 2010; Benson and Cole 2008). Migration of supercritical CO_2 within these geological repositories is controlled by confinement/trapping of CO_2 in the porous structure as well as solubility of CO_2 in the fluids (brine and hydrocarbons) already present in the storage formation (Cole et al. 2010; Doughty 2010). In deep saline aquifers, the dissolution of CO_2 in water generates carbonic acid, which in turn reacts with minerals such as clay, mica and feldspar and carbonates present in the reservoir rocks to generate cations and carbonate/bicarbonate ions (Kaszuba et al. 2003, 2005; Kharaka et al. 2006; Ketzer et al. 2009; Cole et al. 2010; Doughty 2010). Finally, precipitation of metal carbonate occurs either by direct or indirect reaction of the CO_2 with other minerals and organic matter present in the reservoirs (Garcia et al. 2012; Kharaka et al. 2010; Shao et al. 2010, Xu et al. 2004, 2005).

It is essential to understand and predict the chemical reactions and stability of mineral phases formed under sequestration conditions as these could affect the migration of CO_2 and the seal integrity of the geologic reservoir (Kharaka et al. 2006, 2010; Benson and Cole 2008). Carbonation reactions of cations that exist in formation fluids and the transformation of minerals present in the host rocks into metal carbonates would produce the most permanent and desirable form of subsurface CO_2 storage (Xu et al. 2004, 2005; Ketzer et al. 2009). Carbonation and dissolution/precipitation of silicates changes the solid volume in the caprocks, which potentially can lead to either sealing of existing cracks and micropores or the creation of new porosity, depending on where old minerals dissolve and new ones precipitate and on the volume change of the reactions (Matter and Kelemen 2009). Basalt and peridotite rich in Ca, Mg, Mn and Fe silicates, olivine, serpentine, pyroxene and plagioclase, are considered to have the highest potential to react with dissolved CO_2 in water to precipitate solid carbonates (Ferrini et al. 2009; Matter and Kelemen 2009). However, several geological sites under consideration for sequestration are in sedimentary basins and consist of sandstone, siltstone, and shale made up of minerals such as quartz, clay, dolomite, gypsum, anhydrite, and halite. Though simple carbonates, $CaCO_3$, $MgCO_3$, $FeCO_3$, $MnCO_3$ and their solid solutions are

1529-6466/13/0077-0003$05.00 http://dx.doi.org/10.2138/rmg.2013.77.3

commonly considered to be the main carbonation products, a number of other carbonates and mineral phases containing both carbonate and silicate in their structures have been reported and their formation along with metal carbonates must be considered to better characterize long term geologic CO_2 sequestration.

Carbonate mineralization is a slow process since it involves complex rock-H_2O/fluid-CO_2 interactions and the kinetic and thermodynamic aspects of these processes are not well understood. The knowledge of both these aspects for carbonate formation is critical in assessing the feasibility and safety of sequestration. This review focuses on the thermodynamic aspects, stressing the energetics of the progression from aqueous solution to possible prenucleation clusters, to amorphous and nanocrystalline carbonate precipitates, and finally to well-crystallized carbonate phases. In addition to the common carbonate phases in the system $CaCO_3$-$MgCO_3$-$FeCO_3$ and $MnCO_3$, some more exotic carbonate and carbonate-silicate phases are also reviewed. Some issues of carbonate stability under a range of conditions broader than those encountered for sequestration are also addressed because they shed light on structure, bonding, and energetics.

SEQUENCES OF CARBONATE CRYSTALLIZATION

The physical principles governing various phase formation are complex and depend on crystal growth ($\Delta G_{\text{Nucleation}} + \Delta G_{\text{Growth}}$) and subsequent phase transformation ($\Delta G_{\text{Phase–trans}}$). As discussed in detail in other chapters in this volume, the thermodynamics, mechanisms, and kinetics of precipitation of carbonates from aqueous solution, especially at the relatively high temperatures and pressures encountered in the possible CO_2 sequestration environment, are still poorly known. Crystal formation by nucleation and growth is a free energy driven phenomenon and reflects solution supersaturation. The initial solution with high free energy reaches the lower equilibrium free energy state by final solid phase formation. Saturation is reached when concentrations (activities) of reactant components in the initial solution equal their equilibrium concentrations (activities) or solubility product (K_{sp}) and the change in free energy (per mole) $\Delta G = -RT\ln K_{sp}$ (R is the gas constant, and T is the absolute temperature). Supersaturation reflects higher concentrations. Saturation and supersaturation can be brought about by changes in reactant concentrations, pH, pCO_2, pressure, or temperature.

According to classical theory, nucleation of a new phase (particle with radius r) is activation energy driven and is associated with interplay between free energy change per molecule of bulk solid ($4\prod r^3\Delta G_{bulk}/3$) and surface ($4\prod r^2\gamma$) formation. The interfacial free energy (γ) is a positive term that destabilizes the nucleus below a critical size. Above critical size, the bulk free energy (proportional to r^3) overcomes the positive free energy (proportional to r^2) due to generation of an interface, and then nucleation and growth can proceed. Consequently, any factors that cause a change in interface energy (γ) influence nucleation. Thus factors such as formation of intermediate metastable phases, surface adsorbed water/ions or presence of foreign substrates are known to alter nucleation, crystal growth, and phase transformation processes.

Under near-ambient conditions, there is increasing evidence that carbonate crystallization occurs not only by classical nucleation and growth (De Yoreo and Vekilov 2003; De Yoreo and Dove 2004; De Yoreo et al. 2007, 2009), but also by various other non-classical mechanisms involving prenucleation clusters, metastable liquid-like precursors, mesocrystals, amorphous and nanophase precursors in the early stages of crystal growth (Gebauer and Coelfen 2011; Navrotsky 2004; Gebauer et al. 2008; Gower 2008; Meldrum and Colfen 2008; Tribello et al. 2009; Raiteri and Gale 2010; Demichelis et al. 2011; Bewernitz et al. 2012). In classical nucleation, the initial random solute clusters formed in a supersaturated solution are thermodynamically unstable and decompose until they reach a critical size, leaving only a very low, dynamic, and transient concentration of such species in solution (see Fig. 1).

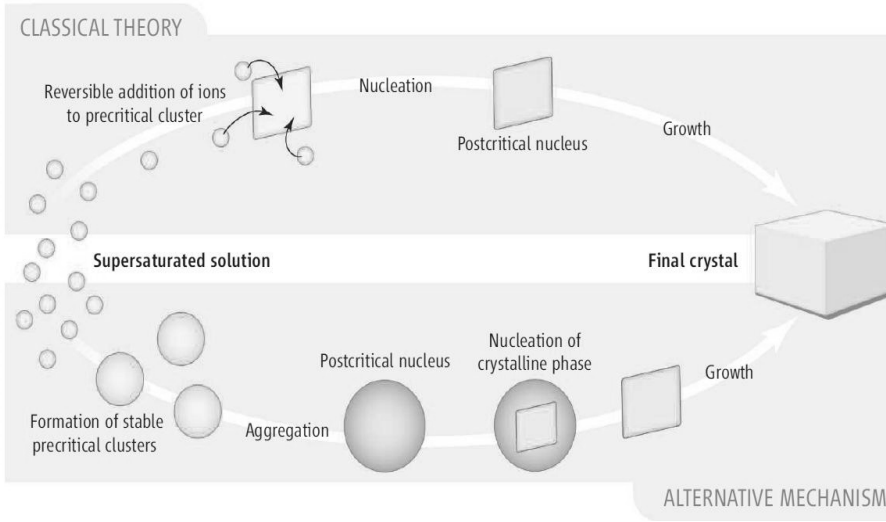

Figure 1. Schematic of carbonate nucleation by (a) classical nucleation theory by addition of ions to a single cluster (top) and (b) alternative mechanism by aggregation of stable, amorphous, precritical clusters (bottom). Reprinted with permission from Meldrum and Sear (2008). Copyright 2008 by the American Association for the Advancement of Science.

In contrast to this classical picture, prior to the carbonate phase nucleation, aqueous solutions often contain "prenucleation clusters", groupings of cations, carbonate groups and water that are intermediate in size between molecules and nanophase precipitates. These clusters, that may or may not resemble the final phase, could act as precursors for the precipitation of nanophase carbonates (see Fig. 1). They are often initially heavily hydrated and amorphous to X-ray diffraction, as discussed below. They may be a thermodynamic intermediate on the road to solid phases, intermediate in free energy between dissolved ions and nanoparticles. Classical and nonclassical nucleation are discussed in detail by De Yoreo et al. (2013, this volume).

Thermodynamics of prenucleation clusters

Prenucleation clusters were initially detected by careful solubility studies that suggested a lowering of thermodynamic activity of ions in solution, leaving not all Ca^{2+} and CO_3^{2-} "free" to precipitate $CaCO_3$ (Gebauer et al. 2008). This implies that bound states of calcium and carbonate ions in clusters may exist in solution and involve a significant fraction of the concentration of these ions (see Fig. 2). These initial observations have been followed by analytical ultracentrifugation (AUC), spectroscopic and cryo-TEM studies that provided stronger evidence for the existence of clusters of about 2 nm in diameter that can grow by colliding and coalescing (Gebauer et al. 2008; Pouget et al. 2009; Gebauer and Coelfen 2011). The cluster formation reaction can be represented as:

$$z\mathrm{Ca}^{2+} + z\mathrm{CO}_3^{\ 2-} + n\mathrm{H}_2\mathrm{O} = [\mathrm{CaCO}_3]_z{\cdot}n\mathrm{H}_2\mathrm{O}$$

Thermodynamic equilibrium for this reaction was established by showing the reversibility of the system with changes in pH and calcium concentration (Gebauer et al. 2008). Unfortunately, unknown cluster structure, size and activity made it impossible to directly determine the thermodynamic equilibrium constant for this reaction. Therefore, in a different approach, the cluster equilibrium was characterized using an ion-binding speciation model with multiple equal and independent equilibrium constants ($K' = K_1 = K_2 = K_3 = \ldots$) as depicted schematically in Figure 3 (Gebauer et al. 2008). The binding strength increases with increased calcium ion bind-

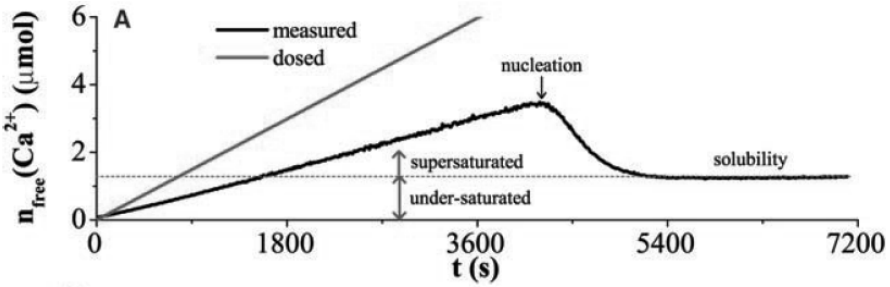

Figure 2. Free calcium ions measured by the calcium ion selective electrode (thick black line) in comparison with the dosed amount of calcium ions (dark grey line) at pH 9.5. The difference between these two gives the bound calcium ions. Reproduced with permission from Gebauer et al. (2008). Copyright 2008 by the American Association for the Advancement of Science.

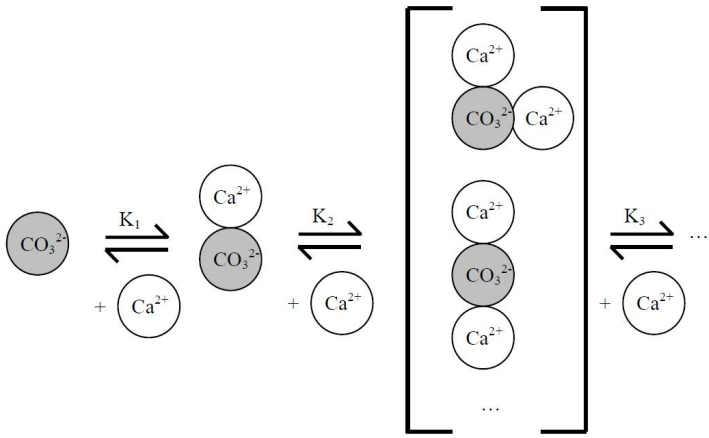

Figure 3. A schematic of multiple-binding equilibrium model depicting a carbonate centre-ion and binding calcium ions. The bracket shows various three dimensional possible bonding structures for the equilibrium steps and the steps are independent with equalized equilibrium constants $K = K_1 = K_2 = K_3 \ldots$ From supporting information of Gebauer et al. (2008) and is reprinted with permission. Copyright 2008 by the American Association for the Advancement of Science.

ing with carbonate in multiple equal steps and finally attains the macroscopic binding strength (K') similar to ion pair formation in the clusters. Hence one can use the macroscopic binding constant to arrive at the standard free energy of ion pair formation in clusters ($-RT\ln K' = \Delta G_{ion-pair}$). The average amount of bound calcium and carbonate ions could be quantified indirectly using a calcium ion sensitive electrode and constant pH titration for carbonate ions (Gebauer et al. 2008). The difference between measured free calcium ion concentration and the dosed amount corresponds to the amount of bound calcium ions in the clusters. The derived equilibrium constants ($K >> 1$, i.e., $\Delta G < 0$) suggest that the clusters are thermodynamically stable with respect to both free ions as well as ion pairs and correspond to a global Gibbs free energy minimum in the solution phase. The average free energy over several equilibria for ion pair formation in the clusters at pH 8.5 to 9.8 range from −17.3 to −18.5 kJ/mol. The clusters formed at lower pH are found to be thermodynamically more stable than ones formed in higher pH solution. Addition of more calcium ions makes the solution state metastable with respect to a solid phase and aggregation of these clusters leads to the nucleation of amorphous nanoparticles in solution and eventually to the calcite phase through various metastable amorphous and crystalline phases.

Figure 4 shows a schematic free energy profile for amorphous calcium carbonate from ion pairs in solution by the nonclassical mechanism and its evolution to the crystalline phase (Gebauer et al. 2008; Meldrum and Colfen 2008; Pouget et al. 2009; Gebauer and Coelfen 2011).

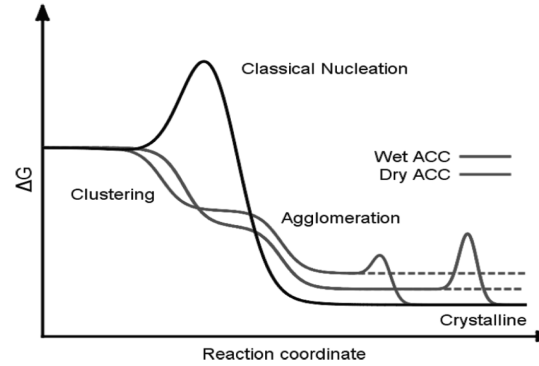

Figure 4. A schematic of free energy profile for calcium carbonate from ion pairs in solution by classical and non-classical methods. Used with permission from Raiteri and Gale (2010). Copyright 2010 by the American Chemical Society.

Prenucleation cluster formation has also been observed in pure magnesium as well as in a mixed calcium and magnesium solution in contact with carbonate ions (Verch et al. 2012). The ultracentrifugation experiments suggest the existence of more than one type of cluster species in pure $MgCO_3$ solutions. In mixed Ca/Mg solutions, the formation of mixed cation pre-nucleation clusters was found to be favored over pure $CaCO_3$ and $MgCO_3$ clusters. In addition, in mixed clusters calcium enrichment over magnesium was observed with respect to the solution composition over the entire Ca/Mg composition range. This could explain high magnesium contents observed in biogenic amorphous calcium carbonates (Gebauer and Coelfen 2011; Verch et al. 2012).

Cluster formation in the early stages of carbonate formation was also suggested by several computational studies (Quigley and Rodger 2008; Tribello et al. 2009; Raiteri and Gale 2010; Raiteri et al. 2010). These studies proved to be very useful in overcoming the experimental difficulties in obtaining the thermodynamic data for cluster formation. Molecular dynamics studies on growth of calcium carbonate in water suggested calcium-carbonate ion pairs binding in clusters is exothermic and falls in the range of −10 and −16 kJ/mol (Raiteri and Gale 2010; Raiteri et al. 2010). The free energy profiles from ion pair binding to clusters to amorphous calcium carbonate (ACC) showed no systematic change in binding energy as a function of increasing size (see Fig. 5). This profile shows a very small (nearly zero) activation energy for the cluster growth process in ACC. The two minima at distances of 2.5-4 Å are due to inclusion of ion pairs into the cluster. These minima become deeper at the point where clusters transform into an ACC precipitate. Therefore, the growth of ACC proceeds without any thermodynamic energy barriers as opposed to a large barrier to calcite crystal growth. Though calcite nanocrystals are stable in solution, at high supersaturation, particles of amorphous material form because they grow much faster than the calcite nanocrystals. The two steps of formation of an ion pair and binding of this ion pair to the cluster in the simulation actually represent ion pair formation in clusters. The average free energy changes for these two steps (the midpoint of the energy range, −20 kJ/mol, gives the free energy of formation of an ion pair in a cluster. This value is in good agreement with the experimentally measured value by Gebauer et al. (−18.5 kJ/mol at pH 8.5). These computational studies match with the experimental data and support the experimental observation of stable prenucleation clusters (Gebauer et al. 2008; Gebauer and Coelfen 2011; Verch et al. 2012).

Thermodynamics of metastable liquid precursors

Calcium carbonate nucleation has also been suggested to occur by a liquid-liquid phase separation mechanism with formation of tiny droplets of a calcium carbonate rich solution from the bulk solution (Gower 2008; Bewernitz et al. 2012). This phenomenon, also known

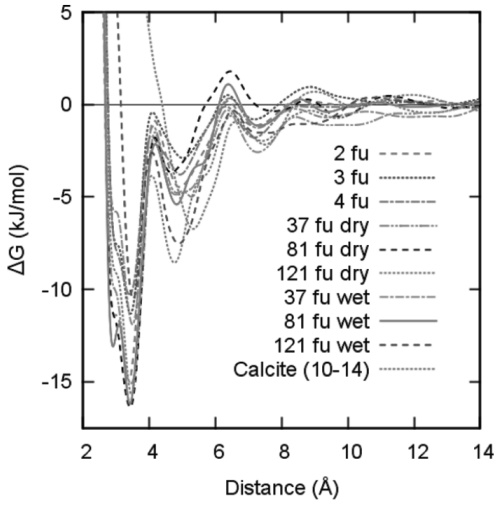

Figure 5. Computed free energy profiles for addition of $CaCO_3$ ion pair to clusters in anhydrous amorphous calcium carbonate and calcite (104) surface. The label of (n + 1) fu indicates the final state of the cluster with (n+1) number of formula units. Used with permission from Raiteri and Gale (2010). Copyright 2010 by the American Chemical Society.

as a polymer induced liquid precursor process (PILP), was first reported by Gower et al. (2008) during calcium carbonate film formation in presence of polyaspartate and was initially thought to be a polymer additive mediated process. Later, evidence of the existence of a liquid drop phase was also demonstrated by acoustic levitation, cryo-TEM and CO_2 outgassing techniques (Faatz et al. 2004; Rieger et al. 2007; Wolf et al. 2011). The thermodynamics of phase separation or PILP formation in the $CaCO_3$ system has been investigated by directly measuring the enthalpy change during punctuated injection of aqueous $CaCl_2$ to a bicarbonate buffer using isothermal titration calorimetry with and without polymer additives (Bewernitz et al. 2012). The enthalpy measurements showed an endothermic process with a discontinuous trend characteristic of a first order phase transition (see Fig. 6). The endothermic enthalpy for liquid droplet formation strongly suggests a major entropic contribution for its stabilization.

In addition, the phase evolution in a similar titration was characterized by a combination of several experimental techniques (light scattering, analytical ultracentrifugation and ^{13}C NMR) (Bewernitz et al. 2012). These studies suggested the emergence of droplets (60 nm size) at the first order transition point, which grew into larger drops of a calcium carbonate rich phase on addition of more Ca^{2+} to the solution. Unlike prenucleation clusters, the liquid condensed phase had a significant amount of calcium bicarbonate ion pairs, which led to an additional energy barrier due to deprotonation of bicarbonate ions during the nucleation of calcium carbonate particles (see Fig. 7). This mechanism thus can lead to ACC formation since crystallization has a large barrier.

Molecular dynamics simulations also showed the formation of stable ionic polymers consisting of linear or branched chains of cations and carbonate/bicarbonate prior to nucleation. These were called dynamically ordered liquid-like oxyanion polymers (DOLLOP) (Demichelis et al. 2011). The chains grew longer on collisions with ions/ion pairs and showed flexibility to distortion similar to a liquid droplet since the free energy cost for changes in radius of gyration is less than ambient thermal energy. The computed free energies for speciation of different ion pairs from this study are listed in Table 1. The transition from DOLLOP to ACC occurs with a significant activation barrier as it involves dehydration of DOLLOP, supporting earlier experimental prediction (Plummer and Busenberg 1982).

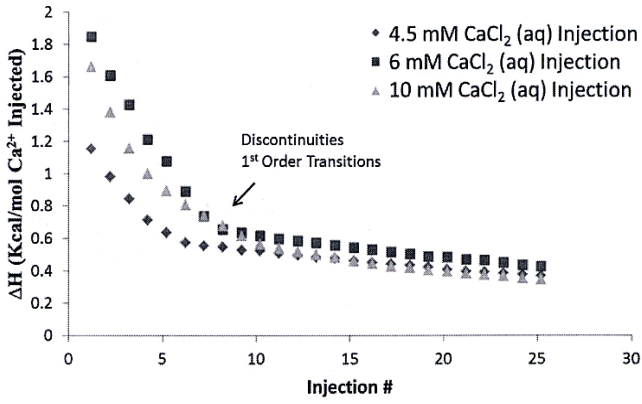

Figure 6. The enthalpy of reaction during the titration of $CaCl_{2(aq)}$ into 20 mM carbonate buffer, pH 8.5. Reprinted from Bewernitz et al. (2012) with permission. Copyright © 2012 Royal Society of Chemistry.

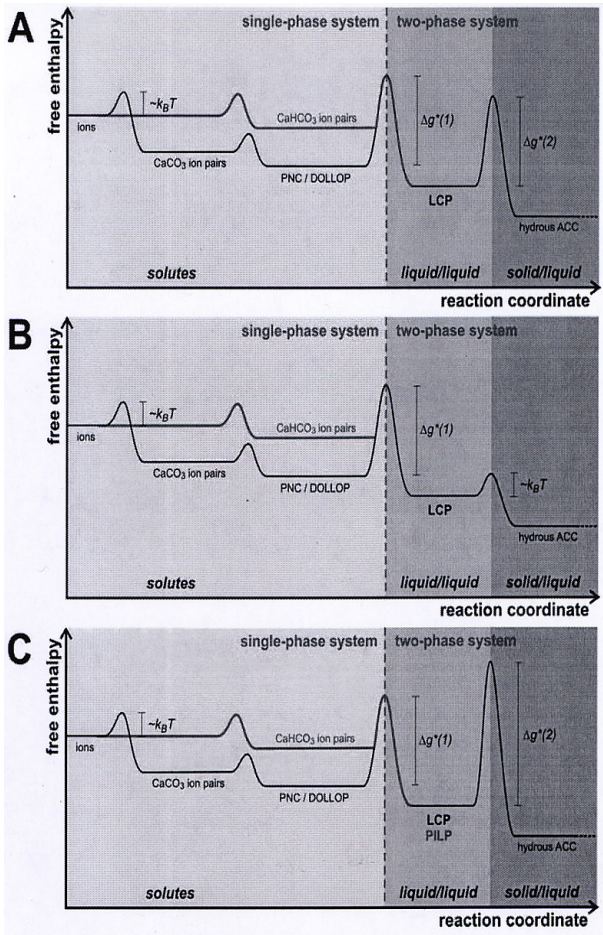

Figure 7. The energetics of calcium carbonate precipitation from supersaturated solution. (A) At neutral pH, nucleation occurs with calcium bicarbonate species with intrinsic kinetic stabilization, $\Delta G^*(2)$. (B) At higher pH, $\Delta G^*(2)$ almost vanishes due to negligible calcium bicarbonate ion pairing and carbonate species dominate the nucleation process with transient liquid condensed phase LCP. (C) In the presence of PAsp polymer, the $\Delta G^*(2)$ barrier increases due to a pronounced role of bicarbonate species in the LCP. Reprinted from Bewernitz et al. (2012) with permission. Copyright © 2012 Royal Society of Chemistry.

Table 1. Free energies from molecular dynamic simulations for three reactions obtained by ion pair speciation model at 0.5, 0.28 and 0.06 M. Reproduced with permission from Demichelis et al. (2011). Copyright © 2011 Nature Publishing Group.

Reaction	Free energies (kJ/mol)		
	pH 9.5	pH 10	Fit to all pHs
$Ca^{2+} + HCO_3^- \rightarrow CaHCO_3^+$	−11.4	−11.4	−11.3
$Ca^{2+} + CO_3^{2-} \rightarrow CaCO_3^0$	−18.6	−20.5	−20.3
$CaCO_3^0 + (CaCO_3^0)_n \rightarrow (CaCO_3^0)_{n+1}$	−22.9	−22.0	−21.7

Mesocrystallization

Mesocrystallization refers to the organization of nanocrystalline particles with various crystallographic registries by different mechanisms as illustrated in Figure 8. Such assemblies form either by oriented attachment of crystalline nano-bricks with surface functionalized polymeric additives or by crystallization of a dense array of amorphous calcium carbonate (ACC) precursor particles. (Colfen and Antonietti 2008; Meldrum and Colfen 2008)

Amorphous carbonates: Energetics of the $CaCO_3$-$MgCO_3$-$FeCO_3$-$MnCO_3$ system

Recent acid solution calorimetric studies have focused on the energetics of amorphous carbonates (amorphous calcium carbonate = ACC, amorphous magnesium carbonate = AMC, ACC-AMC solid solutions, amorphous iron carbonate = AFC and amorphous manganese carbonate = AMNC). Data are summarized in Table 2.

ACC can be precipitated from aqueous solution below room temperature but it is not persistent, crystallizing in hours or less in contact with its mother liquor and within a few days even when separated and dried. ACC is also formed biogenically as a precursor to calcite or aragonite structures in organisms such as molluscs and sea urchins. Calorimetric study (see Fig. 9) shows a complex energy landscape, with ACC progressively dehydrating to more energetically stable amorphous forms, and then crystallizing to nanocrystalline and finally bulk crystalline carbonate (Radha et al. 2010). ACC can be a precursor for vaterite, aragonite, or calcite, lying higher in energy than any of these crystalline forms (Radha et al. 2010). The ACC crystallization energetics reported by various experimental and computational studies are summarized in Table 3.

The ACC–AMC system with $0 \le x = Mg/(Mg+Ca) \le 1$ (see Fig. 10) shows a number of interesting energetic trends (Radha et al. 2012). All solid solution compositions are less metastable than a mixture of the end-members, ACC and AMC (enthalpies of formation from calcite and magnesite less positive for solid solutions than for mechanical mixture). There is a definite break in the energetic trends near $x = 0.5$, a composition corresponding to dolomite (see Fig. 10). This break separates two roughly linear distinct segments in enthalpy; a "homogeneous region for $x < 0.5$ and a heterogeneous one for $x > 0.5$, the latter showing two sets of decomposition peaks in DSC curves. Although powder XRD confirms the amorphous nature over the entire composition range, $0 < x < 1$, characterization by TGA/DSC coupled with FTIR suggests heterogeneous (pseudo two phase) behavior for samples with $0.5 < x < 1$ (Radha et al. 2012). All these data support the coexistence of a mixture of AMC with an amorphous material with composition near $x = 0.5$ for Mg-rich bulk compositions with $x > 0.5$. The length scale of this phase separation may be higher than the coherent domain size and short range order interrogated by the X-ray pair distribution functions (PDF) as the PDF data are not conclusive in determining the existence of heterogeneity (Radha et al. 2012).

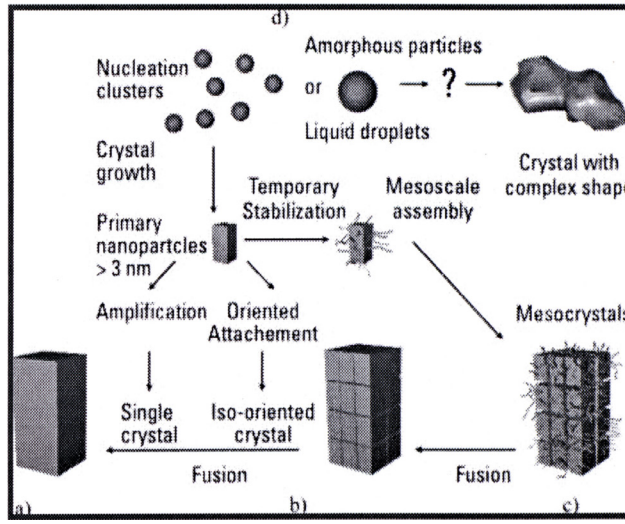

Figure 8. Schematic representation of (a) classical crystal nucleation and growth of a single crystal via primary nanoparticle, (b) single crystal formation from iso-oriented crystal due to oriented attachment of primary nanoparticles (c) mesocrystal formation either from a polymer or additive covered primary nanoparticles or directly from pure nanoparticle and (d) formation of amorphous particles and its transformation to complicated morphologies. Reprinted with permission from Colfen and Antonietti (2008). Copyright 2008 John Wiley & Sons.

Table 2. Calorimetric data for amorphous carbonate phases and corresponding water content per MCO_3. Reproduced with permission of Elsevier Science from Sel et al. (2012). Copyright © 2012 Elsevier Science.

Amorphous $MCO_3 \cdot nH_2O$	**Water from TGA (n) (mol)**	**Enthalpy of Crystallization (ΔH_{crys}) (kJ/mol)**	**Ionic/crystal radius M^{2+} (nm)**	**Refs.**
$MnCO_3 \cdot nH_2O$ (AMNC)	1.2 ± 0.04	−32.44± 0.71	0.083 (0.097)	[1]
$CaCO_3 \cdot nH_2O$ (ACC)	1.13 - 1.58	−17 ± 1 to −24 ± 1	0.1 (0.114)	[2]
$MgCO_3 \cdot nH_2O$ (AMC)	1.28	−35.8 ± 1.2	0.072 (0.086)	[3]
$FeCO_3 \cdot nH_2O$ (AFC)	1.75	−37.8 ± 9.8	0.078 (0.092)	[4]

The values in () is crystal radius.
References: [1] Radha and Navrotsky (in prep); [2] Radha et al. (2010); [3] Radha et al. (2012); [4] Sel et al. (2012)

The enthalpies of crystallization in the homogeneous region vary roughly linearly with x and range from −10.6 ± 0.8 to −16.9 ± 0.6 kJ/mol. Interestingly, the crystallization enthalpy measured for the biogenic spicule sample containing about 5 mol% $MgCO_3$ extracted from California purple sea urchin larval spicules (−13.3 ± 0.5 kJ/mol) falls in this region (Radha et al. 2010). The overlaid histogram in Figure 10 shows the number of reported biominerals containing different amounts of Mg (Addadi et al. 2003). It can be seen that the Mg content in biominerals varies between $x = 0$ and $x = 0.3$ coincides with the low metastability portion of this region ($0.02 < x < 0.20$) (Beniash et al. 1997; Aizenberg et al. 2002; Addadi et al. 2003). This observation suggests that the marine organisms may select this single-phase low-metastability pathway for calcification by controlling the Mg uptake in the early stages of

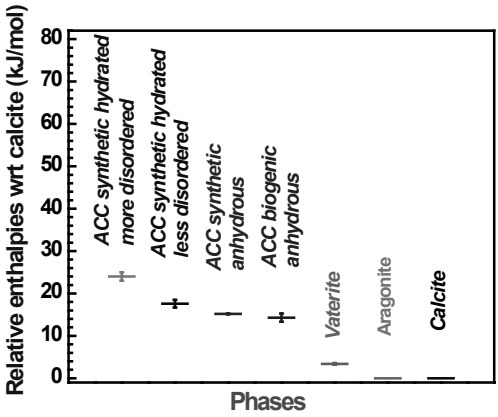

Figure 9. Energetic stabilities of different calcium carbonate phases with respect to calcite. The enthalpy values of vaterite and aragonite are taken from Wolf et al. (2000) and Wolf et al. (1996) respectively. Reprinted from Radha et al. (2010) with permission of the National Academy of Sciences, USA. Copyright © 2010 National Academy of Sciences, USA.

Table 3. Experimental and computational energetic data on various $CaCO_3$ phases with respect to calcite. Modified from Wang and Becker (2012).

ACC	Disordered Vaterite	Ordered Vaterite	Aragonite	Method	Refs.
+26.6	20.7	9.7	–3.0	MD simulations	[1]
+28.5				MD simulations	[1]
			–4.8	MD Force fields	[2]
			12.67	MD Force fields	[2]
		5.0	8.6	DFT (DMol3) plane wave	[1]
	16.39	2.95	0.996	DFT (CASTEP) plane wave	[1]
	17.54	5.72	12.69	DFT (CASTEP) ultrafast pseudopotential	[1]
	19.8	5.8	12.19	DFT (VASP and GGA-PAW)	[1]
			–4.9	DFT (SIESTA) linear scaling	[2]
			+9.3		[2]
+15.0				Thermoanalysis	[3]
+14.3				Anhydrous ACC by calorimetry	[4]
+22.7				More disordered ACC by calorimetry	[4]
+17.2				Less disordered ACC by calorimetry	[4]
+12.3				Thermal analysis	[5]
	6.2		1.2	Dissociation reactions	[6]
	3.4		–0.4	Calorimetric and potentiometric methods	[7]

References: [1] Wang amd Becker (2009, 2012); [2] Raiteri et al. (2010); [3] Wolf and Gunther (2001); [4] Radha et al. (2010); [5] Koga et al. (1998); [6] Plummer and Busenberg (1982); [7] Wolf et al. (1996, 2000)

biomineralization. An earlier study (Wang et al. 2009) suggests that the electrostatic potential around carboxyl groups in proteins regulates Mg uptake, probably by assisting the dehydration of the Mg^{2+} ions, i.e., by assisting the kinetics of Mg^{2+} incorporation. Calorimetric studies suggest that there is an additional thermodynamic driving force to the incorporation of Mg^{2+} into biominerals. It is also interesting that the materials with $x < 0.20$ crystallize more readily than those with higher Mg content. The ability to tune crystallization rates on time scales of hours to days (rather than weeks to months) may be another reason organisms control the Mg content of the amorphous carbonate precursors to be in this range.

The water content appears to influence the enthalpies of crystallization and hence the metastability of samples. The enthalpies of crystallization of more hydrated samples deviate

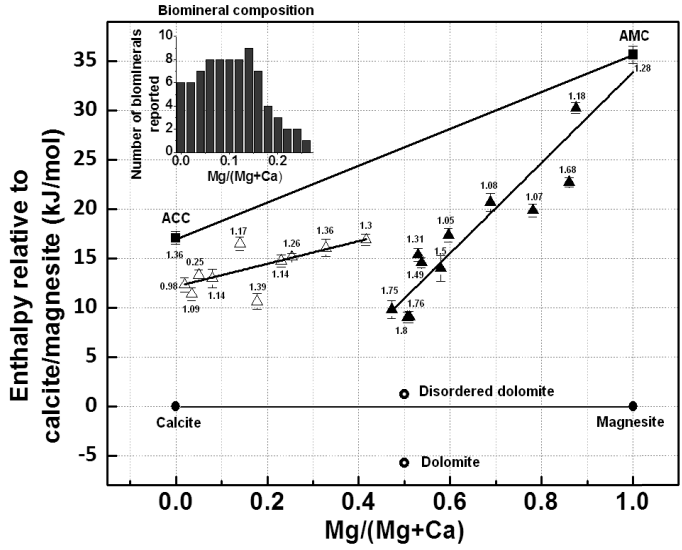

Figure 10. Energetic stabilities of amorphous $Ca_{1-x}Mg_xCO_3{\cdot}nH_2O$ ($0 \le x \le 1$) phases with respect to calcite and magnesite. Open triangles are for homogeneous single phase region and filled triangles represent potentially heterogeneous two phase region. The inset is the histogram of number of binominals as function of their Mg contents (Addadi et al. 2003). The values of disordered dolomite and dolomite are taken from Navrotsky and Capobianco (1987) and Chai et al. (1995). The number on each symbol is the water content of corresponding amorphous phase. Reprinted from Radha et al. (2012) with permission from Elsevier Science. Copyright © 2012 Elsevier Science.

from the linear trend to less exothermic enthalpies of crystallization in both regions, which indicates lower energetic metastability of more hydrated amorphous materials. The most hydrated samples occur at x = 0.47 to 0.51 and have the least exothermic enthalpies of crystallization in the whole system (see Fig. 10). The Mg/Ca ratio in this range is similar to that in dolomite. This suggests that this region, having lesser metastability, could be an amorphous precursor to dolomite formation.

The more exothermic crystallization enthalpy of AMC compared to ACC suggests that AMC is more metastable than ACC. Nevertheless AMC is much more persistent, surviving for a year or more under ambient conditions without crystallizing (Radha et al. 2012). This may be a kinetic effect related to the difficulty of dehydrating the first coordination sphere of the Mg^{2+} ion. The low temperature decomposition of AMC (432 °C) without any sign of crystallization indicates that AMC is thermally less stable than ACC (771 °C). Magnesite, the stable crystalline form of $MgCO_3$, appears to form only under high temperature synthesis conditions either by hydrothermal methods or by reaction of MgO with CO_2. Hence AMC does not appear to be a precursor phase to magnesite and the possible significance of AMC formation in carbonate mineralization under various conditions may require more detailed investigation.

The energetics of the amorphous iron carbonate (AFC) precursor formed during siderite precipitation has been measured by high-temperature oxide-melt solution calorimetry (Sel et al. 2012). The synthesis, isolation and characterization of AFC require maintenance of anaerobic condition (in nitrogen glove box) to prevent Fe^{2+} oxidation and probably for this reason there is not much report of synthetic AFC in the literature. Thermal decomposition of AFC on heating is complex and the oxide phases formed at the end of decomposition are different in inert and oxidizing conditions. In an inert Ar atmosphere, the DSC profile of AFC shows an endothermic

peak near 120 °C due to dehydration and multiple thermal events at 160-325 °C due to simultaneous crystallization (exothermic) and decomposition (endothermic) of $FeCO_3$ to FeO and CO_2. At higher temperature, FeO further reacts with CO_2 (exothermic) to form Fe_3O_4 or Fe_2O_3 and CO gas. Thermal decomposition of AFC in air or oxygen leads to formation of hematite (Fe_2O_3) (for more details, see Sel et al. 2012).

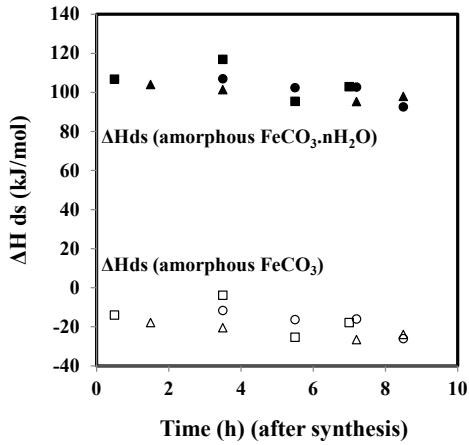

Figure 11. The ethalpies of drop solution ΔH_{ds} data of amorphous iron (II) carbonate (AFC) as a function of time after their synthesis for three different samples. ΔH_{ds} (amorphous $FeCO_3$) is for anhydrous sample corrected for water determined from the TGA/DSC as physically absorbed water. Reproduced with permission of Elsevier Science from Sel et al. (2012). Copyright © 2012 Elsevier Science.

Calorimetric measurements have been done on several freshly prepared samples of AFC to minimize the effects of oxidation (Fe^{2+} to Fe^{3+}), amorphous phase short range structure evolution, and crystallization to siderite. The scatter in the calorimetric data measured within 8-9 h after the synthesis (see Fig. 11) is reasonable considering the sample handling challenges of these highly air sensitive samples. The exothermic crystallization enthalpy (−37.8 ± 9.8 kJ/mol) of AFC suggests that amorphous $FeCO_3$ (AFC) precursor provides a low energy pathway for crystallization of siderite. AFC is energetically similar to amorphous $MgCO_3$ (AMC) and more metastable than amorphous $CaCO_3$ (ACC). AMC is more persistent than either ACC or AFC, despite being more metastable. This may relate to strength of hydration.

The crystallization energetics of amorphous manganese carbonate (AMNC) has been measured by acid solution calorimetry (Radha and Navrotsky 2013). XRD studies suggest that the dry AMNC slowly crystallizes to rhodochrosite, $MnCO_3$, after 40 days. The thermal decomposition reactions of AMNC are analogous to those of AFC. In oxidative conditions, $MnCO_3$ undergoes decomposition with multiple steps and forms various high oxidation state phases such as MnO_2, Mn_2O_3 and Mn_3O_4 at different temperatures. In an inert atmosphere, it decomposes in a single step to MnO and CO_2. At higher temperature, the liberated CO_2 if not flushed out, further reacts with MnO to form Mn_3O_4 and CO. Consequently, the TG-DSC profile of AMNC in argon first shows an endothermic DSC peak (30-200 °C) corresponding to dehydration. The DSC profile for the second step (200-420 °C) shows multiple thermal events with simultaneous crystallization (exothermic) and decomposition (endothermic) occurring at ~ 400 °C. The crystallization enthalpy for freshly prepared AMNC is −32.44 ± 0.71 kJ/mol. This exothermic crystallization of AMNC suggests that the amorphous phase is metastable and could provide a low energy pathway for crystalline rhodochrosite mineralization similar to other carbonate systems with Ca, Mg and Fe cations.

The formation of common carbonates in natural environments occurs in far from equilibrium conditions and the various metastable amorphous and nanoparticulate precursor phases may control the mineralization process (Morse and Casey 1988). Calorimetric studies show that amorphous carbonate precursors provide a low energy crystallization pathway in the (Ca-Mg-Fe-Mn)-CO_3 system. To constrain the driving force for crystallization of carbonates in these systems, we compare the crystallization energetics of amorphous Ca, Mg, Fe and Mn carbonates in Table 2. The crystallization enthalpies become less exothermic with increase in

ionic radius of the cations. The ionic size driven crystallization enthalpy trend in (Ca-Mg-Fe-Mn)-CO_3 system suggests that the crystallization of amorphous phases with smaller cations may be energetically more favored than that for larger cations. A study on patterns of structure - property relationships in carbonate minerals reported many cation-size dependent phenomena in crystalline isostructural carbonates (Railsback 1999). The physical (hardness, and density) and spectroscopic (shifts in IR peak positions) properties of rhombohedral carbonates showed a linear dependency on the cation radius and degree of hydration. Such trends are mainly attributed to variation in metal-oxygen bond lengths (Railsback 1999). Geochemical properties such as solubility and distribution coefficients appear to be controlled by the degree of cationic fit in the crystal structure (Railsback 1999). The comparative study on amorphous carbonates illustrates the influence of cationic radius on thermodynamic properties of carbonate formation via crystallization processes. A critical understanding of these qualitative trends would help in developing a predictive capability for carbonate mineralization processes based on their physical properties

Nanophase carbonates and surface energies

Crystals of the same mineral grow into different shapes and morphologies under different synthetic and natural growth environments. Thermodynamic equilibrium under different conditions drives crystal growth to a minimum free energy state through wide combinations of crystal facets with different surface energies. These surface energies can be affected by the presence of inorganic, organic, and polymeric species in solution. In addition, deviations from equilibrium are common. A detailed discussion of the energetics of various carbonate crystal facets is beyond the scope of this review. When fine-grained carbonates are precipitated rapidly from aqueous solution at relatively low temperature, equilibrium among various growing faces may not be attained or maintained. The surface energies of phases can be determined by both computation and experimental techniques (see Tables 4, 5 and references therein). The computed surface energy values vary depending on the modeled crystal facet, the surface end groups, and the details of the calculation (see Table 4 and references there in). We concentrate here on surface energies measured by solution calorimetry on nanoparticle assemblages, having a range of particle sizes but a well-defined average surface area and showing some average distribution of exposed crystal faces determined by the precipitation conditions. Such materials may in fact be representative of many natural precipitation environments.

Calorimetric studies have demonstrated that nanoscale intermediates can control phase formation and morphology by reversing the order of thermodynamic stability of polymorphs (Navrotsky 2004, 2009, 2011). These size induced crossovers in the free energies of the polymorphs at the nanoscale show a correlation between increasing metastability and decreasing surface energy (Navrotsky 2001, 2004). The free energy crossovers due to increasing specific surface area (decreasing particle size) combined with small energy differences between bulk polymorphs have been exhibited by several oxide systems including alumina, titania, zirconia iron oxides and manganese oxides (McHale et al. 1997; Ranade et al. 2002; Pitcher et al. 2005; Levchenko et al. 2006; Navrotsky et al. 2008, 2010; Radha et al. 2009).

Calcium carbonate exists in five different crystalline polymorphs at ambient pressure as calcite, aragonite, vaterite (anhydrous phases), monohydrocalcite and ikaite (hydrated phases), in addition to various amorphous forms. Thermodynamic stability crossovers in calcium carbonate system at nanoscale regimes would have tremendous geologic and technological implications, including geological sequestration of CO_2. Calcium carbonate precipitation in a geologic CO_2 repository occurs in confined micro/nanopores of the sandstone aquifer and the stability crossovers could alter the dominant calcium carbonate phase precipitated under such conditions. Also the influence of the increased pressures, temperatures, and ionic strength of the environment could alter the precipitation pathway.

Table 4. A summary of computed calcite surface energies. Reproduced with permission from Forbes et al. (2011). Copyright © 2011 Elsevier Science.

Calcite Crystal Face	Energy of hydrous surface (J/m^2)	Energy of anhydrous surface (J/m^2)	Reference
$10\bar{1}4$	0.288	0.86	Kvamme et al. (2009)
	0.232	0.863	Hwang et al. (2001)
	0.387	0.59	Kerisit et al. (2003)
	0.14	0.60	Duffy and Harding (2004)
	0.16	0.59	de Leeuw and Parker (1998)
		0.59	Titloye et al. (1998)
$10\bar{1}0$	0.778	1.50	Kvamme et al. (2009)
		1.37	Hwang et al. (2001)
		0.95	Kerisit et al. (2003)
		1.23	Titloye et al. (1998)
	0.75	0.97	de Leeuw and Parker (1998)
		0.97	Titloye et al. (1998)
$10\bar{1}2$	0.37 or 0.44*	1.06 or 1.25*	Duffy and Harding (2004)
		0.75 or 1.06*	Bruno et al. (2008)
		2.62	Braybrook et al. (2002)
		2.65	Massaro et al. (2008)
$11\bar{2}0$		1.39	Titloye et al. (1998)
	0.43	1.39	de Leeuw and Parker (1998)

* The lower value corresponds to a surface terminated by carbonate groups and the higher value is a surface terminated by calcium ions.

Table 5. A summary of measured calcite surface energies by different experimental methods. Reproduced with permission from Forbes et al. (2011). Copyright © 2011 Elsevier Science.

Surface energy (J/m^2)	Method	Reference
0.085	Homogeneous nucleation	Sohnel and Mullin (1982)
0.064	Heterogeneous nucleation	Lioliou et al. (2007)
0.032-0.035	Heterogeneous nucleation on polymers	Dousi et al. (2003), Gomez-Morales et al. (2010)
0.033	Heterogeneous nucleation	Manoli and Dalas (2002)
0.23	Cleavage experiments	Gilman (1960)
0.347 ± 0.045	Cleavage technique	Gupta and Santhanam (1969)
0.32	Subcritical cracking	Roayne et al. (2011)
0.098	Contact angle measurements	Janczuk et al. (1986)
0.072	Contact angle measurements	Okayama et al. (1997)
0.54-0.76	Heat of immersion	Goujon and Mutaftschiev (1976)
0.762 ± 0.002	Heat of immersion	Wade and Hackerman (1959)

Surface energy data for calcite by both experimental and computational methods show a wide distribution covering several orders of magnitude (see Tables 4 and 5). Generally, calculated surface energies for other oxides agree with the measured values within 10-50%. Computed values are based on the ideal surface, while real surfaces have complex and heterogeneous structures with edge sites and defects (Navrotsky 2009, 2011). It is possible that the less directly determined experimental surface energy values for calcite are low because they are derived based on classical homogeneous and heterogeneous nucleation theory, rather than measured directly (see Table 5). The initial solid formed may be different (e.g. prenucleation clusters leading to amorphous precipitates). The surface energy of such metastable precursor phases (ACC or vaterite) are expected to be lower than that of the stable calcite phase. Furthermore, the induction times used in the surface energy determinations may not correspond to those for the formation of calcite. A similar concern was raised earlier in deriving the interfacial surface tension of calcite based on nucleation experiments (Christoffersen et al. 1991).

To determine the effect of particle size on thermodynamic stability in carbonate systems, the energetics of nanophase calcite and nanophase manganese carbonate phases were measured by acid solution and water adsorption calorimetric techniques (Forbes et al. 2011; Radha and Navrotsky 2013). A critical assessment of three different characterization techniques (XRD, TEM and BET methods) for particle size analysis for calcite phases suggests that the surface area measurement using the BET method is best suited for use in surface energy determination of calcite type structures (Forbes et al. 2011). The enthalpies of solution (ΔH_{sol}) for the nanophase and bulk carbonate phases were measured by acid solution (5 M HCl) calorimetry. The surface energy for a given surface area is the excess enthalpy of nanophase with respect to bulk obtained after subtracting the contribution of adsorbed water from enthalpies of solution (ΔH_{soln}) and can be written as

$$\Delta H_{sol\text{-}bulk} = \Delta H_{sol\text{-}corr\ nano} + SA \times \gamma$$

where SA = surface area of nanocalcite (m^2/mol); γ = surface enthalpy (J/m^2)

Solution enthalpies are corrected for physically ($\Delta H_{sol\text{-}corr\text{-}physi}$) or chemisorbed ($\Delta H_{sol\text{-}corr\text{-}chemi}$) water contents and plotted against the surface area obtained from BET analysis. The negative of the slopes of the linear fits give the surface enthalpies for hydrous and anhydrous surfaces. These surface enthalpy values are good approximations to the surface energy and surface free energy (surface tension) since the contribution of excess volume (*PV* term) and surface entropy ($T\Delta S$ term) are expected to be small (Navrotsky 2009). Figure 12 shows surface energy plots of hydrous and anhydrous surfaces of nanophase calcite and manganese carbonate. From the calorimetric data, the surface energies of hydrous and anhydrous surfaces are 1.48 ± 0.21 and 1.87 ± 0.13 J/m^2 for calcite (Forbes et al. 2011) and 0.64 ± 0.08 J/m^2 and 0.94 ± 0.12 J/m^2 for nano manganese carbonate (Radha and Navrotsky 2013). The measured values are generally larger than predicted from computational models (0.14 to 0.77 J/m^2 for hydrous and 0.59 to 2.65 J/m^2 for anhydrous surface) for idealized calcite surfaces (de Leeuw and Parker 1998; Titloye et al. 1998; Hwang et al. 2001; Braybrook et al. 2002; Kerisit et al. 2003; Duffy and Harding 2004; Bruno et al. 2008; Massaro et al. 2008; Kvamme et al. 2009) probably because the synthetic samples contain a range of planes and defect structures.

Studies of surface energies for aragonite and vaterite phases are in progress. Given the small differences in energy between the polymorphs, there is a good possibility that stability crossovers of the nanoscale may exist for calcium carbonate system as well as for oxide minerals.

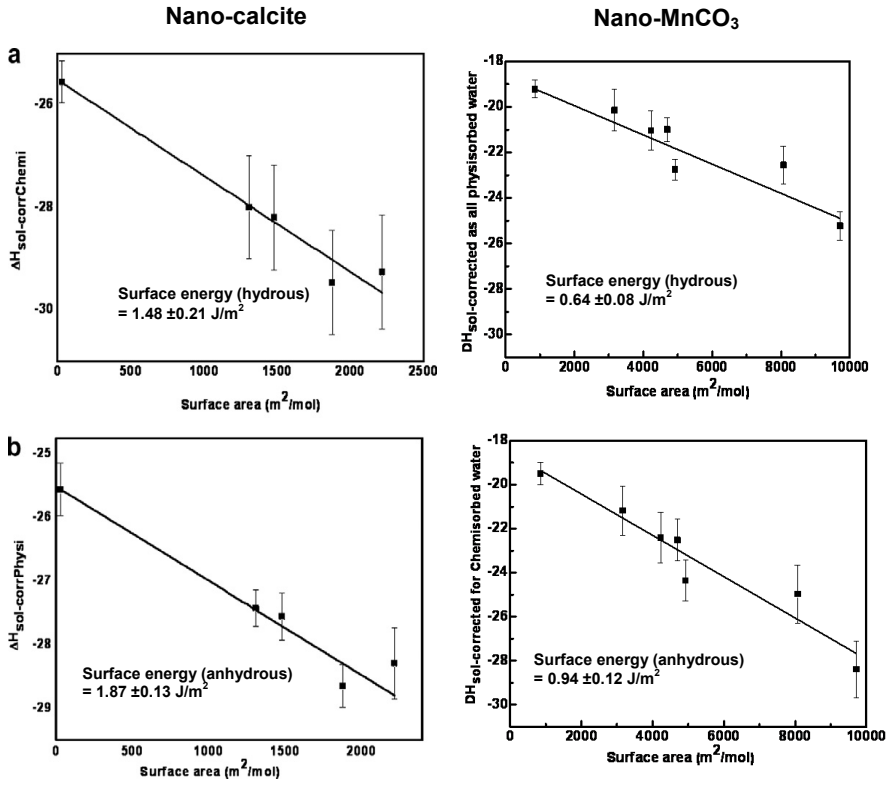

Figure 12. Surface energy plots of hydrous and anhydrous surfaces of nanophase calcite and manganese carbonate phases. Reprinted with permission of Elsevier Science from Forbes et al. (2011). Copyright © 2011 Elsevier Science.

CRYSTALLINE DIVALENT CARBONATES

Thermodynamics of rhombohedral and orthorhombic carbonates

Crystalline anhydrous metal carbonates, $M(II)CO_3$ exist either in rhombohedral (calcite type) or orthorhombic (aragonite-type) structure depending on the cation size (Reeder 1983). Divalent cations smaller than Ca^{2+} form rhombohedral carbonates with six coordinated cations, whereas cations bigger than Ca^{2+} crystallize in the orthorhombic aragonite structure with nine coordinated cations. Ca^{2+} has an intermediate size and exists in both structural forms as calcite and aragonite in addition to a hexagonal vaterite phase (Reeder 1983; Ribbe et al. 1987). The calcite-type rhombohedral structure consists of alternate layers of Ca atoms (A) and carbonate ions (B/C) (Fig. 13). The flat carbonate ions in successive layers stack in reverse (ABAC) orientation to facilitate octahedral co-ordination of cation with six oxygens from different carbonate anions. Consequently, the rhombohedral unit cell parameter along the stacking direction is the height of six layers of carbonate ions. In the aragonite-type orthorhombic carbonate structure; the layer stacking is pseudohexagonal due to nonplanar metal layers having out of plane cation displacements (around ± 0.005 nm) and corrugated carbonate layers with reverse orientations (Speer 1983). This facilitates the formation of 9-coordinated metal cations having six M-O bonds with oxygens at the edges of 3 carbonate groups and three M-O bonds with three corner oxygens from three separate carbonate groups (see Fig. 13).

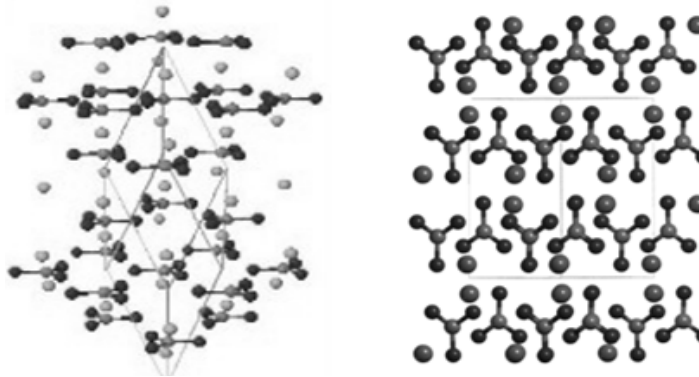

Figure 13. The crystal structures of rhombohedral (calcite-type) and orthorhombic (aragonite-type) carbonates. From *http://www.crystal.unito.it/prtfreq/jmol.html*.

Figure 14 shows the free energy and the solubility data for some common divalent metal carbonate minerals as a function of cation radius (Railsback 1999). For rhombohedral carbonates, the thermodynamic stability generally increases (the free energy of formation from ions at 25 °C becomes more exothermic) with increase in cation radius, although calcite is an exception. The most common rhombohedral minerals, calcite (with largest cation, Ca^{2+}) and magnesite (smaller Mg^{2+} cation) have lower stability and hence are more soluble. The orthorhombic carbonates show a similar trend with phases having intermediate radius being thermodynamically more stable than the end members of the series, aragonite ($CaCO_3$) and witherite ($BaCO_3$). This trend in thermodynamic stability seems to have direct structural correlation with the cation coordination geometries. The distorted 6-fold and 9-fold coordination geometries due to poor fit of largest and smallest cations in the rhombohedral and orthorhombic structures lower the thermodynamic stability. The most abundant sedimentary carbonate minerals calcite ($CaCO_3$), aragonite ($CaCO_3$), magnesite ($MgCO_3$) and dolomite ($CaMg(CO_3)_2$) fall into the lower stability region relative to aqueous solution and hence are more reactive. The large cation aragonite carbonates are far less soluble. The ordered mixed cation carbonates, dolomite [$CaMg(CO_3)_2$], ankerite [$Ca(Fe,Mg,Mn)(CO_3)_2$] and alstonite [$BaCa(CO_3)_2$] are more stable than their respective end members.

Calcite-aragonite phase transition at high pressure and orientational disordering in calcite at high temperature

The calcite-aragonite equilibrium is temperature and pressure dependent and has been studied extensively due to its importance in petrology and geo-thermobarometry (Carlson 1983; Essene 1983). Though these phenomena become important at pressures and temperatures above those envisioned for CO_2 sequestration, they shed light on issues of structure and bonding relevant to carbonate behavior. Pressure extends the carbonate stability field to higher temperature by disfavoring CO_2 evolution. The pressure-temperature *(P-T)* calcite-aragonite equilibrium curve calculated using thermodynamic data from both direct and indirect free energy measurements (Redfern et al. 1989) shows a significant change in slope between low and high *P-T* regimes (see Fig. 15). These changes were initially attributed to a first-order phase transition within the calcite phase (Cohen and Klement 1973). However, comprehensive structural studies by high temperature XRD and neutron scattering indicated gradual orientation disordering in calcite leading to $R\bar{3}c$ *to* $R\bar{3}m$ transition (Markgraf and Reeder 1985; Dove and Powell 1989).

A combined low temperature heat capacity and high-temperature transposed-temperature drop calorimetric study has been used to measure the energetic change associated with the

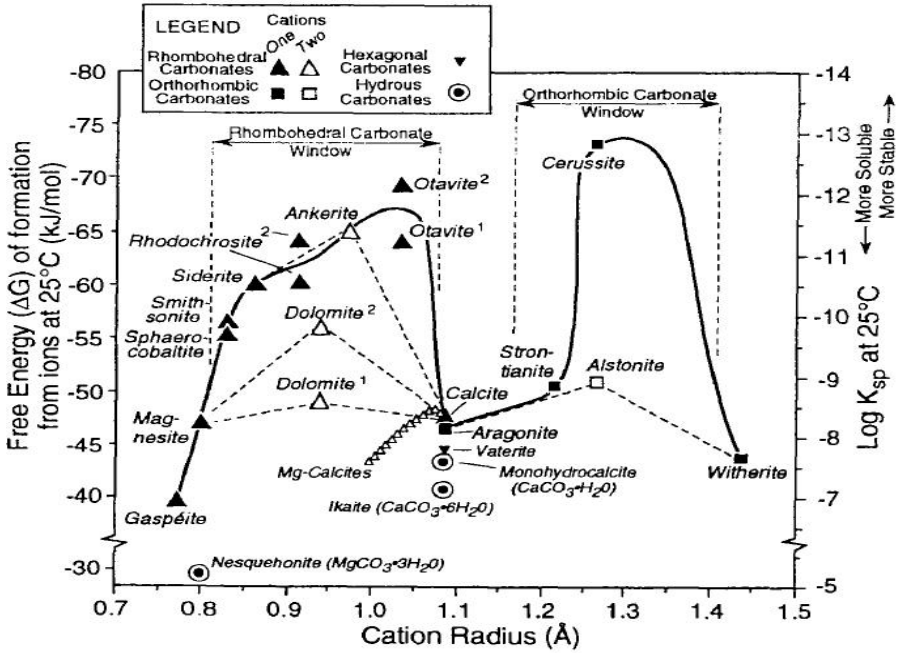

Figure 14. The free energy and the solubility data for common divalent metal carbonate minerals as a function of cationic radius. K_{sp} is the solubility product, and represents the equilibrium constant for dissolution or precipitation. Originally published in Railsback (1999) and reprinted with permission. Copyright © 1999 by Springer Science.

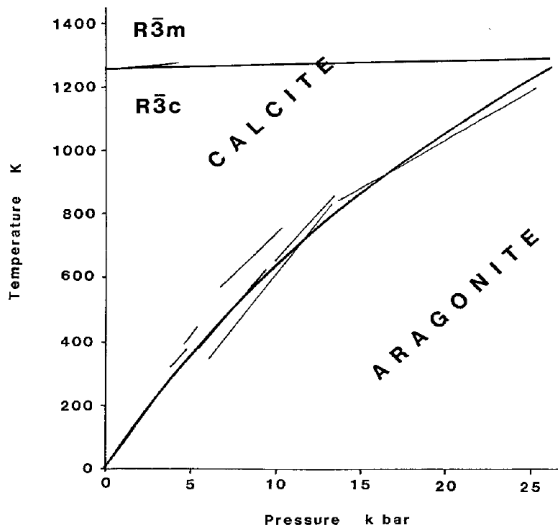

Figure 15. The phase diagram of calcite-aragonite. Thick lines are the phase boundary calculated for the $R\bar{3}c$ to $R\bar{3}m$ disorder transition and thin lines are the experimental data (Jamieson 1953; Simmons and Bell 1963; Crawford and Fyfe 1964; Johannes and Puhan 1971; Zimmermann 1971; Cohen and Klement 1973; Irving and Wyllie 1973). Reprinted from Redfern et al. (1989) with permission. Copyright © 1989 by Springer Science.

orientational order-disorder transition in order to understand its implication for the calcite/aragonite phase boundary behavior (Redfern et al. 1989). The deviation of the calorimetrically measured enthalpy of high temperature calcite phase ($R\bar{3}m$) between 973 K and 1325 K from the extrapolated low temperature phase ($R\bar{3}c$) heat capacity data gives the enthalpy for the orientational order-disorder transition (6.9 ± 1.1 kJ/mol) (Fig. 16). The calculated phase diagram based on excess enthalpy analyzed by Landau theory for tricritical phase transition is in agreement with the experimental observations. This supports the change in slope of the calcite/aragonite phase boundary is due to the $R\bar{3}c$ to $R\bar{3}m$ transition in calcite.

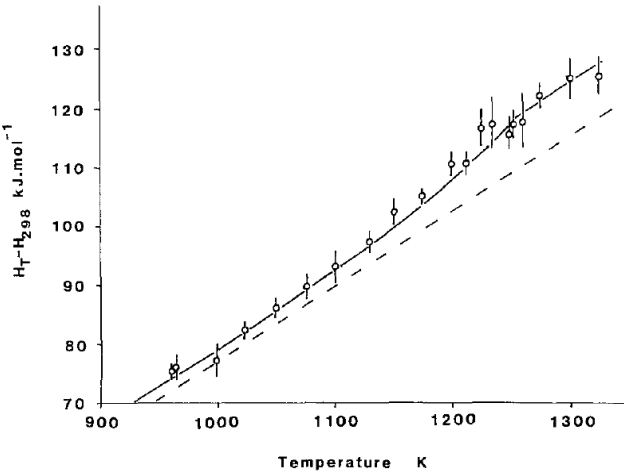

Figure 16. Calorimetric data for the enthalpy of calcite between 900 K and 1350 K (solid line) plotted with extrapolated low temperature heat capacity (dashed line) data from Jacobs et al. (1981). Taken from Redfern et al. (1989) with permission. Copyright © 1989 by Springer Science.

Vaterite

Vaterite is thermodynamically the least stable anhydrous polymorph of calcium carbonate under ambient conditions and is generally found in low temperature environments: biological systems, sediments, cements and as an intermediate phase during calcite synthesis (Plummer and Busenberg 1982; Mann et al. 1988; Friedman et al. 1993; Falini et al. 1998; Friedman 2005; Hu et al. 2010; Natoli et al. 2010). Vaterite transforms to calcite at room temperature on aging and on heating at 693-753 K. However, biomolecules or organic additive templates are shown to stabilize synthetic vaterite under ambient conditions (Pach et al. 1990; Kanakis and Dalas 2000; Kanakis et al. 2001; Lee et al. 2005; Han et al. 2006; Pouget et al. 2010). It is not clear whether such stabilization is purely kinetic or has a thermodynamic basis arising from adsorption of organics. Most vaterite samples are very fine grained (nanophase). There are reports of at least three different types of vaterite structures, (a) disordered hexagonal ($P6_3/mmc$), (b) ordered superstructures (P_6522) and (c) ordered orthorhombic ($Pbnm$) as shown in Figure 17 (Kamhi 1963; Medeiros et al. 2007; Wang and Becker 2009, 2012; Ren et al. 2013).

The hexagonal structure of vaterite has alternate layers of Ca ions and carbonate ions similar to rhombohedral carbonates. However the carbonate layers in vaterite are disordered with CO_3 planes orienting perpendicular to the 001 stacking direction. The presence of stacking faults and their ordering in the (001) plane could lead to superstructure formation. The formation of such superstructure established from *ab initio* calculations and molecular-dynamics (MD)

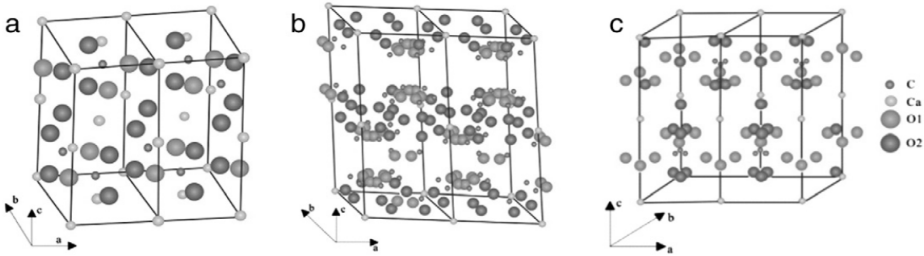

Figure 17. Vaterite models with (a) rhombic (b) hexagonal and (c) ordered hexagonal crystal structures. Reproduced with permission from Ren et al. (2013). Copyright © 2013 Elsevier Science.

simulations (Wang and Becker 2009) is found to be consistent with NMR results (Michel et al. 2008). The ordered orthorhombic structure was proposed recently based on X-ray diffraction data and is 3 to 10 kJ/mol higher than calcite, and the experimentally measured values fall within the computed range (3.4 kJ/mol, (Wolf et al. 1996, 2000) and 6.2 kJ/mol (Plummer and Busenberg 1982). A possible reason for this difference in experimental values could be the existence of a variable degree of disorder in the experimental samples. The computed enthalpy of disordered vaterite is 11-14 kJ/mol above that of ordered vaterite and 16-21 kJ/mol higher than calcite (Wang and Becker 2009, 2012 and also see Table 3). In contact with aqueous solution, the initial vaterite phase is thought to evolve from an amorphous precursor (ACC) phase with orientationally disordered carbonate ions. The degree of disordering in vaterite seems to have a large effect on the relative stability of vaterite with respect to ACC, aragonite, and calcite as indicated by large differences in their energetics. The energy differences among the three ordered crystalline polymorphs (ordered vaterite, aragonite, and calcite) are found to be small (Plummer and Busenberg 1982; Wolf et al. 1996, 2000; Wang and Becker 2009, 2012; Raiteri et al. 2010). Small energy differences between ACC and disordered vaterite are also predicted (Koga et al. 1998; Wolf and Gunther 2001; Radha et al. 2010; Wang and Becker 2009, 2012) (Fig. 18).

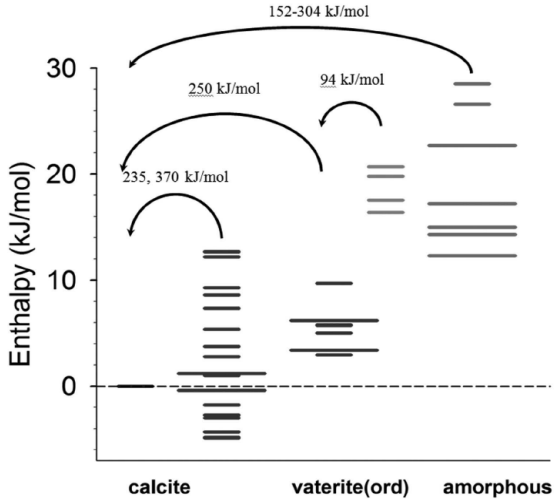

Figure 18. Enthalpies and activation energies for phase transitions among different calcium carbonate polymorphs with respect to calcite as reference (thin dashed line). Long, thick lines are experimental values, short, thick lines are theoretical calculations and the curved lines with arrows are the activation energy of the transition. Reproduced with permission from Wang and Becker (2012).

BINARY DIVALENT METAL CARBONATE SYSTEMS

The binary carbonate systems (MCO_3-NCO_3) form solid solutions with calcite, orthorhombic and dolomite structures. They are completely or partially miscible. The miscibility depends on the differences between the cation sizes of the end members of the binary system for calcite-type structures (see Table 6) and on the temperature of formation. Thermodynamics of formation and mixing properties determines the phase formation in these binary systems. Calorimetric measurements of energetics have revealed interesting mixing behavior in some of the binary carbonate systems and are discussed below.

Table 6. Cation size differences between the end members of the binary system Reproduced with permission from Reeder (1983).

Complete miscibility cation pairs		**Limited miscibility cation pairs**	
M^{2+} - N^{2+}	Δr (nm) in VI coordination	M^{2+} - N^{2+}	Δr (nm) in VI coordination
Fe - Mg	0.006	Ca - Mg	0.028
Ca - Cd	0.005	Ca - Fe	0.022
Mg - Co	0.003	Ca - Mn	0.017
Fe - Mn	0.005	Cd - Mg	0.023
Mg - Mn	0.011	Ca - Co	0.026
		Ca - Ni	0.031

$CaCO_3$-$MgCO_3$

$CaCO_3$-$MgCO_3$ is an important binary system in several geochemical settings involving sedimentary, metamorphic, marine, and mantle processes as well as in biological systems (Bischoff et al. 1983; Mackenzie et al. 1983). This binary system has limited miscibility with disordered rhombohedral $CaCO_3$-$MgCO_3$ solid solution interrupted by the dolomite phase field around the midpoint composition and a miscibility gap in both the Mg-rich and Ca-rich regions (see Fig. 19) (Graf and Goldsmith 1955; Goldsmith and Heard 1961; Bischoff et al. 1983; Mackenzie et al. 1983; Walter and Morse 1984).

Calorimetric studies of magnesian calcite and calcian dolomite have shown different energetic trends (Navrotsky and Capobianco 1987). In the Ca-rich region, Mg substitutes up to 25 mol% $MgCO_3$ to form calcite-type solid solution in low-temperature inorganic and biogenic environments. The biogenic magnesian calcites seem to have greater local disorder and show subtle differences in their crystallographic parameters and vibrational spectra compared to their synthetic analogues (Bischoff et al. 1983). Several studies on magnesian calcites have reported lowering of stability and increase in reactivity with increase in Mg substitution (Bischoff et al. 1983; Mackenzie et al. 1983; Navrotsky and Capobianco 1987; Busenberg and Plummer 1989). However, the calorimetric measurements on synthetic magnesian calcites, $Ca_{1-x}Mg_xCO_3$ for $x < 0.12$ show a small exothermic enthalpy of mixing (see Fig. 20) as opposed to the expected destabilization (hence positive heats of mixing) due to cation size mismatch (Navrotsky and Capobianco 1987; Chai et al. 1995). Gordon and Greenwood (1970) suggested positive deviations from ideal activity-composition relations and hence positive deviations in free energies at high temperature near 700 °C. The combination of positive excess free energies and negative enthalpy of mixing suggest the negative excess entropy of mixing for this system. This could probably associated with some sort of structural ordering such as clustering of Mg that produces a favorable lowering of the enthalpy but a loss of entropy in synthetic magnesian calcites equilibrated at 700 °C. The random stacking of Mg-

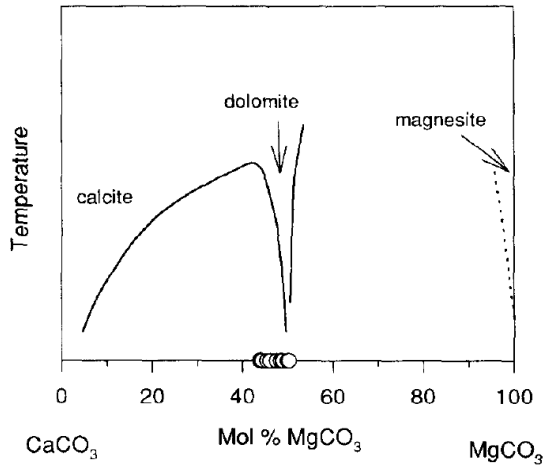

Figure 19. Schematic of $CaCO_3$-$MgCO_3$ *T-X* diagram with open circles showing the Ca-rich dolomite region after Goldsmith and Heard (1961). Reprinted with permission from University of Chicago Press, USA. Copyright © 1961, University of Chicago.

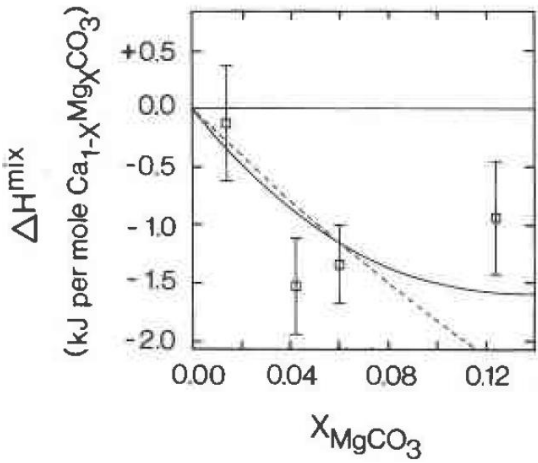

Figure 20. Enthalpy of mixing calculated from calorimetric data in magnesiacn calcites ($Ca_{1-x}Mg_xCO_3$) with a data fit using ideal mixing with equations $\Delta H_{mix} = X(1-X)\ (-20.37 \pm 13.39)$ (solid line) and $\Delta H_{mix} = X\ (1-X)\ [-25.65 \pm 5.94 + (88.49 + 49.71)X]$ (dashed line). Reprinted with permission from Navrotsky and Capobianco (1987).

rich layers between Ca layers rather than random substitution of Mg for Ca could also lead to energetically stable Mg-calcites.

$FeCO_3$-$MgCO_3$

The mixing of Fe^{2+} and Mg^{2+} cations in octahedral sites is a common occurrence in sedimentary and metamorphic carbonate minerals. For $FeCO_3$-$MgCO_3$, the mixing property studies suggest the formation of a complete solid solution (Rosenberg 1963; Davidson 1994). The enthalpy of mixing for this system has been obtained by a two-step calorimetric method at 770 °C (Chai and Navrotsky 1996b). In the first step, sample was decomposed in an oxygen atmosphere and in the second step; the decomposed products (a mixture of $MgFe_2O_4$, spinel and MgO or hematite) were dissolved in lead borate solvent in air. The enthalpies of mixing for the $FeCO_3$-$MgCO_3$ system are slightly positive due to a slight mismatch in Fe^{2+} and Mg^{2+} sizes. Fitting

experimental data with a regular solution model ($\Delta H_{mix} = WX_{Fe}X_{Mg}$, where W = the interaction parameter, and X_{Fe} and X_{Mg} = mole fractions of $FeCO_3$ and $MgCO_3$ in the solid solution) gives the interaction parameter W as 4.44 ± 0.75 kJ/mol (see Fig. 21).

The positive deviation of enthalpy from ideal mixing is a signature of probable low temperature exsolution. The phase diagram of $FeCO_3$-$MgCO_3$ is derived from the Gibbs free energy of mixing by using a regular solution model and the ideal entropy of mixing (see Fig. 22). The miscibility gap and the spinodal curve suggest the complete solid solution in all geological environments for $MgCO_3$-$FeCO_3$ system with possible exsolution at a very low critical temperature of about 267 K (Chai and Navrotsky 1996b).

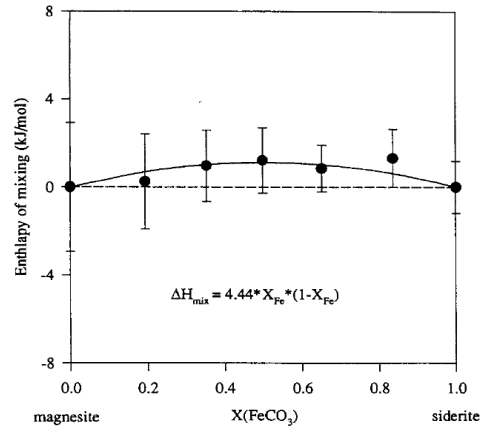

Figure 21. Enthalpy of mixing for the $FeCO_3$-$MgCO_3$ system with a fit using a regular solution parameter of 4.44 kJ/mol (solid line) and the dashed line is for ideal mixing. Reprinted with permission from Chai and Navrotsky (1996b). Copyright © 1996 Elsevier Science.

$CaCO_3$-$MnCO_3$

The $CaCO_3$-$MnCO_3$ (calcite-rhodochrosite) binary system is a part of the rock-forming carbonate tetrahedron, but such carbonates are often found in association with other Mn and Ca minerals. The minerals of this system, Mn-bearing calcites and kutnahorite with dolomite-type structure are found in deep-sea sediments (Pedersen and Price 1982). Thermodynamic studies by phase equilibrium and calorimetric methods showed positive excess free energies (see Fig. 23) and complex endothermic and exothermic enthalpies of mixing (see Fig. 24), which suggest negative excess entropies of mixing supporting short range ordering (Goldsmith and Graf 1957; De and Peters 1981; Capobianco and Navrotsky 1987). For phase equilibrium calculations, the $(Ca,Mn)CO_3$ decomposition and Gibbs-Duhem relation were used to obtain the activity coefficients of $MnCO_3$ (γ_{MnCO3}) and $CaCO_3$ (γ_{CaCO3}) as a function of composition X. The excess free energy of mixing at 700 °C is found to be positive (Fig. 23) and the enthalpy of mixing is asymmetric at 600 °C (Fig. 24). Addition of $MnCO_3$ destabilizes the calcite and $CaCO_3$ addition results in exothermic mixing with rhodochrosite without any kutnahorite as this temperature is above its stability field. This again supports negative excess entropies of mixing. The calculated and the experimentally determined solvi (De and Peters 1981) for this system are shown in Figure 25. The metastable solvus closes at 355 °C, whereas the experimental solvus extends to about 550 °C. The suppression of kutnahorite

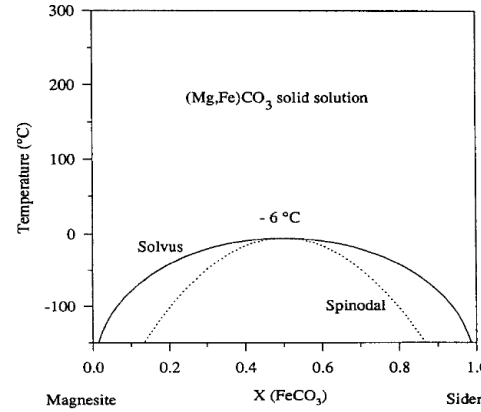

Figure 22. Calculated phase diagram of the $FeCO_3$-$MgCO_3$ system showing the solvus (solid curve) and the spinodal (dashed curve). Reprinted from Chai and Navrotsky (1996b) with permission. Copyright © 1996 Elsevier Science.

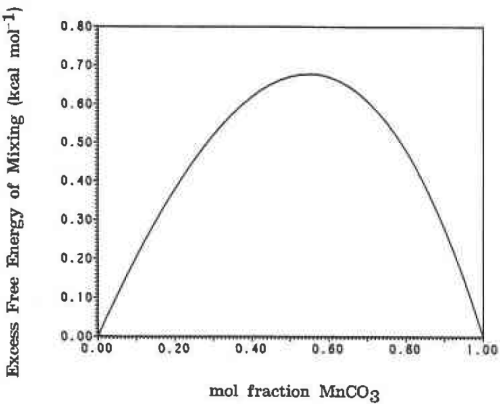

Figure 23. Excess free energy for the calcite-rhodochrosite system as a function of composition at 700 °C. Reproduced with permission from Capobianco and Navrotsky (1987).

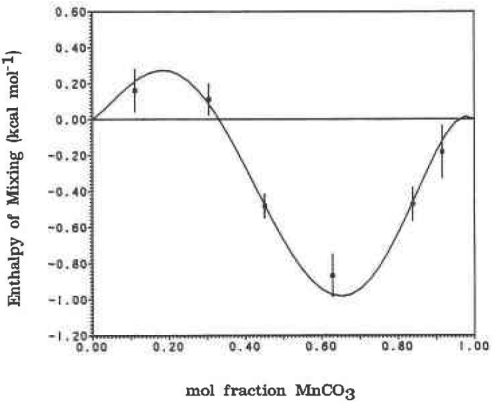

Figure 24. Calorimetric data for 600 °C samples with least-square fit to the data. Reproduced with permission from Capobianco and Navrotsky (1987).

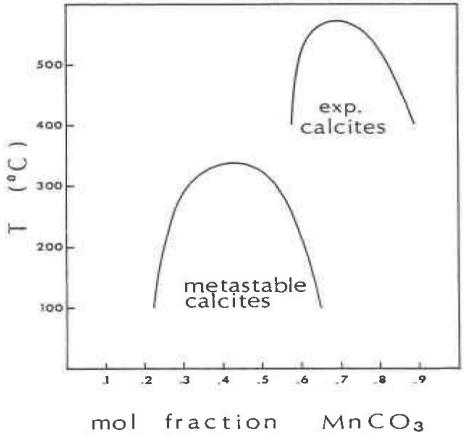

Figure 25. Phased diagram of calcite-rhodochrosite with experimental solvus (De and Peters 1981) and metastable solvus calculated from temperature-dependent excess-free-energy functions. Reproduced with permission from Capobianco and Navrotsky (1987).

phase formation increases the solid solubility in this system.

$CaCO_3$-$SrCO_3$

The $CaCO_3$-$SrCO_3$ system is an important component of solid-aqueous phase interactions in geochemistry and relevant for contaminant of migration (including that of radium) in the environment (Plummer and Busenberg 1987; Koenigsberger and Gamsjager 1990; Plummer et al. 1992). This system crystallizes in the orthorhombic aragonite structure. Thermodynamic data have been determined by solubility studies (Holland et al. 1963; Plummer et al. 1992) electrochemical (Casey et al. 1996b) and calorimetric measurements (Casey et al. 1996a). The calorimetric measurements show positive heats of mixing (ΔH_{mix}) with a positive symmetric deviation that reaches a maximum value of 3.82 ± 0.94 kJ/mol at x = 0.5 (see Fig. 26). The ΔG_{mix} (0.0 < x < 0.9) of mixing for $Ca_{(1-x)}Sr_xCO_3$ solid solution by electrochemical measurements also shows a similar positive trend (+3.0 ± 1.6 kJ/mol at x = 0.7), which suggest small or zero excess entropy of mixing for this system (see Fig. 26).

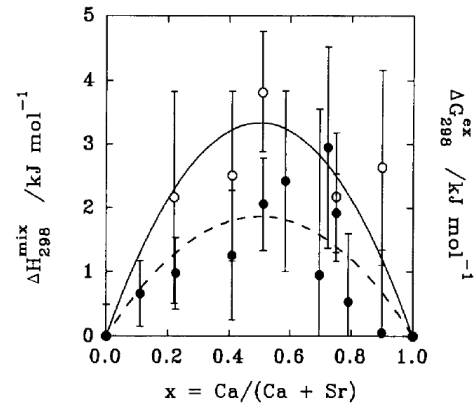

Figure 26. The ΔH_{ds} values from calorimetric data (solid line) and ΔG_{excess} data from Casey et al. (1996b) (dashed line) with fits using the regular-solution model. Reprinted with permision from Casey et al. (1996a). Copyright © 1996 Elsevier Science.

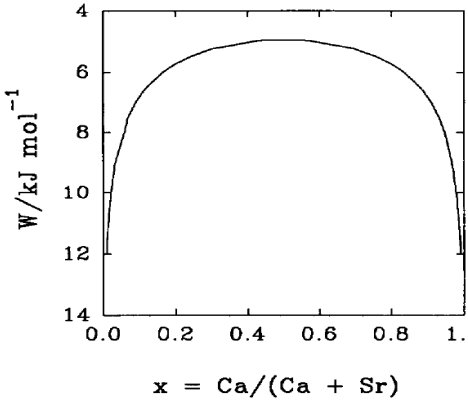

Figure 27. The stable compositions of orthorhombic Sr-CO_3-$CaCO_3$ system at 298 K and 1 bar as a function of the interaction parameter for a regular solution. Reprinted from Casey et al. (1996a) with permission. Copyright © 1996 Elsevier Science.

Therefore a regular solution model, $\Delta H_{mix} = Wx\ (1 - x)$ was used to obtain the interaction parameter (W = 13.5 ± 1.3 kJ/mol) for this system (see Fig. 27). The large interaction parameter suggests very limited miscibility at ambient temperature. But in nature, aragonites having l-2 mol% $SrCO_3$ (a few to 14% $SrCO_3$) and strontianites with 25-30 mol% $CaCO_3$ have been observed (Plummer and Busenberg 1987; Koenigsberger and Gamsjager 1990; Plummer et al. 1992; Casey et al. 1996a). The formation of such phases has been attributed to metastable equilibrium of minerals with aqueous solution.

Dolomite-type structures and energetics of order-disorder phenomena

Dolomite (space group $R\bar{3}$) is a superstructure of calcite or magnesite (space group $R\bar{3}c$) having ordered alternate calcium and magnesium layers. In $CaMg(CO_3)$, the average Ca-O distance is 2.390 Å and Mg-O distance is 2.095 Å (Wyckoff 1964) and this difference in bond length drives the formation of the ordered structure. The ideal composition of dolomite contains

50 mol% each of Ca and Mg carbonates. However, in nature Ca rich dolomite having up to 57-58 mol% of $CaCO_3$ are common (Lumsden and Chimahusky 1980; Sperber et al. 1984; and references therein). Mg rich dolomites are rare and limited to less than 1 mol% from the ideal composition. High temperature experimental studies have reported the existence of dolomite having 5-6 mol% excess $CaCO_3$ with substitutional cation disorder at 900-1100 °C (Goldsmith and Graf 1958; Goldsmith 1967; Reeder 1983; Reeder and Sheppard 1984; Navrotsky and Capobianco 1987). Cation ordering is favored at lower temperature (Reeder and Markgraf 1986) and above 1150 °C dolomite transforms to calcite structure with a largely disordered distribution of Ca and Mg.

The more endothermic enthalpies of formation of Ca-rich dolomites with increase in $CaCO_3$ content indicate that these phases are thermodynamically unstable (see Fig. 28). The substitution of Ca for Mg in the Mg layer of dolomite is energetically unfavorable. This is further supported by thermodynamic cluster variation model calculations that show positive contribution to the enthalpy from interactions within layers and a negative contribution from interactions between layers in the dolomite structure (Burton 1987; Capobianco et al. 1987). Therefore the formation of Ca-rich dolomite in sedimentary environments seems to be controlled more by kinetics than by thermodynamics.

The different trends in formation energetics of magnesian calcite and dolomite solid solutions are shown together in Figure 29 (Chai et al. 1995; Chai and Navrotsky 1996b). The magnesian calcites show a small negative deviation from the mechanical mixtures of stoichiometric dolomite and calcite, as well as a negative heat of mixing between $CaCO_3$ and $MgCO_3$. For calcian dolomites, the formation enthalpies deviate positively from the mechanical mixture to a larger extent. This behavior is related to ionic radii or bond lengths and attributed to energetically more favorable substitution of a smaller Mg cation for a larger Ca in magnesian calcite than of a larger Ca for a smaller Mg in calcian magnesite. However, formation of Mg-rich dolomite seems to be more complicated, involving cation order-disorder and mixed-layer sequences.

$CdCO_3$-$MgCO_3$

This system is considered an analogue for $CaCO_3$-$MgCO_3$, with disordering occurring at lower temperature. The dolomite type phases in $CdCO_3$-$MgCO_3$ system showed different degrees of ordering on quenching at different pressure and temperature (0.1-1 gPa pCO_2 and 600-850 °C). The structures of these phases are well constrained since a large difference in atomic number between Cd and Mg makes it easier to characterize site occupancies by XRD. The completely ordered structure forms at 600 °C and disordered samples form at 800 °C, while the samples with intermediate ordering at 750-775 °C. The calorimetric data of Cd-Mg dolomite type solid solution for samples quenched from 600 to 850 °C has been reported (Capobianco et al. 1987). The enthalpy of formation of ordered $CdMg(CO_3)_2$ from $CdCO_3$ and $MgCO_3$ is -5.6 ± 0.8 kJ/mol; that of the disordered phase is $+8.1 \pm 0.8$ kJ/mol. The long-range order parameter changes from unity to zero in this range and the enthalpy of disordering is 13.7 ± 0.8 kJ/mol. The $CdCO_3$-$MgCO_3$ binary phase equilibrium also has two regions comprising disordered calcite-type and dolomite type solid solutions similar to $CaCO_3$-$MgCO_3$ system. The relationship between the structure and energetics associated with order-disorder phase transformation and phase equilibrium in $CdCO_3$-$MgCO_3$ has been studied by different structural models and is compared with the experimental data. The experimentally determined order-disorder transition is sharper with a narrower temperature range than predicted from the models. (Capobianco et al. 1987). The phase diagrams based on different thermodynamic models produce a reasonably good fit with the data from different experiments with a stability field for two disordered phases.

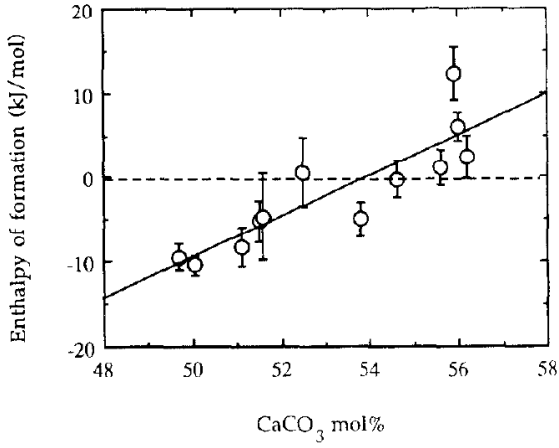

Figure 28. Enthalpies of formation of Ca-rich dolomite with the best fit for the data as a solid line. Reprinted with permission from Chai et al. (1995). Copyright © 1995 Elsevier Science.

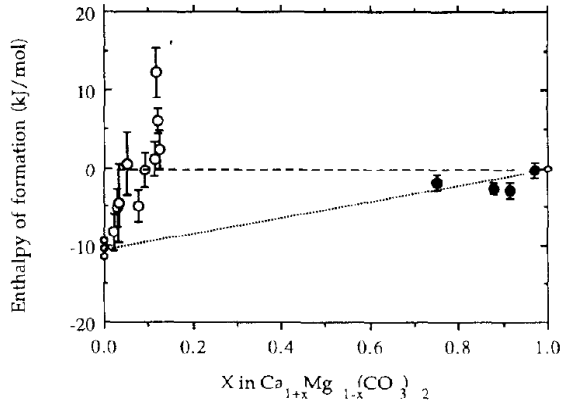

Figure 29. Enthalpy of formation of Ca-rich dolomite (open circles) and magnesian calcite (filled circles) and the small open circles for stoichiometric dolomite and calcite. Reprinted with permission from Chai et al. (1995). Copyright © 1995 Elsevier Science.

$CaMg(CO_3)_2$ - $CaFe(CO_3)_2$ solid solution (dolomite - ankerite join)

Though there is no report of occurrence of pure ordered calcium iron carbonate, ankerite, $CaFe(CO_3)_2$, but dolomite structured solid solution ($Ca(Fe_xMg_{1-x})(CO_3)_2$, $0 \le x \le 0.7$) formed by partial substitution of Fe in Mg sites of dolomite is common in nature (Reeder 1983; Reeder and Dollase 1989; Davidson et al. 1993 and references therein). However, there are reports of existence of synthetic disordered $CaFe(CO_3)_2$ with calcite-type structure at 845 °C and 3 gPa, indicating the possibility of existence of an ordered $CaFe(CO_3)_2$ phase at lower temperature (Davidson et al. 1993).

The calorimetrically measured enthalpy of formation of disordered $CaFe(CO_3)_2$ (6.98 ± 2.08 kJ/mol) (Chai and Navrotsky 1996a,b) agrees with that estimated from the solvus of the $CaCO_3$-$FeCO_3$ system, 8.35 kJ/mol (Davies and Navrotsky 1983; Davidson et al. 1993). Increase in Fe content has opposite effects on stability of ordered and disordered phases. The ordered phase becomes more endothermic and hence less stable and the disordered ankerite becomes more exothermic and hence more stable with increasing Fe content (see Fig. 30). The enthalpy of formation of ordered dolomite $CaMg(CO_3)_2$ is –9.29 ± 1.97 kJ/mol. The enthalpy of disordering in dolomite (~ 25 kJ/mol) is larger than the disordering enthalpy in ankerite, $CaFe(CO_3)_2$ (~ 10 kJ/mol). These factors destabilize ordered $CaFe(CO_3)_2$ (Chai and Navrotsky 1996a,b).

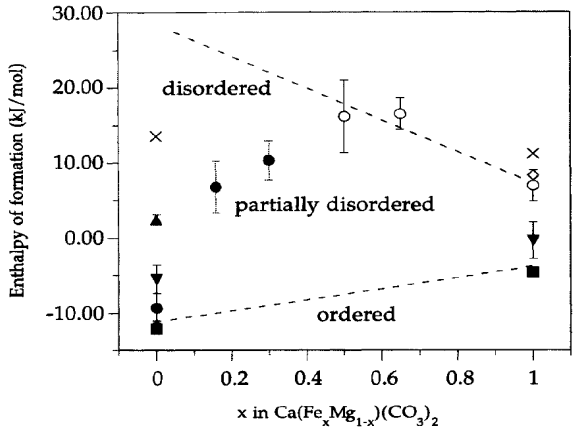

Figure 30. Enthalpy of formation of the ankerite solid solution. The circles are data from calorimetry, the squares are from lattice-energy calculations, the triangle is from (Navrotsky and Capobianco 1987), the inverted triangles are from (Holland and Powell 1990), and the diamond is calculated from the solvus. The Xs are for disordered phases calculated from solid-solution-mixing parameter (Davies and Navrotsky 1983). The Solid symbols indicate complete order; open symbols, complete disorder; and shaded symbols, partial disorder. Reprinted with permission from Chai and Navrotsky (1996a).

CARBONATE BEARING MULTICOMPONENT PHASES

Thermodyanmics of hydrotalcite-type layered double hydroxides (LDH)

Hydrotalcite-like compounds generally known as layered double hydroxides (LDH) are derivatives of the mineral hydrotalcite ($Mg_6Al_2(OH)_{16}(CO_3)\cdot 4H_2O$). The structure is made up of positively charged mixed metal hydroxide layers and the interlayers of anions and water appear to influence the hydroxide layer stacking sequences (Bellotto et al. 1996; Cavani et al. 1991; Radha et al. 2005; Thomas et al. 2006). The composition is $[M(II)_{1-x}M''(III)_x(OH)_2]^{x+}(A^{n-})_{x/n}\cdot mH_2O$, where M(II) = Mg, Ca, Fe, Co, Ni, Cu, Zn; M″ (III) = Al, Cr, Fe, Co and anions (A^{n-}) = CO_3^{2-}, Cl^-, NO_3^-, SO_4^{2-} polyoxometallates, organic anions. The interlayer regions are labile and readily undergo intercalation/deintercalation reactions and ion exchange (Radha et al. 2005b, 2007). Hydrotalcite is white mineral containing Mg-Al cations with carbonate anions and often occurs with other minerals such as serpentine and calcite. The Ni bearing analogue, takovite [$Ni_6Al_2(OH)_{16}(CO_3)\cdot 4H_2O$], is found in karstic bauxites, with minerals such as carrboydite [$(Ni_{10}Cu_4Al_9(SO_4)_4(CO_3)_2(OH)_{43}\cdot 7(H_2O)$], gaspeite [$Ni_{0.6}Mg_{0.3}Fe^{2+}_{0.1}(CO_3)$] and in weathered Ni-sulfide deposits (Bish 1980).

A summary of enthalpies of formation of LDH with different cations and anions, obtained from high temperature oxide melt solution calorimetry, is given in Table 7 (Allada and Navrotsky 2002; Allada et al. 2005a,b, 2006). The third law entropy based on low temperature adiabatic heat capacity measurements suggested that the entropy contribution ($T\Delta S$ term) in Mg-Al-CO_3 LDH is 2-3 kJ/mol at room temperature (Allada et al. 2005a) and is within the uncertainties of formation enthalpies. The formation energetics of LDH with respect to their single cation hydroxides and carbonates and water contents (see Table 7) show about 5 to 20 kJ/mol stabilization (Allada and Navrotsky 2002; Allada et al. 2005a,b, 2006; Mazeina et al. 2008).

In $Mg_{1-x}Al_x(OH)_2(CO_3)_{x/2}\cdot mH_2O$, the enthalpies of formation from oxide and carbonate components change only slightly with variation in Al content (z) (Allada et al. 2005a), suggesting that the Mg/Al ratios are controlled by the activities of cations in solution and the pH rather than by big thermodynamic changes in the solid phase. Kinetic factors also

Table 7. Summary of heat of formation data for $M_{1-x}Al_x(OH)_2(CO_3)_{x/2}{\cdot}mH_2O$. Reproduced with permission from Allada et al. (2006). Copyright © 2006 The Clay Minerals Society.

Sample	ΔH_{dsol} (kJ/mol)	$\Delta_f H_{ox}$ (kJ/mol)	ΔH°_f (kJ/mol)	$\Delta_f H^{scc}$ (kJ/mol)
$Co_{0.68}Al_{0.32}(OH)_2(CO_3)_{0.16}$ 0.78H_2O	226.98 ± 1.24 (4)	−42.80 ± 1.50	−1044.17 ± 2.54	−5.05 ± 2.86
$Co_{0.69}Al_{0.31}(OH)_2(CO_3)_{0.16}$ 0.68H_2O	218.17 ± 1.28 (7)	−41.84 ± 1.32	−1006.26 ± 1.62	−4.42 ± 2.15
$Co_{0.70}Al_{0.30}(OH)_2(CO_3)_{0.16}$ 0.23H_2O	212.18 ± 1.08 (6)	−49.22 ± 1.01	−877.34 ± 1.35	−11.04 ± 1.92
$Co_{0.76}Al_{0.24}(OH)_2(CO_3)_{0.12}$ 0.81H_2O	228.50 ± 1.25 (4)	−43.51 ± 1.42	−991.79 ± 1.72	−9.78 ± 2.07
$Co_{0.80}Al_{0.20}(OH)_2(CO_3)_{0.10}$ 0.76H_2O	215.97 ± 2.46 (4)	−35.23 ± 1.71	−933.36 ± 2.17	−3.88 ± 2.17
$Co_{0.83}Al_{0.17}(OH)_2(CO_3)_{0.09}$ 0.29H_2O	183.47 ± 1.51 (4)	−35.00 ± 1.67	−777.09 ± 1.97	−5.13 ± 2.64
$Mg_{0.67}Al_{0.33}(OH)_2(CO_3)_{0.16}$ 0.70H_2O	222.67 ± 1.26 (5)	−58.61 ± 1.79	−1284.65 ± 1.75	−11.01 ± 1.56
$Mg_{0.66}Al_{0.34}(OH)_2(CO_3)_{0.17}$ 0.69H_2O	224.98 ± 1.42 (5)	−57.99 ± 1.68	−1292.07 ± 1.63	−11.62 ± 1.42
$Mg_{0.69}Al_{0.31}(OH)_2(CO_3)_{0.15}$ 0.30H_2O	200.69 ± 0.85 (5)	−62.68 ± 1.66	−1168.52 ± 1.81	−16.61 ± 1.08
$Mg_{0.74}Al_{0.26}(OH)_2(CO_3)_{0.13}$ 0.39H_2O	197.50 ± 1.18 (5)	−55.43 ± 1.43	−1165.98 ± 2.06	−10.49 ± 1.37
$Mg_{0.73}Al_{0.27}(OH)_2(CO_3)_{0.16}$ 0.83H_2O	226.11 ± 1.06 (4)	−54.42 ± 1.87	−1297.19 ± 1.97	−7.20 ± 1.27
$Ni_{0.69}Al_{0.31}(OH)_2(CO_3)_{0.16}$ 0.37H_2O	211.10 ± 1.01 (4)	−40.71 ± 1.16	−918.42 ± 1.21	−15.83 ± 1.28
$Ni_{0.66}Al_{0.34}(OH)_2(CO_3)_{0.17}$ 0.42H_2O	208.33 ± 0.65 (4)	−43.70 ± 0.86	−904.031 ± 0.93	−8.98 ± 1.28
$Ni_{0.77}Al_{0.23}(OH)_2(CO_3)_{0.12}$ 0.33H_2O	202.84 ± 1.03 (5)	−34.27 ± 1.21	−838.18 ± 1.26	−11.99 ± 1.58
$Ni_{0.67}Al_{0.33}(OH)_2(CO_3)_{0.17}$ 0.41H_2O	217.89 ± 1.95 (5)	−40.07 ± 2.03	−908.42 ± 2.06	−19.46 ± 2.22
$Ni_{0.64}Al_{0.36}(OH)_2(CO_3)_{0.18}$ 0.46H_2O	220.33 ± 1.38 (7)	−33.09 ± 1.48	−942.41 ± 1.53	−17.72 ± 1.72
$Zn_{0.67}Al_{0.33}(OH)_2(CO_3)_{0.17}$ 0.30H_2O	192.84 ± 0.68 (4)	−45.32 ± 0.91	−993.04 ± 0.96	−21.97 ± 1.5

probably play a role. Thus one observes hydrotalcites with different compositions in a variety of conditions (Reichle 1986; Thevenot et al. 1989). However, the nature of divalent cations appears to have greater influence (5 to 20 kJ/mol) on thermodynamic stability (Allada et al. 2005a,b, 2006). The most stable phase is Zn-LDH, followed by the Ni-, Mg- and Co-LDH. These stability trends could not be rationalized based on any specific crystal chemical factors such as cation radius or M-O bond distortions. The solubility products for Co-Al, Mg-Al, Ni-Al and Zn-Al LDHs calculated from MINTEQ code (see Table 8) suggested a decrease in solubility compared to the mechanical mixture and agree with reported log K_{sp} values based on solubility measurements (Allada et al. 2006; Johnson and Glasser 2003).

Table 8. Solubility products for $M_{1-x}Al_x(OH)_2(CO_3)_{x/2}{\cdot}mH_2O$. Reproduced with permission from Allada et al. (2006). Copyright © 2006 The Clay Minerals Society.

Sample	log K_{sp}
$Ni_{0.69}Al_{0.31}(OH)_2(CO_3)_{0.16}{\cdot}0.37H_2O$	2.24
$Co_{0.76}Al_{0.24}(OH)_2(CO_3)_{0.12}{\cdot}0.81H_2O$	7.12
$Zn_{0.67}Al_{0.33}(OH)_2(CO_3)_{0.17}{\cdot}0.30H_2O$	3.73
$Mg_{0.74}Al_{0.26}(OH)_2(CO_3)_{0.13}{\cdot}0.39H_2O$	9.82

Dawsonite type compounds $MAl(OH)_2CO_3$ (M = Na, K, NH_4)

Dawsonite ($NaAlCO_3(OH)_2$ is a naturally occurring mineral with orthorhombic (*Imma*) structure having distorted $AlO_2(OH)_4$ and $NaO_4(OH)_2$ octahedra, and CO_3 groups (Corazza et al. 1977). Potassium dawsonite ($KAl(OH)_2CO_3$) and ammonium dawsonite ($NH_4Al(OH)_2CO_3$) are the other two known dawsonite-type compounds. Dawsonite occurs in various sedimentary rocks associated with volcanics or CO_2-rich alkaline thermal solutions and as hydrothermal alteration products of igneous rocks (Jackson et al. 1972; Baker et al. 1995; Sirbescu and Nabelek 2003). Several geochemical modeling studies have predicted the formation of dawsonite during the long term mineral sequestration of CO_2 in sodium rich brines (Ferrante et al. 1976; Xu et al. 2005; Zerai et al. 2006; Benezeth et al. 2007). However, dawsonite rarely forms in nature or in laboratory experiments under the conditions used in these simulations (Kaszuba et al. 2003). The equilibrium based experimental and modeling studies with following reaction has revealed that these inconsistencies in dawsonite stability field mainly arise due to lack of consistent thermodynamic data on aluminum hydroxide polymorphs and aluminum complexes, which lead to the gross underestimation of dissolved aluminum.

$$NaAlCO_3(OH)_2 \text{ (dawsonite)} + H_2O = Al(OH)_3 + Na^+ + HCO_3^-$$

The interactions among aluminum hydroxide/oxyhydroxide minerals and aqueous complexes compete with dawsonite to constrain aluminum solubility and thus influence the dawsonite stability field (Kaszuba et al. 2011).

Thermodynamic properties of dawsonite have been determined by copper block drop calorimetry and low temperature heat capacity (6 to 307 K) adiabatic calorimetry (Ferrante et al. 1976; Benezeth et al. 2007). These measurements showed $\Delta G^\circ_{f,\,298.1K} = -1786 \pm 4$ kJ/mol, $\Delta H^\circ_{f,\,298.1K} = -1964 \pm 4$ kJ/mol, $S^\circ_{298.1K} = 132 \pm 2$ J /K mol and $C^\circ_{p,\,298.1K} = 142.6 \pm 0.4$ J/ K mol. The data for dawsonite dissolution has been calculated from the solubility measurements for the following dissolution reaction with under- and oversaturated solutions at 50-200 °C in basic media at 1.0 mol/kg NaCl.

$$NaAlCO_3(OH)_2\ (xl) + 2\ H_2O = Al(OH)_4^- + Na^+ + HCO_3^- + H^+$$

The thermodynamic parameters for the above reaction at 25 °C were calculated as $\Delta G° = 102.1$ kJ/mol, $\Delta H° = 97.0$ kJ/mol and $\Delta S° = -17.1$ J mol^{-1} K^{-1}.

Figure 31 shows the phase equilibrium diagram of dawsonite with bayerite and other common sandstone aquifer minerals such as quartz and albite in varying total aluminum and carbon concentrations at 100 °C (Benezeth et al. 2007). Such phase equilibrium study would be useful to understand the relative stability of dawsonite with respect to other minerals in geological sequestration conditions. Dawsonite is quite stable at wide range of pH when log[C] > −2.6 in absence of silica, (Fig. 31a) and has a lower limit of stability relative to bayerite at a pH 4.8 in presence of aluminum (Fig. 31b). Albite-bearing rocks in contact with saline fluids at 100 °C (Fig. 31a) dissolve in acidic solution after CO_2 introduction. This buffered pH drives the equilibrium to the region where dawsonite dominates over either boehmite or bayerite (Benezeth et al. 2007). This suggest that formation of dawsonite could trap CO_2 at lower pH

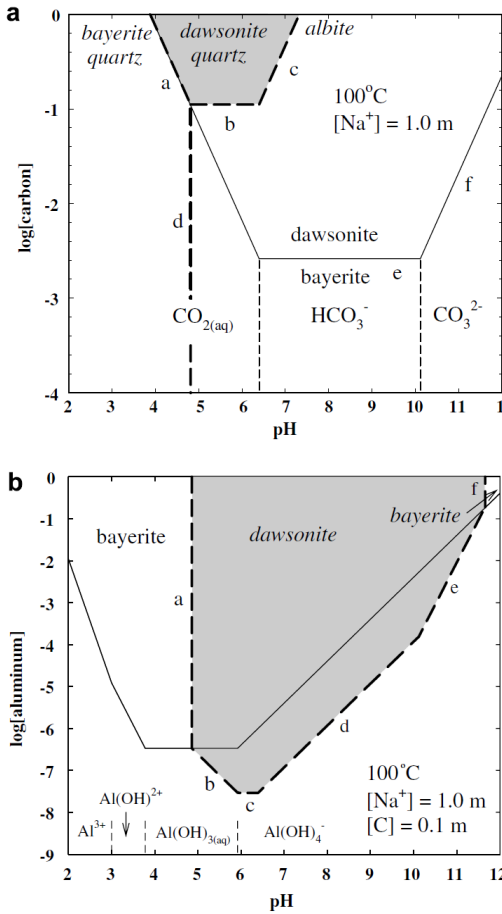

Figure 31. Stability diagram of dawsonite with respect to bayerite, albite and quartz. (a) log[C] versus pH and (b) log[Al] versus pH with [C] = 0.1 mol/kg in the presence of bayerite at an arbitrarily fixed [Na$^+$]. Minerals in italics represent those present when silica is in the system. Reprinted with permission of Elsevier Science from Benezeth et al. (2007). Copyright © 2007 Elsevier Science.

limit due to buffering reaction of albite (Albite + HCO_3^- + H^+ = Dawsonite + 3 Quartz), when total dissolved carbon concentration is above 0.1 mol/ kg.

K_2CO_3-$CaCO_3$ double carbonates

The K_2CO_3-$CaCO_3$ binary system having three intermediate phases is generally found in wood ash, partly burned fir, hemlock, and other trees in the western United States and in the combustion of biomass fuels (Olanders and Steenari 1995). Butschliite and fairchildite are two polymorphs with composition $K_2Ca(CO_3)_2$. The third phase $K_2Ca_2(CO_3)_3$, is an incongruently melting phase (1083 K), which below 800 K decomposes to butschliite and $CaCO_3$. The structure of butschliite comprises atoms centered on mirror planes and the CO_3 groups situated on threefold axes, oriented normal to the *c* axis (Pabst 1974). In fairchildite and $K_2Ca_2(CO_3)_3$, a quarter of the cations are situated on the threefold axes and surrounded by CO_3 groups. The carbonate groups in Fairchildite forms a layered structure with half of the CO_3 groups orientationtally disordered around a common C atom position (Pertlik 1981). The CO_3 groups are ordered but inclined relative to the (001) plane in $K_2Ca_2(CO_3)_3$.

The enthalpies of formation of double carbonates phases of K_2CO_3-$CaCO_3$ were determined by drop solution calorimetry in molten $2PbO{\cdot}B_2O_3$ at 974 K (Navrotsky et al. 1997). The enthalpies of formation from binary carbonates for butschliite and fairchildite polymorphs are −38.7 ± 3.2 kJ/mol and −5.1 ± 3.3 kJ/mol respectively and −7.2 ± 5.8 kJ/mol for $K_2Ca_2(CO_3)_3$. The entropy change for the formation of fairchildite is 40.9 ± 5.1 J/mol·K and of $K_2Ca_2(CO_3)_3$ is 39.4 ± 7.3 J/mol·K and it is zero for ordered butschliite. Thus butschliite is the stable low temperature polymorph and is calculated to transform to fairchildite at 822 K.

Rare earth oxycarbonates

The rare earth (Ln) metal oxides form oxycarbonate ($Ln_2O_2CO_3$) phases with CO_2 at low or moderate temperatures. They exist in three crystalline modifications known as I, IA and II. At ambient pressure, types I and IA are metastable compared with type II lanthanides lighter than Gd and Ln heavier than Gd, form only in type I structure (Turcotte et al. 1969). Thermodynamic data for the formation of rare earth oxy carbonates from their oxides (Ln_2O_3(xl) + CO_2(g) = $Ln_2O_2CO_3$(xl)) are given Table 9 and plotted against ionic potential in Figure 32 (Sjastad et al. 2012). The enthalpy, entropy, and free energy values derived from adiabatic shield calorimetry and drop solution calorimetry are found to be more accurate and are recommended over the data extracted from gas equilibration experiments or DTA studies.

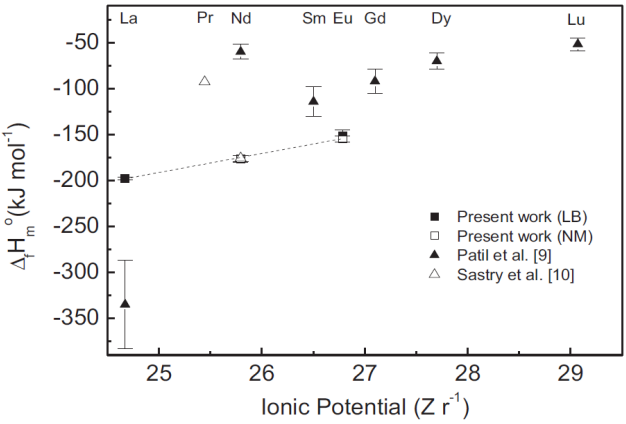

Figure 32. The enthalpy of formation of $Ln_2O_2CO_3$ from their oxide components at 298 K versus ionic potential. Reprinted with permission of Elsevier Science from Sjastad et al. (2012). Copyright © 2012 Elsevier Science.

Table 9. The standard enthalpies (ΔH_m°) and entropies (ΔS_m°) of formation for $Ln_2O_2CO_3$ from the component oxides Ln_2O_3 and CO_2. Modified from Sjastad et al. (2012) and reproduced with permission. Copyright © 2012 Elsevier Science.

Phase	ΔH_m° (*T*) (kJ/mol)	ΔS_m° (*T*) (J/ K·mol)	*T* (K)	Reference
		Calorimetric studies		
$La_2O_2CO_3$	−198.0 ± 1.7		298	Sjastad et al. (2012)
		−170.2 ± 0.6	300	Olafsen et al. (1999)
$Nd_2O_2CO_3$	−176.4± 4.7		298	Sjastad et al. (2012)
		−177.0 ± 0.6	300	Olafsen et al. (1999)
		−166.9 ± 0.9	900	Olafsen et al. (1999)
$Eu_2O_2CO_3$	−153.2 ± 7.2		298	Sjastad et al. (2012)
		DTA studies		
$La_2O_2CO_3$	−322 ± 48		1173	Patil et al. (1968)
$Pr_2O_2CO_3$	−88		813	Sastry et al. (1966)
$Nd_2O_2CO_3$	−50 ± 8		1063	Patil et al. (1968)
	−167		1003	Sastry et al. (1966)
$Sm_2O_2CO_3$	−105 ± 16		1023	Patil et al. (1968)
$Gd_2O_2CO_3$	−84 ± 13		973	Patil et al. (1968)
$Dy_2O_2CO_3$	−63 ± 9		933	Patil et al. (1968)
$Lu_2O_2CO_3$	−46 ± 7		863	Patil et al. (1968)
		Gas equilibration studies		
$La_2O_2CO_3$	−149	−126	1000-1300	Watanabe et al. (1986)
	−145.5 ± 5.0	−119.2 ± 5.0	773-1190	Shirsat et al. (2003)
$Nd_2O_2CO_3$	−213 ± 27	−195 ± 26	800–1100	Olafsen and Fjellvag (1999)
	−198.1 ± 5	−180 ± 5	775–1105	Shirsat et al. (2005)
$Sm_2O_2CO_3$	−131 ± 5	−127 ± 5	755–987	Shirsat et al. (2008)
$Eu_2O_2CO_3$	−155 ± 5	−153 ± 5	773–993	Shirsat et al. (2008)
$Gd_2O_2CO_3$	−187.9 ± 5	−197 ± 5	774–952	Shirsat et al. (2005)

Thermodynamics of calcium silicate carbonate minerals

The silicate carbonate minerals are another class of rock forming minerals that play an important role in CO_2-H_2O-rock interactions (Xu et al. 2004; Matter and Kelemen 2009). There are several silicate carbonates with well-refined crystal structures. The five common silicate carbonate minerals in the CaO-SiO_2-CO_2-H_2O system are spurrite, $Ca_5(SiO_4)_2(CO_3)$ (Smith 1960; Grice 2005), tilleyite, $Ca_5(Si_2O_7)(CO_3)_2$ (Louisnathan and Smith 1970; Grice 2005), scawtite, $Ca_7(Si_6O_{18})(CO_3)\cdot 2H_2O$ (Grice 2005), fukalite, $Ca_4Si_2O_6(OH)_2(CO_3)$ (Henmi et al. 1977) and the recently discovered galuskinite, $Ca_7(SiO_4)_3(CO_3)$ (Lazic et al. 2011).

Spurrite, $Ca_5(SiO_4)_2(CO_3)$ is an orthosilicate having separate layers of silicate and carbonate groups due to their different Lewis-base strengths (Grice 2005). The structure of scawtite $Ca_7(Si_6O_{18})(CO_3)\cdot 2H_2O$, is composed of a $[CaO_{6\text{-}8}]$ polyhedral sheet linked by Si_6O_{18} rings and isolated CO_3 groups parallel to (101) (Grice 2005). The enthalpies of formation determined by high-temperature oxide melt solution calorimetry for scawtite, and spurrite, are given in Table 10 (Zhang et al. 2013). The enthalpy of formation from the oxides is −689.5 ± 14.3 kJ/mol for scawtite and −455.1 ± 9.7 kJ/mol for spurrite, and the enthalpy

Table 10. Enthalpies of drop solution in molten lead borate at 702 °C , as well as the enthalpies of formation, of spurrite, scawtite and constituent oxides. Reproduced with permission from Zhang et al. (2013). Copyright © 2013 Elsevier Science.

Material	ΔH_{ds} (kJ/mol)	$\Delta H^{\circ}_{f,ox}$ (kJ/mol)	$\Delta H^{\circ}_{f,el}$ (kJ/mol)
Scawtite	940.2 ± 0.7 (11) [a]	−689.5 ± 14.3	−11564.5 ± 16.8
Spurrite	457.0 ± 1.2 (8)	−455.1 ± 9.7	−5845.5 ± 10.9
$CaCO_3$	189.6 ± 1.1 [b]	−178.9 ± 1.6	−1207.5 ± 1.3 [f]
CaO	−21.4 ± 1.9		−635.1 ± 0.9 [f]
SiO_2	38.4 ± 0.8 [c]		−910.7 ± 1.0 [f]
CO_2	32.1 ± 0.1 [d]		−393.5 ± 0.1 [f]
H_2O	69.0 ± 0.1 [d]		−285.8 ± 0.1 [f]
$CaSiO_3$	105.4 ± 0.7 [e]		
Ca_2SiO_4	121.44 ± 0.99 (8)		

NOTES:
[a] Uncertainty is two standard deviations of mean; number in paratheses is the number of expriments.
[b] Navrotsky et al. (1994)
[c] Schoenitz et al. (2001)
[d] Calculated from the heat capacity reported by Robie and Hemingway (1995).
[e] Chai and Navrotsky (1993)
[f] Robie and Hemingway (1995)

of formation from the elements is −11564.5 ± 16.8 kJ/mol for scawtite and −5845.5 ± 10.9 kJ/mol for spurrite. The entropy of formation for scawtite was estimated using the enthalpy of formation data with the earlier reported phase equilibrium results. The stability fields of spurrite and scawtite with calcium carbonate at 25 °C and 80 °C are shown in Figure 33. These diagrams suggest that spurrite forms in strongly oversaturated calcium solutions at 25 °C in solutions with a low aqueous silica activity. Scawtite on the other hand could precipitate in a wide range of Ca^{2+}/ H^+ activity ratio and higher a_{H4SiO4} value as well as at saturation with quartz. Calcite is stable at relatively low Ca^{2+}/ H^+ activity but in a very wide range of H_4SiO_4 activity. If the reservoir rock is sandstone, calcium carbonate would be the dominant product at 25 °C. However, scawtite and spurrite can form if the activity of Ca^{2+} is much higher

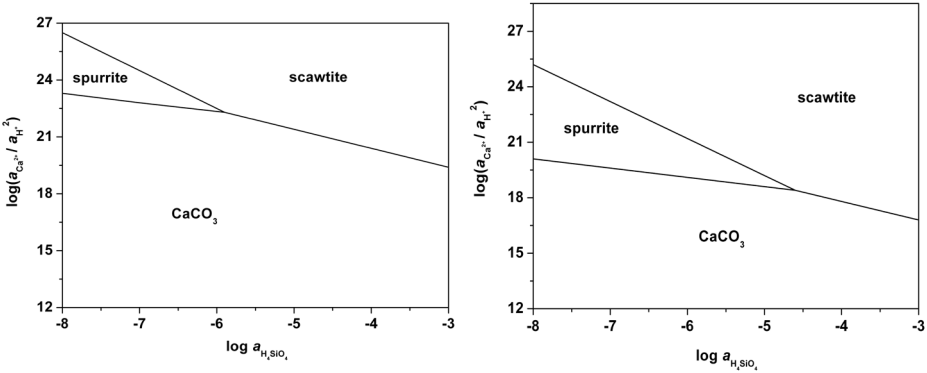

Figure 33. Mineral stability diagrams in the CaO-SiO_2-H_2O-CO_2 system at 25 and 80 °C. Reproduced with permission from Zhang et al. (2013). Copyright © 2013 Elsevier Science.

than that of H^+. Thus scawtite and spurrite may precipitate near the surfaces of dissolving silicate minerals, clays, or cement phases, as may occur in or near the caprocks in a CO_2 sequestration environment. At high temperatutre (80 °C) relevant to CO_2 sequestration, the expanded scawtite and spurrite stability fields suggest their favorable formation over calcite under moderate calcium concentration and pH by direct carbonation reactions.

A SUMMARY OF THERMODYNAMIC DATA FOR CARBONATE MINERALS

The thermodynamic data for different types of carbonate bearing minerals are summarized in Table 11 to give a bird's eye view of the data available in the literature.

CONCLUSIONS AND OUTLOOK

The thermodynamic properties of divalent binary carbonates MCO_3 and the ternary and higher order systems derived from them are dominated by three factors: the initial formation of amorphous phases, the competition between calcite, aragonite, vaterite, and dolomite structures in the crystalline state, and the mixing of cations. When the size mismatch of cations is small (e.g. Mg^{2+} and Fe^{2+}, Ca^{2+} and Sr^{2+}), disordered solid solutions occur, with positive heats of mixing and solvi reflecting lattice strain. When the size difference is larger, e.g. Mg^{2+} and Ca^{2+} or Mg^{2+} and Cd^{2+}, ordering of cations in alternate layers occurs, with negative heats of mixing and formation of ordered dolomite phases. There are also ternary carbonate phases in a number of other carbonate systems, as well as carbonate-containing layered double hydroxide phases and a number of carbonate silicate minerals. Though the thermodynamic picture of stability of these phases is improving, much work remains to be done. Because of the subtle effects of particle size, structural disorder, and inclusion/adsorption of water and organics, thermodynamic and structural and spectroscopic studies must go hand in hand. Kinetic and thermodynamic factors affecting carbonate reactions must be identified and separated. Interactions between carbonates and silicate minerals are important and need further study. To understand carbonate stability in aqueous and hydrothermal environments, the properties of the aqueous phase must be much better known, especially at high pressure, temperature, and salinity.

ACKNOWLEDGMENTS

This material is based upon work supported as part of the Center for Nanoscale Control of Geologic CO_2, an Energy Frontier Research Center funded by the U.S. Department of Energy, Office of Science, Office of Basic Energy Sciences under Award Number DE-AC02-05CH11231. We thank Tori Z. Forbes, Yin-Qing Zhang, Ozlem Sel, Di Wu, Olga Trofymulk, and Alexis Loulier for their contributions toward this project. We are especially thankful to Yin-Qing Zhang for putting together the thermodynamic data table of carbonate bearing minerals.

Table 11. Thermodynamic data of carbonate bearing minerals.

Name	Chemical Formula	ΔH_f from oxides kJ/mol	ΔH_f from elements kJ/mol	ΔG_f from elements kJ/mol	Reference
Natrite	Na_2CO_3	– 241.2 ± 0.8 [a]	– 1049.5 ± 0.4 [f]		Kiseleva et al. (1996), Robie et al. (1978)
Thermonatrite	$Na_2CO_3{\cdot}H_2O$	– 335.5 [f]	– 1429.7 [a]	–1286.1 [a]	Robie and Hemingway (1995)
Natron	$Na_2CO_3{\cdot}10\ H_2O$	– 412.76 [f]	–4079.39 [g]	–3427.66 [g]	Johnson et al. (1992)
Burkeite	$Na_6CO_3(SO_4)_2$			–3592.99 [g]	Johnson et al. (1992)
Cancrinite (NC2)	$Na_{7.770}[Al_{6.003}Si_{5.997}O_{24}](NO_3)_{1.474}(CO_3)_{0.146}{\cdot}2.175H_2O$	–871.65 ± 12.23 [a]	–14258.27 ± 17.34 [a]		Liu et al. (2007)
Cancrinite (NCS5)	$Na_{7.282}[Al_{5.854}Si_{6.146}O_{24}](NO_3)_{1.336}(CO_3)_{0.046}{\cdot}3.365H_2O$	–903.33 ± 15.72 [a]	–14258.27 ± 17.34 [a]		Liu et al. (2007)
Cancrinite (CAN7)	$Na_{7.571}[Al_{6.103}Si_{5.897}O_{24}](NO_3)_{1.242}(CO_3)_{0.113}{\cdot}3.533H_2O$	–871.65 ± 12.23 [a]	–14384.09 ± 15.76 [a]		Liu et al. (2007)
Cancrinite (CAN25)	$Na_{7.887}[Al_{5.982}Si_{6.018}O_{24}](NO_3)_{1.433}(CO_3)_{0.236}{\cdot}2.457H_2O$	–834.63 ± 9.08 [a]	–14207.51 ± 11.62 [a]		Liu et al. (2007)
Cancrinite (CAN50)	$Na_{7.725}[Al_{5.969}Si_{6.031}O_{24}](NO_3)_{1.234}(CO_3)_{0.261}{\cdot}2.829H_2O$	–844.94 ± 8.69 [a]	–14257.26 ± 11.32 [a]		Liu et al. (2007)
Cancrinite (CAN75)	$Na_{8.072}[Al_{6.055}Si_{5.945}O_{24}](NO_3)_{1.320}(CO_3)_{0.348}{\cdot}2.501H_2O$	–822.45 ± 9.75 [a]	–14292.44 ± 12.13 [a]		Liu et al. (2007)
Cancrinite (FB2-49)	$Na_{7.771}[Al_{5.956}Si_{6.004}O_{24}](CO_3)_{0.881}{\cdot}3.480H_2O$	–803.97 ± 12.08 [a]	–14524.07 ± 14.09 [a]		Liu et al. (2007)
Dawsonite	$NaAlCO_3(OH)_2$	–245.46 ± 3.00 [f]	–1963.97 ± 2.93 [b]	–1785.99 ± 2.95 [b]	Ferrante et al. (1976), Robie et al. (1978)
Sodalite	$Na_8Al_6Si_6O_{24}C_{12}$	–899.9 ± 14.3 [a]	–11591.83 ± 16.0 [f]		Liu and Navrotsky (2007)
Magnesite	$MgCO_3$	–118.28 ± 1.37 [f]	–1113.28 ± 1.34 [f]	–1029.48 ± 1.38 [d]	Robie (1965), Robie et al. (1978)

Table 11. Continued.

Name	Chemical Formula	ΔH_f from oxides kJ/mol	ΔH_f from elements kJ/mol	ΔG_f from elements kJ/mol	Reference
Nesquehonite	$MgCO_3 \cdot 3H_2O$	–124.77 ± 0.43 [f]	–1977.26 ± 0.26 [b]	–1723.75 ± 0.50 [b]	Robie and Hemingway (1973), Robie et al. (1978)
Lansfordite	$MgCO_3 \cdot 5H_2O$			–2199.2	Woods and Garrels (1987)
Hydromagnesite	$Mg_5(CO_3)_4(OH)_2 \cdot 4H_2O$	–504.22 ± 1.88 [f]	–6514.86 ± 1.06 [b]	–5864.17 ± 1.09 [b]	Robie and Hemingway (1973), Robie et al. (1978)
Artinite	$Mg_2(OH)_2CO_3 \cdot 3H_2O$	–180.80 ± 0.94 [f]	–2920.61 ± 0.71 [b]	–2568.35 ± 0.75 [b]	Hemingway and Robie (1973), Robie et al. (1978)
Hydrotalcite	$Mg_{0.69}Al_{0.31}(OH)_2(CO_3)_{0.16} \cdot 0.30H_2O$	–62.91 ± 1.66 [a]	–1170.34 ± 1.81 [a]		Allada et al. (2005a,b)
Hydrotalcite	$Mg_{0.74}Al_{0.26}(OH)_2(CO_3)_{0.13} \cdot 0.39H_2O$	–55.44 ± 1.43 [a]	–1165.98 ± 2.06 [a]		Allada et al. (2005a,b)
Hydrotalcite	$Mg_{0.67}Al_{0.33}(OH)_2(CO_3)_{0.17} \cdot 0.69H_2O$	–58.61 ± 1.90 [a]	–1284.65 ± 1.97 [a]		Allada et al. (2005a,b)
Hydrotalcite	$Mg_{0.66}Al_{0.34}(OH)_2(CO_3)_{0.17} \cdot 0.70H_2O$	–57.99 ± 2.00 [a]	–1292.08 ± 2.05 [a]		Allada et al. (2005a,b)
Hydrotalcite	$Mg_{0.73}Al_{0.27}(CO_3)_{0.16}(OH)_{1.95} \cdot 0.83H_2O$	–55.99 ± 1.99 [f]	–1297.19 ± 1.97 [a]		Allada et al. (2005a,b)
Potassium carbonate	K_2CO_3	–234.4± 1.1 [a]	–991.1 ± 2.4 [f]		Kiseleva et al. (1996), Robie et al. (1978)
Butschliite	$K_2Ca(CO_3)_2$	–38.7 ± 3.2 [a]	–1824.0 ± 3.9 [f]		Robie et al. (1978), Navrotsky et al. (1997)
Fairchildite	$K_2Ca(CO_3)_2$	–5.1 ± 3.3 [a]	–1790.4 ± 4.0 [f]		Robie et al. (1978), Navrotsky et al. (1997)
	$K_2Ca_2(CO_3)_3$	–7.2 ± 5.8 [a]	–2821.1 ± 6.4 [f]		Robie et al. (1978), Navrotsky et al. (1997)
Aragonite	$CaCO_3$	–178.83 ± 1.68 [f]	–1207.43 ± 1.42 [a]	–1127.79 ± 1.46 [a]	Robie et al. (1978), Parker et al. (1971)
Calcite	$CaCO_3$	–178.77 ± 1.61 [f]	–1207.37 ± 1.34 [a]	–1128.84 ± 1.38 [a]	

Table 11. Continued.

Name	Chemical Formula	ΔH_f from oxides kJ/mol	ΔH_f from elements kJ/mol	ΔG_f from elements kJ/mol	Reference
Calcite	$CaCO_3$	–193.4 ± 0.7 [a]	–1221.99 ± 1.13 [f]		Kiseleva et al. (1996), Robie et al. (1978)
Vaterite	$CaCO_3$			–1125.540 ± 1.50 [b]	Turnbull (1973)
Monohydrocalcite	$CaCO_3 \cdot H_2O$	–183.86 ± 1.47 [f]	–1498.29 ± 1.17 [a,d]	–1361.600 ± 1.13 [a,d]	Hull and Turnbull (1973), Robie et al. (1978)
Ikaite	$CaCO_3 \cdot 6H_2O$	– 210.5 [f]	–2954.1 [a]	–2540.9 [a]	Robie and Hemingway (1995)
Dolomite	$CaMg(CO_3)_2$	–300.9 ± 0.5 [b]	–2324.5 ± 1.1 [b]	–2161.7 ± 1.1 [b]	Hemingway and Robie (1994)
Dolomite	$CaMg(CO_3)_2$			–2147.82 ± 2.20 [e]	Rock et al. (2001)
Huntite	$CaMg_3(CO_3)_4$	–516.00 ± 2.07 [f]	–4529.60 ± 1.57 [b]	–4203.42 ± 1.63 [b]	Robie et al. (1978), Hemingway and Robie (1973)
Meionite	$Ca_4Al_6Si_6O_{24}CO_3$	–522.8 [f]	–13881.4 [a]	–13131.8 [a]	Robie and Hemingway (1995)
Pirssonite	$Na_2Ca(CO_3)_2 \cdot 2H_2O$			–635.794 [g]	Johnson et al. (1992)
Gaylussite	$Na_2Ca(CO_3)_2 \cdot 5H_2O$			–3372.61 [g]	Johnson et al. (1992)
Rhodochrosite	$MnCO_3$	–110.52 ± 1.30 [f]	–889.27 ± 1.21 [d]	–816.05 ± 1.38 [d]	Robie, (1965), Robie et al. (1978)
Kutnahorite	$CaMn(CO_3)_2$			–1950.6	Woods and Garrels (1987)
Siderite	$FeCO_3$	–71.43 ± 3.08 [f]	–736.98 ± 2.26 [d]	–666.70 ± 2.09 [d]	Robie et al. (1978)
Siderite	$FeCO_3$	–84.95 ± 2.24 [f]	–750.5 ± 0.8 [a]		Chai and Navrotsky (1994), Robie et al. (1978)
Ankerite	$Ca(Fe_{0.1583}Mg_{0.8417})(CO_3)_2$	6.80 ± 3.45 [a]	–1964.65 ± 3.59 [f]		Chai and Navrotsky (1996 a,b), Robie et al. (1978)
Ankerite	$Ca(Fe_{0.2990}Mg_{0.7010})(CO_3)_2$	10.36 ± 2.64 [a]	–1914.73 ± 2.87 [f]		Chai and Navrotsky (1996 a,b), Robie et al. (1978)

Table 11. Continued.

Name	Chemical Formula	ΔH_f from oxides kJ/mol	ΔH_f from elements kJ/mol	ΔG_f from elements kJ/mol	Reference
Ankerite	$Ca(Fe_{0.4996}Mg_{0.5004})(CO_3)_2$	16.21 ± 4.80 [a]	–1842.80 ± 5.00 [f]		Chai and Navrotsky (1996 a,b), Robie et al. (1978)
Ankerite	$Ca(Fe_{0.6482}Mg_{0.3518})(CO_3)_2$	16.54 ± 2.10 [a]	–1793.51 ± 2.66 [f]		Chai and Navrotsky (1996 a,b), Robie et al. (1978)
Ankerite	$CaFe(CO_3)_2$	6.98 ± 2.08 [a]	–1687.17 ± 3.09 [f]		Chai and Navrotsky (1996 a,b), Robie et al. (1978)
Sphaerocobaltite	$CoCO_3$	–114.36 ± 1.10 [a]	–745.82 ± 1.68 [a]		Allada and Navrotsky (2002)
Co-Al hydrotalcite	$Co_{0.68}Al_{0.32}(OH)_2(CO_3)_{0.16}\cdot 0.779H_2O$	–42.80 ± 1.50 [a]	–1044.17 ± 2.54 [a]		Allada and Navrotsky (2002)
Co-Al hydrotalcite	$Co_{0.756}Al_{0.244}(OH)_2(CO_3)_{0.122}\cdot 0.805H_2O$	–43.51 ± 1.42 [a]	–991.79 ± 1.72 [a]		Allada and Navrotsky (2002)
Co-Al hydrotalcite	$Co_{0.756}Al_{0.244}(OH)_2(CO_3)_{0.1202}(NO_3)_{0.0018}\cdot 0.810H_2O$	–21.87 ± 3.47 [f]	–967.89 ± 3.33 [a]		Allada and Navrotsky (2002)
Malachite	$Cu_2CO_3(OH)_2$	–59.97 ± 3.29 [f]	–1053.95 ± 2.09		Richardson and Brown (1974), Robie et al. (1978)
Azurite	$Cu_3(OH)_2(CO_3)_2$	–87.37 ± 4.27 [f]	–1632.18 ± 2.00 [a]		Wagman et al. (1969), Robie et al. (1978)
Smithsonite	$ZnCO_3$	–68.81 ± 2.95 [f]	–812.78 ± 2.93 [a]	–731.48 ± 2.97 [a]	Parker et al. (1971), Robie et al. (1978)
Strontianite	$SrCO_3$	–234.88 ± 1.26 [b]	–1233.43 ± 2.09 [b]	–1153.04 ± 2.09 [b]	Adami and Conway (1966)
Strontianite	$SrCO_3$	–247.4 ± 3.3 [f]	–1231.4 ± 3.2 [a]		Kiseleva et al. (1994), Robie et al. (1978)
Otavite	$CdCO_3$	–98.90 ± 2.65 [f]	–750.61 ± 2.51 [a]	–669.44 ± 2.64 [a]	Wagman et al. (1968), Robie et al. (1978)
Witherite	$BaCO_3$	–269.63 ± 1.26 [b]	–1245.57± 3.35 [b]	–1165.61 ± 3.35 [b]	Adami and Conway (1966)

Table 11. Continued.

Name	Chemical Formula	ΔH_f from oxides kJ/mol	ΔH_f from elements kJ/mol	ΔG_f from elements kJ/mol	Reference
Witherite	$BaCO_3$	–268.29 ± 6.17 [f]	–1209.9 ± 5.8 [a]		Kiseleva et al. (1994), Robie et al. (1978)
Cerussite	$PbCO_3$	–90.43 ± 1.26 [b]	–703.38 ± 1.26 [b]	–629.69 ± 1.26 [b]	Adami and Conway (1966)
Rutherfordine	$(UO_2)(CO_3)$	–99.1 ± 4.2 [a]	–1716.4 ± 4.2 [a]	–1564.7 ± 1.8 [a]	Kubatko et al. (2005)
Andersonite	$Na_2Ca(UO_2)(CO_3)_3(H_2O)_5$	–710.6 ± 9.1 [a]	–5593.6 ± 9.1 [a]	–5651 ± 24 [a]	Kubatko et al. (2005)
Grimselite	$K_3Na(UO_2)(CO_3)_3(H_2O)$	–989.3 ± 14.0 [a]	–4431.6 ± 15.3 [a]	–4051.3 ± 1.8 [a]	Kubatko et al. (2005)
Barentsite	$Na_7AlH_2(CO_3)_4F_4$	N/A			
Shortite	$Na_2Ca_2(CO_3)_3$	N/A			
Zemkorite	$(Na,K)_2Ca(CO_3)_2$	N/A			
Tunisite	$NaCa_2Al_4(CO_3)_4(OH)_8Cl$	N/A			
Carletonite	$Na_4KCa_4Si_8O_{18}(CO_3)_4F{\cdot}H_2O$	N/A			
Spurrite	$Ca_5(SiO_4)_2(CO_3)$	N/A			
Tilleyite	$Ca_5Si_2O_7(CO_3)_2$	N/A			
Scawtite	$Ca_7Si_6O_{18}(CO_3){\cdot}2H_2O$	N/A			
Gaspeite	$(Ni,Mg,Fe)CO_3$	N/A			
Hydrozincite	$Zn_5(CO_3)_2(OH)_6$	N/A			
Minrecordite	$CaZn(CO_3)_2$	N/A			
Rosasite	$(Cu,Zn)_2CO_3(OH)_2$	N/A			
Aurichalcite	$(Cu,Zn)_5(CO_3)_2(OH)_6$	N/A			
Barytocite	$BaCa(CO_3)_2$	N/A			
Kampfite	$Ba_6(Si,Al)_8O_{16}(CO_3)_2Cl_2{\cdot}H_2O$	N/A			

Table 11. Continued.

Name	Chemical Formula	ΔH_f from oxides kJ/mol	ΔH_f from elements kJ/mol	ΔG_f from elements kJ/mol	Reference
Fencooperite	$Ba_6Fe_3Si_8O_{23}(CO_3)_2Cl_3 \cdot H_2O$	N/A			
Bussenite	$Na_2Ba_2FeTiSi_2O_7(CO_3)(OH)_3F$	N/A			
Tundrite	$Na_2Ce_2TiO_2(SiO_4)(CO_3)_2$	N/A			
Hydrocerussite	$Pb_3(CO_3)_2(OH)_2$	N/A			
Phosgenite	$Pb_2(CO_3)Cl_2$	N/A			
Ashburtonite	$Cu_4Pb_4Si_4O_{12}(HCO_3)_4(OH)_4Cl$	N/A			
Zellerite	$Ca(UO_2)(CO_3)_2 \cdot 5H_2O$	N/A			
Limoriite	$Y_2(SiO_4)(CO_3)$	N/A			
Kainosite	$Ca_2Y_2Si_4O_{12}(CO_3) \cdot H_2O$	N/A			
Caysichite	$Ca_4Y_4Si_8O_{20}(CO_3)_6(OH) \cdot 7H_2O$	N/A			
Ashcroftine	$K_5Na_5Y_{12}Si_{28}O_{70}(CO_3)_8(OH)_2 \cdot 8H_2O$	N/A			

Superscripts indicate the method: a. Solution calorimetry; b. Acid calorimetry; c. Oxide melt; d. Solubility equilibrium; e. Electrochemical cells; f. Calculated from ΔH_f from oxides or ΔH_f from elements; g. Calculated from computer models N/A = not available

REFERENCES

Adami LH, Conway KC (1966) Heats and free energies of formation of anhydrous carbonates of barium, strontium, and lead. US Bur Mines Rep Invest No. 6822, p 7

Addadi L, Raz S, Weiner S (2003) Taking advantage of disorder: Amorphous calcium carbonate and its roles in biomineralization. Adv Mater 15:959-970

Aizenberg J, Lambert G, Weiner S, Addadi L (2002) Factors involved in the formation of amorphous and crystalline calcium carbonate: A study of an ascidian skeleton. J Am Chem Soc 124:32-39

Allada RK, Navrotsky A (2002) Thermochemistry and aqueous solubilities of hydrotalcite-like solids. Science 296:721-723

Allada RK, Navrotsky A, Boerio-Goates J (2005a) Thermochemistry of hydrotalcite-like phases in the MgO-Al_2O_3-CO_2-H_2O system: A determination of enthalpy, entropy, and free energy. Am Mineral 90:329-335

Allada RK, Peltier E, Navrotsky A, Casey WH, Johnson CA, Berbeco HT, Sparks DL (2006) Calorimetric determination of the enthalpies of formation of hydrotalcite-like solids and their use in the geochemical modeling of metals in natural waters. Clays Clay Miner 54:409-417

Allada RK, Pless JD, Nenoff TM, Navrotsky A (2005b) Thermochemistry of hydrotalcite-like phases intercalated with CO_3^{2-}, NO_3^-, Cl^-, I^-, and ReO^{4-}. Chem Mater 17:2455-2459

Baker JC, Bai GP, Hamilton PJ, Golding SD, Keene JB (1995) Continental-scale magmatic carbon dioxide seepage recorded by dawsonite in the Bowen-Gunnedah-Sydney basin system, eastern Australia. J Sediment Res Sec A65:522-530

Bellotto M, Rebours B, Clause O, Lynch J, Bazin D, Elkaiem E (1996) A reexamination of hydrotalcite crystal chemistry. J Phys Chem 100:8527-8534

Benezeth P, Palmer DA, Anovitz LM, Horita J (2007) Dawsonite synthesis and reevaluation of its thermodynamic properties from solubility measurements: Implications for mineral trapping of CO_2. Geochim Cosmochim Acta 71:4438-4455

Beniash E, Aizenberg J, Addadi L, Weiner S (1997) Amorphous calcium carbonate transforms into calcite during sea urchin larval spicule growth. Proc R Soc London 264:461-465

Benson SM, Cole DR (2008) CO_2 sequestration in deep sedimentary formations. Elements 4:325-331

Bewernitz MA, Gebauer D, Long J, Colfen H, Gower LB (2012) A metastable liquid precursor phase of calcium carbonate and its interactions with polyaspartate. Faraday Discuss 159:291-312

Bischoff WD, Bishop FC, Mackenzie FT (1983) Biogenically produced magnesian calcite: inhomogeneities in chemical and physical properties; Comparison with synthetic phases. Am Mineral 68:1183-1188

Bish DL (1980) Anion-exchange in takovite: applications to other hydroxide minerals. Bull Mineral 103:170-175

Braybrook AL, Heywood BR, Jackson RA, Pitt K (2002) Parallel computational and experimental studies of the morphological modifications of calcium carbonate by cobalt. J Cryst Growth 243:336-344

Bruno M, Massaro RF, Prencipe M (2008) Theoretical structure and surface energy of the reconstructed {01.2} form of calcite ($CaCO_3$) crystal. Surf Sci 602:2774-2782

Burton BP (1987) Theoretical analysis of cation ordering in binary rhombohedral carbonate systems. Am Mineral 72:329-336

Busenberg E, Plummer LN (1989) Thermodynamics of magnesian calcite solid-solutions at 25 °C and 1 atm total pressure. Geochim Cosmochim Acta 53:1189-1208

Capobianco C, Navrotsky A (1987) Solid-solution thermodynamics in $CaCO_3$-$MnCO_3$. Am Mineral 72:312-318

Capobianco C, Burton BP, Davidson PM, Navrotsky A (1987) Structural and calorimetric studies of order-disorder in cadmium magnesium carbonate ($CdMg(CO_3)_2$). J Solid State Chem 71:214-223

Carlson WD (1983) Polymorphs of calcium carbonate and the aragonite-calcite transformation. Rev Mineral 11:191-225

Casey WH, Chai L, Navrotsky A, Rock PA (1996a) Thermochemistry of mixing strontianite [$SrCO_{3(s)}$] and aragonite [$CaCO_{3(s)}$] to form $Ca_xSr_{1-x}(CO_3)_{(s)}$ solid solutions. Geochim Cosmochim Acta 60:933-940

Casey WH, Rock PA, Chung J-B, Walling EM, McBeath MK (1996b) Gibbs energies of formation of metal-carbonate solid solutions. 2: the $Ca_xSr_{1-z}CO_{3(s)}$ system at 298 K and 1 bar. Am J Sci 296:1-22

Cavani F, Trifiro F, Vaccari A (1991) Hydrotalcite-type anionic clays: preparation, properties and applications. Catal Today 1:173-301

Chai L, Navrotsky A (1993) Thermochemistry of carbonatepyroxene equilibria. Contrib Mineral Petrol 114:139-147

Chai L, Navrotsky A (1994) Enthalpy of formation of siderite and its application in phase equilibrium calculation. Am Mineral 79:921-929

Chai L, Navrotsky A (1996a) Synthesis, characterization, and energetics of solid solution along the dolomite-ankerite join, and implications for the stability of ordered $CaFe(CO_3)_2$. Am Mineral 81:1141-1147

Chai L, Navrotsky A (1996b) Synthesis, characterization, and enthalpy of mixing of the $(Fe,Mg)CO_3$ solid solution. Geochim. Cosmochim. Acta 60:4377-4383

Chai L, Navrotsky A, Reeder RJ (1995) Energetics of calcium-rich dolomite. Geochim Cosmochim Acta 59:939-944

Christoffersen J, Rostrup E, Christoffersen MR (1991) Relation between interfacial surface tension of electrolyte crystals in aqueous suspension and their solubility; Asimple derivation based on surface nucleation. J Crystal Growth 113:599-605

Cohen LH, Klement W Jr (1973) Determination of high-temperature transition in calcite to 5 kbar by differential thermal analysis in hydrostatic apparatus. J Geol 81:724-726

Cole DR, Chialvo AA, Rother G, Vlcek L, Cummings PT (2010) Supercritical fluid behavior at nanoscale interfaces: Implications for CO_2 sequestration in geologic formations. Philos Mag 90:2339-2363

Colfen H, Antonietti M (2008) Mesocrystals and Non-classical Crystallization; John Wiley & Sons: Chichester, UK

Corazza E, Sabelli C, Vannucci S (1977) Dawsonite: new mineralogical data and structure refinement. Neues Jahrb Mineral Monatsh 381-397

Crawford WA, Fyfe WS (1964) Calcite-aragonite equilibrium at 100 °C. Science 144:1569-1570

Davidson PM (1994) Ternary iron, magnesium, calcium carbonates: a thermodynamic model for dolomite as an ordered derivative of calcite-structure solutions. Am Mineral 79:332-339

Davidson PM, Symmes GH, Cohen BA, Reeder RJ, Lindsley DH (1993) Synthesis of the new compound $CaFe(CO_3)_2$ and experimental constraints on the $(Ca,Fe)CO_3$ join. Geochim Cosmochim Acta 57:5105-5109

Davies PK, Navrotsky A (1983) Quantitative correlations of deviations from ideality in binary and pseudobinary solid solutions. J Solid State Chem 46:1-22

De CC, Peters T (1981) The solvus in the system manganese(II) carbonate-calcium carbonate. Contrib Mineral Petrol 76:394-400

de Leeuw NH, Parker SC (1998) Surface structure and morphology of calcium carbonate polymorphs calcite, aragonite, and vaterite: an atomistic approach. J Phys Chem B 102:2914-2922

De Yoreo JJ, Dove PM (2004) Materials science. Shaping crystals with biomolecules. Science 306:1301-1302

De Yoreo JJ, Vekilov PG (2003) Principles of crystal nucleation and growth. Rev Mineral Geochem 54:57-93

De Yoreo JJ, Wierzbicki A, Dove PM (2007) New insights into mechanisms of biomolecular control on growth of inorganic crystals. Cryst Eng Comm 9:1144-1152

De Yoreo JJ, Zepeda-Ruiz LA, Friddle RW, Qiu SR, Wasylenki LE, Chernov A.A, Gilmer GH, Dove PM (2009) Rethinking classical crystal growth models through molecular scale insights: Consequences of kink-limited kinetics. Cryst Growth Design 9:5135-5144

De Yoreo JJ, Waychunas GA, Jun Y-S, Fernandez-Martinez A (2013) *In situ* investigations of carbonate nucleation on mineral and organic surfaces. Rev Mineral Geochem 77:229-257

Demichelis R, Raiteri P, Gale JD, Quigley D, Gebauer D (2011) Stable prenucleation mineral clusters are liquid-like ionic polymers. Nat Commun 2:590

Doughty C (2010) Investigation of CO_2 plume behavior for a large-scale pilot test of geologic carbon storage in a saline formation. Transp Porous Media 82:49-76

Dousi E, Kallitsis J, Chrissanthopoulos A, Mangood AH, Dalas E (2003) Calcite overgrowth on carboxylated polymers. J Crystal Growth 253:496-503

Dove MT, Powell BM (1989) Neutron diffraction study of the tricritical orientational order/disorder phase transition in calcite at 1260 K. Phys Chem Miner 16:503-507

Duffy DM, Harding JH (2004) Growth of polar crystal surfaces on ionized organic substrates. Langmuir 20:7637-7642

Essene EJ (1983) Solid solutions and solvii among metamorphic carbonates, with applications to geologic thermobarometry. Rev Mineral Geochem 11:77-96

Faatz M, Gröhn F, Wegner G (2004) Amorphous calcium carbonate: Synthesis and potential intermediate in biomineralization. Adv Mater 16:996-1000

Falini G, Fermani S, Gazzano M, Ripamonti A (1998) Oriented crystallization of vaterite in collagenous matrixes. Chem Eur J 4:1048-1052

Ferrante MJ. Stuve JM, Richardson DW (1976) Thermodynamic Data for Synthetic Dawsonite. US Bur Mines p. 13

Ferrini V, De Vito C, Mignardi S (2009) Synthesis of nesquehonite by reaction of gaseous CO_2 with Mg chloride solution: Its potential role in the sequestration of carbon dioxide. J Hazardous Mater 168:832-837

Forbes TZ, Radha AV, Navrotsky A (2011) The energetics of nanophase calcite. Geochim Cosmochim Acta 75:7893-7905

Friedman GM (2005) Unusual occurrences: vaterite. An uncommon polymorph of $CaCO_3$. Carbonates Evaporites 20:181

Friedman GM Schultz DJ, Guo B, Sanders JE (1993) Vaterite (an uncommon polymorph of calcium carbonate): occurrences in boreholes demonstrate unexpected longevity. J Sediment Petrol 63:663-664

Garcia DJ, Shao H, Hu Y, Ray JR, Jun Y-S (2012) Supercritical CO_2-brine induced dissolution, swelling, and secondary mineral formation on phlogopite surfaces at 75-95 °C and 75 atm. Energy Environ Sci 5:5758-5767

Garrels RM, Thompson ME, Siever R (1960) Stability of some carbonates at 25 °C and one atmosphere total pressure. Am J Sci 258:402-418

Gebauer D, Coelfen H (2011) Prenucleation clusters and non-classical nucleation. Nano Today 6:564-584

Gebauer D, Voelkel A, Coelfen H (2008) Stable prenucleation calcium carbonate clusters. Science 322:1819-1822

Gilman JJ (1960) Direct measurements of the surface energies of crystals. J Appl Phys 31:2208-2218

Goldsmith JR (1967) Metastability and hangovers in crystals. Geochim Cosmochim Acta 31:913-919

Goldsmith, JR, Graf DL (1957) The system CaO-MnO-CO_2; Solid-solution and decomposition relations. Geochim Cosmochim Acta 11:310-334

Goldsmith JR, Graf DL (1958) Structural and compositional variations in some natural dolomites. J Geology 66:678-693

Goldsmith JR, Heard HC (1961) Subsolidus phase relations in the system $CaCO_3$-$MgCO_3$. J Geology 69:45-74

Gomez-Morales J, Hernandez-Hernandez A, Sazaki G, Garcia-Ruiz JM (2010) Nucleation and polymorphism of calcium carbonate by a vapor diffusion sitting drop crystallization technique. Crystal Growth Design 10:963-969

Gordon TM, Greenwood HJ (1970) The reaction dolomite + quartz + water = talc + calcite + carbon dioxide. Am J Sci 268:225-242

Goujon G, Mutaftschiev B (1976) On the crystallinity and the stoichiometry of the calcite surface. J Colloid Interface Sci 57:148-161

Gower LB (2008) Biomimetic model systems for investigating the amorphous precursor pathway and its role in biomineralization. Chem Rev 108:4551-4627

Graf DL, Goldsmith JR (1955) Dolomite-magnesian calcite relations at elevated temperatures and carbon dioxide pressures. Geochim Cosmochim Acta 7:109-128

Grice JD (2005) The structure of spurrite, tilleyite and scawtite, and relationships to other silicate-carbonate minerals. Can Mineral 43:1489-1500

Gupta YP, Santhanam AT (1969) Cleavage surface energy of calcite crystals. Acta Metall 17:419-424

Han YS, Hadiko G, Fuji M, Takahashi M (2006) Crystallization and transformation of vaterite at controlled pH. J Crys Growth 289:269-274

Hemingway BS, Robie RA (1973) Calorimetric determination of the standard enthalpies of formation of huntite, $CaMg_3(CO_3)_4$, and artinite, $Mg_2(OH)_2CO_3{\cdot}3H_2O$, and their standard Gibbs free energies of formation. J Res US Geol Surv 1:535-541

Hemingway BS, Robie RA (1994) Enthalpy and Gibbs energy of formation of dolomite, $CaMg(CO_3)_2$ at 298.15 K from HCl solution calorimetry. U.S. Department of the Interior, US Geol Surv Open-file Report 94-575

Henmi C, Kusachi I, Kawahara A, Henmi K (1977) Fukalite, a new calcium carbonate silicate hydrate mineral. Mineral J 8:374-381

Holland HD, Borcsik M, Munoz J, Oxburgh UM (1963) Coprecipitation of Sr^{2+} with aragonite and of Ca^{2+} with strontianite between 90 and 100 °C. Geochim Cosmochim Acta 27:957-977

Holland TJB, Powell R (1990) An enlarged and updated internally consistent thermodynamic dataset with uncertainties and correlations: The system K_2O-Na_2O-CaO-MgO-MnO-FeO-Fe_2O_3-Al_2O_3-TiO_2-SiO_2-C-H_2-O_2. J Metamorphic Geol 8:89-124

Hu Q, Zhang J, Becker U (2010) Growth process and crystallographic properties of ammonia-induced vaterite. Mater Res Soc Symp Proc p 1272, Paper: 1272-PP1203-1206

Hull H, Turnbull AG (1973) Thermochemical study of monohydrocalcite. Geochim Cosmochim Acta 37:685-694

Hwang S, Blanco M, Demiralp E, Cagin T, Goddard WA (2001) The MS-Q force field for clay minerals: application to oil production. J Phy Chem B 105:4122-4127

Irving AJ, Wyllie PJ (1973) Melting relations in calcium oxide-carbon dioxide and magnesium oxide-carbon dioxide to 36 kilobars with comments on carbon dioxide in the mantle. Earth Planet Sci Lett 20:220-225

Jackson JJr, Huggins CW, Ampian SG (1972) Synthesis and Characterization of Dawsonite. Bur Mines p. 19

Jacobs GK, Kerrick DM, Krupka KM (1981) The high-temperature heat capacity of natural calcite ($CaCO_3$). Phys Chem Miner 7:55-59

Jamieson JC (1953) Phase equilibrium in the system calcite-aragonite. J Chem Phys 21:1385-1390

Janczuk B, Chibowski E, Bialopiotrowicz T (1986) Time dependence wettability of quartz with water. Chem Pap 40:349-356

Johannes W, Puhan D (1971) Calcite-aragonite transition, reinvestigated. Contrib Mineral Petrol 31:28-38

Johnson CA, Glasser FP (2003) Hydrotalcite-like minerals ($M_2Al(OH)_6(CO_3)0.5{\cdot}xH_2O$, where M = Mg, Zn, Co, Ni) in the environment: Synthesis, characterization, and thermodynamic stability. [Erratum to document cited in CA138:388278]. Clays Clay Miner 51:357

Johnson JW, Oelkers EH, Helgeson HC (1992) SUPCRT92:A software package for calculating the standard molal thermodynamic properties of minerals, gases, aqueous species, and reactions from 1 to 5000 bar and 0 to 1000 °C. Computers Geosci 18:899-947

Kamhi SR (1963) On the structure of vaterite, $CaCO_3$. Acta Crystallogr 16:770-773

Kanakis J, Dalas E (2000) The crystallization of vaterite on fibrin. J Cryst Growth 219:277-282

Kanakis J, Malkaj P, Petroheilos J, Dalas E (2001) The crystallization of calcium carbonate on porcine and human cardiac valves and the antimineralization effect of sodium alginate. J Crystal Growth 223:557-564

Kaszuba JP, Janecky DR, Snow MG (2003) Carbon dioxide reaction processes in a model brine aquifer at 200 °C and 200 bars: implications for geologic sequestration of carbon. Appl Geochem 18:1065-1080

Kaszuba JP, Janecky DR, Snow MG (2005) Experimental evaluation of mixed fluid reactions between supercritical carbon dioxide and NaCl brine: Relevance to the integrity of a geologic carbon repository. Chem Geol 217:277-293

Kaszuba JP, Viswanathan HS, Carey JW (2011) Relative stability and significance of dawsonite and aluminum minerals in geologic carbon sequestration. Geophys Res Lett 38:L08404/08401-L08404/08405

Kerisit S, Parker SC, Harding JH (2003) Atomistic simulation of the dissociative adsorption of water on calcite surfaces. J Phy Chem B 107:7676-7682

Ketzer JM, Iglesias R, Einloft S, Dullius J, Ligabue R, de Lima V (2009) Water-rock-CO_2 interactions in saline aquifers aimed for carbon dioxide storage: Experimental and numerical modeling studies of the Rio Bonito Formation (Permian), southern Brazil. Appl Geochem 24:760-767

Kharaka YK, Campbell P, Thorden JJ, Thomas PB, Cole DR, Hovorka SD (2010) Geologic storage of carbon dioxide: Potential environmental impacts of CO_2-organic interactions. Geochim Cosmochim Acta 74:A511-A511

Kharaka YK, Cole DR, Thordsen JJ, Kakouros E, Nance HS (2006) Gas-water-rock interactions in sedimentary basins: CO_2 sequestration in the Frio Formation, Texas, USA. J Geochem Explor 89:183-186

Kiseleva IA, Kotelnikov AR, Martynov KV, Ogorodova LP, Kabalov JK (1994) Thermodynamic properties of strontianite-witherite solid solution (Sr,Ba)CO_3. Phys Chem Minerals 21:392-400

Kiseleva IA, Navrotsky A, Belitsky IA, Fursenko BA (1996) Thermochemistry of natural potassium sodium calcium leonhardite and its cation-exchanged forms. Am Mineral 81:668-675

Koenigsberger E, Gamsjager, H (1990) Solid-solute phase equilibria in aqueous solution. IV. Calculation of phase diagrams. Z Anorg Allg Chem 584:185-193

Koga N, Nakagoe Y, Tanaka H (1998) Crystallization of amorphous calcium carbonate. Thermochim Acta 318:239-244

Kubatko K-A, Helean KB, Navrotsky A, Burns PC (2005) Thermodynamics of uranyl minerals: Enthalpies of formation of rutherfordine, UO_2CO_3, andersonite, $Na_2CaUO_2(CO_3)_3(H_2O)_5$, and grimselite, $K_3NaUO_2(CO_3)_3H_2O$. Am Mineral 90:1284-1290

Kvamme B, Kuznetsova T, Uppstad D (2009) Modelling excess surface energy in dry and wetted calcite systems. J Math Chem 46:756-762

Lazic B, Armbruster T. Savelyeva VB, Zadov AE, Pertsev NN, Dzierzanowski P (2011) Galuskinite, $Ca_7(SiO_4)_3(CO_3)$, a new skarn mineral from the Birkhin gabbro massif, Eastern Siberia, Russia. Mineral Mag 75:2631-2648

Levchenko AA, Li G, Boerio-Goates J, Woodfield BF. Navrotsky A (2006) TiO_2 stability landscape: polymorphism,surface energy and bound water energetics. Chem Mater 18:6324-6332

Lee HS, Ha TH, Kim K (2005) Fabrication of unusually stable amorphous calcium carbonate in an ethanol medium. Mater Chem Phys 93:376-382

Lioliou MG, Paraskeva CA, Koutsoukos PG, Payatakes AC (2007) Heterogeneous nucleation and growth of calcium carbonate on calcite and quartz. J Colloid Interface Sci 308:421-428

Liu Q, Navrotsky A (2007) Synthesis of nitrate sodalite: An in situ scanning calorimetric study. Geochim Cosmochim Acta 71:2072-2078

Liu Q, Navrotsky A, Jove-Colon CF, Bonhomme F (2007) Energetics of cancrinite: Effect of salt inclusion. Microporous Mesoporous Mater 98:227-233

Louisnathan SJ, Smith JV (1970) Crystal structure of tilleyite. Refinement and coordination. Z Kristallog Kristallgeom Kristallphys Kristallchem 132:288-306

Lumsden DN, Chimahusky JS (1980) Relationship between dolomite nonstoichiometry and carbonate facies parameters. *In:* Concepts and Models of Dolomitization. Zenger DH, Dunham J, Ethington R (ed). Sot Econ Paleontol Mineral, p 123- 137

Mackenzie FT, Bischoff WD, Bishop FC, Loijens M, Schoonmaker J, Wollast R (1983) Magnesian calcites: low-temperature occurrence, solubility, and solid-solution behavior. Rev Mineral 11:87-144

Mann S, Heywood BR, Rajam S, Birchall JD (1988) Controlled crystallization of calcium carbonate under stearic acid monolayers. Nature 334:692-695

Manoli F, Dalas E (2002) The crystallization of calcium carbonate on sodium cholate. J Mater Sci Mater Med 13:69-73

Markgraf SA, Reeder RJ (1985) High-temperature structure refinements of calcite and magnesite. Am Mineral 70:590-600

Massaro FR, Pastero L, Rubbo M, Aquilano D (2008) Theoretical surface morphology of {0112} acute rhombohedron of calcite: A comparison with experiments and {1014} cleavage rhombohedron. J Cryst Growth 310:706-715

Matter JM, Kelemen PB (2009) Permanent storage of carbon dioxide in geological reservoirs by mineral carbonation. Nat Geosci 2:837-841

Mazeina L, Navrotsky A, Dyar D (2008) Enthalpy of formation of sulfate green rusts. Geochim Cosmochim Acta 72: 1143-1153

McHale JM, Auroux A, Perrotta AJ, Navrotsky A (1997) Surface energies and thermodynamic phase stability in nanocrystalline alumina. Science 277:788-791

Medeiros SK, Albuquerque EL, Maia FF, Caetano EWS, Freire VN (2007) First-principles calculations of structural, electronic, and optical absorption properties of $CaCO_3$ Vaterite. Chem Phys Lett 435:59-64

Meldrum FC, Colfen H (2008) Controlling mineral morphologies and structures in biological and synthetic systems. Chem Rev 108:4332-4432

Meldrum FC and Sear RP (2008) Now you see them. Science 322:1802-1803

Michel FM, MacDonald J, Feng J, Phillips BL, Ehm L, Tarabrella C, Parise JB, Reeder RJ (2008) Structural characteristics of synthetic amorphous calcium carbonate. Chem Mater 20:4720–4728

Morse JW, Casey WH (1988) Ostwald processes and mineral paragenesis in sediments. Am J Sci 288:537-560

Natoli A, Wiens M, Schroder H-C, Stifanic M, Batel R, Soldati AL, Jacob DE, Muller WEG (2010) Bio-vaterite formation by glycoproteins from freshwater pearls. Micron 41:359-366

Navrotsky A (2001) Thermochemistry of nanomaterials in nanoparticles and the environment. Rev Mineral Geochem 44:73-103

Navrotsky A (2004) Energetic clues to pathways to biomineralization: precursors, clusters, and nanoparticles. Proc Natl Acad Sci USA. 101:12096-12101

Navrotsky A (2009) Energetics of oxide nanoparticles. Int J Quantum Chem 109:2647-2657

Navrotsky A (2011) Nanoscale Effects on thermodynamics and phase equilibria in oxide systems. Chem Phys Chem 12:2207-2215

Navrotsky A, Capobianco C (1987) Enthalpies of formation of dolomite and of magnesian calcites. Am Mineral 72:782-787

Navrotsky A, Rapp R P, Smelik E, Burnley P, Circone S, Chai L, Bose K, Westrich HR (1994) The behavior of H_2O and CO_2 in high temperature lead borate solution calorimetry of volatile-bearing phases. Am. Mineral 79:1099-1109

Navrotsky A, Putnam RL, Winbo C, Rosen E (1997) Thermochemistry of double carbonates in the K_2CO_3-$CaCO_3$ system. Am Mineral 82:546-548

Navrotsky A, Mazeina L, Majzlan J (2008) Size-driven structural and thermodynamic complexity in iron oxides. Science 319:1635-1638

Navrotsky A, Ma C, Lilova K, Birkner N (2010) Nanophase transition metal oxides show large thermodynamically driven shifts in oxidation-reduction equilibria. Science 330:199-201

Okayama T, Keller DS, Luner P (1997) The wetting of calcite surfaces. J Adhes 63:231-252

Olafsen A, Fjellvag H (1999) Synthesis of rare earth oxide carbonates and thermal stability of $Nd_2O_2CO_3$ II. J Mater Chem 9:2697-2702

Olafsen A, Fjellvag H, Solen S, Atake T, Kawaji H, Matsuo K (1999) Heat capacities and entropies of $La_2O_2CO_3$ from T = (12 to 300) K and of $Nd_2O_2CO_3$ from T = (12 to 930) K, and their interpretation. J Chem Thermodyn 31:433-449

Olanders B, Steenari B-M (1995) Characterization of ashes from wood and straw. Biomass Bioenergy 8:105-115

Pabst A (1974) Synthesis, properties, and structure of $K_2Ca(CO_3)_2$, buetschliite. Am Mineral 59:353-358

Pach L, Hrabe Z, Komarneni S, Roy R (1990) Controlled crystallization of vaterite from viscous solutions of organic colloids. J Mater Res 5:2928-2932

Parker VB, Wagman DD, Evans WH (1971) Selected values of chemical thermodynamic properties. Tables for the alkaline earth elements (elements 92 through 97 in the standard order of arrangement). US Natl Bur Stand Tech Note p. 106

Patil KC, Chandrashekhar GV, George MV, Rao CNR (1968) Infrared spectra and thermal decompositions of metal acetates and dicarboxylates. Can J Chem 46:257-265

Pedersen TF, Price NB (1982) The geochemistry of manganese carbonate in Panama Basin sediments. Geochim Cosmochim Acta 46:59-68

Pertlik F (1981) Structural investigations of synthetic fairchildite, $K_2Ca(CO_3)_2$. Z Kristallogr 157:199-205

Pitcher MW, Ushakov SV, Navrotsky A, Woodfield BF, Li GS, Boerio-Goates J, Tissue BM (2005) Energy crossovers in nanocrystalline zirconia. J Am Ceram Soc 88:160-167

Plummer LN, Busenberg E (1982) The solubilities of calcite, aragonite, and vaterite in carbon dioxide-water solutions between 0 and 90 °C, and an evaluation of the aqueous model for the system calcium carbonate-carbon dioxide-water. Geochim Cosmochim Acta 46:1011-1040

Plummer LN, Busenberg E (1987) Thermodynamics of aragonite-strontianite solid solutions: Results from stoichiometric solubility at 25 and 76 °C. Geochim Cosmochim Acta 51:1393-1411

Plummer LN, Busenberg E, Glynn PD, Blum AE (1992) Dissolution of aragonite-strontianite solid solutions in nonstoichiometric $Sr(HCO_3)_2$-$Ca(HCO_3)_2$-CO_2-H_2O solutions. Geochim Cosmochim Acta 56:3045-3072

Pouget EM, Bomans PHH, Goos JACM, Frederik PM, de With G, Sommerdijk NAJM (2009) The initial stages of template-controlled $CaCO_3$ formation revealed by Cryo-TEM. Science 323:1455-1458

Pouget EM, Bomans PHH, Dey A, Frederik PM, de With G, Sommerdijk NAJM (2010) The development of morphology and structure in hexagonal vaterite. J Am Chem Soc 132:11560-11565

Quigley D, Rodger PM (2008) Free energy and structure of calcium carbonate nanoparticles during early stages of crystallization. J Chem Phys 128:221101-1–221101-4

Radha AV, Navrotsky A (2013) Manganese carbonate formation from amorphous and nanocrystalline precursors: Thermodynamics and geo-elctrochemical relevance. Am Mineral, submitted

Radha AV, Shivakumara C, Kamath PV (2005a) DIFFaX simulations of stacking faults in layered double hydroxides. Clays Clay Miner 53: 521-528

Radha AV, Kamath PV, Shivakumara C (2005b) Mechanism of the anion exchange reactions of the Layered Double Hydroxides (LDHs) of Ca and Mg with Al. Solid State Sciences 7:1180-1187

Radha AV, Kamath PV, Shivakumara C (2007) Conservation of order, disorder and 'crystallinity' during anion exchange reactions among the Layered Double Hydroxides (LDHs) of Zn with Al. J Phys Chem B 111:3411-3418

Radha, AV, Bomati-Miguel O, Ushakov SV, Navrotsky A, Tartaj P (2009) Surface enthalpy, enthalpy of water adsorption and phase stability in nanocrystalline monoclinic Zirconia. J Am Ceram Soc 92:133-140

Radha AV, Forbes TZ, Killian CE, Gilbert PUPA, Navrotsky A (2010) Transformation and crystallization energetics of synthetic and biogenic amorphous calcium carbonate. Proc Natl Acad Sci USA 107:16438-16443

Radha AV, Fernandez-Martinez A, Hu YD, Jun YS, Waychunas GA, Navrotsky A (2012) Energetic and structural studies of amorphous $Ca_{1-x}Mg_xCO_3{\cdot}nH_2O$ ($0 \le x \le 1$). Geochim Cosmochim Acta 90:83-95

Railsback LB (1999) Patterns in the compositions, properties, and geochemistry of carbonate minerals. Carbonates Evaporites 14:1-20

Raiteri P, Gale JD (2010) Water is the key to nonclassical nucleation of amorphous calcium carbonate. J Am Chem Soc. 132:17623-17634

Raiteri P, Gale JD, Quigley D, Rodger PM (2010) Derivation of an accurate force-field for simulating the growth of calcium carbonate from aqueous solution: A new model for the calcite-water interface. J Phys Chem C 114:5997-6010

Ranade MR, Navrotsky A, Zhang HZ, Banfield JF, Elder SH, Zaban A, Borse PH, Kulkarni SK, Doran GS, Whitfield H J (2002) Energetics of nanocrystalline TiO_2. Proc Natl Acad Sci 99:6476–6481

Redfern SAT, Salje E, Navrotsky A (1989) High-temperature enthalpy at the orientational order-disorder transition in calcite: Implications for the calcite/aragonite phase equilibrium. Contrib Mineral Petrol 101:479-484

Reeder RJ (1983) Crystal chemistry of the rhombohedral carbonates. Rev Mineral 11:1-47

Reeder RJ, Dollase WA (1989) Structural variation in the dolomite-ankerite solid-solution series: An x-ray, Moessbauer, and TEM study. Am Mineral 74:1159-1167

Reeder RJ, Markgraf SA (1986) High-temperature crystal chemistry of dolomite. Am Mineral 71:795-804

Reeder RJ, Sheppard CE (1984) Variation of lattice parameters in some sedimentary dolomites. Am Mineral 69:520-527

Reichle WT (1986) Synthesis of anionic clay minerals (mixed metal hydroxides, hydrotalcite). Solid State Ionics 22:135-141

Ren D, Gao Y, Fen Q (2013) Comparative study on nano-mechanics and thermodynamics of fish otoliths. Mater Sci Eng C 33:9-14

Ribbe PH, Rider RJ, Goldsmith JR (eds) (1987) Carbonates: Mineralogy and Chemistry. Reviews in Mineralogy, Volume 11. Mineralogical Society of America

Richardson DW, Brown RR (1974) Enthalpy of formation of malachite. Albany Metall Res Cent p. 5

Rieger J, Frechen T, Cox G, Heckmann W, Schmidt C, Thieme J (2007) Precursor structures in the crystallization/precipitation processes of $CaCO_3$ and control of particle formation by polyelectrolytes. Faraday Discussions 136:265-277

Roayne A, Bisschop J, Dysthe DK, (2011) Experimental investigation of surface energy and subcritical crack growth in calcite. J Geophys Res Solid Earth 116:B04204/04201-B04204/04210

Robie RA (1965) Heat and free energy of formation in herzenbergite, troilite, magnesite, and rhodochrosite calculated from equilibrium data. US Geol Surv Prof Pap. 525-D, 65-72

Robie RA, Hemingway BS (1973) Enthalpies of formation of nesquehonite, $MgCO_3{\cdot}3H_2O$, and hydromagnesite, $5MgO{\cdot}4CO_2{\cdot}5H_2O$. J Res US Geol Surv 1, 543-547

Robie RA, Hemingway BS, Fisher JR (1978) Thermodynamic properties of minerals and related substances at 298.15 K and 1 Bar (105 Pascals) pressure and at higher temperatures. US Geol Sur Bull 1452

Robie RA, Hemingway GS (1995) Thermodynamic properties of minerals and related substances at 298.15 K and 1 bar (105 Pascals) pressure and at higher temperatures. US Geol Sur Bull 2131

Rock PA, Mandell GK, Casey WH, Walling EM (2001) Gibbs energy of formation of dolomite from electrochemical cell measurements and theoretical calculations. Am J Sci 301:103-111

Rosenberg PE (1963) Synthetic solid solutions in the systems $MgCO_3$-$FeCO_3$ and $MnCO_3$-$FeCO_3$. Am Mineral 48:1396-1400

Sastry RLN, Yoganarasimhan SR, Mehrotra PN, Rao CNR (1966) Preparation, characterization, and thermal decomposition of praseodymium, terbium, and neodymium carbonates. J Inorg Nucl Chem 28:1165-1177

Schoenitz M, Navrotsky A, Ross N (2001) Enthalpy of formation of $CaSi_2O_5$, a quenched high-pressure phase with pentacoordinate silicon. Phys Chem Miner 28:57-60

Sel O, Radha AV, Dideriksen K, Navrotsky A (2012) Amorphous iron (II) carbonate: Crystallization energetics and comparison to other carbonate minerals related to CO_2 sequestration. Geochim Cosmochim Acta 87:61-68

Shao H, Ray JR, Jun Y-S (2010) Dissolution and precipitation of clay minerals under geologic CO_2 sequestration conditions: CO_2-brine-phlogopite interactions. Envir Sci Techn 44:5999-6005

Shirsat AN, Ali M, Kaimal KNG, Bharadwaj SR, Das D (2003) Thermochemistry of $La_2O_2CO_3$ decomposition. Thermochim Acta 399:167-170

Shirsat AN, Bharadwaj SR, Das D (2008) Thermochemistry of decomposition of $RE_2O_2CO_3$ (RE=Sm, Eu). Thermochim Acta 477:38-41

Shirsat AN, Kaimal KNG, Bharadwaj SR, Das D (2005) Thermochemical studies on $RE_2O_2CO_3$ (RE = Gd, Nd) decomposition. J Phys Chem Solids 66:1122-1127

Simmons G, Bell P (1963) Calcite-aragonite equilibrium. Science 139:1197-1198

Sirbescu M-LC, Nabelek PI (2003) Dawsonite: An inclusion mineral in quartz from the Tin Mountain pegmatite, Black Hills, South Dakota. Am Mineral 88:1055-1059

Sjastad AO, Fjellvag H, Helean KB, Navrotsky A (2012) Enthalpy of formation of $Ln_2O_2CO_3$ II (Ln = La, Nd, Eu) and thermodynamics of decomposition equilibria. Thermochim Acta 550:76-82

Smith JV (1960) Crystal structure of spurrite, $Ca_5(SiO_4)_2CO_3$. II. Description of structure. Acta Crystallogr 13:454-458

Sohnel O, Mullin JW (1982) Precipitation of calcium carbonate. J Cryst Growth 60:239-250

Speer AJ (1983) Crystal chemistry and phase relations of orthorhombic carbonates. Rev Mineral 11:145-190

Sperber CM, Wilkinson BH, Peacor DR (1984) Rock composition, dolomite stoichiometry, and rock/water reactions in dolomitic carbonate rocks. J Geol 92:609-622

Thevenot F, Szymanski R, Chaumette P (1989) Preparation and characterization of aluminum-rich zinc-aluminum hydrotalcite-like compounds. Clays Clay Miner 37:396-402

Thomas GS, Radha AV, Kamath PV and Kannan S (2006) Thermally induced polytype transformations among the Layered Double Hydroxides (LDHs) of Mg and Zn with Al. J Phys Chem B 110:12365-12371

Titloye JO, de Leeuw NH, Parker SC (1998) Atomistic simulation of the differences between calcite and dolomite surfaces. Geochim Cosmochim Acta 62:2637-2641

Tribello GA, Bruneval F, Liew CC, Parrinello M (2009) A Molecular Dynamics Study of the Early Stages of Calcium Carbonate Growth. J Phys Chem B 113:11680-11687

Turcotte RP, Sawyer JO, Eyring L (1969) Rare earth dioxymonocarbonates and their decomposition. Inorg Chem 8:238-246

Turnbull AG (1973) Thermochemical study of vaterite. Geochim Cosmochim Acta 37:1593-1601

Verch A, Antonietti M, Colfen H (2012) Mixed calcium-magnesium pre-nucleation clusters enrich calcium. Z Kristallogr Cryst Mater 227:718-722

Wade WH, Hackerman N (1959) Heats of immersion. II. Calcite and kaolinite, effect of pretreatment. J Phys Chem 63:1639-1641

Wagman DD, Evans WH, Parker VB, Halow I, Bailey SM, Schumm RH (1968) Selected values of chemical thermodynamic properties. Nat Bur Stand (US), Tech Notes No. 270-3, 264 pp

Wagman DD, Evans WH, Parker VB, Halow I, Bailey SM, Schumm RH (1969) Selected values of chemical thermodynamic properties. Nat Bur Stand p. 141

Walter LM, Morse JW (1984) Magnesian calcite stabilities: a reevaluation. Geochim Cosmochim Acta 48:1059-1069

Wang D, Wallace AF, De Yoreo JJ, Dove PM (2009) Carboxylated molecules regulate magnesium content of amorphous calcium carbonates during calcification. Proc Natl Acad Sci USA 106:21511-21516

Wang J, Becker U (2009) Structure and carbonate orientation of vaterite ($CaCO_3$). Am Mineral 94:380-386

Wang J, Becker U (2012) Energetics and kinetics of carbonate orientational ordering in vaterite calcium carbonate. Am Mineral 97:1427-1436

Watanabe Y, Miyazaki S, Maruyama T, Saito Y (1986) Dissociation pressure of lanthanum dioxide carbonate. J Mater Sci Lett 5:135-136

Wolf G, Gunther C (2001) Thermophysical investigations of the polymorphous phases of calcium carbonate. J Therm Anal Calorim 65:687-698

Wolf G, Konigsberger E, Schmidt HG, Konigsberger LC, Gamsjager H (2000) Thermodynamic aspects of the vaterite-calcite phase transition. J Therm Anal Calorim 60:463-472

Wolf G, Lerchner J, Schmidt H, Gamsjaeger H, Koenigsberger E, Schmidt P (1996) Thermodynamics of $CaCO_3$ phase transitions. J Therm Anal 46:353-359

Wolf SE, Muller L, Barrea R, Kampf CJ, Leiterer J, Panne U, Hoffmann T, Emmerling F, Tremel W (2011) Carbonate-coordinated metal complexes precede the formation of liquid amorphous mineral emulsions of divalent metal carbonates. Nanoscale 3:1158-1165

Woods TL, Garrels RM (1987). Thermodynamic Values at Low Temperature for Natural Inorganic Materials: An Uncritical Summary, Oxford University Press, New York, New York

Wyckoff RWG (1964) Crystal Structures. Volume 2: Inorganic Compounds RXn, $RnMX_2$, $RnMX_3$. Second Edition, Interscience Publishers

Xu T, Apps JA, Pruess K (2004) Numerical simulation of CO_2 disposal by mineral trapping in deep aquifers. Appl Geochem 19:917-936

Xu T, Apps JA, Pruess K (2005) Mineral sequestration of carbon dioxide in a sandstone-shale system. Chem Geol 217:295-318

Zerai B, Saylor BZ, Matisoff G (2006) Computer simulation of CO_2 trapped through mineral precipitation in the Rose Run Sandstone, Ohio. Appl Geochem 21:223-240

Zhang Y-Q, Radha AV, Navrotsky A (2013) Thermochemistry of two calcium silicate carbonate minerals: scawtite, $Ca_7(Si_6O_{18})(CO_3)\cdot 2H_2O$, and spurrite, $Ca_5(SiO_4)_2(CO_3)$. Geochim Cosmochim Acta 115:92-99

Zimmrmann HD (1971) Equilibrium conditions of the calcite/aragonite reaction between 150° and 350 °C. Nature 231:203-204

Reviews in Mineralogy & Geochemistry
Vol. 77 pp. 123-152, 2013
Copyright © Mineralogical Society of America

PVTX Properties of H_2O-CO_2-"salt" at *PTX* Conditions Applicable to Carbon Sequestration in Saline Formations

Robert J. Bodnar, Matthew Steele-MacInnis, Ryan M. Capobianco, J. Donald Rimstidt

Department of Geosciences
Virginia Tech
Blacksburg, Virginia 24061, U.S.A.

rjb@vt.edu; mjmaci@vt.edu; rcapobi@vt.edu; jdr02@vt.edu

Robert Dilmore, Angela Goodman, George Guthrie

U.S. Department of Energy (DOE)
National Energy Technology Laboratory (NETL)
P.O. Box 10940
Pittsburgh, Pennsylvania 15236, U.S.A.

Robert.Dilmore@NETL.DOE.GOV; Angela.Goodman@NETL.DOE.GOV;
George.Guthrie@NETL.DOE.GOV

INTRODUCTION

Among the many scenarios that have been proposed to reduce the amount of carbon dioxide (CO_2) emissions to the atmosphere, carbon-capture and storage (CCS) in geological reservoirs represents the method most technologically feasible and capable of accommodating the large amounts of CO_2 that are generated on an annual basis by combustion of fossil fuels (IPCC, 2005). Geological environments and processes that have been proposed for CCS include deep, unmineable coal seams, depleted oil and gas reservoirs, organic-rich shale basins, deep saline formations, and mineral carbonation of basalts. Of these various options, the one that is most attractive owing to its widespread distribution and capacity to store large amounts of CO_2 is deep saline formations, with the U.S. Department of Energy reporting that saline formations in the United States could potentially store more than 2,100-20,000 billion metric tons of CO_2 (DOE, 2012). A recently released assessment of geologic carbon dioxide storage potential (USGS, 2013) estimates a capacity ranging from 2,400 to 3,700 billion metric tonnes (Gt) of CO_2, which corresponds to the low end of the DOE estimate.

When supercritical CO_2 ($scCO_2$) is injected into a saline formation, it may be stored in various ways. Initially, the CO_2 will be stored by structural and stratigraphic trapping, whereby $scCO_2$ is trapped beneath an impermeable confining layer that prohibits the upward migration of the more buoyant $scCO_2$. Some $scCO_2$ may also be stored by residual trapping in pores via capillary forces. In the discussion to follow, we include residual trapping with structural/stratigraphic trapping as all of these processes involve the storage of a $scCO_2$ phase and, as such, the volume requirements are assumed to be identical for these storage mechanisms for a given mass of CO_2. Over time, some of the $scCO_2$ dissolves into the formation (pore) waters, a process referred to as solubility trapping; solubility trapping may even become significant during the injection phase (accounting for ~20% of the CO_2 distribution) (Goodman et al. 2013). Eventually, some portion of the $scCO_2$ and/or CO_2 dissolved in formation waters will

1529-6466/13/0077-0004$05.00 http://dx.doi.org/10.2138/rmg.2013.77.4

react with minerals and/or dissolved cations in the formation to form carbonate and other minerals via a mechanism referred to as mineral trapping. With time, the storage mechanism evolves from one dominated by structural/stratigraphic trapping with significant solubility trapping (from injection to ~10^1 yr), to one dominated by residual trapping and solubility trapping (~10^1-10^3 yr) to one dominated by solubility trapping (~10^3-10^4 yr) (Kumar et al. 2005; Han et al. 2010, 2011; Goodman et al. 2013). Eventually, mineral trapping (~10^2-10^5 yr) becomes more significant (Benson and Cole 2008) (Fig. 1) (albeit solubility trapping may remain dominant indefinitely; Gilfillan et al. 2009; Kumar et al. 2005).

Each of the various storage mechanisms listed above involves a change in the volume and/or pressure of the system, where "system" refers to $scCO_2$ + formation (pore) waters + minerals within the saline formation (aquifer) (Steele-MacInnis et al. 2013). The volume and concomitant pressure changes associated with $scCO_2$ injection and the subsequent evolution of the system thus affect the storage capacity as well as the long-term storage security of the formation. Here, we summarize available experimental *PVTX* (Pressure-Volume-Temperature-Composition) data for the system H_2O-CO_2-"salt"-"mineral" as well as Equations of State (EOS) that have been developed to estimate the *PVTX* properties at conditions relevant to CCS in geological formations. We also evaluate the various storage mechanisms in terms of the storage volumes required and provide assessments of the volume of brine or aquifer required to accommodate current and projected CO_2 emissions.

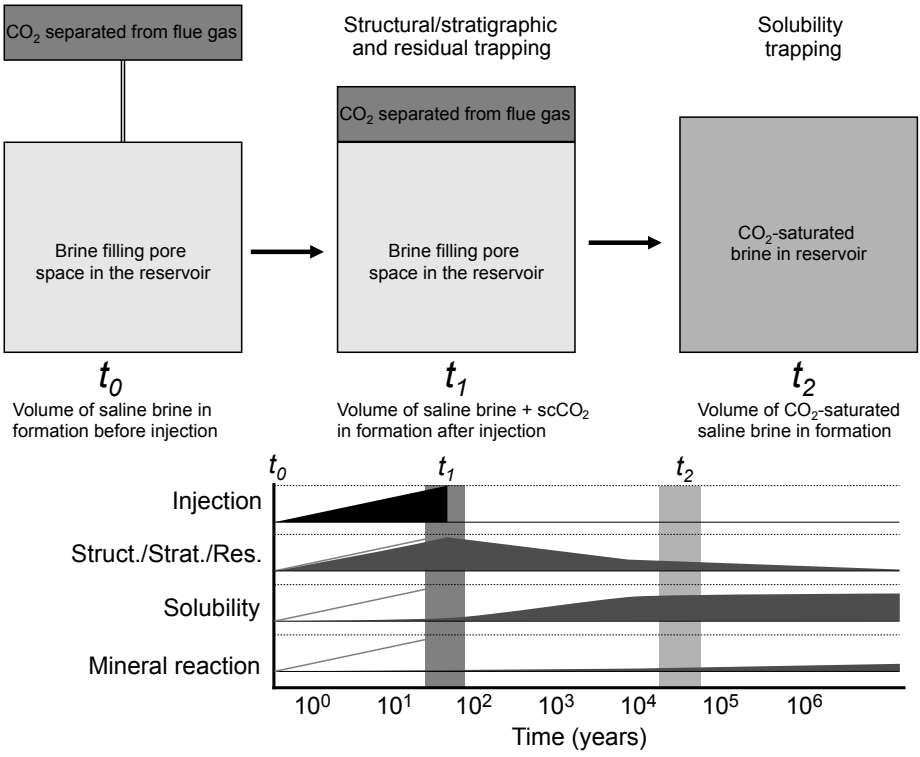

Figure 1. Conceptual model comparing the relative formation volumes required to store CO_2 as a separate supercritical phase (center) and as a dissolved component in the formation brine (right). Also shown at the bottom is the time range over which various storage mechanisms operate (modified from Steele-MacInnis et al. 2013).

SUMMARY OF AVAILABLE *PVTX* DATA AND EOS

A significant experimental database has been developed over the years related to the *PVTX* properties of fluids in the H_2O-CO_2-"salt" system at conditions relevant to storage in geologic formations. Excellent compilations and summaries of *PVTX* data for binary and ternary aqueous systems are provided by Scharlin (1996) and Valyashko (2008), and Hu et al. (2007) provide a detailed assessment of data for the H_2O-CO_2-"salt" system at CCS conditions. Here, we define the likely storage conditions for CO_2 in saline formations as 1.0-4.5 km depth, temperature range of 50-140 °C, and a pressure before injection of 100-750 bar (IPCC 2005; Nordbotten et al. 2005; Benson and Cole 2008). The accessible depth, and thus *PT* range of interest, is based on various economic and geological constraints. Thus, the formation must be sufficiently deep to assure isolation from the surface under an impermeable caprock, but not so deep such that the drilling and infrastructure costs make the project economically unviable. The minimum pressure at a given depth represents hydrostatic pressure, and the maximum pressure represents 0.6 × lithostatic pressure at the depth of interest. At pressures above this value, vertically oriented hydrofractures may develop (Hubbert and Willis 1957; Bredehoeft et al. 1976), allowing leakage of CO_2 from the formation.

H_2O

There have been perhaps several hundred experimental studies of the *PVT* properties of the single component system H_2O, and it is neither practical nor necessary to summarize these studies here. In recent years, the available experimental data have been rigorously evaluated by various workers during the course of developing equations of state to predict the thermodynamic properties of H_2O. Among the more common EOS for H_2O that have been applied to geologic environments are the models of Burnham et al. (1969), Haar et al. (1984) and Wagner and Pruß (2002). This latter EOS, referred to in the literature as IAPWS-95, has been adopted by the International Association for the Properties of Water and Steam (IAPSWS) and is valid from the ice-melting line to 1273 K (1000 °C) and up to 1000 MPa (10 kbar). IAPWS-95 is generally considered to most faithfully reproduce the physical and thermodynamic properties of H_2O over a wide range of *PT* conditions relevant to geological environments, including the CCS environment, and is used in most formulations to predict the *PVTX* properties of aqueous fluids.

CO_2

Similar to H_2O, abundant experimental *PVT* data are available for the one component system CO_2. As with H_2O, these data have been carefully evaluated during the course of EOS development, especially in recent years. The EOS for CO_2 that are valid over significant ranges in *PT* conditions and which have been applied in geologic environments include those of Altunin and Gadetskii (1971), Angus et al. (1976), Bottinga and Richet (1981) and Span and Wagner (1996). The EOS of Span and Wagner (1996) has been adopted by the National Institute of Standards and Technology (NIST) and is valid from the CO_2 triple point (216.6 K (−56.6 °C), 0.52 MPa (5.2 bar)) to 1100 K (827 °C) and 800 MPa (8 kbar). Span and Wagner (1996) note that the EOS shows the smallest uncertainty in the range up to 300 MPa (3 kbar) and 523 K (250 °C), which includes the CCS *PT* range. The EOS of Span and Wagner (1996) is used by most workers today in geologic applications, including CCS.

H_2O-"salt"

Compositions of formation waters in continental sedimentary basins vary significantly, both in terms of salinity or total dissolved solids and chemistry. Hanor (1994) divided subsurface saline waters into three groups based on their salinity and anionic composition. The least common type is represented by formation waters in which Cl is not the dominant anion. These fluids generally have salinities of <10,000 ppm (1 wt%) and include Na-HCO_3

and Na-acetate waters. The other two water types are Cl-dominated, with one represented by halite-unsaturated waters with salinities in the range 10,000-250,000 ppm (1-25 wt%) and the other represented by halite-saturated waters with salinities typically in excess of 300,000 ppm (30 wt%). In Cl-dominated waters, the Ca/Na and K/Na ratios usually increase with increasing salinity. Thus, most brines in sedimentary basins that would be appropriate for CCS are approximated by the system H_2O-NaCl-$CaCl_2$.

As noted above, chloride is the dominant anion in most basinal brines, and numerous experimental studies of the *PVTX* properties of aqueous chloride solutions have been conducted. By far, the largest proportion of these studies has focused on the system H_2O-NaCl. Phase equilibrium and thermodynamic properties for this binary system are used most often in geologic applications, including CCS. Potter et al. (1975) summarized the results of studies that were published between 1928-1974, and Bodnar (1985), Bodnar et al. (1985) and Driesner and Heinrich (2007) have summarized the more recent data.

Haas (1976a,b) developed a numerical model to predict the physical (Haas 1976a) and thermodynamic (Haas 1976b) properties of the coexisting liquid and vapor phases from 80-325 °C and from pure H_2O to halite saturation, and Potter and Brown (1977) provided algorithms and tables describing the density of H_2O-NaCl from 0-500 °C, from the liquid-vapor curve to 2000 bars, and from 0-25 wt% NaCl. Rogers and Pitzer (1982) and Anderko and Pitzer (1993) developed numerical models describing the physical and thermodynamic properties of H_2O-NaCl at elevated *PTX* conditions, and Driesner (2007) and Driesner and Heinrich (2007) presented a numerical model that predicts the physical and thermodynamic properties of coexisting liquid and vapor phases in the H_2O-NaCl system from 0-1000 °C, 1-5000 bar and from pure H_2O to pure NaCl. Compared to the system H_2O-NaCl, fewer data are available for other binary aqueous chloride systems, especially at elevated *PT* conditions (Potter et al. 1975; Valyashko 2008). Among the studies of binary aqueous systems that include *PVTX* data relevant to CCS conditions are those of Ananthaswamy and Atkinson (1985) for aqueous $CaCl_2$ solutions to 100 °C, Apelblat and Korin (2002) for various salts to 50 °C, and Holmes et al. (1994) for aqueous $CaCl_2$ solutions to 250 °C.

H_2O-CO_2

Compared to H_2O-"salt" many fewer experimental studies of gas-bearing aqueous systems have been conducted, owing to the experimental difficulties associated with these systems, especially at elevated *PT* conditions. Among the studies of the *PVTX* properties of H_2O-CO_2 at elevated *PT* conditions are those of Tödheide and Franck (1963), Takenouchi and Kennedy (1964), and Sterner and Bodnar (1991). While these studies are in general agreement for H_2O-rich compositions, they show significant disagreement for CO_2-rich compositions, especially at *PT* conditions applicable to CCS. A more recent study by Capobianco et al. (2013 and unpublished data) shows that the two-phase field extends to higher CO_2 concentration in the CO_2-rich portion of the system, and that the excess volumes are small at these conditions.

Hu et al. (2007) evaluated all available experimental *PVTX* data for the system H_2O-CO_2 at CCS conditions and developed an EOS based on the most consistent data. Figure 2 summarizes the range of *PT* conditions for which experimental *PVTX* data are available for the H_2O-CO_2±"salt" system at CCS conditions, and the fluid compositions are listed in Table 1.

H_2O-CO_2-"salt"

Only relatively few experimental studies of the *PVTX* properties of ternary compositions (H_2O-CO_2-"salt") have been conducted at *PTX* conditions relevant to crustal geologic environments. Takenouchi and Kennedy (1965) investigated three pseudobinary joins in the ternary system H_2O-CO_2-NaCl, including (H_2O-CO_2) + 6 wt% NaCl, (H_2O-CO_2) + 10 wt% NaCl, and (H_2O-CO_2) + 20 wt% NaCl over the *PT* range 100-350 °C and pressures to 1500

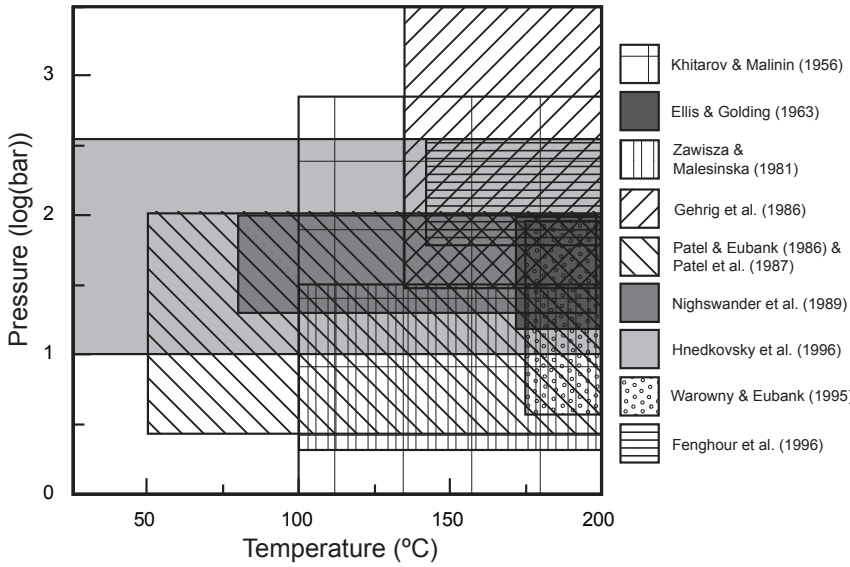

Figure 2. Summary of the *PT* range covered by experimental *PVTX* data for the system H_2O-CO_2±"salt" for various salinities. The studies shown are limited to those that report volumetric *PVTX* data, and the reader is referred to Schlarin (1996), Valyashko (2008) and Springer et al. (2012) for additional compilations of phase equilibrium data for this system. Data shown on Figure 2 are also listed in Table 1.

Table 1. Experimental *PVTX* studies of the system H_2O–CO_2 ± salt at CCS *PT* conditions (modified from Valyashko et al. 2008).

Components	Composition		Temperature (°C)	Pressure (bar)	Refs.
	CO_2	NaCl			
$H_2O + CO_2$	0-50 wt%		100-500	1-590	[1]
$H_2O + CO_2$	6.53-87.9 mol%		100-200	2.08-33.5	[2]
$H_2O + CO_2$	50-98 mol%		50-225	2.7-103.4	[3]
$H_2O + CO_2$	0.29-1.45 mol%		79.7-198	20.4-102.1	[4]
$H_2O + CO_2$	0.15-0.18 *m*		25-432	10-350	[5]
$H_2O + CO_2$	21-94 mol%		142-427	60-350	[6]
$H_2O + CO_2$	50-98 mol%		50-225	2.7-103.4	[7]
$H_2O + CO_2$	90 mol%		175-225	3.7-90	[8]
$H_2O + CO_2$ + NaCl	0.31-1.8 mol%	0.5–2 *m*	172-334	15.7-86.1	[9]
$H_2O + CO_2$ + NaCl	0-100 mol%	6–10 wt%	135-520	30-3000	[10]
$H_2O + CO_2$ + NaCl	0.29-1.66 *m*	1 wt%	80.1-200.5	21.1-100.3	[11]

References: [1] Khitarov and Malinin (1956); [2] Zawisza and Malesinska (1981); [3] Patel and Eubank (1988); [4] Nighswander et al. (1989); [5] Hnedkovsky et al. (1996); [6] Fenghour et al. (1996); [7] Patel el al. (1987); [8] Warowny and Eubank (1995); [9] Ellis & Golding (1963); [10] Gehrig et al. (1986); [11] Nighswander et al. (1989)

bars. Gehrig (1980) conducted experiments in the system H_2O-CO_2-NaCl to 550 °C and 3 kbar, mostly along the 6, 10 and 20 wt% NaCl pseudobinaries. Numerous experimental studies of *PVTX* properties of the system H_2O-CO_2-"salt" have been conducted in recent years using the synthetic fluid inclusion technique (Frantz et al. 1992; Kotelnikov and Kotelnikova 1990; Shmulovich and Graham 1999, 2004; Schmidt and Bodnar 2000), but most of these are at *PT* conditions outside of the range of interest for CCS. Figure 2 summarizes the range of *PT* conditions for which experimental *PTX* data are available for the H_2O-CO_2±"salt" system at CCS conditions.

A summary of phase equilibria for the ternary system H_2O-CO_2-NaCl at CCS conditions is shown on Figure 3. The lower left corner of the ternary shows phase equilibria relevant to the water (brine)-rich phase in the formation, and the lower right corner shows phase equilibria relevant to the CO_2-rich phase in the formation. These two single-phase regions are separated by a large field in which an H_2O + salt-rich phase coexists with a CO_2 ± H_2O-rich phase. Note that a large field in which aqueous liquid + CO_2-rich vapor + halite coexist lies adjacent to all of the above-mentioned fields. This is especially relevant to the interface between the CO_2-rich vapor and the brine in the formation, as the "evaporation" of H_2O from the brine into the CO_2 phase may lead to desiccation of the brine and cause halite precipitation. This, in turn, would affect the permeability of the formation and could hinder the continued diffusion of CO_2 away from the interface and into the brine phase, thus inhibiting the eventual development of a system in which solubility trapping dominates.

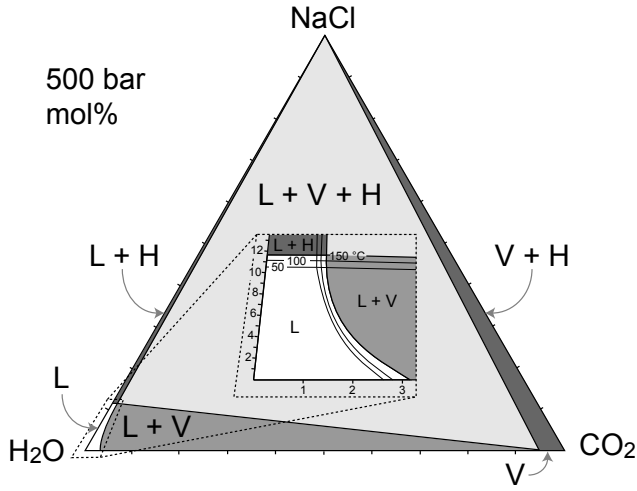

Figure 3. Ternary diagram for the system H_2O-CO_2-NaCl at 150 °C and 500 bars showing the phase fields in which liquid, vapor and halite are stable. The inset shows an enlargement of the H_2O-rich corner that is relevant to the brine phase in the formation, along with the 100 and 50 °C phase boundaries showing the reduction in the size of the liquid stability field with decreasing temperature. Phase relations are based on Rogers and Pitzer (1982), Duan and Sun (2003), and Spycher and Pruess (2005, 2010).

Models and EOS to estimate the *PVTX* properties of H_2O-CO_2-"salt" at CCS conditions

Various theoretical and empirical models have been developed over the years to predict the *PVTX* properties of H_2O-CO_2-"salt" over the range of *PTX* conditions relevant to CCS. The model of Spycher et al. (2003) predicts the mutual solubilities of H_2O and CO_2 and is based on data covering the temperature range from 12-110 °C that were assembled from a variety of sources including King et al. (1992), Teng et al. (1997), Bamberger et al. (2000) and others.

Data above 110 °C (e.g., some of the measurements of Takenouchi and Kennedy (1964) and Müller et al. (1988)) were not included in the analysis of Spycher et al. (2003).

Duan et al. (2008) developed an equation of state for CO_2-H_2O fluids with applications to the CO_2-rich phase (the "vapor" phase) in CO_2 storage environments. The model of Duan et al. (2008) is based on the earlier virial EOS of Duan et al. (1992a), with modified binary interaction parameters. Experimental data used to develop the model of Duan et al. (2008) include those of Wormald et al. (1986), Patel et al. (1987), Patel and Eubank (1988), Warowny and Eubank (1995), and Fenghour et al. (1996).

Spycher and Pruess (2005) presented a model for solubility of CO_2 in the H_2O-rich phase for the systems H_2O-CO_2-NaCl (up to 6 molal) and H_2O-CO_2-$CaCl_2$ (up to 4 molal). This model was based on previous work by these authors and their co-workers (Spycher et al. 2003) and expanded the earlier model of Spycher et al. (2003) to include the effects of salinity, using many of the same experimental data as used by Duan and Sun (2003), supplemented with additional more recent data of Kiepe et al. (2002) and Bando et al. (2003). Spycher and Pruess (2005) evaluated various studies that report activity coefficients for aqueous CO_2 in brine or provide experimental data from which activity coefficients can be calculated. Spycher and Pruess (2005) found that all of the activity coefficient formulations they evaluated predicted CO_2 solubilities in agreement with experimental and computed reference data up to 2 molal NaCl. The model of Duan and Sun (2003) best fit experimental data up to 4 molal NaCl, while the model of Rumpf et al. (1994) provided the best results from 4 to 6 molal NaCl. Likewise, the models of Duan and Sun (2003) and Rumpf et al. (1994) were found to be the most accurate when extended to $CaCl_2$ solutions having salinities ≤4 molal. Noting the paucity of data at pressures of ~100 bar and temperatures <100 °C, Spycher and Pruess (2005) were unable to predict with confidence which formulation was most accurate at these conditions; however they found that both approaches gave satisfactory results. Spycher and Pruess (2005) "tend to favor Duan and Sun (2003) because it was fitted over a wider *PT* range…," because their formulation allows non-iterative computations, and because it "is somewhat easier to implement." Spycher and Pruess (2010) extended their earlier model to higher temperatures (from 100 °C up to 300 °C). In this model, Spycher and Pruess (2010) refitted the activity coefficient model for $CO_{2(aq)}$ up to 300 °C. This revised activity coefficient model compares well with that of Duan and Sun (2003) but is simpler, having no pressure dependence and requiring fewer fitting parameters.

More recently, Akinfiev and Diamond (2010) presented a thermodynamic model for the system H_2O-CO_2-NaCl that is valid from –22-100 °C and from 1-1000 bars. This model also allows predictions of solid-liquid-vapor equilibria, which may be relevant in those cases in which halite saturation is reached.

Zerai et al. (2009) compared five solubility models for CO_2 in brine as well as output from the Geochemist's Workbench computer software (using f_{CO2} calculated from Duan and Sun 2003) to experimental data. Zerai et al. (2009) considered pressures ranging from 70-300 bar, temperatures from 30-127 °C, and salinities of 1-6 molal (however the authors modeled a wider region of *PT* space). Zerai et al. (2009) found that the model of Spycher and Pruess (2005) and that of Duan and Sun (2003) produced good fits to experimental data. The model of Enick and Klara (1990) and the Geochemist's Workbench likewise produced good results if f_{CO2} calculated from Duan and Sun (2003) was used as input. Similar to the conclusions reached by Spycher and Pruess (2005), Zerai et al. (2009) were unable to identify a "best" model due to the lack of experimental data for pressures greater than 100 bars and temperatures between 30 and 130 °C. Zerai et al. (2009) favor the model of Duan and Sun (2003), as it "provides a means to estimate CO_2 solubilities at conditions where experimental data are not available…." Zerai et al. (2009) note that the model of Spycher and Pruess (2005) provides similar results to the model of Duan and Sun (2003).

Thomas et al. (2012) used various combinations of thermodynamic sub-models to predict changes in pH, mineral dissolution, and solubility trapping associated with injection of CO_2 into a saline dolomitic-limestone aquifer. They found that pH and mineral dissolution/precipitation are not very sensitive to the choice of thermodynamic sub-models, but that solubility trapping is dependent on which sub-models are used. These workers do not recommend a preferred combination of sub-models that would produce the most accurate predictions. Gundogan et al. (2011) compared three numerical codes, PHREEQC, GEM and TOUGHREACT, for predicting brine-CO_2-rock reactions and found that differences in predicted values were related mostly to differences in the thermodynamic databases and activity models used in the different codes.

The model of Duan and Sun (2003) is the one most commonly used today to examine *PVTX* behavior of fluids associated with CCS. The model is based on a compilation of experimental data for CO_2 solubility in pure H_2O and saline brines (mostly NaCl solutions, the only exception being the study of Prutton and Savage (1945) on the solubility of CO_2 in aqueous $CaCl_2$ solutions). Data for CO_2 solubility in pure H_2O were drawn from several sources, the most extensive being the studies of Tödheide and Franck (1963) and Takenouchi and Kennedy (1964). Experimental data for CO_2 solubility in NaCl solutions were also taken from several previous studies, of which the most extensive were the studies of Takenouchi and Kennedy (1965) and Drummond (1981).

The equation of state of Duan et al. (2008) for the volumetric properties of H_2O-NaCl-CO_2 fluids is a theoretical-based model that does not include empirical parameters for the ternary system. Instead, the Duan et al. (2008) model combines the molar volume of H_2O with the apparent volumes of NaCl and CO_2. The apparent volume of NaCl is determined from the model of Rogers and Pitzer (1982). The apparent volume of CO_2 is based on an equation of state for the H_2O-CO_2 binary developed by Duan et al. (2008) and is described below.

To determine the *PVTX* properties of the CO_2-rich phase, we calculated the solubility of H_2O in CO_2 using the models of Spycher et al. (2003) for CO_2 in equilibrium with pure H_2O, and the models of Spycher and Pruess (2005, 2010) for CO_2 in equilibrium with chloride brines. The density of scCO_2 was represented by the equation of state (EOS) of Duan et al. (1992a). The densities of H_2O-bearing, CO_2-rich fluids were estimated using either the model of Duan et al. (1992b), or Duan et al. (2008).

PROTOCOL TO ESTIMATE FLUID PVTX PROPERTIES AT CCS CONDITIONS

Recently, Steele-MacInnis et al. (2013) examined the volumetric relationships of CO_2 storage in saline aquifers, and the methodology from that study is modified in the present study and is summarized below. Steele-MacInnis et al. (2013) estimated fluid volumetric properties using recently published equations of state (EOS) that have been rigorously tested at CCS *PVTX* conditions (Duan and Sun 2003; Hu et al. 2007). In the formulation used here, the density of scCO_2 is represented by a virial-type EOS (Duan et al. 1992a), and the solubility of CO_2 in water and brine is based on Pitzer's formalism (Pitzer 1973; Duan and Sun 2003). The density of the aqueous fluid is calculated from the apparent molar volumes of CO_2 (Duan et al. 2008) and NaCl (Rogers and Pitzer 1982) and the molar volume of H_2O (Hu et al. 2007).

Here, we compare the volume required to store CO_2 as a supercritical fluid (structural or stratigraphic trapping) with the volume required to store the same amount of CO_2 as a dissolved component in brine (solubility trapping). We selected initial amounts of brine and CO_2 such that all injected CO_2 could be dissolved to produce CO_2-saturated brine. Later, we added increments of calcite and as much additional CO_2 as can be dissolved by reaction with calcite. This approach allows comparison of volumetric changes for three end-member

scenarios—one in which all CO_2 is stored as a supercritical fluid, one in which all CO_2 is stored as a dissolved component in brine, and another in which additional CO_2 is dissolved by calcite dissolution. These results can then be employed to estimate CO_2 storage capacities in saline formations assuming these various modes of storage.

For reasons described above, we assume that the storage horizon in saline formations is between 1.0-4.5 km depth, with a temperature of 50-140 °C, and a pressure before injection of 100-750 bars. In the following sections, the volumetric changes accompanying 1) CO_2 injection (physical trapping), 2) dissolution in brine, and 3) reaction with calcite, are described at discrete times following injection. The motivation for presenting results at discrete stages is to differentiate the volumetric contributions of each mechanism. We recognize that during and after injection, several trapping mechanisms may contribute to the overall storage capacity simultaneously, and that the dominant mechanism will change with time as the system evolves (Benson and Cole 2008) (Fig. 1). However, as a first approximation it is reasonable to separate the various processes based on the different time scales at which each is dominant. Physical (stratigraphic/structural/capillary) trapping dominates in the first years to decades following injection, dissolution of CO_2 into brine (solubility trapping) becomes significant over centuries, and mineral reactions do not begin to contribute significantly until centuries to millennia after injection (Benson and Cole 2008) (Fig. 1).

In addition to the trapping mechanisms, volume estimates as well as the long-term behavior of the formation, are dependent on whether the system is open or closed (Zhou et al. 2008). We consider both open and closed system scenarios in our evaluation, although we note that volume requirements are relatively insensitive to whether the system is open or closed as described below. The volumetric requirements for open vs. closed systems are shown schematically in Figure 4.

Let us consider the evolution of total fluid volume (brine ± CO_2) during and after CO_2 injection. In this discussion, the thermodynamic system is comprised of brine plus injected CO_2. Prior to injection of CO_2, the system consists only of brine and the system volume is equal to the mass of brine multiplied by the brine specific volume (Fig. 1, time t_0). In a closed system scenario, the mass of brine initially present in the system is unchanged during and after CO_2 injection, and the system volume will increase as CO_2 is added, whereas in an open system scenario some amount of brine will be displaced to accommodate the injected CO_2. Thus, in the closed system scenario we calculate the change in system volume after injection, and in the open system case we calculate the amount of brine displaced. Note that we ignore the small change in volume associated with compression of the pore and pore fluid associated with pressure increase during CO_2 injection. These small volume changes, referred to in the CCS literature as "storage efficiency," are generally on the order of 1-5 % of the original pore volume (USGS 2013).

Immediately following injection of CO_2 the system consists of brine and supercritical CO_2, and the system volume equals the initial volume of brine plus the volume of injected $scCO_2$ (Fig. 1, time t_1). The increase in system volume when CO_2 is injected into an H_2O- or H_2O-NaCl-filled formation is compared to the initial system volume before injection and is computed as

$$\%\ \text{volume change} = \frac{\overline{V}_{CO_2} m_{CO_2}}{\overline{V}_{H_2O\text{-}NaCl}\left(m_{NaCl} + \dfrac{1000\,\text{g/kg}}{M_{H_2O}}\right)} \times 100\% \qquad (1)$$

where $\overline{V}_{CO_2}$ and $\overline{V}_{H_2O\text{-}NaCl}$ are the molar volumes of the CO_2 phase and the aqueous phase, respectively (cm^3/mol), m_{CO_2} and m_{NaCl} are the CO_2 solubility and brine salinity, respectively (mol/kg H_2O), and M_{H_2O} is the molar mass of H_2O (g/mol). The numerator of Equation (1) ($\overline{V}_{CO_2} m_{CO_2}$)

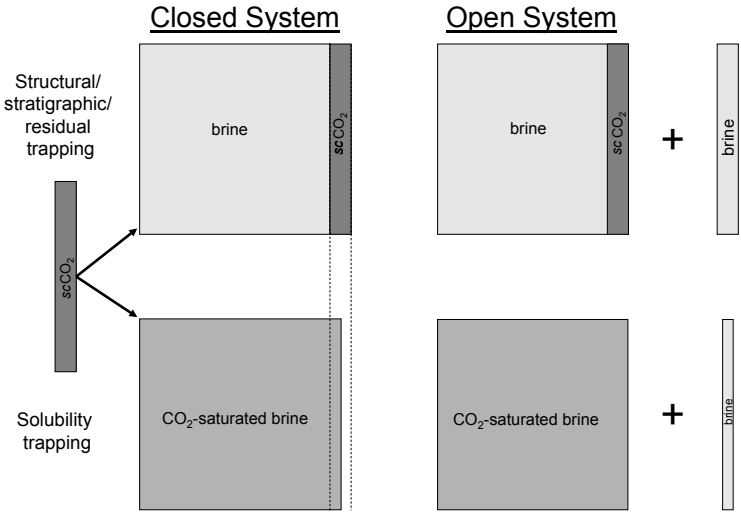

Figure 4. Comparison of the relative volume requirements for storage of $scCO_2$ through structural/stratigraphic/residual trapping and by solubility trapping, for both open and closed systems. The box on the left labeled $scCO_2$ represents the volume of CO_2 injected into the formation. For structural/stratigraphic/residual trapping either the volume of the formation must increase by an amount equal to the volume of the injected CO_2 (closed system) or a volume of brine equal to the amount of injected CO_2 must be displaced (open system). For solubility trapping, the volume occupied by the CO_2-saturated brine in the closed system (bottom left panel) is larger than the volume occupied by the brine in the formation before injection, but less than the volume of brine + $scCO_2$ in the closed system. In the open system scenario, brine still must be displaced to provide space for the CO_2-saturated brine, but the volume of brine that must be displaced is less than that required to store an equal amount of CO_2 via structural/stratigraphic/residual trapping. The amounts of brine that must be displaced for various storage scenarios are plotted as a function of formation *PT* conditions on Figure 5.

represents the volume of injected CO_2 per kg of H_2O, with CO_2 occurring as $scCO_2$. The denominator of Equation (1) represents the volume of brine in the system per kg of H_2O. The result is a dimensionless quantity based on the mass of H_2O being conserved, i.e. a closed system scenario. Thus, Equation (1) assumes a constant mass of H_2O in the system during and after CO_2 injection, representing the pre-existing brine in the pore space. This is because the total mass of H_2O in the system is constant in a closed system, whereas the total amount (number of moles) of fluid in the system is not constant (it increases, as CO_2 is injected).

In an open system scenario, injection of CO_2 causes displacement or removal of some brine from the system, rather than increasing the system volume. In this case, Equation (1) must be modified to account for the amount of brine that is displaced from the reservoir. The volume of displaced brine is equal to the volume of injected $scCO_2$, and the proportion of brine volume displaced is expressed as

$$\%\ \text{brine displaced} = \frac{\overline{V}_{CO_2} m_{CO_2}}{V_{H_2O}\left(m_{NaCl} + \dfrac{1000\,\text{g/kg}}{M_{H_2O}} \right) + \overline{V}_{CO_2} m_{CO_2}} \times 100\% \qquad (2)$$

Equation (2) represents the proportion of brine that must be displaced in order for the system volume to remain constant if an amount of $scCO_2$ equal to the amount that can be dissolved into the brine is injected into the formation.

The CO_2 phase and CO_2-free aqueous brine are not in chemical equilibrium immediately following injection. With time some CO_2 dissolves into the aqueous phase and some H_2O dissolves into the $scCO_2$ phase. The volume change for a closed system scenario as the system evolves from CO_2-free brine to CO_2-saturated brine is calculated as

$$\%\ \text{volume change} = \left[\frac{\overline{V}_{\text{H}_2\text{O-NaCl}} \left(m_{\text{NaCl}} + \dfrac{1000\,\text{g/kg}}{M_{\text{H}_2\text{O}}} \right)}{\dfrac{\overline{V}_{\text{H}_2\text{O-NaCl-CO}_2}}{X_{\text{H}_2\text{O}} M_{\text{H}_2\text{O}}} \times 1000\,\text{g/kg}} - 1 \right] \times 100\% \tag{3}$$

where $\overline{V}_{\text{H}_2\text{O-NaCl-CO}_2}$ is the molar volume of the CO_2-saturated aqueous phase (cm^3/mol) and $X_{\text{H}_2\text{O}}$ is the mole fraction of H_2O in the aqueous phase. This equation represents the difference in volume between a system consisting of free (initial) brine + $scCO_2$, and a system in which all of the CO_2 is dissolved in the brine while conserving the mass of H_2O in the system. Equation (3) neglects volume changes associated with dissolution of H_2O into the CO_2. Note that Equation (3) above is the corrected version of the incorrect Equation (2) from Steele-MacInnis et al. (2013). In the previously published version, the term "−1" was omitted.

In the open system scenario, injection of CO_2 will displace some brine from the system, and thus the amount of brine available for dissolution of CO_2 into brine will be reduced by the amount that is displaced. Assuming that the system volume remains constant during and after injection, the amount of brine (proportion of original brine volume) that will be displaced by injected CO_2 is expressed as

$$\%\ \text{brine displaced} = \left[1 - \frac{\overline{V}_{\text{H}_2\text{O-NaCl}} \left(m_{\text{NaCl}} + \dfrac{1000\,\text{g/kg}}{M_{\text{H}_2\text{O}}} \right)}{\dfrac{\overline{V}_{\text{H}_2\text{O-NaCl-CO}_2}}{X_{\text{H}_2\text{O}} M_{\text{H}_2\text{O}}} \times 1000\,\text{g/kg}} \right] \times 100\% \tag{4}$$

Figure 5 compares the volume requirements for both open and closed systems, and for structural/stratigraphic and for solubility trapping. For a given brine salinity and *PT* condition, the percent volume change associated with CO_2 injection into a closed system and the percent brine displaced in an open system scenario are similar. This reflects the fact that the major difference in volume requirements for closed and open system conditions is that in a closed system CO_2 will dissolve into all the brine that was initially in the reservoir before injection, whereas in an open system some of that brine must be removed and is thus not available to dissolve CO_2. However, because the solubility of CO_2 in brine is generally low at CCS *PT* conditions, removal of a few percent of the brine has little effect on the total amount of CO_2 that can be dissolved, and thus has little effect on the volume requirements.

The storage mechanism that is expected to dominate centuries to millennia after injection is mineral trapping. Reaction of injected CO_2 with calcite promotes dissolution of additional CO_2, according to the reaction

$$CO_{2(v)} + H_2O_{(l)} + CaCO_{3(s)} = Ca^{2+}{}_{(aq)} + 2HCO_3^-{}_{(aq)} \tag{5}$$

The change in volume of the aqueous phase resulting from calcite dissolution is estimated assuming the apparent molar volume of calcium bicarbonate in solution is similar to that of calcium chloride (Oakes et al. 1995). The solubility of calcite (and resulting enhanced CO_2 solubility) was calculated by extrapolating temperature functions (Plummer and Busenberg 1982) for the relevant equilibrium constants over the *PT* range of the model. The resulting volume change is expressed as

$$\%\ \text{volume change} = \frac{S_{cal} V_{Ca(HCO_3)_2(aq)}}{V_{CO_2\text{-saturated solution}} + S_{cal} V_{Ca(HCO_3)_2(aq)}} \times 100\% \quad (6)$$

where $V_{Ca(HCO_3)_2(aq)}$ is the apparent molar volume of dissolved calcium and bicarbonate ions and S_{cal} is the solubility of calcite (mol/kg H_2O).

Our model considers the system H_2O-NaCl-CO_2-$CaCO_3$, whereas natural saline brines contain other salts, and injected CO_2 may contain other gaseous species. Lack of experimental data over the complete *PT* range of interest limits our ability to quantitatively model effects of other components. However, available data suggest that the overall trends in solubility and volumetric properties are reasonably approximated by the H_2O-NaCl-CO_2-$CaCO_3$ system. For example, Dilmore et al. (2008) conducted CO_2 solubility experiments in natural connate brines from the Oriskany formation (eastern USA) at 22 °C and at 75 °C and from 100 to 400 bars and compared the experimental results with the CO_2 solubility predicted by the model used here. The Oriskany brine contains about 214,000 ppm (21.4 wt%) total dissolved solids, with ~4.8 wt% Na^+ and ~2.5 wt% Ca^{2+}. Review of a subset of results from data presented in Figure 1 from Dilmore et al. (2008) shows measured values to be within ~6.5% of calculated values. Additional experimental data on CO_2 solubility in real brines (R. Dilmore, unpub. data) suggest that the majority of the observed difference can be accounted for by experimental error, and that more meticulous data collection is likely to bring experimental results into closer agreement with predictions from Duan and Sun (2003).

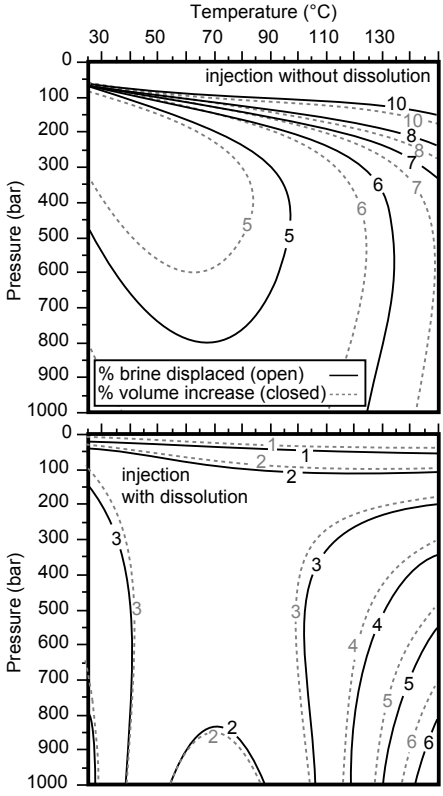

Figure 5. Comparison of the vol% of brine (10 wt% NaCl) displaced in an open-system scenario, and the volume increase to accommodate injected CO_2 for a closed-system scenario, for both structural/stratigraphic/residual trapping (top) and for solubility trapping (bottom). Calculated from Rogers and Pitzer (1982), Duan and Sun (2003), Hu et al. (2007) and Duan et al. (2008).

PVTX PROPERTIES OF H_2O-CO_2-"SALT" AT CCS CONDITIONS

Immediately following injection into the saline formation, CO_2 will be present as a pure, supercritical CO_2 ($scCO_2$) phase (Fig. 1; t_1) and the volume change of the system (saline formation + injected CO_2) may be estimated from the density of $scCO_2$ at formation *PT* conditions. The density of $scCO_2$ estimated from the EOS of (Duan et al. 1992a) is shown in Figure 6. With time, some amount of H_2O that was originally present in the formation will dissolve into the $scCO_2$ phase to produce an H_2O-saturated CO_2 phase. Figure 7 shows the solubility of H_2O in the CO_2-rich phase as a function of pressure and temperature for the case in which the coexisting H_2O-rich phase is either pure H_2O (solid lines) or a brine containing 25 wt% NaCl (dashed lines). The H_2O solubilities in the CO_2-rich

phase shown in Figure 7 were calculated using the models of Spycher et al. (2003) and Spycher and Pruess (2005, 2010). We note that the models of Spycher et al. (2003) and Spycher and Pruess (2005, 2010) are valid to 600 bars, but we have used these models to 1000 bars, and the models appear to give reasonable results at these higher pressures. The solubility of H_2O in the CO_2-rich fluid increases with increasing temperature, reaching maximum values of ~5 mol% at 150 °C. At pressures <200 bar, the solubility of H_2O in CO_2 increases with increasing pressure. However, at higher pressures (>200 bar) the solubility of H_2O in CO_2 is nearly independent of pressure to at least 1000 bar (Fig. 7). The transition from the lower pressure regime in which H_2O solubility increases with increasing pressure, to the higher pressure region in which H_2O solubility is relatively insensitive to pressure, roughly corresponds to the transition from a CO_2-rich fluid with a "vapor-like" density (i.e., a density less than the critical density of ~0.464 g/cm^3), to a "liquid-like" CO_2-rich phase with density greater than the critical density (for a complete discussion of this phenomenon, the reader is referred to (Diamond 2003).

At the *PT* conditions relevant to CCS in saline formations, the solubility of NaCl in the CO_2-rich phase is extremely low, and it is reasonable to approximate the CO_2-rich phase as a binary H_2O-CO_2 fluid (Hu et al. 2007). However, the partitioning of H_2O into the CO_2-rich phase depends on the salinity of the H_2O-rich phase. Specifically, the apparent solubility of H_2O in the CO_2-rich phase is lower in the presence of saline brine compared to the solubility in pure H_2O because addition of NaCl to the aqueous fluid reduces the activity of H_2O in the aqueous phase and this, in turn, affects the partitioning behavior.

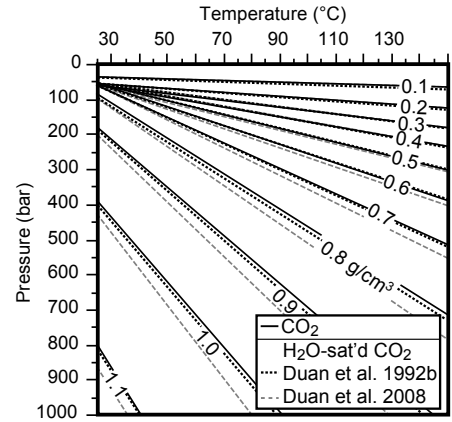

Figure 6. Density (in g/cm^3) of pure CO_2 and H_2O-saturated CO_2 as a function of temperature and pressure at CCS conditions calculated using the models of Duan et al. (1992a,b, 2008).

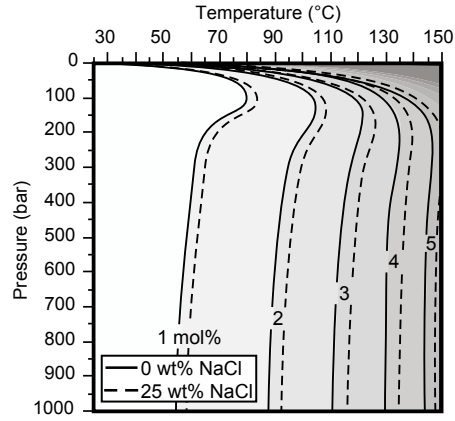

Figure 7. H_2O solubility (in mol%) in CO_2 at CCS *PT* conditions. The dashed line represents the H_2O content of H_2O-saturated CO_2 in equilibrium with a CO_2-saturated, 25 wt% NaCl aqueous solution. Solubilities were calculated using the model of Spycher et al. (2003) and Spycher and Pruess (2005, 2010).

Dissolution of H_2O into the CO_2-rich fluid ($scCO_2$) generally results in small, positive excess volumes of mixing at *PT* conditions relevant to CO_2 storage in saline formations (Capobianco et al. 2013 and unpublished data). Stated differently, the volume occupied by H_2O-saturated, CO_2-rich fluid is greater than the volume occupied by the same mass of H_2O and $scCO_2$ coexisting as pure, separate phases. This means that, following injection, as H_2O gradually dissolves into the $scCO_2$ phase the volume of the system will increase or, if the formation is unable to accommodate the volume increase, the pressure will increase.

Few experimental data are available for the volumetric properties of H_2O-bearing, CO_2-rich fluids. As a result of the dearth of experimental data, existing numerical models show significant variability in the predicted excess volumes for H_2O-saturated CO_2 above ~200 bar. For example, Duan et al. (1992a) developed an equation of state for H_2O-CO_2 mixtures that included segmented temperature functions for the binary interaction parameters. Duan et al. (2008) found that the earlier model of Duan et al. (1992b) did not provide a good fit to the experimental *PVT* data for CO_2-rich fluids, and, therefore, Duan et al. (2008) developed a new set of continuous temperature functions for the binary interaction parameters. Figure 8 shows a comparison of the predicted excess volumes of H_2O-saturated CO_2-rich fluid, based on the binary interaction parameters from Duan et al. (2008) (left) and Duan et al. (1992b) (right). Both models yield excess volumes that show significant anomalies (discontinuities) that are likely artifacts of the fitting and extrapolation beyond the range of experimental data. More importantly, the calculated excess volumes differ substantially between the two models. The model of Duan et al. (1992b) suggests excess volumes close to zero throughout most of the *PT* range relevant to CO_2 storage in saline formations, whereas the model of Duan et al. (2008) predicts positive excess volumes of ~0.5 to 2.5 cm^3/mol over the same *PT* range. Also shown on Figure 8 are high-precision vibrating-tube densimeter data at 150 °C from Capobianco et al. (2013 and unpublished data). These newer measurements are in much better agreement with the model of Duan et al. (1992b), compared to that of Duan et al. (2008). We are unaware of any experimental data at *PT* conditions above ~300 bar and <150 °C, and this represents a significant knowledge gap in terms of assessing the long-term behavior of CCS in saline formations. As such, the data shown on Figure 8 are largely unconstrained by experiments over much of the range of *PT* conditions shown.

Figure 6 shows the densities of CO_2 (solid lines) and H_2O-saturated CO_2 (dashed lines) as functions of pressure and temperature. As noted above, data for molar volumes of H_2O-saturated CO_2 are limited and therefore the dashed contours should be regarded as approximate values at best. However, the data suggest that H_2O-saturated CO_2 is slightly less dense (more buoyant) than "dry" CO_2, and will preferentially fill space at the top of formation. This, in turn, may lead to interaction between the H_2O-saturated CO_2 phase and the minerals in the overlying caprock (c.f., Rother et al. 2012). We note that recent experimental data (Capobianco

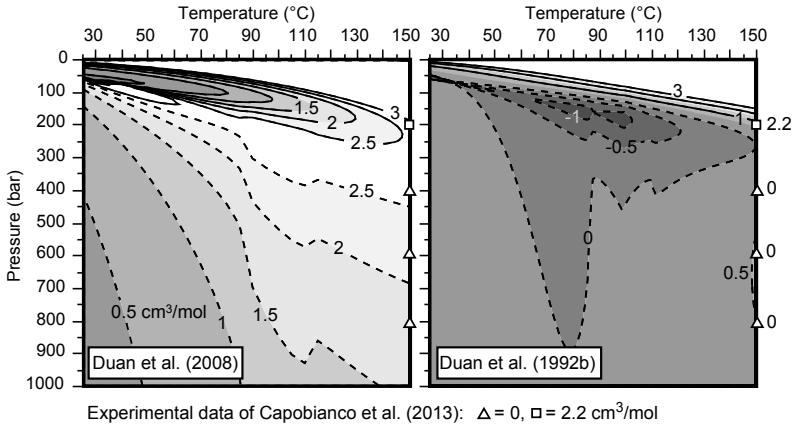

Figure 8. Excess volume of H_2O (in cm^3/mole) in H_2O-saturated CO_2 as a function of temperature and pressure calculated from equations of Duan et al. (2008) and Duan et al. (1992a, b). Also shown on the right ordinate are excess volume at 150 °C at various pressures determined experimentally by Capobianco et al. (2013 and unpublished data).

et al. 2013, and unpublished data) suggest that H_2O-saturated CO_2 may not be less dense than dry CO_2, and additional work is required to reconcile this discrepancy.

Following injection of scCO_2 into the formation, the H_2O-saturated CO_2 phase will develop relatively quickly, with the actual time a function of turbulence of flow during injection, the permeability of the formation, relative permeability of the phases, etc. (Bradshaw et al. 2007). With increasing time following injection, the CO_2 phase will dissolve into the brine in the formation. The rate of dissolution is controlled by the CO_2 phase/brine contact area within the pore space, as well as by the rate of diffusion of CO_2 through the brine and away from the interface. Figure 9 shows the solubility of CO_2 in the aqueous phase, for pure H_2O and for saline solutions with 5, 10, 15, 20 and 25 wt% NaCl. The highest solubility of CO_2 occurs in the lower salinity aqueous phase, and CO_2 solubility decreases with increasing salinity according to the familiar "salting-out" effect that results from the reduction in the activity (chemical potential) of H_2O upon addition of electrolytes. Stated differently, addition of electrolytes results in clustering of H_2O molecules around dissolved ions, and concomitant reduction in the availability of H_2O molecules to dissolve non-polar species (Diamond 2003). Inspection of Figure 9 also reveals that the solubility of CO_2 in the aqueous phase decreases with increasing temperature up to ~80 °C, and then increases with increasing temperature above ~80 °C (at $P >$ 200 bar). In addition, the solubility of CO_2 increases monotonically with increasing pressure.

Figure 10 shows the densities of H_2O and CO_2-saturated H_2O (top left), and of CO_2-free and CO_2-saturated 25 wt% NaCl solution (bottom left). Also shown on Figure 10 (right) are the differences between the densities of CO_2-free and CO_2-saturated H_2O and brine. Dissolution of CO_2 into H_2O and into brine results in a small, negative excess volume of mixing at the *PT* conditions of CO_2 storage in saline formations (Fig. 11) (Capobianco et al. 2013 and unpublished data), coupled with an increase in the mean molar mass of the solution. Thus, the density of CO_2-saturated aqueous fluids is greater than the density of the CO_2-free end-members, and CO_2-saturated fluids will be negatively buoyant in the reservoir. This effect is significantly greater for lower salinity aqueous solutions, mainly owing to the greater solubility of CO_2 in low salinity fluids compared to brines. One result of the increase in density is that as CO_2 dissolves into the formation waters the CO_2-bearing solution will tend to sink, thus promoting mixing and accelerating the dissolution process within the formation. The effect of density-enhanced diffusion associated with dissolution of CO_2 into the brine is discussed by Ennis-King and Paterson (2005, 2007) and Pau et al. (2010).

CO_2-rock reactions

Predicting the effect of a sudden increase of CO_2 pressure on aquifer mineralogy is challenging because of complicated brine chemistry, uncertain thermodynamic data, and poorly known reaction rates. These factors limit our knowledge to rather broad generalizations based on significant simplifications. This discussion is predicated on the assumptions that compared to mineral reaction rates, the rate of transfer of CO_2 from the fluid phase into the aqueous phase is fast and that equilibration among aqueous species is locally effectively instantaneous. The relatively high brine temperatures along with complicated and variable chemistry (Collins 1975) makes detailed solution speciation modeling difficult. This problem combined with differences among the thermodynamic data bases used to model the final equilibrium state results in significant differences in the predicted amount of trapped CO_2 (Dethlefsen et al. 2012). As noted above, Gundogan et al. (2011) compared three numerical codes, PHREEQC, GEM and TOUGHREACT, for predicting brine-CO_2-rock reactions and found that differences in predicted values were related mostly to differences in the thermodynamic databases and activity models used in the different codes.

Although the rate equations compiled by (Palandri and Kharaka 2004) and revised by (Marini 2007) are a valuable first step toward summarizing the existing dissolution rate data,

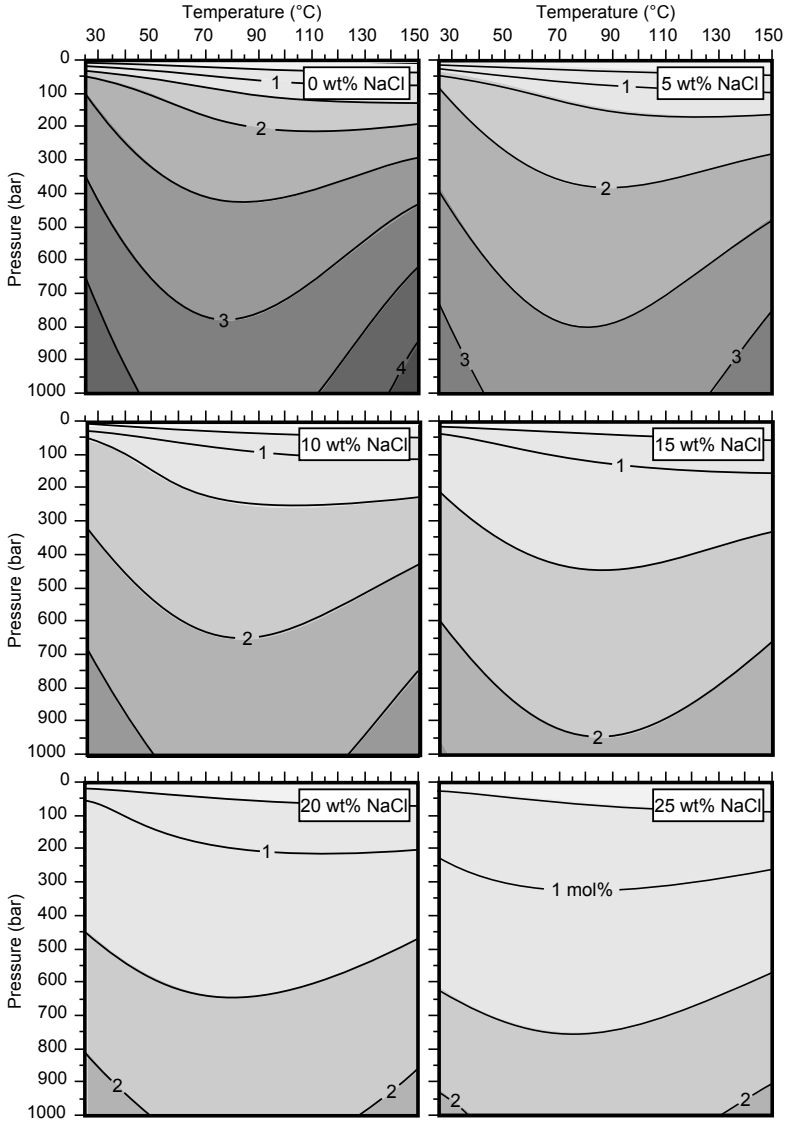

Figure 9. CO_2 solubility in aqueous solutions (in mol%) at CCS *PT* conditions calculated using the models of Duan and Sun (2003).

they are not based on systematic reviews of all of the existing data (Rimstidt et al. 2012) so these rate data must be viewed with caution. Finally, there are few data for the mineral precipitation rates so models of the rates of mineral trapping rely mostly on speculative estimates. These issues no doubt account for the significant variability among the published models of CO_2–rock interactions summarized in Table 1 in Balashov et al. (2013). For example, predictions of the amounts of CO_2 that will eventually be incorporated into the rock range from ~17 to ~90 kg/m^3. In spite of these problems, a few useful generalizations emerge from the existing data and models.

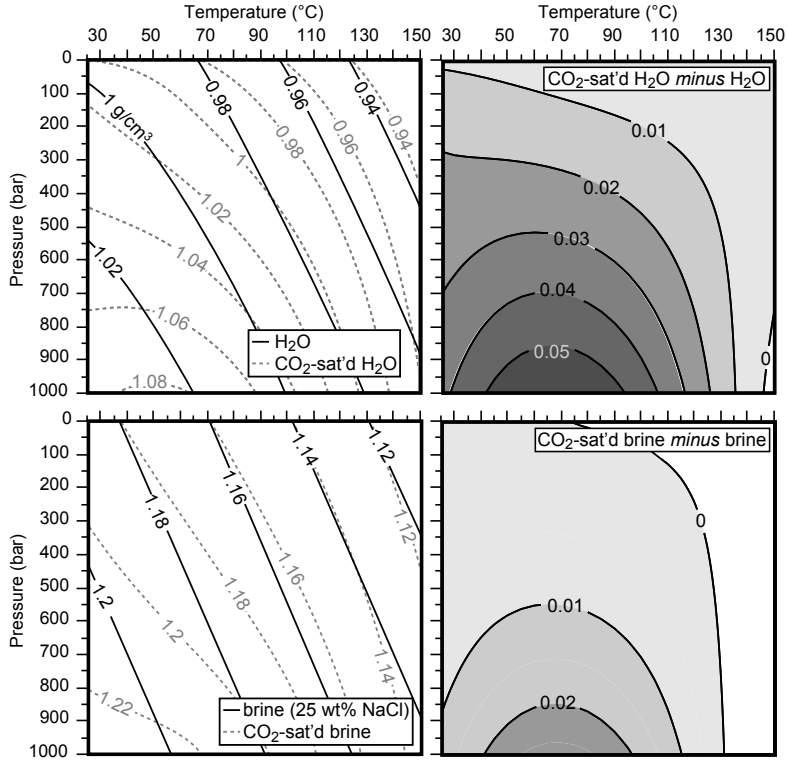

Figure 10. Density of pure H_2O and brine (in g/cm^3) containing 25 wt% NaCl compared to the densities of these same solutions at CO_2 saturation (left panels). The right panels show the difference in density between the CO_2-saturated aqueous phase and the CO_2-free aqueous phase, indicating the negative buoyancy of the CO_2-saturated brine compared to the CO_2-free brine. Calculated from Rogers and Pitzer (1982), Duan and Sun (2003), Hu et al. (2007) and Duan et al. (2008).

The models generally agree that for the first few years to decades after the injection of $scCO_2$ into a saline aquifer the main process is structural or stratigraphic trapping. Solubility trapping becomes important on the time scale of centuries to millennia. During this time some carbonate minerals will dissolve due to the lowered pH associated with CO_2 dissolution. The total amount dissolved, however, will be small, producing a negligible effect on volumes (Steele-MacInnis et al. 2013). On the time scale of centuries to millennia, dissolution of silicate minerals consumes hydrogen ions converting carbonic acid to bicarbonate and carbonate ions, according to:

$$H_2CO_3 = H^+ + HCO_3^-$$

$$HCO_3^- = H^+ + CO_3^{2-}$$

In addition, the dissolution of silicate minerals will release Ca^{2+}, Mg^{2+}, Fe^{2+}, and Al^{3+} into solution where they may react with carbonate ions to form carbonate minerals (mineral trapping). This mineral trapping process may affect the fluid volumes but it occurs on the time scale of centuries to millennia, which means that it will be a post-closure phenomenon. Although attainment of a final equilibrium state appears to require tens of millennia, most of the reactions will be nearly complete after a few thousands of years. For example, the reactive

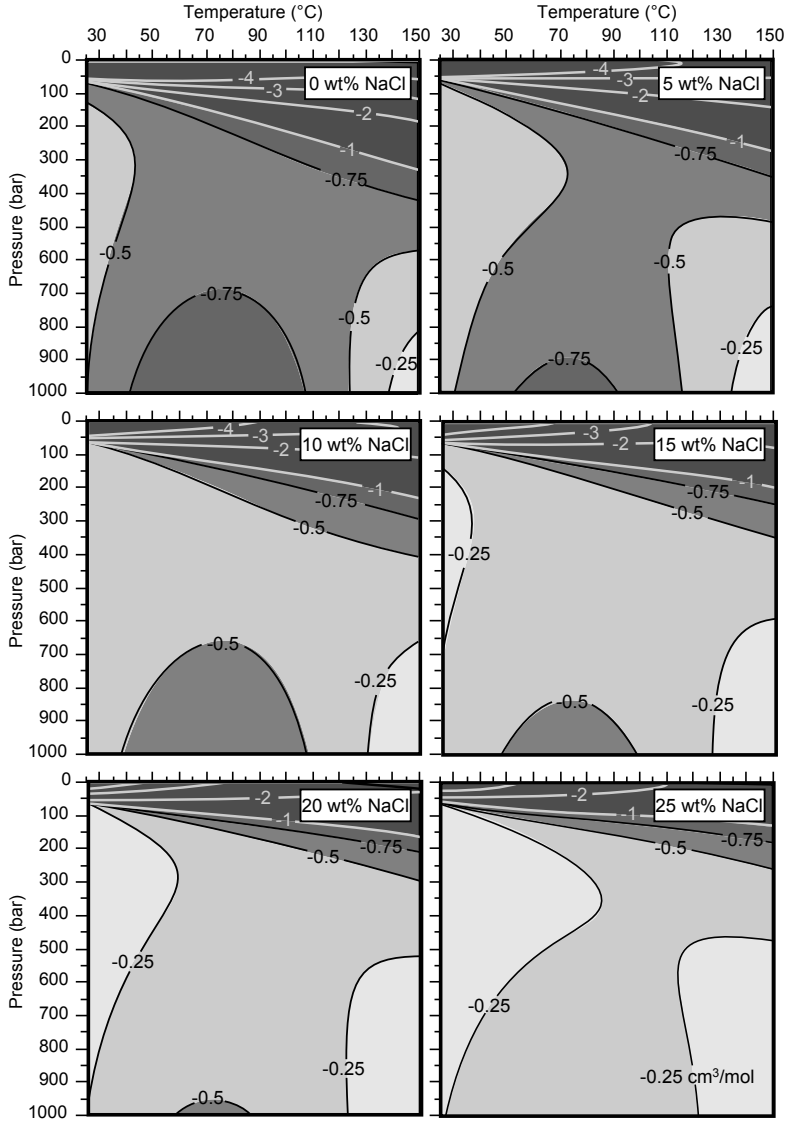

Figure 11. Excess volumes (in cm^3/mole) for CO_2 in the CO_2-saturated aqueous phase calculated as described in the text. Calculated from Rogers and Pitzer (1982), Duan and Sun (2003), Hu et al. (2007) and Duan et al. (2008).

transport model results from Balashov et al. (2013) show mineral dissolution/precipitation effects resulting from injection of $scCO_2$ into a sandstone aquifer are predicted to reach equilibrium at ~25,000 years (Fig. 12). The results suggest that although solubility and mineral trapping will have a positive effect on the sequestration security they will do little to alleviate the volumetric expansion caused by the CO_2 injection.

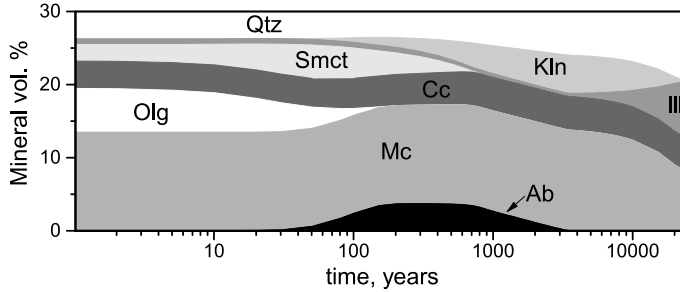

Figure 12. Mineralogy changes over time predicted for a sandstone aquifer after injection injecting $scCO_2$ at time zero. Modified from Balashov et al. (2013).

EFFECT OF TRAPPING MECHANISM ON STORAGE VOLUMES

Using the available *PVTX* data described above, we may estimate the relative volumes required for CO_2 storage under the various scenarios shown in Figure 1. At the *PT* conditions of CO_2 storage in saline formations, the density of CO_2 ranges from about 0.4-0.8 g/cm^3 (Fig. 6). At the same conditions, the solubility of CO_2 ranges from about 2 to ~4 mol% in H_2O and decreases systematically with increasing salinity to <2 mol% in a 25 wt% NaCl solution (Fig. 9). Figure 5 compares the storage volume required for storage of $scCO_2$ and dissolved CO_2 in both open and closed systems. As the volume requirements for open and closed systems are nearly equal, the discussion below is limited to closed systems.

When an amount of CO_2 equal to the amount required to saturate the aqueous phase (i.e., the amount of CO_2 that could be stored as a dissolved component in the brine) is injected, its volume is between 75-140 cm^3 per kg of water, or 50-70 cm^3 per kg of brine. During injection and before any of the CO_2 has dissolved in the brine, the volume of the system (brine + CO_2) increases by approximately 7.3-10% for pure H_2O (Fig. 13) and the volume percent increase decreases with increasing salinity to about 3-5% for a 25 wt% NaCl solution (Fig. 13). The larger volume increase for H_2O compared to brines reflects the higher solubility of CO_2 in pure H_2O compared to its solubility in brine at the same *PT* conditions. One result of this decreased solubility is that more brine, or a larger saline formation volume, is required to eventually store the same amount of CO_2 as a dissolved component, as described below.

The maximum amount of CO_2 that can be dissolved in the brine is limited by the CO_2 solubility at the formation *PT* conditions (Fig. 9). The apparent volume of dissolved CO_2 at saturation is between 40-80 cm^3 per kg of water, and this value decreases to about 25-55 cm^3 per kg as the salinity increases. Moreover, the volume occupied by the CO_2-saturated aqueous phase is greater than the volume of brine in the formation before injection (Fig. 1). This occurs in spite of the fact that the excess volumes are negative, and the volume increases because mass is being added to the system, i.e., the formation contains more fluid. Within the *PT* range considered here, the volume of the CO_2-saturated aqueous phase is greater than the volume of the original brine phase by about 3.5-8% if the pore fluid is pure H_2O (Fig. 14), and the increase in volume decreases with increasing salinity to about 1-2% for a 25 wt% NaCl solution (Fig. 14).

Owing to the low solubility of calcite, dissolution of calcite increases the volume of the aqueous phase by only 0.01-0.04%. Thus, the contribution of calcite dissolution to the net volume change is insignificant compared to the contributions of supercritical CO_2 or dissolved CO_2.

The volume changes described above for CO_2 storage as $scCO_2$ (Fig. 13) and as a dissolved component in the brine (Fig. 14) are compared to the initial brine volume in the

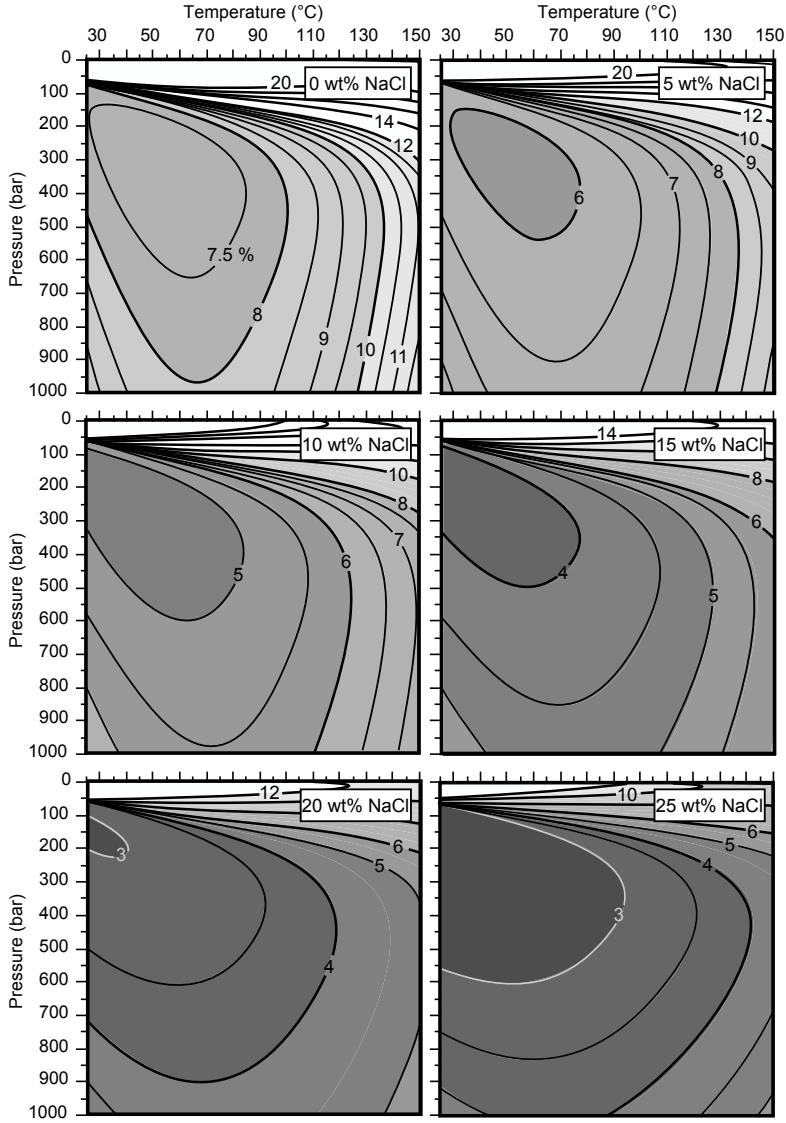

Figure 13. Increase in formation volume (in %) required for structural or stratigraphic trapping of an amount of CO_2 equal to the amount required to saturate the brine. Thus, the panels show the volume of brine + $scCO_2$ (scenario t_1; Fig. 1) minus the volume of brine in the formation before injection (scenario t_0; Fig. 1). Calculated from Rogers and Pitzer (1982), Duan and Sun (2003), Hu et al. (2007) and Duan et al. (2008).

formation before CO_2 injection. We also compared the volume change as the $scCO_2$ phase dissolves into the brine (Fig. 1). As shown by the reduced area of the CO_2-saturated brine box (right side) compared to the combined area of brine and CO_2 (middle boxes), dissolution of CO_2 into brine reduces the net fluid volume compared to the sum of the volumes of brine and CO_2 immediately following injection. *Stated differently, less formation volume is required to store CO_2 as a dissolved component in the brine compared to storage as a separate $scCO_2$*

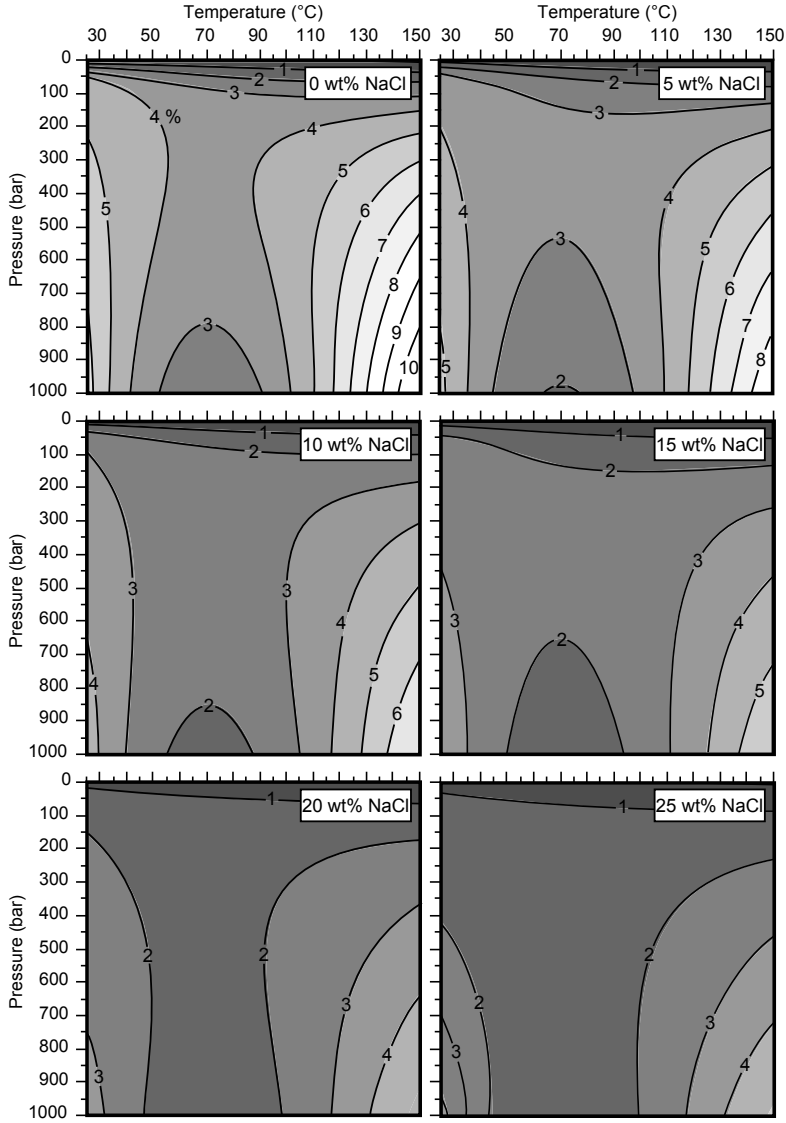

Figure 14. Increase in formation volume (in %) required for solubility trapping of CO_2 compared to the volume of brine before injection. Thus, the panels show the volume of brine + dissolved CO_2 (scenario t_2; Fig. 1) minus the volume of brine in the formation before injection (scenario t_0; Fig. 1). Calculated from Rogers and Pitzer (1982), Duan and Sun (2003), Hu et al. (2007) and Duan et al. (2008).

phase. Throughout most of the *PT* region of CO_2 storage, the apparent volume of dissolved CO_2 is about one half of the volume of the same mass of $scCO_2$ (Fig. 15). Therefore, the volume required for solubility trapping is 45-65% less than the volume required for structural/stratigraphic trapping of the same amount of CO_2, independent of whether the pore fluid is H_2O or brine. In other words, although the volume required to store injected CO_2 is greater than the initial brine volume regardless of whether the CO_2 is dissolved or is present as a separate

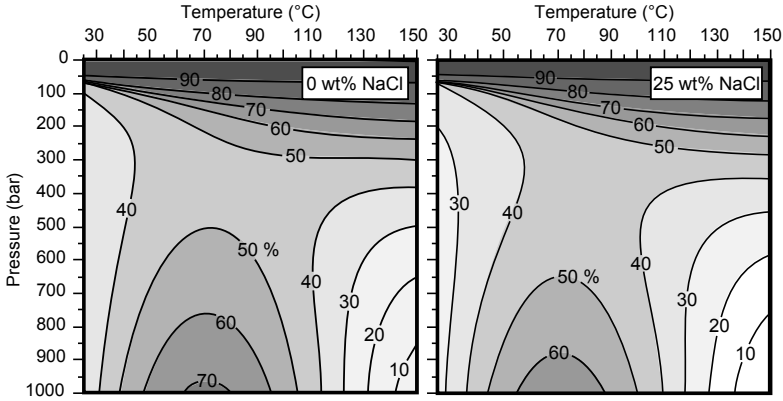

Figure 15. Formation volume (in %) required for solubility trapping of CO_2 compared to the volume of required to store the same amount of $scCO_2$ through structural or stratigraphic trapping. Results are shown as percent increase in storage volume for trapping as $scCO_2$ (shown in Fig. 9), minus the percent increase in formation volume for solubility trapping of CO_2 (Fig. 10). Calculated from Rogers and Pitzer (1982), Duan and Sun (2003), Hu et al. (2007) and Duan et al. (2008).

supercritical fluid, solubility trapping of CO_2 requires only ~50% of the volume required for structural or stratigraphic trapping of the same mass of CO_2. For example, at 60 °C and 250 bar, a CO_2-saturated solution has a composition of ~1.3 molal. At these same conditions, the amount of CO_2 required to saturate 1 kg of H_2O (1006 cm^3) has a volume of about 72 cm^3. Before mixing, the total volume H_2O (l) + $scCO_2$ is 1006 + 72 = 1078 cm^3. After mixing (all of the $scCO_2$ has dissolved), the total volume of the $H_2O + CO_{2(aq)}$ phase is (1000 g +1.3 mol × 44 g/mol) / 1.01 g/cm^3 (from Fig. 10) ≈1047 cm^3. Thus, the volume increase associated with solubility trapping (~41 cm^3) is ~45% less than the volume increase for trapping of $scCO_2$ (72 cm^3). This observation, in turn, has significant implications concerning storage capacity estimates for CCS in saline formations.

Relationship between storage mechanism and storage security

Previous studies (c.f., Lu et al. 2009) have emphasized that dissolution of CO_2 increases the density of the brine, and the CO_2-saturated brine becomes negatively buoyant compared to CO_2-free brine (Fig. 10). Thus, CO_2-saturated brine will sink in the reservoir, enhancing storage security. Based on volumetric modeling that documents that solubility trapping requires only ~50% of the volume required to store the same amount of CO_2 via structural or stratigraphic trapping, this mechanism has the additional advantage of enhancing storage capacity (Fig. 15).

The rate of CO_2 dissolution into the brine following injection depends on the contact area between the CO_2 and brine phases, as well as how quickly aqueous CO_2 diffuses away from the CO_2/brine interface and into the brine. Unassisted, the contribution of solubility trapping becomes significant only after centuries (Fig. 1) (IPCC 2005; Benson and Cole 2008). Some workers have suggested various approaches to accelerate the dissolution of CO_2 into brine, with the aim of enhancing storage security (Leonenko and Keith 2008; Buscheck et al. 2011). Our results suggest that such procedures will also enhance storage capacity.

Applications to estimating required formation volumes

An important consideration when assessing CO_2 storage in saline formations is related to whether the system behaves as an open or closed system. Zhou et al. (2008) define an open system as one in which the brine that is displaced by injected CO_2 can migrate laterally to provide the "space" to accommodate the CO_2, with minimal pressure increase. Zhou et

al. (2008) further describe a closed system as one in which the saline formation is overlain and underlain by completely impermeable units, with faults or other discontinuities inhibiting lateral flow. A semi-closed system is one in which the overlying/underlying units are slightly permeable. In closed and semi-closed systems pressure buildup associated with CO_2 injection and concomitant damage to the formation are likely to limit the storage capacity and security, whereas in open systems storage capacity and injection rates are limited by the ability of the brine to migrate laterally away from the injection well. We also note that closed-system behavior is not believed to be appropriate for the majority of geologic storage targets, and certainly not for the major targets being considered for large-scale sequestration.

PVTX data presented here may be used to estimate storage volume requirements for a given amount of CO_2. For example, according to the U.S. Environmental Protection Agency, 2,221 M metric tons (2.221×10^{12} kg) of CO_2 was emitted from coal-fired plants in the U.S. in 2011. To sequester this amount of CO_2 as a separate CO_2 phase in the subsurface requires a volume of ~2.33 km^3 (assuming a CO_2 density of 0.8 g/cm^3). In an open or semi-closed system, this same volume of brine would have to be displaced, ignoring the small change in formation volume associated with pressure buildup during and following injection. To put this into perspective, this volume of brine is about the same as the annual discharge of the Thames River at London, U.K. (= 65.8 m^3/sec, or 2.07 km^3/yr). For comparison, annual withdrawals of groundwater in the United States are roughly 35-40× larger than this volume of CO_2 emissions.

The Scherer coal-fired power plant in Juliette, Georgia, U.S.A. is the single largest stationary source of CO_2 in the United States, emitting approximately 2.5×10^{10} kg of CO_2 annually. If all of the CO_2 produced in one year is captured and injected into the subsurface as $scCO_2$ it would occupy a volume of 26.3×10^7 m^3 (or 0.0263 km^3), assuming an average CO_2 density of 0.8 g/cm^3. If the CO_2 is dissolved into the brine, approximately 5×10^{11} kg of brine would be required to dissolve all of the CO_2 generated by the Scherer plant in one year, and this CO_2-saturated brine would have a volume of ~0.53 km^3. Szulczewski (2009) have evaluated saline formations in the U.S. and estimate an average thickness of ~1,000 m and an average porosity of ~20% (see also Goodman et al. 2013). Thus, assuming that the formation is 1,000 m thick and has an average porosity of 20%, the formation area required would be ~2.7 km^2. The Scherer plant has been in operation since 1982 and, assuming that it has generated the same amount of CO_2 emissions each year of operation, it would have generated $\sim 7.5 \times 10^{11}$ kg of CO_2 during its operating lifetime. Using the same assumptions as before, storing all of the CO_2 generated by the Scherer plant during the past 30 years as a dissolved component in saline formations would require ~15.9 km^3 of brine and the formation footprint would occupy ~80 km^2. For this reason, most scenarios consider the storage of the bulk of the CO_2 phase as a supercritical fluid, which would require accessing a much smaller formation volume than dissolved CO_2. Although some of this CO_2 would ultimately dissolve into the formation, natural analogs suggest that much would remain as a discrete supercritical phase for long periods of time (Gilfillan et al. 2009). Although these volumes of CO_2 are large, the rates and volumes of CO_2 emissions from a typical power plant are comparable to rates and volumes of fluids produced from large oil and gas reservoirs. Further, various options are being explored to use active reservoir management to address any issues associated with displaced fluid volumes (e.g., Elliot et al. 2013).

According to the U.S. Department of Energy 2012 Carbon Utilization and Storage Atlas (DOE, 2012), deep saline formations in the United States represent a prospective storage resource that is estimated to be in the range 2,100-20,000 billion metric tonnes of CO_2. These estimates of storage resource are not intended to represent all pore space that would ultimately be used for storing CO_2, which will be a function of a range of additional factors including regulatory and economic considerations as well as site-specific factors on the integrity of a storage reservoir. If one were to consider storing CO_2 in all of this prospective pore space,

it would, indeed, represent a large volume of impacted formation (on the order of 10^{15} m^3). However, at realistic deployment scales with CO_2 sequestration as part of a broader portfolio of options, the volumes of CO_2 stored are likely to be a small fraction of the prospective storage resource.

An additional consideration that is related to the volumetrics of CO_2 storage in saline formations ties to rates of injection into the reservoir. Ghaderi et al. (2009) note that most studies of reservoir performance consider an injection rate of 1 Mt/year. However, the Scherer coal-fired plant generates 25 Mt/year of CO_2, or 25× the amount generally considered for performance assessment. Ghaderi et al. (2009) note that the reservoir storage capacity is limited by ability to inject large amounts of CO_2 without exceeding the fracture pressure of the formation. One approach to minimize pressure-buildup during injection is to extract an equal amount of brine from the reservoir. Hassanzadeh et al. (2009) propose a method involving extraction of brine followed by re-injecting the brine on top of the CO_2 plume. These workers note that in simulations without brine injection only about 8% of the CO_2 is dissolved into the brine after 200 years, whereas 50% of the injected CO_2 dissolves within 200 years if brine is reinjected on top of the CO_2. These workers further note that solubility trapping increases storage security and we add, based on results presented here, that the required storage volume is also decreased. As a modification of the process described by Hassanzadeh et al. (2009), we propose that CO_2 could be mixed with the extracted brine at the surface, i.e., at the source, and then the CO_2-saturated brine could be reinjected into the formation. This would achieve 100% solubility trapping instantaneously, rather than the 50% that would be achieved in 200 years according to the Hassanzadeh et al. (2009) model. We note, however, that the increased cost associated with brine extraction and reinjection has not been adequately addressed to our knowledge.

Even if an adequate volume of formation is available for storage, there are engineering challenges associated with injecting large volumes of CO_2 into a reservoir at reasonable rates without damaging the formation. As mentioned above, injection pressure in excess of 0.6 × lithostatic pressure may fracture the formation (Hubbert and Willis 1957; Bredehoeft et al. 1976). The pressure required to induce flow in a well at a given rate will vary according to the hydrologic properties of the target formation, including but not limited to, formation permeability, depth, and thickness; the compressibility, density, and relative permeability of the H_2O and CO_2-rich phases; and mineral compressibility (Ehlig-Economides and Economides 2010; Michael et al. 2010; Szulczewski 2009; Zhou and Birkholzer 2011) and references therein. An injection project may require multiple wells and/or horizontally dispersed injection, such as at In Salah (Algeria), where three wells (each with up to 1500 m horizontally dispersed injection) were required to inject 3500 t/day (Michael et al. 2010). Ehlig-Economides and Economides (2010) estimate that a power plant that produces three million metric tons of CO_2 per year for 30 years (a rate ~2.3× greater than is in being injected at In Salah) would require between 2 and 1155 injection wells depending on the properties of the formation and the lateral extent of the CO_2 plume. However, this model assumes a closed system, and Zhou and Birkholzer (2011) show that closed systems with a large lateral extent behave like open systems on the timescale of injection projects. Consequently, Zhou and Birkholzer (2011) conclude that the model of Ehlig-Economides and Economides (2010) may significantly overestimate the number of injection wells that are needed. The engineering experience needed to inject fluids at this scale is already well established in the oil and gas industry; although much of this experience ties to injection of water, significant experience on injection of CO_2 at scale exists within the enhanced-oil recovery industry.

To date the largest CO_2 sequestration project injecting into a single well is the Sleipner (Norway) project, which injects about 1 Mt/year (Michael et al. 2010). From this we can make a rough estimate that the Scherer plant, which produces ~25 Mt/year, would require ~25

injection wells if the target aquifer had similar hydrologic properties and the wells were spaced widely enough that they do not significantly interfere with each other. The Sleipner site has a relatively high permeability (5000 mD, or about 1000× that of In Salah; Michael et al. 2010) so this may be an idealized case. However, technologies such as the horizontally dispersed injection employed at In Salah may serve to reduce the number of wells needed even in low-permeability formations.

To put the pore volumes and storage capacities discussed above into perspective, Zhou and Birkholzer (2011) compared the pore volume needed to store annual energy-related CO_2 emissions (assuming a CO_2 density of 0.7 g/cm^3) with other "geological fluid volumes." These workers show that the pore volume required to store the world CO_2 emissions generated in 2005 is 9.8× larger than the volume of oil produced that same year. For the United States, the pore volume required is slightly less, at ~7× the volume of crude oil consumption. However, the volume of fresh groundwater extracted in the U.S. was ~20× larger than the storage volume required for all of the CO_2 generated by stationary sources.

Kramer (2012) summarized effects of injecting large amounts of CO_2 into the subsurface, including potential seismic activity. Kramer (2012) quotes Rachel Cleetus of the Union of Concerned Scientists, who states that "seismicity pales in comparison to cost as an impediment to the adoption of CCS." Thus, the volumetric and technical issues associated with CCS, as significant as they are, may not be the limiting factor for its implementation. Costs associated with implementation of CCS may be minimized by minimizing the volume required for storage, and results presented here contribute to understanding the appropriate conditions and protocols to minimize storage volumes.

GAPS IN KNOWLEDGE AND UNDERSTANDING

Our ability to accurately model the behavior of saline formations following CO_2 injection and to better constrain storage capacities and long-term storage security requires reliable experimental data and equations of state (EOS) for the *PVTX* properties of gas-bearing aqueous solutions over the complete range of CCS conditions. As noted above, even for the simple system H_2O-CO_2-NaCl, *PVTX* data are lacking above ~300 bars for temperatures <150 °C (Fig. 2), a range that includes most of the *PT* environment considered to be favorable for CO_2 storage in saline formations. Additionally, data are essentially nonexistent for more complex electrolyte-bearing aqueous solutions, with only a few data available for the system H_2O-NaCl-$CaCl_2$. Similarly, experimental data for mixed-gas systems at CCS conditions are sparse. Hu et al. (2007) note that "There are only a few data sets for the ternary liquids, and they are inconsistent with each other, where only a couple of data sets can be used to test a predictive density model for CO_2 sequestration." We also note that excess volumes in H_2O-rich compositions are slightly negative at 150 °C and 200-800 bars, whereas a single data point at 100 °C and 200 bars obtained by vibrating tube densimetry suggests a positive excess volume (Capobianco et al. 2013 and unpublished data), highlighting the need for additional experiments in this *PTX* range.

CONCLUDING STATEMENT

Results of a rigorous evaluation of the volumetric requirements for CO_2 storage in saline formations shows that the volume needed to store a given amount of CO_2 via solubility trapping is reduced by ~45-65% compared to the volume required for trapping of scCO_2. Solubility trapping further enhances storage security. However, our ability to predict formation behavior and better constrain storage capacities is limited by the lack of experimental data to develop numerical models.

ACKNOWLEDGMENTS

The authors thank Nick Spycher, Ariel Chialvo and Alex Navrotsky for comments on an earlier draft of this manuscript that have led to significant improvements. This research effort was partially performed in support of the National Energy Technology Laboratory under Contract DE-FE-0004000, and through funding from the National Science Foundation to RJB under grant EAR-1019770.

Disclaimer: *"This report was prepared as an account of work sponsored by an agency of the United States Government. Neither the United States Government nor any agency thereof, nor any of their employees, makes any warranty, express or implied, or assumes any legal liability or responsibility for the accuracy, completeness, or usefulness of any information, apparatus, product, or process disclosed, or represents that its use would not infringe privately owned rights. Reference herein to any specific commercial product, process, or service by trade name, trademark, manufacturer, or otherwise does not necessarily constitute or imply its endorsement, recommendation, or favoring by the United States Government or any agency thereof. The views and opinions of authors expressed herein do not necessarily state or reflect those of the United States Government or any agency thereof."*

REFERENCES

Akinfiev NN, Diamond LW (2010) Thermodynamic model of aqueous CO_2-H_2O-NaCl solutions from 22 to 100 degrees C and from 0.1 to 100 MPa. Fluid Phase Equilib 295:104-124

Altunin W, Gadetskii OG (1971)Equation of state and thermodynamic properties of liquid and gaseous carbon dioxide. Teploenergetika 18:120-125

Ananthaswamy J, Atkinson G (1985)Thermodynamics of concentrated electrolyte mixtures 5. A review of the thermodynamic properties of aqueous calcium chloride in the temperature range 273.15 K-373.15 K. J Chem Eng Data 30:120-128

Anderko A, Pitzer KS (1993) Equation-of-state representation of phase equilibria and volumetric properties of the system NaCl-H_2O above 573 K. Geochim Cosmochim Acta 57:1657-1680

Angus S, Armstrong B, de Reuck KM, Altunin VV, Gadestskii OG, Chapela GA, Rowlinson JS (1976) Carbon Dioxide, International Thermodynamic Tables of the Fluid State. Pergamon, p 37-47

Apelblat A, Korin E (2002) The vapour pressure of water over saturated solutions of sodium sulfate, calcium bromide, ferric chloride, zinc nitrate, calcium nitrate, and lithium nitrate at temperatures from 278.15 K to 323.15 K. J Chem Thermodyn 34:1621-1637

Balashov VN, Guthrie GD, Hakala JA, Lopanto CL, Rimstidt JD, Brantley SL (2013) Predictive modeling of CO_2 sequestration in deep saline sandstone reservoirs: Impacts of geochemical kinetics. Appl Geochem 30:41-56

Bamberger A, Sieder G, Maurer G (2000) High-pressure (vapor + liquid) equilibrium in binary mixtures of (carbon dioxide + water or acetic acid) at temperatures from 313 to 353 K. J Supercrit Fluids 17:97-110

Bando S, Takemura F, Nishio M, Hihara E, Akai M (2003) Solubility of CO_2 in aqueous solutions of NaCl at (30 to 60) °C and (10 to 20) MPa. J Chem Eng Data 48:576-579

Benson SM, Cole DR (2008) CO_2 sequestration in deep sedimentary formations. Elements 4:325-331

Bodnar RJ (1985) Pressure-volume-temperature-composition (PVTX) properties of the system H_2O-NaCl at elevated temperatures and pressures. PhD Dissertation, Pennsylvania State University, State College, Pennsylvania

Bodnar RJ, Burnham CW, Sterner SM (1985) Synthetic fluid inclusions in natural quartz. III. Determination of phase equilibrium properties in the system H_2O-NaCl to 1000 °C and 1500 bars. Geochim Cosmochim Acta 49:1861-1873

Bottinga Y, Richet P (1981) High pressure and temperature equation of state and calculation of the thermodynamic properties of gaseous carbon dioxide. Am J Sci 281:615-60

Bradshaw J, Bachu S, Bonijoly D, Burruss RC, Holloway S, Christensen NJ Mathiassen OM (2007) CO_2 storage capacity estimation: Issues and development of standards. Int J Greenhouse Gas Control 1:62-68

Bredehoeft JD, Wolff RG, Keys WS, Shuter E (1976) Hydraulic fracturing to determine regional insitu stress field, Piceance Basin, Colorado. Geol Soc Am Bull 87:250-258

Burnham CW, Holloway JR, Davis NF (1969) Thermodynamic properties of water to 1,000 °C and 10,000 bars. Geological Society of America Special Paper 132

Buscheck TA, Sun Y, Hao Y, Wolery TJ, Bourcier W, Tompson AFB, Jones ED, Friedmann SJ, Aines RD (2011) Combining brine extraction, desalination, and residual-brine reinjection with CO_2 storage in saline formations: Implications for pressure management, capacity, and risk mitigation. Energy Procedia 4:4283-4290

Capobianco RM, Gruszkiewicz MS, Wesolowski DJ, Cole DR, Bodnar RJ (2013) Volumetric properties and fluid phase equilibria of CO_2 + H_2O. *In:* Proceedings, Thirty-Eighth Workshop on Geothermal Reservoir Engineering, Volume 38: Stanford University, Stanford, California, Paper #100

Collins AG (1975) Geochemistry of Oilfield Waters. Elsevier, Amsterdam

Dethlefsen F, Haase C, Evert M, Dahmke A (2012) Uncertainties of geochemical modeling during CO_2 sequestration applying batch equilibrium calculations. Environ Earth Sci 65:1105-1117

Diamond LW (2003) Introduction to gas-bearing, aqueous fluid inclusions. *In:* Fluid Inclusions. Analysis and Interpretation, Vol 32. Samson I, Anderson A, Marshall D (eds) Mineralogical Association of Canada, p 101-158

Dilmore RM, Allen DE, Jones JRM, Hedges SW, Soong Y (2008) Sequestration of dissolved CO_2 in the Oriskany formation. Environ Sci Technol 42:2760-2766

DOE (Department of Energy) (2012) Carbon Sequestration Atlas of the United States and Canada. 4th edition. *http://www.netl.doe.gov/technologies/carbon_seq/refshelf/atlasIV/*

Driesner T (2007) The system H_2O-NaCl. Part II: Correlations for molar volume, enthalpy, and isobaric heat capacity from 0 to 1000 °C, 1 to 5000 bar, and 0 to 1 X_{NaCl}. Geochim Cosmochim Acta 71:4902-4919

Driesner T, Heinrich CA (2007) The system H_2O-NaCl. Part I: Correlation formulae for phase relations in temperature-pressure-composition space from 0 to 1000 °C, 0 to 5000 bar, and 0 to 1 X_{NaCl}. Geochim Cosmochim Acta 71:4880-4901

Drummond JSE (1981) Boiling and Mixing of Hydrothermal Fluids: Chemical Effects on Mineral Precipitation. PhD dissertation, Pennsylvania State University, State College, Pennsylvania

Duan ZH, Sun R (2003) An improved model calculating CO_2 solubility in pure water and aqueous NaCl solutions from 273 to 533 K and from 0 to 2000 bar. Chem Geol 193:257-271

Duan Z, Møller N, Weare JH (1992a) An Equation of State for the CH_4-CO_2-H_2O System: I. Pure Systems from 0 to 1000 °C and 0 to 8000 bar. Geochimica et Cosmochimica Act 56:2605-2617

Duan Z, Møller N, Weare JH (1992b) An equation of state for the CH_4-CO_2-H_2O system: II. Mixtures from 50 to 1000 °C and 0 to 1000 bar. Geochim Cosmochim Acta 56:2619-2631

Duan Z, Hu JW, Li DD, Mao SD (2008) Densities of the CO_2-H_2O and CO_2-H_2O-NaCl systems up to 647 K and 100 MPa. Energy Fuels 22:1666-1674

Ehlig-Economides C, Economides MJ (2010) Sequestering carbon dioxide in a closed underground volume. J Petrol Sci Eng 70:118-125

Elliot, TR, Buscheck, TA, Celia, M (2013) Active CO_2 reservoir management for sustainable geothermal energy extraction and reduced leakage. Greenhouse Gases Sci Technol 3:50-65

Ellis AJ, Golding RM (1963) The solubility of carbon dioxide above 100 degrees C in water and in sodium chloride solutions. Am J Sci 261:47-60

Enick RM, Klara SM (1990) CO_2 Solubility in water and brine under reservoir conditions. Chem Eng Commun 90:23-33

Ennis-King J, Paterson L (2005) Role of convective mixing in the long-term storage of carbon dioxide in deep saline formations. SPE Journal 10:349-356

Ennis-King J, Paterson L (2007) Coupling of geochemical reactions and convective mixing in the long-term geological storage of carbon dioxide. Int J Greenhouse Gas Control 1:86-93

Fenghour A, Wakeham WA, Watson JTR (1996) Densities of (water + carbon dioxide) in the temperature range 415 K to 700 K and pressures up to 35 MPa. J Chem Thermodyn 28:433-446

Frantz JD, Popp RK, Hoering TC (1992) The compositional limits of fluid immiscibility in the system H_2O-NaCl-CO_2 as determined with the use of synthetic fluid inclusions in conjuction with mass-spectrometry. Chem Geol 98:237-255

Gehrig M (1980) Phasengleichgewichte und pVT-Daten ternärer Mischungen aus Wasser, Kohlendioxid und Natriumchlorid bis 3 kbar und 550 °C. PhD dissertation, University of Karlsruhe, Germany [in German]

Gehrig M, Lentz H, Franck EU (1986) The system water carbon-dioxide sodium-chloride to 773 K and 300 MPa. Ber Bunsen Ges Phys Chem 90:525-533

Ghaderi S, Keith DW, Leonenko Y (2009) Feasibility of injecting large volumes of CO_2 into aquifers. Energy Procedia 1:3113-3120

Gilfillan, SM, Sherwood Lollar, B, Holland, G, Blagburn, D, Stevens, S, Schoell, M, Cassidy, M, Ding, Z, Zhou, Z, Lacrampe-Couloume, G, Ballentine, CJ (2009) Solubility trapping in formation water as dominant CO_2 sink in natural gas fields. Nature 458:614-618

Goodman A, Bromhal G, Strazisar B, Rodosta T, Guthrie G (2013) Comparison of publicly available methods for development of geologic storage estimates for carbon dioxide in saline formations. NETL-TRS-1-2013, NETL Technical Report Series, U.S. Department of Energy, National Energy Technology Laboratory. Morgantown, WV.

Gundogan O, Mackay E, Todd A (2011) Comparison of numerical codes for geochemical modelling of CO_2 storage in target sandstone reservoirs. Chem Eng Res Design 89:1805-1816

Haar L, Gallagher JS, Kell GS (1984) NBS/NRC Steam Tables: Hemisphere Publishing Corp., Washington, D.C.

Haas JL Jr (1976a) Physical properties of the coexisting phases and thermochemical properties of the H_2O component in boiling NaCl solutions. U.S. Geological Survey Bulletin 1421-A

Haas JL Jr (1976b) Thermodynamic properties of the coexisting phases and thermochemical properties of the H_2O component in boiling NaCl solutions. U.S. Geological Survey Bulletin 1421-B

Han, WS, Lee, S-Y, Lu, C, McPherson, BJ (2010) Effects of permeability on CO_2 trapping mechanisms and buoyancy-driven CO_2 migration in saline formations. Water Resources Res 46:W07510

Han, WS, Kim, K-Y, Esser, RP, Park, E, McPherson, BJ (2011) Sensitivity study of simulation parameters controlling CO_2 trapping mechanisms in saline formations. Transp Porous Media 90:807-829

Hanor JS (1994) Origin of saline fluids in sedimentary basins. *In* Geofluids: Origin, Migration and Evolution of Fluids in Sedimentary Basins, Vol 78, Parnell J (ed) Geological Society of London, p. 151-174

Hassanzadeh H, Pooladi-Darvish M, Keith DW (2009) Accelerating CO_2 dissolution in saline aquifers for geological storage - Mechanistic and sensitivity studies Energy & Fuels 23:3328-3336

Hnedkovsky L, Wood RH, Majer V (1996) Volumes of aqueous solutions of CH_4, CO_2, H_2S, and NH_3 at temperatures from 298.15 K to 705 K and pressures to 35 MPa. J Chem Thermodyn 28:125-142

Holmes HF, Busey RH, Simonson JM, Mesmer RE (1994) $CaCl_{2(aq)}$ at elevated temperatures – Enthalpies of dilution, isopiestic molalities, and thermodynamic properties. J Chem Thermodyn 26:271-298

Hu JW, Duan,Z, Zhu C, Chou IM (2007) PVTx properties of the CO_2-H_2O and CO_2-H_2O-NaCl systems below 647 K: Assessment of experimental data and thermodynamic models. Chem Geol 238:249-267

Hubbert MK, Willis DG (1957) Mechanics of hydraulic fracturing. Transactions of A. I. M. E. 210:153-166

IPCC (Intergovernmental Panel on Climate Change) (2005) Chapter 5. Underground geological storage, *In* Metz B, Davidson O, de Coninck HC, Loos M, Meyer LA (eds) IPCC Special Report on Carbon Dioxide Capture and Storage. Cambridge University Press, p. 195-276

Khitarov NI, Malinin SD (1956) Eksperimentalnaya kharakteristika chasti sistemy H_2O-CO_2. Geokhimiya 3:18-27 [in Russian]

Kiepe J, Horstmann S, Fischer,K, Gmehling J (2002) Experimental determination and prediction of gas solubility data for CO_2 + H_2O mixtures containing NaCl or KCl at temperature between 313 and 393K and pressures up to 10 MPa. Ind Eng Chem Res 41:4393-4398

King MB, Mubarak A, Kim JD, Bott TR (1992) The mutual solubilities of water with supercritical and liquid carbon dioxide. J Supercrit Fluids 5:296-302

Kotelnikov AR, Kotelnikova ZA (1990) Experimental-study of phase state of the system H_2O-CO_2-NaCl by method of synthetic fluid inclusions in quartz. Geokhimiya 1992:526-537

Kramer D (2012) Scientists poke holes in carbon dioxide sequestration. Phys Today 65:22-24

Kumar A, Ozah R, Noh M, Pope GA, Bryant S, Sepehrnoori K, Lake LW (2005) Reservoir simulation of CO_2 storage in deep saline aquifers. SPE Journal 10:336-348

Leonenko Y, Keith DW (2008) Reservoir engineering to accelerate the dissolution of CO_2 stored in aquifers. Environ Sci Technol 42:2742-2747

Lu C, Han WS, Lee SY, McPherson BJ, Lichtner PC (2009) Effects of density and mutual solubility of a CO_2-brine system on CO_2 storage in geological formations: "Warm" vs. "cold" formations. Adv Water Resources 32:1685-1702

Marini L (2007) Geological Sequestration of Carbon Dioxide: Thermodynamics, Kinetics and Reaction Path Modeling. Developments in Geochemistry 11, Elsevier, Amsterdam

Michael K, Golab A, Shulakova,V, Ennis-King J, Allinson,G, Sharma S, Aiken T (2010) Geological storage of CO_2 in saline aquifers - A review of the experience from existing storage operations. Int J Greenhouse Gas Control 4:659-667

Müller G, Bender E, Maurer G (1988) Vapor liquid equilibrium in the ternary system ammonia-carbon dioxide-water at high water contents in the range 373 K to 473 K. Ber Bunsen Phys Chem 92:148-160

Nighswander JA, Kalogerakis N, Mehrotra AK (1989) Solubilities of carbon-dioxide in water and 1 wt% NaCl solution at pressures up to 10 MPa and temperatures from 80 °C to 200 °C. J Chem Eng Data 34:355-360

Nordbotten JM, Celia, MA, Bachu S (2005) Injection and storage of CO_2 in deep saline aquifers: Analytical solution for CO_2 plume evolution during injection. Transp Porous Media 58:339-360

Oakes CS, Simonson JM, Bodnar RJ (1995) Apparent molar volumes of aqueous calcium chloride to 250 °C, 400 bars, and from molalities of 0.242 to 6.150. J Solution Chem 24:897-916

Palandri JL, Kharaka YK (2004) A compilation of rate parameters of water-mineral interaction kinetics for application to geochemical modeling. U.S. Geological Survey Open-file Report 2004-1068

Patel MR, Eubank PT (1988) Experimental densities and derived thermodynamic properties for carbon dioxide-water mixtures. J Chem Eng Data 33:185-193

Patel MR, Holste JC, Hall KR, Eubank PT (1987) Thermophysical properties of gaseous carbon dioxide-water mixtures. Fluid Phase Equilib 36:279-299

Pau GSH, Bell JB, Pruess K, Almgren AS, Lijewski MJ, Zhang K (2010) High-resolution simulation and characterization of density-driven flow in CO_2 storage in saline aquifers. Adv Water Resources 33:443-455

Pitzer KS (1973) Thermodynamics of electrolytes: I. Theoretical basis and general equations. J Phys Chem 77:268–277

Plummer LN, Busenberg E (1982) The solubilities of calcite, aragonite and vaterite in CO_2-H_2O solutions between 0 and 90 °C, and an evaluation of the aqueous model for the system $CaCO_3$-CO_2-H_2O. Geochim Cosmochim Acta 46:1011-1040

Potter RWI, Brown DL (1977) The Volumetric properties of aqueous sodium chloride solutions from 0° to 500 °C at pressures up to 2000 bars based on a regression of available data in the literature. U.S. Geological Survey Bulletin1421-C

Potter RWI, Shaw DR, Haas JL Jr (1975) Annotated bibliography of studies on the density and other volumetric properties for major components in geothermal waters 1928-1974. U.S. Geological Survey Bulletin 1417

Prutton CF, Savage RL (1945) The solubility of carbon dioxide in calcium chloride-water solutions at 75, 100, 120 °C and high pressures. J Am Chem Soc 67:1550-1554

Rimstidt JD, Brantley SL, Olsen AA (2012) Systematic review of forsterite dissolution data. Geochim Cosmochim Acta 99:159-178

Rogers PSZ, Pitzer KS (1982) Volumetric properties of aqueous sodium-chloride solutions. J Phys Chem Ref Data 11:15-81

Rother G, Krukowski EG, Wallacher D, Grimm N, Bodnar RJ, Cole DR (2012) Pore size effects on the sorption of supercritical CO_2 in mesoporous CPG-10 silica. J Phys Chem C 116:917-922

Rumpf B, Nicolaisen H, Ocal,C, Maurer G (1994) Solubility of carbon dioxide in aqueous solutions of sodium chloride: Experimental results and correlation. J Solution Chem 23:431-448

Scharlin P (1996) Carbon Dioxide in Water and Aqueous Electrolyte Solutions. Solubility data Series 62. International Union of Pure and Applied Chemistry, Oxford University Press

Schmidt C, Bodnar RJ (2000) Synthetic fluid inclusions: XVI. PVTX properties in the system H_2O-NaCl-CO_2 at elevated temperatures, pressures, and salinities. Geochim Cosmochim Acta 64:3853-3869

Shmulovich KI, Graham CM (1999) An experimental study of phase equilibria in the system H_2O-CO_2-NaCl at 800 degrees C and 9 kbar. Contrib Mineral Petrol 136:247-257

Shmulovich KI, Graham CM (2004) An experimental study of phase equilibria in the systems H_2O-CO_2-$CaCl_2$ and H_2O-CO_2-NaCl at high pressures and temperatures (500-800 degrees C, 0.5-0.9 GPa): Geological and geophysical applications. Contrib Mineral Petrol 146:450-462

Span R, Wagner W (1996) A new equation of state for carbon dioxide covering the fluid region from the triple-point temperature to 1100 K at pressures up to 800 MPa. J Phys Chem Ref Data 25:1509-1596

Springer RD, Wang Z, Anderko A, Wang P, Felmy AR (2012) A thermodynamic model for predicting mineral reactivity in supercritical carbon dioxide: I. Phase behavior of carbon dioxide-water-chloride salt systems across the H_2O-rich to the CO_2-rich regions. Chem Geol 322-323:151-171

Spycher N, Pruess K (2005) CO_2-H_2O mixtures in the geological sequestration of CO_2 II. Partitioning in chloride brines at 12-100 degrees C and up to 600 bar. Geochim Cosmochim Acta 69:3309-3320

Spycher N, Pruess K (2010) A phase-partitioning model for CO_2-brine mixtures at elevated temperatures and pressures: Application to CO_2-enhanced geothermal systems. Transp Porous Media 82:173-196

Spycher N, Pruess K, Ennis-King J (2003) CO_2-H_2O mixtures in the geological sequestration of CO_2. I. Assessment and calculation of mutual solubilities from 12 to 100 degrees C and up to 600 bar. Geochim Cosmochim Acta 67:3015-3031

Steele-MacInnis M, Capobianco RM, Dilmore R, Goodman A, Guthrie Jr G, Rimstidt JD, Bodnar RJ (2013) Volumetrics of CO_2 storage in deep saline formations. Environ Sci Technol 47:79-86

Sterner SM, Bodnar RJ (1991) Synthetic fluid inclusions: X. Experimental determination of P-V-T-X properties in the CO_2-H_2O system to 6 kb and 700 degrees C. Am J Sci 291:1-54

Szulczewski ML (2009) Storage Capacity and Injection Rate Estimates for CO_2 Sequestration in Deep Saline Aquifers in the Conterminous United States. MS Thesis, Massachusetts Institute of Technology, Cambridge.

Szulczewski ML, MacMinn CW, Herzog HJ, Juanes R (2009) Lifetime of carbon capture and storage as a climate-change mitigation technology. Proc Natl Acad Sci 109:1-5. doi: 10.1073/pnas.1115347109

Takenouchi S, Kennedy GC (1964) The binary system H_2O-CO_2 at high temperatures and pressures. Am J Sci 262:1055-1074

Takenouchi S, Kennedy GC (1965) The solubility of carbon dioxide in NaCl solutions at high temperatures and pressures. Am J Sci 263:445-454

Teng H, Yamasaki A, Chun MK, Lee H (1997) Solubility of liquid CO_2 in water at temperatures from 278 K to 293 K and pressures from 6.44 MPa to 29.49 MPa and densities of the corresponding aqueous solutions. J Chem Thermodyn 29:1301-1310

Thomas MW, Stewart M, Trotz M, Cunningham JA (2012) Geochemical modeling of CO_2 sequestration in deep, saline, dolomitic-limestone aquifers: Critical evaluation of thermodynamic sub-models. Chem Geol 306:29-39

Tödheide K, Franck EU (1963) Das Zweiphasengebiet und die kritische Kurve im System Kohlenoxid-Wasser bis zu Drucken von 3500 bar. Z Phys Chem Neue Folge 37:387-401 [in German]

USGS (2013) National assessment of geologic carbon dioxide storage resources – Summary. USGS Fact Sheet 2013-3020.

Valyashko VM (2008) Phase equilibria in binary and ternary hydrothermal systems: *In:* Hydrothermal Eexperimental Data. Valyashko VM (ed) John Wiley & Sons, Ltd., Chichester, UK, p 1-133

Wagner W, Pruß A (2002) The IAPWS formulation 1995 for the thermodynamic properties of ordinary water substance for general and scientific use. J Phys Chem Ref Data 31:387-535

Warowny W, Eubank PT (1995) Generalized equations of the Burnett P-V-T methods for adsorbing gases. Fluid Phase Equilib 103:77-95

Wormald C, Lancaster NM, Sellars AJ (1986) The excess molar enthalpies of $\{xH_2O + (1-x)CO\}_{(g)}$ and $\{xH_2O + (1-x)CO_2\}_{(g)}$ at high temperatures and pressures. J Chem Thermodyn 18:135-147

Zawisza A, Malesinska B (1981) Solubility of carbon dioxide in liquid water and of water in gaseous carbon dioxide in the range 0.2-5 MPa and at temperatures up to 473 K. J Chem Eng Data 26:388-391

Zerai B, Saylor BZ, Allen DE (2009) Quantification of CO_2 trapping and storage capacity in the subsurface: Uncertainty due to solubility models. *In:* Carbon Sequestration and its Role in the Global Carbon Cycle, Volume 183. McPherson BJ, Sundquist ET (eds) Washington, D.C., American Geophysical Union, p 249-260

Zhou QL, Birkholzer JT (2011) On scale and magnitude of pressure build-up induced by large-scale geologic storage of CO_2. Greenhouse Gases Sci Technol 1:11-20

Zhou Q, Birkholzer JT, Tsang CF, Rutqvist J (2008) A method for quick assessment of CO_2 storage capacity in closed and semi-closed saline formations. Int J Greenhouse Gas Control 2:626-639

Reviews in Mineralogy & Geochemistry
Vol. 77 pp. 153-188, 2013
Copyright © Mineralogical Society of America

Experimental Perspectives of Mineral Dissolution and Precipitation due to Carbon Dioxide-Water-Rock Interactions

John Kaszuba
Department of Geology & Geophysics
& School of Energy Resources
Dept 3006, 1000 E. University Avenue
University of Wyoming
Laramie, Wyoming 82071, U.S.A.
John.Kaszuba@uwyo.edu

Bruce Yardley
School of Earth and Environment
University of Leeds
Leeds LS2 9JT, United Kingdom
B.W.D.Yardley@leeds.ac.uk

Muriel Andreani
Laboratoire de Géologie de Lyon
UMR 5276, ENS et Université Lyon 1
Bat. Géode - R6
2 rue Raphael Dubois
69622 Villeurbanne CEDEX, France
muriel.andreani@univ-lyon1.fr

INTRODUCTION

Interactions between CO_2 and H_2O fluids and the rocks that host them are of significance for Geological Carbon Storage (GCS) for several reasons. These interactions determine the amount of CO_2 that can be trapped in solution and in minerals. The petrophysical properties of reservoir and cap rocks, especially porosity and permeability, are also affected. Carbon storage in fluids and minerals, coupled with potential changes to the petrophysical properties of rocks, have a direct bearing on the long-term effectiveness of GCS.

Many potential reservoir rocks contain a range of minerals that may react at very different rates. In particular, carbonate minerals are widespread minor components of sedimentary rocks and react much more rapidly than silicates, while clay minerals are often much more reactive than minerals such as quartz or alkali feldspars. It follows that the evolution of pore fluid composition in a reservoir into which CO_2 is injected may be strongly influenced by kinetic factors. Dissolution of fast-reacting minerals may be limited by the transport of reactants to the mineral surface, while minerals whose surfaces react only slowly may persist out of equilibrium with pore fluid for extended periods. Some reactions, such as congruent dissolution, proceed until the reacting mineral is in equilibrium with the pore fluid, but other, incongruent reactions may involve unstable reactants which never attain equilibrium with the pore fluid, resulting in very extensive mineralogical transformations over time.

1529-6466/13/0077-0005$05.00 http://dx.doi.org/10.2138/rmg.2013.77.5

This chapter examines interactions between CO_2 and H_2O fluids and the rocks and minerals that comprise GCS reservoirs, as well as the caprocks that seal these reservoirs, from the perspective of laboratory experiments. Laboratory experiments determine thermodynamic and kinetic parameters and can identify fluid-rock reactions and processes that may have been previously unknown or unappreciated. Experimental studies of equilibrium and kinetic aspects of mineral dissolution and precipitation relevant to GCS are now quite mature, and there is a growing body of work investigating petrophysical consequences of CO_2 injection. This chapter examines fluid-mineral and fluid-rock interactions that take place in water at a range of scales, from the micro- to the core scale. Other chapters evaluate fluid-mineral interactions at the nano-scale (De Yoreo et al. 2013, this volume), the field scale (Kharaka et al. 2013, this volume), and in natural analogues (Bickle et al. 2013, this volume). In addition, this chapter focuses on abiotic CO_2-water-rock interactions; we do not address the role of biological processes relevant to GCS.

This chapter is divided into three major sections. In the first section we discuss relationships between hydrogeology (i.e., flow paths, heterogeneities, porosity-permeability, etc.) and fluid-rock interactions. We also discuss the influence that CO_2 exerts on reactions and processes in a water-rock system. Our discussion assumes that the reader possesses a basic understanding of the geochemistry and mineralogy of water-rock interactions and focuses on the changes that CO_2 brings to these interactions. The reader can consult any of a large number of books that provide the basic theory of mineral precipitation and dissolution, pH control of reactions, and other relevant subjects discussed in this chapter (e.g., Stumm and Morgan 1996; Drever 1997; Langmuir 1997). In addition, much of the kinetic rate data that we present has been recently tabulated (Palandri and Kharaka 2004; Brantley et al. 2008). The second section is a brief summary of the experimental equipment and techniques used to evaluate reactions between fluids and minerals. The third section evaluates fluid-mineral behavior in laboratory experiments. This section focuses on the important rock-forming minerals within reservoirs and cap rocks as well as accessory minerals that are pertinent to GCS. Olivine and pyroxene are discussed because storage as carbonate is likely to be most important in mafic and ultramafic rocks. The common silicate minerals, feldspars, phyllosilicates, and quartz, are then addressed. We subsequently consider carbonate minerals, followed by sulfates, sulfides, and Fe-oxyhydroxides. The section concludes with discussion of fluid-rock behavior in laboratory experiments assessing both reservoir rocks and caprocks as opposed to individual minerals. It is worth noting that the results of experimental studies focused on GCS also provide insights into other geologic environments, including engineered geothermal systems, enhanced oil and gas recovery, and unconventional hydrocarbon resources. The chapter concludes with a summary section and a section that suggests directions for future work.

CARBON DIOXIDE IN A FLUID-ROCK SYSTEM

Under all likely conditions for CO_2 storage, H_2O and CO_2 are immiscible even in the absence of dissolved salts (Kaszuba et al. 2006). Carbon dioxide solubility in water decreases with increasing temperature and salinity at surface conditions, but increases with pressure (Todheide and Franck 1963; Takenouchi and Kennedy 1964, 1965). Over the range of conditions relevant for GCS, CO_2 solubility is almost independent of temperature, but does have a strong pressure dependency. It is also subject to "salting-out" effects (Takenouchi and Kennedy 1965). In a rock-dominated system typical of most natural reservoirs, CO_2 solubility is further influenced by mineral-fluid interactions.

Under conditions likely to prevail in a GCS site, the pH of unreacted CO_2-charged water is markedly acid (<4), and so the dominant carbonate species will be aqueous CO_2 and undissociated carbonic acid. The effect of fluid-mineral interactions is almost invariably

to neutralize some of this carbonic acid acidity, resulting in a rise in pH. Provided the pH remains below the apparent first dissociation constant of carbonic acid (pK_a = ~6 according to temperature and salinity of the fluid (e.g., Bodnar et al. 2013, this volume)), the dominant aqueous carbonate species remain as $CO_{2(aq)}$ and $H_2CO_3°$, and mineral dissolution has little effect on total dissolved inorganic carbon. If mineral reactions result in a rise in pH above pK_a, however, significant additional CO_2 may enter solution as bicarbonate, enabling additional carbon to be stored through solubility trapping.

Targets for modeling

In a storage environment, the starting condition involves rocks that contain formation water which is likely to be saline and already saturated with the minerals in the host rock. Injection of CO_2 leads to the creation of a plume of CO_2 which expands away from the point of injection along the most permeable horizons and whose ascent is prevented by a cap rock (Fig. 1). In the direction of advance of CO_2 along permeable beds, water ahead of the CO_2 front becomes acidified and reacts with the host rock (Kharaka et al. 2009), but is pushed ahead of the advancing plume. The thickness of the zone of acidified water ahead of the plume is controlled by transport processes within the water phase (Kampman et al. 2013). Although initially very reactive, this migrating slug of water will rapidly approach equilibrium with the more reactive minerals in the host rock, probably in a matter of days. Nevertheless, as the radius of the advancing plume increases, the volume of acidified water must also continuously increase. Consequently, there will always be reaction in the rocks at the front of the advancing plume (Fig. 1, location A). While injection continues to drive the plume front forward, reactivity ahead of it will inevitably be limited to rapid reactions.

Behind the advancing plume front, residually trapped water persists and can continue to react with host minerals. The capacity to directly dissolve minerals into this static, acidified water is strictly limited. However, this water can persist for an extended period of time until all the water has completely evaporated into the CO_2 or been consumed as a reactant in, for example, the formation of clays (Fig. 1, location B). In this situation, slow reactions may

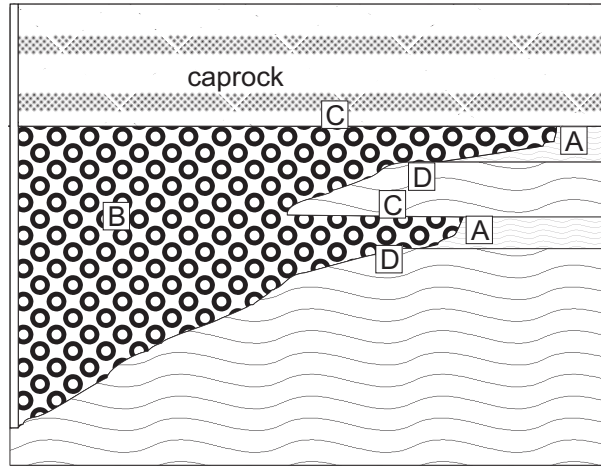

Figure 1. Schematic representation of CO_2 injection into an aquifer sandstone beneath a caprock. The CO_2 fingers ahead down more permeable sandstone beds. A: sites in the most permeable beds where the advancing CO_2 front pushes acidified water ahead of it; B: region behind the CO_2 front containing interconnected CO_2 and residually trapped brine; C: upper surfaces of CO_2 fingers where CO_2 interacts by diffusion with overlying formation brines in less permeable beds; D: lower surfaces of CO_2 fingers where CO_2 interacts with underlying formation brines by diffusion and in some circumstances convection.

nevertheless have a significant impact on rock properties. Comparable reactions may be expected in reservoirs where alternating CO_2 and water injections have been used to stabilize CO_2 through residual trapping (Qi et al. 2009), except that salinity is unlikely to reach extreme values as in a zone of evaporation. The upper and lower surfaces of permeable layers into which CO_2 has preferentially migrated provide relatively stable sites for CO_2-water-mineral interactions (Fig. 1 locations C and D), and these may be particularly effective at the lower surface (location D) where the increase in density triggered by dissolution of CO_2 in water can set up convection cells and enhance mixing (Riaz et al. 2006; Xu et al. 2006). Reactions near persistent interfaces have the potential to continue for extended periods, and could result in changes to the local permeability structure. In addition to the different types of interaction between fluids and minerals that can take place in different settings, short term reactivity is also likely to be affected by temperature fluctuations caused by ongoing and very large scale injections of carbon dioxide.

The significance of these different settings of reactivity is that they involve different timescales and degrees of disequilibrium. It is important to ensure that kinetic experiments address the relevant rate-limiting step for the part of the injection system of interest. For example, it is unlikely that CO_2-water interactions will lead to significant dissolution of additional alumina and silica from aluminum silicates since the original formation water is already saturated with the host rock. Indeed these elements may even be precipitated as a result of dissolution of CO_2 causing a reduction in water activity. On the other hand, reactions involving cation leaching or exchange are likely to be triggered by acidification of formation waters and consequent dissolution of carbonates.

Fluid- and rock-dominated reaction systems

Injection of supercritical CO_2 into a fluid-rock system alters the balance between rock- and fluid-dominated reaction systems (Kaszuba and Janecky 2009). In general, rock-dominated systems such as deep brine formations are not affected by fluid infiltration such as recharge and mineral reactions control the aqueous geochemistry (Langmuir 1997). In contrast, fluids control the mineralogy and aqueous geochemistry in fluid-dominated systems. Examples include aquifers that are replenished by fresh water recharge as well as reservoirs and deep brine formations into which CO_2 is injected.

In experimental studies and in brine formations at GCS sites, injection of supercritical CO_2 initially shifts the pore fluid composition from being dominated by the rock towards one dominated by the injected fluid (Kaszuba et al. 2003, 2005); CO_2-H_2O interactions result in acid-dominated reactions and related mineral dissolution and/or precipitation (Kaszuba and Janecky 2009). This fundamental change from rock- to fluid- control triggers almost all emergent geochemical phenomena. Subsequent mineral-fluid interactions counter carbonic acid acidity as the rock begins to reassert its control.

Within the reservoir, the variability of flow properties due to structural heterogeneity can also lead to spatial variation of the type of reaction control: fluid-dominated reactions occur preferentially along main flow paths of higher permeability, while rock-dominated reactions are favored in more protected areas where flow is reduced. With time, dissolution and precipitation reactions progressively modify flow pathways and may locally shift the reaction control. This phenomenon induces chemical gradients at various scales that can affect the distribution of reactions, especially in multi-mineral reservoirs (e.g., Molins et al. 2012). Heterogeneity of reaction has even been noted at the micrometric to centimetric scale during the experimental percolation of CO_2-enriched brine within olivine-rich sinters (Andreani et al. 2009). Local variations of fluid flow induce variable chemical gradients at the silicate surface and create microenvironments of dissolution (high flow regions) close to microenvironments of precipitation (low flow regions) (Fig. 2). At the sample scale, dissolution reactions

preferentially occur at the inlet of the core while carbonate precipitation is favored toward the core outlet until CO_2 is consumed; phyllosilicates precipitate at the core outlet.

It is evident that the departure from equilibrium of the solution can vary with space and time in massive rock samples. Many experimental studies investigate the reactivity and kinetics of water-rock interactions at conditions that are far from equilibrium (see section discussing olivine and pyroxene) whereas few experiments investigate water-rock reactions at saturation indices approaching equilibrium. The rate-free energy (r-ΔG_r) relationship may be inadequately modeled within the classic Transition-State-Theory framework (Daval et al. 2010; Hellmann et al. 2010). Indeed, experiments on diopside show a considerable departure from models that leads to an overestimation of the reaction rate in the case of CO_2 storage (Daval et al. 2010). Hence, the dependence of the reaction rate of silicates upon ΔG_r is fundamental for GCS. These processes have important implications for determining whether transport or reaction (kinetics) is the rate-limiting process at the macroscopic scale.

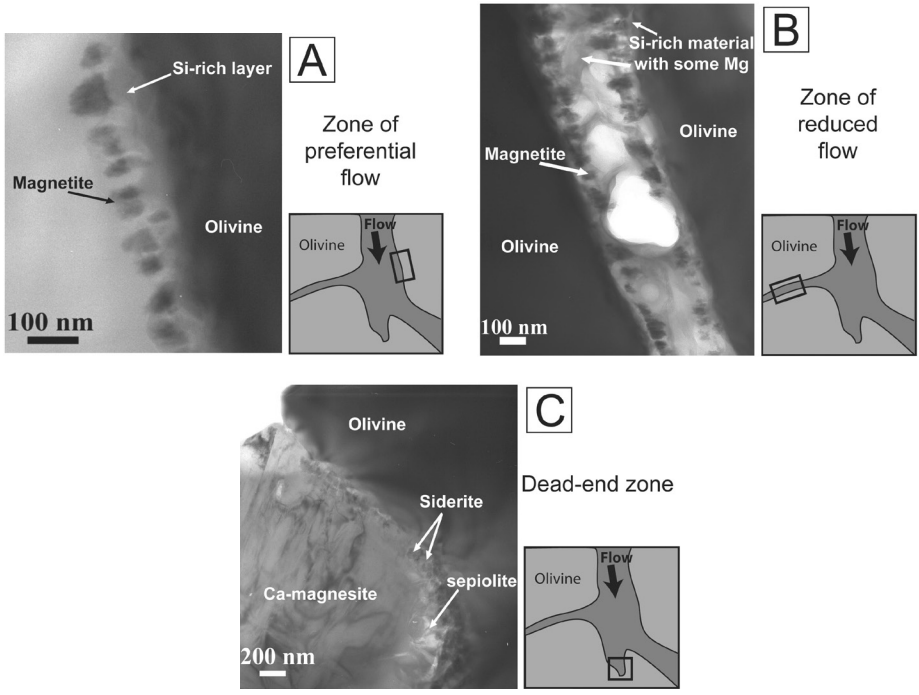

Figure 2. TEM images of main reaction textures observed in samples of sintered olivine and diopside reacted with CO_2-enriched water in a percolation experiment, a type of flow-through experiment. These textures illustrate the variability of transport-reaction resulting from the structural heterogeneity of the sample. Along main flow paths (A), olivine dissolution prevails because of an efficient advective removal of elements due to strong chemical gradients between the fluid and the mineral. A silica-passivation layer is created on olivine surfaces where magnetite precipitates. In reduced flow zones (B), chemical gradients and removal of elements are both reduced. Mg-Si phyllosilicates can precipitate instead of the silica layer. In dead-end-zones (C), chemical gradients are reduced and carbonate supersaturation can be achieved to form magnesite and siderite on olivine surfaces, in addition to an Mg-Si-rich phyllosilicate [Used by permission of the American Chemical Society, from Andreani et al. (2009), *Environ Sci Technol*, Vol. 43, Fig. 4, p. 1228.].

Role of co-contaminants

Geologic storage of CO_2 that contains impurities such as SO_x, NO_x, H_2S, Hg and potentially O_2 and other constituents is known as co-sequestration, a term first used with reference to co-injected CO_2 and H_2S (Williams 2002). While the body of literature regarding experimental evaluation of mineralogic and geochemical effects of CO_2-water-rock interactions is quite extensive, experimental studies of co-injected impurities have only recently received attention (see sections discussing sulfate and sulfide minerals). Chialvo et al. (2013, this volume) address the behavior of CO_2-rich environments containing H_2O, SO_x, H_2S, or NO_x. In this chapter we evaluate the limited data that is available for mineral precipitation and dissolution due to reaction with CO_2-H_2O fluids containing such impurities. In general, SO_x and other impurities provide new sources of acidity and dissolved solutes such as sulfate. Additional acidity is almost invariably neutralized by mineral reactions and additional solutes may lead to precipitation of new minerals and growth of preexisting minerals.

EXPERIMENTAL TECHNIQUES

The various parts of the injection system differ in their physico-chemical conditions due to the pCO_2 gradient created by the injection. Consequently, different CO_2-water-rock interactions take place in different parts of the system. Initial reactions close to the injection well are dominated by acidification of pore waters; either the migrating formation waters pushed ahead of the CO_2 plume or the residual water trapped behind the plume front and progressively evaporated as additional CO_2 is injected. Mineral dissolution includes both direct dissolution (mainly of carbonates, e.g., Kjøller et al. 2011; Canal et al. 2013; Jun et al. 2013) and hydrolysis of feldspars and phyllosilicates leading to precipitation of clays and other secondary silicate minerals (Lin et al. 2008; Hangx and Spiers 2009). Precipitation of secondary carbonates is likely to take place further away, after the initial acidification of formation waters has been neutralized and silicate reactions have disturbed the initial carbonate-fluid equilibrium (Bateman et al. 2010). Interpretations of experiments relevant for GCS have to address these two settings, even if most experiments have been designed to measure dissolution rates under far-from-equilibrium conditions, where reasonably consistent results can be obtained. Many differences in results between studies probably reflect different experimental approaches. No one approach can be said to provide a universal best analogue for what will happen during injection and subsequent storage because of the range of settings in which reactions are possible within even a simple storage site and the range of injection scenarios that might be implemented. Injection of CO_2 as a single continuous process disrupts the equilibria in an existing system in which formation waters are already at saturation with respect to aluminum silicates, whereas alternating injection of water and gas to enhance capillary trapping introduces water that is low in silica and aluminum.

Variations of two different types of apparatus, batch and flow through, are used to reproduce as much as possible these different conditions. Both are used in experiments for reactivity, thermodynamics, kinetics, and hydrodynamic investigations. Schematic drawings of the major types of experimental apparatus we discuss are presented in Figure 3.

Materials for experimental apparatus

Experimental apparatus must be designed to span a wide range of pressure, temperature, and pCO_2 conditions, up to and exceeding supercritical CO_2 pressures, and should be constructed of inert materials so as not to participate in the reactions of interest. The latter is particularly true for experiments conducted with high pCO_2 and high-salinity brines that are extremely corrosive. These conditions require the experimentalist to exercise caution on the nature of the reaction cell chosen for the experiments. Metal alloys, like Hastelloy, titanium,

and gold, are usually favored compared to steel. Most laboratories rely on stainless steel or titanium pressure vessels that can be rated to several tens of MPa and used in an oven to several hundred degrees C. A liner is often used to contain the sample and solution, to minimize corrosion. For experiments with CO_2, rupture discs of Inconel alloy prove susceptible to corrosion and must be frequently replaced unless first coated with gold. However, at pressures of just a few atmospheres, PTFE vessels have been used because they are cheap, allowing many experiments to be run simultaneously. While these pressures are well below the critical pressure of CO_2, they are much greater than the partial pressure of CO_2 in the atmosphere, and so they provide useful pointers to likely behavior at higher pressures.

Specific surface area measurements

At the simplest level, in most of the apparatus, the samples investigated are in powder form, typically sieved to dimensions of 100-200 micrometers, and lie loose in the bottom of the reaction cell. Knowledge of the reactive surface area is essential to interpret the results of dissolution rate experiments. Reactive surface area is most commonly determined by BET measurements of inert gas adsorption or by geometrical estimates. Typically BET surface areas are greater than simple geometrical estimates. The magnitude of the difference varies greatly between different materials and is particularly sensitive to microporosity effects that may vary between samples of the same mineral species (Brantley and Mellott 2000). Brantley and Mellott (2000) reported BET surface areas between 10-40 times greater than geometrical surface areas based on a spherical approximation. Unfortunately, it cannot be assumed that BET surface areas provide an ideal measure of the reactive surface area available during hydrothermal reactions; access of dissolved species to surfaces of micropores beneath the surface may be transport-limited in a way that access to surface sites is not. At the core scale, not all available surface area necessarily reacts because of the variable connectivity of pores and because of localized reaction close to preferential flow paths. Additionally, it is clear from SEM images of grains that have undergone reaction that the surface area is not constant and commonly increases due to selective dissolution along cracks and cleavage planes as the experiment progresses. Dissolution-precipitation reactions may also modify the reactive surface area. To further complicate matters, some studies perform kinetic calculations using surface areas determined before the experiment begins whereas others use surface areas of minerals determined after the experiment is terminated.

A magnetic stirrer is generally used to ensure that the reactions taking place in the experiments are not inhibited by sluggish transport. Possible problems that can arise include changes in grain size due to vigorous stirring and clogging of the dip tube, especially by clay minerals. Some workers have used less vigorous forms of agitation, such as shaking tables, and the dip tube will normally be fitted with a filter. Clay-bearing samples may be retained in a membrane made from dialysis tubing to prevent clay clogging (e.g., Allan et al. 2011), although dialysis tubing material will disintegrate in the course of extended experiments, especially at elevated temperatures.

An alternative solution to the problem of accurately determining surface area is the use of discs of monomineralic rock or part of a mineral single crystal, embedded in resin and with a polished surface of accurately known area (Sjöberg and Rickard 1983). The disc rotates in the vessel, and by comparing rates at different rotation speeds it is possible to evaluate the importance of transport for the dissolution process (Pokrovsky et al. 2005). For minerals which react rapidly with fluid, notably calcite, mineral dissolution rate experiments produce results that are strongly dependent on the configuration inside the vessel and resulting hydrodynamic effects (Sjöberg and Rickard 1983). These factors emphasize the need for care before applying experimental reaction rates to GCS systems. The main lesson in the case of calcite is that it is not the surface reaction but the transport step that is rate controlling.

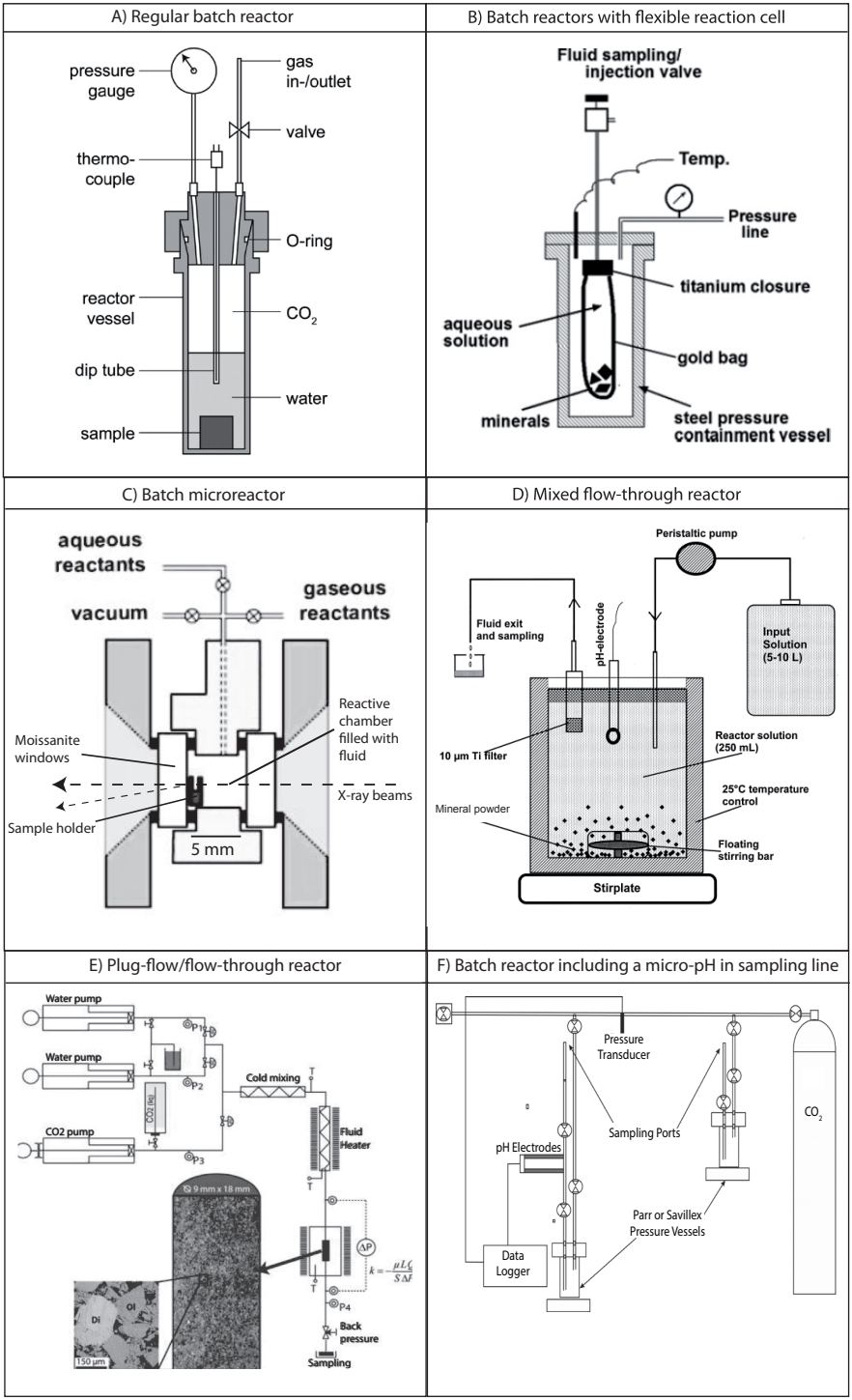

Figure 3. *caption on facing page*

Batch reactors

Batch experiments at specific CO_2 pressures are carried out in closed vessels under elevated pressure, either for dissolution studies of single minerals, or to characterize reaction paths and equilibrium assemblages in more complex polymineralic assemblages in which dissolution and precipitation occur simultaneously (e.g., Hövelmann et al. 2012a). A typical configuration (Fig. 3a) involves a sealed vessel with at least two ports. Carbon dioxide is introduced at the top of the vessel and water is sampled via a dip tube, which may be fitted with a filter to prevent clogging. Some configurations use an additional port to allow the headspace gas to be changed or flushed. The advent of pH electrodes capable of withstanding pressure-temperature conditions appropriate to investigations of GCS permit *in situ* measurement of pH (below). If the fluid is not repeatedly sampled during the experiment, repeated runs of increasing duration are required to characterize the rate of reaction advancement by removing fluids and solids at different times.

A major challenge for high-pressure experiments involving CO_2 is sampling the fluid during the course of the run. It is necessary to take samples with considerable care to prevent water from degassing CO_2 as it is sampled. For determinations of the dissolved CO_2 content, samples may be bled off into a syringe containing alkali hydroxide solution, either using delicate human control of the sampling valve or a syringe pump to control back pressure. Rosenqvist et al. (2012) reported that the pressure drop using manual sampling was measured to less than 0.001 MPa by instrumenting the assembly with pressure transducers. An alternative method for determining dissolved CO_2 content is accomplished by coulometric titration (Huffmann 1977; Kaszuba et al. 2005). In this method, samples are bled off into a glass gas-tight syringe. Carbon dioxide dissolved in brine and exsolved at ambient pressure and temperature are injected together into a carbon coulometer.

Another type of batch reactor, initially described by Dickson et al. (1963) and improved later by different authors (e.g., Seyfried et al. 1979; Seyfried et al. 1987; Rosenbauer et al. 1993), consists of a flexible reaction cell, made of titanium or gold, with a detachable titanium cap (Fig. 3b). This cell is placed in a steel vessel similar to the previously described batch reactor. Pressure and temperature are externally controlled and water ensures pressure transmission to the cell. The cell is plumbed with an exit capillary tube linked to a sampling valve block. This system allows the isobaric and isothermal sampling of reacted fluids during the course of the experiment and permits the injection of fluids such as CO_2 when required (e.g., Kaszuba et al. 2003). Samples are cooled and depressurized to ambient conditions in a few seconds to prevent retrograde reactions that may occur during a prolonged quench process. Measurements of mineral solubilities and determination of coupled dissolution-precipitation rates can then be estimated using measurements of cation and anion concentrations. A related type of batch reactor is known as the Barnes-type rocking autoclave (Barnes 1971). This is a fixed-volume hydrothermal system in which pressures are determined by the liquid-vapor curve for reactant solutions.

Figure 3 *(on facing page)***.** Schematic drawings of the major types of experimental apparatus. A) Typical configuration for a batch reactor [Used by permission of Elsevier, from Hövelmann et al. (2012a), *Chem Geol*, Vol. 334, Fig. 2, p. 258.]. B) Batch reactor containing flexible reaction cell [Used by permission of the American Chemical Society, from McCollom and Seewald (2007), *Chem Rev*, Vol. 107, Fig. 6, p. 388.]. C) Microreactor [Used by permission of the American Chemical Society, from Wolf et al. (2004), *Environ Sci Technol*, Vol. 38, Fig. 1, p. 933.]. D) Mixed flow-through batch reactor [Used by permission of Elsevier, from Pokrovsky and Schott (2000), *Geochim Cosmochim Acta*, Vol. 64, Fig. 1, p. 3314.]. E) Plug-flow reactor, also known as a flow-through and core-flood reactor [Used by permission of the American Chemical Society, from Andreani et al. (2009), *Environ Sci Technol*, Vol. 43, Fig. 2, p. 1227.]. F) Batch reactor including a micro-pH electrode assembly in the sampling line [Used by permission of Elsevier, from Rosenqvist et al. (2012), *Appl Geochem*, Vol. 27, Fig. 1, p. 1611.].

With exceedingly few exceptions, solid samples can only be recovered from batch apparatus after the experiments are terminated. Batch apparatus that permit time sampling of solids are custom-made apparatus not available commercially, such as stacked-vessel autoclaves (Cole et al. 1992). Availability of solid samples only after termination of the experiment may affect the study of reaction mechanisms since some intermediate phases or processes may be missed. In addition, fluid sampling does not always manage to correctly record the reaction in polymineralic assemblages because of assumptions made for mineral compositions and proportions for mass balance. These limitations have motivated the development of "microreactors" capable of *in situ* monitoring of fluid-rock interactions (Fig. 3c) (Béarat et al. 2006; Schaef et al. 2011; Schaef et al. 2012). Microreactors are a few microliters in size and contain transparent windows constructed of diamond or moissanite (SiC). *In situ* monitoring of reactions is performed using methods such as X-Ray diffraction of solid products, X-ray fluorescence for solid and fluid composition, or Infrared or Raman for solids and some dissolved species (e.g., carbonate, bicarbonate ions). This type of approach has been limited so far to mineral physics for high-pressure experiments using diamond-anvil cells (DAC). Development of low-pressure DAC or low-pressure reactors with an external control on the fluid opens new perspectives for the study of CO_2-water-rock interactions using a wider range of characterization tools (e.g., Wolf et al. 2004; Daval et al. 2010). The main constraint of this type of experiment is that the size of the window may require the use of synchrotron radiation in order to get the required spatial resolution and beam intensity for analyzing small volumes of minerals and fluids.

Mixed flow-through reactors

Batch experiments provide measurements of dissolution rates in fluid-dominated settings in which the reaction affinity changes as equilibrium is approached. Progressive sampling of solution in the course of the experiment changes the proportion of mineral to fluid so that the amount of mineral dissolution needed to produce a given change in fluid composition gradually decreases as the experiment proceeds. An alternative approach is to carry out experiments in which fluid flows at a steady rate through the experimental vessel and is sampled at the exit point (Fig. 3d). The composition of the exit fluid is considered representative of that inside the vessel. Mixing ensures fluid homogeneity and stirring rate is fixed in order to avoid mass transport limitations on the reaction rate. In flow-through reactors, the composition of the introduced fluid remains constant, so that the reaction affinity reaches a steady state. As a result, conditions are likely to be further from equilibrium than is the case for batch experiments, but affinity remains constant. Dove and Crerar (1990) developed a hydrothermal mixed flow-through reactor capable of working over the range of pressure-temperature conditions appropriate to GCS. This approach was further developed by Carroll and Knauss (2005) for experiments with CO_2-bearing fluids. Water (or brine) is first saturated with CO_2 at the required pressure in a separate pressure vessel and is then injected into the stirred reactor vessel containing the mineral charge. Since a single fluid phase passes though the reaction vessel and a backpressure is maintained to prevent the dissolved gas from separating, issues with two-phase flow do not arise. Hydrothermal mixed flow-through reactors arguably offer the best-constrained environment for determining far-from equilibrium mineral dissolution rates in CO_2-bearing water. However, depending on the stage of the GCS process that is being investigated, these may not be the key reaction rates for the problem of interest.

Plug-flow/flow-through reactors

Batch reactors and mixed flow-through reactors monitor the dissolution of small mineral volumes in large fluid volumes. In order to predict the consequences of injection of CO_2 into rock-dominated reservoir rocks, there is clearly a case for carrying out experiments where fluid flows through a rock or sediment plug, reacting as it moves. However, it is not normally possible to back out absolute rate information from the results. This type of approach also better emulates the dynamics of CO_2 injection in a natural reservoir where a coupling between chemical

reactions and hydrodynamic properties is expected. Moreover, a rock is a chemically and physically heterogeneous media in which fluid flow and reaction may vary with space, even at the micrometric scale. Most flow-through reactor experiments investigate the characteristics of specific rocks from prospective reservoirs or their caps, but it is also possible to carry out experiments on packed columns containing solids that are well-characterized (Bateman et al. 2010).

An example of a plug-flow reactor, also known as a flow-through or core-flood reactor, is shown schematically in Figure 3e. The fluid to be injected is prepared in a separate vessel and pumped into a cm-scale rock core held in a core holder. The confining pressure around the jacket containing the core is substantially greater than the fluid pressure at the point of injection to prevent leakage. Reservoir conditions (greater than 200 °C and 20 MPa) can be achieved within the core (e.g., Luquot and Gouze 2009). Fluid pressure at the outlet is adjusted to give a pre-determined constant flow rate, and the measured difference of pressure across the core provides a continuous record of permeability (as calculated using Darcy's law). Both dissolution and precipitation reactions can be investigated depending on the inlet fluid composition. Initial porosity measurements correlated to mass balance calculations during the course of the experiment provide the porosity evolution and hence the determinant permeability-porosity (k-ϕ) relationship for reactive transport modeling as a function of fluid reactivity and fluid flow. Some apparatus are ported such that pH is continuously monitored on the outflow line and fluid samples may be collected during the run. Some apparatus are constructed such that the entire assembly is set up in a CT scanner so that changes in the distribution of porosity can be monitored periodically as the run proceeds. NMR can also be used to monitor changes in porosity and pore size distribution. Further measurements can be made at the end of the run, including off-line measurements of permeability and seismic velocities (v_p, v_s). Noiriel et al. (2009) carried out experiments close to atmospheric pressure, which allowed the core to be removed periodically to be scanned in a micro-CT scanner. This approach yielded high-resolution spatial images of the evolution of reactive surface area, porosity and tortuosity while reaction progressed. Experiments of this type do not readily yield fundamental kinetic data, but they do provide a test for the available theoretical models.

pH measurements under GCS conditions

A major consequence of CO_2 injection is acidification of formation waters, but only recently have electrodes been developed to allow pH determinations at elevated pressure and temperature in experimental systems. Many studies with CO_2 still measure pH as quickly as possible after reducing pressure to ambient, and rely on geochemical models to calculate pH at *in situ* conditions.

Solid state pH and reference electrodes that can be inserted into a pressure vessel using additional ports in the lid were used by Pokrovsky et al. (2005), who combined a commercial pH electrode with a home made reference electrode. Comparable electrodes are currently available commercially from Corr Instruments. Because these electrodes remain in place for the entire duration of an experiment they must be both robust and stable, but if they meet this requirement they permit monitoring of pH throughout an experiment. An alternative approach employed by Rosenqvist et al. (2012) is to use small volume solid-state electrodes in-line on the dip tube, between the vessel and sampling syringe (Fig. 3f). This configuration allows measurements to be made whenever a sample is taken, and the same electrode assembly can be used during sampling from a number of vessels rather than being dedicated to just one. Rosenqvist et al. (2012) used Unisense micro pH electrodes, rated to 1 MPa, and so were unable to work at full GCS pressures. The same assembly can be used for plug flow experiments as well as for batch experiments.

A growing number of studies do report high pressure pH measurements. It appears that they are comparable to those obtained by careful thermodynamic modeling, although oversimplistic application of modeling codes can produce misleading results depending on the treatment of

CO_2 fugacity (Allen et al. 2005; Rosenqvist 2012). Until the release of PHREEQC v.3 in 2012 (*http://wwwbrr.cr.usgs.gov/projects/GWC_coupled/phreeqc/index.html*), modeling codes did not allow for the non-ideal behavior of CO_2. To get meaningful results it was necessary to calculate CO_2 fugacity off-line (e.g., Duan et al. 2006) and then input the resulting value as a pressure into the model. PHREEQC now incorporates a fugacity correction.

Both pH and fluid composition have been widely investigated as variables controlling mineral dissolution rates, with or without the presence of CO_2. Studies that specifically address mineral dissolution in the presence of CO_2 report that it is the role of dissolved CO_2 in determining pH that influences dissolution rate, rather than the presence of dissolved carbonate *per se* (e.g., Carroll and Knauss 2005; Pokrovsky et al. 2005). In effect, mineral dissolution experiments relevant to GCS represent a subset of the available data performed over a relatively narrow range of moderately acid conditions.

CARBON DIOXIDE-WATER-ROCK INTERACTIONS IN RESERVOIR ROCKS AND CAPROCKS: EXPERIMENTAL PERSPECTIVES

Olivine and pyroxene

Olivine and pyroxene are the predominant minerals in mafic and ultramafic rocks forming the oceanic lithosphere and the upper mantle. These rocks represent the greatest potential for CO_2 storage capacity by mineral trapping, i.e., ~2 tons and 1.3-1.4 tons of CO_2 per m^3 of rock, respectively (Xu et al. 2004). This capacity is a consequence of 1) the strong disequilibrium of olivine and pyroxene in the presence of aqueous fluids under shallow crustal conditions and 2) the high ratio of divalent cations to silica that provides abundant Mg^{2+}, Fe^{2+} and Ca^{2+} to form carbonates when olivine and pyroxene dissolve in a CO_2-rich aqueous fluid. Hence, in addition to possible oceanic disposal, fragments of ancient oceanic lithosphere and major flood basalts exposed on land constitute large and accessible reservoirs for CO_2 storage (McGrail et al. 2006; Kelemen and Matter 2008). Iceland already hosts the first pilot holes where in situ injection of CO_2 into basalt is currently tested as part of the CARBFIX project (Gislason et al. 2010; Matter et al. 2011). Kelemen and Matter (2008) estimated that present-day, natural weathering of exposed mantle rocks in the Oman ophiolite stores 10^4 to 10^5 tons of CO_2 per year, under atmospheric pCO_2 and temperature < 100 °C (compared to sequestration targets of c. 10^9 tons per year). This natural phenomenon motivated experimental work to identify optimum conditions for accelerating the carbonation reaction (Power et al. 2013, this volume).

As silicate dissolution is assumed to be the rate limited step of the overall carbonation process, several experimental studies evaluated the kinetics of olivine and pyroxene dissolution in the presence of CO_2. This type of experiment has been performed very far from equilibrium in stirred-batch or mixed flow-through reactors. Final solution compositions were undersaturated with respect to expected secondary products (e.g., carbonates, Mg-Fe-hydroxydes or phyllosilicates) such that secondary mineral formation cannot affect dissolution rates. The effect of fluid composition on reactions has sometimes been taken into account. At least two types of effects have been evaluated: the effect of ΔG and the effect of aqueous complexes or formation of secondary minerals that may retard or accelerate the reaction.

With such reactors, numerous studies have been devoted to the dissolution kinetics of forsteritic olivine with Mg > 1.8 atoms per formula unit (see Rimstidt et al. 2012 for a review). Experimental conditions range in temperature from 25 to 120 °C, pCO_2 from 0 to 18 MPa, pH from 2 to 12, and NaCl concentration from 0 to 50 g/L. The pH values were either directly related to the pCO_2 or to $NaHCO_3$ content, or fixed using acid or basic salts such as HCl and LiOH, in order to compare the effect pH to the effect of carbonate ions in

solution. All of these experiments show that the rate of olivine dissolution increases with increasing pCO_2, temperature and NaCl concentration and with decreasing pH. Incongruent dissolution is observed at the initiation of the reaction when fresh olivine is introduced into low pH or high pH solutions. At low pH, magnesium is released faster than silica while the opposite is observed at high pH; dissolution is stoichiometric only near pH 6. Nevertheless, once a steady-state dissolution rate is achieved, it appears to be stoichiometric across the entire pH range. This justifies the use of either magnesium or silica release rate for calculations (Rimstidt et al. 2012). When compiling data for a given temperature of 120 °C, Prigiobbe et al. (2009) show that the rate of olivine dissolution mainly depends on pH for pH values greater than 8 (Fig. 4); pCO_2 and NaCl concentration affect the rate through their effect on pH. This relationship suggests that carbonate ions neither inhibit nor enhance olivine dissolution and that kinetics as a function of pH can be used directly (Fig. 4). However, the importance of the effect of carbonate ions is still debated regarding CO_2 mineralization at high pH and pCO_2 greater than atmospheric levels. Under these conditions, an inhibiting effect of CO_3^{2-} has been observed (Fig. 4) at 25 °C for pH greater than 7 (Wogelius and Walther 1991; Pokrovsky and Schott 2000), and at 120 °C for pH greater than 5 (Hänchen et al. 2006). These authors attribute this behavior to the adsorption of carbonate ions on $>MgOH_2^+$ groups present on the dissolving olivine surface under alkaline conditions. Comparison of predicted rates using regression models for experiments with and without dissolved carbonates indicates that the inhibiting effect of carbonate is the highest around pH 5 for temperature less than 40 °C (0.7 difference in log rate value, Rimstidt et al. 2012). This observation is inconsistent with previous experiments and the authors conclude that the current dataset is too incomplete to correctly estimate this effect.

Some compounds have also been recognized as enhancing olivine dissolution. Organic additives, like citric or oxalic acids that can be important ligands in soils, increase the rate of olivine dissolution around neutral pH at low *T* (25 °C) (Wogelius and Walther 1991; Olsen and Rimstidt 2008). Prigiobbe and Mazzotti (2011) extended this study for high temperature and pCO_2 relevant for CO_2 sequestration. They show that for a pH range of 1 to 7 at temperatures

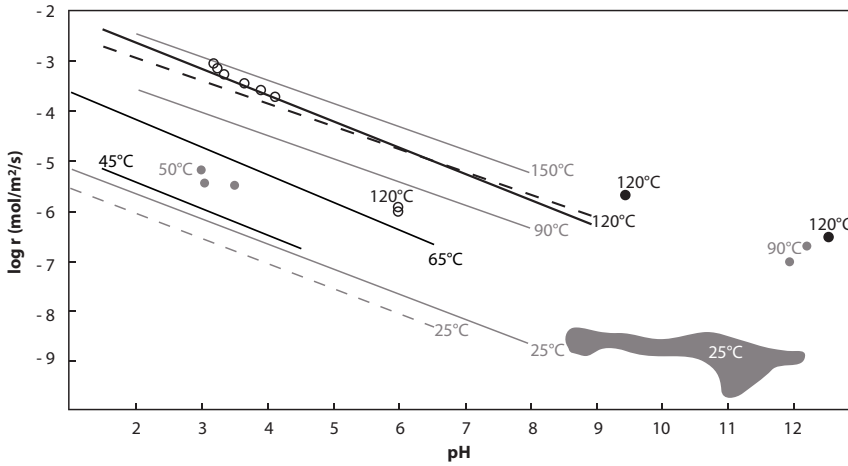

Figure 4. Experimental dissolution rates of olivine as a function of pH at 25 °C (dotted line: data from Blum and Lasaga 1988; Wogelius and Walther 1991; line and grey area: data from Pokrovsky and Schott 2000), at 45 °C (data from Rosso and Rimstidt 2000), at 50 °C (dots: data from Wang and Giammar 2013), at 65 °C (data from Wogelius and Walther 1991; Chen and Brantley 2000), at 90 °C (data from Hänchen et al. 2006), at 120 °C (data from Hänchen et al. 2006: without CO_2 (dotted line and dots), with CO_2 (open circles); line: data from Prigiobbe et al. 2009), and at 150 °C (data from Hänchen et al. 2006).

of 90 and 120 °C, sodium oxalate and sodium citrate increases the rate of olivine dissolution; this effect increases with pH. Chen and Brantley (2000) added aluminum to solution at 25 °C in olivine dissolution experiments but did not notice any effect on the reaction rate. Using a closed microreactor (low-pressure DAC) at higher pressure and temperature conditions (200 MPa, 200 °C and 300 °C), Andreani et al. (2013) observed a significant increase of the hydrothermal alteration rate of olivine. They attributed the rate increase to an enhanced olivine solubility due to alumina-silica complexation, as previously observed for aluminosilicates for pH values greater than 4 (Salvi et al. 1998). No experiments have been performed between these extreme conditions; further investigations under conditions relevant for GCS are warranted since aluminum is present in mafic and ultramafic reservoirs, notably in feldspars.

Very few studies investigate the dissolution rate of fayalite, the pure iron end-member of olivine, but these studies cover a wide range of conditions. Available data provide kinetic rates for 25 °C ≤ T ≤ 100 °C, without CO_2, at pressures up to 30 MPa for pH 1-3, and variable pH at low pressure and temperature (Wogelius and Walther 1992; Daval et al. 2010). Under far from equilibrium conditions, fayalite dissolves faster than forsterite, especially at 25 °C where the rate is about one order of magnitude higher; however, the stoichiometry of dissolution is not yet determined. Similar to forsterite, the dissolution rate of fayalite increases with increasing temperature and acetate concentrations or decreasing pH.

Dissolution of pyroxene has been less well studied than that of olivine, especially in CO_2-bearing fluids. Ca-clinopyroxenes diopside and augite were the most studied, in comparison to the FeMg-orthopyroxene enstatite. Chen and Brantley (1998) provide dissolution rates of diopside at 25 (~10^{-9} mol/m^2/s for pH <4) and 90 °C (~10^{-7} to 10^{-8} mol/m^2/s) under acidic conditions (pH 1 to 4), these values are about an order of magnitude lower than the values of Golubev et al. (2005) for the same pH range. At these conditions and up to pH values of ~10, at which the dissolution rate is ~10^{-9} mol/m^2/s (Knauss et al. 1993; Golubev et al. 2005), diopside dissolves non-stoichiometrically at early stages of reaction and until it reaches a stoichiometric steady state. In more basic solutions a preferential release of silica suggests the formation of a Ca-Mg-rich layer on mineral surfaces (Golubev et al. 2005). Diopside dissolution rates are much slower than other silicates, notably olivine (Fig. 4), with rates 3 orders of magnitude slower at 25 °C and approximately 2 to 3 orders of magnitude slower at 70 and 90 °C, respectively. This is in accordance with common petrographic observations of alteration in mafic rocks. It is worth noting that the values of Chen and Brantley (1998) at 25 °C and acidic pH are slightly lower than those published by other authors (e.g., Schott et al. 1982; Knauss et al. 1993; Golubev et al. 2005), although all of the studies agree that dissolution kinetics are very slow. Augite dissolves more rapidly at 25 °C under very acidic pH of 1 to 3 (approximately 10^{-7} to 10^{-9} mol/m^2/s) but the reaction rate decreases with pH greater than 4. The reported pH-dependence of dissolution for pyroxene also varies from author to author. Variations are possibly the result of the reactive surface area chosen for calculations, since both initial and final surface areas have been used. This effect may be more important for pyroxenes because of preferential dissolution along cleavage planes. However, the reaction rate generally tends to decrease with increasing pH and decreasing temperature. As with olivine, the presence of CO_2 up to 0.1 MPa and of carbonate ions has no direct effect on diopside dissolution (Golubev et al. 2005).

Enstatite dissolution was studied by Oelkers and Schott (2001) at 28 to 168 °C and pH 1 to 11 in CO_2-free solutions containing variable amounts of magnesium and silica. Enstatite dissolution rate follows the same trend as other pyroxenes with very similar values as diopside at 70 °C (10^{-7} to 10^{-9} mol/m^2/s from pH 1 to 12), but the rate decreases with increasing aqueous Mg^{2+} concentration (0 to 4×10^{-4} mol/kg) while aqueous silica (up to 5×10^{-4} mol/kg) has no effect. This observation is interpreted to stem from a peculiar dissolution mechanism controlled by a Mg/H^+ exchange reaction within Mg octahedra that link silica tetrahedral chains. This

mechanism, which depends on aqueous Mg activity and pH, is also expected to occur for other pyroxenes and pyroxenoids in general. This suggests that the role of magnesium has to be taken into account for CO_2 storage in such reservoirs since the concomitant dissolution of neighboring olivine releases abundant magnesium into solution. Experiments performed at 25 °C and higher pH (8 to 13), both with and without atmospheric CO_2, demonstrate an inhibiting effect of CO_3^{2-} on enstatite dissolution at pH greater than 10, attributed to the same mechanism as the one proposed for olivine (Halder and Walther 2011). Wollastonite, a pyroxenoid rarely found in natural systems, has also been studied under ambient and GCS conditions to investigate the behavior of Ca-silicates (Rimstidt and Dove 1986; Weissbart and Rimstidt 2000). While its structure is very close to pyroxene, wollastonite displays much faster dissolution rates than pyroxene (about 3 orders of magnitude higher than diopside at 25 °C); these rates are close to olivine dissolution rates. An explanation for differences between wollastonite and pyroxene dissolution rates has yet to be determined. The pH dependence varies from one author to another but the rate tends to decrease with increasing pH. For example, at 25 °C for a pH ranging from 1 to 6, the dissolution rate is either nearly constant at 10^{-6} mol/m^2/s (Rimstidt and Dove 1986) or decreases to approximately 10^{-7} mol/m^2/s when pH increases (Xie and Walther 1994). The presence of CO_2 has no effect on the dissolution rate of wollastonite, but its dissolution rate increases with HCO_3^- in solution (0.01 to 0.1 molar) at pH 7 to 8 and slightly decreases with CO_2^{3-} in solution (10^{-4} molar) at pH 12 (Golubev et al. 2005).

Batch experiments have been used to investigate the entire process of mineral carbonation, both dissolution and precipitation, under conditions relevant for GCS since mineralization is the main reaction expected in basaltic and ultramafic reservoirs. Batch experiments are able to test the effect of precipitation of secondary minerals on the dissolution rate of primary silicates as well as the rate of carbonation in the reservoir in order to identify optimum conditions for CO_2 storage. In general, the carbonation reaction is much faster than the dissolution reaction of olivine and pyroxene. Olivine and wollastonite are fully transformed to carbonate in few hours to few days, respectively, under favorable conditions (Gerdemann et al. 2007; Daval et al. 2010). In some cases, the solution reaches supersaturated conditions with respect to magnesite, but magnesite does not precipitate. In this case, precipitation is limited by the nucleation process that requires a critical saturation index (Giammar et al. 2005). Surprisingly, olivine carbonation is the highest under alkaline conditions where CO_3^{2-} is dominant, whereas olivine dissolution is inhibited under such conditions (Hänchen et al. 2006). Optimum carbonation conditions identified for olivine are 15 MPa pCO_2, 185 °C, 0.64 molar $NaHCO_3$, and 1 molar NaCl (Gerdemann et al. 2007). The reaction rate increases with temperature and pCO_2 up to these optimum values (see Kelemen and Matter 2008). The exothermic nature of olivine carbonation is also proposed to "self enhance" reaction rates by increasing temperature; energy costs required to heat fluids utilized for *ex situ* CO_2 mineralization (see Power et al. 2013, this volume) are consequently reduced, provided this effect is not overwhelmed by influx of cold fluid.

The role of secondary phase precipitation on the carbonation rate is a matter of debate and depends on the product mineralogy and permeability, and on the primary silicate. The formation of a silica passivation layer on silicate surfaces limits olivine carbonation (Béarat et al. 2006) while it only has a minor effect on diopside and wollastonite carbonation (Daval et al. 2009a,b; 2010). Some studies noticed an inhibition or decrease in the reaction rate when carbonate forms on silicate surfaces (Stockmann et al. 2008; Daval et al. 2009a) while fast precipitation also shifts the composition of the aqueous solution at negative free energy values, promoting the reaction (Daval et al. 2009a). In plug-flow experiments, carbonate, iron oxides and phyllosilicates can precipitate simultaneously near olivine surfaces in areas of reduced permeability, preventing the formation of the passive silica layer (Andreani et al. 2009) (Fig. 2B and 2C).

Feldspars

The feldspars are one of the most widespread groups of potentially reactive minerals in reservoir rocks, and have been the subject of considerable attention from both a theoretical and experimental viewpoint. Classically, studies of feldspar dissolution kinetics have mainly focused on albite, but Ca-bearing plagioclases have been seen as particularly important for GCS because of their potential to promote mineral storage through calcite growth consequent on calcium release (Gunter et al. 1997). Labradorite in particular has been the subject of a number of solubility studies (Stillings and Brantley 1995; Carroll and Knauss 2005; Allan et al. 2011) and is the subject of the GaMin11 interlaboratory comparison study. The application of conventional dissolution rate data on feldspars to GCS sites is particularly fraught because of the strong dependence on aluminum concentrations in solution (Amrhein and Suarez 1992; Schott et al. 2009). Oelkers et al. (1994) developed a treatment to account for the effect of aluminum concentration in solution on feldspar dissolution, linking dissolution to the degree of undersaturation and the formation of silica complexes on mineral surfaces. This is particularly significant for GCS applications because the initial pore fluid is already near feldspar saturation before the introduction of CO_2, so that conventional kinetic experiments starting without dissolved alumina and silica are likely to indicate much faster dissolution than occurs in real systems. An additional factor which has been highlighted in a series of papers by Zhu and co-workers (Lu et al. 2013 and references therein) is that, in a reservoir setting, feldspar dissolution is coupled to precipitation of secondary minerals such as phyllosilicates. Owing to sluggish precipitation of secondary minerals, the pore fluid remains supersaturated with them, and this in turn can significantly inhibit the feldspar dissolution step of the process. Most rate determinations have been made under far-from-equilibrium conditions, whereas rates are greatly reduced as equilibrium is approached (Burch et al. 1993).

Albite dissolution under far from equilibrium conditions has been studied over a wide range of pH values and at temperatures from 25 to greater than 100 °C (Chou and Wollast 1984; Knauss and Wolery 1986; Hellmann 1994) with additional data at pH 3 from Stillings and Brantley (1995) and Allan et al. (2011). There is generally good agreement between these studies despite different experimental approaches. For example, Chou and Wollast (1984) used a fluidized bed reactor, Stillings and Brantley (1995) employed a mixed through-flow reactor, making allowance for increase in surface area in the course of the experiment, while Allan et al. (2011) employed a batch reactor with long run times and minimal stirring to avoid physical damage to mineral powders as the run proceeded. It is clear from all the results (Fig. 5) that dissolution rates range from around 10^{-11} mol/m^2/s at 25 °C to around 10^{-9} mol/m^2/s at 100 °C. Allan et al. (2011) found that an increase in NaCl from 0.01 to 1 molar resulted in a decrease in dissolution rate by around 1 order of magnitude. Albite reaction with CO_2 under more extreme hydrothermal conditions (200 to 300 °C) were studied by Hangx and Spiers (2009), and although no kinetic data were obtained they did show the development of secondary aluminosilicates from albite breakdown, as discussed further by Lu et al. (2013).

Results from studies on labradorite show much less agreement. Dissolution rates based on increases in silica in low salinity fluids at pH 3 and near room temperature range from 10^{-10} mol/m^2/s (Carroll and Knauss 2005) to 10^{-12} mol/m^2/s (Allan et al. 2011). Possible reasons for these discrepancies include the possible effects of increasing surface area noted by Stillings and Brantley (1995) and the very mild agitation used in the work of Allan et al. (2011), coupled with the approach towards equilibrium in these batch experiments. It is also worth noting that there can be considerable variation in the compositions of different natural labradorites. Carroll and Knauss (2005) noted that labradorite dissolution becomes congruent with increasing temperature above 60 °C, but they confirmed the role of aluminum in inhibiting dissolution.

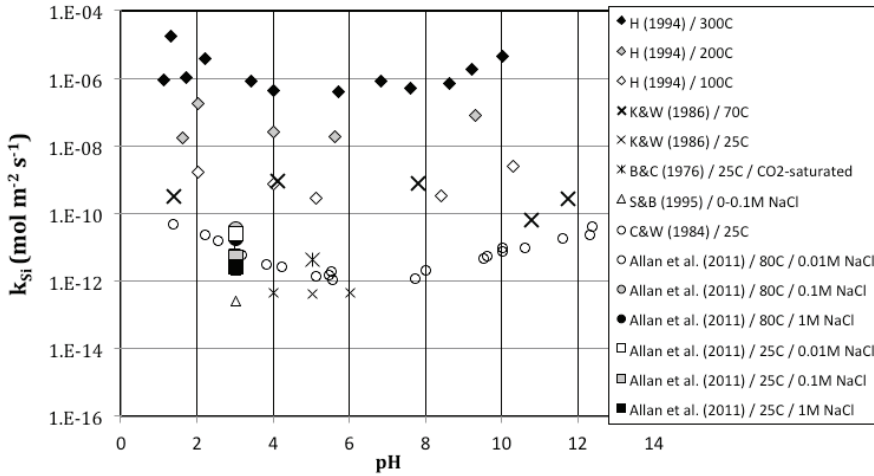

Figure 5. Comparison of a range of experimental dissolution rates for albite (C&W,'84 data from Chou and Wollast 1984; S&B,'95 data from Stillings and Brantley 1995; B&C,'76 data from Busenberg and Clemency 1976; K&W,'86 data from Knauss and Wolery 1986; H,'94 data from Hellmann 1994). [Used by permission of Elsevier, from Allan et al. (2011), *Appl Geochem*, Vol. 26, Fig. 6, p. 1295.].

K-feldspar occurs in a wide range of reservoirs, although since detrital grains are often perthitic it usually coexists with albite. Fu et al. (2009) investigated dissolution of perthitic K-feldspar in batch experiments at relatively high temperatures and pressures for GCS (200 °C and 30 MPa) and an initial pH of 3.1. The metastable coexistence of K-feldspar with kaolinite and sometimes also illite is well known in sandstone diagenesis, suggesting that K-feldspar dissolution can be accompanied by the growth of secondary phases. Fu et al. (2009) were able to document this in their experiments. Contrasting runs of 5 days and 78 days duration, they found evidence for continued dissolution of the albite component of the perthite. After around 400 hours the fluid became supersaturated with K-feldspar, muscovite, boehmite and kaolinite, and secondary precipitates of boehmite and kaolinite began to develop on feldspar surfaces. Further work by Lu et al. (2013) has extended our understanding of secondary mineral formation from alkali feldspar and the effect this has on overall reaction rates. Secondary clay minerals are very significant for reducing sandstone permeability, and these results indicate that extended exposure to acidified formation waters will lead to progressive alteration of K-feldspar to clay.

Phyllosilicates

Phyllosilicates are hydrous minerals that classically form during the aqueous alteration of silicates, such as those forming CO_2 storage reservoirs (e.g., feldspars, olivine). Phyllosilicates can be present in the reservoir before CO_2 is injected or form during CO_2-water-silicate interactions. They are also important components of argillaceous caprocks (mudstone, clays, and shale) where an understanding of their interaction with CO_2-bearing fluids is important for evaluating caprock integrity after injection.

As with most minerals, phyllosilicate dissolution is sensitive to pH and temperature, two determinant parameters for GCS. Dissolution experiments of illite at 5 to 50 °C and pH 1 to 12 in mixed flow-through reactors show the same rate behavior at all temperatures: a decrease of dissolution rate with increasing pH at acid condition, a minimum rate near neutral conditions (5×10^{-14} to 10^{-15} mol/m^2/s), and an increase of dissolution rate with increasing pH at basic conditions (Köhler et al. 2003). The rate also slightly increases with increasing temperature and

is a maximum (10^{-12} to 10^{-13} mol/m^2/s) at low pH. Comparison with available data on other aluminous clay minerals at 25 °C shows similar trends with pH, and very close rate values suggesting similar dissolution behavior despite their chemical variability (Nagy 1995; Huertas et al. 1999) (Fig. 6). A slowing of clay dissolution rate with elapsed time during experiments is generally observed but not yet explained.

Micas can be important phyllosilicates in GCS reservoirs and cap rocks (e.g., Sleipner; Gaus et al. 2005). The reactivity of micas in CO_2-rich brines at conditions relevant to GCS has been investigated using batch reactors. Phlogopite served as a first model for dissolution rates of clays in experiments performed at 95 °C, 10.2 MPa pCO_2, and 1 molar NaCl (Shao et al. 2010). Incongruent dissolution with an enhanced release of the interlayer potassium through ion-exchange is observed, similar to behavior at ambient pressure conditions, while Mg, Si and Al dissolve congruently. The dissolution of phlogopite is more important in CO_2-bearing aqueous solution than in acidic solutions without CO_2, suggesting a role for CO_2 on the dissolution mechanism. Complementary experiments at 75 and 95 °C, 7.6 MPa, with supercritical CO_2 in 1 molar NaCl brines describe the precipitation of illite and amorphous silica on phlogopite surfaces (Garcia et al. 2012a). Similar experiments performed with biotite at 35 to 95 °C and 7.5 to 12 MPa pCO_2 in 1 molar NaCl solutions also suggest a role for CO_2, expressed as a pH decrease, bicarbonate complexation, and an interlayer CO_2 intercalation (Hu and Jun 2012). Interlayer CO_2 intercalation promotes swelling and creation of new surface area that enhances dissolution and, in turn, increases permeability in natural settings. On the other hand, biotite alteration results in the precipitation of fibrous illite grains that become detached and mobilized, altering flow pathways. Experiments on powdered clay-rich shale containing aluminous phyllosilicates like illite show little reactivity in 1 molar NaCl, CO_2-rich solution at 11 MPa pCO_2 between 80 and 150 °C, suggesting little porosity/permeability alteration (Alemu et al. 2011). However, plug-flow experiments on core or fractured core samples reveals processes that may affect caprock integrity. For example, experimental and theoretical studies demonstrate that the formation of small quantities of clay can significantly change the porosity and permeability of reservoirs or caprocks (Gaus et al. 2005; Gaus 2010; Luquot et al. 2012) (Fig. 7 and 8). When clays form along main flow paths, the increased tortuosity can lead to a strong permeability

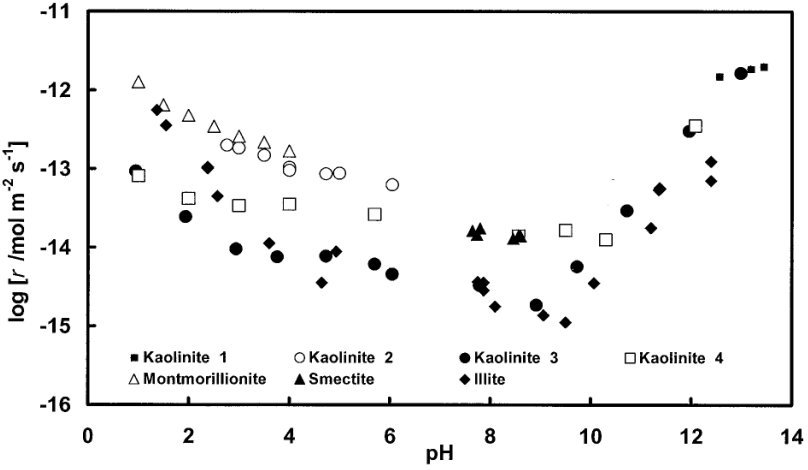

Figure 6. Comparison of apparent dissolution rates for illite and other clay minerals. Dissolution rates are normalized to 10 oxygen atoms. Closed system experiments in excess of 1 month are denoted by open symbols; those of shorter duration are denoted by open symbols [Used by permission of Elsevier, from Köhler et al. (2003), *Geochim Cosmochim Acta*, Vol. 67, Fig. 7, p. 3592.].

decrease without significant porosity change (Godard et al. 2013).

Phyllosilicates are distinctive minerals because they have high specific surface areas due to their sheeted structure and present a wide range of chemical compositions. These characteristics lead to specific properties of phyllosilicate-bearing rocks, such as high tortuosity, but also give rise to high sorption capacity, ion exchange capacity, or swelling ability that can influence macroscopic properties of the rocks. CO_2 sorption experiments on clay minerals in shales performed at 50 °C and total pressure less than 20 MPa (Busch et al. 2008; Wollenweber et al. 2010) demonstrated a maximum sorption capacity of 1 mmol/g for pCO_2 of 7 to 12 MPa. This phenomenon could expand the CO_2 storage capacity of caprocks in case of leakage. However, swelling sorption can decrease permeability and result in microcracks, with an increased risk of leakage. Implications of sorption on caprock integrity are not fully understood and require further research.

To simulate a CO_2 leak through fractured caprocks, CO_2-rich brines and CO_2-gas were alternately flowed through a fractured claystone in a plug flow apparatus (Andreani et al. 2008). An abrupt increase of the fracture aperture occurred after each gas flow. The aperture increase is controlled by the decohesion of the clay framework induced by acidification from the CO_2 gas. Numerical simulation of kaolinite/CO_2-brine/kaolinite interaction at crystal scales suggest repulsion between kaolinite aggregates in acidic solutions (Pèpe et al. 2010). This process is expected to produce a progressive decrease of the capacity of the caprock to maintain its seal. In contrast, an opposing process may be induced in clays with a high swelling capacity, like Na- or Ca-saturated montmorillonite, after exposure to supercritical CO_2, suggesting again that CO_2 may be trapped by intercalating the interlayer region (Schaef et al. 2012; Romanov 2013; Tokunaga and Wan 2013, this volume). However, other studies observed that supercritical CO_2 partially saturated with H_2O can still dehydrate clays (Ilton et al. 2012). Hence, if the supercritical CO_2 flux is significant, the potential increase of permeability may lead to caprock failure.

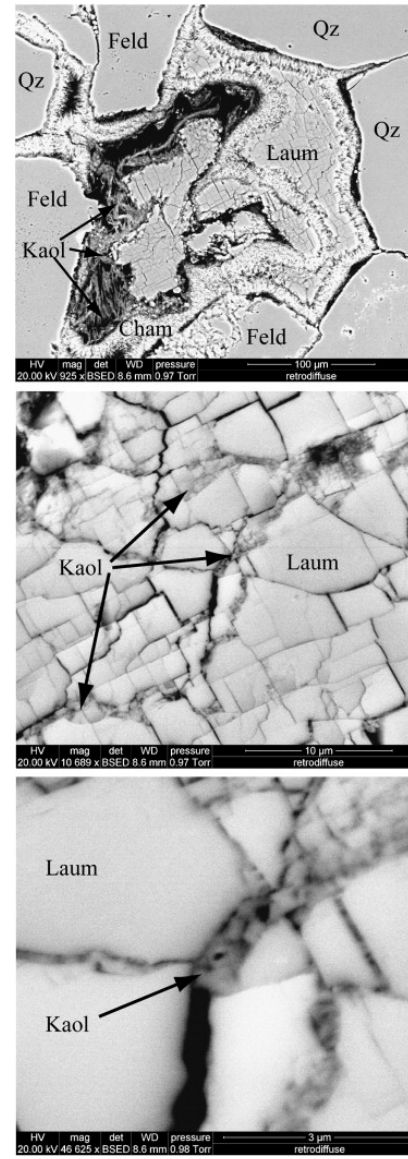

Figure 7. SEM images of laumontite dissolution features and kaolinite precipitation in CO_2 percolation experiments through chlorite/zeolite-rich sandstone samples from the Pretty Hill Formation (Otway Basin, Australia). Dissolution of laumontite and chamosite are the potential sources of calcium, iron and magnesium required for carbonate precipitation. The experiment emulates in situ temperature and pressure conditions (95 °C and 10 MPa) [Used by permission of Elsevier, from Luquot et al. (2012), *Chem Geol*, Vol. 294-295, Fig. 7, p. 82.].

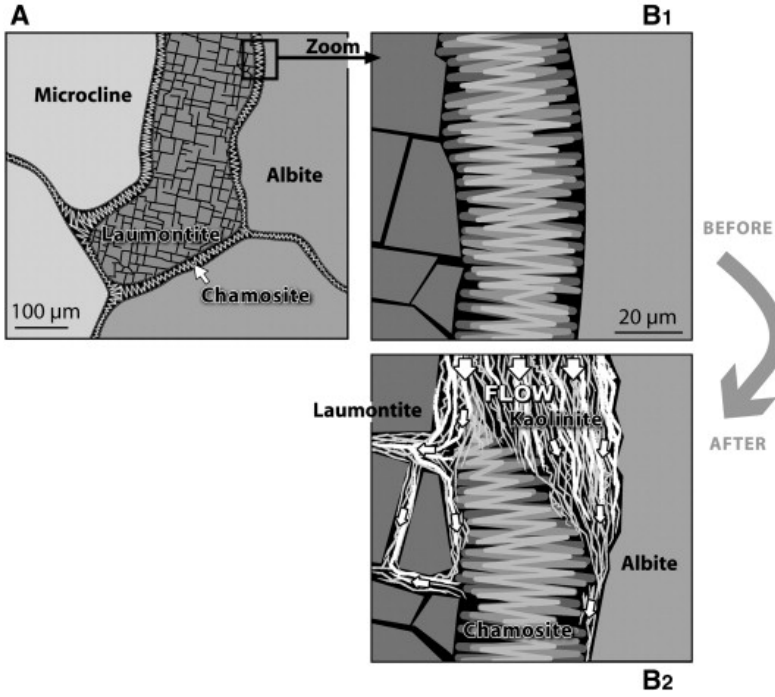

Figure 8. Sketch illustration of laumontite, chamosite and feldspars dissolution and kaolinite precipitation in Figure 7, explaining reactive surface and permeability decrease with time. Permeability decreases of about one order of magnitude due to the localization of the kaolinite precipitation in the main flow paths, while porosity increases. [Used by permission of Elsevier, from Luquot et al. (2012), *Chem Geol*, Vol. 294-295, Fig. 14, p. 86.].

Few phyllosilicates react directly to produce carbonate minerals, instead phyllosilicates serve as a source of divalent cations for formation of carbonates. The only layered phases proposed for direct carbonation reactions are serpentines (phyllosilicate group) and brucite (hydroxide group); both have been tested experimentally under conditions relevant to GCS using batch reactors or microreactors. As with olivine or pyroxene, the reaction kinetics must be accelerated in order to develop an economically feasible GCS process. Exploitation of brucite from mine tailings has been proposed for *ex situ* CO_2 storage via processing in industrial reactors (e.g., Lin et al. 2008; Zhao et al. 2010; Power et al. 2013, this volume). Its dissolution rate increases with decreasing pH and increasing $NaHCO_3$ concentration (Hövelmann et al. 2012b). The rate of the carbonation process increases with pCO_2 and HCO_3^- in solution, similar to olivine. At high pCO_2, the CO_2 uptake is the limiting process (Harrison et al. 2013). Surprisingly, hydrated carbonates like nesquehonite ($MgCO_3 \cdot 3H_2O$) are the predominant product, whereas magnesite is predicted. Magnesite may form after brucite at greater than 50 °C and but definitely at 75 °C (Schaef et al. 2011). These authors also show that brucite carbonation is not effective in anhydrous supercritical CO_2 and that the conversion of brucite to carbonate increases rapidly with increased water content of the fluid. Like brucite, serpentine can be harvested from asbestos mines, but it is also very abundant in ultramafic reservoirs. Hence its behavior with CO_2-rich fluid is of interest for both *ex situ* and *in situ* solutions. As with brucite and olivine, carbonation is optimized by adding NaCl and $NaCO_3$ to the heated solution. The dissolution of serpentine during carbonation first produces an amorphous silica-

rich layer before magnesite precipitates. This layer is the limiting step for cation diffusion and reduces reaction progress (Schulze et al. 2004). Pre-heating (up to 630 °C) and grinding have been proposed to optimize *ex situ* CO_2 processing by causing dehydroxylation and increasing reactive surface area, respectively.

Quartz

Relatively little attention has been paid to the solubility of quartz in the context of GCS, primarily because quartz solubility is not enhanced by reduction in pH (Knauss and Wolery 1988). Indeed, significant dissolution of CO_2 in water lowers quartz solubility (Walther and Orville 1983). Furthermore, detrital quartz grains possess relatively small effective surface areas compared to many other silicates, such as clays or partially weathered feldspars (Sardini et al. 1995). Rates of quartz dissolution are likewise independent of pH below values around 6 (Knauss and Wolery 1988). Under near neutral conditions, rates of quartz dissolution are enhanced by the presence of cations in solution, with sodium and calcium giving rise to a greater enhancement than magnesium (Dove 1999 and references therein, Fig. 9). Interestingly, further investigation of this effect indicates that the mechanism may also enhance release of silica from other silicate minerals (Wallace et al 2010). Most data are for far from equilibrium conditions, but Davis et al. (2011) have reported results for near-equilibrium dissolution in mildly alkaline solutions. At relatively low temperatures appropriate for GCS (up to about 125 °C), quartz dissolution rates agree well with the predictions of Bickmore et al. (2008), but they are slower than expected at higher temperatures (greater than 200 °C) (Davis et al. 2011).

While quartz dissolution rates should be rather slow, Houston et al. (2007) reported evidence for silica dissolution into injected seawater during a seawater enhanced oil recovery operation in the Miller Field, UK North Sea, but suggested that it was released from feldspars or other silicate minerals, rather than directly from quartz dissolution. Carroll et al. (2013), in a study of reactivity of reservoir and caprocks with CO_2, even reported amorphous silica precipitation from silica released during clay transformations. Overall, injection of CO_2 into existing formation waters is unlikely to have a significant effect on the amount of silica in solution, although it may lead to silica being redistributed from feldspars to clays. Where water is also injected and is undersaturated with silica under reservoir conditions, net dissolution of silica can be expected, but this may not be released directly from quartz if other silicates are present. Under relatively high-temperature conditions (200 °C) Kaszuba et al. (2003) did however report the development of etch pits on quartz grain surfaces.

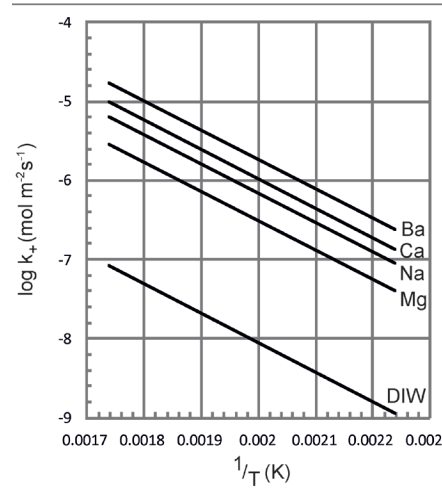

Figure 9. Effect of chloride salts on quartz solubility under conditions relevant to GCS [Used by permission of Publishing Company, from Dove (1999), *Geochim Cosmochim Acta*, Vol. 63, Fig. 3, p. 3722.].

Carbonates

Carbonate behavior in aqueous solutions is often quite distinctive from that of silicates; for example, carbonates exhibit retrograde solubility under conditions relevant to GCS. It has long been appreciated that many carbonates react more quickly than silicates with acidified pore fluids, and they probably play a key role in controlling fluid pH and composition in the rapidly-moving fluid packet ahead of an advancing CO_2 plume (Fig. 1). There are many studies

of calcite and dolomite dissolution rates in the literature and more limited data for magnesite, siderite and other carbonates (e.g., Morse and Arvidson 2002; Golubev et al. 2009; Pokrovsky et al. 2009a,b; Schott et al. 2009).

In addition to classical reaction rate studies on carbonate minerals, some recent studies have used high-resolution imaging to document the movement of specific surface steps on cleavage planes. Xu et al. (2013) used hydrothermal atomic force microscopy to monitor dolomite dissolution in solutions of varying ionic strength. They were able to document increased dissolution rates in more concentrated solutions, although bulk experiments of Pokrovsky et al. (2005) found little influence of ionic strength in solutions up to 1 molar.

Much early work on carbonate mineral solubility was aimed at weathering studies and so used CO_2 pressures less than 0.1 MPa. This work provided an overview of carbonate dissolution rates and allowed the development of models for carbonate dissolution (Pokrovsky et al. 1999a,b; Morse and Arvidson 2002) but could not evaluate whether pCO_2 influenced dissolution rates other than through the effect on pH. Pokrovsky et al. (2005) carried out rotating disc batch experiments to determine calcite and dolomite dissolution rates at pCO_2 greater than 5.5 MPa and 25 °C, with pH measured directly, and also measured dissolution of these minerals as powders in a mixed-flow reactor. Magnesite dissolution rates were also measured at elevated pCO_2 on powders using a batch reactor. Overall, the results of this work showed that carbonate dissolution rates are not strongly dependent on pCO_2 except through the influence that it exerts on pH, and only weakly dependent on ionic strength up to 1 molar NaCl. In particular, the effect of pCO_2 was not significant at pressures greater than about 1 MPa. For magnesite and dolomite, dissolution rates can be predicted at pCO_2 values up to 5 MPa by the Surface Complexation Models of Pokrovsky et al. (1999a,b).

Subsequently, Pokrovsky et al. (2009b) presented experimental results for calcite, magnesite and dolomite in 0.1 molar NaCl at temperatures to 150 °C, and presented an empirical fit to the experimental data for a range of pH values. This work showed only a small dependence of dissolution rate on temperature, with the highest rates at around 100 °C. Figure 10 shows the dissolution rates of these three carbonates at 60, 100 and 150 °C as a function of pCO_2 and demonstrates the order of magnitude differences between them. The calculations were performed for pH of about 4 and a rather dilute (0.1 molar NaCl) matrix. On the basis of these results it appears that carbonate dissolution rates are not strongly dependent on either temperature or pCO_2 over the range of conditions likely to be encountered in GCS sites.

Surface reaction rates of calcite are so fast in acid to neutral fluids that in practice reactivity in a calcite-bearing geological reservoir will always be transport controlled (Sjöberg 1983; Morse and Arvidson 2002). Surface reaction rates of calcite are therefore not in general relevant to GCS problems and it is the rate of dissolution and transport of CO_2 that dictates how fast calcite dissolves. Dolomite is slower to react than calcite but its dissolution may also be transport controlled in many situations (Pokrovsky et al. 2005). Magnesite is, however, even slower to react than dolomite under conditions relevant to GCS, and for magnesite the dissolution rate may well be controlled by surface reaction.

Sulfates

Sulfate minerals, predominantly anhydrite but also gypsum, are common accessory minerals in sedimentary rocks that comprise GCS reservoirs and caprocks. Anhydrite can also be a major mineral in an evaporate caprock. In addition, anhydrite may serve as a mineral trap for sulfur in CO_2-SO_2 co-sequestration (Knauss et al. 2005; Xu et al. 2007; Kaszuba et al. 2011; Chopping and Kaszuba 2012). The predominant reaction involving SO_2 in geologic carbon sequestration, and in water-rock systems in general, is the disproportionation reaction

$$4SO_2 + 4H_2O = 3H_2SO_4 + H_2S \quad (1)$$

(Holland 1965; Getahun et al. 1996; Palandri and Kharaka 2005; Palandri et al. 2005; Kaszuba et al. 2011; Chopping and Kaszuba 2012). Anhydrite may precipitate in response to the subsequent increase in dissolved sulfate.

As with carbonate minerals, sulfates exhibit retrograde solubility under conditions relevant to GCS. Reaction kinetics for sulfate minerals are also orders of magnitude faster than many of the silicate minerals (Palandri and Kharaka 2004 and references therein), thus anhydrite readily precipitates and dissolves at laboratory time scales. The most important control on the precipitation and dissolution of anhydrite is the concentration of dissolved sulfate. Experiments have been conducted with a wide range of aqueous sulfate concentrations. Some experiments contain no aqueous sulfate in the initial brine, others contain sufficient sulfate to saturate or supersaturate brine with respect to anhydrite. Interpretation of anhydrite behavior in experiments must take into account the parameters at which the experiments are performed, including brine chemistry (ionic strength) and temperature.

Anhydrite dissolves in batch experiments evaluating reactions among rocks containing anhydrite, brine containing no aqueous sulfate, and supercritical CO_2. Such is the case for experiments evaluating the Eau Claire Formation, the shale caprock for the Mount Simon sandstone in the Midwestern United States (Liu et al. 2012), and the Stuttgart Formation, the sandstone reservoir for the pilot storage site at Ketzin, Brandenburg, Germany (Fischer et al. 2010). It is conceivable that gypsum may replace anhydrite at the temperatures of these experiments (56 °C and 40 °C, respectively), but no gypsum was reported in either study.

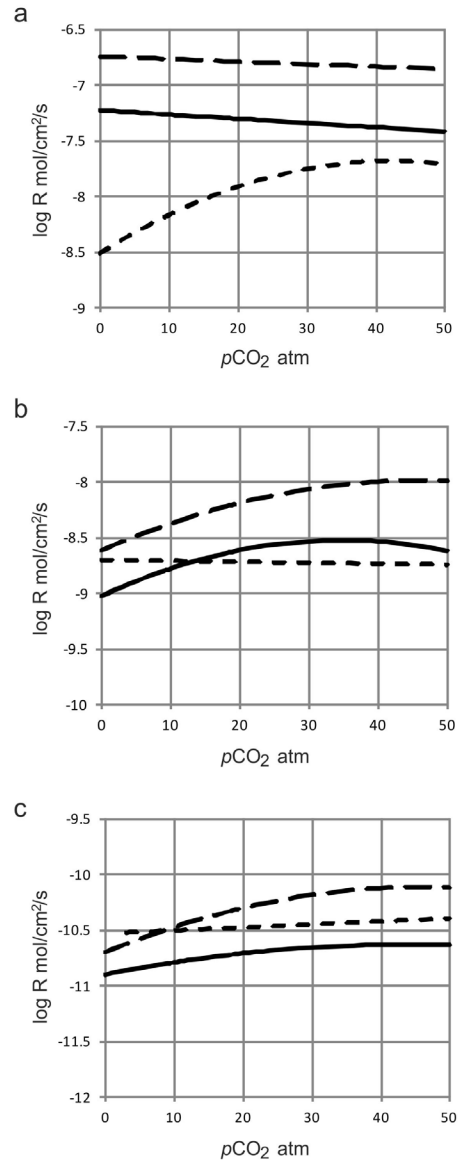

Figure 10. Dissolution rates of carbonate minerals as a function of pCO_2, calculated from the equations of Pokrovsky et al. (2009b) for a 0.1molar NaCl solution with pH = 4. a) calcite, b) dolomite, c) magnesite. Solid lines are calculated for 60 °C, long dashed lines for 100 °C and short dashed lines for 150 °C.

Anhydrite does not react in a coreflood experiment evaluating reactions in the Three Fingers evaporite unit, the lower part of the caprock at the Weyburn-Midale reservoir, Saskatchewan, Canada (Smith et al. 2013). The brine used in this study was formulated to emulate a typical *in situ* brine that is near equilibrium with anhydrite, slightly saturated with respect to calcite and dolomite,

and equilibrated with CO_2 at a pressure of 3 MPa. Dolomite dissolved during the experiment in response to the acidity of the brine. Anhydrite, however, did not react because anhydrite stability is not sensitive to pH and because the brine injected into the rock was already close to equilibrium with anhydrite. Dissolution of the dolomite matrix physically mobilized anhydrite crystals, a finding with potential implications for redistributing permeability and porosity in the rock.

Anhydrite precipitates in a series of hydrothermal batch experiments using Dickson cells that were performed to evaluate CO_2-water-rock interactions in carbonate rocks from the Leadville Limestone Formation, Paradox Valley, Colorado, United States (Rosenbauer et al. 2005). Injection of supercritical CO_2 dissolves calcite in these experiments. Dolomite precipitates in experiments containing high-sulfate brine but dissolves in experiments containing low-sulfate brine. This study reported similar results for carbonate rocks reacted with high-sulfate brine but no CO_2. Anhydrite also precipitated in a series of batch experiments evaluating CO_2-water-rock interactions in the Madison Limestone of the Moxa Arch, Southwest Wyoming, United States (Chopping and Kaszuba 2012). Following injection of supercritical CO_2, dolomite and calcite dissolve due to increased acidity whereas anhydrite precipitates (Fig. 11). Reaction-path calculations suggest that dolomite will become stable and precipitate once acidity in the brine is fully buffered by the rock (Fig. 12).

Similar behavior is observed in experiments that evaluate co-injection of SO_2 with CO_2 into Madison Limestone (Chopping 2011) and into arkose (Mandalaparty et al. 2011). Carbonate minerals dissolve in response to the increased acidity whereas anhydrite precipitates in response to the increase in dissolved sulfate (Eqn. 1). Pronounced calcite dissolution is attributed to increased acidity due to SO_2 co-injection (Chopping 2011). Carbonate dissolution buffers the acidity such that pH values are similar to values observed for CO_2 injection (approximately pH 5); increased acidity predicted by computer models (e.g., Knauss et al. 2005) is not observed.

Collectively, these experiments demonstrate that co-injected SO_2 and CO_2 increases aqueous sulfate concentrations, precipitates anhydrite, acidifies the water and dissolves carbonate minerals. All of these reactions will take place in the acidified water ahead of the CO_2 front (Fig. 1, Location A). These experiments also demonstrate that injection of CO_2 (without SO_2) will lead to anhydrite precipitation if sufficient aqueous sulfate is present. Mineral-fluid interactions will neutralize some of this carbonic acidity, resulting in a rise in pH and reprecipitation of carbonate minerals.

Sulfides

Sulfide minerals, most commonly pyrite, are common accessory minerals in sedimentary rocks that comprise the reservoirs and caprocks targeted for geologic carbon sequestration. Dissolution of pyrite can augment mineral storage by providing Fe^{2+} for siderite and ankerite. Pyrite can also be important in CO_2-SO_2 co-sequestration due to the increase in dissolved sulfide (Eqn. 1). On the other hand, oxidized impurities in the CO_2 will oxidize pyrite, generate sulphuric acid, and potentially decrease pH to values lower than injection of CO_2 without impurities. However, SO_2-CO_2 injection in batch reactions with Madison Limestone showed no significant pH decrease. Much would depend on the rate at which oxidized impurities are supplied; even feldspars will neutralize additional acid as it is generated if oxidants are not delivered too quickly.

Very few experimental studies report results for pyrite precipitation or dissolution. Pyrite precipitates due to alteration of basaltic glass beginning at temperatures of 150-250 °C (Gysi and Stefansson 2012). Siderite precipitates near pyrite in response to CO_2 injection (Liu et al. 2012). In the CO_2-water-Madison Limestone experiments of Chopping and Kaszuba (2012), pyrite exhibits minor dissolution textures that developed in response to injection of CO_2. Finally, pyrite forms in experiments that evaluate hematite and goethite dissolution (section on

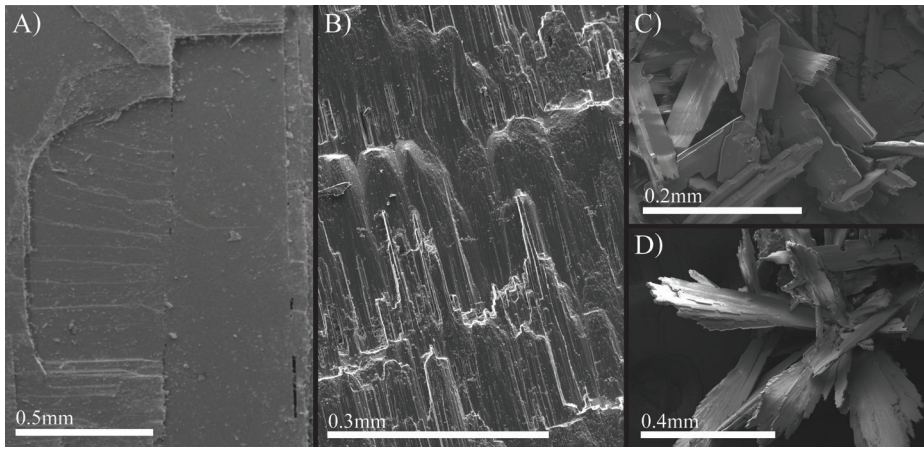

Figure 11. FE-SEM micrographs of anhydrite. Scale bars vary among the images. A) Unreacted anhydrite used in experiments conducted in flexible cell batch reactors at 110 °C and 25 MPa. B) Anhydrite recovered from experiment reacting brine with dolomite, calcite, anhydrite, and pyrite. The brine is approximately saturated with respect to anhydrite. Dissolution textures are evident. C) and D) Euhedral anhydrite crystals that precipitated in experiments containing brine, dolomite, calcite, pyrite, ± anhydrite (C and D, respectively). Anhydrite precipitated in response to injection of supercritical CO_2. The brine is slightly undersaturated with respect to anhydrite at the time the CO_2 was injected [Used by permission of Elsevier, from Chopping and Kaszuba (2012), *Chem Geol*, Vol. 322–323, Fig. 5, p. 231.].

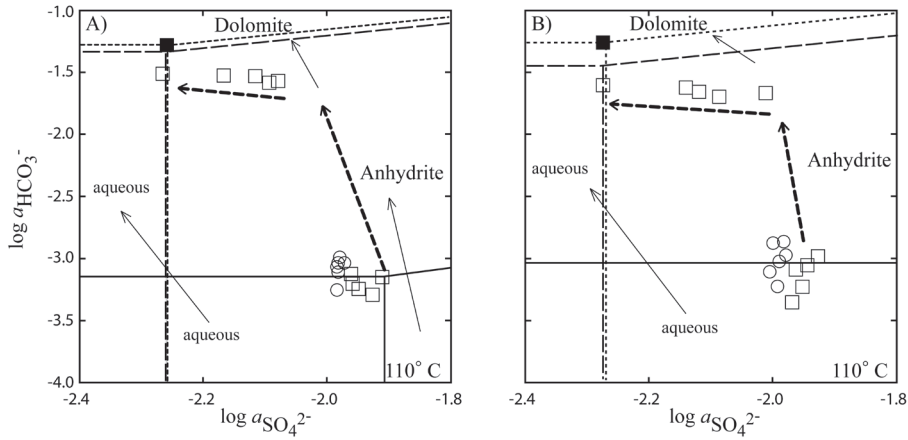

Figure 12. Geochemical evolution of $scCO_2$-brine-rock experiments in the CaO-CO_2-SO_4^{2-}-H_2O system at 110 °C. Stability fields for dolomite, anhydrite, and aqueous fluid at *in situ* conditions prior to (solid lines) and after (long dashed lines) injection of $scCO_2$ are depicted. Stability fields predicted for equilibrium conditions in the $scCO_2$-brine-rock experiments (short dashed lines, filled square) are also depicted. A) Diagram plotting log $a_{HCO_3^-}$ versus log $a_{SO_4^{2-}}$ for ±$scCO_2$-brine-Do-Cc-Anh-Py experiments. Aqueous samples are plotted for brine-Do-Cc-Anh-Py experiment (open circles) and $scCO_2$-brine-Do-Cc-Anh-Py experiment (open squares). The temporal sequence of samples in the $scCO_2$ experiment defines a reaction path trajectory (bold dashed arrows) towards the dolomite saturation boundary. B) Diagram plotting log $a_{HCO_3^-}$ versus log $a_{SO_4^{2-}}$ for ±$scCO_2$-brine-Do-Cc-Py experiments. Aqueous samples are plotted for brine-Do-Cc-Py experiment (open circles) and $scCO_2$-brine-Do-Cc-Py experiment (open squares). The temporal sequence of samples in the $scCO_2$ experiment defines a reaction path trajectory (bold dashed arrows) towards the aqueous stability field. Anhydrite field appears after injection of supercritical CO_2 [Used by permission of Elsevier, from Chopping and Kaszuba (2012), *Chem Geol*, Vol. 322–323, Fig. 7, p. 233.].

iron oxyhydroxides, below).

Iron oxyhydroxides

Although not as abundant as silicate minerals, Fe^{3+}-bearing oxyhydroxide minerals occur in sedimentary rocks, especially redbeds, which are generally thick and widely distributed. Fe^{3+}-bearing oxyhydroxide minerals can promote mineral storage via reactions forming siderite and ankerite, if the minerals can be dissolved and aqueous Fe^{3+} reduced to Fe^{2+}. Hematite and goethite in particular have been the subject of studies coupling mineral dissolution and iron reduction. Hematite has also been proposed as an important mineral for geologic co-sequestration of SO_2

$$Fe_2O_3 \text{ (hematite)} + 2CO_2 + SO_2 + H_2O = 2FeCO_3 \text{ (siderite)} + H_2SO_4 \quad (2)$$

(Palandri and Kharaka 2005; Palandri et al. 2005).

Hydrothermal batch experiments using Dickson cells and performed at 150 °C and 30 MPa in 1.0 molal NaCl solution demonstrate that hematite and goethite dissolve, aqueous Fe^{3+} reduces to Fe^{2+}, and siderite precipitates in response to co-injection of supercritical CO_2 and SO_2 (Palandri et al. 2005; Garcia et al. 2012b). Roughly 0.05 to 0.1 vol% of the hematite and 2.4 vol% of the goethite reacted to siderite in these experiments. Other minerals that precipitated in the hematite-bearing experiment are pyrite (and or amorphous iron sulfide), dawsonite ($NaAlCO_3(OH)_2$), and native sulfur. Dawsonite probably precipitated in response to injection of NaOH immediately before the experiment was terminated (Palandri et al. 2005). As may be expected, goethite reacted to form siderite quicker than hematite (576 vs. 611 hours). Kinetic dissolution rates for goethite have not been determined at low pH. At neutral pH, goethite dissolution rates (~10^{-8} mol/m^2/s) are indeed much faster than hematite dissolution rates (~10^{-15} mol/m^2/s) (Palandri and Kharaka 2004 and references therein). At low pH, hematite dissolution rates are around 10^{-9} mol/m^2/s. Rapid dissolution of Fe^{3+}-bearing oxyhydroxide minerals will be important in continental redbed sandstones (Palandri and Kharaka 2005).

Iron oxyhydroxide minerals also reacted rapidly to form siderite and native sulfur or pyrite in a sequence of experiments performed at lower temperature (70 and 100 °C) and pressure (8.2 to 8.3 MPa) (Murphy et al. 2010; Lammers et al. 2011; Murphy et al. 2011). These studies employed two different types of apparatus, a micoreactor configured to perform *in situ* infrared spectroscopy and a standard batch reactor. Mineral dissolution, reduction of iron, and subsequent precipitation of siderite occurred on exceedingly short time scales (< 1 hour). Nanocrystals of several iron oxyhydroxide minerals were evaluated, including hematite, ferrihydrite, and iron hydroxide polymorphs (goethite, lepidocrocite, or akaganeite). The NaCl solutions injected with supercritical CO_2 in these experiments contained aqueous hydrogen sulfide as a proxy for co-injected SO_2. Finally, hematite nanocrystals precipitated in batch hydrothermal experiments performed at 150 °C and 20 MPa in CO_2-saturated 0.5 molar NaCl solution in a batch reactor (Montes-Hernandez and Pironon 2009). Iron-bearing montmorillinite (plus iron from the reactor walls) reacted to form hematite in 15 days and hematite + siderite in 60 days.

Reservoir and cap rocks

A number of studies have investigated the effect of CO_2-saturated fluids on rocks, most commonly in plug flow reactors. The overwhelming conclusion from such studies is that reactions with natural rocks are dominated by carbonate dissolution, in accordance with results of field trials (Lu et al. 2012). Kjøller et al (2011) found that even after 13 months at 70 °C and 20 MPa, carbonate dissolution was the predominant process with calcite, dolomite and siderite dissolving in different rock types. By comparison, clay minerals and feldspars did not react, possibly because the carbonate reactions prevented low pH conditions from being attained. In contrast, experiments by Carroll et al. (2013) on sandstone and shale at 51 °C and 19.5 MPa

found that Fe-rich clays appear to have dominated the reactions, dissolving incongruently to secondary clays and amorphous silica.

The effects of reactivity on petrophysical properties of reservoir rocks have been investigated in several studies. Canal et al. (2013) measured changes in porosity due to calcite dissolution and found a marked increase in permeability and changes to seismic velocities. Bachaud et al. (2011) measured increased porosity in limestone caprock; in contrast, permeability remained low in these experiments. Hangx et al. (2010) carried out creep tests on sandstones partially cemented by calcite and found that reaction of the calcite did not affect rock strength. Busch et al. (2008) evaluated diffusive loss of CO_2 through a 100 m thick clay-rich, carbonate poor caprock. They determined that diffusive gas breakthrough occurs at the top of the caprock after approximately 0.3 Ma. Their experimental results also suggest that shale caprocks provide additional CO_2 storage capacity, predominantly through sorption (see discussion on phyllosilicates), but the related geochemical and mineralogic processes were not well constrained.

Experiments on natural rock cores provide a test for computer models (Canal et al. 2013) and have been used to investigate trapping mechanisms (Iglauer et al. 2011) and the effect of reactivity on the physical properties of reservoir rocks (Hangx et al. 2010). In the event that GCS is implemented commercially, it seems likely that such measurements will be an important part of site characterization and evaluation. An obvious limitation is the complexity of natural rocks which can make it difficult to extract fundamental data. Some workers have carried out column experiments using packed mineral grains of known composition and abundance instead of natural rock cores to try to address this issue. Bateman et al. (2010) carried out an extended (3.5 month) experiment flowing a synthetic brine pre-saturated with CO_2 through a 1 m column packed with a mix of calcite, labradorite and quartz. In addition to monitoring the outflow fluid, the changes to the solid constituents were investigated along the length of the column. Over much of its length, calcite was completely dissolved and labradorite showed some evidence of pitting. Near the outflow however, there was evidence for new precipitation of calcite cement, apparently the result of neutralizing of acidity by silicate reactions.

SUMMARY AND CONCLUSIONS

This brief review has demonstrated the considerable breadth of experimental data that is available for mineral dissolution and precipitation due to CO_2-water-rock interactions as well as the diversity of laboratory techniques used to acquire these data. In particular, a sizeable dataset quantifying the dissolution rates of minerals likely to be of significance for Geological Carbon Storage has been assembled. We hope this review has also demonstrated that further laboratory experiments, particularly kinetic measurements, are needed for conditions close to those likely to be encountered in CO_2 reservoirs. Here, pore fluids are likely to be already close to equilibrium with their host rocks prior to CO_2 injection, and will respond primarily to the lowering of pH which results as CO_2 dissolves into pore waters.

Despite limitations in our understanding, a number of important conclusions can be drawn about CO_2-water-rock interactions, particularly with respect to relative rates, that may be of value for the design of sequestration schemes. The fastest minerals to respond to the changes in fluid chemistry induced by CO_2 injection are calcite, anhydrite and dolomite. When present in the reservoir, these minerals serve to raise pH on a timescale of days in response to dissolution of CO_2 in formation waters, and as a result may further inhibit the slower response of silicate minerals to injection. Nevertheless, silicate reactions may take place within the lifetime of an injection site. Conversion of feldspars to secondary clay minerals is likely to be an important reservoir reaction, but at present the rates of such reactions are difficult to predict because they may be more dependent on the rate of precipitation of the secondary phases than on feldspar

dissolution. This is important, because the secondary minerals may reduce permeability significantly and if this happens on the timescale of the original injection, it could reduce reservoir capacity. Impurities co-injected with CO_2 may provide new sources of acidity as well as dissolved solutes that may promote precipitation of new minerals and additional growth of preexisting minerals. Along main flow paths exhibiting high permeability, fluid composition will likely be dominated by the injected fluid; more protected areas exhibiting reduced flow may instead retain rock-dominated fluids. Over time, mineral dissolution and precipitation may progressively modify flow pathways and shift the types of reaction taking place. These processes will collectively determine the interplay between reaction kinetics and mass transport processes in CO_2 reservoirs.

DIRECTIONS FOR FUTURE WORK

Upscaling experimental laboratory data to reservoir scale is one of the most challenging issues to predicting the long-term fate of CO_2 in reservoirs that display an evolving reactivity. Reactive-transport modeling uses kinetic data determined from laboratory experiments to predict larger scale behavior, but two main issues need to be addressed to achieve better predictions. First, the interplay between chemical reactions, changing rock geometry, and hydrodynamic properties is crucial but not well constrained. This interplay notably controls fluid accessibility to reaction sites and the evolution of reactive surface areas. The latter may vary significantly in natural systems compared to those estimated for powders used in experiment because preferential flow paths can be created depending on the local flow rate. All these parameters vary from one rock to another and are strongly dependent on the departure from equilibrium (ΔG) of the fluid-rock reaction. Experiments at intermediate ΔG, below values expected for the injection site, are rare but very useful to constrain the evolution of reaction rate, porosity and permeability as a function of pCO_2. The experimental measurement of characteristic non-dimensional numbers that describe the timescale of reaction versus the one of transport (Damkholer number) under various conditions may also help to upscale the laboratory-scale processes. Second, reaction-transport modeling usually follows a macroscopic approach, using chemical properties averaged at the scale of a representative elementary volume (REV) that depends on rock structure. This approach fails to describe the complex spatial arrangement of rock-forming minerals, especially in polymineralic rocks, the connectivity of pores as it relates to accessible reactive surface area (Landrot et al. 2012), or the resulting heterogeneities in geochemical reactions. This has been emphasized in experiments in which dissolution and precipitation can both occur during fluid flow through the rock. From an experimental point of view, it is necessary to combine batch and dynamic approaches to discriminate between the intrinsic properties of minerals and the effect of rock structure on macroscopic reaction rates. Identifying the processes that control the overall behavior of the reservoir will inform decisions and assumptions needed to simplify computer models of reservoir and caprock behavior.

Taking the large-scale view to try to understand reservoir injection and storage, we can identify several areas where more work is needed. Experimental studies performed to date underline difficulties in predicting the behavior of caprocks and clay-rich lithologies in presence of a CO_2-rich fluid. Batch experiments on powders allow characterization of numerous properties of phyllosilicates; however, they fail to predict the macroscopic behavior of a real rock. Many opposing processes, such as CO_2 sorption, swelling, and sheet repulsions in an acidic media can occur simultaneously in nature. The extent to which these processes will occur depends on the fluid composition and the mineralogy and structure of the rock. The resulting macroscopic implications on caprock integrity are not fully understood and require further research.

An important target for GCS is the creation of enhanced residual or capillary trapping of CO_2 as isolated bubbles surrounded by water, and therefore physically captured by capillary

forces (Qi et al. 2009; Tokunaga and Wan 2013, this volume). Although capillary trapping has been achieved in the laboratory on a short time scale (Iglauer et al. 2011), the experiments were only of short duration. Experiments evaluating the long-term stability of capillary trapping are needed because this trapping mechanism will depend on chemical processes since CO_2 is relatively soluble in water. Long-term experiments are also needed to evaluate whether the chemical connectivity between apparently isolated bubbles, through their solubility in the enclosing medium, has any effect on the stability of this trapping mechanism.

Most carbonation experiments conducted under GCS conditions have focused on the conversion of CO_2 into carbonate minerals. However, companion redox reactions may occur. Luquot et al (2012) showed that CO_2 may be converted into reduced carbon when injected in a ferrous iron-bearing sandstone reservoir, resulting in the precipitation of poorly-crystallized graphite. In mafic and ultramafic reservoirs, the oxidation by H_2O of the ferrous iron component of olivine or pyroxene can result in H_2 production (Stevens and McKinley 2000; Marcaillou et al. 2011). In CO_2-poor experiments, a part of the CO_2 is reduced to methane and possibly more complex carbon compounds (McCollom 2013). If magnesite precipitation after olivine is faster than iron oxidation under high pCO_2 (Jones et al. 2010), pCO_2 gradients in natural reservoirs may produce regions where hydration, carbonation and redox reaction compete, inducing a risk of CH_4 production that could alter storage integrity. In addition, the fraction of CO_2 possibly converted abiotically into heavier organic compounds is totally unknown, whatever the type of reservoir and the pressure, temperature, and pCO_2 conditions. The stability of such an organic fraction is also of interest for long-term safety. Redox reactions associated with CO_2 may strongly influence the fate of CO_2 and need to be experimentally investigated. The effect of CO_2 on the redox potential of the system also requires examination. It will be worth considering both problems under abiotic and biotic conditions since H_2 and CH_4 can be associated with autotrophic microbial activity.

ACKNOWLEDGMENTS

John Kaszuba is grateful to his students Curtis Chopping, Virginia Marcon, and Mary Kate McCarney and his colleague Geoffrey Thyne. Acknowledgment is made to the Donors of the American Chemical Society Petroleum Research Fund and to the UW School of Energy Resources for partial support. Bruce Yardley is indebted to his colleagues and students Murray Allan, Jorgen Rosenqvist, Andrew Kilpatrick and Benoit Lamy-Chappuis for many insights into experimental studies of mineral reactivity, and to collaborators in the NERC-funded CRIUS consortium for much advice and discussion, in particular Chris Rochelle and Keith Bateman (BGS) and Mike Bickle, Niko Kampman and Benoit Dubacq (Cambridge). The authors thank Dave Cole for his insightful review.

REFERENCES

Alemu BL, Aagaard P, Munz IA, Skurtveit E (2011) Caprock interaction with CO_2: A laboratory study of reactivity of shale with supercritical CO_2 and brine. Appl Geochem 26(12):1975-1989

Allan MM, Turner A, Yardley BWD (2011) Relation between the dissolution rates of single minerals and reservoir rocks in acidified pore waters. Appl Geochem 26:1289-1301

Allen DE, Strazisar BR, Soong Y, Hedges SW (2005) Modeling carbon dioxide sequestration in saline aquifers: Significance of elevated pressures and salinities. Fuel Proc Tech 86:1569-1580

Amrhein C, Suarez DL (1992) Some factors affecting the dissolution kinetics of anorthite at 25 °C. Geochim Cosmochim Acta 56(5):1815-1826

Andreani M, Gouze P, Luquot L, Jouanna P (2008) Changes in seal capacity of fractured claystone caprocks induced by dissolved and gaseous CO_2 seepage. Geop Res Lett 35(14), doi:10.1029/2008gl034467

Andreani M, Luquot L, Gouze P, Godard M, Hoisé E, Gibert B (2009) Experimental study of carbon sequestration reactions controlled by the percolation of CO_2-rich brine through peridotites. Environ Sci Technol 43(4):1226-1231

Andreani M, Daniel I, Pollet-Villard M (2013) Aluminium speeds up the hydrothermal alteration of olivine. Am Mineral, in press

Bachaud P, Berne P, Renard F, Sardin M, Leclerc JR (2011) Use of tracers to characterize the effects of a CO_2-saturated brine on the petrophysical properties of a low permeability carbonate caprock. Chem Eng Res Design 89(9):1817-1826

Barnes HL (1971) Investigations in hydrothermal sulfide systems. *In*: Research Technques for High Pressure and High Temperature. Ulmer GC (ed) Springer-Verlag, pp 317-335

Bateman K, Rochelle C, Lacinska A, Wagner D (2010) CO_2-porewater-rock reactions – Large scale column experiment (Big Rig II). Energy Procedia 4:4937-4944

Béarat H, McKelvy MJ, Chizmeshya AVG, Gormley D, Nunez R, Carpenter RW, Squires K, Wolf GH (2006) Carbon sequestration via aqueous olivine mineral carbonation: Role of passivating layer formation. Environ Sci Technol 40(15):4802-4808

Bickle M, Kampman N, Wigley M (2013) Natural analogues. Rev Mineral Geochem 77:15-71

Bickmore BR, Wheeler JC, Bates B, Nagy KL, Eggett DL (2008) Reaction pathways for quartz dissolution determined by statistical and graphical analysis of macroscopic experimental data. Geochim Cosmochim Acta 72(18):4521-4536

Blum A, Lasaga A (1988) Role of surface speciation in the low-temperature dissolution of minerals. Nature 331:431-433

Bodnar RJ, Steele-MacInnis M, Capobianco RM, Rimstidt JD, Dilmore R, Goodman A, Guthrie G (2013) PVTX Properties of H_2O-CO_2-"salt" at PTX conditions applicable to carbon sequestration in saline formations. Rev Mineral Geochem 77:123-152

Brantley SL, Kubicki JD, White AF (eds) (2008) Kinetics of Water-Rock Interaction. Springer, New York

Brantley SL, Mellott NP (2000) Surface area and porosity of primary silicate minerals. Am Mineral 85(11-12):1767–1783

Burch TE, Nagy KL, Lasaga AC (1993) Free-energy dependence of albite dissolution kinetics at 80 °C and pH 8.8. Chem Geol 105(1-3):137-162

Busch A, Alles S, Al E (2008) Carbon dioxide storage potential of shale. Int J Greenhouse Gas Control 2(3):297-308

Busenberg E, Clemency CV (1976) The dissolution kinetics of feldspars at 25 °C and 1 atm CO_2 partial pressure. Geochim Cosmochim Acta 40:41-49

Canal J, Delgado J, Falcon I, Juncosa R, Barrientos V (2013) Injection of CO_2-saturated water through a siliceous sandstone plug from the Hontomin Test Site (Spain): Experiment and modelling. Environ Sci Technol 47(1):159-167

Carroll SA, Knauss KG (2005) Dependence of labradorite dissolution kinetics on CO_2(aq), Al(aq), and temperature. Chem Geol 217(3-4):213-225

Carroll SA, McNab WW, Dai Z, Torres SC (2013) Reactivity of Mount Simon Sandstone and the Eau Claire Shale under CO_2 storage conditions. Environ Sci Technol 47(1):252

Chen Y, Brantley SL (1998) Diopside and anthophyllite dissolution at 25° and 90 °C and acid pH. Chem Geol 147:233-248

Chen Y, Brantley SL (2000) Dissolution of forsteritic olivine at 65 °C and $2 < pH < 5$. Chem Geol 165:267-281

Chialvo AA, Vlcek L, Cole DR (2013) Acid gases in CO_2-rich subsurface geologic environments. Rev Mineral Geochem 77:361-398

Chopping C (2011) Supercritical carbon dioxide-brine-rock reactions in the Madison Limestone of Southwest Wyoming: An experimental investigation of a sulfur-rich natural carbon dioxide reservoir. MS Thesis, University of Wyoming, Laramie, Wyoming

Chopping C, Kaszuba JP (2012) Supercritical carbon dioxide-brine-rock reactions in the Madison Limestone of Southwest Wyoming: An experimental investigation of a sulfur-rich natural carbon dioxide reservoir. Chem Geol 322:223-236

Chou L, Wollast R (1984) Study of the weathering of albite at room temperature and pressure with a fluidized bed reactor. Geochim Cosmochim Acta 48(11):2205-2217

Cole DR, Ohmoto H, Jacobs GK (1992) Isotopic exchange in mineral-fluid systems: III. Rates and mechanisms of oxygen isotope exchange in the system granite-H_2O ± NaCl ± KCl at hydrothermal conditions. Geochim Cosmochim Acta 56(1):445-466

Daval D, Martinez I, Corvisier J, Findling N, Goffé B, Guyot F (2009a) Carbonation of Ca-bearing silicates, the case of wollastonite: Experimental investigations and kinetic modeling. Chem Geol 265(1):63-78

Daval D, Martinez I, Guigner J-M, Hellmann R, Corvisier J, Findling N, Dominici C, Goffe B, Guyot F (2009b) Mechanism of wollastonite carbonation deduced from micro- to nanometer length scale observations. Am Mineral 94(11-12):1707-1726

Daval D, Hellmann R, Corvisier J, Tisserand D, Martinez I, Guyot F (2010) Dissolution kinetics of diopside as a function of solution saturation state: Macroscopic measurements and implications for modeling of geological storage of CO_2. Geochim Cosmochim Acta 74(9):2615-2633

Davis MC, Wesolowski DJ, Rosenqvist J, Brantley SL, Mueller KT (2011) Solubility and near-equilibrium dissolution rates of quartz in dilute NaCl solutions at 398–473 K under alkaline conditions. Geochim Cosmochim Acta 75(2):401-415

De Yoreo JJ, Waychunas GA, Jun Y-S, Fernandez-Martinez A (2013) In situ investigations of carbonate nucleation on mineral and organic surfaces. Rev Mineral Geochem 77:229-257

Dickson FW, Blount CW, Tunell G (1963) Use of hydrothermal solutions equipment to determine the solubility of anhydrite in water from 100 °C to 275 °C and from 1 bar to 1,000 bars pressure. Am J Sci 261:61-78

Dove PM (1999) The dissolution kinetics of quartz in aqueous mixed cation solutions. Geochim Cosmochim Acta 63:3715-3727

Dove PM, Crerar DA (1990) Kinetics of quartz dissolution in electrolyte solutions using a hydrothermal mixed flow reactor. Geochim Cosmochim Acta 54(4):955-969

Drever JI (1997) The Geochemistry of Natural Waters: Surface and Groundwater Environments. Prentice Hall, Upper Saddle River, N.J.

Duan ZH, Sun R, Zhu C, Chou IM (2006) An improved model for the calculation of CO_2 solubility in aqueous solutions containing Na^+, K^+, Ca^{2+}, Mg^{2+}, Cl^-, and SO_4^{2-}. Mar Chem 98(2-4):131-139

Fischer S, Liebscher A, Wandrey M, Grp CS (2010) CO_2-brine-rock interaction - First results of long-term exposure experiments at in situ P-T conditions of the Ketzin CO_2 reservoir. Chemie Der Erde-Geochem 70:155-164

Fu Q, Lu P, Konishi H, Dilmore R, Xu H, Seyfried WEJ, Zhu C (2009) Coupled alkali-feldspar dissolution and secondary mineral precipitation in batch systems: 1. New experiments at 200 °C and 300 bars. Chem Geol 258:125-135

Garcia DJ, Shao H, Hu Y, Ray JR, Jun Y-S (2012a) Supercritical CO_2–brine induced dissolution, swelling, and secondary mineral formation on phlogopite surfaces at 75-95 °C and 75 atm. Energy Environ Sci 5(2):5758-5758

Garcia S, Rosenbauer RJ, Palandri J, Maroto-Valer MM (2012b) Sequestration of non-pure carbon dioxide streams in iron oxyhydroxide-containing saline repositories. Int J Greenhouse Gas Control 7:89-97

Gaus I (2010) Role and impact of CO_2-rock interactions during CO_2 storage in sedimentary rocks. Int J Greenhouse Gas Control 4:73-89

Gaus I, Azaroual M, Czernichowski-Lauriol I (2005) Reactive transport modelling of the impact of CO_2 injection on the clayey cap rock at Sleipner (North Sea). Chem Geol 217(3-4):319-337

Gerdemann SJ, O'Connor WK, Dahlin DC, Penner LR, Rush H (2007) Ex situ aqueous mineral carbonation. Environ Sci Technol 41(7):2587-2593

Getahun A, Reed MH, Symonds R (1996) Mount St Augustine volcano fumarole wall rock alteration: Mineralogy, zoning, composition and numerical models of its formation process. J Volcanol Geotherm Res 71(2-4):73-107

Giammar DE, Bruant RG, Peters CA (2005) Forsterite dissolution and magnesite precipitation at conditions relevant for deep saline aquifer storage and sequestration of carbon dioxide. Chem Geol 217(3-4):257-276

Gislason SR, Wolff-Boenisch D, Stefansson A, Oelkers EH, Gunnlaugsson E, Sigurdardottir H, Sigfusson B, Broecker WS, Matter JM, Stute M (2010) Mineral sequestration of carbon dioxide in basalt: A pre-injection overview of the Carbfix project. Int J Greenhouse Gas Control 4(3):537-545

Godard M, Luquot L, Andreani M, Gouze P, Gilbert B (2013) Incipient hydration of mantle lithosphere at ridges: A reactive percolation experiment. Earth Planet Sci Lett 371-372:92-102

Golubev SV, Pokrovsky OS, Schott J (2005) Experimental determination of the effect of dissolved CO_2 on the dissolution kinetics of Mg and Ca silicates at 25 °C. Chem Geol 217(3-4):227-238

Golubev SV, Benezeth P, Schott J, Dandurand JL, Castillo A (2009) Siderite dissolution kinetics in acidic aqueous solutions from 25 to 100 °C and 0 to 50 atm pCO_2. Chem Geol 265(1-2):13-19

Gunter WD, Wiwchar B, Perkins EH (1997) Aquifer disposal of CO_2-rich greenhouse gases: Extension of the time scale of experiment for CO_2-sequestering reactions by geochemical modelling. Mineral Petrol 59(1-2):121-140

Gysi AP, Stefansson A (2012) Mineralogical aspects of CO_2 sequestration during hydrothermal basalt alteration - An experimental study at 75 to 250 °C and elevated pCO_2. Chem Geol 306-307:146

Halder S, Walther JV (2011) Far from equilibrium enstatite dissolution rates in alkaline solutions at earth surface conditions. Geochim Cosmochim Acta 75(23):7486-7493

Hänchen M, Prigiobbe V, Storti G, Seward TM, Mazzotti M (2006) Dissolution kinetics of fosteritic olivine at 90–150 °C including effects of the presence of CO_2. Geochim Cosmochim Acta 70(17):4403-4416

Hangx SJT, Spiers CJ (2009) Reaction of plagioclase feldspars with CO_2 under hydrothermal conditions. Chem Geol 265(1-2):88-98

Hangx SJT, Spiers CJ, Peach CJ (2010) Creep of simulated reservoir sands and coupled chemical-mechanical effects of CO_2 injection. J Geophys Res - Solid Earth 115, doi:10.1029/2009jb006939

Harrison AL, Power IM, Dipple GM (2013) Accelerated carbonation of brucite in mine tailings for carbon sequestration. Environ Sci Technol 47(1):126-134

Hellmann R (1994) The albite-eater system: Part I. The kinetics of dissolution as a function of pH at 100, 200 and 300 °C. Geochim Cosmochim Acta 58(2):595-611

Hellmann R, Daval D, Tisserand D (2010) The dependence of albite feldspar dissolution kinetics on fluid saturation state at acid and basic pH: Progress towards a universal relation. C R Geosci 342(7-8):676-684

Holland HD (1965) Some applications of thermochemical data to problems of ore deposits II. Mineral assemblages and the composition of ore forming fluids. Econ Geol 60(6):1101-1166

Houston SJ, Yardley BWD, Smalley PC, Collins I (2007) Rapid fluid-rock interaction in oilfield reservoirs. Geology 35(12):1143-1146

Hövelmann J, Austrheim H, Jamtveit B (2012a) Microstructure and porosity evolution during experimental carbonation of a natural peridotite. Chem Geol 334:254-265

Hövelmann J, Putnis CV, Ruiz-Agudo E, Austrheim H (2012b) Direct nanoscale observations of CO_2 sequestration during brucite [$Mg(OH)_2$] dissolution. Environ Sci Technol 46(9):5253

Hu Y, Jun Y-S (2012) Biotite dissolution in brine at varied temperatures and CO_2 pressures: Its activation energy and potential CO_2 intercalation. Langmuir 28(41):14633-14641

Huertas FJ, Chou L, Wollast R (1999) Mechanism of kaolinite dissolution at room temperature and pressure. Part II: Kinetic study. Appl Geochem 63:3261-3275

Huffmann E (1977) Performance of a new automatic carbon dioxide coulometer. Microchem J 22(4):567-573

Iglauer S, Paluszny A, Pentland CH, Blunt MJ (2011) Residual CO_2 imaged with x-ray micro-tomography. Geop Res Lett 38(21), doi:10.1029/2011GL049680

Ilton ES, Schaef HT, Qafoku O, Rosso KM, Felmy AR (2012) In situ X-ray diffraction study of Na^+ saturated montmorillonite exposed to variably wet super critical CO_2. Environ Sci Technol 46:4241-4248

Jones LC, Rosenbauer R, Goldsmith JI, Oze C (2010) Carbonate control of H_2 and CH_4 production in serpentinization systems at elevated P-Ts. Geop Res Lett 37, doi:10.1029/2010GL043769

Jun Y-S, Giammar DE, Werth CJ (2013) Impacts of geochemical reactions on geologic carbon sequestration. Environ Sci Technol 47(1):3-8

Kampman N, Bickle M, Wigley M, Dubacq B (2013) Geochemical processes in carbon storage. Chem Geol in press

Kaszuba JP, Janecky DR, Snow MG (2003) Carbon dioxide reaction processes in a model brine aquifer at 200 °C and 200 bars: Implications for geologic sequestration of carbon. Appl Geochem 18(7):1065-1080

Kaszuba JP, Janecky DR, Snow MG (2005) Experimental evaluation of mixed fluid reactions between supercritical carbon dioxide and NaCl brine: Relevance to the integrity of a geologic carbon repository. Chem Geol 217(3-4):277-293

Kaszuba JP, Williams LL, Janecky DR, Hollis WK, Tsimpanogiannis IN (2006) Immiscible CO_2-H_2O fluids in the shallow crust. Geochem Geophys Geosyst 7, doi:10.1029/2005gc001107

Kaszuba JP, Janecky DR (2009) Geochemical impacts of sequestering carbon dioxide in brine formations. *In*: Carbon Sequestration and Its Role in the Global Carbon Cycle. Vol Geophysical Monograph 183. McPherson B, Sundquist E (eds) American Geophysical Union, Washington, DC, pp 239-247

Kaszuba JP, Navarre-Sitchler A, Thyne G, Chopping C, Meuzelaar T (2011) Supercritical carbon dioxide and sulfur in the Madison Limestone: A natural analogue in Southwest Wyoming for geologic carbon-sulfur co-sequestration. Earth Planet Sci Lett 309:131–140

Kelemen PB, Matter J (2008) In situ carbonation of peridotite for CO_2 storage. Proc Natl Acad Sci USA 105(45):17295-17300

Kharaka YK, Thordsen JJ, Hovorka SD, Nance HS, Cole DR, Phelps TJ, Knauss KG (2009) Potential environmental issues of CO_2 storage in deep saline aquifers: Geochemical results from the Frio-I Brine Pilot test, Texas, USA. Appl Geochem 24(6):1106-1112

Kharaka YK, Cole DR, Thordsen JJ, Gans KD, Thomas RB (2013) geochemical monitoring for potential environmental impacts of geologic sequestration of CO_2. Rev Mineral Geochem 77:399-430

Kjøller C, Weibel R, Bateman K, Laier T, Nielsen LH, Frykman P, Springer N (2011) Geochemical impacts of CO_2 storage in saline aquifers with various mineralogy – results from laboratory experiments and reactive geochemical modelling. Energy Procedia 4:4724-4731

Knauss KG, Wolery TJ (1986) Dependence of albite dissolution kinetics on pH and time at 25 °C and 70 °C. Geochim Cosmochim Acta 50:2481-2497

Knauss KG, Wolery TJ (1988) The dissolution kinetics of quartz as a function of pH and time at 70 °C. Geochim Cosmochim Acta 52(1):43-53

Knauss KG, Nguyen SN, Weed HC (1993) Diopside dissolution kinetics as a function of pH, CO_2, temperature, and time. Geochim Cosmochim Acta 57:285-294

Knauss KG, Johnson JW, Steefel CI (2005) Evaluation of the impact of CO_2, co-contaminant gas, aqueous fluid and reservoir rock interactions on the geologic sequestration of CO_2. Chem Geol 217(3-4):339-350

Köhler SJ, Dufaud F, Oelkers EH (2003) An experimental study of illite dissolution kinetics as a function of pH from 1.4 to 12.4 and temperature from 5 to 50 °C. Geochim Cosmochim Acta 67(19):3583-3594

Lammers K, Murphy R, Riendeau A, Smirnov A, Schoonen MAA, Strongin DR (2011) CO_2 sequestration through mineral carbonation of iron oxyhydroxides. Environ Sci Technol 45(24):10422-10428

Landrot G, Ajo-Franklin JB, Yang L, Cabrini S, Steefel CI (2012) Measurement of accessible reactive surface area in a sandstone, with application to CO_2 mineralization. Chem Geol 318:113-125

Langmuir D (1997) Aqueous Environmental Geochemistry. Prentice Hall, Upper Saddle River, New Jersey

Lin H, Fujii T, Takisawa R, Takahashi T, Hashida T (2008) Experimental evaluation of interactions in supercritical CO_2/water/rock minerals system under geologic CO_2 sequestration conditions. J Mater Sci 43:2307-2315

Liu FY, Lu P, Griffith C, Hedges SW, Soong Y, Hellevang H, Zhu C (2012) CO_2-brine-caprock interaction: Reactivity experiments on Eau Claire Shale and a review of relevant literature. Int J Greenhouse Gas Control 7:153-167

Lu JM, Phelps TJ, Manning MA, Cook PJ, Hovorka SD, Kharaka YK, Thordsen JJ, Horita J, Karamalidis A, Griffith C, Hakala JA, Ambats G, Cole DR (2012) CO_2-rock-brine interactions in Lower Tuscaloosa Formation at Cranfield CO_2 Sequestration Site, Mississippi, USA. Chem Geol 291:269-277

Lu P, Fu Q, Seyfried WE, Jr., Hedges SW, Soong Y, Jones K, Zhu C (2013) Coupled alkali feldspar dissolution and secondary mineral precipitation in batch systems - 2: New experiments with supercritical CO_2 and implications for carbon sequestration. Appl Geochem 30:75-90

Luquot L, Gouze P (2009) Experimental determination of porosity and permeability changes induced by injection of CO_2 into carbonate rocks. Chem Geol 265(1-2):148

Luquot L, Andreani M, Gouze P, Camps P (2012) CO_2 percolation experiment through chlorite/zeolite-rich sandstone (Pretty Hill Formation – Otway Basin–Australia). Chem Geol 294-295:75-88

Mandalaparty P, Deo M, Moore J (2011) Gas-compositional effects on mineralogical reactions in carbon dioxide sequestration. Soc Pet Engineers J 16(4):949-958

Marcaillou C, Munoz M, Vidal O, Parra T, Harfouche M (2011) Mineralogical evidence for H_2 degassing during serpentinization at 300 °C/300 bar. Earth Planet Sci Lett 303(3-4):281-290

Matter JM, Broecker WS, Gislason SR, Gunnlaugsson E, Oelkers EH, Stute M, Sigurdardóttir H, Stefansson a, Alfreðsson Ha, Aradóttir ES, Axelsson G, Sigfússon B, Wolff-Boenisch D (2011) The CarbFix Pilot Project–Storing carbon dioxide in basalt. Energy Procedia 4:5579-5585

McCollom TM (2013) Laboratory simulations of abiotic hydrocarbon formation in earth's deep subsurface. Rev Mineral Geochem 75:467-494

McCollom TM, Seewald JS (2007) Abiotic synthesis of organic compounds in deep-sea hydrothermal environments. Chemical Reviews 107(2):382-401

McGrail BP, Schaef HT, Ho AM, Chien Y-J, Dooley JJ, Davidson CL (2006) Potential for carbon dioxide sequestration in flood basalts. J Geophys Res 111(B12), doi:10.1029/2005JB004169

Molins S, Trebotich D, Steefel CI, Shen CP (2012) An investigation of the effect of pore scale flow on average geochemical reaction rates using direct numerical simulation. Water Resour Res 48, doi:10.1029/2011wr011404

Montes-Hernandez G, Pironon J (2009) Hematite and iron carbonate precipitation-coexistence at the iron–montmorillonite–salt solution–CO_2 interfaces under high gas pressure at 150 °C. Appl Clay Sci 45(4):194-200

Morse JW, Arvidson RS (2002) The dissolution kinetics of major sedimentary carbonate minerals. Earth Sci Rev 58:51-84

Murphy R, Lammers K, Smirnov A, Schoonen MAA, Strongin DR (2010) Ferrihydrite phase transformation in the presence of aqueous sulfide and supercritical CO_2. Chem Geol 271(1):26-30

Murphy R, Lammers K, Smirnov A, Schoonen MAA, Strongin DR (2011) Hematite reactivity with supercritical CO_2 and aqueous sulfide. Chem Geol 283(3-4)

Nagy KL (1995) Dissolution and precipitation kinetics of sheet silicates. *In*: Chemical Weathering Rates of Silicate Minerals. Vol 31. White AF, Brantley SL (eds), pp 173-233

Noiriel C, Luquot L, Made B, Raimbault L, Gouze P, van der Lee J (2009) Changes in reactive surface area during limestone dissolution: An experimental and modelling study. Chem Geol 265(1-2):160-170

Oelkers EH, Schott J (2001) An experimental study of enstatite dissolution rates as a function of pH, temperature, and aqueous Mg and Si concentration, and the mechanism of pyroxene/pyroxenoid dissolution. Geochim Cosmochim Acta 65(8):1219-1231

Oelkers EH, Schott J, Devidal JL (1994) The effect of aluminium, pH, and chemical affinity on the rates of aluminosilicate dissolution reactions. Geochim Cosmochim Acta 58:2011-2024

Olsen AA, Rimstidt JD (2008) Oxalate-promoted forsterite dissolution at low pH. Geochim Cosmochim Acta 72(7):1758-1766

Palandri JL, Kharaka YK (2004) A compilation of rate parameters of water-mineral interaction kinetics for application to geochemical modeling. US Geological Survey, Open File Report 2004-1068

Palandri JL, Kharaka YK (2005) Ferric iron-bearing sediments as a mineral trap for CO_2 sequestration: Iron reduction using sulfur-bearing waste gas. Chem Geol 217(3-4):351-364

Palandri JL, Rosenbauer RJ, Kharaka YK (2005) Ferric iron in sediments as a novel CO_2 mineral trap: CO_2-SO_2 reaction with hematite. Appl Geochem 20:2038-2048

Pèpe G, Dweik J, Jouanna P, Gouze P, Andreani M, Luquot L (2010) Atomic modelling of crystal/complex fluid/crystal contacts—Part II. Simulating AFM tests via the Genmol code for investigating the impact of CO_2 storage on kaolinite/brine/kaolinite adhesion. J Crystal Growth 312(22):3308-3315

Pokrovsky OS, Schott J, Thomas F (1999a) Dolomite surface speciation and reactivity in aquatic systems. Geochim Cosmochim Acta 63:3133-3143

Pokrovsky OS, Schott J, Thomas F (1999b) Processes at the magnesium-bearing carbonates solution interface. I: A surface speciation model for magnesite. Geochim Cosmochim Acta 63:863-880

Pokrovsky OS, Schott J (2000) Kinetics and mechanism of forsterite dissolution at 25 °C and pH from 1 to 12. Geochim Cosmochim Acta 64(19):3313-3325

Pokrovsky OS, Golubev SV, Schott J (2005) Dissolution kinetics of calcite, dolomite and magnesite at 25 °C and 0 to 50 atm pCO_2. Chem Geol 217:239-255

Pokrovsky OS, Golubev SV, Jordan G (2009a) Effect of organic and inorganic ligands on calcite and magnesite dissolution rates at 60 °C and 30 atm pCO_2. Chem Geol 265(1-2):33-43

Pokrovsky OS, Golubev SV, Schott J, Castillo A (2009b) Calcite, dolomite and magnesite dissolution kinetics in aqueous solutions at acid to circumneutral pH, 25 to 150 °C and 1 to 55 atm pCO_2: New constraints on CO_2 sequestration in sedimentary basins. Chem Geol 265(1-2):20-32

Power IM, Harrison AL, Dipple GM, Wilson SA, Kelemen PB, Hitch M, Southam G (2013) Carbon mineralization: from natural analogues to engineered systems. Rev Mineral Geochem 77:305-360

Prigiobbe V, Costa G, Baciocchi R, Hänchen M, Mazzotti M (2009) The effect of CO_2 and salinity on olivine dissolution kinetics at 120 °C. Chem Eng Sci 64(15):3510-3515

Prigiobbe V, Mazzotti M (2011) Dissolution of olivine in the presence of oxalate, citrate, and CO_2 at 90 °C and 120 °C. Chem Eng Sci 66(24):6544-6554

Qi R, LaForce TC, Blunt MJ (2009) Design of carbon dioxide storage in aquifers. Int J Greenhouse Gas Control 3(2):195–205

Riaz A, Hesse M, Tchelepi HA, Orr FM (2006) Onset of convection in a gravitationally unstable diffusive boundary layer in porous media. Journal of Fluid Mechanics 548:87-111

Rimstidt JD, Dove PM (1986) Mineral/solution reaction rates in a mixed flow reactor: Wollastonite hydrolysis. Geochim Cosmochim Acta 50:2509-2516

Rimstidt JD, Brantley SL, Olsen AA (2012) Systematic review of forsterite dissolution rate data. Geochim Cosmochim Acta 99:159-178

Romanov VN (2013) Evidence of irreversible CO_2 intercalation in montmorillonite. Int J Greenhouse Gas Control 14:220-226

Rosenbauer RJ, Bischoff JL, Potter JM (1993) A flexible Au-Ir cell with quick assembly for hydrothermal experiments. Am Mineral 78:1286-1289

Rosenbauer RJ, Koksalan T, Palandri JL (2005) Experimental investigation of CO_2–brine–rock interactions at elevated temperature and pressure: Implications for CO_2 sequestration in deep-saline aquifers. Fuel Process Technol 86:1581-1597

Rosenqvist J, Kilpatrick, A.D. Yardley, B.W.D. (2012) Solubility of carbon dioxide in aqueous fluids and mineral suspensions at 294 K and subcritical pressures. Appl Geochem 27:1610-1614

Rosso JJ, Rimstidt JD (2000) A high resolution study of forsterite dissolution rates. Geochim Cosmochim Acta 64(5):797-811

Salvi S, Pokrovsky GS, Schott J (1998) Experimental investigation of aluminum-silica aqueous complexing at 300 °C. Chem Geol 151(1-4):51-67

Sardini P, Ledesert B, Touchard G (1995) Quantification of microscopic porous networks by image analysis and measurements of permeability in the Soultz-sous-Forets granite (Alsace, France). *In*: Fluid Flow and Transport in Rocks. Jamtveit B, Yardley BWD (eds) Chapman & Hall, London, pp 171-189

Schaef HT, Windisch CF, McGrail BP, Martin PF, Rosso KM (2011) Brucite [$Mg(OH_2)$] carbonation in wet supercritical CO_2: An in situ high pressure x-ray diffraction study. Geochim Cosmochim Acta 75(23):7458-7471

Schaef HT, Ilton ES, Qafoku O, Martin PF, Felmy AR, Rosso KM (2012) In situ XRD Study of Ca^{2+} saturated montmorillonite (STX-1) exposed to anhydrous and wet supercritical carbon dioxide. Int J Greenhouse Gas Control 6:220-229

Schott J, Berner RA, Sjoberg EL (1982) Mechanism of pyroxene and amphibole weathering. I: Experimental studies of iron-free minerals. Geochim Cosmochim Acta 45:2123-2135

Schott J, Pokrovsky OS, Oelkers EH (2009) The link between mineral dissolution/precipitation kinetics and solution chemistry. Rev Mineral Geochem 70:207-258

Schulze RK, Hill MA, Field RD, Papin PA, Hanrahan RJ, Byler DD (2004) Characterization of carbonated serpentine using XPS and TEM. Energy Convers Manage 45(20):3169-3179

Seyfried WE, Gordon PC, Dickson F (1979) A new reactive cell for hydrothermal solution equipment. Am Mineral 64:646-649

Seyfried WE Jr, Janecky DR, Berndt ME (1987) Rocking autoclaves for hydrothermal experiments, II. The flexible reaction-cell system. *In*: Hydrothermal Experimental Techniques. Ulmer GC, Barnes HL (eds) John Wiley & Sons, New York, pp 216-239

Shao H, Ray JR, Jun Y-S (2010) Dissolution and precipitation of clay minerals under geologic CO_2 sequestration conditions: CO_2-brine-phlogopite interactions. Environ Sci Technol 44(15):5999-6005

Sjöberg EL, Rickard D (1983) The influence of experimental design on the rate of calcite dissolution. Geochim Cosmochim Acta 47:2281-2285

Smith MM, Sholokhova Y, Hao Y, Carroll SA (2013) Evaporite caprock integrity: An experimental study of reactive mineralogy and pore-scale heterogeneity during brine-CO_2 exposure. Environ Sci Technol 47(1):262-268

Stevens TO, McKinley JP (2000) Abiotic controls on H_2 production from basalt-water reactions and implications for aquifer biogeochemistry. Environ Sci Technol 34(5):826-831

Stillings LL, Brantley SL (1995) Feldspar dissolution at 25 °C and pH 3: Reaction stoichiometry and the effect of cations. Geochim Cosmochim Acta 59:1483-1496

Stockmann G, Wolff-Boenisch D, Gislason SR, Oelkers EH (2008) Dissolution of diopside and basaltic glass: The effect of carbonate coating. Mineral Mag 72(1):135-139

Stumm W, Morgan JJ (1996) Aquatic Chemistry: Chemical Equilibria and Rates In Natural Waters. Wiley-Interscience New York

Takenouchi S, Kennedy GC (1964) The binary system H_2O-CO_2 at high temperatures and pressures. Am J Sci 262:1055-1074

Takenouchi S, Kennedy GC (1965) The solubility of carbon dioxide in NaCl solutions at high temperatures and pressures. Am J Sci 263:445-454

Todheide K, Franck EU (1963) Das Zweiphasengebiet und die kritische kurve in system kohlendioxide-wasser bis zu drucken von 3500 bar. Z Phys Chem (Neue Folge) 37:387-401

Tokunaga TK, Wan J (2013) Capillary pressure and mineral wettability influences on reservoir CO_2 capacity. Rev Mineral Geochem 77:481-503

Walther JV, Orville PM (1983) The extraction quench technique for determination of the thermodynamic properties of solute complexes - Application to quartz solubility in fluid mixtures. Am Mineral 68(7-8):731-741

Wang F, Giammar DE (2013) Forsterite dissolution in saline water at elevated temperature and high CO_2 pressure. Environ Sci Technol 47(1):168-173

Wallace AF, Gibbs GV, Dove PM (2010): Influence of ion-associated water on the hydrolysis of Si-O bonded interactions. J Phys Chem A 114:2534-2542

Weissbart EJ, Rimstidt DJ (2000) Wollastonite: Incongruent dissolution and leached layer formation. Geochim Cosmochim Acta 64:4007-4016

Williams RH (2002) Major roles for fossil fuels in an environmentally constrained world. Sustainability in Energy Production and Utilization in Brazil: The Next Twenty Years, Universidade Estadual de Campinas (Unicamp), Campinas, Sao Paulo, Brazil

Wogelius RA, Walther JV (1991) Forsterite dissolution at 25 °C: Effects of pH, CO_2 and organic acids. Geochim Cosmochim Acta 55:943-954

Wogelius RA, Walther JV (1992) Olivine dissolution kinetics at near-surface conditions. Chem Geol 97:101-112

Wolf GH, Chizmeshya AVG, Diefenbacher J, McKelvy MJ (2004) In situ observation of CO_2 sequestration reactions using a novel microreaction system. Environ Sci Technol 38(3):932-936

Wollenweber J, Alles S, Busch A, Krooss BM, Stanjek H, Littke R (2010) Experimental investigation of the CO_2 sealing efficiency of caprocks. Int J Greenhouse Gas Control 4(2):231-241

Xie Z, Walther JV (1994) Dissolution stoichiometry and adsorption of alkali and alkaline earth elements to the acid-reacted wollastonite surface at 25 °C. Geochim Cosmochim Acta 58:2587-2598

Xu T, Apps JA, Pruess K (2004) Numerical simulation of CO_2 disposal by mineral trapping in deep aquifers. Appl Geochem 19(6):917-936

Xu XF, Chen SY, Zhang DX (2006) Convective stability analysis of the long-term storage of carbon dioxide in deep saline aquifers. Adv Water Resources 29(3):397-407

Xu T, Apps JA, Pruess K, Yamamoto H (2007) Numerical modeling of injection and mineral trapping of CO_2 with H_2S and SO_2 in a sandstone formation. Chem Geol 242(3-4):319-346

Xu M, Sullivan K, VanNess G, Knauss KG, Higgins SR (2013) Dissolution kinetics and mechanisms at dolomite - water interfaces: Effects of electrolyte specific ion strength. Environ Sci Technol 47:110-118

Zhao L, Sang L, Chen J, Ji J, Teng HH (2010) Aqueous carbonation of natural brucite: Relevance to CO_2 sequestration. Environ Sci Technol 44(1):406-411

Reviews in Mineralogy & Geochemistry
Vol. 77 pp. 189-228, 2013
Copyright © Mineralogical Society of America

Molecular Simulation of CO_2- and CO_3-Brine-Mineral Systems

Laura M. Hamm, Ian C. Bourg
Earth Sciences Division
Lawrence Berkeley National Laboratory
Berkeley, California 94720, U.S.A.
icbourg@lbl.gov

Adam F. Wallace
Department of Geological Sciences
University of Delaware
Newark, Delaware 19716, U.S.A.

Benjamin Rotenberg
Laboratoire PECSA
CNRS and UPMC Université Paris 06
75005 Paris, France

INTRODUCTION

Atomistic simulations—molecular dynamics (MD) and Monte Carlo (MC) simulations, *ab initio* and density functional theory (DFT) calculations—have proved useful in gaining insight into the molecular basis of fundamental processes in aquatic geochemistry, such as solvation, ion pair formation, adsorption, molecular diffusion, and the energetics of mineral phases (Rotenberg et al. 2007; Bickmore et al. 2009; Hamm et al. 2010; Kerisit and Liu 2010; Hofmann et al. 2012; Stack et al. 2012; Wallace et al. 2013). Key strengths of these simulations are their ability to examine the behavior of individual atoms (where spectroscopic and other experimental methods probe the average behavior of large numbers of molecules) and to allow constraints that would be difficult or impossible to impose in the laboratory. These features make atomistic simulations powerful tools for elucidating the manner in which collective phenomena arise from molecular scale properties in geochemical systems. The range of length and time scales probed by atomistic simulations (from angstroms to tens of nanometers and from femtoseconds to microseconds, continuously expanding with advances in the availability and sophistication of computational resources) makes them ideally suited to complement several spectroscopic techniques, including X-ray, neutron, and nuclear magnetic resonance approaches.

A well known limitation of the methods described in the present chapter, particularly in the case of classical mechanical (MD and MC) simulations, is the approximate nature of the models that are used to describe interatomic forces. In the simplest of these simulations, bond lengths and angles are fixed; inter-atomic interactions are modeled as the sum of two-body interactions that depend only on the identity of the interacting atoms and the distance between them; and chemical bonds are not allowed to break or form during a simulation (Allen and Tildesley 1987; Frenkel and Smit 2001). The choice of force fields (i.e., interatomic potential models) can strongly influence predicted properties such as the structure of liquid water (Hura

1529-6466/13/0077-0006$05.00 http://dx.doi.org/10.2138/rmg.2013.77.6

et al. 2003; Bickmore et al. 2009), the solubility of CO_2 in water (Lísal et al. 2005), CO_2-water interfacial tension (Nielsen et al. 2012), and the structure of calcite-water interfaces (Fenter et al. 2013). In this chapter, we describe how, despite these limitations, carefully designed atomistic simulations can generate useful fundamental insight into the geochemical properties of mineral-water-CO_2 and -CO_3 systems at conditions relevant to geologic carbon sequestration (GCS).

CO_3-BRINE-MINERAL SYSTEMS

CO_3-brine speciation

The aqueous speciation of carbonate-bearing solutions has been extensively studied due to its importance as the primary buffer system in natural waters and in many engineered settings. Thermodynamic solution speciation models account for the equilibria between gaseous and solvated $CO_{2(aq)}$ as well as the step wise decomposition of carbonic acid, H_2CO_3, into bicarbonate and carbonate ions, HCO_3^- and CO_3^{2-}. As aqueous carbon dioxide and carbonic acid are not easily distinguishable by analytical titration and carbonic acid is far less abundant in solution than aqueous carbon dioxide, it has become commonplace to represent the concentrations of both species collectively as the hypothetical species $H_2CO_3^*$. In addition to these basic relations, speciation models also include mineral solubility products (i.e., $K_{sp} = \{M(II)\}\{CO_3^{2-}\}$) and equilibrium constants for ion hydrolysis (i.e., $K_{hyd} = \{M(II)OH^+\}\{H^+\}/\{M(II)\}$) and ion pair formation (i.e., $K_{ip} = \{M(II)\}\{HCO_3^-\}/\{M(II)HCO_3^+\}$), such that the solubility of a given M(II)-carbonate mineral phase is equal to the sum over the activities of all the M(II)-containing species in solution under a given set of environmental conditions (temperature, pressure, CO_2 fugacity, ionic strength). Although evermore sophisticated activity coefficient corrections must be applied to account for non-ideal interactions between species at higher concentrations (Debye and Hückel 1923; Davies 1962; Pitzer 1973), ion activity models remain the preeminent means by which dilute solutions and brines are modeled.

Recent experimental work on the early stages of homogeneous $CaCO_3$ crystallization, however, has challenged the standard treatment of electrolyte solutions as presented above. Titration experiments (Gebauer et al. 2008) show that the calcium ion activity of a sodium bicarbonate buffer solution deviates from the amount of calcium dosed into the solution. On its own, this result is completely consistent with traditional speciation models that predict non-ideal solution behavior (i.e., ion pairing). However, analytical ultracentrifugation (Gebauer et al. 2008; Gebauer and Coelfen 2011) and cryo-TEM (Pouget et al. 2009) also suggest that ions are concentrated in subnanometer clusters that are not accounted for by ion activity models. While the presence of clusters is expected in supersaturated solutions such as those employed in these experiments, the apparently monodisperse cluster size distribution has been interpreted as evidence that the species are stable or metastable "prenucleation" clusters (PNC), although there are alternative mechanisms that can also produce similar distributions (Faatz et al. 2004; Binder and Fratzl 2005). If indeed ions more favorably reside in cluster species than as ion pairs and free ions, perhaps even at equilibrium (Gebauer et al. 2008, 2010; Gebauer and Coelfen 2011), then presumably the formation of calcium carbonate from solution follows a non-classical nucleation pathway dominated by cluster-cluster aggregation (PNC theory) rather than ion-by-ion addition as assumed by classical theory. Moreover, if ions are concentrated in cluster phases rather than distributed throughout solution, theoretical treatments of mass transport may need to be modified or adjusted to make more accurate predictions of real system behavior.

The possible existence of additional stable calcium carbonate/bicarbonate ion species in solution that are larger than ion pairs is not necessarily inconsistent with the tenants of standard ion activity models. Indeed the presence of triple and quadruple ion species has been suspected

previously in a number of systems including iron bicarbonate solutions (Marcus and Hefter 2006; Fosbøl et al. 2010). However, in order to reconcile the existence of additional ion species with the demonstrated predictive capabilities of existing speciation models, the abundance of the additional species must be negligible near equilibrium such that their omission from standard thermodynamic databases has little effect on model predictions. Since the assertion of PNC theory (Gebauer et al. 2008, 2010; Gebauer and Coelfen 2011; Bewernitz et al. 2012), numerous MD simulation based investigations have probed the onset of $CaCO_3$ formation from supersaturated solutions in search of stable prenucleation clusters. To date, these studies have been unable to attribute special thermodynamic significance to a cluster of any size, which is the hallmark of PNC theory (Tribello et al. 2009; Raiteri and Gale 2010; Demichelis et al. 2011; Wallace et al. 2013). In the high pH limit, it has been demonstrated, by inference (Tribello et al. 2009; Raiteri and Gale 2010) and by direct quantification of the free energy landscape (Demichelis et al. 2011; Wallace et al. 2013), that there is no thermodynamic barrier opposing cluster formation in concentrated solutions (>15 mmol dm^{-3} as $CaCO_3°$). This is most consistent with spinodal decomposition as a phase-separation mechanism (Markov 2004; Binder and Fratzl 2005) and implies that there is a binodal in the system that describes the coexistence of an ion-rich dense liquid phase, and an ion-poor dilute solution phase (Fig. 1) (Faatz et al. 2004; Rieger et al. 2007; Wolf et al. 2008, 2011; Wallace et al. 2013). However, where bicarbonate ions persist at lower pH, the cluster size distribution is exponential (Demichelis et al. 2011), which is in line with the expectations of classical nucleation theory (Markov 2004).

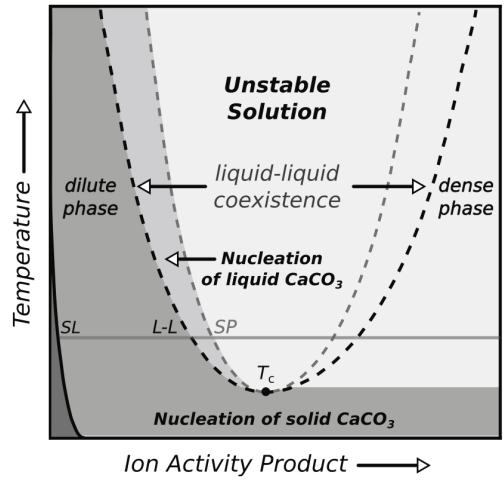

Figure 1. Schematic representation of the presumptive phase relationships in the $CaCO_3$-H_2O system at ambient pressure (Wallace et al. 2013). The gray horizontal line represents a constant temperature slice through the stability fields as the solution ion activity product is increased. The solubility of all polymorphs is represented by a single solubility line (SL), which bounds the undersaturated solution field (dark gray region in the lower left corner). This simplification highlights that the solid phases of $CaCO_3$ (calcite, aragonite, vaterite, presumably ACC) all display the same general retrograde solubility behavior. Indirect nucleation of the solid phases proceeds to the high concentration side of the dashed black liquid-liquid coexistence line (L-L). The phase field bounded by the L-L line and the dashed gray spinodal line (SP) and labeled "Nucleation of liquid $CaCO_3$" indicates the conditions where nucleation of the dense liquid phase (DLP) is possible. In the region bounded by the spinodal line, the solution is unstable to fluctuations and liquid-liquid separation proceeds spontaneously. The retrograde solubility of the DLP (i.e., concave up orientation of the system binodal) is assumed based on the behavior of the $MgSO_4$-H_2O system at high temperature (Wallace et al. 2013) and the arguments in support of a lower critical point temperature presented by Faatz et al. (2004). [Reprinted with permission of AAAS from Wallace et al. (2013) *Science* 341:885-889.]

Recent molecular dynamics studies have also posited that liquid-like or bona fide liquid phases of calcium carbonate may form in solution (Demichelis et al. 2011; Wallace et al. 2013). Demichelis et al. (2011) first noted that at high concentrations (> 50 mmol dm^{-3}) hydrated Ca-carbonate and Ca-bicarbonate cluster phases adopt linear and branched configurations that are highly dynamic and reorder quickly. From these results they coined the term DOLLOP, which stands for "dynamically ordered liquid-like oxyanion polymer." Wallace et al. (2013) later showed that in the high pH limit DOLLOP evolves quickly into a dense liquid phase (DLP) that is stable at lower concentrations (~15 mmol dm^{-3} or less) and that first coalesces and, then, partially dehydrates to form a material whose structure is consistent with hydrated amorphous calcium carbonate. Several experimental studies have also suggested the presence of liquid calcium carbonate based on the interpretation of light scattering (Faatz et al. 2004) and cryo-electron microscopy data (Rieger et al. 2007; Wolf et al. 2008). These studies were unable to convincingly demonstrate that the observed particles were indeed liquid rather than amorphous and solid. However, from the biomineralization literature it is well known that organic molecules can stabilize a metastable liquid form of calcium carbonate called PILP (Polymer Induced Liquid Precursor) (Gower and Odom 2000; Jee et al. 2011; Jiang et al. 2012). It therefore seems plausible that a dense liquid phase may also form in the absence of organics, with the inorganic liquid state being presumably less stable than PILP. The possible coexistence of such a phase with a more dilute liquid suggests that under certain conditions the carbonate system could be buffered by the metastable equilibrium between the two liquid states rather than by the solubility limit of solid $CaCO_3$ (Fig. 1). The case for liquid-liquid separation is also supported in part by the recent experimental documentation of liquid-liquid coexistence in the $MgSO_4$-water system (Wang et al. 2013), albeit at substantially higher temperatures than suggested for $CaCO_3$, and by a nuclear magnetic resonance (NMR) study that supports the notion that liquid calcium carbonate phases can form in the absence of organic polymers (Bewernitz et al. 2012).

Amorphous $M^{(II)}CO_3$ phases

Amorphous phases of Ca, Mg, and Fe(II) carbonate have been characterized to varying degrees experimentally (Michel et al. 2008; Radha et al. 2010, 2012; Sel et al. 2012). While amorphous calcium carbonate is an important precursor phase in the formation of biogenic carbonates, the extent to which such amorphous phases may persist in abiotic environments is unknown. Modeling efforts to date have focused primarily on the structure of the calcium bearing end member, amorphous calcium carbonate (ACC). As synthesized in the laboratory, ACC contains approximately one mole of water per formula unit of $CaCO_3$, though "anhydrous" biogenic forms have been observed with reduced water contents (Radha et al. 2010; Gong et al. 2012). Molecular dynamics simulations have demonstrated that dehydrated ACC is more dense and ordered than hydrous ACC (Saharay et al. 2013). Despite the polyamorphism of ACC demonstrated very recently in high-pressure experiments (Fernandez-Martinez et al. 2013), the aforementioned synthetic variety remains the only non-biogenic form that has been successfully stabilized in the laboratory at ambient temperature and pressure conditions. However, the presence of a transient anhydrous phase has been inferred at high temperatures from the interpretation of Differential Scanning Calorimetry profiles (Radha et al. 2010). ^{1}H and ^{13}C nuclear magnetic resonance spectroscopy has provided some insights into the structural and compositional characteristics of synthetic hydrated ACC (Michel et al. 2008; Nebel et al. 2008). These studies suggested a low abundance of hydroxyl moieties in the structure, as well as the presence of two populations of water molecules that are present in roughly equal proportions. On the millisecond timescale, one of these populations was immobile and the other had a somewhat restricted mobility. Additionally, two distinct populations of carbonate ions were identified that are distinguished by their proximity to immobile water molecules (~25% close to immobile H_2O at room temperature). Another study combining NMR with X-ray

diffraction (XRD) reported ^{13}C spectra for amorphous "proto-calcite" and "proto-vaterite" phases (Gebauer et al. 2010); however, the alternative and more traditional interpretation of these data maintains that the observed line broadening in the NMR spectra (and XRD patterns) arises from the presence of nanocrystalline rather than amorphous material in the samples (Jäger et al. 2006).

The initial theoretical study of the ACC structure (Goodwin et al. 2010) utilized the Reverse Monte Carlo (RMC) approach (McGreevy and Howe 1992; McGreevy 2001), which refines the atomic positions against experimental data using Metropolis-type Monte Carlo moves to minimize the numerical differences between the observed and model data. In the case of ACC, the RMC procedure was applied to the pair distribution function (PDF) of synthetic hydrated ACC as obtained from total X-ray scattering (Fig. 2). Recent work has shown that the PDF of stable biogenic ACC is essentially identical to that obtained from synthetic ACC (Reeder et al. 2013). The RMC-derived structure suggested that ACC is nanoporous and chemically heterogeneous, expressing both water-poor Ca-rich regions and Ca-deficient regions that are relatively enriched in water and carbonate ions. Although this structure model has also been shown to be consistent with the results of calcium K-edge EXAFS and NMR spectroscopy (Michel et al. 2008; Goodwin et al. 2010), subsequent molecular dynamics simulations have shown that the RMC-derived structure corresponds to an unstable state, and that the system tends to become more homogeneous over time (Singer et al. 2012). The observed instability of the RMC structure highlights the main drawbacks of the RMC approach. While RMC modeling generally produces well-converged PDFs, the solution is not necessarily unique and a large number of candidate structures may fit the experimental data equally well; moreover, because the structure refinement is not based upon an underlying energy model, there is no guarantee that the solution will correspond to a locally stable state on the energy landscape. Despite these

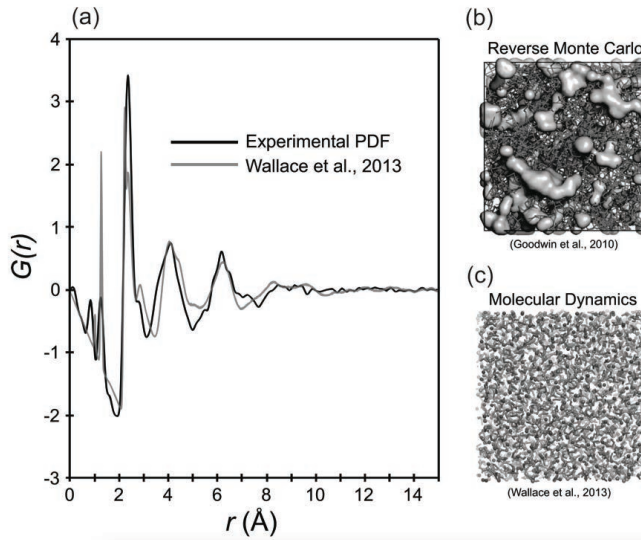

Figure 2. (a) Comparison of the experimental X-ray pair distribution function with the molecular dynamics-derived model structure of amorphous calcium carbonate (Wallace et al. 2013). (b) Snapshot of the RMC fit to the experimental PDF (Goodwin et al. 2010). (c) Model structure of amorphous calcium carbonate obtained from MD simulations of $CaCO_3(nH_2O)$ cluster aggregation and dehydration (Wallace et al. 2013). [Figures 2a and 2c reprinted with permission of AAAS from Wallace et al (2013) *Science* 341:885-889. Figure 2b adapted with permission of American Chemical Society from Goodwin et al. (2010) *Chem Mater* 22:3197-3205.]

limitations, RMC is a valuable technique that can provide insights into the local structure of disordered materials.

As an alternative to RMC, Wallace et al. (2013) constructed a model of hydrated ACC based on the results of MD simulations of calcium carbonate nanoparticle aggregation, coalescence, and dehydration (Fig. 2c). This approach utilized replica-exchange molecular dynamics (REMD) simulations (Sugita and Okamoto 1999; Okur et al. 2006; Chaudhury et al. 2012) to first grow hydrated carbonate clusters into a size regime comparable to the coherent X-ray scattering length in synthetic ACC (~1.5 nm) as well as to the so-called prenucleation clusters, which have an average diameter somewhat less than 1 nm according to cryo-TEM measurements (Pouget et al. 2009). The initial aggregate structure was obtained by randomly packing copies of a single 1.5 to 2 nm diameter $CaCO_3(nH_2O)$ cluster into a solvent-filled cell. Subsequently, the calcium to water ratio was slowly adjusted to match that of synthetic ACC (Ca/H_2O ~1.0) over a series of constant pressure molecular dynamics simulations. At each iteration, a few solvent molecules were removed from the solvent rich volumes between the clusters. The net effect of this procedure is that the clusters were driven to coalesce without disturbing the structural water molecules that are intrinsic to their character. The model ACC structure obtained by this approach, though not as exact a match to the experimental PDF as the RMC results, is locally stable and faithfully reproduces the most salient aspects of the experimental PDF (Fig. 2). Future studies of amorphous carbonate structures may benefit from a hybrid approach that integrates the beneficial aspects of the MD based approach with those of RMC.

Rather than modeling the experimental ACC structure, other workers have focused their efforts on characterizing the free energy landscape underlying structural transitions in anhydrous $CaCO_3$ nanoparticles using the metadynamics approach (Laio and Gervasio 2008; Quigley and Rodger 2008, 2009; Quigley et al. 2009, 2011). The common objective of almost all of these studies has been to determine which phase of $CaCO_3$ is thermodynamically preferred at a given nanoparticle size. The initial results of Quigley and Rodger (2008), performed at constant density for a ~2 nm diameter particle (75 $CaCO_3$ units), displayed two free energy minima corresponding to separate disordered and semi-ordered states, with the disordered state being overwhelmingly preferred. Later work by the same group showed that for larger particles (192 and 300 formula units) the landscape is possibly reversed, with the amorphous state being metastable with respect to both vaterite and calcite-like states (Freeman et al. 2010). The thermodynamic barriers associated with transforming between the disordered and semi-ordered states were predicted to be on the order of several hundred times k_BT, suggesting that reordering of the particles in the solid state is unlikely. However, in their most recent work, Quigley et al. (2011) showed that in constant pressure rather than constant density simulations (i.e., in the *NPT* versus the *NVT* ensemble) this trend reverses for the 75 formula unit cluster and the disordered state was predicted to be metastable with respect to a partially ordered state where more than 25% of the ions occupied calcite-like environments. Additionally, in the NPT simulations the barrier between the disordered and semi-ordered states was substantially reduced to a few tens of times k_BT, which suggests that some degree of ordering in the particles may be possible without partial dissolution. It was suggested that the enhanced stability of the amorphous phase at constant density arises from spatial confinement of the particle and solvent, as observed experimentally (Stephens et al. 2011). However, it is well known that synthetic and biogenic amorphous calcium carbonate contains a certain amount of water that may influence the stability of these phases; to date only anhydrous $CaCO_3$ particles have been investigated with the metadynamics simulation technique.

Crystalline carbonate phases

Bulk properties. Although it has been estimated that calcite and dolomite represent upwards of 90% of all naturally-formed carbonate minerals, according to Railsback (1999) there are at least 277 minerals that contain carbonate in their structure; these comprise a diverse class of

materials that can contain multiple anion species including carbonate, bicarbonate, hydroxide, chloride, fluoride, sulfate, phosphate, and silicate among others. Many of these phases may yet prove to be consequential for carbon capture, storage, and utilization efforts, particularly if impurities from the injection stream are present in significant quantities (Chialvo et al. 2013a, this volume) and if the pH of the brine is too low to support nucleation and growth of pure carbonate phases. This exposes a gap in the theoretical literature, at least as it pertains to mineral trapping of CO_2, in which the vast majority of calculations and simulations continue to be performed on phases that are naturally abundant but not necessarily very important for carbon sequestration. However, this also presents an opportunity for theoretical efforts to provide insights in the phase stability of less abundant carbonate minerals for which thermodynamic data are limited. A report by Krupka et al. (2010) attempted for the first time to consolidate all of the available data for the whole suite of carbonate-containing phases into a single thermodynamic database.

Ab initio and DFT calculations are widely used to determine the structure and properties of crystalline carbonate phases at high pressures where experimental measurements are arduous or impossible (Skorodumova 2005). These methods also are valuable tools for refining and testing structure solutions for difficult phases such as vaterite, for which there is still much disagreement (Demichelis et al. 2012; Mugnaioli et al. 2012; Wang and Becker 2012). Primarily, these simulation studies have aimed to determine the elastic properties (i.e., bulk moduli) (Elstnerová et al. 2010; Brik 2011; Ungureanu et al. 2012; Carteret et al. 2013), vibrational spectra (Medeiros et al. 2007; Kupka et al. 2009), and thermochemical properties such as heat capacity (Ungureanu et al. 2010) that are critical for predicting phase stability. Where comparison with experimental data is possible, good agreement is generally achievable. These data are often useful for constraining empirical potential models that can be used in MD and MC simulations. Several studies have also used quantum and classical methods to investigate the substitution of M(II) cations in the calcite and dolomite structures (de Leeuw and Parker 2000; de Leeuw et al. 2002; Austen et al. 2005; Elstnerová et al. 2010; Stashans and Chamba 2011) and to characterize cation disorder in dolomite (Zucchini et al. 2012). Additionally, the thermodynamics of mixing (described in more detail in Radha and Navrostky 2013, this volume) have been investigated using classical approaches for the $(Ca,Mg)CO_3$ (Vinograd et al. 2007), $(Ca,Mn)CO_3$ (Wang et al. 2011), and $(Ca,Sr)CO_3$ (Kulik et al. 2010) solid solutions (Fig. 3). Density functional theory calculations on transition metal carbonates, particularly iron(II) carbonate (siderite) and manganese(II) carbonate (rhodochrocite) have focused primarily on understanding the electronic band structures of these phases (Sherman 2009; Badaut et al. 2010). In the case of siderite, DFT calculations have also been applied to the analysis of the pressure induced magnetic transition from high spin to low spin iron at 40-50 GPa (Shi et al. 2008; Ming et al. 2012).

Interface with water. Compared to the number of high-precision experimental methods available to characterize the bulk structure of materials, there are relatively few scattering and spectroscopic approaches that can provide high fidelity information about interfacial structure. The only available data concerning the interfacial structure of carbonate mineral surfaces with water comes from specular and non-specular X-ray reflectivity (XR) studies of the calcite-water interface. Specular XR provides a laterally averaged view of the interfacial structure (i.e., only information about the vertical positions of atoms relative to the interface). Non-specular XR is a complimentary technique that can provide information about both the vertical and lateral positions of atoms across the interface, but it is only sensitive to atoms that reside in well defined sites, and much more time is required to make high quality measurements relative to specular XR. On its face it appears that non-specular XR might be generally preferable because of its ability to provide three-dimensional information about the interfacial structure. However, in their recent reexamination of the calcite-water interface, Fenter and Sturchio (2012) suggested that the uncertainties associated with previous studies (Geissbühler et al. 2004; Heberling et al. 2011) are substantially larger than the uncertainties in their present specular XR results due to the likely quantitative instability of the calcite surface during the course of the measurements.

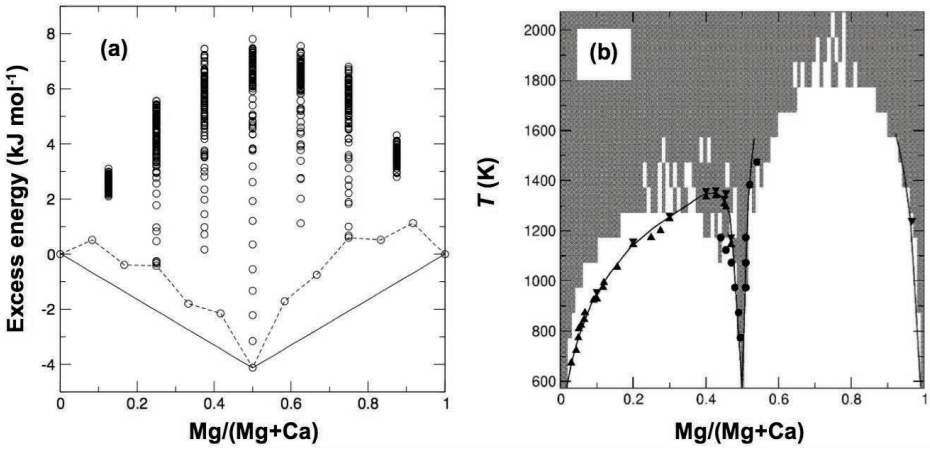

Figure 3. Prediction of the thermodynamics of mixing of the rhombohedral carbonate system $Ca_{1-x}Mg_xCO_3$ based on atomistic simulations (Vinograd et al. 2007). (a) Excess static structure energies of 700 $Ca_{1-x}Mg_xCO_3$ structures ($4 \times 4 \times 1$ supercell with $x = 0.125$ to 0.875 and different distributions of Ca and Mg atoms) predicted with an empirical model of interatomic interactions; the dashed line connects the minimum energy structures. (b) Comparison of predicted and experimental calcite-magnesite phase diagrams. The symbols and solid lines are experimental results (Goldsmith 1983); the gray and white regions indicate predictions of phase stability and instability (or metastability). The model predictions were obtained using a coarse-grained Monte Carlo simulation ($12 \times 12 \times 4$ supercell) where interactions between metal sites were described with an effective pair potential parameterized to fit the all-atom simulation results in (a). [Reprinted with permission of Elsevier from Vinograd et al. (2007) *Geochim Cosmochim Acta* 71, p 974-983.]

While Fenter and Sturchio (2012) observed that their data were inconsistent with previous combined non-specular and specular XR model fits, they reported consistency across the board with respect to the specular XR components of earlier studies (Geissbühler et al. 2004; Heberling et al. 2011). These specular XR results show the presence of at least two structured water layers adjacent to the $\{10\bar{1}4\}$ surface, and indicate that the calcite surface is relaxed (to a depth of up to 4 to 6 unit cells) relative to the bulk structure of calcite (Fenter and Sturchio 2012).

The structure of the calcite-water interface has been studied by molecular orbital calculations (Lardge et al. 2009; Villegas-Jiménez et al. 2009) and classical molecular dynamics (Spagnoli et al. 2006; Cooke and Elliott 2007; Aschauer et al. 2010; Cooke et al. 2010; Miyake and Kawano 2010; Doudou et al. 2012; Wolthers et al. 2012). While *ab initio* and DFT approaches are appealing due to the robust treatment of interatomic forces, their application to the calcite-water interface is challenging because the interfacial region is thick, spanning several unit cell depths of the calcite surface and extending a nanometer or more into the bulk solution. Handling such a large system is not readily tractable for electronic structure methods; therefore, investigations of this kind have been limited to the study of small portions of the calcite surface in contact with very few water molecules; these system sizes may or may not be sufficient to constitute an adequate representation of the interfacial region. Conversely, MD simulations can easily handle large systems due to their more empirical treatment of interatomic forces, but the results can be very sensitive to the parameterization of the forcefield. In a recent study, Fenter et al. (2013) compared experimental specular XR model fits to the results of four different MD simulations that used empirical potentials with different functional forms (nonpolarizable, polarizable, reactive). Quantitative agreement between the measured and predicted XR spectra was found to be poor in each case, primarily because the MD models did not correctly predict the relaxation of the calcite structure in the vicinity of the interface (Fig. 4). Remarkably, the

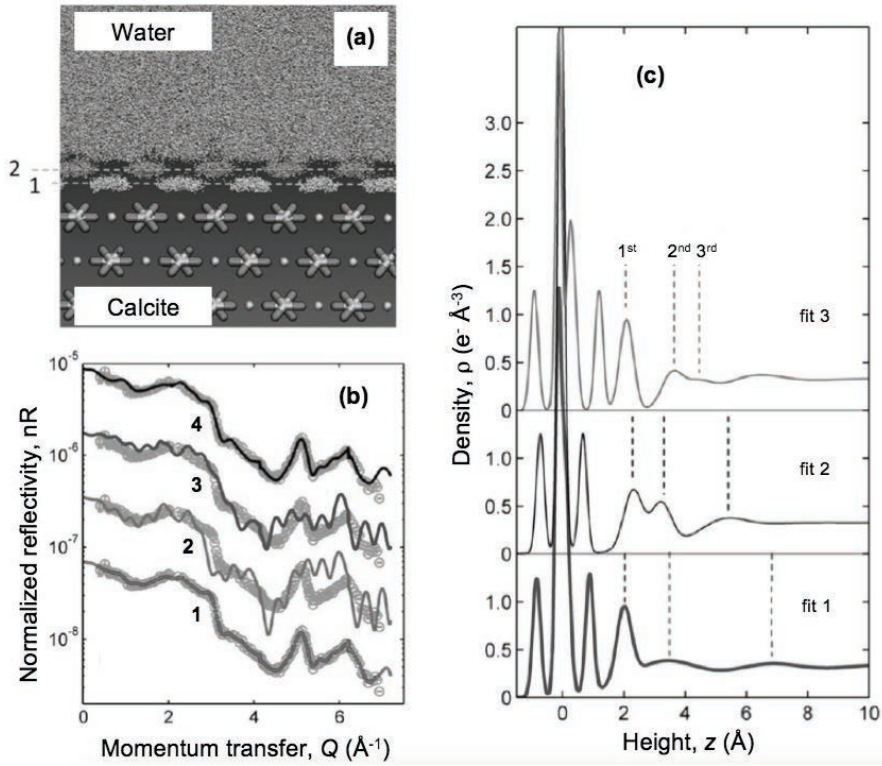

Figure 4. Examination of the structure of water and calcite on terraces of the $\{10\bar{1}4\}$ calcite surface using a combination of X-ray reflectivity (XR) data and MD simulation results (Fenter et al. 2013). (a) MD simulation prediction of water structure on the calcite surface. The lower part of the figure shows the average position of the calcite atoms during the simulation (spheres: Ca atoms; sticks: C and O atoms). The upper part of the figure shows the range of positions of water O atoms during the simulation (O atoms shown as points, with coordinates taken from 500 frames sampled at regular intervals during the simulation). The planes of O atoms coordinated to surface Ca and CO_3 groups are labeled 1 and 2. (b) Comparison of the normalized XR data (circles) with four different fitting schemes (lines): (1) direct fit to the XR data, (2) direct comparison of the MD results with the XR data, (3) hybrid scheme in which only the interfacial calcite structure was taken from the MD results, and (4) hybrid scheme in which only the interfacial water structure was taken from the MD results. (c) Total electron density profile in the direction normal to the interface ($z = 0$ at the location of the plane of surface Ca atoms) calculated by directly fitting to the XR data (fit 1) or by fitting the XR data with a model that was informed by two different MD simulation predictions (fits 2 and 3). All three fits described the XR data equally well. [Adapted with permission by the American Chemical Society from Fenter et al. (2013) *J Phys Chem C* 117:5028-5042.]

two most simple force fields (non-polarizable, non-reactive empirical pair potentials) tested by Fenter et al. (2013) predicted interfacial water structures that were consistent with the XR data, whereas the more complex (polarizable or reactive) force fields did not.

Molecular dynamics simulations and *ab initio* calculations have also been used to assess the acidity of various sites on the $\{10\bar{1}4\}$ surface (defects, terraces, acute and obtuse ledges, kinks, and corner sites). On defect-free terraces, water is favored to adsorb associatively (Kerisit et al. 2003; Lardge et al. 2009). However, defect and edge sites can promote water dissociation (Kerisit et al. 2003). From X-ray photoelectron spectroscopy (XPS) there is evidence of H-CO_3 and Ca-OH type bonding environments being present on the calcite surface (Stipp and Hochella 1991). Two recent studies (Andersson and Stipp 2012; Wolthers et al. 2012) concluded also

that the acidity of surface sites depends strongly on the nature of the local water structure and that dissociative adsorption is promoted to varying degrees at edge, kink, and corner sites, with dissociation being generally most favored at kink and corner sites and along acute step edges. These findings reinforce the experimental observation that obtuse and acute steps behave differently, particularly with respect to their interactions with impurities (Davis et al. 2000, 2004; Wasylenki et al. 2005a,b). Additional insights into the behavior of impurity ions at the calcite-water interface may be gained by revisiting previous studies (de Leeuw and Parker 2000; de Leeuw 2002; de Leeuw et al. 2002; de Leeuw and Cooper 2004) with reactive empirical potentials that can account for variations in surface speciation.

Geochemical kinetics at $M^{(II)}CO_3$-water interfaces

Formation of carbonate minerals. To date, modeling studies of carbonate mineral formation from solution have focused predominantly on the calcite-water system. Typically it is assumed that mineral precipitation occurs by nucleation, which is a specific mechanism of phase-separation by which the free energy of a metastable system is reduced by overcoming a free energy barrier opposing the formation of a new phase (De Yoreo et al. 2013, this volume; Radha and Navrotsky 2013, this volume). Physically, nucleation occurs as thermally driven fluctuations induce the assembly of unstable clusters, which grow ion-by-ion against a free energy barrier until a critical size threshold is surpassed. Beyond the critical size the clusters are stable with respect to dissolution, and unstable with respect to continued growth of the new phase. However, because the height of the free energy barrier opposing nucleation is inversely proportional to supersaturation, the free energy barrier opposing nucleation vanishes if the chemical driving force for precipitation becomes large enough. When the free energy barrier disappears, the phase-separation mechanism changes from nucleation to spinodal decomposition. At the spinodal line, the same fluctuations that in the case of nucleation form clusters that are unstable with respect to dissolution instead produce clusters that are unstable with respect to growth. Furthermore, once the system enters the spinodal regime, the assumption of ion-by-ion growth that is implicit in the classical kinetic treatment of nucleation (Nielsen 1964) no longer applies in a strict sense and phase separation may proceed by cluster coalescence as well as by single ion addition.

The mechanism of phase-separation in $CaCO_3$-water systems is challenging to discern largely because the many varied observations concerning the early stages of mineral formation are difficult to reconcile within a single theoretical framework. It is likely, especially given recent suggestion that there may be a liquid-liquid binodal in the system (Wallace et al. 2013), that much of the observed variability may arise from the particular relationship of a given set of experimental conditions to the supposed liquid-liquid coexistence line. At low driving force, direct nucleation of the solid phases may be the only accessible mechanism. If the system approaches the binodal (and, beyond that, the spinodal) it may also become possible to form a dense liquid phase by nucleation and spinodal decomposition.

Theorists have the potential to quantify free energy landscapes of early stage carbonate mineral formation, although the rarity of nucleation events makes the simulation of systems comparable to experimental conditions difficult for suitably long timescales. Additionally, the ability of potential-based simulation methods to elucidate phase separation processes depends on the development of force fields that accurately describe both solid and aqueous phases. The force field for the $CaCO_3$-water system developed by Raiteri et al. (2010) is a promising step towards the goal of simulating $CaCO_3$ precipitation events as it accurately reproduces free energies of component ions in solution as well as the energy difference for the calcite to aragonite phase transition. The use of non-reactive potentials, however, prevents direct description of carbonate speciation and limits its applicability for studying nucleation events because carbonate-bicarbonate conversion occurs during $CaCO_3$ nucleation at pH levels relevant to natural systems. Development of reactive carbonate models, like the one recently proposed by Gale et

al. (2011) for the aqueous calcium carbonate system, will help future simulation efforts better study carbonate formation processes.

At present, most simulations pertinent to $CaCO_3$ nucleation have utilized MD simulations (Martin et al. 2006; Raiteri and Gale 2010; Demichelis et al. 2011; Finney and Rodger 2012) and enhanced sampling methods including umbrella sampling (Tribello et al. 2009; Demichelis et al. 2011) and metadynamics (Quigley and Rodger 2008) in an attempt to identify $CaCO_3$ species that act as intermediates between ions in solution and post-nucleation amorphous or crystalline $CaCO_3$ phases. Di Tommaso and de Leeuw (2008, 2009) have examined $CaCO_3$ ion pair formation as a first step towards modeling homogeneous nucleation from solution. Such simulations have repeatedly shown that cluster aggregation and ion or cluster addition to amorphous nanoparticles in solution is essentially barrier-less (Fig. 5), unlike ion or cluster addition to ordered $CaCO_3$ phases (Martin et al. 2006; Tribello et al. 2009; Raiteri and Gale 2010).

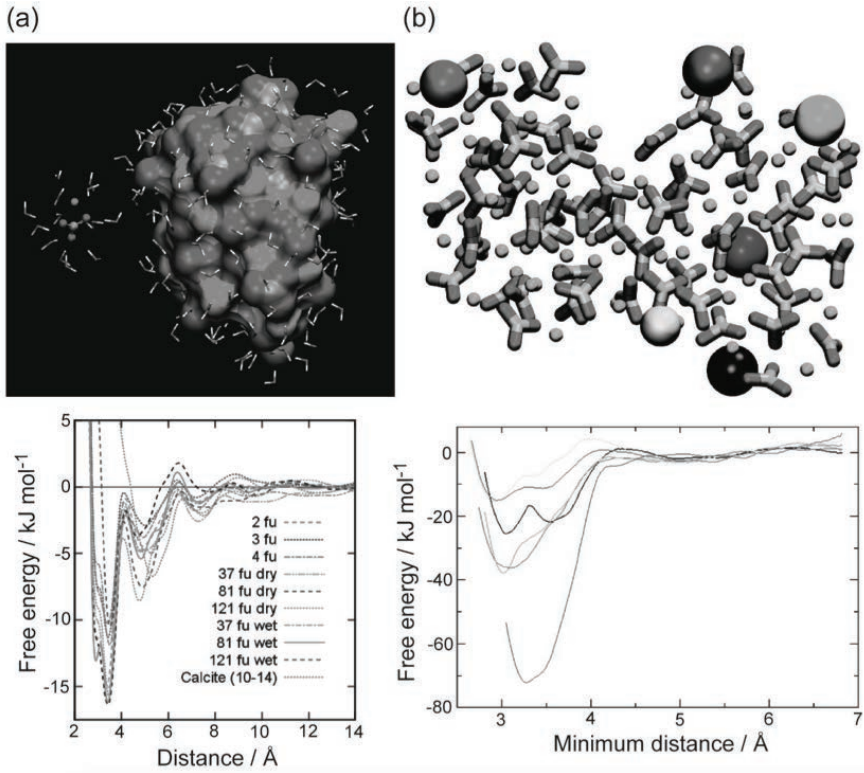

Figure 5. Atomistic scale calculations with model ACC clusters demonstrate that calcium ion and $CaCO_3$ ion pair addition to ACC are energetically favorable processes. (a) Illustration of a $CaCO_3$ ion pair (visible on the left with water molecules in its first solvation shell) being added to a model ACC cluster (the large structure on the right, also shown with its neighboring water molecules) and free energy profiles for the addition of a $CaCO_3$ ion pair to ACC clusters of varying size (formula units, fu) and hydration state (Raiteri and Gale 2010). The equivalent profile for addition to the $\{10\bar{1}4\}$ surface of calcite (light gray line with an overall minimum at ~5 Å instead of ~3 Å) is shown for comparison. (b) Model ACC cluster with potential calcium ion addition sites (shown as large spheres) and free energy profiles for the addition of Ca^{2+} at the different sites (Tribello et al. 2009). [Adapted with permission of the American Chemical Society from Raiteri and Gale (2010) *J Am Chem Soc* 132:17623-17634, and Tribello et al. (2009) *J Phys Chem B* 113:11680-11687.]

An interplay between calcium-carbonate coordination number and ion hydration has been invoked to explain differences in cluster stability based on size (Finney and Rodger 2012), although no specific cluster size or makeup has been identified as a likely candidate for the stable prenucleation clusters. Hydration effects also are influential in modulating the energetic barriers to cluster aggregation and growth—the disorder of water layers at unstructured $CaCO_3$ nanoparticles may explain the low energy barrier to forming and growing these species compared to crystalline particles, which exert stronger ordering on the surrounding water molecules (Tribello et al. 2009; Raiteri and Gale 2010). Additional simulations of heterogeneous nucleation on self-assembled monolayers have examined the roles of monolayer ionization, epitaxial matching, and headgroup orientation on nucleating $CaCO_3$ (Freeman et al. 2008), and successfully predicted the orientations of calcite crystallization on carboxylic-acid terminated surfaces (Quigley et al. 2009).

It should be noted that the majority of these simulations describe high pH and high supersaturation regimes, where CO_3^{2-} is the dominant carbonate species and cluster growth and aggregation can be observed on time scales accessible by simulation. Both of these limitations are problematic because the dominant species in most natural systems is HCO_3^- and because the mechanism of phase separation depends upon supersaturation. Thus, high concentration simulations may only probe those mechanisms, such as spinodal decomposition, that are active at high driving forces.

Ion attachment and detachment at carbonate step edges. The flat $\{10\bar{1}4\}$ surface of calcite is by far the most stable face and dominates the morphology of the mineral. From atomic force microscopy (AFM) experiments, growth and dissolution on these surfaces is known to occur at steps (Gratz et al. 1993) and spiral dislocations (Hillner et al. 1993). Early simulations of ion detachment at steps include a kinetic Monte Carlo model that reproduces AFM data for calcite dissolution (McCoy and LaFemina 1997) and MD simulations that predicted $CaCO_3$ unit removal to be more energetically favorable from the obtuse step compared to the acute step (de Leeuw et al. 1999), as seen experimentally. Subsequent MD calculations of free energy profiles (Spagnoli et al. 2006) and energy minimizations (Kerisit et al. 2003) concluded that ion detachment occurs preferentially at step edges compared to the flat surface, and identified the reaction of water with edge CO_3 groups as the first step in the detachment process. In the case of $BaSO_4$, a potential analog for $CaCO_3$, metadynamics and umbrella sampling calculations showed that metal detachment from step edges is a multi-step process as described in Figure 6 (Stack et al. 2012). Metal detachment from calcite step edges may be equally complex.

Simulations of ion attachment at carbonate step edges have been carried out for MCO_3 (where M = Ca^{2+}, Mg^{2+}, Fe^{2+}, Sr^{2+}, or Cd^{2+}) growth on the calcite $\{10\bar{1}4\}$ surface (de Leeuw 2002). As for attachment of Ca^{2+} ions, the initial incorporation of impurity ions is more exothermic at the obtuse step, with free energies of attachment 44 to 86 kJ mol^{-1} more negative than at the acute step, depending on the cation. The calculated free energies indicate that impurity incorporation competes effectively with calcite formation for a single row of growth, but becomes increasingly endothermic for subsequent rows due to the mismatch with the underlying calcite lattice. Thus, subsequent growth becomes unfavorable (Davis et al. 2000) and growth is poisoned, as seen experimentally (Wasylenki et al. 2005b; Nielsen et al. 2013). The development of a new force field for MD simulations of hydrated calcium carbonate (Raiteri et al. 2010) highlights a few differences from previous models (Jackson and Price 1992; Pavese et al. 1992, 1996) with implications for step growth. Namely, inner-sphere complexation of Ca^{2+} at the flat $\{10\bar{1}4\}$ surface is unfavorable and CO_3^{2-} is only weakly attracted to the interface. Thus, the traditional view of growth wherein ions adsorb to the surface and, then, diffuse to growth sites may be unrealistic for the calcite $\{10\bar{1}4\}$ surface, as ions prefer to diffuse via solution. Continued development of force field parameters that accurately describe the energetics of both aqueous and solid phases will aid in future simulations of carbonate growth mechanisms.

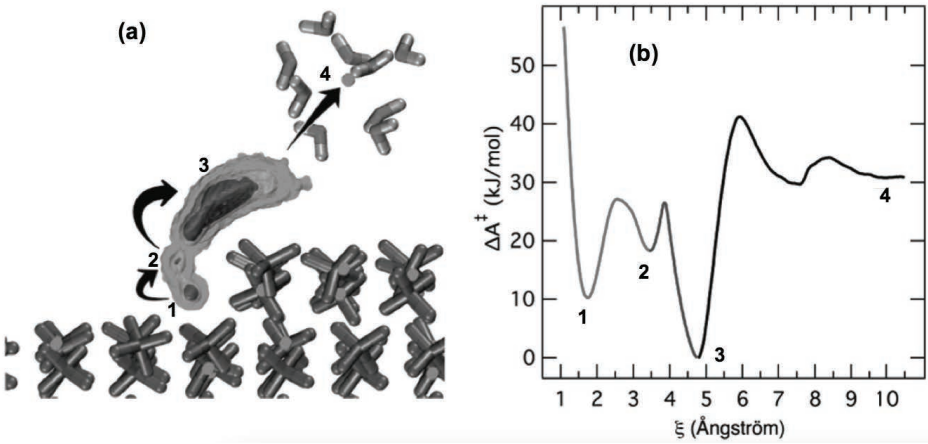

Figure 6. Metadynamics and umbrella sampling calculations reveal that the attachment of Ba^{2+} on a $BaSO_4$ step edge involves several stable states: (1) Ba at the step edge, (2) Ba slightly detached from the step edge, (3) Ba forming an inner-sphere surface complex above the step edge, and (4) Ba in solution (Stack et al. 2012). The different stable states are shown in (a) a two-dimensional map of the potential energy landscape calculated with the metadynamics method, and (b) a plot of the free energy profile along the minimum free energy path as calculated with the umbrella sampling technique (this technique shows a fifth stable state at $\xi \approx 7.5$ Å where Ba forms an outer-sphere surface complex). The potential energy landscape associated with Ca^{2+} attachment to a $CaCO_3$ kink site is likely to be similarly complex. [Adapted with permission of the American Chemical Society from Stack et al. (2012) *J Am Chem Soc* 134:11-14.]

Influence of organic species on carbonate formation and growth. Organic additives have long been known to modify calcium carbonate growth rate (Addadi and Weiner 1985), morphology (Wada et al. 1999), and nucleating phase (Falini et al. 1996). With recent developments in understanding the early stages of $CaCO_3$ crystallization, more attention is being paid to how organic molecules affect the formation, evolution, and stability of amorphous $CaCO_3$ phases and prenucleation species. While the motivation for these studies often lies in understanding biomineralization, organic species are ubiquitous in most environments and are likely to also influence non-biogenic carbonate formation. The specific functions of organic additives and the mechanisms by which they act, however, remain difficult to discern because of their chemical complexity and the fact that a single organic molecule can have multiple roles, and these roles can change depending on concentration and other conditions. Titration work in the presence of organic molecules by Gebauer et al. (2009) constitutes a first effort at developing a framework to categorize additives based on their effects on all stages of $CaCO_3$ formation. Organic species are divided into classes based on their interaction with calcium ions, soluble clusters, nanoparticles, amorphous intermediates, and nucleated crystals.

In an attempt to examine how acetate, aspartate and citrate influence prenucleation clusters of $CaCO_3$ within the context of these categories, the MD simulation study by Raiteri et al. (2012) highlights the complexity of organic-$CaCO_3$ interactions and the difficulty in identifying individual roles and mechanisms. Both aspartate and citrate are classified as nucleation inhibitors from titration data, yet only citrate binds strongly enough to Ca^{2+} in solution to inhibit nucleation through the lowering of supersaturation. The simulations indicate that aspartate, which is also classified as a stabilizer of amorphous intermediates, has a moderate binding affinity for both clusters and amorphous nanoparticles (a weaker affinity than citrate, which is classified as a stabilizer of prenucleation clusters but not of amorphous intermediates). This moderate affinity of aspartate for amorphous nanoparticles presumably allows stabilization of the intermediate

phase, as seen in the experimental formation of polymer-induced liquid precursor (PILP) in the presence of polyaspartate (Gower and Odom 2000) and in agreement with other MD simulation work (Finney and Rodger 2012). Additionally, the strong interaction of citrate with all $CaCO_3$ species except basal calcite surfaces may help explain the experimentally observed bias towards calcite in systems containing citrate. Results from the metadynamics work of Freeman et al. (2010) suggest a similar mechanism at work in the case of eggshell protein OC-17; the protein is proposed to bind to ACC nanoparticles, facilitate the transformation to calcite and, then, desorb from the crystal surface as the mineral begins to grow.

Other computational studies have focused on understanding the mechanisms that underlie experimentally observed effects of organics on $CaCO_3$ step growth kinetics. Atomistic energy minimizations of phosphonates indicate that these molecules bind more strongly to steps than to the flat $\{10\bar{1}4\}$ surface, confirming results of AFM growth experiments (Nancollas et al. 1981; Gratz et al. 1993). More recent MD simulation work again confirms the preference of organic species (in this case polyaspartate and polyacrylic acid) for steps over flat surfaces, and further speculates that the inhibitory ability depends on an interplay between surface/step binding affinity and affinity for ions in solution (Aschauer et al. 2010; Fig. 7). Experimental studies demonstrate that impurities, including organic molecules (peptides and peptoids), influence calcite growth differently depending on their concentration: at low concentrations they accelerate calcite step velocities and growth rates, whereas at high concentrations they inhibit calcite growth (Elhadj et al. 2006a; Chen et al. 2011). The organic concentration at which growth is inhibited is related to the effectiveness of the organic as a growth accelerator (more effective growth promotion corresponds to a lower inhibitory concentration). Elhadj et al. (2006b) modeled polyaspartate (Asp_n) attachment at calcite steps with a quantum mechanics method and determined that binding strength increases with Asp chain length, reducing the Asp_n concentration required to block step growth. Results from molecular simulations have also suggested that enhancements in step growth rate may be explained by the ability of organic molecules to lower dehydration barriers, either of ions (Piana et al. 2007; Hamm et al. 2010) or of the mineral surface (Piana et al. 2006), both of which represent significant barriers to step growth . Lastly, organic self-assembled monolayers, commonly used experimentally as templates for heterogeneous $CaCO_3$ nucleation (Aizenberg et al. 1999; De Yoreo et al. 2013), also have been studied computationally to understand their interaction with nucleating $CaCO_3$ minerals. This work (Quigley et al. 2009) demonstrated that the formation of oriented crystals on self-assembled monolayers does not arise as a consequence of epitaxy, but rather by the cooperative reorganization of both the mineral phase and the organic layer.

CO_2-BRINE-MINERAL SYSTEMS

CO_2-brine two-phase systems

Equation of state. In order to predict the fate of CO_2 in geologic carbon sequestration, it is essential to consider the phase behavior of CO_2 when placed in contact with the geological medium (DePaolo and Cole 2013, this volume). A molecular model used for that purpose should correctly describe the thermodynamic properties of mixtures of CO_2 with brine as a function of thermodynamic conditions: pressure (P) or density (ρ), temperature (T), and composition (nature of the ions and their concentrations) in the aqueous phase. Several force fields have been proposed in the literature to investigate, using various approaches (the most common being the Grand Canonical Monte Carlo, GCMC, simulation technique), the phase behavior of pure CO_2 and its mixture with pure and saline water.

The most popular force field for CO_2, the EPM2 model, was introduced by Harris and Yung (1995). This simple 3-site model, in which C and O atoms interact via pair-wise additive Lennard-Jones (LJ) and Coulomb (with point charges) potentials, is able to correctly capture

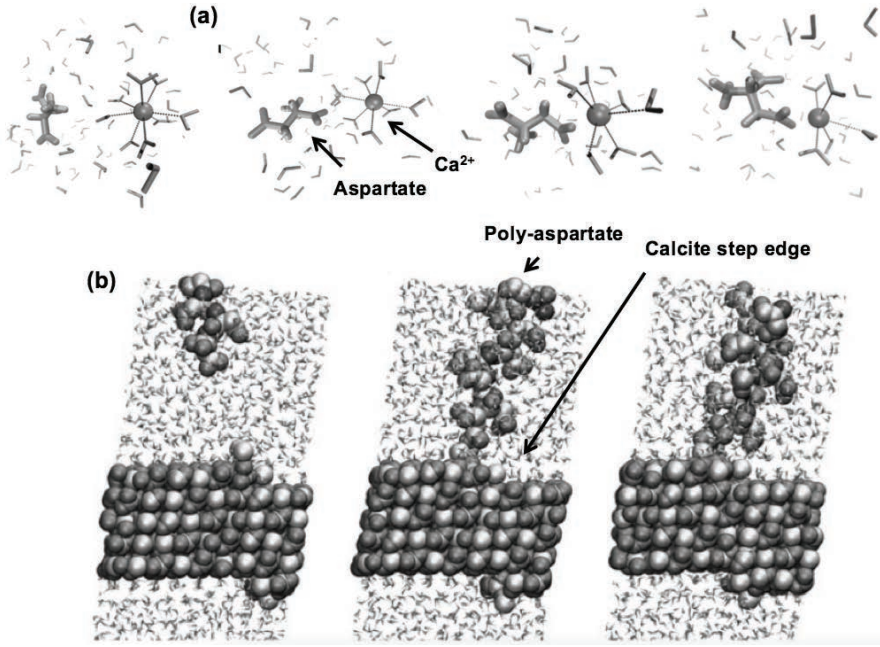

Figure 7. Organic acids may influence calcite growth rates either by (a) interacting with Ca^{2+} in solution, of (b) interacting with growth (kink) sites on the calcite surface. (a) Molecular dynamics simulations show that Asp binding to Ca^{2+} in bulk liquid water strongly disrupts the solvation shell of calcium: the number of water molecules coordinating Ca decreases from 8 to 5 as Asp approaches Ca (Hamm et al. 2010). (b) Molecular dynamics simulations show that n-Asp spontaneously adsorbs on negatively charged kink sites, but not on the uncharged flat surface of calcite (Aschauer et al. 2010). [Figure 7a adapted with permission by the American Chemical Society from Hamm et al. (2010) *J Phys Chem B* 114:10488-10495; Figure 7b reprinted with permission by Elsevier from Aschauer et al. (2010) *J Colloid Interface Sci* 346:226-231.]

the Liquid-Vapor equilibrium (LVE) and the critical properties of pure CO_2 in the (ρ,T) plane. Accounting for bond flexibility in this model does not appreciably change the phase boundaries; therefore, simulations with the EPM2 model usually treat the CO_2 molecule as a rigid entity. The similar Exp-6 and TraPPE (Transferable Potential for Phase Equilibria) models are also able to describe the LVE of pure CO_2 (Potoff et al. 1999; Potoff 2001). Zhang and Duan (2005) optimized parameters of a similar force field for the prediction of the LVE and critical properties. Other force fields have been proposed, either with increased complexity to refine the prediction of CO_2 properties (such as the composition of the coexisting phases or the critical behavior) or with simplified interactions to increase computational efficiency. Examples of the latter type include several 1-site models that differ according to their treatment of electrostatic [point quadrupole (Vrabec et al. 2001), thermally averaged quadrupole (Mognetti et al. 2008) or without explicit electrostatics (Avendano et al. 2011)] and non-electrostatic interactions [isotropic (Vrabec et al. 2001; Mognetti et al. 2008) or anisotropic LJ (Persson 2011), with Lorentz-Berthelot combining rules for interactions between atoms of different type or more elaborate ones (Schacht et al. 2011). A 3-site model with LJ interactions and a point quadrupole, optimized for LVE, has also been proposed (Merker et al. 2010). These simpler models are usually parameterized to reproduce the experimental LVE and/or critical properties or analytical equations of state such as the Statistical Associating Fluid Theory (SAFT) model (Avendano et al. 2011; Schacht et al. 2011). In the opposite direction, refined models have been proposed that introduce flexibility (Zhu et al. 2009; Cygan et al 2012) or polarization effects

using distributed point polarizabilities (Wang et al. 2012a). Finally, *ab initio* calculations have enabled the direct investigation of the effect of dispersion on the properties of supercritical CO_2 ($scCO_2$) (Balasubramanian et al. 2009) and the development of improved force fields accounting for non-additive interactions (Oakley and Wheatley 2009) or based on a rigorous energy decomposition and Symmetry Adapted Perturbation Theory (Yu et al. 2011).

Some studies have been devoted to the properties of a single phase, such as the effect of density on the structure of $scCO_2$ along an isotherm (Ishii et al. 1996), the structure of liquid CO_2 (Neuefeind et al. 2009) or more rarely dynamical properties (In Het Panhuis et al., 1998; Nieto-Draghi et al. 2007; Garcia-Ratés et al. 2012). In all cases, comparison with experimental data provides a critical test of the accuracy of the force fields. For example, Nieto-Draghi et al. (2007) found that the EPM2 model reasonably describes the shear viscosity and thermal conductivity under sub-critical conditions, except for the thermal conductivity at low density. Such a good prediction of dynamical properties by the EPM2 model is remarkable, as the force field was calibrated to reproduce only thermodynamic properties, and suggests that the interactions between CO_2 molecules are relatively well described on the microscopic level.

The phase equilibria of pure CO_2 have been investigated in many simulation studies, not only for their interest per se and their relevance for practical applications, but also as a critical test of molecular models, in particular as a first step towards predicting the phase behavior of mixtures containing CO_2. For example, Errington et al. (1998) used GCMC simulations to predict the LVE of pure CO_2 with the EPM2 model and its binary mixture with water. The same model was investigated by Vorholz et al. (2000) using GCMC simulations in the NVT and NPT ensembles (Fig. 8a). These studies, together with the above-mentioned ones, confirm the ability of the EPM2 model to correctly describe the LVE and critical properties of pure CO_2. The Fluid-Solid equilibria (FSE) have attracted less attention, but have also provided interesting insights. Albo and Müller (2003) discussed the relevance of simulation methods and the choice of force field for the prediction of these equilibria. More recently, Péréz-Sanchez et al. (2013)w analyzed the role of the quadrupole moment on the melting curve of dry ice up to 1000 MPa by comparing several popular force fields. They found that, firstly, while the models were all able to reproduce the experimental LVE, their prediction of the melting curve differed significantly; secondly, of all the models tested, the TraPPE force field yielded the best predictions for melting curve and triple point properties and; thirdly, a large quadrupole moment is required to correctly describe the properties of the solid phase. From the dynamical point of view, molecular simulations have been used by Leyssale et al. (2005) to investigate homogeneous crystal nucleation in supercooled CO_2.

Several groups have built upon the promising results on the thermodynamic properties of pure CO_2 by combining the EPM2 or TraPPE models with popular force fields for water to predict the phase behavior of their binary mixtures. For example, Errington et al. (1998) and Vorholz et al. (2000) investigated the SPC and TIP4P water models. They found that the use of standard combining rules for the LJ parameters of the pure components yielded very good results for the LVE between EPM2 and both SPC or TIP4P, for temperatures of 348 to 393 K and pressures up to 20 MPa. Among several combinations of force fields for the solubility of CO_2 in water over a wide range of thermodynamic conditions, the Exp-6 model (Errington and Panagiotopoulos 1998; Potoff et al. 1999) gives the best agreement with experimental data (Lísal et al. 2005). The most comprehensive comparison of force fields for mixtures of water and CO_2, over a wide range of P (0 to 1000 bar) and T (323 to 623 K) was carried out by Liu et al. (2011). While none of the models could reproduce the experimental data over the whole range of thermodynamic conditions, it was found that, firstly, below 523 K, i.e., away from the critical region of water, the Exp-6 model gives the best predictions for the CO_2-rich phase, whereas the TraPPE/TIP4P2005 combination is more accurate for the H_2O-rich phase (Fig. 8b); secondly, near the critical region (523 to 623 K) none of the models correctly predicts

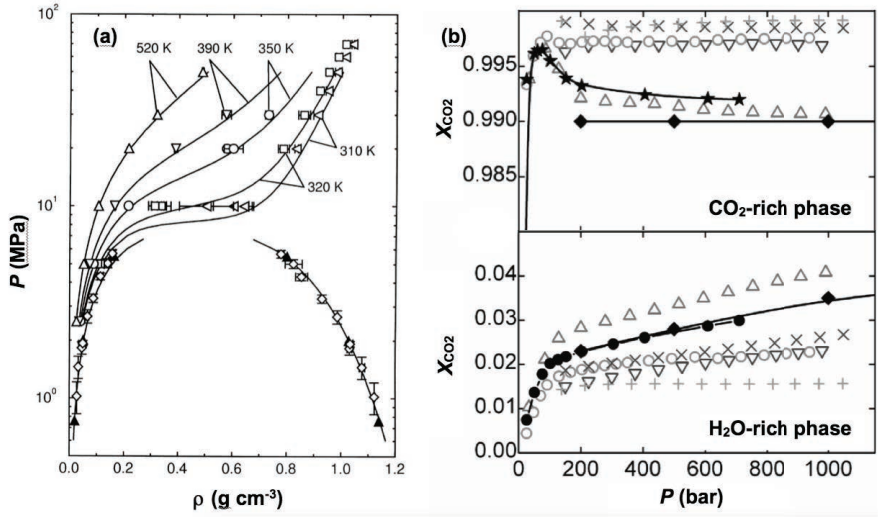

Figure 8. Model predictions of the phase properties of pure CO_2 (left) and CO_2-water mixtures (right). (a) Pressure-density relation of pure CO_2 calculated with the equation of state of Bender (1970) (solid line) or predicted using GCMC simulation with the EPM2 CO_2 model (open symbols) at T = 290 to 520 K (Vorholz et al. 2000). (b) Pressure-composition relation of CO_2-water two-phase mixtures predicted using GCMC simulation (Liu et al. 2011) with different models of water and CO_2 [Exp-6 water and CO_2 (Δ), EPM2+TIP4P/2005 (+), TraPPE+TIP4P2005 (×), EPM2+SPC (o), EPM2+TIP4P (∇)]. The filled symbols are experimental data from Wiebe and Gaddy (1939) (circles), Wiebe (1941) (stars), and Takenouchi and Kennedy (1964) (diamonds). [Figure 8a reprinted with permission by Elsevier from Vorholz et al. (2004) *Fluid Phase Equil* 226:237-250; Figure 8b reproduced with permission of American Chemical Society from Liu et al. (2011) *J Phys Chem B* 115:6629-6635.]

the critical behavior, even though the Exp-6 model gives the correct qualitative features and; thirdly, modified Lorentz-Berthelot combining rules provide only minor improvements. This extensive study highlights the need for improving the force fields for the prediction of binary mixture properties. To achieve this goal, it might be useful to consider in the parameterization process the dynamical properties, which have been only rarely investigated for mixtures (Fernández et al. 2005; Nieto-Draghi et al. 2007; Garcia-Ratés et al. 2012). An alternative approach consists in designing modified Lorentz-Berthelot combining rules for the CO_2-water interaction that are fitted to the mutual solubility of water and CO_2, but with the mole fraction of water in CO_2 corrected to account for the polarization change associated with water evaporation (Vlcek et al. 2011; Chialvo et al. 2013a, this volume). This approach follows naturally from the fact that non-polarizable water models will necessarily underestimate the enthalpy of vaporization of water because they inherently cannot account for the different dipole moments of water in scCO_2 and in liquid water.

Finally, a few studies have considered the more complex mixtures of CO_2 with brine. Vorholz et al. (2004) tested the ability of the SPC and TIP4P (for water) and EPM2 (for CO_2) models, with various potentials for sodium and chloride ions, to reproduce the solubility of CO_2 in NaCl aqueous solutions, for temperatures of 373 to 433 K and pressures up to 10 MPa. Several salt molalities, including above the solubility limit, were simulated. While the "salting-out" effect observed in experiments was qualitatively reproduced, the decrease in CO_2 solubility in the presence of salt was overestimated. Improvements can be obtained by introducing modified combining rules for the interactions between unlike species. Molecular dynamics simulations further provided data on the diffusion and electric conductivity of CO_2-

brine mixtures, for which few experimental results are available, as well as molecular scale information, such as rotational relaxation times. Garcia-Ratés et al. (2012) investigated these properties with the SPC/E and EPM2 models for water and CO_2 and two models for the ions. Finally, the solvation of cations in $scCO_2$-water mixtures at 300 K was studied by Criscenti and Cygan (2013). This study investigated the partitioning of alkali and alkaline Earth metals between the liquid aqueous and supercritical CO_2-rich phases. Although ions consistently prefer the aqueous phase, the partitioning of cations into CO_2 increases with ion size, because of the inverse relation between ion size and solvation energy. When both phases are in contact, cations can be found in the CO_2 phase as partially (e.g., K^+ or Cs^+) or fully (Sr^{2+}) hydrated complexes.

Interfacial tension. Once the composition of the co-existing fluid phases is known under given thermodynamic conditions, molecular simulations allow computing another important property in the context of CO_2 sequestration, namely the interfacial tension between the two phases, and interpreting its microscopic origin. Such simulations usually involve slabs of fluids and the determination of the normal and tangential components of the local pressure tensor: the interfacial tension (IFT) is then given by the integral of the difference between these components across the interface. In fact, these interfacial components are also related to the bulk phase stability. Kraska et al. (2009) exploited this connection to the LVE of CO_2 in order to predict the spinodal (limit of metastability) and the equation of state in the unstable region. The interface between pure water and $scCO_2$ was investigated with the SPC and EPM2 models by Zhao et al. (2011). By analyzing the relative contribution of the water-water, CO_2-CO_2 and water-CO_2 interactions to the IFT, they showed that the overall IFT is dominated by the water "self" contribution (consistently with the very large IFT for the water liquid-vapor interface) and that the CO_2-water interactions contribute negatively, i.e., they lower the IFT. The decomposition of the IFT according to the various terms of the force field (electrostatic, bond stretching, angle bending, LJ) indicated that only the LJ interactions contribute favorably to the surface tension. Nevertheless, one should keep in mind that such a decomposition in the design of a force field is not without its ambiguities and, therefore, the last point should be considered with caution. Finally, the authors considered the orientation of interfacial molecules and found that both water and CO_2 are aligned nearly parallel to the Gibbs Dividing Surface. The brine-water interface was also investigated by Zhao et al. (2011) who considered a 2.7 M $CaCl_2$ aqueous solution. They predicted that IFT increases with salinity, as observed experimentally, and they suggested that this salinity-dependence results from a change in the orientation of interfacial water caused by the ions.

The most comprehensive molecular simulation study of the water-CO_2 IFT was performed by Nielsen et al. (2012). They assessed the ability of several force fields to predict the IFT at pressure and temperature conditions relevant to GCS (Fig. 9). The combinations of three CO_2 models and two water models all predicted the same qualitative trends: at fixed T, the IFT decreases strongly with increasing P below the critical CO_2 pressure, then levels off, while it depends only slightly on T at fixed P, as observed experimentally. Quantitative differences were observed between the different force fields, mainly due to variations in the description of short-range interactions that dominate the overall value of the IFT. The PPL CO_2 model (In Het Panhuis et al. 1998) combined with the TIP4P/2005 CO_2 model (Abascal and Vega 2005) provided the best agreement with experimental data over the whole 5-45 MPa range at 383 K. The PPL model combined with the SPC/E water model underestimated the IFT by ~10 mN/m, i.e., the amount by which the SPC/E model underestimates the IFT of pure liquid water. The simulation results of Nielsen et al. (2012) showed that the P-dependence of IFT is consistent with the Gibbs adsorption equation ($d\gamma_{wg} = -\Gamma_{CO_2}^{(H_2O)} d\mu_{CO_2}$, where γ_{wg} is the CO_2-water IFT, μ_{CO_2} is the chemical potential of CO_2, and $\Gamma_{CO_2}^{(H_2O)}$ is the surface excess of CO_2 at the interface—calculated using water as a reference phase). The difference between the IFT values predicted with different CO_2 models was shown to result from differences in the

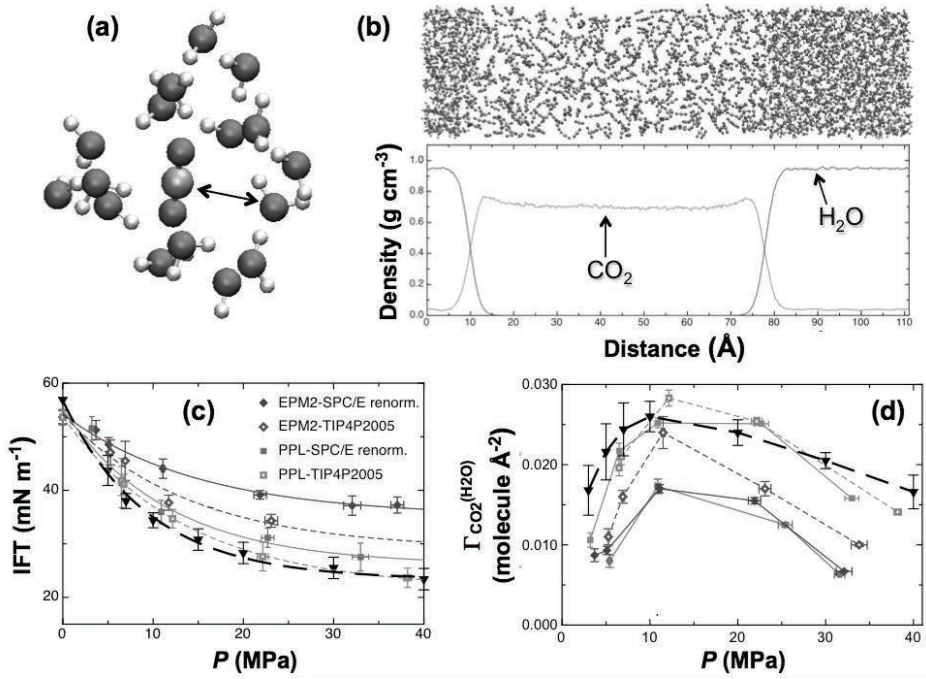

Figure 9. Molecular dynamics simulation prediction of CO_2-water IFT and CO_2 adsorption on the surface of liquid water (Nielsen et al. 2012). (a) Snapshot of a single CO_2 molecule and the water molecules in its first solvation shell. (b) Snapshot of a MD simulation cell containing two coexisting fluid phases (liquid water and $scCO_2$) and two parallel interfaces; the graph shows the density profile of water and CO_2 molecules in the direction normal to the CO_2-water interfaces; adsorption of CO_2 on the water surface is evidenced by the small enhancement in CO_2 density near the interface. (c) Experimental data on IFT vs. *P* at 383 K (black triangles and dashed line; Chiquet et al. 2007a) compared with MD simulation predictions obtained with different combinations of water (SPC/E, TIP4P/2005) and CO_2 (EPM2, PPL) models (gray symbols and lines). Simulation results with the SPC/E water model were renormalized to the surface tension of TIP4P2005 water by adding 8.4 mN m^{-1} to the predicted IFT values. (d) Experimental data and MD simulation predictions of CO_2 surface excess $\Gamma_{CO_2}^{(H_2O)}$ vs. *P*. The experimental values were calculated from the experimental data on IFT vs. *P* in (c) using the Gibbs adsorption equation. [Figure modified by permission of Elsevier from Nielsen et al. (2012) *Geochim Cosmochim Acta* 81:28-38.]

CO_2-water LJ interaction predicted by different models: the PPL model predicts a stronger short-range CO_2-water attraction, hence more CO_2 adsorption on the water surface and a larger *P*-dependence of IFT, in agreement with experimental data.

As mentioned above, IFT results from various contributions, whose subtle balance depends on the arrangement of the interfacial molecules. Willard and Chandler (2010) demonstrated that the interfacial structure cannot be understood properly by considering only the Gibbs Dividing Surface (GDS), which is smeared out by capillary fluctuations. Rather, they introduced the notion of an instantaneous interface that fluctuates in time and showed that when the structure of molecules is analyzed with respect to this interface one recovers a layered structure that is progressively damped over a few molecular layers, as in the vicinity of a solid object. Zhang and Singer (2011) re-examined the structure of the interface between water and sub-critical CO_2 using this concept. Under these conditions, they observed, as in experiments, the adsorption of a CO_2 layer on the water surface (which is at the origin of the decrease in IFT compared to pure water, as noted above). In addition, the density profile

decays almost exponentially from the interface, with a characteristic length that diverges with increasing pressure according to an inverse power law. No effect of CO_2 adsorption on the orientation of interfacial water molecules was observed.

CO_2-brine-mineral systems with a single fluid phase

Clay interlayer nanopores. Much of the atomistic simulation research on CO_2 near mineral surfaces has used clay minerals, a well-characterized nanoporous medium (Rotenberg et al. 2007; Bourg and Sposito 2010; Ferrage et al. 2011; Marry et al. 2011) of relevance to the geochemistry of clayshale and mudstone caprocks of GCS sites (Carey 2013, this volume; Kaszuba et al. 2013, this volume). The adsorption of CO_2 in clay nanopores has been mainly considered in the absence of water. Experimentally, the incorporation of CO_2 in pyrophyllite during dehydroxylation has been observed by infrared spectroscopy (Wang et al. 2003) and X-ray diffraction has allowed following the intercalation of CO_2 in Na-fluorohectorite near ambient conditions: the expansion in basal spacing is similar to that obtained during intercalation with water, but it occurs at a rate that is several orders of magnitude slower (Hemmen et al. 2012). The density of CO_2 confined in Na-montmorillonite with a sub-single hydration layer depends on the bulk $scCO_2$ density (Rother et al. 2013). Yang and Zhang (2005) used MD simulations to investigate the structure and diffusion of CO_2 in clay-like slit pores, finding in particular a decrease in the diffusion coefficient under confinement. Cole et al. (2010) carried out MD simulations of dry $scCO_2$ in mica interlayers and observed, in line with the behavior of water, a layering of the fluid and a decrease in mobility compared to bulk $scCO_2$. It would be interesting to investigate how some of the observed features, such as the formation of hydrogen bonds between CO_2 oxygens and surface hydroxyl groups, are affected by the presence of water. The swelling of Na-montmorillonite in contact with CO_2 was studied by Yang and Yang (2011) using GCMC simulations. Whereas swelling is thermodynamically favorable under supercritical conditions (10 MPa and 318.15 K), it is unfavorable at lower CO_2 pressure (0.1 MPa). In the former case, it was found that Na^+ counterions were not well solvated by CO_2 and remained close to the surface. The swelling of organoclays, where inorganic counterions are replaced by alkylammonium chains, by $scCO_2$ has also been simulated by Yu and Yang (2011).

More relevant in the context of geological sequestration is the case where clay is in contact with both CO_2 and water. Recent experiments have shown that the uptake of CO_2 depends on the initial water content—hence also on the nature of the counterion (Giesting et al. 2012; Schaef et al. 2012). Botan et al. (2010) used molecular simulations to investigate the thermodynamics, structure and transport in Na-montmorillonite in contact with water and CO_2 (Fig. 10). They considered clay interlayer nanopores in equilibrium with a reservoir at 348 K and two pressures in which two bulk phases coexist: an H_2O-rich liquid phase and a CO_2-rich gas (at 25 bars) or supercritical fluid (at 125 bar). This bulk phase coexistence determines the chemical potentials of water and CO_2 used in GCMC simulations, with the rigid SPC and EPM2 models, to determine the swelling free energy curves and composition of the metastable states. The bihydrated state, which is the most stable in the absence of CO_2 under the investigated conditions, remains the most stable in the presence of CO_2, i.e., no swelling (by CO_2 uptake) or shrinkage (by water removal) was predicted if the clay remains in contact with the water reservoir. The CO_2 uptake is limited to its dissolution in interlayer water without dramatic changes in the overall fluid density and the water structure. The CO_2 molecules tend to stay close to the clay surface, oriented so as to partially enter the hexagonal cavities. The diffusion coefficient of CO_2 is reduced compared to its value in bulk liquid water by a factor 50 and 5 in the mono- and bihydrated states, respectively. The presence of CO_2 also slows down the diffusion of interlayer water and cations.

Cygan et al. (2012) recently developed a fully flexible CO_2 model for the simulation of CO_2 and water in clays. This model better reproduces the vibrational properties of bulk CO_2 than earlier flexible force fields and, when used in conjunction with the flexible SPC or TIP4P

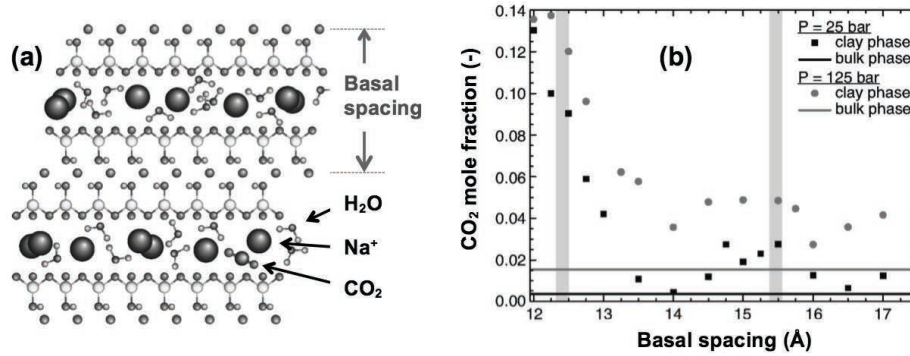

Figure 10. Grand Canonical Monte Carlo prediction of the solubility of CO_2 in water-filled smectite clay interlayer nanopores at 348 K and 25 or 125 bar as a function of clay basal spacing (Botan et al. 2010). (a) Schematic view of the simulated system containing stacked smectite lamellae and interlayer nanopores filled with water, Na^+, and $CO_{2(aq)}$. (b) Predictions of the solubility of CO_2 in nanopore water as a function of clay basal spacing (black and gray squares at 25 and 125 bar, respectively). The solubility of CO_2 in bulk liquid water at 25 and 125 bar is shown by the horizontal black and gray lines. The vertical shaded bars indicate the stable swelling states of the clay mineral (the one- and two-layer hydrates). The results show that CO_2 is more soluble in clay interlayer water than in bulk liquid water. [Figure modified with permission by American Chemical Society from Botan et al. (2010) *J Phys Chem C* 114:14962-14969.]

water models, more accurately predicts the diffusion coefficient of CO_2 in bulk water at 0.1 MPa compared to its rigid counterparts (which overestimate it). In simulations of a hydrated Na-montmorillonite clay, the addition of two CO_2 molecules per unit cell in the interlayer space was predicted to cause an increase in the interlayer distance (i.e., swelling) for all considered water contents. This finding does not contradict the results of Botan et al. (2010), because Cygan et al. (2012) simulated systems with a fixed number of interlayer water and CO_2 molecules, whereas Botan et al. (2010) simulated systems with fixed chemical potential. Flexibility of water and CO_2 does not have a large impact on the structure of the interlayer fluid but is obviously essential for the prediction of vibrational properties. In particular, Cygan et al. (2012) predicted that the bending motion of CO_2 is blue-shifted by 10 to 15 cm^{-1} in the clay interlayer while the asymmetric stretch mode is virtually unaffected by confinement, in qualitative agreement with their diffuse-reflectance infrared spectroscopy results.

Nanoporous silica and zeolites. A significant body of atomistic simulation research exists on the adsorption of CO_2 in nanoporous silica and zeolites at relatively low pressures and in the absence of water, because of the potential utility of these materials in carbon capture. These studies show that CO_2 has a significant affinity for silica surfaces that is strongly dependent on the details of the pore structure and the presence of surface charge sites (Kim et al. 2013). At conditions more relevant to GCS (high P and T, presence of water), few atomistic simulation studies have been carried out. Gravimetric and neutron scattering data show that confinement in silica nanopores can promote the formation of a dense adsorbed phase even in pores as large as 35 nm (Melnichenko et al. 2010; Cole et al. 2010; Rother et al. 2012) but this has never been tested by atomistic simulation, to our knowledge. Molecular dynamics simulations described elsewhere in this volume show that the solubility of CO_2 in water-filled silica nanopores is highly sensivity to nanopore size and the hydrophilicity of the silica surface (Chialvo et al. 2013a,b, this volume).

CO_2-brine-mineral systems with two fluid phases

Thin films of adsorbed water at CO_2-mineral interfaces. Hydrophilic mineral surfaces (such as silica, mica, and carbonates), when exposed to humid air, are well known to adsorb

thin films of liquid water (up to hundreds of nanometers thick) with a chemical potential lower than that of bulk liquid water (Pashley and Kitchener 1979; Balmer et al. 2008; Asay et al. 2009; Salmeron et al. 2009; Tokunaga 2009, 2012; Bohr et al. 2010; Rubasinghege and Grassian 2013). These adsorbed water films influence the hydrogeology of unsaturated porous media (Tokunaga 2009; Diaz et al. 2010) and the geochemistry of mineral-air interfaces (Kendall and Martin 2005; Rubasinghege and Grassian 2013). On quartz and silica surfaces at low relative vapor pressures ($P/P_{sat} \leq 0.8$), the thickness of these films ranges from zero to about two statistical water monolayers (Asay et al. 2009; Tokunaga 2009, 2012). These two water monolayers are strongly adsorbed as measured by their isosteric heat of adsorption (Asay et al. 2009). Beyond the first two water monolayers, water is weakly adsorbed (Pashley 1980; Asay et al. 2009); nevertheless, water film thickness continues to increase with relative vapor pressure and reaches tens to hundreds of nanometers at $P/P_{sat} > 0.975$ (Pashley and Kitchener 1979; Tokunaga 2012). Mica surfaces are somewhat less hydrophilic than silica and they carry only one water monolayer at $P/P_{sat} \approx 0.65$ (Balmer et al. 2008).

In geological CO_2 storage formations, adsorbed water films may play important roles by mediating the interaction of humid $scCO_2$ with mineral surfaces (McGrail et al. 2009; Kwak et al. 2011; Loring et al. 2011; Shao et al. 2011; Tokunaga and Wan 2013, this volume). At present, however, the properties of adsorbed water films at mineral-CO_2 interfaces remain poorly understood. Loring et al. (2011) roughly estimated the thickness of water films at forsterite-$scCO_2$ interfaces by infrared spectroscopy as 0.1, 0.2, 1.0 and 2.0 nm at $P/P_{sat} = 0.47$, 0.81, 0.95 and 1.36, respectively (for comparison, a single water monolayer has a thickness of about 0.3 nm). Kim et al. (2012) probed water films at silica-$scCO_2$ interfaces at low capillary pressures (P_c = 0.18 to 3.7 kPa, equivalent to P/P_{sat} ~0.99999) using X-ray synchrotron fluorescence. At the conditions of their study, water film thickness was less than 2 nm, but a more precise quantification of adsorbed film thickness was prevented by capillary condensation on surface roughness features.

Molecular dynamics and Monte Carlo simulations have been used to study adsorbed water films in the absence of CO_2, for example on silica (Wensink et al. 2000; Romero-Vargas Castrillón et al. 2011), calcite (Stöckelmann and Hentschke 1999; Rahaman et al. 2008), mica (Malani and Ayappa 2009), and talc surfaces (Rotenberg et al. 2011). In these studies, plots of the average water density as a function of distance from the surface showed that up to two water monolayers are structured by the surface. In the presence of CO_2, to our knowledge, only two atomistic simulations have probed adsorbed water films, on forsterite (Kerisit et al. 2012) and quartz (Bagherzadeh et al. 2012). In atomistic simulations, film thickness can be controlled by imposing the vapor pressure of water in the gas phase (Stöckelmann and Hentschke 1999; Rahaman et al. 2008; Malani and Ayappa 2009), the total number of water molecules in the simulation cell (Romero-Vargas Castrillón et al. 2011; Kerisit et al. 2012), or the radius of curvature r_m of a bubble of water vapor or CO_2 in the simulated system (Wensink et al. 2000; Bagherzadeh et al. 2012). This last property is related to the relative vapor pressure P/P_{sat} through the Kelvin equation (Wensink et al. 2000):

$$\frac{P}{P_{sat}} = e^{\frac{\gamma_{wg} V_m}{RT r_m}} \quad (1)$$

where γ_{wg} is the interfacial tension between liquid water and the non-wetting phase (CO_2 or water vapor) and V_m is the molar volume of water. Overall, atomistic simulations show that, in both mineral-water-air and mineral-water-CO_2 systems, water molecules located in the first one or two monolayers on hydrophilic mineral surfaces have a large isosteric heat of adsorption (in agreement with experimental results) and a low diffusivity relative to bulk liquid water (Wensink et al. 2000; Rahaman et al. 2008; Malani and Ayappa 2009; Kerisit et al. 2012). These distinct properties of the first one or two water monolayers result from the participation of

interfacial water in the solvation of adsorbed (Malani and Ayappa 2009) or structural (Rahaman et al. 2008; Kerisit et al. 2012) surface metal cations (Fig. 11a) and in hydrogen bonding with surface O atoms and OH groups (Rahaman et al. 2008; Romero-Vargas Castrillón et al. 2011). Water molecules located beyond the first two monolayers behave essentially as bulk water (Kerisit et al. 2012).

Grand Canonical Monte Carlo simulation predictions of water film thickness vs. P/P_{sat} on silica (Leroch and Wendland 2012), mica (Malani and Ayappa 2009), and calcite surfaces (Rahaman et al. 2008) in mineral-water-vapor systems predict that these surfaces have similar hydration properties at P/P_{sat} values up to 0.7, where they carry a single statistical water monolayer (Fig. 11b). The apparent discrepancy between the monolayer coverage of silica at P/P_{sat} ~0.7 predicted by GCMC simulation (Leroch and Wendland 2012) and the bilayer coverage observed experimentally at the same relative vapor pressure (Asay et al. 2009) may arise from the pH-dependence of silica surface charge: at near-neutral pH values, silica has a negative surface charge density because of the deprotonation of silanol groups (>Si-OH = >Si-O^- + H^+, with pK_a = 7.0 ± 0.6; Sonnefeld et al. 2001; Carroll et al. 2002; Dove and Craven 2005). The uncharged silica surface (with fully protonated silanol groups) simulated by Leroch and Wendland (2012) is representative of acidic conditions, the point of zero net charge of silica being located near pH 3 (Wang et al. 2012b). Figure 11b includes data obtained in systems where $P/P_{sat} < 1$ was imposed by placing a bubble of water vapor (Wensink et al. 2000; Bagherzadeh et al. 2012) or CO_2 (Bagherzadeh et al. 2012) in contact with the adsorbed water film. Experimental and simulation results show that at P/P_{sat} ~ 0.7, negatively charged)silica surfaces carry two water monolayers (Asay et al. 2009), uncharged silica surfaces (representative of pH ~ 3) carry one

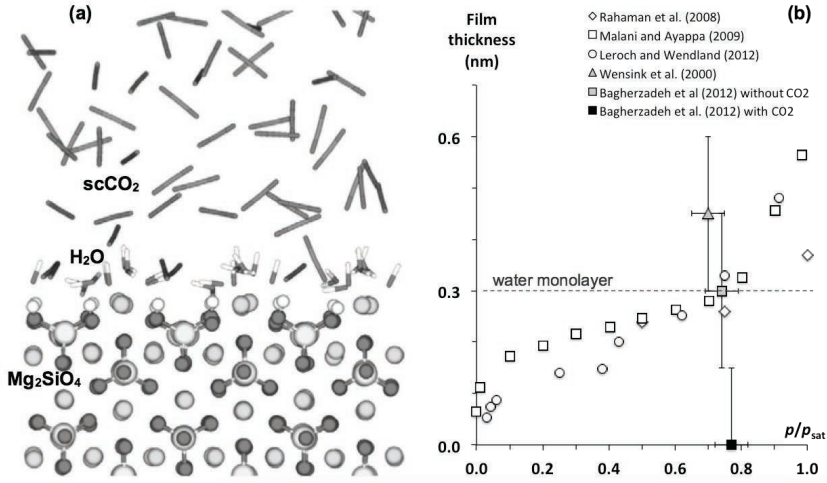

Figure 11. (a) Molecular dynamics simulation snapshot of a sub-monolayer adsorbed water film at the forsterite-scCO$_2$ interface (Kerisit et al. 2012). The figure shows that adsorbed water molecules are attracted to the forsterite surface because of their affinity for structural Mg^{2+} ions (light gray spheres). (b) Compilation of MD and GCMC simulation predictions of the thickness of adsorbed water films on flat mineral surfaces at T = 298 to 300 K on silica (Bagherzadeh et al. 2012; Leroch and Wendland 2012; Wensink et al. 2000), calcite (Rahaman et al. 2008), and mica (Malani and Ayappa 2009). Values of film thickness and P/P_{sat} in the simulations of Wensink et al. (2000) and Bagherzadeh et al. (2012) were estimated by visual inspection of MD simulation snapshots and by applying Equation (1) with γ_{gw} = 54.7 mN m^{-1} and r_m = 1.1 ± 0.2 nm (Wensink et al. 2000) or with γ_{gw} = 80.1 or 70.1 mN m^{-1} (in the absence or presence of CO_2, respectively) and r_m = 1.93 ± 0.4 nm (Bagherzadeh et al. 2012) [γ_{gw} values were roughly estimated from the results of Vega and deMiguel (2007) and Nielsen et al. (2012)]. [Figure 11a reprinted by Elsevier from Kerisit et al. (2012) *Geochim Cosmochim* Acta 84:137-151.]

water monolayer (Leroch and Wendland 2012), and uncharged silica surfaces exposed to a bulk CO_2 fluid carry zero water monolayers (Bagherzadeh et al. 2012).

CO_2-brine-mineral wetting angles. The wettability of mineral surfaces by brine vs. CO_2—characterized by the mineral-brine-CO_2 wetting angle θ—is an important property of rock formations used in GCS (Tokunaga and Wan 2013, this volume). Knowledge of θ is required to convert mercury intrusion porosimetry data into a CO_2-brine capillary pressure-saturation relation (Espinoza and Santamarina 2010; Pini et al. 2012), to predict the maximum column height of CO_2 that can be immobilized under a seal formation (Chiquet et al. 2007b; Chalbaud et al. 2009; Iglauer et al. 2012b), and to derive correlations for the residual CO_2 saturation $S_{g,r}$ (Spiteri et al. 2008; Iglauer et al. 2012a). These relationships arise from the well-known Young-Laplace equation ($P_c = \gamma_{wg}/r_m$), where r_m is the radius of curvature of the CO_2-brine interface. If r_m is expressed as a function of the wetting angle and pore aperture, this yields for a cylindrical pore of radius r_p:

$$P_c = \frac{2\gamma_{wg}\cos\theta}{r_p} \tag{2}$$

Despite their importance, the θ values of mineral surfaces in GCS-relevant conditions are poorly characterized. Experimental results obtained at the most widely studied conditions (silica surfaces, $T \sim 298$ K, low salinity) show significant discrepancies in both the magnitude of θ and its pressure dependence (Fig. 12a). Experimental studies also disagree on the influence of salinity: θ either increases (Espinoza and Santamarina 2010; Jung and Wan 2012; Farokhpoor et al. 2013) or decreases with NaCl concentration (Chiquet et al. 2007b; Wang et al. 2012b). There is disagreement about the hysteresis of measured θ values, reported as either negligible (Bikkina 2011; Jung and Wan 2012) or up to ~20° (Dickson et al. 2006; Chiquet et al. 2007b; Broseta et al. 2012). The influence of pH is almost entirely unexamined (Wang et al. 2012) and few studies have measured the θ values of minerals other than silica, such as calcite (Espinoza and Santamarina 2010; Bikkina 2011; Wang et al. 2012b; Farokhpoor et al. 2013) and phyllosilicates (Chiquet et al. 2007b; Wang et al. 2012b; Farokhpoor et al. 2013). Figure 12 shows that $\theta = 21 \pm 11°$ in silica-water-CO_2 systems at low P (Chiquet et al. 2007b; Espinoza and Santamarina 2010; Bikkina 2011; Jung and Wan 2012; Wang et al. 2012b; Farokhpoor et al. 2013). For comparison, $\theta = 0°$ in silica-water-air systems (Lamb and Furlong 1982). This difference suggests that the presence of CO_2 decreases the hydrophilicity of silica, perhaps because it causes the pH to approach the point of zero net charge of silica (Chiquet et al. 2007b; Wang et al. 2012b).

The range of behaviors shown in Figure 12a illustrates the difficulty of accurately characterizing θ. Experimental measurements of θ are highly sensitive to trace levels of impurities that can accumulate at interfaces (Pashley and Kitchener 1979; Lamb and Furlong 1982; Stipp and Hochella 1991). Another experimental difficulty is the hysteresis between wetting angles measured during imbibition (θ_i) and drainage ($\theta_d < \theta_i$). This hysteresis may be enhanced by surface roughness (Dickson et al. 2006; Chiquet et al. 2007b; Broseta et al. 2012), but it can also occur on atomically smooth surfaces (Diaz et al. 2010). The few studies that measured a wetting angle hysteresis reported drainage wetting angles θ_d (Dickson et al. 2006; Chiquet et al. 2007b; Farokhpoor et al. 2013), but some studies may have reported θ values that are intermediate between θ_d and θ_i. Finally, the θ-values themselves may be influenced by surface roughness, a poorly controlled parameter that may evolve upon exposure to CO_2 (Espinoza and Santamarina 2010).

Atomistic simulations can readily predict the wetting angle θ on atomically-smooth surfaces and its dependence on pressure and salinity and provide insight into the molecular-scale phenomena that control θ. To our knowledge, only three such simulation studies have been carried out (Fig. 12b). A probable cause of the range of predicted θ-values is that the

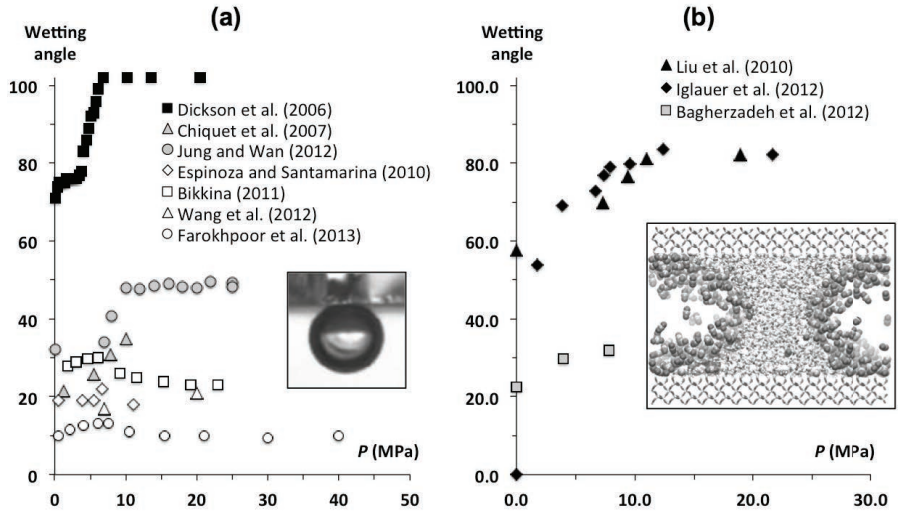

Figure 12. Compilation of (a) measurements and (b) MD simulations of the mineral-water-CO_2 wetting angle θ on silica surfaces at low ionic strengths ($I \leq 0.2$ M NaCl) as a function of pressure. The inset images show a photograph of a CO_2 droplet on a quartz surface in water during a goniometric contact angle experiment (Wang et al. 2012) and a MD simulation cell containing a CO_2 bubble confined in an otherwise water-filled pore between quartz surfaces (Bagherzadeh et al. 2012). All studies used pristine quartz surfaces and $T = 293$ to 309 K unless otherwise noted. Dickson et al. (2006) used a reduced-hydrophilicity silica surface treated by silanization to remove 63% of silanol groups. Wang et al. (2012b) used $T = 303$ K at 7 MPa and 323 K at 20 MPa. Jung and Wan (2012) used $T = 318$ K and an amorphous silica surface. Liu et al. (2010) used $T = 318$ K and a crystobalite surface with ~35% of the hydroxyl site density of a pristine silica surface. Iglauer et al. (2012b) used a dehydroxylated quartz surface with no silanol surface functional groups. Pressure in the simulations of Liu et al. (2010) was estimated from the reported CO_2 densities using National Institute of Standards and Technology (NIST) data on the pressure-density relation of pure CO_2 at 318 K. Pressure in the simulations of Bagherzadeh et al. (2012) was roughly estimated as the average value of the diagonal pressure tensor components in directions parallel to the silica surfaces (calculated by the authors for the entire simulation cell), renormalized such that $P = 0$ in the absence of CO_2. [Figure 12a inset reproduced by American Chemical Society with permission from Wang et al. (2012) *Environ Sci Technol* 47:234-241. Figure 12b inset reproduced with permission by American Chemical Society from Bagherzadeh et al (2012) *J Phys Chem C* 116:24907-24915.]

studies in Figure 12b used very different models of the silica surface structure: Liu et al. (2010) simulated a surface with bare Si atoms and a few protonated silanol (>Si-OH) functional groups; Iglauer et al. (2012b) simulated a surface with only siloxane (>Si-O-Si<) functional groups; and Bagherzadeh et al. (2012) simulated a surface with only silanol functional groups. The first two types of surfaces should are quite different from the pristine silica surfaces probed experimentally, because the formation of silanol sites on silica surfaces is highly favorable (Lamb and Furlong 1982; Du and de Leeuw 2006; Salmeron et al. 2009), but they may be analogous to the synthetically dehydroxylated silica surface studied by Dickson et al. (2006).

A notable difficulty in predicting θ from atomistic simulations is the lack of a set of interatomic potential parameters known to accurately predict the solid-water (γ_{sw}), solid-CO_2 (γ_{sg}), and water-CO_2 (γ_{wg}) interfacial tensions. These interfacial tensions determine the wetting angle through the well-known Young equation:

$$\cos\theta = \frac{\gamma_{sg} - \gamma_{sw}}{\gamma_{wg}} \tag{3}$$

In the absence of a well-tested set of force fields for CO_2-water-mineral wettability studies, Iglauer et al. (2012b) used a combination of CO_2 and water models (EPM2, TIP4P/2005) that predicts γ_{wg} within ~10 mN m^{-1} (Nielsen et al. 2012), but they selected a silica-water interaction model (van Beest et al. 1990) that overestimates the strength of the silica-water interaction (in the absence of CO_2, they predicted $\theta = 0°$ for water on a silica surface that carries only siloxane functional groups, whereas the experimental value for a fully dehydroxylated silica surface is about 42°; Lamb and Furlong 1982). Bagherzadeh et al. (2012) used a water model (TIP4P/Ice) that significantly overestimates the surface tension of liquid water (Vega and de Miguel 2007) and a silica-water interaction model (Lopes et al. 2006) that was not designed for use with the TIP4P/Ice water model and that performs less than optimally when used with at least one other water model (Skelton et al. 2011). In recent years, the CLAYFF model (Cygan et al. 2004b) has emerged as a remarkably accurate model of the interaction between silicate minerals and liquid water (Bourg and Sposito 2010; Ferrage et al. 2011; Marry et al. 2011; Skelton et al. 2011; Bourg and Steefel 2012; Leroch and Wendland 2012), but this model has been exclusively used with two water models (the SPC and SPC/E water models; Berendsen et al. 1981, 1987) that underestimate the surface tension of liquid water (Vega and de Miguel 2007; Nielsen et al. 2012). When used with the SPC water model, the CLAYFF model underestimates the adhesive energy caused by a water meniscus between silica surfaces in humid air (P/P_{sat} = 0.3 to 0.8) by 5 to 22% (Leroch and Wendland 2012).

Another notable difficulty associated with atomistic simulation predictions of θ is that systems larger than ~10^5 atoms are difficult to model at a reasonable computational cost for the durations (tens of nanoseconds) required to probe wetting angles. Therefore, atomistic simulations of wetting phenomena necessarily probe very small CO_2 bubbles or water droplets (with diameters on the order of 5 nm) that may have distinct properties from those of macroscopic bubbles and drops. For example, pressure may be difficult to define in nanoscale bubbles that are too small to contain a bulk-fluid-like region (Cosden and Lukes 2011). Furthermore, interfacial energies are sensitive to long-range interactions; therefore, they may be influenced by interfacial curvature (Cosden and Lukes 2011; Rezaei Nejad et al. 2011) and by the choice of approximations used in evaluating long-range van der Waals interactions (Wensink et al. 2000; Biscay et al. 2009; Cosden and Lukes 2011).

The θ values of Si oxide surfaces reported in Figure 12 can be grouped into two distinct datasets. The first set includes all studies of partly or completely de-hydroxylated silica surfaces (Dickson et al. 2006; Liu et al. 2010; Iglauer et al. 2012b). These surfaces are weakly hydrophilic in the absence of CO_2 and they show a strong wettability alteration with increasing CO_2 pressure. The second set includes all studies of pristine silica surfaces (Chiquet et al. 2007b; Espinoza and Santamarina 2010; Bikkina 2011; Jung and Wan 2012; Wang et al. 2012b). The density of silanol functional groups determines whether a silica surface belongs to one or the other group. Within the second dataset, the MD simulation results of Bagherzadeh et al. (2012) are most closely consistent with the experimental results of Chiquet et al. (2007b). The origin of the difference between studies that show a *P*-dependence of θ (Chiquet et al. 2007b; Bagherzadeh et al. 2012; Jung and Wan 2012) and those that do not (Espinoza and Santamarina 2010; Bikkina 2011; Wang et al. 2012b) is not known. This question should lend itself readily to an atomistic scale analysis of the *P*-dependence of the interfacial energies γ_{gs}, γ_{gw}, and γ_{ws} (Iglauer et al. 2012b).

CO_2 clathrate hydrates

Gas clathrate hydrates (Fig. 13a) play important roles in certain GCS concepts, such as carbon sequestration in deep ocean sediments (House et al. 2006; Tohidi et al. 2010) and CO_2-CH_4 substitution in natural methane hydrate formations (Ota et al. 2005; Park et al. 2006; Espinoza and Santamarina 2011). The potential usefulness of gas hydrates as a CO_2 storage medium is illustrated by the fact that the molecular CO_2:H_2O ratio in these hydrates can be

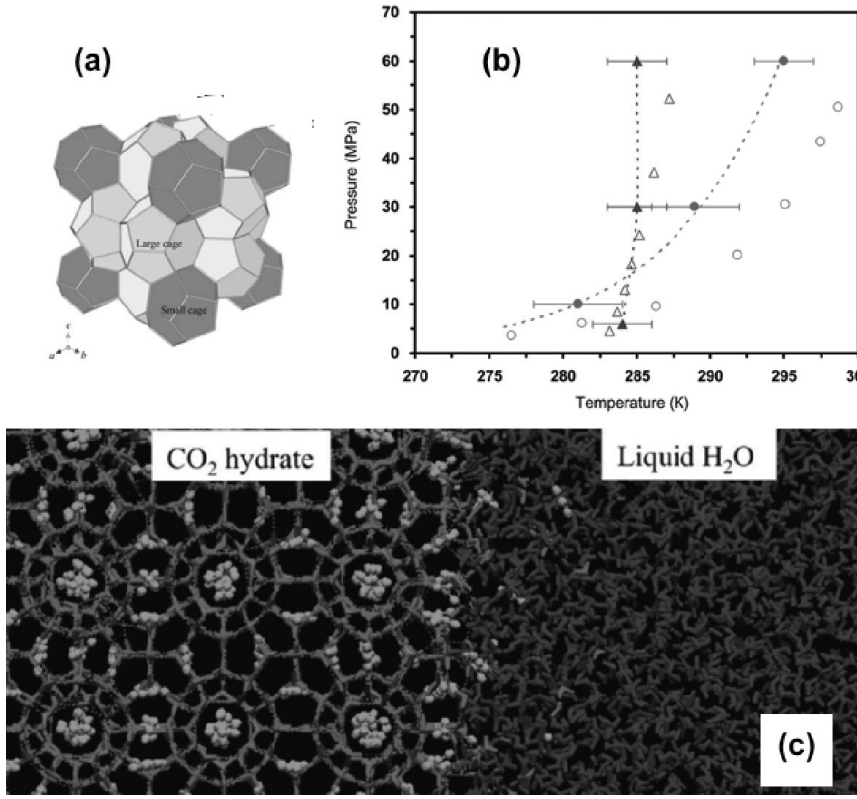

Figure 13. Prediction of the properties of CO_2 hydrates in contact with bulk liquid water. (a) Structure of the host lattice in the sI clathrate hydrate; the large and small cages are shown in light and dark gray, respectively (Hoshikawa et al. 2006). (b) Comparison of experimental measurements (open symbols; Takenouchi and Kennedy 1965; Jager and Sloan 2001; Yang et al. 2001) and MD simulation predictions (filled symbols; Tung et al. 2010, 2011a) of the three-phase coexistence conditions of CO_2 and CH_4 hydrates (triangles and circles, respectively) (Tung et al. 2011b). (c) Interface between CO_2 hydrate and bulk liquid water during a simulation of CO_2 hydrate dissociation; water molecules are displayed in lighter or darker gray depending on whether their local coordination is more clathrate-like or liquid-like (Sarupria and Debenedetti 2011). [Figure 13a reprinted with permission by AIP Publishing LLC from Hoshikawa et al (2006) *J Chem Phys* 125:034505. Figure 13b reproduced with permission by American Chemical Society from Tung et al (2011) *J Phys Chem B* 115:15295-15302. Figure 13c reproduced with permission by American Chemical Society from Sarupria and Debenedetti (2011) *J Phys Chem A* 115:6102-6111.]

as high as 1:5.75, about 300 times the solubility of CO_2 in water at ambient conditions. A substantial fraction of the molecular modeling research on CO_2-H_2O systems has focused on CO_2 hydrates—their bulk properties (Chialvo et al. 2002; Ota and Ferdows 2005; Geng et al. 2009; Jiang and Jordan 2010), their nucleation (Radhakrishnan and Trout 2002), growth (Tung et al. 2011a), and dissolution (Sarupria and Debenedetti 2011), their stability near mineral surfaces (Bai et al. 2011), and the conversion from CH_4 to CO_2 hydrates (Geng et al. 2009; Tung et al. 2011b).

From a technical point of view, atomistic simulations of CO_2 hydrates benefit from the existence of well-tested force fields that are known to predict the properties of these crystals with reasonable accuracy (Jiang and Jordan 2010; Sarupria and Debenedetti 2011; Tung et al. 2011a). In particular, the combination of the TIP4P/Ew water model (Horn et al. 2004), the

EPM2 CO_2 model (Harris and Yung 1995), and the CO_2-water interaction parameters of Sun and Duan (2005) (parameterized to fit the quantum mechanical calculations of Sadlej et al. 1998) yields a remarkably good prediction of CO_2 hydrate melting temperature (Fig. 13b; Tung et al. 2011a). One complicating aspect of the atomistic modeling of CO_2 hydrates is that the cage occupancy of real CO_2 hydrates is lower than one CO_2 molecule per cage: it ranges from 0.8 to 1.0 and depends on cage size (the large cages of the gas hydrate sI structure are almost fully occupied, the small cages are partly occupied; Circone et al. 2003; Sun and Duan 2005; Takeya et al. 2010). Molecular simulation studies have almost always probed the condition of full cage occupancy (Jiang and Jordan 2010; Tung et al. 2011a). In a rare study of CO_2 hydrates with partial cage occupancy, Sarupria and Debenedetti (2011) showed that the melting temperature of CO_2 clathrate hydrate decreases by 2 to 4 K as cage occupancy decreases from 1.0 to 0.87 and that this destabilization is greater if CO_2 is removed from the larger cages of the clathrate structure.

Atomistic simulations of bulk CO_2 hydrates and their interfaces with liquid water have yielded several insights into the nano-scale properties of CO_2 hydrates. For example, simulations of bulk CO_2 hydrates revealed that their thermal conductivity is ~20% smaller than that of CH_4 hydrates (Jiang and Jordan 2010), a difference that could have important implications for the process of storing CO_2 in CH_4 hydrate formations. Simulations of CO_2 hydrate growth showed that the growth rate is on the order of 0.10 to 0.16 m s^{-1}, with little pressure-dependence, and that growth proceeds through the formation of a transient amorphous phase that contains more large cages and fewer small cages than the bulk CO_2 hydrate (Tung et al. 2011a), a finding consistent with simulations showing that the binding energy of CO_2 is about 4.0 kJ mol^{-1} greater in the large cages than in the small cages (Jiang and Jordan 2010). Simulations of the dissolution of CO_2 hydrates show that dissolution is a collective phenomenon with an activation energy of 62 to 70 kJ mol^{-1} (consistent with the breaking of 3-5 hydrogen bonds) and a rate that increases as cage occupancy decreases (Sarupria and Debenedetti 2011). Simulations of CO_2 hydrate dissolution and growth (Fig. 13c) have not detected the formation of transient ice-like structures (Sarupria and Debenedetti 2011; Tung et al. 2011a). Finally, simulations show that the replacement of CH_4 by CO_2 in clathrate hydrate crystals can occur in the absence of clathrate melting (Tung et al. 2011b) and that the CH_4-CO_2 mixed hydrate, with CH_4 occupying the small clathrate cages, is more stable than either the CH_4 or the CO_2 hydrates (Geng et al. 2009), in agreement with experimental evidence that CO_2 displaces CH_4 much more readily from large cages than from small cages (Ota et al. 2005).

An emerging research area in the simulation of gas hydrates is the influence of mineral surfaces on hydrate nucleation, growth, and dissolution. Experimental studies suggest that mineral surfaces influence the kinetics and thermodynamics of methane hydrate growth in porous media (Cha et al. 1988; Uchida et al. 2004; Koster van Groos and Guggenheim 2009), but the details of this effect are not well established (Park and Sposito 2003; Cygan et al. 2004a) and its existence in the case of CO_2 hydrates is unknown. To our knowledge, only two atomistic-scale simulation studies have studied CO_2 or CH_4 hydrate crystals near mineral surfaces (Bai et al. 2011; Liang et al. 2011). Both studies simulated uncharged silica surfaces and found that a thin water film (0.5 to 1.0 nm thick) separates the gas hydrate from the mineral surface (Bai et al. 2011; Liang et al. 2011). This finding is consistent with the well-established observation that a 0.4 to 0.6 nm thick layer of surface water in silica nanopores freezes at a much lower temperature than bulk liquid water and does not form a crystalline ice phase (Hansen et al. 1996; Schreiber et al. 2001) and with the strong adsorption of one or two water monolayers on flat silica surfaces (discussed in the section on adsorbed water films). The simulation study by Liang et al. (2011) provides tantalizing evidence that MD simulations may allow evaluating the silica-water-gas hydrate wetting angle.

FUTURE RESEARCH OPPORTUNITIES

Atomistic simulations can play an important role in helping to improve thermodynamic models of mineral-brine-CO_2 systems, one of the poorly constrained inputs of current GCS models (Xu et al. 2007). In particular, MD simulation techniques can probe the stability of metal carbonate/bicarbonate ion species in solution that are larger than ion pairs (Marcus and Hefter 2006; Fosbøl et al. 2010) and the thermodynamics of CO_2 impurities such as H_2S and SO_2 (Chialvo et al. 2013a, this volume). Classical or quantum mechanical calculations also could be used to inform thermodynamic models of aqueous Al species (Gaus et al. 2005).

Continued development of force field parameters that accurately describe the energetics of both aqueous and solid phases will aid in future simulations of carbonate growth mechanisms. Comparisons of experimental and atomistic simulation results will continue to play a central role in this effort as shown by recent XR data on the structure of the calcite-water interface (Fenter et al. 2013). *Ab initio* and DFT predictions of calcite-water interfaces can play an important role in constraining new force fields. Development of reactive carbonate models, like the one proposed by Gale et al. (2011) for the aqueous-calcium carbonate system, could also play an important role in this effort because of the possible importance of water dissociation at calcite kink sites.

Investigations of synthetic and biogenic ACC should elucidate the water content of these phases and its influence on their stability. For example, the metadynamics technique (so far been applied only to anhydrous $CaCO_3$ particles) should be applied to hydrated ACC.

Simulations of the interplay between organic and inorganic species in solution during mineralization remain challenging because the mechanisms of $CaCO_3$ crystallization are still not fully understood. In a simpler crystallization system like urea, for which MD and kinetic Monte Carlo modeling has successfully described the mechanisms of crystal growth and dissolution (Piana and Gale 2005), simulation is able to predicts growth rates and morphologies in the presence of organic species in good agreement with experiment (Salvalaglio et al. 2012). For carbonates, the information gained from simulations of additive effects during the early stages of crystallization will be much less complicated to interpret once the pathways to mineral formation are known.

Atomistic simulations are barely beginning to be applied to the study of wetting properties (behavior of adsorbed water, wetting angles) in mineral-brine-CO_2 systems. Carefully designed simulations can provide information on the dependence of these properties on the type of mineral surface, and the influence of solutes such as electrolyte ions, dissolved organic molecules, or CO_2 impurities (H_2S, SO_2). Advances in this area will require the identification of a set of force fields that can accurately predict the interfacial energies of mineral-water, mineral-CO_2, and water-CO_2 interfaces. Future simulations should aim to determine the origin of the difference between studies that show a *P*-dependence of θ in silica-water-CO_2 systems (Chiquet et al. 2007b; Bagherzadeh et al. 2012; Jung and Wan 2012) and those that do not (Espinoza and Santamarina 2010; Bikkina 2011; Wang et al. 2012b).

ACKNOWLEDGMENTS

This material was prepared by LMH, AFW, and ICB with support from the Center for Nanoscale Control of Geologic CO_2 (NCGC), an Energy Frontiers Research Center funded by the U.S. Department of Energy, Office of Science, Office of Basic Energy Sciences under Award Number DE-AC02-05CH11231.

REFERENCES

Abascal JLF, Vega C (2005) A general purpose model for the condensed phases of water: TIP4P/2005. J Chem Phys 123:234505

Addadi L, Weiner S (1985) Interactions between acidic proteins and crystals: stereochemical requirements in biomineralization. Proc Natl Acad Sci USA 82:4110-4114

Aizenberg J, Black AJ, Whitesides GM (1999) Control of crystal nucleation by patterned self-assembled monolayers. Nature 398:495-498

Albo S, Müller EA (2003) On the calculation of supercritical fluid–solid equilibria by molecular simulation. J Phys Chem B 107:1672-1678

Allen MP, Tildesley DJ (1987) Computer Simulation of Liquids. Oxford University Press, Oxford

Andersson MP, Stipp SLS (2012) How acidic is water on calcite? J Phys Chem C 116:18779-18787

Asay DB, Barnette AL, Kim SH (2009) Effects of surface chemistry on structure and thermodynamics of water layers at solid–vapor interfaces. J Phys Chem C 113:2128-2133

Aschauer U, Spagnoli D, Bowen P, Parker SC (2010) Growth modification of seeded calcite using carboxylic acids: atomistic simulations. J Colloid Interface Sci 346:226-231

Austen KF, Wright K, Slater B, Gale JD (2005) The interaction of dolomite surfaces with metal impurities: a computer simulation study. Phys Chem Chem Phys 7:4150-4156

Avendaño C, Lafitte T, Galindo A, Adjiman CS, Jackson G, Müller EA (2011) SAFT-gamma force field for the simulation of molecular fluids. 1. A single-site coarse grained model of carbon dioxide. J Phys Chem B 115:11154-11169

Badaut V, Zeller P, Dorado B, Schlegel ML (2010) Influence of exchange correlation on the symmetry and properties of siderite according to density-functional theory. Phys Rev B 82:205121

Bagherzadeh SA, Englezos P, Alavi S, Ripmeester JA (2012) Influence of hydrated silica surfaces on interfacial water in the presence of clathrate hydrate forming gases. J Phys Chem C 116:24907-24915

Bai D, Chen G, Zhang X, Wang W (2011) Microsecond molecular dynamics simulations of the kinetic pathways of gas hydrate formation from solid surfaces. Langmuir 27:5961-7

Balasubramanian S, Kohlmeyer A, Klein ML (2009) Ab initio molecular dynamics study of supercritical carbon dioxide including dispersion corrections. J Chem Phys 131:144506

Balmer TE, Christenson HK, Spencer ND, Heuberger M (2008) The effect of surface ions on water adsorption to mica. Langmuir 24:1566-1569

Bender E (1970) Equations of state exactly representing the phase behavior of pure substances. *In*: Proceedings of the 5th Symposium on Thermophysical Properties. The American Chemical Society of Mechanical Engineers, Columbia, p 227

Berendsen HJC, Grigera JR, Straatsma TP (1987) The missing term in effective pair potentials. J Phys Chem 91:6269-6271

Berendsen HJC, Postma JPM, van Gunsteren WF, Hermans J (1981). Interaction models for water in relation to protein hydration. *In*: Intermolecular Forces. Pullman B (ed) Reidel Publishing, Amsterdam, p 331-342

Bewernitz MA, Gebauer D, Long J, Cölfen H, Gower LB (2012) A metastable liquid precursor phase of calcium carbonate and its interactions with polyaspartate. Farad Discuss 159:291-312

Bickmore BR, Rosso KM, Brown ID, Kerisit S (2009) Bond-valence constraints on liquid water structure. J Phys Chem A 113:1847-1857

Bikkina PK (2011) Contact angle measurements of CO_2–water–quartz/calcite systems in the perspective of carbon sequestration. Int J Greenhouse Gas Control 5:1259-1271

Binder K, Fratzl P (2005) Spinodal decomposition. *In*: Phase Transformations in Materials. Kostorz G (ed) Wiley-VCH Verlag GmbH & Co. KGaA, Weinheim, p 409-480

Biscay F, Ghoufi A, Lachet V, Malfreyt P (2009) Monte Carlo simulations of the pressure dependence of the water-acid gas interfacial tensions. J Phys Chem B 113:14277-14290

Bohr J, Wogelius RA, Morris PM, Stipp SLS (2010) Thickness and structure of the water film deposited from vapour on calcite surfaces. Geochim Cosmochim Acta 74:5985-5999

Botan A, Rotenberg B, Marry V, Turq P, Noetinger B (2010) Carbon dioxide in montmorillonite clay hydrates: thermodynamics, structure, and transport from molecular simulation. J Phys Chem C 114:14962-14969

Bourg IC, Sposito G (2010) Connecting the molecular scale to the continuum scale for diffusion processes in smectite-rich porous media. Environ Sci Technol 44:2085-2091

Bourg IC, Steefel CI (2012) Molecular dynamics simulations of water structure and diffusion in silica nanopores. J Phys Chem C 116:11556-11564

Brik MG (2011) First-principles calculations of structural, electronic, optical and elastic properties of magnesite $MgCO_3$ and calcite $CaCO_3$. Phys B: Condens Matter 406:1004-1012

Broseta D, Tonnet N, Shah V (2012) Are rocks still water-wet in the presence of dense CO_2 or H_2S? Geofluids 12: 280-294

Carey JW (2013) Geochemistry of wellbore integrity in CO_2 sequestration: Portland cement-steel-brine-CO_2 interactions. Rev Mineral Geochem 77:505-539

Carroll SA, Maxwell RS, Bourcier W, Martin S, Hulsey S (2002) Evaluation of silica-water surface chemistry using NMR spectroscopy. Geochim Cosmochim Acta 66:913-926

Carteret C, De La Pierre M, Dossot M, Pascale F, Erba A, Dovesi R (2013) The vibrational spectrum of $CaCO_3$ aragonite: a combined experimental and quantum-mechanical investigation. J Chem Phys 138:014201

Cha SB, Ouar H, Wildeman TR, Sloan ED (1988) A third-surface effect on hydrate formation. J Phys Chem 92:6492-6494

Chalbaud C, Robin M, Lombara J-M, Martin F, Egermann P, Bertin H (2009) Interfacial tension measurements and wettability evaluation for geological CO_2 storage. Adv Water Resour 32:98-109

Chaudhury S, Olson MA, Tawa G, Wallqvist A, Lee MS (2012) Efficient conformational sampling in explicit solvent using a hybrid replica exchange molecular dynamics method. J Chem Theory Comput 8:677-687

Chen CL, Qi J, Zuckermann RN, De Yoreo JJ (2011) Engineered biomimetic polymers as tunable agents for controlling $CaCO_3$ mineralization. J Am Chem Soc 133:5214-5217

Chialvo AA, Houssa M, Cummings PT (2002) Molecular dynamics study of the structure and thermophysical properties of model sI clathrate hydrates. J Phys Chem B 106:442-451

Chialvo AA, Vlcek L, Cole DR (2013) Acid gases in CO_2-rich subsurface geologic environments. Rev Mineral Geochem 77:361-398

Chialvo AA, Vlcek L, Cole DR (2013b) Aqueous CO_2 solutions at silica surfaces and within nanopore environments. Insights from isobaric-isothermal molecular dynamics. J Phys Chem C 116:13904-13916

Chiquet P, Daridon J-L, Broseta D, Thibeau S (2007a) CO_2/water interfacial tensions under pressure and temperature conditions of CO_2 geological storage. Energy Convers Manage 48:736-744

Chiquet P, Broseta D, Thibeau S (2007b) Wettability alteration of caprock minerals by carbon dioxide. Geofluids 7:112-122

Circone S, Stern LA, Kirby SH, Durham WB, Chakoumakos BC, Rawn CJ, Rondinone AJ, Ishii Y (2003). CO_2 hydrate: synthesis, composition, structure, dissociation behavior, and a comparison to structure I CH_4 hydrate. J Phys Chem B 107:5529-5539

Cole DR, Chialvo AA, Rother G, Vlcek L, Cummings PT (2010) Supercritical fluid behavior at nanoscale interfaces: Implications for CO_2 sequestration in geologic formations. Philos Mag 90:2339-2363

Cooke DJ, Elliott JA (2007) Atomistic simulations of calcite nanoparticles and their interaction with water. J Chem Phys 127:104706

Cooke DJ, Gray RJ, Sand KK, Stipp SLS, Elliott JA (2010) Interaction of ethanol and water with the $\{10\bar{1}4\}$ surface of calcite. Langmuir 26:14520-14529

Cosden LA, Lukes JR (2011) Effect of cutoff radius on the surface tension of nanoscale bubbles. J Heat Transfer 113:101501

Criscenti LJ, Cygan RT (2013) Molecular simulations of carbon dioxide and water: cation solvation. Environ Sci Technol 47:87-94

Cygan RT, Guggenheim S, Koster van Groos AF (2004a) Molecular models for the intercalation of methane hydrate complexes in montmorillonite clay. J Phys Chem B 108:15141-15149

Cygan RT, Liang J-J, Kalinichev AG (2004b) Molecular models of hydroxide, oxyhydroxide, and clay phases and the development of a general force field. J Phys Chem B 108:1255-1266

Cygan RT, Romanov VN, Myshakin EM (2012) Molecular simulation of carbon dioxide capture by montmorillonite using an accurate and flexible force field. J Phys Chem C 116:13079-13091

Davies CW (1962) Ion Association. Butterworths, London, 190 p

Davis KJ, Dove PM, De Yoreo JJ (2000) The role of Mg^{2+} as an impurity in calcite growth. Science 290:1134-1137

Davis KJ, Dove PM, Wasylenki LE, De Yoreo JJ (2004) Morphological consequences of differential Mg^{2+}-incorporation at structurally distinct steps on calcite. Am Mineral 89:714-720

de Leeuw NH (2002) Molecular dynamics simulations of the growth inhibiting effect of Fe^{2+}, Mg^{2+}, Cd^{2+}, and Sr^{2+} on calcite crystal growth. J Phys Chem B 106:5241-5249

de Leeuw NH, Cooper TG (2004) A computer modeling study of the inhibiting effect of organic adsorbates on calcite crystal growth. Cryst Growth Des 4:123-133

de Leeuw NH, Harding JH, Parker SC (2002) Molecular dynamics simulations of the incorporation of Mg^{2+}, Cd^{2+} and Sr^{2+} at calcite growth steps: Introduction of a $SrCO_3$ potential model. Mol Simul 28:573-589

de Leeuw NH, Parker SC (2000) Modeling absorption and segregation of magnesium and cadmium ions to calcite surfaces: introducing $MgCO_3$ and $CdCO_3$ potential models. J Chem Phys 112:4326-4333

de Leeuw NH, Parker SC, Harding JH (1999) Molecular dynamics simulation of crystal dissolution from calcite steps. Phys Rev B 60:13792-13799

De Yoreo JJ, Waychunas GA, Jun Y-S, Fernandez-Martinez A (2013) *In situ* investigations of carbonate nucleation on mineral and organic surfaces. Rev Mineral Geochem 77:229-257

Debye P, Hückel E (1923) Zur Theorie der Elektrolyte. I. Gefrierpunktserniedrigung und verwandte Erscheinungentle. Physik Z 24:185-206

Demichelis R, Raiteri P, Gale JD, Dovesi R (2012) A new structural model for disorder in vaterite from first-principles calculations. CyrstEngComm 14:44-47
Demichelis R, Raiteri P, Gale JD, Quigley D, Gebauer D (2011) Stable prenucleation mineral clusters are liquid-like ionic polymers. Nature Commun 2:590
DePaolo DJ, Cole DR (2013) Geochemistry of geologic carbon sequestration: an overview. Rev Mineral Geochem 77:1-14
Di Tommaso D, de Leeuw NH (2008) The onset of calcium carbonate nucleation: a density functional theory molecular dynamics and hybrid microsolvation/continuum study. J Phys Chem B 112:6965-6975
Di Tommaso D, de Leeuw NH (2009) Theoretical study of the dimerization of calcium carbonate in aqueous solution under natural water conditions. Geochim Cosmochim Acta 73:5394-5405
Diaz ME, Fuentes J, Cerro RL, Savage MD (2010) Hysteresis during contact angles measurement. J Colloid Interface Sci 343:574-583
Dickson JL, Gupta G, Horozov TS, Binks BP, Johnston KP (2006) Wetting phenomena at the CO_2/water/glass interface. Langmuir 22:2161-2170
Doudou S, Vaughan DJ, Livens FR, Burton NA (2012) Atomistic simulations of calcium uranyl(VI) carbonate adsorption on calcite and stepped-calcite surfaces. Environ Sci Technol 46:7587-7594
Dove PM, Craven CM (2005) Surface charge density on silica in alkali and alkaline earth chloride electrolyte solutions. Geochim Cosmochim Acta 69:4963-4970
Du Z, de Leeuw NH (2006) Molecular dynamics simulations of hydration, dissolution and nucleation processes at the alpha-quartz (0001) surface in liquid water. Dalton Trans 22:2623-2634
Elhadj S, De Yoreo JJ, Hoyer JR, Dove PM (2006a) Role of molecular charge and hydrophilicity in regulating the kinetics of crystal growth. Proc Natl Acad Sci USA 103:19237-19242
Elhadj S, Salter EA, Wierzbicki A, De Yoreo JJ, Han N, Dove PM (2006b) Peptide controls on calcite mineralization: Polyaspartate chain length affects growth kinetics and acts as a stereochemical switch on morphology. Cryst Growth Des 6:197-201
Elstnerová P, Friák M, Fabritius HO, Lymperakis L, Hickel T, Nikolov S, Raabe D, Ziegler A, Hild S, Neugebauer J (2010) Ab initio study of thermodynamic, structural, and elastic properties of Mg-substituted crystalline calcite. Acta Biomater 6:4506-4512
Errington JR, Panagiotopoulos AZ (1998) A fixed point charge model for water optimized to the vapor-liquid coexistence properties. J Phys Chem B 102:7470-7475
Errington JR, Kiyohara K, Gubbins KE, Panagiotopoulos AZ (1998) Monte Carlo simulation of high-pressure phase equilibria in aqueous systems. Fluid Phase Equil 150-151:33-40
Espinoza DN, Santamarina JC (2010) Water-CO_2-mineral systems: Interfacial tension, contact angle, and diffusion—Implications to CO_2 geological storage. Water Resour Res 46:W07537
Espinoza DN, Santamarina JC (2011) P-wave monitoring of hydrate-bearing sand during CH_4-CO_2 replacement. Int J Greenhouse Gas Control 5:1031-1038
Faatz M, Gröhn F, Wegner G (2004) Amorphous calcium carbonate: synthesis and potential intermediate in biomineralization. Adv Mater 16:996-1000
Falini G, Albeck S, Weiner S, Addadi L (1996) Control of aragonite or calcite polymorphism by mollusk shell macromolecules. Science 271:67-69
Farokhpoor R, Bjørkvik BJA, Lindeberg E, Torsæter O (2013) Wettability behaviour of CO_2 at storage conditions. Int J Greenhouse Gas Control 12:18-25
Fenter P, Kerisit S, Raiteri P, Gale JD (2013) Is the calcite–water interface understood? Direct comparisons of molecular dynamics simulations with specular X-ray reflectivity data. J Phys Chem C 117:5028-5042
Fenter P, Sturchio NC (2012) Calcite (104)–water interface structure, revisited. Geochim Cosmochim Acta 97:58-69
Fernández GA, Vrabec J, Hasse H (2005) Self-diffusion and binary Maxwell–Stefan diffusion coefficients of quadrupolar real fluids from molecular simulation. Int J Thermophys 26:1389-1407
Fernandez-Martinez A, Kalkan B, Clark SM, Waychunas GA (2013) Pressure-induced polyamorphism and foramtion of 'aragonitic' amorphous calcium carbonate. Angew Chem Int Ed 52:8354-8357
Ferrage E, Sakharov BA, Michot LJ, Delville A, Bauer A, Lanson B, Grangeon S, Frapper G, Jiménez-Ruiz M, Cuello GJ (2011) Hydration properties and interlayer organization of water and ions in synthetic Na-smectite with tetrahedral layer charge. Part 2. Toward a precise coupling between molecular simulations and diffraction data. J Phys Chem C 115:1867-1881
Finney AR, Rodger PM (2012) Probing the structure and stability of calcium carbonate pre-nucleation clusters. Farad Discuss 159:47-60
Fosbøl PL, Thomsen K, Stenby EH (2010) Review and recommended thermodynamic properties of $FeCO_3$. Corros Eng Sci Technol 45:115-135
Freeman CL, Harding JH, Duffy DM (2008) Simulations of calcite crystallization on self-assembled monolayers. Langmuir 24:9607-9615

Freeman CL, Harding JH, Quigley D, Rodger PM (2010) Structural control of crystal nuclei by an eggshell protein. Angew Chem Int Ed 49:5135-5137

Frenkel D, Smit B (2001) Understanding molecular simulation: From algorithms to applications. Academic Press, San Diego

Gale JD, Raiteri P, van Duin ACT (2011) A reactive force field for aqueous-calcium carbonate systems. Phys Chem Chem Phys 13:16666-16679

Garcia-Ratés M, de Hemptinne J-C, Avalos JB, Nieto-Draghi C (2012) Molecular modeling of diffusion coefficient and ionic conductivity of CO_2 in aqueous ionic solutions. J Phys Chem B 116:2787-2800

Gaus I, Azaroual M, Czernichowski-Lauriol I (2005) Reactive transport modelling of the impact of CO_2 injection on the clayey cap rock at Sleipner (North Sea). Chem Geol 217:319-337

Gebauer D, Coelfen H (2011) Prenucleation clusters and non-classical nucleation. Nano Today 6:564-584

Gebauer D, Colfen H, Verch A, Antonietti M (2009) The multiple roles of additives in $CaCO_3$ crystallization: A quantitative case study. Adv Mater 21:435-439

Gebauer D, Gunawidjaja PN, Ko JYP, Bacsik Z, Aziz B, Liu L, Hu YF, Bergström L, Tai C-W, Sham T-K, Edén M, Hedin N (2010) Proto-valcite and proto-vaterite in amorphous calcium carbonates. Agnew Chem Int Ed 49:8889-8891

Gebauer D, Voelkel A, Coelfen H (2008) Stable prenucleation calcium carbonate clusters. Science 322:1819-1822

Geissbühler P, Fenter P, DiMasi E, Srajer G, Sorensen LB, Sturchio NC (2004) Three-dimensional structure of the calcite–water interface by surface X-ray scattering. Surf Sci 573:191-203

Geng C-Y, Wen H, Zhou H (2009) Molecular simulation of the potential of methane reoccupation during the replacement of methane hydrate by CO_2. J Phys Chem A 113:5463-5469

Giesting P, Guggenheim S, Koster van Groos AF, Busch A (2012) Interaction of carbon dioxide with Na-exchanged montmorillonite at pressures to 640 bars: Implications for CO_2 sequestration. Int J Greenhouse Gas Control 8:73-81

Goldsmith JR (1983) Phase relations of rhombohedral carbonates. Rev Mineral 11:49-76

Gong YUT, Killian CE, Olson IC, Appathurai NP, Amasino AL, Martin MC, Holt LJ, Wilt FH, Gulbert PUPA (2012) Phase transitions in biogenic amorphous calcium carbonate. Proc Natl Acad Sci USA 109:6088-6093

Goodwin AL, Michel FM, Phillips BL, Keen DA, Dove MT, Reeder RJ (2010) Nanoporous structure and medium-range order in synthetic amorphous calcium carbonate. Chem Mater 22:3197-3205

Gower LB, Odom DJ (2000) Deposition of calcium carbonate films by a polymer-induced liquid-precursor (PILP) process. J Cryst Growth 210:719-734

Gratz AJ, Hillner PE, Hansma PK (1993) Step dynamics and spiral growth on calcite. Geochim Cosmochim Acta 57:491-495

Hamm LM, Wallace AF, Dove PM (2010) Molecular dynamics of ion hydration in the presence of small carboxylated molecules and implications for calcification. J Phys Chem B 114:10488-10495

Hansen EW, Stöcker M, Schmidt R (1996) Low-temperature phase transition of water confined in mesopores probed by NMR. Influence on pore size distribution. J Phys Chem 100:2195-2200

Harris JG, Yung KH (1995) Carbon dioxide's liquid-vapor coexistence curve and critical properties as predicted by a simple molecular model. J Phys Chem 99:12021-12024

Heberling F, Trainor TP, Lützenkirchen J, Eng P, Denecke MA, Bosbach D (2011) Structure and reactivity of the calcite-water interface. J Colloid Interface Sci 354:843-857

Hemmen H, Rolseth EG, Fonseca DM, Hansen EL, Fossum JO, Plivelic TS (2012) X-ray studies of carbon dioxide intercalation in Na-fluorohectorite clay at near-ambient conditions. Langmuir 28:1678-1682

Hillner PE, Manne S, Hansma PK, Gratz AJ (1993) Atomic force microscope: a new tool for imaging crystal growth processes. Farad Discuss 95:191-197

Hofmann AE, Bourg IC, DePaolo DJ (2012) Ion desolvation as a mechanism for kinetic isotope fractionation in aqueous systems. Proc Natl Acad Sci USA 109:18689-18694

Horn HW, Swope WC, Pitera JW, Madura JD, Dick TJ, Hura GL, Head-Gordon T (2004) Development of an improved four-site water model for biomolecular simulations: TIP4P-Ew. J Chem Phys 120:9665-9678

Hoshikawa A, Igawa N, Yamauchi H, Ishii Y (2006) Observation of hydrogen in deuterated methane hydrate by maximum entropy method with neutron powder diffraction. J Chem Phys 125:034505

House KZ, Schrag DP, Harvey CF, Lackner KS (2006) Permanent carbon dioxide storage in deep-sea sediments. Proc Natl Acad Sci USA 103:12291-12295

Hura G, Russo D, Glaeser RM, Head-Gordon T, Krack M, Parrinello M (2003). Water structure as a function of temperature from X-ray scattering experiments and ab initio molecular dynamics. Phys Chem Chem Phys 5:1981-1991

Iglauer S, Fernø MA, Shearing P, Blunt MJ (2012a) Comparison of residual oil cluster size distribution, morphology and saturation in oil-wet and water-wet sandstone. J Colloid Interface Sci 375:187-192

Iglauer S, Mathew MS, Bresme F (2012b) Molecular dynamics computations of brine-CO_2 interfacial tensions and brine-CO_2-quartz contact angles and their effects on structural and residual trapping mechanisms in carbon geo-sequestration. J Colloid Interface Sci 386:405-414

In Het Panhuis M, Patterson CH, Lynden-Bell RM (1998) A molecular dynamics study of carbon dioxide in water: diffusion, structure and thermodynamics. Mol Phys 94: 963-972

Ishii R, Okazaki S, Okada I, Furusaka M, Watanabe N, Misawa M, Fukunaga T (1996) Density dependence of structure of supercritical carbon dioxide along an isotherm. J Chem Phys 105:7011-7021

Jackson RA, Price GD (1992) A transferable interatomic potential for calcium carbonate. Mol Simul 9:175-177

Jager MD, Sloan ED (2001) The effect of pressure on methane hydration in pure water and sodium chloride solutions. Fluid Phase Equil 185:89-99

Jäger C, Welzel T, Meyer-Zaika W, Epple M (2006) A solid-state NMR investigation of the structure of nanocrystalline hydroxyapatite. Magn Reson Chem 44:573-580

Jee SS, Kasinath RK, DiMasi E, Kim Y-Y, Gower L (2011) Oriented hydroxyapatite in turkey tendon mineralized via the polymer-induced liquid-precursor (PILP) process. CyrstEngComm 13:2077-2083

Jiang H, Jordan KD (2010) Comparison of the properties of xenon, methane, and carbon dioxide hydrates from equilibrium and nonequilibrium molecular dynamics simulations. J Phys Chem C 114:5555-5564

Jiang Y, Gower L, Volkmer D, Cölfen H (2012) The existence region and composition of a polymer-induced liquid precursor phase for DL-glutamic acid crystals. Phys Chem Chem Phys 14:914-919

Jorgensen WL, Chandrasekhar J, Madura JD, Impey RW, Klein ML (1983) Comparison of simple potential functions for simulating liquid water. J Chem Phys 79:926-935

Jung J-W, Wan J (2012) Supercritical CO_2 and ionic strength effects on wettability of silica surfaces: equilibrium contact angle measurements. Energy Fuels 26:6053-6059

Kaszuba J, Yardley B, Andreani M (2013) Experimental perspectives of mineral dissolution and precipitation due to carbon dioxide-water-rock interactions. Rev Mineral Geochem 77:153-188

Kendall TA, Martin ST (2005) Mobile ions on carbonate surfaces. Geochim Cosmochim Acta 69:3257-3263

Kerisit S, Liu C (2010) Molecular simulation of the diffusion of uranyl carbonate species in aqueous solution. Geochim Cosmochim Acta 74:4937-4952

Kerisit S, Parker SC, Harding JH (2003) Atomistic simulation of the dissociative adsorption of water on calcite surfaces. J Phys Chem B 107:7676-7682

Kerisit S, Weare JH, Felmy AR (2012) Structure and dynamics of forsterite–scCO_2/H_2O interfaces as a function of water content. Geochim Cosmochim Acta 84:137-151

Kim J, Lin L-C, Swisher JA, Haranczyk M, Smit B (2013) Predicting large CO_2 adsorption in aluminosilicate zeolites for postcombustion carbon dioxide capture. J Am Chem Soc 134:18940-18943

Kim TW, Tokunaga TK, Shuman DB, Sutton SR, Newville M, Lanzirotti A (2012) Thickness measurements of nanoscale brine films on silica surfaces under geologic CO_2 sequestration conditions using synchrotron X-ray fluorescence. Water Resour Res 48:W09558

Koster van Groos AF, Guggenheim S (2009) The stability of methane hydrate intercalates of montmorillonite and nontronite: Implications for carbon storage in ocean-floor environments. Am Mineral 94:372-379

Kraska T, Romer F, Imre AR (2009) The relation of interface properties and bulk phase stability: molecular dynamics simulations of carbon dioxide. J Phys Chem B 113:4688-4697

Krupka KM, Cantrell KJ, McGrail PB (2010) Thermodynamic data for geochemical modeling of carbonate reactions associated with CO_2 sequestration - literature review. Pacific Northwest National Laboratory, Richland, WA, 135 p; http://www.pnl.gov/main/publications/external/technical_reports/pnnl-19766.pdf

Kulik DA, Vinograd VL, Paulsen N, Winkler B (2010) (Ca,Sr)CO_3 aqueous–solid solution systems: From atomistic simulations to thermodynamic modelling. Phys Chem Earth 35:217-232

Kupka T, Lin HM, Stobinski L, Chen C-H, Liou W-J, Wrzalik R, Flisak Z (2009) Experimental and theoretical studies on corals. I. Toward understanding the origin of color in precious red corals from Raman and IR spectroscopies and DFT calculations. J Raman Spec 41:651-658

Kwak JH, Hu JZ, Turcu RVF, Rosso KM, Ilton ES, Wang C, Sears JA, Engelhard MH, Felmy AR, Hoyt DW (2011) The role of H_2O in the carbonation of forsterite in supercritical CO_2. Int J Greenhouse Gas Control 5:1081-1092

Laio A, Gervasio FL (2008) Metadynamics: a method to simulate rare events and reconstruct the free energy in biophysics, chemistry and material science. Rep Prog Phys 71:126601

Lamb RN, Furlong DN (1982). Controlled wettability of quartz surfaces. J Chem Soc Faraday Trans 1 78:61-73

Lardge JS, Duffy DM, Gillan MJ (2009) Investigation of the interaction of water with the calcite $\{10\bar{1}4\}$ surface using ab initio simulation. J Phys Chem C 113:7207-7212

Leroch S, Wendland M (2012) Simulation of forces between humid amorphous silica surfaces: A comparison of empirical atomistic force fields. J Phys Chem C 116:26247-26261

Leyssale JM, Delhommelle J, Millot C (2005) Molecular simulation of the homogeneous crystal nucleation of carbon dioxide. J Chem Phys 122:184518

Liang S, Rozmanov D, Kusalik PG (2011) Crystal growth simulations of methane hydrates in the presence of silica surfaces. Phys Chem Chem Phys 13:19856-19864
Lísal M, SmithWR, Aim K (2005) Analysis of Henry's constant for carbon dioxide in water via Monte Carlo simulation. Fluid Phase Equil 228-229:345-356
Liu S, Yang X, Qin Y (2010) Molecular dynamics simulation of wetting behavior at CO_2/water/solid interfaces. Chin Sci Bull 55:2252-2257
Liu Y, Panagiotopoulos AZ, Debenedetti PG (2011) Monte Carlo simulations of high-pressure phase equilibria of CO_2-H_2O mixtures. J Phys Chem B 115:6629-6635
Lopes PE, Murashov V, Tazi M, Demchuk E, MacKerell AD Jr (2006) Development of an empirical force field for silica. Application to the quartz-water interface. J Phys Chem B 110:2782-2792
Loring JS, Thompson CJ, Wang Z, Joly AG, Sklarew DS, Schaef HT, Ilton ES, Rosso KM, Felmy AR (2011) In situ infrared spectroscopic study of forsterite carbonation in wet supercritical CO_2. Environ Sci Technol 45:6204-6210
Malani A, Ayappa KG (2009) Adsorption isotherms of water on mica: redistribution and film growth. J Phys Chem B 113:1058-1067
Marcus Y, Hefter G (2006) Ion pairing. Chem Rev 106:4585-4621
Markov IV (2004) Crystal Growth for Beginners: Fundamentals of Nucleation, Crystal Growth and Epitaxy. World Scientific, Singapore, 546 p
Marry V, Dubois E, Malikova N, Durand-Vidal S, Longeville S, Breu J (2011) Water dynamics in hectorite clays: influence of temperature studied by coupling neutron spin echo and molecular dynamics. Environ Sci Technol 45:2850-2855
Martin P, Spagnoli D, Marmier A, Parker SC, Sayle DC, Watson G (2006) Application of molecular dynamics DL_POLY codes to interfaces of inorganic materials. Mol Simul 32:1079-1093
McCoy JM, LaFemina JP (1997) Kinetic Monte Carlo investigation of pit formation at the $CaCO_3$ $\{10\bar{1}4\}$ surface-water interface. Surf Sci 373:288-299
McGrail BP, Schaef HT, Glezakou V-A, Dang LX, Owen AT (2009) Water reactivity in the liquid and supercritical CO_2 phase: Has half the story been neglected? Energy Procedia 1:3415-3419
McGreevy RL (2001) Reverse Monte Carlo modelling. J Phys Condens Matter 13:R877-R913
McGreevy RL, Howe MA (1992) RMC: modeling disordered structures. Ann Rev Mat Sci 22:217-242
Medeiros SK, Albuquerque EL, Maia FF Jr, Caetano EWS, Freire VN (2007) First-principles calculations of structural, electronic, and optical absorption properties of $CaCO_3$ vaterite. Chem Phys Lett 435:59-64
Melnichenko YB, Mayama H, Cheng G, Blach T (2010) Monitoring phase behavior of sub- and supercritical CO_2 confined in porous fractal silica with 85% porosity. Langmuir 26:6374-6379
Merker T, Engin C, Vrabec J, Hasse H (2010) Molecular model for carbon dioxide optimized to vapor-liquid equilibria. J Chem Phys 132:234512
Michel FM, MacDonald J, Feng J, Phillips BL, Ehm L, Tarabrella C, Parise JB, Reeder RJ (2008) Structural characteristics of synthetic amorphous calcium carbonate. Chem Mater 20:4720-4728
Ming X, Wang X-L, Du F, Yin J-W, Wang C-Z, Chen G (2012) First-principles study of pressure-induced magnetic transition in siderite $FeCO_3$. J Alloys Compd 510:L1-L4
Miyake A, Kawano J (2010) High-temperature molecular dynamics simulation of aragonite. J Phys: Condens Matter 22:225402
Mognetti BM, Yelash L, Virnau P, Paul W, Binder K, Müller M, MacDowell LG (2008) Efficient prediction of thermodynamic properties of quadrupolar fluids from simulation of a coarse-grained model: The case of carbon dioxide. J Chem Phys 128:104501
Mugnaioli E, Andrusenko I, Schüler T, Loges N, Dinnebier RE, Panthöfer M, Tremel W, Kolb U (2012) Ab initio structure determination of vaterite by automated electron diffraction. Angew Chem Int Ed 51:7041-7045
Nancollas GH, Kazmierczak TF, Schuttringer E (1981) A controlled composition study of calcium carbonate crystal growth: The influence of scale inhibitors. Corrosion 37:76-81
Nebel H, Neumann M, Mayer C, Epple M (2008) On the structure of amorphous calcium carbonate--a detailed study by solid-state NMR spectroscopy. Inorg Chem 47:7874-7879
Neuefeind J, Fischer HE, Simonson JM, Idrissi A, Schöps A, Honkimäki V (2009) The structure of liquid carbon dioxide and carbon disulfide. J Chem Phys 130:174503
Nielsen AE (1964) Kinetics of precipitation. International Series of Monographs on Analytical Chemistry, Vol. 18. Pergamon Press limited, Oxford
Nielsen LC, Bourg IC, Sposito G (2012) Predicting CO_2–water interfacial tension under pressure and temperature conditions of geologic CO_2 storage. Geochim Cosmochim Acta 81:28-38
Nielsen LC, De Yoreo JJ, DePaolo DJ (2013) General model for calcite growth kinetics in the presence of impurity ions. Geochim Cosmochim Acta 115:100-114
Nieto-Draghi C, de Bruin T, Pérez-Pellitero J, Bonet Avalos J, Mackie AD (2007) Thermodynamic and transport properties of carbon dioxide from molecular simulation. J Chem Phys 126:064509

Oakley MT, Wheatley RJ (2009) Additive and nonadditive models of vapor-liquid equilibrium in CO_2 from first principles. J Chem Phys 130:034110

Okur A, Wickstrom L, Layten M, Geney R, Song K, Hornak V, Simmerling C (2006) Improved efficiency of replica exchange simulations through use of a hybrid explicit/implicit solvation model. J Chem Theory Comput 2:420-433

Ota M, Ferdows M (2005) Monte Carlo approach to structure and thermodynamic property of CO_2 hydrate. JSME Int J Ser B 48:802-809

Ota M, Morohashi K, Abe Y, Watanabe M, Smith RL Jr, Inomata H (2005) Replacement of CH_4 in the hydrate by use of liquid CO_2. Energy Convers Manage 46:1680-1691

Park S-H, Sposito G (2003) Do montmorillonite surfaces promote methane hydrate formation? Monte Carlo and molecular dynamics simulations. J Phys Chem B 107:2281-2290

Park Y, Kim D-Y, Lee J-W, Huh D-G, Park K-P, Lee J, Lee H (2006). Sequestering carbon dioxide into complex structures of naturally occurring gas hydrates. Proc Natl Acad Sci USA 103:12690-12694

Pashley RM (1980) Multilayer adsorption of water on silica: An analysis of experimental results. J Colloid Interface Sci 78:246-248

Pashley RM, Kitchener JA (1979) Surface forces in adsorbed multilayers of water on quartz. J Colloid Interface Sci 71:491-500

Pavese A, Catti M, Parker SC, Wall A (1996) Modelling of the thermal dependence of structural and elastic properties of calcite, $CaCO_3$. Phys Chem Miner 23:89-93

Pavese A, Catti M, Price GD, Jackson RA (1992) Interatomic potentials for $CaCO_3$ polymorphs (calcite and aragonite), fitted to elastic and vibrational data. Phys Chem Miner 19:80-87

Perez-Sanchez G, Gonzalez-Salgado D, Pineiro MM, Vega C (2013) Fluid-solid equilibrium of carbon dioxide as obtained from computer simulations of several popular potential models: the role of the quadrupole. J Chem Phys 138:084506

Persson RAX (2011) Simple one-center model for linear molecules: application to carbon dioxide. J Phys Chem B 115:10073-10078

Piana S, Gale JD (2005) Understanding the barriers to crystal growth: dynamical simulation of the dissolution and growth of urea from aqueous solution. J Am Chem Soc 127:1975-1982

Piana S, Jones F, Gale JD (2006) Assisted desolvation as a key kinetic step for crystal growth. J Am Chem Soc 128:13568-13574

Piana S, Jones F, Gale JD (2007) Aspartic acid as a crystal growth catalyst. CyrstEngComm 9:1187-1191

Pini R, Krevor SCM, Benson SM (2012) Capillary pressure and heterogeneity for the CO_2/water system in sandstone rocks at reservoir conditions. Adv Water Res 38:48-59

Pitzer KS (1973) Thermodynamics of electrolytes. I. Theoretical basis and general equations. J Phys Chem 77:268-277

Potoff JJ, Siepmann JI (2001) Vapor-liquid equilibria of mixtures containing alkanes, carbon dioxide, and nitrogen. AIChE J 47:1676-1682

Potoff JJ, Errington JR, Panagiotopoulos AZ (1999) Molecular simulation of phase equilibria for mixtures of polar and non-polar components. Mol Phys 97:1073-1083

Pouget EM, Bomans PHH, Goos JACM, Frederik PM, de With G, Sommerdijk NAJM (2009) The initial stages of template-controlled $CaCO_3$ formation revealed by cryo-TEM. Science 323:1455-1458

Quigley D, Freeman CL, Harding JH, Rodger PM (2011) Sampling the structure of calcium carbonate nanoparticles with metadynamics. J Chem Phys 134:044703

Quigley D, Rodger PM (2008) Free energy and structure of calcium carbonate nanoparticles during early stages of crystallization. J Chem Phys 128: 221101

Quigley D, Rodger PM (2009) A metadynamics-based approach to sampling crystallisation events. Mol Simul 35:613-623

Quigley D, Rodger PM, Freeman CL, Harding JH, Duffy DM (2009) Metadynamics simulations of calcite crystallization on self-assembled monolayers. J Chem Phys 131:094703

Radha AV, Fernandez-Martinez A, Hu Y, Jun Y-S, Waychunas GA, Navrotsky A (2012) Energetic and structural studies of amorphous $Ca_{1-x}Mg_xCO_3{\cdot}nH_2O$ ($0 \le x \le 1$). Geochim Cosmochim Acta 90:83-95

Radha AV, Forbes TZ, Killian CE, Gilbert PUPA, Navrotsky A (2010) Transformation and crystallization energetics of synthetic and biogenic amorphous calcium carbonate. Proc Natl Acad Sci USA 107:16438-16443

Radha AV, Navrotsky A (2013) Thermodynamics of carbonates. Rev Mineral Geochem 77:73-121

Radhakrishnan R, Trout BL (2002) A new approach for studying nucleation phenomena using molecular simulations: Application to CO_2 hydrate clathrates J Chem Phys 117:1786-1797

Rahaman A, Grassian VH, Margulis CJ (2008) Dynamics of water adsorption onto a calcite surface as a function of relative humidity. J Phys Chem C 112:2109-2115

Railsback LB (1999) Patterns in the compositions, properties, and geochemistry of carbonate minerals. Carbonates Evaporites 14:1-20

Raiteri P, Demichelis R, Gale JD, Kellermeier M, Gebauer D, Quigley D, Wright LB, Walsh TR (2012) Exploring the influence of organic species on pre- and post-nucleation calcium carbonate. Farad Discuss 159:61-85

Raiteri P, Gale JD (2010) Water is the key to nonclassical nucleation of amorphous calcium carbonate. J Am Chem Soc 132:17623-17634

Raiteri P, Gale JD, Quigley D, Rodger PM (2010) Derivation of an accurate force-field for simulating the growth of calcium carbonate from aqueous solution: A new model for the calcite-water interface. J Phys Chem C 114:5997-6010

Reeder RJ, Tang Y, Schmidt MP, Kubista LM, Cowan DF, Phillips BL (2013) Characterization of structure in biogenic amorphous calcium carbonate: pair distribution function and nuclear magnetic resonance studies of lobster gastrolith. Cryst Growth Des 13:1905-1914

Rezaei Nejad H, Ghassemi M, Mirnouri Langroudi SM, Shahabi A (2011) A molecular dynamics study of nano-bubble surface tension. Mol Simul 37:23-30

Rieger J, Frechen T, Cox G, Heckmann W, Schmidt C, Thieme J (2007) Precursor structures in the crystallization/precipitation processes of $CaCO_3$ and control of particle formation by polyelectrolytes. Farad Discuss 136:265-277

Romero-Vargas Castrillón S, Giovambattista N, Aksay IA, Debenedetti PG (2011) Structure and energetics of thin film water. J Phys Chem C 115:4624-4635

Rotenberg B, Marry V, Vuilleumier R, Malikova N, Simon C, Turq P (2007) Water and ions in clays: Unraveling the interlayer/micropore exchange using molecular dynamics. Geochim Cosmochim Acta 71:5089-5101

Rotenberg B, Patel AJ, Chandler D (2011) Molecular explanation for why talc surfaces can be both hydrophilic and hydrophobic. J Am Chem Soc 133:20521-20527

Rother G, Krukowski EG, Wallacher D, Grimm N, Bodnar RJ, Cole DR (2012) Pore size effects on the sorption of supercritical CO_2 in mesoporous CPG-10 silica. J Phys Chem C 116:917-922

Rother G, Ilton ES, Wallacher D, Hauß T, Schaef HT, Qafoku O, Rosso KM, Felmy AR, Krukowski EG, Stack AG, Grimm N, Bodnar RJ (2013) CO_2 sorption to subsingle hydration layer montmorillonite clay studied by excess sorption and neutron diffraction measurements. Environ Sci Technol 47:205-211

Rubasinghege G, Grassian VH (2013) Role(s) of adsorbed water in the surface chemistry of environmental interfaces. Chem Commun 49:3071-3094

Sadlej J, Makarewicz J, Chałasiński G (1998) Ab initio study of energy, structure and dynamics of the water–carbon dioxide complex J Chem Phys 109:3919-3928

Saharay M, Yazaydin AO, Kirkpatrick RJ (2013) Dehydration-induced amorphous phases of calcium carbonate. J Phys Chem B 117:3328-3336

Salmeron M, Bluhm H, Tatarkhanov M, Ketteler G, Shimizu TK, Mugarza A, Deng X, Herranz T, Yamamoto S, Nilsson A (2009) Water growth on metals and oxides: binding, dissociation and role of hydroxyl groups. Farad Discuss 141:221-229

Salvalaglio M, Vetter T, Giberti F, Mazzotti M, Parrinello M (2012) Uncovering molecular details of urea crystal growth in the presence of additives. J Am Chem Soc 134:17221-17233

Sarupria S, Debenedetti PG (2011) Molecular dynamics study of carbon dioxide hydrate dissociation. J Phys Chem A 115:6102-6111

Schacht CS, Vlugt TJH, Gross J (2011) Using an analytic equation of state to obtain quantitative solubilities of CO_2 by molecular simulation. J Phys Chem Lett 2:393-396

Schaef HT, Ilton ES, Qafoku O, Martin PF, Felmy AR, Rosso KM (2012) In situ XRD study of Ca^{2+} saturated montmorillonite (STX-1) exposed to anhydrous and wet supercritical carbon dioxide. Int J Greenhouse Gas Control 6:220-229

Schreiber A, Ketelsen I, Findenegg GH (2001) Melting and freezing of water in ordered mesoporous silica materials. Phys Chem Chem Phys 3:1185-1195

Sel O, Radha AV, Dideriksen K, Navrotsky A (2012) Amorphous iron (II) carbonate: Crystallization energetics and comparison to other carbonate minerals related to CO_2 sequestration. Geochim Cosmochim Acta 87:61-68

Shao H, Ray JR, Jun Y-S (2011) Effects of salinity and the extent of water on supercritical CO_2-induced phlogopite dissolution and secondary mineral formation. Environ Sci Technol 45:1737-1743

Sherman DM (2009) Electronic structures of siderite ($FeCO_3$) and rhodochrosite ($MnCO_3$): Oxygen K-edge spectroscopy and hybrid density functional theory. Am Mineral 94:166-171

Shi H, Luo W, Johansson B, Ahuja R (2008) First-principles calculations of the electronic structure and pressure-induced magnetic transition in siderite $FeCO_3$. Phys Rev B 78:155119

Singer JW, Yazaydin AO, Kirkpatrick RJ, Bowers GM (2012) Structure and transformation of amorphous calcium carbonate: A solid-state ^{43}Ca NMR and computational molecular dynamics investigation. Chem Mater 24:1828-1836

Skelton AA, Fenter P, Kubicki JD, Wesolowski DJ, Cummings PT (2011) Simulations of the quartz (10−11)/water interface: A comparison of classical force fields, ab initio molecular dynamics, and X-ray reflectivity experiments. J Phys Chem C 115:2076-2088

Skorodumova NV (2005). Stability of the $MgCO_3$ structures under lower mantle conditions. Am Mineral 90:1008-1011
Sonnefeld J, Löbbus M, Vogelsberger W (2001) Determination of electric double layer parameters for spherical silica particles under application of the triple layer model using surface charge density data and results of electrokinetic sonic amplitude measurements. Colloid Surface A 195:215-225
Spagnoli D, Kerisit S, Parker SC (2006) Atomistic simulation of the free energies of dissolution of ions from flat and stepped calcite surfaces. J Cryst Growth 294:103-110
Spiteri EJ, Juanes R, Blunt MJ, Orr FM Jr (2008) A new model of trapping and relative permeability hysteresis for all wettability characteristics. Soc Petrol Eng J 13:277-288
Stack AG, Raiteri P, Gale JD (2012) Accurate rates of the complex mechanisms for growth and dissolution of minerals using a combination of rare-event theories. J Am Chem Soc 134:11-14
Stashans A, Chamba G (2011) A new insight on the role of Mg in calcite. Int J Quant Chem 111:2436-2443
Stephens CJ, Kim Y-Y, Evans SD, Meldrum FC, Christenson HK (2011) Early stages of crystallization of calcium carbonate revealed in picoliter droplets. J Am Chem Soc 133:5210-5213
Stipp SL, Hochella MF Jr (1991) Structure and bonding environments at the calcite surface as observed with X-ray photoelectron spectroscopy (XPS) and low energy electron diffraction (LEED). Geochim Cosmochim Acta 55:1723-1736
Stöckelmann E, Hentschke R (1999) Adsorption isotherms of water vapor on calcite: A molecular dynamics–Monte Carlo hybrid simulation using a polarizable water model. Langmuir 15:5141-5149
Sugita Y, Okamoto Y (1999) Replica-exchange molecular dynamics method for protein folding. Chem Phys Lett 314:141-151
Sun R, Duan Z (2005) Prediction of CH_4 and CO_2 hydrate phase equilibrium and cage occupancy from ab initio intermolecular potentials. Geochim Cosmochim Acta 69:4411-4424
Takenouchi S, Kennedy GC (1964) Binary system H_2O-CO_2 at high temperatures + pressures. Am J Sci 262:1055-1074
Takenouchi S, Kennedy GC (1965) Dissociation pressures of the phase $CO_2{\cdot}5¾H_2O$. J Geol 73:383-390
Takeya S, Udachin KA, Moudrakovski IL, Susilo R, Ripmeester JA (2010) Direct space methods for powder X-ray diffraction for guest-host materials: applications to cage occupancies and guest distributions in clathrate hydrates. J Am Chem Soc 132:524-531
Tohidi B, Yang J, Salehabadi M, Anderson R, Chapoy A (2010) CO_2 hydrates could provide secondary safety factor in subsurface sequestration of CO_2. Environ Sci Technol 44:1509-1514
Tokunaga TK (2009) Hydraulic properties of adsorbed water films in unsaturated porous media. Water Resour Res 45:W06415
Tokunaga TK (2012) DLVO-based estimates of adsorbed water film thicknesses in geologic CO_2 reservoirs. Langmuir 28:8001-8009
Tokunaga TK, Wan J (2013) Capillary pressure and mineral wettability influences on reservoir CO_2 capacity. Rev Mineral Geochem 77:481-503
Tribello GA, Bruneval F, Liew C, Parrinello M (2009) A molecular dynamics study of the early stages of calcium carbonate growth. J Phys Chem B 113:11680-11687
Tung Y-T, Chen L-J, Chen Y-P, Lin S-T (2010) The growth of structure I methane hydrate from molecular dynamics simulations. J Phys Chem B 114:10804-10813
Tung Y-T, Chen L-J, Chen Y-P, Lin S-T (2011a) Growth of structure I carbon dioxide hydrate from molecular dynamics simulations. J Phys Chem C 115:7504-7515
Tung Y-T, Chen L-J, Chen Y-P, Lin S-T (2011b) In situ methane recovery and carbon dioxide sequestration in methane hydrates: A molecular dynamics simulation study. J Phys Chem B 115:15295-15302
Uchida T, Takeya S, Chuvilin EM, Ohmura R, Nagao J, Yakushev VS, Istomin VA, Minagawa H, Ebinuma T, Narita H (2004) Decomposition of methane hydrates in sand, sandstone, clays, and glass beads. J Geophys Res 109:B05206.
Ungureanu CG, Prencipe M, Cossio R (2010) Ab initio quantum-mechanical calculation of $CaCO_3$ aragonite at high pressure: thermodynamic properties and comparison with experimental data. Eur J Mineral 22:693-701
Ungureanu CG, Cossio R, Prencipe M (2012) An ab-initio assessment of thermo-elastic properties of $CaCO_3$ polymorphs: Calcite case. Calphad 37:25-33
van Beest BWH, Kramer GJ, van Santen RA (1990) Force fields for silicas and aluminophosphates based on ab initio calculations. Phys Rev Lett 64:1955-1958
Vega C, de Miguel E (2007) Surface tension of the most popular models of water by using the test-area simulation method. J Chem Phys 126:154707
Villegas-Jiménez A, Mucci A, Whitehead MA (2009) Theoretical insights into the hydrated $\{10\bar{1}4\}$ calcite surface: structure, energetics, and bonding relationships. Langmuir 25:6813-6824
Vinograd VL, Winkler B (2010) An efficient cluster expansion method for binary solid solutions: Application to the halite-silvite, NaCl-KCl, system. Rev Mineral Geochem 71:413-436

Vinograd VL, Burton BP, Gale JD, Allan NL, Winkler B (2007) Activity–composition relations in the system $CaCO_3$–$MgCO_3$ predicted from static structure energy calculations and Monte Carlo simulations. Geochim Cosmochim Acta 71:974-983

Vlcek L, Chialvo AA, Cole DR (2011) Optimized unlike-pair interactions for water-carbon dioxide mixtures described by the SPC/E and EPM2 models. J Phys Chem B 115:8775-8784

Vorholz J, Harismiadis VI, Rumpf B, Panagiotopoulos AZ, Maurer G (2000) Vapor+liquid equilibrium of water, carbon dioxide, and the binary system, water+carbon dioxide, from molecular simulation. Fluid Phase Equil 170:203-234

Vorholz J, Harismiadis VI, Panagiotopoulos AZ, Rumpf B, Maurer G (2004) Molecular simulation of the solubility of carbon dioxide in aqueous solutions of sodium chloride. Fluid Phase Equil 226:237-250

Vrabec J, Stoll J, Hasse H (2001) A set of molecular models for symmetric quadrupolar fluids. J Phys Chem B 105:12126-12133

Wada N, Yamashita K, Umegaki T (1999) Effects of carboxylic acids on calcite formation in the presence of Mg^{2+} ions. J Colloid Interface Sci 212:357-364

Wallace AF, Hedges LO, Fernandez-Martinez A, Raiteri P, Gale JD, Waychunas GA, Whitelam S, Banfield JF, De Yoreo JJ (2013) Microscopic evidence for liquid-liquid separation in supersaturated $CaCO_3$ solutions. Science 341:885-889

Wang J, Becker U (2012) Energetics and kinetics of carbonate orientational ordering in vaterite calcium carbonate. Am Mineral 97:1427-1436

Wang L, Zhang M, Redfern SAT (2003) Infrared study of CO_2 incorporation into pyrophyllite [$Al_2Si_4O_{10}(OH)_2$] during dehydroxylation. Clay Clay Miner 51:439-444

Wang Q, Grau-Crespo R, de Leeuw NH (2011) Mixing thermodynamics of the calcite-structured (Mn,Ca)CO_3 solid solution: a computer simulation study. J Phys Chem B 115:13854-13861

Wang F-F, Kumar R, Jordan KD (2012a) A distributed point polarizable force field for carbon dioxide. Theor Chem Acc 131:1132

Wang S, Edwards IM, Clarens AF (2012b) Wettability phenomena at the CO_2-brine-mineral interface: implications for geologic carbon sequestration. Environ Sci Technol 47:234-241

Wang X, Chou I-M, Hu W, Burruss RC (2013) In situ observations of liquid–liquid phase separation in aqueous $MgSO_4$ solutions: Geological and geochemical implications. Geochim Cosmochim Acta 103:1-10

Wasylenki LE, Dove PM, De Yoreo JJ (2005a) Effects of temperature and transport conditions on calcite growth in the presence of Mg^{2+}: Implications for paleothermometry. Geochim Cosmochim Acta 69:4227-4236

Wasylenki LE, Dove PM, Wilson DS, De Yoreo JJ (2005b) Nanoscale effects of strontium on calcite growth: An in situ AFM study in the absence of vital effects. Geochim Cosmochim Acta 69:3017-3027

Wensink EJW, Hoffmann AC, Apol MEF, Berendsen HJC (2000) Properties of adsorbed water layers and the effect of adsorbed layers on interparticle forces by liquid bridging. Langmuir 16:7392-7400

Wiebe R (1941) The binary system carbon dioxide-water under pressure. Chem Rev 29:475-481

Wiebe R, Gaddy VL (1939) The solubility in water of carbon dioxide at 50, 75, and 100°, at pressures to 700 atmospheres. J Am Chem Soc 61:315-318

Willard AP, Chandler D (2010) Instantaneous liquid interfaces. J Phys Chem B 114:1954-1958

Wolf SE, Leiterer J, Kappl M, Emmerling F, Tremel W (2008) Early homogenous amorphous precursor stages of calcium carbonate and subsequent crystal growth in levitated droplets. J Am Chem Soc 130:12342-12347

Wolf SE, Müller L, Barrea R, Kampf CJ, Leiterer J, Panne U, Hoffmann T, Emmerling F, Tremel W (2011) Carbonate-coordinated metal complexes precede the formation of liquid amorphous mineral emulsions of divalent metal carbonates. Nanoscale 3:1158-1165

Wolthers M, Di Tommaso D, Du Z, de Leeuw NH (2012) Calcite surface structure and reactivity: molecular dynamics simulations and macroscopic surface modelling of the calcite-water interface. Phys Chem Chem Phys 14:15145-15157

Xu T, Apps JA, Pruess K, Yamamoto H (2007) Numerical modeling of injection and mineral trapping of CO_2 with H_2S and SO_2 in a sandstone formation. Chem Geol 242:319-346

Yang N, Yang X (2011) Molecular simulation of swelling and structure for Na-Wyoming montmorillonite in supercritical CO_2. Mol Simul 37:1063-1070

Yang X, Zhang C (2005) Structure and diffusion behavior of dense carbon dioxide fluid in clay-like slit pores by molecular dynamics simulation. Chem Phys Lett 407: 427-432

Yang SO, Cho SH, Lee H, Lee CS (2001) Measurement and prediction of phase equilibria for water + methane in hydrate forming conditions. Fluid Phase Equil 185:53-63

Yu Y, Yang X (2011) Molecular simulation of swelling and interlayer structure for organoclay in supercritical CO_2. Phys Chem Chem Phys 13:282-290

Yu K, McDaniel JG, Schmidt JR (2011) Physically motivated, robust, ab initio force fields for CO_2 and N_2. J Phys Chem B 115:10054-10063

Zhang H, Singer SJ (2011) Analysis of the subcritical carbon dioxide-water interface. J Phys Chem A 115:6285-6296

Zhang Z, Duan Z (2005) An optimized molecular potential for carbon dioxide. J Chem Phys 122:214507
Zhao L, Lin S, Mendenhall JD, Yuet PK, Blankschtein D (2011) Molecular dynamics investigation of the various atomic force contributions to the interfacial tension at the supercritical CO_2–water interface. J Phys Chem B 115:6076-6087
Zhu A, Zhang X, Liu Q, Zhang Q (2009) A fully flexible potential model for carbon dioxide. Chin J Chem Eng 17:268-272
Zucchini A, Prencipe M, Comodi P, Frondini F (2012) Ab initio study of cation disorder in dolomite. Calphad 38:177-184

Reviews in Mineralogy & Geochemistry
Vol. 77 pp. 229-257, 2013
Copyright © Mineralogical Society of America

In situ Investigations of Carbonate Nucleation on Mineral and Organic Surfaces

James J. De Yoreo
Physical Sciences Division
Pacific Northwest National Laboratory
Richland, Washington 99352, U.S.A.
James.DeYoreo@pnnl.gov

Glenn A. Waychunas
Earth Sciences Division
Lawrence Berkeley National Laboratory
Berkeley, California 94720, U.S.A.

Young-Shin Jun
Department of Energy, Environment and Chemical Engineering
Washington University
St. Louis, Missouri 63130, U.S.A.

Alejandro Fernandez-Martinez
ISTerre, CNRS & Universite Joseph-Fourier Grenoble I
B.P. 53X
38041 Grenoble Cedex 9, France

INTRODUCTION

Nucleation is the seminal event in formation of new mineral phases. The subject has a long history, finding its modern roots in the work of Gibbs in the late 1800's (Gibbs 1876, 1878) and continuing through the efforts of Stransky and others in the mid-20th century (Gutzow 1997). What emerged has come to be known as classical nucleation theory (CNT). Within this model, mineral nucleation comes about through ion-by-ion addition to a growing cluster (Fig. 1A), whose origin lies in the inherent thermodynamic fluctuations of the solution. In recent years, this well-accepted theory has been called into question by an increasing number of studies, both experimental and theoretical, reporting so-called "non-classical" pathways of nucleation involving aggregation of clusters or nanoparticles that exist in equilibrium with the free ions (Fig. 1B). Moreover, such studies often report the nuclei consist of an amorphous precursor, which transforms to the more stable crystalline products only after nucleation has long ended. Presumably, if these cluster-based and multi-stage processes dominate, it is because they offer a lower barrier pathway to nucleation than does the pathway through ion-by-ion addition. Based on the many years of surface science research since the development of CNT, we now know that energy landscapes are unlikely to be flat; i.e., the free energy of a cluster of ions should depend on its size and/or configuration, and composition, including that of the solvent. The resulting peaks and valleys in the energy landscape will naturally create cluster populations, which could give rise to unexpected pathways. In the context of a geological reservoir, consideration of mineral surfaces, organic films, and pores is crucial, because both substrates and pores can reduce the classical barrier to nucleation and, hence, may play a large role in modifying energy

1529-6466/13/0077-0007$05.00 http://dx.doi.org/10.2138/rmg.2013.77.7

landscapes, re-directing pathways, and determining nucleation rates. The purpose of this chapter is to examine the impact of cluster-based pathways, surfaces, and complex energy landscapes on CNT, and then examine findings from *in situ* studies of nucleation on mineral substrates and organic films. We finish by discussing the implications for geologic CO_2 sequestration.

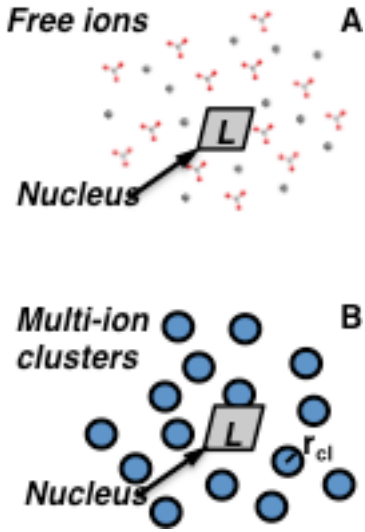

Figure 1. Schematic of ion-by-ion and cluster-based nucleation pathways. (A) Homogeneous nucleation of a crystalline nucleus of length L from ions in solution. (B) Nucleation of a crystalline nucleus of length L from clusters of radius r_{cl} with excess free energy ΔG_{ex}. [Used by permission of Royal Society of Chemistry, from Hu et al. (2012a), *Faraday Disc*, Vol. 159, Fig. 1, p. 512.]

THERMODYNAMIC DRIVERS OF NUCLEATION

Mineral nucleation occurs because the free energy of the initial solution phase is greater than the sum of the free energies of the crystalline phase plus the final solution phase (Gibbs 1876, 1878). In terms of solution activities (which are often well approximated by solution concentrations), an equivalent statement is that the actual activity product of the reactants, AP, exceeds the equilibrium activity product of those reactants, the latter being simply the equilibrium constant, K_{sp}. In cases where a single chemical component crystallizes, the driving force has been expressed not in terms of total free energy change during crystallization, but rather as the change in chemical potential of the crystallizing species, $\Delta\mu$. This $\Delta\mu$ measures the free energy response to molecules transferring from one phase to the other. The larger $\Delta\mu$ becomes, the greater is the driving force for crystallization (Mullin 1992).

Not surprisingly, both the change in free energy and the change in chemical potential are directly related to the activity products (Johnson 1982). For the precipitation reaction:

$$aA + bB + \ldots + nN \rightarrow A_aB_b\bullet\bullet\bullet N_n \quad (1)$$

the activity product of the reactants, AP, and the value of K_{sp} are given by:

$$AP = [A]^a[B]^b[C]^c\bullet\bullet\bullet[N]^n \quad (2)$$

$$K_{sp} = [A]_e^a[B]_e^b[C]_e^c\bullet\bullet\bullet[N]_e^n \quad (3)$$

where the subscript "e" refers to the activity at equilibrium. In turn, the free energy of solution per molecule, ΔG_s, and the change in chemical potential are:

$$\Delta G_s = -k_B T \ln K_{sp} \quad (4)$$

$$\Delta\mu = k_B T \ln AP - \Delta G_s \quad (5a)$$

$$= k_B T \ln(AP/K_{sp}) \quad (5b)$$

where k_B is Boltzmann's constant and T is the absolute temperature. Rather than use $\Delta\mu$, most crystal growth analyses refer to the supersaturation, σ, which is related to $\Delta\mu$ by:

$$\Delta\mu = k_B T\sigma \quad (6)$$

$$\sigma = \ln\{AP/K_{sp}\} \quad (7)$$

Readers may often see σ defined as $AP/K_{sp} - 1$ or even $C/C_e - 1$ where C and C_e are the equilibrium reactant concentrations. These are referred to as absolute supersaturations. They are valid approximations only at small values of σ and, in the case of the expression that utilizes concentrations, only useful when either the activity coefficients, $\chi = [M]/C$ and $\chi_e = [M_e]/C_e$ for the reactants are close to unity, or when $\chi = \chi_e$. Nonetheless the absolute supersaturation is important when considering the kinetics of growth. This will become clear later in the chapter.

CLASSICAL NUCLEATION THEORY

Nucleation is one of the two major mechanisms of the first order phase transition, the process of generation of a new phase from an old phase whose free energy has become higher than that of the emerging new phase (Hohenberg and Halperin 1977; Chaikin and Lubensky 1995). Nucleation occurs via the formation of small embryos of the new phase inside the large volume of old phase. Another prominent feature of nucleation is metastability of old phase, i.e., the transformation requires passage over a free energy barrier (Kashchiev 1999). This is easily understood by considering the free energy changes associated with the formation of the nucleus. The statement that the free energy per molecule of the new phase is less than that of the solvated phase only applies to the bulk of the new phase. The surface is a different matter. Because the surface molecules are less well bound to their neighbors than are those in the bulk, their contribution to the free energy of the new phase is greater (Fig. 2A). The difference between the free energy per molecule of the bulk and that of the surface is referred to as the interfacial free energy. (It is sometimes called the surface free energy but, strictly speaking, this term should be reserved for surfaces in contact with vacuum.) The interfacial free energy is always a positive term and acts to destabilize the nucleus. As a consequence, at very small size when many of the molecules reside at the surface, the nucleus is unstable. Adding even one more molecule increases the free energy of the system. On average, such a nucleus will dissolve rather than grow. But once the nucleus gets large enough, the drop in free energy associated with formation of the bulk phase becomes sufficiently high that the surface free energy is unimportant and every addition of a molecule to the lattice lowers the free energy of the system (Fig. 2B). There is an intermediate size at which the free energy of the system is decreased whether the nucleus grows or dissolves, and it is known as the critical size. This phenomenon of size-dependent stability is referred to as the Gibbs-Thomson effect. Of course, if the supersaturation is high enough, the critical size can be reduced to less than one growth unit. Then the barrier vanishes and the old phase becomes thermodynamically unstable relative to the new so that an infinitesimal fluctuation of an order parameter, such as density, can lead to the appearance of the new phase. The rate of generation and growth of the new phase is then only limited by the rate of transport of mass or energy. This second process is referred to as spinodal decomposition, and the boundary between the regions of metastability and instability of the old phase is called spinodal line (Binder and Fratzl 2001; Kashchiev 2003).

Homogeneous nucleation

Below the spinodal, the rate of nucleation is largely controlled by two important energetic barriers. The first is the excess free energy associated with the creation of the new interface as discussed above. This is an ensemble property that creates a thermodynamic barrier ΔG_c due to the collective behavior of the ions in the solid and liquid phases. The second is an effective kinetic barrier E_A arising from the individual reactions associated with transport of energy and mass, such as desolvation of solute ions, attachment to the forming nucleus, and structural rearrangements. Both barriers appear exponentially in the expression for the rate of nucleation J through (De Yoreo and Vekilov 2003):

$$J = Ae^{-\frac{E_A}{k_B T}} e^{-\frac{\Delta G_c}{k_B T}} \tag{8}$$

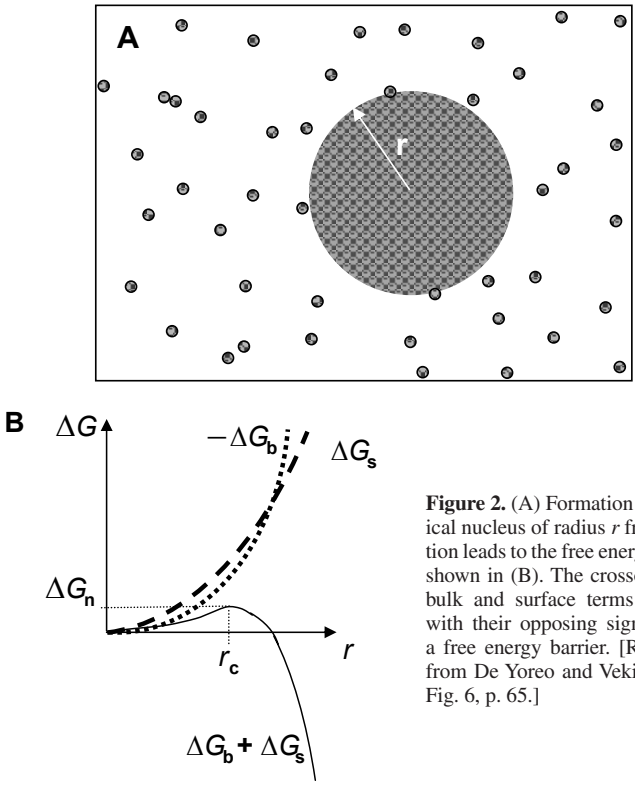

Figure 2. (A) Formation of a spherical nucleus of radius *r* from a solution leads to the free energy changes shown in (B). The crossover of the bulk and surface terms combined with their opposing signs leads to a free energy barrier. [Reproduced from De Yoreo and Vekilov (2003) Fig. 6, p. 65.]

where A is a pre-factor that is determined by geometric factors and material-dependent parameters (e.g., density) and ΔG_c is a decreasing function of the chemical potential $\Delta\mu = \sigma/k_B T$, where σ is the supersaturation, k_B is Boltzmann's constant and T is the absolute temperature.

While the exponential dependence of J on σ through the free energy barrier is a universal hallmark of nucleation that, in essence, distinguishes it from a simple chemical reaction, the exact forms of A and ΔG_c are model dependent. The source of ΔG_c is a positive excess free energy ΔG_{ex} of the solid phase that adds to the change in free energy for a simple chemical reaction, which is simply given by $(dG/dn)\Delta n$ where Δn is the number of molecules passing from the solution to the solid phase. Note that for a supersaturated solution, $(dG/dn) < 0$. Thus without ΔG_{ex} there would be no barrier and precipitation would happen spontaneously at infinitesimal supersaturation *without nucleation*. As discussed above, in classical nucleation theory (CNT), ΔG_{ex} arises from the free energy of the interface between the mineral and the surrounding solvent and substrate (Fig. 1A). When the free energy landscape is flat—that is, the excess free energy is simply determined by the surface area times the interfacial free energy α, which is independent of size—then ΔG_c is given by (De Yoreo and Vekilov 2003; Hu et al. 2012a):

$$\Delta G_c = B\frac{\alpha^3}{\sigma^2} \tag{9}$$

where B is a constant that depends on the shape and density of the nucleating solid, as well as the temperature (see De Yoreo and Vekilov 2003 and Hu et al. 2012a for detailed derivations).

Equations (8) and (9) show that the magnitude of the interfacial free energy has a great influence over nucleation rates, because it appears as a cubic term in an exponential. Sohnel (1982) and Sohnel and Mullin (1978) showed that interfacial energies scale inversely with the logarithm of solubility. Consequently, for sparingly soluble crystals the interfacial energy is quite high and, hence, the thermodynamic barrier to homogeneous nucleation is formidable. In the case of calcite, based on the literature value of 109 mJ/m^2 for the interfacial free energy (Sohnel 1982; Sohnel and Mullin 1978) the predicted classical barrier to homogeneous nucleation of a calcite rhomb ranges from 175 k_BT to 93 k_BT for $CaCl_2$ and $NaHCO_3$ concentrations between 10 mM and 29 mM—the latter marking the literature value for the solubility limit of amorphous calcium carbonate (Brecevic and Nielsen 1989) (ACC) (Fig. 3, bottom curve, σ = 4.8). (Note that, at 300 K, 1 k_BT = 2.6 kJ/mol = 0.62 kcal/mol.)

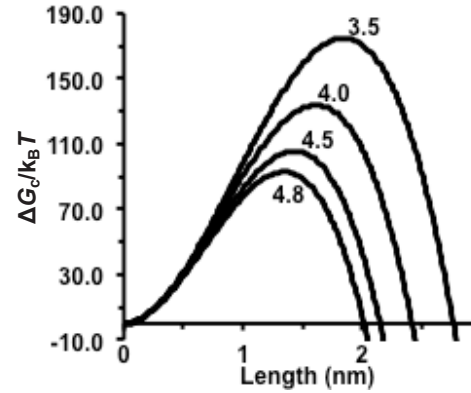

Figure 3. Dependence of free energy ΔG on the length L of one side of an equilateral calcite rhombohedron for homogeneous nucleation from solutions formed from equal mixtures of $CaCl_2$ and $NaHCO_3$ for the indicated values of supersaturation. The corresponding final Ca^{2+} concentrations are from top to bottom: 10 mM, 15 mM, 23 mM and 28 mM. [Used by permission of Royal Society of Chemistry, from Hu et al. (2012a), *Faraday Disc,* Vol. 159, Fig. 2, p. 515.]

Equation (9) also reveals the extreme level of supersaturation needed to reduce the classical free energy barrier for nucleation of ACC below that for calcite. Based on the scaling of interfacial free energy with solubility, the ratio of α for ACC to that of calcite is of order 0.75. Taking into account the differences in the parameter B for calcite and ACC, one finds that the free energy barrier to forming calcite will be less than the barrier to forming ACC until the solution concentration is increased to the point where the supersaturation relative to ACC exceeds ~65% of the supersaturation relative to calcite (Hu et al. 2012a). Because the solubility of ACC is so much higher than that of calcite, for equal mixtures of $CaCl_2$ and $NaHCO_3$, this condition can only be reached if the solution Ca^{2+} concentration is far in excess of 100 mM. Even if the solubility of ACC is considerably smaller than reported in the literature as seems likely based on recent titration studies (Gebauer et al. 2008) as well as in situ observations of nucleation in which bulk ACC formation was observed at less than half the literature value of the solubility (i.e., 13 mM vs. 28 mM final Ca^{2+} concentration) (Hu et al. 2012a), the required concentration for ACC to be favored thermodynamically is still extreme. For example, even if we take the equilibrium solubility to be as small as 10 mM (final Ca^{2+} concentration), a Ca^{2+} concentration of approximately 100 mM is required before there is a crossover in barriers. Even at that concentration, the classical barrier is still in excess of 53 k_BT. The clear conclusion of this analysis is that, for a flat energy landscape, the concentrations required to achieve homogeneous nucleation of either phase are extreme and inconsistent with experimental observations of both calcite and ACC nucleation at significantly lower concentrations. Hence, either nucleation is heterogeneous or other pathways of precipitation that avoid this barrier must be at work.

Heterogeneous nucleation

The presence of a foreign surface can be used to exert even greater control over nucleation because, quite often, the interfacial energy between a crystal nucleus and a solid substrate is lower than that of the crystal in contact with the solution (Nielsen 1964; Abraham 1974;

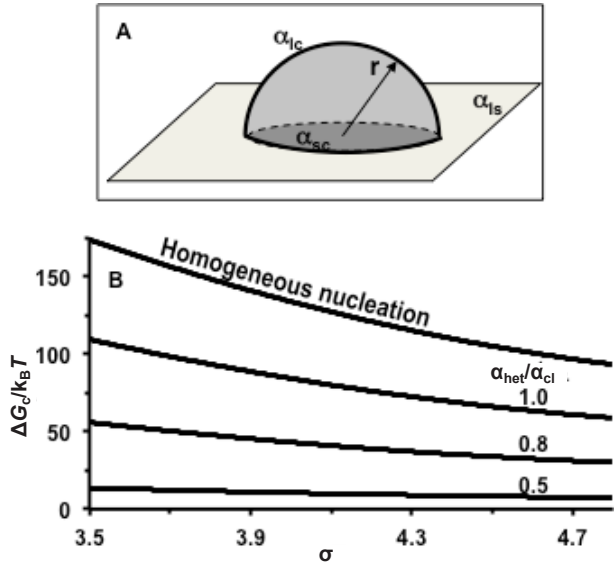

Figure 4. (**A**) Heterogeneous formation of a hemispherical nucleus at a foreign substrate. The interfacial free energies for the crystal-liquid, crystal-substrate and liquid-substrate interfaces are α_{cl}, α_{cs}, and α_{ls}, respectively. (B) Dependence of free energy barrier ΔG_c on σ for homogeneous nucleation of a calcite rhomb with α = 109 mJ/m^2 and heterogeneous nucleation of a calcite rhomb on an (012) face with the indicated values of α_{het}/α_{cf}. [Reproduced from De Yoreo and Vekilov (2003) Fig. 6, p. 65.]

Chernov 1984; Mullin 1992; Mutaftschieve 1993). This is because the molecules in the crystal can form bonds with those in the substrate that are stronger than the bonds of solvation. Because the enthalpic contribution to the free energy comes primarily from chemical bonding, stronger bonds lead to a smaller interfacial free energy. This is likely to be a physical phenomenon of great importance in mineral environments, where a range of mineral-types and crystallographic faces are exposed. Clearly the strength of bonding at the interface is strongly dependent on the structure and chemistry of the substrate surface. If the atomic structure of the substrate surface closely matches a particular plane of the nucleating phase so that lattice strain is minimized and, in addition, the substrate presents a set of chemical functionalities that promote strong bonding to the nucleus, then the enthalpic contribution to the interfacial free energy becomes small and nucleation occurs preferentially on that crystal plane.

Because the thermodynamic barrier depends upon the cube of the interfacial energy, heterogeneous nucleation on surfaces (Fig. 4A) that reduce the interfacial energy can proceed at dramatically altered rates. In this case, α becomes an effective interfacial energy α_{het} that depends on the interfacial energies of the crystal-fluid, fluid-substrate, and crystal-substrate interfaces through:

$$\alpha_{het} = \alpha_{cl} - h(\alpha_{ls} - \alpha_{cs}) \tag{10}$$

where h is a factor that depends on the aspect ratio of the nucleus (see SI of Hu et al. 2012a for details). As long as $\alpha_{cs} < \alpha_{ls}$, the value of α_{het} will be reduced from that for the homogeneous nucleus. However, even if the effective α_{ls} equals α_{cs}, that is, the interfacial energies for the crystal-substrate and fluid-substrate interfaces are equal, the barrier will already be reduced by a factor of 1.6 (Fig. 4B, α_{het}/α_{cl} = 1.0) simply because a surface that would have been generated during homogeneous nucleation is now a crystal-substrate interface that carries no energy penalty. A further reduction in α_{het} by only 20% to 50% due to $\alpha_{cs} < \alpha_{ls}$ would lead to a decrease

in the barrier by a factor of 3 to 13 (Fig. 4B, $\alpha_{het}/\alpha_{cl} = 0.8$ and 0.5). Given that nucleation rate depends exponentially on this barrier, these large reductions mean that surfaces have the potential to completely alter the dynamics and pathways of calcite formation.

Based on Equation (10), it is worth pointing out that a substrate for which the interfacial energy with the surrounding solution is extremely high can drive nucleation to occur on the substrate rather than in the surrounding solution even on a crystal-substrate interface that is not particularly well matched, simply because covering a patch of the substrate with the crystalline nucleus hides it from the solution and thus reduces the overall free energy of the system.

The impact of heterogeneous surfaces on nucleation rates is expected to be enhanced when those surfaces contain steps, grooves or pores (Page and Sear 2006; Hedges and Whitelam 2012). The essential reason for the effect is that the presence of a corner increases the fraction of the forming nucleus in contact with the surface. The magnitude of the effect depends strongly on pore size and aspect ratio, and for a given driving force there is an optimum size. When the interaction between the surface and the crystal is favorable, the impact is dramatic. For example, Hedges and Whitelam (2012) show that, for conditions in which the bulk barrier to nucleation is 67 k_BT and the interaction between the surface and the mineral reduces that barrier to 45 k_BT placing an appropriately sized square pore in that surfaces reduces the barrier to only 20 k_BT. When these barriers are translated to nucleation rates, the surface alone enhances the rate by 9 orders of magnitude over the bulk rate, a square groove increases it by another 7 orders of magnitude, and a square pore further increases it by a factor of 70, giving a total enhancement of nearly 18 orders of magnitude (Fig. 5)!

Deviations from a flat energy landscape: Cluster aggregation and size dependent α

In truth, the free energy landscape is unlikely to be flat (Fig. 6, long-dashes) at small sizes. ΔG_{ex} must approach zero at the size of a molecule (shown schematically in Fig. 6 by dotted curve) and probably exhibits local minima and maxima at very small cluster size as certain configurations expose more or less favorable coordination geometries for the surface ions (shown schematically in Fig. 6 solid and short-dashed curve). While these variations in ΔG_{ex} are easy to account for by expressing α as a function of size, they do little to change the basic physics of the nucleation process. Nonetheless, they can potentially have significant effects on the magnitude of the barrier (Figs. 7A and 7B) if the size at which that barrier is reached—i.e., the critical size—becomes comparable to the dimensions at which size effects begin to emerge (dotted curve in Fig. 6), or where local or global minima in the free energy landscape create a population of metastable or stable clusters, respectively (solid and short dashed curves in Fig. 6). These can aggregate to form a critical nucleus (Fig. 1B).

Unfortunately, not much is known about the size dependence of the interfacial free energy α. What little data do exist suggest a slight rise with decreasing size, followed by the beginning of a decrease in magnitude (Zhang et al. 2009), but those data do little to constrain the dependence in the region below 5 nm diameter, which is greater than the 1-3 nm critical size seen in Figure 2A. Theoretical treatments suggest that even a single formula unit already possesses much of the energetic features of the bulk (Gibbs et al. 2011). This suggests the fall-off in interfacial energy may not occur until diameters below 1 nm, though these simulations were performed for molecular solids and cannot be directly translated to ionic crystals like calcite. However, metadynamics simulations of equilibrium calcite structure suggest the energetic features of the bulk are still manifest below 2 nm (Harding 2011). Indirect evidence for a complex dependence on size comes from both cryoTEM (Pouget et al. 2009) and ultra-centrifugation data (Gebauer et al. 2008) that suggest there is indeed a population of sub-critical clusters (commonly referred to as pre-nucleation clusters) with a tight size distribution, which implies there is indeed a minimum in the free energy vs. size, as shown schematically in Figure 6 (solid and short-dashed curves). In fact, titration-based studies on the amount of calcium inferred to be bound

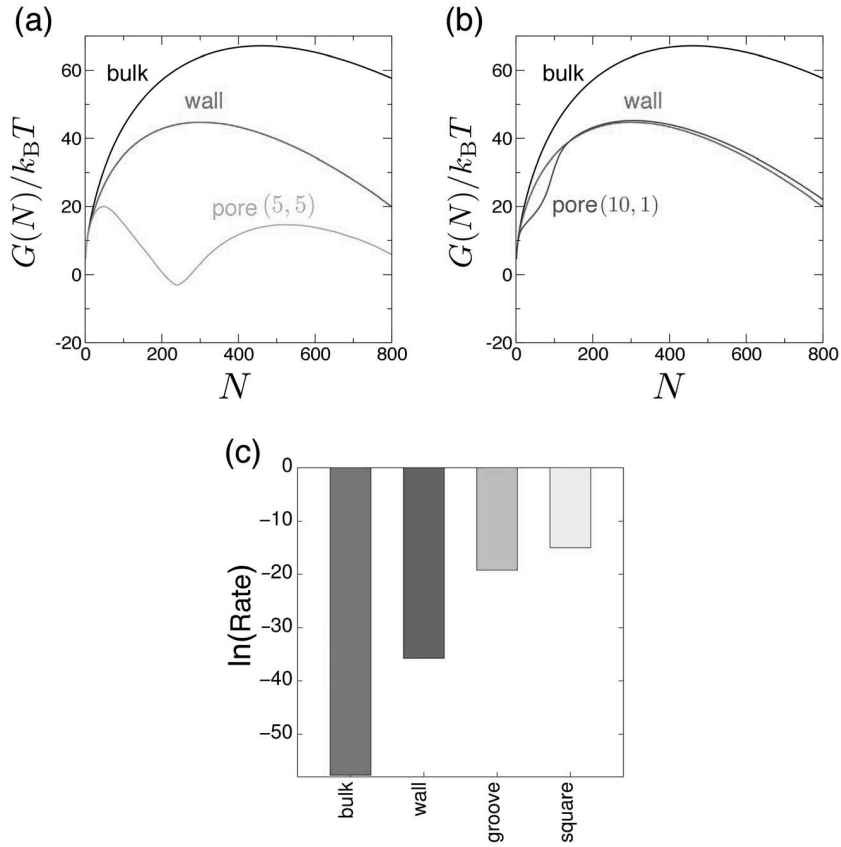

Figure 5. Predictions of 3D Ising model for dependence of absolute free energy G divided by k_BT vs. number of growth units N showing well-chosen pores should dramatically enhance nucleation relative to a planar surface made of the same material, while badly chosen pores do little except take up space on the substrate. (a) Under conditions where the bulk nucleation barrier is about 67 k_BT and the attractive interaction with the surface reduces the barrier to 45 k_BT, a pore of optimum geometry reduces the barrier to about 20 k_BT. (b) By contrast, a badly chosen pore offers no enhancement of nucleation over a flat surface of the same material. Given a pore so narrow that droplets are unstable within it, nucleation takes place instead on the surrounding surface. (c) Nucleation at the planar surface is 9 orders of magnitude faster than in the bulk, while a long groove of optimum width promotes nucleation rate by a further 7 orders of magnitude and a square pore of optimum width gives rise to nucleation that is about 70 times faster still. [Used by permission of Royal Society of Chemistry, from Hedges and Whitelam (2012), *Soft Matter*, Vol. 8, Fig. 8, p. 8632.]

in these clusters concluded that they occupy a global minimum, i.e., the free energy of the pre-nucleation clusters lies *below* that of the free ions (Fig. 6, short dashed curve) (Gebauer et al. 2008; Gebauer and Coelfen 2011).

Deviations from a flat landscape will change the dependence of ΔG_c on σ (Eqn. 9). In the case of a size dependent α, the change can be complex and depends on the form of the size dependence. For nucleation by aggregation of clusters that occupy a local minimum in the free energy, the dependence becomes (Hu et al. 2012a):

$$\Delta G_c = B\frac{\alpha^3}{\left(\sigma \pm C\right)^2} \tag{11}$$

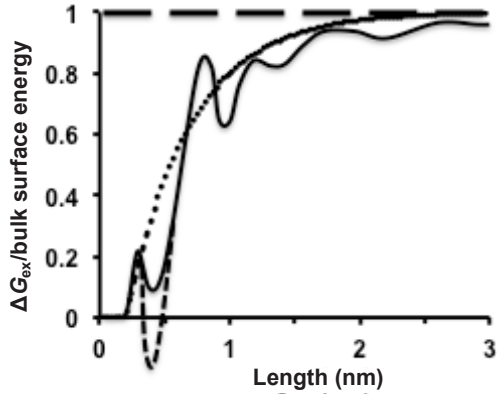

Figure 6. Dependence of excess free energy (ΔG_{ex}) on particle size. Long dashed line – flat energy landscape; Dotted line – simple size dependence; Solid line – Size dependence with local minima and maxima; Short dashed line illustrates global minimum defining stable population of clusters with narrow size distribution. [Used by permission of Royal Society of Chemistry, from Hu et al. (2012a), *Faraday Disc*, Vol. 159, Fig. 2, p. 515.]

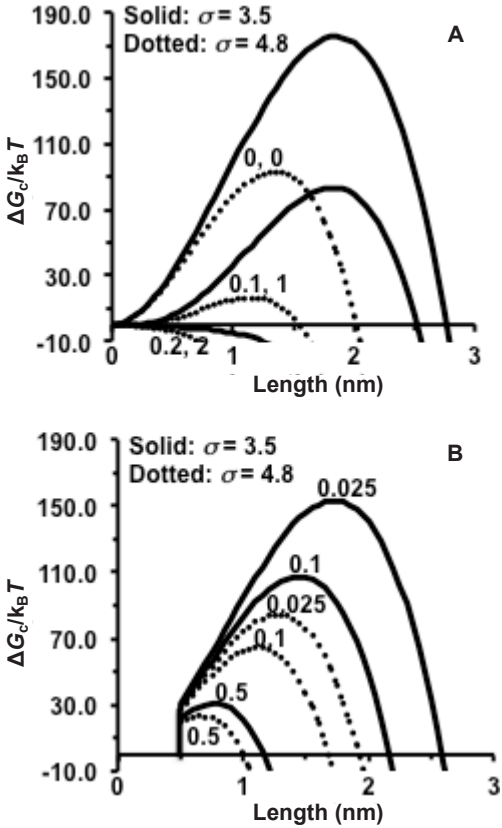

Figure 7. (A) Effect of size dependent excess free energy on ΔG, where $\alpha = \alpha_\infty\{1-\exp[-(L-L_0)/L_\infty]\}$ and α_∞ is the bulk interfacial energy, for two different supersaturations and the indicated values for of L_0 and L_∞ where L_0 is the length at which ΔG_{ex} reaches zero in Figure 5 and L_∞ is the size at which it reaches $1-\exp[-(1-L_0/L_\infty)]$ of its bulk value. (B) Effect on ΔG of aggregation by clusters of size $L = 0.5$ nm occupying a local minimum in excess free energy for two different supersaturations and the indicated values for the ratio of excess free energy to bulk surface energy. Note that values of ΔG make no sense below $L = 0.5$ nm, because clusters of this size are assembled to make the critical nucleus. [Used by permission of Royal Society of Chemistry, from Hu et al. (2012a), *Faraday Disc,* Vol. 159, Fig. 2, p. 515.]

where C is a constant that depends on the shape factor, the cluster radius and the excess free energy of the cluster, and the plus or minus sign depends on whether the minimum in ΔG is local or global (for details, see Hu et al. 2012a). If it is a local minimum (Fig. 1D, solid green line), then the clusters are metastable, they carry excess free energy above the free ions, the plus sign applies, and the barrier is reduced. If it is a global minimum (Fig. 1D, dashed green line), then the clusters lie below the free ions, the minus sign applies and nucleation by cluster

aggregation brings with it an extra energy cost. This is the case for pre-nucleation clusters, which were found to lie about 18 kJ/mol below the free ions (Gebauer and Coelfen 2011). Thus creation of a super-critical nucleus by aggregation of pre-nucleation clusters would bring with it a larger barrier than aggregation of free ions, regardless of whether the end product is an amorphous or crystalline phase.

One interesting implication of Equation (11) is that the impact of clusters—stable or metastable—is to effectively alter the supersaturation from σ to $\sigma \pm C$, making it larger for metastable clusters and smaller for stable clusters. The result is that the existence of metastable clusters *increases* the probability of nucleating ACC rather than calcite, while the existence of stable clusters *decreases* that probability. This effect was further explored in a number of recent studies. Habraken et al. (2013) found that calcium phosphate nuclei formed by aggregation of nm-sized metastable complexes, which carried an excess free energy above the free ions, leading to a reduced barrier and appearance of the amorphous phases at anomalously low supersaturations. In the iron oxide system, Baumgartner et al. (2013) observed formation of the magnetite phase through aggregation of highly disordered ferrihydrite precursor particles. Similarly, Van Driessche et al. (2012) discovered that gypsum formed through a two-step process in which bassanite nanoparticles first formed at concentrations *below* the solubility limit for that phase and transformed into gypsum as they grew in size, or upon attachment to existing gypsum crystals. These latter cases harken to an effect predicted by Navrotsky (2004), who pointed out that, because enthalpies of formation of polymorphs can cross over as the particle size decreases into the nanoscale, one might observe an inversion of the relative solubilities. As a consequence, the less ordered phase, which is typically is more soluble at macroscopic size and has a lower interfacial energy, would become the thermodynamically favored phase. Because the disordered phase also typically exhibits the lower interfacial energy, considering Equation (2), it follows that, if this size effect on phase stability is indeed manifest, the less ordered phase would appear first at *all* supersaturations, forcing the system to follow a two-step pathway to formation of the final stable phase.

GISAXS MEASUREMENTS OF INTERFACE PRECIPITATION AND NUCLEATION RATES

GISAXS is a versatile extension of the well-known SAXS technique applied to interfaces between materials of different electron density (Levine et al. 1989). By suitable selection of experimental geometry it is possible to probe buried interfaces in solid materials (Naudon 1995), or at solid/liquid interfaces. The technique relies on the density differences at the interface to set up a grazing incidence geometry allowing total reflection of X-rays into the lower density medium (Fig. 8). Such scattering geometry allows scattering normal to the interface (z direction), and along the interface (xy direction or 2θ direction) to be probed independently, so that scattering information for all directions along and normal to the surface can be measured. Such data conveys detailed particle size and shape, as well as interparticle separation information unavailable with classical SAXS measurements, where all scattering directions in the detector plane are equivalent.

For aqueous interfaces the technique is ideal for probing the evolution of precipitates from initial nucleation, through growth and evolution (Fig. 9), and into development of faceted crystallites (Fig. 10). The practical limits of the technique depend on range of the scattering vector (q, in dimensions of reciprocal length) available, which in turn is determined by the X-ray scattering setup, detector size, sample to detector distance, and incident beam divergence. Given highly brilliant X-radiation from a synchrotron undulator beamline, precipitates down to less than 1 nm can be detected, and growth followed up to sizes 2π/(lowest q value), typically on the order of 50-100 nm, but extendable to microns using long sample to detector distances

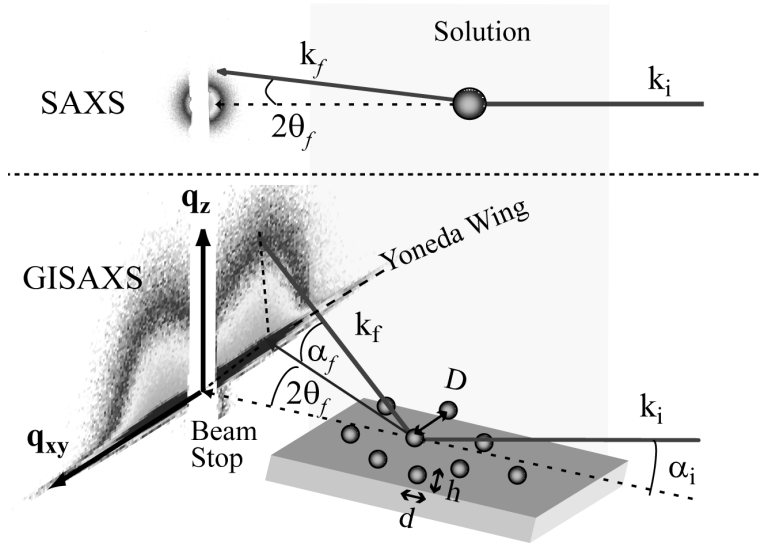

Figure 8. GISAXS scattering geometry. The incident beam is the k_i vector, and scattered beam is k_f. α_i and α_f are the incidence and reflected beam angles, respectively, with α_i generally set below the critical angle for total external scattering of the substrate. In practice the direct reflected beam along the q_z direction is blocked by a narrow beam stop to protect the detector. [From Jun et al. (2010), *Environ Sci Technol*, Vol. 44, Fig. 1A, p. 8183, used with permission from the American Chemical Society.]

with highly collimated X-rays. The technique is also fast, as scattering consists of a fraction of the incident beam (typically several %) and thus good counting statistics can be obtained in fractions of one second.

GISAXS combines elements of classical SAXS and grazing-incidence diffraction, hence for accurate analysis one would consider scattering not only involving particles at an interface, but also higher order scattering such as involving reflection from the surface first, then subsequent particle scattering, along with other scattering paths. For aqueous mineral interfaces with relatively low reflectivity, we might generally neglect the higher order scattering, a model known as the Born approximation. However in the case where reflectivity is high, e.g., at highly perfect surfaces below the critical angle, the second order scattering must be considered, and the distorted wave Born approximation (DWBA) is used in modeling to take account of several important scattering contributions (Rauscher et al. 1995; Lazzari 2002). In general the scattered intensity is related to the scattering power of the atoms in the precipitate, the difference in density between precipitate and contacting medium, and the number of scattering particles. One may speak of X-ray "contrast" which is proportional to the square of the electron density differences between precipitate and surrounding medium. Precipitates having low contrast are difficult to measure, even if abundant. The intensity is also modulated by the particular arrangement of particles in the precipitate, the structure factor or S(q), and the shape of the particles, the form factor P(q). Hence we have

$$\mathrm{I}(q) = \frac{N}{V}\,(\rho_1 - \rho_2)^2 V_\mathrm{p}^2 \mathrm{P}(q)\mathrm{S}(q) \tag{13}$$

where N is the number of particles, V_p is the particle volume, V is the X-ray illuminated volume, ρ_1 is the particle density and ρ_2 is the matrix density. Data analysis is commonly first done with *direct* methods, i.e. methods that do not require use of specific model fitting or assumptions.

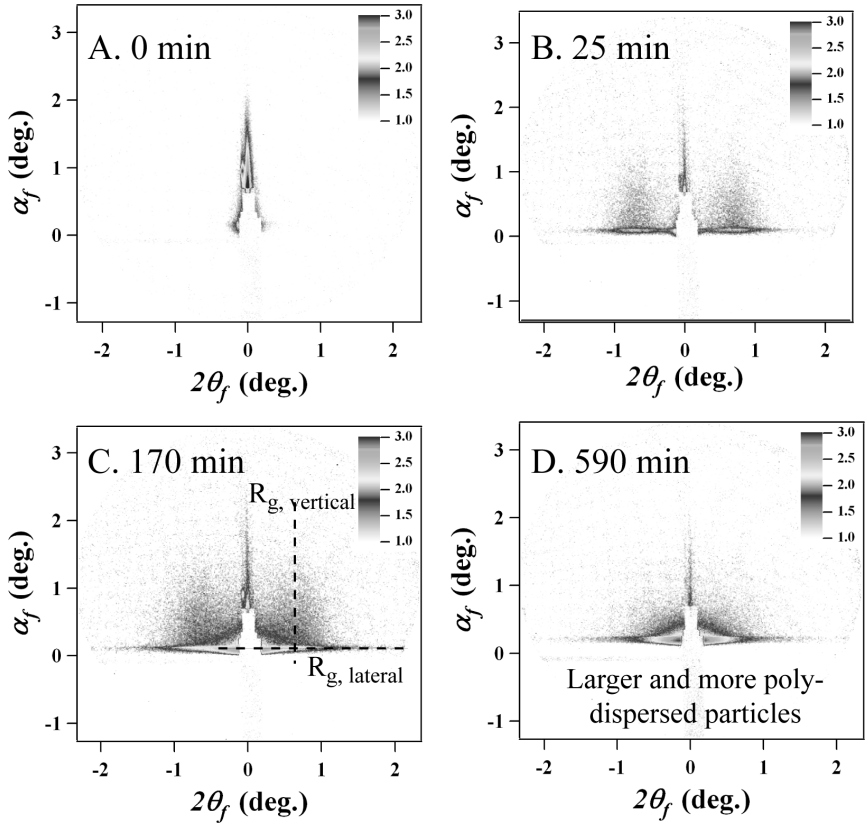

Figure 9. GISAXS patterns from Fe oxyhydroxide heterogeneous precipitation on quartz surfaces. Two symmetric lobes of scattering intensity appear at 25 minutes into the reaction showing particle nucleation, and these evolve with time to smaller q values (smaller 2π) indicating both lateral and vertical particle growth. The data are frequently analyzed by slicing the pattern along the lateral and vertical directions (12 C), producing one dimensional scattering profiles as in Figure 14. [From Jun et al. (2010), *Environ Sci Technol*, Vol. 44, Fig. 2, p. 8184, used with permission from the American Chemical Society].

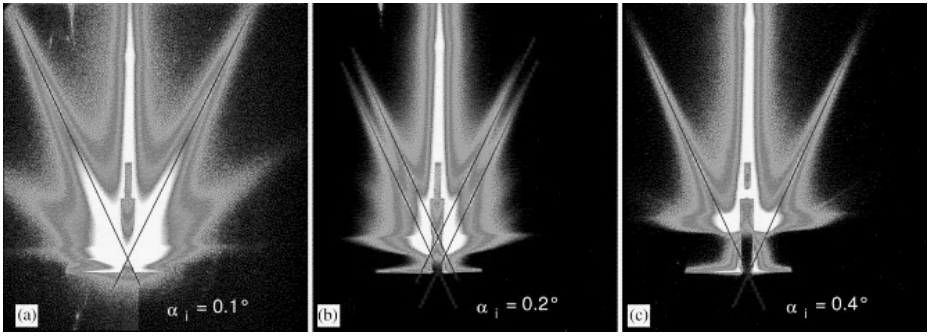

Figure 10. Strong scattering features created by faceting of nanoscale islands of Ge grown epitaxial on Si developed during *in situ* GISAXS. Similar features have been observed in aqueous Fe oxyhydroxide growth on quartz. [Reproduced with permission of Elsevier from Leroy et al. (2005), *J Cryst Growth*, Vol. 275, Fig. 4, p. e2195-e2200.]

Rather than process an entire 2D pattern, the image file is generally "sliced" to separate out the intensity change with q both vertically (z direction) and horizontally (lateral or xy direction). Such slice positions are shown in dashed lines in Figure 9. Analysis of these one dimensional patterns begins by subtracting the background scattering from the GISAXS pattern followed by proper scattering curve normalization using the incident beam intensity. For aqueous systems involving precipitation, it is important to consider the absorption of the X-rays in the liquid phase. If a high flow rate in a reaction cell is maintained, the liquid composition should remain stable, but if the solution is not continuously refreshed then a separate measurement of the solution absorption must be made to allow for solute loss to the interface. For cases of high dilution where the particle separation is relatively large (e.g. less than 1% interface coverage), interparticle scattering effects are negligible, and we can work on the basis of analysis of a single averaged particle and neglect the structure factor. This allows use of the Guinier approximation, applicable to the smallest q region in the scattering curve. In this region the slope of the scattering curve plotted as log I vs. q^2 is related to the size of this average particle, known as its radius of gyration (R_g). R_g is representative of the rms distance from the edges of the particle to its center of scattering, and for the Guinier region the slope of the scattering curve will be $-R_g^2/3$.

In the high q limit of the GISAXS scattering, before approaching the wide angle X-ray scattering (WAXS) region (where interatomic distances within the particles become important) at still larger q, another useful approximation is due to Porod. Here if sharp interfaces are present between particles, the integrated surface area of the particles, S, can be estimated from

$$\mathrm{I}(q) = 2\pi S(\rho_1 - \rho_2)^2 q^{-4} \tag{14}$$

from a log I versus log q plot. Other slopes are consistent with rough interfaces of fractal dimension D (slope = $1/q^{6-D}$), or other complex shapes. Figure 11 also shows other aspects of the scattering curve, e.g. the presence of knees indicative of particle shapes, e.g. elongate rods will have knees indicative of both the thickness and length. Additional data analysis can be done using the invariant function, Q, which is equivalent to the area under the weighted scattering curve, or

$$Q = \sum \mathrm{I}(q) q^2 dx \tag{15}$$

taken over the full range of the SAXS data from small q limit to the beginning of the WAXS region. The invariant is proportional to the scattered volume and hence can be used to estimate

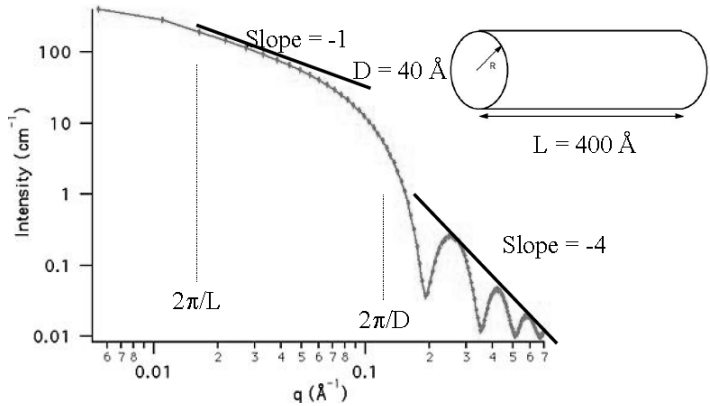

Figure 11. One dimensional GISAXS scattering curve, log I versus log q, showing Porod slope region and two "knees" indicative of the length and diameter of nanoscale rods. In practice the finite size oscillations may not be measureable. [From Eliot Gilbert tutorial, SANS instrumentation, ANSTO, at *http://capsicum.me.utexas.edu/ChE386K/docs/SAS_intro.pdf*.]

precipitate volume. However it must be integrated well beyond the range where q shows any finite size features to be accurate.

The first application of the GISAXS method applied to aqueous geochemical interfaces has conducted by Jun et al. (2010) on precipitation of Fe oxide on quartz. Here the precipitate geometry, particle size and nucleation rate are seen to vary substantially as a function of saturation index or ionic strength. In addition, utilizing this method, the effect of environmentally abundant anions (Hu et al. 2012b) and organic coated mineral surfaces (Ray et al. 2012) on the nucleation and growth of Fe oxide were observed. If only nuclei contribute to the bulk of the scattering, and if there is little growth once nuclei form, one can use the invariant function as a proxy for nuclei density without use of a specific fitting model. Then changes in the invariant can be used to obtain nucleation rates. However if there is growth of nuclei in addition to new nuclei formation, then the various particle components must be fitted and the quantitative numbers of nuclei extracted. An additional consideration is the presence of homogeneous nucleation in solution, where the resulting particles can be collected by the interface and thus miscounted as heterogeneous nuclei. In synchrotron GISAXS experiments one can move the aligned sample in the z direction to allow the beam to transit only the solution, thus examining the scattering intensity from any homogeneous nuclei. Experiments may also be done in inverted mode so that gravity is used to frustrate homogeneous particle collection by the interface.

The first GISAXS studies of nucleation and growth of $CaCO_3$ on high quality single crystal quartz substrates (Fernandez-Martinez et al. 2013) examined a range of solution saturations, each producing different nucleation rates (see next section). If all nuclei can be assumed to be the same phase, then the various nucleation rates can be directly related to precipitate/substrate interfacial energy. In principle similar analysis can be applied to any nucleation system to determine interfacial energies using the assumptions of classical nucleation theory. This is especially valuable as information on interfacial energies for mineral precipitation on contrasting mineral substrates is extremely limited.

GISAXS: from scattered intensity to interfacial energy

The use of time-resolved *in situ* GISAXS experiments using a flow-cell allows keeping a constant supersaturation in the solution, i.e., allows working in an open system and probing the thermodynamics of carbonate mineral nucleation. Experiments are performed measuring scattering patterns at different time points while the mineral substrate of interest is being exposed to a saturated carbonate solution. By placing the mineral substrate in total reflection conditions, the particles nucleated on the surface scatter the incident radiation onto a 2D detector, generating a scattering pattern that contains 3D information about the precipitate. This is illustrated here with the example of $CaCO_3$ particles nucleated onto a quartz (100) substrate (Fernandez-Martinez et al. 2013) With time, an increase in the scattered intensity is observed at intermediate q values, which is associated with the formation of $CaCO_3$ particles on the quartz substrate. As mentioned above, the average vertical and lateral particle sizes of the nucleated particles can be obtained from the distribution of the scattering intensity along the momentum transfer directions perpendicular and parallel to the plane of the substrate, respectively. Figure 12a shows a horizontal integration of the intensity at different times during the nucleation experiment.

In this particular case, the scattering intensity is for that of an isotropic system, and is proportional to:

$$I_{\mathrm{GISAXS}}(q) = I(0) \times \mathrm{P}(q, R, \sigma_d) \tag{16}$$

where $\mathrm{P}(q,R,\sigma_d)$ is the form factor and q is the scattering vector (Renaud et al. 2003). The intensity can be modeled using a log-normal polydisperse model of non-interacting spherical particles (Guinier 1994) with:

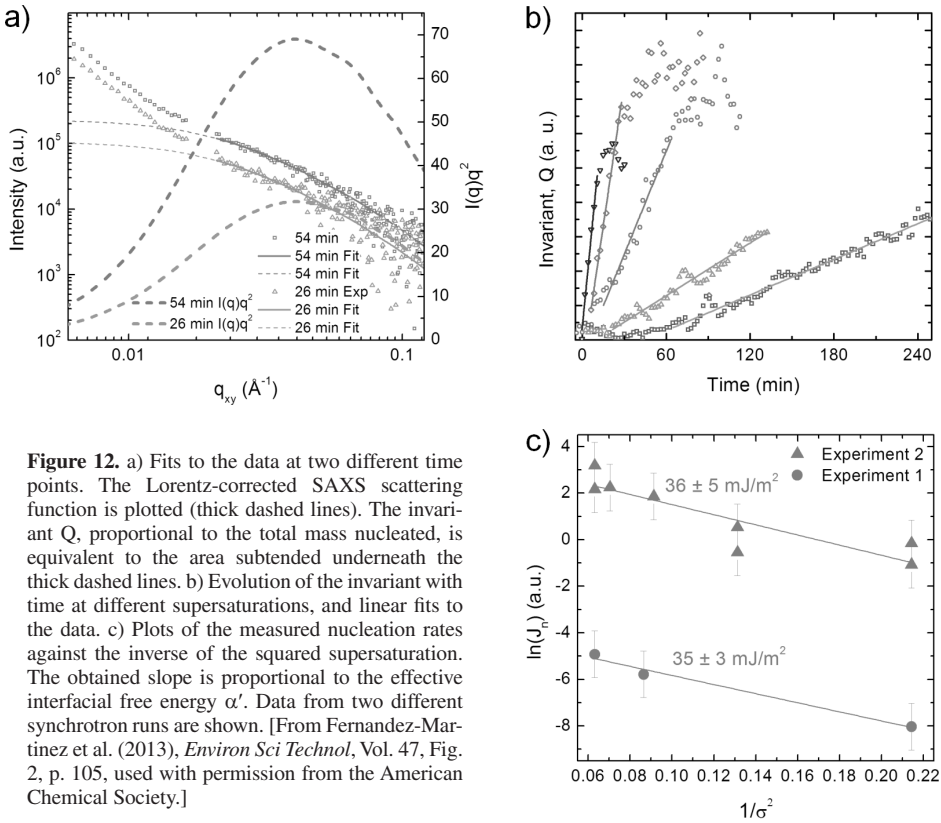

Figure 12. a) Fits to the data at two different time points. The Lorentz-corrected SAXS scattering function is plotted (thick dashed lines). The invariant Q, proportional to the total mass nucleated, is equivalent to the area subtended underneath the thick dashed lines. b) Evolution of the invariant with time at different supersaturations, and linear fits to the data. c) Plots of the measured nucleation rates against the inverse of the squared supersaturation. The obtained slope is proportional to the effective interfacial free energy α'. Data from two different synchrotron runs are shown. [From Fernandez-Martinez et al. (2013), *Environ Sci Technol*, Vol. 47, Fig. 2, p. 105, used with permission from the American Chemical Society.]

$$P(q,R,\sigma) = (\Delta\rho)^2 \int n(R,\sigma_d) V^2 \frac{9\left(\sin(qr) - qR\cos(qR)\right)^2}{(qR)^6} dR \tag{17}$$

where $n(R,\sigma_d)$ is the log-normal distribution, which is used to represent the observed size polydispersity of the nucleated particles, with R being the mean radius of the particle and σ_d its standard deviation. V and $\Delta\rho$ are the particle volume and the electronic density difference (or contrast) between the particle and the surrounding solution. The low-q part of the curves shows a power law behavior associated with the formation of aggregates. A fit to the data in the high-q region using a log-normal distribution of polydisperse spherical particles yields a mean particle size (radius) of ~2 nm, with typical standard deviation values of ~0.09 nm.

Analyzing the development of particle scattering at the initial stages of the experiments under different supersaturation conditions allows us to obtain thermodynamic information of the $CaCO_3$-quartz system. According to Equations (16) and (17), three factors affect the total level of scattered intensity, namely the contrast ($\Delta\rho$), the square of the particle volume (V) and the number of particles (n). In the case of $CaCO_3$ nucleation of quartz (100), the size of these primary particles remains constant during these initial stages, which suggest that nucleation, instead of growth, is the dominant precipitation mechanism contributing to the increase of the GISAXS intensity. This allows using the time-evolution of the GISAXS invariant (Eqn. 15) as a proxy for the nucleation rate, under the assumption that the nature of the $CaCO_3$ polymorph that is being formed remains unchanged, and hence that V and $\Delta\rho$ are constant. Plots of the so-called

Lorentz-corrected GISAXS intensity ($f(q) = I(q)\cdot q^2$) for two different time points are shown in Figure 12a. These curves have been calculated from the fitted function to the experimental data, which allows extrapolating the data at high-q values and obtaining a converged value for the invariant at each time point. The invariant is equivalent to the subtended area underneath the Lorentz-corrected GISAXS intensity curves. Plots with the time-evolution of the invariant for a set of experiments at different solution supersaturation values are shown in Figure 12b, together with linear fits to the data. Following the observation that the size of the primary particles is constant throughout the early stages of the experiment, the slope of each of these curves is then equivalent to the rate of heterogeneous nucleation of $CaCO_3$ on quartz.

In the case of systems showing nucleation and growth (and in the absence of Ostwald ripening processes), fitting polydisperse size distributions to the data is required. Nucleation rates can then be extracted then by integrating the derived particle number distributions at each time point, and making a linear regression to these data.

The effective interfacial energies can be extracted from these data with the help of classical nucleation theory discussed earlier. A plot of the natural logarithm of J against $1/\sigma^2$ is shown in Figure 12c. A linear regression of this plot yields a value for the slope that can be interpreted in terms of an interfacial free energy α_{het} by using Equation (10). The fact that the obtained α_{het} value is smaller than $\alpha_{water\text{-}calcite} = 109$ mJ/m^2 (the interfacial energy that governs $CaCO_3$ homogeneous nucleation) implies that the thermodynamic driving force for heterogeneous nucleation of $CaCO_3$ on quartz is higher than for homogenous nucleation. A comparison between the height of the molar free energy barriers for nucleation (ΔG_c) for both processes gives a ratio $\Delta G_{c\text{-}hete}/\Delta G_{c\text{-}homo} \times 100 = 2.5\%$ for calcite and an estimated ratio of $\Delta G_{c\text{-}hete}/\Delta G_{c\text{-}homo} \times 100 = 15\%$ lower if ACC is the nucleated polymorph. This implies that heterogeneous nucleation will be more significant over homogeneous nucleation given that kinetically-limiting factors for both processes are unimportant.

AFM OBSERVATIONS OF NUCLEATION AND GROWTH OF NEWLY FORMED PRECIPITATES

Atomic force microscopy (AFM) is a powerful tool for qualitatively and quantitatively observing *in situ* surface reactions. It also provides a means to observe *in situ* nucleation at solution-substrate interfaces in real-time while allowing for changing bulk aqueous conditions, but it cannot detect nuclei in solution (Jun et al. 2005). The technique has sub Angstrom vertical resolution, but the lateral resolution is limited to ~40-60 nm features at solution-solid interfaces depending on the specific instrument. If the nuclei are smaller than the lateral resolution, one cannot make an assessment of shape. In addition, newly formed nuclei are often very soft and can be easily wiped out by interactions with the AFM tip. Therefore, careful operations are needed.

The AFM operates a piezo feedback loop based on the force relationship between the tip and sample, which leads to deflection of the cantilever. AFM height mode images provide vertical and lateral dimensional information and phase mode images (see inset images in Fig. 15 below) provide variations in composition, adhesion, friction, viscoelasticity, and other properties (Babcock and Prater 2004). Surface morphology changes by dissolution of pre-existing phases and nucleation and growth of new phases at a solution-solid interface can be observed using an AFM equipped with a fluid cell (Fig. 13). For example, metal carbonate surfaces can be reacted with solutions introduced into the fluid cell by a syringe pump and effluent from the fluid cell can be collected and analyzed off-line for aqueous metal concentrations using inductively coupled plasma mass spectrometry (ICP-MS) or atomic absorption spectroscopy. The setup in Figure 13 allows for real-time molecular scale observations of film growth while controlling factors such as ionic strength, pH, and saturation ratio.

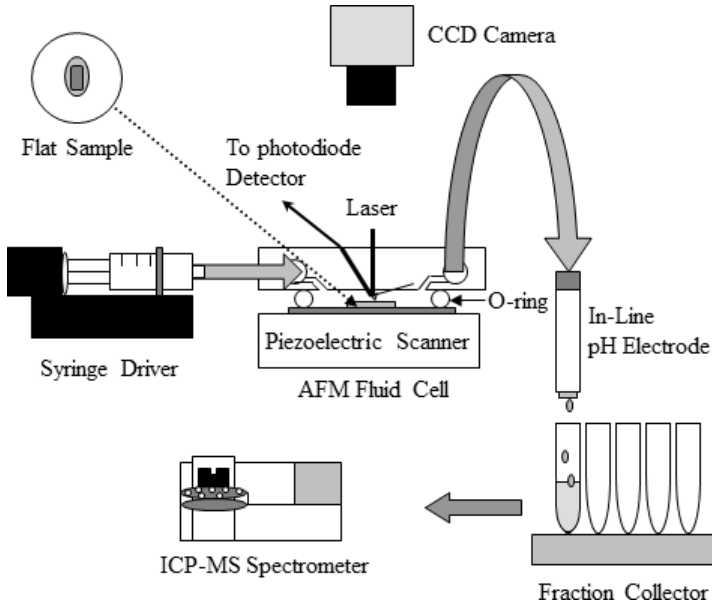

Figure 13. Experimental setup for *in situ* AFM/flow-through reactor experiments. A syringe pump introduces solution via tubing to the fluid cell. The effluent can pass through an in-line pH electrode and the solution is collected for off-line ICP-MS analysis of dissolved aqueous metal concentrations. [From Jun and Martin (2003), *Environ Sci Technol*, Vol. 37, Fig. 2, p. 2364, used with permission from the American Chemical Society.]

This technique has been previously used to investigate thin film growth on carbonate substrates. Lea et al. (2001, 2003) reported that by introducing 150 mM $[CO_3^{2-}]$ and $10^{-5.7}$ M Mn^{2+} at pH = 8.9 $Mn_{0.5}Ca_{0.5}CO_3$ nucleates and grows on the $(10\bar{1}4)$ surface of $CaCO_3$. In particular, the shape of the new $Mn_{0.5}Ca_{0.5}CO_3$ precipitate grows parallel to the $[2\bar{2}1]$ direction of the $CaCO_3$ substrate. Astilleros et al. (2002) also observed *in situ* precipitate film growth on the $(10\bar{1}4)$ $CaCO_3$ surface by adding Ca^{2+}, Mn^{2+}, and $[CO_3^{2-}]$ at pH = 10.2 and showed that, for low $[Mn^{2+}]_{(aq)}$, a $Mn_xCa_{1-x}CO_3$ film initiates at steps, whereas at high $[Mn^{2+}]_{(aq)}$ 2D nuclei form on terraces. Jun et al. (2005) also reported the heterogeneous nucleation and growth of a Mn(III) oxide thin film on the $(10\bar{1}4)$ surface of $MnCO_3$ at circumneutral pH and 1 atm O_2. Heteroepitaxial nucleation and oriented growth of Mn(III) oxide islands on the carbonate substrates $MnCO_3$, $MgCO_3$, and $CaCO_3$ was also observed (Fig. 14). These islands grow on $MnCO_3$ terraces with a rhombohedral 2D shape. On highly stepped surfaces, the islands lack a euhedral form and additional aqueous Mn^{2+} created rounded precipitate islands rather than rhombohedral shaped islands. Interestingly, the Mn(III) oxide islands were observed on $MgCO_3$, but not on $CaCO_3$ due to lattice mismatch between the new precipitate film and $CaCO_3$ substrate. While these studies provide good qualitative descriptions of nucleation and growth processes, statistically improved quantitative analyses are required to obtain the nucleation rates for larger surface areas.

Ex situ AFM observations of GISAXS samples

AFM also can be used to observe surface morphological changes *ex situ*. Figure 15 shows *ex situ* AFM observations of $CaCO_3$ nucleation on the (100) surface of quartz as function of saturation (defined as the natural log of the ion activity product divided by the calcite solubility product, or ln $IAP/K_{sp,}$). The measurements were made within 5 hours of nucleation

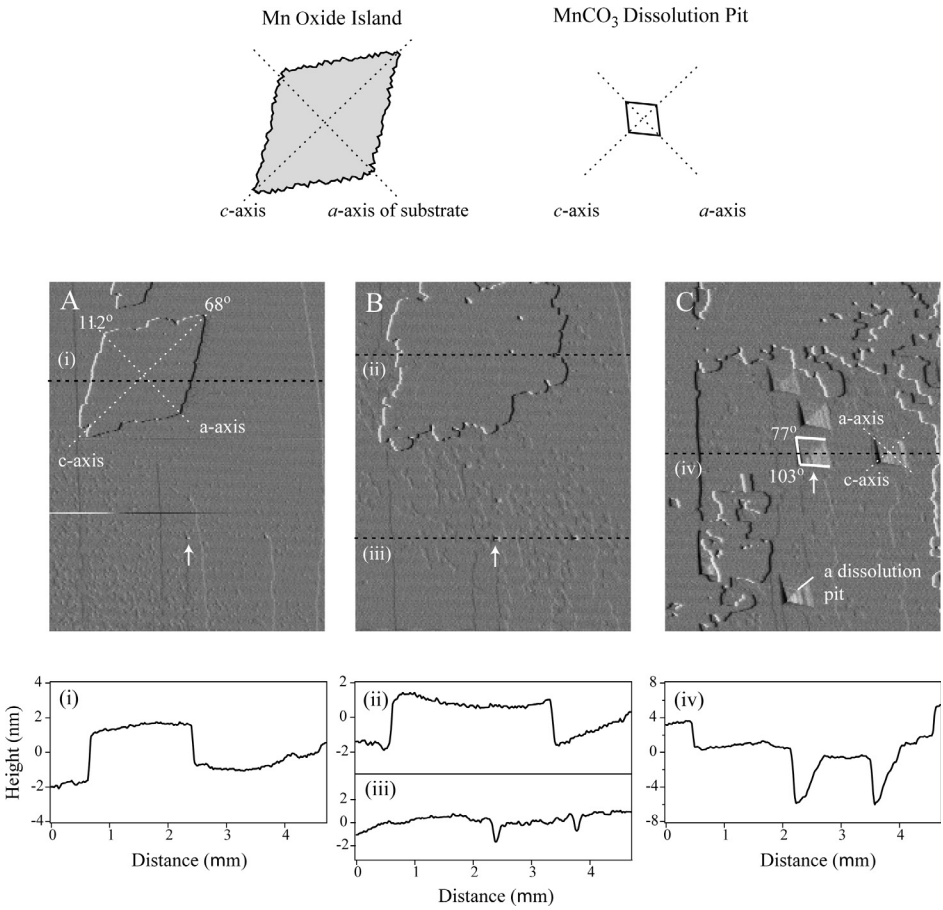

Figure 14. Concurrent island precipitation and substrate dissolution. Top: Illustration of the relative 90° rotation between the dissolution pit and the island growth. Bottom: (A) A rhombohedral island after 120 min exposure to solution. The island grows with 90° rotation relative to the crystallographic axis of the substrate. (B) Growth of the island after 290 min and appearance of a dissolution pit. (C) Coalescence of islands, forming a film, after 950 min and contemporaneous appearance of many dissolution pits. The AFM micrographs are recorded in deflection mode (4.7×6.0 mm^2) at 298 K. The solution has pH = 6.1, no added aqueous Mn^{2+}, and 1 atm $O_{2(aq)}$. The *z*-scale of the image is 10 nm. The white arrows show a common point of reference in images *A* to *C* (image drift). [Used by permission of American Chemical Society, from Jun et al. (2003), *Environ Sci Technol*, Vol. 39, Fig. 2, p. 1242.]

completion, and the images were shown here in height mode. The solution conditions were similar to analogous GISAXS experiments described above. For AFM imaging water was removed, first by washing with pure ethanol to remove remaining dissolved metal ions and solution, and then with drying by application of a high purity nitrogen gas jet. As predicted from classical nucleation theory, the nucleus size at lower saturation was the largest observed, and the size decreased with saturation. The observed sizes from AFM measurements can be somewhat smaller than from GISAXS observations due to particle dehydration. A few larger particles were observed that were formed by homogeneous nucleation and collected by the interface. However, their particle sizes were much larger than the 10 nm range exhibited by the heterogeneously nucleated particles, as also expected from classical nucleation theory.

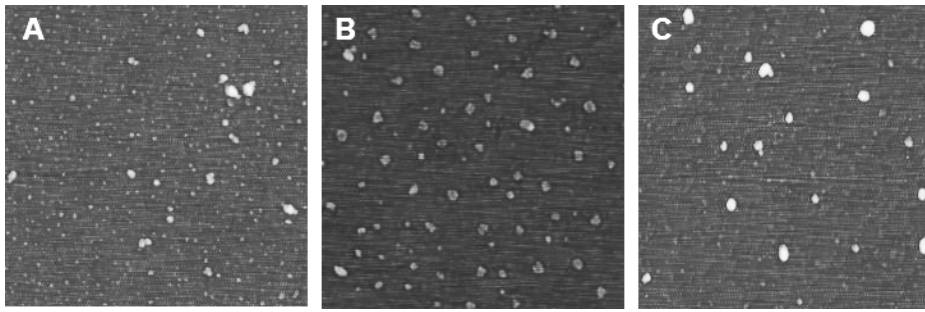

Figure 15. Newly formed calcium carbonates on the (100) surface of quartz as a function of saturation. (A) Saturation (ln IAP/K_{sp}) with respect to calcite is 3.73. The average particle size is 1.2 ± 0.6 nm (B) Saturation with respect to calcite is 3.05. The average particle size is 1.8 ± 0.6 nm (C) Saturation with respect to calcite is 2.72. The average particle size is 4.2 ± 2.5 nm. All solutions were at pH = 8.00 ± 0.06, and the reaction time was two hours. The scan sizes of the images are 1 μm × 1 μm.

Morphology and preliminary Raman spectroscopy indicate that these can particles may be vaterite. Further investigation is needed to confirm whether there is a phase transformation after the nucleation process, perhaps from amorphous calcium carbonate (ACC) to vaterite.

CALCIUM CARBONATE NUCLEATION ON ORGANIC FILMS

The recognition that organic films could have a large impact on nucleation came from investigations in the field of biomineralization where an organic matrix composed of proteins and/or polysaccharides is often found in association with highly organized mineral elements of hard tissues ranging from the carbonate shells of marine organisms (Addadi et al. 2006) to the phosphate-based bones of humans and other mammals (Weiner et al. 2005). Early work on control over calcium carbonate nucleation by organic films focused on either Langmuir monolayers at an air-water interface, polydiacetylene films on mica, or organothiol self-assembled monolayers (SAMs) on noble metal surfaces. Following the landmark paper by Aizenberg et al. (1999a), showing that SAMs could be used to control the location and orientation of calcite crystals with high specificity and fidelity, many studies, both experimental and theoretical, explored the source of structural control in this system (Aizenberg 1999b; Han and Aizenberg 2003; Travaille et al. 2003; Duffy and Harding 2004; Lee et al 2007). Even small modifications in SAM composition or structure, such as changing the endgroup functionality (Aizenberg 1999b) or hydrocarbon chain length (Han and Aizenberg 2003), or altering the noble metal substrate (Aizenberg et al. (1999a) were shown to alter the preferred orientation of the final suite of crystals.

More recently, in situ AFM studies of calcium phosphate nucleation on collagen demonstrated that the effective interfacial energy was greatly decreased from that expected for bulk solution (Habraken et al. 2013), while *in situ* optical studies of calcium carbonate nucleation came to a similar conclusion in the case of organothiol SAMs on gold for both odd and even parity hydrocarbon chain length (Hu et al. 2012a), as well as a range of different headgroup chemistries Hamm et al. 2013). In the latter case, a direct correlation between crystal-SAM binding energy and interfacial energy was established. Similar studies using polysaccharide films revealed a systematic relationship between the barrier to nucleation and the surface charge of the film (Giuffre et al. 2013). The latter two studies provided further insights into the terms within the effective interfacial energy α_{het} (Eqn. 4) that are responsible for the reduced barriers. As we show below, these studies reveal the powerful impact surfaces can have on controlling the pathway and enhancing the rate of nucleation.

In situ studies of calcium carbonate nucleation on organic films have been based on the use of a quartz cuvette modified to allow continuous flow of solution and placed in an inverted optical microscope (Hu et al. 2012a; Nielsen et al. 2012) (Fig. 16A). Calcium and carbonate buffers from two syringe pumps are mixed at a T-junction some distance from the inlet to the cell and a substrate coated with the organic film is placed upside down within the cell. Images are recorded using a CCD camera and the number of crystals forming on the substrate (Fig. 16B-D) is measured as a function of time (Fig. 17A). Once a necessary incubation time has passed, the number of crystals grows linearly with time until the spacing between them becomes too small to allow for independent nucleation events, at which point the increase in number density begins to level off. The nucleation rate is then defined by the slope of the linear region in the plot of number vs. time. These measurements are repeated over a range of supersaturation, giving the dependence of nucleation rate on supersaturation.

Combining Equations (8) through (10), we see that CNT predicts the dependence of the heterogeneous nucleation rate on supersaturation to be described by:

$$\ln J = \ln A' - B\frac{\alpha_{het}^3}{\sigma^2} \tag{18}$$

Hu et al. (2012a) measured J for a range of supersaturations on SAMs of 16-mercaptohexadecanoic acid (MHA) and 11-mercaptoundecanoic acid (MUA) to determine if indeed the prediction of CNT was obtained and whether these surfaces led to a reduction in interfacial free energy. Qualitatively similar behavior was observed for both the even chain-length (MHA, C-16) and

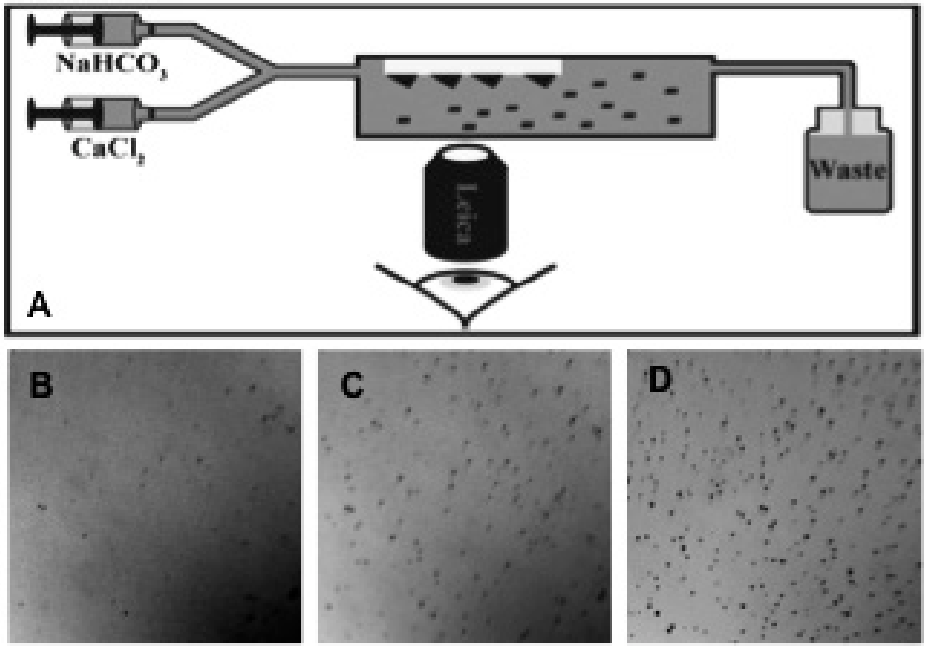

Figure 16. (A) Experimental set-up for optical measurements of nucleation rates. The SAM is suspended upside-down in a flow-through cell and imaged using an inverted optical microscope to measure nucleation rates as supersaturated calcium carbonate solutions are continuously pumped through the cell to maintain constant supersaturation. (B-D) Sequential optical images collected at t = 300, 350 and 450 s. Each image is: 0.43 mm × 0.43 mm. [Used by permission of Royal Society of Chemistry, from Nielsen et al. (2012), *Faraday Disc,* Vol. 159, Fig. 5, p. 112.]

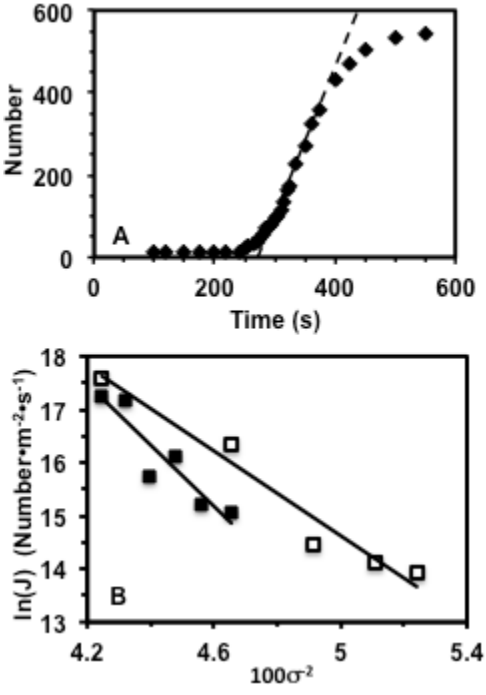

Figure 17. Rate of calcite nucleation on MHA and MUA SAMs. (A) Example showing dependence of number of nuclei on time. (B) Dependence of ln(J) on σ^{-2} showing that data follow dependence predicted by CNT and that MHA films produce shallower slope (lower value of α_{het}) and lower intercept (smaller value of E_A) than MUA films. [Used by permission of Royal Society of Chemistry, from Hu et al. (2012a), *Faraday Disc,* Vol. 159, Fig. 3, p. 516.]

odd chain-length (MUA, C-11) films, but the nucleation rate was greater on MHA. In addition, in accord with previous reports, nucleation occurred on distinct crystallographic planes for the two different SAMs (Travaille et al. 2002; Han and Aizenberg 2003). In contrast, under identical conditions, nuclei on SAM-free gold films were few in number and exhibited random orientations with sporadic occurrences of vaterite.

In accordance with the prediction of Eqn. 12, plots of ln(J) vs. σ^{-2} were found to be linear (Fig. 17B). From these data Hu et al. (2012a) obtained an α_{het} of 72 mJ/m^2 for MHA and 81 mJ/m^2 for MUA, both of which were substantially smaller than previous estimates of 109 mJ/m^2 for α in the case of (homogeneous) calcite nucleation in bulk solution (Sohnel and Mullin 1978; Sohnel 1982). In the middle of the concentration range of the study, these differences in interfacial energy corresponded to free energy barriers for nucleation on MHA, MUA and in bulk solution of 19 k_BT, 27 k_BT and 105 k_BT, respectively. All other factors being equal, these differences alone would correspond to relative nucleation rates J_{MHA}:J_{MUA}:J_{sol} of 1:3.4×10^{-4}:4.5×10^{-38}. The results of these studies showed that calcite nucleation on canonical carboxyl-terminated SAMs proceeded as expected from CNT and that both the enhancement of nucleation on the SAMs relative to bulk solution and the advantage of the SAM with even parity over that with odd parity could be explained in purely classical terms through differences in interfacial energy. This conclusion in no way pre-supposes whether the fundamental units that comprise the nucleus are individual ions or pre-nucleation clusters, because, as Equation (11) indicates, the form of the rate equations is the same in either case and, in fact, for the range of supersaturations used in this study, the value of C never exceeded 10% of σ.

In a subsequent study, Hamm et al. (2013) performed the same experiments for a series of SAMs with distinct headgroup chemistries including COOH, SH and PO_4. As in the study of Hu et al. (2012a), the data were described well by the classical expression, despite the fact that the supersaturations used in this study straddled the solubility limit of ACC as given in the literature. (Though as discussed above, there is good evidence that this limit is substantially lower than previously reported.) Figure 18A, which shows the dependence of ΔG_c on supersaturation for each type of surface in comparison to the barrier to homogeneous nucleation of a calcite rhomb estimated from the literature value for α in pure solution, demonstrates that: 1) the thermodynamic barrier to nucleation onto the SAM surfaces is significantly lower than estimates for homogeneous nucleation; and 2) substrate functional group chemistry and alkanethiol chain length have significant effects on the barrier. For example, comparisons of

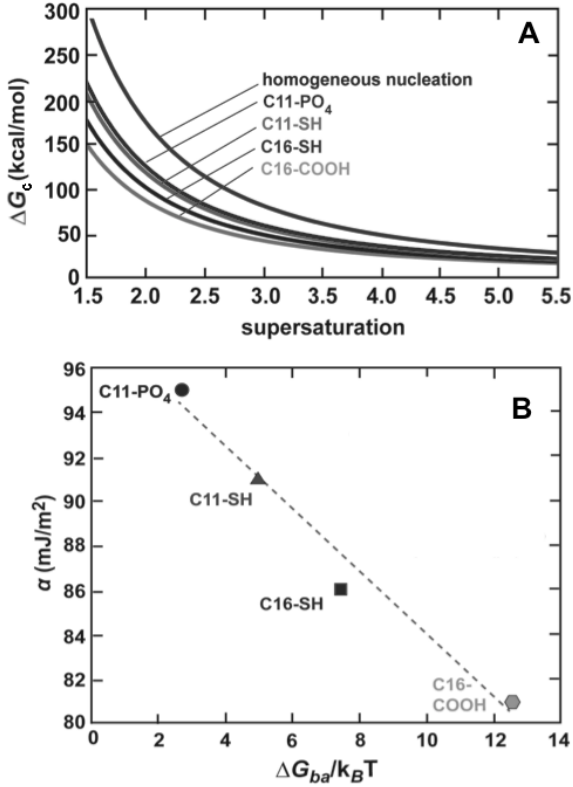

Figure 18. (A) Dependence of ΔG_c on supersaturation as determined from measurements of nucleation rate using method illustrate in Figs. 16 and 17. (B) Interfacial energies (α) derived from nucleation rate measurements in (A) vs. free energies of binding (ΔG_{ba}) for alkanethiol SAM molecules on calcite (104) surfaces as measured by dynamic force spectroscopy. Lower α correlates with strong calcite-SAM interactions (large ΔG_{ba}).

substrates with the same chain length but different head groups show that ΔG_c is lower for C16-COOH than C16-SH and that C11-SH gives a value that is lower than for C11-PO_4. The influence of chain length is seen by the lower ΔG_c value for C16-SH as compared to C11-SH.

Extraction of the interfacial energy from the barriers showed that α_{het} ranges from 81 to 95 mJ/m^2 for these SAMs, which is considerably less than the bulk value of 109 mJ/m^2. Considering the expression for α_{het} in terms of the individual interfacial energies given by Equation (10), Hamm et al. (2013), reasoned that the crystal-liquid interfacial energy should be nearly the same for all films, as should the SAM-liquid interfacial energy given the pk_A of the films and the pH of the experiments. The only term that should differ significantly from one film to the other is the interfacial energy between the SAM and the crystal α_{cs} with smaller values leading to lower barriers. Moreover, α_{cs} should be largely controlled by the binding free energy between the crystal and the SAM. Using dynamic force spectroscopy (DFS) with gold-coated AFM probes, Hamm et al. (2013) measured the free energy of binding between the SAMs and the surfaces of calcite single crystals. The results, shown in Figure 18B, reveal a direct, linear correlation between these two quantities. A large crystal-SAM binding free energy leads to a small crystal-SAM interfacial energy, resulting in a small barrier to nucleation.

Using the same in situ optical technique, Giuffre et al. (2013) looked at nucleation on polysaccharide films deposited by electrodeposition onto gold substrates. They considered five different films including de-N-sulfated Heparin containing amine, acetylamine, carboxyl, and sulfate groups; LG and HG sodium alginates containing carboxyl groups with different proportions of guluronic acid monomer content, hyaluronate containing acetylamine and carboxyl groups, and chitosan containing amine and acetylamine groups. As in the studies of Hu et al. (2012a) and Hamm et al. (2013), the nucleation rates were found to vary with supersaturation according to the dependence expected classically and given by Equation (12). Extracting the barrier, Giuffre et al. (2013) found a systematic variation with polysaccharide charge density, with the most negatively charged film giving the highest barrier (Fig. 19A). Moreover, when the data from Hamm et al. were put on the same plot, they found this correlation extended smoothly from the polysaccharide films to the SAMs. Considering, once again, the terms in Equation (10), Giuffre et al. (2013) reasoned that, as in the study of Hamm et al. (2013), the magnitude of the crystal-liquid interfacial energy was the same in all cases. However, because the polysaccharides have very different charge densities, the film-liquid interfacial energy might be very different for each polysaccharide. Taking the film-air interfacial energy as a surrogate for the film-liquid interfacial energy—with larger values of one corresponding to smaller values of the other—they found that, indeed, the nucleation barrier scaled linearly with the film-air interfacial energy as expected (Fig. 19B).

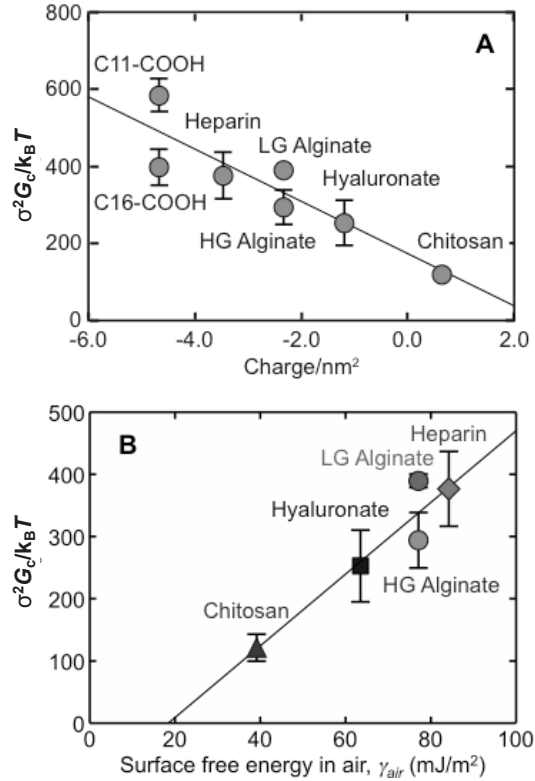

Figure 19. (A) Slope of ln(J) vs. $1/\sigma^2$ (equal to $B\alpha^2$ in Eqn. 12) for calcite nucleation on polysaccharide substrates vs. (A) charge density of the polysaccharide substrates and (B) polysaccharide substrate surface tension in air. [Used by permission of National Academy of Sciences, from Giuffre et al. (2013), *Proc Natl Acad Sci USA*, *www.pnas.org/cgi/doi/10.1073/pnas.1222162110*, Fig. 3, p. 4.]

There are three major conclusions of these studies of calcite nucleation on organic films: First, they demonstrate the dependence of nucleation rate on supersaturation is in accordance with the predictions of CNT without consideration of "non-classical" behavior. Second, the film-to-film differences are controlled by the effective interfacial energy α_{het}, also as expected from CNT. Third, both the substrate-liquid and substrate-crystal interfacial energies can be manipulated to alter α_{het} in a systematic manner.

IMPLICATIONS OF NUCLEATION INFORMATION ON GEOLOGIC CO_2 SEQUESTRATION

Nucleation information is pertinent to both mineral trapping in geologic carbon sequestration (GCS) reservoirs, and geochemical processes occurring in caprock formations, especially changes in porosity and flow due to precipitation. For GCS applications requiring effective mineral trapping of carbonate, it is essential to understand the factors affecting both the volume and specific location of carbonate produced from exposure of porous media to carbonate rich brines. If nucleation occurs preferentially in the throats of pores near an injection site, then brine infiltration of the reservoir may be restricted by rapidly decreasing permeability, limiting the effectiveness of the effort (Armstrong and Ajo-Franklin 2011). On the other hand, if nucleation is limited, leaking of the emplaced fluid into caprock is a concern. In a typical scenario, the degree of saturation increases after brine implacement, due to the dissolution by the brine of minerals having Ca^{2+}, Mg^{2+} and Fe^{2+}. Once saturation with respect to a crystalline phase is exceeded, the nucleation rate is then determined in part by the interfacial energy between the precipitate and the substrate mineral. A low interfacial energy supports easier nucleation, and hence certain minerals are more likely to support early and high-density nucleation. However at very high saturations, for example when the reservoir fluid already contains high cation concentrations, homogeneous nucleation becomes important, allowing nucleation to become significant within the fluid. Nuclei formed in this way may travel further into the reservoir, leading to reduced porosity and flow, depending on permeability. We are thus concerned about where precipitation occurs and to what extent, and require the ability to model the process from knowledge of the fluid composition, types of minerals in the reservoir, and the likely hydrological networks in the reservoir. Basic information supplied by GISAXS, optical and AFM nucleation studies includes: a) estimation of precipitate/mineral surface interfacial energies, b) locations for high nucleation density and topology of growth following nucleation, and c) effects of solution composition on nucleation and growth rates. In actual GCS field situations, these considerations are all likely to have influence, perhaps strongly coupled to local mineralogical, biological, and geochemical characteristics in the reservoir. Hence they must be considered together to effectively understand the precipitation process on all appropriate length scales.

Precipitate/mineral interfacial energies

Significant differences in interfacial energies can dictate where nucleation is likely to first occur, and will affect the density of nuclei. Both factors influence further growth (trapping) of carbonate precipitates. The observations for quartz indicate that it supports nucleation at ambient conditions, but comparisons with other phases, though in progress, are not yet available. With increasing temperature, retrograde solubility of $CaCO_3$ will increase saturation, so nucleation and growth are expected to be robust in reservoirs dominated by quartz, e.g. sandstones. However the effect of pressure and temperature on interfacial energies is not yet known, and requires investigation. Another factor is the wettability of mineral surfaces, which are known to become more hydrophobic after contact with $scCO_2$ (Chiquet et al. 2007; Espinoza and Santamarina 2010). Additional hydrophobicity will alter the thermodynamics of nucleation by affecting the difference between the α_{ls} and α_{cs} terms in the nucleation rate equation (see Eqns. 9 and 10). α_{ls} will increase while a change in α_{cs}, ostensibly due to lattice mismatch between substrate and

nucleating crystal, is difficult to predict. Lattice mismatch strain assumes coherency between precipitate and substrate, and coherency may be reduced in a hydrophobic interface. However, assuming nil change in α_{cs}, the net effect would be a lowering of the effective interface energy for nucleation, α_{het}, increasing the driving force for heterogeneous nucleation. It is important to note that both precipitate/substrate interfacial energies and relevant solution/substrate interfacial energies are not yet known for most of the cases expected in GCS. This affects not only modeling of nucleation processes, but also determination of thermodynamic and kinetic factors affecting dissolution (Lasaga and Blum 1986).

Location and topology of high-density nucleation and subsequent growth

There is evidence from simulations (Hedges and Whitelam 2012) that confined pore spaces can enhance nucleation rates, leading to rapid cutoff of pore flow and reduction in permeability after nucleation. This may be further enhanced if the nucleation density is favored by interfacial energy. However the combined effect of dimensionality, roughness of surfaces, and interfacial energies on nucleation in pore throats has not been treated. Particular nucleation environments may favor increased precipitate growth, or conversely, lead to much reduced growth, given varied topological factors. For example, nucleation in narrow pore throats may produce limited growth due to rapid reduction in solution flow, while nucleation in wide pores may lead to extensive growth. Growth may also be affected by the shape of nuclei and the phase nucleated, e.g. if it is an amorphous carbonate phase, or if it has variable composition, such as might be expected in the presence of significant Mg levels.

A further example of how nucleation may be affected by interface and mineral types is afforded by the work of Shao et al. (2010), which reported the evolution of nanoscale amorphous silica precipitation on phlogopite surfaces reacted with $scCO_2$ in 1 M NaCl under 102 atm of CO_2 at 95 °C, conditions relevant to GCS. The actual nanophase formed depends on temperature, pressure and salinity, but amorphous silica is overall dominant. Images depicting a range of reaction times are shown in Figure 20, where parts A, B, C, E and F refer to 5, 8, 22, 43 and 159 h reaction times, and D is an enlargement from a small area of B. All are AFM images shown here in height mode, with insets in the lower left corners collected in phase mode, which can be used to identify the nanoparticle phase. Insets in right upper corners indicate schematic particle positions, and the height cross sections below the images correspond to the white dotted lines in height images. Arrows indicate the position of particles on the edge of dissolution pits. The dotted curved line in image D indicates the evolution of a single dissolution pit. An interesting aspect is that the nanoparticles prefer to form at the edges of dissolution pits rather than on flat surfaces. If the particles grow continuously, they may close over the dissolution pit, locally passivating the reaction. Dissolution pits might be considered analogous to pore structures in GCS sites, and must be considered when there are simultaneous dissolution and nucleation processes. As the location of nucleation is important owing to the impacts on CO_2 permeability changes in porous media, the mineralogical constituents of caprocks and formation rocks in GCS sites are also crucial to understand. Mineralogical distributions in GCS sites are quite diverse and often their heterogeneities create more complex interactions with CO_2 and brines (Landrot et al. 2012). Consequently, nucleation of secondary precipitates can form with totally different kinetics and extent as a function of exposed reactive mineral (for examples, quartz, mica, or feldspar). These differences can then further affect pore-scale microstructure and reactive fluid transport. Hence, a better understanding of the location, morphology, and their mineralogy of the pre-existing mineral substrates in GCS would be needed.

Effects of solution composition on nucleation and growth rates

Solution composition is expected to mitigate nucleation in several ways apart from degree of supersaturation and effects associated with $scCO_2$ exposure. An important characteristic environmental factor is high salinity (Shao et al. 2011a), which can cause an increase in α_{ls}, as shown by Mizele et al. (1985) in amorphous silica surface in 1 M NaCl solutions. This

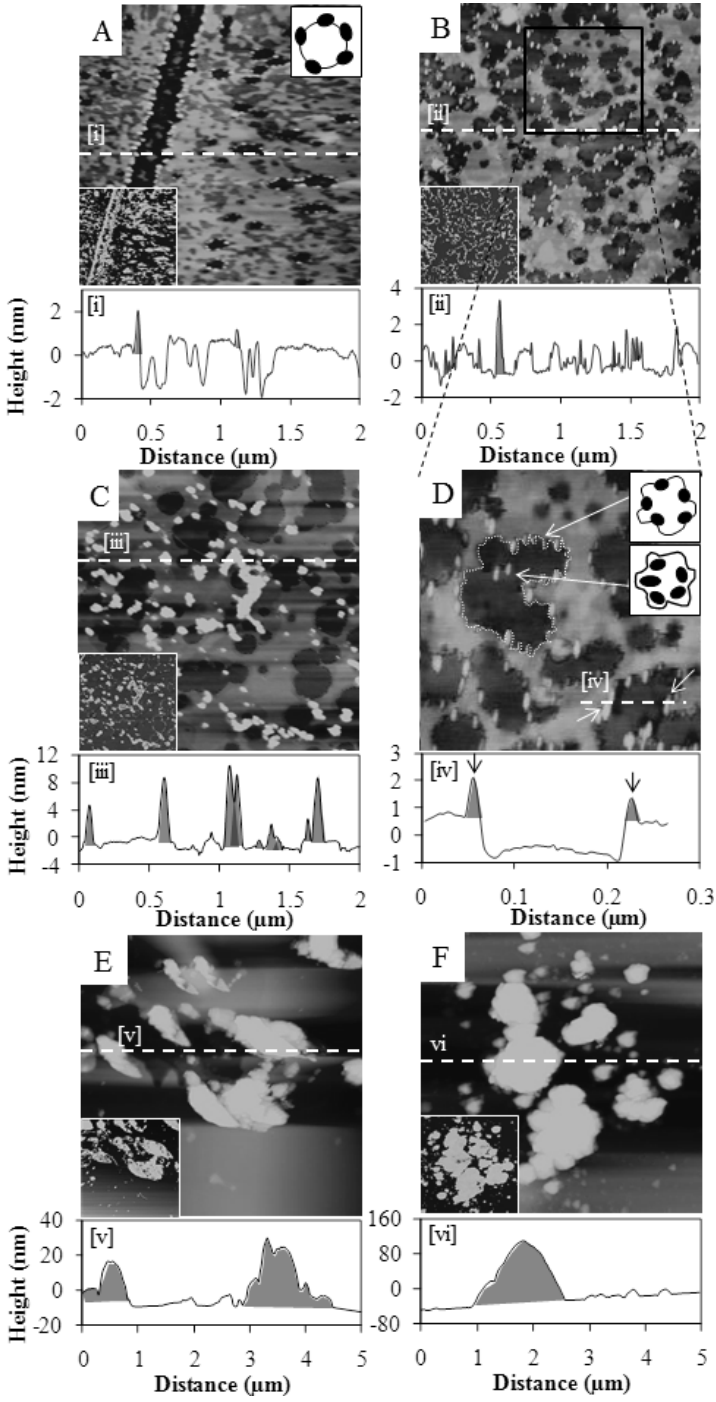

Figure 20. Amorphous silica nanoparticle formation (2-7 nm in height, identification corroborated by HR-TEM and FTIR) on phlogopite sample under GCS conditions (see text) for 5-159 hours of reaction. [From Shao et al. (2010), *Environ Sci Technol*, Vol. 44, Fig. 3, p. 6002, used by permission of the American Chemical Society.]

factor is relevant in especially relevant in sedimentary reservoir rocks where salt domes are coexistant, and which can have salinities up to 2 M NaCl in the pore-space water (Kharaka et al. 2006). Another important aspect is the presence of organic species that may contaminate interfaces, affect near interface water structure, or bind ions which result in slowed growth, e.g., by chelation (Yang et al. 2011, 2013). Because supercritical CO_2 is well known as a good organic solvent, the injection of supercritical CO_2 can also increase concentrations of organic species in brine (Shao et al. 2011b). Recent work on peptoid effects on calcite growth show that some of these organic species can enhance growth at low concentrations, but retard growth as concentration increases (Chen et al. 2011). Natural organics may have similar effects (Ray et al. 2012), although the more important considerations may be increased hydrophobicity of pore space surfaces by nonpolar hydrocarbons, or the complete blockage of hydrological channels by larger concentrations of organics such as remaining after natural oil recovery (Butkus and Grasso 1998). These considerations require knowledge of both fluid composition and the response of mineral surfaces and confined spaces to dissolved and particulate organic matter.

ACKNOWLEDGMENTS

J.J.D., G.A.W, Y.-S.J. were supported as part of the Center for Nanoscale Control of Geologic CO_2, an Energy Frontier Research Center funded by the U.S. Department of Energy, Office of Science, Office of Basic Energy Sciences under Award Number DE-AC02-05CH11231. A.F.-M. was supported as part of Le Centre national de la recherche scientifique (CNRS) at Institut des Sciences de la Terre, Universite Joseph-Fourier Grenoble I and CNRS.

REFERENCES

Abraham FF (1974) Homogeneous Nucleation Theory, Academic Press, New York

Addadi L, Joester D, Nudelman F, Weiner S (2006) Mollusk shell formation: a source of new biomineralization processes. Chem Eur J 12:980-987

Aizenberg J, Black AJ, Whitesides GM (1999a) Control of crystal nucleation by patterned self-assembled monolayers. Nature 398:495-498

Aizenberg J, Black AJ, Whitesides GM (1999b) Oriented growth of calcite controlled by self-assembled monolayers of functionalized alkanethiols supported on gold and silver. J Am Chem Soc 121:4500-4509

Armstrong R, Ajo-Franklin J (2011) Investigating biomineralization using synchrotron based X-ray computed microtomography. Geophys Res Lett 38:L08406

Astilleros JM, Pina CM, Fernandez-Diaz A, Putnis A (2002) Molecular-scale surface processes during the growth of calcite in the presence of manganese. Geochim Cosmochim Acta 66:3177-3189

Babcock KL, Prater CB (2004) Phase Imaging: Beyond Topography. Veeco Instruments Inc. Santa Barbara CA USA

Baumgartner J, Dey A, Bomans, PHH, Le Coadou C, Fratzl P, Sommerdijk NAJM, Faivre D (2013) Nucleation and growth of magnetite from solution. Nat Mater 12:310-314

Binder K, Fratzl P (2001) Spinodal decomposition. *In:* Phase Transformation in Materials. Kostorz G (ed) Wiley, New York, p 414-416

Brecevic L, Nielsen AE (1989) Solubility of amorphous calcium carbonate. J Cryst Growth 98:504-510

Butkus M, Grasso D (1998) Impact of aqueous electrolytes on interfacial energy. Colloid Interface Sci 181:172-181

Chaikin PM, Lubensky TC (1995) Principles of Condensed Matter Physics. Cambridge University Press, Cambridge

Chen CL, Qi J, Zuckermann RN, De Yoreo JJ (2011) Engineered biomimetic polymers as tuneable agents for controlling $CaCO_3$ mineralization. J Am Chem Soc 133:5214-5217

Chernov AA (1984) Modern Crystallography III: Crystal Growth. Springer, Berlin

Chiquet P, Broseta D, Thibeau S (2007) Wettability alteration of caprock minerals by carbon dioxide. Geofluids 7:112-122

De Yoreo JJ, Vekilov PG (2003) Principles of Crystal Nucleation and Growth. Rev Mineral Geochem 54:57-93

Duffy DM, Harding JH (2004) Simulations of organic monolayers as templates for the nucleation of calcite crystals. Langmuir 20:7630-7636

Espinoza DN, Santamarina JC (2010) Water - CO_2 - mineral systems: Interfacial tension, contact angle, and diffusion — Implications to CO_2 geological storage. Water Resour Res 46:1-10

Fernandez-Martinez A, Hu Y, Lee B, Jun YS, Waychunas GA (2013) In situ determination of interfacial energies between heterogeneously nucleated $CaCO_3$ and quartz substrates: thermodynamics of CO_2 mineral trapping. Environ Sci Technol 47:102-109

Gebauer D, Volkel A, Colfen H (2008) Stable prenucleation calcium carbonate clusters. Science 322:1819-1822

Gebauer D, Coelfen H (2011) Prenucleation clusters and non-classical nucleation. NanoToday 6:564-584

Gibbs GV, Crawford TD, Wallace AF, Cox DF, Parrish RM, Hohenstein EG, Sherril CD (2011) The role of long-range intermolecular forces in the formation of inorganic nanoparticle clusters. J Phys Chem A 115:12933-12940

Gibbs JW (1876) On the equilibrium of heterogeneous substances. Trans Connect Acad Sci 3:108-248

Gibbs JW (1878) On the equilibrium of heterogeneous substances. Trans Connect Acad Sci 16:343-524

Giuffre AJ, Hamm LM, Han N, De Yoreo JJ, Dove PM (2013) Polysaccharide chemistry regulates kinetics of calcite nucleation through competition of interfacial energies. Proc Natl Acad Sci USA 110(23):9261-9266

Guinier A(1994) X-Ray Diffraction in Crystals, Imperfect Crystals, and Amorphous Bodies. Dover Publications Inc

Gutzow IA (1997) In Memoriam Prof. Dr. Ivan N. Stranski (1897-1979). Cryst Res Technol 32:753-758

Habraken WJEM, Tao J, Brylka LJ, Friedrich H, Bertinetti L, Schenk AS, Verch A, Dmitrovic V, Bomans PHH, Frederik PM, Laven J, van der Schoot P, Aichmayer B, de With G, De Yoreo JJ, Sommerdijk NAJM (2013) Ion association complexes unite classical and non-classical theories for the biomimetic nucleation of calcium phosphate. Nat Commun 4:1507, doi: 10.1038/ncomms2490

Hamm LM, Giuffre AJ, Dove PM, De Yoreo JJ (2013) Free energy of binding is key to understanding templated calcite nucleation. In review

Han YJ, Aizenberg, J (2003) Face-selective nucleation of calcite on self-assembled monolayers of alkanethiols: effect of the parity of the alkyl chain. Angew Chem Int Ed 42:3668-3670

Harding J (2011) Sampling the structure of calcium carbonate nanoparticles with metadynamics. J Chem Phys 134:044703

Hedges LO, Whitelam S (2012) Patterning a surface so as to speed nucleation from solution. Soft Matter 8:8624-8635

Hohenberg PC, Halperin BI (1977) Theory of dynamic critical phenomena. Rev Mod Phys 49:435-479

Hu Q, Nielsen MH, Freeman CL, Hamm LM, Tao J, Lee JRI, Han TYJ, Becker U, Harding JH, Dove PM, De Yoreo JJ (2012a) Classical vs. non-classical pathways of crystallization. Faraday Disc 159:509-523

Hu YD, Lee B, Bell C, Jun YS (2012b) Environmentally abundant anions influence the nucleation, growth, ostwald ripening, and aggregation of hydrous Fe(III) oxides. Langmuir 28:7737-7746

Johnson DA (1982) Some Thermodynamic Aspects of Inorganic Chemistry. Cambridge University Press, Cambridge

Jun YS, Kendall TA, Martin ST, Friend CM, Vlassak JJ (2005) Heteroepitaxial nucleation and oriented growth of manganese oxide islands on carbonate minerals under aqueous conditions. Environ Sci Technol 39:1239-1249

Jun YS, Lee B, Waychunas GA (2010) In situ observations of nanoparticle early development kinetics at mineral-water interfaces. Environ Sci Technol 44:8182-8189

Kharaka YK, Cole DR, Thordsen JJ, Kakouros E, Nance HS (2006) Gas-water-rock interactions in sedimentary basins: CO_2 sequestration in the Frio Formation, Texas, USA. J Geochem Explor 89:183-186

Kashchiev D (1999) Nucleation: Basic Theory with Applications. Butterworths, Heinemann, Oxford

Kashchiev D (2003) Thermodynamically consistent description of the work to form a nucleus of any size. J Chem Phys 118:1837-1851

Landrot G, Ajo-Franklin JB, Yang L, Cabrini S, Steefel CI (2012) Measurement of accessible reactive surface area in a sandstone, with application to CO_2 mineralization. Chem Geol 318-319:113-125

Lasaga AC, Blum AE (1986) Surface chemistry, etch pits and mineral-water reactions. Geochim Cosmochim Acta 50:2363-2379

Lazzari R (2002) IsGISAXS: a program for grazing-incidence small-angle scattering analysis of supported islands. J Appl Crystallogr 35:406-421

Lee JRI, Han TYJ, Willey TM, Wang D, Meulenberg RW, Dove PM, Nilsson J, Terminello LJ, van Buuren T, De Yoreo JJ (2007) Structural development of mercaptophenol self-assembled monolayers and the overlying mineral phase during templated $CaCO_3$ crystallization from a transient amorphous film. J Am Chem Soc 129:10370-10381

Lea AS, Amonette JE, Baer DR, Linag Y, Colton NG (2001) Microscopic effects of carbonate, manganese, and strontium ions on calcite dissolution. Geochim Cosmochim Acta 65:369-379

Lea AS, Hurt TT, El-Azab A, Amonette JE, Baer DR (2003) Heteroepitaxial growth of a manganese carbonate secondary nano-phase on the (10-14) surface of calcite in solution. Surf Sci 524:63-77

Leroy F, Eymert J, Buttard D, Renaud G, Lazzari R (2005) Growth of Ge on Si (001) studied in situ by grazing incidence small angle scattering. J Cryst Growth 275:e2195-e2200

Levine JR, Cohen JB, Chung YW, Georgopoulos P (1989) Grazing-Incidence small angle scattering: A new tool for studying thin film growth. J Appl Crystallogr 22:528-532

Mizele J, Dandurand J, Schott J (1985) Determination of the surface energy of amorphous silica from solubility measurements in micropores. Surf Sci 162:830-837

Mullin JW (1992) Crystallization, 3rd Edition. Butterworths, Oxford

Mutaftschiev B (1993) Nucleation theory. *In:* Handbook on Crystal Growth, Volume 1. Hurle DTJ (ed) Elsevier, Amsterdam, p 189-247

Naudon A (1995) Modern Aspects of Small Angle Scattering. Kluwer Academic Publishers

Navrotsky A (2004) Energetic clues to pathways to biomineralization: Precursors, clusters, and nanoparticles. Proc Natl Acad Sci USA 101:12096-12101

Nielsen AE (1964) Kinetics of Precipitation. Pergamon, Oxford

Nielsen MH, Lee JRI, Hu Q, Han TYJ, De Yoreo JJ (2012) Structural evolution, formation pathways and energetic controls during template-directed nucleation of $CaCO_3$. Faraday Disc 159:105-121

Page AJ, Sear RP (2006) Heterogeneous Nucleation in and out of Pores. Phys Rev Lett 97:65701

Pouget EM, Bomans PHH, Goos JACM, Frederik PM, de Wilth G, Sommerdijk NAJM (2009) The initial stages of template-controlled $CaCO_3$ formation revealed by cryo-TEM. Science 323:1455-1458

Rauscher M, Salditt T, Spohn H (1995) Small angle x-ray scattering under grazing incidence: the cross section in the distorted-ave Born approximation. Phys Rev B 52:16855-16863

Ray, JR, Lee B, Baltrusaitis J, Jun YS (2012) Formation of Iron(III) hydroxides on polyaspartate- and alginate-coated SiO_2: effects of substrate hydrophilicity and functional groups at the surface. Environ Sci Technol 46:13167-13175

Renaud G, Lazzari R, Revenant C, Barbier A, Noblet M, Ulrich O, Leroy F, Jupille J, Borensztein Y, Henry CR, Deville JP, Scheurer F, Mane-Mane J, Fruchard O (2003) Real-time monitoring of growing nanoparticles. Science 300:1416-1419

Shao H, Ray JR, Jun YS (2010) Dissolution and precipitation of clay minerals under geological CO_2 sequestration conditions:CO_2-brine-phlogopite interactions. Environ Sci Technol 44:5999-6005

Shao H, Ray JR, Jun YS (2011a) Effects of salinity and the extent of water on supercritical CO_2-induced phlogopite dissolution and secondary mineral formation. Environ Sci Techno. 45:1737-1743

Shao H, Ray JR, Jun YS (2011b). Effects of organic ligands on supercritical CO_2-induced phlogopite dissolution and secondary mineral formation. Chem Geol 290:121-132

Sohnel O (1982) Electrolyte crystal-aqueous solution interfacial tensions from crystallization data. J Cryst Growth 57:101-108

Sohnel O, Mullin JW (1978) A method for the determination of precipitation induction periods. J Cryst Growth 44:377-382

Travaille AM, Donners JJJM, Gerritsen JW, Sommerdijk NAJM, Nolte RJM, van Kempen H (2002) Aligned growth of calcite crystals on a self-assembled monolayer. Adv Mater 14:492-495

Travaille AM, Kaptijn L, Verwer P, Hulsken B, Elemans, JAAW, Nolte, RJM, van Kempen, H (2003) Highly oriented self-assembled monolayers as templates for epitaxial calcite growth. J Am Chem Soc 125:11573-11577

Van Driessche, AES, Benning LG, Rodriguez-Blanco JD, Ossorio M, Bots P, Garcia-Ruiz JM (2012) The role and implications of bassanite as a stable precursor phase to gypsum precipitation. Science 336:69-72

Weiner S, Sagi I, Addadi L (2005) Choosing the crystallization path less travelled. Science 309:1027-1028

Yang Y, Ronzio C, Jun YS (2011) The effects of initial acetate concentration on $scCO_2$–brine–anorthite interactions under geologic CO_2 sequestration conditions. Energy Environ Sci 4:4596-4606

Yang Y, Min Y, Jun YS (2013) Structure-dependent interactions between alkali feldspars and organic compounds: implications for reactions in geologic carbon sequestration. Environ Sci Technol 47(1):150-158

Zhang H, Chen B, Banfield JF (2009) The size dependence of the surface free energy of titania nanocrystals. Phys Chem Chem Phys 11:2553-2558

Reviews in Mineralogy & Geochemistry
Vol. 77 pp. 259-303, 2013
Copyright © Mineralogical Society of America

Pore Scale Processes Associated with Subsurface CO_2 Injection and Sequestration

Carl I. Steefel[1], Sergi Molins[1], David Trebotich[2]

[1] *Earth Sciences Division*
[2]*Computational Research Division*
Lawrence Berkeley National Laboratory
Berkeley, California 94720, U.S.A.

cisteefel@lbl.gov *smolins@lbl.gov* *DPTrebotich@lbl.gov*

INTRODUCTION

The injection of CO_2 into the Earth's subsurface drives the fluid-rock system into "far-from-equilibrium" conditions, which means that the fluxes that return the system to equilibrium are nonlinearly related to the generalized driving forces (e.g., chemical affinities and gradients in the fluid pressures and chemical potentials). The nonlinear response results in emergent structures and self-organization (Prigogine 1968, 1980; Ortoleva 1994; Lasaga 1998; Jamtveit and Meakin 1999), of which the reactive infiltration instability is a well-known example in the Earth Sciences that is directly applicable to CO_2 injection and caprock integrity (Ortoleva et al. 1987; Hoefner and Fogler 1988; Steefel and Lasaga 1994; Steefel and Maher 2009). Flow, solute transport, colloid transport, mineral dissolution and mineral precipitation combine within the mechanical framework of the porous medium to generate precipitate structures in individual pores correlated over many thousands to millions of pores, and immiscible fluid structures with fractal geometry over scales from millimeters to kilometers (Feder 1988). The focus in this chapter is on processes, emergent and otherwise, taking place at the pore scale, defined here as the scale where individual grains and fluid interfaces can be resolved.

The chief focus of research in recent years has been to improve the understanding of the nonlinear dynamics specifically associated with biogeochemical and microbially induced processes coupled to physical processes such as flow and diffusion at the pore scale. When coupled, whether in field-scale applications, bench-scale experiments, or in models, emergent behavior may result, including changes in permeability, diffusivity, and reactivity. The pore scale is an important scale to analyze these emergent behaviors given that it provides the architecture within which the smaller scale (nano and molecular scale) processes occur. For the individual processes to interact, transport is typically necessary and the resulting behavior is not predictable from consideration of the individual processes alone. The continuum scale, in which the detailed properties of the pore structure are averaged in some fashion, is an abstraction that may not preserve all of the dynamics at the micro-scale.

The final equilibrium states and the time scales to reach equilibrium, which are critical to meaningful predictions of system behavior, cannot be assessed in the absence of proper governing equations applicable to large scales that are rooted in correct descriptions of molecular-to-pore scale processes. The interest is on how bulk properties such as permeability, diffusivity and reactivity can be related back to pore scale and smaller phenomena, as well as how they change as a result of the stresses associated with CO_2 injection.

1529-6466/13/0077-0008$05.00 http://dx.doi.org/10.2138/rmg.2013.77.8

Pore scale structure and CO_2 sequestration

Natural subsurface materials have their own pore scale architecture that regulates how physical and chemical processes are coupled. Pore spaces are filled with brine (water) and/or CO_2 and are bordered by a range of solid phases that may be reactive (Fig. 1). While cations for carbonate formation are generally present in the brine, their concentrations are typically not high enough in the brine to precipitate all of the CO_2 that is locally present. Another important effect has to do with the fact that gaseous or supercritical CO_2 dissolves in the aqueous phase to form carbonic acid according to the reaction

$$CO_2 + H_2O \rightleftarrows H_2CO_3 \tag{1}$$

thus lowering the pH of the aqueous phase as the carbonic acid dissociates to the bicarbonate ion

$$H_2CO_3 \rightarrow HCO_3^- + H^+ \tag{2}$$

Since the solubility of all carbonate phases is higher at low pH than at high or circumneutral pH, this effect tends to reduce the amount of carbonate that can be formed. Formation of a significant mass of carbonate, therefore, requires that the pH be raised, generally as a result of the dissolution of cation and alkalinity-bearing phases (e.g., silicates). Within the pore structure of the subsurface materials, therefore, transport effects become important insofar as cations and alkalinity must be moved from dissolving phases to nucleation and growth sites, whether in pore throats or pore bodies (Fig. 1). At high CO_2 (and low water) saturation, transport within the aqueous phase may become slower due to the increased tortuosity, even though water serves as the wetting phase providing a reactive medium adjacent to the mineral surfaces. An additional effect is that a small amount of water (up to 5%) may dissolve in the supercritical CO_2 phase, thus potentially leading to drying out in those portions of the system that experience high CO_2 fluxes (McGrail et al. 2009). This has been observed to lead to halite precipitation, which can have the effect of reducing permeability in the near well-bore regions where the CO_2 flux is the highest (e.g., Muller et al. 2009). Additional discussion of CO_2 injection and sequestration impacts can be found in Jun et al. (2013).

A generic reaction in which silicates dissolve under acidic conditions and precipitate carbonates can be written using Ca-bearing plagioclase (An_{50}, or labradorite), calcite, and kaolinite as model phases (Fig. 1):

$$\underset{Ca\text{-}Na\ plagioclase}{(Ca_{0.5}Na_{0.5})Al_{1.5}Si_{2.5}O_8} + H_2CO_3 + 5H^+ \rightarrow \tag{3}$$

$$0.5Ca^{2+} + 0.5Na^+ + 2.5SiO_{2,aq} + 1.5Al^{3+} + HCO_3^- + 3H_2O$$

$$0.5Ca^{2+} + 0.5HCO_3^- \rightarrow \underset{calcite}{0.5CaCO_3} + 0.5H^+ \tag{4}$$

$$1.5SiO_{2,aq} + 1.5Al^{3+} + 3.75H_2O \rightarrow \underset{kaolinite}{0.75Al_2Si_2O_5(OH)_4} + 4.5H^+ \tag{5}$$

where the reaction has been balanced on the Ca^{2+} and Al^{3+} ions released from the plagioclase dissolution. Note that while it is customary in geochemistry textbooks to write reactions as perfectly balanced between dissolving and precipitating phases, in nature (or in numerical reactive transport models) this is rarely the case because of the effects of transport and kinetics (Brimhall 1979; Steefel and Lichtner 1994). Note also that the plagioclase dissolution, in addition to releasing the calcium ion needed to precipitate the calcite, provides alkalinity and thus consumes protons. It should be noted in this regard that not all Ca-bearing minerals contribute alkalinity upon dissolution (the sulfate-bearing minerals gypsum and anhydrite are good examples), so their tendency to drive carbonate precipitation is not as great. In general, the dissolution of silicate minerals containing metals that can readily form carbonates (Ca^{2+}, Mg^{2+}, and Fe^{2+}) also provide alkalinity to neutralize the carbonic acid associated with CO_2.

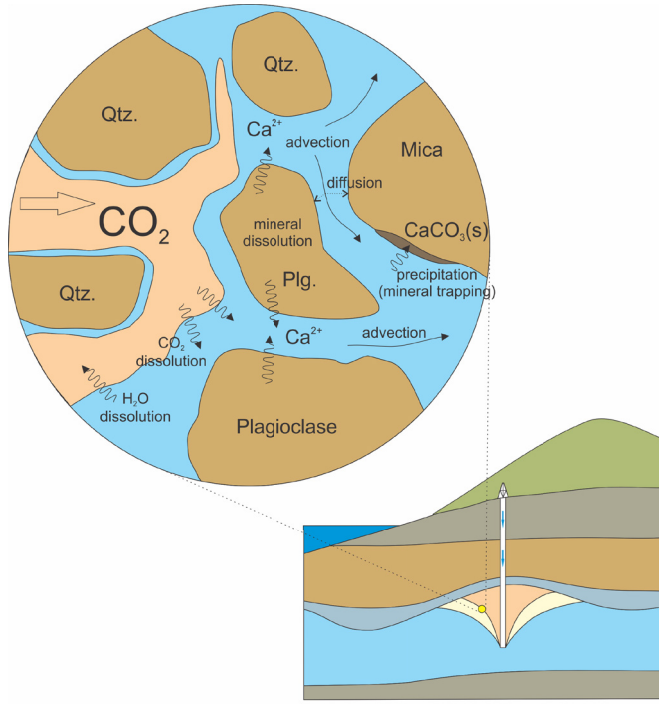

Figure 1. Schematic representation of chemical and physical processes associated with CO_2 (tan color) injection and sequestration at the pore scale (brine is in blue). Qtz = quartz, Plg = plagioclase.

It should also be readily apparent from what we know of the pore architecture, as represented for example as in Figure 1, that the various phases dissolving and precipitating, as well as the CO_2 itself, need not be strictly co-located. While carbonate may form directly on the dissolving phase, in other cases there can be a significant separation in space between the neoformed carbonate and the metal and alkalinity source, particularly under acidic conditions (Daval et al. 2009). In part this may be the result of the tendency for nucleation of carbonate phases preferentially on some mineral surfaces versus others because of the lower interfacial energy of these phases (De Yoreo et al. 2013, this volume). This implies that the physical processes of flow and transport at the pore scale are likely to be important in mediating reaction rates, which implies in turn that pore scale CO_2 sequestration is a mesocale rather than a strictly molecular or microscale problem. An example of the pore structure in a sandstone imaged with X-ray microtomographic techniques and the associated flow calculated using the Navier-Stokes equation is shown in Figure 2. Distributions of CO_2 may be even more heterogeneous (Sato et al. 2011), separated in some cases from the dissolving phases by centimeters and even meters (i.e., well beyond the pore scale that we address here).

Pore scale methods

An improved understanding of the pore scale dynamics associated with CO_2 injection and sequestration require an advanced set of experimental, imaging and modeling tools. The rapidly developing field of 3D imaging techniques (X-ray, neutron, and magnetic resonance) allow for the characterization and observation of dynamic geological and hydrological processes on unprecedented temporal and spatial resolutions (Carlson 2006). Among these three techniques, X-ray computed tomography has been most widely used for 3D imaging of geologic materials

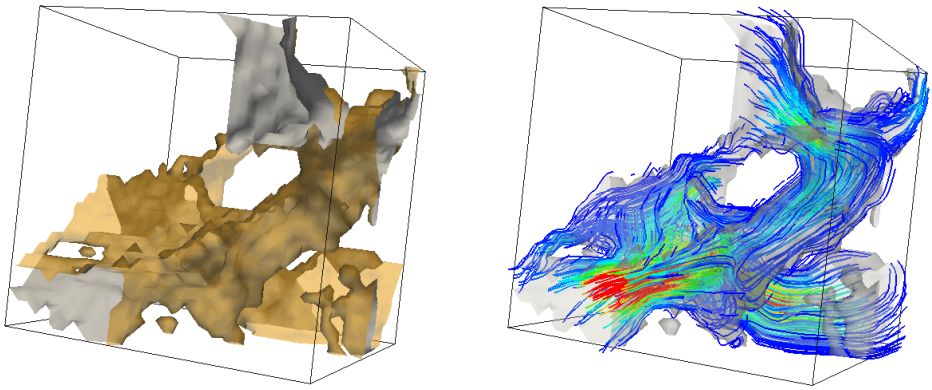

Figure 2. Image of a set of connected pores from X-ray microtomographic imaging (300 μm each side), with calculation of the flow streamlines and their magnitude (from Molins et al. 2011).

(Mees et al. 2003; Wildenschild and Sheppard 2013). Another important technique is Small Angle Neutron Scattering (SANS), which although not a 3D microtomographic approach, is useful in detecting changes in pore size at scales much smaller than what can be imaged with the tomographic methods. Complementary 2D imaging of CO_2 invasion dynamics at the pore scale can be carried out using two-dimensional optically transparent pore networks called "micromodels."

To complement the imaging of CO_2 injection, a second equally important requirement is the use of pore-scale reactive transport modeling tools. Pore scale models differ from continuum models in that each of the phases involved and their interfaces must be resolved explicitly. High resolution and extreme computing capabilities are necessary. Methods employed include particle methods, lattice Boltzmann or Direct Numerical Simulation. Pore networks are also been used, especially in multiphase applications.

Organization of chapter

In what follows, the physics of single phase flow (CO_2 dissolved in brine) and multiphase flow (CO_2 and brine) are briefly discussed. Geochemical processes operating at the pore scale are then reviewed, particularly those that are relevant to the emergent processes that are the focus of the remainder of the chapter. Pore scale experimental and characterization approaches are summarized, followed by a discussion of modeling approaches and results specific to this scale and architecture. Finally, the set of emergent behaviors associated with pore scale physical and chemical processes are reviewed. Ultimately, the focus is on insights from the pore scale that can be used to develop phenomenological laws that will provide an improved predictive capability for CO_2 injection and sequestration at the porous-continuum scale.

PHYSICS OF SINGLE PHASE FLOW AT THE PORE SCALE

Owing to its relatively high solubility in water, dissolution of CO_2 into the pore solution can contribute significantly to its trapping in the subsurface both in the short and long term (DePaolo and Cole 2013, this volume). As a dissolved component in the aqueous phase, the fate of CO_2 in the subsurface will depend on the flow of water in the pore space. In particular, transport in the aqueous phase mediates dissolution and precipitation processes driven by elevated CO_2 concentrations and resulting low pH conditions by enabling chemical transformations in solution and at mineral surfaces.

Single-phase aqueous flow in the pore space is subject to inertial, viscous and other body forces such as gravity ($\mathbf{f}_b = \boldsymbol{g}$). Inertial forces have their origin in the convective acceleration of the fluid as it flows through the tortuous pore space. Viscous forces originate in the friction between water molecules and are responsible for the dissipation of energy. Given the small compressibility of water, in most subsurface conditions, the incompressible Navier-Stokes equations can be used to accurately describe aqueous flow via the conservation of momentum and mass, respectively

$$\rho\left(\frac{\partial \mathbf{u}}{\partial t} + (\mathbf{u}\cdot\nabla)\mathbf{u}\right) = -\nabla P + \mu\nabla^2\mathbf{u} + \mathbf{f}_b \tag{6}$$

$$\nabla\cdot\mathbf{u} = 0 \tag{7}$$

where $\mathbf{u}$ is the fluid velocity, ∇P is the pressure gradient, ρ is the fluid density, μ is the dynamic viscosity. The left hand side of Equation (6) represents the inertial terms, while the right hand represents the divergence of the stress and the body forces.

The ratio between inertial and viscous forces is expressed by the Reynolds number, Re:

$$\mathrm{Re} = \frac{|u|l}{\nu} \tag{8}$$

where $|u|$ is the fluid velocity magnitude, ν is the kinematic viscosity, and l is a characteristic length of the porous medium (e.g., average grain size). At low Reynolds numbers (i.e., Re << 1), inertial forces can be neglected and Stokes flow is valid. Under steady-state conditions, the Navier-Stokes equation simplifies to the Stokes equation

$$\nabla P = \mu\nabla^2\mathbf{u} + \mathbf{f}_b \tag{9}$$

which is solved again together with Equation (7).

Even when inertial forces are not negligible, consideration of viscous forces is necessary to account for energy dissipation. In no-slip flow, the velocity of the fluid is zero at the mineral grain surface and a thin region forms around mineral grains where viscosity dominates. This boundary layer generates most of drag exerted on the mineral grain (Fig. 3).

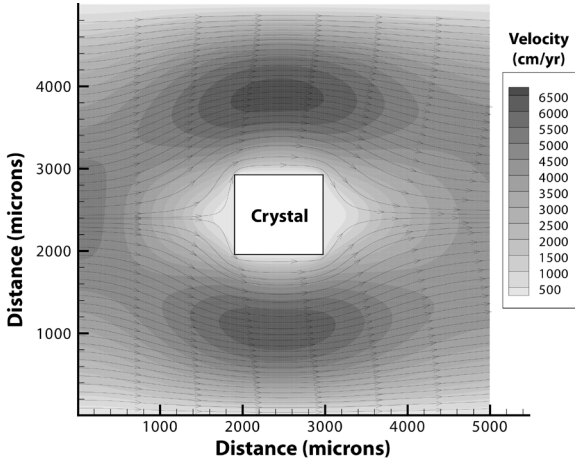

Figure 3. 2D pore scale simulation of Navier-Stokes flow past a crystal using the Chombo software.

PHYSICS OF MULTIPHASE FLOW AT THE PORE SCALE

The injection of CO_2 in the subsurface clearly involves multiphase flow. A recent review of modeling of pore scale multiphase fluid flow in fractured and porous media devoted to general applications, including the vadose zone and hydrocarbon reservoirs, is given by Meakin and Tartakovsky (2009) along with a thorough general description of the fundamentals of multiphase flow at the pore scale. Here, the basic concepts of multiphase flow applicable at the pore scale are reviewed, focusing on the CO_2-brine system.

The injection of CO_2 in the subsurface involves the displacement of a wetting phase (brine) that initially occupies the pore space by a non-wetting phase (supercritical CO_2), a drying process. The resulting dynamic system is characterized by CO_2-brine fluid-fluid interfaces and the contact angles of these interfaces at the mineral surfaces that evolve with time. The concept of capillary surface is commonly employed to describe the interface between two fluids such as CO_2 and brine. Implicit in the concept of surface is the assumption of a sharp or infinitely thin transition between fluids. Due to the surface tension, a pressure discontinuity exists at this fluid-fluid interface. This pressure discontinuity or capillary pressure P_c is related to the interfacial tension γ_{wc} and the surface mean curvature $(1/r_1+1/r_2)$ through the Young-Laplace equation:

$$P_c = P_{CO_2} - P_{brine} = \gamma_{wc}\left(\frac{1}{r_1}+\frac{1}{r_2}\right) \tag{10}$$

The curvature of this interface controls the capillary pressure, which dominates over viscous forces under typical conditions. At the fluid-fluid-solid interface, the contact or wetting angle between phases at equilibrium under static conditions on an ideal surface is given by

$$\cos\theta = \frac{\gamma_{sc}-\gamma_{sw}}{\gamma_{wc}} \tag{11}$$

where γ_{sc} is the interfacial tension between the solid and the CO_2, and γ_{sw} is the interfacial tension between solid and brine. In the dynamic conditions driven by CO_2 injection, Equation (11) is not applicable and the contact angle depends on displacement of the interface (e.g., whether CO_2 is displacing brine or the opposite), the velocity of this moving interface at the solid surface, and the direction of motion of the fluid-fluid-solid contact line. Capillary pressure variations may also arise from the mineral contact angle heterogeneity inherent in geological formations (Ellis and Bazylak 2012, 2013). Mineral surfaces are not perfectly smooth or chemically homogeneous, which may explain differences between the advancing (θ_a) and receding (θ_r) contact angles that are observed. This difference is commonly referred to as the contact angle hysteresis. Hysteretic behavior also exists because of the breakup in symmetry once the non-wetting fluid goes from small to large pore versus the opposite (ink-bottle effect). Empirical models for contact angle hysteresis exist (de Gennes 1985), but recent experimental studies with $scCO_2$ on silica surfaces (Fig. 4) suggest also a time-dependent evolution of the wettability (Jung and Wan 2012; Kim et al. 2012).

The invasion of a non-wetting phase (e.g., c = CO_2) in a saturated porous medium can be characterized by the capillary number ($Ca = u_c\mu_c/\gamma_{wc}$), the viscosity ratio ($M = \mu_c/\mu_w$) (and the Bond number ($Bo = \Delta\rho g l^2/\gamma_{wc}$), where $\Delta\rho$ is the density difference (Lenormand et al. 1988; Ewing and Berkowitz 1998; Blunt 2001). When viscosity forces dominate (e.g., near an injection point) and the viscosity ratio is high, stable front propagation is expected. However, when that is not the case, displacement leads to unsteady front propagation. In this case, capillary, viscous or gravity fingering may be observed depending on whether capillary forces (small Ca), viscosity of the brine (small M) or gravitational forces dominate, respectively (Lenormand et al. 1988; Ewing and Berkowitz 1998; Blunt 2001). In CO_2 sequestration scenarios, the displacement process is considered unstable due to the unfavorable viscosity ratio between the invading

scCO$_2$ and the resident brine (log M < 0) (e.g., Zhang et al. 2011; Wang et al. 2013). After CO$_2$ injection has stopped, buoyant rise of the CO$_2$ continues (Fig. 5), capillary forces become dominant and non-wetting CO$_2$ bubbles and stringers that are not physically connected are left behind, an effect referred to as capillary trapping (Fig. 5). The ratio of buoyancy to viscous forces can also be expressed as a function of Ca and Bo.

Multiphase interfacial processes and contact angles relevant for CO$_2$ sequestration are reviewed in detail in three other chapters in this volume and will not be discussed in depth here. Hamm et al. (2013, this volume) reviews the current knowledge of interfacial tension between brine and CO$_2$, while Tokunaga and Wan (2013, this volume) reviews the current knowledge of mineral surface wettability under relevant sequestration conditions.

Although a sharp interface is often assumed, real CO$_2$-brine interfaces may not necessarily be accurately described as infinitely thin at the pore scale. Diffuse-interface theories replace the sharp interface with a continuous variation of an order parameter (e.g., density). Surface

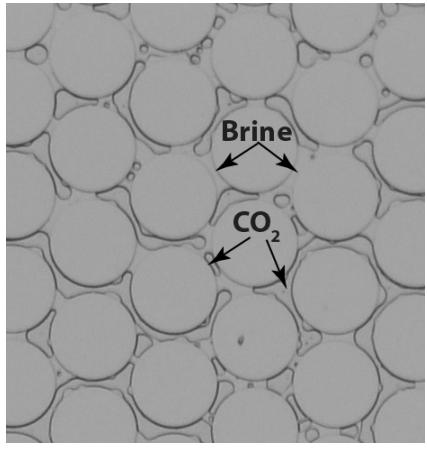

Figure 4. Photograph of a micromodel experiment at high supercritical CO$_2$ saturation showing isolated water (brine) droplets. The microscopic image was taken 2 hours after an invasion experiment at 8.5 MPa and 45 °C and a 1 M NaCl brine (Kim et al. 2012).

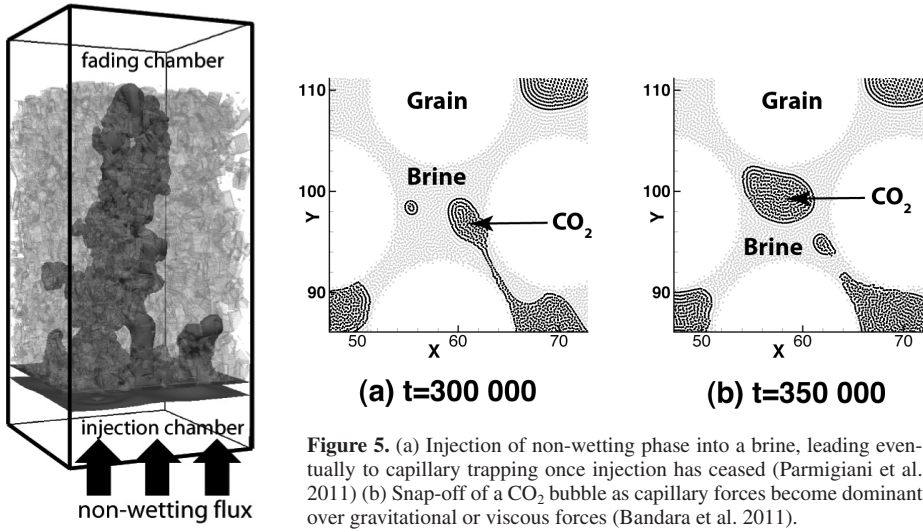

Figure 5. (a) Injection of non-wetting phase into a brine, leading eventually to capillary trapping once injection has ceased (Parmigiani et al. 2011) (b) Snap-off of a CO$_2$ bubble as capillary forces become dominant over gravitational or viscous forces (Bandara et al. 2011).

tension effects then need to be considered through the stress tensor in the Navier-Stokes equations. The Cahn-Hilliard diffuse interface model describes the free energy density (free energy per unit volume) of a binary two-component fluid or a single component fluid by a free energy functional (Cahn and Hilliard 1958). Further details of the Cahn-Hilliard model and its application in multiphase pore scale models may be found in de Gennes (1985), Meakin and Tartakovsky (2009), Xu et al. (2009), Bogdanov et al. (2011), and Parmigiani et al. (2011).

PHYSICS OF MULTICOMPONENT SOLUTE TRANSPORT AT THE PORE SCALE

Steefel and Maher (2009) provide a review of transport processes in porous media from the perspective of their role as driving force for many of the reactions in the water-rock interaction processes. In particular, transport processes are responsible for continuously introducing fluid out of equilibrium with respect to the reactive solid phase. Injection of CO_2 in the subsurface is an extreme case of this scenario. The review by Steefel and Maher (2009) emphasizes concepts applicable when the porous medium can be treated as a continuum in which a representative elementary volume (REV) is significantly larger than the average grain size. When considering the pore scale, however, phenomenological laws such as Darcy's law, the concept of tortuosity applied to diffusion or the Fickian treatment of mechanical dispersion are not necessary. These processes are captured naturally from a pore scale description of fluid flow and transport of chemical species because the detailed flow paths are explicitly considered. Understanding how these parameters are upscaled from the pore scale to the continuum scale is an active field of research. In this section, we introduce the fundamentals of transport at the pore scale and discuss how these pore scale transport processes relate to continuum scale parameters.

Advection

Advection involves the translation in space of dissolved or suspended material at the rate of movement of a bulk fluid phase. The advective flux, J_i^{adv}, of a dissolved species in the pore space of a porous medium can be described mathematically as

$$J_i^{adv} = \mathbf{u} \cdot c_i \tag{12}$$

where c_i is the concentration of the i^{th} species. The fluid velocity vector $\mathbf{u}$ is calculated as a solution of the Navier-Stokes equations (Eqns. 6 and 7) or Stokes equation (Eqns. 9 and 7).

Diffusion

In contrast to advection, where mass transport involves the motion of a bulk fluid phase, diffusion results in mixing of the multicomponent mixture of solutes. Although it can also be derived atomistically (Lasaga 1998), Fick's First Law, which is applicable at the pore scale, provides a phenomenological theory for diffusion relating the diffusive flux to the "driving force" given by the concentration gradient:

$$J_i^{diff} = -D_i \nabla c_i \tag{13}$$

where D_i is the diffusion coefficient specific to the chemical component considered as indicated by the subscript i. In the more general case, a diffusive flux is driven by gradients in chemical potential

$$J_i^{diff} = -L_{ij} \nabla \mu_i \tag{14}$$

where μ_i is the chemical potential of the i^{th} species and the L_{ij} are the Onsager coefficients that couple the individual chemical components in the system (Steefel and Maher 2009). The more rigorous treatment of the chemical potential as providing the driving force for molecular diffusion implies that gradients in activity coefficients as well as concentration need to be considered.

Electrochemical migration

In the case of diffusion of charged species in dilute solutions, it is also necessary to consider an electrochemical migration term derived from the Nernst-Planck equation that is most commonly related to diffusion of charged species at different rates (Ben-Yaakov 1972; Lasaga 1979; Felmy and Weare 1991; Van Cappellen and Gaillard 1996; Giambalvo et al. 2002; Boudreau et al. 2004; Maher et al. 2006; Appelo and Wersin 2007; Li et al. 2008; Steefel and Maher 2009; Liu et al. 2011). Molins et al. (2012) showed that neglecting electrochemical migration in the single pore calcite dissolution experiment of Li et al. (2008) can introduce significant errors, especially under low-pH conditions. Ovaysi and Piri (2013) also observe that for weakly acidic conditions, electrostatic forces only affect transport slightly; however, when SO_2 and CO_2 are injected simultaneously, electrostatic forces significantly influence the solution composition in the pore space. More recently, Rolle et al. (2013) explored the effects of multicomponent diffusion on transverse dispersion/diffusion, an effect that could be important at the smaller length scales associated with the pore structure. Molecular diffusion and electrochemical migration are described by

$$J_i^{migr} = -z_i u_i F c_i \nabla \Phi \tag{15}$$

where z_i is the charge of the species, u_i is its mobility, F is Faraday's constant (= 96,487 Coulombs per mole of electrons), and Φ is the electrical potential. The mobility refers to the average velocity of a species in solution acted upon by a unit force, independent of the origin of the force.

Péclet number

The Péclet number, $\mathrm{Pe} = (|u| l / D_i)$ is commonly used to evaluate the relative importance of advective and diffusive transport processes, where l is a characteristic length of the porous medium (at the pore scale, typically the average grain size). Even in the dynamic flow conditions induced by the CO_2 injection, a large portion of the reactivity of target storage formations may be located in low porosity and permeability material, where molecular diffusion is the dominant transport mechanism. So while the high permeability zones are disproportionately important for the consideration of flow, low permeability zones may be extremely important when reactive processes are considered. In addition, at the scale of a pore, even when advective transport dominates in the bulk solution far from the mineral surface, the no-slip condition at the mineral grain surface results in low fluid velocities in a thin boundary layer around the grains. In this region diffusive processes can be of significance, in particular insofar as this limits the mass flux to reactive surfaces. Well mixed conditions cannot be assumed in pores where gradients in concentrations lead to rate limiting conditions (Li et al. 2008). An example of flow and transverse diffusion in a cylindrical pore developed in calcite is shown in Figure 6. Note the development of a characteristic parabolic velocity profile associated with Poiseuille Flow and the diffusion boundary layer adjacent to the no-slip reactive boundaries of the pore.

Damköhler numbers

The Damköhler numbers, $\mathrm{Da_I}$ and $\mathrm{Da_{II}}$, are another set of important dimensionless parameters that are useful in the context of pore scale processes. They provide a comparison of the characteristic times for reaction (t_R) and advective (t_A) and diffusive (t_D) transport

$$\mathrm{Da_I} = \frac{t_A}{t_R} = \frac{kl}{|u|} \tag{16}$$

$$\mathrm{Da_{II}} = \frac{t_D}{t_R} = \frac{kl^2}{D} \tag{17}$$

where k is the reaction rate constant, l is again the length scale of interest (typically the grain

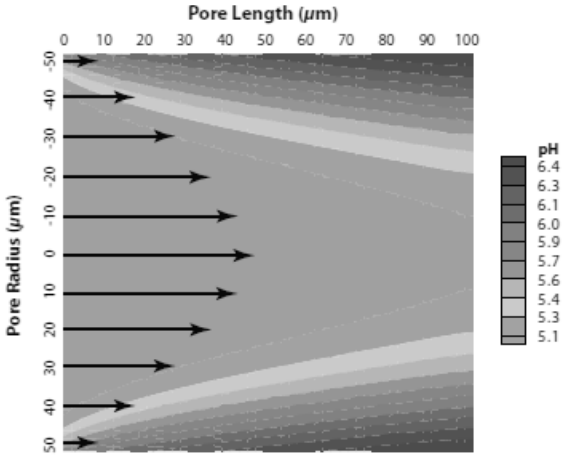

Figure 6. pH distribution in a single cylindrical pore developed in calcite (Li et al. 2008). The solution entering from the left is slightly acidic and therefore undersaturated with respect to calcite, which dissolves. Dissolution only occurs at the calcite-solution interface.

diameter at the pore scale), and D is the diffusion coefficient. Because of the variations in velocity at the pore scale (which are often not resolved at the larger continuum scale), the Da_I number in particular can be expected to vary significantly in space and time.

Upscaling of flow and transport processes to continuum scale parameters

***Darcy flow and permeability*.** In a cylindrical core subject to a single phase flow through experiment, permeability in the flow direction can be calculated using the one-dimensional Darcy's equation (e.g., Noiriel et al. 2004; Luquot and Gouze 2009):

$$k = \frac{\mu L}{S}\frac{Q}{\Delta P} \tag{18}$$

where L is the length of the sample in the flow direction, and S is the cross sectional area of the sample.

For two-phase CO_2-brine flow at steady state, the relative permeability of the non-wetting phase at the inlet ($k_{r,nw}(\Delta P_{c,1})$) is proportional to the slope of the curve formed by the plot of the injection flow rate Q as a function of the steady-state pressure drop $\Delta P_{c,1} = \Delta P - P_{c,e}$ (Pini and Benson 2013):

$$\frac{dQ}{d\Delta P_{c,e}} = k_{r,nw}\left(\Delta P_{c,e}\right)\frac{Sk}{L\mu_{nw}} \tag{19}$$

where $P_{c,e}$ is the entry capillary pressure, i.e., the minimum pressure at which the permeability to the nonwetting phase takes a finite value.

Diffusion and tortuosity. Tortuosity is defined as the ratio of the path length the solute would follow in water alone, L_p, relative to the tortuous path length it would follow in porous media, L_e (Bear 1988) (see Fig. 7):

$$\tau = \left(\frac{L_p}{L_e}\right)^2 \tag{20}$$

In this definition, the value of the tortuosity is always < 1 and the effective diffusion coefficient in porous media is obtained by multiplying the tortuosity by the diffusion coefficient for the solute in pure water. With this formulation, the diffusion coefficient in porous media is given by

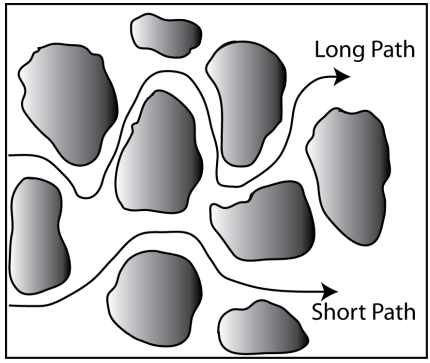

Figure 7. Tortuous diffusion paths in porous material, from Steefel and Maher (2009).

$$D_i^* = \tau D_i \tag{21}$$

At the pore scale, the effective diffusion coefficient D_i^* can be determined directly and thus used to calculate a tortuosity coefficient applicable at continuum scale. In a CO_2 experiment, Gouze and Luquot (2011) used segmented microtomographic images to calculate a tortuosity value with a random walk method based on the principles of Einstein (1956). The method involves computing the mean square displacement of a large ensemble of N_p particles at long time ($t \to \infty$):

$$D_i^* = \lim_{t\to\infty} \frac{\sum_{n=1}^{N_p} \left| \mathbf{x}_n(t) - \mathbf{x}_{n(0)} \right|^2}{N_p \cdot 6t} \tag{22}$$

where $\mathbf{x}_n(t)$ is the position of the n^{th} particle at time t.

Dispersion. As a result of the fact that variations in the velocities exist within the pore space, a non-reactive tracer released up gradient will not advance as a sharp front, but rather will appear as a disperse or gradual breakthrough at the down gradient end of the porous medium. This process, known as mechanical dispersion, was first clearly discussed for the case of laminar flow and transport within a cylindrical tube (Taylor 1953). A cylinder can be used for a first order description of an individual pore in which velocities adjacent to a solid grain are slower than the velocities in the center of the pore (Li et al. 2008). This effect is referred to as Taylor-Aris dispersion (Bear 1988; Steefel and Maher 2009), as in Figure 8.

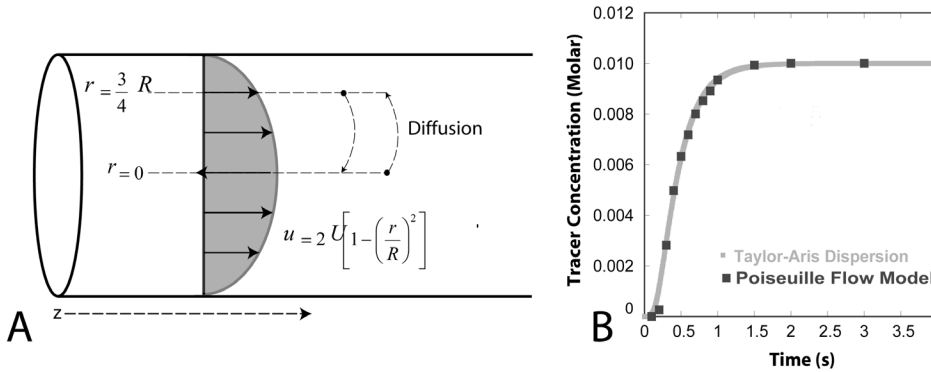

Figure 8. Taylor-Aris dispersion within a cylindrical pore (after Steefel and Maher 2009).

Additional effects in porous media are related to the tortuosity of flow paths and to differences in pore size, since velocities will be higher in those pores with wider apertures. When concentrations are resolved at the pore scale, the asymptotic longitudinal dispersion coefficient can be quantified using the second moment of the concentration of a non-reactive tracer (Le Borgne et al. 2011; Blunt et al. 2013; Varloteaux et al. 2013)

$$D_e = \frac{1}{2}\lim_{t\to\infty}\frac{d}{dt}\left\{\frac{\int c(\mathbf{x},t)x^2 d\mathbf{x}}{\int c(\mathbf{x},t)d\mathbf{x}} - \left[\frac{\int c(\mathbf{x},t)x d\mathbf{x}}{\int c(\mathbf{x},t)d\mathbf{x}}\right]^2\right\} \tag{23}$$

GEOCHEMICAL PROCESSES AT THE PORE SCALE

The various trapping mechanisms for CO_2 in the subsurface have been summarized by Gaus et al. (2008). The mechanisms involving geochemistry include 1) solubility trapping, in which the CO_2 gas or supercritical phase dissolves in the aqueous phase up to its solubility according to Equation (1), and 2) mineral trapping. The long term trapping of CO_2 in the subsurface is generally considered to involve carbonate precipitation. Capillary trapping can be influenced by chemistry through the mineralogical influence on interfacial free energy (see Tokunaga and Wan 2013, this volume), and is also important as an intermediate step between capillary and mineral trapping. In addition to carbonate precipitation reaction, other reactions that include precipitation of salt or silicate phases may play a role in modifying the pore structure of the subsurface and thus may need to be considered as well, even though they do not contribute to CO_2 sequestration.

Mineral dissolution is important as a cation source for carbonate precipitation, as well as serving as a source of alkalinity (and thus raising the pH) to decrease the solubility of the carbonate phases that can precipitate. In addition, dissolution can modify the pore structure, potentially increasing the porosity and permeability of the subsurface medium and/or fractures. In the case of the dissolution of carbonate minerals under the acidic conditions characterizing CO_2 injection and sequestration, wormholing or "reaction fingering" may occur (Steefel and Lasaga 1990; Steefel and Maher 2009; Carroll et al. 2013; Elkhoury et al. 2013). Precipitation of halite, clays, sulfate (gypsum), and carbonate phases can potentially result in clogging (Muller et al. 2009).

In general, the geochemical processes operating at the pore scale are the same as those investigated at the continuum scale, even if additional issues associated with pore scale transport and kinetics emerge (Steefel et al. 2005). Audigane et al. (2007) presented many of the relevant reactions for the Sleipner site in the North Sea, including the replacement of chlorite and calcite by siderite, dolomite, kaolinite, and chalcedony

$$\underset{chlorite}{Fe_{2.5}Mg_{2.5}Al_2Si_3O_{10}(OH)_8} + 2.5\underset{calcite}{CaCO_3} + 5CO_2 \rightarrow \tag{24}$$
$$2.5\underset{siderite}{FeCO_3} + 2.5\underset{dolomite}{MgCa(CO_3)_2} + \underset{kaolinite}{Al_2Si_2O_5(OH)_4} + \underset{chalcedony}{SiO_2} + 2H_2O$$

This represents an idealized stoichiometry that assumes perfect conservation of some of the components, an unlikely scenario when transport and kinetics are involved. Similar reactions may be written for the dissolution of the micas under high CO_2 conditions (mica and biotite), as well as the clay minerals kaolinite and illite. Another reaction much discussed in the literature involves the replacement of albite (Na-plagioclase) by dawsonite (Audigane et al. 2007)

$$\underset{albite}{NaAlSi_3O_8} + CO_2 + H_2O \rightarrow \underset{dawsonite}{NaAlCO_3(OH)_2} + SiO_{2,aq} \tag{25}$$

where the reaction has been modified to produce aqueous silica rather than a specific silica

phase. As pointed out by Hellevang et al. (2011), this is potentially an important point, since many of the geochemical simulations that have predicted the formation of dawsonite did so because of the assumption of the formation of quartz, which is associated with a low silica activity in solution that favors dawsonite precipitation (see also Benezeth et al. 2007 for a discussion of the thermodynamics of dawsonite).

In more mafic rocks, reactions involving the formation of Fe and Mg carbonates become more important. For example, the dissolution of serpentine under high CO_2 conditions to form magnesite can be written as (e.g., Boschi et al. 2009)

$$\underset{serpentine}{Mg_3Si_2O_5(OH)_4} + 3CO_2 \rightarrow 3\underset{magnesite}{MgCO_3} + 2SiO_{2,aq} + 2H_2O \tag{26}$$

Olivine (written here as Fo_{50}, or 50% Mg and 50% Fe) present in basaltic or ultramafic rocks can react similarly with CO_2 (e.g., Daval et al. 2009)

$$\underset{olivine}{MgFeSiO_4} + 2CO_2 \rightarrow \underset{magnesite}{MgCO_3} + \underset{siderite}{FeCO_3} + SiO_{2,aq} \tag{27}$$

as can the mineral pyroxene

$$\underset{pyroxene}{Mg_{0.5}Fe_{0.5}SiO_3} + CO_2 \rightarrow 0.5\underset{magnesite}{MgCO_3} + 0.5\underset{siderite}{FeCO_3} + SiO_{2,aq} \tag{28}$$

Other minerals than silicates may dissolve under high CO_2 conditions, as for example the Fe-oxyhydroxides described from the Green River Formation (Wigley et al. 2012)

$$\underset{hematite}{Fe_2O_3} + 0.25CH_4 + 3.2CO_2 + 0.95H_2O + 0.55H^+ \rightarrow 2Fe^{2+} + 3.45HCO_3^- \tag{29}$$

leading potentially to the formation of siderite

$$2Fe^{2+} + 2HCO_3^- \rightarrow 2\underset{siderite}{FeCO_3} + 2H^+ \tag{30}$$

In carbonate aquifers, the dissolution of carbonate phases calcite and dolomite may have a significant effect on aquifer porosity, permeability and pH, even if they do not contribute to net CO_2 sequestration

$$\underset{calcite}{CaCO_3} + CO_2 \rightarrow Ca^{2+} + 2HCO_3^- \tag{31}$$

$$\underset{dolomite}{CaMg(CO_3)_2} + CO_2 \rightarrow Ca^{2+} + Mg^{2+} + 3HCO_3^- \tag{32}$$

Mineral dissolution and precipitation reaction rates

Bulk mineral reversible dissolution and precipitation reaction rates have been described by transition state theory (TST) (Lasaga 1981; Burch et al. 1993; Hellmann and Tisserand 2006) as the product of a far-from-equilibrium term and an affinity (or Gibbs Free Energy, ΔG) term that goes to zero at equilibrium

$$r_m = k_m \exp\left[-\frac{E_a}{RT}\right] \prod a_i^n \left[1 - \exp\left(m_2\left(\frac{\Delta G}{RT}\right)^{m_3}\right)\right]^{m_1} \tag{33}$$

where k_m is the intrinsic rate constant (mol m^{-2} mineral s^{-1}), E_a is the activation energy (kcal mol^{-1}), Πa_i^n is a product representing the inhibition or catalysis of the reaction by various ions in solution raised to the power n, ΔG is the Gibbs free energy (kcal) with m_1, m_2 and m_3 being three parameters that affect the affinity dependence, R is the ideal gas constant, and T is the temperature. In the case of far from equilibrium dissolution, the affinity or ΔG term can often be neglected, as in the studies of chlorite dissolution under high pCO_2 conditions (Smith et

al. 2013a), although care must be taken to ensure that this can be justified, particularly in the case of the silicate minerals where there may be a dependence of the rates over a very broad range of ΔG values (Burch et al. 1993; Hellmann and Tisserand 2006). For application to CO_2 injection and sequestration problems, the parameters in Equation (33) need to be determined under the relevant conditions, e.g., high salinity and high pCO_2 (Pokrovsky et al. 2009; Smith et al. 2013a,b).

For modeling of carbonate dissolution at the pore scale, Molins et al. (2012) used the rate laws proposed and parameterized by Plummer et al. (1978) and Chou et al. (1989):

$$\begin{aligned} k_1 &: CaCO_3 + H^+ \rightarrow Ca^{2+} + HCO_3^- \\ k_2 &: CaCO_3 + H_2CO_3^* \rightarrow Ca^{2+} + 2HCO_3^- \\ k_3 &: CaCO_3 \rightarrow Ca^{2+} + CO_3^{2-} \end{aligned} \tag{34}$$

The rate of calcite dissolution is described by the transition state theory as the product of a far-from-equilibrium term and an affinity (or ΔG) term that goes to zero at equilibrium

$$r_{CaCO_3}[\text{mol m}^{-2}\text{mineral s}^{-1}] = \left(k_1 a_{H^+} + k_2 a_{H_2CO_3^*} + k_3\right)\left(1 - \frac{a_{Ca^{2+}} a_{CO_3^{2-}}}{K_{eq}}\right) \tag{35}$$

where k_1, k_2 and k_3 are the rate constants [mol m^{-2} mineral s^{-1}]; K_{eq} is the equilibrium constant of the reaction; and a_{H^+}, $a_{H_2CO_3^*}$, $a_{CO_3^{2-}}$, and $a_{Ca^{2+}}$ are the activities of H^+, $H_2CO_3^*$, CO_3^{2-}, and Ca^{2+} [dimensionless] respectively. At 25 °C, $k_1 = 0.89$, $k_2 = 5.01\times10^{-4}$, $k_3 = 6.6\times10^{-7}$ mol m^{-2} s^{-1} (Chou et al. 1989), and $\log K_{eq} = -8.234$ (Wolery et al. 1990). The pCO_2 dependent parameter provided by Chou et al. (1989) is not adequate to describe rates at higher pCO_2 values and the data given by (Pokrovsky et al. 2009) should be used instead.

More recently, the applicability of the TST rate formulations have been called into question on several levels. One issue has to do with the reversibility implied in the TST formulation(s), since it appears that for most (or all) of the silicates and even carbonate phases, precipitation and dissolution cannot be described with the same rate law and set of parameters (Yang and Steefel 2008; Hellevang et al. 2011; Saldi et al. 2012). For both dissolution and precipitation, multiple rate laws may need to be used in order to capture the behavior over the entire range of ΔG. For dissolution, there may be a transition from nearly linear dissolution close to equilibrium to a more nonlinear dependence on ΔG farther from equilibrium as etch pit formation and propagation become more important (Burch et al. 1993). For precipitation, the situation is even more complicated, with transitions from spiral growth to 2D surface nucleation occurring as the supersaturation increases (Teng et al. 2000; De Yoreo and Vekilov 2003; Noiriel et al. 2012).

A more fundamental issue has to do with the lack of an atomistic treatment of mineral dissolution and precipitation. Atomistic treatments of mineral dissolution and precipitation demonstrate clearly the limitations of the bulk TST approaches (e.g., Teng et al. 2000; Nielsen et al. 2012; Wolthers et al. 2012). For example, a simple TST rate law like that given in Equation (33) or in Equation (35) fails to capture the dependence of the rate on the calcium to carbonate activity ratio (Nehrke et al. 2007; Gebrehiwet et al. 2012; Nielsen et al. 2012; Wolthers et al. 2012; Bracco et al. 2013). Perhaps even more telling is the inability of the simpler forms of the TST to capture kinetic isotopic fractionation adequately (Nielsen et al. 2012; Druhan et al. 2013). Certainly a more atomistic treatment of dissolution and precipitation is required as the interest increases in developing mesoscale models for mineral reactions at the pore scale (Bracco et al. 2013).

The major obstacle to the use of the atomistic models is the lack of a dynamic description of time-dependent mineral surface reactivity. The types and density of specific reactive

sites on the mineral surface is poorly constrained by the theoretical models, and numerical techniques like Kinetic Monte Carlo have not yet been routinely developed that can capture the thermodynamic and kinetic controls associated with multicomponent solution chemistry. In fact, one is hard pressed to find an adequate reconciliation of site densities and bulk reactive surface area, despite the importance of this topic and the large amount of work being carried out on atomistic crystal growth and dissolution rates. Arguably, the first successful example of this reconciliation has been provided by Bracco et al. (2013). Thus, additional work needs to be done to implement fully dynamic atomistic mineral dissolution and precipitation rate laws in the modeling tools that can be used to describe pore scale CO_2 injection and sequestration at the meso to macroscale.

Another issue has to do with the potential rate limitation associated with transport to and from the mineral surface, a topic that has been relatively neglected in the geochemical literature in recent years. When the transport of reactants to the reactive surface is very fast, the dissolution or precipitation reaction rate is controlled by the kinetic barrier, i.e., the rate of attachment and detachment of ions from the mineral surface. However, in general, transport processes will exert some control on the overall reaction rates, particularly when interface reaction rates are high. This effect is potentially most important in the case of calcium carbonate, which shows a partial diffusion rate control in rotating disk experiments even at 25 °C and circumneutral pH (Pokrovsky et al. 2005; Noiriel et al. 2012). It is generally agreed that calcite dissolution is completely transport controlled at pH values below 4—at higher pH values, calcite dissolution shows a mixed control, which is more difficult to treat in larger scale, continuum models (Noiriel et al. 2012). If a sufficiently high spatial resolution (order micron scale) is available at the pore scale, however, the interplay between molecular diffusion and surface reaction may be captured naturally (Molins et al. 2012; Yoon et al. 2012; Hiorth et al. 2013). When the reaction is assumed to take place at the mineral-fluid interface, the mass flux $\mathbf{J}$ perpendicular to the surface for mineral precipitation-dissolution reaction must be equal to reaction rate $\overline{r}$ expressed per unit of physical interfacial area (mol m^{-2} s^{-1})

$$\mathbf{J} \cdot \mathbf{n} = \overline{r} \tag{36}$$

where $\mathbf{n}$ is a unit vector normal to the interface. Figure 9 shows an example 2D calculation of flow, diffusion, and reaction around a calcite crystal using the Chombo-Crunch pore scale modeling software (Molins et al. 2012) and the rate laws given in Equation (35) at 25 °C and pH 7.5 to 9 (injection solution is pH 7.5). The presence of concentration gradients, which are most pronounced for larger grain sizes (> 200 microns), indicates a partial diffusion control of the dissolution rate. A square geometry for the calcite grain was assumed so as to avoid grid orientation effects, although the verification subsequently indicated that this was not necessary for Chombo-Crunch.

PORE SCALE CHARACTERIZATION AND EXPERIMENTATION

A number of new pore scale experimental and characterization approaches have emerged or matured in recent years that have made it possible, along with the new modeling approaches (see below), to investigate the physical and chemical processes associated with CO_2 injection and sequestration with unprecedented spatial resolution and process fidelity. These methods include 2D backscattered electron mapping (BSE), 3D microtomography based on X-ray computed microtomography diffraction (XMCT) and focused ion beam-scanning electron microscopy (FIB-SEM), small angle neutron scattering (SANS), nuclear magnetic resonance (NMR), and 2D micromodels. On the experimental side, there is great potential for progress in understanding CO_2 injection and sequestration processes with the use of engineered microfluidic and nanofluidic devices that simulate natural pores, although we are only just beginning to see applications in this field (Yoon et al. 2012).

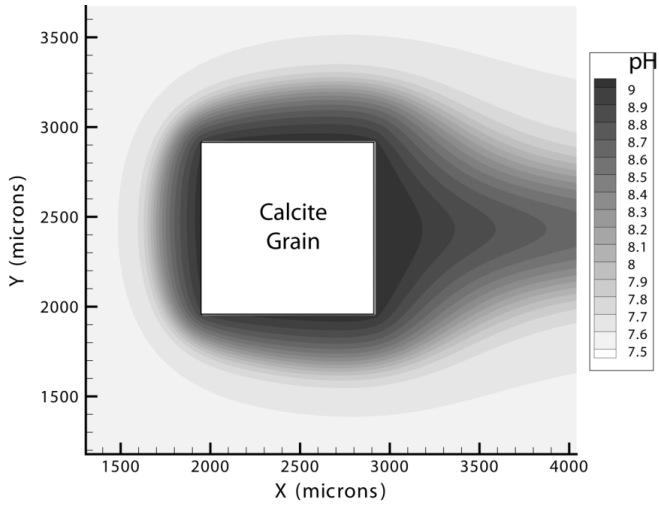

Figure 9. Diffusion boundary layer in solution pH developed around a dissolving calcite grain in two dimensions, the flow field of which is shown in Figure 3. The simulation was carried out with the software Chombo-Crunch (Molins et al. 2012) and verified against simulations using CrunchFlow with a velocity field imported from Chombo.

2D backscattered electron mapping

Backscattered electron microscopy is a powerful technique for mapping porosity and mineral distributions at the pore scale, as first demonstrated by Peters (2009) in her analysis of CO_2 reservoir sandstones from the Alberta Basin in Canada. The technique is based on the use of scanning electron microscopy (SEM) operated in backscatter mode to produce elemental maps that, when combined with the appropriate thresholding technique, can be used to produce mineral distribution maps. The approach is generally supplemented by local or point X-ray dispersive (EDX) analysis for semi-quantitative or quantitative (when combined with standards) determination of mineral chemistry. The technique is particularly powerful in that it can be combined with mapping of porosity (both connected and unconnected) so as to quantify the hydrologically accessible reactive surface area (Peters 2009; Landrot et al. 2012). Since the approach is based on surface backscattering, it is usually treated as a 2D technique, although if combined with FIB-SEM, in which successive layers of the solid material are destructively interrogated, it can be made fully 3D.

Peters (2009) investigated the Viking sandstone in the Alberta sedimentary basin in Canada and found that porosities ranged from 20% to as low as 8%. Based on their thresholding analysis, they were able to map kaolinite as the dominant secondary mineral phase in the sediment ranging from 5% to 31% of the mineral content on a volume basis. However, Peters (2009) also found that kaolinite comprised 65% to 86% of the pore-mineral contacts based on the mapping, indicating that it accounted for most of the reactive surface area in the sediment. On this basis, Peters (2009) determined that reactive surface area (RSA) could be overestimated by as much as 3 to 5 times if mineral volume fractions alone were used as the basis for the estimate (i.e., by simply multiplying the concentration of the mineral by its specific surface area).

Similar conclusions were reached by Landrot et al. (2012), who investigated the accessible RSA of a reservoir sand from the Cranfield Formation in Mississippi. Landrot et al. (2012) employed a hybrid approach in which 2D BSE mapping supplemented by EDX chemical

analysis with resolution as high as 330 nm was combined with 3D X-ray microtomography at a resolution of 880 nm (Fig. 10). Scale-dependent correction factors for the porosity and mineral distributions were obtained by carrying out the BSE mapping at both the higher resolution of 330 nm and at the 880 nm resolution of the X-ray microtomography (Landrot et al. 2012). Locally, they also collected FIB-SEM data at a 14 nm resolution to map chlorite-filled pores.

Anovitz et al. (2013) used BSE on samples of the St. Peter Sandstone to extend their Ultra Small Angle Neutron Scattering (USANS) and Small Angle Neutron Scattering (SANS) results to larger scales (see below).

3D microtomography (XCMT and FIB-SEM)

Ideally, the pore structure of a sediment or rock intended as part of a CO_2 reservoir or a caprock intended to prevent its buoyant rise should be mapped in three dimensions. The X-ray CT technique involves an X-ray source, an object, and a detector. The source generates X-rays that are directed toward an object that is rotated in a stepwise manner. The X-rays are attenuated as they pass through the object and the emerging or transmitted X-ray intensity is measured and recorded by the detector for every step of rotation. The data is typically collected as a series of 2D radiographs that are then stacked together to provide spatially resolved 3D images. The attenuation of X-rays by an object may be modeled using Beer's law, which is valid for monochromatic radiation passing though homogeneous materials. Nanometer scale resolution is achievable in some cases, but only with a tradeoff in the volume of material that can be investigated. Synchrotron-based X-ray sources like those at the Advanced Photon Source (Argonne National Laboratory) and the Advanced Light Source (Lawrence Berkeley National Labora-

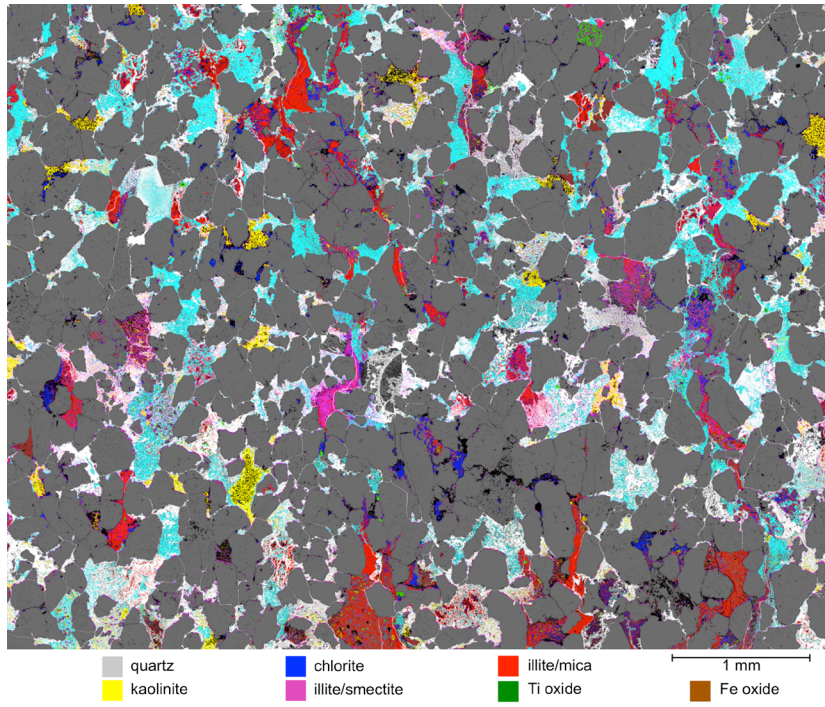

Figure 10. BSE map of reactive phases and porosity in a 2D sample from the Cranfield Formation in Mississippi, a CO_2 injection test site (Landrot et al. 2012). Connected porosity is uncolored. Both shades of blue represent chlorite, with the lighter blue made up of nanoporous chlorite.

tory) provide higher energy than is achievable typically with commercially available units.

X-ray based microtomography (μCT or XCMT) techniques have been used in a number of studies of the physics and chemistry of CO_2 injection and sequestration. Noiriel et al. (2004, 2009) used periodic X-ray microtomographic analysis at a resolution of 4.91 μm to map local changes in porosity, pore roughness, and reactive surface area in a limestone subjected to CO_2-acidified water. In the case where a single mineral is present and dissolving, the increase in porosity also represents the net amount of the mineral dissolved. Estimates based on the volume of mineral lost can be compared to the estimate of total dissolution over the length of the sample determined from effluent chemistry (e.g., based on the flux of calcium). Similarly, Luquot and Gouze (2009) and Gouze and Luquot (2011) used the technique to map dissolution of carbonate as a function of time, demonstrating that slower flow conditions (corresponding to high Damköhler numbers) resulted in "wormholing" or reaction fingering (Ortoleva et al. 1987; Hoefner and Fogler 1988; Steefel and Lasaga 1990). Smith et al. (2013a) used the approach to contrast dissolution rates and pore geometry evolution in an evaporite caprock. Carroll et al. (2013) extended the analysis to two contrasting rock types, a vuggy limestone (which showed extensive wormholing) and a marly dolostone (which did not), both from the Weyburn CO_2 injection site in Alberta, Canada (Fig. 11). They also took the novel next step of using the microtomography data to provide conditions to initialize a 3D reactive transport model, the results from which were then compared to post-experiment microtomographic maps of the same rock. Although not a true pore scale analysis, based as it was on a continuum representation of a porosity-permeability relationship, it made use of micron scale resolution data of the evolving porosity structure of the rock.

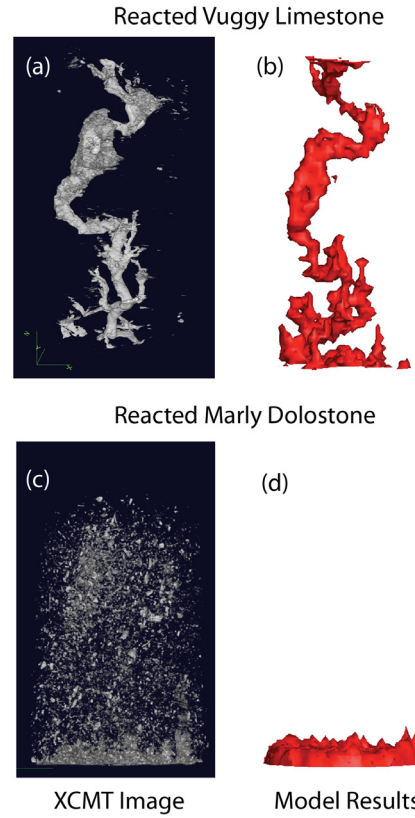

Figure 11. XCMT images of dissolution features in a) a vuggy limestone, and c) a marly dolostone from the Weyburn Formation CO_2 injection site in Alberta, Canada. Panels (b) and (d) on the right represent model results that made use of the initial porosity distribution and an assumed porosity-permeability relationship (Carroll et al. 2013).

Noiriel et al. (2012) carried out a combined XMCT and chemical analysis of carbonate precipitation as a result of mixing. The experimental scenario was intended to represent the processes likely to occur when the CO_2-rich acidic brine is neutralized and mixed with a source of calcium ions. As in the case of limestone dissolution, calcite was determined to be the only phase to form, so the porosity decrease determined at a 4.4 micron resolution could be treated as local precipitation of calcite. The addition of carbonate precipitate after 28 days of reaction is clearly visible in the reconstructed images from the XCMT analysis (Noiriel et al. 2012) (Fig. 12). The study demonstrated that the rates of local (micron scale) reaction could be reconciled with independently determined reaction calcite precipitation rates in the absence of transport or "porous medium" effects (Noiriel et al. 2012).

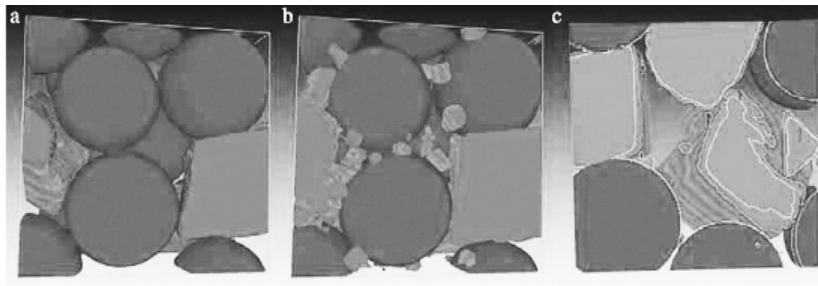

Figure 12. Carbonate precipitation on glass beads (dark gray spheres) and calcite spar (medium gray rhombic crystals) before reaction (Panel A) and after 28 days of reaction with a flowing supersaturated solution (Panel B) Panel C shows the displacement of the crystal-solution interface (pale lines)as a result of precipitation. From Noiriel et al., 2012.

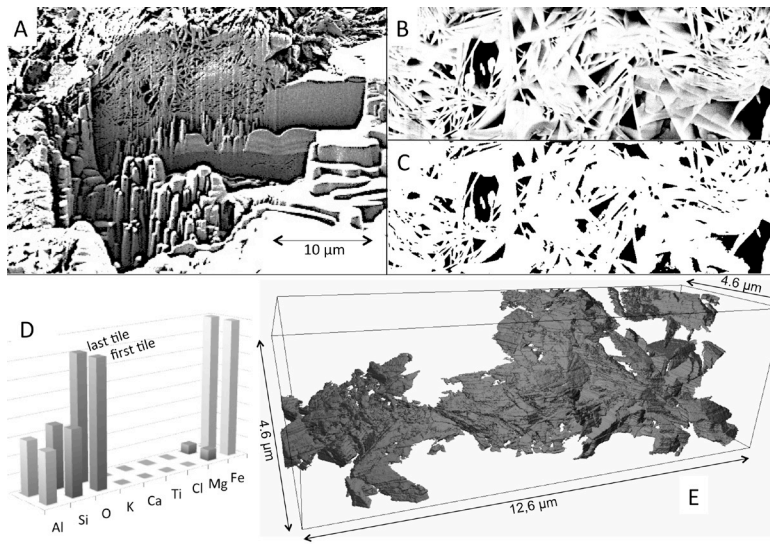

Figure 13. FIB-SEM microtomography of chlorite from a pore in the reservoir sandstone from the Cranfield, Mississippi $scCO_2$ injection site (Landrot et al. 2012). A) Excavated portion of the chlorite-filled pore, with a quartz grain on the right. B and C) SEM close up of chlorite showing nanoporosity. D) EDX results showing Fe-chlorite composition. E) Microtomographic image of chlorite-filled pore.

Focused Ion Beam-Scanning Electron Microscopy (FIB-SEM) was used to provide 3D microtomographic data at scales below the resolution of the XCMT techniques (Landrot et al. 2012) (Fig. 13). FIB-SEM is a destructive technique that gradually excavates new 2D layers, which are then imaged with the SEM (supplemented by EDX analysis, if available). The technique provides data that can be interpreted in a similar fashion to the XCMT, with counting of voxels to establish porosity and the use of a burning algorithm to determine connected porosity (Landrot et al. 2012). Landrot et al. (2012) applied the technique to chlorite filled pores in a reservoir sandstone from the Cranfield Formation in Mississippi at a resolution of 14.2 nanometers. Landrot et al. (2012) were able to determine that essentially all of the porosity (or nanoporosity) within the chlorite was connected. FIB-SEM was also used for the quantitative analysis of nanopore structures in a Cretaceous chalk sample (Yoon and Dewers 2013), revealing a nano-scale basis for strong anisotropy in the presence of fractures.

Multiphase studies of CO_2 injection and/or sequestration have been fewer, in part because of the difficulty in capturing the highly transient injection stage with time-consuming X-ray microtomographic techniques. Silin et al. (2011) and Blunt et al. (2013) used XCMT to image the two-phase fluid resolution resulting from CO_2 invasion of the Frio sandstone and the Doddington sandstone, respectively. Kneafsey et al. (2013) carried out a core-scale experiment in which supercritical carbon dioxide ($scCO_2$) was flowed through a brine-saturated sample consisting of a layer of silica sand, a layer of calcite sand, and then another layer of silica sand. The results were compared with an otherwise identical experiment in which nitrogen was the invading gas. Both experiments were carried out at 46.7 °C and 8.28 MPa. Panel A of Figure 14 shows the XCMT data before injection of the gases, with the contrast between the silica (dark grey, or purple in the original reference) and the calcite (light grey, or yellow in the original reference) clearly visible as a result of their density difference (Kneafsey et al. 2013). The upper left circular slice (3 mm thick) is closest to the injection port, while the lower right circular slice is furthest downstream. Panels B and C of Figure 14 show the distribution of nitrogen and $scCO_2$, respectively. Both gases show a buoyant rise to the top of the core after about 4 to 5 slices, flow through a very narrow pathway along the top of the core within the calcite sand, while taking a slightly broader pathway through the silica sand downstream. Presumably this difference in behavior reflects the difference in wetting behavior of the two non-aqueous fluids.

Pini and Benson (2013) presented a novel method to measure drainage capillary pressure curves both at the core and sub-core scale using CO_2 and water at reservoir conditions. Capillary pressure measurements were made at the inlet face of the sample by successively increasing the flow rate of the non-wetting phase while measuring the saturation with a medical X-ray Computed Tomography (CT) scanner. They found excellent agreement between the new method and data from mercury intrusion porosimetry, while also allowing for an estimate of the wetting and interfacial properties of the CO_2/water system.

Bauer et al. (2012) calculated macro and microporosity values for three carbonate rock samples (assumed monomineralic) by applying two thresholds to the distribution of measured intensities. These values were in close agreement with those measured from mercury intrusion.

Small Angle Neutron Scattering

Small Angle Neutron Scattering (SANS) and Ultra Small Neutron Scattering (USANS) are powerful techniques that make it possible to investigate a large range of pore sizes, although they are statistical rather than tomographic techniques (pore shapes are not directly imaged, but must be reconstructed on the basis of a geometric model). Nonetheless, their ability to extend analysis to nanometer sized pores makes them the methods of choice for investigating water-rock and CO_2-water-rock interaction as a function of pore size, particularly when nanoporosity is of interest. Anovitz et al. (2013) recently studied samples of St. Peter Sandstone that contain significant volumes of large-scale porosity, modified by quartz overgrowths, along with significant sub-micron porosity based on the neutron scattering results. In their study, autocorrelation data from BSE was used to extend the neutron scattering range (~1 nm to 10 μm) to investigate structures up to 1 cm. While data from sandstones collected previously suggested scattering is dominated by surface fractal behavior over many orders of magnitude, careful analysis of the St. Peters Sandstone data showed both fractal (high Q values in Fig. 15b) and pseudo-fractal behavior. The scattering curves are composed of subtle steps that can be modeled as polydispersed assemblages of pores with log-normal distributions (Fig. 15b).

Nuclear Magnetic Resonance (NMR) and Magnetic Resonance Imaging (MRI)

Nuclear Magnetic Resonance (NMR) and Magnetic Resonance Imaging (MRI) are additional techniques for directly imaging CO_2 injection at the pore scale. Suekane et al. (2005) used a magnetic resonance imaging (MRI) technique to directly visualize the distribution of supercritical CO_2 injected into a packed bed of glass beads containing water. After the CO_2

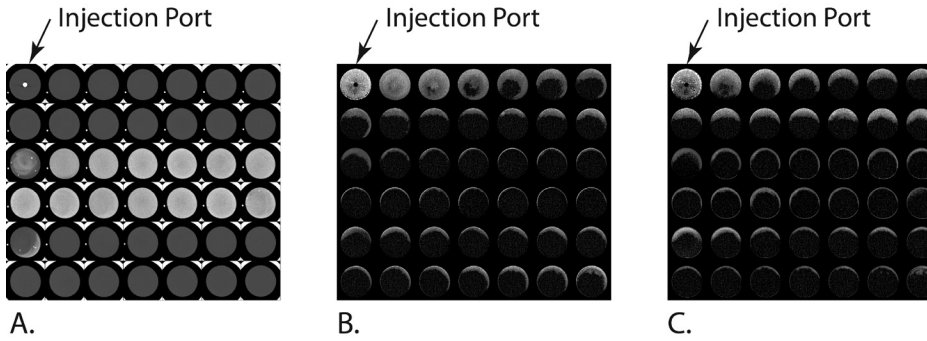

Figure 14. XCMT images of A) the pre-experiment silica (dark grey, or purple in the original reference) and calcite (light grey, or yellow in the original reference) sand distribution, clearly visible from the density contrast between the two minerals, B) the distribution of nitrogen, and C) the distribution of $scCO_2$. The experiment was carried out at 46.7 °C and 8.28 MPa (Kneafsey et al. 2013).

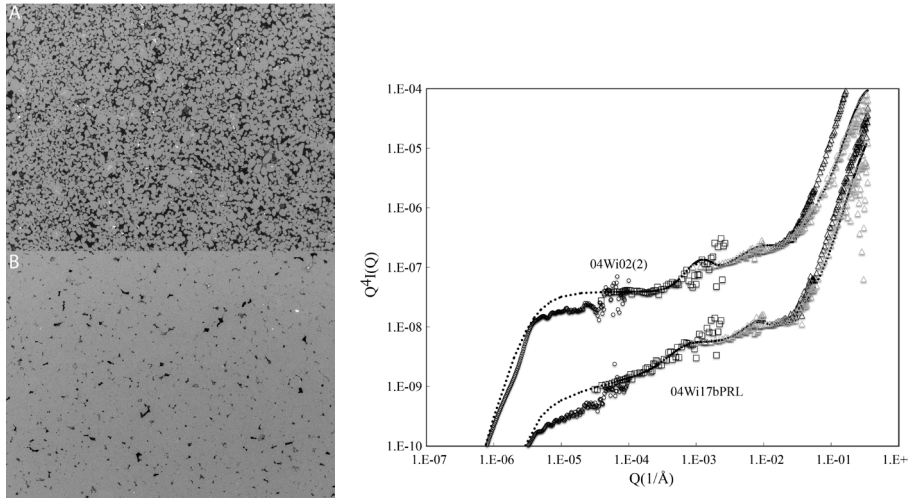

Figure 15. (a) SEM/BSE images of two samples from the St. Peter Sandstone (Anovitz et al. 2013) (b) Porod transform of the scattering curve for these samples (USANS data in boxes, SANS data in circles, BSE data in dashed lines). The lines show the log-normal, monodispersed sphere and form factor fits to the datasets (Anovitz et al. 2013).

displaced much of the water, some water remained near the central axis, although there were several millimeter-sized, CO_2-rich channels running through this water-rich region. In a parallel channel with hydrophilic surfaces, a high velocity of water between the bubbles along the flow direction results in a high relative permeability at low water saturations. At high CO_2 saturations, a stable layer flow occurred, indicating that the relative permeability of water decreased sharply with saturation decreasing. In Suekane et al. (2009) a noninvasive nuclear magnetic resonance (NMR) technique was presented to measure the amount of CO_2 dissolved in water in porous rock. The relaxation time of the NMR signal was evidently shortened by the porous material surfaces and CO_2 dissolution. Hussain et al. (2011) used NMR techniques to quantify the spatial distribution and pore environment associated with CO_2 capillary trapping in a model porous medium (random glass bead packing). 3D images revealed relatively homogeneous (at

the macroscopic scale) CO_2 entrapment, even though the image resolution was insufficient to resolve individual CO_2 ganglia. Quantification of the pore environment of the CO_2 ganglia was achieved using NMR displacement propagators (displacement probability distributions), acquired both before and after CO_2 entrapment.

Micromodels

Micromodels are transparent pore networks used for laboratory studies of microscopic distribution and transport of fluids in porous media, with application to research related to oil recovery from reservoirs, nonaqueous phase liquid dissolution, and colloid transport (see also Crawshaw and Boek 2013, this volume). Micromodels have also been applied in reactive systems (e.g., Yoon et al. 2012). Few micromodel experiments have been conducted under elevated pressure and temperature, and even fewer have been conducted under supercritical $scCO_2$ conditions. Chalbaud et al. (2009) investigated distributions of CO_2 and water in glass micromodels having different wettabilities. Er et al. (2010) investigated the behavior of CO_2 and oil in homogeneous and heterogeneous fractured micromodels. Micromodel studies have been used to identify the crossover conditions from viscous to capillary fingering during invasion of liquid and supercritical CO_2, in heterogeneous and heterogeneous pore networks (Zhang et al. 2011; Wang et al. 2013). Discussion of the emergent features of associated with CO_2 invasion is provided below.

Kim et al. (2012) studied pore-scale wettability and wettability alteration in $scCO_2$-silica-brine systems using engineered micromodels at 8.5 MPa and 45 °C over a wide range of NaCl concentrations up to 5.0 M (Fig. 4). Dewetting of silica surfaces upon reactions with $scCO_2$ was observed through water film thinning, water droplet formation, and contact angle increases within single pores. The brine contact angles increased from initial values near 0° up to 80° with larger increases under higher ionic strength conditions. Given the abundance of silica surfaces in reservoirs and caprocks, these results indicate that CO_2-induced dewetting may have important consequences on CO_2 sequestration, including the reduction of capillary entry pressure, as well as the modification of CO_2 residual trapping, relative permeability, and caprock integrity.

INCORPORATING MICROSCOPIC CHARACTERIZATION INTO NUMERICAL PORE SCALE MODELS

Significant advancements in imaging techniques and processing capabilities have made it possible to resolve the porous media at micrometer scale. To incorporate these data into numerical models, images captured experimentally by microtomography need to be converted into input data for numerical models. Wildenschild and Sheppard (2013) have provided a comprehensive review of the approaches that can be used to segment images to obtain the morphology and topology of the pore space, the porosity, fluid saturation and spatial distribution, and the interface curvature estimation.

Segmentation is used to identify the discrete materials in an image, frequently by binarization of an image into just two materials, e.g., pore and solid. Noiriel et al. (2009) presented an approach to segmenting the images collected from X-ray microtomographic analysis of cores. They used a segmentation technique based on region growing (Gonzalez and Woods 2008) to avoid the errors associated with simple thresholding. Before the segmentation procedure, the data sets were normalized through a linear interpolation procedure to achieve consistency within a dynamic range of intensity values on the different images. The noise was reduced by running a 3D median filter. Then, the different parameters for segmentation were chosen by visual inspection of the grey-level histogram, and the results were validated by comparison of the segmented volumes with the greyscale ones. In the fitting procedure, the parameters used were forced to be the same for all of the sample intervals investigating. In the study by Noiriel

et al. (2012), a similar approach was taken, although in this case simple thresholding would have been sufficient because of the strong contrast between the two materials, glass beads and calcite spar. Armstrong and Ajo-Franklin (2011) also found that after applying a median filter (3×3×3 kernel), it was possible to use a simple threshold to segment the solid (glass and calcium carbonate) and liquid phases.

Following the segmentation procedure, the porosity of the sample can be evaluated. The next step consists in determining the percolation clusters, or sample spanning clusters, which are the networks of pores connected to the boundaries of the sample, and the unconnected pores using a cluster-labeling algorithm (Stauffer et al. 1994). A similar burning algorithm was employed by Landrot et al. (2012).

Beyond the morphology and topology of the pore space, geometric methods such the Method of Inscribed Spheres (MIS) can provide insights into two-phase fluid distributions in porous media (Silin and Patzek 2006). The method of MIS models these distributions from segmented micron-scale 3D images of natural rock assuming equilibrium dominated by the capillary forces (Silin et al. 2011). Kneafsey et al. (2013) computed characteristic curves for an experimental core of silica and calcite sand layers for a range of contact angles using the method of maximal inscribed spheres. Simple physical arguments and analysis using MIS indicated that CO_2 was wetting the calcite under the experimental conditions and duration of the experiment.

Most recently, Yoon and Dewers (2013) extended combination of image analysis and pore-scale modeling to 3D nanopore structures, suggesting the multiscale reconstruction was possible by mapping FIB-SEM data onto microCT dataset. Blunt et al. (2013) also described the underlying technology, namely imaging of the pore space of rocks from the nanometer scale upwards, coupled with a suite of different numerical techniques for simulating single and multiphase flow and transport through these images.

MODELING APPROACHES FOR THE PORE SCALE

Simulation of flow in the subsurface has historically relied on the treatment of the porous medium as a continuum in which a representative volume or REV is defined (Bear 1988). Within the REV at each point in space, all phases are assumed to exist simultaneously. At the pore scale, however, each point of space is occupied by a discrete phase (CO_2 or brine or solid). This requires incorporating directly the spatial distribution of the fluid and solid phases and their evolution with time. The initial phase distribution in actual rock or sediment samples is available from experimental characterization techniques as outlined in the previous section. Often for convenience and simplicity, especially for model validation or for testing of fundamental concepts, many modeling efforts are performed on synthetically generated domains where mineral grains are represented by spheres or other basic geometric shapes, rather than using actual porous media (Chen and Zhang 2010; Bandara et al. 2011). Sometimes these basic geometries correspond to those etched in experimental micromodels (e.g., Jung and Wan 2012; Yoon et al. 2012). Stochastic porous medium structures have also been generated by computer simulation (Sadhukhan et al. 2012) assuming a fractal pore-grain interface distribution (Dutta and Tarafdar 2003).

Recent literature reviews of pore scale models (Meakin and Tartakovsky 2009; Joekar-Niasar and Hassanizadeh 2012) reveal a large number of pore scale modeling studies of significance in problems ranging from hydrocarbons reservoir processes, vadose zone contamination or water-rock interaction, but only a limited number of works are devoted to CO_2 sequestration scenarios (Table 1). The availability of pore scale simulation methods and the recent interest in the subject suggest that the next few years will likely see a remarkable increase in pore scale models applied specifically to CO_2 sequestration problems.

Table 1. Selected list of published pore scale models relevant to CO_2 sequestration

Reference	Model	Sample	Approach	Resolution	Domain size
Ovaysi and Piri (2013)	sF-T	Berea and Bentheimer sandstones	MMPS particle method	5.345 μm	0.51×0.51×1.09 mm
Chen and Zhang (2010)	mF	Square grains and fracture in 2D	Lattice Boltzmann	25 μm	0.01×0.01 m
Flukiger and Bernard (2009)	sF-T-R	Packed spheres obtained from XCMT	Direct Numerical Simulation	10 μm	0.5×0.5×1.5 mm
Varloteaux et al. (2013)	T-R	Fontainebleau sandstone	Pore Network	80 μm	18.4 mm^3 &
Sadhukhan et al. (2012)	sF-T-R	2D stochastic	Finite difference, random walk method		128×1000 (unreported units)
Molins et al. (2012)	sF-T-R	Packed virtual spheres	Pore Network	7.8 μm	1.0 cm length, 0.5 cm diameter
Molins et al. (2012)	sF-T-R	Crushed calcite grains in capillary tube	Direct Numerical Simulation	1.1 μm	0.7 cm length, 0.5 mm in diameter
Yoon et al. (2012)	sF-T-R	Cylindrical grains from micromodel	Hybrid lattice Boltzmann and DNS	5 μm	2 cm length, 1 cm in width
Kang et al. (2007)	sF-T-R	2D Synthetic porous medium	Lattice Boltzmann	117 μm 125 μm	0.75×0.75 cm 5×0.75 cm
Blunt et al. (2013)	mF-T	Estaillades carbonate, Ketton limestone, Mount Gambier carbonate	Pore Network	36-91μm *&	18.7-31.3 mm^3
Ellis and Bazylak (2013)	mF	Rectangular lattice	Pore Network	3.2±1.5 μm	0.09×0.09×0.24 mm #&
Kim et al. (2011)	sF-T-R	Sandstones, Viking formation	Pore Network	67 μm *&	2.9×2.9×1.4 mm

NOTES:
sF = single fluid
mF = multiple fluid phases
T = transport
R = reactions)
* = estimated assuming cubic pores
# = estimated assuming a porosity of 0.14
& = estimated assuming pore bodies make up entire pore space

Here we review the generic pore scale modeling approaches specifically as they can be or have been applied to modeling CO_2 sequestration scenarios. To address these scenarios, pore scale models need to resolve the relevant physical and chemical processes in complex pore geometries with interfaces between CO_2 and brine. This requirement demands very fine model resolution (on the order of a few microns) so that the physics and chemistry are accurately captured. However, the ultimate interest of many modeling applications is to be able to draw conclusions that are applicable over a representative volume of porous medium. For this purpose, large simulation domains are required. The two broad categories of approaches used to simulate pore scale processes are those that extract the pore space geometry to construct a pore network and those that consider the actual pore space geometry directly. Pore network models sacrifice the resolution of the complex pore space geometry of most rocks and soils by replacing it with a network of pore volumes connected by channels so as to enable simulations of large porous domains. Pore scale models that preserve the fine scale resolution include lattice Boltzmann methods, particle methods or grid-based direct numerical simulation methods. This group of approaches has faced a computational limitation in terms of the size of domains that can be simulated.

An approach that does not fall in these two broad categories, but has also been successfully applied in some pore scale studies is the so-called micro-continuum approach. In this approach, continuum model concepts are applied to very small volumes of porous medium (micron scale), often at the scale where pore scale processes take place (e.g., Noiriel et al. 2012; Carroll et al. 2013).

Models that combined different approaches for various components of the model have also been employed. Mixed approach models are usually developed for practical reasons: to take advantage of existing, time-tested methods or software packages, or because specific approaches are computationally advantageous. For example, conventional discretization methods have been used to simulate pore scale processes when a solution of the flow field was obtained with a lattice Boltzmann method (Yoon et al. 2012), or a random walk method has been used for reactive transport while a direct finite difference solver was used for Navier Stokes flow (Sadhukhan et al. 2012).

The dynamics of physical and chemical processes at the continuum scale are controlled by phenomena that take place in a localized region of the domain where the continuum scale models break down and resolving the pore scale is necessary. However, in most of the domain, the computationally demanding pore scale resolution is not necessary. Hybrid multiscale models (Scheibe et al. 2007), where the different spatial scales are resolved in different parts of the domain, can be used to overcome the limitations regarding the size that "brute force" pore scale models would require. Pore scale and continuum scales are coupled by enforcing the continuity of pressures and mass fluxes at the pore/continuum interfaces (Battiato et al. 2011). Coupling between subdomains can be done using finite-element spaces to determine interface conditions, such as in the mortar method (Balhoff et al. 2008). Mortar coupling is a domain decomposition approach in which subdomain are coupled together using a low-degree of freedom mortar space defined on a coarse grid in such a way that fluxes match weakly. Mortars have been used primarily for coupling continuum-scale models, but were recently extended to model flow at multiple spatial scales (Balhoff et al. 2008) and applied to upscale reactive transport processes associated with CO_2 sequestration using a pore network model as the underlying pore scale model (Mehmani et al. 2012). Another approach to multiscale CO_2 modeling is that of (Varloteaux et al. 2013), where pore network model simulations are used to evaluate continuum scale parameters as the pore space evolves due to geochemical processes. We are not aware of the existence of any adaptive hybrid multiscale model, an approach in which the pore scale description would be adaptively applied where needed depending on the physical or chemical evolution of the system (e.g., where sharp geochemical gradients exist).

Pore network models

In pore network models, the pore space geometry is conceptualized as a network of pore volumes connected by channels or pore throats (Fatt 1956; Payatakes et al. 1973) (e.g., Fig. 16). Mass fluxes are calculated for each channel or pore throat and a mass balance equation is solved at each pore volume. For flow of a single phase fluid, the mass balance in the i^{th} pore volume can be written as a sum of fluxes from all pore volumes j connected to i, q_{ij} (e.g., Mehmani et al. 2012):

$$\sum_j q_{ij} = \sum_j G_{ij}\left(P_i - P_j\right) = 0 \tag{37}$$

where P_i and P_j are the fluid pressures, and G_{ij} is a coefficient that is a function of the properties of the connection. Often specific geometrical shapes are used for the connection and G_{ij} has a definite form e.g., $G_{ij} = (\pi r_{ij}^4 / 8\mu L_{ij})$ for a cylinder of radius r_{ij} and length L_{ij} as in Mehmani et al. (2012). In general, the major practical challenge of single phase pore network models is to find accurate way of representing real porous media. For that, the structure of the pore network can be extracted from 3D images such as those obtained from XMCT (e.g., Bauer et al. 2012; Varloteaux et al. 2013). Pore network extraction based on skeletonization using a medial axis analysis is a common approach in the work of Lindquist and co-workers (Lindquist and Venkatarangan 1999; Lindquist et al. 2000; Kim et al. 2011). Other techniques, such as the distance ordered homotopic thinning technique (Pudney 1998; Bauer et al. 2012), have also been used for pore network extraction.

The mass balance of each species subject to reactive transport can be written for each pore of volume V_i (e.g., Kim et al. 2011)

$$V_i \frac{\partial C_k}{\partial t} = \sum_{q_{ij}>0} q_{ij} C_{k,j} + \sum_{q_{ij}<0} q_{ij} C_{k,j} + \sum_j D A_{ij} \frac{C_{k,j} - C_{k,i}}{L_{ij}} + V_i R_{k,i} \tag{38}$$

where $R_{k,i}$ is the reaction rate contribution to component k in the i^{th} pore volume, and A_{ij} is the cross-sectional area of the throat.

If mineral precipitation-dissolution is considered, the volume change of the pores can be calculated and translated into a change in the conductance G_{ij} of the connection. Different assumptions are made in translating this volume change and conductance change (see for example Mehmani et al. 2012; Varloteaux et al. 2013), but the resulting simulations make it possible to

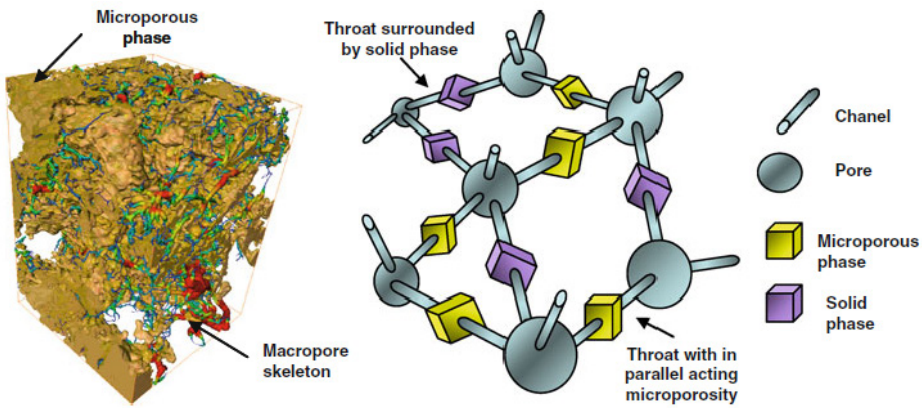

Figure 16. Dual pore network conceptualization (right) for a carbonate rock sample (left) with micro and macroporosity domain (Bauer et al. 2012).

evaluate feedback processes between reactions and flow at larger scales under different reactive transport regimes. Heterogeneous mineral distributions can also be incorporated in pore networks based on XCMT image analysis (Kim et al. 2011).

Due to the computational challenges associated with pore scale models based on a direct representation of the pore space and the fluid-fluid interfaces, pore network models are by far the most common approach for simulating multiphase flow in the literature. However, applications to CO_2 injection and sequestration are lagging behind other applications such as oil reservoirs and other environmental applications. Comprehensive reviews of quasi-static and dynamic multiphase pore network models are provided in Blunt (2001), Blunt et al. (2002, 2013), and Joekar-Niasar and Hassanizadeh (2012). Blunt et al. (2013) recognized that for multiphase flow, network modeling offers the most proven approach for predicting relative permeability and capillary pressure. In Blunt et al. (2013), imaging, network extraction, assignment of contact angle and pore network simulation of displacement of water by a non-wetting phase (oil) on three carbonates samples are presented.

Kang et al. (2005) applied the invasion percolation theory in a pore network to two-phase immiscible displacement of seawater by liquid CO_2 in deep oceanic sediments. The invasion percolation theory was used to model the slow immiscible displacement controlled by capillary forces of two phases within a porous medium where a non-wetting phase such as CO_2 displaces a wetting phase. In the system considered by Kang et al. (2005), CO_2 and seawater are assumed to react to form hydrate and the depth of CO_2 invasion in the sediments is controlled by changes in the pore-scale porosity close to the hydrate formation front. The effects of contact angle heterogeneity on CO_2 saturation involving quartz and mica were modeled in 2D and 3D pore networks over a range of viscosity ratios (M) and capillary numbers (Ca) relevant to carbon sequestration (Ellis and Bazylak 2012, 2013).

Lattice Boltzmann method

Rather than solving the conservation equations for the concentrations or momentum directly, the lattice Boltzmann (LB) method simulates the fluid/s as consisting of particles on a discrete lattice that perform consecutive propagation and collision steps. The LB method recovers the macroscopic pore-scale equations (e.g., Navier-Stokes) and is easily parallelizable.

The Bhatnagar-Gross-Krook (BGK) collision operator (Bhatnagar et al. 1954) is commonly used in the discrete Boltzmann equation:

$$f_i\left(\mathbf{x}+\mathbf{e}_i\Delta t, t+\Delta t\right)-f_i\left(\mathbf{x},t\right)=-\omega\left(f_i(\mathbf{x},t)-f_i^{eq}(\mathbf{x},t)\right) \tag{39}$$

where f_i is the discrete particle distribution function and Δt is the time step size. The term on the left hand side expresses the propagation of particles according to the lattice velocity $\mathbf{e}_i$, a set of vectors which depend on the choice of lattice. The term on the right-hand side represents the BGK rule for collision. The BGK collision expresses how the particle distribution f_i relaxes to the local equilibrium distribution function f_i^{eq} with a single relaxation frequency ω. The relaxation frequency determines the kinematic viscosity of the fluid, e.g., $v=c_s^2(1/\omega-1/2)$ in Kang et al. (2005). The form of the local equilibrium distribution function f_i^{eq} depends on the macroscopic equations that one wants to recover and the order of accuracy desired.

The LB method has the advantage of describing non-equilibrium dynamics, especially in fluid flow applications involving interfacial dynamics and complex boundaries (Chen and Doolen 1998). For multiphase flow, most lattice Boltzmann models (e.g., Shan and Doolen 1995) treat the interface as a diffuse one, where for the case of an immiscible binary mixture at equilibrium the two fluids are separated by an interface of finite thickness.

Complex fluid-solid interfaces are usually treated with a bounce back boundary condition. Kang and co-workers have applied the LB method to reactive transport problems (e.g., Kang

et al. 2007), with consideration of aqueous speciation reactions and the evolution of the pore space geometry as a result of precipitation-dissolution. Hiorth et al. (2013) constructed a LB model that includes non-linear dissolution–precipitation kinetics, surface complexation, and ion exchange and applied to the injection of seawater into a chalk core. Chen and Zhang (2010) simulate density driven convection driven by the dissolution of $scCO_2$ in the brine occupying the pore space of a single fracture. Model results show that after the onset of convective instability, the increase in the interfacial area between CO_2-rich brine and unaffected brine may favor the migration of CO_2 into the fracture and adjacent porous medium.

Although the works mentioned above have been limited to rather simple geometries and 2D problems (Kang et al. 2007; Chen and Zhang 2010), recent lattice Boltzmann studies dealing with immiscible multiphase reactive systems in complex 3D porous geometries (Parmigiani et al. 2011) show that the LB method is capable of addressing the requirements of computational pore scale simulations of CO_2 injection and sequestration (Fig. 5a).

Particle methods: Smooth particle hydrodynamics and moving particle

In particle methods such as the smooth particle hydrodynamics method (SPH) and moving particle method (MPS), fluids are represented by N_p particles with intensive properties (e.g., mass m_i) that are tracked in time as they move in the pore space. Continuous variables (e.g., density) are represented as the superposition of kernel functions centered on a set of discrete particle points $\mathbf{r}_i$. In continuous form, this superposition for variable $A(\mathbf{r})$ at point $\mathbf{r}$ can expressed in integral form as

$$A(\mathbf{r}) = \int A(\mathbf{r}')W(\mathbf{r}-\mathbf{r}',h)d\mathbf{r}' \tag{40}$$

where W is the kernel and the parameter h is the kernel size that defines the domain of influence of the kernel for each particle. To reduce the computational costs in numerical calculations, the domain of influence is chosen to be finite such that $W(\mathbf{r}-\mathbf{r}',h)=0$ when $|\mathbf{r}-\mathbf{r}'|>h$. In SPH, the kernel function satisfies $\int W(\mathbf{r}-\mathbf{r}',h)d\mathbf{r}'=1$ and the discrete approximation to $A(r)$ at particle point r_i is

$$A(\mathbf{r}_i) \approx A^*(\mathbf{r}_i) = \sum_i^{N_h} A^*(\mathbf{r}_j)W(|\mathbf{r}_i-\mathbf{r}_j|) \tag{41}$$

where N_h is the number of particles within the region defined by h. In the moving particle method, the kernel function does not necessarily need to satisfy the normalization conditions, however, for convenience we will not present these expressions here. The gradient of the continuous field $A(r)$ can also be written as a function of the kernel functions

$$\nabla A(\mathbf{r}_i) \approx A^*(\mathbf{r}_i) = \sum_i^{N_h} A^*(\mathbf{r}_j)\nabla W(|\mathbf{r}_i-\mathbf{r}_j|) \tag{42}$$

Variables in the equations describing fluid flow, transport and reactions and their gradients are discretized as particle equations using Equations (41) and (42). As a result, the discretized forms of the differential equations are a function of the relative position of the particles $W(\mathbf{r}_i-\mathbf{r}_j,h)$, and the kernel function W. The kernel function is in practice defined as a spline or polynomial function defined piece-wise between $0<|\mathbf{r}_i-\mathbf{r}_j|<h$.

Particle methods have recently been applied to the simulation of multiphase flow involving CO_2 and brine (Bandara et al. 2011) and multicomponent transport associated with elevated CO_2 and SO_2 concentrations (Ovaysi and Piri 2013). Bandara et al. (2011) developed an SPH model for multiphase CO_2-brine flow. Rather than prescribing an interface between fluids, fluid-fluid and fluid-fluid-solid interfaces are simulated via an approach similar to molecular dynamics in which a combination of short repulsive and medium range attractive forces are included, leading to a diffuse interface. These forces are added in the momentum balance equation according to

$$\frac{\partial\left(m_i \mathbf{u}_i\right)}{\partial t} = \mathbf{F}_i + \mathbf{F}_i^{\text{interaction}} \tag{43}$$

$$\mathbf{F}_i^{\text{interaction}} = \sum\nolimits_j \mathbf{F}_{i,j}^{\text{interaction}} \tag{44}$$

The form of $\mathbf{F}_{i,j}^{\text{interaction}}$ ensures that it is repulsive in the short range, attractive in the medium range and zero when particles *i* and *j* are separated by a distance greater than *h*:

$$\mathbf{F}_{i,j}^{\text{interaction}} = \begin{cases} s_{ij} \cos\left(\dfrac{3\pi}{2h}\left|\mathbf{r}_i - \mathbf{r}_j\right|\right) \dfrac{\mathbf{r}_i - \mathbf{r}_j}{\left|\mathbf{r}_i - \mathbf{r}_j\right|} & \left|\mathbf{r}_i - \mathbf{r}_j\right| \le h \quad \left|\mathbf{r}_i - \mathbf{r}_j\right| \le h \\ 0 & \left|\mathbf{r}_i - \mathbf{r}_j\right| > h \end{cases} \tag{45}$$

where s_{ij} is the strength of the particle-particle interaction. In this model, the immiscible behavior of the CO_2 and brine phases is simulated with the interaction strengths between particles of same type (s_{ij}) larger than that of different fluids (brine and CO_2). Wetting and non-wetting are represented by a set of stationary particles that have different strengths s_{solids} with respect to brine or CO_2. With this method, Bandara et al. (2011) were able to reproduce the processes by which isolated CO_2 bubbles are left trapped in the pore space: division, leave behind, snap-off (Fig. 5b), and coalescence.

Ovaysi and Piri (2013) used a modified moving particle method to simulate multicomponent advection, diffusion, and electrochemical migration of CO_2 and SO_2, while also considering aqueous equilibrium complexation reactions associated with these species. The simulation was performed on a domain generated from microtomographic images of Berea and Bentheimer sandstones.

Although a significant body work exists in the application of SPH in reactive systems with mineral-precipitation processes that result in evolving pore geometry, in particular by A. Tartakovsky and co-workers (Tartakovsky et al. 2007a,b), widespread application of this method to CO_2 problems is still not available in the literature. The ability of particle methods to simulate processes with dynamically evolving interfaces, e.g., fluid-solid (Tartakovsky et al. 2007a,b), fluid-fluid-solid employing methods akin to molecular dynamics (Bandara et al. 2011), or fluid-fluid with the Cahn-Hilliard diffuse interface theory (Xu et al. 2009) suggest they are a useful tool to address coupled simulation of the physical and chemical processes associated with CO_2 injection and sequestration. However, one of the main challenges faced by particle methods is the size of problems that can be addressed. The simulations by Bandara et al. (2011) and Tartakovsky et al. (2007a,b) were performed on 2D domains with mineral grains represented as circular shapes, while the work of Ovaysi and Piri (2013) simulates a relatively small domain (0.51×0.51×1.09 mm). This challenge can be overcome with the use of massively parallel implementations such as in the recent application for single-component conservative transport in a 3D sphere pack of dimensions 2×2×4 mm (Scheibe et al. 2013).

Direct numerical simulation

Direct numerical simulation involves the use of conventional discretization methods to solve the flow, transport and geochemical equations introduced in earlier sections. These Eulerian, mesh-based methods include finite volume, finite differences and finite element methods (Patankar 1980; de Marsily 1986; Zienkiewicz et al. 2005). Complex geometries of the pore space that do not evolve with time can be captured well and simulated efficiently with the mesh-based methods. However, pore scale processes associated with CO_2 sequestration involve multiple evolving interfaces. Specific methods must be employed to capture within the resolution of the discretization the moving interfaces. These methods can be broadly classified between those that track the interface, such the volume-of-fluid method for multiphase processes (Huang et al. 2005; Huang and Meakin 2008; Raeini et al. 2012), or the embedded

boundary methods for mineral-fluid interfaces (Miller and Trebotich 2012; Molins et al. (2012) (see Fig. 17), and those that mark both sides of the interface by means of a level set function e.g., for geometry update (Li et al. 2008, 2010) or a phase-field variable, e.g., for geometry evolution (Xu and Meakin 2008, 2011) or for multiphase flow according to the Cahn Hilliard model (Bogdanov et al. 2011).

While multiphase application of direct numerical simulation methods to the processes that take place in petroleum reservoirs are more common (e.g., Raeini et al. 2012), applications to the CO_2 problem are mostly work in progress. The effect of a single phase flow of a solution rich in CO_2 on the dissolution of calcite in a 0.5×0.5×1.5 mm 3D geometry of packed spheres has been studied by Flukiger and Bernard 2009) using a finite volume method.

EMERGENT PROCESSES

Physical evolution of the pore space

As a result of dissolution or precipitation associated with CO_2 injection and sequestration, the mineral surface evolves with time, thus modifying the pore space. Assuming uniform dissolution-precipitation of a single mineral phase the velocity of the moving interface $\mathbf{u}^{\Gamma}$ can be described by (e.g., Li et al. 2010)

$$\mathbf{u}^{\Gamma} \cdot \mathbf{n} = \frac{\overline{r}}{\rho_m} \tag{46}$$

where ρ_m is the molar density of the mineral phase and $\overline{r}$ is the reaction rate.

As a result of these changes in the pore space, the flow paths available for the transport of reactants evolve with time. Evolution of the flow paths in turn may hinder further reaction progress in the case of clogging or enhance it by opening new flow channels. This pore space evolution depends on the relative importance of reactive and transport processes. The Damköhler numbers are usually employed to evaluate the relative importance of transport and reactions (see Eqns. 16 and 17). The length scale for pore scale studies is typically given by the grain or pore size, which suggests that kinetics and diffusion become increasingly important at these and smaller scales—the local equilibrium assumption, for example, is much harder to justify as a general approach at the pore scale.

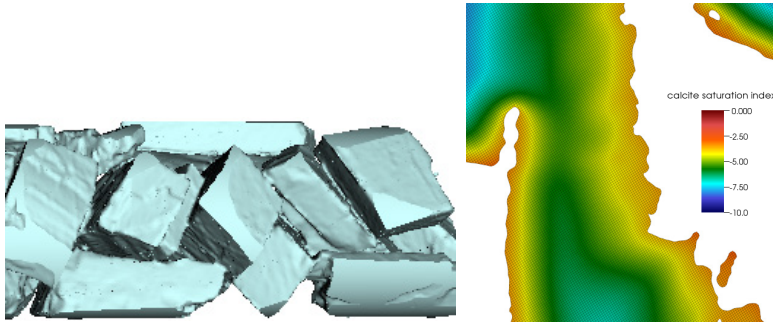

Figure 17. (a) Portion of the computational domain constructed from XCMT data showing mineral grains (~200 μm in size) represented as embedded boundaries on a Cartesian grid using the methods in Trebotich et al. (2008) and Molins et al. (2012). The capillary tube was 0.7 cm in length and 0.5 mm in diameter, with approximately 1.3 billion grid points used to provide a spatial resolution of 1.12 μm. (b) Diffusion boundary layer around dissolving calcite grain as shown by the calcite saturation index (log Q/K_{eq}) in the solution in the pore space (Molins et al. 2012).

A well-known phenomenon is that of formation of wormholes as a result of the reactive infiltration instability (Ortoleva et al. 1987; Hoefner and Fogler 1988; Steefel and Lasaga 1990; Daccord et al. 1993; Fredd and Fogler 1998; Steefel and Maher 2009; Smith et al. 2013a). In this emergent process, mineral dissolution under transport-controlled conditions leads to the more rapid growth of high flow velocity pathways over slower pathways. This is a form of geochemical self-organization or pattern formation that is characteristic of advection-dominant (high Péclet number) reactive flow systems. As shown experimentally by Hoefner and Fogler (1988) and computationally by Steefel and Lasaga (1990) and Steefel and Maher (2009), the wormholes become more highly ramified and ultimately diffuse when the Damköhler number is small (surface reaction-controlled) for a given system.

The injection of CO_2 at depth drives the subsurface environment into far from equilibrium, undersaturated conditions, similar to the environment in the near-well bore region when matrix acidization is used for the purposes of permeability enhancement (Cohen et al. 2008). Smith et al. 2013a) demonstrated that wormholing of a caprock sample consisting of dolomite and anhydrite occurred when CO_2-acidified solution was injected. Heterogeneous dissolution at the pore scale has been observed in experiments performed under conditions relevant for CO_2 sequestration: at pCO_2 = 10 MPa and 100 °C for an oolitic limestone from the Mondeville formation (Paris basin, France) (Luquot and Gouze 2009) and at pCO_2 = 3 MPa and 60 °C for a Vuggy limestone from the Weyburn-Midale field, Saskatchewan, Canada (Carroll et al. 2013). At lower pCO_2 values (0.7 MPa), such features are not observed for the same oolitic limestone from the Mondeville formation (Luquot and Gouze 2009). Heterogeneous dissolution was not observed at pCO_2 = 3 MPa and 60 °C for a Midale Marly dolostone from the Weyburn-Midale field that contained a much higher abundance of dolomite relative to calcite and higher initial porosity and permeability compared to the Vuggy limestone (Carroll et al. 2013), although this is likely due to the combination of slower reaction kinetics and smaller experimental length scales such that the effective Damköhler number remains small (Fig. 11). Carroll et al. (2013) proposed that their data could be described by a porosity-permeability relationship of the form

$$k = k_o \left(\frac{\phi}{\phi_0} \right)^3 \tag{47}$$

that captures the evolution of permeability associated with reaction-induced porosity (ϕ) change.

A number of different formulations have been used for a porosity-permeability relationship in reactive rocks, although it should be pointed out that few have been tested carefully against reaction-induced (either dissolution or precipitation) permeability change. Exceptions are the experimental study of Armstrong et al. (2012) and the computational study of Molins et al. (2011). In modeling studies of reaction-induced porosity and permeability change (note that we do not specifically focus on CO_2 here, since the behavior should be fairly general for acidified brines when the dissolution of carbonate is involved), the Kozeny-Carman equation was used by Steefel and Lasaga (1990) to simulate wormholing

$$k = C_k \frac{\phi^3}{(1-\phi)^2} \frac{1}{S^2} \tag{48}$$

where S is the surface area of the solids per unit volume solids, and thus proportional to the inverse of the average grain diameter (Bear 1988). An equivalent formulation is based on a specification of the initial porosity and permeability

$$k_t = k_o \frac{(\phi_t)^3}{\left(1-\phi_t\right)^2} \frac{\left(1-\phi_0\right)^2}{(\phi_0)^3} \tag{49}$$

where the subscript *t* refers to the permeability or porosity over time and the subscript 0 refers to the initial permeability or porosity. For rocks in which the porosity and permeability is dominated by approximately planar fractures, a cubic law relationship has been proposed and used (Phillips 1991; Steefel and Lasaga 1994; Steefel and Lichtner 1998)

$$k = \frac{\phi_f \delta^3}{12} \tag{50}$$

where ϕ_f is the fracture porosity and δ is the average fracture aperture. Other formulations have been proposed, included a simple power law relationship (Noiriel et al. 2004)

$$k \propto \phi^n \tag{51}$$

with the exponent *n* decreasing continuously with time as dissolution of the microcrystalline phase progressed as a result of injection of CO_2-rich, acidic solution. The same concepts can be used to model the permeability of caprock fractures (Ellis et al. 2011; Deng et al. 2013; Elkhoury et al. 2013) as discussed by Fitts and Peters (2013, this volume).

In the Noiriel et al. (2004) study, once the microcrystalline phase in the limestone was locally depleted, dissolution shifted to the sparitic phase, resulting in a constant value of the constant n and a decrease in the roughness of the pore walls as recorded by XCMT analysis (Fig. 18).

Another set of limestone dissolution experiments that coupled XCMT to quantify pore structure changes with solution effluent analysis were undertaken by Luquot and Gouze (2009). They carried out experiments at three different flow rates, resulting in three different Damköhler numbers as evaluated across the length of the core sample. At the highest flow rate (and thus lowest Damköhler number designated as D3), no gradients in porosity developed—dissolution was effectively homogeneous over the length of the core (Fig. 19).

As discussed initially by Hoefner and Fogler (1988) and Steefel and Lasaga (1990), the case of low Damköhler number flow and reaction results in diffuse reaction with little tendency to "wormhole". At lower flow rates and higher Damköhler number, Luquot and Gouze (2009)

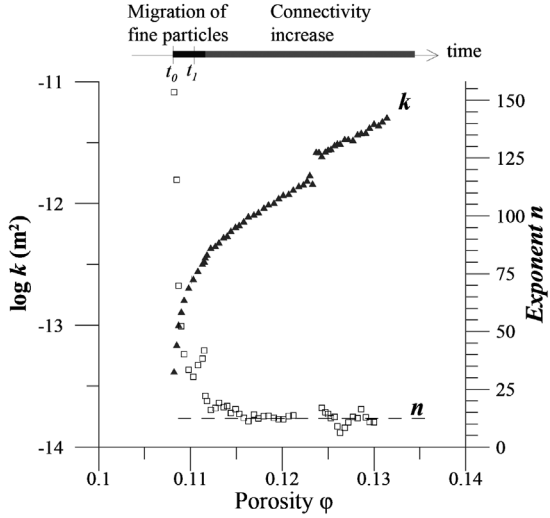

Figure 18. Permeability (log axis) and power law exponent *n* versus porosity for CO_2-induced dissolution of a limestone (Noiriel et al. 2004).

demonstrated that gradients in reaction developed and the dominant dissolution feature were fingers or wormholes that resulted in highly heterogeneous porosity development. XCMT images of the three Damköhler regimes (D1>D2>D3) investigated in the study are shown in Figure 20, in this case with the range in the Damköhler number resulting from the use of different flow velocities (in contrast to the study by Carroll et al. (2013), where reactivity was the adjustable parameter).

Analyzing these experimental results, Gouze and Luquot (2011) concluded that the low Damköhler experiment in which the dissolution was homogeneous resulted in a decrease in tortuosity, while the higher Damköhler number experiment (heterogeneous porosity develop-

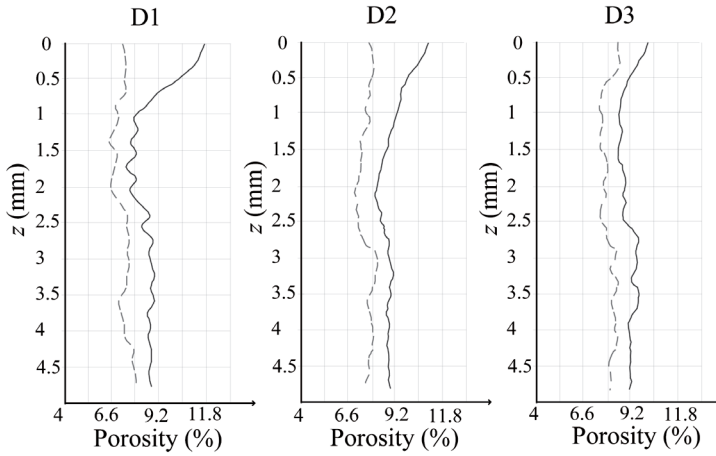

Figure 19. X-Y averaged porosity profiles for three different Damköhler numbers (D1>D2>D3), with pre-experiment results shown with a dotted line, post-experiment results shown with a solid line (Luquot and Gouze 2009).

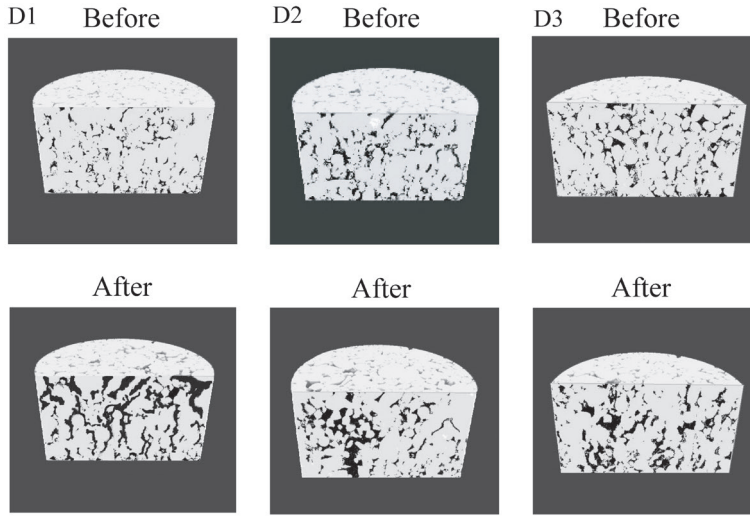

Figure 20. XCMT before and after injection of a CO_2-acidified solution for the 3 Da numbers (Luquot and Gouze 2009).

ment) also resulted in a tortuosity decrease, but accompanied by an increase in hydraulic radius. They proposed a porosity-permeability relationship based on a percolation threshold in which a critical porosity, ϕ_c, is defined

$$k(t) = k_o \left[\phi(t) - \phi_c\right]^{\alpha} \left(\frac{B_\tau}{\tau}\right) \tag{52}$$

where α is the power dependence of the relationship that typically varies over time, τ is the tortuosity and B_τ is an experimentally determined coefficient. Based on their experimental data, they estimated a critical porosity corresponding to the percolation threshold of 5.9%. Carroll et al. (2013) pursued this general approach of combining XCMT to quantify pore structure changes with effluent chemistry to determine bulk reaction rates.

Chemical evolution of the pore space: reactive surface area

The reaction rate in Equation (36) and (46) is expressed per units of physical interfacial area between the mineral and the fluid phase. It can be related to the actual rate r in Equation (33) (per units of reactive surface area) via a parameter ψ (m^2 physical surface m^{-2} reactive surface). For a surface with a heterogeneous mineralogy, ψ represents the portion of surface with mineral reactions, but ψ can also be used to represent enhanced reactivity due to surface roughness not resolved at the pore scale, i.e., nanometer scale roughness, or atomic scale density of reactive sites (Bracco et al. 2013). The reactive surface area has traditionally been estimated from adsorption isotherms (Brunauer-Emmett-Teller, or BET) (Brunauer et al. 1938) or geometrically based on the average physical grain size. However, these approaches do not account for the hydrologic accessibility of the reactive phases within the pore structure (Peters 2009; Landrot et al. 2012).

In a study by Noiriel et al. (2009) of limestone infiltrated by CO_2-rich solution, Sr and Ca release rates were used to assess the relative dissolution rates of the sparitic and microcrystalline phases in the limestone subjected to infiltration of CO_2-rich solution. The results demonstrate that the RSA of the sparite in this case increased greatly, as recorded by the rate of dissolution of that phase over time. In contrast, its geometric surface area, as recorded by XCMT, decreased slightly. To describe the time dependent behavior, Noiriel et al. (2009) proposed a "sugar cube" model in which disaggregation of the granular network (presumably resulting in the large increase in RSA of the sparitic phase, which is now exposed to more of the reactive infiltrating solution) precedes dissolution of the individual grains of sparite. Noiriel et al. (2009) described the time-dependent RSA, Sr, mathematically with the expression

$$S_r = \left(S_{r0} + S_{rm}\left[1 - \left(\frac{C}{C_0}\right)^{n_1}\right]^{n_2}\right)\left(\frac{C}{C_0}\right)^{n_3} \tag{53}$$

where S_{r0} is the initial surface area, S_{rm} is the maximum surface area given by the sum of all of the surface areas of the individual particles, C is the concentration of the mineral calcite over time, C_0 is its initial concentration, and n_1, n_2, and n_3 are empirical coefficients that depend on the geometry of the aggregate.

Focusing on the low Damköhler case (D3) in which reaction rates over the length of the core are largely homogeneous, Luquot and Gouze (2009) proposed an expression for the average effective reactive surface area (m^2 mineral m^{-3} porous medium) over time, $\overline{\sigma}(t)$

$$\overline{\sigma}(t) = \overline{\sigma}^{*}\left(\frac{\overline{\phi}(t)}{\overline{\phi}^{*}}\right)^{-w} \tag{54}$$

where $\overline{\sigma}^{*}$ and $\overline{\phi}^{*}$ are the initial reactive surface area and the porosity, respectively, and w is an

experimentally-determined positive coefficient. This leads to an expression for the porosity change with time Luquot and Gouze (2009) of the form

$$\overline{\phi}(t) = \overline{\phi}^{*}\left(1 + A(w)t\right)^{1/w} \tag{55}$$

with the coefficient $A(w)$ is given by

$$A(w) = \overline{r}'\,\overline{\sigma}^{*}\,vw \tag{56}$$

where w and $\overline{r}'$ (the average reaction rate) characterize the reaction regime and v is the molar volume of calcite. According to these expressions, this leads to an evolution of the reactive surface area in the limestone for the three Damköhler cases shown in Figure 21.

For the case of carbonate precipitation that occurs when carbonate-forming metal cations and alkalinity are available from either mineral dissolution or the local brine, Noiriel et al (2012) investigated the change in reactive surface area using two approaches: 1) based on XCMT mapping of mineral-fluid interfaces, and 2) based on the ability to capture time-dependent reactivity with a micro-continuum model. Based on an XCMT analysis using a voxel size of 4.4 microns at the Advanced Light Source (Lawrence Berkeley National Laboratory), surface area was determined geometrically by counting the interfaces between solid (either glass spheres or calcite spar) and fluid (porosity). The data show a distinct nucleation or surface roughening event between the column inlet and a distance of about 2 mm downstream in the core (Fig. 22), a result consistent with the fact that the supersaturation was highest in this portion of the column (which gradually decreases downstream as a result of reaction).

The conclusion that reactive surface area increased locally in the column due to nucleation and/or crystal growth was reinforced by micro-continuum modeling results using the code CrunchFlow (Noiriel et al. 2012). Figure 23 contrasts the ability of the micro-continuum model to capture the increase in calcite volume fraction based on the XCMT. The panel on the left uses only the initial BET-determined specific surface area value of 0.012 m^2/g for the calcite and thus underpredicts significantly the amount of carbonate accumulated in the first 2 mm of the column (supersaturated solution is injected from the left). In contrast, the panel on the right uses a specific surface area value of 0.21 m^2/g for newly formed calcite based on a post-experiment five point krypton BET analysis. Note that the modeling here is based entirely

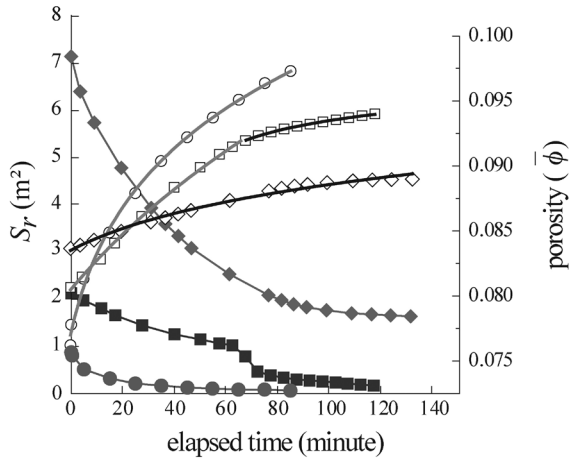

Figure 21. Reactive surface area (S_r filled symbols) and porosity (ϕ, empty symbols) versus elapsed time for experiments D1 (circles), D2 (squares), and D3 (diamonds) investigated by Gouze and Luquot (2011).

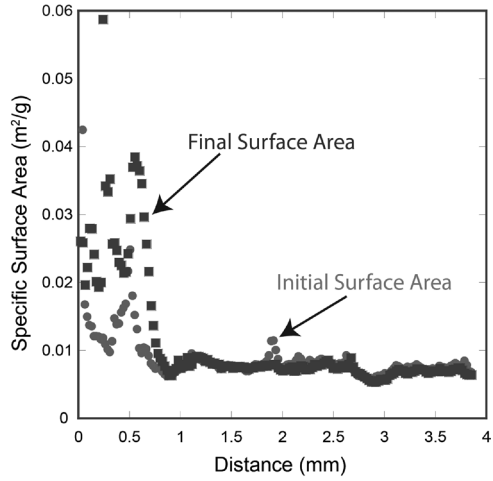

Figure 22. Nucleation or surface roughening event with 2 mm of the column inlet, which was injected with a supersaturated solution of sodium bicarbonate and calcium chloride (Noiriel et al. 2012). The initial specific surface area based on the XCMT mapping is shown as solid circles, while the final specific surface area is represented by solid squares.

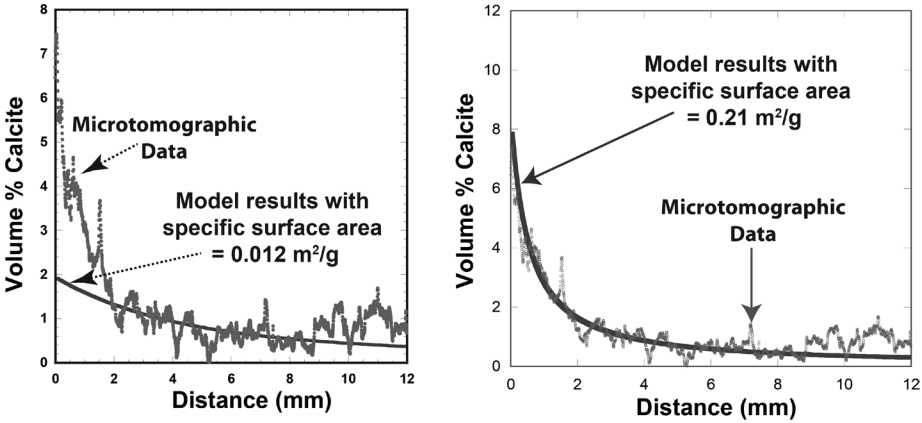

Figure 23. Comparison of micro-continuum modeling of the accumulation of calcite (volume %) using the code CrunchFlow for the case in which a specific surface based on the initial BET determination on unreacted calcite spar (Left Panel) and for the case in which a higher specific surface area based on post-experiment BET determination is used. The results do not involve any fitting of the microtomographic data, as they make use of independently determined parameters (rate constants, BET surface area, porosity). The results demonstrate the importance of the spatial and temporal evolution of reactive surface area (Noiriel et al. 2012).

on independently determined parameters and makes no attempt to calibrate these parameters based on the XCMT data.

CO_2 invasion

The invasion of CO_2 in the brine-saturated porous medium is an energetically unfavorable process due to the low viscosity ratio (M) between CO_2 and brine. Under these conditions, the front propagation during the immiscible displacement is unstable, and fingering, an emergent process, is observed. Depending on the dimensionless capillary number (Ca), capillary fingering or viscous fingering may develop. Capillary fingering takes place when the capillary force of the wetting fluid is the dominant force and is characterized by fluid phase geometries characterized by wider lateral nonwetting (CO_2) phase flowpaths. Viscous fingering takes place

when the viscous driving force of the nonwetting fluid is lower and is characterized by narrow flowpaths that propagate forward rather than laterally. Figure 24 illustrates viscous fingering (top left) and capillary fingering (bottom left) compared to stable displacement (top right) in the Pore Network simulations of Ellis and Bazylak (2013).

Micromodel experiments by Wang et al. (2013) showed that capillary fingering was the dominant mechanism for all $scCO_2$ injection rates in a continuous-rate experiment, where the rate was increased after quasi-steady conditions were reached for a given injection rate. However, in a discontinuous-rate injection, where the micromodel was saturated with brine before each $scCO_2$ injection rate was imposed, crossover from capillary to viscous fingering was observed for logCa = −5.91 to −5.21. This resulted in a large decrease in $scCO_2$ saturation. The discontinuous-rate experimental results confirmed the decrease in nonwetting fluid saturation during crossover from capillary to viscous fingering predicted by numerical simulations carried out by Lenormand et al. (1988).

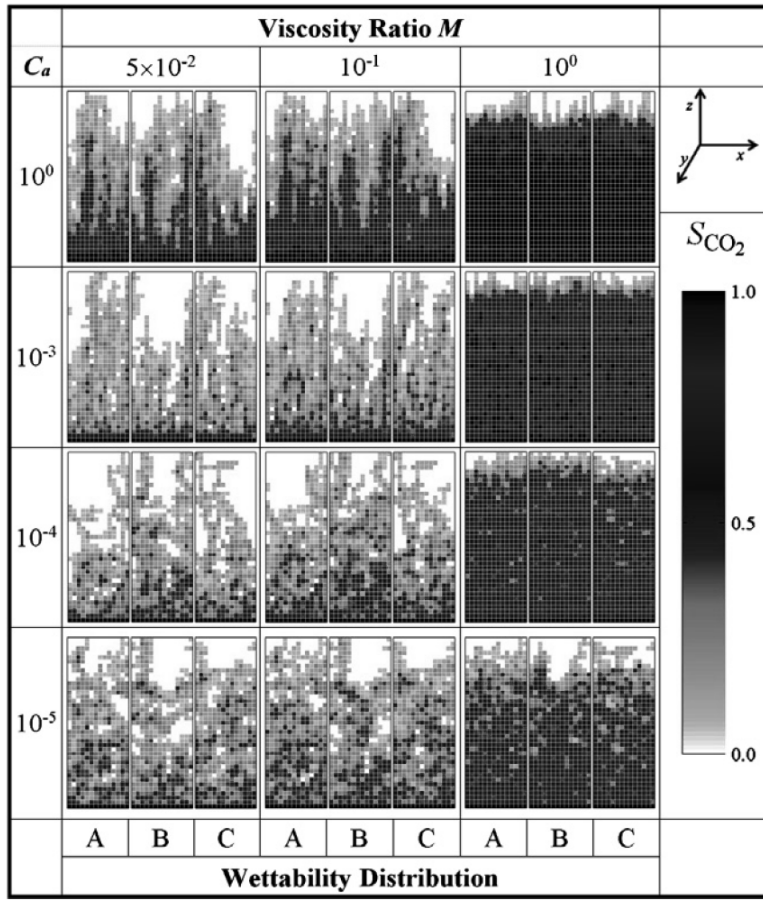

Figure 24. Pore network simulation results from Ellis and Bazylak (2013) showing the saturation patterns for various Ca, M, and wettability conditions A (homogeneous), B (heterogeneous), and C (homogeneous). The grey scale values indicate the averaged relative CO_2 saturation in the direction normal to the page. The bottom face is the inlet in each case, and the mean pore diameter is 5 μm. (The reader is referred to the web version of this article for a color version.)

While the experiments by Wang et al. (2013) were for a homogeneous medium, heterogeneity can have a significant effect on CO_2 invasion. Zhang et al. (2011) investigated liquid CO_2 (LCO_2) water displacement in a pore network micromodel with two distinct permeability zones. LCO_2 displaced water only in the high permeability zone at low injection rates, while at high injection rates, LCO_2 displaced water in the low permeability zone with capillary fingering as the dominant mechanism. Microtomographic images of the distribution of CO_2 in a flooding experiment by Blunt et al. (2013) suggests that CO_2 is trapped in the pore space surrounded by brine as clusters of all sizes, from small blobs in the center of a single pore to ramified, extensive ganglia spanning several pores.

Using pore network modeling of multiphase flow, Ellis and Bazylak (2013) investigated the effects of contact angle heterogeneity on CO_2 saturation (S_{CO_2}) in a system containing quartz and mica over a range of viscosity ratios (M) and capillary numbers (Ca) relevant to carbon sequestration (Fig. 24). Simulations showed that at $Ca = 10^{-4}$, CO_2 saturations were 20% higher for heterogeneous contact angle distributions compared to similar networks with homogeneous distributions. The results were quantified based on a power law correlation similar to that proposed by Al-Fossail and Handy (1990) relating the dimensionless M to the brine saturation. The power-law expression has the form

$$S_{CO_2} = AM^n \tag{57}$$

where A and n are fitting parameters. Good qualitative agreement was found between fitted curves and simulated results, with fitting parameters differing between homogeneous and heterogeneous cases only at low capillary numbers.

NEW DIRECTIONS

Despite the length of this chapter, in fact the research into pore scale processes associated with CO_2 injection and sequestration has only just scratched the surface of the topic. Much remains to be done to achieve a mechanistic understanding of the pore scale processes that could be captured in a defensible predictive model. The field is clearly far from mature. For example, the characterization of pore scale physical and chemical properties at sufficiently high resolution that the data can be incorporated into true pore scale models is only just beginning—collecting 3D geochemical data at high spatial resolution is arguably the biggest challenge here. While the resolution available for mapping of the physical structure of porous media is improving, there is a corresponding tradeoff in the size of the sample that can be investigated. This is a problem when one of the objectives is to upscale pore scale parameters and processes to the larger continuum scale. An even more significant challenge will be to develop and apply methods for chemical/mineralogical mapping in 3D—as discussed in this chapter, most of the chemical mapping methods are based on 2D geometries. There is also a need to further develop techniques that can span a significant range of spatial scales, particularly so as to be able to resolve the entire pore size distribution. Right now, SANS and USANS are probably the best techniques available, but they produce statistical data that can only be interpreted in terms of the 3D porous medium geometry using model assumptions. Without these new techniques, the nanoporosity within the subsurface sediment, which contributes so much in the way of reactivity to the porous medium, cannot be factored in.

To go with the advances in characterization, we need a new generation of pore scale models that scale efficiently on high performance computing frameworks. While the pore network models have already demonstrated their usefulness in analyzing pore scale dynamics, especially for multi-phase systems, there is a clear need for fully resolved pore scale models where this is possible. This implies that work on conceptual and computational models for pore scale physical and chemical processes, especially for the case of multi-phase flow characterizing CO_2

injection and sequestration, will continue. At the pore scale, there is a need (and even requirement) to be able to address full multicomponent chemistry, while resolving pore scale gradients in flow velocity, solute concentration, and reaction rates.

Probably the single most important process coupling that needs to be explored further is that between chemical and mechanical processes. The force of crystallization needs to be factored into pore scale models and the associated stress field. Conversely, the stress field needs to affect the thermodynamics and kinetics of the biogeochemical reaction networks. Further progress is also needed on the explicit incorporation of microbial communities into pore scale models, since these communities (which compete and collaborate) may regulate the overall chemistry (especially redox) of the subsurface system.

The upside here is that this approach has the potential to finally provide mechanistic explanations for many of the long-standing conundrums in reactive geochemistry in porous media, not least of which is the so-called discrepancy between laboratory and field rates. It is clear that the pore scale approach offers the chance to understand reaction-induced porosity, permeability, and reactivity change, although one still expects that molecular to nanometer scale effects will need to be integrated into the otherwise mesoscale (pore scale) studies. The combination of new microscopic characterization, experimental, and modeling approaches presents the opportunity for a new paradigm in the cross disciplinary fields of geochemistry, hydrology, and geophysics. Of course, this progress goes well beyond the narrower topic of subsurface CO_2 injection and sequestration and in fact will improve our understanding of water-rock interaction as a whole.

ACKNOWLEDGMENTS

This material is based upon work supported as part of the Center for Nanoscale Control of Geologic CO_2, an Energy Frontier Research Center funded by the US Department of Energy, Office of Science, Office of Basic Energy Sciences under Award No. DE-AC02-05CH11231. Additional support for the chapter preparation was provided by the Office of Basic Energy Sciences (Geosciences Program) of the U.S. Department of Energy. We are also grateful for the constructive reviews of the manuscript provided by Hongkyu Yoon, Christian Huber, and Ian Bourg.

REFERENCES

Al-Fossail K, Handy LL (1990) Correlation between capillary number and residual water saturation. J Colloid Interface Sci 134:256-263

Anovitz L, Cole D, Rother G, Allard L, Jackson A, Littrell K (2013) Diagenetic changes in macro- to nano-scale porosity in the St. Peter Sandstone: An (ultra) small angle neutron scattering and backscattered electron imaging analysis. Geochim Cosmochim Acta 102:280-305

Appelo CAJ, Wersin P (2007) Multicomponent diffusion modeling in clay systems with application to the diffusion of tritium, iodide, and sodium in Opalinus clay. Environ Sci Technol 41:5002-5007

Armstrong R, Ajo-Franklin J (2011) Investigating biomineralization using synchrotron based X-ray computed microtomography. Geophys Res Lett 38:L08406, doi: 10.1029/2011GL046916

Armstrong RT, Porter ML, Wildenschild D (2012) Linking pore-scale interfacial curvature to column-scale capillary pressure. Adv Water Resour 46:55-62

Audigane P, Gaus I, Czernichowski-Lauriol I, Pruess K, Xu T (2007) Two-dimensional reactive transport modeling of CO_2 injection in a saline aquifer at the Sleipner site, North Sea. Am J Sci 307:974-1008

Balhoff M, Thomas S, Wheeler M (2008) Mortar coupling and upscaling of pore-scale models. Comput Geosci 12:15-27

Bandara UC, Tartakovsky AM, Palmer BJ (2011) Pore-scale study of capillary trapping mechanism during CO_2 injection in geological formations. Int J Greenhouse Gas Control 5:1566-1577

Battiato I, Tartakovsky DM, Tartakovsky AM, Scheibe T (2011) Hybrid models of reactive transport in porous and fractured media. Adv Water Resour 34:1140-1150

Bauer D, Youssef S, Fleury M, Bekri S, Rosenberg E, Vizika O (2012) Improving the estimations of petrophysical transport behavior of carbonate rocks using a dual pore network approach combined with computed microtomography. Transport Porous Med 94:505-524

Bear J (1988) Dynamics of Fluids in Porous Media. Dover Books on Physics and Chemistry, Dover

Benezeth P, Palmer DA, Anovitz LM, Horita J (2007) Dawsonite synthesis and reevaluation of its thermodynamic properties from solubility measurements: Implications for mineral trapping of CO_2. Geochim Cosmochim Acta 71:4438-4455

Ben-Yaakov S (1972) Diffusion of sea water ions-I. Diffusion of sea water into a dilute solution. Geochim Cosmochim Acta 36:1395-1406

Bhatnagar PL, Gross EP, Krook M (1954) A model for collision processes in gases. I. Small amplitude processes in charged and neutral one-component systems. Phys Rev 94:511-525

Blunt MJ (2001) Flow in porous media - pore-network models and multiphase flow. Curr Opin Colloid Interface Sci 6:197-207

Blunt MJ, Bijeljic B, Dong H, Gharbi O, Iglauer S, Mostaghimi P, Paluszny A, Pentland C (2013) Pore-scale imaging and modelling. Adv Water Resour 51:197-216

Blunt MJ, Jackson MD, Piri M, Valvatne PH (2002) Detailed physics, predictive capabilities and macroscopic consequences for pore-network models of multiphase flow. Adv Water Resour 25:1069-1089

Bogdanov I, Guerton F, Kpahou J, Kamp A (2011) Direct pore-scale modeling of two-phase flow through natural media. *In:* Proceedings of the 2011 COMSOL Conference in Stuttgart; http://www.comsol.com/paper/download/83497/bogdanov_paper.pdf

Boschi C, Dini A, Dallai L, Ruggieri G, Gianelli G (2009) Enhanced CO_2-mineral sequestration by cyclic hydraulic fracturing and Si-rich fluid infiltration into serpentinites at Malentrata (Tuscany, Italy). Chem Geol 265:209-226

Boudreau BP, Meysman FJ, Middelburg JJ (2004) Multicomponent ionic diffusion in porewaters: coulombic effects revisited. Earth Planet Sci Lett 222:653-666

Bracco JN, Stack AG, Steefel CI (2013) Upscaling calcite growth rates from the mesoscale to the macroscale. Environ Sci Technol 47:7555-7562

Brimhall (1979) Lithologic determination of mass transfer mechanisms of multiple-stage porphyry copper mineralization at Butte, Montana; vein formation by hypogene leaching and enrichment of potassium-silicate protore. Econ Geol 74:556-589

Brunauer S, Emmett PH, Teller E (1938) Adsorption of gases in multimolecular layers. J Am Chem Soc 60:309-319

Burch T, Nagy K, Lasaga A (1993) Free energy dependence of albite dissolution kinetics at 80°C and pH 8.8. Chem Geol 105:137-162

Cahn JW, Hilliard JE (1958) Free energy of a nonuniform system. I. Interfacial free energy. J Chem Phys 28:258-267

Carlson WD (2006) Three-dimensional imaging of earth and planetary materials. Earth Planet Sci Lett 249:133-147

Carroll SA, McNab WW, Dai Z, Torres SC (2013) Reactivity of Mount Simon sandstone and the Eau Claire shale under CO_2 storage conditions. Environ Sci Technol 47:252-261

Chalbaud C, Robin M, Lombard JM, Martin F, Egermann P, Bertin H (2009) Interfacial tension measurements and wettability evaluation for geological CO_2 storage. Adv Water Resour 32:98-109

Chen C, Zhang D (2010) Pore-scale simulation of density-driven convection in fractured porous media during geological CO_2 sequestration. Water Resour Res 46:W11527, doi: 10.1029/2010WR009453

Chen S, Doolen G (1998) Lattice Boltzmann method for fluid flows. Annu Rev Fluid Mech 30:329-364

Chou L, Garrels R, Wollast R (1989) Comparative-study of the kinetics and mechanisms of dissolution of carbonate minerals. Chem Geol 78:269-282

Cohen CE, Ding D, Quintard M, Bazin B (2008) From pore scale to wellbore scale: Impact of geometry on wormhole growth in carbonate acidization. Chem Eng Sci 63:3088-3099

Crawshaw JP, Boek ES (2013) Multi-scale imaging and simulation of structure, flow and reactive transport for CO_2 storage and EOR in carbonate reservoirs. Rev Mineral Geochem 77:431-458

Daccord G, Lenormand R, Liétard O (1993) Chemical dissolution of a porous medium by a reactive fluid–I. Model for the "wormholing" phenomenon. Chem Eng Sci 48:169-178

Daval D, Martinez I, Corvisier J, Findling N, Goffe B, Guyot F (2009) Carbonation of Ca-bearing silicates, the case of wollastonite: Experimental investigations and kinetic modeling. Chem Geol 265:63-78

de Gennes PG (1985) Wetting: statics and dynamics. Rev Mod Phys 57:827-863

de Marsily G (1986) Quantitative Hydrogeology: Groundwater Hydrology for Engineers. Academic Press

De Yoreo JJ, Vekilov PG (2003) Principles of crystal nucleation and growth. Rev Mineral Geochem 54:57-93

De Yoreo JJ, Waychunas GA, Jun Y-S, Fernandez-Martinez A (2013) *In situ* investigations of carbonate nucleation on mineral and organic surfaces. Rev Mineral Geochem 77:229-257

Deng H, Ellis BR, Peters CA, Fitts JP, Crandall D, Bromhal GS (2013) Modifications of carbonate fracture hydrodynamic properties by CO_2-acidified brine flow. Energy Fuels 27:4221-4231

DePaolo DJ, Cole DR (2013) Geochemistry of geologic carbon sequestration: an overview. Rev Mineral Geochem 77:1-14

Druhan JL, Steefel CI, Williams KH, DePaolo DJ (2013) Calcium isotope fractionation in groundwater: Molecular scale processes influencing field scale behavior. Geochim Cosmochim Acta 119:93-116

Dutta T, Tarafdar S (2003) Fractal pore structure of sedimentary rocks: Simulation by ballistic deposition. J Geophys Res-Solid Earth 108(B2):2062, doi: 10.1029/2001JB000523

Einstein A (1956) Investigations on the Theory of the Brownian Movement. R Firth, translated by AD Cowper, New York: Dover

Elkhoury JE, Ameli P, Detwiler RL (2013) Dissolution and deformation in fractured carbonates caused by flow of CO_2-rich brine under reservoir conditions. Int J Greenhouse Gas Control 16, Supplement 1:S203-S215

Ellis B, Peters C, Fitts J, Bromhal G, McIntyre D, Warzinski R, Rosenbaum E (2011) Deterioration of a fractured carbonate caprock exposed to CO_2-acidified brine flow. Greenhouse Gases Sci Technol 1:248-260

Ellis JS, Bazylak A (2012) Dynamic pore network model of surface heterogeneity in brine-filled porous media for carbon sequestration. Phys Chem Chem Phys 14:8382-8390

Ellis JS, Bazylak A (2013) Investigation of contact angle heterogeneity on CO_2 saturation in brine-filled porous media using 3D pore network models. Energy Convers Manage 68:253-259

Er V, Babadagli T, Xu Z (2010) Pore-scale investigation of the matrix fracture interaction during CO_2 injection in naturally fractured oil reservoirs. Energy Fuel 24:1421–1430

Ewing RP, Berkowitz B (1998) A generalized growth model for simulating initial migration of dense non-aqueous phase liquids. Water Resour Res 34:611-622

Fatt I (1956) The network model of porous media. 1. Capillary pressure characteristics. Petroleum Transactions, AIME 207:144-159

Feder J (1988) Fractals, Physics of Solids and Liquids. Springer

Felmy AR, Weare JH (1991) Calculation of multicomponent ionic diffusion from zero to high concentration: I. The system Na-K-Ca-Mg-Cl-SO_4-H_2O at 25°C. Geochim Cosmochim Acta 55:113-131

Fitts JP, Peters CA (2013) Caprock fracture dissolution and CO_2 leakage. Rev Mineral Geochem 77:459-479

Flukiger F, Bernard D (2009) A new numerical model for pore scale dissolution of calcite due to CO_2 saturated water flow in 3D realistic geometry: Principles and first results. Chem Geol 265:171-180

Fredd CN, Fogler HS (1998) Influence of transport and reaction on wormhole formation in porous media. AIChE J 44:1933-1949

Gaus I, Audigane P, Andre L, Lions J, Jacquemet N, Durst P, Czernichowski-Lauriol I, Azaroual M (2008) Geochemical and solute transport modelling for CO_2 storage, what to expect from it? Int J Greenh Gas Con 2:605-625

Gebrehiwet T, Redden G, Fujita Y, Beig M, Smith R (2012) The effect of the CO_3^{2-} to Ca^{2+} ion activity ratio on calcite precipitation kinetics and Sr^{2+} partitioning. Geochem Trans 13:1, doi: 10.1186/1467-4866-13-1

Giambalvo ER, Steefel CI, Fisher AT, Rosenberg ND, Wheat CG (2002) Effect of fluid-sediment reaction on hydrothermal fluxes of major elements, eastern flank of the Juan de Fuca Ridge. Geochim Cosmochim Acta 66:173-1757

Gonzalez R, Woods R (2008) Digital Image Processing. Pearson/Prentice Hall

Gouze P, Luquot L (2011) X-ray microtomography characterization of porosity, permeability and reactive surface changes during dissolution. J Contam Hydrol 120-121:45-55

Hamm LM, Bourg IC, Wallace AF, Rotenberg B (2013) Molecular simulation of CO_2- and CO_3-brine-mineral systems. Rev Mineral Geochem 77:189-228

Hellevang H, Declercq J, Aagaard P (2011) Why is dawsonite absent in CO_2 charged reservoirs? Oil Gas Sci Technol 66:119-135

Hellmann R, Tisserand D (2006) Dissolution kinetics as a function of the Gibbs free energy of reaction: An experimental study based on albite feldspar. Geochim Cosmochim Acta 70:364-383

Hiorth A, Jettestuen E, Cathles L, Madland M (2013) Precipitation, dissolution, and ion exchange processes coupled with a lattice Boltzmann advection diffusion solver. Geochim Cosmochim Acta 104:99-110

Hoefner ML, Fogler HS (1988) Pore evolution and channel formation during flow and reaction in porous media. AIChE J 34:45-54

Huang H, Meakin P (2008) Three-dimensional simulation of liquid drop dynamics within unsaturated vertical Hele-Shaw cells. Water Resour Res 44: W03411, doi: 10.1029/2007WR006158

Huang H, Meakin P, Liu M (2005) Computer simulation of two-phase immiscible fluid motion in unsaturated complex fractures using a volume of fluid method. Water Resour Res 41:W12413, doi: 10.1029/2005WR004204

Hussain R, Pintelon T, Mitchell J, Johns M (2011) Using NMR displacement measurements to probe CO_2 entrapment in porous media. AIChE J 57:1700-1709

Jamtveit B, Meakin P (1999) Growth, Dissolution and Pattern Formation in Geosystems. Springer

Joekar-Niasar V, Hassanizadeh SM (2012) Analysis of fundamentals of two-phase flow in porous media using dynamic pore-network models: a review. Crit Rev Env Sci Technol 42:1895-1976

Jun YS, Giammar DE, Werth CJ (2013) Impacts of geochemical reactions on geologic carbon sequestration. Environ Sci Technol 47:3-8

Jung JW, Wan J (2012) Supercritical CO_2 and ionic strength effects on wettability of silica surfaces: equilibrium contact angle measurements. Energy Fuel 26:6053-6059

Kang Q, Lichtner PC, Zhang D (2007) An improved lattice Boltzmann model for multicomponent reactive transport in porous media at the pore scale. Water Resour Res 43:W12S14, doi: 10.1029/2006WR005551

Kang Q, Tsimpanogiannis IN, Zhang D, Lichtner PC (2005) Numerical modeling of pore-scale phenomena during CO_2 sequestration in oceanic sediments. Fuel Process Technol 86:1647-1665

Kim D, Peters CA, Lindquist WB (2011) Upscaling geochemical reaction rates accompanying acidic CO_2-saturated brine flow in sandstone aquifers. Water Resour Res 47:W01505, doi: 10.1029/2010WR009472

Kim Y, Wan J, Kneafsey TJ, Tokunaga TK (2012) Dewetting of silica surfaces upon reactions with supercritical CO_2 and brine: pore-scale studies in micromodels. Environ Sci Technol 46:4228-4235

Kneafsey TJ, Silin D, Ajo-Franklin JB (2013) Supercritical CO_2 flow through a layered silica sand/calcite sand system: Experiment and modified maximal inscribed spheres analysis. Int J Greenhouse Gas Control 14:141-150

Landrot G, Ajo-Franklin JB, Yang L, Cabrini S, Steefel CI (2012) Measurement of accessible reactive surface area in a sandstone, with application to CO_2 mineralization. Chem Geol 318-319:113-125

Lasaga AC (1979) The treatment of multi-component diffusion and ion pairs in diagenetic fluxes. Am J Sci 279:324-346

Lasaga A (1998) Kinetic Theory in the Earth Sciences. Princeton Series in Geochemistry. Princeton University Press

Lasaga AC (1981) Transition State Theory. Rev Mineral Geochem 8:135-168

Le Borgne T, Bolster D, Dentz M, de Anna P, Tartakovsky A (2011) Effective pore-scale dispersion upscaling with a correlated continuous time random walk approach. Water Resour Res 47:W12538, doi: 10.1029/2011WR010457

Lenormand R, Touboul E, Zarcone C (1988) Numerical-models and experiments on immiscible displacements in porous-media. J Fluid Mech 189:165-187

Li L, Steefel CI, Yang L (2008) Scale dependence of mineral dissolution rates within single pores and fractures. Geochim Cosmochim Acta 72:360-377

Li X, Huang H, Meakin P (2008) Level set simulation of coupled advection-diffusion and pore structure evolution due to mineral precipitation in porous media. Water Resour Res 44:W12407, doi: 10.1029/2007WR00674

Li X, Huang H, Meakin P (2010) A three-dimensional level set simulation of coupled reactive transport and precipitation/dissolution. Int J Heat Mass Transfer 53:2908-2923

Lindquist W, Venkatarangan A (1999) Investigating 3D geometry of porous media from high resolution images. Phys Chem Earth Part A 24:593-599

Lindquist WB, Venkatarangan A, Dunsmuir J, Wong Tf (2000) Pore and throat size distributions measured from synchrotron X-ray tomographic images of Fontainebleau sandstones. J Geophys Res-Solid Earth 105:21509-21527

Liu C, Shang J, Zachara JM (2011) Multispecies diffusion models: A study of uranyl species diffusion. Water Resour Res 47:W12514, doi:10.1029/2011WR010575

Luquot L, Gouze P (2009) Experimental determination of porosity and permeability changes induced by injection of CO_2 into carbonate rocks. Chem Geol 265:148-159

Maher K, Steefel CI, DePaolo DJ, Viani BE (2006) The mineral dissolution rate conundrum: Insights from reactive transport modeling of U isotopes and pore fluid chemistry in marine sediments. Geochim Cosmochim Acta 70:337-363

McGrail B, Schaef H, Glezakou VA, Dang L, Owen A (2009) Water reactivity in the liquid and supercritical CO_2 phase: Has half the story been neglected? Energy Procedia 1:3415-3419

Meakin P, Tartakovsky AM (2009) Modeling and simulation of pore-scale multiphase fluid flow and reactive transport in fractured and porous media. Rev Geophys 47:RG3002

Mees F, Swennen R, Geet MV, Jacobs P (2003) Applications of X-ray computed tomography in the geosciences. Geol Soc London Spec Publ 215:1-6

Mehmani Y, Sun T, Balhoff M, Eichhubl P, Bryant S (2012) Multiblock pore-scale modeling and upscaling of reactive transport: application to carbon sequestration. Transport Porous Med 95:305-326

Miller G, Trebotich D (2012) An embedded boundary method for the Navier-Stokes equations on a time-dependent domain. Commun Appl Math Comp Sci 7:1-31

Molins S, Silin D, Trebotich D, Steefel CI (2011) Direct pore-scale numerical simulation of precipitation and dissolution. Mineral Mag 75:1487

Molins S, Trebotich D, Shen C, Yang L, Ajo-Franklin J, Steefel C (2012) Calcite dissolution driven by a CO_2-rich solution in a flow-through capillary tube: experiment and pore-scale modeling. Abstract H52C-06 presented at 2012 Fall Meeting AGU, San Francisco, Calif. 3-7 Dec.

Molins S, Trebotich D, Steefel CI, Shen C (2012) An investigation of the effect of pore scale flow on average geochemical reaction rates using direct numerical simulation. Water Resour Res 48:W03527, doi:10.1029/2011WR011404

Muller N, Qi R, Mackie E, Pruess K, Blunt MJ (2009) CO_2 injection impairment due to halite precipitation. Energy Procedia 1:3507-3514

Nehrke G, Reichart G, Cappellen PV, Meile C, Bijma J (2007) Dependence of calcite growth rate and Sr partitioning on solution stoichiometry: Non-Kossel crystal growth. Geochim Cosmochim Acta 71:2240-2249

Nielsen LC, Bourg IC, Sposito G (2012) Predicting CO_2-water interfacial tension under pressure and temperature conditions of geologic CO_2 storage. Geochim Cosmochim Acta 81:28-38

Noiriel C, Gouze P, Bernard D (2004) Investigation of porosity and permeability effects from microstructure changes during limestone dissolution. Geophys Res Lett 31:L24603

Noiriel C, Luquot L, Madé B, Raimbault L, Gouze P, van der Lee J (2009) Changes in reactive surface area during limestone dissolution: An experimental and modelling study. Chem Geol 265:160-170

Noiriel C, Steefel CI, Yang L, Ajo-Franklin J (2012) Upscaling calcium carbonate precipitation rates from pore to continuum scale. Chem Geol 318-319:60-74

Ortoleva P (1994) Geochemical Self-Organization. Oxford University Press

Ortoleva P, Chadam J, Merino E, Sen A (1987) Geochemical self-organization II; the reactive-infiltration instability. Am J Sci 287:1008-1040

Ovaysi S, Piri M (2013) Pore-scale dissolution of CO_2+SO_2 in deep saline aquifers. Int J Greenhouse Gas Control 15:119–133

Parmigiani A, Huber C, Bachmann O, Chopard B (2011) Pore-scale mass and reactant transport in multiphase porous media flows. J Fluid Mech 686:40-76

Patankar S (1980) Numerical Heat Transfer and Fluid Flow, Series in Computational Methods in Mechanics and Thermal Sciences. Taylor & Francis

Payatakes AC, Tien C, Turian RM (1973) A new model for granular porous media: Part I. Model formulation. AIChE J 19:58-67

Peters CA (2009) Accessibilities of reactive minerals in consolidated sedimentary rock: An imaging study of three sandstones. Chem Geol 265:198-208

Phillips O (1991) Flow and Reactions in Permeable Rocks. Cambridge University Press

Pini R, Benson SM (2013) Simultaneous determination of capillary pressure and relative permeability curves from core-flooding experiments with various fluid pairs. Water Resour Res 49:3516-3530, doi: 10.1002/wrcr.20274

Plummer L, Wigley T, Parkhurst D (1978) Kinetics of calcite dissolution in CO_2-Water systems at 5°C to 60°C and 0.0 to 1.0 atm CO_2. Am J Sci 278:179-216

Pokrovsky OS, Golubev SV, Schott J (2005) Dissolution kinetics of calcite, dolomite and magnesite at 25 °C and 0 to 50 atm pCO_2. Chem Geol 217:239-255

Pokrovsky OS, Golubev SV, Schott J, Castillo A (2009) Calcite, dolomite and magnesite dissolution kinetics in aqueous solutions at acid to circumneutral pH, 25 to 150°C and 1 to 55 atm pCO_2: New constraints on CO_2 sequestration in sedimentary basins. Chem Geol 265:20-32

Prigogine I (1968) Introduction to Thermodynamics of Irreversible Processes. Interscience Publishers

Prigogine I (1980) From Being to Becoming: Time and Complexity in the Physical Sciences. W H Freeman & Company

Pudney C (1998) Distance-ordered homotopic thinning: a skeletonization algorithm for 3D digital images. Comput Vision Image Understanding 72:404-413

Raeini AQ, Blunt MJ, Bijeljic B (2012) Modelling two-phase flow in porous media at the pore scale using the volume-of-fluid method. J Comput Phys 231:5653-5668

Rolle M, Muniruzzaman M, Haberer CM, Grathwohl P (2013) Coulombic effects in advection-dominated transport of electrolytes in porous media: Multicomponent ionic dispersion. Geochim Cosmochim Acta 120:195-205

Sadhukhan S, Gouze P, Dutta T (2012) Porosity and permeability changes in sedimentary rocks induced by injection of reactive fluid: A simulation model. J Hydrol 450-451:134-139

Saldi GD, Schott J, Pokrovsky OS, Gautier Q, Oelkers EH (2012) An experimental study of magnesite precipitation rates at neutral to alkaline conditions and 100-200 °C as a function of pH, aqueous solution composition and chemical affinity. Geochim Cosmochim Acta 83:93-109

Sato K, Mito S, Horie T, Ohkuma H, Saito H, Watanabe J, Yoshimura T (2011) Monitoring and simulation studies for assessing macro- and meso-scale migration of $\{CO_2\}$ sequestered in an onshore aquifer: Experiences from the Nagaoka pilot site, Japan. Int J Greenhouse Gas Control 5:125-137

Scheibe TD, Hou Z, Palmer BJ, Tartakovsky AM (2013) Pore-scale simulation of intragranular diffusion: Effects of incomplete mixing on macroscopic manifestations. Water Resour Res 49:4277-4294, doi: 10.1002/wrcr.20333

Scheibe TD, Tartakovsky AM, Tartakovsky DM, Redden GD, Meakin P (2007) Hybrid numerical methods for multiscale simulations of subsurface biogeochemical processes. J Phys Conf Ser 78:012063

Shan X, Doolen G (1995) Multicomponent lattice-Boltzmann model with interparticle interaction. J Stat Phys 81:379-393

Silin D, Patzek T (2006) Pore space morphology analysis using maximal inscribed spheres. Physica A 371:336-360

Silin D, Tomutsa L, Benson S, Patzek T (2011) Microtomography and pore-scale modeling of two-phase fluid distribution. Transport Porous Med 86:495-515

Smith MM, Sholokhova Y, Hao Y, Carroll SA (2013) Evaporite caprock integrity: an experimental study of reactive mineralogy and pore-scale heterogeneity during brine-CO_2 exposure. Environ Sci Technol 47:262-268

Smith MM, Wolery TJ, Carroll SA (2013) Kinetics of chlorite dissolution at elevated temperatures and CO_2 conditions. Chem Geol 347:1-8

Stauffer D, Adler J, Aharony A (1994) Universality at the three-dimensional percolation threshold. J Phys A 27:L475

Steefel C, Lichtner P (1998) Multicomponent reactive transport in discrete fractures: II: Infiltration of hyperalkaline groundwater at Maqarin, Jordan, a natural analogue site. J Hydrol 209:200-224

Steefel CI, DePaolo DJ, Lichtner PC (2005) Reactive transport modeling: An essential tool and a new research approach for the Earth sciences. Earth Planet Sci Lett 240:539-558

Steefel CI, Lasaga AC (1990) Evolution of dissolution patterns: Permeability change due to coupled flow and reaction. *In:* Chemical Modeling of Aqueous Systems II. ACS Symposium Series 416:212-225

Steefel CI, Lasaga AC (1994) A coupled model for transport of multiple chemical species and kinetic precipitation/dissolution reactions with application to reactive flow in single phase hydrothermal systems. Am J Sci 294:529-592

Steefel CI, Lichtner PC (1994) Diffusion and reaction in rock matrix bordering a hyperalkaline fluid-filled fracture. Geochim Cosmochim Acta 58:3595-3612

Steefel CI, Maher K (2009) Fluid-rock interaction: A reactive transport approach. Rev Mineral Geochem 70:485-532

Suekane T, Furukawa N, Tsushima S, Hirai S, Kiyota M (2009) Application of MRI in the measurement of two-phase flow of supercritical CO_2 and water in porous rocks. J Porous Med 12:143-154

Suekane T, Soukawa S, Iwatani S, Tsushima S, Hirai S (2005) Behavior of supercritical CO_2 injected into porous media containing water. Energy 30:2370-2382

Tartakovsky AM, Meakin P, Scheibe TD, West RME (2007) Simulations of reactive transport and precipitation with smoothed particle hydrodynamics. J Comput Phys 222:654-672

Tartakovsky AM, Meakin P, Scheibe TD, Wood BD (2007) A smoothed particle hydrodynamics model for reactive transport and mineral precipitation in porous and fractured porous media. Water Resour Res 43:W05437

Tartakovsky AM, Redden G, Lichtner PC, Scheibe TD, Meakin P (2008) Mixing-induced precipitation: Experimental study and multiscale numerical analysis. Water Resour Res 44:W06S04, doi: 10.1029/2006WR005725

Taylor G (1953) Dispersion of soluble matter in solvent flowing slowly through a tube. Proc Roy Soc Lond Ser-A 219:186-203

Teng H, Dove PM, Yoreo JJD (2000) Kinetics of calcite growth: surface processes and relationships to macroscopic rate laws. Geochim Cosmochim Acta 64:2255-2266

Tokunaga TK, Wan J (2013) Capillary pressure and mineral wettability influences on reservoir CO_2 capacity. Rev Mineral Geochem 77:481-503

Trebotich D, Straalen BV, Graves D, Colella P (2008) Performance of embedded boundary methods for CFD with complex geometry. J Phys Conf Ser 125:012083

Van Cappellen P, Gaillard JF (1996) Biogeochemical dynamics in aquatic sediments. Rev Mineral 34:335-376

Varloteaux C, Bekri S, Adler PM (2013) Pore network modeling to determine the transport properties in presence of a reactive fluid: From pore to reservoir scale. Adv Water Resour 53:87-100

Wang Y, Zhang C, Wei N, Oostrom M, Wietsma TW, Li X, Bonneville A (2013) Experimental study of crossover from capillary to viscous fingering for supercritical CO_2-water displacement in a homogeneous pore network. Environ Sci Technol 47:212-218

Wigley M, Kampman N, Dubacq B, Bickle M (2012) Fluid-mineral reactions and trace metal mobilization in an exhumed natural CO_2 reservoir, Green River, Utah. Geology 40:555-558

Wildenschild D, Sheppard AP (2013) X-ray imaging and analysis techniques for quantifying pore-scale structure and processes in subsurface porous medium systems. Adv Water Resour 51:217-246

Wolery T, Jackson K, Bourcier W, Bruton C, Viani B, Knauss K, Delany J (1990) Chemical Modeling of Aqueous Systems II, chap. Current status of the EQ3/6 software package for geochemical modeling. *In:* Chemical Modeling of Aqueous Systems II. ACS Symposium Series 416:104-116

Wolthers M, Nehrke G, Gustafsson JP, Cappellen PV (2012) Calcite growth kinetics: Modeling the effect of solution stoichiometry. Geochim Cosmochim Acta 77:121-134

Xu Z, Meakin P (2008) Phase-field modeling of solute precipitation and dissolution. J Chem Phys 129:014705, http://dx.doi.org/10.1063/1.2948949

Xu Z, Meakin P (2011) Phase-field modeling of two-dimensional solute precipitation/dissolution: Solid fingers and diffusion-limited precipitation. J Chem Phys 134:044137

Xu Z, Meakin P, Tartakovsky AM (2009) Diffuse-interface model for smoothed particle hydrodynamics. Phys Rev E 79:036702

Yang L, Steefel CI (2008) Kaolinite dissolution and precipitation kinetics at 22 C and pH 4. Geochim Cosmochim Acta 72:99-116

Yoon H, Dewers TA (2013) Nanopore structures, statistically representative elementary volumes, and transport properties of chalk. Geophys Res Lett 40, doi:10.1002/grl.50803

Yoon H, Valocchi AJ, Werth CJ, Dewers T (2012) Pore-scale simulation of mixing-induced calcium carbonate precipitation and dissolution in a microfluidic pore network. Water Resour Res 48

Zhang C, Oostrom M, Grate JW, Wietsma TW, Warner MG (2011) Liquid CO_2 displacement of water in a dual-permeability pore network micromodel. Environ Sci Technol 45:7581-7588

Zienkiewicz O, Taylor R, Zhu J (2005) The Finite Element Method: Its Basis and Fundamentals: Its Basis and Fundamentals. Elsevier Science

Reviews in Mineralogy & Geochemistry
Vol. 77 pp. 305-360, 2013
Copyright © Mineralogical Society of America

Carbon Mineralization: From Natural Analogues to Engineered Systems

Ian M. Power, Anna L. Harrison, Gregory M. Dipple*
Mineral Deposit Research Unit, Department of Earth, Ocean and Atmospheric Sciences, The University of British Columbia
Vancouver, British Columbia V6T 1Z4, Canada
**gdipple@eos.ubc.ca*

Siobhan A. Wilson
School of Geosciences, Monash University
Clayton, VIC 3800, Australia

Peter B. Kelemen
Lamont Doherty Earth Observatory
Columbia University
Palisades, New York 10964, U.S.A.

Michael Hitch
Norman B. Keevil Institute of Mining Engineering
The University of British Columbia
Vancouver, British Columbia V6T 1Z4, Canada

Gordon Southam
School of Earth Sciences, The University of Queensland
Brisbane, St Lucia, QLD 4072, Australia

INTRODUCTION

Carbon mineralization sequesters CO_2 by reaction of alkaline earth metal bearing silicate and hydroxide minerals with CO_2 to form stable carbonate minerals. Seifritz (1990) proposed harnessing this natural process as a method for sequestration of anthropogenic CO_2. It was first studied in detail as an industrial process by Lackner et al. (1995), which is often referred to as "mineral carbonation." Much of this early research aimed to capitalize on the globally abundant natural deposits of ultramafic and mafic rocks, which are rich in alkaline earth metals, in addition to the long-term stability of the resultant carbonate minerals (Lackner et al. 1995). More recently, other process routes have been investigated that rely on feedstocks other than naturally occurring minerals (e.g., industrial wastes) as a source of cations for carbonate precipitation. Therefore, we use the more general term "carbon mineralization" to refer to any process that sequesters CO_2 as a solid carbonate phase. The main advantages of carbon mineralization as a CO_2 storage method are that the reactions are thermodynamically favored, the carbonation processes can be readily controlled and manipulated, and the resulting product is benign and stable over geological time.

We begin this review with an overview of the fundamental processes that are relevant to carbon mineralization, which provides a basic framework in which to understand CO_2

1529-6466/13/0077-0009$05.00 http://dx.doi.org/10.2138/rmg.2013.77.9

sequestration strategies based on carbon mineralization. We next discuss natural analogues to engineered systems, focusing on (1) exhumed hydrothermal systems in peridotite that have formed listvenite (magnesite + quartz) and soapstone and (2) shallow subsurface peridotite weathering processes and related alkaline springs that form carbonate veins, surficial travertine deposits, and hydromagnesite–magnesite playas. The propensity to form carbonate minerals in these ultramafic terranes reflects the thermodynamic instability of Mg-silicate minerals in the presence of CO_2. These systems provide greater understanding of the key processes that may be exploited—and the limitations that must be minimized—to accelerate carbon mineralization (Fig. 1).

Carbon mineralization strategies are often divided into *ex situ* processes—involving carbonation of a feedstock removed from its original location—and *in situ* processes, involving transport and injection of CO_2 and other carbon sources into existing rock formations. In this chapter, we review the pertinent research on *ex situ* and *in situ* carbon mineralization in systems that operate over a variety of temperatures and pressures, utilize either chemical or biological processes, and that range from passive to fully engineered. *Ex situ* carbon mineralization strategies include (1) enhanced weathering, (2) carbonation at industrial sites, (3) biologically mediated carbonation, and (4) carbon mineralization in industrial reactors. All of these strategies rely on a feedstock that is rich in divalent cations. *In situ* carbon mineralization aims to promote subsurface carbonation in place. Depending on the carbon mineralization strategy employed, the efficiency and security of CO_2 storage may be monitored directly as part of an industrial process circuit or assessed on the scale of landscapes and geologic formations using geophysical and geochemical techniques.

The challenge is to develop carbon mineralization technologies that operate at a scale and rate commensurate to the scale of anthropogenic greenhouse gas (GHG) emissions. Currently, global anthropogenic CO_2 emissions are estimated at 38 Gt CO_2/yr (IPCC 2007), which increases

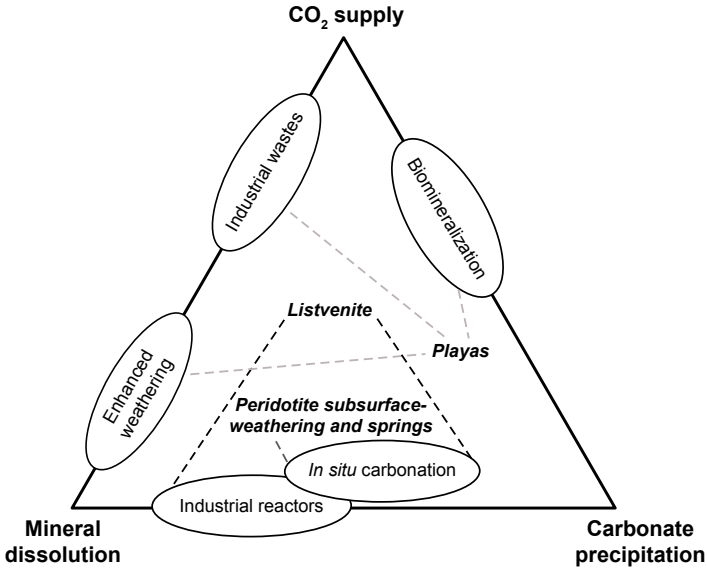

Figure 1. Conceptual diagram illustrating the three fundamental processes that may be rate-limiting for carbon mineralization. Natural environments and carbon mineralization strategies are plotted relative to one another with their interrelationships indicated by dashed lines.

the atmospheric CO_2 concentration by approximately 2 ppm annually (NOAA 2013). Given the magnitude of global GHG emissions, it is unlikely that any single carbon sequestration strategy will achieve the desired reduction in CO_2 concentrations. For this reason, we summarize the individual capacity and rate of various carbonation strategies, which in combination could yield a rate of CO_2 sequestration that is significant on the scale of global emissions.

FUNDAMENTAL PROCESSES OF CARBON MINERALIZATION

Carbon mineralization is the conversion of silicate and hydroxide minerals to form carbonate minerals as a stable sink for CO_2. A range of mineral feedstocks or natural rock formations may be used, which produce a wide variety of alkaline-earth carbonate mineral products. Aqueous and crystal chemical controls on carbon mineralization must be understood in order to optimize this process for industrial deployment. The mineralogical composition of both feedstock and carbonate precipitates impacts the sequestration capacity of the reactants and the mass of CO_2 sequestered (Table 1; Power et al. 2013b). Formulae for many of the relevant feedstock minerals and carbonate products are given in Table 1. The mass ratio of CO_2 sequestered to reactant mineral consumed depends on the mass proportion of divalent cations (e.g., Mg^{2+}) in the mineral feedstock as well as the CO_2:MgO ratio and H_2O content of the resulting carbonate mineral (Table 1). For instance, less reactant mineral is required to sequester 1 tonne of CO_2 in minerals with a 1:1 CO_2:MgO ratio (e.g., magnesite) than in minerals with lower ratios (e.g., hydromagnesite). These are important considerations in the overall efficiency of the process, and may have implications for the mass of material that must be mined or transported and for the water budget of carbon mineralization technologies.

Numerous process routes involving both high and low temperature chemical reactions, as well as biologically mediated reactions, have been proposed in the literature to achieve carbon

Table 1. Reactants for and products of carbon mineralization.

Mineral/ Formula	CO_2:MgO ratio	Tonnes of mineral required to sequester 1 t of CO_2				
		Serpentine[a] [$Mg_3Si_2O_5(OH)_4$]	Brucite [$Mg(OH)_2$]	Forsterite [Mg_2SiO_4]	Diopside[b] [$CaMgSi_2O_6$]	Enstatite [$Mg_2Si_2O_6$]
Magnesite $MgCO_3$	1:1	2.10	1.33	1.60	2.46	2.28
Hydromagnesite $Mg_5(CO_3)_4(OH)_2{\cdot}4H_2O$	4:5	2.62	1.66	2.00	2.73	2.85
Dypingite $Mg_5(CO_3)_4(OH)_2{\cdot}{\sim}5H_2O$	4:5	2.62	1.66	2.00	2.73	2.85
Pokrovskite $Mg_2(CO_3)(OH)_2$	1:2	4.20	2.65	3.20	3.28	4.56
Artinite $Mg_2(CO_3)(OH)_2{\cdot}3H_2O$	1:2	4.20	2.65	3.20	3.28	4.56
Nesquehonite $MgCO_3{\cdot}3H_2O$	1:1	2.10	1.33	1.60	2.46	2.28
Lansfordite $MgCO_3{\cdot}5H_2O$	1:1	2.10	1.33	1.60	2.46	2.28

[a]Serpentine group minerals include antigorite, lizardite, and chrysotile.
[b]Tonnes of diopside required to sequester 1 t of CO_2 in Mg-carbonate minerals of varying CO_2:MgO ratio plus $CaCO_3{\cdot}xH_2O$ (e.g., x = 0 for calcite, aragonite and vaterite, x = 1 monohydrocalcite, x = 6 ikaite). Hydration state of Mg- and Ca-carbonate mineral products impacts water budget, but not C or Mg (Power et al. 2013b).

mineralization at a scale and rate sufficient to help mitigate global climate change. At the core of these process routes are the geochemical processes fundamental to carbon mineralization: (1) mineral dissolution to provide cations, (2) the supply of CO_2, and (3) carbonate mineral precipitation that sequesters CO_2. These processes operate in natural systems, but may be manipulated in engineered systems that are specifically designed to sequester CO_2 at faster rates (Fig. 1). Biological processes that mediate these reactions are discussed separately in a section on biologically mediated carbonation.

Mineral dissolution

The suitability of solid materials as carbon mineralization feedstock depends primarily on their reactivity and chemical composition, in addition to their availability. Igneous and metamorphic rocks are rich in alkaline earth metals, making them ideal sources of divalent metal cations for carbon mineralization (e.g., ultramafic and mafic rocks). Furthermore, carbonation of Mg- and Ca-silicate minerals is thermodynamically favored (Lackner et al. 1995). For these reasons, basic silicate and hydroxide minerals such as wollastonite [$CaSiO_3$] (Daval et al. 2009; Miller et al. 2013), olivine [Mg-end-member forsterite] (O'Connor et al. 2005; Giammar et al. 2005; Chizmeshya et al. 2007; Daval et al. 2011), brucite (Zhao et al. 2010, Harrison et al. 2013), and serpentine group minerals (Park and Fan 2004; Teir et al. 2007b; Zevenhoven et al. 2008), as well as aluminosilicates such as plagioclase [Ca-end-member anorthite; $CaAl_2Si_2O_8$] (Gislason et al. 2010; Munz et al. 2012), and natural volcanic glasses (Gislason et al. 2010; Stockmann et al. 2011) have been investigated as potential feedstock for carbon mineralization. In addition, many industrial processes produce Ca- and Mg-rich wastes that could provide readily available material for carbon mineralization (Bobicki et al. 2012; Sanna et al. 2012). The dissolution rate of these natural minerals and industrial by-products depends largely on crystal chemistry and solution chemistry, temperature, and available surface area.

Effect of crystal chemistry on dissolution rates. Silicate dissolution may be rate-limiting for certain carbon mineralization strategies such as mineral carbonation in industrial reactors. The elemental composition and crystal structure of a mineral largely govern the rate of dissolution at far from equilibrium conditions, and consequently the rate at which a rock dissolves is controlled by modal mineralogy. For example, the dissolution rates of peridotite, pyroxenite, and basalt are ~2 orders of magnitude faster than those of rhyolite and granite at comparable temperature and pH (Kelemen and Matter 2008; Gislason et al. 2010; Kelemen et al. 2011). The dissolution rate of a mineral is related to the strength of metal-oxygen bonds (controlled by cation size and co-ordination number) and, in the case of silicate minerals, the degree of silica polymerization. The dissolution of single oxide minerals (e.g., brucite) requires that only one type of bond be broken, whereas the dissolution of multi-oxide minerals (e.g., olivine, pyroxene, aluminosilicates, glasses) requires the breakage of numerous types of metal-oxygen bonds (Schott et al. 2009). The destruction of the slowest-breaking metal-oxygen bond that is essential to the crystal structure (typically, the shortest and strongest bond) is the rate-limiting step for dissolution (Schott et al. 2009). Under acidic conditions, the rate of metal-oxygen bond breakage in common silicate minerals generally decreases with increasing metal ion valence from monovalent to trivalent (Oelkers 2001). The Si-O bond is typically the strongest bond in the structure of a silicate mineral and is consequently the slowest to break. The relative difference in Si-O and metal-oxygen bond strength may lead to non-stoichiometric dissolution and the development of Si-rich layers that may passivate the reactive surface, potentially slowing dissolution (Luce et al. 1972; Pokrovsky and Schott 2000a; Béarat et al. 2006; Jarvis et al. 2009; Schott et al. 2009, 2012). For example, in the case of olivine dissolution at 25 °C, when the pH is <8, a thin Mg-depleted and silica-rich layer tends to form due to the preferential release of Mg (Luce et al. 1972; Wogelius and Walther 1991; Pokrovsky and Schott 2000b; Rosso and Rimstidt 2000). However, a Si-depleted and Mg-rich

surface layer is created at higher pH values and dissolution is governed by the decomposition of hydrated Mg complexes, with a preferential release of Si into solution (Pokrovsky and Schott 2000b). Similar behavior was also documented at higher temperatures between 90 and 150 °C and with pH values between 2 and 12.5 (Hänchen et al. 2006). This effect can be minimized in industrial reactors by optimization of slurry flow parameters to control particle abrasion (Béarat et al. 2006; Daval et al. 2011).

Dissolution rates tend to decrease with increasing silica polymerization which is defined by the average number of Si-O-Si bonds in a crystal structure (given by Q^i; Brantley 2008a). Orthosilicates, such as forsterite, are completely unpolymerized (Q^0) and will therefore tend to dissolve more rapidly than pyroxenes (Q^2), such as diopside and enstatite, and phyllosilicates (Q^3), such as serpentine group minerals like chrysotile (Fig. 2A; Schott et al. 2009). Similarly, the rate of brucite dissolution is orders of magnitude greater than that of Mg-silicate minerals, as it lacks the strong Si-O bonding (e.g., Bales and Morgan 1985; Pokrovsky and Schott 2004). Due to the comparatively weak Ca-O bond, Ca-silicates tend to dissolve at faster rates than Mg-silicates for a given connectedness (Fig. 2A; Brantley 2003; Schott et al. 2009). The crystallinity (i.e., extent of long-range structural order) of the solid also influences its rate of dissolution. For instance, Gislason and Oelkers (2003) and Wolff-Boenisch et al. (2006) documented that dissolution of glassy rocks was approximately two orders of magnitude faster than compositionally similar crystalline phases. The crystal chemistry of feedstock for carbon mineralization may therefore determine the method of artificial acceleration that should be employed.

Effects of solution chemistry on dissolution rates. In general, the dissolution rates of different basic silicates exhibit a similar dependence on pH, with rates decreasing with increasing pH up to moderately alkaline pH (Schott et al. 2009). This behavior has been documented for both chrysotile and forsterite (Bales and Morgan 1985; Pokrovsky and Schott 2000b; Thom et al. 2013). In contrast, aluminosilicates tend to exhibit minimum dissolution rates at circumneutral pH (the pH where the surface charge of the mineral equals zero), and accelerate above and below this point (Brantley 2003; Schott et al. 2009). This is also the case for basaltic glass (Gislason and Oelkers 2003). Thus, the effect of pH on the extraction of cations for carbon mineralization depends on the feedstock. However, under acidic conditions a decline in pH will generally accelerate dissolution for most mineral feedstocks.

In natural systems, soil microbes and plant roots produce natural organic ligands that accelerate the weathering of bedrock (e.g., Wu et al. 2007). The presence of ligands (e.g., oxalate and citrate) can significantly enhance or inhibit mineral dissolution rates in comparison to pH effects alone (Fig. 2B; e.g., Hänchen et al. 2006; Krevor and Lackner 2011; Prigiobbe and Mazzotti 2011). In the range of natural concentrations found in soils, the effect of organic ligands on dissolution rates of brucite and silicates is relatively weak (Pokrovsky et al. 2005; Brantley 2008b). However, artificial enrichment of organic ligand concentrations could significantly enhance dissolution rates of phases of interest for carbon mineralization (Krevor and Lackner 2011).

Inorganic ligands, such as sulfate, carbonate, and phosphate may also inhibit or enhance mineral dissolution rates depending on the type of surface complex they form (e.g., Pokrovsky et al. 2005). The effect of carbonate ligands on mineral dissolution rates is of particular relevance for carbon mineralization. In natural soils, CO_2 concentrations can be elevated by 10 to 100 times over atmospheric concentrations due to respiration (Brady and Carroll 1994). Although the decline in pH associated with the uptake of CO_2 into solution is generally expected to enhance dissolution rates, the direct effect of carbonate species is less straightforward, and has the potential to enhance or inhibit dissolution (Fig. 2C; c.f., Malmstrom and Banwart 1997; Berg and Banwart 2000; Golubev et al. 2005; Pokrovsky et al. 2005; Hänchen et al. 2006). On the other hand, Olsen (2007) measured no effect on forsterite dissolution rates in the presence of inorganic salts, such as KNO_3, $Mg(NO_3)_2$, Na_2SO_4, and $MgSO_4$ in CO_2-free solutions with a

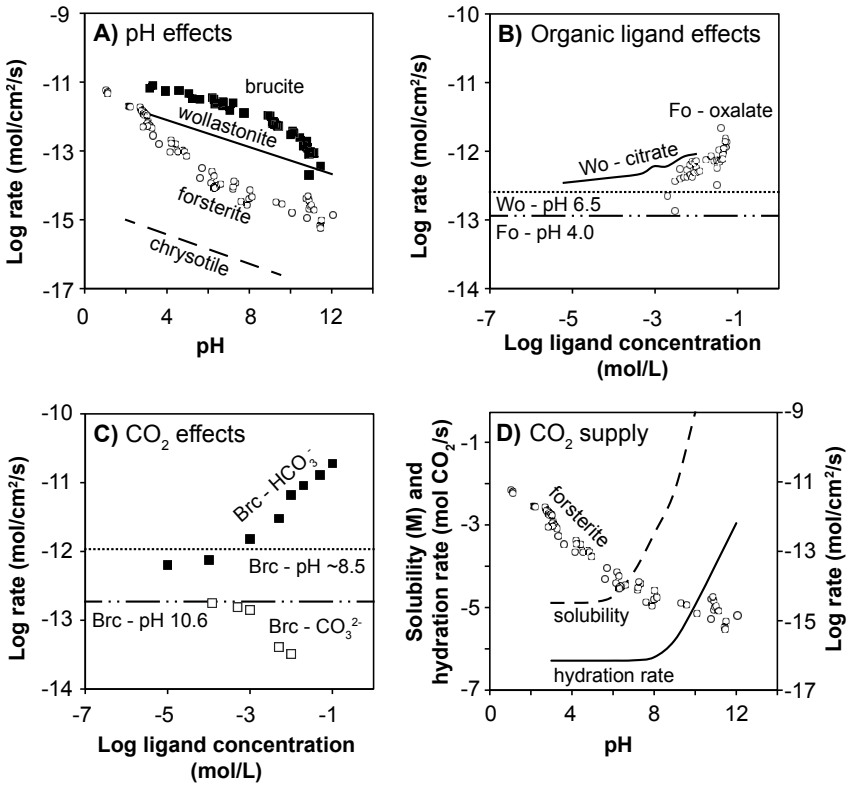

Figure 2. (A) Log dissolution rate versus pH for brucite (Pokrovsky and Schott 2004), wollastonite (Pokrovsky et al. 2009), forsterite (Pokrovsky and Schott 2000a), and chrysotile (Thom et al. 2013). (B) Log dissolution rate versus log ligand concentration for organic ligand-affected silicate dissolution. Citrate promoted wollastonite (Wo) dissolution at pH ~6.5-7.5 is represented by the black line (Pokrovsky et al. 2009), and oxalate promoted forsterite (Fo) dissolution at pH ~4.0 is shown by the open circles (Olsen and Rimstidt 2008). The pH-promoted dissolution rates at the appropriate pH for each mineral are presented by the horizontal dashed lines. (C) Log dissolution rate versus log ligand concentration for brucite dissolution in the presence of dissolved carbonate. Brucite (brc) dissolution rates in HCO_3^- and CO_3^{2-} dominated solutions are shown by the shaded and open squares, respectively (Pokrovsky et al. 2005). The effect of HCO_3^- was measured in a solution at pH ~8.5, whereas the effect CO_3^{2-} was measured in a solution with a pH of ~10.6 (Pokrovsky et al. 2005). The horizontal dashed lines indicate the pH-promoted dissolution rates in a ligand-free solution at these pH values. (D) CO_2 solubility (mol/L) and $CO_{2(aq)}$ hydration rate (mol CO_2/s) versus pH plotted on the left y-axis, compared to pH-promoted forsterite dissolution rate (Pokrovsky and Schott 2000a) versus pH plotted on the right y-axis. CO_2 solubility at each pH value was calculated for equilibrium with atmospheric CO_2 using PHREEQC (Parkhurst and Appelo 1999). The CO_2 hydration rate was calculated as the initial rate based on equations provided by Stumm and Morgan (1996) assuming no CO_2 is initially in solution.

pH range of 1 to 4 at 25 °C. Prigiobbe et al. (2009) arrived at the same conclusions as a result of their comprehensive studies on Mg-silicate dissolution kinetics at 120 °C in the pH range of 3 to 8.

Effects of temperature on dissolution rates. Silicate mineral dissolution rates are typically accelerated with increased temperature at the laboratory and field scales (Brady and Carroll 1994; White and Blum 1995; White et al. 1999). An important consequence of the temperature dependence of silicate dissolution is the feedback between climate and natural weathering rates, and therefore CO_2 drawdown (e.g., White et al. 1999). For instance, Gislason et al.

(2009) calculated a 4-14% increase in chemical weathering rates per degree of temperature increase in eight Icelandic river catchments over a 44-year period. Mineral dissolution can proceed in minutes under high temperature and pressure conditions as is discussed in the section on industrial reactors.

Effects of surface passivation and surface area. High reactive surface area results in faster dissolution rates. However, the surface area must be accessible to reactants for the reaction to proceed. Precipitation of secondary phases such as carbonate minerals or amorphous silica may occur directly on the surface of the primary phase during carbonation (Béarat et al. 2006; Andreani et al. 2009; Hövelmann et al. 2012). This has the potential to passivate the reactive surface and inhibit dissolution, although the effect is variable. For instance, experimental studies suggest that surface coatings do not inhibit dissolution of anorthite, diopside, or basaltic glass (Hodson 2003; Stockmann et al. 2011, 2013). Conversely, the development of amorphous silica and Fe-oxide layers at the mineral surface has a deleterious effect on the dissolution rates of olivine and serpentine (Park et al. 2003; Béarat et al. 2006; Teir et al. 2007c; Chizmeshya et al. 2007; Andreani et al. 2009; Daval et al. 2011; Assima et al. 2012; Hövelmann et al. 2012). Similarly, precipitation of secondary carbonate minerals has been linked to declining carbonation rates of Ca-rich steel making slags (Lekakh et al. 2008). The effect of surface coatings on dissolution rates may depend strongly on the mechanism of precipitation (i.e., epitaxial vs. random heterogeneous nucleation; Cubillas et al. 2005). As such, the effect of surface coatings on carbon mineralization rates varies depending on the type of feedstock and secondary precipitate, and should be evaluated experimentally to better predict the potential extent of surface passivation.

CO_2 supply

The carbon mineralization reaction is in some cases limited by the supply of CO_2 (e.g., Wilson et al. 2010). The rate of CO_2 supply into solution relates to the phase transition from gaseous to aqueous CO_2, and the subsequent hydration of $CO_{2(aq)}$ and dissociation to form HCO_3^- and CO_3^{2-} anions. Carbonate anions may then react with alkaline earth cations to precipitate carbonate minerals (Eqn. 1-5).

$$CO_{2(g)} \leftrightarrow CO_{2(aq)} \quad (1)$$

$$CO_{2(aq)} + H_2O_{(l)} \leftrightarrow H_2CO_{3(aq)} \quad (2)$$

$$H_2CO_{3(aq)} \leftrightarrow HCO_3^-{}_{(aq)} + H^+{}_{(aq)} \quad (3)$$

$$HCO_3^-{}_{(aq)} \leftrightarrow CO_3^{2-}{}_{(aq)} + H^+{}_{(aq)} \quad (4)$$

$$M^{2+}{}_{(aq)} + CO_3^{2-}{}_{(aq)} \leftrightarrow MCO_{3(s)} \quad (5)$$

Many natural waters are not in equilibrium with atmospheric CO_2 due to the slow gas to solution transfer reaction, poor mixing conditions, and the relatively slow hydration of aqueous CO_2 (Clark et al. 1992; Stumm and Morgan 1996; Wilson et al. 2011). The dissolved inorganic carbon (DIC) concentration is governed by the $CO_{2(g)}$ partial pressure in the gas phase in contact with the water and the solution pH, with increased DIC capacity positively correlated to pH (Fig. 2D). Additionally, the hydration rate of $CO_{2(aq)}$ increases with increasing pH values at alkaline pH, due to changing hydration mechanisms (Fig. 2D; Stumm and Morgan 1996). However, as previously discussed, dissolution rates for basic silicates typically decrease with increasing pH. As such, optimal conditions for carbonation are likely to occur at pH values that balance CO_2 supply and mineral dissolution rates (Fig. 2D).

The solubility of CO_2 tends to decrease with salinity (Harned and Davis 1943), which may negatively impact the supply of CO_2 in natural and industrial systems with high salinities, such as mine waste process waters and produced waters from oil fields (Mignardi et al 2011). Wilson et al. (2010) performed experiments to study carbonation of brucite to dypingite within

saline, Mg-rich solutions of similar composition to the tailings waters at ultramafic mines. The only available source of carbon in these experiments was ambient atmospheric CO_2 that was bubbled into solution. Wilson et al. (2010) found that during uptake of atmospheric CO_2 into high salinity, high pH solutions, neither DIC concentrations nor $\delta^{13}C_{DIC}$ reached predicted equilibrium values. Upon precipitation of dypingite, DIC concentrations decreased and $\delta^{13}C_{DIC}$ values became increasingly negative, indicating that the rate of mineral precipitation outpaced the rate of CO_2 uptake (i.e., CO_2 dissolution and hydration) in solution. Therefore, CO_2 uptake may be rate limiting for carbon mineralization in saline, high pH solutions of the type typically found in tailings storage facilities. However, Mignardi et al. (2011) documented that the increased residence time of CO_2 in saline waters helps to counter the effect of decreased solubility, and Harrison et al. (2013) report that increasing CO_2 supply into similar solutions (i.e., using CO_2-rich gas) helps to overcome this effect.

Carbonate mineral precipitation

In carbon mineralization processes, a number of studies have shown that Mg-carbonate precipitation can be rate limiting (Hänchen et al. 2008; Saldi et al. 2010, 2012; Haug et al. 2011), but relatively few studies have focused on Mg-carbonate precipitation rates compared to Mg-silicate dissolution rates (e.g., Saldi et al. 2010, 2012). Precipitation consists of two separate processes: nucleation of a solid phase followed by crystal growth. The rate of nucleation is controlled by the degree of supersaturation, temperature, and the cluster-water interfacial free energy. The crystal growth rate is a function of the reactive surface area of the precipitate, solution chemistry and pH, temperature, and reaction affinity (Giammar et al. 2005; Morse et al. 2007).

The rate of carbonate precipitation is related to the rate of exchange of water molecules in the metal coordination sphere, which is considerably faster for the large Ca^{2+} ion than the smaller Mg^{2+} ion (Schott et al. 2009). Consequently, the precipitation rates of the anhydrous Mg-bearing carbonates, magnesite and dolomite [$CaMg(CO_3)_2$], can be 6 and 4 orders of magnitude slower than precipitation of calcite [$CaCO_3$] at 25 °C (Saldi et al. 2009; Schott et al. 2009). As a consequence of the comparatively slow kinetics of desolvation of Mg^{2+} ions in solution, the precipitation of magnesite and dolomite is kinetically inhibited at surface conditions, whereas calcite precipitation occurs readily (e.g., Giammar et al. 2005; Morse et al. 2007; Hänchen et al. 2008; Case et al. 2011). Instead, formation of metastable hydrated Mg-carbonate minerals is kinetically favored (e.g., Hänchen et al. 2008), and may occur at ambient temperature and pressure (e.g., O'Neil and Barnes 1971; Power et al. 2007, 2009; Wilson et al. 2009a, 2010).

Hydrated Mg-carbonate minerals have long been recognized as low-temperature weathering products of natural serpentine minerals and brucite (e.g., Hostetler et al. 1966; O'Neil and Barnes 1971). These minerals can be organized into three groups on the basis of their chemical formulae (after Canterford et al. 1984; see Table 1 for mineral formulae). The first group comprises minerals with formulae based on magnesite with variable waters of hydration. Two such minerals are known to occur in nature: nesquehonite (Stephan and MacGillavry 1972; Giester et al. 2000), and lansfordite (Hill et al. 1982). The second group is distinguished from the first by the addition of hydroxyl groups or a brucite-like formula component. Artinite (Akao and Iwai 1977a) and pokrovskite (Perchiazzi and Merlino 2006) are both members of this group. Three minerals with the chemical formula $Mg_5(CO_3)_4(OH)_2{\cdot}xH_2O$ comprise the third group: hydromagnesite with $x = 4$ (Akao et al. 1974; Akao and Iwai 1977b), dypingite with $x = 5$ (Raade 1970; Wilson et al. 2010; Ballirano et al. 2013), and giorgiosite with $x = 5$ or 6 (Friedel 1975; Canterford et al. 1984). Hydromagnesite is the only one of the latter three minerals for which the crystal structure has been determined (Akao and Iwai 1977b). A synthetic hydrated Mg-carbonate phase, of possible composition $Mg_5(CO_3)_4(OH)_2{\cdot}8H_2O$, has been described by Hopkinson et al. (2008, 2012) as a decomposition product of nesquehonite, but it has yet to be characterized from a natural setting. The hydrated Mg-carbonate minerals decompose in

sequence from lansfordite, nesquehonite, dypingite, and hydromagnesite to thermodynamically stable magnesite (Davies and Bubela 1973; Suzuki and Ito 1973; Hill et al. 1982; Canterford et al. 1984; Zhang et al. 2000; Botha and Strydom 2001).

The degree of supersaturation with respect to Mg-carbonate minerals is an important control on the rate and extent of precipitation. For homogeneous nucleation to occur, a threshold supersaturation must be achieved with smaller degrees of supersaturation resulting in a longer induction period prior to precipitation (Pokrovsky 1998; Giammar et al. 2005). For instance, magnesite precipitation rates increase systematically with increasing saturation state (Saldi et al. 2010, 2012).

Giammar et al. (2005) concluded that the interfacial free energy of magnesite-olivine is lower than magnesite-water when they observed that magnesite nucleation and crystal growth are closely related to the olivine crystal surface. It was also documented that a grain size reduction from 125-250 μm (0.088 m^2/g) to 20-50 μm (15 m^2/g) corresponded to a greater extent of magnesite precipitation due to the increased surface area (Giammar et al. 2005). Yet, Case et al. (2011) found no measurable effect on the rate or extent of magnesite precipitation in the presence of olivine when compared to solid-free systems. The effects of the olivine surface on magnesite precipitation thus require further investigation. However, the rate of magnesite precipitation may be accelerated if an initial magnesite seed is present (Giammar et al. 2005).

Due to the kinetic barriers affecting precipitation of Mg-carbonate minerals, elevated temperatures can accelerate the rate of precipitation (e.g., Case et al. 2011), until the free energy change of the precipitation reaction begins to drop significantly (e.g., Kelemen and Matter 2008). In addition, the ion activity ratio at a given saturation index affects the rate of calcite precipitation, which is maximized at a Ca^{2+}:CO_3^{2-} ratio of 1 (Perdikouri et al. 2009). Magnesite precipitation, on the other hand, is relatively insensitive to the Mg^{2+}:CO_3^{2-} ratio, yet the rate declines with CO_3^{2-} activity (Saldi et al. 2012). The rate of precipitation of both calcite and magnesite declines with increasing pH (Ruiz-Agudo et al. 2011; Saldi et al. 2012).

The presence of ligands and other cations in solution can also influence the rate of precipitation of carbonates due to complexation and adsorption effects. For instance, chemisorption of certain ligands, such as citrate and sulfate, on reactive sites has been found to inhibit calcite precipitation (Morse et al. 2007 and references therein). Similarly, the presence of aqueous Mg inhibits calcite precipitation, although aragonite [$CaCO_3$] precipitation is unaffected (e.g., Morse et al. 2007). Aqueous complexation of cations with ligands also decreases the saturation state of the carbonate mineral, and may thus have adverse effects on precipitation. On the other hand, Schott et al. (2009) suggest that ligands have the potential to enhance precipitation rates by increasing the rate of exchange of water molecules and facilitating the entrance of carbonate species into the metal coordination sphere.

The importance of Mg-carbonate precipitation rates are exemplified by magnesite. For saturation indices of up to 1.14 at 95 °C and 100 bar, magnesite nucleation was not detected by Giammar et al. (2005). Moreover, recent research indicates that the carbonation reaction of olivine at the preferred carbonation conditions (as determined by O'Connor et al. 2005) is limited by magnesite precipitation and not by the olivine dissolution rate (Haug et al. 2011). Saldi et al. (2012) determined that at 150 °C, magnesite precipitation is 3 to 4 orders of magnitude slower than forsterite dissolution at neutral to alkaline pH for their experimental conditions. A shift in emphasis towards optimizing precipitation kinetics is thus essential in order to fully optimize carbon mineralization processes.

The fastest known olivine carbonation rate was observed in studies at the U.S. Department of Energy's Albany Research Center (O'Connor et al. 2005) and at Arizona State University (Chizmeshya et al. 2007), described in more detail in the subsequent "carbon" mineralization in industrial reactors section. Carbonation rates were 10^3 times faster at the same conditions

in solutions with bicarbonate than solutions without. Importantly, it seems that there are no experiments on dissolution of plagioclase or basalt with high $NaHCO_3$. If high-$NaHCO_3$ solutions catalyze rapid basalt carbonation, comparable with the effect for olivine, then basalt might be a more favorable feedstock than peridotite, because basalt is the most common rock type in Earth's crust. However, note that there are few, if any, natural analogues of basalt alteration that achieve 100% mineral carbonation, whereas this is common for natural peridotite alteration.

Implications for carbon mineralization

For carbon mineralization processes in which cation extraction and carbonate precipitation must occur concurrently (e.g., direct aqueous carbonation), the solution chemistry must promote both mineral dissolution and carbonate precipitation (Krevor and Lackner 2011). Both kinetic and thermodynamic constraints must be considered. For example, the dissolution rates of silicates are enhanced with a decline in pH toward acidic values. Yet, carbonate minerals are generally more stable at alkaline pH, at which the equilibrium DIC concentration is also greater. Therefore, to enhance carbonate precipitation without compromising the silicate dissolution rate, a balance must be struck (O'Connor et al. 2002). Other proposed process routes separate the dissolution and precipitation reactions into different stages, providing optimal conditions for each stage independently. For instance, Park and Fan (2004) developed a "pH-swing" process that dissolves silicates at low pH and subsequently precipitates carbonates at higher pH. This allows the entire mineral carbonation process to be manipulated and controlled but costs may be much greater.

In some cases, the inherent production of alkalinity during mineral dissolution may be sufficient to permit carbonate precipitation without external pH manipulation. This requires the mineral dissolution rate to be rapid enough to counteract the pH reduction associated with dissolution of CO_2. Dissolution of highly reactive phases such as brucite at ambient conditions is sufficient to allow precipitation of hydrated Mg-carbonate minerals within a single reactor (Harrison et al. 2013). The production of alkalinity via alkaline mineral dissolution is particularly relevant for carbonation of highly reactive industrial wastes such as waste cements and mine tailings.

NATURAL ANALOGUES

Peridotite (40-98% olivine) comprises most of the Earth's upper mantle and is exposed along plate boundaries by tectonic uplift. Mantle peridotite is very far from equilibrium with the atmosphere and surface waters, providing a readily available source of chemical potential energy. Mg-olivine (forsterite) plus water or CO_2 has an energy density (J/m^3) that is ~5% of the energy density of petroleum fuels (Kelemen and Hirth 2012). This chemical potential drives geologically rapid hydration and carbonation reactions (Matter and Kelemen 2009), and the associated volume changes convert some energy to work (Kelemen and Hirth 2012), enhancing permeability and reactive surface area via reaction-driven cracking. For this reason, peridotite and its hydrated equivalent, serpentinite, have long been considered potential feedstocks for mineral carbonation (Lackner et al. 1995; O'Connor et al. 2005; IPCC 2005; Chizmeshya et al. 2007).

One of the unique and important features of proposed methods for CO_2 storage via mineral carbonation in partially serpentinized peridotite is the abundance of well-exposed, extensively studied natural analogues, ranging from "high temperature" carbonate alteration (100-300 °C, at a few kilometers depth), through near-surface weathering, to the precipitation of calcite-rich travertine and hydromagnesite–magnesite playas on the surface. These natural analogues provide an indication that carbon mineralization of peridotite is a spontaneous, rapid geological process. They also yield insight into processes, such as reaction-driven cracking, that can

achieve 100% carbonation (i.e., all Mg and Ca within the rock is in carbonate minerals), which could aid in design of engineered systems that emulate these natural processes.

High-temperature carbonate alteration of peridotite: listvenite and soapstone

Magnesite–quartz rocks (listvenite, also spelled listwanite and listwaenite) and talc–magnesite rocks (soapstone) are common in ultramafic terranes on Earth (reviews in Nasir et al. 2007; Akbulut et al. 2006; Boschi et al. 2006; Halls and Zhao 1995; Hess 1933), where they have replaced partially serpentinized peridotites (Fig. 3A-B). Their abundance demonstrates that conditions favorable for efficient and complete carbonation exist at shallow levels of the crust. While modest carbonation may accompany lower temperature serpentinization, more extensive carbonate alteration typically occurs at higher temperature and greater depths (ca. 100 to 300 °C and 3–5 km; Naldrett 1966; Madu et al. 1990; Schandl and Wicks 1991; Hansen et al. 2005; Kelemen et al. 2011; Streit, Kelemen, Eiler unpublished clumped isotope data) at the limit of existing CO_2 injection systems (Bodnar et al. 2013, this volume). For surface temperatures (~25 °C) and typical geotherms of 25 °C/km, fitting to experimental data of O'Connor et al. 2005; Kelemen and Matter (2008) predict a 500 to 5000 fold increase in olivine carbonation rates at depths of 3 to 5 km, compared to surface weathering. With pCO_2 >70 bars in this range of temperature and depths, a ~10^4 to 10^6 times increase in carbonation rates compared to surface weathering is expected.

In ultramafic terranes, carbonation reactions at temperatures greater than 100 °C and pressures less than 5 kb are driven by infiltration of CO_2-rich fluids. Listvenites can form in the presence of fluids with a mole fraction of CO_2, $X(CO_2)$, greater than ~5×10^{-5} at 5 kb, and >5×10^{-4} at 3 kb (Fig. 4). Reaction sequences correlate with changes in the nature of permeability. Phase equilibrium calculations indicate that reaction sequences preserved in carbonate-altered peridotites can be attributed to changes in the CO_2 content of the fluid phase (e.g., Hansen et al. 2005), which could be controlled in a CO_2 injection scenario.

Sharp reaction fronts in exhumed peridotite carbonation systems indicate that reaction rate and progress are governed by the rate of CO_2 supply to the reaction site (Beinlich et al. 2012). It is uncertain how fluid supply is sustained, given that many peridotite carbonation reactions potentially involve negative feedbacks that limit the extent of reaction. Carbonation reactions reduce solid density, increase solid mass, and decrease fluid mass, leading to solid volume increases and, potentially, compaction of pore space. Further, they precipitate phases in pore space, decreasing permeability and armoring reactive surfaces. A notable exception is talc–magnesite alteration of completely serpentinized peridotite, which is nearly isovolumetric because volume increase due to carbonation is approximately balanced by volume loss due to dehydration (Naldrett 1966). However, in general, carbonation of partially serpentinized rocks, and formation of listvenite from serpentinite, likely produces increasing solid volume. One manifestation of this is the presence of extension veins (Fig. 3C) (Hansen et al. 2005), attributed to reaction-driven cracking (MacDonald and Fyfe 1985; Jamtveit et al. 2000, 2008, 2012; Iyer et al. 2008; Rudge et al. 2010; Kelemen and Hirth 2012). Theoretical and observational constraints suggest that stresses of hundreds of MPa can be generated by these volume changes (Kelemen and Hirth 2012). Reaction-driven cracking may provide a positive feedback mechanism that sustains or increases permeability and reactive surface area, leading to 100% carbonation as is commonly observed in listvenite occurrences. Carbonate alteration of peridotite provides useful guidance toward efficient pathways for 100% mineral carbonation in *in situ* and industrial reactor carbon mineralization systems (Fig. 1).

Shallow subsurface peridotite weathering and related alkaline springs

Near-surface carbonation of partially serpentinized peridotites is known to occur in low-temperature spring systems worldwide (Barnes et al. 1978), and has received focused study in Italy, California, Oman, and on the seafloor (Barnes and O'Neil 1969; Bruni et al. 2002; Neal

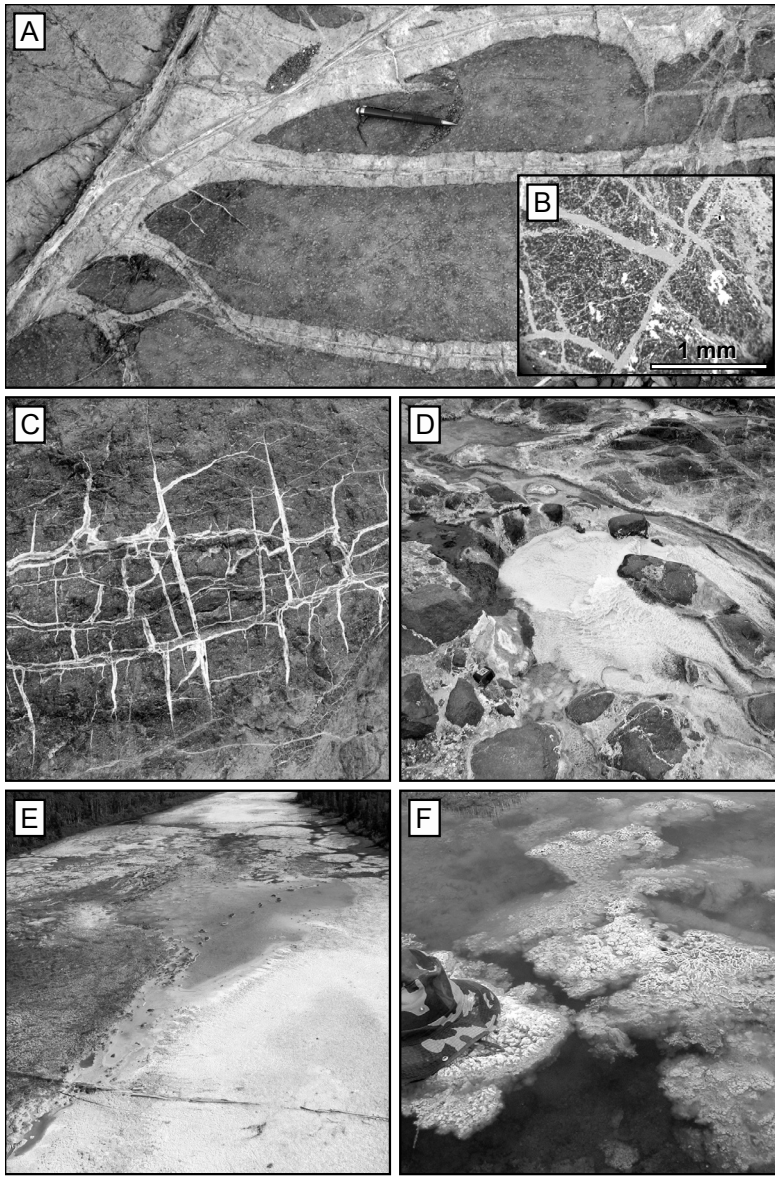

Figure 3. (A) Outcrop where light colored soapstone (talc + dolomite) has partially replaced darker, partially serpentinized peridotite, Wadi Bani Karous, Oman. Pencil for scale. Photograph by Peter Kelemen. (B) Backscattered electron micrograph of listvenite [magnesite (grey) + quartz (light grey veins) + chromite (bright white)] from ~10 m thick band replacing peridotite in Oman parallel to, and about 500 m above, a thrust fault emplacing hanging wall peridotite over footwall carbonate-bearing metasediments. Micrograph by Lisa Streit. (C) White magnesite veins filling extensional cracks in darker partially serpentinized peridotite, Wadi Fins, Oman. Field of view ~2 m wide. Photograph by Sara Kelemen. (D) Small travertine terrace growing at outlet of a peridotite-hosted alkaline spring, Wadi Tayin, Oman. Field of view ~3 m wide. Photograph by Peter Kelemen. (E) Hydromagnesite–magnesite playas near Atlin, British Columbia, Canada seen from a helicopter, white sediments at the surface are mixtures of hydromagnesite and magnesite. Field of view ~30 m wide at bottom of photograph. Photograph by Ian Power. (F) Floating microbial mats encrusted with hydrated Mg-carbonate minerals. Hat for scale. Photograph by Ian Power.

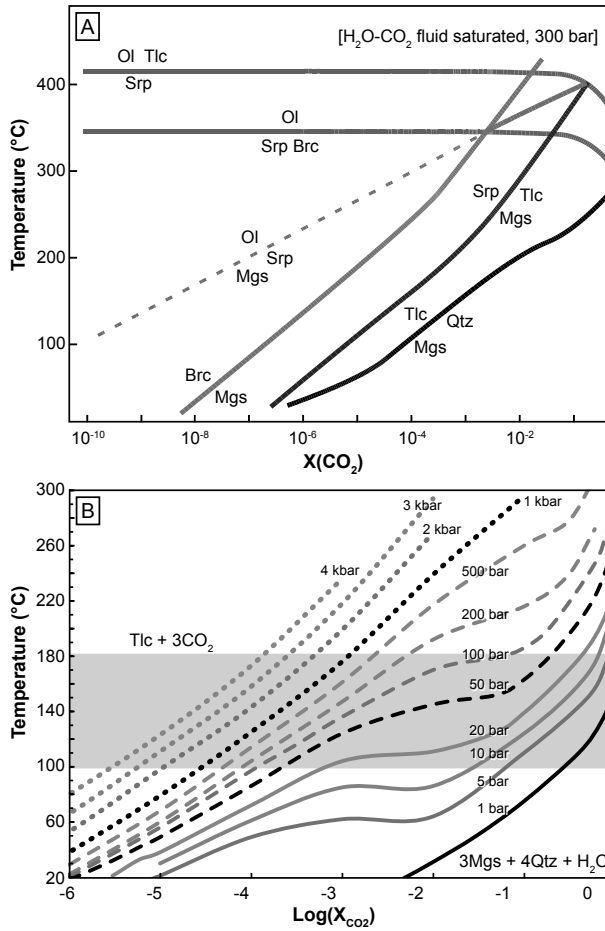

Figure 4. (A) Schematic phase diagram for reactions involving brucite (Brc), olivine (Ol), the serpentine polymorph chrysotile (Srp), talc (Tlc), quartz (Qtz), and magnesite (Mgs) in the system $MgO\text{-}SiO_2\text{-}H_2O\text{-}CO_2$, saturated in $H_2O\text{-}CO_2$ fluid at 300 bar, calculated using Thermocalc (Holland and Powell 1998). (B) Mole fraction of CO_2 in $H_2O\text{-}CO_2$ fluid XCO_2 versus temperature, for the reaction talc (Tlc) + CO_2 = magnesite (Mgs) + quartz (Qtz) + H_2O, calculated for Mg-end-members using Thermocalc (Holland and Powell 1998). At a given pressure, the assemblage magnesite + quartz at high temperature is stable only in the presence of CO_2-rich fluids. The shaded band shows the likely temperature of formation of Oman listvenites (Streit, Kelemen, Eiler et al. unpublished clumped isotope data). Figures reproduced from Kelemen et al. (2011).

and Stanger 1985; Kelley et al. 2001). Natural carbonation of these Mg-rich rocks produces alkaline springs that form carbonate fracture and vein fillings (Fig. 3C), large travertine deposits (Fig. 3D), and carbonate chimneys at submarine hydrothermal vents.

Weathering of ultramafic rocks produces two types of waters: (Type I) shallow, pH 8-9, $Mg\text{–}HCO_3$ groundwater, which develops from interaction of meteoric water with Mg-rich bedrock; (Type II) deep, high-pH (≥11) Ca–OH groundwater that develops from $Mg\text{–}HCO_3$ water when isolated from the atmosphere during alteration of peridotite at depth (Barnes and O'Neil 1969; Paukert et al. 2012). Type II waters form because, although Mg^{2+} and Ca^{2+} are released via dissolution of peridotite, Mg^{2+} is incorporated into solid reaction products such

as serpentine, brucite and magnesite, while Ca^{2+} is concentrated in solution. Subsurface Mg-carbonate veins in Oman formed via this process, have $^{18}O/^{16}O$ and clumped isotope ratios indicative of crystallization at 20 to 60 °C, ^{14}C ages generally less than 50,000 years, and very low temperature alteration assemblages including serpentine (chrysotile) + quartz (Streit et al. 2012), all of which are indicative of recent formation in a near-surface weathering environment.

Type II waters are extremely depleted in Mg^{2+} and DIC, and generally emerge at the surface with temperatures close to the mean annual air temperature, suggesting that they did not rise from more than a few hundred meters below the surface. Where they emerge at the surface as alkaline springs, they rapidly absorb CO_2 and precipitate Ca-carbonate minerals, generally calcite, to form travertine deposits. Comparison of carbon concentration in Type I and Type II provides an estimate of the proportion of Mg-carbonate minerals precipitated at depth, while the Ca^{2+} concentration in Type II yields an upper bound on the amount of Ca-carbonate that can precipitate at alkaline springs. These estimations show that for every kg of calcite in travertines, ~10 kg of Mg-carbonate minerals are precipitated in subsurface veins (Kelemen et al. 2011). In Oman, ~10^4 tonnes of CO_2 per year are consumed in peridotite carbonation via formation of subsurface veins and surficial travertines (Kelemen et al. 2011).

An interesting feature of travertines forming from peridotite-hosted, alkaline springs is that they commonly show strong depletions in both ^{18}O and ^{13}C, compared to subsurface veins, and to carbonate in equilibrium with typical surface and spring waters with $\delta^{18}O$ values of approximately −2‰ to 3‰ relative to VSMOW (Kelemen et al. 2011). Also, alkaline spring waters retain high pH and Ca^{2+} concentrations for days to weeks in artificial holding tanks in Oman. These effects are attributed to incomplete, disequilibrium transfer of atmospheric CO_2 into alkaline spring water, which limits the rate of calcite precipitation and produces light carbon isotope ratios, together with participation of OH^- with low $^{18}O/^{16}O$, in the calcite precipitation reaction.

Long-term precipitation of calcite from Ca–OH spring water over tens to hundreds of thousands of years (Früh-Green et al. 2003; Ludwig et al. 2006; Kelemen and Matter 2008; Kelemen et al. 2011) produces extensive subaerial travertines and seafloor chimneys composed of Ca-carbonates. This highlights two important features: (1) natural systems maintain permeability and reactive surface area on this time scale, and (2) alkaline solutions have a high capacity to absorb CO_2 directly from the atmosphere and the ocean. The long-term rate of carbon fixation is likely limited by the flow rate of the springs. An important, unknown quantity is the extent of microbial catalysis in these systems, though there have been extensive studies of the related microbial ecosystem at the seafloor, Lost City site (Brazelton et al. 2012; Lane and Martin 2012; Ménez et al. 2012).

Hydromagnesite–magnesite playas

Discharge of Mg–HCO_3 groundwater (Type I) into closed basins can lead to the formation of hydromagnesite–magnesite playas, a natural analogue for carbon mineralization strategies at near-surface conditions (Fig. 3E) (Renaut and Long 1989; Renaut 1990, 1993; Power et al. 2009). Study of hydromagnesite–magnesite playas offers an opportunity to examine mineral carbonation of ultramafic bedrock involving low-temperature silicate dissolution and carbonate precipitation occurring on a watershed scale. Importantly, both abiotic and biotic processes are involved in silicate dissolution and carbonate precipitation.

Biological processes enhance silicate weathering by orders of magnitude over purely abiotic processes. Soils overlying bedrock accelerate weathering by the production of chelating agents, and organic and inorganic acids produced by soil biota (Ullman et al. 1996). The stabilization of soil on bedrock, combined with biological effects, can result in weathering rates that are 100 to 1000 times greater than those of a purely abiotic rock surface (Schwartzman and Volk 1989). Consequently, an abiotic Earth would be 20-40 °C warmer if biotic weathering were

100 times faster; 35-60 °C warmer if the biotic enhancement were 1000 times abiotic rates, based on increased atmospheric CO_2 content (Schwartzman and Volk 1989). The enhanced weathering induced by biological process also results in an increase of the flux of DIC from the continents to the oceans (Andrews and Schlesinger 2001). For example, in ultramafic terranes, groundwaters at relatively shallow depths typically have pH values of ~8, alkalinity of >2500 mg/L HCO_3^-, and Mg concentrations of ~500 mg/L (Mg/Ca ratio ~70:1) (Power et al. 2009).

Mg–HCO_3 groundwater may discharge into topographic lows creating unique environments for carbonate precipitation. Upon discharge, evaporation and CO_2 degassing are important abiotic physicochemical drivers of carbonate precipitation, as they concentrate dissolved components in groundwater and cause an increase in pH, respectively. Carbonate precipitation is also facilitated by biotic processes. A variety of biofilms and microbial mats dominated by filamentous cyanobacteria inhabit these water bodies (Fig. 3F) (Power et al. 2007). Modern hydromagnesite microbialites have also been documented in water bodies associated with ultramafic terranes (Braithwaite and Zedef 1994, 1996). Biological processes including alkalinization through photosynthesis and microbial sulfate reduction operate in water bodies, and help facilitate carbonate precipitation. For instance, cyanobacteria are able to induce the precipitation of aragonite, dypingite (Power et al. 2007) and hydromagnesite (Braithwaite and Zedef 1994, 1996). Lansfordite and nesquehonite may form abiotically as hardpans and evaporative crusts (Power et al. 2009). Nesquehonite (Fig. 5A) typically forms prismatic elongated crystals, whereas dypingite may form rosette-like crystal aggregates (Fig. 5B). Hydromagnesite forms either rosettes or plates (Fig. 5C) and magnesite has a rhombic crystal habit (Fig. 5D). Over millennia, these carbonate sediments eventually fill water bodies, culminating in the formation of hydromagnesite–magnesite playas.

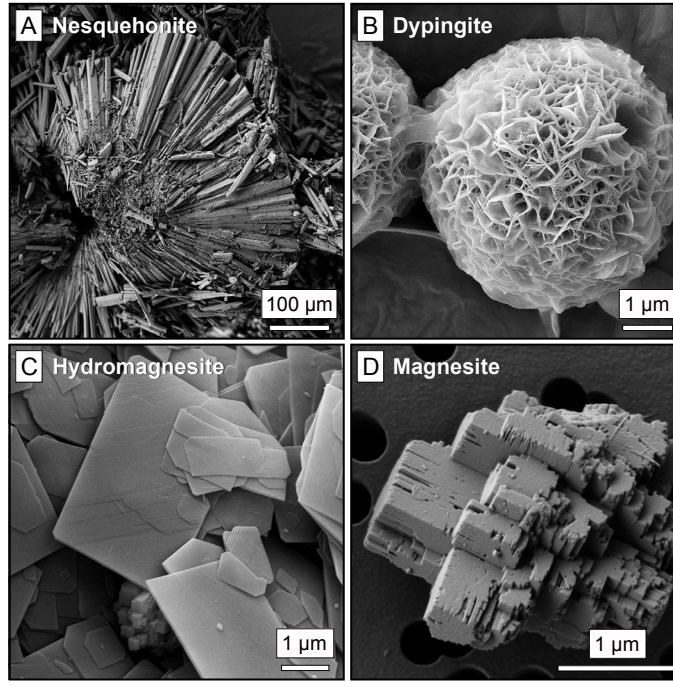

Figure 5. Representative scanning electron micrographs of (A) nesquehonite, (B) dypingite, (C) hydromagnesite, and (D) magnesite collected from hydromagnesite–magnesite playas near Atlin, British Columbia, Canada. These minerals are potential products in carbon mineralization processes. Micrographs by Ian Power.

Diagenesis of hydrated Mg-carbonate minerals appears to occur through Ostwald ripening, favoring the transformation to less hydrated phases over time (Morse and Casey 1988; Hopkinson et al. 2008, 2012). Anhydrous Mg-carbonate, magnesite, is the most stable Mg-carbonate phase and is thought to form either by dissolution–precipitation or dehydration of hydromagnesite. It is estimated that the conversion of hydromagnesite to magnesite requires 10s to 100s of years (Zhang et al. 2000). Glacial deposits underlie the hydromagnesite–magnesite playas in British Columbia, Canada, demonstrating that these deposits formed after the last deglaciation approximately 11 ka (Renaut 1993; Power et al. 2009). This implies that they provide the level of stability required of artificial carbon sinks, and that hydrated Mg-carbonate minerals are effective long-term traps for CO_2. Hydromagnesite–magnesite playas are a biogeochemical analogue for carbon mineralization via enhanced weathering, carbonation of alkaline industrial wastes at low temperatures, and biomineralization (Fig. 1).

ENHANCED WEATHERING

Enhanced weathering is a geoengineering approach that aims to accelerate natural weathering rates of silicate minerals to remove CO_2 from the atmosphere as DIC and subsequently carbonate minerals. Enhanced weathering capitalizes on the well-studied natural geochemical process of silicate weathering, which has been an important regulator of atmospheric CO_2 concentration over geologic time (Holland et al. 1986; Kump et al. 2000). Chemical weathering of silicate minerals by dissolution in natural waters may lead to precipitation of carbonate minerals under conditions of atmospheric pressure and temperature. This weathering process is one of the most significant mechanisms for exchange of CO_2 between the atmosphere and Earth's critical zone (the zone that ranges from the deepest groundwater to the outer limits of vegetation) (Schwartzman and Volk 1989; Berner 1990; Brantley 2008b). Natural silicate weathering typically follows this series of reactions (after Berner 1990): (1) atmospheric CO_2 dissolves in meteoric or surface water to form carbonic acid and bicarbonate (Eqns. 1-3); (2) divalent cations and silica are released into solution by the neutralization reaction between carbonic acid or bicarbonate with silicate minerals; (3) carbonate minerals precipitate from available divalent cations and DIC (Eqn. 6 using forsterite as an example), provided that saturation is reached and reactions are kinetically favored.

$$Mg_2SiO_{4(s)} + 2HCO_3^-{}_{(aq)} + 2H^+_{(aq)} \leftrightarrow 2MgCO_{3(s)} + SiO_{2(s)} + 2H_2O_{(l)} \quad (6)$$

Natural chemical weathering of minerals depends not only on solution chemistry and crystal chemistry but also on (1) tectonic controls on erosion and (2) climatic controls on hydrological transport and temperature-dependent dissolution kinetics (White and Blum 1995; West et al. 2005; Gislason et al. 2009). Chemical weathering rates are typically determined at the catchment level by measuring solute fluxes, water fluxes and drainage basin area in major rivers (e.g., Gislason et al. 2009). Weathering rates can also be estimated based on the time-dependent production and accumulation of cosmogenic radionuclides, such as ^{10}Be and ^{36}Cl, within the crystal structures of mineral grains in the topmost few meters of rock and soil at Earth's surface (Granger and Riebe 2007). In recognition of the strong coupling between the carbon and silicon cycles (Berner et al. 1983; Berner 1995), chemical weathering rates are commonly expressed in terms of the flux of CO_2 consumed by mineral dissolution or the flux of alkalinity (as aqueous HCO_3^-) to the oceans. Ludwig et al. (1998) have used a compilation of chemical weathering data for 35 major river catchments to provide a range of baseline fluxes of HCO_3^- between 16×10^3 mol/km^2/yr and 1411×10^3 mol/km^2/yr. This range may also be expressed in masses of CO_2 per square meter per year (i.e., 0.70 g CO_2/m^2/yr to 62.10 g CO_2/m^2/yr) for more meaningful comparison with sites where weathering and carbonation occur at accelerated rates. Currently, natural weathering results in the export of 2.3 Gt of atmospheric CO_2 to the oceans each year (Ludwig et al. 1998).

Basaltic terranes occupy less than 10% of Earth's land surface, but account for approximately 33% of CO_2 consumption by natural chemical weathering (Dessert et al. 2003). Peridotites and serpentinites are an order of magnitude less abundant than basalts (Lee et al. 2004), but represent localized regions of intense chemical weathering. The natural rate of chemical weathering is typically higher in mafic and ultramafic terranes, compared to regions underlain by quartzo-feldspathic rocks. For instance, Cleaves et al. (1974) conducted a comparative study of chemical weathering of biotite-feldspar-quartz schist and serpentinite that underlie a watershed at Soldiers Delight in the Eastern Piedmont Province of Maryland, USA. Although they do not report bicarbonate fluxes, Cleaves et al. (1974) report that 3.24 g/m^2/yr of dissolved silica, Na^+, K^+, Ca^{2+} and Mg^{2+} were removed from the schist, whereas 5.93 g/m^2/yr of the same aqueous species were leached from the serpentinite.

Implementation of enhanced weathering would involve mining, crushing and spreading of reactive Mg-silicate minerals such as olivine in agricultural and forest soils and along coastlines (Schuiling and Krijgsman 2006; Schuiling and de Boer 2011). Enhanced weathering seeks to exploit the high reactivity of Mg-silicate minerals with meteoric water, seawater and soils. This is due to the ability of these minerals to neutralize carbonic acid by generating aqueous bicarbonate and to promote the precipitation of Mg-carbonate minerals. Fertilization of soils using wollastonite, Mg- and Ca-carbonates, and fly ash has been reported to accelerate CO_2 uptake in soils and biomass (Hartmann and Kempe 2008 and references therein), but awaits rigorous testing and costing in the context of large scale implementation.

Schuiling and de Boer (2011) propose that dissolution of olivine may be enhanced by abrasion and grain size reduction in high-energy, shallow coastal environments. Based on modeling and cost estimates, Hangx and Spiers (2009) suggest that implementation of these strategies at a global scale may not be cost-effective (given expenses associated with mining, milling and transport of olivine) or sufficiently rapid within seawater (pH ~8.2) in temperate regions. They suggest that enhanced weathering in coastal settings and soils may be most feasible in tropical regions where weathering rates are greater. Enhanced weathering may be limited by the accumulation of silicic acid (Fig. 1). Schuiling et al. (2011) propose that the build-up of aqueous silica may be minimized by precipitation of secondary phases and uptake by the biosphere. Song et al. (2012) suggest that it may also be possible to manipulate the biological pump for silicon by enhancing silicon uptake by plants to accelerate the biogeochemical sequestration of atmospheric CO_2. Stimulating biological processes that accelerate mineral dissolution or increasing reactive surface areas *in situ* could further enhance weathering. It remains unknown to what extent enhanced weathering in natural settings will contribute to ocean alkalinity should drainage into catchments be transported to the ocean prior to mineral precipitation.

CARBONATION AT INDUSTRIAL SITES

Many industrial wastes are appropriate feedstock for carbon mineralization owing to high Mg and Ca-silicate, -oxide, and -hydroxide contents (Renforth et al. 2011; Bobicki et al. 2012). Carbonation of industrial wastes has several key advantages. Processed mineral wastes and other industrial wastes are inherently more reactive than natural minerals due to processes such as comminution, and because, like ultramafic rocks from Earth's mantle, they are often formed at conditions far from equilibrium with Earth's surface conditions. Carbonation may decrease the hazardous nature of certain wastes such as asbestos mine tailings and red mud (Bobicki et al. 2012). In addition, such wastes are typically produced near point sources of CO_2 (Huntzinger et al. 2009b; Gunning et al. 2010; Renforth et al. 2011; Bobicki et al. 2012). Carbonation of wastes offers the opportunity for industries to use this material to provide an environmental benefit, and possibly a financial advantage in the case of a carbon tax or

emissions cap-and-trade systems (e.g., Bobicki et al. 2012; Hitch and Dipple 2012). In certain industries, carbonation of industrial wastes provides an opportunity to "close the loop" on CO_2 emissions. Moreover, implementation of carbon mineralization strategies for industrial wastes also provides a valuable proving ground before deployment of such technologies at a larger scale for carbonation of natural minerals (Huntzinger and Eatmon 2009; Bobicki et al. 2012; Power et al. 2013b).

Passive weathering and carbonation

Immense quantities of Mg- and Ca-rich alkaline wastes have been generated since the Industrial Revolution (Renforth et al. 2011; Renforth 2012; Bobicki et al. 2012; Sanna et al. 2012), and are weathering and carbonating as a consequence of prolonged exposure to Earth's atmosphere, hydrosphere and biosphere. We refer to this as passive weathering and carbonation, which occurs via natural hydrologic and element cycles without human mediation. The potential for passive carbonation of alkaline wastes to provide a sink for CO_2 has only recently been recognized. Consequently, the rate of passive carbonation in waste materials has only been assessed in detail for urban soils contaminated by Ca-rich building materials (Renforth et al. 2009; Washbourne et al. 2012; Manning and Renforth 2013) and for ultramafic mining environments (Wilson et al. 2006, 2009a,b, 2011; Bea et al. 2012; Beinlich and Austrheim 2012; Pronost et al. 2012).

Soils contaminated with alkaline building waste. Soils are a significant sink for both organic and inorganic carbon; the latter typically takes the form of pedogenic calcite. Extensive deposits of caliche (synonymous with calcrete, which is an accumulation of predominantly microcrystalline calcite) may form within soils in arid environments by weathering of Ca-rich bedrock or evaporation of Ca-bearing groundwater (Goudie 1973; Watts 1980; Schlesinger 1985; Knauth et al. 2003). Manning (2008) suggested that the extent of pedogenic carbonate formation could be greater within urban soils contaminated with Ca-rich alkaline wastes such as cement from demolition of buildings and slag from the manufacture of steel. Renforth et al. (2009) measured the $CaCO_3$ content of two contaminated urban soils near Newcastle upon Tyne, UK. One soil contained concrete demolition waste (to a depth of 3 m) and had pH values as high as 11.8, while the second was from a slag-contaminated field adjacent to a former steel works that produced runoff with a pH of 12.5. Renforth et al. (2009) used stable carbon and oxygen isotopic data for soil carbonate to establish that organic carbon and atmospheric CO_2 were being mineralized. They estimate that these contaminated soils are passively sequestering 25 ± 12.8 t C/ha/yr, which is equivalent to 9160 ± 4690 g $CO_2/m^2/yr$; more than two orders of magnitude greater than the highest weathering rates estimated for river catchments.

Ultramafic mine tailings. Milled mineral wastes (tailings) produced by mining of mafic- and ultramafic-hosted ore deposits are rich in Mg-silicate and -hydroxide minerals, such as serpentine, forsterite, and brucite. The reactivity of mine tailings is enhanced relative to natural deposits due to the high reactive surface areas that result from ore processing (Wilson et al. 2009a, 2011). Passive weathering and carbonation of mine tailings has been documented at historical and active mine sites in Canada, USA, Australia, and Norway (Wilson et al. 2006, 2009a,b, 2011; Levitan et al. 2009; Bea et al. 2012; Pronost et al. 2012; Beinlich and Austrheim 2012). Lansfordite, nesquehonite, dypingite and hydromagnesite have been found as weathering products of ultramafic mine tailings (Wilson et al. 2006, 2009a,b, 2011; Bea et al. 2012; Beinlich and Austrheim 2012). These Mg-carbonate minerals commonly form in two distinct environments within ultramafic mine tailings storage facilities (Fig. 6): (1) at tailings surfaces as efflorescent crusts, thick hardpans and coatings on loose cobbles and (2) at depth within tailings as a cement that forms between mineral grains (Wilson et al. 2009a). The surface expression of passive mineral carbonation in mine tailings is likely related to ingress of atmospheric CO_2 into near-surface tailings waters coupled with evapoconcentration of these Mg-rich solutions. High abundances of hydrated Mg-carbonate minerals may develop

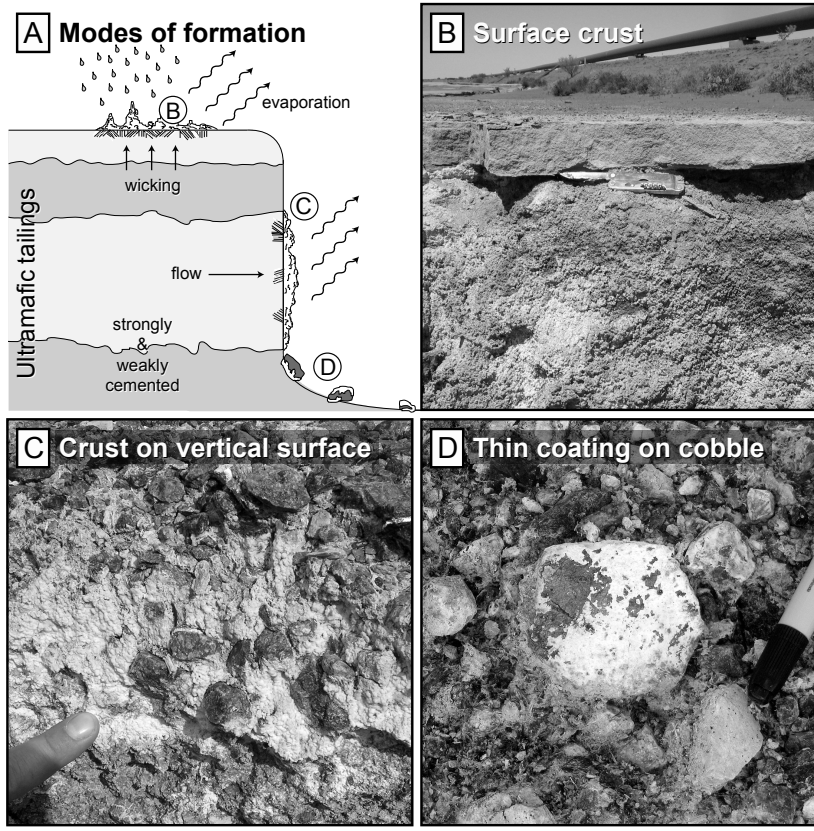

Figure 6. (A) Conceptual diagram illustrating the mechanisms of secondary carbonate mineral formation in mine tailings; note labels for photographs in B, C, and D (modified after Wilson et al. 2009a). Photographs were taken at the Mount Keith Nickel Mine in Western Australia (B) and Clinton Creek Chrysotile Mine in Yukon, Canada (C-D). (B) Hydromagnesite-rich crust formed on top surface of mine tailings. (C) Mg-carbonate-rich efflorescence on horizontal surface of tailings formed by outflow from tailings. (D) Coatings of dypingite ± hydromagnesite on cobbles of serpentinite. Marker for scale. Photographs by Gregory Dipple and Siobhan Wilson.

at depth as carbonated surfaces become buried or as a consequence of ongoing reaction post burial (e.g., Pronost et al. 2012). Estimated rates of CO_2 uptake into Mg-carbonate minerals at several chrysotile, diamond and nickel mines range from 374 to 6200 g $CO_2/m^2/yr$ (Wilson et al. 2009a, 2011; Schuiling et al. 2011; Bea et al. 2012), which is 2-5 orders of magnitude greater than natural weathering rates for Earth's major river catchments.

Stable carbon and oxygen isotopic data for hydrated Mg-carbonate minerals from the Diavik Diamond Mine in Canada (Wilson et al. 2011), the Mount Keith Nickel Mine in Australia (Wilson et al. 2010), and 12 mines in the Feragen Ultramafic Body in Norway (Beinlich and Austrheim 2012) are consistent with brucite and serpentine carbonation under CO_2-limited conditions. Additionally, reactive transport modeling and modal mineralogical data for the Mount Keith Nickel Mine also support this interpretation showing that ingress of atmospheric CO_2 is restricted to the upper 50 cm of mine tailings deposits at Mount Keith (Bea et al. 2012). Carbon mineralization technologies that rely upon low-temperature weathering of minerals must therefore target this rate limitation by enhancing the supply of CO_2 into solution

(Fig. 1). Additionally, laboratory experiments suggest that carbonation of mining residues is limited by high water contents when diffusion of atmospheric CO_2 provides the only carbon source (Assima et al. 2013).

Accelerated carbonation

A potential strategy for accelerating carbonation rates of pulverized industrial wastes is to increase the supply of CO_2. Increasing exposure to atmospheric CO_2 may be sufficient to accelerate carbonation of highly reactive materials, such as waste from acetylene production (e.g., Morales-Flórez et al. 2011). Therefore, simple modifications of waste management practices to optimize atmospheric exposure may offer substantial benefits in terms of carbonation rates. For instance, at the Diavik Diamond Mine in the Canadian subarctic, rates of passive carbonation in tailings are two orders of magnitude higher than natural silicate weathering rates predicted for the geographic region (Wilson et al. 2011). Yet, carbonation is hindered by tailings management practices that leave tailings largely submerged, which limits the ingress of atmospheric CO_2 (Wilson et al. 2011). Therefore, adjusting tailings management practices to avoid high water contents in tailings could enhance passive carbonation rates. Similar modifications could be made for management of wastes that carbonate passively such as construction and demolition wastes and steel making slag. Urban soil engineering, for instance, aims to exploit the natural carbon cycling processes in soils to optimize the uptake of atmospheric CO_2 through the addition of waste Mg- and Ca-silicates to urban soils (Renforth et al. 2009; Manning and Renforth 2013; Washbourne et al. 2012). This process is advantageous, as it requires minimal intervention and management (Washbourne et al. 2012).

An active approach would accelerate rates of carbonation by circulation of CO_2-rich fluids or gases through feedstock such as mine tailings or cement kiln dust (Fig. 7A). For instance, Harrison et al. (2013) documented an acceleration of ~240 times over passive rates of brucite carbonation in an alkaline slurry by supplying gas similar in composition to flue gas. Similarly, Huntzinger et al. (2009b) achieved ~100% carbonation of landfilled cement kiln dust in column experiments by supplying gas with ~8.5% CO_2, similar to CO_2 concentration in flue gas. In the case of industrial waste products such as mine tailings, cement kiln dust, and Ca-rich combustion products, the wastes are generated at or near the location of point sources of CO_2 emissions (Bobicki et al. 2012). Consequently, CO_2 emissions from these sources could be directly sup-

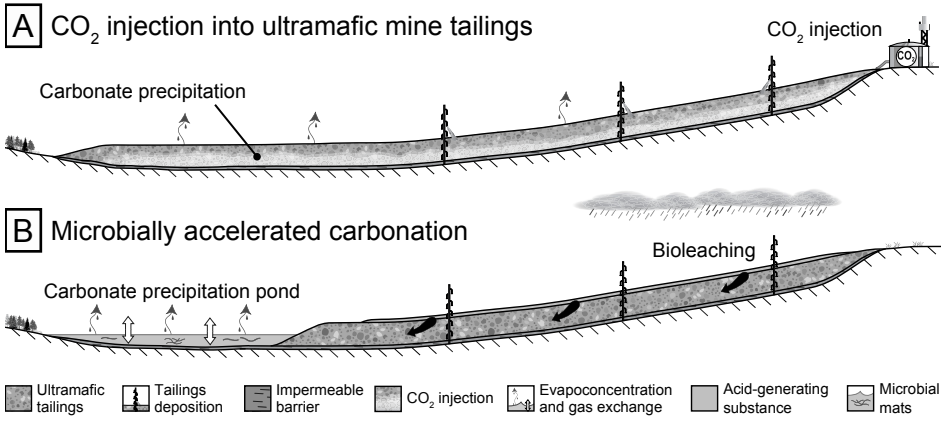

Figure 7. A schematic of two mine tailings facilities depicting (A) an abiotic strategy employing CO_2 injection, and (B) use of bioleaching and microbial carbonate precipitation as strategies for carbon mineralization (modified after Power et al. 2013b).

plied to waste materials. For example, Arickx et al. (2006) utilized emissions at a municipal solid waste incinerator (MSWI) plant to successfully carbonate the MSWI ash produced at the plant. This strategy is advantageous, as it provides a direct and easily monitored offset of industry-specific emissions. Industrial scale carbonation of alkaline wastes could act as a testing ground for more widespread implementation of enhanced weathering at the global scale.

BIOLOGICALLY MEDIATED CARBONATION

Microbially enhanced mineral dissolution

Bacteria exploit a wide range of thermodynamically favorable redox reactions to support metabolism (Barns and Nierzwicki-Bauer 1997; Nealson and Stahl 1997), and these reactions can directly and indirectly affect the solubility and dissolution of minerals. The small size of bacteria, i.e., the scale on which they process materials (Pirie 1973), is key to understanding their contributions to mineral dissolution. Biogeochemical processing at low Reynold's Number (Purcell 1977) generates steep concentration gradients that can extend several micrometers outwards from the cell surface, creating unique chemical environments around individual cells, around microcolonies of cells and within/throughout biofilms. When combined with the close association between bacteria and mineral substrates (e.g., Mielke et al. 2003), or the growth of bacteria as biofilms, the concentration of reactive by-products, such as organic acids, can be orders of magnitude greater at the mineral surface than the bulk fluid phase. This ability to alter the chemistry of their surrounding environment is what enables bacteria to promote mineral dissolution, typically to their benefit (Southam and Saunders 2005). The biological influence on weathering in the critical zone in soils is orders of magnitude greater than pure abiotic reaction rates (Brantley et al. 2011). Biological processes, which accelerate geochemical phenomena through enzyme catalysis, offer fundamental strategies to enhance weathering of Ca- and Mg-silicates (Schuiling and deBoer 2010; Yao et al. 2013).

Both aerobic and anaerobic microorganisms can have a profound effect on the geochemistry of dissolved metals and metal-bearing minerals. Heterotrophy, the use of organic carbon as a source of energy, is employed by aerobic bacteria that use oxygen as their terminal electron acceptor (Eqn. 7) and by anaerobic, respiring bacteria that employ alternative electron acceptors, e.g., iron-oxyhydroxide (Eqn. 8), and sulfate, ultimately producing CO_2 as a by-product of metabolism by the step-wise oxidation of organic carbon.

$$C_6H_{12}O_6 + 6O_2 \rightarrow 6CO_2 + 6H_2O \quad (7)$$

$$C_2H_4O_2 + 2Fe(OH)_3 \rightarrow C_2H_2O_2 + 2Fe^{2+} + 4OH^- + 2H_2O \quad (8)$$

Microbially enhanced mineral dissolution is not restricted to carbon dioxide/carbonic acid production (Olsson et al. 2012), but is dramatically enhanced by a wide range of inorganic and organic acids produced via microbial activity (Schwartzman and Volk 1989; Southam and Saunders 2005; Salek et al. 2013). In natural systems, the microbial degradation of complex organic compounds such as cellulose and hemicellulose to simpler, intermediate organic carbon molecules such as acetate, oxalate and citrate, can also enhance mineral solubility by forming metal-organic complexes and can cause active dissolution of silicate minerals (Bennett 1991; Hiebert and Bennett 1992; Bennett et al. 1996, 2001; Rogers and Bennett 2004).

Sulfuric acid, considered the most effective chemical for cation extraction from serpentine minerals (Maroto-Valer et al. 2005), is generated through the bio-oxidation of reduced sulfur-bearing materials, e.g., metal sulfides (biogeochemical cycling between Eqn. 9 and 10) and the bio-oxidation of elemental sulfur (Eqn. 11) (Nordstrom and Southam 1997; Enders et al. 2006). The bacteria that catalyze these processes include *Leptospirillum ferrooxidans* (an iron oxidizer), *Acidithiobacillus ferrooxidans* (an iron and sulfur oxidizer), and *A. thiooxidans* (a

sulfur oxidizer), all of which are common in acidic environments containing pyrite (Edwards et al. 1999; Nordstrom and Southam 1997). Under acidic conditions (pH < 4; Kirby et al. 1999), these bacteria can generate acid up to 10^5 times faster than the abiotic rate (Singer and Stumm 1970). The oxidation of iron (Eqn. 9) also contributes to acid production through hydrolysis (Eqn. 12).

$$Fe^{2+} + ¼O_2 + H^+ \rightarrow Fe^{3+} + ½H_2O \quad (9)$$

$$FeS_2 + 14Fe^{3+} + 8H_2O \rightarrow 15Fe^{2+} + 2SO_4^{2-} + 16H^+ \quad (10)$$

$$S^\circ + 1.5O_2 + H_2O \rightarrow SO_4^{2-} + 2H^+ \quad (11)$$

$$Fe^{3+} + 3H_2O \rightarrow Fe(OH)_3 + 3H^+ \quad (12)$$

The acids produced through microbial activity promote the aqueous dissolution of Ca- and Mg-silicate minerals that can subsequently contribute to carbon mineralization reactions (Olsson et al. 2012).

Biological processes that aid in silicate dissolution could be utilized to further enhance carbonation of alkaline wastes. There has been preliminary research regarding the bioleaching of alkaline wastes such as slag (Willscher and Bosecker 2003), red mud (Vachon et al. 1994), and ultramafic mine tailings (Power et al. 2010). Biological processes require minimal energy input, and in conjunction with physical and chemical processes, could be applied to create the conditions that are favorable for carbonate precipitation. For example, mine tailings generally lack overlying soil; therefore, without sufficient energy sources for acid-generating microbes, biological weathering is limited. Sulfuric acid could be generated *in situ* in tailings storage facilities through the use of *A. ferrooxidans* and *A. thiooxidans* to accelerate the oxidation of reduced sulfur and iron compounds that are intrinsic to, or layered onto, tailings (Fig. 7B). Experimental systems possessing an acid-generating substance colonized with *Acidithiobacillus* spp. produced leachates with Mg concentrations that were at least one order of magnitude greater than in control systems, thereby increasing the availability of dissolved Mg^{2+} ions for carbon mineralization (Power et al. 2010).

Carbonate biomineralization

Weathering of silicate minerals is often biogeochemically coupled to the precipitation of carbonate minerals by microorganisms (Ferris et al. 1994). In ancient and contemporary systems, microorganisms have substantially contributed to carbonate precipitation and sedimentation within oceans, lakes, springs, caves, and soils (Riding 2000; Pomar and Hallock 2008). There are three types of biomineralization: (1) biologically controlled mineralization, (2) biologically induced mineralization, and (3) organomineralization. Biologically controlled mineralization is when cellular activity directs the nucleation, growth, morphology, and final location of a mineral; whereas biologically induced mineralization refers to the indirect process of mineral precipitation as a result of interactions between biological activity and the environment (Frankel and Bazylinski 2003). Organomineralization is a more passive process in which organic matter may create conditions for mineral precipitation in the absence of a living organism (Dupraz et al. 2009).

Fundamentally, microbial processes that induce carbonate precipitation include photosynthesis, ammonification, denitrification, manganese and iron oxide reduction, sulfate reduction, anaerobic sulfide oxidation and methanogenesis (Ferris et al. 1994; Riding 2000; Roberts et al. 2004). Experimental studies have demonstrated biologically induced precipitation of a wide-range of carbonate minerals including aragonite (Sanchez-Moral et al. 2003 and references therein), calcite (Thompson and Ferris 1990), dolomite (van Lith et al. 2003), and the hydrated Mg-carbonate minerals, dypingite and hydromagnesite (Power et al. 2007; Shirokova et al. 2013).

Carbonated microbial mats, whiting events, and microbialites are striking examples of biologically induced carbonate precipitation (Thompson et al. 1997; Riding 2000; Dupraz et al. 2009). Microbial carbonate precipitation is known to play an active role in the formation of landscape features, such as hydromagnesite–magnesite playas, that result from ultramafic bedrock weathering (Power et al. 2009). While several approaches for biological carbon sequestration have been examined elsewhere, we focus on (1) carbonate precipitation induced by photoautotrophs, and (2) carbonic anhydrase facilitated carbonate precipitation, which are relevant to *ex situ* carbon mineralization in continental systems. Biologically controlled mineralization (e.g., forams) and geoengineered biomineralization in the oceans are not considered here.

Coupling photosynthesis and carbonate precipitation. Globally, tens of Gt of CO_2 are fixed and respired by microorganisms each year (Sarmiento and Gruber 2002; Van Cappellen 2003). Photoautotrophs, such as cyanobacteria and algae, are microorganisms that use sunlight for energy and CO_2 as a carbon source (Fig. 8). These microbes are ideally suited for carbon sequestration purposes because they harness their own energy and do not require organic carbon. Microbial processes can dramatically alter the microenvironment relative to the bulk water chemistry. For instance, adsorption of cations by the net-negative microbial cell wall increases their concentration within the microenvironment of the cell (Schultze-

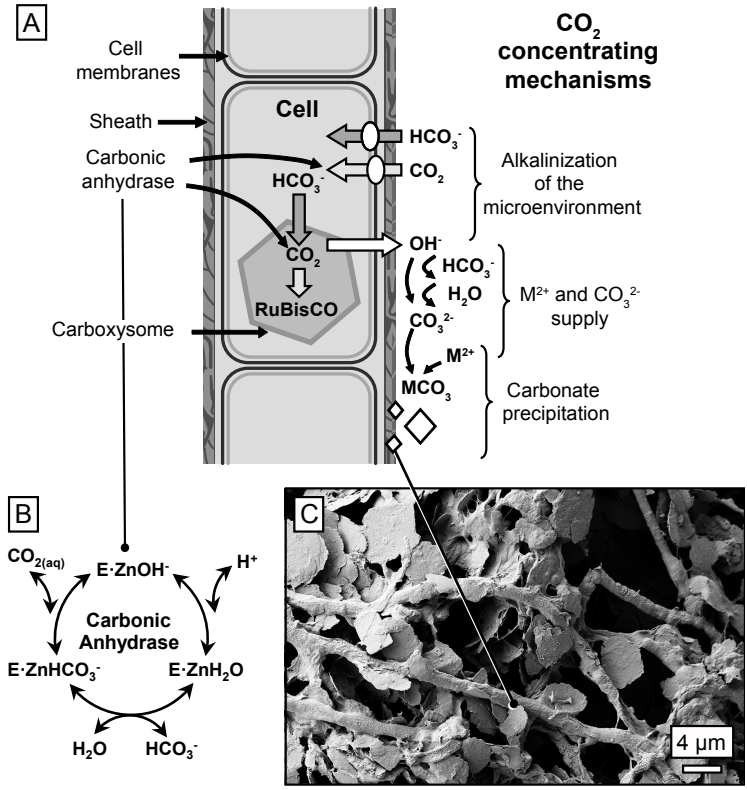

Figure 8. (A) Conceptual diagram of cyanobacteria showing carbon concentrating mechanism that may result in the alkalinization of the microenvironment (modified from Riding 2006). (B) Reaction mechanism of catalytic CO_2 hydration by carbonic anhydrase. (C) Scanning electron micrograph of filamentous cyanobacteria associated with plates of the Mg-carbonate mineral, dypingite. Micrograph by Ian Power.

Lam and Beveridge 1994; Obst et al. 2006) and hence can facilitate mineral precipitation. In addition, microbial cell walls offer an ideal surface for mineral nucleation with large numbers of regularly-spaced, chemically identical nucleation sites such as carboxyl groups and amino functional groups. Extracellular polymeric substances (EPS) that act as a barrier between a cell and its environment may also possess abundant functional groups that aid in inducing carbonate precipitation (Dupraz et al. 2009). Organic ligands (e.g., carboxyl functional groups, $R.COO^-$) within a biofilm or on the cell wall may cause partial dehydration of cations (e.g., Mg^{2+}) and allow for increased association with carbonate anions (Eqn. 13)(Dudev et al. 1999; Zhang et al. 2012).

$$R.COO^- + [Mg(H_2O)_6]^{2+} \rightarrow [Mg(H_2O)_5(R.COO)]^+ \quad (13)$$

Lowering the hydration state of cations could facilitate carbonate precipitation, perhaps allowing for the precipitation of less hydrated and more stable minerals (Zhang et al. 2012).

Photosynthesis may drive a pH increase, referred to as alkalinization. Thompson and Ferris (1990) demonstrated that the unicellular cyanobacterium, a *Synechococcus* sp., could induce the precipitation of carbonate minerals primarily through alkalinization of its microenvironment. Photoautotrophs, such as cyanobacteria, possess CO_2 concentrating mechanisms (CCM) that enable them to concentrate CO_2 up to 1000 times relative to their external environment (Fig. 8) (Kaplan and Reinhold 1999; Badger and Price 2003). CO_2 and HCO_3^- are actively transported into the cell, where the carbonic anhydrase enzyme converts all forms of DIC to HCO_3^-. HCO_3^- anions then diffuse into the carboxyzome, a protein-enclosed compartment hosting RuBisCO, the key enzyme for fixing carbon. In the carboxysome, carbonic anhydrase again converts HCO_3^- into CO_2, thereby releasing an OH^- ion from the cell (Thompson and Ferris 1990; Riding 2006; Power et al. 2011a) (Eqn. 14 representing the overall process of alkalinization by photosynthesis).

$$HCO_3^- + H_2O + h\nu \rightarrow CH_2O + OH^- + O_2\uparrow \quad (14)$$

Alkalinization of the microenvironment may occur within the interstitial waters of a biofilm or microbial mat, but may also extend to macroscopic scales, i.e., a lake. Given adequate cation and DIC concentration, alkalinization may cause waters to become saturated with respect to carbonate minerals. Conventional knowledge asserts that carbonate precipitation causes a release of CO_2 from solution as described by Equation (15) (Wollast et al. 1980; Ware et al. 1992; Frankignoulle et al. 1994).

$$M^{2+} + 2HCO_3^- \rightarrow MCO_3 + CO_2 + H_2O \quad (15)$$

The ratio of CO_2 release to carbonate precipitated depends on the alkalinity of the water. Carbonate precipitation in freshwater should theoretically release an equal amount of CO_2; seawater with a greater buffering capacity should release 0.6 moles of CO_2 for each mole of carbon precipitated as carbonate mineral (Ware et al. 1992; Frankignoulle et al. 1994). Precipitation of carbonate minerals results in net carbon sequestration if there is an external supply of alkalinity (Lackner 2002). Whether carbonate precipitation acts as a net source or sink of CO_2 also depends on two key biological processes. First, calcification is often coupled to photosynthesis (e.g., cyanobacterial carbonate precipitation and coccolithophores), which generates alkalinity that can act to neutralize acidity generated from carbonate precipitation (Eqn. 14). Dupraz et al. (2009) refer to those microbial processes that generate carbonate anions as the "alkalinity engine." The net impact by calcifying organisms on CO_2 partial pressure depends on the calcification to photosynthesis ratio (C:P) (Soetaert et al. 2007). CO_2 partial pressure will remain constant for both coccolithophores and corals if the C:P ratio is approximately 1.2 or 1.7. In the case of cyanobacterial carbonate precipitation, e.g., direct measurement of CO_2 fluxes from marine whiting events found in association with cyanobacteria and microalgae (e.g., *Synechococcus*, *Synechoecystis*, and *Chlorella*) in the

Bahamas demonstrated a drawdown of CO_2 at an average rate of 8.1×10^{-11} moles CO_2/m^2/s (Robbins and Yates 2001). Second, it must also be considered that CO_2 released during carbonate precipitation may be metabolized into biomass, another sink for CO_2. Consequently, if the rate of photosynthesis in seawater is at least 0.6 times the calcification rate, there is no change in CO_2 partial pressure (Suzuki 1998). Coupling carbonate precipitation to a biological mediator is highly advantageous as it uses a renewable energy source (sunlight), generates alkalinity (e.g., OH^- ions) and fixes CO_2 into biomass.

Sequestering CO_2 would involve stimulating the growth of photoautotrophs (e.g., microalgae and cyanobacteria) that are capable of precipitating carbonates within specifically designed ponds or basins with excess alkalinity (Fig. 7B; Lackner 2002). Ponds and photobioreactors using microalgae are actively being developed for production of biofuel and valuable by-products (Schenk et al. 2008; Mata et al. 2010). Microalgae and cyanobacteria are very attractive for biofuel production because they can be grown on non-arable land in saline and sub-saline waters and their photosynthetic efficiencies can be several times greater than terrestrial plants, resulting in greater biomass production and CO_2 fixation as organic matter per unit area (Chisti 2007). Cyanobacteria and microalgae that are currently being assessed for biofuel production in terms of growth rate and quality of biomass (e.g., lipid content; Rodolfi et al. 2009) have also been independently assessed for their ability to induce carbonate precipitation (e.g., Power et al. 2011b). Growth of cyanobacteria and microalgae requires an aqueous habitat with suitable environmental conditions (e.g., pH, light, nutrients, and salinity). An ideal scenario would involve specially designed carbonate precipitation ponds with saline waters rich in Mg and Ca that would cultivate the growth of photoautotrophs (Power et al. 2011b). Furthermore, cyanobacteria occupy a wide-range of environments on Earth; many species are halophilic or thermophilic, and thus may tolerate saline waters or the higher temperatures of CO_2-rich flue gases, both of which may be used for sequestering CO_2 (Jansson and Northen 2010). Waste brines or seawater could act as a feedstock for dissolved cations that are necessary for precipitation of carbonate minerals. There is also the possibility of genetically modifying cyanobacteria to enhance their ability to precipitate carbonate minerals (e.g., Chen et al. 2012). Without a carbon source in addition to atmospheric CO_2, biomineralization may be limited by the supply of CO_2 (Fig. 1; Power et al. 2011b).

Enzymatic carbonation. The use of the carbonic anhydrase (CA) enzyme can be advantageous in cases where the supply of CO_2 into solution is rate-limiting. CA is ubiquitous in nature and acts to catalyze the dissociation/association of $CO_{2(aq)}$ to HCO_3^-. CA plays an important role in the carbon concentrating mechanism of photoautotrophic, chemoautotrophic, and heterotrophic prokaryotes (Prabhu et al. 2011). CA (represented by $E{\cdot}ZnH_2O$) first deprotonates, which is followed by nucleophilic attack of the carbon atom of the $CO_{2(aq)}$ molecule to form HCO_3^- that is then replaced by a water molecule (Eqn. 16-18).

$$E{\cdot}ZnH_2O \leftrightarrow E{\cdot}ZnOH^- + H^+ \quad (16)$$

$$E{\cdot}ZnOH^- + CO_{2(aq)} \leftrightarrow E{\cdot}ZnHCO_3^- \quad (17)$$

$$E{\cdot}ZnHCO_3^- + H_2O \leftrightarrow E{\cdot}ZnH_2O + HCO_3^- \quad (18)$$

CA operates at rates that are typically between 10^4 and 10^6 reactions per CA molecule per second, thereby accelerating the rate of DIC supply (Mirjafari et al. 2007; Sharma et al. 2011). Consequently, CA has been shown to enhance the precipitation of Ca- and Mg-carbonate minerals (Bond et al. 2001; Dilmore et al. 2009; Favre et al. 2009; Lee et al. 2010; Sharma and Bhattacharya 2010; Vinoba et al. 2011; Power et al. 2013a). CA could be utilized in CO_2 scrubbers to capture CO_2 at industrial point sources, or for direct air capture (e.g., Bond et al. 2001; Figueroa et al. 2008; Savile and Lalonde 2011; Zhang et al. 2011; Power et al. 2013a). It may also be used in combination with conventional technologies for capture of CO_2 in absorption-desorption processes that utilize alkanolamines such as monoethanolamine (MEA),

diethanolamine (DEA), and N-methyl-diethanolamine (MDEA) (Penders-van Elk et al. 2012). The lifespan of CA may be increased substantially by immobilizing it onto a solid substrate (e.g., Mateo et al. 2007; Ozdemir 2009). In terms of production, many microorganisms are capable of producing CA (Ramanan et al. 2009; Li et al. 2010; Sharma and Bhattacharya 2010; Prabhu et al. 2011). Genetic modifications may be possible for increasing the production of CA or expressing CA production in different organisms (Chen et al. 2012; Ki et al. 2012). Immobilizing CA or continual production of microbial CA could provide a chemical environment that is conducive to CO_2 sequestration. For instance, *Saccharomyces cerevisae*, a yeast commonly used in the food industry, was engineered to express several CA isoforms and mineralization peptides for enhancing calcite precipitation using coal fly ash as a source of CaO (Barbero et al. 2013).

CARBON MINERALIZATION IN INDUSTRIAL REACTORS

Carbon mineralization using industrial reactors to carbonate mineral feedstock was first studied experimentally by Lackner and co-workers at the Los Alamos National Laboratory (LANL) (Lackner et al. 1995; Lackner 2003; Fig. 9). The experimental process they used originated from efforts to address a magnesium shortage in the United States during World War II (Houston 1945; Barnes et al. 1950). Magnesium was extracted from peridotite and serpentinite in hydrochloric acid, followed by gas-solid carbonation of $Mg(OH)_2$ at high temperature to form $MgCO_3$. The energy consumption and associated theoretical CO_2 emissions (assuming coal generated electricity) of this process was about four times the energy embodied in the sequestered CO_2 (Nilsen and Penner 2001). Although this initial study revealed the process to be economically impractical as well as carbon intensive, it encouraged subsequent research on improving the efficiency of industrialized carbon mineralization as a method of CO_2 sequestration. Since then, many carbonation approaches have emerged, and several gas-solid and aqueous-solid carbonation processes have been proposed. The majority of this work has focused on the development of fast, large-scale methods for fixing and storing CO_2 at industrial point sources. The IPCC Special Report on Carbon Dioxide Capture and Storage, plus five other reviews, provide a comprehensive description of the status of research

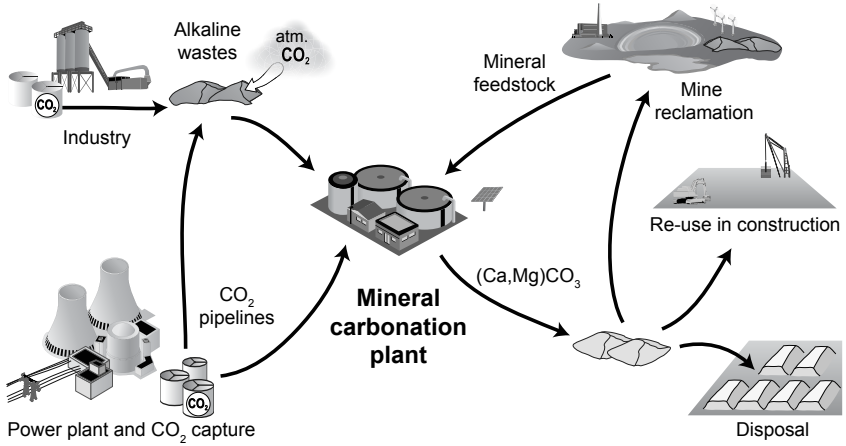

Figure 9. Material fluxes and processes associated with industrial carbonation of mineral feedstock and industrial alkaline wastes (modified after IPCC 2005). Graphical elements are courtesy of the Integration and Application Network, University of Maryland Center for Environmental Sciences (ian.umces.edu/symbols).

on these methods (Huijen and Comans 2003, 2005; IPCC 2005; Sipliä et al. 2008; Yang et al. 2008; Zevenhoven et al. 2011). Carbonation rates can be accelerated by elevating temperatures and pressures, the addition of chemical additives in the reaction fluid, and/or pre-treatment of the minerals. Recent research has focused on operational scale-up and demonstration of high temperature reaction apparatus (Zevenhoven et al. 2010). Although most industrial carbonation research has largely focused on the carbonation of natural minerals such as olivine and serpentine, the approach may also be applied to carbonation of Mg- and Ca-rich industrial wastes such as certain mine tailings (e.g., Gerdemann et al. 2007; Fig. 9). Carbonation of highly reactive and accessible industrial wastes using these process routes may help bring these technologies towards more widespread usage for reaction of more abundant natural mineral feedstocks (e.g., Bobicki et al. 2012).

Process routes for carbon mineralization in industrial reactors

Recent research has focused on two broad process routes: direct and indirect carbon mineralization. Direct carbon mineralization is completed in a single reaction step. Indirect carbonation first extracts the reactive cation from the mineral feedstock prior to carbonation in a pre-treatment step known as chemical activation. Both direct and indirect methods can be done as either a gas-solid process or as an aqueous process. In the gas-solid process, carbonation occurs by chemisorption of CO_2 to the solid by strong chemical bonds or by physisorption by weaker inter-molecular bonds (Kwon et al. 2011). In aqueous sorption, CO_2 is initially dissolved into the solvent and is subsequently reacted with the mineral feedstock.

Gas-solid carbonation. The major benefits of the gas-solid carbonation process are its simple design and that less energy is required to bring this two-phase system to temperature in comparison to a gas-water-solid system. Forsterite (Eqn. 19), serpentine (Eqn. 20), and brucite (Eqn. 21) may act as potential mineral feedstock for gas-solid carbonation**.**

$$Mg_2SiO_{4(s)} + CO_{2(g)} \leftrightarrow MgCO_{3(s)} + SiO_{2(s)} \quad (19)$$

$$Mg_3Si_2O_5(OH)_{4(s)} + CO_{2(g)} \leftrightarrow MgCO_{3(s)} + SiO_{2(s)} + H_2O_{(l/g)} \quad (20)$$

$$Mg(OH)_{2(s)} + CO_{2(g)} \leftrightarrow MgCO_{3(s)} + H_2O_{(l/g)} \quad (21)$$

High gas pressures and reaction temperatures improve the reaction rate, but these are subject to thermodynamic limitations. Rates can be further enhanced using supercritical CO_2 (Zevenhoven and Kohlmann 2001). However, atmospheric pressure decomposition of Mg-carbonate begins at 680 K, and the rate of olivine carbonation begins to decrease at even lower temperatures due to the decreasing chemical potential for reaction (O'Connor et al. 2005; Kelemen and Matter 2008). At higher pressure, the range of temperatures that promote carbonation is considerably larger (Lackner et al. 1997).

In addition to CO_2 pressure and temperature conditions, the extent of carbonation is also influenced by the pre-treatment of minerals and the presence of water in the process. For instance, untreated serpentine that was unreactive at 200 °C and 1-15 bar of 15% CO_2 (N_2 balance) underwent modest carbonation (~3% CO_2) after heat-treatment at 1000 °C (Zevenhoven and Kohlmann 2001). This is consistent with results on rate enhancement via heat treatment of serpentine (O'Connor et al. 2005). In static and stirred experiments at 483 bar and 140 °C, Martinez et al. (2000) found that the addition of water increased the degree of carbonation from 5.2% to 43%.

Experimental rates of Mg-silicate carbonation using gas-solid processes are too slow for large-scale applications (Zevenhoven 2004; Huijgen and Comans 2005). On the other hand, direct dry carbonation of Ca- and Mg-hydroxides is kinetically favorable. Even under highly favorable conditions (340 bar, 500 °C), a powdered (20 μm) Mg-silicate sample does not react appreciably. In contrast, the carbonation of brucite was nearly complete after two

hours under the same conditions (Lackner et al. 1997). By manipulating the dehydroxylation/rehydroxylation reactions of brucite, one can further promote the carbonation process (Butt et al. 1996; Béarat et al. 2002). A detailed thermodynamic and kinetic study of dehydroxylation and carbonation of brucite found that the most rapid carbonation kinetics were 375 °C at 0.765 atm (Butt et al. 1996). Conversely, Béarat et al. (2002) discovered that the highest carbonation rate of brucite occurs at the minimum pressure for magnesite stability, and that at 537 °C the optimum reaction pressure is 25.2 atm. Above this pressure, the rates of dehydroxylation and carbonation of brucite decrease. Using an atmospheric bubbling fluidized bed, batch reactors showed higher levels of carbonation because magnesite coatings were removed from particles by attrition (Zevenhoven and Teir 2004).

Brucite is a better feedstock for gas-solid carbonation, compared to silicate minerals. However, magnesium hydroxides are not abundant in nature and extracting them from Mg-silicate minerals without using large chemical or energy inputs remains the principle challenge to achieving significant, large-scale gas-solid carbonation.

Aqueous carbonation. Although dry carbonation is simpler in comparison to aqueous carbonation, its slow reaction kinetics is problematic. As a result, there is a focus on aqueous carbonation pathways (e.g., Goff and Lackner 1998; O'Connor et al. 2000; Herzog 2002; Park and Fan 2004). Aqueous carbonation can be divided into direct and indirect routes.

Direct aqueous carbonation involves reaction of CO_2 and water directly with solids, whereas indirect carbonation has an additional step of cation extraction from the feedstock followed by an acid-base reaction between metal (hydro) oxides and CO_2. A chemical model proposed by Guthrie et al. (2001) illustrates the aqueous carbonation of Mg-silicates. The model is based on two assumptions: first, that dissolution/precipitation occurs in the aqueous phase and not in the supercritical CO_2 phase and second, that the carbonation process takes place mainly by dissolution and precipitation, and not by the direct carbonation of silicate minerals. Under these assumptions, aqueous carbon mineralization can be divided into the following steps: the dissolution and hydration of CO_2 in water (Eqn. 22), the dissolution of silicate minerals using forsterite as an example (Eqn. 23), and the precipitation of carbonate (Eqn. 24) and silica (Eqn. 25).

$$CO_{2(g)} + H_2O_{(l)} \rightleftarrows H_2CO_{3(aq)} \leftrightarrow H^+_{(aq)} + HCO_3^-{}_{(aq)} \leftrightarrow 2H^+_{(aq)} + CO_3^{2-}{}_{(aq)} \quad (22)$$

$$Mg_2SiO_{4(s)} + 4H^+_{(aq)} \leftrightarrow 2Mg^{2+}_{(aq)} + H_4SiO_{4(aq)} \quad (23)$$

$$Mg^{2+}_{(aq)} + CO_3^{2-}{}_{(aq)} \leftrightarrow MgCO_{3(s)} \quad (24)$$

$$H_4SiO_{4(aq)} \leftrightarrow SiO_{2(s)} + 2H_2O_{(l)} \quad (25)$$

The overall reaction rate for the carbonation process is dependent on the slowest, rate-limiting step but identifying this step *a priori* is challenging (Hänchen et al. 2008). Because CO_2 is actively supplied to an industrial reactor, either mineral dissolution or precipitation will be rate-limiting (Fig. 1). Several operating conditions that influence the reaction rate of the aqueous carbonation process include pH, CO_2 fugacity, salinity, fluid composition, and temperature (O'Connor et al. 2005; Hänchen et al. 2006, 2008; Chizmeshya et al. 2007; Prigiobbe et al. 2009).

Kelemen et al. (2011) reviewed other effects of aqueous fluid composition on mafic minerals (olivine, pyroxene, Ca-rich plagioclase) and rock (peridotite, basalt) dissolution and carbonation reactions. The fastest known olivine carbonation was observed in studies at the U.S. Department of Energy's Albany Research Center (O'Connor et al. 2005) and at Arizona State University (Chizmeshya et al. 2007). These studies combined olivine dissolution with carbonate precipitation at an olivine-to-water ratio of 1:4. Olivine in saline aqueous solutions with 1 M NaCl and high bicarbonate (e.g., $NaHCO_3$, $KHCO_3$) concentrations was held in a

closed reaction vessel at high pCO_2 (>70 bar). The fastest rates were at 185 °C. Rates were 10^3 times faster than for the same conditions without bicarbonate, and more than 10^6 times faster than rates observed and calculated at 25 °C, pH 8, and atmospheric pCO_2.

Pre-treatment of minerals

In some instances, the reactivity of Ca- and Mg-silicate minerals, particularly serpentine, cannot be enhanced sufficiently by the careful selection of process route and conditions alone. Pre-treatment options can improve mineral dissolution kinetics for some feedstocks by activating the constituent minerals for carbonation. All pre-treatment options aim to create disorder in the mineral structure and/or increase the specific surface area. Pre-treatment can be conducted by thermal (McKelvy et al. 2004; O'Connor et al. 2005), chemical (Maroto-Valer et al. 2005; Alexander et al. 2007) or mechanical means (O'Connor et al. 2005; Chizmeshya et al. 2007). Accelerations in mineral dissolution rates achieved through pre-treatment must be balanced with the energy and operational cost penalties that they induce.

Thermal activation. Thermal pre-treatment removes chemically bound water, which can increase porosity and surface area as well as create structural disorder. Serpentine contains up to 13 wt% chemically bound water. By heating it to 600-650 °C, the hydroxyl groups are removed, structural disorder is created, and a significant improvement in the carbonation reaction rate can be achieved (O'Connor et al. 2000). In addition, heat-treatment of antigorite, a serpentine group mineral, increased its surface area from 8.5 m^2/g to 18.7 m^2/g (O'Connor et al. 2001). Steam treatment resulted in a 59.4% conversion to magnesite, while an untreated serpentine sample only carbonated to 7.2% magnesite. Heat treatment of serpentine at higher temperatures created well-ordered decomposition products (e.g., pyroxene) that were less reactive.

Heat treatment of serpentine group minerals may be impractical for large scale implementation because of the excessive energy penalty (300-500 kW h/tonne) that results in a net negative amount of CO_2 being sequestered if fossil fuels are used to generate the required energy (O'Connor et al. 2005). Alternatively, there may be specific applications in which carbon-free energy generation is available, and/or waste heat could be used. Although heat treatment leads to the highest conversion rate of serpentine, it has nearly no effect on olivine minerals, as they do not contain hydroxyl bonds in their structures.

Chemical activation. The principle aim of this method is to polarize and weaken the Mg bonds within the Mg-silicate structure, resulting in enhanced dissolution kinetics. For instance, Lackner et al. (1995) used hydrochloric acid to leach serpentine for the indirect carbonation of the released Mg. Hydrated magnesium chloride [$MgCl_2 \cdot 6H_2O$] was formed. After it was heated to 250 °C, the associated water was removed, followed by hydrochloric acid (HCl) separation creating Mg(OH)Cl. When water was re-introduced, $Mg(OH)_2$ was formed which was readily carbonated. By using HCl as the leaching agent, the liberation of Mg ions is enhanced. However, the considerable energy it takes to produce $Mg(OH)_2$ limits its applicability.

To increase the reactivity of serpentine, various complexing agents have been investigated, including inorganic acids (acetic, hydrochloric, phosphoric and sulfuric acid), organic acids (formic and acetic), bases (sodium and potassium hydroxide), and salts (ammonium chloride, sulfate, and nitrate) (e.g., Maroto-Valer et al. 2005; Teir et al. 2007c; Wang and Maroto-Valer 2011). Sulfuric acid is recognized as a very effective complexing agent, as it can extract more than 70% of the Mg from serpentine and produce a silica by-product with a high surface area (Maroto-Valer et al. 2005). Park et al. (2003) found that a mixture of orthophosphoric acid, oxalic acid, and ethylenediaminetetraacetic acid (EDTA) yielded 1.5 times greater Mg concentrations than did hydrochloric acid. Although acid leaching effectively extracts Mg from the serpentine matrix, it is not selective. For selective leaching, ammonium salts have

performed better (Wang and Maroto-Valer 2011). For example, only 17.6% Si was measured in the solution after 3 h of leaching at 100 °C using 1.4 M NH_4HSO_4, whereas 100% Mg and 98% Fe were extracted (Wang and Maroto-Valer 2011).

Disadvantages of chemical activation include an increase in cost, particularly because there are challenges in recycling and disposing of additives (Maroto-Valer et al. 2005). For example, Teir et al. (2007c), found that chemical consumption for indirect aqueous carbonation of serpentinite was 2.4 t NaOH and 2.1 t HCl (or 3.6 t HNO_3) per tonne of CO_2, resulting in a chemical cost of 1300 US$/t CO_2 ($1600 using HNO_3; Teir et al. 2007b). Furthermore, pre-treatment by chemical activation of olivine has had limited success (O'Connor et al. 2000).

Mechanical activation. The increase in mineral surface area accompanying grain size reduction leads to increases in mineral dissolution rates. For example, a reduction of olivine from 106-150 μm to <37 μm increased the extent of carbonation from 10% to 90% within 24 hours in distilled water with a reaction temperature of 185 °C and CO_2 partial pressure of 115 atm (O'Connor et al. 2000), consistent with similar studies by Chizmeshya et al. (2007). High-energy attrition grinding additionally introduces imperfections into the crystal structure which may facilitate carbonation (Gerdemann et al. 2003). Olivine carbonation is dramatically increased by 1 h of mechanical activation (O'Connor et al. 2001) attributed to the structural disordering of its surfaces (Kleiv and Thornhill 2006). The mechanical activation of serpentine often focuses on the structural changes accompanying the loss of hydroxyl molecules. Liao and Senna (1992) and Ryu et al. (1992) have concluded that mechanical activation gives an effect similar to that produced by calcination, but others have concluded that chemically bound water does not inhibit carbonation (O'Connor et al. 2000).

Nelson (2004) proposed a mechanochemical process whereby grinding and carbonation are integrated. Reactions are thought to proceed faster as fresh reactive surfaces are regenerated. In theory, processing costs could be lower due to simplification of the process. Kalinkina et al. (2001a,b) tested dry mechanochemical carbonation of Ca- and Mg-silicates, including enstatite, diopside, akermanite [$Ca_2MgSi_2O_7$] and wollastonite. The amount of CO_2 consumed due to grinding increases with increasing CaO content in the minerals, and correlates with the Gibbs free energy of the carbonation reactions. However, due to stronger Mg-O bonds in comparison to Ca-O bonds, the absence of calcium in enstatite limits its carbonation (Kalinkin et al. 2004). Sandvik et al. (2011) found that simultaneous mechanical activation and exposure of olivine to CO_2 for 30 min resulted in a concentration of 2.5 ± 0.1 wt% CO_2 in the final product. In contrast, there was no measurable carbonation in samples exposed to CO_2 for 1 h, before or after mechanical activation. It is possible that conventional grinding in a tumbling mill in a CO_2 atmosphere could compete with high energy efficiency mills for large-scale carbon mineralization (Sandvik et al. 2011). It is widely believed that due to its energy intensive nature, attrition grinding is impractical on a large scale (Huijgen and Comans 2003). However, if mechanical activation is implemented as an integrated part of the total milling, the operational energy consumption could be reduced to practical levels.

Summary and combination of pre-treatments. A pre-treatment step can greatly enhance carbon mineralization. These benefits are balanced by the additional costs and energy consumption of pre-treatment methods. The main benefits of mechanical activation are an increase in the available reactive surface area and the generation of thermodynamically unstable materials without the use of chemicals, while producing high activation extent that is similar to calcinations. In addition, there is some indication that the effectiveness of mechanical activation decreases over time, suggesting that grinding modifies surfaces to produce a transient catalytic effect. These advantages may render this process preferable to thermal and chemical activation.

Combining pre-treatment methods can achieve unexpected activation effects. For instance, O'Connor et al. (2005) found the combination of chemical activation and mechanical

activation most effective. Grinding of serpentine in a caustic solution (1 M NaOH, 1 M NaCl) for 3 h resulted in a higher carbonation conversion and reaction rate than through thermal activation (O'Connor et al. 2001). A combination of thermal activation using recycled "waste heat" ranging from 300-600 °C and mechanical activation by grinding achieved carbonation rates of serpentine equivalent to those achieved via thermal activation alone at >850 °C (Yu et al. 2011). Similarly, the disintegration of serpentine (chrysotile) fibers through a combination of chemical (sulfuric acid) and mechanical treatments has been proposed (Uddin et al. 2012).

IN SITU CARBON MINERALIZATION

In situ carbon mineralization aims to promote subsurface carbonation reactions by injecting CO_2, or aqueous solutions containing dissolved CO_2, into hydraulically fractured or porous subsurface formations such as peridotite, basalt or serpentinite (e.g., Cipolli et al. 2004; Kelemen and Matter 2008; Gislason et al. 2010). There are both high temperature (listvenite) and low temperature (shallow subsurface peridotite weathering) carbonation systems that represent natural analogues for proposed engineered systems for *in situ* subsurface carbon mineralization (Kelemen et al. 2011).

Two end-member, high-temperature systems can be conceived. In one approach, a volume of peridotite at depth is hydraulically fractured and heated to optimal reaction temperature prior to injection of CO_2 (Kelemen and Matter 2008). Kelemen and Matter (2008) propose that the heat generated from the exothermic olivine carbonation reaction could be exploited to maintain the optimal temperature for peridotite carbonation while injecting fluid at ambient surface temperature. Injection of CO_2-rich fluid could drive carbonation at a rate of up to 1 t CO_2/m^3 aquifer/yr, if the fluid injection rate is controlled to balance exothermic heat generation to maintain the rock mass near optimal conditions (Kelemen et al. 2011). A second approach relies on thermal convection of seawater to provide CO_2 to a reaction site below the sea floor (Kelemen and Matter 2008). CO_2-depleted water would then return to the surface to draw down atmospheric CO_2. Injection and production drill holes connected at depth by a zone of hydraulically fractured peridotite would be used to induce thermal convection. Maximum carbonation rates of up to 1000 t CO_2/yr/well are estimated. These rates would not be limited by olivine carbonation kinetics, but instead by CO_2 supply, controlled by the CO_2 concentration in seawater and flow rates in standard industry borehole casings. Pumping would not be feasible, due to the high cost per tonne of CO_2 in seawater, unless geothermal power were also generated using the same circulation system. At these rates, *in situ* geothermal carbonation at a rate of 1 Gt CO_2 per year would require 1 million drill holes, which is approximately equal to the total number of producing oil and gas wells in the United States (Kelemen et al. 2011). Both systems would be safest and most cost-effective if shallow marine peridotite is accessed from shore-based boreholes. The natural process of reaction-driven cracking, if it can be engineered, converts chemical potential energy to work, offering a significant energy savings compared to grinding feedstock for *ex situ* mineral carbonation. These strategies are advantageous because no pre-treatment of minerals by comminution or thermal activation is required (Kelemen and Matter 2008; Kelemen et al. 2011)

CO_2 injection into ultramafic-hosted aquifers could offer yet another means of subsurface carbon mineralization. Based on serpentine dissolution rates, Cipolli et al. (2004) estimated that 33 g CO_2/kg H_2O could be sequestered annually in serpentinite-hosted aquifers at ambient conditions of 60 °C and pCO_2 of 250 bars achieved through injection. Geothermal heating accelerates mineral dissolution and may allow for the precipitation of more stable mineral phases such as magnesite. Using a very similar modeling approach to simulate *in situ* carbonation of a peridotite aquifer at 30 to 90 °C and pCO_2 of 10 MPa, including standard values for mineral dissolution kinetics, Paukert et al. (2012) predict average uptake rates of

0.2-20 g CO_2/kg peridotite/yr over 30 years (10-1000 g CO_2/kg H_2O). The model aquifer in their study achieves almost 100% carbonation after 30 years at 90 °C.

A key limitation of proposed, *in situ* mineral carbonation techniques is the potential for negative feedbacks involving (1) compaction due to increasing solid mass and decreasing solid density, (2) precipitation of product phases in pore space, and (3) armoring of reactive surfaces with product phases that would slow mineral dissolution (Fig. 1). Thus, for example, Xu et al. (2004) concluded that porosity would rapidly fill with reaction products during peridotite alteration, limiting the extent of carbonation. On the other hand, the fact that natural peridotite carbonation systems persist in the same location for tens to hundreds of thousands of years, and that some attain 100% carbonation on meter to km scale (Fig. 3b; Beinlich et al. 2012), indicates that this process is not always self-limiting. One possible explanation is that the large volume changes associated with peridotite hydration and carbonation cause "reaction-driven cracking," in a positive feedback mechanism that maintains or enhances permeability and reactive surface area throughout the alteration process (MacDonald and Fyfe 1985; Jamtveit et al. 2000, 2008, 2012; Iyer et al. 2008; Rudge et al. 2010; Kelemen and Hirth 2012). The specific conditions determining whether positive or negative feedbacks dominate reaction progress for *in situ* carbon mineralization remain to be determined.

MONITORING AND STABILITY

Continuous process monitoring is readily implemented within industrial reactors; however, other *ex situ* carbon mineralization strategies (e.g., enhanced weathering and carbonation) as well as *in situ* carbonation requires systematic field-based and laboratory-based monitoring using techniques adapted from environmental and geological disciplines.

To date, enhanced weathering experiments have not been undertaken in natural landscapes and monitoring strategies for this technology have yet to be developed. Hartmann et al. (2013) suggest that monitoring the progress of mineral dissolution in soils, and its impact on soil and aquatic geochemistry, will be the most critical monitoring priorities for enhanced weathering. Implementation of enhanced weathering in agricultural and forested regions of river catchments would likely require routine and systematic monitoring of solute fluxes to rivers in order to assess the rate and extent of enhanced weathering on a regional scale. Finer scale monitoring of the abundance of mineral feedstock and carbonate minerals in soils and sediments – as well as regular monitoring of soil and watershed health – would also be necessary.

The feasibility of a number of monitoring techniques has been tested for quantification of carbon mineralization in industrial settings. Continued development and vetting of monitoring strategies at the scale of industrial sites will facilitate their adaptation and application to large scale *ex situ* and *in situ* carbon mineralization projects. Systematic coring and trenching of rocks, soils and waste stockpiles is becoming more routine (Renforth et al. 2009; Wilson et al. 2009a,b, 2011; Bea et al. 2012; Washbourne et al. 2012) and statistical and geospatial methods for displaying and interpreting CO_2 uptake are under development (Washbourne et al. 2012). Stable oxygen and carbon isotopic data and radiogenic ^{14}C analysis, used in combination with elemental abundance data or modal mineralogical data from quantitative powder X-ray diffraction methods, may be used to measure the extent and rate of CO_2 sequestration from atmospheric, organic or industrial sources (Renforth et al. 2009; Wilson et al. 2006, 2009a,b; Washbourne et al. 2012; Harrison et al. 2013).

Mg- and Ca-carbonate minerals that precipitate within high-pH soils and saline, high-pH waste and process waters commonly form out of isotopic equilibrium with the atmosphere and/or DIC (Renforth et al. 2009; Wilson et al. 2009a, 2010, 2011; Beinlich and Austrheim 2012; Washbourne et al. 2012). Therefore, it can be challenging to identify whether CO_2 is being

sequestered within minerals from an atmospheric, organic or industrial source or merely being recycled via dissolution and reprecipitation of pre-existing carbonate minerals (Wilson et al. 2009a). Wilson et al. (2009a, 2011) and Kelemen et al. (2011) have demonstrated the effectiveness of $\delta^{13}C$–$\delta^{18}O$–^{14}C–$^{87}Sr/^{86}Sr$ multi-tracer approaches to assess the source of carbon and other elements within carbonate minerals in industrial and natural settings.

Some systems, such as ultramafic mine tailings storage facilities, may contain "primary" igneous or metamorphic carbonate minerals in addition to "secondary" carbonate minerals produced by recent weathering of silicate or hydroxide minerals. In such cases, it becomes important to identify the source of carbon within each carbonate mineral phase and to use crystallographic methods, such as diffraction techniques and vibrational spectroscopy, to determine the abundance of specific carbonate minerals that are trapping and storing CO_2 from atmospheric, ancient geological, modern organic or industrial sources (Wilson et al. 2006, 2009b; Kelemen et al. 2011). Pronost et al. (2012) have also demonstrated the effectiveness of the combined use of (1) infrared imaging to monitor heat released by exothermic carbonation reactions and (2) direct measurement of atmospheric CO_2 concentration immediately above waste piles to monitor the progress of carbon mineralization within mine tailings storage facilities.

As discussed previously, the most common products of weathering and surficial carbonation of Mg-rich silicate and hydroxide minerals are metastable hydrated Mg-carbonate phases. Diagenesis of hydrated Mg-carbonate minerals to magnesite may occur on the timescale of tens to hundreds of years (Zhang et al. 2000). Allen and Brent (2010) investigated possible impacts of acid rain on hypothetical stockpiles of magnesite, produced by *ex situ* industrial carbonation, to assess the risk of CO_2 release. They concluded that release rates of stored CO_2 are likely to be minimal using average rainfall pH data from industrialized regions of the USA, China, Europe and Australia. Hydrated Mg-carbonate minerals are more susceptible to dissolution in acidic solutions than magnesite (Königsberger et al. 1999), but are stable under alkaline conditions on millennial timescales (Renaut 1993; Power et al. 2009). Therefore, a degree of care should be taken in choosing sites for implementation of enhanced weathering and carbonation of Mg-rich minerals.

In considering monitoring of mineral storage, it is also evident that *in situ*, sub-surface mineral carbonation sites are essentially permanent, as they are protected from surficial weathering, so that time-series measurements after storage is completed are less important, compared to *ex situ* sites. However, the total mass of mineralized carbon is more difficult to assess for *in situ* as compared to *ex situ* sites.

CAPACITY AND RATES OF CARBON MINERALIZATION STRATEGIES

Annual global CO_2 emissions are estimated at 38 Gt, with 29 Gt of CO_2 emitted from fossil fuel combustion (IPCC 2007). A significant reduction in CO_2 emissions is unlikely to be achieved by any one technology alone, but would require large-scale deployment of several technologies in parallel. Pacala and Socolow (2004) suggest that seven emission reducing activities, referred to as "stabilization wedges," each capable of reducing emissions by 3.7 Gt CO_2/yr (1 Gt C/yr) could achieve stabilization of atmospheric CO_2 concentrations at ~500 ppm. One of their wedges relies on geological carbon capture and storage (CCS) in subsurface pore space, which could be more broadly interpreted to include carbon mineralization. A combination of these CO_2 sequestration technologies operating in parallel could thus comprise a stabilization wedge.

At present, the largest geological CCS projects inject ~1-3 Mt CO_2/yr into subsurface pore space (Michael et al. 2009; Whittaker et al. 2011), with an estimated 16 Mt CO_2 stored in three of the largest commercial CCS operations at the end of 2010 (Sleipner, In Salah, Snohvit; Eiken et al. 2011). Thus, between ~1200 and 3700 large-scale CO_2 sequestration projects

operating simultaneously might constitute one stabilization wedge. Subsurface geologic storage of CO_2 in pore space is not practical in all geographic areas, for instance in seismically active regions and where appropriate geological formations are unavailable. Thus, alternative CO_2 sequestration strategies, such as *ex situ* carbon mineralization should also be considered to provide more opportunities for CO_2 sequestration globally.

The capacity for CO_2 storage via carbonation of abundant, rock-forming minerals is immense; ultramafic rock formations are of sufficient abundance to completely offset anthropogenic CO_2 emissions. Lackner et al. (1995) estimate that carbonation of natural Ca- and Mg-silicates could sequester the CO_2 produced from combustion of all known coal reserves, while Kelemen and Matter (2008) calculated that 100% carbonation of the peridotite within 3 km of the surface would consume ~30 trillion tons of CO_2 in the Sultanate of Oman alone. The CO_2 sequestration capacity of these materials could be harnessed through a combination of *ex situ* and *in situ* technologies. In addition, many industrial wastes are comprised of Mg- and Ca-rich materials that are typically more reactive and easily accessible than natural minerals. Although carbonation of industrial wastes provides a much lower total sequestration capacity than natural deposits, it offers the opportunity to offset emissions at the industrial level. Industrial emissions comprise ~19% of annual GHG emissions (~7 Gt CO_2/yr; IPCC 2007); so that widespread reduction of industrial emissions would provide a meaningful CO_2 offset on the scale of global emissions.

Enhanced weathering

The CO_2 sequestration capacity of enhanced weathering is considerable (e.g., 1.25 t CO_2/t olivine) with the sequestration rate largely depending on the same factors that affect natural weathering rates. Köhler et al. (2010) estimate the amount of olivine that could be spread in the Amazon and Congo catchments for enhanced weathering while maintaining a river pH no higher than that of the ocean (i.e., pH = 8.2). The maximum annual dissolution of olivine could maintain the appropriate pH within these river catchments while leading to sequestration of 1.8 and 0.4 Gt of CO_2, respectively. The modeling results of Köhler et al. (2010) suggest that enhanced weathering in these two catchments has the potential to sequester approximately 40-190 g CO_2/m^2/yr over the combined catchment area of 9.43×10^{12} m^2. This represents a two to ten times increase of the natural rate of weathering, 20.33 g CO_2/m^2/yr, in the Amazon River basin (Ludwig et al. 1998). Globally, Köhler et al. (2010) indicate that up to 3.7 Gt CO_2/yr could be dissolved as bicarbonate using this strategy, although there are large uncertainties associated with any global estimates. Nevertheless, this process could offset on the order of 10% of global CO_2 emissions. Renforth (2012) provides an account of the potential for enhanced weathering in the United Kingdom (UK) based on the volume and chemistry of igneous formations. It is estimated that a total of 430 Gt CO_2 could be sequestered *ex situ*. However, in order to consume ~50 Mt CO_2/yr (10% of UK emissions), tripling of current igneous rock mining rates would be required (Renforth 2012).

Industrial waste carbonation

Mine tailings. The CO_2 sequestration capacity of mine tailings can be significant, with the potential to more than completely offset mine emissions (e.g., Wilson et al. 2009a). Passive carbonation rates are on the order of 10^{-4} to 10^{-2} t CO_2/t tailings/yr (Wilson et al. 2009a,b, 2011; Bea et al. 2012; Pronost et al. 2012; Harrison et al. 2013). These rates represent a non-optimized baseline for weathering of mine tailings that could be further enhanced by site engineering. A number of mine types may produce tailings appropriate for carbonation, such as asbestos, nickel, diamond, and platinum group metal mines (Wilson et al. 2009a, 2011; Vogeli et al. 2011; Bea et al. 2012; Pronost et al. 2012)

Asbestos production only occurs in a limited number of countries, producing ~20-80 Mt tailings/yr (Bobicki et al. 2012). This would provide a total sequestration capacity of ~8-32

Mt CO_2 annually. Tailings stockpiles are also available in a number of locations, including an estimated 5-8 Mt in the United States (Gerdemann et al. 2007), and >2 Gt of chrysotile mining residues in Canada (Gerdemann et al. 2007; Wilson et al. 2009a; Larachi et al. 2010). This provides the potential to store >0.8 Gt CO_2 as hydromagnesite.

The tailings of active mines provide ongoing opportunities for sequestration because tailings are continually replenished. Vogeli et al. (2011) calculate a theoretical sequestration capacity for tailings from platinum group metal (PGM) mining in South Africa of ~14 Mt CO_2/yr, which would be sufficient to offset the emissions of several mining operations in the region. Similarly, complete carbonation of the ~11 Mt/yr of tailings produced at the Mount Keith Nickel Mine in Western Australia (BHP Billiton 2005) would sequester ~4 Mt CO_2/yr as hydromagnesite. This is more than ten times greater than the mine emissions of ~0.37 Mt CO_2 equivalent/yr (BHP Billiton 2005). Yet, passive carbonation at Mount Keith currently sequesters only ~15% of annual mine emissions (Harrison et al. 2013), suggesting that engineered methods are necessary to achieve the full sequestration capacity.

Power et al. (2010) investigated the use of bioleaching techniques to enhance dissolution rates of asbestos tailings, which might in turn enhance carbonation rates. They estimate that 458 kt CO_2 could be captured at an historic asbestos mine in Yukon, Canada, via bioleaching and subsequent hydromagnesite precipitation in an artificial wetland downstream of the tailings pile (Power et al. 2010). Alternatively, injection of CO_2-rich gas into could significantly enhance carbonation rates, particularly by targeting highly reactive phases such as brucite. Although brucite is typically present at relatively low abundance in ultramafic tailings (1-15 wt%), its carbonation could offer significant sequestration capacity (e.g., up to ~20-60% of mine emissions at Mount Keith; Harrison et al. 2013).

At the global production rates of Ni, PGMs, asbestos, diamond, chromite, and talc in 2010 (USGS 2010) at typical ore grades (after Thayer 1964; Yehia and Al-Wakeel 2000; Rio Tinto 2010; Glaister and Mudd 2010; Mudd 2010; Bobicki et al. 2012) we estimate that approximately 419 Mt ultramafic and mafic tailings are produced annually. Assuming complete carbonation, this provides the potential to sequester ~175 Mt CO_2/yr, equivalent to more than 100 "conventional" sites for injection and storage of CO_2 in subsurface pore space, such as at the Sleipner gas field (after Michael et al. 2009). If accelerated carbonation techniques are successfully applied to these tailings types, then the technologies could be extended for carbonation of less reactive felsic tailings. Some Ag, Au, Pb, Cu, Mo, Sn, Zn, and W mines produce tailings that could potentially be used for carbon mineralization. Based on the typical grade of deposits mined for these metals and their production rates in 2010, it is estimated that ~5560 Mt tailings are produced annually (after Sillitoe et al. 1975; Ruvalcaba-Ruiz and Thompson 1988; MacDonald and Arnold 1994; Edgerton 1997; Sillitoe 1997; Walters and Bailey 1998; Love et al. 2004; Jiang et al. 2004; Peng et al. 2006; Singer et al. 2008; USGS 2010; Thompson Creek Metals Company Inc. 2011; USGS 2013a), with the potential to sequester up to ~441 Mt CO_2/yr. Thus, in combination, carbonation of different tailings types could sequester up to ~16% of one carbon sequestration stabilization wedge, or ~1.5% of annual global CO_2 emissions (Figs. 10 and 11).

Iron and steel making slag. Renforth et al. (2011) estimate that global slag production from iron and steel manufacture is 250-300 Mt/yr and 130-200 Mt/yr, respectively. This could provide a total CO_2 sequestration potential of 161-216 Mt CO_2/yr (Renforth et al. 2011). Iron and steel manufacture is responsible for 6-7% of total CO_2 emissions worldwide (Doucet 2010; Bobicki et al. 2012). Carbonation of slag could offset ~6-10% of annual emissions from this industry (Fig. 10), which equates to ~0.4-0.6% of global total annual CO_2 emissions. At an individual steel mill operation, there is the potential to offset emissions by 8-21% (Eloneva et al. 2008). Renforth et al. (2011) estimate that between 5.8 and 8.3 Gt of slag stockpiles have accumulated since the mid-19th century, providing a total storage capacity of 1.8-4.0 Gt CO_2.

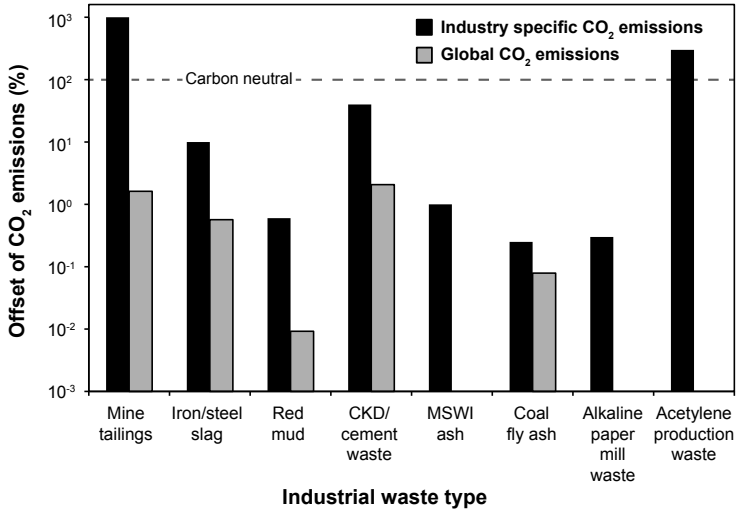

Figure 10. Percent offset of CO_2 emissions for specific industries and global annual emissions provided via carbonation of various industrial waste materials. CKD = cement kiln dust; MSWI = municipal solid waste incinerator. The data were insufficient to calculate the offset of total annual global CO_2 emissions provided via carbonation of MSWI ash, acetylene production, and alkaline paper mill waste.

Nearly complete conversion (e.g., ~74%) of iron and steel making slag occurs in minutes in high temperature/high pressure reactors (e.g., 100 °C; 19 bar CO_2; Huijgen et al. 2005; Huijgen and Comans 2006), whereas hours are required to leach the majority of Ca under ambient conditions (Stolaroff et al. 2005; Lekakh et al. 2008). The latter method is estimated to cost only ~$8/t CO_2 sequestered, and provides the added benefit of not requiring a point source of CO_2 (Stolaroff et al. 2005). However, slag can also be efficiently carbonated with gas streams similar in composition to power plant flue gas (~10-20% CO_2), which would allow direct use of power plant flue gases (e.g., Uibu et al. 2011; Yu and Wang 2011; van Zomeren et al. 2011). The carbonation of these materials is much more rapid than for the natural Ca-silicate mineral, wollastonite, under the same conditions (Huijgen and Comans 2006; Teir et al. 2007a).

Red mud. Red mud is a highly alkaline slurry (pH >13) that is generated as a by-product of the Bayer process for production of alumina from bauxite ore (Bonenfant et al. 2008). Its primary constituents include, in descending order of abundance: Fe_2O_3, Al_2O_3, SiO_2, Na_2O, CaO and TiO_2 (Bobicki et al. 2012). The caustic nature of red mud makes it hazardous and difficult to store safely (Johnston et al. 2010; Bobicki et al. 2012), yet also provides suitable conditions for the precipitation of carbonate minerals. Several studies have investigated the use of red mud for carbon mineralization, either by supplying CO_2 at ambient conditions (Bonenfant et al. 2008; Sahu et al. 2010; Yadav et al. 2010), or taking advantage of its alkalinity for the carbonation of saline wastewaters (Dilmore et al. 2008; Johnston et al. 2010). Both methods have reaction timescales on the order of hours and result in neutralization of the slurry, thereby decreasing its hazardous nature (Dilmore et al. 2008; Sahu et al. 2010). Although the carbonation capacity of red mud alone is relatively low (~0.05 kg CO_2/kg slurry; Bobicki et al. 2012), it is produced in large quantities (~70 Mt/yr; Dilmore et al. 2008). The products of red mud carbonation are primarily Na_2CO_3 and $NaHCO_3$, whereas carbonation of added saline wastewater produces more stable Mg- and Ca-carbonate minerals, making the latter process more appropriate for long term CO_2 storage (Bobicki et al. 2012). Carbonation of red mud alone would capture ~3.5 Mt CO_2/yr, or ~0.01% of global annual CO_2 emissions (Fig. 10; Bobicki et al. 2012). The world

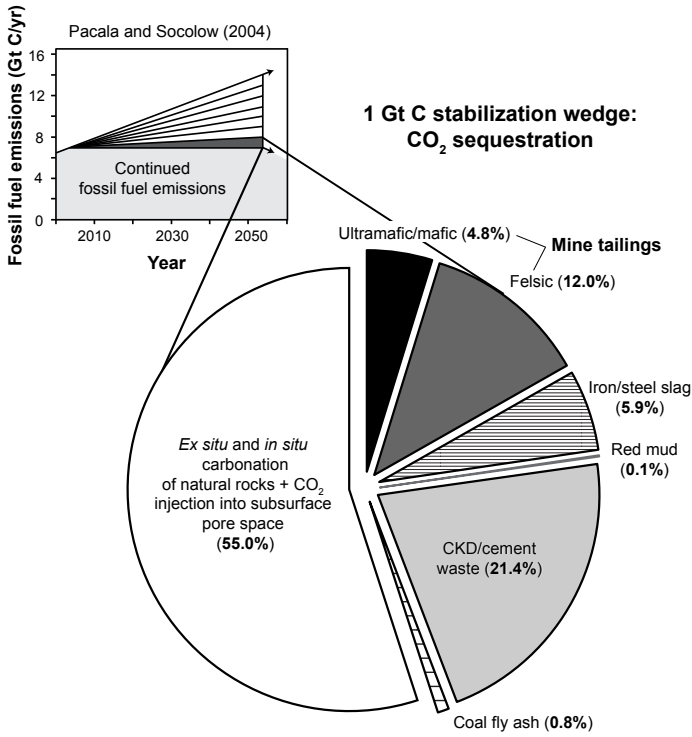

Figure 11. Contribution of different carbon sequestration technologies towards a 1 Gt C/yr "stabilization wedge" (3.67 Gt CO_2/yr; modified after Pacala and Socolow 2004). "CKD" is the abbreviation for cement kiln dust.

average of CO_2 emissions from alumina production in 2002 was 12.7 t CO_2 equivalent/t Al (Gao et al. 2009), implying that with ~44 Mt aluminum produced in 2011 (World Aluminum 2013), approximately 0.56 Gt CO_2 equivalent was released globally. Thus, carbonation of red mud would offset ~0.6% of emissions from the aluminum industry. A treatment plant in Western Australia operated by Alcoa employs this technology to sequester 0.07 Mt CO_2/yr (ICMM 2008), demonstrating that this is a feasible technology. The carbonation capacity is dependent upon the initial mineralogy, and CO_2 uptake rate is affected by solution pH (Dilmore et al. 2008; Yadav et al. 2010).

Cement kiln dust and waste cement. The cement industry is one of the largest industrial emitters of CO_2, with annual emissions estimated at 5% of global totals (~2 Gt CO_2; Worrell et al. 2001; Huntzinger and Eatmon 2009). Approximately 0.81 t CO_2 are emitted per tonne cement produced (Worrell et al. 2001), with ~2.8 Gt/yr of cement produced globally (Schneider et al. 2011). In addition, cement manufacturing yields massive quantities of waste "cement kiln dust" (CKD), at 150-200 kg of CKD produced per 1 t of cement (van Oss and Padovani 2003). Thus, an estimated 0.42-0.56 Gt of CKD are produced globally per year. CKD is typically stored in landfills or quarries and is potentially hazardous due to its alkaline nature and as a respiratory irritant; carbonation could help reduce these hazards (Huntzinger and Eatmon 2009; Huntzinger et al. 2009b; Gunning et al. 2010). Assuming an average CaO content in cement waste of 65% (Renforth et al. 2011), complete carbonation of the CKD produced annually would sequester 286 Mt CO_2/yr, or 15% of emissions from cement manufacture. The

overall sequestration capacity of CKD depends primarily on the initial mineralogy, with high proportions of Ca-oxides and -hydroxides being ideal (Huntzinger et al. 2009a; Gunning et al. 2010).

Waste concrete and cement from construction and demolition also offers significant carbonation potential, with CaO contents in construction wastes ranging from 10-20% (Renforth et al. 2011). Bobicki et al. (2012) summarize current annual waste concrete production values of 663 Mt in the European Union, ~239 Mt in China, and 200 Mt in the United States, which they suggest could collectively sequester 61 Mt CO_2/yr. This equates to ~3% of annual emissions from cement manufacture globally. Renforth et al. (2011) estimate that between 120-500 Mt CO_2/yr could be stored in construction and demolition wastes worldwide using population as a proxy for waste production; this would offset 6-26% of cement manufacturing emissions. In combination, carbonation of construction and demolition wastes and CKD could offset up to ~40% of annual cement industry emissions or ~2% of global CO_2 emissions (Fig. 10).

Due to the high CaO content and fine particle size of CKD, carbonation is likely to be rapid at relatively mild conditions. Huntzinger et al. (2009b) documented a carbonation efficiency of up to 100% of theoretical conversion for landfilled CKD supplied with ~8.5% CO_2 gas at ambient conditions in column experiments on a time scale of days. Similarly, Huntzinger et al. (2009a) documented 60% of theoretical conversion of CKD in 8 h at ambient conditions in batch experiments. The limiting factors for reaction rate recorded in experimental studies include diffusion of reactants through a carbonate product layer and the liquid:solid ratio.

Waste ash and combustion products. There are a number of waste ash materials that are suitable for carbonation owing to high CaO contents, including municipal solid waste incinerator (MSWI) fly and bottom ash (Rendek et al. 2006; Arickx et al. 2006; X. Li et al. 2007; Jiang et al. 2009), coal fly ash (Montes-Hernandez et al. 2009; Uliasz-Bocheńczyk et al. 2009; Nyambura et al. 2011), and oil shale ash (Uibu et al. 2010, 2011). Although Jiang et al. (2009) documented a lower carbonation extent of MSWI fly ash when using gas streams representative of MSWI flue gas (~12 vol.% CO_2) compared to pure CO_2, close to 20 g CO_2/100 g ash could still be captured within 40 min. Rendek et al. (2006) estimate that carbonation of MSWI bottom ash at incinerator plants would offset emissions by 0.5-1.0%, assuming a capacity of ~2 g CO_2/100 g bottom ash based on their experimental results. Bottom ash comprises 80-90% of the residue from MSWI (Arickx et al. 2006) and is therefore more representative of the total sequestration capacity of MSWI ash than is the more reactive fly ash. In the United States, ~29 Mt of municipal solid waste (MSW) was combusted in 2010 (USEPA 2010). This would produce ~7.25 Mt bottom ash (after Rendek et al. 2006). It is estimated that 0.15 Mt CO_2 per year could be captured via bottom ash carbonation (after Rendek et al. 2006), or ~0.002% of total CO_2 emissions in the United States (USEPA 2008). Although this is a relatively small impact on the scale of CO_2 emissions, the rapidity at which this material can be carbonated and its proximity to CO_2 point sources makes it a convenient option. In addition, accelerated carbonation of MSWI ash helps to decrease its environmental toxicity by limiting heavy metal leaching and neutralizing alkalinity (Rendek et al. 2006; Li et al. 2007; Jiang et al. 2009).

Coal fly ash is also available in large quantities near point sources of CO_2, and has a lime (CaO) content of ~4-10 wt% (Montes-Hernandez et al. 2009; Nyambura et al. 2011). However, its carbonation capacity is relatively low (Bobicki et al. 2012). Experimental studies employing water/ash slurries exposed to elevated pressure (~10-40 atm) and relatively low temperature (20-90 °C) have recorded carbonation capacities between ~2.60-7.85 g CO_2/100 g ash (Uliasz-Bocheńczyk et al. 2009; Montes-Hernandez et al. 2009), and up to 7.15 g CO_2/100 g ash in brine/ash slurries (Nyambura et al. 2011), both on a timescale of hours. On the other hand, at ambient conditions, the carbonation capacity in slurry reactors was found to be only

0.8 g CO_2/100 g ash (Jo et al. 2012b), and ~2 g CO_2/100 g ash in a flow through system on a timescale of hours (Jo et al. 2012a). Approximately 12 Gt of CO_2 are released annually from coal-fired power plants, which produces 600 Mt coal fly ash (Bobicki et al. 2012). Bobicki et al. (2012) estimate that with an average uptake of ~5% CO_2/mass ash, carbonation of coal fly ash would offset only ~0.25% (~30 Mt CO_2) of emissions from coal-fired power plants globally. However, although coal fly ash carbonation offers limited capacity on the scale of coal combustion emissions, the sequestration capacity is comparable to that of 10-30 large-scale operations storing CO_2 in subsurface pore space.

Oil shale ash has a greater specific sequestration capacity than the other ash types discussed due to its higher free lime content (22.4% CaO; Uibu et al. 2011; Bobicki et al. 2012). At ambient temperature and pressure conditions, Uibu et al. (2011) found that oil shale ash could be carbonated to contain 29 g CO_2/100 g ash within 37 min when exposed to a simulated flue gas (15% CO_2). Uibu et al. (2010) estimate that ~1 Mt CO_2/yr could be captured from flue gases at oil shale fired power plants in Estonia, which is equivalent to 5-6% of Estonia's total CO_2 emissions (Bobicki et al. 2012).

Alkaline paper mill and acetylene production waste. A limited number of studies have investigated carbonation of alkaline paper mill waste for the purpose of CO_2 sequestration (e.g., Pérez-López et al. 2008; Sun et al. 2013). Alkaline paper mill waste is a $Ca(OH)_2$-rich solid generated during the kraft pulping process of paper manufacture (Pérez-López et al. 2008). Pérez-López et al. (2008) carbonated paper mill waste in slurry reactors at moderate temperature (30 or 60 °C) and pressures of up to ~40 atm for 2 h. Extrapolation of their experimental rates suggests up to ~22 g CO_2/100 g paper mill waste could be stored, which is approximately ten times greater than reported for most CaO rich ash materials (e.g., Montes-Hernandez et al. 2009). However, only ~0.3% of emissions at a paper mill operation would be offset by carbonation of its paper mill waste (Bobicki et al. 2012). In the United States, approximately 6% of industrial emissions are sourced from the "forest products" sector, which includes paper manufacture (USEPA 2008), suggesting a maximum offset of <0.4 Mt CO_2 annually, or <1 subsurface geologic CCS operation.

The production of acetylene generates an aqueous $Ca(OH)_2$ slurry (~95% CaO) that offers the potential to completely offset the emissions from its production (Morales-Flórez et al. 2011). The $Ca(OH)_2$ particles have a high surface area, lending to a relatively rapid rate of reaction under ambient conditions (Morales-Flórez et al. 2011). Morales-Flórez et al. (2011) experimentally investigated the carbonation of "weathering pools" of thinly spread slurry samples at ambient conditions, and CO_2 sourced solely from the atmosphere. It is estimated that 800 t CO_2/yr could be sequestered using these "weathering pools," which would more than offset the indirect emissions from acetylene production of 288 t CO_2/yr at a single plant, or ~30% of CO_2 emissions from production of calcium carbide, the precursor to acetylene (assuming a 1 ha "weathering pool;" Morales-Flórez et al. 2011).

Waste brines. Waste brines are produced in massive quantities worldwide and often contain significant concentrations of dissolved cations (e.g., Ca^{2+}, Mg^{2+}) that are available for carbonate precipitation. An external source of alkalinity is also required. For instance, the oil industry generates ~8 Gt/yr of produced water, and ~10 Gt/yr of reject brines (Mignardi et al. 2011). Ferrini et al. (2009) have demonstrated that sequestration of CO_2 in the form of nesquehonite can be achieved on a timescale of minutes by supplying CO_2 gas to Mg-rich brine buffered by ammonia. Moreover, Mignardi et al. (2011) demonstrate that the high salinity of simulated industrial wastewaters does not significantly decrease the efficiency of carbonation, despite the decrease in CO_2 solubility in saline waters. Power et al. (2013a) demonstrate that CO_2 uptake into saline solutions for mineralization can be accelerated by up to 600% through the use of the carbonic anhydrase enzyme. It is difficult to estimate the total emissions offset that could be achieved via wastewater carbonation, as it will depend largely on the cation

concentrations and the amount of wastewater available for carbonation globally. However, this could have industry specific applications with significant sequestration potential. For instance, Power et al. (2013a) estimate that precipitation of Mg and Ca ions in the process waters used at the Mount Keith Nickel Mine in Australia would sequester ~15% of the mine's annual emissions. As another example, a USGS compilation of (highly variable) produced water compositions in North Dakota from 1949 to 1979 yields about 9000 ± 9500 ppm Ca and 1500 ± 1400 ppm Mg (1 σ) (USGS 2013b). Together, these average values yield ~200 μmol Ca + Mg/kg; complete carbonation of these cations would consume ~0.87 wt% CO_2. This value represents a maximum that does not account for solution alkalinity. For the total 18 Gt of oil industry wastewater estimated above, this corresponds to a maximum of ~160 Mt of CO_2/yr.

Carbonate biomineralization

Biological carbonate precipitation could offer a low-energy strategy for sequestering CO_2 with the added benefit of producing valuable biomass (e.g., biofuel, pharmaceuticals and nutraceuticals). Whiting events, the widespread precipitation of microcrystalline $CaCO_3$, in the oceans provide an estimate of the potential for carbonate biomineralization at a large scale. Whiting events induced by growth of cyanobacteria on the Great Bahama Bank have been investigated as a natural analogue for CO_2 sequestration (Robbins and Yates 2001; Lee et al. 2006). Estimates of the carbonate precipitation rates for a strain of *Synechococcus* sp. (cyanobacteria) are up to 1.1 Mt C as $CaCO_3$ per year over an area of 70 km^2 with 5 m water depth (3.1 g C/L) (Lee et al. 2006). In addition, a survey of freshwater and marine microalgae shows that lipid (i.e., bio-oil) productivity can be 10-142 mg/L/day with the lipid content comprising 2-65% of the dry mass (Mata et al. 2010). Cyanobacteria may also produce valuable by-products such as ethanol at 240 mg/L/day (Dexter and Fu 2009). Production of these by-products in conjunction with carbonate precipitation could be of significant economic value, potentially more than offsetting operational costs (Williams and Laurens 2010). In a small raceway experiment coupling carbonate and biomass production, growth of the algae, *Spirulina platensis*, sequestered 53%, 41% and 39% of the CO_2 supplied at concentrations of 1%, 5% and 10%, CO_2 respectively. The biomass yield was 2.91 g/L (calorific value of 4303 kcal/kg) and calcite deposition rate was 3.52 g/L/day with an input CO_2 concentration of 10% (Ramanan et al. 2010). The coccolithophorid, *Pleurochrysis carterae* grown in a raceway pond had an annual total biomass productivity of about 60 t/ha/yr, with 21.9 t/ha/yr of total lipid and 5.5 t/ha/yr total $CaCO_3$ produced (Moheimani and Borowitzka 2006). Ca-rich fly ash and cement kiln dust could be used as feedstock for alkaline pond systems utilizing photoautotrophs and iron-reducing bacteria that facilitate precipitation of calcite and siderite [$FeCO_3$] (Roh et al. 2000). Ponds of 8-10 m in depth with residence times of weeks could handle 10,000 tons of ash per day while sequestering a large portion (e.g., 1/3) of the CO_2 bubbled through the ponds each day. Saline brines are another potential medium for biologically mediated carbonation.

The capacity of post-combustion capture of CO_2 using an enzyme-based system (i.e., immobilized carbonic anhydrase) is dependent on the overall deployment, i.e., retrofitting of existing power plants. An enzyme-based system using carbonic anhydrase within a membrane is able to remove 90% of the supplied CO_2 at the laboratory scale (Figueroa et al. 2008).

Carbon mineralization in industrial reactors

Carbonation in industrial reactors aims for rapid carbonation of silicate minerals (e.g., serpentine and olivine) at rates commensurate to the CO_2 emissions of coal burning electricity generation facilities (~100-1000 t CO_2/hour; Power et al. 2013b). This requires 100% mineral carbonation in a few hours. A number of *ex situ* carbonation routes may achieve sufficient reaction rates (e.g., O'Connor et al. 2005; Chizmeshya et al. 2007; Sipila et al. 2008), but may require high energy and financial inputs. Although the technologies for the previously

discussed process routes are feasible, the associated costs have limited their implementation. The estimated costs associated with pre-treatments, mining and processing of feedstock, chemical additives, and the energy required at each stage are ~$100/t CO_2, approximately 20 times greater than the current cost of carbon ($5/t; Power et al. 2013b). Application of these processes for carbonation of industrial waste material that is already pre-treated to a certain extent (e.g., mine tailings; Gerdemann et al. 2007; Hitch and Dipple 2012) would offset some of the costs associated with mining and grinding natural material. However, the total CO_2 storage capacity of waste materials is much lower than that of natural mineral deposits.

Ex situ carbonation of natural minerals at a globally significant scale, via use in industrial reactors and/or for enhanced weathering, would require new mining activities at a scale comparable to total existing global mining operations for fossil fuels, aggregate, minerals, and metals combined (Power et al. 2013b). Therefore, implementation of industrial *ex situ* carbonation at rates sufficient to offset anthropogenic CO_2 emissions is unlikely in the foreseeable future unless considerable incentives are introduced.

In situ carbon mineralization

In situ carbon mineralization could allow storage of CO_2 at a rate of >1 Gt CO_2/yr, or >2.6% of global CO_2 emissions, provided optimal reaction rates were attained by maintaining a high partial pressure of CO_2 in rocks at temperatures between 160 to 200 °C (Kelemen and Matter 2008). Large, near-surface peridotite massifs similar to that in Oman are exposed on land in Albania and neighboring countries, New Caledonia, and Papua New Guinea. Smaller peridotite bodies exposed in the 48 contiguous US states have a cumulative mass equivalent to that in Oman (Krevor et al. 2009). Notable peridotite exposures near European population centers include the large Ronda massif in southern Spain and its "sister," the Beni Boussera massif in Morocco, both on the Mediterranean coastline.

Terrestrial basalts also offer significant sequestration capacity (e.g., McGrail et al. 2006), with an estimated 100 Gt CO_2 storage capacity in the Columbia River basalts alone (Gislason et al. 2010). Carbonation of deep sea basalts is also proposed; Goldberg et al. (2008) estimate that ~920 Gt CO_2 could be stored as calcite on the Juan de Fuca plate, providing sufficient sequestration capacity to store all annual emissions from the United States (~7 Gt CO_2/yr; USEPA 2008) for ~122 years. Basalts have a lower intrinsic carbonation capacity than peridotites and serpentinites but are much more abundant than peridotites at and near the Earth's surface. Results from Wolff-Boenisch et al. (2011) indicate that Si release rates (as a proxy for dissolution rate) from basalt are within 0.6 log units of those from olivine-rich peridotite under some experimental conditions. Injection of CO_2-charged seawater into basalt may therefore be nearly as efficient as injection into peridotite. However, full carbonation of peridotite in aqueous solutions with 1 M NaCl and 0.6 to 3 M $NaHCO_3$ is reported to be orders of magnitude faster than dissolution of plagioclase, basalt or other geologically abundant materials (O'Connor et al. 2005; Chizmeshya et al. 2007; Kelemen et al. 2011). In Iceland, a subsurface basalt formation located at the Hellesheidi geothermal power plant is being supplied with CO_2 charged water, and has the capacity to accommodate ~12 Mt CO_2 (Gislason et al. 2010). If CO_2 were injected at the rate of annual emissions from the geothermal power plant (60 kt CO_2/yr), it would take ~200 years to reach this capacity. Goldberg et al. (2013) estimate that ~75 Mt CO_2/yr could be collected from the atmosphere via air capture supported by wind energy and sequestered below the seafloor in the Kerguelen plateau, a large igneous province in the Indian Ocean.

Thus, *in situ* mineral carbonation could, in principle, account for more than one stabilization wedge. This would require a substantial up-scaling of current drilling activities globally, and better understanding of feedbacks between mineral carbonation, permeability, and reactive surface area.

SUMMARY

Carbon sequestration research and technology is motivated by concerns that increasing atmospheric CO_2 concentrations are causing changes to Earth's climate and ecosystems that have the potential to cause serious, negative impacts on human welfare (IPCC 2005, 2007). As a global society, we will need to greatly improve energy efficiency and conservation, and develop alternative and renewable energy sources, while implementing carbon sequestration strategies to stabilize the concentration of atmospheric CO_2. The carbon mineralization strategies reviewed in this chapter complement CO_2 storage in subsurface pore space. This promising approach for sequestering CO_2 is grounded in the fundamental processes that govern natural mineral dissolution and carbonate precipitation. Natural analogue sites allow for the study of the geochemical and biological transformation of CO_2 at the field-scale; drawing our attention to potential reaction pathways that can be exploited and utilized, but also to the limitations that must be overcome in geoengineered and industrial systems designed to accelerate carbonation. Further study of natural analogues may yield a better understanding of the reaction pathways required for efficient carbonation, the long-term stability of carbonate minerals at Earth's surface, and the monitoring required for long-term storage.

Enhanced weathering of natural minerals or alkaline wastes under near-surface conditions offers a low-energy means of sequestering CO_2. Although this method offers the ability to aid in remediating the atmosphere, its effectiveness remains untested at large-scales. Accelerated carbonation of alkaline wastes may offer a means of reducing net greenhouse gas emission at the industrial level, while providing a testing ground for more widespread implementation. Biologically mediated carbonate precipitation is an alternate, low-energy means of sequestering CO_2 that could be incorporated into efforts to produce biofuels. *In situ* carbon mineralization of peridotite offers substantial capacity and relatively fast carbonation rates. Industrial reactors for *ex situ* carbonation are technologically feasible, yet the estimated costs exceed current carbon prices. Further research and development of process routes is therefore required. Industries that produce alkaline wastes may adopt these technologies as a means of reducing their carbon footprints, while helping to further develop these technological solutions.

The largest scale geologic carbon capture and storage operations currently inject ~1-3 Mt CO_2/yr into subsurface pore space (Michael et al. 2009; Whittaker et al. 2011). Use of industrial wastes for carbonation may rival these rates. In the future, these two strategies may be roughly equivalent in rate and capacity: global implementation of accelerated waste carbonation could exceed the sequestration capacity of 700 CO_2 injection sites. Use of a variety of industrial wastes in parallel could provide ~45% of a "stabilization wedge," and deliver significant offsets at the industry-specific level (Figs. 10 and 11). Implementation of accelerated waste carbonation technologies may allow establishment of viable *ex situ* technologies that could then be applied to larger scale carbonation of abundant, rock forming minerals, both *ex situ* and *in situ*. Although mafic and ultramafic deposits are present in sufficient quantity to completely offset anthropogenic CO_2 emissions for more than 1000 years, large-scale deployment of *ex situ* carbonation would require new mining activities at a scale comparable to total existing global mining operations (Power et al. 2013b). In principle, enhanced weathering and/or *in situ* carbonation of natural deposits could comprise an entire "stabilization wedge," but these techniques are very much at the basic research stage.

The capacity and rates of carbon mineralization are sufficient to offset significant portions of global greenhouse gas emissions. To realize this potential requires an interdisciplinary effort from fields ranging from the physical sciences to engineering to social sciences. Many of the strategies discussed in this chapter are technologically feasible at a level required for large-scale experimentation and even implementation at the industrial scale. In practice, a combination of *ex situ* carbonation of industrial waste and natural minerals, *in situ* carbonation of rock

formations, and ongoing CO_2 storage in subsurface pore space, could achieve a "stabilization wedge" (Fig. 11). However, financial incentives, either via a cap-and-trade mechanism or a carbon tax, are required to stimulate further innovation and research of CO_2 sequestration technologies that will lead to significant CO_2 sequestration via carbon mineralization or any other method proposed to date. Investigation of all of these techniques should proceed in parallel, followed by gradual adoption of a range of successful methods, using a variety of optimal strategies that depend on specific local conditions and opportunities.

ACKNOWLEDGMENTS

We acknowledge funding by the Carbon Management Canada National Centre of Excellence and the Natural Sciences and Engineering Research Council of Canada. Kelemen's work on this paper was supported by the Arthur D. Storke Chair at Columbia University, NSF Research Grant EAR-1049905, and DOE Award Number: DE-FE0002386. We are grateful for the detailed and thorough review by Bill Carey. This is publication 326 of the Mineral Deposit Research Unit.

REFERENCES

Akao M, Iwai S (1977a) The hydrogen bonding of artinite. Acta Crystallogr Sect B Struct Sci B33:3951-3953

Akao M, Iwai S (1977b) The hydrogen bonding of hydromagnesite. Acta Crystallogr Sect B Struct Sci B33:1273-1275

Akao M, Marumo F, Iwai S (1974) Crystal structure of hydromagnesite. Acta Crystallogr Sect B Struct Sci 30:2670-2672

Akbulut M, Piskin O, Karayigit AI (2006) The genesis of the carbonatized and silicified ultramafics known as listvenites: A case study from the Mihaliccik region (Eskisehir), NW Turkey. Geol J 41:557-580

Alexander G, Maroto-Valer MM, Gafarova-Aksoy P (2007) Evaluation of reaction variables in the dissolution of serpentine for mineral carbonation. Fuel 86:273-281

Allen DJ, Brent GF (2010) Sequestering CO_2 by mineral carbonation: Stability against acid rain exposure. Environ Sci Technol 44:2735-2739

Andreani M, Luquot L, Gouze P, Godard M, Hoisé E, Gibert B (2009) Experimental study of carbon sequestration reactions controlled by the percolation of CO_2-rich brine through peridotites. Environ Sci Technol 43:1226-1231

Andrews JA, Schlesinger WH (2001) Soil CO_2 dynamics, acidification, and chemical weathering in a temperate forest with experimental CO_2 enrichment. Glob Biogeochem Cycle 15:149-162

Arickx S, Van Gerven T, Vandecasteele C (2006) Accelerated carbonation for treatment of MSWI bottom ash. J Hazard Mat 137:235-243

Assima GP, Larachi F, Beaudoin G, Molson JW (2012) CO_2 sequestration in chrysotile mining residues - Implication of watering and passivation under environmental conditions. Ind Eng Chem Res 51:8726-8734

Badger MR, Price GD (2003) CO_2 concentrating mechanisms in cyanobacteria: molecular components, their diversity and evolution. J Exp Bot 54:609-622

Bales RC, Morgan JJ (1985) Dissolution kinetics of chrysotile at pH 7 to 10. Geochim Cosmochim Acta 49:2281-2288

Ballirano P, De Vito C, Mignardi S, Ferrini V (2013) Phase transitions in the Mg–CO_2–H_2O system and the thermal decomposition of dypingite, $Mg_5(CO_3)_4(OH)_2{\cdot}5H_2O$: Implications for geosequestration of carbon dioxide. Chem Geol 340:59-67

Barbero R, Carnelli L, Simon A, Kao A, Monforte AD, Ricco M, Bianchi D, Belcher A (2013) Engineered yeast for enhanced CO_2 mineralization. Energy Environ Sci 6:660-674

Barnes I, O'Neil JR (1969) Relationship between fluids in some fresh alpine-type ultramafics and possible modern serpentinization, western United States. Geol Soc Am Bull 80:1947-60

Barnes VE, Shock DA, Cunningham WA (1950) Utilization of Texas serpentine. The University of Texas, No. 5020, Bureau of Economic Geology.

Barnes I, O'Neil JR, Trescases JJ (1978) Present-day serpentinization in New Caledonia, Oman and Yugoslavia. Geochim Cosmochim Acta 42:144-45

Barns SM, Nierzwicki-Bauer SA (1997) Microbial diversity in ocean, surface and subsurface environments. Rev Mineral 35:35-79

Bea SA, Wilson SA, Mayer KU, Dipple GM, Power IM, Gamazo P (2012) Reactive transport modeling of natural carbon sequestration in ultramafic mine tailings. Vadose Zone J 11, doi: 10.2136/vzj2011.0053

Béarat H, McKelvy MJ, Chizmeshya AVG, Sharma R, Lowell S, Shield JE, Thoma SA, Thommes M (2002) Magnesium hydroxide dehydroxylation/carbonation reaction processes: Implications for carbon dioxide mineral sequestration. J Am Ceram Soc 85:742-748

Béarat H, McKelvy MJ, Chizmeshya AVG, Gormley D, Nunez R, Carpenter RW, Squires K, Wolf GH (2006) Carbon sequestration via aqueous olivine mineral carbonation: Role of passivating layer formation. Environ Sci Technol 40:4802-4808

Beinlich A, Austrheim H (2012) In situ sequestration of atmospheric CO_2 at low temperature and surface cracking of serpentinized peridotite in mine shafts. Chem Geol 323-333:32-44

Beinlich A, Plümper O, Hövelmann J, Austrheim H, Jamtveit B (2012) Massive serpentinite carbonation at Linnajavri, N–Norway. Terra Nova 24:446-455

Bennett PC (1991) Quartz dissolution in organic-rich aqueous systems. Geochim Cosmochim Acta 55:1781-1797

Bennett PC, Hiebert FK, Choi W (1996) Rates of microbial weathering of silicates in ground water. Chem Geol 132:45-53

Bennett PC, Rogers JA, Hiebert FK, Choi WJ (2001) Silicates, silicate weathering, and microbial ecology: Geomicrobiol J 18:3-19

Berg A, Banwart SA (2000) Carbon dioxide mediated dissolution of Ca-feldspar: Implications for silicate weathering. Chem Geol 163:25-42

Berner RA (1990) Atmospheric carbon dioxide levels over Phanerozoic time. Science 249:1382-1386

Berner RA (1995) Chemical weathering and its effect on atmospheric CO_2 and climate. Rev Mineral 31:565-583

Berner RA, Lasaga AC, Garrels RM (1983) The carbonate–silicate geochemical cycle and its effect on atmospheric carbon dioxide over the past 100 million years. Am J Sci 283:641-683

BHP Billiton (2005) Mt Keith Nickel Operations: Environmental Data. BHP Billiton Sustainability Reports, BHP Billiton, *http://hsecreport.bhpbillton.com/wmc/2004/performance/mko/data*

Bobicki ER, Liu Q, Xu Z, Zeng H (2012) Carbon capture and storage using alkaline industrial wastes. Prog Energy Combust Sci 38:302-320

Bodnar RJ, Steele-MacInnis M, Capobianco RM, Rimstidt JD, Dilmore R, Goodman A, Guthrie G (2013) PVTX Properties of H_2O-CO_2-"salt" at PTX conditions applicable to carbon sequestration in saline formations. Rev Mineral Geochem 77:123-152

Bond GM, Stringer J, Brandvold DK, Simsek FA, Medina MG, Egeland G (2001) Development of integrated system for biomimetic CO_2 sequestration using the enzyme carbonic anhydrase. Energy Fuels 15:309-316

Bonenfant D, Kharoune L, Sauvé S, Hausler R, Niquette P, Mimeault M, Kharoune M (2008b) CO_2 sequestration by aqueous red mud carbonation at ambient pressure and temperature. Ind Eng Chem Res 47:7617-7622

Boschi C, Früh-Green G, Escartin J (2006) Occurrence and significance of serpentinite-hosted talc- and amphibole-rich fault rocks in modern oceanic settings and ophiolite complexes: An overview. Ofioliti 31:129-140

Botha A, Strydom CA (2001) Preparation of a magnesium hydroxy carbonate from magnesium hydroxide. Hydrometallurgy 62:175-183

Brady PV, Carroll SA (1994) Direct effects of CO_2 and temperature on silicate weathering: Possible implications for climate control. Geochim Cosmochim Acta 58: 1853-1856

Braithwaite CJR, Zedef V (1994) Living hydromagnesite stromatolites from Turkey. Sediment Geol 92:1-5

Braithwaite CJR, Zedef V (1996) Hydromagnesite stromatolites and sediments in an alkaline lake, Salda Gölü, Turkey. J Sediment Res 66:991-1002

Brantley SL (2003) Reaction kinetics of primary rock-forming minerals under ambient conditions. Treatise Geochem 5:73-117

Brantley SL (2008a) Kinetics of mineral dissolution. *In:* Kinetics of water-rock interaction. Vol 1. Brantley SL, Kubicki JD, White AF (eds) Springer, New York, p 151-210

Brantley SL (2008b) Understanding soil time. Science 321:1454-1455

Brantley SL, Megonigal JP, Scatena FN, Balogh-Brunstad Z, Barnes RT, Bruns MA, Van Cappellen P, Dontsova K, Hartnett HE, Hartshorn AS, Heimsath A, Herndon E, Jin L, Keller CK, Leake JR, McDowell WH, Meinzer FC, Mozdzer TJ, Petsch S, Pett-Ridge J, Pregitzer KS, Ratmond PA, Riebe CS, Shumaker K, Sutton-Grier A, Walter R and Yoo K (2011) Twelve testable hypotheses on the geobiology of weathering. Geobiol 9:140-165

Brazelton WJ, Nelson B, Schrenk MO (2012) Metagenomic evidence for H_2 oxidation and H_2 production by serpentinite-hosted subsurface microbial communities. Front Microbiol 2:268

Bruni J, Canepa M, Chiodini G, Cioni R, Cipolli F, Longinelli A, Marini L, Ottonello G, Zuccolini MV (2002) Irreversible water-rock mass transfer accompanying the generation of the neutral, Mg-HCO_3 and high-pH, Ca-OH spring waters of the Genova province, Italy. Appl Geochem 17:455-474

Butt DP, Lackner KS, Wendt CH, Conzone SD, Kung H, Lu Y, Bremser JK (1996) Kinetics of thermal dehydroxylation and carbonation of magnesium hydroxide. J Am Ceram Soc 79:1892-1898

Canterford JH, Tsambourakis G, Lambert B (1984) Some observations on the properties of dypingite, $Mg_5(CO_3)_4(OH)_2{\cdot}5H_2O$, and related minerals. Mineral Mag 48:437-442

Case DH, Wang F, Giammar DE (2011) Precipitation of magnesium carbonates as a function of temperature, solution composition, and presence of a silicate mineral substrate. Environ Eng Sci 28:881-889

Chen PH, Liu HL, Chen YJ, Cheng H, Lin WL, Yeh CH, Chang CH (2012) Enhancing CO_2 bio-mitigation by genetic engineering of cyanobacteria. Energy Environ Sci 5:8318-8327

Chisti Y (2007) Biodiesel from microalgae. Biotechnol Adv 25:294-306

Chizmeshya AVG, McKelvy MJ, Squires K, Carpenter RW, Béarat H (2007) A novel approach to mineral carbonation: enhancing carbonation while avoiding mineral pretreatment process cost. U.S. Dep. Energy Final Rep. 924162, Arizona State University, Tempe, Arizona

Cipolli F, Gambardella B, Marini L, Ottonello G, Zuccolini MV (2004) Geochemistry of high-pH waters from serpentinites of the Gruppo di Voltri (Genova, Italy) and reaction path modeling of CO_2 sequestration in serpentinite aquifers. Appl Geochem 19:787-802

Clark ID, Fontes JC, Fritz P (1992) Stable Isotope disequilibria in travertine from high pH waters: Laboratory investigations and field observations from Oman. Geochim Cosmochim Acta 56:2041-2050

Cleaves ET, Fisher DW, Bricker OP (1974) Chemical weathering of serpentinite in the Eastern Piedmont of Maryland. Geol Soc Am Bull 85:437-444

Cubillas P, Köhler S, Prieto M, Causserand C, Oelkers EH (2005) How do mineral coatings affect dissolution rates? An experimental study of coupled $CaCO_3$ dissolution—$CdCO_3$ precipitation. Geochim Cosmochim Acta 69:5459-5476

Daval D, Martinez I, Corvisier J, Findling N, Goffé B, Guyot F (2009) Carbonation of Ca-bearing silicates, the case of wollastonite: Experimental investigations and kinetic modeling. Chem Geol 265:63-78

Daval D, Sissmann O, Menguy N, Saldi GD, Guyot F, Martinez I, Corvisier J, Garcia B, Machouk I, Knauss KG, Hellmann R (2011) Influence of amorphous silica layer formation on the dissolution rate of olivine at 90 °C and elevated pCO_2. Chem Geol 284:193-209

Davies PJ, Bubela B (1973) The transformation of nesquehonite into hydromagnesite. Chem Geol 12:289-300

Dessert C, Dupré B, Gaillardet J, François LM, Allègre CJ (2003) Basalt weathering laws and the impact of basalt weathering on the global carbon cycle. Chem Geol 202:257-273

Dexter J, Fu P (2009) Metabolic engineering of cyanobacteria for ethanol production. Energy Environ Sci 2:857-864

Dilmore R, Lu P, Allen D, Soong Y, Hedges S, Fu JK, Dobbs CL, Degalbo A, Zhu C (2008) Sequestration of CO_2 in mixtures of bauxite residue and saline wastewater. Energy Fuels 22:343-353

Dilmore R, Griffith C, Liu Z, Soong Y, Hedges SW, Koepsel R, Ataai M (2009) Carbonic anhydrase-facilitated CO_2 absorption with polyacrylamide buffering bead capture. Int J Greenhouse Gas Control 3:401-410

Doucet FJ (2010) Effective CO_2-specific sequestration capacity of steel slags and variability in their leaching behaviour in view of industrial mineral carbonation. Miner Eng 23:262-269

Dudev T, Cowan JA, Lim C (1999) Competitive binding in magnesium coordination chemistry: Water versus ligands of biological interest. 121:7665-7673

Dupraz C, Reid RP, Braissant O, Decho AW, Norman RS, Visscher PT (2009) Processes of carbonate precipitation in modern microbial mats. Earth-Sci Rev 96:141-162

Edgerton D (1997) Reconstruction of the Red Dog Zn-Pb-Ba orebody, Alaska: implications for the vent environment during the mineralizing event. Can J Earth Sci 34:1581-1602

Edwards KJ, Goebel BM, Rodgers TM, Schrenk MO, Gihring TM, Cardona MM, Hu B, McGuire MM, Hamers RJ, Pace NR, Banfield JF (1999) Geomicrobiology of pyrite (FeS_2) dissolution: Case study at Iron Mountain, California. Geomicrobiol J 16:155-179

Eiken O, Ringrose P, Hermanrud C, Nazarian B, Torp TA, Høier L (2011) Lessons learned from 14 years of CCS operations: Sleipner, In Salah and Snøhvit. Energy Procedia 4:5541-5548

Eloneva S, Teir S, Salminen J, Fogelholm C-J, Zevenhoven R (2008) Fixation of CO_2 by carbonating calcium derived from blast furnace slag. Energy 33:1461-1467

Enders MS, Knickerbocker C, Titley SR, Southam G (2006) The role of bacteria in the supergene environment of the Morenci porphyry copper deposit, Greenlee County, Arizona. Econ Geol 101:59-70

Favre N, Christ ML, Pierre AC (2009) Biocatalytic capture of CO_2 with carbonic anhydrase and its transformation to solid carbonate. J Mol Catal B Enzym 60:163-170

Ferrini V, De Vito C, Mignardi S (2009) Synthesis of nesquehonite by reaction of gaseous CO_2 with Mg chloride solution: Its potential role in the sequestration of carbon dioxide. J Hazard Mater 168:832-837

Ferris FG, Wiese RG, Fyfe WS (1994) Precipitation of carbonate minerals by microorganisms: Implications for silicate weathering and the global carbon dioxide budget. Geomicrobiol J 12:1-13

Figueroa JD, Fout T, Plasynski S, McIlvried H, Srivastava RD (2008) Advances in CO_2 capture technology—The U.S. Department of Energy's Carbon Sequestration Program. Int J Greenhouse Gas Control 2:9-20

Frankel RB, Bazylinski DA (2003) Biologically induced mineralization by bacteria. Rev Mineral Geochem 54:95-114

Frankignoulle M, Canon C, Gattuso J-P (1994) Marine calcification as a source of carbon dioxide - Positive feedback of increasing atmospheric CO_2. Limnol Oceanogr 39:458-462

Friedel B (1975) Synthetic giorgiosite. Neues Jahrb Mineral Monatsh 196-208

Früh-Green GL, Kelley DS, Bernasconi SM, Karson JA, Ludwig KA, Butterfield DA, Boschi C, Proskurowski G (2003) 30,000 years of hydrothermal activity at the Lost City vent field. Science 301:495-498

Gao F, Nie Z, Wang Z, Li H, Gong X, Zuo T (2009) Greenhouse gas emissions and reduction potential of primary aluminum production in China. Sci China Ser E Technol Sci 52:2161-2166

Gerdemann SJ, Dahlin DC, O'Connor WK, Penner LR (2003) Carbon dioxide sequestration by aqueous mineral carbonation of magnesium silicate minerals. *In*: Proceedings of the 2nd Annual Conference on Carbon Sequestration, Alexandria, VA, May 5-8, 2003. *http://netl.doe.gov/publications/proceedings/03/carbon-seq/PDFs/074.pdf*

Gerdemann SJ, O'Connor WK, Dahlin DC, Penner LR, Rush H (2007) Ex situ aqueous mineral carbonation. Environ Sci Technol 41:2587-2593

Giammar DE, Bruant Jr RG, Peters CA (2005) Forsterite dissolution and magnesite precipitation at conditions relevant for deep saline aquifer storage and sequestration of carbon dioxide. Chem Geol 217:257-276

Giester G, Lengauer CL, Rieck B (2000) The crystal structure of nesquehonite, $MgCO_3{\cdot}3H_2O$, from Lavrion, Greece. 70:153-163

Gislason SR, Oelkers EH (2003) Mechanism, rates, and consequences of basaltic glass dissolution: II. An experimental study of the dissolution rates of basaltic glass as a function of pH and temperature. Geochim Cosmochim Acta 67:3817-3832

Gislason SR, Oelkers EH, Eiriksdottir ES, Kardjilov MI, Gisladottir G, Sigfusson B, Snorrason A, Elefsen S, Hardardottir J, Torssander P, Oskarsson N (2009) Direct evidence of the feedback between climate and weathering. Earth Planet Sci Lett 277:213-222

Gislason SR, Wolff-Boenisch D, Stefansson A, Oelkers EH, Gunnlaugsson E, Sigurdardottir H, Sigfusson B, Broecker WS, Matter JM, Stute M (2010) Mineral sequestration of carbon dioxide in basalt: A pre-injection overview of the CarbFix project. Int J Greenhouse Gas Control 4:537-545

Glaister BJ, Mudd GM (2010) The environmental costs of platinum–PGM mining and sustainability: Is the glass half-full or half-empty? Miner Eng 23:438-450

Goff F, Lackner KS (1998) Carbon dioxide sequestering using ultramafic rocks. Environ Geosci 5:89-101

Goldberg DS, Takahashi T, Slagle AL (2008) Carbon dioxide sequestration in deep-sea basalt. Proc Natl Acad Sci USA 105:9920-9925

Goldberg DS, Lackner KS, Han P, Slagle AL, Wang T (2013) Co-location of air capture, subseafloor CO_2 sequestration, and energy production on the Kerguelen plateau. Environ Sci Technol 47:7521-7529

Golubev SV, Pokrovsky OS, Schott J (2005) Experimental determination of the effect of dissolved CO_2 on the dissolution kinetics of Mg and Ca silicates at 25 °C. Chem Geol 217:227-238

Goudie AS (1973) Duricrusts of Tropical and Subtropical Landscapes. Oxford University Press, UK. p 174

Granger DE, Riebe CS (2007) Cosmogenic nuclides in weathering and erosion. Treatise Geochem 5:1-43

Gunning PJ, Hills CD, Carey PJ (2010) Accelerated carbonation treatment of industrial wastes. Waste Manage 30:1081-1090

Guthrie GD Jr, Carey JW, Bergfeld D, Byler D, Chipera S, Ziock HJ (2001) Geochemical aspects of the carbonation of magnesium silicates in an aqueous medium. First National Conference on Carbon Sequestration. National Energy Technology Laboratory, Washington, DC, *http://netl.doe.gov/publications/proceedings/01/carbon_seq/6c4.pdf*

Halls C, Zhao R (1995) Listvenite and related rocks: Perspectives on terminology and mineralogy with reference to an occurrence at Cregganbaun, Co. Mayo, Republic of Ireland: Mineral. Deposita 30:303-313

Hänchen M, Prigiobbe V, Storti G, Seward TM, Mazzotti M (2006) Dissolution kinetics of fosteritic olivine at 90-150 °C including effects of the presence of CO_2. Geochim Cosmochim Acta 70:4403-4416

Hänchen M, Prigiobbe V, Baciocchi R, Mazzotti M (2008) Precipitation in the Mg-carbonate system—effects of temperature and CO_2 pressure. Chem Eng Sci 63:1012-1028

Hangx SJT, Spiers CJ (2009) Coastal spreading of olivine to control atmospheric CO_2 concentrations: A critical analysis of viability. Int J Greenhouse Gas Control 3:757-767

Hansen LD, Dipple GM, Gordon TM, Kellett DA (2005) Carbonated serpentinite (listwanite) at Atlin, British Columbia: a geological analogue to carbon dioxide sequestration. Can Mineral 43:225-239

Harned HS, Davis R Jr (1943) The ionization constant of carbonic acid in water and the solubility of carbon dioxide in water and aqueous salt solutions from 0 to 50°. J Am Chem Soc 65:2030-2037

Harrison AL, Power IM, Dipple GM (2013) Accelerated carbonation of brucite in mine tailings for carbon sequestration. Environ Sci Technol 47:126-134

Hartmann J, Kempe S (2008) What is the maximum potential for CO_2 sequestration by "stimulated" weathering on the global scale? Naturwissenschaften 95:1159-1164

Hartmann J, West JA, Renforth P, Köhler P, De La Rocha CL, Wolf-Gladrow DA, Dürr HH, Scheffran J (2013) Enhanced chemical weathering as a geoengineering strategy to reduce atmospheric carbon dioxide, supply nutrients, and mitigate ocean acidification. Rev Geophys 51:2012RG000404

Haug TA, Munz IA, Kleiv RA (2011) Importance of dissolution and precipitation kinetics for mineral carbonation. Energy Procedia 4:5029-5036

Herzog HJ (2002) Carbon sequestration via mineral carbonation: Overview and assessment. MIT Laboratory for Energy and the Environment. Cambridge, Massachusetts.

Hess HH (1933) The problem of serpentinization and the origin of certain chrysotile asbestos, talc and soapstone deposits. Econ Geol 28:634-657

Hiebert F, Bennett PC (1992) Microbial control of silicate weathering in organic-rich ground water. Science 258:278-281

Hill RJ, Canterford JH, Moyle FJ (1982) New data for lansfordite. Mineral Mag 46:453-457

Hitch M, Dipple GM (2012) Economic feasibility and sensitivity analysis of integrating industrial-scale mineral carbonation into mining operations. Miner Eng 39:268-275

Hodson ME (2003) The influence of Fe-rich coatings on the dissolution of anorthite at pH 2.6. Geochim Cosmochim Acta 67:3355-3363

Holland TJB, Powell R (1998) An internally consistent thermodynamic data set for phases of petrological interest. J Metamorph Geol 16:309-343

Holland HD, Lazar B, McCaffrey M (1986) Evolution of the atmosphere and oceans. Nature 320:27-33

Hopkinson L, Rutt K, Cressey G (2008) The transformation of nesquehonite to hydromagnesite in the system CaO-MgO-H_2O-CO_2: An experimental spectroscopic study. J Geol 116:387-400

Hopkinson L, Kristova P, Rutt K, Cressey G (2012) Phase transitions in the system MgO–CO_2–H_2O during CO_2 degassing of Mg-bearing solutions. Geochim Cosmochim Acta 76:1-13

Hostetler PB, Coleman RG, Mumpton FA, Evan BW. (1966) Brucite in alpine serpentinites. Am Mineral 51:75:98

Houston EC (1945) Magnesium from olivine. Metals Technology XII:1-14

Hövelmann J, Putnis CV, Ruiz-Agudo E, Austrheim H (2012) Direct nanoscale observations of CO_2 sequestration during brucite [$Mg(OH)_2$] dissolution. Environ Sci Technol 46:5253-5260

Huijgen WJ, Comans RN (2003) Carbon dioxide sequestration by mineral carbonation: Literature review. Energy Research Center of the Netherlands, Petten, Netherlands, ECN-C-03-016

Huijgen WJ, Comans RN (2005) Carbon dioxide sequestration by mineral carbonation: Literature review update 2003-2004. Energy Research Center of the Netherlands, Petten, Netherlands, ECN-C-05-022

Huijgen WJJ, Comans RNJ (2006) Carbonation of steel slag for CO_2 sequestration: leaching of products and reaction mechanisms. Environ Sci Technol 40:2790-2796

Huijgen WJJ, Witkamp G-J, Comans RNJ (2005) Mineral CO_2 sequestration by steel slag carbonation. Environ Sci Technol 39:9676-9682

Huntzinger DN, Eatmon TD (2009) A life-cycle assessment of Portland cement manufacturing: Comparing the traditional process with alternative technologies. J Cleaner Prod 17:668-675

Huntzinger DN, Gierke JS, Kawatra SK, Eisele TC, Sutter LL (2009a) Carbon dioxide sequestration in cement kiln dust through mineral carbonation. Environ Sci Technol 43:1986-1992

Huntzinger DN, Gierke JS, Sutter LL., Kawatra SK, Eisele TC (2009b) Mineral carbonation for carbon sequestration in cement kiln dust from waste piles. J Hazard Mater 168:31-37

ICMM (2008) Case study: Alcoa develops carbon capture process. *http://www.icmm.com/page/2420/alcoa-develops-carbon-capture-process*

IPCC (2005) IPCC Special Report on Carbon Dioxide Capture and Storage. Prepared by Working Group III of the Intergovernmental Panel on Climate Change. Metz B, Davidson O, de Coninck HC, Loos M, Meyer LA (eds) Cambridge University Press, Cambridge, United Kingdom and New York, USA

IPCC (2007) IPCC Climate Change 2007: Synthesis Report, An Assessment of the Intergovernmental Panel on Climate Change, *http://www.ipcc.ch/pdf/assessment-report/ar4/syr/ar4_syr.pdf*

Iyer K, Jamtveit B, Mathiesen J, Malthe-Sorenssen A, Feder J (2008) Reaction-assisted hierarchical fracturing during serpentinization. Earth Planet Sci Lett 267:503-516

Jamtveit B, Austrheim H, Malthe-Sørenssen A (2000) Accelerated hydration of the Earth's deep crust induced by stress perturbations. Nature 408:75-78

Jamtveit B, Malthe-Sørenssen A, Kostenko O (2008) Reaction enhanced permeability during retrogressive metamorphism. Earth Planet Sci Lett 267:620-627

Jamtveit B, Kobchenko M, Austrheim H, Malthe-Sørenssen A, Royne A, Svensen H (2011) Porosity evolution and crystallization-driven fragmentation during weathering of andesite. J Geophys Res-Solid Earth 116:B12204, http://dx.doi.org/ 10.1029/12011JB008649

Jansson C, Northen T (2010) Calcifying cyanobacteria-the potential of biomineralization for carbon capture and storage. Curr Opin Biotechnol 21:365-371

Jarvis K, Carpenter RW, Windman T, Kim Y, Nunez R, Alawneh F (2009) Reaction mechanisms for enhancing mineral sequestration of CO_2. Environ Sci Technol 43:6314-6319
Jiang S-Y, Yu J-M, Lu J-J (2004) Trace and rare-earth element geochemistry in tourmaline and cassiterite from the Yunlong tin deposit, Yunnan, China: Implication for migmatitic–hydrothermal fluid evolution and ore genesis. Chem Geol 209:193-213
Jiang J, Du X, Chen M, Zhang C (2009) Continuous CO_2 capture and MSWI fly ash stabilization, utilizing novel dynamic equipment. Environ Pollut 157:2933-2938
Jo HY, Ahn J-H, Jo H, (2012a) Evaluation of the CO_2 sequestration capacity for coal fly ash using a flow-through column reactor under ambient conditions. J Hazard Mater 241-242:127-136
Jo HY, Kim J H, Lee YJ, Lee M, Choh S-J (2012b) Evaluation of factors affecting mineral carbonation of CO_2 using coal fly ash in aqueous solutions under ambient conditions. Chem Eng J 183:77-87
Johnston M, Clark MW, McMahon P, Ward N (2010) Alkalinity conversion of bauxite refinery residues by neutralization. J Hazard Mater 182:710-715
Kalinkina EV, Kalinkin AM, Forsling W, Makarov VN (2001a) Sorption of atmospheric carbon dioxide and structural changes of Ca and Mg silicate minerals during grinding: I. Diopside. Int J Miner Process 61:273-288
Kalinkina EV, Kalinkin AM, Forsling W, Makarov VN (2001b) Sorption of atmospheric carbon dioxide and structural changes of Ca and Mg silicate minerals during grinding: II. Enstatite, akermanite and wollastonite. Int J Miner Process 61:289-299
Kalinkin AM, Kalinkina EV, Politov AA, Makarov VN, Boldyrev VV (2004) Mechanochemical Interaction of Ca Silicate and Aluminosilicate Minerals with Carbon Dioxide. Springer, the Netherlands
Kaplan A, Reinhold L (1999) CO_2 concentrating mechanisms in photosynthetic microorganisms. Annu Rev Plant Physiol Plant Molec Biol 50:539-570
Kelemen PB, Hirth G (2012) Reaction-driven cracking during retrograde metamorphism: Olivine hydration and carbonation. Earth Planet Sci Lett 345:81-89
Kelemen PB, Matter J (2008) In situ carbonation of peridotite for CO_2 storage. Proc Natl Acad Sci 105:17295-17300
Kelemen PB, Matter J, Streit EE, Rudge JF, Curry WB, Blusztajn J (2011) Rates and mechanisms of mineral carbonation in peridotite: natural processes and recipes for enhanced, in situ CO_2 capture and storage. Annu Rev Earth Planet Sci p 39:545-576
Kelley DS, Karson JA, Blackman DK, Fruh-Green GL, Butterfield DA, Lilley MD, Olson EJ, Schrenk MO, Roe KK, Lebon GT, Rivizzigno P, Party ATS (2001) An off-axis hydrothermal vent field near the Mid-Atlantic Ridge at 30°N. Nature 412:145-149
Ki MR, Kanth BK, Min KH, Lee J, Pack SP (2012) Increased expression level and catalytic activity of internally-duplicated carbonic anhydrase from *Dunaliella* species by reconstitution of two separate domains. Process Biochem 47:1423-1427
Kirby CS, Thomas HM, Southam G, Donald R (1999) Relative contributions of abiotic and biological factors in Fe(II) oxidation in mine drainage. Appl Geochem 14:511-530
Kleiv RA, Thornhill M (2006) Mechanical activation of olivine. Miner Eng 19:340-347
Knauth LP, Brilli M, Klonowski S (2003) Isotope geochemistry of caliche developed on basalt. Geochim Cosmochim Acta 67:185-195
Köhler P, Hartmann J, Wolf-Gladrow DA (2010) Geoengineering potential of artificially enhanced silicate weathering of olivine. Proc Natl Acad Sci 107:20228-20233
Königsberger E, Königsberger L, Gamsjager H (1999) Low-temperature thermodynamic model for the system Na_2CO_3-$MgCO_3$-$CaCO_3$-H_2O. Geochim Cosmochim Acta 63:3105-3119
Krevor SCM, Lackner KS (2011) Enhancing serpentine dissolution kinetics for mineral carbon dioxide sequestration. Int J Greenhouse Gas Control 5:1073-1080
Krevor SC, Graves CR, Van Gosen BS, McCafferty AE (2009) Mapping the mineral resource base for mineral carbon-dioxide sequestration in the conterminous United States: U.S. Geological Survey Digital Data Series 414, 14 p., 1 plate, http://pubs.usgs.gov/ds/414
Kump LR, Brantley SL, Arthur MA (2000) Chemical weathering, atmospheric CO_2, and climate. Annu Rev Earth Planet Sci 28:611-667
Kwon S, Fan M, DaCosta HFM, Russell AG, Berchtold KA, Dubey MK (2011) CO_2 Sorption. *In:* Coal Gasification and its applications. William Andrew Publishing, Boston, p 293-339
Lackner KS (2002) Carbonate chemistry for sequestering fossil carbon. Annu Rev Energy Env 27:193-232
Lackner KS (2003) Climate change - A guide to CO_2 sequestration. Science 300:1677-1678
Lackner KS, Wendt CH, Butt DP, Joyce EL, Sharp DH (1995) Carbon dioxide disposal in carbonate minerals. Energy 20:1153-1170
Lackner KS, Butt DP, Wendt CH (1997) Process on binding CO_2 in mineral substrates. Energy Convers Manage 38:S259-S264
Lane N, Martin WF (2012) The origin of membrane bioenergetics. Cell 151:1406-1416

Larachi F, Daldoul I, Beaudoin G (2010) Fixation of CO_2 by chrysotile in low-pressure dry and moist carbonation: Ex-situ and in-situ characterizations. Geochim Cosmochim Acta 74:3051-3075

Lee BD, Graham RC, Laurent TE, Amrhein C (2004) Pedogenesis in a wetland meadow and surrounding serpentinitic landslide terrain, northern California, USA. Geoderma 118:303-320

Lee BD, Apel WA,Walton MR (2006) Whitings as a potential mechanism for controlling atmospheric carbon dioxide concentrations – Final project report final report. INL/EXT-06-01351. Idaho National Laboratory

Lee SW, Park SB, Jeong SK, Lim KS, Lee SH, Trachtenberg MC (2010) On carbon dioxide storage based on biomineralization strategies. Micron 41:273-282

Lekakh SN, Rawlins CH, Robertson DGC, Richards VL, Peaslee KD (2008) Kinetics of aqueous leaching and carbonization of steelmaking slag. Metall Mater Trans B 39:125-134

Levitan DM, Hammarstrom JM, Gunter ME, Seal RR II, Chou I-M, Piatek NM (2009) Mineralogy of mine waste at the Vermont Asbestos Group mine, Belvidere Mountain, Vermont. Am Mineral 94:1063-1066

Li X, Bertos MF, Hills CD, Carey PJ, Simon S (2007) Accelerated carbonation of municipal solid waste incineration fly ashes. Waste Manage 27:1200-1206

Li W, Liu LP, Chen WS, Yu LJ, Li WB, Yu HZ (2010) Calcium carbonate precipitation and crystal morphology induced by microbial carbonic anhydrase and other biological factors. Process Biochem 45:1017-1021

Liao J, Senna M (1992) Thermal behavior of mechanically amorphized talc. Thermochim Acta 197:295-306

Love DA, Clark AH, Glover JK (2004) The lithologic, stratigraphic, and structural setting of the Giant Antamina Copper-Zinc skarn Deposit, Ancash, Peru. Econ Geol 99:887-916

Luce RW, Bartlett RW, Parks GA (1972) Dissolution kinetics of magnesium silicates. Geochim Cosmochim Acta 36:35-50

Ludwig W, Amiotte Suchet P, Munhoven G, Probst JL (1998) Atmospheric CO_2 consumption by continental erosion: Present-day control and implications for the Last Glacial Maximum. Global Planet Change 16-17:107-120

Ludwig KA, Kelley DS, Butterfield DA, Nelson BK, Früh-Green G (2006) Formation and evolution of carbonate chimneys at the Lost City hydrothermal field. Geochim Cosmochim Acta 70:3625-3645

Macdonald AH, Fyfe WS (1985) Rate of serpentinization in seafloor environments. Tectonophys 116:123-135

MacDonald GD, Arnold LC (1994) Geological and geochemical zoning of the Grasberg Igneous Complex, Irian Jaya, Indonesia. J Geochem Explor 50:143-178.

Madu BE, Nesbitt BE, Muehlenbachs K (1990) A mesothermal gold-stibnite-quartz vein occurrence in the Canadian Cordillera. Econ Geol 85:1260-1268

Malmstrom M, Banwart S (1997) Biotite dissolution at 25°C: The pH dependence. Geochim Cosmochim Acta 61:2779-2799

Manning DAC (2008) Biological enhancement of soil carbonate precipitation: passive removal of atmospheric CO_2. Mineral Mag 72:639:649

Manning DAC, Renforth P (2013) Passive sequestration of atmospheric CO_2 through coupled plant-mineral reactions in urban soils. Environ Sci Technol 47:135-141

Maroto-Valer MM, Fauth DJ, Kuchta ME, Zhang Y, Andrésen JM (2005) Activation of magnesium rich minerals as carbonation feedstock materials for CO_2 sequestration. Fuel Process Technol 86:1627-1645

Martinez AM, Rubin JB, Hollis WK, Ziock LHJ, Guthrie GD, Chipera SJ, Lackner KS (2000) Sequestration of carbon dioxide by carbonation of minerals at supercritical fluid conditions. Mexican American Engineers Scientists MAES 26th Annual International Symposium: 2800

Mata TM, Martins AA, Caetano NS (2010) Microalgae for biodiesel production and other applications: A review. Renewable Sustainable Energy Rev 14:217-232

Mateo C, Palomo JM, Fernandez-Lorente G, Guisan JM, Fernandez-Lafuente R (2007) Improvement of enzyme activity, stability and selectivity via immobilization techniques. Enzyme Microb Technol 40:1451-1463

Matter JM, Kelemen PB (2009) Permanent storage of carbon dioxide in geological reservoirs by mineral carbonation. Nature Geoscience 12:837-841

McGrail BP, Schaef HT, Ho AM, Chien Y-J, Dooley JJ, Davidson CL (2006) Potential for carbon dioxide sequestration in flood basalts. J Geophys Res 111:1-13

McKelvy MJ, Chizmeshya AVG, Diefenbacher J, Béarat H, Wolf G (2004) Exploration of the role of heat activation in enhancing serpentine carbon sequestration reactions. Environ Sci Technol 38:6897-6903

Ménez B, Pasini V, Brunelli D (2012) Life in the hydrated suboceanic mantle. Nat Geosci 5:133-137

Michael K, Allinson G, Golab A, Sharma S, Shulakova V (2009) CO_2 storage in saline aquifers II – experience from existing storage operations. Energy Procedia 1:1973-1980

Mielke RE, Pace DL. Porter T, Southam G (2003) A critical stage in the formation of acid mine drainage: Colonization of pyrite by *Acidithiobacillus ferrooxidans* under pH-neutral conditions. Geobiology 1:81-90

Mignardi S, De Vito C, Ferrini V, Martin RF (2011) The efficiency of CO_2 sequestration via carbonate mineralization with simulated wastewaters of high salinity. J Hazard Mater 191:49-55

Miller QRS, Thompson CJ, Loring JS, Windisch CF, Bowden ME, Hoyt DW, Hu JZ, Arey BW, Rosso KM, Schaef HT (2013) Insights into silicate carbonation processes in water-bearing supercritical CO_2 fluids. Int J Greenhouse Gas Control 15:104-118

Mirjafari P, Asghari K, Mahinpey N (2007) Investigating the application of enzyme carbonic anhydrase for CO_2 sequestration purposes. Ind Eng Chem Res 46:921-926

Moheimani NR, Borowitzka MA (2006) The long-term culture of the coccolithophore *Pleurochrysis carterae* (Haptophyta) in outdoor raceway ponds. J Appl Phycol 18:703-712

Montes-Hernandez G, Pérez-López R, Renard F, Nieto JM, Charlet L (2009) Mineral sequestration of CO_2 by aqueous carbonation of coal combustion fly-ash. J Hazard Mater 161:1347-1354

Morales-Flórez V, Santos A, Lemus A, Esquivias L (2011) Artificial weathering pools of calcium-rich industrial waste for CO_2 sequestration. Chem Eng J 166:132-137

Morse JW, Casey WH (1988) Ostwald processes and mineral paragenesis in sediments. Am J Sci 288:537-560

Morse JW, Arvidson RS, Lüttge A. (2007) Calcium carbonate formation and dissolution. Chem Rev 107:342-381

Mudd GM (2010) Global trends and environmental issues in nickel mining: Sulfides versus laterites. Ore Geol Rev 38:9-26

Munz IA, Brandvoll Ø, Haug TA, Iden K, Smeets R, Kihle J, Johansen H (2012) Mechanisms and rates of plagioclase carbonation reactions. Geochim Cosmochim Acta 77:27-51

Naldrett AJ (1966) Talc-carbonate alteration of some serpentinized ultramafic rocks south of Timmins, Ontario. J Petrol 7:489-499

Nasir S, Al Sayigh AR, Al Harthy A, Al-Khirbash S, Al-Jaaldi O, Musllam A, Al-Mishwat A, Al-Bu'saidi S (2007) Mineralogical and geochemical characterization of listwaenite from the Semail Ophiolite, Oman. Chem Erde-Geochem 67:213-228

Neal C, Stanger G (1985) Past and present serpentinization of ultramafic rocks: an example from the Semail ophiolite nappe of northern Oman. *In*: The Chemistry of Weathering. Drever JI (ed) Reidel Publishing, Dordrecht, Netherlands, p 249-275

Nealson KH, Stahl DA (1997) Microorganisms and biogeochemical cycles: what can we learn from layered microbial communities? Rev Mineral 35:5-34

Nelson MG (2004) Carbon dioxide sequestration by mechanochemical carbonation of mineral silicates. University of Utah, United States. doi:10.2172/826304

Nilsen DN, Penner LR (2001) Reducing greenhouse gas emissions: Engineering and cost assessment of direct mineral carbonation technology (Process development information for the olivine process). Albany Research Center, US DOE:DOE/ARC-TR-01-015

NOAA (2013) National Oceanic and Atmospheric Administration. Mauna Loa Observatory, *http://www.esrl.noaa.gov/gmd/ccgg/trends/*

Nordstrom DK, Southam G (1997) Geomicrobiology of sulfide mineral oxidation. Rev Mineral 35:361-390

Nyambura MG, Mugera GW, Felicia PL, Gathura NP (2011) Carbonation of brine impacted fractionated coal fly ash: Implications for CO_2 sequestration. J Environ Manage 92: 655-664

O'Connor WK, Dahlin DC, Nilsen DN, Rush GE, Walters R, Turner PC (2000) CO_2 storage in solid form: a study of direct mineral carbonation. Proceedings of the 5th international conference on greenhouse gas technologies. DOE/ARC-2000-011, *http://www.osti.gov/bridge/servlets/purl/896225-BXda6a/896225.pdf*

O'Connor WK, Dahlin DC, Rush GE, Dahlin CL, Collins WK (2002) Carbon dioxide sequestration by direct mineral carbonation: Process mineralogy of feed and products. Miner Metall Process 19:95-101

O'Connor WK, Dahlin DC, Rush GE, Gerdemann SJ, Penner LR, Nilsen DN (2005) Aqueous mineral carbonation: Mineral availability, pretreatment, reaction parametrics, and process studies. Albany Research Center. US DOE: DOE/ARC-TR-04-002

O'Neil JR, Barnes I (1971) C^{13} and O^{18} compositions in some fresh-water carbonates associated with ultramafic rocks and serpentinites: western United States. Geochim Cosmochim Acta 35:687-697

Obst M, Dittrich M, Kuehn H (2006) Calcium adsorption and changes of the surface microtopography of cyanobacteria studied by AFM, CFM, and TEM with respect to biogenic calcite nucleation. Geochem Geophys Geosyst 7(6), doi: 10.1029/2005GC001172

Oelkers EH (2001) General kinetic description of multioxide silicate mineral and glass dissolution. Geochim Cosmochim Acta 65:3703-3719

Olsen AA (2007) Forsterite Dissolution Kinetics: Applications and Implications for Chemical Weathering. PhD Dissertation, Virginia Polytechnic Institute & State University, Blacksburg, Virginia

Olsen AA, Rimstidt DJ (2008) Oxalate-promoted forsterite dissolution at low pH. Geochim Cosmochim Acta 72:1758-1766

Olsson J, Bovet N, Makovicky E, Bechgaard K, Balogh Z, Stipp SLS (2012) Olivine reactivity with CO_2 and H_2O on a microscale: Implications for carbon sequestration. Geochim Cosmochim Acta 77:86-97

Ozdemir E (2009) Biomimetic CO_2 Sequestration: 1. Immobilization of carbonic anhydrase within polyurethane foam. Energy Fuels 23:5725-5730

Pacala S, Socolow R (2004) Stabilization Wedges: Solving the climate problem for the next 50 years with current technologies. Science 305:968-972

Park AA, Fan L (2004) CO_2 mineral sequestration: Physically activated dissolution of serpentine and pH swing process. Chem Eng Sci 59:5241-5247

Park AA, Jadhav R, Fan L (2003) CO_2 mineral sequestration: Chemically enhanced aqueous carbonation of serpentine. Can J Chem Eng 81:885-890

Parkhurst DL, Appelo CAJ (1999) User's guide to PHREEQC (version 2) A computer program for speciation, batch reaction, one-dimensional transport, and inverse geochemical calculations: U.S., Geological Survey Water-Resources Investigations Report 99-4259, p 312

Paukert AN, Matter JM, Kelemen PB, Shock EL, Havig JR (2012) Reaction path modeling of enhanced in situ CO_2 mineralization for carbon sequestration in the peridotite of the Samail Ophiolite, Sultanate of Oman. Chem Geol 330:86-100

Penders-van Elk NJMC, Derks PWJ, Fradette S, Versteeg GF (2012) Kinetics of absorption of carbon dioxide in aqueous MDEA solutions with carbonic anhydrase at 298 K. Int J Greenhouse Gas Control 9:385-392

Peng J, Zhou M-F, Hu R, Shen N, Yuan S, Bi X, Du A, Qu W (2006) Precise molybdenite Re–Os and mica Ar–Ar dating of the Mesozoic Yaogangxian tungsten deposit, central Nanling district, South China. Mineralium Deposita 41:661-669

Perchiazzi N, Merlino S (2006) The malachite-rosasite group: crystal structures of glaukosphaerite and pokrovskite. Eur J Mineral 18:787-792

Perdikouri C, Putnis CV, Kasioptas A, Putnis A (2009) An atomic force microscopy study of the growth of a calcite surface as a function of calcium/total carbonate concentration ratio in solution at constant supersaturation. Cryst Growth Des 9:4344-4350

Pérez-López R, Montes-Hernandez G, Nieto JM, Renard F, Charlet L (2008) Carbonation of alkaline paper mill waste to reduce CO_2 greenhouse gas emissions into the atmosphere. App Geochem 23:2292-2300

Pirie NW (1973) On being the right size. Ann Rev Microbiol 27:119-131

Pokrovsky OS (1998) Precipitation of calcium and magnesium carbonates from homogeneous supersaturated solutions. J Cryst Growth 186:233-239

Pokrovsky OD, Schott J (2000a) Kinetics and mechanism of forsterite dissolution at 25°C and pH from 1 to 12. Geochim Cosmochim Acta 64:3313-3325

Pokrovsky OD, Schott J (2000b) Forsterite surface composition in aqueous solutions: A combined potentiometric, electrokinetic, and spectroscopic approach. Geochim Cosmochim Acta 64:3299-3312

Pokrovsky O, Schott J (2004) Experimental study of brucite dissolution and precipitation in aqueous solutions: Surface speciation and chemical affinity control. Geochim Cosmochim Acta 68:31-45

Pokrovsky OD, Schott J, Castillo A (2005) Kinetics of brucite dissolution at 25°C in the presence of organic and inorganic ligands and divalent metals. Geochim Cosmochim Acta 69:905-918

Pokrovsky OS, Shirokova LS., Benezeth P, Schott J, Golubev SV (2009) Effect of organic ligands and heterotrophic bacteria on wollastonite dissolution kinetics. Am J Sci 309:731-772

Pomar L, Hallock P (2008) Carbonate factories: A conundrum in sedimentary geology. Earth-Sci Rev 87:134-169

Power IM, Wilson SA, Thom JM, Dipple GM, Southam G (2007) Biologically induced mineralization of dypingite by cyanobacteria from an alkaline wetland near Atlin, British Columbia, Canada. Geochem Trans 8:13

Power IM, Wilson SA, Thom JM, Dipple GM, Gabites JE, Southam G (2009) The hydromagnesite playas of Atlin, British Columbia, Canada: A biogeochemical model for CO_2 sequestration. Chem Geol 260:286-300

Power IM, Dipple GM, Southam G (2010) Bioleaching of ultramafic tailings by *Acidithiobacillus* spp. for CO_2 Sequestration. Environ Sci Technol 44:456-462

Power IM, Wilson SA, Dipple GM, Southam G (2011a) Modern carbonate microbialites from an asbestos open pit pond, Yukon, Canada. Geobiology 9:180-195

Power IM, Wilson SA, Small DP, Dipple GM, Wan WK, Southam G (2011b) Microbially mediated mineral carbonation: Roles of phototrophy and heterotrophy. Environ Sci Technol 45:9061-9068

Power IM, Harrison AL, Dipple GM, Southam G (2013a) Carbon sequestration via carbonic anhydrase facilitated magnesium carbonate precipitation. Int J Greenhouse Gas Control 16:145-155

Power IM, Wilson SA, Dipple GM (2013b) Serpentinite carbonation for CO_2 sequestration. Elements 9:115-121

Prabhu C, Wanjari S, Puri A, Bhattacharya A, Pujari R, Yadav R, Das S, Labhsetwar N, Sharma A, Satyanarayanan T, Rayalu S (2011) Region-specific bacterial carbonic anhydrase for biomimetic sequestration of carbon dioxide. Energy Fuels 25:1327-1332

Prigiobbe V, Mazzotti M (2011) Dissolution of olivine in the presence of oxalate, citrate, and CO_2 at 90 °C and 120 °C. Chem Eng Sci 66:6544-6554

Prigiobbe V, Costa G, Baciocchi R, Hänchen M, Mazzotti M (2009) The effect of CO_2 and salinity on olivine dissolution kinetics at 120 °C. Chem Eng Sci 64:3510-3515

Pronost J, Beaudoin G, Lemieux J-M, Hebert R, Constantin M, Marcouiller S, Klein M, Duchesne J, Molson JW, Larachi F, Maldague X (2012) CO_2-depleted warm air venting from chrysotile milling waste (Thetford Mines, Canada): Evidence for in-situ carbon capture from the atmosphere. Geology 40:275-278

Purcell E (1977) Life at low Reynold's number. Am J Phys 45:3-11

Raade G (1970) Dypingite, a new hydrous basic carbonate of magnesium, from Norway. Am Miner 55:1457-1465

Ramanan R, Kannan K, Sivanesan SD, Mudliar S, Kaur S, Tripathi AK, Chakrabarti T (2009) Bio-sequestration of carbon dioxide using carbonic anhydrase enzyme purified from *Citrobacter freundii*. 25:981-987

Ramanan R, Kannan K, Deshkar A, Yadav R, Chakrabarti T (2010) Enhanced algal CO_2 sequestration through calcite deposition by *Chlorella* sp. and *Spirulina platensis* in a mini-raceway pond. Bioresour Technol 101:2616-2622

Renaut RW (1990) Recent carbonate sedimentation and brine evolution in the saline lake basins of the Cariboo Plateau, British Columbia, Canada. Hydrobiologia 197:67-81

Renaut RW (1993) Morphology, distribution, and preservation potential of microbial mats in the hydromagnesite-magnesite playas of the Cariboo Plateau, British Columbia, Canada. Hydrobiologia 267:75-98

Renaut RW, Long PR (1989) Sedimentology of the saline lakes of the Cariboo Plateau, Interior British Columbia, Canada. Sediment Geol 64:239-264

Rendek E, Ducom G, Germain P (2006) Carbon dioxide sequestration in municipal solid waste incinerator (MSWI) bottom ash. J Hazard Mater 128:73-79

Renforth P (2012) The potential of enhanced weathering in the UK. Int J Greenhouse Gas Control 10:229-243

Renforth P, Manning DAC, Lopez-Capel E (2009) Carbonate precipitation in artificial soils as a sink for atmospheric carbon dioxide. Appl Geochem 24:1757-1764

Renforth P, Washbourne C-L, Taylder J, Manning DAC (2011) Silicate production and availability for mineral carbonation. Environ Sci Technol 45:2035-1041

Riding R (2000) Microbial carbonates: The geological record of calcified bacterial-algal mats and biofilms. Sedimentology 47:179-214

Riding R (2006) Cyanobacterial calcification, carbon dioxide concentrating mechanisms, and Proterozoic–Cambrian changes in atmospheric composition. Geobiology 4:299-316

Rio Tinto (2010) Mining Diamonds in the Arctic North. *http://www.diavik.ca/index_ouroperations.asp*

Robbins LL, Yates KK (2001) Direct measurement of CO_2 fluxes in marine whitings. U.S. Geological Survey - Center for Coastal and Regional Marine Studies, p 10

Roberts JA, Bennett PC, Gonzalez LA, Macpherson GL, Milliken KL (2004) Microbial precipitation of dolomite in methanogenic groundwater. Geology 32:277-280

Rodolfi L, Zittelli GC, Bassi N, Padovani G, Biondi N, Bonini G, Tredici MR (2009) Microalgae for oil: Strain selection, induction of lipid synthesis and outdoor mass cultivation in a low-cost photobioreactor. Biotechnol Bioeng 102:100-112

Rogers JR, Bennett PC (2004) Microbial release and utilization of inorganic nutrients from feldspar, basalt, and glass. Chem Geol 203:91-108

Roh Y, Phelps TJ, McMillan AD, Lauf RJ (2000) Utilization of biomineralization processes with fly ash for carbon sequestration. http://www.netl.doe.gov/publications/proceedings/01/carbon_seq/5a2.pdf

Rosso JJ, Rimstidt JD (2000) A high resolution study of forsterite dissolution rates. Geochim Cosmochim Acta 64:797-811

Rudge JF, Kelemen PB, Spiegelman M (2010) A simple model of reaction-induced cracking applied to serpentinization and carbonation of peridotite. Earth Planet Sci Lett 291:215-227

Ruiz-Agudo E, Putnis CV, Rodriguez-Navarro C, Putnis A (2011) Effect of pH on calcite growth at constant ratio and supersaturation. Geochim Cosmochim Acta 75:284-296

Ruvalcaba-Ruiz DC, Thompson TB (1988) Ore deposits at the Fresnillo Mine, Zacatecas, Mexico. Econ Geol 83:1583-1596

Ryu H, Kasai E, Saito F (1992) Effect of Mixed Grinding of Kaolinite-Gibbsite Mixture on Formation of Mullite. J Min Mater Process Inst Japan 108:221-226

Sahu RC, Patel RK, Ray BC (2010) Neutralization of red mud using CO_2 sequestration cycle. J Hazard Mater 179:28-34

Saldi GD, Jordan G, Schott J, Oelkers EH (2009) Magnesite growth rates as a function of temperature and saturation state. Geochim Cosmochim Acta 73:5646-5657

Saldi GD, Schott J, Pokrovsky OS, Gautier Q, Oelkers EH (2010) An experimental study of magnesite precipitation rates at neutral to alkaline conditions and 150–200 °C as a function of pH, aqueous solution composition and chemical affinity. Geochim Cosmochim Acta 74:6344-6356

Saldi GD, Schott J, Pokrovsky OS, Gautier Q, Oelkers EH (2012) An experimental study of magnesite precipitation rates at neutral to alkaline conditions and 100–200°C as a function of pH, aqueous solution composition and chemical affinity. Geochim Cosmochim Acta 83:93-109

Salek SS, Kleerebezem R, Jonkers HM, Voncken JHL, van Loosdrecht MCM (2013) Determining the impacts of fermentative bacteria on wollastonite dissolution kinetics. Appl Microbiol Biotechnol 97:2743-2752

Sanchez-Moral S, Canaveras JC, Laiz L, Saiz-Jimenez C, Bedoya J, Luque L (2003) Biomediated precipitation of calcium carbonate metastable phases in hypogean environments: A short review. Geomicrobiol J 20:491-500

Sandvik KL, Kleiv RA, Haug TA (2011) Mechanically activated minerals as a sink for CO_2. Adv Powder Technol 22:416-421

Sanna A, Dri M, Hall MR, Maroto-Valer M (2012) Waste materials for carbon capture and storage by mineralisation (CCSM) – A UK perspective. Appl Energy 99:545-554

Sarmiento JL, Gruber N (2002) Sinks for anthropogenic carbon. Phys Today 55:30-36

Savile CK, Lalonde JJ (2011) Biotechnology for the acceleration of carbon dioxide capture and sequestration. Curr Opin Biotechnol 22:818-823

Schandl ES, Wicks FJ (1991) Carbonate and associated alteration of ultramafic and rhyolitic rocks at the Hemingway Property, Kidd Creek Volcanic Complex, Timmins, Ontario. Econ Geol 88:1615-1635

Schenk PM, Thomas-Hall SR, Stephens E, Marx UC, Mussgnug JH, Posten C, Kruse O, Hankamer B (2008) Second Generation Biofuels: High-Efficiency Microalgae for Biodiesel Production. BioEnergy Res 1:20-43

Schlesinger WH (1985) The formation of caliche in soils of the Mojave Desert, California. Geochim Cosmochim Acta 49:57-66

Schneider M, Romer M, Tschudin M, Bolio H (2011) Sustainable cement production—present and future. Cem Concr Res 41:642-650

Schott J, Pokrovsky OS, Oelkers EH (2009) The Link Between Mineral Dissolution/Precipitation Kinetics and Solution Chemistry. Rev Mineral Geochem 70:207-258

Schott J, Pokrovsky OS, Spalla O, Devreux F, Gloter A, Mielczarski JA (2012) Formation, growth and transformation of leached layers during silicate minerals dissolution: The example of wollastonite. Geochim Cosmochim Acta 98:259-281

Schuiling RD, de Boer PL (2010) Coastal spreading of olivine to control atmospheric CO_2 concentrations: A critical analysis of viability. Comment: Nature and laboratory models are different. Int J Greenhouse Gas Control 4:855-856

Schuiling RD, de Boer PL (2011) Rolling stones; fast weathering of olivine in shallow seas for cost-effective CO_2 capture and mitigation of global warming and ocean acidification. Earth Syst Dyn Discuss 2:551-568

Schuiling RD, Krijgsman P (2006) Enhanced weathering: An effective and cheap tool to sequester CO_2. Climatuc Change 74:349-354

Schuiling RD, Wilson SA, Power IM (2011) Enhanced silicate weathering is not limited by silicic acid saturation. Proc Natl Acad Sci 108:E41

Schultze-Lam S, Beveridge TJ (1994) Physicochemical characteristics of the mineral-forming S-layer from the cyanobacterium *Synechococcus* strain Gl24. Can J Microbiol 40:216-223

Schwartzman DW, Volk T (1989) Biotic enhancement of weathering and the habitability of Earth. Nature 340:457-460

Seifritz W (1990) CO_2 disposal by means of silicates. Nature 345:486

Sharma A, Bhattacharya A (2010) Enhanced biomimetic sequestration of CO_2 into $CaCO_3$ using purified carbonic anhydrase from indigenous bacterial strains. J Mol Catal B-Enzym 67:122-128

Sharma A, Bhattacharya A, Shrivastava A (2011) Biomimetic CO_2 sequestration using purified carbonic anhydrase from indigenous bacterial strains immobilized on biopolymeric materials. Enzyme Microb Technol 48:416-426

Shirokova LS, Mavromatis V, Bundeleva IA, Pokrovsky OS, Benezeth P, Gerard E, Pearce CR, Oelkers EH (2013) Using Mg isotopes to trace cyanobacterially mediated magnesium carbonate precipitation in alkaline lakes. Aquat Geochem 19:1-24

Sillitoe RH (1997) Characteristics and controls of the largest porphyry copper-gold and epithermal gold deposits in the circum-Pacific region. Aust J Earth Sci 44:373-388

Sillitoe RH, Halls C, Grant JN (1975) Porphyry tin deposits in Bolivia. Econ Geol 70:913-927

Singer PC, Stumm W (1970) Acidic mine drainage: The rate determining step. Science 167:1121-1123

Singer DA, Berger VI, Moring BC (2008) Porphyry copper deposits of the world: Database and grade and tonnage models. Open File Report- U.S. Department of the Interior and U.S. Geological Survey, *http://geopubs.wr.usgs.gov/open-file/of02-268/*

Sipilä J, Teir S, Zevenhoven R (2008) Carbon dioxide sequestration by mineral carbonation: Literature review update 2005-2007. Report 2008-1; Åbo Akademi University Heat Engineering Laboratory

Soetaert K, Hofmann AF, Middelburg JJ, Meysman FJR, Greenwood J (2007) The effect of biogeochemical processes on pH (Reprint of Marine Chemistry, vol 105, pg 30-51, 2007). Mar Chem 106:380-401

Song Z, Wang H, Strong PJ, Li Z, Jiang P (2012) Plant impact on the coupled terrestrial biogeochemical cycles of silicon and carbon: Implications for biogeochemical carbon sequestration. Earth Sci Rev 115:319-331

Southam G, Saunders JA (2005) Geomicrobiology in contemporary natural systems: Implications for Economic Geology. Econ Geol 100:1067-1084
Stephan GW, MacGillavry CH (1972) The crystal structure of nesquehonite, $MgCO_3 \cdot 3H_2O$. Acta Crystallogr Sect B: Struct Sci B28:1031-1033
Stockmann GJ, Wolff-Boenisch D, Gislason SR, Oelkers EH (2011) Do carbonate precipitates affect dissolution kinetics? 1: Basaltic glass. Chem Geol 284:306-316
Stockmann GJ, Wolff-Boenisch D, Gislason SR, Oelkers EH (2013) Do carbonate precipitates affect dissolution kinetics? 2. Diopside. Chem Geol 337-338:56-66
Stolaroff JK, Lowry GV, Keith DW (2005) Using CaO- and MgO-rich industrial waste streams for carbon sequestration. Energy Convers Manage 46:687-699
Streit E, Kelemen PB, Eiler J (2012) Coexisting serpentine and quartz from carbonate-bearing serpentinized peridotite in the Samail Ophiolite, Oman. Contrib Mineral Petrol 164:821-837
Stumm W, Morgan JJ (1996) Aquatic Chemistry - Chemical Equilibria and Rates in Natural Waters. Wiley, New York
Sun R, Li Y, Liu C, Xie X, Lu C (2013) Utilization of lime mud from paper mill as CO_2 sorbent in calcium looping process. Chem Eng J 221: 124-132
Suzuki A (1998) Combined effects of photosynthesis and calcification on the partial pressure of carbon dioxide in seawater. J Oceanogr 54:1-7
Suzuki J, Ito M (1973) A new magnesium carbonate hydrate mineral, $Mg_5(CO_3)_4(OH)_2 \cdot 8H_2O$, from Yoshikawa, Aichi Prefecture, Japan. J Japan Assoc Mineral Petrol Econ Geol 68:353-361
Teir S, Eloneva S, Fogelholm C-J, Zevenhoven R (2007a) Dissolution of steelmaking slags in acetic acid for precipitated calcium carbonate production. Energy 32:528-539
Teir S, Kuusik R, Fogelholm C-J, Zevenhoven R (2007b) Production of magnesium carbonates from serpentine for long-term storage of CO_2. Int J Miner Process 85:1-15
Teir S, Revitzer H, Eloneva S, Fogelholm C-J, Zevenhoven R (2007c) Dissolution of natural serpentinite in mineral and organic acids. Int J Miner Process 83:36-46
Thayer TP (1964) Principal features and origin of podiform chromite deposits, and some observations on the Guleman-Soridag district, Turkey. Econ Geol 59:1497-1524
Thom JGM, Dipple GM, Power IM, Harrison AL (2013) Chrysotile dissolution rates: Implications for carbon sequestration. Appl Geochem 35:244-254
Thompson Creek Metals Company Inc. (2011) Thompson Creek Mine operations, *http://www.thompsoncreekmetals.com/s/Thompson_Creek_Mine.asp*
Thompson JB, Ferris FG (1990) Cyanobacterial precipitation of gypsum, calcite, and magnesite from natural alkaline lake water. 18:995-998
Thompson JB, Schultze-Lam S, Beveridge TJ, DesMarais DJ (1997) Whiting events: Biogenic origin due to the photosynthetic activity of cyanobacterial picoplankton. Limnol Oceanogr 42:133-141
Uddin S, Rao SR, Mirnezami M, Finch JA (2012) Processing an ultramafic ore using fiber disintegration by acid attack. Int J Miner Process 102-103:38-44
Uibu M, Velts O, Kuusik R (2010) Developments in CO_2 mineral carbonation of oil shale ash. J Hazard Mater 174:209-214
Uibu M, Kuusik R, Andreas L, Kirsimäe K (2011) The CO_2-binding by Ca-Mg-silicates in direct aqueous carbonation of oil shale ash and steel slag. Energy Procedia 4:925-932
Uliasz-Bocheńczyk A, Mokrzycki E, Piotrowski Z, Pomykała R (2009) Estimation of CO_2 sequestration potential via mineral carbonation in fly ash from lignite combustion in Poland. Energy Procedia 1: 4873-4879
Ullman WJ, Kirchman DL, Welch SA, Vandevivere P (1996) Laboratory evidence for microbially mediated silicate mineral dissolution in nature. Chem Geol 132:11-17
USEPA (2008) Quantifying greenhouse gas emissions from key industrial sectors in the United States. *http://www.epa.gov/sectors/pdf/greenhouse-report.pdf*
USEPA (2010) Municipal solid waste generation, recycling, and disposal in the United States: Facts and figures for 2010. *http://www.epa.gov/osw/nonhaz/municipal/msw99.htm*
USGS (2010) 2010 Minerals Yearbook: Statistical Summary. *http://minerals.usgs.gov/minerals/pubs/commodity/statistical_summary/myb1-2010-stati.pdf*
USGS (2013a) Mineral Commodity Summaries 2013. *http://minerals.usgs.gov/minerals/pubs/mcs/2013/mcs2013.pdf*
USGS (2013b) Produced Waters Database, *http://energy.cr.usgs.gov/prov/prodwat/data2.htm*
Vachon P, Tyagi RD, Auclair J-C, Wilkinson KJ (1994) Chemical and biological leaching of aluminum from red mud. Environ Sci Technol 28:26-30
Van Cappellen P (2003) Biomineralization and global biogeochemical cycles. Rev Mineral Geochem 54:357-381

van Lith Y, Warthmann R, Vasconcelos C, McKenzie JA (2003) Microbial fossilization in carbonate sediments: a result of the bacterial surface involvement in dolomite precipitation. 50:237-245

van Oss HG, Padovani AC (2003) Cement manufacture and the environment and opportunities. J Ind Ecol 7:93-126

van Zomeren A, van der Laan SR, Kobesen HBA, Huijgen WJJ, Comans RNJ (2011) Changes in mineralogical and leaching properties of converter steel slag resulting from accelerated carbonation at low CO_2 pressure. Waste Manage 31:2236-2244

Vinoba M, Kim DH, Lim KS, Jeong SK, Lee SW, Alagar M (2011) Biomimetic Sequestration of CO_2 and Reformation to $CaCO_3$ Using Bovine Carbonic Anhydrase Immobilized on SBA-15. Energy Fuels 25:438-445

Vogeli J, Reid DL, Becker M, Broadhurst J, Franzidis J-P (2011) Investigation of the potential for mineral carbonation of PGM tailings in South Africa. Miner Eng 24:1348-1356

Walters S, Bailey A (1998) Geology and mineralization of the Cannington Ag-Pb-Zn deposit: An example of Broken Hill-type mineralization in the Eastern succession, Mount Isa Inlier, Australia. Econ Geol 93:1307-1329

Wang X, Maroto-Valer MM (2011) Dissolution of serpentine using recyclable ammonium salts for CO_2 mineral carbonation. Fuel 90:1229-1237

Ware JR, Smith SV, Reakakudla ML (1992) Coral reefs - sources or sinks of atmospheric CO_2. Coral Reefs 11:127-130

Washbourne C-L, Renforth P, Manning DAC (2012) Investigating carbonate formation in urban soils as a method for capture and storage of atmospheric carbon. Sci Total Environ 431:166-175

Watts NL (1980) Quaternary pedogenic calcretes from the Kalahari (southern Africa): mineralogy, genesis and diagenesis. Sedimentology 27: 661-686

West AJ, Galy A, Bickle M (2005) Tectonic and climatic controls on silicate weathering. Earth Planet Sci Lett 235:211-228

White AF, Blum AE (1995) Effects of climate on chemical weathering in watersheds. Geochim Cosmochim Acta 59:1729-1747

White AF, Blum AE, Bullen TD, Vivit DV, Schulz M, Fitzpatrick J (1999) The effect of temperature on experimental and natural chemical weathering rates of granitoid rocks. Geochim Cosmochim Acta 63:3277-3291

Whittaker S, Rostron B, Hawkes C, Gardner C, White D, Johnson J (2011) A decade of CO_2 injection into depleting oil fields: Monitoring and research activities of the IEA GHG Weyburn-Midale CO_2 Monitoring and Storage Project. Energy Procedia 4:6069-6076

Williams PJB, Laurens LML (2010) Microalgae as biodiesel & biomass feedstocks: Review & analysis of the biochemistry, energetics & economics. Energy Environ Sci 3:554-590

Willscher S, Bosecker K (2003) Studies on the leaching behaviour of heterotrophic microorganisms isolated from an alkaline slag dump. Hydrometallurgy 71:257-264

Wilson SA, Raudsepp M, Dipple GM (2006) Verifying and quantifying carbon fixation in minerals from serpentine-rich mine tailings using the Rietveld method with X-ray powder diffraction data. Am Mineral 91:1331-1341

Wilson SA, Dipple GM, Power IM, Thom JM, Anderson RG, Raudsepp M, Gabites JE, Southam G (2009a) Carbon dioxide fixation within mine wastes of ultramafic-hosted ore deposits: Examples from the Clinton Creek and Cassiar chrysotile deposits, Canada. Econ Geol 104:95-112

Wilson SA, Raudsepp M, Dipple GM (2009b) Quantifying carbon fixation in trace minerals from processed kimberlite: A comparative study of quantitative methods using X-ray powder diffraction data with applications to the Diavik Diamond Mine, Northwest Territories, Canada. Appl Geochem 24:2312-2331

Wilson SA, Barker SLL, Dipple GM, Atudorei V (2010) Isotopic disequilibrium during uptake of atmospheric CO_2 into mine process waters: Implications for CO_2 sequestration. Environ Sci Technol 44:9522-9529

Wilson SA, Dipple GM, Power IM, Barker SLL, Fallon SJ, Southam G (2011) Subarctic weathering of mineral wastes provides a sink for atmospheric CO_2. Environ Sci Technol 45:7727-7736

Wogelius RA, Walther JV (1991) Forsterite dissolution at 25°C: Effects of pH, CO_2, and organic acids. Geochim Cosmochim Acta 55:943-954

Wolff-Boenisch D, Gislason SR, Oelkers EH (2006) The effect of crystallinity on dissolution rates and CO_2 consumption capacity of silicates. Geochim Cosmochim Acta 70:858-870

Wolff-Boenisch D, Wenau S, Gislason SR, Oelkers EH (2011) Dissolution of basalts and peridotite in seawater, in the presence of ligands, and CO_2: Implications for mineral sequestration of carbon dioxide. Geochim Cosmochim Acta 75:5510-5525

Wollast R, Garrels RM, Mackenzie FT (1980) Calcite-seawater reactions in ocean surface waters. Am J Sci 280:831-848

World Aluminum (2013) World aluminum production statistics. *http://www.world-aluminium.org/statistics/*

Worrell E, Price L, Martin N, Hendriks C, Meida LO (2001) Carbon dioxide emissions from the global cement industry. Annu Rev Energy Environ 26:303-329

Wu L, Jacobson AD, Chen H-C, Hausner M (2007) Characterization of elemental release during microbe–basalt interactions at T = 28 °C. Geochim Cosmochim Acta 71:2224-2239

Xu WY, Apps JA, Pruess K (2004) Numerical simulation of CO_2 disposal by mineral trapping in deep aquifers. Appl Geochem 19:917-936

Yadav VS, Prasad M, Khan J, Amritphale SS, Singh M, Raju CB (2010) Sequestration of carbon dioxide (CO_2) using red mud. J Hazard Mater 176:1044-1050

Yang H, Xu Z, Fan M, Gupta R, Slimane RB, Bland AE, Wright I (2008) Progress in carbon dioxide separation and capture: A review. J Environ Sci 20:14-27

Yao M, Lian B, Teng HH, Tian Y, Yang X (2013) Serpentine dissolution in the presence of bacteria *Bacillus mucilaginosus*. Geomicrobiol J 30:72-80

Yehia A, Al-Wakeel MI (2000) Technical note talc separation from talc-carbonate ore to be suitable for different industrial applications. Miner Eng 13:111-116

Yu J, Wang K (2011) Study on characteristics of steel slag for CO_2 capture. Energy Fuels 25:5483-5492

Yu HL, Xu Y, Shi PJ, Wang HM, Zhang W, Xu BS (2011) Effect of thermal activation on the tribological behaviours of serpentine ultrafine powders as an additive in liquid paraffin. Tribol Int 44:1736-1741

Zevenhoven R (2004) Mineral carbonation for long-term CO_2 storage: An exergy analysis. Int J Thermodyn 7:23-31

Zevenhoven R, Kohlmann J (2001) CO_2 Sequestration by magnesium silicate mineral carbonation in Finland. Second Nordic Mini-symposium on Carbon Dioxide Capture and Storage, Göteborg *http://www.entek.chalmers.se/~anly/symp/01zevenhoven.pdf*

Zevenhoven R, Teir S (2004) Long-term storage of CO_2 as magnesium carbonate in Finland. 3rd Annual conference on carbon capture and sequestration, Alexandria

Zevenhoven R, Teir S, Eloneva S (2008) Heat optimisation of a staged gas–solid mineral carbonation process for long-term CO_2 storage. Energy 3:362-370

Zevenhoven R, Fagerlund J, Songok JK (2010) Mineral carbonation for long-term CO_2 storage: An energy analysis. Int J Thermodyn 7:23

Zevenhoven R, Fagerlund J, Songok JK (2011) CO_2 mineral sequestration: Developments toward large-scale application. Greenhouse Gases Sci Technol 1:48-57

Zhang P, Anderson HLJ, Kelly JW, Krumhansl JL, Papenguth HW (2000) Kinetics and mechanisms of formation of magnesite from hydromagnesite in brine. Sandia National Laboratories, Albuquerque, p 26

Zhang SH, Zhang ZH, Lu YQ, Rostam-Abadi M, Jones A (2011) Activity and stability of immobilized carbonic anhydrase for promoting CO_2 absorption into a carbonate solution for post-combustion CO_2 capture. Bioresour Technol 102:10194-10201

Zhang FF, Xu HF, Konishi H, Shelobolina ES, Roden EE (2012) Polysaccharide-catalyzed nucleation and growth of disordered dolomite: A potential precursor of sedimentary dolomite. Am Mineral 97:556-567

Zhao L, Sang L, Chen J, Ji J, Teng HH (2010) Aqueous carbonation of natural brucite: relevance to CO_2 sequestration. Environ Sci Technol 44:406-411

Reviews in Mineralogy & Geochemistry
Vol. 77 pp. 361-398, 2013
Copyright © Mineralogical Society of America

Acid Gases in CO_2-rich Subsurface Geologic Environments

Ariel A. Chialvo, Lukas Vlcek

Geochemistry & Interfacial Sciences Group. Chemical Sciences Division
Oak Ridge National Laboratory
Oak Ridge, Tennessee 37831-6110, U.S.A.

chialvoaa@ornl.gov

David R. Cole

School of Earth Sciences and Chemistry Department
Ohio State University
Columbus, Ohio 43210, U.S.A.

cole.618@osu.edu

INTRODUCTION

The analysis of species behavior involving dilute fluid environments has been crucial for the advance of modern solvation thermodynamics through molecular-based formalisms to guide the development of macroscopic regression tools in the description of fluid behavior and correlation of experimental data (Chialvo 2013). Dilute fluid environments involving geologic formations are of great theoretical and practical relevance regardless of the thermodynamic state conditions. The most challenging systems are those involving highly compressible and reactive confined environments, i.e., where small perturbations of pressure and/or temperature can trigger considerable density changes. This in turn can alter significantly the species solvation, their preferential solvation, and consequently, their reactivity with one another and with the surrounding mineral surfaces whose outcome is the modification of the substrate porosity and permeability, and ultimately, the integrity of the mineral substrates. Considering that changes in porosity and permeability resulting from dissolution and precipitation phenomena in confined environments are at the core of the aqueous CO_2-mineral interactions, and that caprock integrity (e.g., sealing capacity) depends on these key parameters, it is imperative to gain fundamental understanding of the mineral-fluid interfacial phenomena and fluid-fluid equilibria under mineral confinement at subsurface conditions. In order to understand the potential effects of acid gases as contaminants of supercritical CO_2 streams, in the next section we will discuss the thermodynamic behavior of CO_2 fluid systems by addressing two crucial issues in the context of carbon capture, utilization and sequestration (CCUS) technologies: (i) *Why should we consider (acid gas)* CO_2 *impurities?* and (ii) *Why are* CO_2 *fluid - mineral interactions of paramount relevance?*

Background on flue gas sources, composition, and CO_2 - acid gases co-injection

The control of anthropogenic greenhouse gases emissions in the atmosphere by means of their capture and sequestration in deep geological reservoirs has emerged as a potential technology for the middle- to long-term mitigation of the greenhouse effect on climate change (Metz et al. 2005; Benson and Cole 2008; Figueroa et al. 2008; Oelkers and Cole 2008) as well as to reduce the emission of other pollutants that might potentially contribute to acid rain (Chestnut and Mills 2005). Steam power generation is probably the largest source of emissions

1529-6466/13/0077-0010$05.00 http://dx.doi.org/10.2138/rmg.2013.77.10

of CO_2 and companion pollutants including SO_x, H_2S, NO_x, H_2O, and CO where the flue gas composition depends strongly on the type of fuel used, the combustion conditions/type of generator, and the capture process involved (Miller and van Atten 2004; Metz et al. 2005). For example, N_2, O_2, H_2O, NH_3, SO_x, and NO_x are typically encountered in post-combustion CO_2 capture; N_2, O_2, SO_2, H_2S, and Ar are usually present in oxy-combustion capture; while H_2, N_2, CO, H_2S, and CH_4 may be found in pre-combustion capture. Though in principle there are no technological impediments to separating highly purified CO_2 from flue gases (Pipitone and Bolland 2009; Posch and Haider 2012), this option is seldom pursued unless strictly necessary, for example for limiting pipeline corrosion during CO_2 transport (Mohitpour et al. 2008; Race et al. 2012), to avoid the additional energy requirement in the separation process and consequent loss of net plant efficiency (Davison 2007). Note that the amount of SO_2 and NO_x co-emitted with the CO_2 is a relatively small fraction, i.e., less than either 1/100 for SO_2 or 1/250 for NO_x, of the total CO_2 emissions (e.g., Fig. 1).

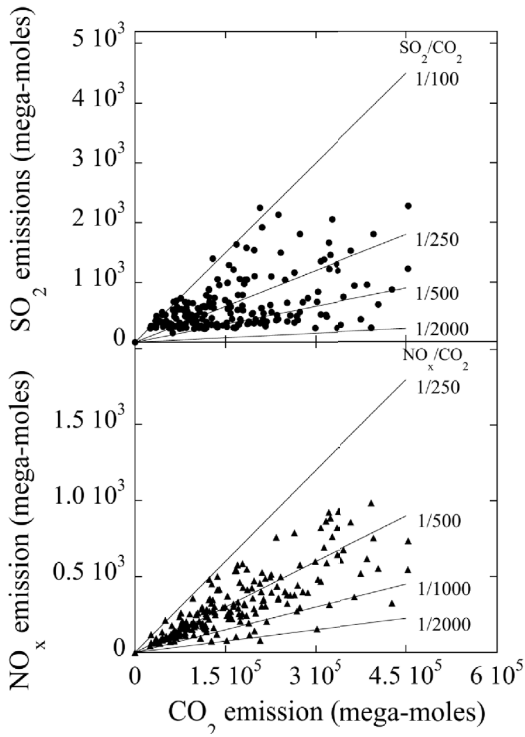

Figure 1. Annual emissions of SO_2 and NO_x relative to CO_2 from the 200 largest SO_2 emitting power plants in the United States based on data from Miller and van Atten (2004).

Two main factors might determine the best course of action to pursue for a more cost effective CCUS strategy to deal with the CO_2 contaminants, namely (a) feasibility of co-sequestering, say, H_2S, SO_x, and/or NO_x, compatible with the mineralogy of the sub-surface geological formations and (b), ability to retrofit and/or adapt the three current technologies of CO_2 capture and storage (i.e., pre-combustion capture, post-combustion capture, and oxy-fuel technology; Posch and Haider 2012) to reduce or avoid entirely the need for the elimination of those pollutants from the CO_2 streams prior to sequestration. The first factor requires addressing the impact of these supercritical environments on the pH of the formation water and, consequently, on the potential changes in permeability resulting from mineral dissolution, secondary mineral precipitation, and their effect on the stability of the porous reservoir formation and caprock integrity (Kharaka et al. 2006; Pauwels et al. 2007). The second factor points to lowering the cost of the CO_2 separation process by co-capturing the acid gases, as CO_2 contaminants, while safely releasing the non-condensable gases (i.e., O_2, N_2, H_2, and Ar) to the atmosphere. In fact, according to studies carried out at Sweden's Vattenfall Research and Development (Anheden et al. 2005), it appears feasible to get a Cost-Of-Electricity (COE) cost reduction of about 10% through SO_2-CO_2 co-capture within the oxy-fuel process, while another study by the International Energy Agency Greenhouse Gas R&D program (IEAGHG) suggested that H_2S-CO_2 co-capture could translate into a 20% reduction of the total capture cost (GHG 2003).

These two reports support the principles behind the co-capture, co-injection, and eventually co-sequestration of some contaminants (air pollutants) together with the CO_2 as a more cost effective approach to CCUS as long as the interactions between the contaminants and the geologic formation do not lead to a degradation in process integrity (Wang et al. 2011). In other words, the unavoidable presence of acid gases in the flue streams should not be taken as a limiting factor in the CCUS process, but as an opportunity to investigate and develop innovative strategies to handle systems that must be "overwhelmingly CO_2" (Gale 2009), yet, to avoid either costly separations or troubling releases of pollutants to the atmosphere.

Consequences of the presence of acid gases on water-rock geochemical reactions

The solubility and reactivity of CO_2, H_2S, SO_2 and NO_2 in aqueous systems are remarkably different (NIST 2013), especially at the state conditions of CCUS processes. At normal conditions aqueous CO_2 generates weak acid solutions ($pK_a \sim 6.3$), the CO_2 contaminants react with water to form H_2SO_3 ($pK_a \sim 1.9$), H_2SO_4 ($pK_a \sim -3.0$) if dissolved O_2 is present, and HNO_3 ($pK_a \sim -1.3$), while H_2S ($pK_a \sim 7.0$) might regulate the SO_2 disproportionation reaction ($pK_{eq} \sim -2.7$) (de Hemptinne and Behar 2000; Housecroft and Sharpe 2008; Ellis et al. 2010). According to the corresponding pK_a values, and despite their dilution, the aqueous H_2S, SO_2 and NO_2 contaminants should in principle have stronger chemical interactions with the mineral substrates than those expected from "pure" aqueous CO_2 (Crandell et al. 2010; Ellis et al. 2010) and consequently, considerably greater impact on the integrity of reservoir rocks and caprocks.

While already recognized (Cole et al. 2011; Verma et al. 2011; Race et al. 2012; Ruhl and Kranzmann 2012), the thermophysical behavior and phase equilibria of CO_2 contaminants and their impact on the CCUS process design have rarely been addressed. Most of these studies focused on the interactions of "pure food grade CO_2" (Kaszuba et al. 2005, 2013, this volume; Gaus et al. 2008), rather than "overwhelmingly" (Gale 2009), CO_2 with representative caprock substrates. There has been however a few outstanding exceptions including experimental and macroscopic simulation efforts involving impure CO_2 streams.

The experimental effort includes petrophysical studies such as those of Nogueira and Mamora (2008) (i.e., SO_2+O_2+N_2+NO_2+CO up to 10.4 MPa and 70 °C), Kummerow and Spangenberg (2011) (i.e., 1.0 vol % SO_2 and brines in contact with reservoir sandstones at 40 °C and 15MPa), and Bennion and Bachu (2008) (i.e., CO_2-H_2S mixtures and brines effects on the relative permeability of reservoir rocks), as well as geochemical studies by Palandri and Kharaka (2005) (i.e., SO_2-bearing CO_2 and 1.0 molar aqueous NaCl solutions in contact with hematite at 150 °C and 30 MPa), and Jacquemet and coworkers (Jacquemet et al. 2005, 2008; Pironon et al. 2007) (i.e., effects of CO_2-H_2S mixtures on the chemical alteration of wellbore cements). Unfortunately, most experiments involving H_2S-bearing CO_2 have been carried out at compositions similar to the mixtures currently injected in several Canadian depleted hydrocarbon reservoirs (Chakma 1997; Shah et al. 2008), i.e., 66 mole% H_2S, 34 mole% CO_2 in the presence of a 2.75 molal NaCl brine under typical state conditions of deep sour-oil-fields (e.g., $T < 200$ °C and $P < 50$ MPa) rather than the highly dilute systems typically encountered in CCUS technologies (e.g., Fig. 1). Moreover, while the reactivity experiments are usually performed in well-stirred batch reactors (Wilke et al. 2012), conditions that are obviously not encountered in the CCUS process, the porosity and permeability measurements are conducted in flow-through setups (Kummerow and Spangenberg 2011) which resembles more closely the actual CCUS environments.

There seems to be just one experimental study conducted at realistic CCUS conditions to investigate the chemical interactions of rock forming minerals (including albite, microcline, kaolinite, biotite, muscovite, calcite, dolomite and anhydrite) with SO_2- or NO_2-bearing supercritical CO_2 in the presence of brines (Wilke et al. 2012). Their batch experiments,

involving mixtures of supercritical CO_2 (99.5 vol%) with either (0.5 vol%) SO_2 or NO_2, indicated the formation of H_2SO_4 or HNO_3 resulting in $1 < pH < 4$ for silicates and anhydrite and $5 < pH < 6$ for carbonates. In contrast, when the experiments were carried out using pure CO_2 the resulting pH was around 4 for silicates and anhydrite, and 7-8 for carbonates. Note that an important point of contention on all these batch experiments, and a source of controversy in the interpretation of reactivity (Gaus 2010), is the fact that the actual CCUS process is a flow-through (continuous) setup where water is available by diffusion, i.e., not in excess as in most experiments.

The macroscopic simulation effort has been conducted by reactive transport modeling (Knauss et al. 2005; Xu et al. 2007; Bacon et al. 2009; Bacon and Murphy 2011; Zhang et al. 2011), whose realistic outcome relies on the availability of accurate macroscopic correlations (typically regressed from experimental data) for the properties of pure fluid and their mixtures. Unfortunately, bulk thermophysical properties for the required mixtures at reservoir conditions are scarce or simply nonexistent (Jacquemet et al. 2009), and our microscopic understanding of their interaction with caprocks is rather limited (Shukla et al. 2010; Kim et al. 2012; Liu et al. 2012; Song and Zhang 2013).

Most published research on CO_2-SO_2 co-sequestration involved macroscopic modeling approaches that typically predict highly reactive water-rock interactions (Gunter et al. 2000; Knauss et al. 2005; Palandri and Kharaka 2005; Xu et al. 2007; Koenen et al. 2011), resulting in (i) strongly acidic environments (pH~1) that prevent carbonate precipitation, (ii) sulfur trapping by precipitation of sulfate minerals, (iii) significant mineral alteration around injection points, and (iv) redistribution of substrate porosity and permeability. In contrast, two more recent modeling studies (Crandell et al. 2010; Ellis et al. 2010) predicted a rather different outcome, i.e., CO_2-SO_2 co-sequestration cannot yield highly reactive water-rock systems because SO_2 cannot readily diffuse from the co-injected supercritical CO_2 solution into the aqueous surroundings. In fact, as reported by Peters and co-workers (Crandell et al. 2010; Ellis et al. 2010) SO_2 in brine solutions could follow three main reaction paths, i.e., (i) hydrolysis to produce the weak sulfurous acid ($pK_a \sim 1.9$), (ii) hydro-oxidation, whenever oxidation conditions exist, will produce a strong sulfuric acid environment ($pK_a \sim -3.0$), and (iii) disproportionation reaction leading to a 3:1 mixture of sulfuric acid and hydrogen sulfide ($pK_a \sim 7.0$). Moreover, their modeling results confirm that SO_2 co-injection can lower the pH of the local environment relative to that of a pure CO_2 injection (i.e., 4.6 under typical CCUS state conditions), even though the magnitude and time scale of the acidification depend not only on the rate of the CO_2 stream injection, but also on the rate of SO_2 dissolution and diffusion from the CO_2-rich phase.

Interestingly, their model predictions for a co-injection of 1% SO_2 (99% CO_2) under the unrealistic process conditions of SO_2-CO_2-brine phase equilibrium, indicate a pH ~ 1.0 for either the oxidation or the disproportionation reaction, and a pH ~ 2.0 for the hydrolysis (see Fig. 3 in Ellis et al. 2010). However, under more realistic diffusion controlled conditions and SO_2 uniformly distributed in the advecting phase, their modeling suggests that SO_2 oxidation would lead to a pH ~ 2.5 about 400 years after injection, while SO_2 hydrolysis under the same scenario would lead to a slight decrease of pH from that expected from the injection of pure CO_2 (see Fig. 5 in Ellis et al. 2010). In summary, the Ellis et al. (2011) study indicates that the effect of co-injected SO_2 on brine acidity is controlled by the diffusion-limited dissolution of SO_2 from the CO_2 phase, and could be limited by the accessibility of oxidants to generate the stronger H_2SO_4 solutions.

Obviously, these contrasting modeling outcomes provide a cautionary note about (i) our imperfect understanding of the physico-chemical interactions between mineral formation and CO_2-contaminant mixtures in CCUS environments, (ii) the underlying difficulties in gaining microscopic insights into the fluid behavior of mixtures for which we have scarce experimen-

tal data, (iii) the need to go beyond the well-stirred batch reactor description through the incorporation of mineral-fluid interfacial phenomena to account for potential confinement effects, concentration gradients, and consequent diffusion-controlled reactions in the development of reactive transport modeling, and (iv) the limitations of the current reactive transport modeling associated with the description of the real (as opposed to the thermodynamic "ideal" mixture typically used; Palandri and Kharaka 2005) behavior of CO_2-rich gas mixtures including the solubility of acid gases in the presence of brines (Jacquemet et al. 2009).

As a matter of fact, there is a crucial shortage of published thermophysics and thermodynamic data for relevant sets of CO_2-X binaries (and consequently, multicomponent for that matter) systems including X = NO_x, SO_x, and H_2S (Li et al. 2011a,b). We are aware of only six reported studies on the CO_2-SO_2 system in the last hundred years (Bluemcke 1888, 1889; Caubet 1902; Thiel and Schulte 1920; Cummings 1931; Lachet et al. 2009), six publications on CO_2-H_2S mixtures (Thiel and Schulte 1920; Klemenc and Bankowski 1932; Steckel 1945; Bierlein and Kay 1953; Sobocinski and Kurata 1959; Kellerman et al. 1995), and about four on the CO_2-NO_x systems (Caubet 1904; Cook 1953; Rowlinson et al. 1957; Camy et al. 2011).

While the actual CCUS environments involve at best quaternary CO_2 mixtures (i.e., CO_2-brine-SO_x or H_2S, or NO_x) in contact with, and confined by mineral substrates, there have been little published reports on experimental and modeling efforts toward the geochemical, petrophysical, and thermodynamic understanding of these challenging systems. An obvious reason for this lack of data is the toxicity of the acid gases, but probably the most significant one hinges around the limitations of the methodology of low-pressure gas solubility measurements that involve the determination of the gas phase pressure, before and after equilibrium, with no aqueous phase sampling (Ricaurte et al. 2012). To overcome this shortcoming Savary et al. (2012) have recently developed a novel technique to sample the aqueous solutions at equilibrium with the CO_2-H_2S mixtures and simultaneously measure the gas solubility, by working at relatively high pressure to avoid the formation of three-phase systems, i.e., the equilibrium involving aqueous liquid phase, the CO_2- or H_2S-rich liquid phases, and the CO_2- or H_2S-rich gas phases.

These experiments provided not only crucial solubility data for CO_2-H_2S mixtures in pure water and 2.0 molar aqueous NaCl solutions at 120 °C and up to 35 MPa, but also new insights into the synergistic behavior of co-dissolved species in the aqueous phase. In particular, the Savary et al. (2012) experiments indicate a strong effect of dissolved CO_2 on the H_2S pressure-solubility dependence, i.e., with a reversal of the trend with increasing CO_2 concentration in the aqueous phase, a behavior that could result in a pressure-driven fractionation of the two species between the gas and the aqueous phase. Their corresponding modeling was based on an earlier effort by Søreide and Whitson (1992), aimed at describing the effect of salts on the solubility of gases in aqueous phase equilibria, via variations of the Peng-Robinson equation of state (PR-EoS). After using the default binary interaction parameters (BIP) for the CO_2-H_2O and H_2S-H_2O systems, they concluded that the observed complex behavior for the CO_2-H_2S-brine might require further improvements in the ability of the EoS formalisms to describe the gas solubility in pure water at high pressure.

In that sense, recent efforts toward the macroscopic modeling CO_2+X mixtures have focused on the development of more elaborate correlations comprising not only variations of the traditional cubic EoS (Li and Han 2009a,b; Pellegrini et al. 2012), but also cubic EoS plus association combinations (CPA) (Kontogeorgis et al. 2006; Li and Firoozabadi 2009), CPA plus mean spherical approximation (CPA-MSA)(Perfetti et al. 2008a,b), Statistical Associating Fluid Theory (SAFT) and Perturbed-Chain SAFT (PC-SAFT) (Diamantonis and Economou 2011, 2012; Diamantonis et al. 2013), as well as Perturbed-Chain Polar SAFT (PCP-SAFT) (Tang and Gross 2010) to deal with the different types of cross interactions encountered in mixtures of polar-nonpolar systems such as those involving X = H_2S, H_2O, NO_x, SO_2 and light

hydrocarbons (Tsivintzelis et al. 2010, 2011). The main idea behind these macroscopic correlations is to make them more flexible by combining the simplicity of a cubic EoS (e.g., Soave-Redlick-Kwong; Soave 1972) to account for the intermolecular (non-directional) interactions, the association contribution from Wertheim's theory (Wertheim 1984) (e.g., as in SAFT; Chapman et al. 1989) to describe specific site-site interactions resulting from hydrogen bonding, as well as the incorporation of non-primitive MSA theory to represent ion-dipole dipole-dipole interactions (Blum and Wei 1987). These developments for mixtures are typically accompanied by setting mixing rules for the EoS term as well as combining rules and BIPs for the cross interactions, based on experimental and *ab initio* calculations (Tsivintzelis et al. 2011).

Obviously, the limited availability of thermophysical data for these fluid mixtures and their physico-chemical interactions with subsurface formations complicates all attempts to simulate reliably the fate of CO_2 and its co-injected species. Considering that the feasibility and safety of the CCUS process for long-term storage of CO_2 depend on both the low hydraulic permeability of the caprock and the ability of the porous mineral formation to hold in place the brine-CO_2 fluids, it becomes crucial to gain fundamental understanding of the fluid-mineral interfacial (and concomitant confinement) behavior in order to attempt the manipulation of the system aimed at controlling the process. Perhaps the most troubling aspect of the suggested co-sequestration is the chemical reactivity of those contaminants in the presence of water because it could potentially trigger a significant pH reduction (Ellis et al. 2010; Wilke et al. 2012) as a consequence of complex, yet not well understood, chemical reaction mechanism.

Geochemical interactions are typically water-mediated, yet in the CCUS process we must account for more complex (heterogeneous) fluid phases interacting with mineral surfaces, including water rich-CO_2 and CO_2 rich-water phases as well as dry solutions of contaminant in supercritical CO_2 fluid phases (Wilke et al. 2012). Under these circumstances we must expect that the injection of supercritical CO_2 will perturb the geochemical equilibrium between mineral species and the formation water, by inducing dehydration (drying out; Rochelle et al. 2004; Song and Zhang 2013). This is especially problematic for clay and clay/sand formations that naturally contain formation water, because its extraction by (and dissolution into) the dryer supercritical CO_2 might induce shrinkage (Albrecht and Benson 2001) and eventually cracking (Osinubi and Nwaiwu 2008), whose effects on the morphology, porosity, permeability, and wettability of the substrate are poorly understood or unknown (Rochelle et al. 2004; Sadhukhan et al. 2012; Yoon et al. 2012).

NEED FOR ACCURATE DESCRIPTIONS OF FLUID – FLUID INTERACTIONS

The state of affairs described in the previous section highlighted the need for an integrated effort between experiment and modeling to gain essential microscopic-based understanding of fluid-fluid and fluid-mineral interactions at realistic CCUS environmental conditions. In the sections that follow we discuss current and recent developments regarding fluid-fluid interactions, involving CO_2 and its companion impurities, aimed at achieving that goal through the interplay of statistical mechanical formalisms and molecular-based simulation tools.

Molecular modeling of CO_2-X phase equilibria at CCUS relevant conditions

From a process design perspective, the CCUS requires an accurate description of the CO_2 interactions with the aqueous environments in contact with, and confined by, minerals surfaces at moderate temperatures and pressures (Benson and Cole 2008; Cole et al. 2010). From a microscopic perspective, the required accuracy highlights the crucial need for physically sound molecular models to predict fluid behavior and physicochemical interactions with mineral formations at such subsurface conditions.

In fact, we could invoke numerous theoretical, modeling, and economical reasons behind the need for a quantitative realistic description of the thermophysical fluid behavior of CO_2-rich phases containing different amounts of impurities (a.k.a., "CO_2 contaminants" or "CO_2-associated components") that will impact the design and operation of their capture, transport, injection, and final storage/sequestration processes (Li et al. 2009). The most basic one is that, whereas some of these CO_2-contaminant systems including CO_2-N_2 and CO_2-O_2, have been studied over wide ranges of state conditions (Li et al. 2011a; Mantovani et al. 2012; Mazzoccoli et al. 2012), there is a troubling lack of experimental data regarding the (phase equilibrium) thermodynamic, thermophysical, and transport properties for most relevant CO_2-contaminant mixtures such as CO_2-SO_x, CO_2-H_2S, and CO_2-NO_x as well as their multicomponent counterparts involving H_2O (Ji and Zhu 2013).

For example, in these highly compressible (supercritical) environments even traces amounts of contaminants can have significant effects on the mechanical partial molar properties (Chialvo 2013) as well as on the resulting phase envelopes (Li et al. 2009; Lachet et al. 2012; Mazzoccoli et al. 2012), i.e., the systems cannot be described based on the behavior of the pure CO_2 phase (Verma et al. 2011; Wang et al. 2011). Moreover, even though water might be considered an innocuous impurity, its presence increases the risk of gas clathrate formation with the consequent pipe plugging and damage to pumping equipment (Carroll 2003; Tohidi et al. 2012), as well as the likelihood of corrosion (Xiang et al. 2011, 2012; Ruhl and Kranzmann 2012).

From transport and storage viewpoints CO_2-rich streams must be as "dense" as possible (above critical pressure, P_c, and under critical temperature, T_c), so that for the same volumes we maximize the transported mass and the storage capacity. Thus, it is highly desirable to eliminate non-condensable associated gases such as N_2, Ar, and especially O_2 in the presence of either SO_x or NO_x to hinder the formation of strong acids (Ruhl and Kranzmann 2012), as well as H_2 due to the related high specific compression work involved (Posch and Haider 2012).

The scarcity of experimental data for CO_2-SO_x, CO_2-H_2S, and CO_2-NO_x systems is most certainly associated to their toxicity and reactivity that make their handling and measurement extremely difficult to tackle. Consequently, it is not surprising that molecular-based simulation has taken the lead in the study of the thermodynamic phase equilibrium and thermophysical properties of these problematic systems (Kamath et al. 2005; Hansen et al. 2007; Ungerer et al. 2007; Ketko et al. 2011). The main idea behind this effort involves the use of the limited experimental data, supplemented with minimal additional measurements when possible, to develop reliable force field parameterizations (Bourasseau et al. 2008; Lachet et al. 2009; El Ahmar et al. 2011) and subsequently to generate by molecular simulation the much needed properties of interest.

The reliability of the resulting force fields is usually measured by the degree of transferability of the parameterizations, i.e., their ability to represent not only the systems at state conditions different from the ones used in the regressions, but also different properties, e.g., thermodynamic, microstructural, or transport. Obviously, the accuracy and transferability of the resulting force fields in representing real systems depend heavily on the ability of the model representation to capture the most essential physical insights into the actual intermolecular interactions underlying the system of interest, without resorting to oversimplifications or unnecessary modeling complexities. As a matter of fact, the most widely used force fields in chemical, biochemical, and geochemical molecular-based simulations of aqueous electrolyte solutions are mostly based on relatively simple and effective (non-polarizable) interaction-site descriptions, in conjunction with different prescriptions (i.e., combining rules) for the unlike-pair interaction parameters (von Ragué Schleyer 1998).

Force fields for CO_2-acid gas systems

This approach usually comprises reaction ensemble Monte Carlo (RxMC) (Smith and Triska 1994), Gibbs Ensemble Monte Carlo (GEMC) (Panagiotopoulos 1987), and classical molecular dynamics (Allen and Tildesley 1987; Haile 1992) simulation of (usually non-polarizable) model systems, i.e., whose interactions are characterized by pairwise additive force fields. These representations involve typically multi-site Lennard-Jones intermolecular potentials for the van der Waals interactions, where unlike-pair interaction-parameters are most frequently given by combining rules, plus a Coulomb potential to account for the point charge electrostatic interactions (Maple 1998).

The three acid gases under explicit consideration here, i.e., SO_2, H_2S, and NO_2, as well as the ubiquitous H_2O in CO_2-rich phases are described by rigid geometries and their intermolecular potential energy is defined as follows,

$$\phi_{ij}(r_{ij}) = \sum_{i>j}\sum_{\alpha,\beta}\left\{4\varepsilon_{\alpha\beta}\left[\left(\sigma_{\alpha\beta}/r_{ij}^{\alpha\beta}\right)^{12} - \left(\sigma_{\alpha\beta}/r_{ij}^{\alpha\beta}\right)^{6}\right] + q_i^{\alpha}q_j^{\beta}/r_{ij}^{\alpha\beta}\right\} \quad (1)$$

where $r_{ij}^{\alpha\beta}$ is the magnitude of the vector $\mathbf{r}_{ij}^{\alpha\beta} = \mathbf{r}_i + \mathbf{d}_i^{\alpha} - \mathbf{r}_j - \mathbf{d}_j^{\beta}$, when $\mathbf{r}_\ell$ and $\mathbf{d}_\ell^{\gamma}$ define the vector position of the center of mass of molecule ℓ and that of its site γ. Moreover, $\varepsilon_{\alpha\beta}$ and $\sigma_{\alpha\beta}$ are the Lennard-Jones energy and size parameters for the $\alpha\beta$-pair interactions, while q_ℓ^{γ} denotes the electrostatic charge located at site γ of molecule ℓ. Note that for a more flexible parameterization not all charges in these molecular models are centered at atomic sites, i.e., similar to the description of water by the TIPnP models (Baranyai et al. 2006); this approach can account for polarization contributions through augmented electrostatic partial charges without resorting to explicit polarizable models (Chialvo and Cummings 1996a).

Over the years CO_2 has been the target of numerous parameterizations based mostly on non-polarizable force-field descriptions, including one-site Lennard-Jones (Chialvo and Debenedetti 1992; Galliero et al. 2007), two-site Lennard-Jones (Gibbons and Klein 1974), and combinations of *n*-site Lennard-Jones with either electrostatic point charges (Harris and Yung 1995; Potoff et al. 1999; Zhang and Duan 2005; Zhu et al. 2009; Cygan et al. 2012) or point quadrupoles (Murthy et al. 1981; Moller and Fischer 1994; Vrabec et al. 2001; Muller and Gelb 2003; Merker et al. 2010). Among them, the so-called *Elementary Physical Model* 2 (EPM2) model proposed by Harris and Yung (1995) describes CO_2 as a quadrupolar rigid-linear molecule involving three sites, centered at the carbon and oxygen atoms. In contrast to other models, the Lennard-Jones unlike-pair interaction parameters σ_{OC} and ε_{OC}, are both described by Berthelot's combining rule (see also a related comment by Nieto-Draghi et al. (2007), around Fig. 13, associated with the use of Lorentz's rule for σ_{OC} in the study of NO_2/N_2O_4-CO_2 mixtures).

EPM2 model has become the favorite for modeling purposes because it was originally developed to describe properly the thermodynamics of near critical CO_2, and consequently, the vapor-liquid phase equilibrium (Harris and Yung 1995; Vorholz et al. 2000; Nieto-Draghi et al. 2007) (e.g., Fig. 2b). More recently, the model was shown to provide accurate description for the transport properties (Nieto-Draghi et al. 2007; Yoo et al. 2012) (e.g., Fig. 3), and the surface tension (Ghoufi et al. 2008) of CO_2 over wide ranges of state conditions (e.g., Fig. 2a).

Water and aqueous solutions have been most frequently studied with the SPC-E model (Berendsen et al. 1987), a force field that has been extensively characterized in terms of fluid (Chialvo and Cummings 1996b; Vega et al. 2005) and crystalline ice (Baranyai et al. 2005; Vega et al. 2005) microstructures, solid-solid phase equilibrium (Sanz et al. 2004), vapor-liquid phase equilibrium (Guissani and Guillot 1993; Boulougouris et al. 1998; Errington et al. 1998; Vorholz et al. 2000; Hayward and Svishchev 2001), shear viscosity (Delgado-Barrio et al. 2008; Gonzalez and Abascal 2010; Medina et al. 2011; Fanourgakis et al. 2012), and surface tension

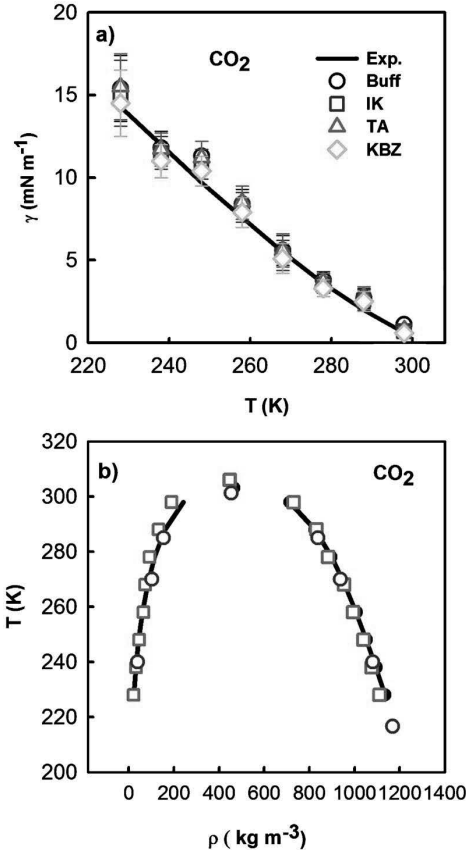

Figure 2. Surface tension (a) and vapor-liquid phase equilibrium (b) for pure CO_2 according to experiment and simulation. The acronyms in these figures refer to the approach used in the calculations, i.e., Buff for Kirkwood-Buff, IK for Irving-Kirkwood, TA for test area, and KBZ for local Kirkwood-Buff. [Adapted with permission from Ghoufi et al. (2008). Copyright © 2008, American Institute of Physics.]

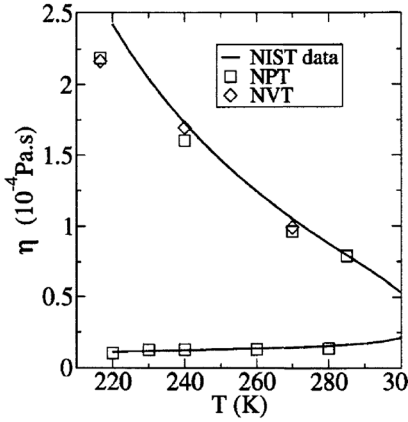

Figure 3. Shear viscosity for pure CO_2 along its vapor-liquid envelope according to experiment and simulation. [Adapted with permission from Nieto-Draghi et al. (2007). Copyright © 2007, American Institute of Physics.]

(Ismail et al. 2006; in't Veld et al. 2007; Vega and de Miguel 2007; Sakamaki et al. 2011). This model originated from its predecessor SPC (Berendsen et al. 1981), involving a Lennard-Jones site centered at the oxygen and three embedded partial charges in a planar geometry, giving rise to a permanent dipole moment $\mu_z = 2.35D$ along the bisectrix of the $\measuredangle$HOH angle. In contrast to SPC, SPC-E includes a "polarization correction" to the enthalpy of vaporization to account for the "missing" water self-polarization in the liquid phase. This contribution comprises the enthalpy change required to polarize a water molecule from its original dipole moment $\left|\vec{\mu}_W^{vac}\right| = 1.85D$ representing an isolated molecule in vacuum, to that of the SPC-E water molecule, $\left|\vec{\mu}_W^{SPC/E}\right| = 2.35D$, i.e., $\Delta H_{pol}^{SPC/E} = (\vec{\mu}_W^{SPC/E} - \vec{\mu}_W^{vac})^2 / 2\alpha_m$ (see Fig. 4a) where α_m is the molecular polarizability.

On the one hand, the introduction of this self-polarization correction results in an additional enhancement of the permanent dipole moment from $2.27D$ for the original SPC to $2.35D$ for the SPC-E model, a contribution that greatly improves the description of various liquid phase properties (see Table I in Berendsen et al. 1987). On the other hand, this improvement comes with an unavoidable downside, i.e., the significant deviations of the orthobaric vapor densities and corresponding equilibrium pressure from the experimental values as a consequence of an unrealistic over-polarization in vapor-like environments (see Fig. 4b). This over-polarization that characterizes all fixed-charge water models also plays a crucial role in the adjustment of the cross interactions between dipolar (H_2O) and non-polar (CO_2) species for the accurate description of the solubility of water in CO_2-rich phases, as we will discuss below.

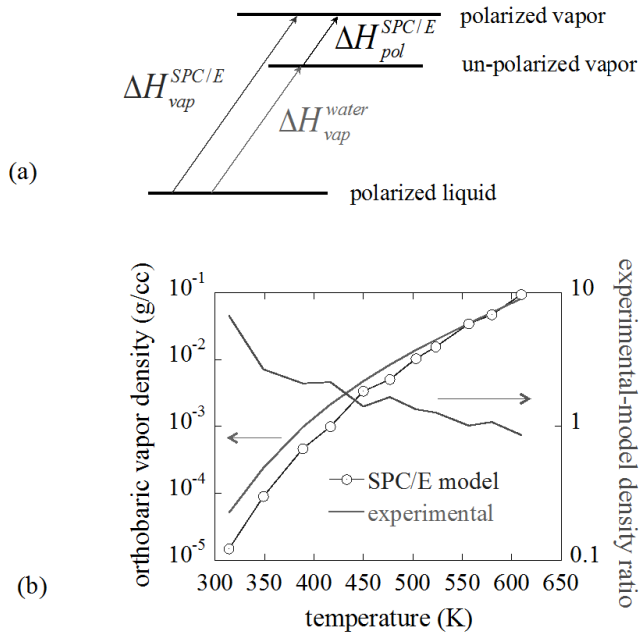

Figure 4. Change in the enthalpy of vaporization due to polarization (a), and comparison between the behavior of water and that of SPC-E model predicted by GEMC simulation (b). [Adapted with permission from Vlcek et al. (2011). Copyright © 2011, American Chemical Society.]

Early modeling by Sokolic et al. (1985, 1986) provided the foundations for the newest SO_2 model developed by Lachet et al. (2009) for a more accurate representation of the vapor-liquid phase equilibria of pure SO_2 and mixtures with N_2 and O_2. According to the point electrostatic charges in Table 1, this model describes SO_2 as a dipolar molecule characterized by a permanent dipole moment $\mu_z = -1.64D$, where z is the direction of the bisectrix of the $\measuredangle$OSO angle. The accuracy of this force field is clearly demonstrated in Figs. 5a-b where the simulated behavior of the interfacial tension and vapor-liquid phase envelope of pure SO_2 is compared against the corresponding experimental data (Neyt et al. 2011).

The modeling of fluid H_2S was initially tackled by Jorgensen (1986) as part of his OPLS force field development for sulfur compounds, and further pursued by Forester et al. (1989) in terms of rigid molecular geometries. Aided by the development of new GEMC tools, Kristof and Liszi (1997) tested those models and developed an improved parameterization to describe properly the vapor-liquid phase envelope, including the critical conditions. Their model describes H_2S as a dipolar molecule, comprising a set of four partial charges resulting in a permanent dipole moment $\mu_z = 1.43D$, where z is the direction of the bisectrix of the $\measuredangle$HSH angle. This model has been further validated by Ghoufi et al. (2008), who used an isothermal-isochoric MC approach to calculate the temperature dependence of the surface tension of H_2S, and simultaneously, the corresponding vapor-liquid phase envelope (Figs. 6a,b). Moreover, using this model Nieto-Draghi et al. (2005) were able to predict the shear viscosity of H_2S along the vapor-liquid envelope in good agreement with the available experimental data (Fig. 7).

Under the label of NO_x as a CO_2 contaminant we might include NO, N_2O, NO_2, and N_2O_4, however we have selected NO_2 as a representative compound for which we have available a recently developed force field parameterization by Bourasseau et al. (2008). This model was

Table 1. Geometry and force field parameters for the acid gases and the aqueous carbon dioxide solutions *

Species	Site	q (e^-)	σ (Å)	ε/k (K)	Reference
CO_2	C	0.6512	2.757	28.129	(Harris and Yung 1995)
	O	−0.3256	3.033	80.507	
	ℓ_{CO} = 1.149 Å; ∡OCO = 180°; μ = 0.0D				
H_2O	O	−0.8476	3.166	78.23	(Berendsen et al. 1987)
	H	0.4238	0.0	0.0	
	ℓ_{OH} = 1.0 Å; ∡HOH = 109.54°; μ_z = 2.35D				
SO_2	S	—	3.583	126.08	(Lachet et al. 2009)
	O	−0.414	2.990	46.41	
	q^+	0.828	—	—	
	ℓ_{SO} = 1.434 Å; ℓ_{Sq+} = 0.312 Å; ∡OSO = 119.3°; μ_z = −1.64D				
H_2S	S	0.40	3.730	250.0	(Kristof and Liszi 1997)
	H	0.250	—	—	
	q^-	−0.90	—	—	
	ℓ_{SH} = 1.34 Å; ℓ_{Sq-} = 0.1862 Å; ∡HSH = 92.0°; μ_z = 1.43D				
NO_2	N	0.146	3.24	50.36	(Bourasseau et al. 2008).
	O	−0.073	2.93	62.51	
	ℓ_{NO} = 1.193 Å; ∡ONO = 134.1° ;μ_z = −0.33D				

* Unlike-pair interactions described by Lorentz-Berthelot combining rules, except for CO_2 that involves only Berthelot's for size and energy Lennard-Jones parameters.

parameterized simultaneously with the dimerized species N_2O_4 when the two species dissolved in model CO_2 were undergoing vapor-liquid phase and chemical equilibration according to an isobaric-isothermal RxMC/GEMC protocol (Smith and Triska 1994). According to the electrostatic point charges in Table 1, this model describes NO_2 as a dipolar species characterized by a permanent dipole moment $\mu_z = -0.33D$ along the bisectrix of the ∡ONO angle. The accuracy of this model is illustrated in Fig. 8, where the simulated vapor-liquid coexistence envelope is compared with the experimental data of Reamer and Sage (1952), and the two variations of an equation of state (de Souza and Deiters 2000).

All geometric and force field parameters for the involved models are summarized in Table 1. Obviously the CO_2 associated compounds exhibit rather different dipolar features (Fig. 9), and consequently, this behavior will translate into contrasting solid-fluid interfacial and confinement outcome, as we will discuss below. Note also that because the van der Waals contributions in Equation (1) are consistently described in terms of Lennard-Jones functions, there is a seamless transition from the study of pure components to their mixtures with the well-characterized EPM2 CO_2 model (Harris and Yung 1995) and the SPC-E water model (Berendsen et al. 1987).

Note that even though we might start with a reasonably realistic account of the pure component properties by the model under consideration (as it is the case for all models described above), the successful description of the mixture properties requires an adequate representation of the unlike-pair ("cross") interactions between distinct molecular species. Typically these unlike-pair interactions are prescribed by combining rules, following numerous empirical and theoretical approaches (Kohler 1957; Hudson and McCoubrey 1960; Fender and Halsey 1962; Good and Hope 1970; Hiza and Duncan 1970; Sikora 1970; Kong 1973a; Kohler et al. 1982, 1989; Pena et al. 1982; Tang and Toennies 1991; Halgren 1992; Waldman and

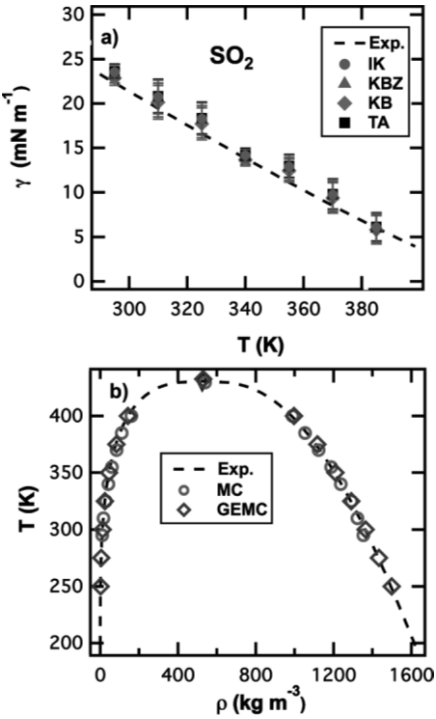

Figure 5. Surface tension (a) and vapor-liquid phase equilibrium (b) for pure SO_2 according to experiment and simulation. The acronyms in these figures refer to the approach used in the calculations, i.e., KB for Kirkwood-Buff, IK for Irving-Kirkwood, TA for test area, and KBZ for local KB. [Adapted with permission from Neyt et al. (2011). Copyright © 2011, American Chemical Society.]

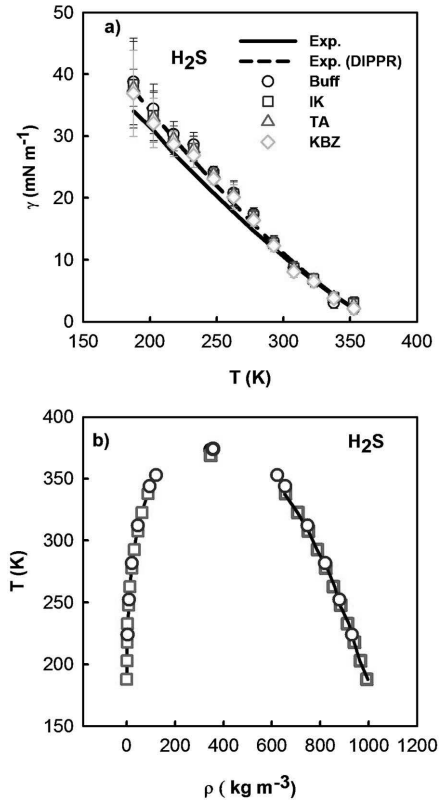

Figure 6. Surface tension (a) and vapor-liquid phase equilibrium (b) for pure H_2S according to experiment and simulation. [Adapted with permission from Ghoufi et al. (2008). Copyright © 2008, American Institute of Physics.]

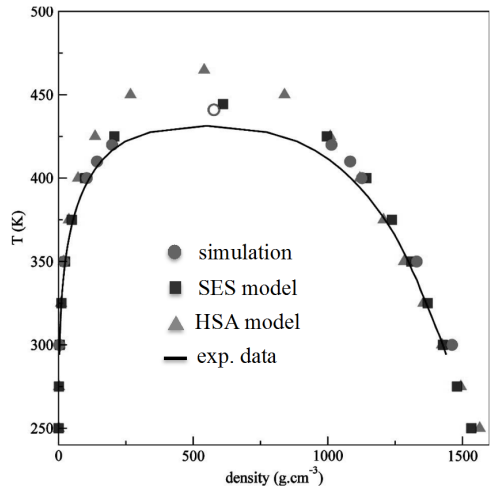

Figure 7. Shear viscosity for pure H_2S along its vapor-liquid envelope according to experiment and simulation. [Adapted with permission from Nieto-Draghi et al. (2005). Copyright © 2005, American Institute of Physics.]

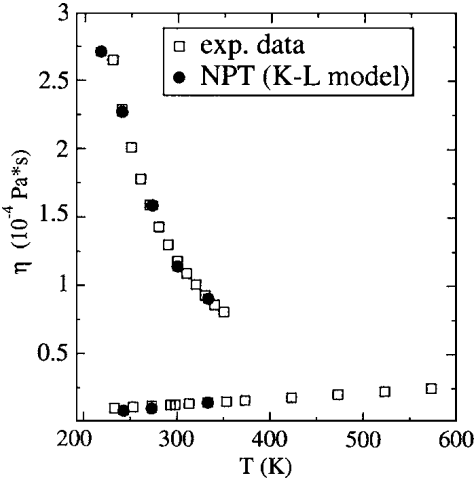

Figure 8. Vapor-liquid equilibrium of the NO_2-N_2O_4 system according to molecular simulation in comparison with experimental data and two types of macroscopic correlations. [Adapted with permission from Bourasseau et al. (2008). Copyright © 2008, American Chemical Society.]

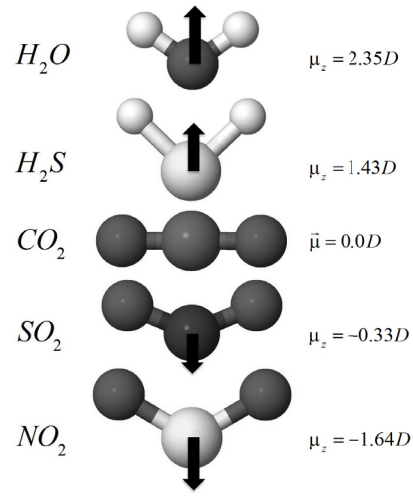

Figure 9. View of molecular geometry and dipole moment of involved models.

Hagler 1993), that can invariably be written as deviations from the popular Lorentz-Berthelot rule (Chialvo 1991), i.e.,

$$\eta_{\alpha\beta} \equiv \frac{\sigma_{\alpha\beta}}{\sigma^{L}_{\alpha\beta}} = \frac{2\sigma_{\alpha\beta}}{\left(\sigma_{\alpha\alpha} + \sigma_{\beta\beta}\right)} \qquad (2)$$

$$\xi_{\alpha\beta} \equiv \frac{\varepsilon_{\alpha\beta}}{\varepsilon^{B}_{\alpha\beta}} = \frac{\varepsilon_{\alpha\beta}}{\sqrt{\varepsilon_{\alpha\alpha}\varepsilon_{\beta\beta}}}$$

where $\sigma^{L}_{\alpha\beta} = 0.5(\sigma_{\alpha\alpha} + \sigma_{\beta\beta})$ and $\varepsilon^{B}_{\alpha\beta} = (\varepsilon_{\alpha\alpha}\varepsilon_{\beta\beta})^{1/2}$ are Lorentz and Berthelot combining rules, respectively (Lorentz 1881; Berthelot 1898). Note however that unlike-pair interaction parameters do not necessarily have to conform to these rules, i.e., they could be regressed independently from the like-pair interactions in order to achieve accurate representations of the phase equilibria in fluid mixtures (Chialvo 1991) as we describe below for the solubility of H_2O in CO_2-rich phases as encountered in CCUS systems.

For the ability of unlike-pair parameters to describe the interactions between polar and non-polar species, such as the case of H_2O and CO_2, we must consider two significant requirements. First, in order for this adjustment to be sound the models of the pure components must describe accurately the microstructural and thermodynamic behavior of these fluids at the state conditions of interest, i.e., the adjustment should not absorb the inaccuracies of the pure component model representations. This is precisely the case for the study of CO_2-H_2O mixtures when the EPM2 (Harris and Yung 1995) and the SPC/E (Berendsen et al. 1987) models are used in the description of the behavior of pure CO_2 and H_2O, respectively. Second, the adjustment strategy depends on whether the system comprises a single phase or two- (or for that matter *n*-) phases in equilibrium. For example, if we are dealing with dilute one-phase aqueous systems the adjustment of the unlike-pair interactions could be achieved by invoking the deviation parameters (η,ξ), Equation (2), to match the simulated and experimental solute solubility

in the desired phase as illustrated in Figure 10 (Chialvo et al. 2012). However, if the target of the study involves two fluid-phases in equilibrium involving species with low mutual solubilities, we need to perform the adjustment of the unlike-pair interactions to describe accurately the two phases simultaneously.

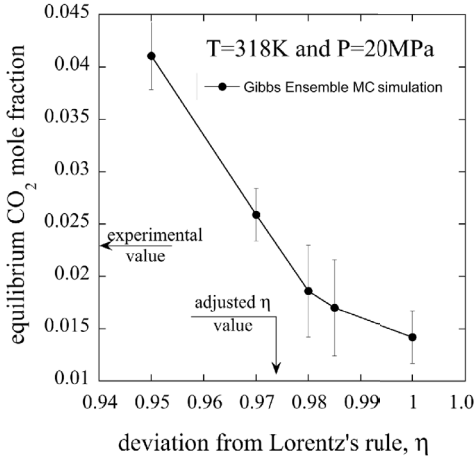

Figure 10. Solubility of CO_2 in the H_2O-rich phase in equilibrium with the CO_2-rich phase. Comparison between experiment and GEMC simulations. [Adapted with permission from Chialvo et al. (2012). Copyright © 2012, American Chemical Society.]

Obviously, the last scenario makes the adjustment more challenging and requires a novel approach to deal with the equilibrium between fluid phases of disparate polarities (Vlcek et al. 2011). In fact, the dissolution of H_2O in CO_2-rich phases at CCUS conditions involves highly dilute polar molecules in dense non-polar and less polarizing phases (Spycher et al. 2003); consequently, any fixed-charge (i.e., non-polarizable) water model adjusted to describe properly liquid-like environments must be 'depolarized' in order to account accurately for the water dipolar behavior in non-polar environments. Otherwise, the mere (η,ξ)-adjustment of the combining rules cannot counter the effect of the over-polarized water in a non-polar environment, and will not provide the desired agreement with the experimental data (Liu et al. 2011), a fact that reminds us about the inherent deficiencies of non-polarizable models in describing systems with significant polarity asymmetries.

We have recently developed a method to tackle these issues during the calibration of the CO_2-H_2O unlike-pair interactions to accurately represent these species solubilities in fluid-fluid phase equilibria at state conditions relevant to the geological CCUS process (Vlcek et al. 2011). The strategy was based on the perturbative adjustment (from a suitable reference cross-interaction parameters) of electrostatic and non-electrostatic interactions for an existing force field, leaving the pure fluid models unchanged (i.e., adherence to the first requirement above), while correcting for the over-polarization of the SPC-E H_2O in the EPM2 CO_2-rich non-polar environment (adherence to the second requirement). The end result of the proposed strategy leads to the following derived expression, Equation (3), that relates the solubility ratio—between actual (experimental) value for H_2O (w) in the CO_2-rich phase and that predicted by the original combining rules—with the adjusted cross-interactions and the de-polarization correction.

$$\frac{x_W^C(\eta,\xi,\Omega)}{x_W^C(1,1,0)} \approx \exp\left[\beta\Delta H_{pol}^{SPC/E}\right] \times \left\langle \exp\left[-\beta\sum(\eta,\xi)\right]\right\rangle_C \tag{3}$$

After identifying $\Omega = -\Delta H_{pol}^{SPC/E}$ and (η = ξ = 1) as the Lorentz-Berthelot combining rules, the two terms in the right hand side of Equation (3) account for the de-polarization correction and the contribution from the perturbation of the combining rules from the corresponding Lorentz-Berthelot, respectively. In fact, the second term in Equation (3) is actually the simulation quantity evaluated during the (η,ξ)-adjustment, where Σ(η,ξ) denotes the perturbation contribution to the configuration energy, β = 1/kT, and $\langle\cdots\rangle_C$ represents an ensemble average in the CO_2-rich phase. For a detailed account on its derivation, application, and general discussion the reader should consult Vlcek et al. (2011).

The resulting Lennard-Jones cross-interaction parameters, after applying the de-polarization correction and simultaneous (η,ξ)-adjustment, are presented in Table 2 together with the original representations based on the Lorentz-Berthelot combining rules. Note that the solubilities of H_2O in a CO_2-rich phase, determined by GEMC simulation at representative CCUS state condition, is about an order of magnitude smaller than the corresponding experimental values. However, the application of the approach embodied in Equation (3) brings the simulated solubilities within ~10% of the experimental values along the 298 and 323 K isotherms as illustrated in Figure 11.

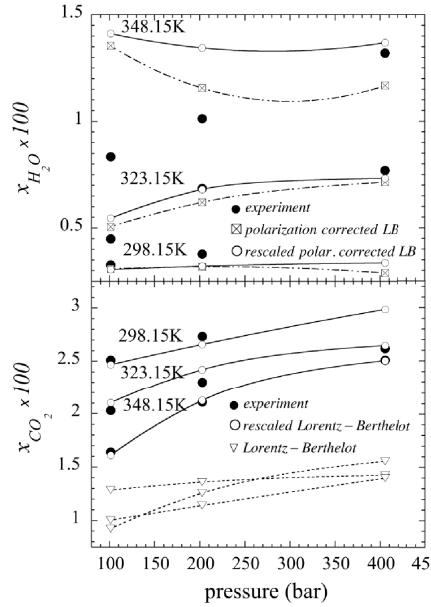

Figure 11. Solubility isotherms of CO_2 in a H_2O-rich phase in fluid-fluid equilibrium with H_2O in a CO_2-rich phase according to the original and the corrected combining rules in comparison with experimental data. [Adapted with permission from Vlcek et al. (2011). Copyright © 2011, American Chemical Society.]

Note that while the simulation results along the 348 K isotherm are not as accurate as those for the lower isotherms, the improvement over those based on the original cross-interactions is still significant. The larger discrepancy of water solubility in the CO_2-rich phase at 348 K and 100 bar, is not surprising considering the increasing unscreened attractive SPC-E dipole-dipole interactions at the least polar phase environment, a condition that again highlights the limitations of non-polarizable models to describe the behavior of phases involving species with significant polarity asymmetries. The adjusted cross-interaction parameters were then used to predict the species diffusivities at state condition for which experimental data are available.

According to Table 3, the resulting CO_2 diffusivity in H_2O is in fairly good agreement with experimental values within the studied temperature range, and translates into a significant improvement over the predictions from the Lorentz-Berthelot counterparts. In fact, the latter over-predict the CO_2 diffusivity in H_2O by 30%. However, the H_2O diffusivity in CO_2 at 298 K and $10 < P$ (MPa) < 40 is about 20% higher than the experimental values and closer to the experimental data than those predicted by the Lorentz-Berthelot systems, and exhibit the cor-

Table 2. Adjusted Lennard-Jones potential parameters for the unlike-pair interactions between the SPC-E and EPM2 models after de-polarization correction (Vlcek et al. 2011).

ij-interaction	ε_{ij}**/k (Å)**	σ_{ij} (Å)	ξ_{ij}	η_{ij}
C_C-O_W (#)	64.20	2.9615	1	1
C_C-O_W	78.04	2.8412	1.4143	0.9594
O_C-O_W (#)	79.36	3.0995	1	1
O_C-O_W	90.08	3.1524	1.1351	1.017

[#] Unlike-pair interactions parameters according to Lorentz-Berthelot combining rules

Table 3. Comparison between simulated (sim) and experimental (exp) diffusion coefficients of infinitely dilute CO_2 in water, D_{CO_2}, and H_2O in CO_2, D_{H_2O} (Vlcek et al. 2011).

T(K)/P(bar)	$10^5 \times D_{CO_2}$ (cm^2s^{-1}) sim/exp	T(K)/P(bar)	$10^4 \times D_{H_2O}$ (cm^2s^{-1}) sim/exp
298/1.0325	1.98/1.95[a]	298/202.65	1.54/1.59[b]
323/1.0325	3.57/3.03[a]	323/202.65	1.96
348/1.0325	5.74/5.40[a]	348/202.65	2.70
298/101.325	2.00	298/101.325	2.65
298/202.65	2.10	298/202.65	1.86
298/405.3	1.98	298/405.3	1.71

[(a)] Xu et al. (2003) [(b)] Espinoza and Santamarina (2010)

rect pressure dependence (e.g., Fig. 6b of Vlcek et al. 2011). As for the case of the lower H_2O solubility in a CO_2-rich phase, the simulated higher H_2O diffusivity in CO_2 based on the optimized parameterization might have the same origin, but we did not find higher temperature data to test this conjectured link.

For the case of the CO_2-SO_2 and CO_2-NO_2 binaries, based on the force field parameterization of Table 1 for the pure components, the reported description of the unlike-pair interactions have involved the usual Lorentz-Berthelot rules for the unlike-pair interactions. In fact, Lachet et al. (2009) successfully applied their SO_2 model to study the fluid phase equilibrium of SO_2-CO_2, SO_2-O_2, and SO_2-N_2 binary mixtures (El Ahmar et al. 2011). For example, Figure 12 illustrates the accuracy of the model representation for the CO_2-SO_2 *P-x* phase behavior along a representative isotherm in comparison with the scarce experimental data (Lachet et al. 2009).

In addition, Bourasseau et al. (2008) have recently parameterized the NO_2/N_2O_4-CO_2 system to study vapor-liquid phase and chemical equilibration. For this purpose, the CO_2 phase was described by the EPM2 model (Harris and Yung 1995) where, instead of the original Berthelot combining rule for the Lennard-Jones unlike-pair size parameter σ_{CO}, Bourasseau et al.

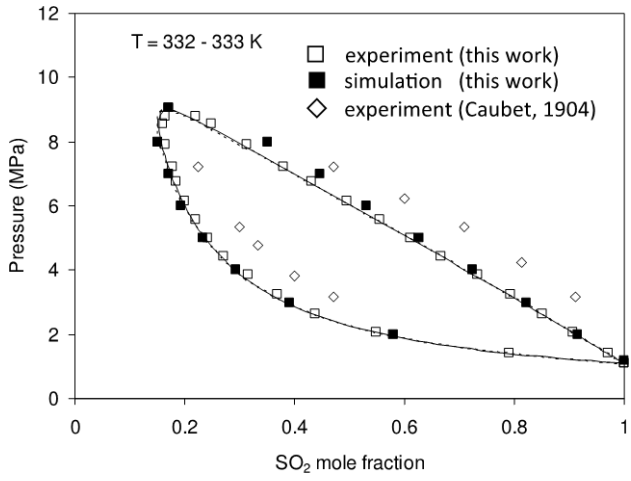

Figure 12. Isothermal *PX* phase diagram for the CO_2-SO_2 mixture according to the experimental data and simulation results. [Adapted with permission from Lachet et al. (2009). Copyright © 2009, Elsevier.]

invoked the usual Lorentz combining rule. This modification translates into a slight change from the original value of σ_{CO} = 2.895 Å to σ_{CO} = 2.8917 Å with a negligible effect on the resulting properties (Nieto-Draghi et al. 2007). The agreement of their parameterization for the model NO_2/N_2O_4-CO_2 system becomes evident in the description of the *P-T-x* phase behavior in comparison with the limited experimental data (Belkadi et al. 2008), and corresponding equation of state correlation (Fig. 13).

Even though there was no intention to optimize the cross interaction parameters for the CO_2-H_2S system, Galliero et al. (2007) tested the accuracy of the models to describe the mixture densities for a few system compositions and state conditions from isobaric-isothermal simulations as shown in Table 4. The immediate conclusion from Table 4 is that Kong's combining rules (Kong 1973b) appear to provide a significant improvement in the predicted mixture densities over those from the Lorentz-Berthelot rules. In fact, by recalling that,

$$\sigma_{\alpha\beta}^{KG} = \sqrt[6]{2^{-13}\left(\varepsilon_{\alpha\alpha}/\varepsilon_{\beta\beta}\right)^{0.5}\left(\sigma_{\alpha\alpha}^{9}/\sigma_{\beta\beta}^{3}\right)\left\{\left[1+\left(\varepsilon_{\beta\beta}\sigma_{\beta\beta}^{12}/\varepsilon_{\alpha\alpha}\sigma_{\alpha\alpha}^{12}\right)^{1/13}\right]/2\right\}^{13}} \qquad (4)$$

$$\varepsilon_{\alpha\beta}^{KG} = \varepsilon_{\beta\beta}\left(\sigma_{\beta\beta}/\sigma_{\alpha\alpha}\right)^{6}\sqrt[13]{\left[2/1+\left(\varepsilon_{\beta\beta}\sigma_{\beta\beta}^{12}/\varepsilon_{\alpha\alpha}\sigma_{\alpha\alpha}^{12}\right)^{1/13}\right]}$$

which, after invoking Equation (2), can be written as $\eta_{\alpha\beta} = \sigma_{\alpha\beta}^{KG} / \sigma_{\alpha\beta}^{L}$ and $\xi_{\alpha\beta} \equiv \varepsilon_{\alpha\beta}^{KG} / \varepsilon_{\alpha\beta}^{B}$. For the particular case described in Table 4, and recalling the parameters from Table 1, we have that η_{CS} = 1.0432, ξ_{CS} = 0.725, η_{OS} = 1.0156 and ξ_{OS} = 0.8822.

Note that based on their TraPPE force field parameterization of H_2S and CO_2 models, Kamath and Potoff (2006) performed GEMC simulations of these mixtures using Lorentz-Berthelot combining rules. Their comparison between experimental data (Bierlein and Kay 1953) and simulation results (Fig. 4 in Kamath and Potoff 2006) for the *PTx* phase envelopes at *T* = 293 K and 313 K indicated significant discrepancies, an outcome in agreement with Galliero et al.'s (2007) findings in Table 4. The fact that Kamath and Potoff (2006) models include flexible, while those from Table 1 involve rigid, geometries is inconsequential. The

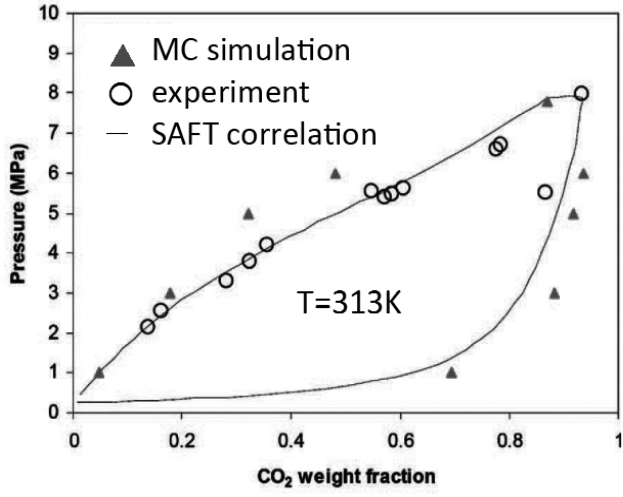

Figure 13. Isothermal pressure-composition diagram for CO_2 -NO_2/N_2O_4 mixtures according to experiment, macroscopic correlation, and simulation. [Adapted with permission from Bourasseau et al. (2008). Copyright © 2008, American Chemical Society.]

Table 4. Comparison between experimental (*exp*) and simulated mixture densities for the system CO_2-H_2S according to two sets of combining rules (Galliero et al. 2007).

x_{H_2S}	T (K)	P (MPa)	ρ_{exp} (g cm^{-3})	ρ_{LB} (g cm^{-3})[(a)]	ρ_{KG} (g cm^{-3}) [(b)]
0.095	273	15	0.9519	1.0021	0.9645
0.293	273	15	0.9138	0.9876	0.926
0.5	273	2.7	0.846	0.9314	0.8538
0.095	400	7.5	0.1139	0.113	0.1112
0.293	400	7.5	0.111	0.110	0.1075
0.5	400	7.5	0.1079	0.109	0.105

[(a)] Lorentz-Berthelot combining rules, [(b)] Kong combining rules (Kong 1973b)

message here is that the cross interaction parameters must adjust to account properly for the significant polarity asymmetry between CO_2 and H_2S following a mechanism similar to that we discussed above for the analogous CO_2-H_2O system.

Considering that all three CO_2 impurities in Table 1 are dipolar species (Fig. 9) and that SO_2 bears the largest dipole moment, it appears surprising that the CO_2-SO_2 model mixture was able to predict the VLE in a good agreement with the experimental data (Lachet et al. 2009) when using the simple Lorentz-Berthelot combining rules. For the second largest dipolar solute, H_2S, the agreement came as a result of a large deviation from these rules, while for the smallest dipolar solute, NO_2, these rules appear to describe adequately the corresponding unlike-pair interactions.

THE SIGNIFICANT ROLE OF CO_2 FLUID – MINERAL INTERACTIONS

The interaction of fluids with mineral surfaces gives rise to a gamut of interfacial and confined environments whose microstructural, dynamical, and thermophysical behavior contrast significantly with those of their bulk counterparts (Alba-Simionesco et al. 2006; Puibasset and Pellenq 2008; Argyris et al. 2009; Malani et al. 2009; Giovambattista et al. 2012). Such interfacial behavior originates in the underlying asymmetry between fluid-fluid and solid-fluid interactions, translates into inhomogeneous fluid density distributions whose eventual overlapping will induce confined environments (see Fig. 14). These inhomogeneous fluid distributions develop within a nanometer length scale, i.e., a few molecular diameters from the mineral surface, and play a key role in defining the local physicochemical fluid behavior including the fluid's composition, species diffusivity, and ultimately its reactivity with the mineral surface. In what follows we discuss the coexistence of solvation and confinement phenomena and then provide molecular-based evidence to support the contention that confined fluids behave radically different from their bulk counterparts.

Coexistence of solvation and confinement phenomena

The injection of CO_2 (and its associated components) into mineral confinement can disturb the existing equilibrium between ionic species, through the induction of either mineral surface dissolution or carbonate precipitation (Gaus 2010). Because the CCUS process relies on a permanent geologic retention of CO_2 involving hydrodynamic, solubility, and/or mineral trapping mechanisms, its success will greatly depend on our ability to manipulate (and eventually control) fluid-mineral interfacial phenomena at the actual subsurface conditions.

Obviously, any realistic attempt toward the manipulation of the fluid-mineral interfacial behavior, and eventual engineering of a robust mineral retention, will require an atomic-level

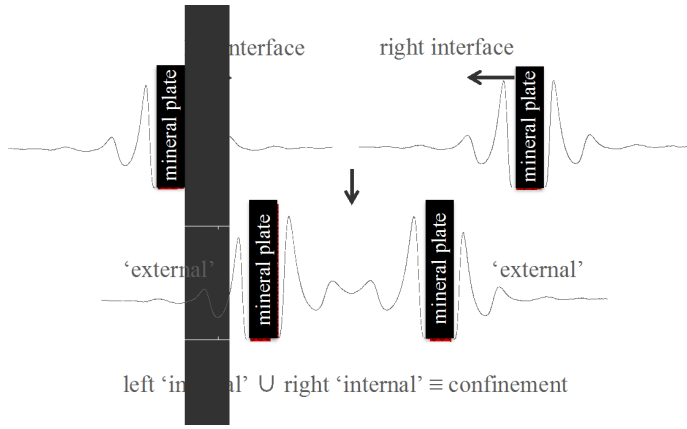

Figure 14. Formation of a confined environment as a result of the overlapping of two approaching solid-fluid ("internal") interfacial structures.

understanding of the cause-effect connections between the nature of the mineral formations, their porosity, local fluid composition, and thermodynamic state conditions. Unfortunately, we currently lack that required understanding regarding the structural and dynamic behavior of CO_2-rich phases in contact with, and adsorbed within, mineral substrates, i.e., subsurface fluid environments interacting with formations characterized by a wide range of nano-porosity and hydrodynamic permeability.

A key factor behind our deficient understanding of fluid behavior under mineral confinement is the intrinsic difficulty to probe directly—i.e., without the use of either untested hypothesis or conjectured behavior in the interpretation of the observations—this type of environments that precludes the gathering of experimental data needed to test and validate macroscopic modeling as well as to improve the simulation capabilities. An immediate consequence is the inherent inability of current macroscopic modeling efforts to capture the essential physics that describes fluid-rock and fluid-fluid interfacial phenomena associated with the geological CO_2 capture and sequestration.

Therefore, it is crucial for us to gain microscopic insights into the interfacial CO_2 fluid-caprock phenomena for a relevant range of pore sizes and geometries as well as pore-wall chemistry (e.g., from hydrophobic to hydrophilic) at representative CCUS conditions. Fortunately, molecular-based simulation can provide a wealth of microstructural and dynamical information for precisely defined intermolecular potential models, to connect unambiguously the microscopic details characterizing the mineral surfaces, their effects on the surrounding fluids, and their potential impact on phase equilibria and transport phenomena (Botan et al. 2011; Giovambattista et al. 2012). However, we should be mindful of the time- and length-scale limitations of these versatile simulation tools, and consequently, apply them either to situations not accessible by other means or to provide complementary insights toward the microscopic interpretation of macroscopic properties.

One such scenario is the microscopic behavior of the caprock-fluid interfaces and the formation of confinement as a result of their overlapping (Fig. 14), where the fluid phase might comprise a CO_2-rich phase in the presence of contaminants and small amounts of H_2O, while in contact with a shale caprock such as quartz-clay rock (Cole et al. 2010). From a microscopic modeling standpoint the study of the behavior of CO_2-rich fluid in contact with fine-grained quartz component can be pursued by invoking pure silica substrate proxies, for which we have

available reliable intermolecular potential models that will facilitate the interrogation of the system properties over a wide range of pore sizes and surface chemistry.

Caprocks are essentially mineral formations that should work as sealers above the storage to prevent the leakage of CO_2 to the atmosphere; they are characterized by low permeability, i.e., in the order of a few nano-Darcy and low porosity (≤ 25%). As in any other geologic formation, the presence of fractures and cracks can accelerate the migration of the CO_2 fluids into and through these caprock nano-environments, facilitate the chemical interactions (dissolution/precipitation) between the fluid and the solid substrates and eventually will affect the substrate permeability.

Typical mineral formations of interest in CCUS include natural sandstones involving a pore-size distribution in the range 10 Å - 50 μm (Radlinski et al. 2004), shale formations with a primary porosity between 6nm and 800 μm (Angeli et al. 2009), tight shale samples exhibiting uni-modal 3 Å - 600 Å pore-size distributions (Katsube and Williamson 1994), natural silica minerals (including chalcedony, chert, quartz, and volcanic glass) comprising 1.5 Å - 3.5 Å pore-size distributions (Yoshizawa et al. 2009), and sedimentary (equi-granular quartzite) sands exhibiting bimodal 4 Å - 200 Å pore-size distributions (Chesta et al. 2009). In particular we focus on the interfacial and confinement behavior of fluids involving the smallest pore sizes because, the smallest pores will ultimately be the ones determining the required impermeability of the caprock.

Grand canonical molecular dynamics simulation of mineral confined fluids

In what follows we illustrate how molecular dynamics simulation can be used to probe and interrogate the behavior of model CO_2-contaminant solutions at, and under extreme confinement between, finite model silica plates for which reliable and precisely defined intermolecular potential models describe the fluids and mineral surfaces. From a thermodynamic viewpoint, the fluids under confinement define open systems, i.e., subject to constant temperature and pressure with a fluctuating number of particles (and resulting composition) to equilibrate the species chemical potentials with the surroundings (O'Connell and Haile 2005). From a molecular simulation standpoint these open environments are straightforwardly studied by a globally isobaric-isothermal ensemble (NPT), that behaves locally as a grand canonical ensemble (μVT) (Giovambattista et al. 2006; Rodriguez et al. 2009; Chialvo et al. 2012).

Using this configuration we have recently analyzed the impact of the surface chemistry of the silica plates, represented by a (111) face of cristobalite, on the interfacial/confinement behavior of H_2O-rich CO_2 fluid phases based on hydroxylated (hydrophilic) and non-hydroxylated (hydrophobic) surface modifications according to the scheme developed by Debenedetti and colls. (Giovambattista et al. 2006). Obviously, this simulation approach provides the opportunity to analyze the effect of a continuous variation of surface polarity on the confined fluid behavior by a simple scaling of the partial charges defining the silanol dipole (Castrillon et al. 2009). In fact, as illustrated in Figure 15, under the current parameterization (i.e., Table 5) (Lee and Rossky 1994) the silanol group bears a rather strong dipole moment with a magnitude comparable to the SPC-E molecule, whose z-component points to the mineral surface with a maximum value of ~1.8*D*.

Moreover, by adjusting the surface polarity through γ , Figure 15, Giovambattista et al. (2007) found that the silica-water contact angle $\vartheta(\gamma)$ varies as $25° < \vartheta(0 \le \gamma \le 1.0) < 115°$, with a hydrophobic-to-hydrophilic crossover at $\gamma = 0.4$, i.e., $\vartheta(\gamma = 0.4) \approx 90°$ so that the transition occurs when the *z*-component of the surface dipole $\mu_{z,tot}(\gamma = 0.4) \approx -0.72D$. Therefore, this description affords the chance to interrogate the model system under precisely defined state and configurational conditions, while keeping complete control of the microscopic details of the system. Specifically, we have already applied this approach to address some fundamental issues regarding the behavior of CO_2 in H_2O-rich phases at representative CCUS conditions, including

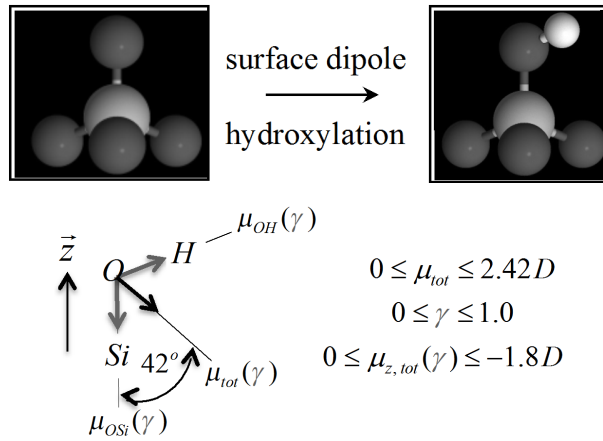

Figure 15. Geometry and magnitude of the surface dipole in a silanol group at a silica surface.

(a) how the degree of surface polarity affects the interfacial structure, (b) how the overlapping of approaching interfacial structures affects the confined fluid composition and consequently, (c) how these inhomogeneous fluid distributions modify the species local mobility (Chialvo et al. 2012). In order to extract valuable microscopic insights they tackled the analysis of three cases of extreme surface polarities, where the mineral surfaces are either both non-hydroxylated or hydroxylated, and the mismatched combination, i.e., the hydrophobic-hydrophobic plates, hydrophilic-hydrophilic, and the hydrophobic-hydrophilic (Janus) configurations. Moreover, to rationalize the observations and facilitate the understanding of these effects Chialvo et al. (2012) have studied first the interfacial behavior of H_2O rich-CO_2 environments in contact with the silica plates at the CCUS representative conditions of 318 K and 20 MPa as illustrated in Figures 16 and 17 in terms of the axial density distributions of H_2O and CO_2, respectively.

These figures emphasize the contrasting interfacial profiles between the external (or purely interfacial), and the internal (or confined) regions. Note that regardless of the nature of the plate surfaces, H_2O and CO_2 exhibit layering within 10-15 Å from the plane containing the silanol's oxygen at the silica surface, beyond which the axial structure is completely lost. Moreover, the strength of the layering depends on the polarity of the plate surface, i.e., H_2O exhibits more significant layering when interfacing with hydrophilic than with hydrophobic plates, resulting from the stronger dipolar water-surface interactions at the aqueous CO_2-hydroxylated surface interfaces. In fact, the bottom portion of Figure 16 clearly illustrates the transition from strong to weak water layering within the confined environment between mismatched plates, i.e., when the left plate is hydrophilic and the right plate is hydrophobic.

Due to its non-polar nature CO_2 displays an interfacial behavior that mirrors the H_2O trend in that it interacts (i) significantly with the non-hydrated hydrophobic plates (resulting from the wa-

Table 5. Lennard-Jones potential parameters and partial charges for the silica sites (Lee and Rossky 1994) [#]

***ii*-interaction**	ε_{ii}/k (K)	σ_{ii} (Å)	q_i (*e*)
Si-Si	64.20	3.795	0.31[(a)]
O_{Si}-O_{Si} (bulk)	78.04	3.154	—
O_{Si}-O_{Si} (surface)	78.04	3.154	–0.71[(a)]
H_{Si}-H_{Si} (surface)	—	—	0.40[(a)]

[#] Unlike-pair interactions parameters are based on Lorentz-Berthelot combining rules
[(a)] Electrostatic charges on Si-O-H units for hydrophilic surfaces

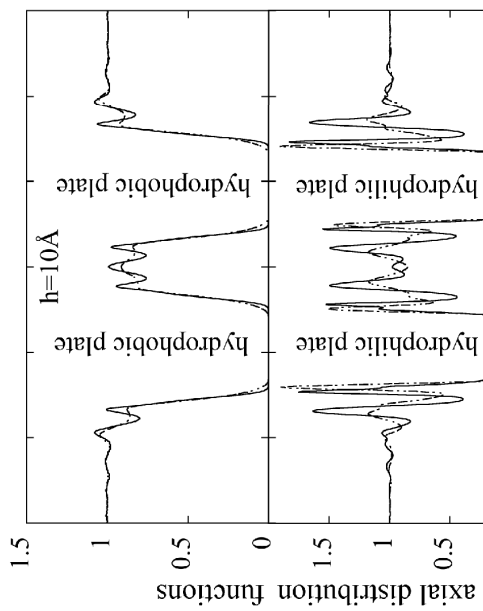

Figure 16. (on left) Water-sites axial distribution functions for H_2O-rich CO_2 solutions interfacing with, and under confinement between, hydrophobic (top), hydrophilic (middle), and mismatched (bottom) silica plates at T = 318 K and P = 20 MPa for an interpolate separation h = 10 Å.

Figure 17. (on right) Interplate dependence of the axial distribution functions of CO_2 for H_2O-rich CO_2 solutions interfacing with, and under confinement between, hydrophobic (top), hydrophilic (middle), and mismatched (bottom) silica plates at T = 318 K and P = 20 MPa for an interpolate separation h = 10 Å.

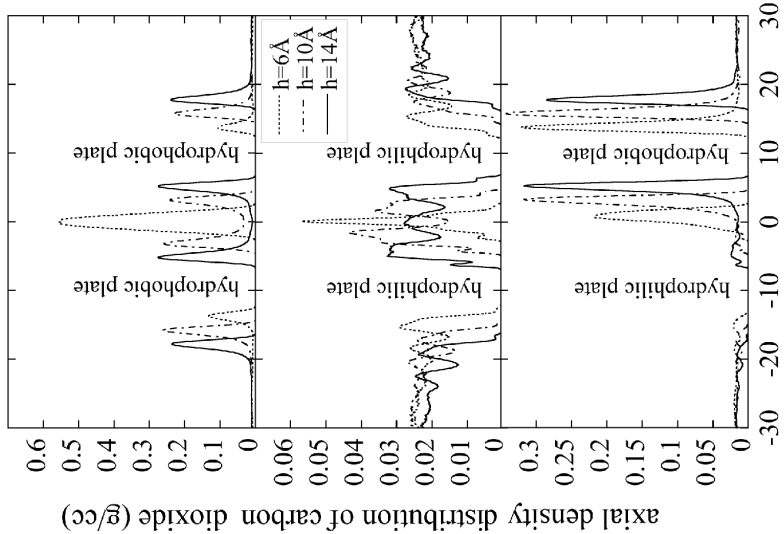

ter expulsion from the plate surfaces, Fig. 17-top), but (ii) rather weakly with fully hydrated hydrophilic plates (through water mediating layers, Fig. 17-middle). In fact, the preferential interaction of CO_2 with the hydrophobic plate surfaces becomes clearly manifested in Fig. 17-top as single strong adsorption peaks, representing local CO_2 environments at the external and internal interfaces over one order of magnitude denser than the corresponding to their bulk counterparts. In contrast the H_2O mediated CO_2 interaction with the hydrophilic plates translates into weak multiple peaks representing local densities of the same order of magnitude as the bulk counterparts (Fig. 17-middle).

Confined fluids behave radically different from their bulk counterparts

An aspect often overlooked when dealing with solid-fluid interaction regards the overlapping of interfacial structures that results in confined environments, as depicted in Figure 14, with a potential for "internal" interface-"external" interface correlations via mineral-mediated interactions whose occurrence might have strong effect on the surface wettability (Olivares et al. 2002). The contrasting behavior of confined fluids depicted in Figures 16-17 has significant implications in the analysis of the caprock reliability associated with the CCUS processes. In fact, it becomes clear that the combination of confinement, surface polarity, and surface mismatch has profound effects on the interfacial fluid composition, species mobility, and surface wettability. As an example, the increasing confinement of H_2O rich-CO_2 phase in equilibrium with its bulk counterpart at 318 K and 20 MPa induces a significant dry out within the silica pore with an inter-plate separation $h = 6$ Å, characterized by a condensed gas-like environment that translates into significantly larger CO_2 diffusivity than the liquid-like environment counterparts (Chialvo et al. 2012).

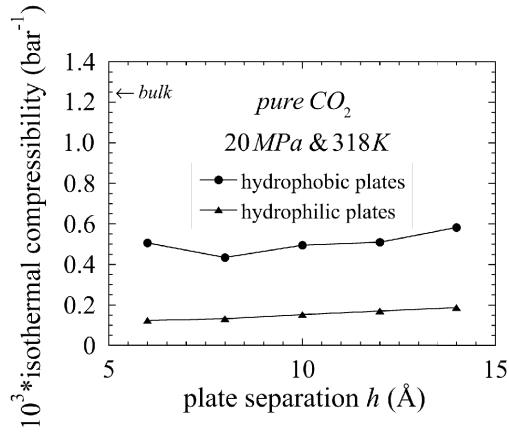

Figure 18. Confinement effect on the isothermal compressibility of fluid CO_2 between silica plates. Contrasting behavior between hydroxylated and non-hydroxylated surfaces.

Another crucial aspect of fluid confinement barely discussed under the CCUS context is the impact of mineral confinement alone and, in combination with, surface polarity on the thermodynamic response functions such as the fluid's isobaric thermal expansivity $\alpha_P = -(\partial \ln\rho/\partial T)_P$ and isothermal compressibility $\kappa_T = (\partial \ln\rho/\partial P)_T$. In Figures 18-19 we illustrate the molecular simulation behavior of those response functions for a pure CO_2 confined phase (EPM2

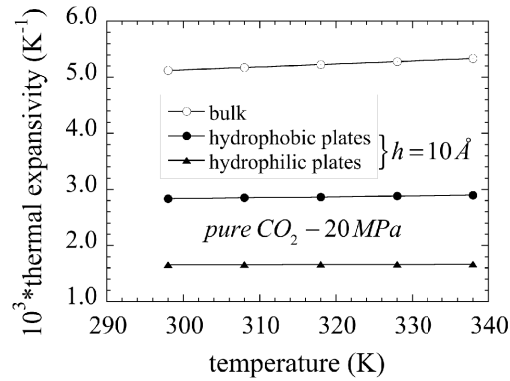

Figure 19. Confinement effect on the isobaric thermal expansivity of fluid CO_2 between silica plates. Contrasting behavior between hydroxylated and non-hydroxylated surfaces.

model of Table 1) in equilibrium with its bulk counterpart at CCUS representative state conditions.

These simulation results provide evidence of the strong contribution of fluid confinement and surface polarity on the isothermal compressibility and thermal expansivity. In particular, note that confinement lowers significantly the values of both properties with respect to the corresponding bulk counterparts, while the surface polarity accentuates the effect, i.e., the larger the surface polarity the stronger the reduction. This behavior is consistent with the fact that the two responses are linked by the slope $(\partial P/\partial T)_\rho$ where ρ denotes the fluid density, and indicates the equivalent environmental response of the confined CO_2 to an isothermal compression and an isobaric cooling.

Moreover, it is instructive to highlight the contrasting behavior between confined CO_2 and confined H_2O under the same type (and model) of silica plates but rather different state conditions and slightly larger inter-plate separations, i.e., $-0.05 \le P(\text{GPa}) \le 0.3$, $220 \le T(\text{K}) \le 300$, and $h = 16$ Å. Giovambattista et al. (2009) found that interfacial water exhibits similar behavior under isobaric cooling or isothermal compression, i.e., water becomes more compressible than its bulk counterpart specially when confined within hydrophobic plates (Giovambattista et al. 2006). In other words, under the same dipolar surface confined CO_2 appears less compressible, while confined H_2O, more compressible than their corresponding bulk counterparts. Note that the observed behavior for the two response functions are more than an academic curiosity, it highlights an frequently overlooked fact that the behavior of a fluid under extreme confinement cannot be described by an EoS (or any other fluid correlation for that matter) at the prevailing state conditions (e.g., pressure, temperature and average confined-fluid density) because it incorporates neither the confinement effect nor the contribution of solid-fluid interactions (Chialvo et al. 2013).

The combination of solid-fluid interactions and confinement effects translates into contrasting behaviors when compared to representative bulk fluid counterparts (e.g., the so called pore-size controlled solubility effect; Rijniers et al. 2005; Emmanuel and Berkowitz 2007) with significant implications in the understanding of microscopic phenomena underlying the basic ideas behind CCUS technologies.

THE CRUCIAL ROLE OF (ACID GAS) CO_2 CONTAMINANTS

As discussed in the previous sections the asymmetry between fluid-fluid and solid-fluid interactions dictates not only the mineral-fluid interfacial structure, Figure 14, but also drives the mineral-surface wettability, the species' local diffusivity and solubility, and ultimately, their reactivity. Therefore, it is imperative to analyze the effect of common CO_2 contaminants on the interfacial behavior of CO_2 rich-mineral interfaces at CCUS conditions in order to gain valuable microscopic insights for the interpretation of experimental evidence and to suggest necessary improvements of the conjectured or *ad hoc* hypotheses involved in current reactive transport modeling. In what follows we highlight some relevant features of the interfacial and confined behavior of these common contaminants, including the selective species co-adsorption driven by surface polarity, as well as the species partition between confinement and bulk based on a research effort currently underway (Chialvo et al. 2013).

Contrasting interfacial behavior of CO_2-rich environments containing H_2O, SO_2, H_2S, or NO_x species

As illustrated in Figure 9, these CO_2 contaminants are all polar species characterized by a (model) dipole moment $-1.64 \le \mu_z(D) \le 2.35$, in comparison with the (model) silica surface polarity of $0.0 \le \mu_z(D) \le -1.8$ (Fig. 15) depending on the degree of surface hydroxylation γ. This scenario anticipates the occurrence of significant changes of interfacial structures resulting

from two effects, i.e., the differential solvation behavior of the dipolar contaminants in the non-polar CO_2, and the preferential adsorption on a polar surface by the minority polar species competing against the overwhelming non-polar CO_2.

Because of its ubiquitous nature, we illustrate first the adsorption behavior of H_2O on partially hydrophilic silica plates, described by the parameter $0.4 \leq \gamma \leq 0.8$, and under confinement with an inter-plate separation of 10 Å (Fig. 20). The outstanding features in this Figure are (a) the strong water adsorption for $\gamma = 0.8$ represented by a liquid-like water layer with the simultaneous expulsion of CO_2 from the silica surface, (b) the stronger adsorption of CO_2 over H_2O for $\gamma = 0.4$, resulting from a weaker (surface)dipole-(water)dipole interactions.

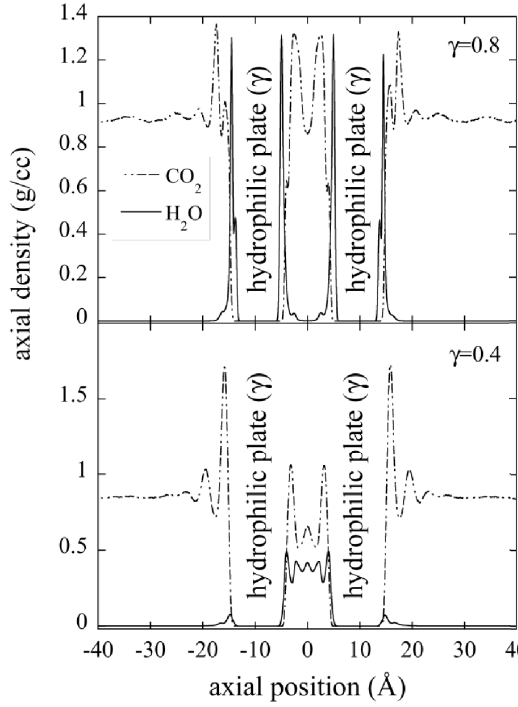

Figure 20. Axial density distribution of H_2O and CO_2 in contact with hydrophilic plates with two different values of surface polarity characterized by the parameter γ, at $T = 318$ K and $P = 20$ MPa.

Note also that as $\gamma \to 0$, i.e., decrease of surface polarity or increase of surface hydrophobicity, water develops a multi-layer adsorption under confinement and exhibits larger local concentration than that of the surrounding fluid environment. In fact, the average mole fraction of confined H_2O is about 0.61 for $\gamma = 0.8$ and decreases to about 0.4 for $\gamma = 0.4$, yet, they are much larger (i.e., by a factor > 50) than the H_2O solubility in CO_2 at the same external state conditions. This behavior bears some similarities to the behavior of dilute CO_2 aqueous solutions under extreme confinement of hydrophobic plates (e.g., Fig. 17 and Fig. 13b of Chialvo et al. 2012).

The location of the adsorbed H_2O on these hydrophilic surfaces is driven by hydrogen bonding between the surface silanol hydrogen and water oxygen. The adsorption is further stabilized by hydrogen bonds between water hydrogens and two other silanol oxygens. Despite the abundance of CO_2 in the bulk phase, the preferential adsorption of H_2O lowers the availability of the most attractive sites and leads to more even water-mediated adsorption of CO_2 over the surface (Fig. 21). The open circles in this Figure denote the positions of the surface Si and O atoms, the dashed lines correspond to the chemical bonds between these atoms, and Si(OH) represents the location of a hydroxylated Si atom, i.e., silanol group.

Unlike H_2O, CO_2 can only form one hydrogen bond between its oxygen and the silanol hydrogen, as well as one weak bond between carbon and hydroxyl oxygen. This different bonding pattern results in the shift of the density maxima away from the positions above Si atom or the center of the hexagonal ring. In contrast, H_2O and CO_2 adsorbed on a less hydrophilic surface, i.e., $\gamma \leq 0.4$, is more evenly distributed between the center of the hexagonal ring and above the Si atom, which is a result of the reduced influence of surface hydrogen bonding of the less polar surface (Fig. 22).

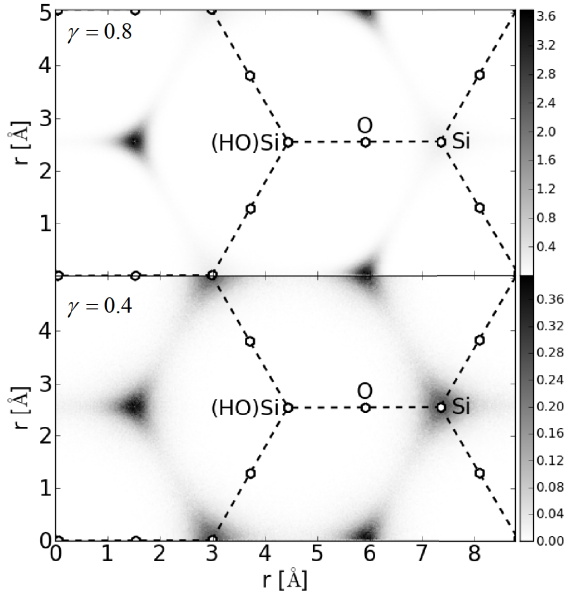

Figure 21. In plane distribution of H_2O within the first adsorption layer on hydrophilic plates with two different values of surface polarity characterized by the parameter γ. Grayscale in units of particles/Å^2.

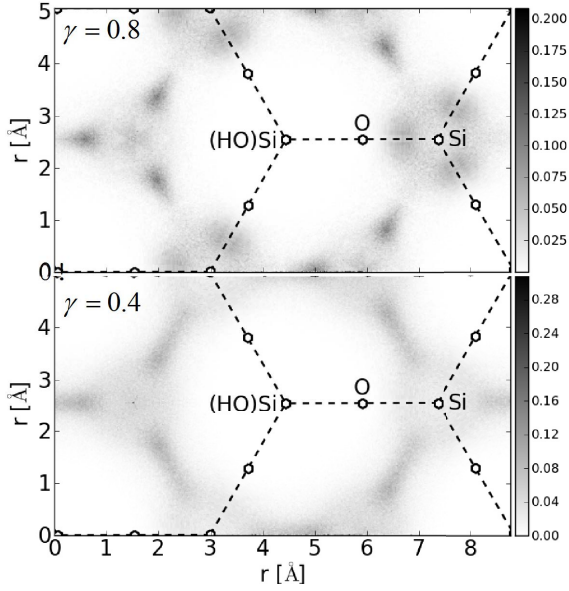

Figure 22. In plane distribution of CO_2 within the first adsorption layer on hydrophilic plates with two different values of surface polarity characterized by the parameter γ. Grayscale in units of particles/Å^2.

In Figures 23-24 we compare the interfacial behavior of SO_2 in the CO_2-rich phase in terms of the corresponding species axial distribution functions for two decreasing inter-plate separations. Due to the high solubility of SO_2 in CO_2, the two species are co-adsorbed within the same layers, i.e., at essentially the same distances from the hydrophobic plates regardless of the nature of the surface. However, there is a clear difference between the "external" and 'internal" interfacial structures; while the strength of the species adsorption in the "external" interfaces appears independent of the interplate separation, fluid layering within the confined region is strongly affected by the overlap of the left and right "internal" interfaces. This

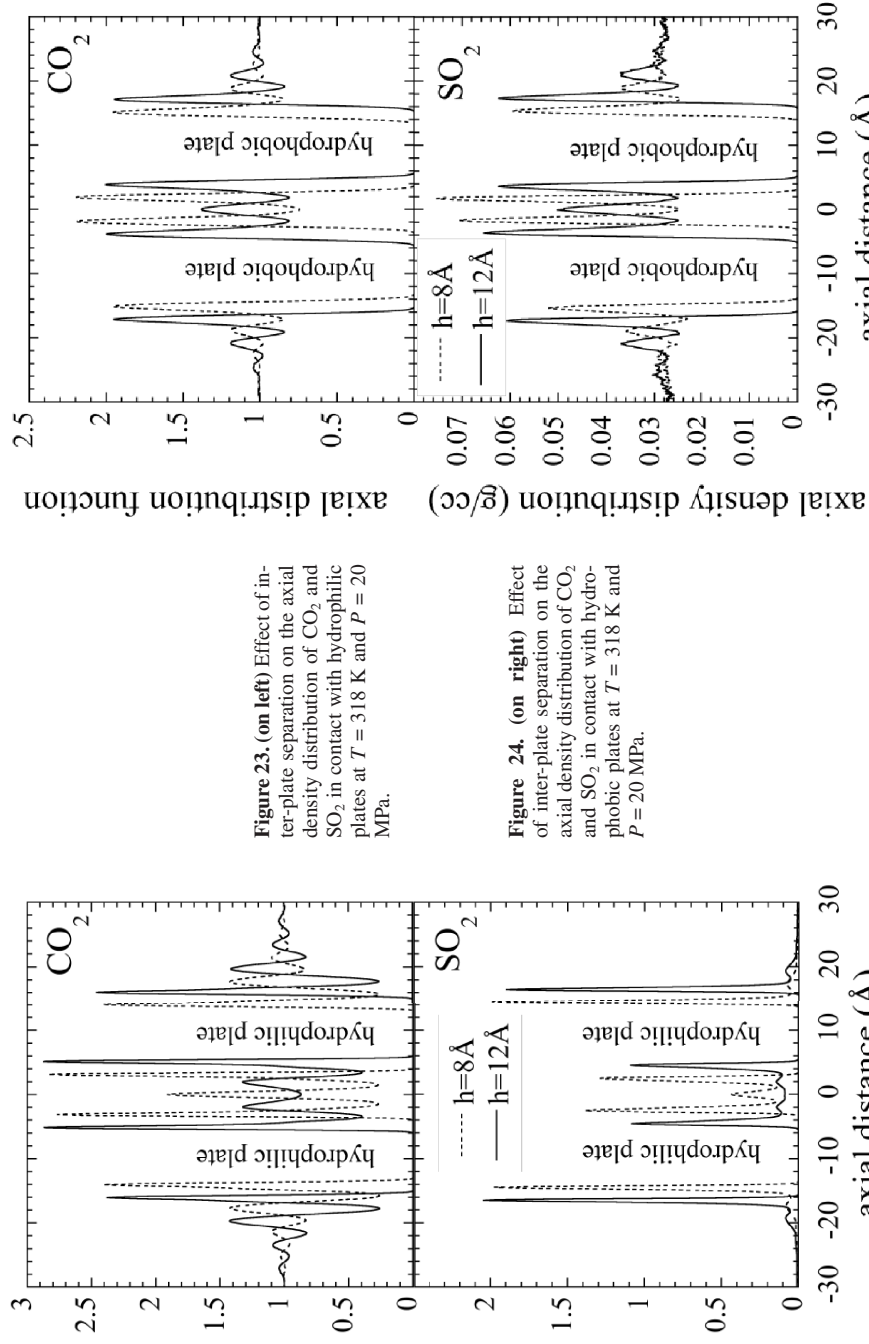

Figure 23. (on left) Effect of inter-plate separation on the axial density distribution of CO_2 and SO_2 in contact with hydrophilic plates at $T = 318$ K and $P = 20$ MPa.

Figure 24. (on right) Effect of inter-plate separation on the axial density distribution of CO_2 and SO_2 in contact with hydrophobic plates at $T = 318$ K and $P = 20$ MPa.

extreme confinement effect, previously observed for the case of dissolved CO_2 in H_2O-rich

solutions under hydrophobic confinement (Chialvo et al. 2012), translates into significant local changes of fluid composition and is yet another manifestation of species partitioning between confined and un-confined solutions.

The adsorption patterns of H_2S and SO_2 follow those of H_2O and CO_2, respectively, reflecting their similar topology with the more electronegative atom either in the central or the end position (Fig. 25). Similar to H_2O, H_2S forms three hydrogen bonds with surrounding hydroxyls, whereas SO_2 typically forms only two stronger bonds (Fig. 26).

While SO_2 and H_2S in CO_2-rich phases exhibits similar interfacial behavior resulting from comparable yet significant dipole moments (despite their opposite signs), the rather small dipole moment of NO_2 provides a better opportunity to interrogate the combined effect of confinement and fluid-fluid intermolecular asymmetry on the species partition. According to Figure 27, the NO_2 adsorption under confinement between hydrophilic plates, separated by an inter-plate distance of 10 Å, appears independent of the solute concentration for the studied state conditions and compositions. This behavior would indicate that $\rho_{NO_2}^{slit} / \rho_{NO_2}^{bulk} \cong H(T,P)$ where $H(T,P) = \int_{V_{slit}} g_{NO_2}(z) dV(z)$ and therefore, that under these conditions the adsorption of NO_2 follows a Henry's law behavior resulting from a rather weak (surface) dipole-(NO_2) dipole interactions.

The simulation results in this section illustrate the significant differences between the properties of bulk, interfacial, and confined environments; they unambiguously highlight the existence of pronounced inhomogeneous density and concentration distributions with profound implications on the transport toward and away from mineral surfaces. In particular, the dramatic confinement-driven concentration en-

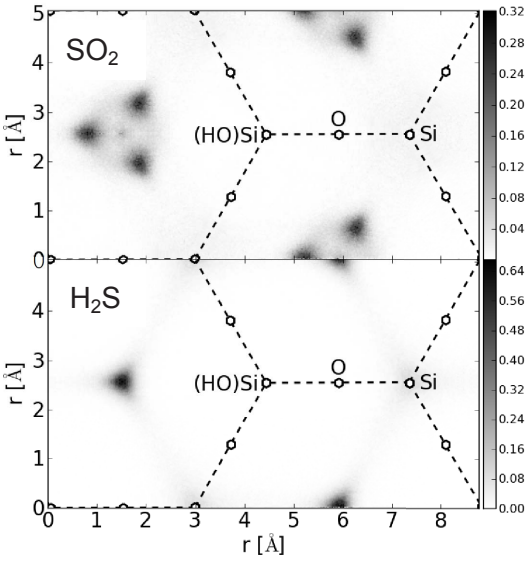

Figure 25. Lateral density (particles/Å^2) profiles of the central atoms within the first adsorption layer of SO_2 (top) and H_2S (bottom) in CO_2-rich phases in contact with hydrophilic silica plates at T = 318 K and P = 20 MPa.

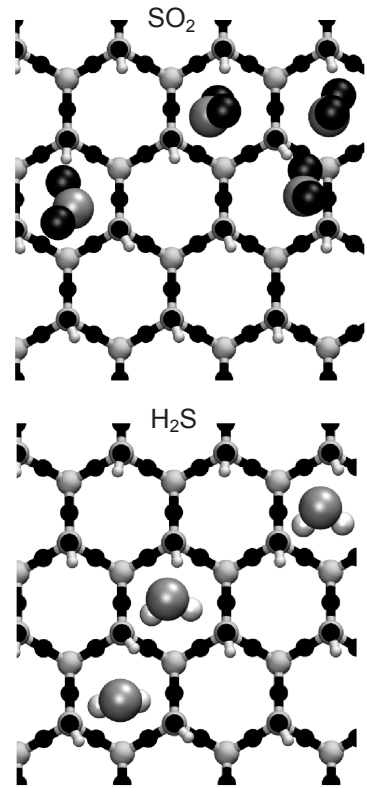

Figure 26. Top view of typical configurations of SO_2 (top) and H_2S (bottom) species in CO_2-rich phases adsorbed in hydrophilic silica plates at T = 318 K and P = 20 MPa.

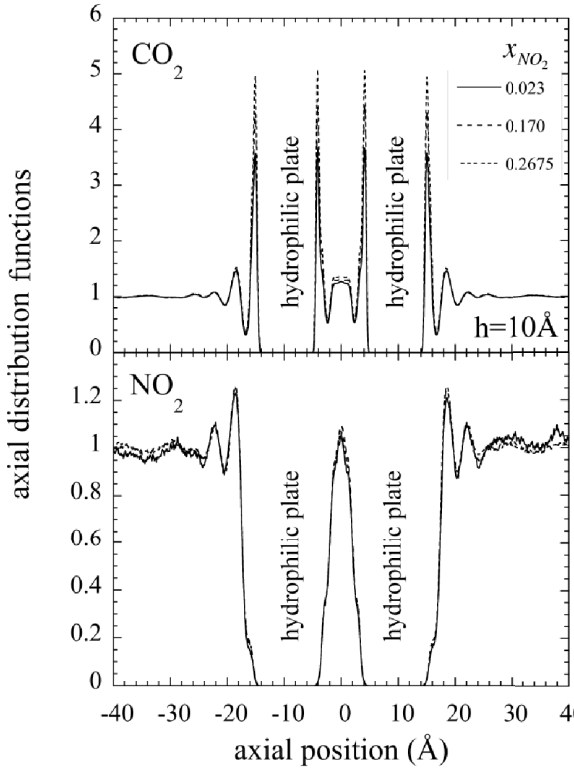

Figure 27. Effect of bulk composition on the axial density distribution of CO_2 and NO_2 in contact with hydrophilic plates at $T = 318$K and $P = 20$ MPa.

hancement of the contaminant species, with respect to the original bulk composition, provides a cautionary note regarding the use of 'well-stirred' conditions for the analysis and reactive transport modeling of these systems, and points again to the crucial need for thermodynamic data for these CO_2-acid gas mixtures as well as their macroscopic correlations to be incorporated into the process modeling.

SUMMARY OF MOLECULAR-BASED OBSERVATIONS AND THEIR IMPLICATIONS IN MACROSCOPIC MODELING

At this point it is quite evident that we have to confront a significant knowledge gap in the area of thermodynamic and thermophysic properties of CO_2-rich phases containing typical contaminants (including water), and consequently, it appears equally obvious that there is a crucial need for an integrated effort to bridge that gap in order to assure success in the design and implementation of the CCUS technology. The lack of experimental data (e.g., for the phase equilibrium of SO_2-H_2S, SO_2-NO_x, H_2S-NO_x, the corresponding aqueous CO_2 multicomponent mixtures, and the kinetics of their aqueous reactivity), and consequently, of suitable macroscopic correlations such as EoS formalisms and reliable mixing rules (including BIP's) to describe accurately the behavior of those fluid phases under proper conditions for pipeline transport and sub-surface storage, pose significant challenges to modelers whose reactive transport codes might not be able to provide realistic solubility calculations.

For the same reasons, most reactive transport simulations of acid gas-bearing CO_2 injections have typically treated the CO_2 and acid gas co-injections as dissolved species in separate liquid brine streams, as opposed to the injection of a supercritical acid-gas bearing CO_2 stream that will ultimately contact the subsurface liquid brines (Gunter et al. 2000; Xu et al. 2007; Xiao et al. 2009). This *ad hoc* approach cannot account for the actual partitioning of the CO_2 contaminants between the CO_2-rich and the aqueous (brine)-rich phases due to differential solubility of the contaminants in the two phases (Bachu and Bennion 2009; Pooladi-Darvish et al. 2009; Savary et al. 2012; Ji and Zhu 2013). A more detailed discussion of the limitations of current reactive transport modeling packages for the interested readers is given elsewhere (Jacquemet et al. 2009, 2011).

Considering the expertize and capabilities in this area, we see no technical obstacles to broad our experimental effort by pursuing thermodynamics and phase equilibria measurements for the missing systems involving CO_2-rich phases (e.g., where SO_2, H_2S, NO_x, and H_2O are the minor components) at CCUS relevant conditions. These activities must be complemented by not only a modeling component aimed at developing accurate macroscopic correlations required in the reactive transport modeling packages but also, a molecular-based parameterization effort of the desired force fields to support the concomitant microscopic modeling.

It has become also much clearer that we have a considerably precarious understanding of the thermochemical behavior of acid gas-bearing CO_2 fluids under mineral confinement, due in part to the confluence of limited experimental data, difficult interpretation of raw data, and the involvement of indirect probes. This scenario advocates the need for a concerted effort to probe experimentally the physico-chemical interactions between acid gas-contaminated CO_2 and (synthetic or otherwise) porous mineral substrates under diffusion- and reaction-controlled conditions, within dry and wet environments. This effort should include volumetric/density determinations (Gruszkiewicz et al. 2012) involving acid gas-CO_2 adsorption, in situ pH measurements, and chemical analysis to characterize the outcome of the fluid-mineral reactivity.

The success of the CCUS technology depends on the caprock ability to prevent gas leakage, i.e., the capillary-sealing efficiency of the caprock that according to the Laplace law, depends on caprock surface wettability and becomes controlled by the fluid-gas interfacial tension (Israelachvili 1992). Therefore, it becomes crucial to understand how the CO_2 contaminants can modify the fluid-mineral wettability, the corresponding fluid-gas interfacial tension, and consequently, the caprock's sealing efficiency. In particular, there is a wide knowledge gap regarding the pressure, temperature, and composition dependence of the interfacial tension of CO_2-rich phases containing acid-gas contaminants, as well as their wetting behavior involving subsurface minerals. Moreover, the lack of experimental data for the thermodynamic and transport properties of CO_2-X systems also limits the experimental probes via non-invasive approaches, to extract microscopic insights needed in the force-field parameterization of mineral-fluid interactions, and subsequently, the interpretation and characterization of sought after interfacial phenomena.

Even though the non-polarizable force field parameterizations described in the section "Force fields for CO_2-acid gas systems" (e.g., Tables 1 and 4) have been rather successful in the description of the pure component behavior, this success transfers only partially to their mixtures because the adjustment of the combining rules to define the unlike-pair interactions cannot always counter the effects of the large polarity asymmetry between CO_2 and the solute species. In fact, as we have argued previously for the case of CO_2-H_2O mixtures (Vlcek et al. 2011), the adjustment of unlike-pair interaction parameters must be achieved with the simultaneous correction for over-polarization involving the fixed-charge non-polarizable species. The current molecular simulation effort involving the polar species H_2O, SO_2, H_2S, and NO_2 dissolved in CO_2-rich phases, suggests the need for the explicit incorporation of

polarizable interactions in order to account properly for the significant variation of polarity asymmetry in dilute solute solutions. This is by no means an easy task or a straightforward target but the soundest way to deal properly with these molecular asymmetries.

CONCLUDING REMARKS

We have discussed the rationale behind the need for a molecular-based understanding of the interaction of acid gases, as contaminants of CO_2, with subsurface mineral formations, and consequently, the interpretation of mineral-fluid interfacial and confinement phenomena aimed at their manipulation and ultimate control in the context of the CCUS process. Toward that end, we have highlighted selected but significant knowledge gaps, identified relevant molecular modeling challenges, suggested potential approaches to pursue them, and provided the pertinent and up to date supporting references.

ACKNOWLEDGMENTS

Support for this work comes from the U.S. Department of Energy, Office of Science, Office of Basic Energy Sciences, through the Center for Nanoscale Control of Geologic CO_2, an Energy Frontier Reseearch Center, (FWP ERKCC67) under contract DE-AC05-00OR22725 to Oak Ridge National Laboratory, managed and operated by UT-Battelle, LLC.

REFERENCES

Alba-Simionesco C, Coasne B, Dosseh G, Dudziak G, Gubbins KE, Radhakrishnan R, Sliwinska-Bartkowiak M (2006) Effects of confinement on freezing and melting. J Phys Condens Matter 18:R15-R68

Albrecht BA, Benson CH (2001) Effect of desiccation on compacted natural clays. J Geotech Geoenviron Eng 127:67-75

Allen MP, Tildesley DJ (1987). Computer Simulation of Liquids. Oxford University Press, Oxford

Angeli M, Soldal M, Skurtveit E, Aker E (2009) Experimental percolation of supercritical CO_2 through a caprock. Energy Procedia 1:3351-3358

Anheden M, Andersson A, Bernstone C, Eriksson S, Yan J, Liljemark S, Wall C (2005) CO_2 quality requirement for a system with CO_2 capture, transport and storage. *In:* Greenhouse Gas Control Technologies 7. Volume II – Part 2. Wilson M, Gale J, Rubin ES, Keith DW, Gilboy CF, Morris T, Thambimuthu K (eds) Elsevier, p 2559-2564

Argyris D, Cole DR, Striolo A (2009) Dynamic behavior of interfacial water at the silica surface. J Phys Chem C 113: 19591-19600

Bachu S, Bennion DB (2009) Chromatographic partitioning of impurities contained in a CO_2 stream injected into a deep saline aquifer: Part 1. Effects of gas composition and in situ conditions. Int J Greenhouse Gas Control 3:458-467

Bacon DH, Murphy EM (2011) Managing chemistry underground: is co-sequestration an option in selected formations? Energia Procedia 4:4457-4464

Bacon DH, Sass BM, Bhargava M, Sminchak J, Gupta N (2009) Reactive transport modeling of co_2 and so_2 injection into deep saline formations and their effect on the hydraulic properties of host rocks. Energy Procedia 1:3283-3290

Baranyai A, Bartok A, Chialvo AA (2005) Computer simulation of the 13 crystalline phases of ice. J Chem Phys 123:54502

Baranyai A, Bartok A, Chialvo AA (2006) Limitations of the rigid planar non-polarizable models of water. J Chem Phys 124:74507

Belkadi A, Llovell F, Gerbaud V, Vega LF (2008) Modeling the vapor-liquid equilibrium and association of nitrogen dioxide/dinitrogen tetroxide and its mixtures with carbon dioxide. Fluid Phase Equilib 266:154-163

Bennion DB, Bachu S (2008) Drainage and imbibition relative permeability relationships for supercritical CO_2/brine and H_2S/brine systems in intergranular sandstone, carbonate, shale, and anhydrite rocks. SPE Reservoir Eval Eng 11:487-496

Benson SM, Cole DR (2008) CO_2 sequestration in deep sedimentary formations. Elements 4:325-331

Berendsen HJC, Postma JPM, van Gunsteren WF, Hermans J (1981) Interaction models for water in relation to protein hydration. *In:* Intermolecular Forces: Proceedings of the Fourteenth Jerusalem Symposium on Quantum Chemistry and Biochemistry. Pullman B (ed) Reidel, p 331-342

Berendsen HJC, Grigera JR, Straatsma TP (1987) The missing term in effective pair potentials. J Phys Chem 91:6269-6271

Berthelot D (1898) Sur le mélange des gaz. CR Hebd Seances Acad Sci 126:1703-1855

Bierlein JA, Kay WB (1953) Phase equilibrium properties of system carbon dioxide-hydrogen sulfide. Ind Eng Chem 45:618-624

Bluemcke A (1888) Determination of the specific weight and of the vapour-pressure of mixtures of sulphurous and carbonic anhydrides. Ann Phys Chem 34:10-21

Bluemcke A (1889) Isotherms of a mixture of sulphurous and carbonic anhydrides. Ann Phys Chem 36:911-923

Blum L, Wei DQ (1987) Analytical solution of the mean spherical approximation for an arbitrary mixture of ions in a dipolar solvent. J Chem Phys 87:555-565

Botan A, Rotenberg B, Marry V, Turq P, Noetinger B (2011) Hydrodynamics in clay nanopores. J Phys Chem C 115: 16109-16115

Boulougouris GC, Economou IG, Theodorou DN (1998) Engineering a molecular model for water phase equilibrium over a wide temperature range. J Phys Chem B 102:1029-1035

Bourasseau E, Lachet V, Desbiens N, Maillet JB, Teuler JM, Ungerer P (2008) Thermodynamic behavior of the CO_2 + NO_2/N_2O_4 mixture: a Monte Carlo simulation study. J Phys Chem B 112:15783-15792

Camy S, Letourneau JJ, Condoret JS (2011) Experimental study of high pressure phase equilibrium of (CO_2 + NO_2/N_2O_4) mixtures. J Chem Thermodyn 43:1954-1960

Carroll JJ (2003) Problem is the result of industry's move to use higher pressures. Pipeline Gas J 230:60-61

Castrillon SRV, Giovambattista N, Aksay IA, Debenedetti PG (2009) Effect of surface polarity on the structure and dynamics of water in nanoscale confinement. J Phys Chem B 113:1438-1446

Caubet F (1902) The liquefaction of gas mixtures. Z Physik Ch 40:257-367

Caubet F (1904) Liquefaction of gas mixtures group: carbon dioxide, nitrous oxide. Z f Physik Ch 49:101-116

Chakma A (1997) Acid gas re-injection - a practical way to eliminate CO_2 emissions from gas processing plants. Energy Convers Manage 38:S205-S209

Chapman WG, Gubbins KE, Jackson G, Radosz M (1989) SAFT equation of state solution model for association fluids. Fluid Phase Equilib 52:31-38

Chesta MA, Ramia ME, Jeandrevin S, Martin CA (2009) Nano-pore size and porosity study by means of nuclear magnetic resonance and positronium annihilation lifetime. Appl Phys A 97:301-307

Chestnut LG, Mills DM(2005) A fresh look at the benefits and costs of the US acid rain program. J Environ Manage 77:252-266

Chialvo AA (1991) Excess properties of liquid mixtures from computer simulation: a coupling-parameter approach to the determination of their dependence on molecular asymmetry. Mol Phys 73:127-140

Chialvo AA (2013) Solvation phenomena in dilute solutions: formal, experimenta evidence, and modeling implications. *In:* Fluctuation Theory of Solutions: Applications in Chemistry, Chemical Engineering and Biophysics. Matteoli E, Smith PE, O'Connell JP (eds). CRC Press. Boca Raton Florida, p 191-224

Chialvo AA, Cummings PT (1996a) Engineering a simple polarizable model for the molecular simulation of water applicable over wide ranges of state conditions. J Chem Phys 105:8274-8281

Chialvo AA, Cummings PT (1996b) Microstructure of ambient and supercritical water. a direct comparison between simulation and neutron scattering experiments. J Phys Chem 100:1309-1316

Chialvo AA, Debenedetti PG (1992) Molecular dynamics study of solute-solute microstructure in attractive and repulsive supercritical mixtures. Ind Eng Chem Res 31:1391-1397

Chialvo AA, Vlcek L, Cole DR (2012) Aqueous CO_2 solutions at silica surfaces and within nanopore environments. insights from isobaric-isothermal molecular dynamics. J Phys Chem C 116:13904-13916

Chialvo AA, Vlcek L, Cole DR (2013) Selective partitioning of CO_2 contaminants in silica nano-pores. To be submitted.

Cole DR, Chialvo AA, Rother G, Vlcek L, Cummings PT (2010) Supercritical fluid behavior at nanoscale interfaces: Implications for CO_2 sequestration in geologic formations. Philos Mag 90:2339-2363

Cole IS, Corrigan P, Sim S, Birbilis N (2011) Corrosion of pipelines used for CO_2 transport in CCS: Is it a real problem? Int J Greenhouse Gas Control 5:749-756

Cook D (1953) The carbon dioxide-nitrous oxide system in the critical region. Proc R Soc London Ser A 219:245-256

Crandell LE, Ellis BR, Peters CA (2010) Dissolution potential of SO_2 co-injected with CO_2 in geologic sequestration. Environ Sci Technol 44:349-355

Cummings LWT (1931) High-pressure rectification. Ind Eng Chem 23:900-902

Cygan RT, Romanov VN, Myshakin EM (2012) Molecular simulation of carbon dioxide capture by montmorillonite using an accurate and flexible force field. J Phys Chem C 116:13079-13091

Davison J (2007) Performance and costs of power plants with capture and storage of CO_2. Energy 32:1163-1176

de Hemptinne JC, Behar E (2000) Thermodynamic properties of acid gas containing systems: Literature review. Oil Gas Sci Technol 55:617-637

de Souza LES, Deiters UK (2000) Modeling of the N_2O_4-NO_2 reacting system. Phys Chem Chem Phys 2:5606-5613

Delgado-Barrio G, Prosmiti R, Villarreal P, Winter G, Medina JS, Gonzalez B, Aleman JV, Gomez JL, Sangra P, Santana JJ, Torres ME (2008). Viscosity of liquid water via equilibrium molecular dynamics simulations. *In:* Frontiers in Quantum Systems in Chemistry and Physics. Vol 18. Wilson S, Grout PJ, Maruani J, Delgado-Barrio G, Piecuch P (eds) Springer, Dordrecht, p 351-361

Diamantonis NI, Economou IG (2011) Evaluation of statistical associating fluid theory (SAFT) and perturbed chain-SAFT equations of state for the calculation of thermodynamic derivative properties of fluids related to carbon capture and sequestration. Energy Fuels 25:3334-3343

Diamantonis NI, Economou IG (2012) Modeling the phase equilibria of a H2O-CO_2 mixture with PC-SAFT and tPC-PSAFT equations of state. Mol Phys 110:1205-1212

Diamantonis NI, Boulougouris GC, Mansoor E, Tsangaris DM, Economou IG (2013) Evaluation of cubic, SAFT, and PC-SAFT equations of state for the vapor–liquid equilibrium modeling of CO_2 mixtures with other gases. Ind Eng Chem Res 52:3933-3942

El Ahmar E, Creton B, Valtz A, Coquelet C, Lachet V, Richon D, Ungerer P (2011) Thermodynamic study of binary systems containing sulphur dioxide: Measurements and molecular modelling. Fluid Phase Equilib 304:21-34

Ellis BR, Crandell LE, Peters CA (2010) Limitations for brine acidification due to SO_2 co-injection in geologic carbon sequestration. Int J Greenhouse Gas Control 4:575-582

Emmanuel S, Berkowitz B (2007) Effects of pore-size controlled solubility on reactive transport in heterogeneous rock. Geophys Res Lett 34:L06404, doi:10.1029/2006GL028962

Errington JR, Kiyohara K, Gubbins KE, Panagiotopoulos AZ (1998) Monte Carlo simulation of high-pressure phase equilibria in aqueous systems. Fluid Phase Equilib 151:33-40

Espinoza DN, Santamarina JC (2010) Water-CO_2-mineral systems: Interfacial tension, contact angle, and diffusion-Implications to CO_2 geological storage. *Water Resources Research* 46:W07537, doi:10.1029/2009WR008634

Fanourgakis GS, Medina JS, Prosmiti R (2012) Determining the bulk viscosity of rigid water models. J Phys Chem A 116:2564-2570

Fender BEF, Halsey GD (1962) Second virial coefficients of argon, krypton, and argon-krypton mixtures at low temperatures. J Chem Phys 36:1881, doi: 10.1063/1.1701284

Figueroa JD, Fout T, Plasynski S, McIlvried H, Srivastava RD (2008) Advances in CO_2 capture technology - The US Department of Energy's Carbon Sequestration Program. Int J Greenhouse Gas Control 2:9-20

Forester TR, McDonald IR, Klein ML (1989) intermolecular potentials and the properties of liquid and solid hydrogen-sulfide. Chem Phys 129:225-234

Gale J (2009) Impure thoughts. Int J Greenhouse Gas Control 3:1-2

Galliero G, Nieto-Draghi C, Boned C, Avalos JB, Mackie AD, Baylaucq A, Montel F (2007) Molecular dynamics simulation of acid gas mixtures: A comparison between several approximations. Ind Eng Chem Res 46:5238-5244

Gaus I (2010) Role and impact of CO_2-rock interactions during CO_2 storage in sedimentary rocks. Int J Greenhouse Gas Control 4:73-89

Gaus I, Audigane P, Andre L, Lions J, Jacquemet N, Dutst P, Czernichowski-Lauriol I, Azaroual M (2008) Geochemical and solute transport modelling for CO_2 storage, what to expect from it? Int J Greenhouse Gas Control 2:605-625

GHG (2003) Potential for improvements in Gasification Combined Cycle Power Generation with CO_2 Capture. International Energy Agency Greenhouse Gas R&D program {IEA GHG}. Chetenham, U.K.

Ghoufi A, Goujon F, Lachet V, Malfreyt P (2008) Multiple histogram reweighting method for the surface tension calculation. J Chem Phys 128:154718

Gibbons TG, Klein ML (1974) Thermodynamic properties for a simple model of solid carbon dioxide. monte carlo, cell model, and quasiharmonic calculations. J Chem Phys 60:112-126

Giovambattista N, Debenedetti PG, Rossky PJ (2007) Effect of surface polarity on water contact angle and interfacial hydration structure. J Phys Chem B 111:9581-9587

Giovambattista N, Rossky PJ, Debenedetti PG (2006) Effect of pressure on the phase behavior and structure of water confined between nanoscale hydrophobic and hydrophilic plates. Phys Rev E 73:041604

Giovambattista N, Rossky PJ, Debenedetti PG (2009) Effect of temperature on the structure and phase behavior of water confined by hydrophobic, hydrophilic, and heterogeneous surfaces. J Phys Chem B 113:13723-13734

Giovambattista N, Rossky PJ, Debenedetti PG (2012) Computational studies of pressure, temperature, and surface effects on the structure and thermodynamics of confined water. Annu Rev Phys Chem 63:179-200

Gonzalez MA, Abascal JLF (2010) The shear viscosity of rigid water models. J Chem Phys 132:96101
Good RJ, Hope CJ (1970) New combining rule for intermolecular distances in intermolecular potential functions. J Chem Phys 53:540-543
Gruszkiewicz MS, Rother G, Wesolowski DJ, Cole DR, Wallacher D (2012) Direct measurements of pore fluid density by vibrating tube densimetry. Langmuir 28:5070-5078
Guissani Y, Guillot BJ (1993) A computer simulation study of the liquid-vapor coexistence curve of water. J Chem Phys 98:8221-8235
Gunter WD, Perkins EH, Hutcheon I (2000) Aquifer disposal of acid gases: modelling of water-rock reactions for trapping of acid wastes. Appl Geochem 15:1085-1095
Haile JM (1992) Molecular Dynamics Simulation. John Wiley & Sons. New York
Halgren TA (1992) Representation of Van der waals (Vdw) interactions in molecular mechanics force-fields - potential form, combination rules, and vdw parameters. J Am Chem Soc 114:7827-7843
Hansen N, Agbor FAB, Keil FJ (2007) New force fields for nitrous oxide and oxygen and their application to phase equilibria simulations. Fluid Phase Equilib 259:180-188
Harris JG, Yung KH (1995) Carbon dioxide liquid-vapor coexistence curve and critical properties as predicted by a simple molecular model. J Phys Chem 99:12021-12024
Hayward TM, Svishchev IM (2001) Equations of state and phase coexistence properties for simulated water. Fluid Phase Equilib 182:65-73
Hiza MJ, Duncan AG (1970) A correlation for prediction of interaction energy parameters for mixtures of small molecules. AiChE J 16:733-738
Housecroft CE, Sharpe AG (2008). Inorganic Chemistry. Person/Prentice Hall. Harlow
Hudson GH, McCoubrey JC (1960) Intermolecular forces between unlike molecules - a more complete form of the combing rules. Trans Faraday Soc 56:761-766
in't Veld PJ, Ismail AE, Grest GS (2007) Application of Ewald summations to long-range dispersion forces. J Chem Phys 127:144711
Ismail AE, Grest GS, Stevens MJ (2006) Capillary waves at the liquid-vapor interface and the surface tension of water. J Chem Phys 125:14702
Israelachvili J (1992). Intermolecular & Surface Forces. Academic Press. London
Jacquemet N, Pironon J, Caroli E (2005) A new experimental procedure for simulation of H_2S+CO_2 geological storage. Oil Gas Sci Technol Rev IFP 60:193-203
Jacquemet N, Pironon J, Saint-Marc J (2008) Mineralogical changes of a well cement in various H_2S-CO_2(-brine) fluids at high pressure and temperature. Environ Sci Technol 42:282-288
Jacquemet N, Le Gallo Y, Estublier A, Lachet V, von Dalwigk I, Yan J, Azaroual M, Audigane P (2009) CO_2 streams containing associated components - a review of the thermodynamic and geochemical properties and assessment of some reactive transport codes. Energy Procedia 1:3739-3746
Jacquemet N, Picot-Colbeaux G, Vong CQ, Lions J, Bouc O, Jeremy R (2011) Intrusion of CO_2 and impurities in a freshwater aquifer - impact evaluation by reactive transport modelling. Energy Procedia 4:3202-3209
Ji XY, Zhu C (2013) Predicting possible effects of H_2S impurity on CO_2 transportation and geological storage. Environ Sci Technol 47:55-62
Jorgensen WL (1986) Intermolecular potential functions and Monte Carlo simulations for liquid sulfur compounds. J Phys Chem 90:6379-6388
Kamath G, Lubna N, Potoff JJ (2005) Effect of partial charge parametrization on the fluid phase behavior of hydrogen sulfide. J Chem Phys 123:124505
Kamath G, Potoff JJ (2006) Monte Carlo predictions for the phase behavior of H_2S + n-alkane, H_2S+CO_2, CO_2+CH_4 and H_2S+CO_2+CH_4 mixtures. Fluid Phase Equilib 246:71-78
Kaszuba JP, Janecky DR, Snow MG (2005) Experimental evaluation of mixed fluid reactions between supercritical carbon dioxide and NaCl brine: Relevance to the integrity of a geologic carbon repository. Chem Geol 217:277-293
Kaszuba J, Yardley B, Andreani M (2013) Experimental perspectives of mineral dissolution and precipitation due to carbon dioxide-water-rock interactions. Rev Mineral Geochem 77:153-188
Katsube TJ, Williamson MA (1994) Effects of diagenesis on shale nano-pore structure and implications for sealing capacity. Clay Miner 29:451-461
Kellerman SJ, Stouffer CE, Eubank PT, Holste JC, Hall KR, Gammon BE, March KN (1995). Thermodynamic Properties of CO_2+H_2S Mixtures. College Station, Texas A&M
Ketko MH, Kamath G, Potoff JJ (2011) Development of an optimized intermolecular potential for sulfur Dioxide. J Phys Chem B 115:4949-4954
Kharaka YK, Cole DR, Hovorka SD, Gunter WD, Knauss KG, Freifeld BM (2006) Gas-water-rock interactions in Frio Formation following CO_2 injection: Implications for the storage of greenhouse gases in sedimentary basins. Geology 34:577-580
Kim Y, Wan JM, Kneafsey TJ, Tokunaga TK (2012) Dewetting of silica surfaces upon reactions with supercritical CO_2 and brine: pore-scale studies in micromodels. Environ Sci Technol 46:4228-4235

Klemenc A, Bankowski O (1932) Properties of volatile hydrides. III. The system: H_2S-CO_2. Z Anorg Allg Chem 209:225-235

Knauss KG, Johnson JW, Steefel CI (2005) Evaluation of the impact of CO_2, co-contaminant gas, aqueous fluid and reservoir rock interactions on the geologic sequestration of CO_2. Chem Geol 217:339-350

Koenen M, Tambach TJ, Neele FP (2011) Geochemical effects of impurities in CO_2 on a sandstone reservoir. Energy Procedia 4:5343-5349

Kohler F (1957) Zur Berechnung der Wechselwirkungsenergie zwischen ungleichen Molekülen in binären flüssigen Mischungen. Monatsh Chem 88:857-877

Kohler F, Fischer J, Wilhelm E (1982) Intermolecular force parameters for unlike pairs. J Mol Struct 84:245-250

Kohler F, Pfennig A (1989) Molecular fluids and mixtures. Pure Appl Chem 61:1041-1050

Kong CL (1973a) Atomic distortion and repulsive interactions of noble-gas atoms. J Chem Phys 59:968-969

Kong CL (1973b) Combining rules for intermolecular potential parameters. 2. Rules for Lennard-Jones (12-6) potential and Morse potential. J Chem Phys 59:2464-2467

Kontogeorgis GM, Michelsen ML, Folas GK, Derawi S, von Solms N, Stenby EH (2006) Ten years with the CPA (Cubic-Plus-Association) equation of state. Part 1. Pure compounds and self-associating systems. Ind Eng Chem Res 45:4855-4868

Kristof T, Liszi J (1997) Effective intermolecular potential for fluid hydrogen sulfide. J Phys Chem B 101:5480-5483

Kummerow J, Spangenberg E (2011) Experimental evaluation of the impact of the interactions of CO_2-SO_2, brine, and reservoir rock on petrophysical properties: A case study from the Ketzin test site, Germany. Geochem Geophys Geosys 12:Q05010, doi:10.1029/2010GC003469

Lachet V, de Bruin T, Ungerer P, Coquelet C, Valtz A, Hasanov V, Lockwood F, Richon D (2009) Thermodynamic behavior of the CO_2 + SO_2 mixture: experimental and Monte Carlo simulation studies. Energia Procedia 1:1641-1647

Lachet V, Creton B, de Bruin T, Bourasseau E, Desbiens N, Wilhelmsen O, Hammer M (2012) Equilibrium and transport properties of CO_2+N_2O and CO_2+NO mixtures: Molecular simulation and equation of state modelling study. Fluid Phase Equilib 322:66-78

Lee SH, Rossky PJ (1994) A comparison of the structure and dynamics of liquid water at hydrophobic and hydrophilic surfaces - a molecular-dynamics simulation study. J Chem Phys 100:3334-3345

Li H, Yan J (2009a) Evaluating cubic equations of state for calculation of vapor-liquid equilibrium of CO_2 and CO_2-mixtures for CO_2 capture and storage processes. Appl Energy 86:826-836

Li H, Yan J (2009b) Impacts of equations of state (EOS) and impurities on the volume calculation of CO_2 mixtures in the applications of CO_2 capture and storage (CCS) processes. Appl Energy 86:2760-2770

Li ZD, Firoozabadi A (2009) Cubic-plus-association equation of state for water-containing mixtures: is "cross association" necessary? AiChE J 55:1803-1813

Li H, Yan J, Yan J, Anheden M (2009) Impurity impacts on the purification process in oxy-fuel combustion based CO_2 capture and storage system. Appl Energy 86:202-213

Li HL, Jakobsen JP, Wilhelmsen O, Yan JY (2011a) PVTxy properties of CO_2 mixtures relevant for CO_2 capture, transport and storage: Review of available experimental data and theoretical models. Appl Energy 88:3567-3579

Li HL, Wilhelmsen O, Lv YX, Wang WL, Yan JY (2011b) Viscosities, thermal conductivities and diffusion coefficients of CO_2 mixtures: Review of experimental data and theoretical models. Int J Greenhouse Gas Control 5:1119-1139

Liu Y, Panagiotopoulos AZ, Debenedetti PG (2011) Monte Carlo simulations of high-pressure phase equilibria of CO_2-H_2O Mixtures. J Phys Chem B 115:6629-6635

Liu FY, Lu P, Griffith C, Hedges SW, Soong Y, Hellevang H, Zhu C (2012) CO_2-brine-caprock interaction: Reactivity experiments on Eau Claire shale and a review of relevant literature. Int J Greenhouse Gas Control 7:153-167

Lorentz HA (1881) Ueber die Anwendung des Satzes vom Virial in der kinetischen Theorie der Gase. Ann Phys 248:127-136

Malani A, Ayappa KG, Murad S (2009) Influence of hydrophilic surface specificity on the structural properties of confined water. J Phys Chem B 113:13825-13839

Mantovani M, Chiesa P, Valenti G, Gatti M, Consonni S (2012) Supercritical pressure-density-temperature measurements on CO_2-N_2, CO_2-O_2 and CO_2-Ar binary mixtures. J Supercrit Fluids 61:34-43

Maple JR (1998). Force fields: general discussion. *In:* Encyclopedia of Computational Chemistry. Vol 2. von Ragué Schleyer P (ed) John Wiley & Sons, Chichester, p 1015-1024

Mazzoccoli M, Bosio B, Arato E (2012) Pressure-density-temperature measurements of binary mixtures rich in CO_2 for pipeline transportation in the CCS process. J Chem Eng Data 57:2774-2783

Medina JS, Prosmiti R, Villarreal P, Delgado-Barrio G, Winter G, Gonzalez B, Aleman JV, Collado C (2011) Molecular dynamics simulations of rigid and flexible water models: Temperature dependence of viscosity. Chem Phys 388:9-18

Merker T, Engin C, Vrabec J, Hasse H (2010) Molecular model for carbon dioxide optimized to vapor-liquid equilibria. J Chem Phys 132:234512

Metz B, Davidson O, Coninck H, Loos M, Meyer L (2005). Carbon Dioxide Capture and Sorage. New York, Intergovernmental Panel on Climate Change 2005

Miller PJ, van Atten C (2004). North American Power Plant Air Emissions. Commission for Environmental Cooperation of North America. Montreal, Canada

Mohitpour M, Jenkins A, Gabe N (2008) A generalized overview of requirements for the design, construction, and operation of new pipelines for CO_2 sequestration. J Pipeline Eng 7:237-252

Moller D, Fischer J (1994) Determination of an effective intermolecular potential for carbon-dioxide using vapor liquid-phase equilibria from npt plus test particle simulations. Fluid Phase Equilib 100:35-61

Muller EA, Gelb LD (2003) Molecular modeling of fluid-phase equilibria using an isotropic multipolar potential. Ind Eng Chem Res 42:4123-4131

Murthy CS, Singer K, McDonald IR (1981) Interaction site models for carbon dioxide. Mol Phys 44:135-143

Neyt JC, Wender A, Lachet V, Malfreyt P (2011) Prediction of the temperature dependence of the surface tension Of SO_2, N_2, O_2, and Ar by Monte Carlo molecular simulations. J Phys Chem B 115:9421-9430

Nieto-Draghi C, de Bruin T, Perez-Pellitero J, Avalos JB, Mackie AD (2007) Thermodynamic and transport properties of carbon dioxide from molecular simulation. J Chem Phys 126:64509

Nieto-Draghi C, Mackie AD, Avalos JB (2005) Transport coefficients and dynamic properties of hydrogen sulfide from molecular simulation. J Chem Phys 123:14505

NIST (2013) "NIST Webbook." from *http://webbook.nist.gov/chemistry/*

Nogueira M, Mamora DD (2008) Effect of flue-gas impurities on the process of injection and storage of CO_2 in depleted gas reservoirs. J Energy Res Technol 130:013301, doi: 10.1115/1.2825174

O'Connell JP, Haile JM (2005). Thermodynamics: Fundamentals for Applications. New York, Cambridge University Press

Oelkers EH, Cole DR (2008) Carbon dioxide sequestration: a solution to a global problem. Elements 4:305-310

Olivares W, Degreve L, Villegas JC, Lozada-Cassou M (2002) Liquid correlation across the walls in a slit pore: Effect on the wetting and drying transition. Phys Rev E 65:061702

Osinubi KJ, Nwaiwu CMO (2008) Desiccation-induced shrinkage in compacted lateritic soils. Geotech Geol Eng 26:603-611

Palandri JL, Kharaka YK (2005) Ferric iron-bearing sediments as a mineral trap for CO_2 sequestration: Iron reduction using sulfur-bearing waste gas. Chem Geol 217:351-364

Panagiotopoulos AZ (1987) Direct determination of phase coexistence properties of fluids by Monte Carlo simulation in a new ensemble. Mol Phys 61:813-826

Pauwels H, Gaus I, le Nindre YM, Pearce J, Czernichowski-Lauriol I (2007) Chemistry of fluids from a natural analogue for a geological CO_2 storage site (Montmiral, France): Lessons for CO_2-water-rock interaction assessment and monitoring. Appl Geochem 22:2817-2833

Pellegrini LA, Moioli S, Gamba S, Ceragioli P (2012) Prediction of vapor-liquid equilibrium for reservoir mixtures with cubic equations of state: Binary interaction parameters for acidic gases. Fluid Phase Equilib 326:45-49

Pena MD, Pando C, Renuncio JAR (1982) Combination rules for intermolecular potential parameters. 2. Rules based on approximations for the long-range dispersion energy and an atomic distortion model for the repulsive interactions. J Chem Phys 76:333-339

Perfetti E, Thiery R, Dubessy J (2008a) Equation of state taking into account dipolar interactions and association by hydrogen bonding: II - Modelling liquid-vapour equilibria in the H_2O-H_2S, H_2O-CH_4 and H_2O-CO_2 systems. Chem Geol 251:50-57

Perfetti E, Thiery R, Dubessy J (2008b) Equation of state taking into account dipolar interactions and association by hydrogen bonding. I: Application to pure water and hydrogen sulfide. Chem Geol 251:58-66

Pipitone G, Bolland O (2009) Power generation with CO_2 capture: Technology for CO_2 purification. Int J Greenhouse Gas Control 3:528-534

Pironon J, Jacquemet N, Lhomme T, Teinturier S (2007) Fluid inclusions as micro-samplers in batch experiments: A study of the system C-O-H-S-cement for the potential geological storage of industrial acid gas. Chem Geol 237:264-273

Pooladi-Darvish M, Hong H, Stocker RK, Bennion B, Theys S, Bachu S (2009) Chromatographic partitioning of H_2S and CO_2 in acid gas disposal. J Can Pet Technol 48:52-57

Posch S, Haider M (2012) Optimization of CO_2 compression and purification units (CO_2CPU) for CCS power plants. Fuel 101:254-263

Potoff JJ, Errington JR, Panagiotopoulos AZ (1999) Molecular simulation of phase equilibria for mixtures of polar and non-polar components. Mol Phys 97:1073-1083

Puibasset J, Pellenq RJM (2008) Grand canonical Monte Carlo simulation study of water adsorption in silicalite at 300 K. J Phys Chem B 112:6390-6397

Race JM, Wetenhall B, Seevam PN, Downie MJ (2012) Towards a CO_2 pipeline specification defining tolerance limits for impurities. J Pipeline Eng 173-190

Radlinski AP, Ioannidis MA, Hinde AL, Hainbuchner M, Baron M, Rauch H, Kline SR (2004) Angstrom-to-millimeter characterization of sedimentary rock microstructure. J Colloid Interface Sci 274:607-612

Reamer HH, Sage BH (1952) Volumetric behavior of nitrogen dioxide in the liquid phase. Ind Eng Chem 44:185-187

Ricaurte M, Torre JP, Asbai A, Broseta D, Dicharry C (2012) experimental data, modeling, and correlation of carbon dioxide solubility in aqueous solutions containing low concentrations of clathrate hydrate promoters: application to CO_2-CH_4 gas mixtures. Ind Eng Chem Res 51:3157-3169

Rijniers LA, Huinink HP, Pel L, Kopinga K (2005) Experimental evidence of crystallization pressure inside porous media. Phys Rev Lett 94:075503, doi: 10.1103/PhysRevLett.94.075503

Rochelle C, Czernichowski-Lauriol I, Milodowski AE (2004) The impact of chemical reactions on CO_2 storage in geological formations: a brief review. *In:* Geological Storage of Carbon Dioxide. Baines SJ, Worden RH (eds) The Geological Society, London. Special Publications 233:87-233, doi: 10.1144/GSL.SP.2004.233.01.07

Rodriguez J, Elola MD, Laria D (2009) Polar mixtures under nanoconfinement. J Phys Chem B 113:12744-12749

Rowlinson JS, Sutton JR, Weston JF (1957) Liquid-vapor equilibrium in the ternary system carbon dioxide-nitrous oxide-ethylene. *In:* Proceedings of the International conference on Thermodynamic and Transport Properties of Fluids. Institution of Mechanical Engineers (London), p 10-14

Ruhl AS, Kranzmann A (2012) Corrosion behavior of various steels in a continuous flow of carbon dioxide containing impurities. Int J Greenhouse Gas Control 9:85-90

Sadhukhan S, Gouze P, Dutta T (2012) Porosity and permeability changes in sedimentary rocks induced by injection of reactive fluid: A simulation model. J Hydrol 450:134-139

Sakamaki R, Sum AK, Narumi T, Yasuoka K (2011) Molecular dynamics simulations of vapor/liquid coexistence using the nonpolarizable water models. J Chem Phys 134:124708

Sanz E, Vega C, Abascal JLF, MacDowell LG (2004) Phase diagram of water from computer simulation. Phys Rev Lett 92

Savary V, Berger G, Dubois M, Lacharpagne JC, Pages A, Thibeau S, Lescanne M (2012) The solubility of CO_2+H_2S mixtures in water and 2 M NaCl at 120 degrees C and pressures up to 35 MPa. Int J Greenhouse Gas Control 10:123-133

Shah V, Broseta D, Mouronval G, Montel F (2008) Water/acid gas interfacial tensions and their impact on acid gas geological storage. Int J Greenhouse Gas Control 2:594-604

Shukla R, Ranjith P, Haque A, Choi X (2010) A review of studies on CO_2 sequestration and caprock integrity. Fuel 89:2651-2664

Sikora PT (1970) Combining rules for spherically symmetric intermolecular potentials. J Phys B At Mol Phys 3:1475-1482

Smith WR, Triska B (1994) The reaction ensemble method for the computer simulation of chemical and phase equilibria. I. Theory and basic examples. J Chem Phys 100:3019-3027

Soave G (1972) Equilibrium constants from modified Redlich-Kwong equation of state. Chem Eng Sci 27:1197-1203

Sobocinski DP, Kurata F (1959) Heterogeneous phase equilibria of hydrogen sulfide-carbon dioxide systems AiChE J 5:545-551

Sokolic F, Guissani Y, Guillot B (1985) Molecular dynamics simulation of thermodynamic and structural properties of liquid SO_2. Mol Phys 56:239-253

Sokolic F, Guissani Y, Baranovic G (1986) Intermolecular pair potentials and the second virial coefficient of suphur dioxide vapor. Chem Phys Lett 131:513-516

Song J, Zhang DX (2013) Comprehensive review of caprock-sealing mechanisms for geologic carbon sequestration. Environ Sci Technol 47:9-22

Søreide I, Whitson CH (1992) Peng-Robinson predictions for hydrocarbons, CO_2, N_2, and H_2S with pure water and NaCl brine. Fluid Phase Equilib 77:217-240

Spycher N, Pruess K, Ennis-King J (2003) CO_2-H_2O mixtures in the geological sequestration of CO_2. I. Assessment and calculation of mutual solubilities from 12 to 100 degrees C and up to 600 bar. Geochim Cosmochim Acta 67:3015-3031

Steckel F (1945) Vapor-liquid equilibria under pressure of some binary hydrogen sulfide-containing systems. Sven Kem Tidskr 57:209-216

Tang KT, Toennies JP (1991) A combining rule calculation of the Vanderwaals potentials of the rare-gas hydrides. Chem Phys 156:413-425

Tang XH, Gross J (2010) Modeling the phase equilibria of hydrogen sulfide and carbon dioxide in mixture with hydrocarbons and water using the PCP-SAFT equation of state. Fluid Phase Equilib 293:11-21

Thiel A, Schulte E (1920) Binary equilibrium system with solid carbon dioxide. Z Phys Chem 96:312-342

Tohidi B, Anderson R, Chapoy A, Yang JH, Burgass RW (2012) Do we have new solutions to the old problem of gas hydrates? Energy Fuels 26:4053-4058

Tsivintzelis I, Kontogeorgis GM, Michelsen ML, Stenby EH (2010) Modeling phase equilibria for acid gas mixtures using the CPA equation of state. I. Mixtures with H_2S. AiChE J 56:2965-2982

Tsivintzelis I, Kontogeorgis GM, Michelsen ML, Stenby EH (2011) Modeling phase equilibria for acid gas mixtures using the CPA equation of state. Part II: Binary mixtures with CO_2. Fluid Phase Equilib 306:38-56

Ungerer P, Nieto-Draghi C, Rousseau B, Ahunbay G, Lachet V (2007) Molecular simulation of the thermophysical properties of fluids: From understanding toward quantitative predictions. J Mol Liquids 134:71-89

Vega C, de Miguel E (2007) Surface tension of the most popular models of water by using the test-area simulation method. J Chem Phys 126:154707

Vega C, McBride C, Sanz E, Abascal JLF (2005) Radial distribution functions and densities for the SPC/E, TIP4P and TIP5P models for liquid water and ices I-h, I-c, II, III, IV, V, VI, VII, VIII, IX, XI and XII. Phys Chem Chem Phys 7:1450-1456

Verma S, Oakes CS, Chugunov N, Ramakrishnan TS (2011) Effect of contaminants on the thermodynamic properties of CO_2-rich fluids and ramifications in the design of surface and injection facilities for geologic CO_2 sequestration. Energia Procedia 4:2340-2347

Vlcek L, Chialvo AA, Cole DR (2011) Optimized unlike-pair interactions for water-carbon dioxide mixtures described by the SPC/E and EPM2 models. J Phys Chem B 115:8775-8784

von Ragué Schleyer P (1998) Encyclopedia of Computational Chemistry, John Wiley & Sons. Chichester

Vorholz J, Harismiadis VI, Rumpf B, Panagiotopoulos AZ, Maurer G (2000) Vapor plus liquid equilibrium of water, carbon dioxide, and the binary system, water plus carbon dioxide, from molecular simulation. Fluid Phase Equilib 170:203-234

Vrabec J, Stoll J, Hasse H (2001) A set of molecular models for symmetric quadrupolar fluids. J Phys Chem B 105:12126-12133

Waldman M, Hagler AT (1993) New combining rules for rare-gas Van-Der-Waals parameters. J Comput Chem 14:1077-1084

Wang JS, Ryan D, Anthony EJ, Wildgust N, Aiken T (2011) Effects of impurities on CO_2 transport, injection and storage. Energy Procedia 4:3071

Wertheim MS (1984) Fluids with highly directional attractive forces. I. Statistical thermodynamics J Stat Phys 35:19-34

Wilke FDH, Vasquez M, Wiersberg T, Naumann R, Erzinger J (2012) On the interaction of pure and impure supercritical CO_2 with rock forming minerals in saline aquifers: An experimental geochemical approach. Appl Geochem 27:1615-1622

Xiang Y, Wang Z, Xu C, Zhou CC, Li Z, Ni WD (2011) Impact of SO_2 concentration on the corrosion rate of X70 steel and iron in water-saturated supercritical CO_2 mixed with SO_2. J Supercrit Fluids 58:286-294

Xiang Y, Wang Z, Yang XX, Li Z, Ni WD (2012) The upper limit of moisture content for supercritical CO_2 pipeline transport. J Supercrit Fluids 67:14-21

Xiao YT, Xu TF, Pruess K (2009) The effects of gas-fluid-rock interactions on CO_2 injection and storage: insights from reactive transport modeling. Energy Procedia 1:1783-1790

Xu B, Nagashima K, DeSimone JM, Johnson CS (2003) Diffusion of water in liquid and supercritical carbon dioxide: An NMR study. J Phys Chem A 107:1-3

Xu TF, Apps JA, Pruess K, Yamamoto H (2007) Numerical modeling of injection and mineral trapping of CO_2 with H_2S and SO_2 in a sandstone formation. Chem Geol 242:319-346

Yoo JH, Breitholz A, Iwai Y, Yoo KP (2012) Diffusion coefficients of supercritical carbon dioxide and its mixtures using molecular dynamic simulations. Korean J Chem Eng 29:935-940

Yoon H, Valocchi AJ, Werth CJ, Dewers T (2012) Pore-scale simulation of mixing-induced calcium carbonate precipitation and dissolution in a microfluidic pore network. Water Resour Res 48:W02524, doi:10.1029/2011WR011192

Yoshizawa K, Sato K, Murakami H, Shikazono N, Fujimoto K, Nakata M (2009) Open-nano pores in natural minerals studied by positron lifetime spectroscopy. *In:* Positron and Positronium Chemistry. Vol 607. Wang SJ, Chen ZQ, Wang B, Jean YC (eds). Trans Tech Publ Ltd. Zurich, p 189-191

Zhang W, Xu TF, Li YL (2011) Modeling of fate and transport of coinjection of H_2S with CO_2 in deep saline formations. J Geophys Res [Solid Earth] 116:B02202, doi: 10.1029/2010JB007652

Zhang ZG, Duan ZH (2005) An optimized molecular potential for carbon dioxide. J Chem Phys 122:214507

Zhu AM, Zhang XB, Liu QL, Zhang QG (2009) A fully flexible potential model for carbon dioxide. Chinese J Chem Eng 17:268-272

Reviews in Mineralogy & Geochemistry
Vol. 77 pp. 399-430, 2013
Copyright © Mineralogical Society of America

Geochemical Monitoring for Potential Environmental Impacts of Geologic Sequestration of CO_2

Yousif K. Kharaka[§], David R. Cole*, James J. Thordsen, Kathleen D. Gans, R. Burt Thomas

U. S. Geological Survey
345 Middlefield Rd
Menlo Park, California 94025, U.S.A.

**Ohio State University*
School of Earth Sciences
Columbus, Ohio 43210, U.S.A.
[§]*ykharaka@usgs.gov*

INTRODUCTION

Carbon dioxide sequestration is now considered an important component of the portfolio of options for reducing greenhouse gas emissions to stabilize their atmospheric levels at values that would limit global temperature increases to the target of 2 °C by the end of the century (Pacala and Socolow 2004; IPCC 2005, 2007; Benson and Cook 2005; Benson and Cole 2008; IEA 2012; Romanak et al. 2013). Increased anthropogenic emissions of CO_2 have raised its atmospheric concentrations from about 280 ppmv during pre-industrial times to ~400 ppmv today, and based on several defined scenarios, CO_2 concentrations are projected to increase to values as high as 1100 ppmv by 2100 (White et al. 2003; IPCC 2005, 2007; EIA 2012; Global CCS Institute 2012). An atmospheric CO_2 concentration of 450 ppmv is generally the accepted level that is needed to limit global temperature increases to the target of 2 °C by the end of the century. This temperature limit likely would moderate the adverse effects related to climate change that could include sea-level rise from the melting of alpine glaciers and continental ice sheets and from the ocean warming; increased frequency and intensity of wildfires, floods, droughts, and tropical storms; and changes in the amount, timing, and distribution of rain, snow, and runoff (IPCC 2007; Sundquist et al. 2009; IEA 2012). Rising atmospheric CO_2 concentrations are also increasing the amount of CO_2 dissolved in ocean water lowering its pH from 8.1 to 8.0, with potentially disruptive effects on coral reefs, plankton and marine ecosystems (Adams and Caldeira 2008; Schrag 2009; Sundquist et al. 2009). Sedimentary basins in general and deep saline aquifers in particular are being investigated as possible repositories for the large volumes of anthropogenic CO_2 that must be sequestered to mitigate global warming and related climate changes (Hitchon 1996; Benson and Cole 2008; Verma and Warwick 2011).

Currently there are eight large-scale commercial projects worldwide that inject ~23 Mt CO_2/yr and that provide valuable experience for assessing the efficacy of carbon capture and storage (CCS); there are another 13 projects in advanced planning to inject 27 Mt CO_2/yr (IEA 2012; Global CCS Institute 2012). There are also more than 100 commercial enhanced oil recovery (EOR) projects worldwide with ~80% in the USA, primarily in the prolific oil reservoirs of the Permian Basin of Texas and New Mexico. In the USA, EOR started in 1973 and currently 6% of oil production is from EOR operations; CO_2 sales for EOR reached 56 Mt CO_2/yr (~3 billion ft^3/d) in 2008 (Moritis 2009; Hovorka and Tinker 2010). In addition

1529-6466/13/0077-0011$05.00 http://dx.doi.org/10.2138/rmg.2013.77.11

there are approximately 25 geologic sequestration field demonstration projects in the US at various stages of planning and deployment, and an equal number of projects in other countries (including the Minami-Nagaoka in Japan, the Otway and Gorgon in Australia, the Pembina Cardium in Canada, and the Ketzin in Germany) that are investigating the storage of CO_2 in various clastic and carbonate rock formations using different injection schemes, monitoring methods, hazards assessment protocols, and mitigation strategies (Torp and Gale 2003; Litynski et al. 2008; Mito et al. 2008, 2013; Cook 2009; Haszeldine 2009; Hitchon 2009; Matter et al. 2009, 2011; Michael et al. 2009; Johnson et al. 2011; IEA 2012; Global CCS Institute 2012; Humez et al. 2013).

Results of geochemical studies from these sites and from natural analogues proved powerful in: (i) Tracking the successful injection of CO_2 in the reservoir rocks (e.g., Hovorka et al. 2006; Kharaka and Cole 2011; Kharaka et al. 2013); (ii) detecting the leakage of CO_2 and brine using natural and added chemical and isotopic tracers (e.g., Wells et al. 2007; Kharaka et al. 2009); (iii) showing mobilization of metals and organics, and major changes in chemical and isotopic compositions of brine (e.g., Kharaka et al. 2006; Cantucci et al. 2009; Lu et al. 2012); (iv) indicating that mineral trapping is a strong function of the chemical composition of formation brine and reservoir minerals (e.g., Audigane et al. 2007; Oelkers et al. 2008; Matter et al. 2009; Xu et al. 2010); and (v) indicating that dissolution in brine is a major long-term sink for CO_2 (e.g., Gilfillan et al. 2009).

Considerable uncertainties and scientific gaps, however, still exist in understanding CO_2-brine-mineral interactions at reservoir conditions, because supercritical CO_2 is buoyant, displaces huge volumes of formation water and becomes reactive when dissolved in the formation water (Haszeldine 2009; Zuddas 2010; Lu et al. 2012). Dissolved CO_2 is likely to react with the reservoir and cap rocks, causing dissolution, precipitation and transformation of minerals, and changing the porosity, permeability and injectivity of the reservoir, as well as impacting the extent of CO_2 and brine leakage that, as noted by Kharaka et al. (2006, 2009, 2013) and Benson and Cole (2008), could contaminate underground sources of drinking water (USDW).

In this review, we discuss the geochemistry of CO_2 sequestration in subsurface reservoirs, emphasizing CO_2-brine-mineral interactions in sedimentary basins at reservoir conditions. We discuss geochemical results obtained from natural CO_2 analogues (e.g., Baines and Worden 2004; Gilfillan et al. 2009), and from the major CO_2 injection field sites, especially our reported results from the Frio Brine Pilot tests and the Cranfield CO_2-EOR and sequestration site, both US DOE funded multi-laboratory field experiments located near Dayton, Texas, and western Mississippi, respectively (Hovorka et al. 2006; Kharaka et al. 2006; 2009; Lu et al. 2012). We emphasize temporal changes in the chemical and isotopic composition of formation brine and gases that were used for tracking the injected CO_2 in the reservoir and for investigating potential leakage of CO_2 and brine into the overlying sandstones or into shallow groundwater. Significant isotopic and chemical changes, including the lowering of pH, increases in alkalinity and electrical conductance (EC), and mobilization of metals, were also observed in samples obtained from shallow groundwater following controlled CO_2 injection at the zero emission research and technology (ZERT) site, located in Bozeman, Montana (Spangler et al. 2009; Kharaka et al. 2010b; Lewicki et al. 2010; Wells et al. 2010; Zhou et al. 2012). The importance of natural and man-made aqueous and gaseous tracers for both the "deep" and "shallow" monitoring is emphasized (Wells et al. 2007; Kharaka et al. 2009, 2011; Nimz and Hudson 2005; Hogan et al. 2012; Myers et al. 2013). Results from both the deep and shallow field tests investigated by us and those reported by others show that highly sensitive chemical and isotopic tracers are available to monitor injection performance and for early detection of any CO_2 and brine leakages (Kharaka et al. 2009, 2013; Romanak et al. 2012a, b).

FIELD AND LABORATORY METHODS

Much of the detailed information that has been generated on the composition of deep waters in sedimentary basins has come from the analysis of aqueous fluids coproduced with crude oil and natural gas. Approximately 4 million oil and gas wells have been drilled in the United States since 1859; fewer than one million of these wells are currently producing oil and/or gas (Breit et al. 2001; Kharaka et al. 2009). Most fluid sampling takes place from valves at the wellhead or at a separator rather than downhole. The fluids are therefore subjected to major reductions in temperature and pressure, to gas loss, and to exposure to oxidizing conditions during sampling. The special methods that must be used in sample collection, preservation, and field and laboratory determinations of chemical components and isotopes in formation waters are detailed in Lico et al. (1982), Kharaka et al. (1985) and Kharaka and Hanor (2013).

Because of the importance of understanding water-rock-gas interactions in field experiments conducted to investigate the potential for geologic storage of CO_2, a more rigorous sampling protocol has been introduced using evacuated and/or syringe-like downhole samplers (500-1000 ml volume) that provided accurate data on water and gas compositions of the subsurface fluids (Kharaka et al. 2006, 2009; Hovorka et al. 2006). During the CO_2 injection in the Frio brine tests, intensive fluid sampling was obtained from an observation well using a novel downhole U-tube system designed for this experiment to track the arrival of CO_2. The brine enters at the bottom of the tube, which is placed just above the perforated zone and is pushed to the surface using N_2, Ar, or even groundwater (Freifeld et al. 2005). Following its use in the Frio brine tests, the U-tube has been used at other sites, including Ketzin (Martens et al. 2012), Otway (Boreham et al. 2011; Underschultz et al. 2011), Cranfield (Lu et al. 2012) and Citronelle (Conaway et al. 2012). The drilling and circulation fluids used in the well were tagged with Rhodamine WT, and fluorescein, to allow for the identification of uncontaminated formation water (Kharaka et al. 2006). Tracer gases, including SF_6, noble gases, tagged CH_4, and several perfluorocarbon tracer gases (PFTs), were injected with the CO_2 to map its flow path in the reservoir sandstone and identify any leakage into the overlying sandstones (Phelps et al. 2006; Kharaka et al. 2009).

For conventional sampling of petroleum wells, production fluids are collected in pre-washed and prerinsed 8 or 20 L carboys with a bottom spigot. Water and oil require from 5 min to several hours to separate, depending on the temperature, the proportion of water, and the composition of oil and water. Immediately after separation of water from oil, the water is passed through glass wool to remove solids and oil droplets before the samples are collected in separate 125 ml flint-glass bottles with Polyseal caps for the field determination of EC, pH, Eh, alkalinity, and H_2S and for laboratory determination of the carbon isotopes (Lico et al. 1982; Kharaka and Hanor 2013). A different method for the determination of DIC carbon isotopes, involving purified CO_2 released by acidification of a water sample is described in Evans et al. (2002).

Filtration and preservation of water samples immediately after collection is important to prevent loss of constituents through precipitation and sorption. Filtration through a 0.45 μm filter, using either compressed nitrogen or compressed air as the pressure source, is adequate for the determination of the major cations and all of the anions. Filtration through a 0.1 μm filter, however, is required for the determination of aluminum, mercury, and other trace metals, because colloidal oxyhydroxides of iron and manganese and clay particles can pass through larger pores; these particles would then dissolve upon sample acidification, increasing the concentration of these and other trace metals (Kennedy et al. 1974; Kharaka et al. 1987, 2009). Filtration and field chemical determinations are better performed in a mobile laboratory equipped with pH meters, a spectrophotometer, filtration, titration, and other field equipment. Because of the presence of oil, the measurement of Eh is difficult for oil-field waters, even when using flow-through cells (Kharaka et al. 1987).

Samples collected for heavy and trace metals (iron, manganese, lead, zinc, and mercury) require additional care to minimize contact of the sample with air during collection and filtration. Contact with air will lead to oxidation of some metals (e.g., Fe^{2+}) and their precipitation as oxyhydroxides, leading to coprecipitation and adsorption of other metals. Contact with air is minimized by (1) flushing the air in the carboy with nitrogen or argon or even natural gas; (2) inserting the tubing from the wellhead as far down in the carboy as possible through a hole drilled through the cap; (3) filling the carboy completely with the fluids; (4) plugging the hole in the cap with a rubber stopper after the carboy is filled; (5) minimizing the length of the Tygon tubing connecting the filtration unit to the carboy and filling it with formation water prior to filtration; (6) discarding the first 250 ml of the filtered sample; and (7) using the next liter of filtered water to rinse the collection bottles (Kharaka et al. 1987).

Samples for the analysis of dissolved organic compounds are filtered through a 0.45 μm Teflon or silver filter and stored in amber bottles fitted with Teflon inserts in the caps. To minimize contamination of organics, stainless steel filtration units and copper or metal tubing are used for collection and filtration of these samples. Mercuric chloride (40 mg/l mercury) is added as a bactericide and the filtered samples are stored chilled at ~4 °C until analysis.

Methodologies for the laboratory analysis of cations and metals include the use of inductively coupled plasma optical emission spectrometry (ICP/OES) or the combination of ICP with mass spectrometry (ICP/MS) (Ivahnenko et al. 2001; Harmon and Vannucci 2006). The advantages of plasma techniques include (1) a wide and linear dynamic concentration range, (2) multi element capability, and (3) relative freedom from matrix interferences. The use of ion chromatography (IC), gas chromatography (GC), and GC/MS has increased for the analysis of anions and dissolved organics (Barth 1987; Ivahnenko et al. 2001; Kharaka and Hanor 2013).

GEOLOGIC STORAGE OF CO_2

Combustion of fossil fuels releases large amounts of greenhouse gases (GHGs), primarily CO_2 to the atmosphere. In 2011, 31.6 Gt CO_2 were added to the atmosphere from these sources, and the amount is projected to increase to 43 Gt by 2030 (Haszeldine 2009; Global CCS Institute 2012; EIA 2012). Sedimentary basins in general and deep saline aquifers in particular are being investigated as possible repositories for the large volumes of anthropogenic CO_2 that must be sequestered to mitigate global warming and related climate changes (Hitchon 1996; Benson and Cole 2008). Depleted petroleum fields and saline aquifers in these basins are attractive for CO_2 storage, because they have huge potential storage capacity, estimated at >10,000 Gt CO_2 worldwide, and advantageous locations close to major CO_2 sources (Holloway 1997; Oelkers and Cole 2008; Rubin 2008). In addition, a great deal of relevant geological, geochemical and hydrologic information can be obtained from the large number of wells (~4 million in USA) drilled for oil and gas operations. Most of the new CCS projects in North America, China, Europe and the Middle East, however, are targeting EOR and enhanced gas recovery (EGR) operations that also provides an additional source of revenue (Hovorka and Tinker 2010; Global CCS Institute 2012).

Initially, the bulk of injected CO_2 will be stored as supercritical fluid because the target reservoirs are likely to have temperatures and pressures higher than 31 °C and 74 bar, the critical values for CO_2. Some of the injected CO_2 will rapidly dissolve in formation water, but mineral trapping, which would depend largely on the availability of reactive Ca, Mg, Fe and other divalent cations in formation water or the reservoir rocks, would be slower, yet more permanent, because many carbonate phases can remain stable for geologically significant time periods (Gunter et al. 1993; Hitchon 1996; Palandri and Kharaka 2005; Oelkers et al. 2008; Matter et al. 2009). Understanding gas-water-mineral-interactions in sedimentary basins could facilitate the isolation of anthropogenic CO_2 in the subsurface for thousands of years (White

et al. 2003; Kharaka et al. 2006). Because of economic benefits and more than 30 years of commercial application, it is expected that injection into depleted petroleum fields for EOR will be the earliest method of CO_2 disposal. However, as the amounts of CO_2 to be sequestered increase, deep saline aquifers will likely become preferred storage sites, because of their huge potential capacity and advantageous locations close to CO_2 sources (Holloway 1997; Hitchon et al. 1999; Cantucci et al. 2009). In addition to storage capacity, key environmental questions include CO_2 leakage related to the storage integrity, and the physical and chemical processes that are initiated by injecting CO_2 underground (Allis et al. 2005; Hepple and Benson 2005; Knauss et al. 2005; Birkholzer et al. 2008; Kharaka and Cole 2011; Lu et al. 2012).

CO_2 trapping mechanisms

Reservoir capacity, performance and integrity are strongly affected by the four possible CO_2 trapping mechanisms (Benson and Cook 2005; Friedmann 2007; Benson and Cole 2008): (1) "Structural and stratigraphic trapping," where the injected CO_2 is stored as a supercritical and buoyant fluid below a cap rock or adjacent to an impermeable barrier; (2) "residual trapping" of CO_2 by capillary forces in the pores of reservoir rocks away from the supercritical plume; (3) "solution trapping," where the CO_2 is dissolved in formation water forming aqueous species such as $H_2CO_3^\circ$, HCO_3^-, and CO_3^{-2}; and (4) "mineral trapping," with the CO_2 precipitated as calcite, magnesite, siderite and dawsonite (Gunter et al. 1993; Palandri et al. 2005; Bénézeth et al. 2007, 2009; Oelkers et al. 2008; Matter et al. 2011). Results from general (Benson and Cook 2005) and site-specific (Han 2008; Han and McPherson 2008; Xu et al. 2010) simulations indicate that initially the bulk of CO_2 will be stored as supercritical fluid, because the target reservoirs are likely to have temperature and pressure values higher than the critical values for CO_2. The amount of CO_2 residually trapped is likely to be small until the injection is terminated and the CO_2 plume migrates away from the injection wells (Han and McPherson 2008). As the injected CO_2 contacts the formation water, it rapidly dissolves in it to saturation, with the dissolved CO_2 comprising 1-5% of brine weight at the likely injection reservoir conditions at 1-4 km below ground level (Spycher et al. 2003; Spycher and Pruess 2005; Benson and Cole 2008; Burruss et al. 2009). Equations of state for CO_2 indicate that its solubility increases with decreasing salinity of formation water, increasing proportion of dissolved Ca to Na and increasing pressure of CO_2; solubility decreases with increasing temperature to about 150 °C, with solubility increasing at higher temperatures (Duan and Sun 2003; Rosenbauer et al. 2005; Spycher and Pruess 2005; Li and Duan 2007). Results from natural gas fields dominated by a CO_2 phase that provide a natural analogue for assessing the geological storage of anthropogenic CO_2 over millennial time scales (Ballentine et al. 2001) indicated that solution in formation water was the sole or the major sink for CO_2 (Gilfillan et al. 2008, 2009).

Computer simulations, laboratory experiments, and field tests indicate that mineral trapping would be slower but more permanent, and the amount sequestered dependent on the chemical composition of the formation water and reservoir pressure and temperature, but primarily on the chemical composition and reactivity of the reservoir minerals (Hitchon 1996; Kaszuba et al. 2005; Knauss et al. 2005; Palandri and Kharaka 2005; Marini 2007; Parry et al. 2007; Han and McPherson 2008). Injection of CO_2 into limestone reservoirs will result in relatively rapid dissolution of carbonate minerals to saturation with calcite and a ~2% increase in porosity (Emberley et al. 2005; Rosenbauer et al. 2005). Field results and geochemical modeling indicated that injection of CO_2 into the Frio sandstone beds resulted in initially lowered pH values (as low as ~3.0) and dissolution of calcite and iron oxyhydroxides; brine pH then would increase as a result of the slower dissolution of feldspar minerals (oligoclase), causing calcite, dawsonite and other minerals to ultimately precipitate (Bénézeth et al. 2007, 2009; Hellevang et al. 2005, 2011; Xu et al. 2010; Kaszuba et al. 2011). More carbonate minerals would ultimately precipitate from sandstones that have abundant feldspar minerals and where the feldspars are more calcic (e.g., anorthite).

General and site-specific simulations indicate that the proportions of CO_2 stored as supercritical fluid in structural and stratigraphic traps will decrease with time relative to the other three trapping mechanisms during the period required (up to 10,000 years) for sequestration (Benson and Cook 2005; Han 2008; Han and McPherson 2008). This decrease likely would lead to increased storage security, especially with regard to the upward leakage of the buoyant (density 0.5-0.8 g/cm^3) supercritical CO_2. The slightly increased density (up to 1%) of brine saturated with CO_2, and the more stable CO_2 residually trapped and stored as carbonate minerals add to the increased overall stability of the system (Benson and Cook 2005). Because the proportions of CO_2 stored as carbonate or in solution increase with storage time relative to that of the supercritical CO_2, the storage capacity should increase with time and will be higher in reservoirs with high proportions of carbonate precipitating minerals (e.g., arkosic sandstones high in Ca-plagioclase feldspar).

CO_2 injection into basalts and ultramafic rocks

Geological sequestration of CO_2 as stable carbonate minerals is favored if the CO_2 is injected into basalts and peridotites, which are high in reactive Mg, Fe and Ca silicates (Lackner 2002; Goldberg et al. 2008; Gysi and Stefansson 2008; Flaathen et al. 2009; Paukert et al. 2012; Power et al. 2013). Carbonation reactions are exothermic and reaction rates are favorable over experimental time scales. In addition, basalts and ultramafic rocks are abundant and widely distributed in accessible and suitable continental and marine systems (Broecker 2008; Matter and Kelemen 2009). Natural carbonation reactions are common in many basalts and most ultramafic rocks, which have sufficient permeability and pore space to react with CO_2-rich fluids (Oelkers et al. 2008; Matter et al. 2009), forming calcite, dolomite, magnesite, siderite and Mg-Fe carbonate solid solution (Brown et al. 2009; Maher et al. 2006; Flaathen et al. 2009; Power et al. 2013). During *in situ* mineral sequestration, CO_2 is injected into an aquifer where it dissolves in water and produces carbonic acid that can react with forsterite (Eqn. 1). The dissociation into bicarbonate releases a proton (H^+) which is free to react with the host rock, here shown as basaltic glass from Stapafell, Iceland (Oelkers et al. 2008):

$$2H_2CO_3 + Mg_2SiO_4 \leftrightarrow 2MgCO_3 + SiO_{2(am)} + 2H_2O \quad (1)$$

$$SiAl_{0.36}Ti_{0.02}Fe^{III}_{0.02}Ca_{0.26}Mg_{0.28}Fe^{II}_{0.17}Na_{0.08}K_{0.008}O_{3.45} + 2.82H^+ \leftrightarrow \quad (2)$$
$$SiO_{2(aq)} + 0.36Al^{3+} + 0.02TiO_{2(aq)} + 0.02Fe^{3+} + 0.26Ca^{2+} + 0.28Mg^{2+}$$
$$+ 0.17Fe^{3+} + 0.08Na^+ + 0.008K^+ + 1.41H_2O$$

This reaction releases carbonate-forming cations, Ca, Fe and Mg into the solution at the same time as it consumes protons (H^+), which leads to a pH increase and promotes the precipitation of secondary minerals, especially carbonates.

The carbonation reaction of CO_2 with basalt and ultramafic rocks, however, results in substantial volume increases that occur during the transformation from Mg- and Ca-silicate minerals to carbonates and the associated by-products of the reactions, including secondary silicate minerals. The large volume change and precipitation of SiO_2 minerals will result in sealing of rock porosity and reduction in the efficiency of carbonation reactions. A pilot study investigating the possibility of sequestering CO_2 captured from a geothermal power plant as carbonate minerals in Icelandic basalt is being performed by the CarbFix research group (Matter et al. 2009, 2011; Gislason et al. 2010).

Sequestration of CO_2 in sedimentary basins

Sedimentary basins, as already mentioned are attractive for CO_2 storage because: (i) they generally have large estimated local and global (> 10,000 Gt CO_2) storage capacities (Holloway 1997; Bradshaw et al 2007; DOE 2008); (ii) they often have advantageous locations

close to power plants and other major CO_2 sources (Hitchon 1996; Friedmann 2007; Burruss et al. 2009); and (iii) there is a great deal of geologic and other relevant information gained from petroleum exploration and production, and disposal of produced water and other wastes (Benson and Cook 2005; Kharaka et al. 2006; Bachu et al. 2007). Currently there are eight large-scale commercial projects worldwide that capture and inject ~23 Mt CO_2 annually, with an additional 17 projects under constructions that would increase injection to ~50 Mt CO_2 annually by 2015 (Global CCS Institute 2012). Large-scale commercial projects with substantial geochemical data include the Sleipner and the Snøhvit projects, offshore Norway, the In Salah gas field project in Algeria, the Illinois Industrial CCS Project, USA. There are also two commercial EOR projects (Weyburn-Midale, Canada, and Cranfield, Mississippi, USA) that capture and inject close to five million tons of CO_2 annually, but these differ from the more than 100 EOR projects worldwide, because they aim to integrate EOR with CO_2 sequestration (Cantucci et al. 2009; Moritis 2009; Hovorka et al. 2010; Hansen et al. 2012; Lu et al. 2012; Nazarian et al. 2013).

The Sleipner Project, operated by the StatoilHydro since 1996, is the world's first industrial-scale operation. Approximately one million tons of CO_2 is being extracted annually from the produced gas that has ~10% CO_2 to meet quality specifications, and stored ~1000 m below sea level in the Utsira Formation (Chadwick et al. 2004, 2009; Hermanrud et al. 2009). The Utsira Formation consists of thick and poorly consolidated sandstones of high porosity (35-40%) and permeability (1-3 darcies), and is overlain by the thick Nordland shale caprock (Bickle 2009). The sand is comprised of 75% quartz, 13% K-feldspar, and 3% calcite (Chadwick et al. 2004). The thickness of the formation varies between 150 and 250 m and the top is located ~800 m beneath the bottom of the North Sea (Bickle 2009).

Results from the 4D seismic imaging indicate that CO_2, though injected into the bottom of the Utsira sandstone, has migrated through intervening shale beds into nine different sandstone layers. However, results from these seismic investigations show that no CO_2 is leaking out of the formation (Chadwick et al. 2004; Bickle 2009). Two-dimensional reactive transport modeling of CO_2 injected at the Sleipner site indicates that after 10,000 years, only ~5% of the injected gas will be trapped into minerals while 95% will be dissolved in the brine (Audigane et al. 2007). The relatively small percentage of mineral trapping is due mainly to the low concentrations of divalent cations in the reservoir sandstones.

The In Salah Gas Joint Venture CO_2 storage project, located in the Algerian Sahara, is currently the largest onshore project in the world (Iding and Ringrose 2009; Nazarian et al. 2013). Approximately ~1 million tons/yr of CO_2 are injected into the water leg of the Carboniferous Krechba sandstone gas-reservoir (20 m thick) via three horizontal wells at a depth of ~1,900 m. The CO_2 is obtained from several local natural gas fields that contain up to 10% CO_2, which has to be reduced to 0.3% before the gas is sold (Rutqvist et al. 2009). CO_2 is injected into sandstones with relatively low porosity (11-20%) and permeability (~10 md) with some fractures and small faults in both the reservoir unit and in the Carboniferous mudstone and siltstone beds of the caprock. Despite the evidence of fractures, the thick mudstone caprock sequence provides an effective mechanical seal for containing the CO_2 (Iding and Ringrose 2009). A number of key technologies to monitor the injection, and the subsurface movement and storage of CO_2 have been, and will continue to be, deployed to provide long term assurance of sequestration (Mathieson et al. 2010; McNab and Carroll 2011). Time-lapse satellite images (using PSInSAR Technology), which measure ground deformation, show a surface uplift on the order of 5 mm/yr above active CO_2 injection wells and the uplift pattern extends several km from the injection wells. The observed surface uplift is used to constrain the coupled reservoir-geomechanical model, and to show that surface deformations from InSAR can be useful for tracking the fluid pressure and for detection of a leakage path (e.g., in a permeable fault) through the overlying caprock (Rutqvist et al. 2009; Nazarian et al. 2013).

Injection at In Salah started in 2004, but was suspended in June 2011 due to concerns about the integrity of the seal and geomechanical issues (In Salah web site accessed February 2013).

The Weyburn-Midale project (Williston Basin, Canada) started injecting CO_2 into the Weyburn field in 2000, combining CO_2 sequestration with EOR by injecting the gas and brine into an almost depleted oil field to increase fluid pressure and oil production (Emberley et al. 2005). The CO_2 used is obtained from the Dakota gasification plant near Beulah, North Dakota, where the gas is captured after coal gasification, liquefied by compression and piped 320 km north to the oil fields. It is the first man-made source of CO_2 being used for EOR. The oil field consists of shallow marine carbonate (depth of ~1500 m) and the injection rate is now >3 million tons of CO_2/yr. The chemical and C-isotope composition of both brine and H_2O exhibit significant changes resulting from CO_2 injection. Geochemical modeling and monitoring of the aquifer indicate that the injected CO_2 reacts with the brine and the host rock, dissolving carbonate minerals, increasing alkalinity, and lowering the pH of produced water; slow dawsonite precipitation is also predicted (Emberley et al. 2005; Cantucci et al. 2009).

In January 2011, the Kerr family, who owns property near the Weyburn field, feared that their groundwater and soil had been contaminated by CO_2 leaking from the EOR project. Cenovus, the company that operates the Weyburn field, and the International Performance Assessment Centre for Geologic Storage of CO_2 (IPAC-CO_2) both initiated studies to investigate this complaint. Results of detailed near-surface geochemical investigations from three independent international experts reported in Sherk et al. (2011) and in local newspapers (e.g., Weyburn Review by Greg Nikkel, December 14, 2011) found no evidence to suggest that CO_2 is leaking from the Weyburn-Midale EOR field.

The Cranfield oil field is a depleted oil reservoir in the Mississippi Interior Salt Basin, with production from the lower Tuscaloosa Formation sandstones (depth ~3000 m). As part of the SEACARB Phase III team, we are continuing our geochemical monitoring of brine and gases at the Cranfield CO_2-EOR and sequestration site, to investigate the potential for the geologic storage of large volumes of CO_2 in saline aquifers. Brine and gas samples were collected from selected production wells at several time intervals following CO_2 injection in July 2008. In addition, brine and gas samples were collected in December, 2009 using installed U-tubes and a downhole Kuster tool, from the three DAS (Detailed Area of Study) wells located down dip of the oil-water contact, with the two monitoring wells situated 69 and 112 m from the CO_2 injector.

Results from all the wells to date show that Tuscaloosa formation water is a Na-Ca-Cl brine of relatively uniform salinity (~150,000 mg/L TDS) and major solute concentrations. Initial results from the production well sampling, and from the DAS wells, indicate only modest water-rock interaction following CO_2 injection, especially when compared with results from the Frio Brine tests (Kharaka et al. 2009). For example, alkalinity (as HCO_3) increased (from ~375 to 500 mg/L), Fe increased (from ~90 to 120 mg/L) and major divalent cations (Ca, Mg, Sr) increased <10%. This has been interpreted as being due to low reactivity of well tubing and of dominant reservoir minerals, quartz, kaolinite, and chlorite (Lu et al. 2012). However, results from the most recent re-sampling (November 2011) of four of the longer producing wells indicate a larger increase in carbonate alkalinity to up to 874 mg/L as HCO_3 and Fe to up to 230 mg/L (Thordsen et al. 2012). These higher alkalinity and Fe values are still lower than those obtained from Frio tests by a factor of four, but are more in line with values observed from other CO_2 injection sites, such as the Minami-Nagaoka in Japan, the Otway and Gorgon in Australia, Weyburn-Midale in Canada and the Ketzin in Germany (Kharaka et al. 2009; Cantucci et al. 2009; Underschultz et al. 2011; Martens et al. 2012).

The concentrations of organic species in general and the toxic components, including benzene, toluene, ethyl benzene and xylene (BTEX), polycyclic aromatic hydrocarbons

(PAHs), and phenols in particular, that potentially could be mobilized by the supercritical CO_2 and transported by any CO_2 leakage into USDW are being carefully investigated in the Cranfield brine and gases (Kharaka et al. 2011; Kharaka and Hanor 2013; Burant et al. 2013). Results to date show the concentrations of n-alkanes in brine from the Cranfield oil wells increased from ~40 to 200 ng/L, as the percentage of CO_2 in the co-produced gas increased from ~6 to 95 vol%. Similar trends were observed in the concentrations of organic acid anions and some of the PAHs. The BTEX and some PAHs showed increases (up to 20 mg/L for benzene, 100 ppb for naphthalene) in the mid-range of CO_2 concentrations, but then tapered off as the CO_2 increased to 95 %. Prior to the CO_2 injection, the brine from the DAS wells was CH_4 saturated (~60 mM), CO_2 was 2-3 vol%, and concentrations of organics were comparable to those initially obtained from the oil wells. Results indicate that the injected supercritical CO_2, which is an effective solvent for some organic compounds, could mobilize and transport BTEX, phenols, and PAHs that are highly toxic to biota. Preventing the leakage of CO_2 into overlying sources of drinking water is already regulated, but becomes of greater importance as a result of these mobilized toxins (Kharaka et al. 2009).

Storage of CO_2 in the Frio Formation. The Frio Brine field test conducted during 2004-2008 was the first scientific project of its kind to investigate the potential for the long-term geologic storage of CO_2 in saline aquifers (Hovorka et al. 2006; Cole et al. 2008; Kharaka et al. 2006, 2009). There are approximately 25 additional geologic sequestration field demonstration projects in the US at various stages of planning, deployment and completion, and an equal number of projects in other countries, including the Minami-Nagaoka in Japan, the Otway and Gorgon in Australia, the Pembina Cardium in Canada, Beitang depression, Tianjin, North China Basin, and the Ketzin in Germany, that have or are investigating the storage of CO_2 in various clastic and carbonate rock formations using different injection schemes, monitoring methods, hazards assessment protocols, and mitigation strategies (Litynski et al. 2008; Cook 2009; Hitchon 2009; Matter et al. 2009; Michael et al. 2009; Zhang et al. 2009; Pang et al. 2010; Johnson et al. 2011; Martens et al. 2012; IEA 2012; Global CCS Institute 2012).

The Frio Brine test was a multi-laboratory field experiment funded by the US Department of Energy that involved injecting food-grade CO_2 into two sandstone members of the Frio Formation. For Frio Brine I test, approximately 1,600 metric tons of CO_2 were injected into a 24-m thick sandstone, named the "C" sandstone, of the Oligocene Frio Formation—an extensive regional petroleum and brine reservoir in the U. S. Gulf Coast (Hovorka et al. 2006). Down-hole and surface samples of formation water and gas were obtained from the injection well and an observation well completed about 30 m updip using a variety of sampling tools and methodologies (Kharaka et al. 2006, 2009). Samples were obtained from both wells before CO_2 injection for baseline data. A large number of samples were taken from the observation well during the injection to track its breakthrough and to investigate temporal changes in fluid composition; some were collected post-injection to investigate the "residual" CO_2 (Hovorka et al. 2006) and its leakage into the overlying "B" sandstone (Kharaka et al. 2006, 2009). Also, surface and wellbore geophysical logging using electrical, seismic, and the Schlumberger reservoir saturation tool (RST) were carried out to provide baseline characterization and to investigate changes in the composition and distribution of the CO_2 plume (Hovorka et al. 2006; Daley et al. 2007, 2008).

Results of chemical analyses for Frio I samples prior to CO_2 injection show that the brine is a Na-Ca-Cl type water, with a salinity of ~93,000 mg/L TDS , with relatively high concentrations of Mg and Ba, but low values for SO_4, HCO_3, DOC and organic acid anions. The high salinity and the low Br/Cl ratio (0.0013) relative to sea water indicate dissolution of halite from the nearby salt dome (Kharaka et al. 2006). The brine has 40-45 mM dissolved CH_4, which is close to saturation at reservoir conditions (60 °C and 150 bar); CH_4 comprises ~95% of total gas, but the CO_2 content is low at ~0.3% (Table 1).

Table 1. Composition (volume %) of gas obtained from Frio "C" and "B" sandstones, during Frio I field test near Houston, Texas, USA (from Kharaka et al. 2009).

Gas	[1] "C"	[2] "C"	[3] "B"
He	0.0077	0	0.014
H_2	0.040	0.19	0.30
Ar	0.041	0	0.063
CO_2	0.31	96.8	2.90
N_2	3.87	0.037	2.46
CH_4	93.7	2.94	96.8
$C_2H_6^+$	1.95	0.0052	0.11

(1) From the injection well before CO_2 injection; (2) from the observation well after CO_2 breakthrough; (3) from the observation well 6 months after CO_2 injection.

During CO_2 injection, October 4–14, 2004, on-site measurements of EC exhibited only a small increase from a pre-injection value of ~120 mS/cm at ~22 °C. However, there were major changes in some chemical parameters (Fig. 1) when the CO_2 reached the observation well, including a sharp drop in pH, from 6.5 to 5.7 (measured at surface conditions), and large increases in alkalinity, from 100 to 3000 mg/L as HCO_3^- (Kharaka et al. 2006). Additionally, laboratory determinations showed major increases in dissolved Fe (from 30 to 1100 mg/L) and Mn (Fig. 2), and significant increases in the concentration of Ca. The most dramatic changes in chemistry occurred at CO_2 breakthrough, 51 h after injection (Fig. 1 and 2). These dramatic changes were also evidenced by determination of PFT gases (Phelps et al. 2006), showing CO_2 concentrations increasing from 0.3% to 3.6% and then quickly to 97% of total gas (Table 1).

Field-measured pH proved the most sensitive and rapid parameter for tracking the arrival of CO_2 at the observation well, especially when an inline pH probe was successfully deployed during Frio II test, when 300 t CO_2 were injected into the Blue sandstone member of the Frio

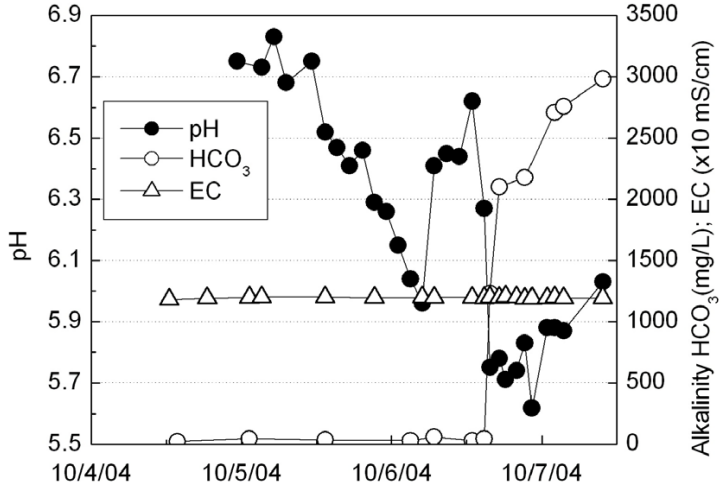

Figure 1. Electrical conductance (EC), pH and alkalinity of Frio I brine obtained from the monitoring well and determined on site during CO_2 injection. Note the sharp drop of pH and alkalinity increase with the breakthrough of CO_2 (from Kharaka et al. 2006).

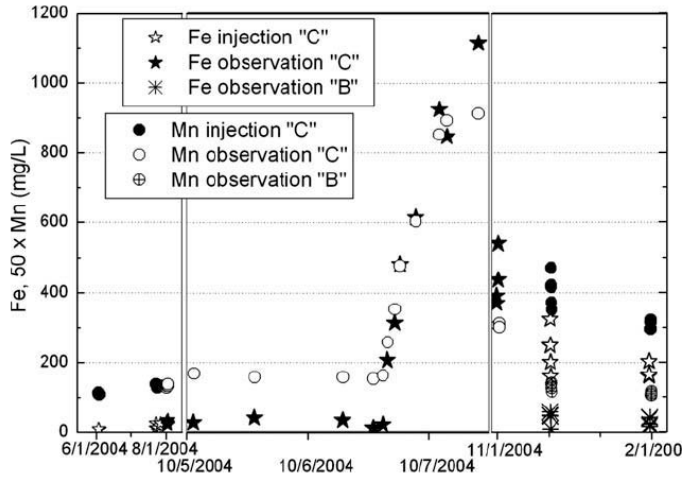

Figure 2. The concentrations of Fe and Mn for selected brine samples from Frio I. See also the high Fe values obtained from Frio II (Fig. 5) together with δ^{56}Fe values that fall between those of the carbon steel tubing and preinjection brine, indicating a mixed origin for dissolved Fe in Frio I and Frio II (Kharaka et al. 2010a).

Formation in 2006 (Fig. 3). The pH values obtained from the online probe in particular, but also from bench measurement at ambient conditions could be used also to indicate the arrival of the dissolved CO_2, which is expected to reach the observation well before the supercritical phase. The sharp drop in pH and increases in alkalinity, dissolved iron, measured CO_2 (Freifeld et al. 2005) and other constituents in the sample collected at 15:45 on 6th of October, marked the time of breakthrough of the supercritical CO_2 plume (Kharaka et al. 2009).

Results of geochemical modeling, using updated SOLMINEQ (Kharaka et al. 1988) indicate that the Frio brine in contact with the supercritical CO_2 would have a pH of ~3 at

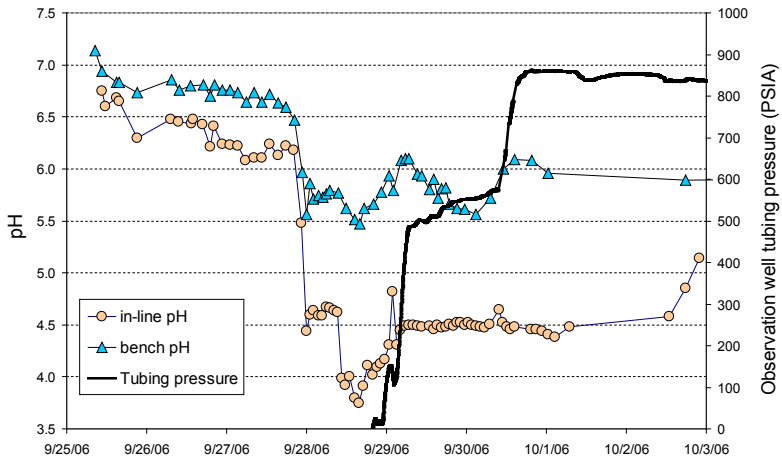

Figure 3. Bench and in-line pH values obtained from Frio II brines before and following CO_2 breakthrough at the observation well. Note the sharp drops of pH, especially values from in-line probe following the breakthrough of CO_2 (Kharaka and Cole 2011).

subsurface conditions, and this low pH causes the brine to become highly undersaturated with respect to carbonate, aluminosilicate and most other minerals present in the Frio Formation (Fig. 4). Because mineral dissolution rates are generally higher by orders of magnitude at such low pH values, the observed increases in concentrations of HCO_3^- and Ca^{2+} likely result from the rapid dissolution of calcite via the reaction:

$$H_2CO_3^0 + CaCO_{(3(s)} \leftrightarrow Ca^{2+} + 2HCO_3^- \quad (3)$$

The large increases observed in concentrations of dissolved Fe and equivalent bicarbonate alkalinity could result from dissolution of siderite, but no siderite was observed in the retrieved core. Alternatively, these increases could be caused by dissolution of the observed iron oxyhydroxides, depicted in redox-sensitive reaction:

$$2Fe(OH)_{3(s)} + 4H_2CO_3^0 + H_2 \leftrightarrow 2Fe^{2+} + 4HCO_3^- + 6H_2O \quad (4)$$

However, some of the increase in dissolved Fe and equivalent bicarbonate could also result from corrosion of pipe and well casing that come in contact with low-pH brine (Hitchon 2000; Kharaka et al. 2009), as indicated by the redox-sensitive reaction:

$$Fe_{(s)} + 2H_2CO_3^0 \leftrightarrow Fe^{2+} + 2HCO_3^- + H_{2(g)} \quad (5)$$

Similarly, a redox-sensitive reaction may be written for Mn, which increased from 3 to 18 mg/L. There were also increases in the concentration of other metals, including Zn, Pb and Mo, which are generally associated (sorbed and coprecipitated) with iron oxyhydroxides, but could also be present in the low-carbon steel pipe used in petroleum wells (Celia et al. 2006).

Even higher concentrations of Fe (up to 1200 mg/L as Fe^{++}) and other metals were obtained in brines collected from Frio II, the Blue sandstone (Fig. 5). For selected samples from Frio II, the $\delta^{56}Fe$ were determined and compared with three values obtained from carbon steel tubing used in the wells. The steel pipe, as expected, has $\delta^{56}Fe$ values of 0±0.5‰, whereas brine samples before CO_2 injection had $\delta^{56}Fe$ values of −2.0±0.5‰. Brine samples following

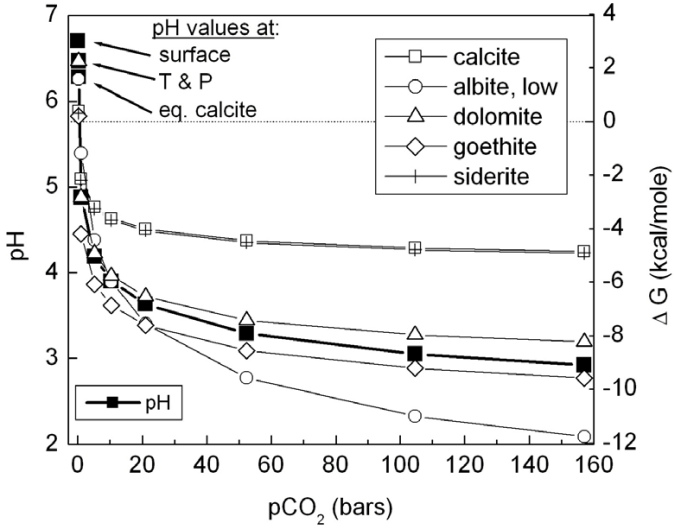

Figure 4. Computed pH values and saturation states of selected minerals in Frio I brine as a function of CO_2 partial pressure at subsurface conditions. Note the sharp initial drop of pH from ~6.4, the average value computed at T & P, and calcite saturation before CO_2 injection (modified from Kharaka et al. 2006).

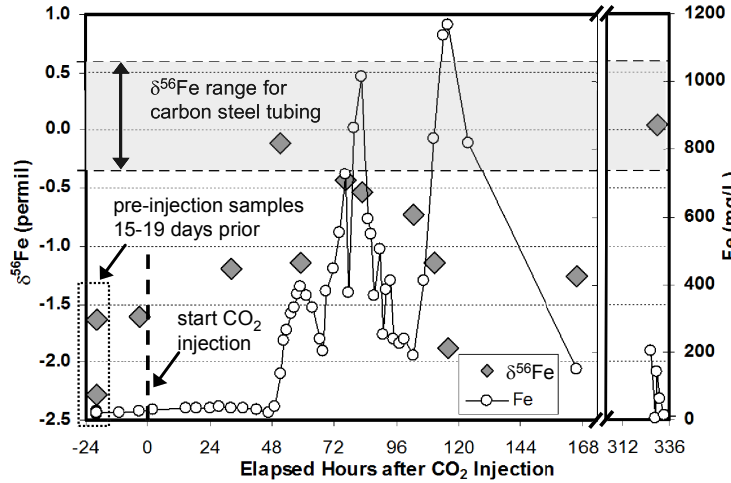

Figure 5. The concentrations of Fe and δ^{56}Fe values for selected brine samples from Frio II. Samples with high Fe values following CO_2 injection have δ^{56}Fe values that fall between those of the carbon steel tubing and preinjection brine, indicating a mixed origin for dissolved Fe (Kharaka et al. 2010a).

CO_2 injection have δ^{56}Fe values that fall between those of the steel pipe and brine before CO_2 injection (Fig. 5). Fe isotopes, geochemical modeling, and other chemical data support the conclusion that dissolution of Fe-oxyhydroxides and corrosion of well pipe contributed to the very high dissolved Fe concentrations.

Geochemical modeling indicates that the brine pH would increase from dissolution of carbonate and iron oxyhydroxide minerals discussed above, as well as from dissolution of oligoclase and other aluminosilicate minerals present in the Frio. Aluminosilicate mineral dissolution generally is not congruent, but likely follows the incongruent reaction described by Equation (6) below, in which dawsonite, gibbsite and amorphous silica are precipitated, and/or kaolinite and amorphous silica are precipitated (White et al. 2003).

$$0.4H^{+} + Ca_{0.2}Na_{0.8}Al_{1.2}Si_{2.8}O_{8(s)} + 0.8CO_{2(g)} + 1.2H_2O \leftrightarrow \quad (6)$$
$$0.2Ca^{2+} + 0.8NaAlCO_3(OH)_{2(s)} + 0.4Al(OH)_{3(s)} + 2.8SiO_{2(s)}$$

As the pH increases from mineral interactions and the mixing of CO_2-saturated and pristine brines, modeling indicates that mineral saturations reverse the trend shown in Figure 4, resulting in precipitation of carbonate and other minerals. These mineral dissolution and precipitation reactions could impact reservoir and caprock porosity and permeability, and thus CO_2 injectivity and leakage.

Dissolved organic carbon (DOC) values obtained in Frio I samples before CO_2 injection are expectedly low (1-5 mg/L); the values obtained from the "C" sandstone during the CO_2 injection increased moderately to 5-6 mg/L. DOC values, however, increased unexpectedly by a factor of 100 on samples collected ~20 days after injection stopped (Fig. 6). The concentrations of organic acid anions and BTEX in these samples were relatively low (<1 mg/L), but values of formate, acetate, and toluene were generally higher in the enriched DOC samples. Results from a more detailed sampling protocol for samples collected six and fifteen months after injection show oil and grease values below detection limit, low levels (up to 30 ppb phenol) of volatile organic compounds (VOCs) and semi-VOCs (30 ppb naphthalene), and only slightly elevated DOC values (5-8 mg/L) (Fig. 6).

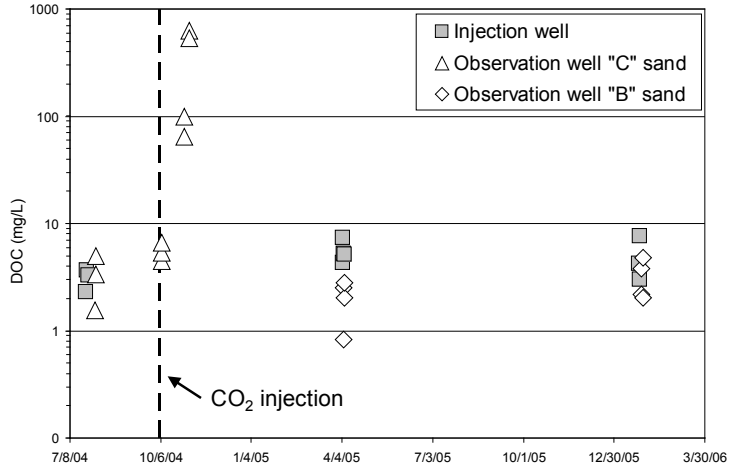

Figure 6. Concentration of dissolved organic carbon (DOC) in Frio I brine. Note the extremely high values obtained on November, 2004, ~20 days after the end of CO_2 injection (Kharaka et al. 2009).

It is difficult to rule out contamination from well operations for the very high DOC values, but they likely represent a "slug" of organic matter mobilized by the injected CO_2, as reported in laboratory experiments simulating carbon dioxide storage in deep coal beds (Kolak and Burruss 2006) and in EOR operations (Shiraki and Dunn 2000). These results suggest that mobilization of organics from depleted oil reservoirs and non-oil-bearing aquifers could have major implications for the environmental aspects of CO_2 storage and containment. The concern here is warranted as high concentrations of toxic organic compounds, including benzene, toluene (up to 60 mg/L for BTEX), phenols (up to 20 mg/L), and polycyclic aromatic hydrocarbons (up to 10 mg/L for PAHs), have been reported in oil-field waters (Kharaka et al. 2009; Burant et al. 2013). These highly toxic organic compounds are partitioned preferentially into the supercritical CO_2, and were measured in high concentrations in brines from the Cranfield EOR field following CO_2 injection as discussed earlier (Kharaka et al. 2010a).

Significant shifts were observed in the isotopic compositions of H_2O (Fig. 7) and DIC (Fig. 8) following CO_2 injection, but only subtle changes in the δD and $\delta^{13}C$ values of CH_4. The $\delta^{13}C$ values of DIC became profoundly lighter, shifting from −3 to −33‰, reflecting the fact that the injected CO_2 is the dominant C source and is depleted, with $\delta^{13}C = -44$ to −34‰, depending on the mixing proportions of the two gas sources used. The $\delta^{18}O$ values of brine became isotopically lighter with time, shifting from 0.80 to −11.1‰, and there was a corresponding increase in the $\delta^{18}O$ values of CO_2, from 9 to 43‰. Because water and CO_2 rapidly exchange oxygen isotopes even at low temperature, it is possible to use their $\delta^{18}O$ values in mass balance equations to estimate the brine to CO_2 mass and volume ratios in the reservoir. The equation for a closed system and no isotopic exchange with minerals is given (Clark and Fritz 1997) by:

$$\frac{X_{brine}}{X_{CO_2}} = \frac{\delta^{18}O^{f}_{CO_2} - \delta^{18}O^{i}_{CO_2}}{\delta^{18}O^{i}_{H_2O} - \delta^{18}O^{f}_{H_2O}} \quad (7)$$

where the superscripts "i" and "f" are the initial and final δ values for brine and CO_2, respectively, and X is the atomic oxygen in the subscripted component.

Results from the observation well (Table 2) show that initially the system is brine dominated, with CO_2 comprising ~10% of the fluid at reservoir conditions from one day after

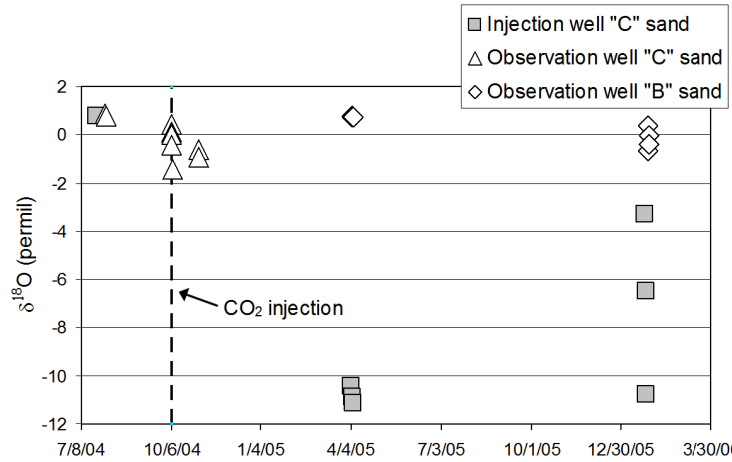

Figure 7. The $\delta^{18}O$ values of Frio I brine samples collected before, during and after CO_2 injection. Note the depleted values obtained from the "C" sandstone following CO_2 injection relative to those before injection. The $\delta^{18}O$ values obtained from the "B" sandstone show some depletion, especially in samples collected ~15 months after completion of injection (Kharaka et al. 2009).

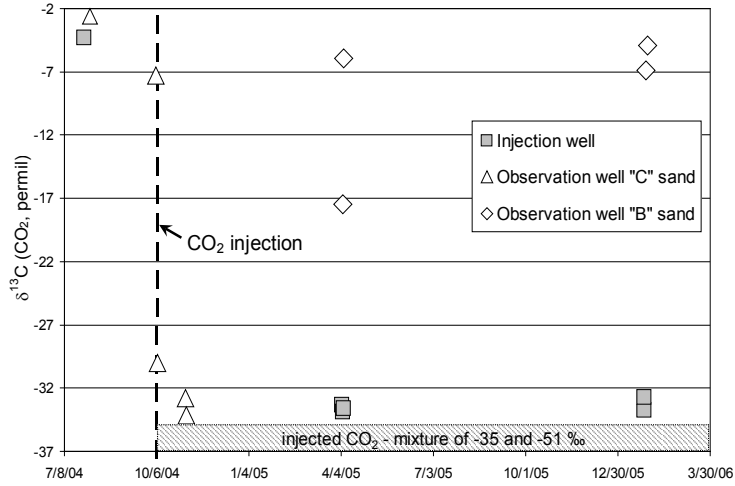

Figure 8. The $\delta^{13}C$ values of DIC in Frio I samples obtained before, during and after CO_2 injection. Note the highly depleted values obtained from the "C" sandstone following CO_2 injection relative to those before injection. The $\delta^{13}C$ values obtained from the "B" sandstone show some depletion, especially in samples collected ~6 months after completion of injection (Kharaka et al. 2009).

the CO_2 breakthrough on October 7, 2004 through November 3, 2004. However, samples collected from the injection well from April 4-6, 2005, yield a value of ~50% for the volume of CO_2 at reservoir conditions. The initial brine dominated system could indicate that the injected CO_2 acts like a piston pushing the pore water out with minimal mixing and isotopic exchange. Contact and isotopic equilibration with a larger volume of injected CO_2 is indicated from data of April, 2005. These results are comparable to "residual" CO_2-saturation values obtained with the RST and other geophysical tools used (Hovorka et al. 2006), indicating the usefulness of this isotopic approach.

Table 2. Calculated brine/CO_2 volume ratios in the Frio "C" sandstone following CO_2 injection based on the $\delta^{18}O$ values for brine and CO_2 (from Kharaka et al. 2006).

Date	Brine $\delta^{18}O$ shift	CO_2 $\delta^{18}O$ shift	vol. ratio* Brine/ CO_2
10-5-04	0	0	$\rightarrow\infty$
10-6-04	0.37	32	43
10-6-04	0.69	32	23
10-6-04	0.77	32	21
10-6-04	1.22	32	13
10-7-04	2.24	32	7.1
11-3-04	1.43	32	11
11-3-04	1.74	32	9.1
4-4-05	11.2	22	0.97
5-4-05	11.7	22	0.93
6-4-05	11.9	22	0.92

* To convert from mole oxygen basis (eq. 4 in text) to brine/CO_2 vol. ratio at reservoir conditions, we multiply by 0.495, using a density (gm/cm^3) of CO_2 = 0.60 and brine= 1.0

POTENTIAL IMPACTS AND RISKS OF GEOLOGIC STORAGE OF CO_2

The major environmental risks associated with a CO_2 storage site, potentially may include induced seismicity in vulnerable locations (Friedmann 2007; Zoback and Gorelick 2012; Juanes et al. 2012), and leakage of CO_2 and brine that may damage USDW and other natural resources or cause harm to humans, animals and ecosystems (EPA 2008, 2009; Kharaka et al. 2009; Smyth et al. 2009; Humez et al. 2013). Fluid leakage could occur along unmapped fracture systems and faults, improperly sealed abandoned and orphaned wells (Celia et al. 2006; Nordbotten et al. 2009), corroded well casings and cements (Carey et al. 2007) or even via pathways created in the rock seals as a result of CO_2-brine-rock interactions (Kharaka et al. 2006, 2009). Maintaining reservoir integrity that limits CO_2 leakage to very low levels (less than 0.01%) is essential to the long term success of injection operations (Hepple and Benson 2005). Preventing brine migration into overlying drinking water supplies is equally important, because dissolution of minerals following CO_2 injection would mobilize Fe, Mn, and other metals, as well as toxic organics, including BTEX, phenols and other toxic compounds observed in the Frio Brine tests (Kharaka et al. 2009).

To evaluate these risks requires a detailed geologic site characterization and an improved understanding of formation properties and how the injected CO_2 spreads and interacts with the rock matrix and reservoir fluids (Bachu 2003; Friedmann 2007; Kharaka et al. 2009, 2013). Geologic formations typically consist of layers of rock with different porosities, permeabilities, thicknesses, and brine and mineral compositions. All of these factors, together with the presence of faults and fracture systems, affect the suitability of the formation as a site for CO_2 sequestration. Porosity and thickness determine the storage capacity of the formation, and chemical composition determines the interaction of CO_2 with the minerals in place. Also, an impervious cap rock and absence of high-permeability faults are necessary to prevent the sequestered buoyant CO_2 from migrating to the surface. Finally, if the geological section consists of a series of aquifers, it is necessary to ensure that CO_2 stored in a saline formation does not migrate to a potable aquifer (Oldenburg 2007; Birkholzer et al. 2008).

Environmental impacts

From an environmental point of view, leakage of CO_2 is the most serious potential problem. Leakage to the atmosphere negates the original environmental benefit and economic effort expended in sequestering the CO_2 (Friedman 2007; Stenhouse et al. 2009). Another potential problem is accumulation of CO_2 in pockets in soil and on the surface of the earth, where it could present a health hazard to humans, animals and ecosystems. Furthermore, CO_2 could migrate into other strata, with the potential for contaminating valuable and at times limited USDW (Reilly et al. 2008; Birkholzer et al. 2008) or causing other problems. If the formation into which CO_2 is being injected is below the ocean, leakage of CO_2 into the marine environment could affect ocean pH and chemistry and have potentially serious consequences for marine life.

Results from the Frio Brine tests, the Cranfield EOR and sequestration test, and other field sites indicate that the injected supercritical CO_2, which is a very effective solvent for organic compounds (Kolak and Burruss 2006), could mobilize and transport organics, including BTEX, phenols, PAHs and other toxic organic compounds that have been reported in relatively high concentrations (10-60 mg/L) in oil field brines (Kharaka et al. 2009; Kharaka and Hanor 2013; Zheng et al. 2013). Preventing brine migration into overlying USDW is equally important, because dissolution of minerals following CO_2 injection would mobilize Fe, Mn and other metals, in addition to the high concentration of other chemicals (salinity 5000 to more than 200,000 mg/L TDS) present in the original brine (Kharaka and Hanor 2013). Additional risks could arise from potential damage to nearby hydrocarbon resources caused by the displacement of fluids by the injected CO_2, such as saline water production at wells that had been producing oil or gas. Finally, if a project does not operate within prescribed injection rates and pressures, there is some potential for initiating seismic activity (Friedmann 2007; Zoback and Gorelick 2012). On the other hand, injection sites should not be located near major active faults (Juanes et al. 2012), such as the San Andreas fault in California, because results from recent simulations indicate that large earthquakes along such faults would cause intense ground motions leading to rock fracturing and possible CO_2 leakage over large areas (up to 300 km by 50 km) (US Geological Survey 2008, *http://www.shakeout.org/).*

Health and safety impacts

Information on the responses of humans, animals and plants to elevated and potentially hazardous levels of CO_2 and low levels of oxygen can be found in literature (Deel et al. 2006; Bergfeld et al. 2006; NIOSH/OSHA 1981; EPA 2008). The National Institute of Occupational Safety and Health (NIOSH/OSHA) has determined that human time weighted average (8-hours TWA) exposure limits to CO_2 of 1% (10,000 ppm), and short term exposure limit (15-minute STEL) of 3% are appropriate (NIOSH/OSHA 1981, 1989). Human exposure to elevated levels of CO_2 can be hazardous in two ways—by a reduction in the oxygen content of the ambient air causing hypoxia or through direct CO_2 toxicity. In most cases of hazardous CO_2 exposure, the gas is presumed to act as a simple asphyxiant. However, extensive research indicates that exposure to elevated CO_2 concentrations higher than 3% has significant effects, including kidney damage before oxygen dilution becomes physiologically significant. Concentrations higher than 10% have caused difficulty in breathing, impaired hearing, nausea, vomiting, a strangling sensation, sweating, and loss of consciousness within 15 minutes. As O_2 concentration drops below 17%, increasingly severe physiological effects occur until below 6% O_2, loss of consciousness is rapid, and death takes place within minutes.

Another potential safety problem could result from accidents while working around the facilities required to capture, condense, transport, and inject the CO_2. If H_2S is sequestered along with CO_2, health risks are significantly increased, as H_2S is highly toxic. Also, the health impacts would increase substantially if significant amounts of BTEX, PAHs and other mobilized organics are carried with the leaking CO_2 (Kharaka et al. 2009).

In order to minimize the environmental hazards and risks associated with CO_2 storage, a rigorous program should be implemented for the measurement, monitoring, and verification (MMV) of the injected CO_2 and associated brine (Benson and Cook 2005; Friedmann 2007; Doughty et al. 2008). MMV is concerned with the capability to measure the amount of CO_2 stored at a specific sequestration site, map its spatial disposition through time, develop techniques for surface and subsurface monitoring for the early detection of leakage, and verify that the CO_2 is stored or isolated as intended and will not adversely impact the host ecosystem, including USDW. MMV for geologic sequestration consists of three areas: i) Modeling and analysis of the geology and hydrology of the total injection system before injection starts; ii) tracking and monitoring the movement of the CO_2 plume; and iii) above-surface measurements that verify that the CO_2 remains sequestered (EPA 2008). Optimization of the MMV technologies is needed to ensure that the full range of spatial and temporal scales are covered. Results from pilot studies highlight the importance of using the more sensitive geochemical markers (Kharaka et al. 2006, 2009; Wells et al. 2007, 2010) and the importance of subsurface monitoring for detecting any early leakage of injected CO_2 and brine to minimize damage to groundwater and the local environment.

GEOCHEMICAL TRACERS OF CO_2 FLOW AND LEAKAGE

Supercritical CO_2 in reservoir rocks is buoyant, displaces huge volumes of formation water, and becomes reactive when dissolved in formation brine. Dissolved CO_2 is likely to react with minerals in reservoir and caprocks, well pipes and cements causing dissolution, precipitation and transformation of minerals that may impact the extent of CO_2 and brine leakage that could contaminate USDW (e.g., Benson and Cook 2005; Kharaka and Cole 2011; May and Waldmann 2013; de Caritat et al. 2013; Myers et al. 2013). Reaction of dissolved CO_2 with reservoir minerals generally results in measurable changes in a large number of chemicals (inorganic and organic) and isotopes that can be used as natural tracers to map the CO_2 plume in the reservoir rocks as well as identify its leakage into other reservoirs or into USDW (Kharaka et al. 2009 2010b; Kharaka and Cole 2011). Man-made chemical and isotopic tracers added to the brine or the injected CO_2 have also been used extensively in CCS operations to complement the natural tracers (Friefield et al. 2005; Phelps et al. 2006; Wells et al. 2007, 2010).

It is important to ascertain that the formation water sampled for CCS operations is pristine, because it often is contaminated by water used in the drilling and circulation fluids. Tagging the drilling fluids with Rhodamine WT, fluorescein, or even tritiated water (if allowed) has proven straightforward, allowing for the identification of uncontaminated formation water (Kharaka et al. 2006, 2009). Tracer gases, including SF_6, noble gases, tagged CH_4, and several PFTs, have been used extensively, especially in the field-pilot operations by injecting them with the CO_2 to map its flow path in the reservoir rocks and to identify any leakages into the overlying reservoir rocks or USDW (Friefield et al. 2005; Phelps et al. 2006; Kharaka et al. 2009; Wells et al. 2007, 2010; Myers et al. 2013). The man-made PFTs have proven extremely valuable in tracking the injected CO_2 in reservoir rocks as well as in deep and shallow monitoring sites (Fig. 9 and 10) because of their ultrasensitive detection limits, at fL/L levels (Begley et al. 1988; Phelps et al. 2006; Wells et al. 2007). Finally, measuring the changes in the $\delta^{18}O$ and the $\delta^{13}C$ values of CO_2 and those of the brine and its DIC have proven extremely powerful tracers for tracking injected CO_2 and understanding CO_2-brine-mineral interactions (Kharaka et al. 2006, 2009; Johnson and Mayer 2011; Johnson et al. 2011; Lu et al. 2012).

Though successfully used in many pilot-scale CCS operations, many of the man-made tracers could not be used in major industrial sequestration operations due to environmental laws and for economic reasons (Myers et al. 2013). Radioactive isotopes, including tritiated

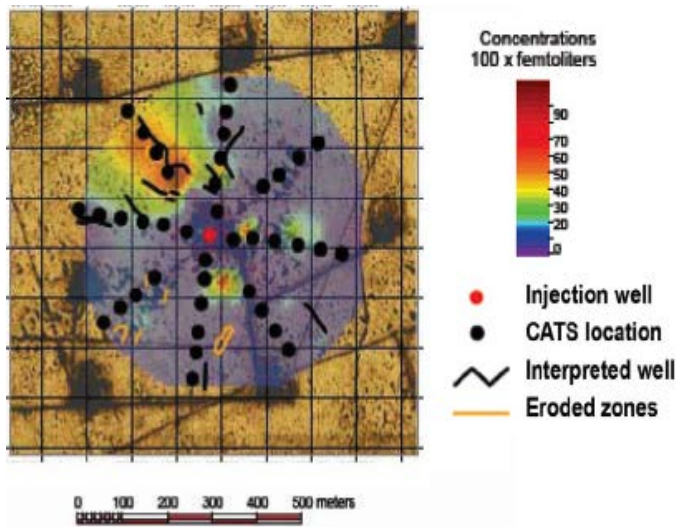

Figure 9. Contour map of the concentrations of the PDCH tracer fluxes obtained with CATS placed ~2 m below ground at the West Pearl Queen oil field, New Mexico after 54 day exposure. Modified from Wells et al. (2007).

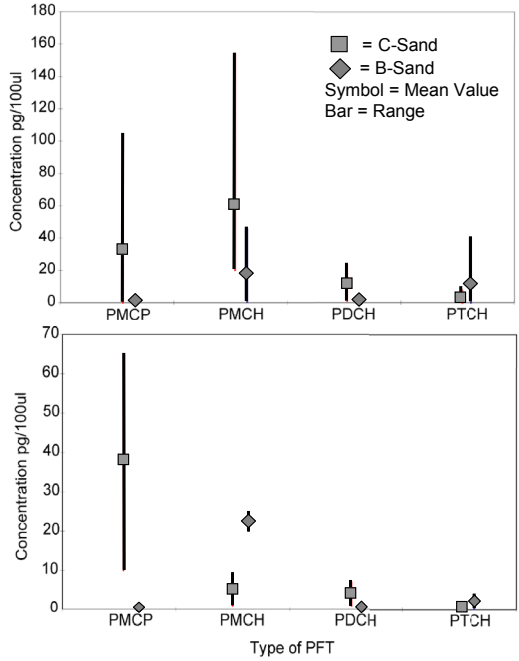

Figure 10. Concentration of perfluorocarbon tracers (PFT) in Frio I brine samples. Mean (dot) and range (bar) for each perfluorocarbon tracer in the Frio "C" sandstone (squares) and the "B" sandstone (diamonds). Data from samples collected 6 (top) and 15 months (bottom) after CO_2 injection (modified from Phelps et al. 2006).

water and CH_4 are not used significantly in the petroleum industry and would not be used in CCS operations due to environmental and health safety regulations. Also, since the adoption of the Montreal Protocol in 1987, chlorofluorocarbons have not been used as tracers as they cause ozone depletion. Finally, the use of SF_6 as a tracer has been banned in the European Union since 2006 due to its very high global warming potential as a greenhouse gas.

Because of these limitations, it becomes essential to rely on natural tracers that require an in-depth understanding of the chemical (organic and inorganic) and isotopic changes in water, gases and minerals when CO_2 is injected into a deep reservoir (detailed for the Frio, for example, in Kharaka et al. 2006, 2009; Lu et al. 2012) or when CO_2 leaks into shallow groundwater (Detailed for the ZERT in Spangler et al. 2009; Kharaka et al. 2010b, and many others). The chemical and isotopic changes described in these and other reports provide extremely sensitive techniques that would lead to the early detection of CO_2 and brine leakages.

Seismic and other geophysical measurements, which are beyond the scope of this report, have been used extensively, at times alone, to track the flow of CO_2 and monitor its leakage in CCS sites (Chadwick et al. 2004, 2009; Daley et al. 2007, 2008; Hermanrud et al. 2009; Bohnhoff et al. 2010). However, in many cases, these techniques alone may not be sufficient to discern the changes caused by carbon dioxide injection relative to initial or baseline conditions. Seismic measurements are not able to detect a change until a separate CO_2 phase is present and are particularly difficult for thin layers where the resolution may not be sufficient or for depleted gas fields where the contrast between natural gas and carbon dioxide may not be adequate. Monitoring changes in downhole pressure has also been used as the pressure front is typically the earliest indication of plume migration; however, this technique is limited by the number and accuracy of downhole pressure gauges (Hovorka 2011; Nogues et al. 2011). Geochemical, pressure and geophysical tracer methods can complement each other, but chemical tracers, as discussed below for two well-studied field cases, can be used for early detection of even small CO_2 and brine leaks that cannot be adequately or readily determined with geophysical measurements alone (Kharaka et al. 2009).

Deep subsurface monitoring for early detection: The Frio I Brine test

The Frio site is located within the South Liberty oil field, near Dayton, Texas, a region of the Gulf Coast where large industrial sources of CO_2 are present. The Frio Formation has a dip of 16° to the south, and comprises several reworked fluvial sandstone and siltstone beds that are separated by transgressive marine shale. The Frio sandstones are generally subarkosic fine-grained, moderately sorted quartz and feldspar sandstone, with minor amounts of illite/smectite, calcite and iron oxyhydroxides. The sandstones have high mean porosity >30% and very high permeability of 2–3 darcies. Approximately 1600 and 300 tons of CO_2 were respectively injected into the Frio "C" and Frio Blue sandstones at a depth of about 1500 m. Situated above the "C", the "B" sandstone has a ~4 m thick reworked fluvial sandstone bed at the top, but is separated from "C" by ~15 m of shale, muddy sandstone and siltstone beds. However, the regional cap—the main barrier to CO_2 leakage to shallow groundwater—is expected to be the overlying thick marine shale beds of the Miocene-Oligocene Anahuac Formation (Hovorka et al. 2006).

In this section, we discuss results from Frio I that are pertinent to the leakage of CO_2; the changes in the chemical and isotopic compositions of brine and gases from Frio I and II have been described in an earlier section of this chapter. Most of the water and gas samples for Frio I were obtained from Frio "C" sandstone before CO_2 injection for baseline data, during the injection to track its breakthrough and post-injection to investigate temporal changes in fluid composition (Kharaka et al. 2006, 2009). Fluid samples were also obtained from the overlying Frio "B" sandstone of the observation well about 6 and 15 months after CO_2 injection to investigate CO_2 flow (leakage) from Frio "C".

Monitoring for CO_2 and brine leakage signals at and close to the ground level and from four shallow groundwater wells (~30 m depth), was not effective at the Frio site, primarily because of perturbation caused by injection operations (Nance et al. 2005; Kharaka et al. 2009). Because of this difficulty, we carried out a rigorous program for subsurface monitoring immediately above the injection zone. Results of brine and gas analyses of fluid samples obtained from the "B" sandstone, first perforated and sampled six months after CO_2 injection, showed: 1) Slightly elevated concentrations of bicarbonate, Fe, and Mn; 2) significantly depleted $\delta^{13}C$ values (−5.9 to −17.5 vs. ~−4‰) of DIC (Fig. 8); and 3) somewhat depleted $\delta^{18}O$ values of brine, relative to preinjection values obtained for the "C" samples (Fig. 7). A more definitive proof of the migration of injected CO_2 into the "B" sandstone was obtained from the presence (Fig. 10) of the two PFT tracers (PMCH and PTCH) that were added to the injected CO_2, and migrated with the initial CO_2 breakthrough (Phelps et al. 2006; Kharaka et al. 2009). Additional proof of the migration of injected CO_2 into the "B" sandstone is obtained from the high concentration (2.9 vs. ~0.3 %) of CO_2 in dissolved gas obtained from one of the two downhole Kuster samples (Table 2).

Results of samples collected approximately 15 months after CO_2 injection were more ambiguous, with gas and brine compositions that are similar to those obtained from the "C" sandstone before CO_2 injection. The $\delta^{13}C$ values of DIC and the $\delta^{18}O$ values of brine are slightly depleted in the heavy isotopes relative to preinjection values obtained for the "C" samples. These overall results indicate the absence of significant amounts of injected CO_2 in the "B" fluids sampled. However, a contrary conclusion is indicated from the fact that PMCH and PTCH were measured in the six samples also analyzed for PFT tracers (Phelps et al. 2006). It is possible that the PMCH and PTCH measured during this sampling represent desorbed PFT tracers that were introduced into "B" earlier and do not require migration of additional injected CO_2 into the "B" sandstone.

Results from the "B" sandstone clearly show some CO_2 migration from the "C" sandstone after about 6 months following injection. However, our results could not be used to estimate the volume of CO_2 that migrated to "B", because large volumes of brine, >300 bbl (48 m^3) during April 2005, and ~200 bbl (32 m^3) during January, 2006, that was a mixture of formation water and drilling mud (used while perforating "B" and also while running geophysical and other tests) had to be produced to clean the well. Our results also could not be used to show the flow path of CO_2 from Frio "C" to "B". We cannot rule out migration through the intervening 15 m beds of shale, muddy sandstone and siltstone, but a short-term leakage through the failed squeeze on perforations in the "C" or remedial cement around the casing of a 50 year old well is much more likely. These results highlight the importance of subsurface monitoring for detecting early leaks, and the importance of investigating the integrity of cement seals, especially in nearby abandoned wells, prior to and post injection of large quantities of reactive and buoyant CO_2 (Carey et al. 2007; Kharaka et al. 2009).

Near surface monitoring: The ZERT site, Bozeman, Montana

Since 2007, the Zero Emission Research and Technology (ZERT) field site, located on a relatively flat 12 hectare agricultural plot at the western edge of the Montana State University (MSU)-Bozeman campus in Bozeman, Montana, USA, has been developed into a facility to conduct controlled multidisciplinary studies aimed at evaluating atmospheric and near-surface monitoring and detection techniques applicable to the subsurface storage and potential leakage of CO_2 (Spangler et al. 2009, 2010). At this site and for the last 6 years, controlled shallow releases of approximately 200-300 kg/day of food-grade CO_2 have been carried out for a period of about a month during summer through a perforated pipe placed horizontally 2-2.3 m beneath the ground surface, a depth that is approximately 1 m below the water table (Spangler et al. 2009: Kharaka et al. 2010b). At the ZERT site, there is a 0.2-1.2 m thick topsoil layer of organic-rich silt and clay with some sand, and a caliche layer, high in calcite (~15%), observed

at depths of ~50-80 cm. Beneath the topsoil layer is a cohesionless deposit of coarse sandy gravel extending to 5 m, the maximum depth investigated (Spangler et al. 2009). Gravels comprise ~70% of rock volume, and andesite is the chief rock fragment among the gravels and coarse sands, but minor amounts of detrital limestone and dolostone are also observed. The sand and silt sized fraction of this sediment consists of approximately 40% quartz, 40% magnetite and magnetic rock fragments, and 20% grains of amphibole, biotite/chlorite, and feldspar.

A wide variety of geophysical, chemical, isotopic and biological detection techniques, some novel, have been deployed at this site by the large number of collaborators from universities, national laboratories and public and private institutes, with the goal of establishing detection limits for various methods and determining efficacy of monitoring strategies. Additionally, modeling of CO_2 transport and concentrations has been conducted to better understand its transport in the shallow groundwater, in the vadose zone and near ground level (Lewicki et al. 2007, 2010; Strazisar et al. 2009; Fessenden et al. 2010; Zheng et al. 2012; Zhou et al. 2012; Hogan et al. 2013). An overview of these investigations and some results are presented in Spangler et al. (2009, 2010). More details of the completed or currently ongoing research at the ZERT site can be obtained from the web site: *http://www.montana.edu/zert.*

As part of this research program, we participated in three annual field samplings of groundwater, and carried out laboratory investigations of CO_2-sediment-groundwater interactions and sequential extractions of sediments from the ZERT site (Beers 2011). The groundwater samples were collected from 10 observation wells (1.5 or 3.0 m deep) located 1-6 m from the injection pipe, and from two distant monitoring wells. The samples were collected before, during and following CO_2 injection. The main objective of our study was to investigate changes in the concentrations of major, minor and trace inorganic and organic compounds during and following CO_2 injection. The ultimate goals were (1) to better understand the potential of groundwater quality impacts related to CO_2 leakage from deep storage operations, (2) to develop geochemical tools that could provide early detection of CO_2 intrusion into USDW, and (3) to test the predictive capabilities of geochemical codes against field data (Kharaka et al. 2010b).

The most complete groundwater sampling and detailed chemical analysis occurred in the summer of 2008, when approximately 80 samples of water were collected from 5 shallow monitoring wells (1.5 m deep) installed 1-6 m from the CO_2 injection pipe, and from two distant monitoring wells; the samples were collected before, during and following CO_2 injection. The chemical data obtained prior to CO_2 injection show that the groundwater in the area is a Ca-Mg-Na-HCO_3 type water, with a salinity of about 600 mg/L TDS (Fig. 11). The groundwater has a pH of approximately 7, HCO_3 is the dominant anion, and the concentrations of Cl and SO_4 are relatively low. The concentrations of Fe, Mn, Zn, Pb and other trace metals are expectedly low, at ppb levels.

Field determinations showed rapid and systematic changes in pH, from 7.0 to values as low as 5.6, alkalinity increased from ~400 to values as high as 1330 mg/L as HCO_3 and electrical conductance increased from 600 to 1800 μS/cm following CO_2 injection (Fig. 11). Laboratory results show major increases in the concentrations of Ca (90 to 240 mg/L), Mg (25 to 70 mg/L), Fe (5 to 1200 ppb) and Mn (5 to 1400 ppb) following CO_2 injection. The very low Fe and Mn concentration during July 20 to July 26 (Fig. 12) following significant precipitation events are attributed to the oxidizing conditions possibly caused by increased dissolved O_2 content in groundwater transported with percolating water from precipitation events (Kharaka et al. 2010b).

The concentrations of Pb, As, Zn and other trace metals generally show an increase with increasing alkalinity (lower pH value) following CO_2 injection. The concentration increases

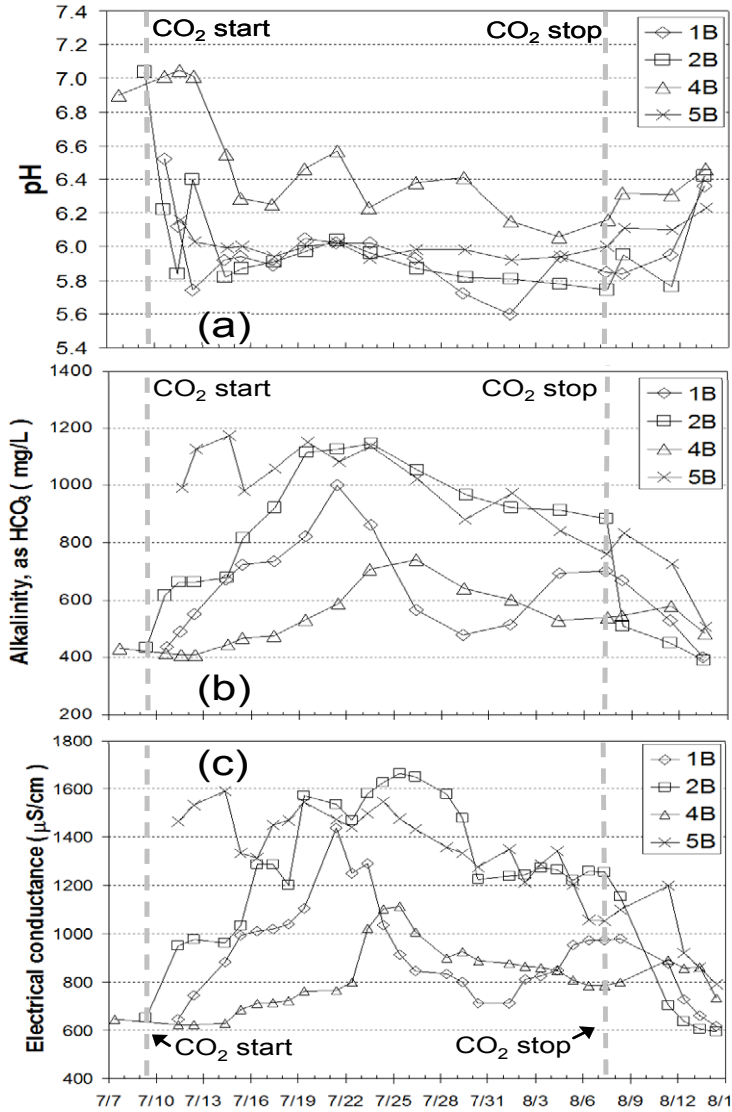

Figure 11. Field measured groundwater pH (4a), alkalinity (4b), and electrical conductance (4c), obtained from selected ZERT wells as a function of sampling time. Note the systematic decrease in pH from ~7.0 before CO_2 injection to values as low as 5.6 during injection. Alkalinities increased from about 400 mg/L to values close to 1200 mg/L as HCO_3, and electrical conductance also increased from about 600 µS/cm before CO_2 injection to values higher than 1,600 µS/cm during injection (Kharaka et al. 2010b).

are likely caused by desorption-ion exchange reactions with H^+, Ca and Mg resulting from lowered pH values. The concentrations of trace metals, it should be noted, are all significantly below the maximum contaminant levels (MCLs) for the respective trace metals (e.g., 15 ppb for Pb, 6 ppb for As). The initial values and the increases in concentrations of these trace metals, although small, are readily measured by the sampling and analytical methods used in this study (see Kharaka et al. 2010b, for details).

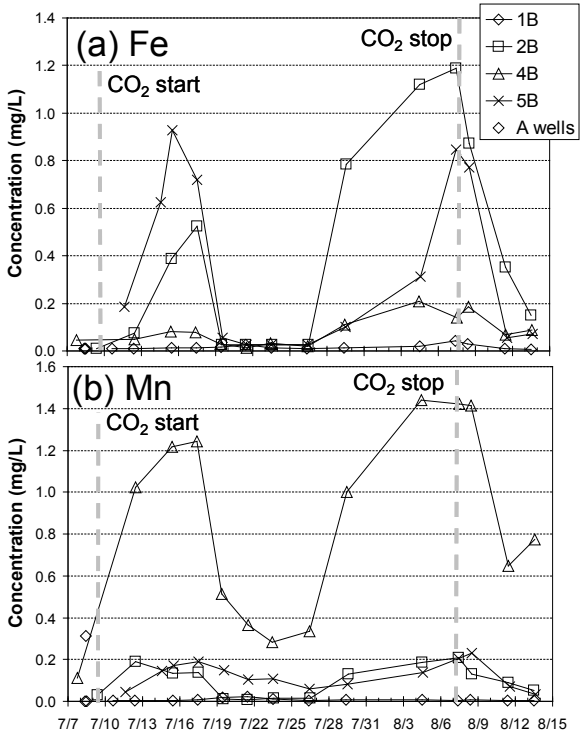

Figure 12. Concentrations of Fe (a) and Mn (b) in groundwater from selected ZERT wells plotted as a function of time of sampling. Note the low Fe and Mn concentrations during July 20 to July 26, which we are attributing to the oxidizing conditions possibly caused by increased dissolved O_2 content in groundwater transported with percolating water from precipitation events (Kharaka et al. 2010b).

The chemical changes observed in the ZERT groundwater following CO_2 injection, are similar in trends, though much lower in concentration values, to the changes observed in the Frio Brine Pilot tests described earlier (Kharaka et al. 2009), and similar to changes observed at other CO_2 sequestration sites described in this chapter (e.g., Cantucci et al. 2009; Underschultz et al. 2011; Martens et al. 2012; Lu et al. 2012). The chemical changes observed at the ZERT site following CO_2 injection, especially in pH, EC and alkalinity that can be readily measured and remotely monitored with relatively inexpensive tools, could provide early detection of CO_2 leakage into shallow groundwater from deep CO_2 storage operations (Kharaka et al. 2010b).

CONCLUDING REMARKS

Geologically sequestered CO_2 is buoyant, has a low viscosity and, when dissolved in brine, becomes reactive to minerals, cements and well pipes. These properties of CO_2 may cause it to leak upward from the major storage reservoirs, possibly contaminating underground sources of drinking water (Kharaka and Cole 2011, and many listed references). We have participated in several multi-laboratory field experiments to investigate the changes in natural chemical and isotopic parameters and added tracers that are applicable to the monitoring of the flow of injected CO_2 into deep reservoirs and into potable shallow groundwater. Geochemical

results from the Frio Brine I and II pilot tests located in the S. Liberty oil field, Dayton, Texas and from the deep SECARB Phase III tests at Cranfield oil field, Mississippi, proved powerful tools in: 1) Tracking the successful injection and flow of CO_2 into the injection sandstones; 2) showing major changes in the chemical (pH, alkalinity, and major divalent cations) and isotopic ($\delta^{13}C$ values of CO_2, and $\delta^{18}O$ values of CO_2, and brine) compositions of formation water; 3) showing mobilization of metals, including Fe Mn and Pb, and organic compounds, including DOC, BTEX, PAHs, and phenols following CO_2 injection; and 4) showing that some of the CO_2 injected into the Frio "C" sandstone was detected in the overlying "B" sandstone that is separated by 15 m of shale and muddy siltstone.

Rapid, significant and systematic changes were also observed in the isotopic and chemical compositions of shallow groundwater at the ZERT site located in Bozeman, MT, in response to four yearly controlled injections of CO_2 gas through a slotted pipe placed horizontally at a depth of ~2 m below ground level. The observed changes, included the lowering of groundwater pH from ~7.0 to values as low as 5.6, increases in the alkalinity from about 400 mg/L as HCO_3 to values of up to 1330 mg/L, increases in the electrical conductance from ~600 μS/cm to up to 1800 μS/cm, as well as increases in the concentrations of cations and metals following CO_2 injection. Geochemical modeling, sequential extractions of cations from the ZERT-aquifer sediments, and controlled laboratory CO_2-groundwater-sediment interactions demonstrated that calcite dissolution and ion exchange on organic material and inorganic mineral surfaces are responsible for the observed chemical changes.

Results from both the deep and shallow field tests investigated by us and those reported by others show that geochemical methods have highly sensitive chemical and isotopic tracers that are needed at CO_2 injection sites to monitor injection performance and for early detection of any CO_2 and brine leakages. For a more detailed discussion of the geochemistry of the geologic storage of CO_2, see a recent review by Kharaka and Cole (2011).

ACKNOWLEDGMENTS

We would like to thank William Evans and Christopher Conaway (both at USGS, Menlo Park, CA) and John Kaszuba (U. of Wyoming) for reviewing this manuscript and suggesting significant improvements. Much of Cole's research on gas chemistry and isotope monitoring of CO_2 injection tests in sedimentary basins is supported by the Department of Energy, National Energy Technology Laboratory (Michael McMillan, Program Coordinator). Cole was also supported as part of the Center for Nanoscale Control of Geologic CO_2, an Energy Frontier Research Center funded by the U.S. Department of Energy, Office of Science, Office of Basic Energy Sciences under Award Number DE-AC02-05CH11231. The Frio and Cranfield projects were managed by Sue Hovorka (Bureau of Economic Geology, University of Texas, Austin), with financial support from Department of Energy (DOE)-National Energy Technology Laboratory (NETL). The zero emission research and Technology (ZERT) research was conducted within the ZERT project directed by Lee Spangler and managed by Laura Dobeck, Montana State University (MSU), Bozeman, MT. The ZERT research was funded primarily by the Electric Power Research Institute, EPRI, but funds were also obtained from EPA, DOE, Lawrence Berkeley National Laboratory (LBNL) and United States Geological Survey (USGS).

REFERENCES

Adams EE, Caldeira K (2008) Ocean storage of CO_2. Elements 4:319-324

Allis R, Bergfeld D, Moore J, McClure K, Morgan C, Chidsey T, Heath J, Macpherson B (2005) Implications of results from CO_2 flux surveys over known CO_2 systems for long-term monitoring. *In:* Proceedings Fourth Annual Conference on Carbon Capture and Sequestration DOE/NETL, May 2-5, 2005, CD-ROM:1367-1388

Audigane P, Gaus I, Czernichowski-Lauriol I, Pruess K, Xu TF (2007) Two-dimensional reactive transport modeling of CO_2 injection in a saline Aquifer at the Sleipner site, North Sea. Am J Sci 307:974-1008

Bachu S (2003) Screening and ranking of sedimentary basins for sequestration of CO_2 in geological media in response to climate change. Environ Geol 44:277-289

Bachu S, Bonijoly D, Bradshaw J, Burruss, R, Holloway, S, Christensen, NP, and Mathiassen OM (2007) CO_2 storage capacity estimation: Methodology and gaps. Int J Greenhouse Gas Control 1:430-443

Baines SJ, Worden RH (2004) The long-term fate of CO_2 in the subsurface: natural analogues for CO_2 storage. In: Geological Storage of Carbon Dioxide. Baines SJ Worden RH (eds) Geological Geol, Soc London Spec Pub 233:59-85

Ballentine CJ, Schoell M, Coleman D, Cain BA (2001) 300-Myr-old magmatic CO_2 in natural gas reservoirs of the west Texas Permian basin. Nature 409:327–331

Barth T (1987) Quantitative determination of volatile carboxylic acids in formation waters by isotachophoresis. Anal Chem 59: 2232–2237

Beers SR (2011) Investigation of the impact of CO_2 on water-rock interactions using sequential extractions. M.S., California State University, San Jose 210p

Begley P, Foulger B, Simmonds P (1988) Femtogram detection of perfluorocarbon tracers using capillary gas chromatography-electron-capture negative-ion chemical ionization mass-spectrometry. J Chromatogr 445(1):119-128

Bénézeth P, Ménez B, Noiriel C (2009) CO_2 geological storage: Integrating geochemical, hydrodynamical, mechanical and biological processes from the pore to the reservoir scale. Chem Geol 265:1-2

Bénézeth P, Palmer AD, Anovitz LM, Horita J (2007) Dawsonite synthesis and re-evaluation of its thermodynamic properties from solubility measurements: Implications for mineral trapping of CO_2. Geochim Cosmochim Acta 71:4438-4455

Benson SM, Cook P (2005) Underground geological storage. *In:* Carbon Dioxide Capture and Storage: Special Report of the Intergovernmental Panel on Climate Change (IPCC). Cambridge University Press, Interlachen, Switzerland, p 5-1 to 5-134

Benson SM Cole DR (2008) CO_2 sequestration in deep sedimentary formations. Elements 4(5):325-331

Bergfeld D, Evans WC, Howle JF, Farrar CD (2006) Carbon dioxide emissions from vegetation-kill zones around the resurgent dome of Long Valley caldera, Eastern California, USA. J Volcanol Geotherm Res 152:140-156

Bickle MJ (2009) Geological carbon storage. Nat Geosci 2(12):815-818

Birkholzer JT Zhou Q (2009) Basin–scale hydrogeologic impacts of CO_2 storage: Capacity and regulatory implications. Int J Greenhouse Gas Control 3:745-756

Birkholzer J, Apps JA, Zheng L, Zhang Y, Xu, T, Tsang, CF (2008) Research project on CO_2 geological storage and groundwater resources: water quality effects caused by CO_2 intrusion into shallow groundwater. Lawrence Berkeley National Laboratory Technical Report, LBNL-1251E:450

Bohnhoff M, Zoback MD, Chiaramonte L, Gerst JL, Gupta N (2010) Seismic detection of CO_2 leakage along monitoring wellbores. Int J Greenhouse Gas Control 4(4):687-697

Boreham C, Underschultz J, Stalker L, Kirste D, Freifeld B, Jenkins C, Ennis-King J (2011) Monitoring of CO_2 storage in a depleted natural gas reservoir: Gas geochemistry from the CO_2CRC Otway Project, Australia. Int J of Greenhouse Gas Control 5:1039-1054

Bradshaw J, Bachu S, Bonijoly D, Burruss R, Holloway, S, Christensen NP, Mathiassen OM (2007) CO_2 storage capacity estimation: Issues and development of standards. Int J Greenhouse Gas Control 1:62-68

Breit GN, Kharaka YK, Rice CA, and Sublette KL (2001) Proceedings of the 7th IPEC Meeting: Environmental Issues and Solutions in Petroleum Exploration, Production, and Refining, November 2000. National Database on the Chemical Composition of Formation Waters from Petroleum Wells, Albuquerque, NM, Tulsa, OK

Broecker WS (2008) CO_2 capture and storage: Possibilities and perspectives. Elements 4:295-297

Brown GE Jr, Bird DK, Kendelewicz T, Maher K, Mao W, Johnson N, Rosenbauer RJ, García Del Real P (2009) Geological Sequestration of CO_2: Mechanisms and Kinetics of CO_2 Reactions with Mafic and Ultramafic Rock Formations (2009). Annual Report to the Global Climate and Energy Project, Stanford University, Stanford, CA, *http://wwwstanfordedu/~gebjr/*

Burant A, Lowry GV, Karamalidis AK (2013) Partitioning behavior of organic contaminants in carbon storage environments: A critical review. Environ Sci Technol 47: 37-54

Burruss R, Brennan ST, Freeman PA, Merrill MD, Ruppert LF, Becker MF, Herkelrath WN, Kharaka YK, Neuzil CE, Swanson, SM, Cook TA, Klett TR, Nelson PH, Schenk CJ (2009) Development of a Probabilistic Assessment Methodology for Evaluation of Carbon Dioxide Storage. USGS Open-File Report No 09–1035

Cantucci B, Montegrossi G, Vaselli O, Tassi F, Quattrocchi F, Perkins EH (2009) Geochemical modeling of CO_2 storage in deep reservoirs: The Weyburn Project (Canada) case study. Chem Geol 265:181-197

Carey JW, Wigand M, Chipera SJ, Wolde G, Pawar R, Lichtner PC, Wehner SC, Raines MA, Guthrie GD (2007) Analysis and performance of oil well cement with 30 years of CO_2 exposure from the SACROC Unit, West Texas, USA. Int J Greenhouse Gas Control 1:75-85

Celia MA, Kavetski D, Nordbotten JM, Bachu S, Gasda SE (2006) Implications of abandoned wells for site selection. *In:* CO_2SC 2006 International Symposium on Site Characterization for CO_2 Geological Storage, March 20-22, 2006. Proceedings: Berkeley, CA, Lawrence Berkeley National Laboratory, 157-159

Chadwick RA, Noy D, Arts R, Eiken O (2009) Latest time-lapse seismic data from Sleipner yield new insights into CO_2 plume development. Energy Procedia 1:2103-2110

Chadwick RA, Zweigel P, Gregersen U, Kirby GA, Holloway S, Johannessen PN (2004) Geological reservoir characterization of a CO_2 storage site: The Utsira Sand, Sleipner, northern. North Sea Energy 29:1371-1381

Clark ID, Fritz P (1997) Environmental Isotopes in Hydrogeology CRC Press, New York

Cole DR, Phelps TJ, Kharaka YK, Horita J, Hovorka SD, Knauss KG, Thordsen JJ Nance HS (2008) Application of gas and fluid chemistry, stable isotopes and perfluorocarbon tracers as MMV tools in assessing water-rock interaction during the Frio CO_2 injection test. Proceedings of the 7th Annual Conf Carbon Capture and Sequestration, Pittsburgh, PA May 5-8, 2008

Conaway CH, Thordsen JJ, Manning MA, Cook PJ, Abedini AA, Trautz RC, Thomas RB, Kharaka YK (2012) Pre-injection comparison of methods for sampling formation water and associated gas from a monitoring well at a carbon dioxide Injection Site, Citronelle oil field, Alabama. Poster presentation at the American Geophysical Union 2012 Fall Meeting, San Francisco, California.

Cook PJ (2009) Demonstration and deployment of carbon dioxide capture and storage in Australia. Energy Procedia 1:3859-3866

Daley TM**,** Solbau RD, Ajo-Franklin JB, Benson SM (2007) Continuous active-source monitoring of CO_2 injection in a brine aquifer. Geophysics 72(5):A57-A61

Daley TM, Myer LR, Peterson JE, Majer EL, Hoversten GM (2008) Time-lapse crosswell seismic and VSP monitoring of injected CO_2 in a brine aquifer. Environ Geol 54(8):1657-1665

de Caritat P, Hortle A, Raistrick M, Stalvies C, Jenkins C (2013) Monitoring groundwater flow and chemical and isotopic composition at a demonstration site for carbon dioxide storage in a depleted natural gas reservoir. Appl Geochem 30:16-32

Deel D, Mahajan K, Mahoney CR, McIlvried HG, Srivastava RD (2006) Risk assessment and management for long-term storage of CO_2 in geologic formations United States. DOE R&D J Systemics, Cybernetics and Informatics 5:79-85

DOE (2008) Carbon Sequestration Atlas II of the United States and Canada, p 142; US Department of Energy, Office of Fossil Energy, National Energy Technology Laboratory

Doughty C, Freifeld BM, Trautz RC (2008) Site characterization for CO_2 geologic storage and vice versa: the Frio brine pilot, Texas, USA as a case study. Environ Geol 54(8):1635-1656

Duan A, Sun R (2003) An improved model calculating CO_2 solubility in pure water and aqueous NaCl solutions from 273 to 533 K and from 0 to 2000 bar. Chem Geol 193:257-271

EIA (2012) Annual Energy Outlook with Projections to 2035. Report #: DOE/EIA-0383; US Energy Information Administration

Emberley S, Hutcheon I, Shevalier M, Durocher K, Mayer B, Gunter WD, Perkins EH (2005) Monitoring of fluid-rock interaction and CO_2 storage through produced fluid sampling at the Weyburn CO_2-injection enhanced oil recovery site, Saskatchewan, Canada. Appl Geochem 20:1131-1157

EPA (2008) Vulnerability evaluation framework for geologic sequestration of carbon dioxide EPA430-R-08-009, p 85; US Environmental Protection Agency

EPA (2009) National Primary Drinking Water Regulations: <http://wwwepagov/safewater/consumer/pdf/mclpdf> (accessed September 18, 2009). US Environmental Protection Agency

Evans WC, Sorey ML, Cook AC, Kennedy BM, Shuster DL, Colvard EM, White LD, Huebner MA (2002) Tracing and quantifying magmatic carbon discharge in cold groundwaters: lessons learned from Mammoth Mountain, USA. J Volcanol Geotherm Res 114: 291-312

Fessenden JE, Clegg SM, Rahn TA, Humphries SD, Baldridge WS (2010) Novel MVA tools to track CO_2 seepage, tested at the ZERT controlled release site in Bozeman, MT. Environ Earth Sci 60:325-334, doi: 101007/s12665-010-0489-3

Flaathen TK, Gislason SR, Oelkers EH, Sveinbjörnsdóttir ÁE (2009) Chemical evolution of the Mt Hekla, Iceland, groundwater: A natural analogue for CO_2 sequestration in basaltic rocks. Appl Geochem 24:463-474

Freifeld BM, Trautz RC, Kharaka YK, Phelps TJ, Myer LR, Hovorka SD, Collins DJ (2005) The U-tube: A novel system for acquiring borehole fluid samples from a deep geologic CO_2 sequestration experiment. J Geophys Res 110:B10203

Friedmann SJ (2007) Geological carbon dioxide sequestration Elements 3:179-184

Gilfillan SMV, Ballentine CJ, Holland G, Blagburn D, Sherwood-Lollar B, Stevens S, Schoell M, Cassidy M (2008) The noble gas geochemistry of natural CO_2 gas reservoirs from the Colorado Plateau and Rocky Mountain provinces, USA. Geochim Cosmochim Acta 72:1174-1198

Gilfillan SMV, Sherwood-Lollar B, Holland G, Blagburn D, Stevens S, Schoell M, Cassidy M, Ding Z, Zhou Z, Lacrampe-Couloume G, Ballentine CJ (2009) Solubility trapping in formation water as dominant CO_2 sink in natural gas fields. Nature 458:614-618

Gislason SR, Wolff-Boenisch D, Stefansson A, Oelkers E, Gunnlaugsson E, Sigurdardóttir H, Sigfússon, Broecker W, Matter J, Stute M, Axelsson G, Fridriksson T (2010) Mineral sequestration of carbon dioxide in basalt: The CarbFix project. Int J Greenhouse Gas Control 4:537-545

Global CCS Institute (2012) The Global Status of CCS: 2012. Canberra, Australia, 218 p *http://www.globalccsinstitute.com/publications/global-status-ccs-2012*

Goldberg DS, Takahashi T, Slagle AL (2008) Carbon dioxide sequestration in deep-sea basalt. Proc Natl Acad Sci USA 105(29):9920-9925

Gunter WD, Perkins EH, McCann TJ (1993) Aquifer disposal of CO_2-rich gases: reaction design for added capacity. Energy Convers Manage 34:941-948

Gysi AP, Stefánsson A (2008) Numerical modeling of CO_2-water-basalt interaction. Mineral Mag 72:55-59

Han WS (2008) Evaluation of CO_2 trapping mechanisms at the SACROC northern platform: Site of 35 years of CO_2 injection: Socorro. The New Mexico Institute of Mining and Technology PhD dissertation, 426

Han WS, McPherson B (2008) Comparison of two different equations of state for application of carbon dioxide sequestration. Adv Water Resourc 31:877-890

Hansen O, Gilding D, Nazarian B, Osdal B, Ringrose P, Kristoffersen JB, Eiken O, Hansen H (2012) Snøhvit: The history of injecting and storing 1 Mt CO_2 in the fluvial Tubåen Fm, 11th Int. Conference on Greenhouse Gas Technology (GHGT11), 18th-22nd November 2012, Kyoto, Japan

Harmon RS, Vannucci R (2006) Frontiers in analytical geochemistry – An IGC 2004 perspective. Appl Geochem 21:727-729

Haszeldine SR (2009) Carbon Capture and Storage: How Green Can Black Be? Science 325:1647-1652

Hellevang H, Declercq J, Aagaard P (2011) Why is dawsonite absent in CO_2 charged reservoirs? Oil Gas Sci Technol – Rev. IFP En. Nouv. 66:119-135

Hellevang HP, Aagaard P, Oelkers EH, Kvamme B (2005) Can dawsonite permanently trap CO_2? Environ Sci Technol 39:8281-8287

Hepple RP, Benson SM (2005) Geologic storage of carbon dioxide as a climate change mitigation strategy: performance requirements and the implications of surface seepage. Environ Geol 47:576-585

Hermanrud C, Andresen T, Eiken O, Hansen H, Janbu A, Lippard J, Bolas HN, Simmenes TH, Teige GMG, Ostmo S (2009) Storage of CO_2 in saline aquifers: lessons learned from 10 years of injection into the Utsira Formation in the Sleipner area. Energy Procedia 1:1997-2004

Hitchon B (ed) (1996) Aquifer Disposal of Carbon Dioxide Geoscience Publishing Ltd, Sherwood Park, Alberta, Canada, p 165

Hitchon B (2000) ''Rust'' contamination of formation waters from producing wells. Appl Geochem 15:1527-1533

Hitchon B (ed) (2009) Pembina Cardium CO_2 Monitoring Pilot: A CO_2-EOR Project, Alberta, Canada. Geoscience Publishing, Box 79088, Sherwood Park, Alberta, Canada p 360

Hitchon B, Gunter WD, Gentzis T, Bailey RT (1999) Sedimentary basins and greenhouse gases: A serendipitous association. Energy Convers Manage 40:825-843

Hogan JA, Shaw JA, Lawrence RL (2012) Detection of leaking CO_2 gas with vegetation reflectances measured by a low-cost multi-spectral imager. IEEE J Selected Topics Appl Earth Observ Remote Sensing 5:699-706

Holloway S (1997) An overview of the underground disposal of carbon dioxide. Energy Convers Manage 38:193-198

Hovorka SD (2011) Test bed for design of commercial monitoring approach - SECARB early test at Cranfield. Abs Proceeding AGU 2011 Fall Meeting, December 5-9, San Francisco, California

Hovorka S, Tinker S (2010) EOR as sequestration: Geoscience perspective. *In:* Symposium on the role of enhanced oil recovery in accelerating the deployment of carbon capture and storage, 23 July 2010, Cambridge, MA, USA.

Hovorka SD, Choi JW, Menckel TA, Trevino RH, Zeng H, Kordi M, Wang FP, Nicot JP (2010) Measured and modeled CO_2 flow through heterogeneous reservoir – early results of SECARB test at Cranfield Mississippi. Abstract, Ninth Annual Conference on Carbon Capture and Sequestration DOE/NETL, May, 2010

Hovorka SD, Benson SM, Doughty CK, Freifeld BM, Sakurai S, Daley TM, Kharaka YK, Holtz MH, Trautz RC, Nance HS, Myer LR, Knauss KG (2006) Measuring permanence of CO_2 storage in saline formations: the Frio experiment. Environ Geosci 13:105-121

Humez P, Lagneau V, Lions J, Negrel P (2013) Assessing the potential consequences of CO_2 leakage to freshwater resources: A batch-reaction experiment towards an isotopic tracing tool. Appl Geochem 30:178-190

Iding M, Ringrose P (2009) Evaluating the impact of fractures on the long-term performance of the In-Salah CO_2 storage site. Energy Procedia 1:2021-2028

IEA (2012) Energy Technology Perspectives 2012--Pathways to a Clean Energy System. 690 p, ISBN 978-92-64-17488-7

Intergovernmental Panel on Climate Change (IPCC) (2005) Special Report on Carbon Dioxide Capture and Storage Prepared by the Working Group III of the Intergovernmental Panel on Climate Change. Metz BO, Davidson HC, de Coninck M, Loos, Meyer LA (eds) Cambridge University Press, Cambridge, United Kingdom and New York, NY, USA, 442 p

Intergovernmental Panel on Climate Change (IPCC) (2007) Climate Change 2007: The Physical Science Basis Contribution of Working Group I to the Fourth Assessment Report of the Intergovernmental Panel on Climate Change. (Solomon S, Qin D, Manning M, Chen Z, Marquis M, Averyt KB, Tignor M, Miller HL (eds) Cambridge University Press, Cambridge, United Kingdom and New York, NY, USA, 996 p

Ivahnenko T, Szabo Z, Gibs J (2001) Changes in sample collection and analytical techniques and effects on retrospective comparability of low-level concentrations of trace elements in ground water. Water Res 35: 3611-3624

Johnson G, Mayer B (2011) Oxygen isotope exchange between H2O and CO_2 at elevated CO_2 pressures: Implications for monitoring of geological CO_2 storage. Appl Geochem 26: 1184-1191

Johnson G, Mayer B, Nightingale M, Shevalier M, Hutcheon I (2011) Using oxygen isotope ratios to quantitatively assess trapping mechanisms during CO_2 injection into geological reservoirs: The Pembina Case Study. Chem Geol 283:185-193

Juanes R, Hager BH, Herzog HJ (2012) No geologic evidence that seismicity causes fault leakage that would render large-scale carbon capture and storage unsuccessful. Proc Natl Acad Sci USA 109:E3623

Kaszuba JP, Janecky DR, Snow MG (2005) Experimental evaluation of mixed fluid reactions between supercritical carbon dioxide and NaCl brine: Relevance to the integrity of a geologic carbon repository. Chem Geol 217(3-4):277-293

Kaszuba JP, Viswanathan HS, Carey JW (2011) Relative stability and significance of dawsonite and aluminium minerals in geologic carbon sequestration. Geophys Res Lett 38, doi:10.1029/2011GL046845, p 1-5

Kennedy VC, Zellsegar GW, Jones BF (1974) Filter pore size effects on the analysis of Al, Fe, Mn, and Ti in water. Water Resourc Res 10:785-789

Kharaka YK, Cole DR (2011) Geochemistry of geologic sequestration of carbon dioxide. *In:* Frontiers in geochemistry: Contribution of Geochemistry to the Study of the Earth. Harmon RS, Parker A (eds) Blackwell Publishing Ltd, p 136-174

Kharaka YK, Hanor JS (2013) Deep fluids in sedimentary basins. In Surface and Ground Water, Weathering and Soils; Treatise on Geochemistry 2nd Edition. Drever JI (ed) Elsevier, 45 p *http://dx.doi.org/10.1016/B978-0-08-095975-7.00516-7*

Kharaka YK, Hull RW, Carothers WW (1985) Water–rock interactions in sedimentary basins. *In:* Gautier DL, Kharaka YK, and Surdam RC (eds.) Series Relationship of Organic Matter and Mineral Diagenesis, Short Course 17, pp. 79-176. Tulsa: Society of Economic Paleontologists and Mineralogists

Kharaka YK, Maest AS, Carothers WW, Law LM, Fries TL (1987) Geochemistry of metal-rich brines from central Mississippi Salt Dome Basin, USA. Appl Geochem 2:543-561

Kharaka YK, Gunter WD, Agarwal PK, Perkins EH, DeBrall JD (1988) SOLMINEQ88: A computer program for geochemical modeling of water-rock interactions. US Geological Survey Water Resources Invest Rep 88-4227

Kharaka YK, Cole DR, Hovorka SD, Gunter WD, Knauss KG, Freifeld BM (2006) Gas-water-rock interactions in Frio Formation following CO_2 injection: implications to the storage of greenhouse gases in sedimentary basins. Geology 34:577-580

Kharaka YK, Thordsen JJ, Kakouros E, Birkholzer J, Apps J, Trautz R, Rauch H, Gullickson K (2009) Potential environmental issues of CO_2 storage in deep saline aquifers: Geochemical results from the Frio-I Brine Pilot test, Texas, USA. Appl Geochem 24:1106-1112

Kharaka YK, Thordsen JJ, Bullen TD, Cole DR, Phelps TJ, Birkholzer JT, Hovorka SD (2010a) Near surface and deep subsurface monitoring for successful geologic sequestration of CO_2. *In:* Birkle P, Torres-Alvarado IS (eds) Proceedings of WRI-13, pp. 867-870. Rotterdam: A. A. Balkema.

Kharaka YK, Thordsen JJ, Kakouros E, Ambats G, Herkelrath WN, Birkolzer JT, Apps JA, Spycher NF, Zheng L, Trautz RC, Rauch HW, Gullickson KS (2010b) Changes in the chemistry of shallow groundwater related to the 2008 injection of CO_2 at the ZERT field site, Bozeman, Montana. Environ Earth Sci 60:273-284

Kharaka YK, Campbell PL, Thordsen JJ, Thomas RB, Cole DR (2011) Environmental impacts of the geologic sequestration of CO_2: Potential impacts from mobilized organic species. Proc 242nd ACS National Meeting, August 30- September 3, 2011, Denver, CO.

Kharaka YK, Thordsen JJ, Conaway CH, Thomas RB, Cole DR (2013) Geochemistry of geologic sequestration of CO_2: Lessons learned from pilot tests and active CCS projects. Proceedings Le Studium Conference: Geochemical reactivity in CO_2 geological storage sites – Orléans, February 25-26, 2013

Knauss KG, Johnson JW, Steefel CI (2005) Evaluation of the impact of CO_2, co-contaminant gas, aqueous fluid and reservoir-rock interactions on the geologic sequestration of CO_2. Chem Geol 217:339-350

Kolak JJ, Burruss RC (2006) Geochemical investigation of the potential for mobilizing non-methane hydrocarbons during carbon dioxide storage in deep coal beds. Energy Fuels 20(2):566-574

Lackner KS (2002) Carbonate chemistry for sequestering fossil carbon. Annu Rev Energy Environ 27:193-232

Lewicki J, Oldenburg C, Dobeck L, Spangler L (2007) Surface CO_2 leakage during the first shallow subsurface CO_2 release experiment. Geophys Res Lett 34:L24402, doi:101029/2007GL032047

Lewicki JL, Hilley GE, Fischer ML, Pan L, Oldenburg CM, Dobeck L, Spangler L (2010) Eddy covariance observations of surface leakage during shallow subsurface CO_2 releases. J Geophys Res Atmos 114:D12302, doi:101029/2008JD011297

Li D, Duan Z (2007) The speciation equilibrium coupling with phase equilibrium in the H_2O–CO_2–NaCl system from 0 to 250 °C, from 0 to 1000 bar, and from 0 to 5 molality of NaCl. Chem Geol 244:730-751

Lico MS, Kharaka YK, Carothers WW, Wright VA (1982) Methods for collection and analysis of geopressured geothermal and oil-field waters. US Geological Survey Water-Supply Paper, Report: W 2194

Litynski JT, Plasynski S, Mahoney HG, Srivastava RD (2008) The United States Department of Energy's regional carbon sequestration partnerships program validation phase. Environ Int 34:127-138

Lu J, Kharaka YK, Thordsen JJ, Horita J, Karamalidis A, Griffith C, Hakala JA, Ambats A, Cole DR, Phelps TJ, Manning MA, Cook PJ, Hovorka SD (2012) CO_2-rock-brine interactions in the Lower Tuscaloosa Formation at the Cranfield CO_2 sequestration site, Mississippi, USA. Chem Geol 291:269-277

Maher K, Steefel CI, Depaolo DJ, Viani BE (2006), The mineral dissolution rate conundrum: Insights from reactive transport modeling of U isotopes and pore fluid chemistry in marine sediments. Geochim Cosmochim Acta 70(2):337-363

Marini L (2007) Geological Sequestration of Carbon Dioxide: Thermodynamics, Kinetics and Reaction Path Modeling. Elsevier, Amsterdam

Martens S, Kempka T, Liebscher A, Lüth S, Möller F, Myrttinen A, Norden B, Schmidt-Hattenberger C, Zimmer M, Kühn M (2012) Europe's longest-operating on-shore CO_2 storage site at Ketzin, Germany: a progress report after three years of injection. Environ Earth Sci 67(2):323-334, doi:10.1007/s12665-012-1672-5

Mathieson A, Midgely J, Wright I, Saoula N, Ringrose P (2010) In Salah CO_2 Storage JIP: CO_2 sequestration monitoring and verification technologies applied at Krechba, Algeria. Energy Procedia 10:1063-1071

Matter JM, Kelemen PB (2009) Permanent storage of carbon dioxide in geological reservoirs by mineral carbonation. Nat Geosci 2(12):837-841

Matter JM, Broecker WS, Stute S, Gislason SR, Oelkers EH, Stefánsson A, Wolff-Boenisch D, Gunnlaugsson E, Axelsson G, Björnsson G (2009) Permanent carbon dioxide storage into basalt: The CarbFix Pilot Project, Iceland. Energy Procedia 1:3641-3646

Matter JM, Broecker WS, Gislason SR, Gunnlaugsson E, Oelkers EH, Stute M, Sigurdardottir H, Stefansson A, Alfredsson HA, Aradottir ES, Axelsson G, Sigfuson B, Wolff-Boenisch D (2011) The CarbFix Pilot Project- Storing carbon dioxide in basalt. Energy Procedia 4:5579-5585

May F, Waldmann S (2013) Tasks and challenges of geochemical monitoring. *In:* Proceedings Le Studium Conference "Geochemical reactivity in CO_2 geological storage sites" – Orléans, February 25-26, 2013

McNab W, Carroll SA (2011) Wellbore integrity at the Krechba Carbon Storage Site, In Salah, Algeria: 2. Reactive transport modeling of geochemical interactions near the Cement–Formation interface. Energy Procedia 4:5195-5202

Michael K, Arnot M, Cook P, Ennis-King J, Funnell R, Kaldi J, Kirste D, Paterson L (2009) CO_2 storage in saline aquifers I: current state of scientific knowledge. Energy Procedia 1:3197-3204

Mito S, Xue Z, Ohsumi T (2008) Case study of geochemical reactions at the Nagaoka CO_2 Injection Site. Japan Int J Greenhouse Gas Control 2:309-318

Mito S, Xue Z, Sato T (2013) Effect of formation water composition on predicting CO_2 behavior: A case study at the Nagaoka post-injection monitoring site. Appl Geochem 30:33-40

Moritis G (2009) Special Report: More CO_2-EOR projects likely as new CO_2 supply sources become available. Dec 2009, Oil & Gas J, *http://www.ogj.com/articles/print/volume-107/issue-45/drillng-production/special-report-more.html*

Myers MB, Stalker L, Pejcic B, Ross A (2013) Tracers - past, present and future applications in CO_2 geosequestration. Appl Geochem 30:125-135

Nance HS, Rauch H, Strazisar B, Bromhal G, Wells A, Diehl R, Klusman R, Lewicki JL, Oldenberg CM, Kharaka YK, Kakouros E (2005), Surface environmental monitoring at the Frio Test site. Proceedings of the Fourth Annual Conference on Carbon Capture and Sequestration, Alexandria, VA, May 2-5, 16 p, CD-ROM

Nazarian B, Ringrose P, Held R (2013) Geochemistry of CO_2 injection in operating CCS projects. Proceedings Le Studium Conference: Geochemical reactivity in CO_2 geological storage sites – Orléans, February 25-26, 2013

NIOSH/OSHA (1981) Occupational Health Guidelines for Chemical Hazards: Department of Health and Human Services (National Institute for Occupational Safety and Health) Publication No 81-123, United States Government Printing Office, Washington, DC

NIOSH/OSHA (1989) Toxicologic review of selected chemicals: Carbon dioxide, *http://wwwcdcgov/niosh/pel88/124-38html*

Nimz GJ, Hudson GB (2005) The use of noble gas isotopes for monitoring leakage of geologically stored CO_2. *In:* Carbon Dioxide Capture for Storage in Deep Geologic Formations. Thomas D, Benson S (Eds) Elsevier Press, Amsterdam, p 1113-1130

Nogues JP, Nordbotten JM, Celia MA (2011) Detecting leakage of brine or CO_2 through abandoned wells in a geological sequestration operation using pressure monitoring wells. Energy Procedia 4:3620-3627

Nordbotten JM, Kavetski D, Celia MA, Bachu S (2009) Model for CO_2 leakage including multiple geological layers and multiple leaky wells. Environ Sci Technol 43:743-749

Oelkers EH, Cole DR (2008) Carbon dioxide sequestration: A solution to a global problem. Elements 4:305-310

Oelkers EH, Gislason SR, Matter J (2008) Mineral carbonation of CO_2. Elements4(5):333-337

Oldenburg CM (2007) Migration mechanisms and potential impacts of CO_2 leakage and seepage. *In:* Carbon Capture and Sequestration: Integrating Technology, Monitoring and Regulation. Wilson EJ, Gerard D (eds) Blackwell Publishing, p 127-146

Pacala S, Socolow R (2004) Stabilization wedges: Solving the climate problem for the next 50 years with current technologies. Science 305(5686):968-972

Palandri JL, Kharaka YK (2005) Ferric iron-bearing sediments as a mineral trap for CO_2 sequestration: iron reduction using sulfur-bearing waste gas. Chem Geol 217:351-364

Palandri JL, Rosenbauer RJ, Kharaka YK (2005) Ferric iron in sediments as a novel CO_2 mineral trap: CO_2-SO_2 reaction with hematite. Appl Geochem 20:2038-2048

Pang Z, Yang F, Li YH, Duan Z (2010) Integrated CO_2 sequestration and geothermal development: Saline aquifers in Beitang depression, Tianjin, North China Basin. *In:* Proceedings of the 13th International Symposium on the Water Rock Interaction. Taylor & Francis, London, p 31-36

Parry WT, Forester CB, Evans JP, Bowen BB, Chan MA (2007) Geochemistry of CO_2 sequestration in the Jurassic Navajo Sandstone: Colorado Plateau, Utah. Environ Geosci 14:91-109

Paukert AN, Matter JM, Kelemen PB, Shock EL, Havig JR (2012). Reaction path modeling of enhanced in situ CO_2 mineralization for carbon sequestration in the peridotite of the Samail Ophiolite, Sultanate of Oman. Chem Geol 330-331:86-100

Phelps TJ, McCallum SD, Cole DR, Kharaka YK, Hovorka SD (2006) Monitoring geological CO_2 sequestration using perfluorocarbon gas tracers and isotopes. Proc Fifth Annual Conference on Carbon Capture and Sequestration, Alexandria, VA, May 8-11, p 8 CD-ROM

Power IM, Wilson SA, Dipple GM (2013) Serpentinite carbonation for CO_2 sequestration. Elements 9:115-121

Reilly TE, Dennehy KF, Alley WM, Cunningham WL (2008) Ground-water availability in the United States. US Geological Survey Circular 1323:70; *http://pubsusgsgov/circ/1323/*

Romanak KD, Bennett PC, Yang C, Hovorka SD (2012a) Process-based approach to CO_2 leakage detection by vadose zone gas monitoring at geologic CO_2 storage sites. Geophys Res Lett 39:L15405, doi:101029/2012GL052426

Romanak KD, Smyth RC, Yang C, Hovorka SD, Rearick M, Lu J (2012b) Sensitivity of groundwater systems to CO_2: application of a site-specific analysis of carbonate monitoring parameters at the SACROC CO_2-enhanced oil field. Int J Greenhouse Gas Control 6(1):142-152

Romanak K, Russell H, Kharaka Y (2013) Geochemical aspects of geologic carbon storage. Editors' introduction. Appl Geochem 30:1-3

Rosenbauer RJ, Koksalan T, Palandri JL (2005) Experimental investigation of CO_2-brine-rock interactions at elevated temperature and pressure: Implications for CO_2 sequestration in deep-saline aquifers. Fuel Process Technol 86:1581-1597

Rubin ES (2008) CO_2 capture and transport. Elements 4:311-317

Rutqvist J, Vasco DW, Myer L (2009) Coupled reservoir-geomechanical analysis of CO_2 injection at In Salah, Algeria. Energy Procedia 1(1):1847-1854

Schrag DP (2009) Storage of carbon dioxide in offshore sediments. Science 325:1658-1659

Sherk GW, Romanak KD, Dale J, Gilfillan SMV, Haszeldine RS, Ringler ES, Wolaver BD, Yang C (2011) The Kerr investigation: findings of the investigation into the impact of CO_2 on the Kerr property: IPAC Research Inc, final report prepared for property owners. Cameron and Jean Kerr, 181 p

Shiraki R, Dunn TL (2000) Experimental study on water-rock interactions during CO_2 flooding in the Tensleep Formation, Wyoming, USA. Appl Geochem 15:265-279

Smyth R C, Hovorka W D, Lu J, Romanak KD, Partin JWC, and Yang WC (2009) Assessing risk to fresh water resources from long term CO_2 injection-laboratory and field studies. Energy Procedia 1:1957-1964

Spangler LH, Dobeck LM, Repasky, Nehrir A, Humphries S, Barr J, Keith C, Shaw J, Rouse J, Cunningham A, Benson S, Oldenburg CM, Lewicki JL, Wells A, Diehl R, Strazisar B, Fessenden J, Rahn T, Amonette J, Barr J, Pickles W, Jacobson SE, Male E, Rauch H, Gullickson K, Trautz R, Kharaka YK, Birkholzer J, Wielopolski L (2009) A controlled field pilot for testing near surface CO_2 detection techniques and transport models. Energy Procedia 1:2143-2150

Spangler LH, Dobeck LM, Repasky, Nehrir A, Humphries S, Barr J, Keith C, Shaw J, Rouse J, Cunningham A, Benson S, Oldenburg CM, Lewicki JL, Wells A, Diehl R, Strazisar B, Fessenden J, Rahn T, Amonette JE, Pickles W, Jacobson SE, Silver EA, Male EJ, Rauch HW, Gullickson KS, Trautz R, Kharaka YK, Birkholzer J, Wielopolski L (2010) A shallow subsurface controlled release facility in Bozeman, Montana, USA, for testing near surface CO_2 detection techniques and transport models. Environ Earth Sci 60:227-239

Spycher N, Pruess K (2005) CO_2-H_2O mixtures in the geological sequestration of CO_2 II: Partitioning in chloride brines at 12-100°C and up to 600 bar. Geochim Cosmochim Acta 69:3309-3320

Spycher N, Pruess K, Ennis-King J (2003) CO_2-H_2O mixtures in geological sequestration of CO_2, I: Assessment and calculation of mutual solubilities from 12 to 100ºC and up to 600 bar. Geochim Cosmochim Acta 67:3015-3031

Stenhouse M, Arthur R, Zhou W (2009) Assessing environmental impacts from geological CO_2 storage. Energy Procedia 1:1895-1902

Strazisar BR, Wells AW, Diehl JR, Hammack RW, Veloski GA (2009) Soil gas monitoring for the ZERT shallow CO_2 injection project. Int J Greenhouse Gas Control 3(6):736-744

Sundquist ET, Ackerman KV, Parker L Huntzinger DN (2009) An introduction to global carbon cycle. *In:* Carbon Sequestration and Its Role in the Global Carbon Cycle. McPherson BJ, Sundquist ET (eds) American Geophysical Union, Geophysical Monograph 183, Washington, DC, p 1-23

Thordsen JJ, Kharaka, YK, Thomas RB, Ambats, G, Abedini A, Manning MA, Lu J (2012) Evolving geochemistry of Tuscaloosa Formation brine in response to continuing CO_2 injection at Cranfield EOR site, Mississippi, USA. Abs 361, Proceedings, 11th Annual Conference on Carbon Capture & Sequestration; April 30-May3, 2012, Pittsburgh, Pennsylvania

Torp TA, Gale J (2003) Demonstrating storage of CO_2 in geological reservoirs: the Sleipner and SACS projects. *In:* Proceedings of the 6th International Conference on Greenhouse Gas Control Technologies. Gale J, Kaya J (eds) (GHGT-6), 1-4 October 2002, Kyoto, Japan, Pergamon, Amsterdam, Vol 1. p 311-316

Underschultz J, Boreham C, Dance T, Stalker L, Freifeld B, Kirste D, Ennis-King J (2011) CO_2 Storage in a Depleted Gas Field: An Overview of the CO_2CRC Otway Project and Initial Results. Int J Greenhouse Gas Control 5:922-932

US Geological Survey (2008) The Great Southern California ShakeOut. *http://wwwshakeoutorg/*

Verma MK, Warwick PD (2011) Development of an assessment methodology for hydrocarbon recovery potential using carbon dioxide and associated carbon sequestration—Workshop findings: U.S. Geological Survey Fact Sheet 2011–3075, 2 p., available at *http://pubs.usgs.gov/fs/2011/3075/*

Wells A, Strazisar B, Diehl JR, Veloski G (2010) Atmospheric tracer monitoring and surface plume development at the Zert Pilot Test in Bozeman, Montana, USA. Environ Earth Sci 60(2):299-305

Wells AW, Diehl JR, Bromhal G, Strazisar BR, Wilson TH, White CM (2007) The use of tracers to assess leakage from the sequestration of CO_2 in a depleted oil reservoir, New Mexico, USA. Appl Geochem 22:996-1016

White CM, Strazisar BR, Granite EJ (2003) Separation and capture of CO_2 from large stationary sources and sequestration in geological formations: coalbeds and deep saline aquifers. J Air Waste Manage Assoc 53:645–715

Xu T, Kharaka YK, Doughty CBM, Daley TM (2010) Reactive transport modeling to study changes in water chemistry induced by CO_2 injection at the Frio-I Brine Pilot. Chem Geol Chem Geol 271:153-164

Zhang W, Li Y, Xu T, Cheng H, Zheng Y, Xiong P (2009) Long-term variations of CO_2 trapped in different mechanisms in deep saline formations: A case study of the Songliao Basin, China. Greenhouse Gas Control Technol 3(2):161-180

Zheng L, Apps JA, Spycher N, Birkholzer JT, Kharaka,YF, Thordsen J, Beers SR, Herkelrath WN, Kakouros E, Trautz RC (2012) Geochemical modeling of changes in shallow groundwater chemistry observed during the MSU-ZERT CO_2 injection experiment. Int J Greenhouse Gas Control 7:202-217

Zheng L, Spycher N, Birkholzer J, Xu T, Apps J, Kharaka Y (2013) On modeling the potential impacts of CO_2 sequestration on shallow groundwater: Transport of organics and co-injected H_2S by supercritical CO_2 to shallow aquifers. Int J Greenhouse Gas Control 14:113-127

Zhou X, Wielopolski L, V. R. Lakkaraju VR, Apple M, Dobeck LM, Gullickson K, Shaw JA, Cunningham AB, Spangler LH (2012) Experimental observations of signature changes of bulk soil electrical conductivity (EC) due to CO_2 leakage. Int J Greenhouse Gas Control, 7: 2012

Zoback MD, Gorelick SM (2012) Earthquake triggering and large-scale geologic storage of carbon dioxide. Proc Natl Acad Sci USA 109(26):10164-10168 *www.pnas.org/cgi/doi/101073/pnas1202473109*

Zuddas P (2010) Water-rock interaction processes seen through thermodynamics. Elements 6: 305-308

Reviews in Mineralogy & Geochemistry
Vol. 77 pp. 431-458, 2013
Copyright © Mineralogical Society of America

Multi-scale Imaging and Simulation of Structure, Flow and Reactive Transport for CO_2 Storage and EOR in Carbonate Reservoirs

John P. Crawshaw and Edo S. Boek

Qatar Carbonates and Carbon Storage Research Centre (QCCSRC)
Department of Chemical Engineering
Imperial College London, London SW7 2AZ, United Kingdom

j.crawshaw@imperial.ac.uk *e.boek@imperial.ac.uk*

INTRODUCTION

As we continue to use fossil fuels for our energy supply, the concentration of CO_2 in the Earth's atmosphere is likely to continue to increase. It has been shown that this is correlated with an increase in the temperature of the atmosphere and potential associated climate change. To mitigate this problem, Carbon Capture and Storage (CCS) has been mooted over the past decade. In this chapter, we will focus on CO_2 storage in downhole rock formations. Rock formations suitable for storage include saline aquifers and depleted oil and gas reservoirs. Also coal bed methane (CBM) reservoirs may be suitable for storage, but we will not consider these in the current chapter. In the case of saline aquifers, we consider only the storage of CO_2. In the case of depleted oil/gas reservoirs, the storage of CO_2 can be combined with Enhanced Oil Recovery (EOR). This may lead to a more favorable economic scenario and has recently been coined as CCUS (Carbon Capture and Utilized Storage). In particular we will focus in this chapter on carbonate reservoirs. Sandstone reservoirs have been relatively well studied. However, much less is known about the storage properties of carbonate rocks, which have very different petrophysical and flow properties. Moreover, carbonate rocks constitute a significant fraction of existing depleted hydrocarbon reservoirs. Our aim is to study the pore scale properties of carbonates and upscale these to the core and field scales. First, carbonates have a very different structure from sandstones, associated with their composition and diagenesis. Carbonates usually have a much broader pore size distribution (PSD) than sandstones with extensive microporosity (Cantrell and Hagerty 1999). In addition, carbonates are often naturally fractured (Ameen et al. 2010). This leads to a broad range of heterogeneity as a function of length scale, in comparison with sandstones which often have more homogeneous properties. The degree of heterogeneity may be quantitatively measured using the concept of Representative Element of Volume (REV) originally introduced by (Bear 1972). Following Bear (1972), let us first define the porosity

$$n_i = \frac{\left(\Delta U_v\right)_i}{\Delta U_i} \tag{1}$$

where $(\Delta U_v)_i$ is the volume of void space within ΔU_i. For large values of ΔU_i , the porosity may change gradually with decreasing ΔU_i, particularly if the domain is heterogeneous (e.g., due to fractures or layering). Below a certain value of ΔU_i, the large scale fluctuations decay, leaving only small scale fluctuations associated with a random distribution of pore sizes. Below a certain value ΔU_0, large-scale fluctuations in the porosity may emerge, as ΔU_i approaches the size of a single pore. Finally, in the limit $\Delta U_i \to 0$, the value of n_i will become either 0 or 1, depending on whether our reference point P is inside a pore or inside the solid matrix of the porous

1529-6466/13/0077-0012$05.00 http://dx.doi.org/10.2138/rmg.2013.77.12

medium. Figure 1 shows the relationship between n_i and ΔU_i. The volume ΔU_0 is defined as the Representative Elementary Volume (REV). From the definition of the REV, it follows that a slight variation in its dimensions does not significantly influence the value of the porosity n_i.

Obviously the REV concept is not limited to the porosity but can be extended to other porous media properties. Please note that the value of the REV will be a function of the property under consideration. Properties relevant to CO_2 storage and EOR include porosity, single-phase permeability, hydrodynamic dispersion and relative permeability. Sandstones are often found to become homogeneous media at sufficiently large length scales. Carbonates, on the other hand, often have REVs larger than those of sandstones for the property under consideration. Sometimes, carbonates remain heterogeneous with increasing length scale.

Second, chemical reactions may occur during the CO_2 storage process. This may affect carbonates and sandstones in different ways. In the case of carbonates, reactive flow may alter the pore space due to dissolution of the matrix or precipitation of carbonate minerals.

This makes the prediction of flow and transport properties in carbonates a particular challenge. We aim to address this challenge by a combination of experiments, modeling and theory:

1. Multi-scale imaging of reservoir rock samples at different length scales, using different scanning techniques including medical CT, micro-CT, confocal microscopy and FIB-SEM, generating 3D pore space images at different spatial resolutions;
2. Multi-scale simulation and micro-fluidic experiments to characterize flow and (reactive) transport directly on pore space images obtained from the scanning experiments above;
3. Upscaling the flow and transport properties from pore to core to field scale

In the following sections, we will address and review the points above systematically and conclude with future research opportunities.

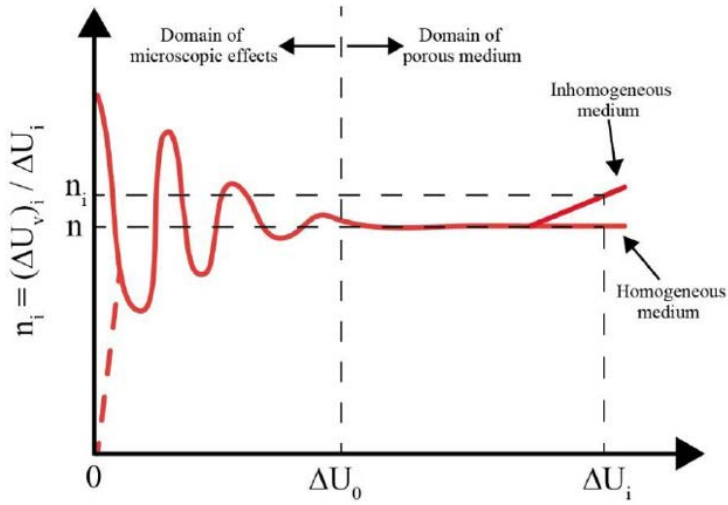

Figure 1. Definition of representative element of volume (REV) based on porosity n_i (adapted from Bear 1972).

MICRO-FLUIDIC EXPERIMENTS OF FLOW IN ETCHED MICRO-MODELS

Various techniques have been used to visualize the transport of fluids in porous media by optical means. Packings of glass beads offer some insight into flow processes, but it is difficult to see clearly displacements happening in individual pores due to the distortion caused by the light from the region of interest passing through materials of different refractive index. Micro-models avoid this problem by adopting a two dimensional structure of channels etched into a flat plate. While this allows unrestricted optical access to flow processes in the model, some compromises have to be made when attempting to represent realistic rock pore geometries. For a detailed review of micro-model development, see Buckley (1991).

Networks of channels chemically etched into glass plates were used as early as 1961 (Mattax and Kyte 1961) but the shape of the duct cross-section in such early attempts was not well defined. This was overcome by Lenormand (1981) using a molding technique in transparent polyester resin which resulted in channels of rectangular cross-section that were convenient for both observation and analysis. The presence of a sharp corner was particularly desirable as this provides a corner meniscus to connect the wetting phase through channels mostly occupied by the non-wetting phase.

A variety of such polymer-based models was subsequently developed, but they lacked the resolution required to represent pores at the sizes found in natural rocks. Models based on channels etched into silicon and covered with a glass plate offered this capability with channel sizes as small as a few micrometers so that pore shapes taken from thin section images of rocks could be represented at 1:1 scale. A glass plate was anodically bonded to the silicon, sealing the etched channels effectively without distortion of the channel walls. Details of the fabrication of silicon/glass micro-models can be found in (Hornbrook et al. 1991; Buchgraber et al. 2012)

An alternative approach to the fabrication of micro-models is to use an all glass construction. Early versions had a much larger minimum channel size than the silicon/glass versions as channels smaller than around 50 micrometers were difficult to etch. However, this limitation has been overcome and pore dimensions can now approach 50 micrometers (Wan et al. 1996).

Drainage and imbibition

In the pioneering work of Lenormand (Lenormand et al. 1983) drainage and imbibition were analyzed in terms of the Young Laplace equation for the pressure across an interface with two principle radii of curvature r_1, r_2 of a fluid pair with interfacial tension meeting the solid surface at an angle θ,

$$P_C = \gamma \cos\theta \left(\frac{1}{r_1} + \frac{1}{r_2} \right) \tag{2}$$

Simple geometric arguments lead to predictions for the capillary pressure at which the advancing meniscus will invade a pore throat during drainage and a pore body during imbibition. The pressure at which snap-off occurs in a throat can also be established by considering the swelling of the corner menisci (Li and Wardlaw 1986); when two of the menisci meet and merge, the interface is unstable and the interface will contract into the middle of the duct and collapse. When the geometry of the network is known exactly, as in Lenormand's array of rectangular ducts (Lenormand et al. 1983), the sequence of filling of the pore space elements can be predicted when the change of the capillary pressure is slow and viscous forces are negligible. This is particularly important for the snap-off events that are fed by the wetting fluid creeping along wetting films and corner menisci. A continuous wetting phase allows snap-off to happen

at positions far from the advancing fluid front, but only if the thin layers have time to conduct the wetting fluid to the position at which snap-off is allowed by the prevailing capillary force. Another key observation was that the pressure (or curvature) at which a pore body can be filled during imbibition depends on the number of connected elements filled with the wetting phase. While this can be allowed for in micro-models where the geometry is relatively simple and known exactly, it is problematic to extend this to real rocks where there are infinitely many permutations of geometry.

Mathematical network models elaborated from the micro-model observations have been successful at predicting petrophysical properties such as relative permeability in a computationally efficient way by reducing the real pore shapes to a network of simple ducts with circular, triangular or rectangular cross-sections (Valvatne and Blunt 2004).

Fractured media

In CO_2 storage in fractured reservoirs, the exchange of fluids between the matrix and the fracture is of great importance. Micro-model investigations of matrix-fracture transfer have been carried out by etching a wide channel at the edge of a pattern representing the rock matrix (Rangel-German and Kovscek 2006). Fluid ports at either end of the wide channel representing the fracture allow it to be filled with a wetting fluid after the micro-model was initially filled with the non-wetting fluid initiating a spontaneous imbibition process. This allows detailed observation of the exchange of fluids between the fracture and the matrix as the fracture is filled (Fig. 2).

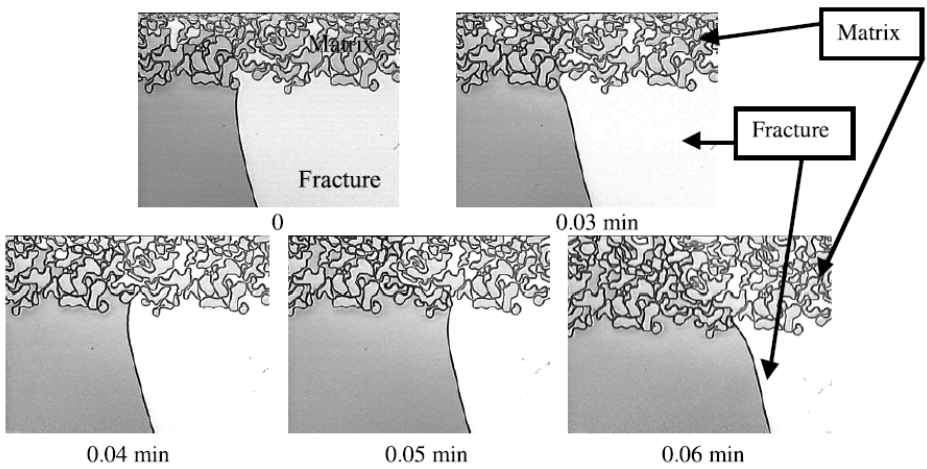

Figure 2. Fluid exchange between the matrix and fracture, where the fluid is invading the fracture from the left, in a silicon micro-model from (Rangel-German and Kovscek 2006) [Used by permission of John Wiley & Sons, from Rangel-German and Kovscek (2006), *Water Resourc Res*, Vol. 42 , Fig. 5.]

High pressure studies

So far we have considered micromodel studies of the fundamentals of multiphase flow at the pore scale that can be carried out only at close to ambient conditions. Now we turn our attention to studies at reservoir conditions, which are particularly important for CO_2 sequestration as the range of conditions encountered spans the critical point where the fluid properties can change significantly.

At low temperatures and high pressures CO_2 can form hydrates and this process has been imaged by Tohidi et al. (2001) using a glass micro-model mounted in a vessel where a confining pressure is applied to balance the pressure inside the channels of the model. As is shown in Figure 3, CO_2 hydrates can form from dissolved gas without the presence of a separate gas phase. Under these conditions, some parts of the pore space behind the crystallization front contained no hydrate (region X in Fig. 3), presumably because in those regions the water was depleted of dissolved CO_2.

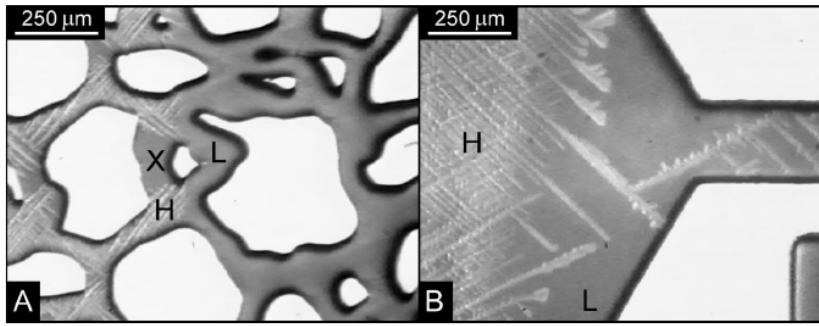

Figure 3. Hydrate formation front (H) and liquid water (L) observed in a high-pressure micro-model showing. [Used by permission of the Geological Society of America from Tohidi et al. (2001).]

The wettability of rock surfaces is an important factor in the flow and trapping of CO_2 in sequestration operations. Glass micromodels have been used to directly image changes in wetting for the CO_2/brine system on silica as the pressure was changed (Kim et al. 2012). The solid surface was initially water wet and when CO_2 invaded a pore, the water remained as a thick film between the silica surface and the CO_2 phase. However as the supercritical CO_2 dissolved into the brine, the surface became less water-wet, resulting in a thinning of the water film on flat surfaces and accumulation of water in corners as is shown in Figure 4.

In many applications, sequestration of CO_2 has been combined with oil recovery. This is a mature technology where large volumes of cheap CO_2 are available but its low viscosity and buoyancy can result in low sweep efficiency. Injecting CO_2 pre-dissolved in water is one potential solution to this issue and this process has also been imaged in high-pressure micro-models (Sohrabi et al. 2011). The observations indicated that there was significant swelling and mobilization of the disconnected oil ganglia that had been trapped during conventional water flooding.

Micro-models are not limited to observations of the movement of fluid-fluid interfaces as has been discussed so far. Optical access also allows spectroscopic analysis and therefore chemical information can be mapped within the model. As an example of this interesting development, high-pressure micro-models have been combined with Raman spectroscopy to determine the concentration of CO_2 dissolved in brine (Liu et al. 2012). In this study a bubble-train micro reactor is proposed as a rapid way of measuring solubility, but the spatially resolved chemical analysis has great potential for studying reactive flow in porous media in general and sequestration processes in particular.

During sequestration CO_2 dissolves into the water phase in the reservoir, providing one of the major mechanisms of trapping. However, if the pressure on the solution is reduced, during an upward movement of the fluid due to a leak for example, then CO_2 will come out of solution as small bubbles distributed throughout pore space. In an elegant study of this exsolution

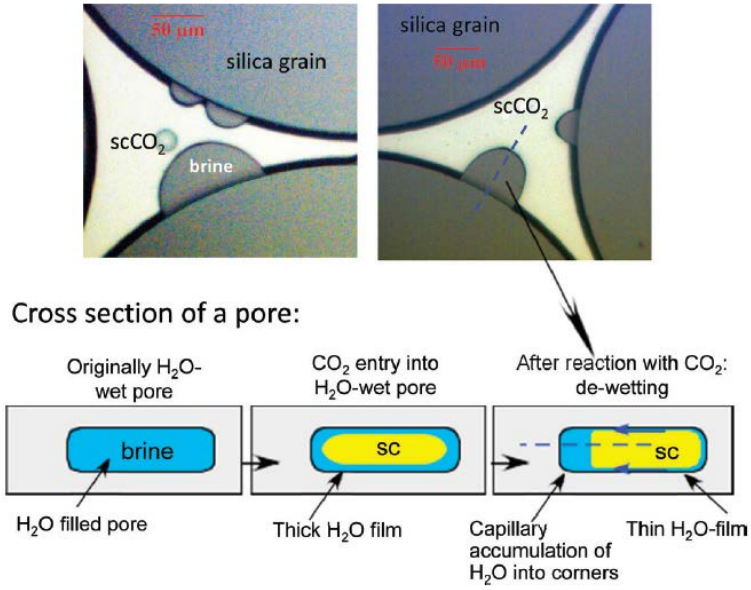

Figure 4. Dewetting process in a pore. (top) images of single pores from the micromodels. (below) sketches of the cross section of a pore as the surface becomes less water wet. [Reprinted with permission from Kim et al. (2012). © 2012 American Chemical Society.]

process, Zuo et al. (2013) showed that the gas phase developed in this way remains very poorly connected compared to the configuration arrived at by a drainage process (Fig. 5). This will have a significant impact on the relative permeability of the CO_2 phase, reducing its mobility compared to the better connected structure arrived at through drainage.

Reactive transport

Chemical reaction is a feature of many sequestration processes. In particular the precipitation of carbonate minerals from the brine is considered one of the safest ways to lock up CO_2 in the formation. Precipitation, particularly of calcite, is likely as the brine in carbonate formations will be saturated with respect to the mineral ions and small changes in the thermodynamic conditions can lead to over saturation. One scenario leading to precipitation is the mixing of brines of different compositions and micro-models have recently been used to investigate this process (Willingham et al. 2008; Zhang et al. 2010). The mixing of the two fluids was strongly influenced by the precipitation that tended to block the channels connecting the regions occupied by the reacting fluids, limiting the deposition to a narrower region than might be expected from the unaltered pore space.

Future research opportunities

While considerable progress has been made in adapting micro-model techniques to the pressure and temperature conditions relevant to CO_2 sequestration, limitations still persist in two aspects: geometry and surface chemistry.

The constant etch depth used in the majority of micro-models limits the range of capillary entry pressures that can be achieved such that it is impossible to fabricate a model representative of many real rocks. This could be overcome by using multiple etch depths at the cost of significantly complicating the manufacturing process. There are also limitations on the range of pore sizes that hinder development of models based on carbonate rock structures

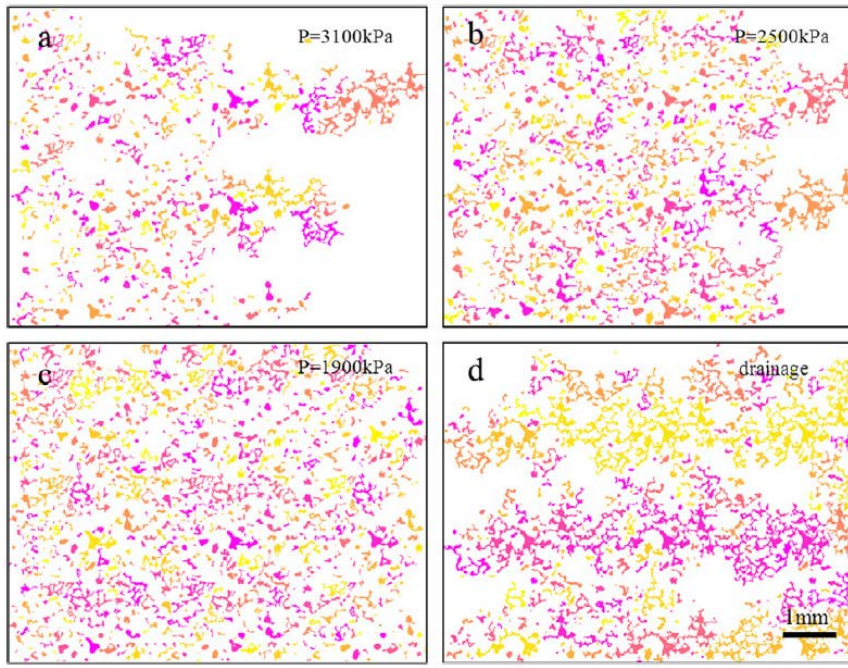

Figure 5. Morphology of the gas phase during exsolution (a, b, c) compared to drainage (d), where the grains and the aqueous phase were merged in white; each individual bubble was labeled with a distinct grey level (color online) from adjacent bubbles. [Reprinted from Zuo et al. (2013) with permission from Elsevier.]

where extensive micro-porosity is the norm. The typical size of micro-pores in carbonates (< 1 μm) makes them too small to be observed by light microscopy. However, it should be possible to observe the consequences such as the exchange of fluids between the observable macro-pores and the micro-porous regions. In addition, direct calculation of immiscible flow in the micro-model geometry may confirm and complement the flow experiments (Boek and Venturoli 2010).

The glass/silicon construction of most high-pressure models is a good representation of the surface chemistry of sandstones (although differences in contact angle between the glass and the silicon surfaces can cause problems). However, a model more representative of the surface chemistry of carbonates would be valuable, particularly given the more reactive nature of calcium carbonate. Experiments on calcite deposition point to one way of achieving a carbonate micro-model surface: deposition of a layer of small calcite crystals on a conventional glass/silicon model would give the appropriate surface chemistry and if the particle size were small enough the geometry would be broadly preserved.

MULTI-SCALE IMAGING OF STRUCTURE AND FLOW IN CARBONATE ROCKS

Carbonate rocks have a notoriously complex structure that is evident across a wide range of length scales. Therefore multi-scale imaging is particularly important. Two-dimensional images, from both light and electron microscopy, have long been used to investigate the pore structure of rocks. The preparation of thin sections has become an essential component

of core analysis. However, the flow of fluids in the rock pore space is strongly influenced by the three-dimensional connectivity of the pores. If the rock is isotropic, the 2D section gives representative estimates of simple, average, properties such as porosity and statistical techniques have been used to generate 3D representations from sections but such approaches, while valuable, rely on assumptions that direct 3D imaging circumvents.

Early methods to measure the 3D pore shapes directly employed serial polishing alternated with either optical (Lin et al. 1986) or electron microscopy (Koplik 1984). However such approaches are laborious and in this review we will focus on inherently 3D imaging techniques.

Macroscopic X-ray CT

X-ray computer tomography was introduced in 1972, revolutionizing medical radiography. The basic quantity measured in CT (McCullough 1975) is the linear attenuation coefficient, μ, defined from Beer's law,

$$\frac{I}{I_0} = \exp(-\mu x) \tag{3}$$

where I_0 is the incident X-ray intensity and I is the intensity after passing through a thickness x of material. In CT, an X-ray source and a detector array are rotated around a sample to obtain a series of projections of attenuation at various angles. This allows a 3D reconstruction of the attenuations in the sample with a resolution of around a mm. This is too coarse a resolution to see any but the largest pores in rocks so each voxel represents the volume fraction weighted attenuation of the mixture of materials occupying that volume.

The use of CT for imaging fluids in rock cores dates back to Vinegar and Wellington (Vinegar and Wellington 1987). They established a method of measuring the fluid saturation of a core during flow experiments that has been widely exploited since. This has become the method of choice for determining relative permeability in core samples. Direct observation of the saturation during two-phase flow experiments eliminates the uncertainty associated with estimating the saturation by a mass balance using only the core effluent. This is particularly advantageous in steady state relative permeability experiments where the saturation changes slowly over many pore volumes injected.

While determination of relative permeability requires only an average of fluid saturation in the core, the three-dimensional nature of CT data allows for other interesting possibilities that are beginning to be explored. In particular, maps of the saturation inside the core can be obtained at different fractional flows showing the heterogeneity of the rock at the sub core scale (Perrin et al. 2009). Figure 6 shows an example of the CO_2 saturation distribution obtained during drainage in a core from the CO_2CRC-Otway project in Australia. In addition to revealing heterogeneity in the rock properties, this level of resolution also allows experimental artifacts such as gravity override and end effects to be identified or eliminated from consideration as is the case in this example.

One novel approach reported recently (Pini et al. 2012) exploits the pressure distribution in the core when only the non-wetting (CO_2) phase is flowing. When the wetting (water) phase is stationary its pressure is everywhere constant and equal to the pressure at the core outlet. The capillary pressure, therefore, is known at the inlet face and is equal to the difference between the injection pressure and the outlet pressure. A two-dimensional saturation image at the inlet can then be used to determine the capillary pressure/ saturation relationship on a pixel-by-pixel basis (Fig. 7). Additionally, if an independent measurement of capillary pressure has been made on the same core with a fluid of known contact angle, such as mercury, then this approach can be used to estimate the effective contact angle of CO_2 in the core.

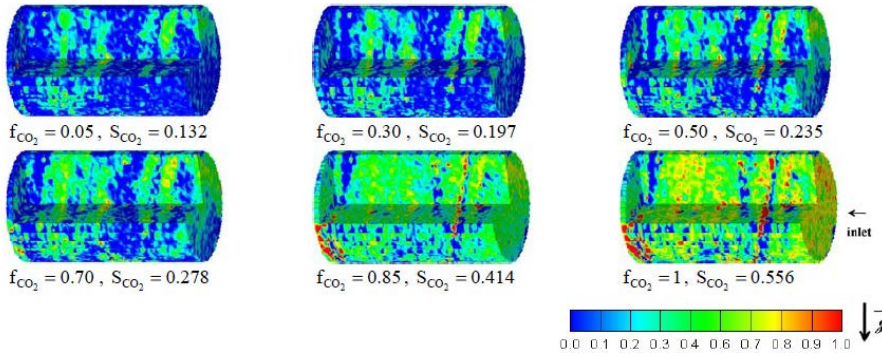

Figure 6. Saturation images for the system CO_2, brine sandstone at a range of different fractional flows showing heterogeneity at the sub core scale. [Reprinted from Perrinet al. (2009) with permission from Elsevier.]

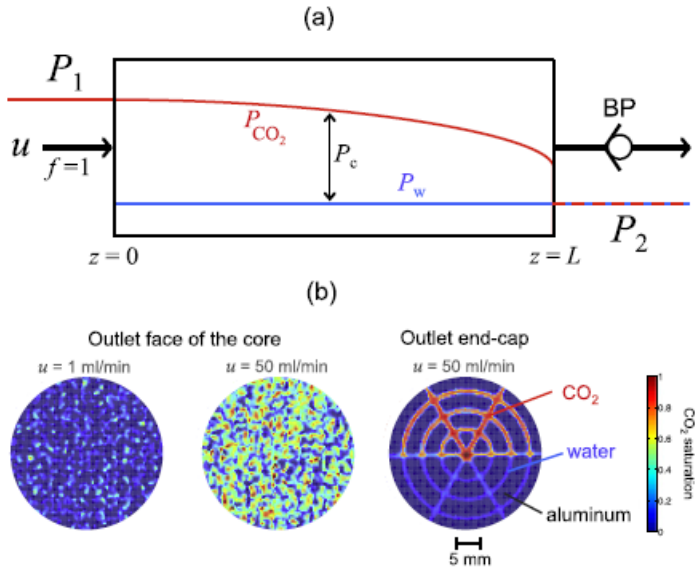

Figure 7. Capillary pressure determination using saturation imaged at the entrance to the core. [Reprinted from Pini et al. (2012) with permission from Elsevier.]

Confocal Laser Scanning Microscopy (CLSM)

Three-dimensional images of the pore space can be obtained by CLSM after the rock is impregnated by a low viscosity resin containing a fluorescent dye (Fredrich et al. 1993, 1995). The key difference between conventional microscopy and confocal microscopy is that the latter has a pinhole placed in front of the detector to eliminate out of focus light. Each measurement is of a single point in space that is scanned along parallel lines to obtain two-dimensional images of sequential planes at specific depths within the sample. Ultimately the depth of penetration of CLSM into the rock is limited by absorption and scattering of the light emitted from the fluorescent dye by the material above. In a rock, the depth that can be reliably reconstructed is less than 100 μm (Petford et al. 2001). However, the field of view in the plane of the scanning can be very large when multiple images are stitched together in the post-processing (Fig. 8).

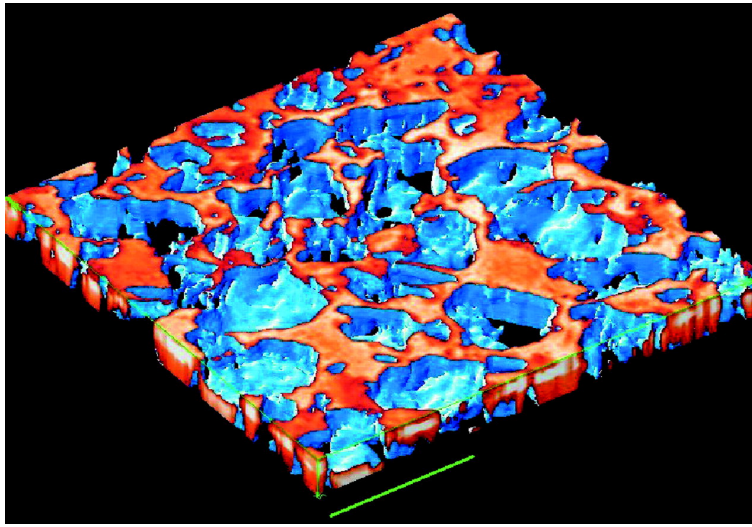

Figure 8. Forty-three slice voxel reconstruction (negative imaging) of a porous sandstone sample made up of individual CLSM images taken at 2.1 μm increments with a depth resolution of 0.1 μm. Opaque areas are impregnated regions that define the pore space. Hollows show the locations of individual grains. Image depth is 90.3 μm. Scale bar 300 μm. [Reprinted from Petford et al. (2001) with permission from Geological Society of London.]

micro-CT

High-resolution X-ray Computed Tomography or micro-CT shares the same basic physics as the macro (medical) CT discussed above. However the implementation is different, allowing much greater resolution with voxel sizes as small as a few hundred nanometers. The principles, advantages and limitations of micro-CT have been recently reviewed (Cnudde and Boone 2013) and here only a brief outline of the technique will be given. The boundary between medical CT and micro-CT is not distinct, but a resolution of around 500 micrometers is a practical division between the techniques. Another difference between the techniques at the two scales is that in micro-CT it is the sample that is rotated to obtain the projections while the source and detector remain stationary. This has implication for the implementation of flow experiments, particularly at reservoir conditions, with *in situ* imaging.

Both synchrotron radiation and bench-top X-ray tubes can be used in micro-CT imaging. The synchrotron offers a clear advantage in the flux of photons, allowing more rapid image acquisition, but the number of such facilities is limited and the advent of the lab based instruments has allowed access to become available to a much larger number of researchers.

Rock structure imaging. The earliest applications of micro-CT in geosciences were 3D pore and grain characterization (Saadatfar et al. 2006; Cnudde and Boone 2013). Extraction of pore geometry for simulation of fluid displacements by networks of geometrically simplified channels (Hazlett 1995) has led to predictive models for absolute and relative permeability (Valvatne and Blunt 2004) for some rocks. However, carbonates are particularly challenging in this regard as a substantial fraction of the porosity is below the resolution of micro-CT (Fig. 9), and neglecting this fraction of the pore space can lead to significant errors in predicting flow (Arns et al. 2005; Blunt et al. 2013).

Reactive transport. The reaction between rock and fluids in general has been reviewed by Steefel and Maher (2009) who considered transport processes and reaction at the Darcy scale.

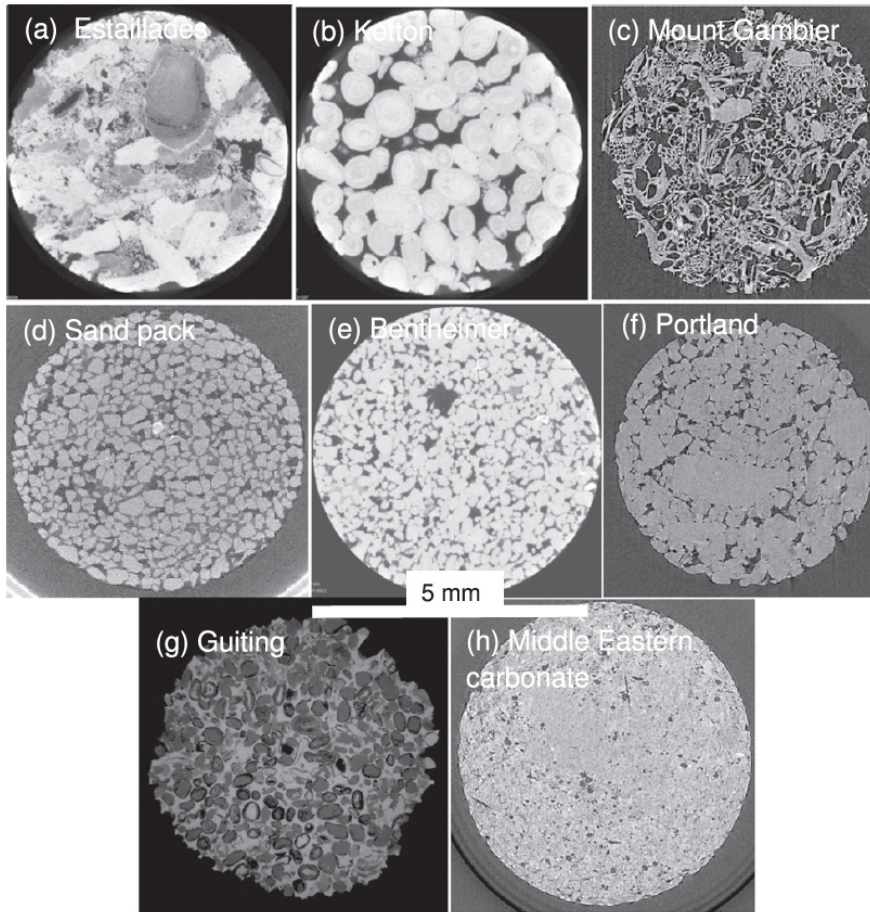

Figure 9. Two-dimensional cross-sections of three-dimensional micro-CT images of a variety of carbonate rocks compared to a sand pack and Bentheimer sandstone. All the carbonates have unresolved micro-pores within the grains. [Reprinted from Blunt et al. (2013) with permission from Elsevier.]

Two dimensionless numbers characterize the fluid-rock interaction; the Péclet number, *Pe*, for the relative importance of advective versus dispersive transport and the Damköhler number, *Da*, for the ratio of the characteristic times for transport and reaction. We note in passing that for carbonates using conventional measures of dispersion may not be adequate due to their complex pore structure (Bijeljic et al. 2011). This aside, the changes to the rock structure, seen when carbonates dissolve due to the acidification of the formation brine by injected CO_2, generally follow a pattern determined by *Da*. When reaction is slow and advection fast (small *Da*) dissolution is rather uniform and existing pores are enlarged. When the reaction is very fast compared to advection (large *Da*) then the rock will be completely dissolved in a front advancing from the point of injection. At intermediate *Da*, worm-holes can form. Imaging studies of CO_2 saturated brine injection into carbonates (Luquot and Gouze 2009) have shown this worm-holing process under conditions relevant to sequestration operations. Figure 10 shows the changes to the limestone cores at three different experimental conditions corresponding to a range of *Da*.

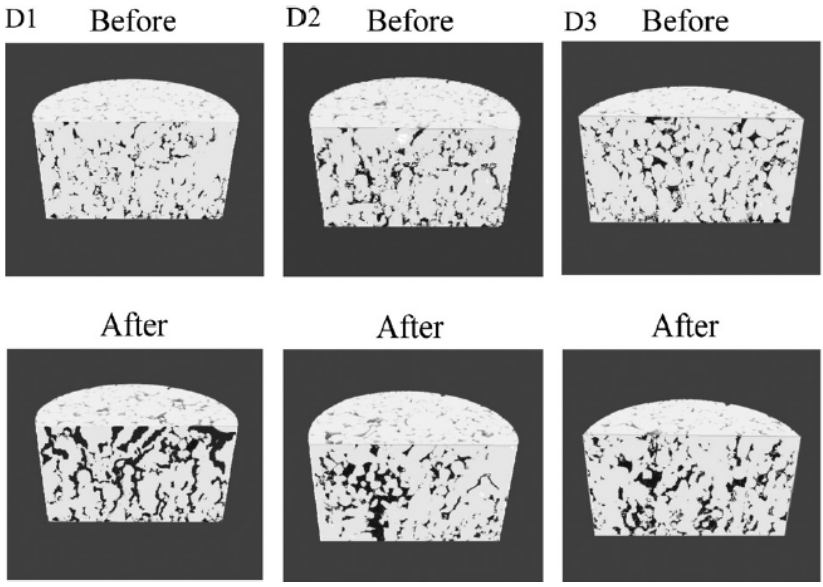

Figure 10. Changes in pore space after injection of CO_2 saturated brine. D1, D2 and D3 show the response to reducing the Damköhler number. [Reprinted from Luquot and Gouze (2009) with permission from Elsevier.]

Estimating the effective reaction rate and therefore the Damköhler number, in reactive transport studies is problematic, as this requires an estimate of the effective surface area (Gouze and Luquot 2011) together with the intrinsic reaction rate. The effective surface area remains difficult to determine as it differs from the geometric surface area due to the non-uniform flow field through the pore space.

Salt precipitation is the other pore space altering process likely when dry CO_2 is injected into brine saturated formations and this topic has recently received attention from the micro-CT community (Ott et al. 2011; Peysson et al. 2011). Images of the distribution of precipitated salt show that it is possible for the locally precipitated amount of salt to be substantially higher than the amount of salt in the brine initially present in the brine in the same volume. This surprising result is due to capillary action pulling additional brine into the volume during the dry out process. Despite the large local concentrations of deposited salt, complete blocking of the pore space was not observed.

Fluid imaging. So far we have considered applications of pore-scale imaging techniques to determining the geometry of the rock. Now we turn our attention to direct imaging of the fluids occupying the pore space. Studies of the pore scale distribution of CO_2 under conditions relevant to sequestration are relatively few, principally due to difficulties inherent in making a core holder transparent to X-rays and suitable for the micro-CT scale. Some progress has been made recently and (Iglauer et al. 2011) have reported imaging of trapped CO_2 in sandstones at reservoir conditions (Fig. 11).

The image acquisition time in the above study, which used a lab based micro-CT, was far too long to observe dynamic transport processes that can be rapid, particularly at the pore scale. The more rapid imaging possible at synchrotron facilities have recently been used (Berg et al. 2013) to overcome this issue and observe the elementary pore-scale displacement processes in real-time. Figure 12 shows one such process, a Haynes jump during drainage in which a single pore is filled as the capillary pressure required to enter the upstream constriction is exceeded.

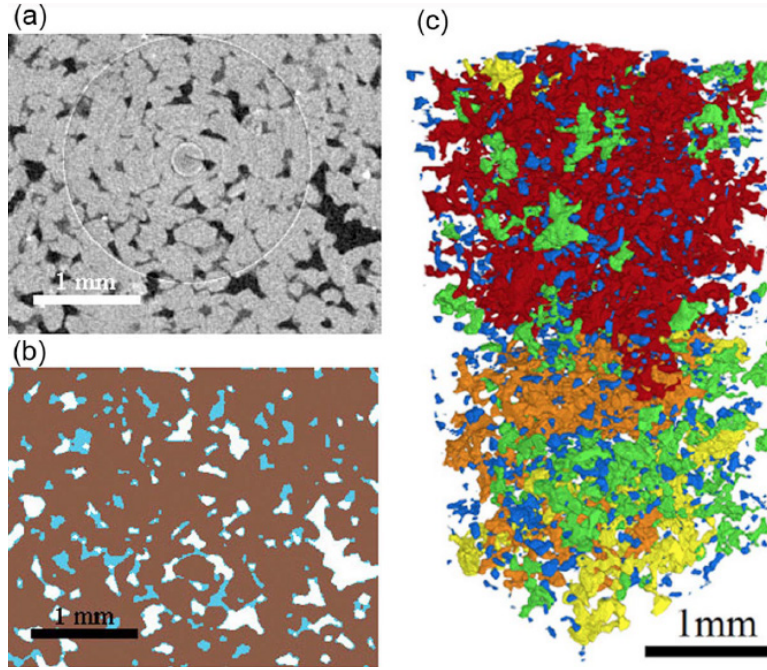

Figure 11. Images showing the core after primary drainage with $scCO_2$: (a) two dimensional slice through the core; $scCO_2$ is black, brine is dark grey and sandstone is light grey. (b) same slice with phases segmented. (c) $scCO_2$ clusters in three dimensions, where different cluster sizes have different shades. [Reprinted from Iglauer et al. (2011) with permission from the American Geophysical Union.]

FIB-SEM

At several stages during the above discussion of micro-CT imaging, micro-porosity below the available resolution has proved to be a limitation on the quantitative application of the technique to carbonate rocks. This can be overcome by using focused ion beam scanning electron microscopy, FIB-SEM, which allows the superior resolution of SEM to be used in three dimensions. FIB-SEM is a serial sectioning technique in which a beam of heavy ions, typically Ga^+, is used to mill away a thin layer of the sample for subsequent imaging using electrons (Holzer et al. 2004, 2006). The process is shown in Figure 13. The sample is initially polished to reduce the time required for the subsequent ion milling. Then the volume selected for imaging is made accessible for scanning by using the ion beam to mill a U shaped trench around it. The imaging plane is then sequentially cut back into the sample, after electron beam scanning of each slice. While the technique is destructive, in contrast to X-ray CT, the resolution available in the SEM imaging (better than 10nm) makes the micro-porosity of carbonates accessible to true 3D characterization.

The technique has recently been applied to chalk (Tomutsa et al. 2007) and carbonates (Sok et al. 2010), resulting in the first direct 3D images of the smallest pores in these difficult samples.

Future research opportunities

Micro-CT – the reactivity of rocks during CO_2 sequestration is determined by the surface area of each reactive mineral exposed to the acidified brine phase. Imaging the mineral

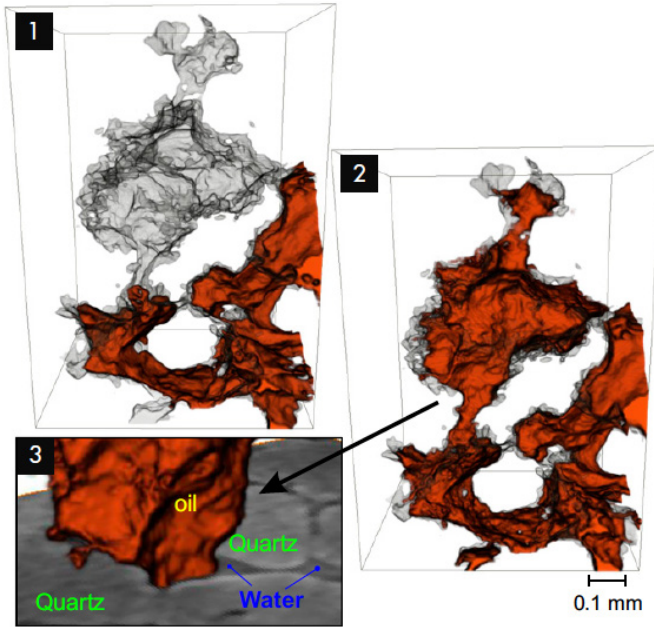

Figure 12. Oil filling event in a single pore during drainage. (Berg et al. 2013). (3) shows a cross section at the toroidal pore throat with the water wetting films and the oil neck after the transition from step (1) to (2).

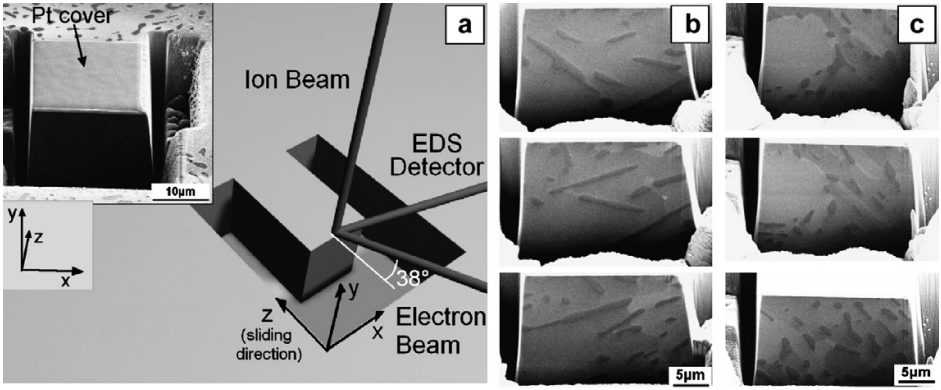

Figure 13. (a) Schematic illustration of FIB-SEM 3D imaging method indicating the beam directions, the sectioning and SEM imaging plane xy. Series of parallel 2D-FIB cross-sections (xy) in (b) and (c). [Reprinted from Lasagni et al. (2007) with permission from Elsevier.]

distribution on the surface of the pores, as opposed to the bulk mineralogy, would assist in this challenging problem. More generally the coupling of the fluid movement within the pores to the reaction at the surface should be the ultimate goal.

FIB-SEM – as the volume of investigation is inherently small in this approach, site selection and sampling of representative structures is of vital importance.

Integration of the imaging techniques at different length scales is vital for quantitative analysis of carbonate rocks which display structure at all scales.

MULTI-SCALE SIMULATION OF FLUID FLOW AND TRANSPORT IN CARBONATE ROCKS

In the previous chapters, we have discussed different methods to image the structure and flow in carbonate rocks, using multi-scale imaging and micro-fluidic flow experiments. In this chapter, we will complement this by considering different methods to model and simulate flow and (reactive) transport in porous media.

As discussed, carbonate rocks have a highly complex structure with heterogeneities across a wide range of length scales. For this reason, the flow and transport in these rocks is a multi-scale modeling and simulation problem. For this purpose, we will consider the imaging techniques discussed in the previous section, including medical and micro-CT, CLSM and FIB-SEM. Using these methods, it is possible to generate 3D pore space images at different length scales. It then becomes possible to calculate flow and transport directly from these pore scale images.

As pointed out by (Meakin and Tartakovsky 2009), pore scale simulation of single-phase fluid flow in porous media may be straightforward, at least in comparison with multi-component flow. However, in some cases, the complex geometry of the pore space and fractures may give rise to complications. This is particularly the case for flow in carbonate rocks, which, as discussed above, are generally very heterogeneous in comparison with, e.g., sandstones. As noted in the Introduction of this chapter (see Fig. 1), typical properties of porous media such as the porosity n_i, may fluctuate as a function of volume ΔU_i on scales that are significantly smaller and larger than a Representative Elementary Volume (REV). In this framework, the fluctuations are small on the intermediate scale of the REV, assumed to be the scale over which the structural details can be averaged (Bear 1972). In reservoir simulations, macroscopic parameters including porosity and permeability are assigned to each REV, based on experimental, digital rock and statistical information. Heterogeneities on the REV scale may be upscaled to the grid block scale used in reservoir simulations. One of the objectives of pore scale simulations is to calculate the properties of porous media at the REV scale. Unfortunately, the concept of a REV is not always well founded, particularly for fluid flow in heterogeneous media, including fractures, such as carbonates. The REV concept is also used in reservoir simulation of multi-component fluid flow. Often, multi-component flow exhibits hysteresis that cannot be rigorously described by simple macroscopic parameters such as relative permeability, saturation and capillary pressure. In that perspective, it may be easier use to pore scale simulations than experiments to systematically vary fluid properties, pore space geometries and boundary conditions. This may result in improved qualitative understanding of the governing physics. Unfortunately, it is generally still very difficult to systematically homogenize the results of pore-scale simulations to generate improved input for reservoir simulations.

As mentioned above, pore-scale simulations of multiphase fluid flow in confined systems are more challenging than single-phase flow simulations. First, it is computationally difficult and expensive to track the complex dynamics of fluid-fluid interfaces. Second, many direct methods struggle with the accurate description of the behavior of multiphase fluids with large density, viscosity and compressibility contrasts. Third, the behavior of fluid-fluid-solid contact lines (and the associated dynamic contact angles) is inherently complex and sensitive to small length-scale physico-chemical heterogeneities and impurities that may influence the wetting behavior and/or surface tension. This review is concerned with multi-component fluid flow and reactive transport at the pore scale. All the methods that will be described below are trying to tackle the problems outlined above in different ways.

Traditionally, pore network models (Blunt 1998) have been used to simulate multi- and single-phase fluid flow in porous media, and these models will continue to provide important

insight and information in the future. However, pore network models are based on simplified models for the pore space geometry and, in the case of multiphase fluid flow, simplified physics. In addition, pore network models may not be suited for the simulation of multiphase fluid flow in fracture apertures, fractured porous media, vuggy carbonates, or other systems with complex macro-pores. More recently, a number of direct methods based more firmly on first principles have been developed. Some of these methods are particle based and include LGA and lattice Boltzmann simulations (Frisch et al. 1986; d'Humieres et al. 1986), dissipative particle dynamics (Hoogerbrugge and Koelman 1992; Espanol and Warren 1995; Boek et al. 1997) and smoothed particle hydrodynamics (SPH) (Gingold and Monahan 1977). We will not describe the SPH method in this chapter as an excellent overview has recently been provided by (Meakin and Tartakovsky 2009). However, as an example of reactive flow in porous media, we mention Tartakovsky et al.'s (2007) study of mineral precipitation in a fracture using the SPH method (Fig. 14).

Other methods are based on continuum concepts, including Density Functional Theory (Demianov et al. 2011), and fluid-fluid interface tracking including velocity-dependent contact angles (Huang et al. 2005). These newer methods are computationally less efficient than pore network models, but increases in the capability of computing systems are making them more attractive. Despite recent advances, it is still not possible to accurately and reliably simulate multiphase fluid flow for the full range of density ratios, viscosity ratios, compressibility and wetting behavior found in porous media flow. For this reason, due to the limitations listed above, in the literature to date, the most computationally efficient and successful predictions of multiphase flow still come from network modeling (Blunt et al. 2013). In the near future, however, it may be expected that efficient multiscale multiphysics models for multiphase fluid flow and reactive transport will be developed and implemented on high-performance computing systems, including CPU and GPU platforms, to generate accurate and efficient predictions of multi-component flow in porous media.

We will now discuss various methods for pore scale flow and transport problems at different length scales. We will pay particular attention to problems associated with CO_2 transport in porous media saturated with reservoir fluids. In the case of CO_2 injection in brine

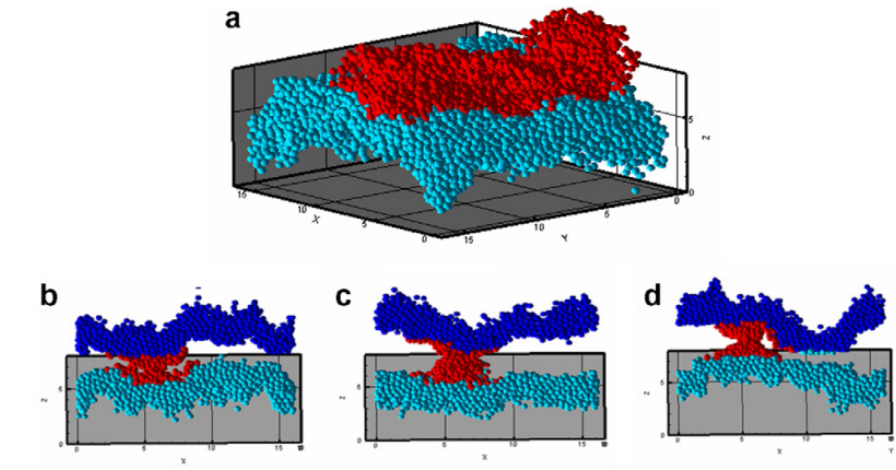

Figure 14. Mineral precipitation in a fracture aperture with self-affine walls resulting from reactive transport. 3D view of precipitated minerals red (medium grey), lower fracture walls light blue (light grey) and upper fracture walls dark blue (dark grey). [Reprinted from Tartakovsky et al. (2007) with permission from Elsevier.]

saturated media, this includes potential matrix dissolution and salt precipitation; in the case of CO_2 storage in depleted oil fields, for the purpose of Enhanced Oil Recovery (EOR), this includes potential precipitation and deposition of asphaltenes. In both cases, reactive flow processes may lead to alteration of the pore space and associated change in permeability.

Fundamental aspects

The properties of fluids and their behavior near solid surfaces can, in principle, be understood in terms of the interactions between their molecular components, solids, and the effect of temperature. In general, the intermolecular interactions consist of a combination of electrostatic and van der Waals interactions (Allen and Tildesley 1990), including long-range attractive and short-range repulsive interactions. To predict physical structural and dynamic fluid properties from intermolecular interactions, numerical Monte Carlo and Molecular Dynamics simulations can be used, respectively, provided that the (classical) interaction potentials are accurate as described by Hamm et al. (2013, this volume). For more complex systems, including chemical reaction, quantum mechanical effects may be included and *ab initio* MD simulations are an option (Suter et al. 2012), although system size and time scales are limited for computational reasons.

Let us now consider dynamic properties. The flow of Lennard-Jones fluids can be described quite accurately by the incompressible Navier-Stokes equations consisting of mass and momentum conservation equations. The flow of most simple fluids can be described by the Navier-Stokes equations, irrespective of their composition. This is an important universal behavior which can be used to describe flow fluid flow at the meso- and macro scales. In more complex fluids, such as polymer solutions and colloidal dispersions, the structure is more sensitive to the strain rate. In this case the fluid may exhibit non-Newtonian behavior. However, this is outside the scope of the current review.

Pore network models

As pointed out by (Meakin and Tartakovsky 2009), the value of pore network model simulations is limited by the approximations and simplifications used. In most pore network models, the physics of the processes taking place in the idealized porous medium is simplified (Valvatne and Blunt 2004). Often information from experiments (Lenormand et al. 1983) or computer models based on conservation principles and more rigorous physics is required. We will now discuss these underlying models in the following sections. For this purpose, we will start at the smallest level with Molecular Dynamics and follow coarse-graining procedures to arrive at mesoscopic and continuum CFD models.

Molecular Dynamics

Molecular Dynamics (MD) simulations are used to investigate structural properties of reservoir fluids and their flow using individual molecules as the smallest unit. Newton's equations of motion are integrated for an ensemble (Allen and Tildesley 1990) of either atomistically detailed or coarse-grained molecules on time and length scales ranging typically from nano- to micro-scale:

$$m_i \frac{d\mathbf{v}_i}{dt} = \mathbf{f}_i \tag{4}$$

where $\mathbf{v}_i$ is the velocity of the i^{th} particle, $\mathbf{f}_i$ is the force acting due to interaction with the other particles in the system and external forces, and m_i is the mass of the i^{th} particle. By taking ensemble averages over the system, we can calculate average properties such as diffusion coefficients, viscosity and flow characteristics in a single pore. For details of the fundamentals of MD simulations, we refer to (Allen and Tildesley 1990).

In principle, MD simulations can be used to simulate fluid flow, and there is evidence that continuum hydrodynamics can be applied on scales on the order of a few nm in some systems. However, experiments and MD simulations indicate that the structure of a variety of liquids is much more ordered adjacent to atomically smooth solid surfaces than in bulk fluids (Christenson 1983). In typical atomistic MD simulations with realistic interactions, the integration time step must be on the order of a femtosecond to obtain accurate results, and the duration of the simulation (in physical time units) is typically on the order of a nano- or micro-second. This is the most important limitation of the application of molecular dynamics to multiphase fluid flow on the pore scale.

Despite these limitations, MD could be used to simulate multiphase fluid flow on the pore scale if the molecular system provided an accurate scale model for pore-scale systems of interest. This would be possible if the size of the system used in the MD simulation were large enough to reach the hydrodynamic limit and to ensure that the effects of the solid boundaries on the adjacent fluid could be neglected. In addition the critical dimensionless ratios should essentially be the same in the MD model and the system of interest. In the case of fluid flow in porous media, these typically include Reynolds (*Re*), Peclet (*Pe*), capillary (*Ca*), Mach (*Ma*) and Bond (*Bo*) numbers. In addition, the Knudsen number *Kn*, defined as $Kn = \lambda/L$, where λ is the mean free path and L is a typical pore length scale, must match with the corresponding physical system. Although MD simulations with realistic interactions are generally not used to simulate multiphase fluid flow in complex porous media for computational reasons, they are important in studying the behavior of thin fluid films on solid surfaces, fluids near solid surfaces, confined systems, contact line dynamics, and velocity-dependent contact angle behavior associated with moving contact lines. Hybrid MD/continuum models have been developed, using MD to simulate fluids near solid surfaces (where continuum models are inadequate) and using standard continuum incompressible Navier-Stokes equation solvers farther from the solid surface. Another example is the hybrid method investigated by (Nie et al. 2004), where the overlap region consists of three layers of cells used in the continuum fluid dynamics model. Nie et al. (2004) showed that the hybrid solution agrees very well with the full MD solution, whereas the continuum model significantly deviates from the hybrid solution indicating inadequacy of the continuum description of fluid flow near rough walls. Russo et al. (2010) studied nano-flows through dilute disordered media using Molecular Dynamics (MD) and Lattice-Boltzmann (LB) simulations. They observed that for solid fraction $\phi > 0.01$, molecular-size effects in the MD simulations lead to a decrease of the permeability, as compared to the Navier-Stokes predictions.

Coarse-grained MD studies have shown that both wettability and surface roughness affect the flow properties in single rough capillaries (see Fig. 15; Stukan et al. 2010).

In addition to dynamic properties, structural studies can be carried out using MD (and Monte Carlo or MC) simulations. A number of atomistic MD studies have been performed of direct relevance to CO_2 storage and EOR in carbonate rocks. These include CO_2 induced asphaltene precipitation and asphaltene adsorption (Headen and Boek 2011a) on a calcite surface (see Fig. 16; Headen and Boek 2011b).

Dissipative Particle Dynamics

The Dissipative Particle Dynamics (DPD) method was developed by (Hoogerbrugge and Koelman 1992) to address fluid flow problems at mesoscopic length and time scales. For this purpose, the fluid is represented by an ensemble of particles subject to the combined effects of forces acting, including conservative $\mathbf{f}^C$, dissipative $\mathbf{f}^D$, fluctuating (random) $\mathbf{f}^R$, and external $\mathbf{f}^{ext}$ forces. The combined equation of motion is

$$m_i \frac{d\mathbf{v}_i}{dt} = \mathbf{f}_i^C + \mathbf{f}_i^D + \mathbf{f}_i^R + \mathbf{f}_i^{\text{ext}} = \sum_{i \neq j} \left(\mathbf{f}_{ij}^C + \mathbf{f}_{ij}^C + \mathbf{f}_{ij}^C \right) + \mathbf{f}_i^{\text{ext}} \tag{5}$$

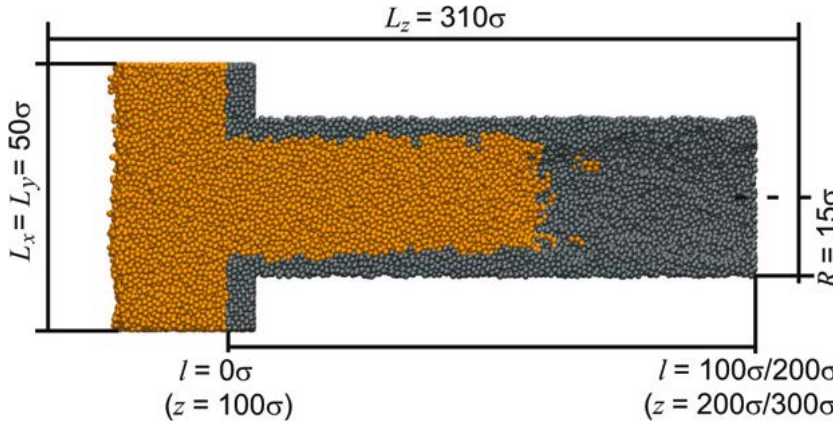

Figure 15. Snapshot of coarse-grained MD study of imbibition in rough nano-pore. [Reprinted from Stukan et al. (2010). © 2010 American Chemical Society.]

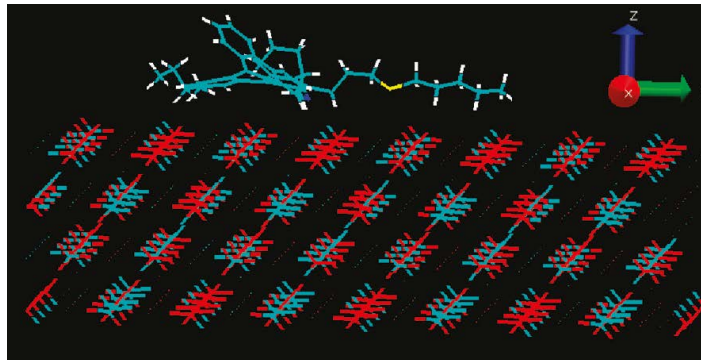

Figure 16. Simulation snapshot of the calcite surface and asphaltene molecules. [Reprinted from Headen and Boek (2011). © 2011 American Chemical Society.]

where $\mathbf{v}_i$ is the velocity of particle i and m_i is its mass. For more details we refer to (Espanol and Warren 1995). Multicomponent systems can be modeled by defining particles with different repulsive interaction strengths to generate phase separation (Coveney and Espanol 1997). A combination of short-range repulsive and long range attractive interactions between fluid and solid can also be used to model different wetting conditions (see e.g., Kong and Yang 2006). DPD has not been as extensively applied as lattice Boltzmann (LB) methods to the simulation of multiphase fluid flow in confined geometries. The reason is that its advantages and disadvantages are less well understood. DPD is well suited to the simulation of small multi-component systems as thermal fluctuations are properly included (Kang and Landman 2007). Because of the soft particle-particle interactions, the compressibility of DPD fluids is large relative to real liquids. In addition, the excluded volume associated with the soft interactions may lead to spurious effects, including depletion interactions, as noted by Boek and van der Schoot (1998). For LB models, on the other hand, the simplicity of the microscopic dynamics allows the fluid viscosity to be analytically calculated. In addition, the LB model is more computationally efficient than DPD. On the other hand, DPD is numerically stable and rigorously Galilean invariant under all conditions (Espanol and Warren 1995). DPD has been used quite extensively to study polymer solutions, colloidal suspensions (Boek et

al. 1997), emulsions, membranes, etc. In these applications, DPD serves as a coarse-grained non-equilibrium MD model. It retains sufficient molecular detail to investigate the effects of size, shape and rigidity of large molecules on the behavior of complex fluids. As noted, DPD has also been applied to investigate the flow behavior of colloids (Boek et al. 1997). This may be extended to the aggregation and deposition of colloidal asphaltene in CO_2 EOR operations. We will further elaborate this in the next sections.

Stochastic Rotation Dynamics (SRD)

Stochastic Rotation Dynamics (SRD) a.k.a. Multi Particle Collision Dynamics (MPCD) simulations are used to investigate properties of reservoir fluid flow at mesoscopic length and time scales. This method has recently been developed to solve the hydrodynamics of complex fluids (Malevanets and Kapral 1999). Although SRD is a fairly recent method, its statistical mechanical and hydrodynamic fundamentals have been thoroughly studied and validated (Ihle and Kroll 2001; Padding and Louis 2006). It is a mesoscopic particulate method where the solvent is represented by N_f point-like (ideal gas) particles. This is different from the DPD method discussed above, where the solvent particles have a finite excluded volume, which may lead to depletion effects as reported in (Boek and van der Schoot 1998). MPCD is similar in spirit to the lattice-Boltzmann (LB) method (Succi 2001; Venturoli and Boek 2006) which will be discussed in the next section. In contrast to LB however, it includes Brownian motion which emerges naturally from the thermal fluctuations of the SRD particles (N_f). This makes the SRD method particularly useful to study the hydrodynamics of colloidal particles, such as precipitated asphaltene. The colloidal particles are described by means of a coarse-grained Molecular Dynamics method (Allen and Tildesley 1990). The SRD hydrodynamics emerges from collisions between solvent particles in coarse-grained cells at coarse-grained time intervals. It is a simple and computationally cheap algorithm ($O(N_f)$), that can be easily coupled to solutes such as polymers and colloids. The algorithm proceeds in two steps (Kikuchi et al. 2004; Padding and Louis 2004). In the first of these, a free streaming step, the positions of the solvent particles, $\mathbf{r}_i(t)$, are updated simultaneously according to

$$\mathbf{r}_i(t+\delta t) = \mathbf{r}_i(t) + \mathbf{v}_i(t)\delta t \tag{6}$$

where $\mathbf{v}_i(t)$ is the velocity of a particle and δt is the discretised time step of the solvent. The second part of the algorithm is the collision step. The simulation system is coarse-grained into cells. Stochastic multi-particle collisions are performed within each individual cell, by rotating the velocity of each particle relative to the center-of-mass velocity $\mathbf{v}_{cm}(t)$ of all the particles within that cell:

$$\mathbf{v}_i(t+\delta t) = \mathbf{v}_{cm}(t) + \mathbf{R}\left(\mathbf{v}_i(t) - \mathbf{v}_{cm}(t)\right) \tag{7}$$

R is a rotation matrix which rotates velocities by a fixed angle α around a randomly oriented axis. The aim of the collision step is to transfer momentum between the particles while conserving the total momentum and energy of each cell. Because mass, momentum and energy are conserved locally, the thermo-hydrodynamic equations of motion are captured in the continuum limit (Kikuchi et al. 2004). Hence hydrodynamic interactions can be propagated by the solvent. Note, however, that any molecular details of the solvent are excluded—this allows the hydrodynamic interactions to be modeled with minimal computational expense. This procedure conserves mass, momentum and energy and yields the correct hydrodynamic behavior, in the sense that the Navier-Stokes equations are recovered (Padding and Louis 2004). The fluid particles only interact with each other through the rotation procedure, which can be viewed as a coarse-graining of particle collisions over space and time. For this reason, the SRD solvent should not be considered as an ensemble of molecules, but rather as a Navier-Stokes solver that naturally includes Brownian noise. The SRD simulation technique has been applied to colloids in solution (Boek et al. 2010), colloidal sedimentation (Padding and Louis

2006), clay particles, polymer fluids, amphiphilic systems, flow in porous media, binary fluid mixtures, flow around solid objects and reactive fluids. The SRD-MPCD method has been used to study reactive flow with aggregation and deposition of colloids in single capillaries (Boek et al. 2008). This is of direct relevance to problems associated with the aggregation and deposition of colloidal asphaltene in CO_2 storage and EOR in depleted carbonate reservoirs. This may lead to increased viscosity and reduced permeability respectively during CO_2 injection operations. Snapshots of MPCD capillary flow simulations (Boek et al. 2008) are presented in Figure 17.

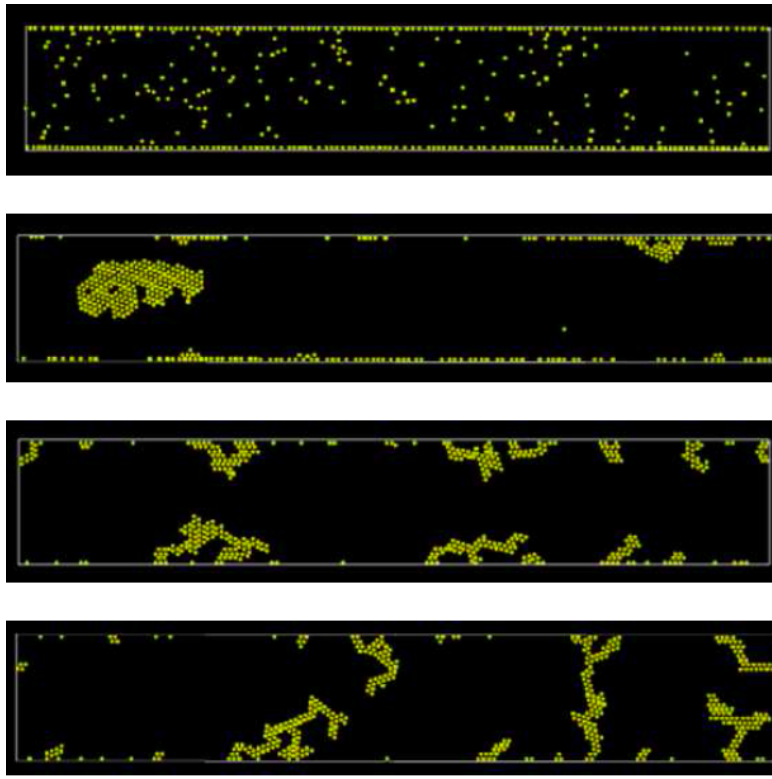

Figure 17. SRD Simulation snapshots for colloidal asphaltene deposition as a function of increasing inter-colloidal potential well depths: from top to bottom $\varepsilon_{cc} = -2, -5, -10$ and $-20\ k_B T$. [Reprinted from Boek et al. (2008). © 2008 American Chemical Society.]

Lattice Gas and lattice-Boltzmann models

Pore network models are an attractive option to calculate single- and multi-phase flow properties in porous media, due to their relative simplicity and small computational burden. However, one important limitation is the systematic and unique generation of a simplified model of pores and throats from a real geometry. For this reason, the calculation of flow properties directly on pore space images has recently become of great interest. The pore space images are obtained from multi-scale imaging techniques, including X-ray tomography, as discussed in the previous sections. These images are then used to directly calculate single- and multi-phase flow properties. A variety of Computational Fluid Dynamics (CFD) methods

is available to solve for the flow. Here we will consider the lattice-Boltzmann (LB) method due to its efficiency to solve flow in systems with complex boundaries such as porous media (Sukop and Thorne 2007).

LB models originate in the early work on lattice gas automata (LGA) models (Frisch et al. 1986) (d'Humieres et al. 1986). In LGA, discrete particles move synchronously from node to node on a regular lattice and collide whilst conserving momentum. However, major deficiencies of lattice gas models are their noisy small-scale dynamics and lack of Galilean invariance. In the lattice-Boltzmann (LB) method, this is overcome by replacing the discrete particles with real valued particle distribution functions. In this sense, LB can be considered as a pre-averaged LGA model. For this reason, LGA models have been largely superseded by LB models for most applications. Instead of tracking individual atoms or molecules, the LB method describes the dynamics of the single-particle distribution function of mesoscopic fluid "packets." In a continuum description, the single-particle distribution function $f_1(\mathbf{r}, \mathbf{v}, t)$ represents the density of fluid particles with position $\mathbf{r}$ and velocity $\mathbf{v}$ at time t, such that the density ρ and velocity $\mathbf{u}$ of the fluid are given by

$$\rho(\mathbf{r},t) = \int f_1(\mathbf{r},\mathbf{v},t)d\mathbf{v} \tag{8}$$

and

$$\mathbf{u}(\mathbf{r},t) = \int f_1(\mathbf{r},\mathbf{v},t)\mathbf{v}d\mathbf{v} \tag{9}$$

respectively. In the non-interacting, long mean free path limit, with no externally applied forces, the evolution of this function is described by the Boltzmann equation

$$(\partial_t + v \cdot \nabla) f_1 = \Omega[f_1] \tag{10}$$

While the left hand side describes changes in the distribution function due to free particle motion, the right hand side models pairwise collisions. The collision operator is an integral expression that is often simplified to the linear Bhatnagar-Gross-Krook (BGK) (Bhatnagar et al. 1954) form as

$$\Omega[f_1] = \frac{1}{\tau}[f - f^{(eq)}] \tag{11}$$

The collision operator describes the relaxation, at a rate controlled by a characteristic time τ towards the local Maxwell-Boltzmann equilibrium distribution $f^{(eq)}$. It can be shown that distributions governed by the simple Boltzmann-BGK equation conserve mass, momentum and energy. The Navier-Stokes equations can be recovered at sufficiently coarse length and time scales (Succi 2001).

The application of LB models to flow in porous media applications requires appropriate boundary conditions. In particular, flow in confinement, such as fractures and porous media requires no-slip, no-flow boundary conditions at solid-fluid interfaces. These boundary conditions are most easily implemented by means of a bounce back procedure that reverses particle velocities when they contact a solid-liquid interface (Sukop and Thorne 2007). The fluid can then be driven through the porous medium by using a body force, pressure boundary conditions or velocity boundary conditions (Fig. 18). The LB approach can also be used to simulate diffusion. This provides a way of simulating coupled flow and diffusion (dispersion) that is consistent with LB flow simulations (Flekkoy et al. 1995; Sukop and Thorne 2007). Using this approach, molecular displacement distributions in porous media have been obtained in good agreement with experimental NMR studies (Bijeljic et al. 2013; Yang and Boek 2013b).

This method also provides a basis for reactive transport simulations. In such cases, a separate distribution function may be used to describe the scalar intensive variable field

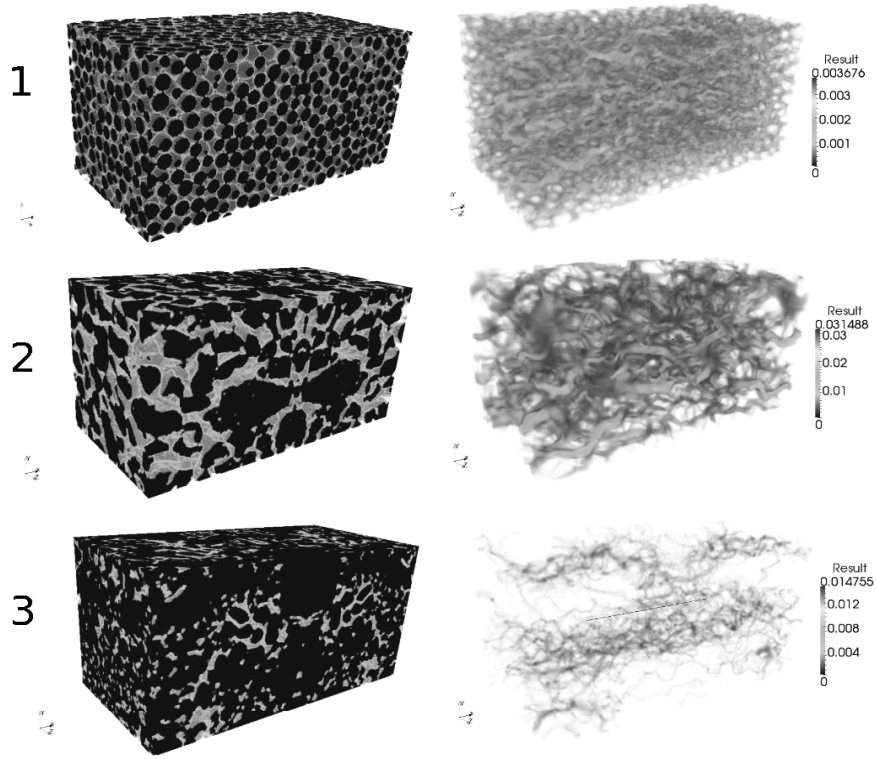

Figure 18. Pore space images (left: pore is light, solid is dark) and velocity distributions (right) of different porous media with increasing heterogeneity. (Yang and Boek 2013b)

associated with the concentration of a diffusing substance. In this fashion, Kaandorp et al. (1996) investigated the influence of nutrient diffusion and flow rate on coral morphology (Fig. 19). Gray and Boek (2013) have investigated dissolution of a solid cube using a dispersion method based on streamline tracing (Mostaghimi et al. 2012) in combination with chemical reaction (Fig. 20). Crystal growth from supersaturated solutions has been studied at different Damköhler numbers, *Da*, defined as the ratio of the characteristic times for transport and reaction (Kang et al. 2004). In addition, both precipitation and dissolution in pore geometries and fractures have been studied by this method (Kang et al. 2005, 2010).

LB methods have been used extensively to simulate both single- and multicomponent multiphase fluids. Multiphase fluids are simulated by adding forces that represent the effects of molecular fluid-fluid interactions. There are various ways to achieve this. (Shan and Chen 1993) have developed a bottom-up scheme that has become popular due to its simple implementation (Chin et al. 2002). A top-down approach was developed based on the Cahn-Hilliard free energy functional model (Swift et al. 1996). Finally, the color gradient model (Gunstensen et al. 1991) has recently gained renewed interest for multi-component flow in large complex geometries, as this scheme turns out to be very efficient in many respects (Yang and Boek 2013a). Using this scheme, it is now possible to carry out multi-component multi-phase flow simulations directly on large 3D tomography images to calculate relative permeabilities and capillary pressures (see Fig. 21; Ramstad et al. 2012; Yang and Boek 2013c).

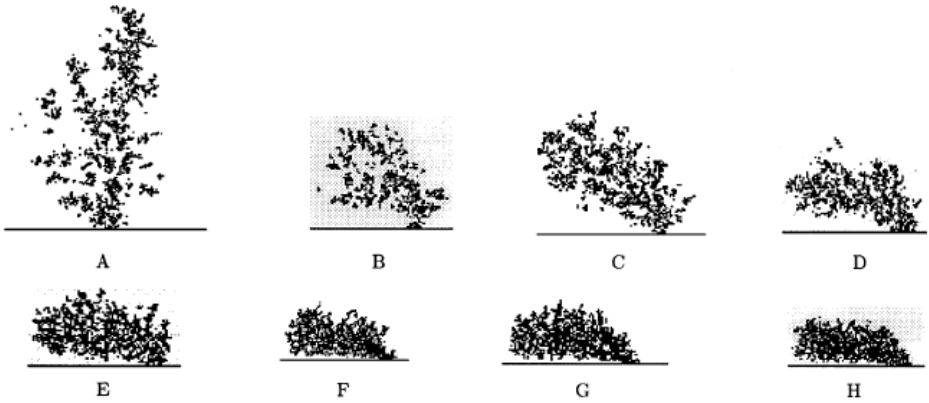

Figure 19. Effect of nutrient diffusion and flow on coral morphology. Flow is directed from left to right. Peclet numers are increasing from A to H. [Reprinted from Kaandorp et al. (1996) © 1996 by permission of the American Physical Society.]

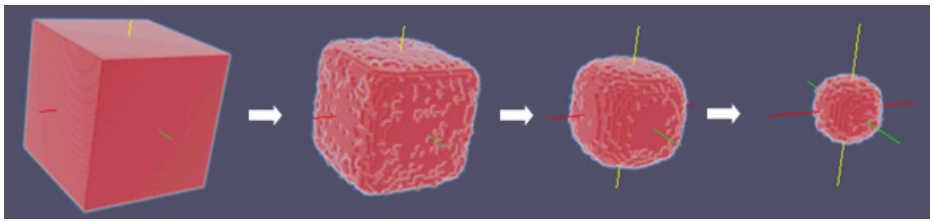

Figure 20. Dissolution of solid cube using dispersion model in combination with chemical reaction (Gray and Boek 2013).

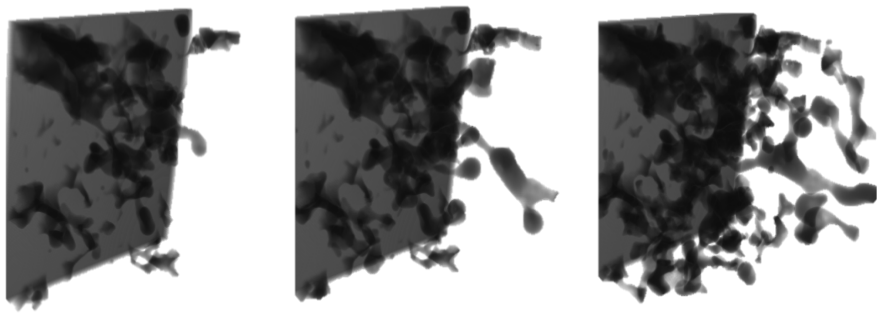

Figure 21. Lattice Boltzmann simulation of unsteady state primary drainage process in Bentheimer sandstone (Yang and Boek 2013c).

Future research opportunities

The extension of LB to multiphase reactive flow is going to be a challenge with particular applications to CO_2 storage and EOR applications. In addition, system sizes and time scales will need to be extended to improve comparison with experimental data. This may require a paradigm shift in computing approaches, possibly including GPU and heterogeneous computing methodologies.

CONCLUSIONS

Carbonate rocks have a structural complexity that makes predicting their flow performance challenging. The combination of a broad (and multimodal) pore size distribution, including a significant micro-porosity, together with a large REV, requires a combination of different experimental techniques to fully characterize the pore geometry. The reactivity of brine acidified by CO_2 in sequestration operations adds the requirement to consider changes to the pore structure during flow.

The scanning methods include medical CT, micro-CT, CLSM and (in the near future) FIB-SEM, to generate 3D pore space images at different spatial resolutions. These tomograms may then be used directly in flow simulation calculations to calculate flow properties. The simulation techniques, including MD, DPD, SRD and LB, may be applied at different length and time scales. Ultimately, the pore scale results will be upscaled to the core and field scale.

ACKNOWLEDGMENTS

This work was carried out as part of the activities of the Qatar Carbonates and Carbon Storage Research Centre (QCCSRC). We gratefully acknowledge the funding of QCCSRC provided jointly by Qatar Petroleum, Shell, and the Qatar Science and Technology Park, and their permission to publish this research.

REFERENCES

Allen M, Tildesley D (1990) Computer Simulation of Liquids. Oxford: Clarendon Press

Ameen MS, Buhidma IM, Rahim Z (2010) The function of fractures and in-situ stresses in the Khuff reservoir performance, onshore fields, Saudi Arabia. AAGP Bulletin 94(1):27-60

Arns CH, Bauget F, Limaye A, Sakellariou A, Senden T, Sheppard A, Sok RM, Pinczewski V, Bakke S, Berge LI, Oren PE, Knackstedt MA (2005) Pore-scale characterization of carbonates using X-ray microtomography. SPE J 10(4):475-484

Bear J (1972) Dynamics of Fluids in Porous Media. New York: Elsevier

Berg S, Ott H, Klapp SA, Schwing A, Neiteler R, Brussee N, Makurat A, Leu L, Enzmann F, Schwarz JO, Kersten M, Irvine S, Stampanoni M (2013) Real-time 3D imaging of Haines jumps in porous media flow. Proc Natl Acad Sci 110(10):3755-3759

Bhatnagar P, Gross E, Krook M (1954) Model for collision processes in gases. I. Small amplitude processes in charged and neutral one-component systems. Phys Rev 94:511-524

Bijeljic B, Mostaghimi P, Blunt MJ (2011) Signature of non-Fickian solute transport in complex heterogeneous porous media. Phys Rev Lett 107:204502

Bijeljic B, Raeini A, Mostaghimi P, Blunt M (2013) Predictions of non-Fickian solute transport in different classes of porous media using direct simulation on pore-scale images. Phys Rev E 87:013011

Blunt MJ (1998) Physically-based network modeling of multiphase flow in intermediate-wet porous media. J Pet Sci Eng 20:117-125

Blunt MJ, Bijeljic B, Dong H, Gharbi O, Iglauer S, Mostaghimi P, Paluszny A, Pentland C (2013) Pore-scale imaging and modelling. Adv Water Res 51:197-216

Boek ES, van der Schoot P (1998). Resolution effects in dissipative particle dynamics simulations. Int J Mod Phys C 9:1307-1318

Boek ES, Venturoli M (2010) Lattice-Boltzmann studies of fluid flow in porous media with realistic rock geometries. Comput Math Appl 59:2305-2314
Boek ES, Coveney PV, Lekkerkerker H, van der Schoot P (1997) Simulating the rheology of dense colloidal suspensions using dissipative particle dynamics. Phys Rev E 55:3124-3133
Boek ES, Ladva H, Crawshaw J, Padding JT (2008) Deposition of colloidal asphaltene in capillary flow: experiments and mesoscopic simulation. Energy Fuels 22:805-813
Boek ES, Padding JT, Headen T (2010) Multi-scale simulation of asphaltene aggregation and deposition in capillary flow. Faraday Disc 144:271-284
Buchgraber M, Al-Dossary M, Ross CM, Kovscek AR (2012) Creation of a dual-porosity micromodel for pore-level visualization of multiphase flow. J Pet Sci Eng 86-87:27-38
Buckley JS (1991) Multiphase displacements in micromodels. *In:* Interfacial Phenomenon in Oil Recovery. Morrow NR (ed) CRC Press, New York, p 157-189
Cantrell DL, Hagerty RM (1999) Microporosity in Arab formation carbonates, Saudi Arabia. GeoArabia 4(2):129-154
Chin J, Boek ES, Coveney P (2002) Lattice Boltzmann simulation of the flow of binary immiscible fluids with different viscosities using the Shan-Chen microscopic interaction model. Philos Trans R Soc London A 360:547-558
Christenson H (1983) Experimental measurements of solvation forces in nonpolar liquids. J Chem Phys 78:6906
Cnudde V, Boone MN (2013) High-resolution X-ray computed tomography in geosciences: A review of the current technology and applications. Earth Sci Rev 123:1-17
Coveney P, Espanol P (1997) Dissipative particle dynamics for interacting multicomponent systems. J Phys A Math Gen 30:779-784
d'Humieres D, Lallemand P, Frisch U (1986) Lattice gas models for 3D hydrodynamics. Europhys Lett 2:291-297
Demianov A, Dinariev O, Evseev N (2011) Density functional modelling in multiphase compositional hydrodynamics. Can J Chem Eng 89:207-226
Espanol P, Warren P (1995) Statistical mechanics of dissipative particle dynamics. Europhys Lett 30:191-196
Flekkoy E, Oxaal U, Feder J, Jossang T (1995) Hydrodynamic dispersion at stagnation points—Simulations and experiments. Phys Rev E 52:4952-4962
Fredrich JT, Greaves KH, Martin JW (1993) Pore geometry and transport properties of Fountainebleau Sandstone. Int J Rock Mech Min Sci 30:691-697
Fredrich JT, Menendez B, Wong T (1995) Imaging the pore structure of geomaterials. Science 268:276-279
Frisch U, Hasslacher B, Pomeau Y (1986) Lattice-gas automata for the Navier-Stokes equation. Phys Rev Lett 56:1505-1508
Gingold R, Monahan J (1977) Smoothed particle hydrodynamics: Theory and application to non spherical stars. Mon Not R Astron Soc 181:375-389
Gouze P, Luquot L (2011) X-ray microtomography characterization of porosity, permeability and reactive surface area changes during dissolution. J Contam Hydrol 120-121:45-55
Gray F, Boek ES (2013) Hydrodynamic dispersion in pore space images. In prep
Gunstensen A, Rothman D, Zaleski S, Zanetti G (1991) Lattice Boltzmann model of immiscible fluids. Phys Rev A 43:4320-4327
Hamm LM, Bourg IC, Wallace AF, Rotenberg B (2013) Molecular simulation of CO_2- and CO_3-brine-mineral systems. Rev Mineral Geochem 77:189-228
Hazlett RD (1995) Simulation of capillary-dominated displacements in microtomographic images of reservoir rocks. Transp Porous Media 20(1-2):21-35
Headen T, Boek E (2011a) Molecular dynamics simulations of asphaltene aggregation in supercritical carbon dioxide with and without limonene. Energy Fuels 25:503-508
Headen T, Boek E (2011b) Potential of mean force calculation from molecular dynamics simulation of asphaltene molecules on a calcite surface. Energy Fuels 25:499-502
Holzer L, Indutnyi F, Gasser P, Munch B, Wegmann M (2004) Three-dimensional analysis of porous BaTiO using FIB nanotomography. J Microsc 216(1):84-95
Holzer L, Muench B, Wegmann M, Gasser P (2006) FIB-nanotomography of particulate systems—Part I: particle shape and topology of interfaces. J Am Ceram Soc 89(8):2577-2585
Hoogerbrugge P, Koelman J (1992) Simulating microscopic hydrodynamic phenomena with dissipative particle dynamics. Europhys Lett 19:155-160
Hornbrook JW, Castanier LM, Petit PA (1991) Observation of foam/oil interactions in a new, high-resolution micromodel. *In:* Proceedings of the SPE Annual Technical Conference and Exhibition. Dallas, TX. Manuscript # 22631-MS, doi: 10.2118/22631-MS
Huang H, Meakin P, Liu M (2005) Computer simulation of two-phase immiscible fluid motion in unsaturated complex fractures using a volume of fluid method. Water Resour Res 41:W12413

Iglauer S, Paluszny A, Pentland CH, Blunt MJ (2011) Residual CO_2 imaged with X-ray micro-tomography. Geophys Res Lett 38 L21403, doi: 10.1029/2011GL049680
Ihle T, Kroll D (2001) Stochastic rotation dynamics: A Galilean-invariant mesoscopic model for fluid flow. Phys Rev E 63:020201
Kaandorp JA, Lowe CP, Frenkel D, Sloot P (1996) Effect of nutrient diffusion and flow on coral morphology. Phys Rev Lett 77:2328-2331
Kang Q, Lichtner P, Viswanathan H, Abdel-Fattah A (2010) Pore scale modeling of reactive transport involved in geologic CO_2 sequestration. Transp Porous Media 82:197-213
Kang Q, Tsimpanogiannis I, Zhang D, Lichtner P (2005) Numerical modeling of pore-scale phenomena during CO_2 sequestration in oceanic sediments. Fuel Process Technol 86:1647-1665
Kang Q, Zhang D, Lichtner P, Tsimpanogiannis I (2004) Lattice Boltzmann model for crystal growth from supersaturated solution. Geophys Res Lett 31:L21604
Kang W, Landman U (2007) Universality crossover of the pinch-off shape profiles of collapsing liquid nanobridges in vacuum and vapor environments. Phys Rev Lett 98:064504
Kikuchi N, Pooley C, Ryder J, Yeomans J (2004) Transport coefficients of a mesoscopic fluid dynamics model. J Chem Phys 119:6388
Kim Y, Wan J, Kneafsey TJ, Tokunaga TK (2012) Dewetting of silica surfaces upon reactions with supercritical CO_2 and brine: pore-scale studies in micromodels. Environl Sci Technol 46:4228-4235
Kong B, Yang X (2006) Dissipative particle dynamics simulation of contact angle hysteresis on a patterned solid/air composite surface. Langmuir 22:2065-2073
Koplik JL (1984) Conductivity and permeability from microgeometry. J Appl Phys 56(11):3127-3131
Lasagni F, Lasagni A, Marks E, Holzapfel C, Mucklich F, Degischer H (2007) Three-dimensional characterization of 'as-cast'and solution-treated AlSi12 (Sr) alloys by high-resolution FIB tomography. Acta Mater 55:3875-3882
Lenormand R (1981) Displacements Polyphasiques en Milieu Poreux sous l'Influence des Forces Capillaires; Etude Experimentale et Modelisation de Type Percolation. Ph.D. dissertation. L'Institut National Polytechnique de Toulouse, France
Lenormand R, Zarcone C, Sarr A (1983) Mechanisms of the displacement of one fluid by another in a network of capillary ducts. J Fluid Mech 135:337-353
Li NC, Wardlaw Y (1986) The influence of wettability and critical pore-throat size ratio on snap-off. J Colloid Interface Sci 109:461-472
Lin C, Pirie G, Trimmer DA (1986), Low permeability rocks: Laboratory measurements and three-dimensional microstructural analysis. J Geophys Res 91(B2):2173-2181
Liu N, Aymonier C, Lecoutre C, Garrabos Y, Marre S (2012) Microfluidic approach for studying CO_2 solubility in water and brine using confocal Raman spectroscopy. Cheml Phys Lett 551:139-143
Luquot L, Gouze P (2009) Experimental determination of porosity and permeability changes induced by injection of CO_2 into carbonate rocks. Cheml Geol 265:148-159
Malevanets A, Kapral R (1999) Mesoscopic model for solvent dynamics. J Chem Phys 110:8605
Mattax CC, Kyte JR (1961) Ever see a water flood? Oil Gas J 1961:115-128
McCullough EC (1975) Photon attenuation in computed tomography. 2(6):307-320
Meakin P, Tartakovsky AM (2009) Modeling and simulation of pore scale multiphase fluid flow and reactive transport in fractured and porous media. Rev Geophys 47:RG3002
Mostaghimi P, Bijeljic B, Blunt MJ (2012) Simulation of flow and dispersion on pore-space images. *In:* Proceedings of the 2010 SPE Annual Technical Conference and Exhibition, Florence, Italy. SPE J 17(4):1131-1141. SPE-135261-PA. doi: 10.2118/135261-PA
Nie X, Chen S, W E, Robbins M (2004) A continuum and molecular dynamics hybrid method for micro and nano-fluid flow. J Fluid Mech 500:55-64
Ott H, de Kloe K, Marcelis F, Makurat A (2011) Injection of supercritical CO_2 in brine saturated sandstone: pattern formation during salt precipitation. Energy Procedia 4:4425-4432
Padding J, Louis A (2004) Hydrodynamic and Brownian fluctuations in sedimenting suspensions. Phys Rev Lett 93:220601
Padding J, Louis A (2006) Hydrodynamic interactions and Brownian forces in colloidal suspensions: coarse-graining over time and length scales. Phys Rev E 74:031402
Perrin J-C, Krause M, Kuo C-W, Miljkovic L, Charoba C, Benson SM (2009) Core-scale experimental study of relative permeability properties of CO_2 and brine in reservoir rocks. Energy Procedia 1:3515-3522
Petford N, Davidson G, Miller JA (2001) Investigation of the petrophysical properties of a porous sandstone sample using confocal scanning laser microscopy. Pet Geosci 7:99-105
Peysson Y, Bazin B, Magnier C, Youssef S (2011) Permeability alteration due to salt precipitation driven by drying in the context of CO_2 injection. Energy Procedia 4:4387-4394
Pini R, Krevor SC, Benson SM (2012) Capillary pressure heterogeneity for the CO_2/water system in sandstone rocks at reservoir conditions. Adv Water Resour 38:48-59

Ramstad T, Idowu N, Nardi C, Oren P (2012) Relative permeability calculations from two-phase flow simulations directly on digital images of porous rocks. Transp Porous Media 94:48-504

Rangel-German ER, Kovscek AR (2006) A micromodel investigation of two-phase matrix-fracture transfer mechanisms. Water Resour Res 42:W03401, doi: 10.1029/2004WR003918

Russo J, Horbach J, Sciortino F, Succi S (2010) Nanoflows through disordered media: A joint lattice Boltzmann and molecular dynamics investigation. Europhys Lett 89:44001

Saadatfar M, Sheppard A, Knackstedt M (2006) Grain partitioning and its applications. *In:* Advances in X-ray Tomography for Geomaterials. Desrues J, Viggiani G, Besuelle P (eds) ISTE Publishing Knowledge, London, p 269-276

Shan X, Chen H (1993) Lattice Boltzmann model for simulating flows with multiple phases and components. Phys Rev E 47:1815-1819

Sohrabi M, Kechut NI, Riazi M, Jamiolahmady M, Ireland S, Robertson G (2011) Safe storage of CO_2 together with improved oil recovery by by CO_2-enriched water injection. Chem Eng Res Design 89:1865-1872

Sok R, Varslot T, Ghous A, Latham S, Sheppard AP, Knackstedt MA (2010) Pore scale characterization of carbonates at multiple scales integration of micro-CT, BSEM, and FIBSEM. Petrophys 51(6):379-387

Steefel C, Maher K (2009) Fluid-rock interaction: a reactive transport approach. Rev Mineral Geochem 70:485-532

Stukan M, Ligneul P, Crawshaw J, Boek ES (2010) Spontaneous imbibition in nanopores of different roughness and wettability. Langmuir 26:13342–13352

Succi S (2001) The Lattice Boltzmann Equation for Fluid Dynamics and Beyond. Oxford: Oxford University Press

Sukop M, Thorne D Jr (2007) Lattice Boltzmann Modeling: An Introduction for Geoscientists and Engineers. Berlin Heidelberg New York: Springer Publishing Company

Suter J, Sprik M, Boek E (2012) Free energies of absorption of alkali ions onto beidellite and montmorillonite surfaces from constrained molecular dynamics simulations. Geochim Cosmochim Acta 91:109-119

Swift M, Orlandini E, Osborn W, Yeomans J (1996) Lattice Boltzmann simulations of liquid-gas and binary fluid systems. Phys Rev E 54:5041-5052

Tartakovsky AM, Meakin P, Scheibe TD, Eichler West RM (2007) Simulations of reactive transport and precipitation with smoothed particle hydrodynamics. J Comput Phys 222:654-672

Tohidi B, Anderson R, Clennell MB, Burgass RW, Biderkab AB (2001) Visual observation of gas-hydrate formation and dissociation in synthetic porous media by means of glass micromodels. Geology 29:867-870

Tomutsa L, Silin DB, Radmilovic V (2007) Analysis of chalk petrophysical properties by means of submicron-scale pore imaging and modeling. SPE Reservoir Eval Eng 10(3):285-293

Valvatne PH, Blunt MJ (2004) Predictive pore-scale modeling of two-phase flow in mixed wet. Water Resour Res 40:W07406, doi: 10.1029/2003WR002627

Venturoli M, Boek ES (2006) Lattice-Boltzmann simulations of single phase flow in a pseudo two-dimensional micromodel. Physica A 362:23-29

Vinegar HJ, Wellington SL (1987) Tomographic imaging of three-phase flow experiments. Rev Sci Instrum 58:96; doi: 10.1063/1.1139522

Wan J, Tokunaga T, Tsang C-F, Bodvarsson GS (1996) Improved glass micromodel methods for studies of flow and transport in fractured porous media. Water Resour Res 32(7):1955-1964

Willingham TW, Werth CJ, Valocchi AJ (2008) Evaluation of the effects of porous media structure on mixing-controlled reactions using pore-scale modeling and micromodel experiments. Environ Sci and Technol 42:3185-3193

Yang J, Boek E (2013a) A comparison study of multi-component lattice-Boltzmann models for ow in porous media applications. Comput Math Appl 65:882-890

Yang J, Boek ES (2013b) Quantitative determination of molecular propagator distributions for solute transport in homogeneous and heterogeneous porous media using lattice Boltzmann simulations. In prep

Yang J, Boek ES (2013c) Lattice-Boltzmann simulation of immiscible flow in 3D tomographic pore space images. In prep

Zhang C, Dehoff K, Hess N, Oostrom M, Wietsma TW, Valocchi AJ, Fouke BW, Werth CJ (2010) Pore-scale study of transverse mixing induced $CaCO_3$ precipitation and permeability reduction in a model subsurface sedimentary system. Environ Sci Technol 44:7833-7838

Zuo L, Zhang C, Faltac RW, Bensona SM (2013) Micromodel investigations of CO_2 exsolution from carbonated water in sedimentary rocks. Adv Water Resour 53:188-197

Reviews in Mineralogy & Geochemistry
Vol. 77 pp. 459-479, 2013
Copyright © Mineralogical Society of America

Caprock Fracture Dissolution and CO_2 Leakage

Jeffrey P. Fitts and Catherine A. Peters

Department of Civil and Environmental Engineering
Princeton University
Princeton, New Jersey 08544, U.S.A.

fitts@princeton.edu cap@princeton.edu

INTRODUCTION

Caprocks are impermeable sedimentary formations that overlie prospective geologic CO_2 storage reservoirs. As such, caprocks will be relied upon to trap CO_2 and prevent vertical fluid migration and leakage. Natural and industrial analogues provide evidence of long-term performance of caprocks in holding buoyant fluids. However, the large volumes of CO_2 that must be injected and stored to meaningfully reduce anthropogenic greenhouse gas emissions will exert unprecedented geomechanical and geochemical burdens on caprock formations due to elevated formation pressures and brine acidification.

Caprocks have inherent vulnerabilities in that wellbores, faults and fractures that transect caprock formations may provide conduits for CO_2 and/or brine to leak out of the intended storage formation. As a result, a critical criterion for CO_2 storage reservoir siting assessments will be to predict and reliably quantify the risk of leakage through caprock formations. We use "flow paths" as a catchall term for any fluid conduit through caprocks including pore networks, fractures and faults along with any combination of the three elements. It is useful to assess leakage rates through flow paths in terms of their individual transmissivity, T [m^4], which is the product of the permeability and the cross-sectional area of the flow path. Darcy's law can be used to relate these intrinsic flow path characteristics and the hydraulic potential (pressure) gradient to determine a volumetric flow rate, Q, or a leakage rate for the individual flow path:

$$Q = -\frac{T}{\mu}\frac{\Delta P}{\Delta z} = -\frac{Ak}{\mu}\frac{\Delta P}{\Delta z} \tag{1}$$

Where P is the hydraulic potential [Pa], z is the depth [m], μ is the fluid viscosity [Pa s] and A [m^2] is the cross-sectional area of the flow path perpendicular to flow, and A equals the product of average fracture aperture and fracture length normal to the flow direction. Predicting leakage potential, however, is extremely complex because assessments must consider not only leakage through existing flow paths, but also the potential for the geomechanical and geochemical burdens to increase caprock transmissivity by creating new flow paths, increasing their cross-sectional area and/or increasing their permeability for decades and centuries to come.

This chapter reviews experimental observations and model developments that have advanced our ability to predict how the geochemical burdens of CO_2 storage might alter leakage rates through caprocks. Our review is motivated by the question: *Under what conditions and to what extent might mineral dissolution increase leakage rates through caprocks?* This question anchors the focus of this paper on practical assessment tools, highlighting simplifying assumptions and the tradeoffs between assessment complexity and uncertainty. Thus far, assessments indicate that leakage risks will be manageably low at properly sited geologic CO_2 storage reservoirs. Economic and commercial viability of GCS, concerns over environmental

1529-6466/13/0077-0013$05.00 http://dx.doi.org/10.2138/rmg.2013.77.13

protection, as well as social dimensions of public acceptance will likely demand reductions in uncertainty about caprock performance that can only be addressed by improving the parameterization and computational efficiency of predictive models.

This chapter does not consider the geochemistry of well cements, and therefore, the reader should refer to the review by Carey (2013, this volume) for a detailed review of the geochemistry of leakage through wellbores. While this chapter does not cover geomechanical processes that play a role in leakage risk, we acknowledge that geomechanical and geochemical processes are often coupled (Sonnenthal et al. 2004). Furthermore, the relevance of geochemical alteration of flow paths is predicated on the existence of flow paths, as might result from independent geomechanical forces (Shukla et al. 2010; Heath et al. 2012; Manga et al. 2012) such as induced seismicity (Zoback and Zinke 2001). We also acknowledge that it is unlikely that geochemical processes alone will create new caprock breaches through impermeable rock (Gaus et al. 2005; Gherardi et al. 2007).

In this chapter, we first survey efforts to define caprock performance standards, reviewing bounding analyses used to assess leakage risk through caprocks in terms of global emissions targets, geologic carbon sequestration (GCS) regulations, siting assessments, and barriers to market penetration and public acceptance of GCS. The review then summarizes the mineralogical reactivity criteria for the event of geochemical reaction induced changes to permeability in caprock flow paths, as well as what is known about the relevant flow paths through caprocks, and processes of brine acidification. We make the case for the development of simplified geochemical reactive transport models to predict permeability evolution, and we demonstrate this with an illustrative example of reactive flow through a 100 m one-dimensional flow path in a calcite-containing caprock. The final section brings together the experiments and simulations that reveal complex processes that are currently not part of existing reactive transport models. Such processes will require further research both to fully understand as well as to determine appropriate means of upscaling for application in practical models of caprock performance.

BIG PICTURE PERSPECTIVE OF CAPROCK PERFORMANCE

Structural or stratigraphic trapping by caprock formations is projected to be the most important mechanism keeping injected CO_2 out of the atmosphere for 100's to 1000's of years. However, it has been recognized that given the necessity for storage over such long periods of time at many large storage sites distributed globally throughout sedimentary basins, leakage at some sites should be expected (Bachu 2008; Benson and Cole 2009). The longevity of CO_2 storage is essential to providing the intended atmospheric greenhouse gas reductions, and while capillary, solubility and mineral trapping are projected to gradually reduce the relative importance of stratigraphic trapping, caprocks will remain the primary seal throughout the lifecycle of a CO_2 geologic storage reservoir (Emberley et al. 2004; Xu et al. 2004). Therefore, we begin with the question: *How good does a caprock need to be?* The answer requires that we define acceptable leakage rates: acceptable in terms of reducing and maintaining reductions in atmospheric CO_2 levels, acceptable in terms of human health and environmental impact, and acceptable economically and with respect to near- and long-term liability. The acceptable level of uncertainty in projections of caprock performance will also need to be defined and will depend both on the spatial scale over which the leakage rate estimates are applied [i.e., global vs. sedimentary basin vs. specific injection/storage site(s)] and the timeframe over which they are projected.

Hepple and Benson (2005) indirectly estimated caprock performance standards by considering the amount of CO_2 that must remain underground in order to achieve different scenarios for global greenhouse gas emissions reductions and climate stabilization targets. Their modeling results showed how the range of acceptable rates of CO_2 "seepage" to the atmo-

sphere (0.01-0.1%/yr) depends on the global quantity of CO_2 emissions reductions stored in geologic reservoirs, from 1000's of Gt to 10-100's of Gt for the relatively high allowable leakage. The authors also evaluated the sensitivity of their global performance standard to emission scenarios and sequestration requirements to achieve climate stabilization goals. This type of analysis is instructive in that it demonstrates the large uncertainties associated with the underlying parameters, and how acceptable leakage rates will need to be revised downward if CO_2 emissions continue unabated. Global performance standards define an upper boundary for acceptable leakage to the atmosphere, and as a result, the greatest tolerance of uncertainty. The performance goal of 99% storage permanence was set by the U.S. Department of Energy (DOE) for its demonstration CO_2 injection projects and storage projects being implemented in the Regional Carbon Sequestration Partnerships. Figure 1, based on the analysis by Hepple and Benson (2005), shows the amount of CO_2 that would need to be offset, such as through geologic sequestration, to achieve climate stabilization of 550 ppm of CO_2 under a rapid economic growth emissions scenario. Their analysis also showed that the 1% performance target may not be effective because by the year 2150 the leakage rate exceeds the allowable emissions. Siting assessments, however, will likely be held to more strict caprock performance standards as stakeholders demand assurances that leakage risk to economic, human health, environmental and societal interests will be low and manageable (Bielicki et al. 2013). Therefore, refined analyses of flow paths in the subsurface will be needed as required to predict both low probability high impact events and geospatial migration in a heavily utilized subsurface.

All currently proposed GCS regulatory frameworks are based on some formulation of what the United States Environmental Protection Agency (USEPA) refers to as an "Area of Review" (AoR). The USEPA currently defines the AoR as the region surrounding the geologic sequestration project where underground sources of drinking water may be endangered by the injection activity. The AoR is delineated using computational modeling that accounts for the physical and chemical properties of all phases of the injected carbon dioxide stream and displaced fluids, and is based on available site characterization, monitoring, and operational data (USEPA 2012). The purpose of the AoR is to determine the presence of flow paths through which significant

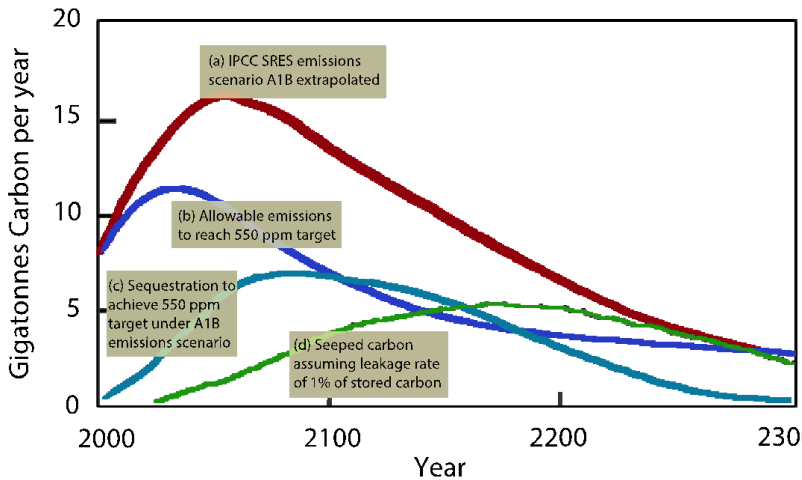

Figure 1. (a) Carbon emissions for the IPCC SRES A1B emissions scenario that assumes rapid global economic growth. (b) Allowable carbon emissions to achieve climate stabilization for CO_2 at 550 ppm. (c) The difference between curves (a) and (b) gives the reduction in CO_2 emissions needed, which here is assumed to be accomplished entirely by geologic sequestration. (d) Seepage of CO_2 assuming a leakage rate of 1% of the amount of CO_2 currently sequestered. [Adapted from: Hipple and Benson 2005].

amounts of injected CO_2 or displaced native brine could migrate out of the targeted storage formation. While the USEPA draft regulations consider the potential leakage risk of CO_2 and displaced native brine to freshwater aquifers, any comprehensive regulations will need to regulate a number of important dimensions of leakage including interference with other subsurface resources and releases of CO_2 back into the atmosphere. For example, hydraulic fracturing of shale formations for methane production has been highlighted as a subsurface activity that should be assessed for its potential impact on the seal quality of deep saline aquifer CO_2 storage formations (Elliot and Celia 2012). Therefore, site-specific caprock assessments would ideally consider the permeability and areal extent of all potential flow paths within the AoR. Nogues et al. (2012a) bounded leakage for a prospective injection site in the Alberta basin by only considering leakage through wellbores (Fig. 2). This approach could be adapted to include leakage through fractures and faults by characterizing/assigning the occurrence, areal extent and permeabilities. This study also demonstrates the application of probability distributions and Monte Carlo simulations to bound leakage rates through individual flow paths. The knowledge gaps in relation to fracture and fault occurrence and characteristics are still too large to yield adequate uncertainties and satisfy statistical criteria of Monte Carlo analyses.

The most stringent caprock performance standards, however, will likely be required to overcome economic and commercial barriers to GCS implementation as well as to facilitate regulatory compliance and public acceptance. The potential risks of CO_2 leakage have already stirred local opposition to GCS implementation (e.g., see refs in Little et al. 2010). Much work has been dedicated to evaluating the cost of GCS (see citations of Rubin et al. 2007), while a more limited number of studies have considered the additional costs of leakage risk. Pollak et al. (2013) developed the Leakage Impact Valuation (LIV) method, a systematic and thorough scenario-based approach to identify these costs, their drivers, and who incurs the costs across four potential leakage outcomes: 1) leakage only; 2) leakage that interferes with a subsurface activity; 3) leakage that affects groundwater; and 4) leakage that reaches the surface. The

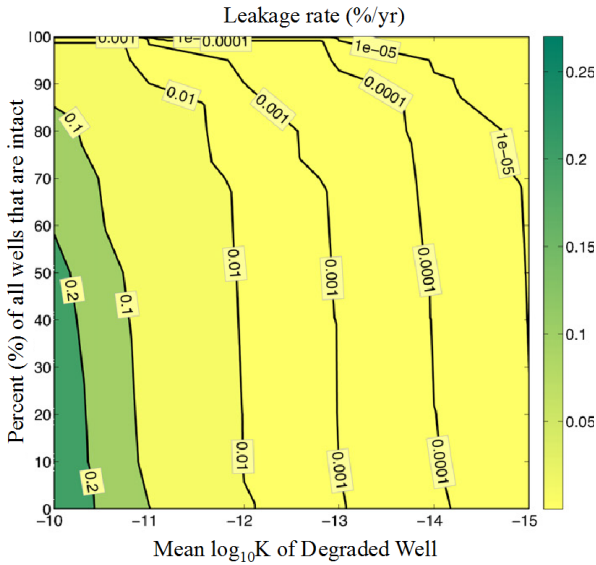

Figure 2. Contour map of leakage rate (%/yr) as a function of the wellbore permeability (log10K) and the percent of wells penetrating the injection formation that provide leakage conduits to the uppermost two aquifers in the stratigraphic column [Used by permission of Elsevier Ltd, from Nogues et al. (2012a), *Int J Greenhouse Gas Control* , Vol. 7, Fig. 4, p. 39.].

LIV method is flexible and can be used to investigate a wide range of leakage scenarios for subsurface activities and resources. The financial consequences of leakage estimated by the LIV method will vary across case studies due to differences in geologic, institutional, and regulatory settings. Bielicki et al. (2013) developed a methodology to monetize leakage risk throughout a basin, based on simulations of fluid flow, subsurface data, and estimates of costs triggered by leakage. Figure 3 shows the geospatial specificity of this method, where the semi-analytical code ELSA (Nordbotten et al. 2005a) was used to simulate leakage rates through existing wellbores into overlying permeable formations for the case of injection into the Mt. Simon formation in the Michigan basin. The results show how leakage infiltration into a formation varies with depth according to the physical extent and permeability of each sedimentary unit, pressure buildup in the injection formation (Cihan et al. 2013), and the flow path characteristics and proximity to the CO_2 source. While the amounts of infiltration to drinking water aquifers and the atmosphere are extremely small over 30 years of injection, the leakage rates of CO_2 and displaced native brine into deeper units are significant enough to impact other subsurface activities including wastewater injection and oil/gas extraction (Bielicki et al. 2013). Furthermore, this study shows how leakage risk is site-specific, and how assessments that account for geospatial variation of caprock performance can be applied to prioritize CO_2 storage site selection based on the location and hydrodynamic properties of flow paths and their proximity to other subsurface activities.

In summary, the goals for caprock performance should guide the appropriate level of detail required to predict leakage rates and their evolution with time. Furthermore, this paradigm can be used to identify risk factors (susceptibilities) and guidelines to limit model complexity.

BASELINE ASSESSMENTS OF CAPROCK DISSOLUTION POTENTIAL

Caprocks are sedimentary formations with relatively low permeability deriving from the low porosity of the rock as well as the unconnected structure of the pore network. Caprocks generally fall into three categories: (i) argillaceous rocks which are highly compacted clays, shales or mudstones, (ii) consolidated clastic rocks that are compacted and highly cemented due to long-term diagenesis, and (iii) evaporites which are precipitated chlorides, sulfates and

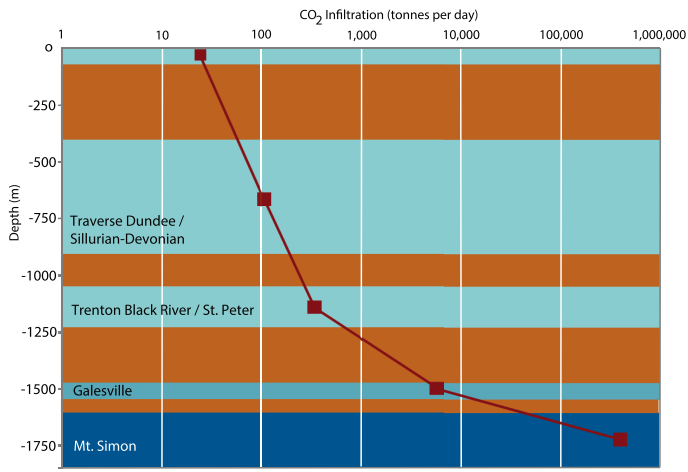

Figure 3. Leakage of CO_2 from the Mt. Simon formation in the Michigan basin and subsequent infiltration through the overlying geologic sequence after 30 years of continuous CO_2 injection and unabated leakage. [Modified with permission of JM Bielicki, see Bielicki et al. 2013].

carbonates that usually contain some detrital materials such as chert, sand, clay or carbonate remnants of marine organisms. Figure 4 shows electron microscopy images of three caprock samples, all with low permeability but each with very different lithology and mineralogy. Even at this small spatial scale, mineral heterogeneity can produce complexity in flow path permeability evolution.

The Nordland shale is an argillaceous rock overlying the Utsira sand, the target in the Sleipner Field for the CO_2 injection project in the North Sea. It is a shaley mudstone containing silt-grade grains of quartz, K-feldspar and calcite in a compacted but uncemented clay matrix of primarily mica and kaolinite (Harrington et al 2009). Specimens of this shale have porosity less than 1%, with permeability on the order of 10^{-19} m^2 (Harrington et al. 2009). This is negligible compared with the underlying Utsira formation which has a porosity between 30% and 40% and a permeability of 10^{-12} m^2 (Bickle et al 2007).

The Eau Claire formation is a highly compacted and consolidated clastic rock overlying the Mt. Simon sandstone in both the Michigan and Illinois sedimentary basins. In the Illinois basin, the Mt. Simon is the target for CO_2 injection for FutureGen 2.0. The Eau Claire formation has been characterized by several lithofacies, which have in common a detrital clastic mix of quartz and K-feldspar in cement matrices of clays such as illite or carbonates such as dolomite (Liu et al. 2012; Neufelder et al. 2012). Organics have also been found (Deng et al. 2013). Calcite is found nearly everywhere in the Eau Claire formation, with percentages as high as 41% particularly in the muddy siltstone and shale lithofacies (Neufelder et al. 2012). The study reported porosities ranging from less than 5% to more than 20%, and permeabilities mostly in the range of 10^{-22} m^2 to 10^{-16} m^2.

The Amherstburg is a dolomitic limestone evaporite that is considered as the primary seal for the Bass Islands dolostone, which was the target for the 2008-2009 CO_2 injection demonstration project in Michigan (Ellis et al. 2011; Gupta et al. 2011). The Amherstburg is

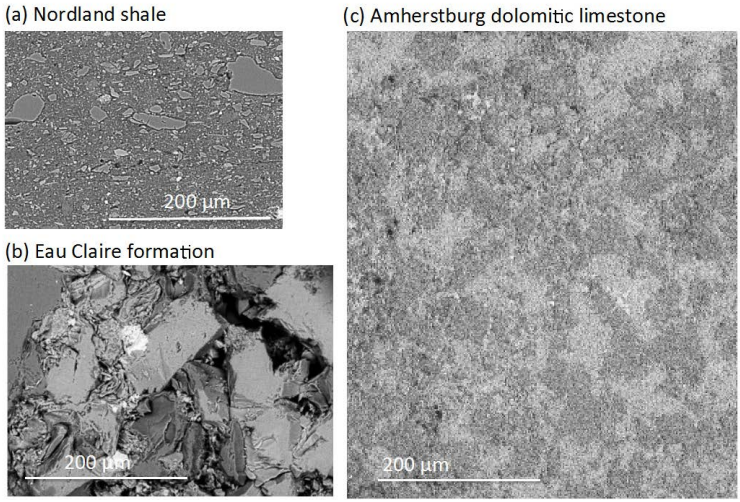

Figure 4. Backscattered electron micrographs of three different caprocks: (a) Nordland shale overlying the Utsira formation in the Sleipner Field, (b) Eau Claire formation overlying the Mt. Simon sandstone in the Illinois basin, (c) Amherstburg dolomitic limestone overlying the Bass Islands dolostone in the Michigan basin. Source for (a) is Harrington et al. (2009) [Used by permission of the British Geological Survey, from Harrington et al. (2009), *Carbon dioxide sequestration in geological media—State of the science: AAPG Studies in Geology*, Vol. 59, Fig. 4, p. 521.].

roughly equal parts calcite and dolomite with numerous well-formed fossil remnants. It has negligible porosity and permeability.

These three caprock formations are all considered to be excellent seals that would prevent upward migration of buoyant fluids. At the Sleipner field, time-lapse seismic observations have provided evidence that the Nordland shale is performing as an effective seal (Bickle et al. 2007). At the Bass Islands injection site, an array of monitoring approaches including wellhead measurements, downhole monitoring, crosswell seismic observation, and brine and cement sampling, indicated no evidence of CO_2 migration outside of the injection formation (Battelle 2011).

While reliable containment was achieved at the Michigan site, is being achieved at the Sleipner field, and is projected for the FutureGen 2.0 site, current leakage risk assessments do not account for possible geochemical evolution of caprock breaches. Caprock reliability assessments have historically been based on physical caprock integrity and hydrologic flow considerations. Implicit is an assumption that there is no risk of migration of acidified brines and reaction-induced erosion due to mineral dissolution. *Under what conditions might this be a concern, and how should computationally tractable models be developed for inclusion into practical basin-scale leakage models?*

To answer this question, we examine the mineralogical and geochemical conditions that present a risk for acid erosion of caprock flow paths. The minerals at risk are ones that are thermodynamically unstable at low pH as well as have negligible kinetic limitations for dissolution. There is only one mineral that fits this description: calcite. For formation brines that are near equilibrium with respect to calcite, if this system is perturbed by introduction of CO_2, the dissolved gas will lead to carbonic acid production. The resulting decrease in pH and increase in bicarbonate ion will lead to an increase in the thermodynamic driving force for calcite dissolution.

In addition to being quite soluble in acidic water, calcite's dissolution kinetics are extremely fast. According to kinetic data compiled by Palandri and Kharaka (2004), calcite's acid-driven dissolution rate constant is an order of magnitude larger than the next fastest reacting minerals, which are dolomite and anorthite, which have rate constants that are orders of magnitude faster than other minerals. Thus, while thermodynamics favors acid-driven dissolution for a host of minerals, calcite is the only one that is both highly soluble and will dissolve very fast. In reactive transport models that account for transport typical of deep subsurface conditions, it is often appropriate to model calcite dissolution as being locally instantaneous (e.g., Nogues et al 2012b, 2013).

In addition to being highly soluble in acid and fast reacting, calcite is quite often abundant in sufficient quantity that its dissolution could substantially alter the volume of a flow path and alter its hydrodynamic properties. In the three caprock examples discussed above, calcite was present in all cases to various degrees. For other minerals that are fairly soluble and with fast dissolution kinetics, such as anorthite, even complete dissolution would not significantly change the permeability because these minerals are not present in sufficient quantities in typical sedimentary formations to cause a substantial porosity change.

The abundance of calcite is critical for permeability evolution of flow paths to be important, but the other necessary condition is a low concentration of calcium. A high calcium concentration in the brine would provide alkalinity that would effectively buffer the addition of acid, and may even favor calcite precipitation rather than dissolution. Formation waters, site to site, are extremely variable in calcium content.

In summary, we argue that geochemical modeling efforts developed for the purpose of predicting reaction-induced permeability evolution focus on the system of equations that describe aqueous phase chemistry of pH, carbonate ions and calcium as well as water-rock

interactions with calcite. This tremendously simplifies the range of complexity normally considered in geochemical reactive transport modeling.

CAPROCK CHARACTERISITICS

To support geochemical modeling to predict reaction-induced permeability evolution, mineralogical, lithological and brine chemistry data are needed for potential injection formations and the overlying caprocks. Reviews of caprock characteristics specific to caprock seal performance assessments are limited. Griffith et al (2011) reviewed available information on the physical and chemical characteristics of geological seal strata within a number of geographically important basins considered for CO_2 sequestration in the US. They found limited published core analyses and downhole geophysical data describing the subsurface mineral and physical properties of the seals, and as a result, much of their tabulated data were derived from published studies of outcrops. An important finding for the basins examined was that fractures and faults penetrate seal strata, and calcite is among the common minerals found in caprocks. Michael et al. (2010) reviewed the seals of active injection sites and demonstration sites, and identified various seal lithofacies for sixteen injection operations as of 2009.

The basin scale reviews all point to the need for site-specific assessments with core data and geophysical measurements tailored on a site-by-site basis. The spatial scope of these site-specific reviews, which the US EPA calls Area of Review, is still being debated and researchers generally recommend that site characterization criteria be allowed to evolve as experience is gained. Birkholzer and Zhou (2009) modeled the areal extent of the pressure pulse and suggest that the area characterized in a permitting process may comprise a very large region within the basin. Understanding the reactive potential of caprock minerals, under relevant temperatures, pressures, and salinities, should be part of site-specific assessments. Sedimentological assessments of caprocks are even more rare in terms of assessing geochemical reactivity. Transverse sedimentary features, however, can be the predominant control on the permeability evolution of fractures (Deng et al. 2013).

FLOW PATHS THROUGH CAPROCKS

Wellbores have been the primary flow paths considered in leakage risk assessments of caprocks (Birkholzer et al. 2011; Celia et al. 2011). The geochemistry of wellbores and the potential for geochemically-driven permeability evolution is reviewed by Carey (2013, this volume). We face even greater uncertainties when assessing the occurrence, potential for creation and reactivation, and hydrodynamic properties of all other types of flow paths through caprocks. Aydin (2000) categorizes the two most common types of structural heterogeneities that facilitate hydrocarbon migration and flow as dilatant fractures (joints, veins, and dikes) and shear fractures/faults. These flow paths are typically characterized using geophysical methods, analog outcrop studies, conceptual models, and core logs. Both natural and induced fractures have been widely documented in consolidated sedimentary formations (Curtis 2002; Long and Ewing 2004), including geothermal (Wood et al. 2001) and CO_2 storage sites (Iding and Ringrose 2010; Griffith et al. 2011).

The hydrodynamic properties needed to evaluate the leakage rate through caprock flowpaths are most practically characterized according to transmissivity (T) and permeability (k) as shown in Equation (1). Studies that assign hydrodynamic properties of these flowpaths are limited. Permeability of these structures may, on average, be a few orders of magnitude higher than those of the corresponding matrix rocks. Fractures are especially important flowpaths due to their prevalence (Bonnet et al. 2001), and potential impacts on flow and reactive transport (Singurindy and Berkowitz 2005).

Creation and reactivation of flow paths through caprocks is an especially important consideration given the large volumes of fluid that must be injected at each well. Induced seismicity (see citations of Chiaramonte et al. 2008) and formation overpressure (Birkholzer et al. 2011) produced by injecting large fluid volumes have been shown to create, activate and propagate fractures in consolidated sedimentary formations (Zoback and Zinke 2002). Geomechanical studies have demonstrated that during CO_2 injection caprocks are exposed to shear stresses (Chiaramonte et al. 2008), thermal stresses (Gor et al. 2013) and crystallization (Noiriel et al. 2010). Morris et al. (2011) simulated the effect of injection pressures from multi-million ton injection scenarios on fault reactivation. Although they were able to devise plausible injection scenarios where faults were reactivated and the seal was compromised, they report significant parameter sensitivity that suggests the need for further model development and detailed site-specific characterization.

In combination, the widespread occurrence of calcite and the network of flow paths point to a significant influence of calcite dissolution on flow path hydrodynamic properties. We must first consider the geochemical driving forces created by brine acidification.

RELEVANT BRINE ACIDIFICATION PROCESSES

The acidification of native brine will be the primary geochemical burden on caprocks and the greatest geochemical challenge to long-term caprock performance. A typical pH range for CO_2-acidified brine is 3 to 4.5 depending on alkalinity, which represents a substantial perturbation to typical formation brines that range from pH 6 to 8. Three factors of brine acidification, however, are especially important to predict caprock dissolution and must be considered in order to quantify the spatial distribution of the proton driving force: 1) the relative distribution and migration of fluid phases within the pore-space (e.g., supercritical, liquid and gaseous CO_2, and brine), 2) the source of the acid, which is primarily carbonic acid, but may also include oxidized sulfur species and organic acids, and 3) mass transfer rates into the brine.

The distribution of acidity within the native brine depends on mass transfer rates and the proximity to the source of acidity, in this case the pure phase CO_2. During injection and as the plume extends, the chemistry of the fluid that will be accessible to a flow path will change. Nordbotten et al. (2005b) modeled the advance of the plume front. However, detailed models of spatial and temporal variation of pH in an injection formation are lacking. Ellis et al. (2010) modeled pH profiles for three simplified acid mass transfer scenarios ranging from rapid brine phase dispersion to slow diffusive mass transfer, and found that it may take several hundred years for a large portion of the brine in an injection formation to be saturated with acid. However, such acid transport must be coupled with plume and brine transport models to provide reliable results.

When the CO_2 plume reaches the entry point for a caprock flow path, two-phase flow of brine and CO_2 is expected to occur. Nordbotten et al. (2005b) predicted upconing would prolong the time that mixed phase fluids would flow through the flow path. Phase changes and two-phase flow can have important implications for the quantity, continuity and duration of the source of acidity (e.g., Oldenburg et al. 2012; Gor et al. 2013; Suekane et al., 2005). Multiphase flow impacts on leakage through a fracture were modeled by Lu et al. (2012). Accounting for phase changes and the relative abundance of different phases is predicted to become especially complex over long flow paths (Oldenburg et al. 2012). Andreani et al. (2008) alternated the flow of CO_2-saturated brine and CO_2 gas through a fractured limestone and suggested that the pure phase CO_2 created locally acidic waters that were trapped in the diffusion controlled regime of the fracture boundary.

Previous authors have evaluated the implications of co-injecting SO_2 with CO_2 as this would potentially bring both environmental and economic benefits. The potential for increased acidification is substantial given the strong acidic nature of sulfurous and sulfuric acid (Knauss et al. 2005; Xu et al. 2007). The additional acidification contributed by SO_2 depends, however on solubility and mass transfer kinetics, which vary with temperature and pressure, as determined by Crandell et al. (2010). The extent to which SO_2 may be oxidized to sulfate is also an important factor (Ellis et al. 2010) as shown in Figure 5.

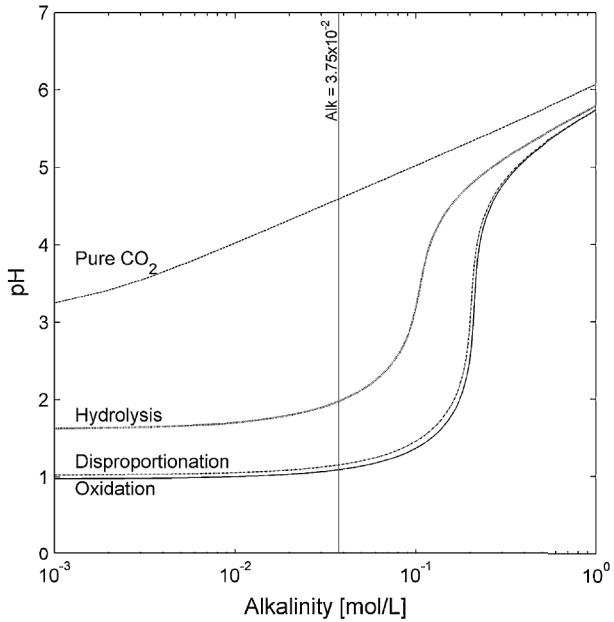

Figure 5. Brine acidification (pH) as a function of brine alkalinity for pure CO_2, CO_2 plus SO_2 with hydrolysis of SO_2, and CO_2 plus SO_2 with SO_2 disproportionation or oxidation [Used by permission of Elsevier Ltd, from Ellis et al. (2010), *Inter. J. Greenhouse Gas Control*, Vol. 4, Fig. 5, p. 575.].

PREDICTING THE EVOLUTION OF CAPROCK FLOW PATHS

Baseline assessments of caprock mineralogy, formation water composition, flow paths, and brine acidification help bound the conditions and geologic storage settings where flow path permeability evolution may occur. Reactive transport modeling, however, is the only practical method capable of exploring the vast parameter space that is beyond the reach of experimental observation. This is especially true for downhole conditions that are difficult to replicate in the laboratory, the complex combination of variables that determine permeability evolution, and the need to predict caprock leakage potential over long time periods.

Here we demonstrate the power of the simple modeling approach we advocate with a reactive transport model that accounts for pH, carbonate ions and calcium, and reactions with only calcite. We present a simulation of permeability evolution due to CO_2-acidified flow through a one-dimensional vertical flow path in a caprock. The system domain is a 100 m long by 0.2 m diameter cylindrical flow path containing a porous rock matrix with an initial porosity of 30% and initial permeability of 10^{-13} m^2. The porous rock matrix within the flow path contains calcite according to a specified initial volume fraction of calcite, over which a

sensitivity analysis is conducted. For simplicity, this simulation assumes a fixed cylindrical boundary beyond which there is no flow and mineral erosion does not occur. Permeability evolution manifests due to calcite dissolution within the system boundary. In reality, it is expected that the walls of the flow path would erode and the system domain would increase especially near the bottom where the acidity is the greatest. However, this is beyond the scope of this simple illustrative modeling exercise.

The water entering the system from the bottom has a typical brine composition, with calcium concentration assumed to be 0.3 mol/L, total carbon concentration 0.8 mol/L, and pH 3.3. This is a substantial perturbation from the initial brine chemistry in the model system, which is assumed to have calcium concentration of 0.3 mol/L, total carbon concentration 1.5×10^{-3} mol/L, and pH 6.9. The pH 3.3 boundary condition is a worst-case scenario in that it corresponds to a case in which the inflowing brine is equilibrated with supercritical CO_2 with no buffering. If the storage reservoir were to have substantial soluble carbonate minerals, then the brine flowing from it into the leakage pathway would already be buffered to some extent and the pH would be higher. One way in which this simulation condition is not the worst case is that the flowing fluid is single-phase brine. If there were two-phase flow of both brine and CO_2, this would be a worst-case scenario as there is little chance for depleting the acidity through buffering along the leakage flow path. The flow of CO_2 as a separate phase serves as a persistent source of acidity.

In this reactive transport simulation, the model accounts for Darcy flow in one dimension, performs geochemical aqueous phase speciation, and treats calcite to be at local equilibrium with the fluid. The pressure gradient is fixed at 10.5 kPa/m. The permeability evolution is related to porosity change through the cubic law (discussed below), and the permeability for the entire domain is the harmonic average of the permeabilities of the nodes in the grid.

Even with a simplified geochemical model, with only one reactive mineral phase, the resulting behavior is complex because of the interplay between mineral dissolution and the buffering that results from the increased alkalinity. Figure 6 shows the simulation results for the permeability evolution over a one hundred year time frame, for initial calcite volume fraction (CVF) values ranging from 5% to 50%. These values might represent the range of conditions in the Eau Claire caprock, for example. For a given curve, the domain permeability evolves slowly early on, as calcite dissolves only near the inlet. As a result the increased concentration of calcium ions near the inlet neutralizes the acid and reduces its effect up the column. Over time, the calcite is depleted near the inlet and the reaction front advances up the column. The permeability remains constrained by the original permeability at the top until the reaction front breaks through. At this point, the permeability has reached a maximum.

For a small amount of calcite mineral (e.g. CVF = 0.05), the acid neutralization effect is smaller than for a larger CVF, and the reaction front advances more quickly. However, it is also the case that for a system with a small amount of calcite mineral, the net potential for volume change is smaller so the reaction reaches a limit earlier than for a larger CVF. This behavior leads to the counter-intuitive result that after 100 years the system with the biggest increase in permeability is the system with the intermediate calcite volume fraction. That is, the worst-case scenario is the system for which the reaction is not so buffered and is advancing at a significant rate, and for which the ultimate permeability change is substantial. If the CVF is too large, the acid neutralization is so substantial that the reaction front advances insignificantly.

Note that these results are purely illustrative and are not intended to be representative for at any particular site. The resulting tripling of the permeability shown in Figure 6 may actually be underestimated, as this model does not allow for a moveable system boundary. In reality, reactive flow in a caprock flow path will dissolve not only the rock matrix inside the flow domain, but will also erode the walls of the flow path thus increasing the transmissivity, not just the permeability.

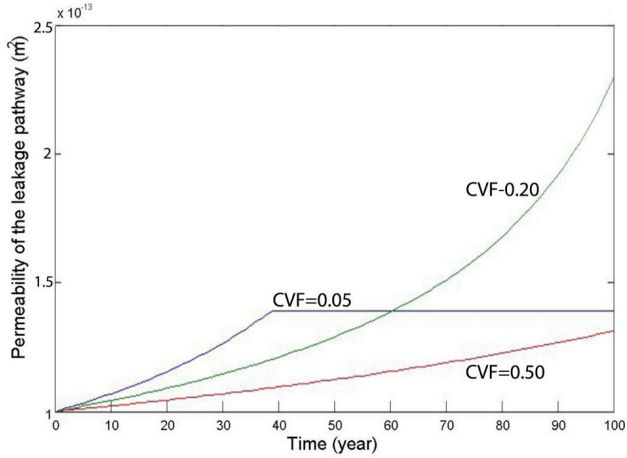

Figure 6. Simulated permeability evolution of a 100 m long flow path through a caprock as a function of time, for three different initial calcite volume fraction (CVF) values.

The ultimate goal is to develop generalizable approaches to modeling flow path alterations with appropriate and justifiable simplifying assumptions. Such models will be computationally tractable and can be plugged into field-scale and basin-scale models that estimate CO_2 containment reliability and leakage risk. However, recent experimental and modeling activities at Princeton and elsewhere have revealed additional levels of complexity that are not currently accounted for in any model. In the next section, we describe the complex permeability evolution processes that derive from heterogeneities and variations in mineral spatial patterns, flow path geometry, and fluid composition and flow rate.

GEOCHEMICALLY-DRIVEN EVOLUTION OF FLOW PATHS

In this section we summarize experimental and simulation studies suggesting that when acidified brines dissolve calcite within caprock flow paths a complex set of factors and processes will determine not only the magnitude and rate of permeability evolution, but also whether the permeability will increase or decrease. Importantly, existing reactive transport models being used to predict flow path permeability evolution do not account for these factors and processes.

Three dimensional (3D) imaging with micro X-ray computed tomography (xCT) (Gouze et al. 2003; Karpyn et al. 2007; Werth et al. 2010; Wildenschild et al. 2013) provides non-invasive geometric measurement tools, and their application has enabled observations of acid-driven geometric evolution of fractures (Nicholl et al. 1999; Detwiler et al. 2003; Gouze et al. 2003; Noiriel et al. 2007; Detwiler et al. 2008). Ellis et al. (2011) flowed CO_2–acidified brine through an artificially fractured carbonate core from the Amherstburg formation of the Michigan sedimentary basin. The experimental conditions were selected to approach storage formation conditions including 14 MPa confining pressure, 10 MPa hydrostatic pressure and 27 °C core temperature. X-ray CT analysis provided a means of quantifying the volumetric changes of the fracture caused by mineral dissolution, and a spatial map of the fracture volume, as shown in Figure 7. Along the 6.5 cm length of the core, the fracture void volume prior to flow of CO_2-acidified brine was ~0.6 mL, the median aperture was 270 μm, and the average cross-sectional area was 0.09 cm^2. After seven days of reaction, the fracture had a void volume of ~1.6 mL, the median aperture was 860 μm, and average cross-sectional area of 0.24 cm^2.

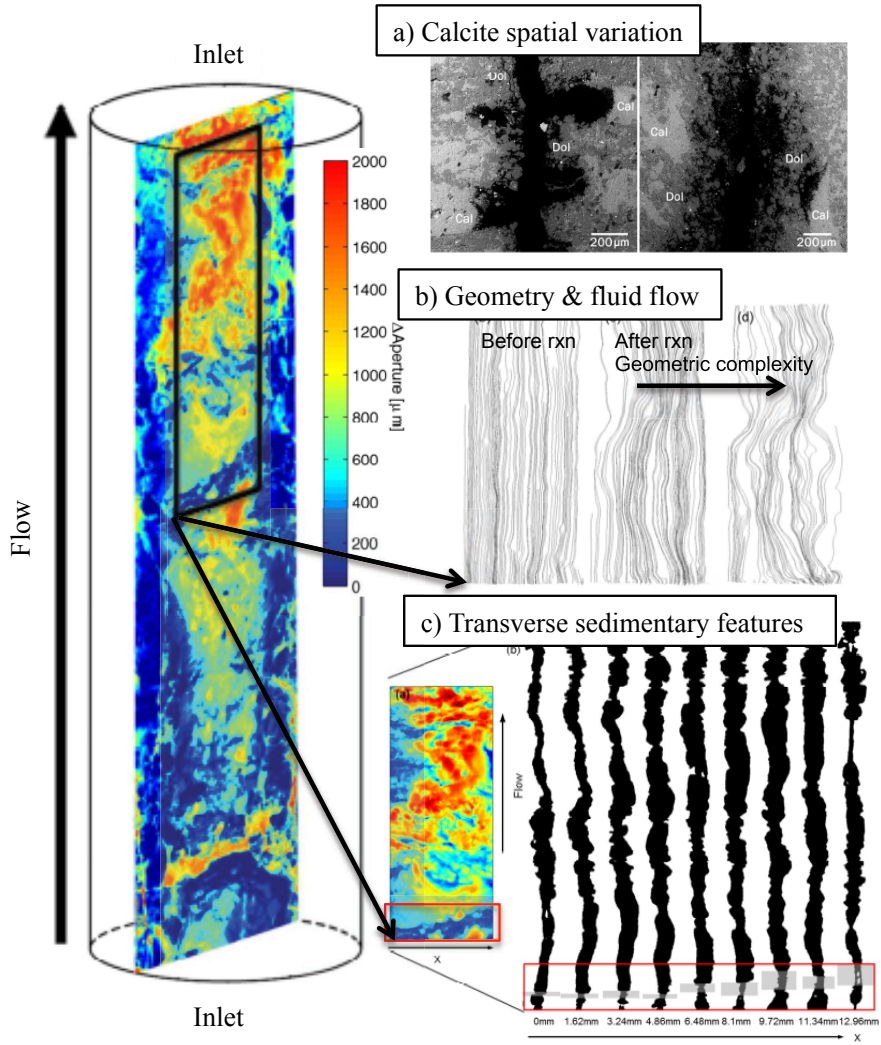

Figure 7. Delta aperture map showing the increase in aperture resulting from calcite dissolution along a fractured core from the Amherstburg formation: (a) Scanning electron microscopy images of two thin sections from the reacted core showing the two most common patterns of calcite dissolution observed in the reacted fracture, (b) streamlines of the velocity fields of fluid flow calculated from CFD simulations comparing the unreacted fracture with the post-reacted geometry with and without considering 'degraded zones' as part of the rock, and (c) vertical cross-sections of the reacted fracture highlighting the transverse sedimentary feature stricture in gray at the bottom. [Adapted from Deng et al. 2013].

This represents an increase in flow area of ~2.7 times. This observation of extensive dissolution confirmed what was expected given the known high calcite content of the rock. This was important to demonstrate the vulnerability of carbonate caprocks that, if fractured, can erode quickly and may jeopardize sealing integrity when hydrodynamic conditions promote flow of CO_2-acidified brine.

Additional important findings were revealed by post-experiment scanning electron microscopy (SEM). Complex geometric alterations of the fracture were created by preferential

dissolution patterns, as shown in Figure 7. For example, where the relatively fast reacting calcite is banded with slower reacting dolomite, preferential dissolution of calcite created 'comb-tooth' shaped roughness (Fig. 7a). In contrast, where calcite is homogeneously mixed with dolomite or non-reactive clay minerals and quartz, very porous calcite-depleted areas were formed, which we refer to as "degraded zones" (Fig. 7a). This suggested that increases in fracture permeability due to mineral dissolution may be offset by unaltered constrictions along the flow path and increases in surface roughness. Thus, the evolution of fracture permeability will depend in complex ways on the carbonate content as well as the heterogeneity of the minerals and their spatial patterning.

To examine the effects of evolving surface roughness on fracture hydrodynamics, we used computational fluid dynamics (CFD) to simulate flow in this experimental fractured core, before and after reaction, and to compare these simulations results with predictions from simpler models. The relationship between fracture roughness and fluid flow has been represented with models of different levels of complexity. One-dimensional models based on the distribution of local apertures account for roughness by using a weighted average or standard deviation of apertures (Tsang and Witherspoon 1981; Renshaw 1995; Zimmerman and Bodvarsson 1996). The Local Cubic Law (LCL) assumes that the cubic law for smooth parallel wall fractures holds locally, and solves Reynolds' equation locally (Cvetkovic et al. 1999; O'Brien et al. 2003; Yasuhara and Elsworth 2006; Ghassemi and Kumar 2007; Chaudhuri et al. 2008). These models have been shown to under-estimate the impact of roughness on fracture flow at relatively high, yet realistic roughness (Nicholl et al. 1999; Petchsingto and Karpyn 2009; Crandall et al. 2010). CFD simulations have been shown to provide accurate calculations for flow in fractures across a range of relevant values for fracture roughness (Petchsingto and Karpyn 2009; Crandall et al. 2010; Javadi et al. 2010). While CFD simulations have shown that increased roughness generally results in more tortuous flow and lower transmissivity, Deng et al. (2013) was the first to observe this relationship by coupling SEM and xCT images showing the spatial distribution of minerals and resulting dissolution patterns in CFD simulations of the core-flooding experiments. The impact of increasing roughness on tortuosity can be seen in Figure 7b, where the inclusion of "degraded zones" in the CFD simulations clearly increases the tortuosity of the streamlines. Therefore, while calcite dissolution greatly increased the fracture volume, the geometric alterations increased roughness, which in turn reduced the impact of fracture volume increase on transmissivity. Noiriel et al. (2007) similarly observed a decrease in permeability that they attributed partly to the increase of fracture roughness even though flowing acidified brine had dissolved calcite in a fractured argillaceous limestone rock.

While the banding of soluble and insoluble minerals is a common type of sedimentary feature that can result in increased fracture roughness, a lens of relatively insoluble minerals can also create a contiguous transverse stricture that controls fracture transmissivity no matter how much calcite dissolution is occurring throughout the fracture. Figure 7c shows the cross-sections of the fracture along the flow direction where such a transverse sedimentary layer of insoluble clay and silicates has maintained a mechanical aperture roughly equivalent to the fracture in the unreacted core. Deng et al. (2013) point out that sharp changes in fracture geometry such as fracture closure may occur if the geomechanical strength of the non-reactive bands is compromised.

Evidence that dissolution can initiate mobilization and physical rearrangement of less soluble minerals has been observed in core-flooding experiments with acidified brines (Noiriel et al. 2007; Andreani et al. 2008; Ellis et al. 2013; Smith et al. 2013). Andreani et al. (2008) and Noiriel et al. 2007 were the first to observe dissolution of calcite that created a clay matrix with 40-50% increased porosity at the fracture boundary. The breakup, rearrangement and mobilization of this porous clay matrix resulted in complex and contradictory changes to permeability – flushing of the clay matrix increased permeability while fracture closure and

clogging reduced permeability. Similarly, Ellis et al. (2013) presented imaging evidence for calcite dissolution that led to the release of less soluble feldspar and dolomite particles. These particles went on to occlude regions of the fracture, demonstrating that extensive dissolution may sometimes lead to a reduction in fracture permeability.

The final complexity that we consider is the development of preferential flow paths due to acid-driven mineral dissolution. There is a growing body of imaging studies investigating the development of preferential flow paths, ranging from studies of reactive flow through idealized fractures (Szymczak and Ladd 2012) to core-flooding experiments with rock cores (Noiriel et al. 2007). The studies with idealized parallel plate geometry and homogeneous mineralogy have observed a transition from uniform dissolution to channelization with increasing Damkohler number and decreasing Peclet number (Detwiler et al. 2003; Detwiler 2008). Furthermore, Szymczak and Ladd (2009) found that channelization occurs above a roughness threshold and is favored under the conditions of high reaction rates and intermediate Peclet number. Detwiler and Rajaram (2007) were able to predict channelization along an idealized single fracture surface using a depth-averaged model of fracture flow and reactive transport that explicitly calculates local dissolution-induced alterations of fracture apertures. Mineral spatial heterogeneity and variation present serious challenges to the application of these relationships beyond homogeneous mineralogy, especially in any realistic field setting.

Given the complexities observed in experimental observations, how does one mathematically relate permeability evolution to the porosity change that results from mineral reactions? A power law relationship has been most widely applied to relate changes in permeability to changes in porosity:

$$k = k_o \left(\frac{\phi}{\phi_o} \right)^{\alpha} \tag{2}$$

where k_o and ϕ_o represent initial permeability and porosity, respectively, and α is the power law parameter. While many experimental observations and theoretical studies suggest a cubic relationship is appropriate, a number of recent studies of CO_2-acidified brine driven permeability evolution have observed a much larger range of values for the power law parameter. Nogues et al. (2013) simulated permeability evolution in a pore network that contained heterogeneous distribution and abundance of calcite (ref. Fig. 8), and found that appropriate α values ranged from 4 to 10. Although Carroll et al. (2013) fit the power law to experimental observations of permeability evolution driven by CO_2-acidified brine flow through limestone cores, they observed a similarly strong dependence of the power law parameter on initial pore connectivity and mineralogy. They found the highest α values for the samples with greatest anisotropy of pore space, connectivity and mineral heterogeneity.

The greatest challenge to predicting permeability evolution in flow paths will be to account for this diverse set of factors unique to the unprecedented geochemical burdens while developing computationally efficient continuum, hybrid continuum-numerical and fully numerical models.

CONCLUDING REMARKS

Caprock formations are known to be reliable in containing buoyant fluids, including natural hydrocarbon and CO_2 reservoirs (e.g., Bravo Dome, Sheep Mountain, McElmo Dome), stored natural gas, as well as injected CO_2 in numerous demonstration projects. Caprocks perform well because they are compacted matrices of fine particles, have undergone diagenic cementation, or are solid evaporite precipitates. However, the large volumes of CO_2 that will need to be injected and stored to meaningfully mitigate climate change will exert unprecedented

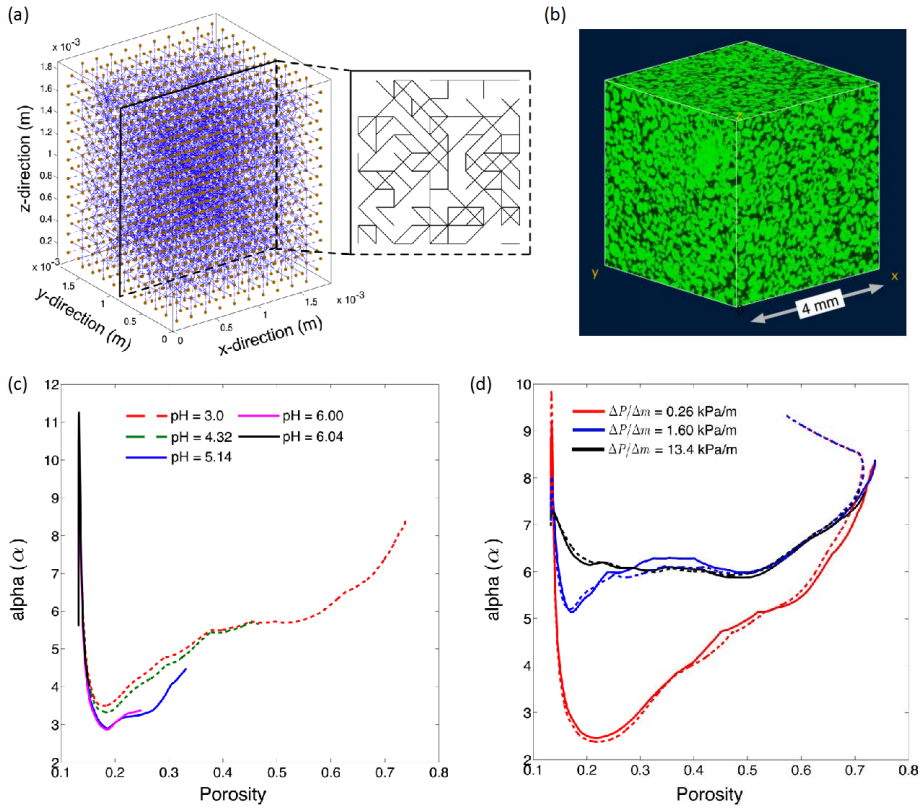

Figure 8. (a) Ball and stick representation of the pore network with a cross-sectional slice of the pore-to-pore connectivity derived from (b) dolomitized oolithic grainstone from Biswal et al. (2009), and used to model permeability changes due to calcite dissolution and derive values of power law parameter α as a function of network porosities, for (c) different inflowing chemistries and (d) different pressure gradient conditions, where solid lines correspond to an inflowing pH=3 and dashed lines for an inflowing pH=5. [Adapted from Nogues et al. 2013].

burdens on caprocks and their potential flow paths. Stringent caprock performance standards will likely be required to overcome economic and commercial barriers to GCS implementation and to facilitate regulatory compliance and public acceptance.

Allowable leakage rates of 1% are generally believed to be an acceptable target for GCS projects. Evidence to date indicates that leakage risks will be manageably low at properly sited storage reservoirs. However, there are challenges in predicting leakage rates for individual geologic strata. One such challenge comes from the plausibility of geochemical alterations of caprock flow paths given the acidity of CO_2-saturated brines and the reactivity of calcite present in most caprocks. Dissolution of caprock minerals in flow paths can conceivably increase the permeability and transmissivity and promote CO_2 and brine leakage. That is, if a flow path exists or is created during the injection process, flow of acidified brine through this flow path can adversely alter its hydrodynamic properties and promote leakage.

The single most important reactive mineral in the context of permeability evolution of flow paths is calcite because it has the necessary criteria of being soluble and fast-reacting, and it is ubiquitous in tight sedimentary rocks and in some formations is sufficiently abundant that

dissolution would lead to important porosity changes. Therefore, we recommend that caprock calcite content be viewed as a critical siting assessment metric. Furthermore, because calcite dissolution is promoted not only by low pH (high carbonic acid concentration) but also by low concentration of dissolved calcium, the calcium concentration of formation brines is also a critical siting assessment metric.

Prediction of permeability evolution of a caprock flow path resulting from acid perturbation requires a reactive transport model that couples Darcy or fracture flow with geochemical speciation and reaction. Normally such a model would be computationally complex and not amenable to practical analytical leakage risk assessments. However, given the rationale for focusing on calcite as the most important mineral, we argue that simplified reactive transport models can be developed that limit the geochemical equations to those relating to pH, calcium, and the carbonate system. Furthermore, there are good arguments for using local equilibrium assumptions for calcite dissolution, rather than including the complexity of kinetic limitations. Such a model would vastly simplify the range of complexity ordinarily considered in geochemical reactive transport modeling, and would be computationally tractable for application in large-scale leakage risk models.

In this chapter, we presented a simple example of such a model simulation for one-dimensional reactive transport through a reactive flow path in a calcite-bearing caprock. We showed that it is conceivable that permeability could triple over the course of a century if the conditions are favorable to drive calcite dissolution. Even with plausible simplifying assumptions, the chemistry is sufficiently complex that the simulation results reveal a non-monotonic relationship between permeability change and calcite content.

Recent experimental and modeling activities at Princeton and elsewhere have revealed additional levels of complexity that are not currently accounted for in any reactive transport model. As an example, reactive evolution of fracture surfaces in rocks with mixtures of calcite and dolomite produces roughness and calcite-depleted porous zones. This makes it difficult to predict permeability evolution using conventional fracture flow models such as the Local Cubic Law model. Furthermore, vertical transport is orthogonal to sedimentary bedding layers so contiguous transverse features may remain undissolved and constrict flow even when there is extensive calcite dissolution. Another complexity that has been observed is the case of reduced fracture permeability resulting from calcite dissolution, explained by the mobilization of clay particles that clog the flow path downstream. Finally, pore-network reactive transport modeling revealed a broad range of possibilities for the power law that relates changes in permeability to changes in porosity, which often is assumed to be a cubic law. Clearly, the process of reaction-induced permeability evolution in caprock flow paths is fraught with complexities that make it difficult to develop computationally tractable models of permeability evolution.

The following list highlights the experimental and modeling research priorities to reduce prediction uncertainties.

- Develop simple permeability evolution models based on calcite as the only reactive mineral, and conduct laboratory core-scale flow experiments and field tests to determine the extent to which such simplified geochemical reactive transport models are effective in predicting permeability change.
- Advance X-ray and electron microscopy and image processing methods to enable i) more accurate and precise quantification of pore space, pore-to-pore connectivity, and mineral spatial heterogeneity and variation; ii) real-time imaging of interfacial processes at flow path boundaries during acidified brine and multi-phase flow at caprock *P*/*T* conditions.
- Conduct more controlled experiments to explore the complex processes that accompany acid-driven mineral dissolution and contribute to flow path permeability

evolution, including: i) the effects of mineral spatial heterogeneity and variation on the complex evolution of flow path geometry and surface roughness, ii) the importance of strictures resulting from relatively insoluble transverse sedimentary features, iii) the mobilization and physical rearrangement of less soluble minerals, iv) the initiation and development of preferential flow paths.

- Develop the means of representing these phenomena in reactive transport models that predict permeability evolution.

ACKNOWLEDGMENT

We would like to acknowledge Hang Deng's substantial contribution to the literature review for "Geochemically-Driven Evolution of Flow Paths" section, and Bin Guo's contribution of the modeling and Figure 6. We would also like to thank T. Tokunaga and I. Bourg for their thoughtful reviews, and J. Rosso for editorial support. This material is based upon work supported by the Department of Energy under Award Number DE-FE0000749. In addition, research is presented that was funded through grants from the National Science Foundation, CMMI-0919140 and CBET-1134397. Finally, the authors acknowledge support from the Siebel Energy Grand Challenges Fund administered through the Princeton Environmental Institute.

DISCLAIMER

This report was prepared as an account of work sponsored by an agency of the United States Government. Neither the United States Government nor any agency thereof, nor any of their employees, makes any warranty, express or implied, or assumes any legal liability or responsibility for the accuracy, completeness or usefulness of any information, apparatus, product, or process disclosed, or represents that its use would not infringe privately owned rights. Reference herein to any specific commercial product, process, or service by trade name, trademark, manufacturer, or otherwise does not necessarily constitute or imply its endorsement, recommendation, or favoring by the United States Government or any agency thereof. The views and options of authors expressed herein do not necessarily state or reflect those of the United States Government or any agency thereof.

REFERENCES

Andreani M, Gouze P, Luquot L, Jouanna P (2008) Changes in seal capacity of fractured claystone caprocks induced by dissolved and gaseous CO_2 seepage. Geophys Res Lett 35:L14404, doi: 10.1029/2008GL034467

Aydin A (2000) Fractures, faults, and hydrocarbon entrapment, migration and flow. Mar Pet Geol 17(7):797-814

Bachu S (2008) CO_2 storage in geological media: Role, means, status and barriers to deployment. Prog Energy Combustion Sci 34(2):254-273

Battelle (2011) Michigan Basin Phase II Geologic CO_2 Sequestration Field Test. Battelle, Columbus, OH

Benson SM, Cole DR (2008) CO_2 sequestration in deep sedimentary formations. Elements 4(5):325-331

Bickle M, Chadwick A, Huppert HE, Hallworth M, Lyle S (2007) Modeling carbon dioxide accumulation at Sleipner: Implications for underground carbon storage. Earth Planet Sci Lett 255(1-2):164-176

Bielicki JM, Pollak MF, Wilson EJ, Fitts JP, Peters CA (2013) A methodology for monetizing basin-scale leakage risk and stakeholder impacts. Energy Procedia 37:4665-4672

Birkholzer JT, Nicot JP, Oldenburg CM, Zhou Q, Kraemer S, Bandilla K (2011) Brine flow up a well caused by pressure perturbation from geologic carbon sequestration: Static and dynamic evaluations. Int J Greenhouse Gas Control (4):850-861

Birkholzer JT, Zhou Q (2009) Basin-scale hydrogeologic impacts of CO_2 storage: Capacity and regulatory implications. Int J Greenhouse Gas Control 3(6):745-756

Biswal B, Held RJ, Khanna V, Wang J, Hilfer R (2009) Towards precise prediction of transport properties from synthetic computer tomography of reconstructed porous media. Phys Rev E 80(4):041301

Bonnet E, Bour O, Odling NE, Davy P, Main I, Cowie P, Berkowitz B (2001) Scaling of fracture systems in geological media. Rev Geophys 39(3):347-383

Carey JW (2013) Geochemistry of wellbore integrity in CO_2 sequestration: Portland cement-steel-brine-CO_2 interactions. Rev Mineral Geochem 77:505-539

Carroll S, Hao Y, Smith M, Sholokhova Y (2013) Development of scaling parameters to describe CO_2–rock interactions within Weyburn-Midale carbonate flow units. Int J Greenhouse Gas Control 16S:S185-S193

Celia MA, Nordbotten JM, Court B, Dobossy M, Bachu S (2011) Field-scale application of a semi-analytical model for estimation cif CO_2 and brine leakage along old wells. Int J Greenhouse Gas Control 5(2):257-269

Chaudhuri A, Rajaram H, Viswanathan H (2008) Alteration of fractures by precipitation and dissolution in gradient reaction environments: Computational results and stochastic analysis. Water Resourc Res 44(W10410):1-19

Chiaramonte L, Zoback MD, Friedmann J, Stamp V (2008) Seal integrity and feasibility of CO_2 sequestration in the Teapot Dome EOR pilot: geomechanical site characterization. Environ Geol 54(8):667-1675

Cihan A, Birkholzer JT, Zhou Q (2013) Pressure buildup and brine migration during CO_2 storage in multilayered aquifers. Ground Water 51(2):252-267

Crandall D, Bromhal G, Karpyn ZT (2010) Numerical simulations examining the relationship between wall-roughness and fluid flow in rock fractures. Int J Rock Mech Min Sci 47(5):784-796

Crandell LE, Ellis BR, Peters CA (2010) Dissolution potential of SO_2 co-injected with CO_2 in geologic sequestration. Environ Sci Technol 44(1):349-355

Curtis JB (2002) Fractured shale-gas systems. AAPG Bulletin 86(11):1921-1938

Cvetkovic V, Selroos JO, Cheng H (1999) Transport of reactive tracers in rock fractures. J Fluid Mech 378:335-356

Deng H, Ellis BR, Peters CA, Fitts JP, Crandall D, Bromhal GS (2013) Modifications of carbonate fracture hydrodynamic properties by CO_2-acidified brine flow. Energy Fuels 27(8):4221-4231; DOI: 10.1021/ef302041s

Detwiler RL (2008) Experimental observations of deformation caused by mineral dissolution in variable-aperture fractures. J Geophys Res Solid Earth 113:B08202, doi: 10.1029/2008JB005697

Detwiler RL, Rajaram H (2007) Predicting dissolution patterns in variable aperture fractures: Evaluation of an enhanced depth-averaged computational model. Water Resourc Res 43:W04403, doi: 10.1029/2006WR005147

Detwiler RL, Glass RJ, Bourcier WL (2003) Experimental observations of fracture dissolution: The role of Peclet number on evolving aperture variability. Geophys Res Lett 30(12):1648-1651

Elliot TR, Celia MA (2012) Potential restrictions for CO_2 sequestration sites due to shale and tight gas production. Environ Sci Technol 46(7):4223-4227

Ellis BR, Crandell LE, Peters CA (2010) Limitations for brine acidification due to SO_2 co-injection in geologic carbon sequestration. Int J Greenhouse Gas Control 4(3):575-582

Ellis BR, Fitts JP, Bromhal GS, McIntyre DL, Tappero R, Peters CA (2013) Dissolution-driven permeability reduction of a CO_2 leakage pathway in a carbonate caprock. Environ Eng Sci 30(4):87-193

Ellis BR, Peters CA, Fitts JP, Bromhal GS, McIntyre DL, Warzinski RP, Rosenbaum EJ (2011) Deterioration of a fractured carbonate caprock exposed to CO_2-acidified brine flow. Greenhouse Gases Sci Technol 1(3):248-260

Emberley S, Hutcheon I, Shevalier M, Durocher K, Gunter WD, Perkins EH (2004) Geochemical monitoring of fluid-rock interaction and CO_2 storage at the Weyburn CO_2-injection enhanced oil recovery site, Saskatchewan, Canada. Energy 29(9-10):1393-1401

Gaus I, Azaroual M, Czernichowski-Lauriol I (2005) Reactive transport modelling of the impact of CO_2 injection on the clayey cap rock at Sleipner (North Sea). Chem Geol 217(3-4):319-337

Ghassemi A, Kumar GS (2007) Changes in fracture aperture and fluid pressure due to thermal stress and silica dissolution/precipitation induced by heat extraction from subsurface rocks. Geothermics 36(2):115-140

Gherardi F, Xu TF, Pruess K (2007) Numerical modeling of self-limiting and self-enhancing caprock alteration induced by CO_2 storage in a depleted gas reservoir. Chem Geol 244(1-2)103-129

Gor GY, Elliot TR, Prevost JH (2013) Effects of thermal stresses on caprock integrity during CO_2 storage. Int J Greenhouse Gas Control 12:300-309

Gouze P, Noiriel C, Bruderer C, Loggia D, Leprovost R (2003) X-ray tomography characterization of fracture surfaces during dissolution. Geophys Res Lett 30(5):1267

Griffith CA, Dzombak DA, Lowry GV (2011) Physical and chemical characteristics of potential seal strata in regions considered for demonstrating geological saline CO_2 sequestration. Environ Earth Sci 64(4):925-948

Gupta N, Ball D, Sminchak J, Gerst J, Kelley M, Place M, Bradbury J, Cumming L (2011) Geologic storage field tests in multiple basins in Midwestern USA–Lessons learned and implications for commercial deployment. Energy Procedia 4:5565-5572

Harrington JF, Noy DJ, Horseman ST, Birchall DJ, Chadwick RA (2009) Laboratory study of gas and water flow in the Nordland Shale, Sleipner, North Sea. *In:* Carbon Dioxide Sequestration in Geological Media. State of the Science. Grobe M, Pashin JC, Dodge RL (eds) AAPG Studies in Geology, p 521-543

Heath JE, Dewers TA, McPherson BJOL, Nemer MB, Kotula PG (2012) Pore-lining phases and capillary breakthrough pressure of mudstone caprocks: Sealing efficiency of geologic CO_2 storage sites. Int J Greenhouse Gas Control 11:04-220

Hepple RP, Benson SM (2005) Geologic storage of carbon dioxide as a climate change mitigation strategy: performance requirements and the implications of surface seepage. Environ Geol 47(4):576-585

Iding M, Ringrose P (2010) Evaluating the impact of fractures on the performance of the In Salah CO_2 storage site. Int J Greenhouse Gas Control 4(2):242-248

Javad, M, Sharifzadeh M, Shahriar K (2010) A new geometrical model for non-linear fluid flow through rough fractures. J Hydrol 389(1-2):18-30

Karpyn ZT, Grader AS, Halleck PM (2007) Visualization of fluid occupancy in a rough fracture using micro-tomography. J Colloid Interface Sci 307(1):181-187

Knauss KG, Johnson JW, Steefel CI (2005) Evaluation of the impact of CO_2, co-contaminant gas, aqueous fluid and reservoir rock interactions on the geologic sequestration of CO_2. Chem Geol 217(3-4):339-350

Little MG, Jackson RB (2010) Potential impacts of leakage from deep CO_2 geosequestration on overlying freshwater aquifers. Environ Sci Technol 44(23):9225-9232

Liu F, Lu P, Griffith C, Hedges SW, Soong Y, Hellevang H, Zhu C (2012) CO_2-brine-caprock interaction: Reactivity experiments on Eau Claire shale and a review of relevant literature. Int J Greenhouse Gas Control 7:153-167

Long JCS, Ewing RC (2004) Yucca Mountain: Earth-science issues at a geologic repository for high-level nuclear waste. Annu Rev Earth Planet Sci 32:363-401

Lu C, Sun Y, Buscheck TA, Hao Y, White JA, Chiaramonte L (2012) Uncertainty quantification of CO_2 leakage through a fault with multiphase and nonisothermal effects. Greenhouse Gases Sci Technol 2(6):445-459

Manga M, Beresnev I, Brodsky EE, Elkhoury JE, Elsworth D, Ingebritsen SE, Mays DC, Wang C-Y (2012) Changes in permeability caused by transient stresses: field observations, experiments, and mechanisms Rev Geophys 50:RB2004, doi: 10.1029/2011RG000382

Michael K, Golab A, Shulakova V, Ennis-King J, Allinson G, Sharma S, Aiken T (2010) Geological storage of CO_2 in saline aquifers-A review of the experience from existing storage operations. Int J Greenhouse Gas Control 4(4):659-667

Morris JP, Detwiler RL, Friedmann SJ, Vorobiev OY, Hao Y (2011) The large-scale geomechanical and hydrogeological effects of multiple CO_2 injection sites on formation stability. Int J Greenhouse Gas Control 5(1):69-74

Neufelder RJ, Bowen BB, Lahann RW, Rupp JA (2012) Lithologic, mineralogical, and petrophysical characteristics of the Eau Claire Formation: Complexities of a carbon storage system seal. Environ Geosci 19:81-104

Nicholl MJ, Rajaram H, Glass RJ, Detwiler R (1999) Saturated flow in a single fracture: Evaluation of the Reynolds equation in measured aperture fields. Water Resourc Res 35(11):3361-3373

Nogues JP, Celia MA, Peters CA (2012b) Pore network model development to study dissolution and precipitation of carbonate rocks. *In:* Proceedings of the XIX International Conference on Water Resources, University of Illinois, *http://cmwr2012.cee.illinois.edu/SubsurfaceBiogeochemReactiveTrans(Proceedings).html*

Nogues JP, Court B, Dobossy M, Nordbotten JM, Celia MA (2012a) A methodology to estimate maximum probable leakage along old wells in a geological sequestration operation. Int J Greenhouse Gas Control 7:39-47

Nogues JP, Fitts JP, Celia MA, Peters CA (2013) Permeability evolution due to dissolution and precipitation of carbonates using reactive transport modeling in pore networks. Water Resourc Res, doi: 10.1002/wrcr.20486

Noiriel C, Made B, Gouze P (2007) Impact of coating development on the hydraulic and transport properties in argillaceous limestone fracture. Water Resourc Res 43(9):W09406, doi: 10.1029/2006WR005379

Noiriel C, Renard F, Doan M-L, Gratier J-P (2010) Intense fracturing and fracture sealing induced by mineral growth in porous rocks. Chem Geol 269(3-4):197-209

Nordbotten JM, Celia MA, Bachu S, Dahle HK (2005a) Semianalytical solution for CO_2 leakage through an abandoned well. Environ Sci Technol 39(2):602-611

Nordbotten JM, Celia MA, Bachu S (2005b) Injection and storage of CO_2 in deep saline aquifers: Analytical solution for CO_2 plume evolution during injection. Transport Porous Media 58(3):339-360

O'Brien GS, Bean CJ, McDermott F (2003) Numerical investigations of passive and reactive flow through generic single fractures with heterogeneous permeability. Earth Planet Sci Lett 213(3-4):271-284

Oldenburg CM, Doughty C, Peters CA, Dobson PF (2012) Simulations of long-column flow experiments related to geologic carbon sequestration: effects of outer wall boundary condition on upward flow and formation of liquid CO_2. Greenhouse Gases Sci Technol 2(4):279-303

Palandri JL, Kharaka YK (2004) A Compilation of Rate Parameters of Water-Mineral Interaction Kinetics for Application to Geochemical Modeling. U.S. Geological Survey Open File Report (OF 2004-1068). U.S. Geological Survey, Menlo Park, CA

Petchsingto T, Karpyn ZT (2009) Deterministic modeling of fluid flow through a CT-scanned fracture using computational fluid dynamics. Energy Sources Part A 31(11):897-905

Pollak MF, Bielicki JM, Dammel JA, Wilson EJ, Fitts JP, Peters CA (2013) The leakage impact valuation (LIV) method for leakage from geologic CO_2 storage reservoirs. Energy Procedia 37:2819-2827

Renshaw CE (1995) On the relationship between mechanical and hydraulic apertures in rough-walled fractures. J Geophys Res Solid Earth 100(B12):24629-24636

Rubin ES, Chen C, Rao AB (2007) Cost and performance of fossil fuel power plants with CO_2 capture and storage. Energy Policy 35(9):4444-4454

Shukla R, Ranjith P, Haque A, Choi X (2010) A review of studies on CO_2 sequestration and caprock integrity. Fuel 89(10):2651-2664

Singurindy O, Berkowitz B (2005) The role of fractures on coupled dissolution and precipitation patterns in carbonate rocks. Adv Water Resourc 28(5):507-521

Smith MM, Sholokhova Y, Hao Y, Carroll SA (2013) Evaporite caprock integrity: an experimental study of reactive mineralogy and pore-scale heterogeneity during brine-co_2 exposure. Environ Sci Technol 47(1):262-268

Sonnenthal EL, Spycher NF, Conrad M, Apps J (2004) A Conceptual and numerical model for thermal-hydrological-chemical processes in the yucca mountain drift scale test. *In:* Coupled Thermo-Hydro-Mechanical-Chemical Processes in Geo-Systems, Fundamentals, Modelling, Experiments and Applications. Elsevier Geo-Engineering Book Series, Volume 2. Stephansson O, Hundson JA, Jing L (eds) Elsevier, p 347-352

Suekane T, Soukawa S, Iwatani S, Tsushima S, Hirai S (2005) Behavior of supercritical CO_2 injected into porous media containing water. Energy 30(11-12):2370-2382

Szymczak P, Ladd AJC (2009) Wormhole formation in dissolving fractures. J Geophys Res Solid Earth 114 B06203, doi: 10.1029/2008JB006122

Szymczak P, Ladd AJC (2012) Reactive-infiltration instabilities in rocks. Fracture dissolution. J Fluid Mech 702:239-264

Tsang YW, Witherspoon PA (1981) Hydromechanical behavior of a deformable rock fracture subject to normal stress. J Geophys Res 86(NB10):9287-9298

USEPA (2012) Criteria and Standards Applicable to Class VI Wells. 40 CFR 146.81. Retrieved June 01, 2013 from www.ecfr.gov.

Werth CJ, Zhang CY, Brusseau ML, Oostrom M, Baumann T (2010) A review of non-invasive imaging methods and applications in contaminant hydrogeology research. J Contaminant Hydrol 113(1-4):1-24

Wildenschild D, Sheppard AP (2013) X-ray imaging and analysis techniques for quantifying pore-scale structure and processes in subsurface porous medium systems. Adv Water Resourc 51:217-246

Wood CP, Brathwaite RL, Rosenberg MD (2001) Basement structure, lithology and permeability at Kawerau and Ohaaki geothermal fields, New Zealand. Geothermics 30(4):461-481

Xu T, Apps JA, Pruess K, Yamamoto H (2007) Numerical modeling of injection and mineral trapping of CO_2 with H_2S and SO_2 in a sandstone formation. Chem Geol 242(3-4):319-346

Xu TF, Apps JA, Pruess K (2004) Numerical simulation of CO_2 disposal by mineral trapping in deep aquifers. Appl Geochem 19(6):917-936

Yasuhara H, Elsworth D (2006) A numerical model simulating reactive transport and evolution of fracture permeability. Int J Numer Anal Methods Geomech 30(10):039-1062

Zimmerman RW, Bodvarsson GS (1996) Hydraulic conductivity of rock fractures. Transport Porous Media 23(1):1-30

Zoback MD, Zinke JC (2002) Production-induced normal faulting in the Valhall and Ekofisk oil fields. Pure Appl Geophys 159(1-3):403-420

Reviews in Mineralogy & Geochemistry
Vol. 77 pp. 481-503, 2013
Copyright © Mineralogical Society of America

Capillary Pressure and Mineral Wettability Influences on Reservoir CO_2 Capacity

Tetsu K. Tokunaga and Jiamin Wan

Earth Sciences Division
Lawrence Berkeley National Laboratory
Berkeley, California, 94720, U.S.A.

tktokunaga@lbl.gov jwan@lbl.gov

INTRODUCTION

The movement of injected CO_2 through permeable pore networks determines its distribution and stability within reservoirs used for carbon sequestration (Fig. 1), and this process is dependent on capillary interactions with the displaced brine (IPCC 2005; Benson and Cole 2008). Capillary phenomena controlling the distribution of CO_2 and reservoir brine depend on pore size (from mm to nm), wetting and interfacial properties. The pressure of the usually nonwetting CO_2 phase relative to that of the native brine is the capillary pressure, P_c, which in combination with pore size, wettability, and interfacial properties determines the saturation of each fluid phase. In typically reservoirs used for geologic carbon sequestration, CO_2 exists as a supercritical (sc) fluid because pressures and temperatures associated with storage depths exceed the critical point values for CO_2 (7.38 MPa, 31.1 °C). Thus, predicting carbon sequestration in reservoirs require understanding of interfacial tension, mineral surface wettability, and the capillary pressure dependence on saturation, for interactions between $scCO_2$, brine, and reservoir mineral surfaces. Investigations into these aspects of $scCO_2$ behavior, especially at elevated pressures and temperatures characteristic of geologic carbon sequestration, have largely only recently begun. Given the fairly early stage of research, many models for CO_2 transport in reservoirs rely heavily on the better understood capillary characteristics of other immiscible fluid pairs such as air-water, oil-water, and oil-

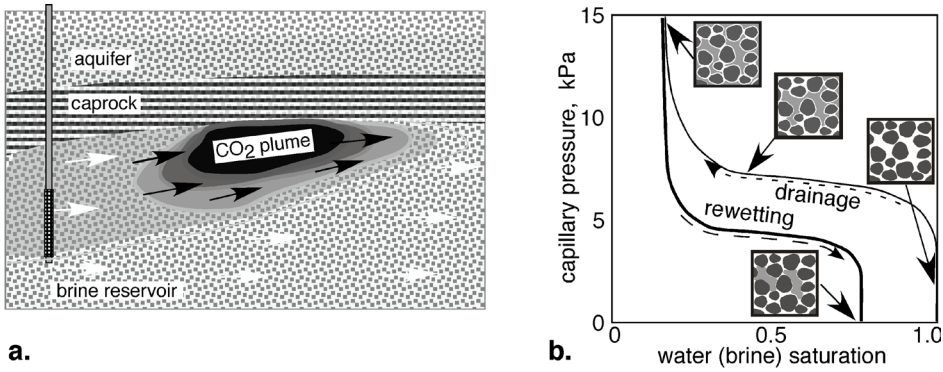

Figure 1. (**a**) Conceptual model of $scCO_2$ movement in a reservoir and its relation to $P_c(S_w)$ relations. (**b**) The drainage $P_c(S_w)$ curve describes regions in the reservoir being invaded by $scCO_2$, and the rewetting curve describes the lowest $P_c(S_w)$ achievable during the post-injection phase. Water and $scCO_2$ are depicted in the pore network schematics along the saturation curves in white and gray, respectively.

1529-6466/13/0077-0014$05.00 http://dx.doi.org/10.2138/rmg.2013.77.14

gas, supplemented with properties of $scCO_2$. However, a growing number of experimental studies are being published on the behavior of $scCO_2$ under reservoir conditions, leading to better understanding of C sequestration while also giving rise to new questions. In this chapter, we review aspects of the current (mostly laboratory-based) understanding of equilibrium capillary interactions between $scCO_2$ and brines, and their implications for $scCO_2$ behavior in brine reservoirs. Although coal seams and depleted oil/gas reservoirs are also very important environments for CO_2 sequestration, they are outside the scope of this chapter.

Capillary and wetting phenomena are important during the $scCO_2$ injection phase in brine reservoirs as well as during the much longer post-injection phase of carbon sequestration. Usually being the nonwetting fluid, $scCO_2$ requires injection at pressures high enough to overcome capillary entry into reservoir pores. As P_c is increased, brine is displaced by $scCO_2$ initially from larger pores and progressively from smaller pores, leaving residual brine films along drained pore walls (Fig. 1b). After cessation of $scCO_2$ injection, brine begins to refill pores by spontaneous imbibition and P_c decreases toward zero. The P_c relation with the wetting phase saturation S_w is hysteretic, such that pore refilling generally occurs at lower P_c than that of its drainage. Moreover, in this rewetting (brine imbibition) process, some fraction of the $scCO_2$ phase becomes occluded in pores, rather than being displaced as a continuous plume. The saturation of this occluded $scCO_2$ is often referred to as the nonwetting phase residual saturation S_{nr}, and represents the important sequestration mechanism of "capillary trapping."

A useful starting point for closer examination of interactions between $scCO_2$ and brine in reservoirs is the Young-Laplace equation,

$$P_c = \frac{2\gamma\cos(\theta)}{R} \tag{1}$$

where γ is the $scCO_2$-brine interfacial tension, θ is the contact angle (measured through the aqueous phase), and R is the characteristic radius of the pore in which the $scCO_2$-brine interface resides. The inverse dependence on R accounts for why the very fine pores of caprocks can provide resistance to capillary entry of $scCO_2$ migration, in addition to their very low permeability.

In the next sections, we survey the recent literature addressing various components of these capillary and wetting processes controlling the pore-scale fate of $scCO_2$ in reservoirs. We begin with a brief overview of studies on $scCO_2$-brine interfacial tension, followed by consideration of more complex and less consistent accounts addressing contact angles. We then review studies addressing aqueous films on mineral surfaces under $scCO_2$ confinement. We then summarize recent studies on $P_c(S_w)$ relations. It is important to recognize that each of these phenomena depend on T and P, which are in turn constrained to approximately follow geothermal and hydrostatic depth gradients in the subsurface. Common ranges of variations in P and T with depth below the land surface are indicated in the shaded band superimposed on the CO_2 phase diagram in Figure 2, showing that CO_2 exists as a supercritical fluid under common reservoir conditions.

$scCO_2$-BRINE INTERFACIAL TENSION

The brine-$scCO_2$ interfacial tension, γ, is important because it (along with wettability, pore-size, and P_c), controls capillary exclusion or entry of $scCO_2$ into originally brine-filled pores during injection, and at later stages influences pore refilling with brine. Some recent studies have investigated water/brine-$scCO_2$ interfaces through molecular simulations (Nielsen et al. 2012; Li et al. 2013). Hamm et al. (2013, this volume) provides an up to date review of molecular simulation studies of the aqueous-$scCO_2$ interface. The present section briefly reviews the experimental data on γ for brine-$scCO_2$ systems. Measurements of γ have recently

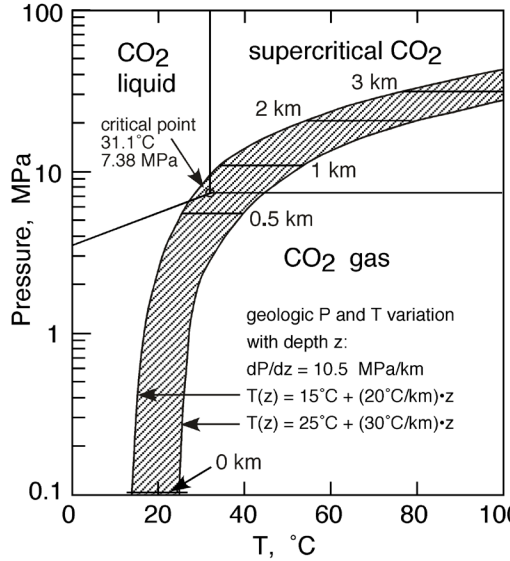

Figure 2. Phase diagram of CO_2, showing typical ranges of *T* and *P* variation with depth. [Modified from Celia 2008.]

been reported by different research groups, and are for the most part in fair to good agreement. Values of γ vary widely over the range of salinities, pressures, and temperatures associated with deep reservoirs used for CO_2 sequestration. Reported γ values range from 22 to 53 mN m^{-1} under typical CO_2 sequestration conditions (pressures of 7 to 27 MPa, temperatures up to 100 °C, and salinities up to about 334 g/L) (Bachu and Bennion 2009). Brine-CO_2 γ values undergo large decreases with pressure up to the critical *P*, then exhibit relatively smaller decreases at more elevated *P* (Fig. 3a). Increases in brine-CO_2 γ values with increased salinity (Fig. 3a) are consistent with the Gibbs adsorption equation for negative surface excesses of ions at the brine-CO_2 interface (Espinoza and Santamarina 2010; Duchateau and Broseta 2012; Iglauer et al. 2012). One the other hand, increased CO_2 solubility at higher P leads to lowering of γ, and these opposing effects of ionic strength and pressure have been shown to have approximately additive effects on γ (Duchateau and Broseta 2012). Brine-CO_2 γ values exhibit discontinuities in the vicinity of the critical *T*, but otherwise increase with temperature Fig. 3b), consistent with lower CO_2 solubility in the aqueous phase (Bachu and Bennion 2009). Differences in assumed values of fluid densities and experimental equilibration times have been identified as contributors to discrepancies among some reported brine-scCO_2 γ values (Bikkina et al. 2011).

CONTACT ANGLE MEASUREMENTS

Background

The importance of reservoir rock wettability has long been known to influence capillary entry pressure, residual fluid saturation, and relative permeability in the context of petroleum recovery (Anderson 1986, 1987; Morrow 1990; Dullien 1992). Fluid imbibition and drainage techniques have been developed to evaluate the wettability of immiscible fluid-oil combinations in rock cores (Amott index method and the US Bureau of Mines method). Direct determination of contact angles can be obtained from goniometric contact angle measurements on solid surfaces, through the captive drop technique. Reservoir rocks are categorized as water-wet, in-

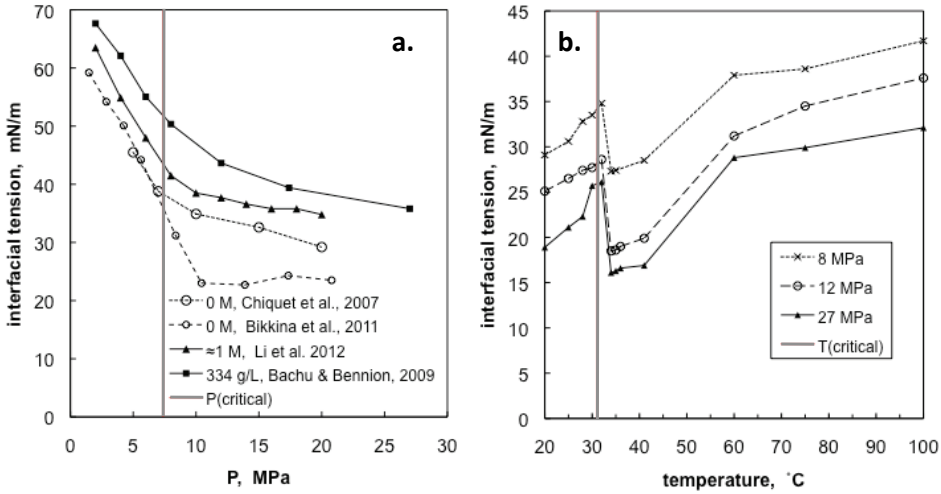

Figure 3. CO_2-water(brine) interfacial tension. (**a**) Variation in γ with *P*, for *T* = 50 °C, for waters of different salinities. The data from Li et al. (2012) are from NaCl + KCl solutions. The values from Bachu and Bennion (2009) were interpolated from their measurements at 41 and 60 °C. Note that γ decreases with *P,* and increases with salinity. (**b**) Variation in γ with *T*, for CO_2-water (no salts) at three pressures (subset of data presented in Bachu and Bennion 2009). Note that γ increases with *T,* with a discontinuity in the vicinity of the critical *T*.

termediate wet, and oil-wet when the advancing contact angle (θ) of the aqueous phase on a reservoir rock surface is in the range of 0-75°, 75-105°, and 105-180°, respectively (Morrow 1990).

Wettability is also recognized to be a critical factor in geological CO_2 sequestration, influencing flow paths within the reservoir's porous network, CO_2 migration rates, and CO_2 residual trapping (Iglauer et al. 2011b; Pentland et al. 2011). Moreover, wettability exerts an important role on caprock performance as well, through preventing or allowing CO_2 leakage from a reservoir. Thus, much of the research on mineral wettability in the presence of $scCO_2$ is motivated by the need to understand caprock performance (Li et al. 2005, 2006; Angeli et al. 2009; Wollenweber et al. 2009, 2010; Fleury et al. 2010). The contact angle can also be related to interfacial tensions through the Young-Dupré equation,

$$\cos\theta = \frac{\gamma_{sb} - \gamma_{sc}}{\gamma} \tag{2}$$

where γ_{sb} and γ_{sc} are the interfacial tension of the solid-brine and solid-$scCO_2$ interfaces, respectively. However, because these latter interfacial tensions involving solids cannot be independently measured, and because of surface roughness and questionable achievement of equilibrium, the predictive value of the Young-Dupré equation is limited (Hiemenz and Rajagopalan 1997). Moreover, the meaning of "γ_{sc}" is unclear in the presence of an adsorbed brine film rather than a dry solid-$scCO_2$ interface. Nevertheless, any factors that alter these interfacial energies can cause changes in the contact angle (Decker et al. 1999; Dickson et al. 2006).

Recent measurements

Contact angles for aqueous solutions (pure water to concentrated brines) and condensed (liquid and sc) CO_2 on various solid substrates have been measured by a number of researchers (Dickson et al. 2006; Siemons et al. 2006; Chiquet et al. 2007a; Yang et al. 2008a; Chalbaud et al. 2009; Espinoza and Santamarina 2010; Fleury et al. 2010; Bikkina 2011; Mills et al.

2011; Li et al. 2012; Farokhpoor et al. 2013; Saraji et al. 2013; Wang et al. 2013). Because CO_2 is lower in density than water over P and T associated with geologic sequestration, θ can be measured using either a CO_2 droplet in water captive against the substrate's lower horizontal surface, or using a water (brine) droplet in CO_2 resting (sessile) on the upper surface of the solid. Wide ranges of conditions are of interest because of the need to understand how θ depends on P, T, mineral substrates, solution chemistry, and wetting history. Most of these studies focused on θ values for smooth surfaces of major minerals as functions of P, and in some cases ionic strength. Quartz and silica are substrates having received the most investigation for wettability in the presence of CO_2 (Bikkina 2011; Mills et al. 2011; Broseta et al. 2012; Jung and Wan 2012; Farokhpoor et al 2013; Saraji et al. 2013; Wang et al. 2013). Contact angle measurements with CO_2-water have also been reported by several sources for micas and calcite (Espinoza and Santamarina 2010; Bikkina 2011; Mills et al. 2011; Broseta et al. 2012; Farokhpoor et al 2013; Wang et al. 2013).

Wettabilities for several other mineral substrates in the presence of CO_2 were determined in a few of the aforementioned studies. Mills et al. (2011) measured contact angles for brine-CO_2 (gas and supercritical) at 40 °C on a variety of common minerals (quartz, muscovite, biotite, calcite, labradorite, and orthoclase), and found all to be hydrophilic, with mica and calcite decreased in wettability, while quartz and biotite increased with higher pressure. Wang et al. (2013) recently reported θ measurements on a wide variety of minerals (quartz, microcline, kaolinite, calcite, phlogopite, illite), at 30 °C and 7 MPa (near the CO_2 triple point) and 50 °C and 20 MPa ($scCO_2$) with a variety of aqueous solutions, and also concluded that all of these substrates remained hydrophilic ($\theta < 30°$). Wang et al. (2013) showed that important predictors for wettability are ionic strength and pH (for minerals with relatively low permanent surface charge. Farokhpoor et al (2013) measured θ of water (0 to 0.8 M NaCl) on quartz, calcite, muscovite, and feldspar at 36 and 66 °C, at pressures up to 40 MPa, and reported fairly stable strongly wetting behavior for most samples, with muscovite being the exception. In the case of muscovite, θ increased from 16° up to 36° as pressure was increased up to 30 MPa, with most of the increase occurring in the vicinity of the critical pressure of CO_2. Moreover, Farokhpoor et al (2013) reported that longer term experiments (up to 48 days) at 10.5 MPa (36 °C) lead to θ increasing from 35° up to 60°.

Contact angles for brine-CO_2 have also been determined for rock samples of mixed mineralogy. Yang et al. (2008) reported θ increases from 44° to 106° (decreased wettability) with increases in P (0.4 to 31.2 MPa) for a limestone sample from the Weyburn oilfield in Canada. In contrast, Broseta et al. (2012) reported relatively constant θ of ~ 32 to 35° for a Rousse carbonate caprock over (low to moderate salinity, 70 and 140 °C, 0.8 to 15.5 MPa). Siemons et al. (2006) measured θ on anthracite coal at 45 °C, over P from atmospheric up to 14.1 MPa, and found large values from about 110° up to 140°, approximately linearly increasing with P. Only their measured θ ~ 90° for anthracite at atmospheric P deviated from this trend, and they hypothesized that this resulted from patches of stable water films.

The P-dependence of θ is important to understand because geologic C sequestration occurs at and above the critical P of CO_2, such that physicochemical properties affecting wetting (density, solubility, interfacial tension) undergo wide variation. Chiquet et al. (2007a) observed that as pressure is increased from 1 to 11 MPa (unspecified T), θ increased to about 35° for quartz. Jung and Wan (2012) obtained wettability measurements at 45 °C for 0 to 5.0 M NaCl and CO_2 on silica surfaces over a wider P range (0.1 to 25 MPa), and showed increases in θ up to ~70° (Fig. 4), primarily occurring within the narrower P range of 7 to 10 MPa. Saraji et al. (2013) reported increases in θ in going from subcritical to $scCO_2$ pressures, especially at higher T (60 °C) for water-advancing conditions. Broseta et al. (2012) reviewed the P-dependence of θ for a variety of substrates (quartz, mica, calcite), and commonly observed $d\theta/dP > 0$ for experiments on mica. However, results from others indicate that changes in

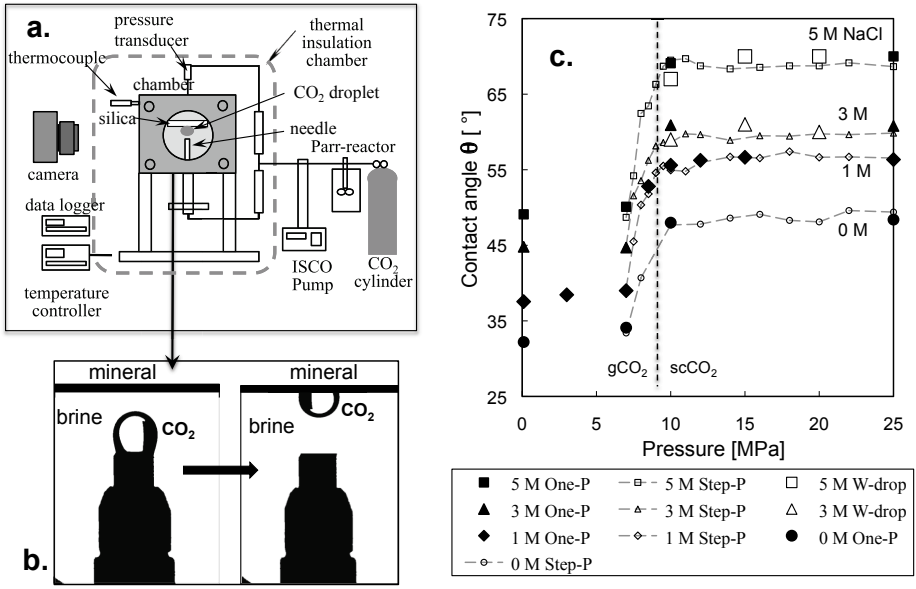

Figure 4. Contact angle measurements with CO_2 (g and sc) and water (0 to 5 M NaCl). (**a**) Experimental apparatus. (**b**) images of CO_2 bubble generated at needle and captive against silica surface. (**c**) Results showing θ dependence on *P* and salinity, obtained consistently using three different methods.

wettability with pressure are minor (Espinoza and Santamarina 2010; Fleury et al. 2010; Wang et al. 2013), and even show increased wettability (Bikkina 2011).

The chemistry of the aqueous phase is also recognized to affect θ. Contact angles have usually been found to increase with ionic strength (Chalbaud et al. 2009; Jung and Wan 2012). Jung and Wan also found nearly linear increases in θ values with ionic strength, and that *P* and ionic strength effects on θ are approximately additive. Brine pH decreases with increased CO_2 pressure, leading to less negative mineral surface charge. For minerals with low permanent charge and low pH_{pzc}, decreased pH-dependent charge diminishes electric double layer stabilization of aqueous films, and is expected decreased wettability (Chiquet et al. 2007a; Wang et al. 2013).

Wettability is further complicated by mineral surface roughness and temporal changes in θ. Surface roughness leads to complex deviation from wetting relative to intrinsic θ values measured on smooth surfaces. During CO_2 entry into pores, the aqueous phase is being displaced, such that a receding θ is representative of the brine drainage process. Over fairly broad ranges of intrinsic θ values (0° to about 45°), receding θ have been found to be practically indistinguishable from that of perfectly wetting (θ = 0°) (Morrow 1975). Conversely, during rewetting, the advancing θ is operative, and takes on values greater than that associated with the intrinsic θ (Morrow 1975). Such trends in θ hysteresis are consistent with recently measured $scCO_2$-brine $P_c(S_w)$ curves for $scCO_2$-brine in sands discussed later.

Surface chemical heterogeneity and changes in surface chemistry can also lead to hysteresis in θ, although recent studies have lead to diverse conclusions. Hysteresis or time-dependence in θ has been observed for CO_2-water(brine) on mica, quartz, and calcite, with widely different magnitudes of this phenomenon reported by different researchers (Chiquet et al. 2007a; Tonnet et al. 2008; Bikkina 2011; Broseta et al. 2012; Kim et al. 2012b; Wang et al. 2013). Of these recent studies, the largest values of θ (80° to 85°) to were reported for

quartz surfaces under longer term liquid CO_2 exposure (Bikkina 2011), and in pores of silica micromodels (Kim et al. 2012b). In the micromodel study, θ ranging from 66° to 87° for 5 M NaCl brine droplets in contact with $scCO_2$ at 8.5 MPa and 45°C (Fig. 5). In contrast to these accounts, Wang et al. found practically identical receding and advancing θ of relatively low magnitude (θ < 30°) for mica, quartz, calcite, and phlogopite, and no discernible changes in their θ over times up to three weeks (Wang et al. 2013).

Further investigations are clearly needed to resolve these differing conclusions, and also to understand potential wettability alteration resulting from long-term chemical reactions in the presence of $scCO_2$ (Bikkina 2011). Although the loss of water-wettability is recognized to decrease and even reverse the capillary exclusion of CO_2 from caprocks (Chiquet et al. 2007a), the consequences of decreased wettability on capillary trapping in reservoirs are unclear, as discussed later. Retraction of water into droplets of increased θ naturally leads to the issue of residual water films remaining on "drained" surfaces. Some microscopic visual evidence relating films to contact angles in $scCO_2$-brine systems now exists (Kim et al. 2012b). Analyses of equilibrium between θ and wetting film thicknesses have undergone considerable development for understanding petroleum recovery, foams, and adhesion (Hirasaki 1991a,b; Li and Neumann 1991; Sharma 1993; Amirfazli 2004). In contrast, studies of systems involving $scCO_2$ are still in early stages. In the next section aqueous films confined by $scCO_2$ on solid surfaces will only be considered on their own (i.e., apart from contact angles).

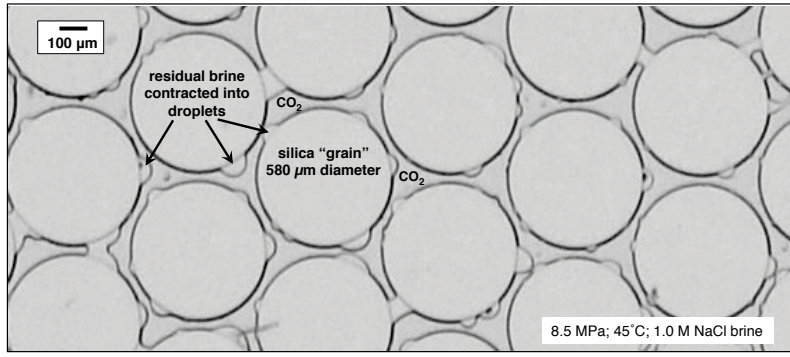

Figure 5. Brine dewetting process observed at the pore-scale during $scCO_2$ invasion into a silica glass micromodel (1 M NaCl, 8.5 MPa 45 °C). Originally thick, smooth water films contracted into droplets with θ up to 80°.

WETTING FILMS CONFINED BY CO_2

Background

As noted in the previous section, most common minerals are hydrophilic, at least during initial exposure to $scCO_2$. Thus, at early stages of $scCO_2$ injection, aqueous films reside between the solid substrate and $scCO_2$. When $scCO_2$ enters reservoir pores, brine films are expected to remain coated on mineral surfaces. The presence of aqueous films on mineral surfaces is important in influencing surface reactions (McGrail et al. 2009; Loring et al. 2011; Shao et al. 2011; Schaef et al. 2013), and pore-scale fluid flow and redistribution in reservoirs during CO_2 sequestration (Suekane et al. 2005; Xu 2008), as well as during CO_2 enhanced oil recovery, CO_2-EOR (Bijeljic et al. 2003). Experimental evidence for the existence of aqueous phase films on mineral surfaces equilibrated with $scCO_2$ has emerged of the past few years. Loring et al.'s (2011) recent study on forsterite carbonation from "wet" $scCO_2$ included measurements of

adsorbed water based on in-situ IR spectroscopy, through normalizing absorbance in the O-H stretching band to forsterite surface area. For $scCO_2$ with H_2O saturations of 47%, 81%, 95%, and "excess water," they reported water films of about 0.1, 0.2, 1 and 2 nm thicknesses (Loring et al. 2011). That study demonstrated that hydration of the mineral surface was energetically favorable, even when contacted with undersaturated $scCO_2$. Shao et al. (2011) inferred the presence of water films on phlogopite contacted with wet $scCO_2$ through the measurement of dissolution pits and new surface phases determined through AFM and DRIFTS. Thus, even in microenvironments within reservoirs filled with $scCO_2$ and containing relatively little water, water films may be present to facilitate surface reactions.

The aforementioned studies point to the importance of wetting films when $scCO_2$ is not necessarily H_2O-saturated. However, as CO_2 pumping into reservoirs proceeds, practically complete H_2O saturation of the $scCO_2$ phase is likely to be very closely approached at moderate distances away from injection wells. Under these conditions, it is advantageous to consider P_c as a controlling factor. It is further useful to consider a broader definition of P_c in order to quantify film behavior on the rough microtopography of reservoir grain surfaces. Wetting films on rough pore walls invaded by $scCO_2$ are retained by adsorption and capillarity (Fig. 6). Analyses of film equilibria on complex surfaces is commonly done with the augmented Young-Laplace equation (AYL)

$$P_c = 2\gamma H + \Pi(f) \tag{3}$$

where H is the mean interfacial curvature, f is the adsorbed film thickness, and $\Pi(f)$ is the film thickness dependent disjoining pressure (Novy et al. 1989). As illustrated in Figure 6b, P_c is equal to the ordinary Young-Laplace capillary pressure in regions with capillary interfaces suspended away from the solid surface, and is equal to $\Pi(f)$ where the fluid-fluid interface is compressed directly onto the solid surface. We next consider how adsorbed film thickness depends on environmental conditions associated with geologic C sequestration.

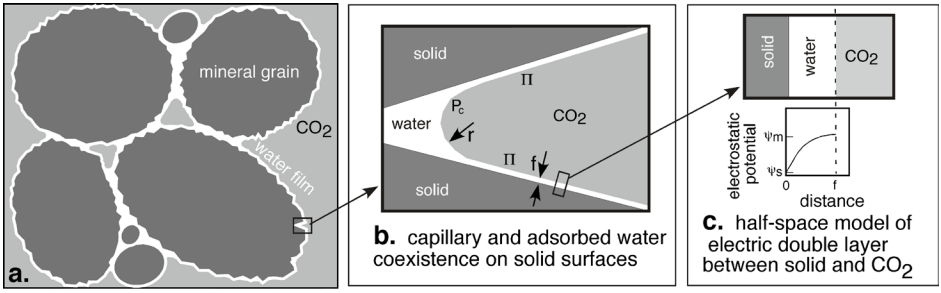

Figure 6. Conceptual model of water (depicted in white) distributions in pores of a granular reservoir filled with $scCO_2$ (gray). (**a**) Water is retained at grain-grain contacts, and along surfaces of grains. At grain-grain contacts and within surface microtopograchic depressions, capillarity primarily controls water retention. (**b**) On microtopographically rough surfaces, water redistributes to equilibrate Π and capillary pressure P_c. (**c**) Along surfaces of drained microtopographic maxima, water films are stabilized through adsorption.

A DLVO model for aqueous films on mineral surfaces, confined by $scCO_2$

Adsorbed films are generally stabilized through electrostatic and van der Waals forces, making them amenable to analysis using the approach developed by Derjaguin, Landau, Verwey and Overbeek (Verwey and Overbeek 1948; Derjaguin et al. 1987). In drained pores, the DLVO framework can be applied to describe how the adsorbed film thickness f depends on disjoining pressure Π, acting between the opposing solid-aqueous and aqueous-$scCO_2$

interfaces. The net pressure from van der Waals dispersion, $\Pi_{vdW}(f)$, and electrostatic $\Pi_{el}(f)$ (Hirasaki 1991b; Mazzoco and Wayner 1999), is

$$\Pi(f) = \Pi_{vdW}(f) + \Pi_{el}(f) \tag{4}$$

For geologic C sequestration, the dispersion and electrostatic components must be evaluated under *P-T* conditions characteristic of deep reservoirs. The DLVO treatment presented here does not include "structural" contributions of surface bound H_2O because this continuum (mean field) approach does not have sub-nm resolution. Structural water can certainly be added to more elaborate film models once sufficient spectroscopic evidence obtained under $scCO_2$ reservoir conditions becomes available.

The van der Waals pressure component on flat substrates varies with the reciprocal of the third power of film thickness, *f*, through

$$\Pi_{vdW}(f) = -\frac{A_{132}}{6\pi f^3} \tag{5}$$

where A_{132} is the Hamaker constant for the interactions between (1) solid substrate, (3) water film, and (2) CO_2. Thus, the van der Waals film thickness relation is

$$f = \left(-\frac{A_{132}}{6\pi\Pi_{vdW}}\right)^{1/3} \tag{6}$$

These relations underscore the importance of determining A_{132} values suitable for $scCO_2$ reservoir conditions. For this purpose, A_{132} can be estimated from A_{ii} of individual components. The Lifshitz equation can be used to obtain these A_{ii} through

$$A_{ii} = \frac{3}{4}k_B T\left(\frac{\varepsilon_i - 1}{\varepsilon_i + 1}\right)^2 + \frac{3h\nu_e}{16\sqrt{2}}\frac{\left(n_i^2 - 1\right)^2}{\left(n_i^2 + 1\right)^{3/2}} \tag{7}$$

where k_B is the Boltzmann constant, T is the Kelvin temperature, ε_i is the relative permittivity of the i^{th} phase, n_i is its refractive index, h is the Planck constant, and ν_e is the primary electronic absorption frequency in the ultraviolet region (ca. 3×10^{15} s^{-1}). These A_{ii} can then be substituting into the combining relation to estimate the nonretarded A_{132} (Israelachvili 1991),

$$A_{132} = \left(\sqrt{A_{11}} - \sqrt{A_{33}}\right)\left(\sqrt{A_{22}} - \sqrt{A_{33}}\right) \tag{8}$$

Hamaker constants of many common minerals (A_{11}) at room temperature and pressure are available in the literature (Hough and White 1980; Bergstrom 1997). Most measurements of A_{11} have been obtained over limited ranges of *P-T* for common minerals, but indicate negligibly changes for conditions associated with CO_2 sequestration (Parsegian 2006; Lefevre and Jolivet 2009). Values for A_{11} of some common minerals have been tabulated (Tokunaga 2011), and A_{132} of silica and smectite have been calculated for CO_2 reservoir conditions using Equations (7) and (8), and range from ~ -6×10^{-21} to -4×10^{-20} J (Tokunaga 2012). Negative values of A_{132} are indicative of film stabilization by van der Waals interactions.

Electrostatic interactions between films and interfaces constitute the other component controlling thicknesses of adsorbed films within the DLVO model. A conceptual model of distributions of water and electrostatic potentials with the electric double layer are shown in Figure 5c. Adsorption controls water film thickness along microtopographic maxima that become progressively exposed at lower water saturations. Ions in the film phase confined between the solid-water and CO_2-water interfaces distribute relative to charged interfaces to achieve a film thickness-dependent chemical potential equilibrium. The equilibrium electrical

double layer developed on flat interfaces is described by the 1D Poisson-Boltzmann equation (Verwey and Overbeek 1948; Israelachvili 1991), which describes the variation in electrostatic potential ψ_e normal to the solid-water interface. For symmetric electrolyte solutions

$$\frac{d^2\psi_e}{dx^2} = \frac{ezn_\infty}{\varepsilon_o\varepsilon_3}\left[\exp\left(\frac{ez\psi_e}{k_BT}\right) - \exp\left(-\frac{ez\psi_e}{k_BT}\right)\right] \tag{9a}$$

or

$$\frac{d^2\psi_e}{dx^2} = \frac{2ezn_\infty}{\varepsilon_o\varepsilon_3}\sinh\left(\frac{ez\psi_e}{k_BT}\right) \tag{9b}$$

where e is the electron charge, z is the ion valence, n_∞ is the ion concentration (number density) in the bulk solution, ε_o is the vacuum permittivity, and ε_3 is the dielectric constant of water. The characteristic electric double layer length or Debye length, κ^{-1} is given by

$$\kappa^{-1} = \sqrt{\left(\frac{\varepsilon_o\varepsilon_3 k_BT}{2e^2z^2n_\infty}\right)} \tag{10}$$

Substituting κ^{-1} and the dimensionless electrostatic potential $Y_e = ze\psi_e/k_BT$, into Equation (9b) gives the Poisson-Boltzmann equation in dimensionless form

$$\frac{d^2}{dx^2}Y_e = \kappa^2 \sinh Y_e \tag{11}$$

In pore waters, κ^{-1} commonly ranges from a few tens of nm to ~1 nm, becoming more compressed in brine systems because of the inverse square-root dependence on ionic strength. Although ε_3 varies with P and T, κ^{-1} itself is relatively insensitive to depth because of counterbalancing changes in ε_3 and T with depth (Tokunaga 2012).

The Poisson Boltzmann equation can be solved numerically for different geometries and boundary conditions ($Y_{e,i}$ at the film-solid surface $i = 1$, and at the film-scCO$_2$ interface $i = 2$) in order to obtain $\Pi_{el}(f)$ over wide ranges of configurations. However, approximate analytical solutions for the one-dimensional case with moderately low values of Y_e are also available. The compression approximation (CA) developed by Gregory (1975)

$$\Pi_{el}(f) = n_\infty k_BT\left\{2\left[1+0.25\left(Y_{e,1}+Y_{e,2}\right)^2\operatorname{csch}^2\left(\frac{\kappa f}{2}\right)\right]^{1/2} - \frac{\left(Y_{e,1}-Y_{e,2}\right)^2\exp(-\kappa f)}{1+0.25\left(Y_{e,1}+Y_{e,2}\right)^2\operatorname{csch}^2\left(\frac{\kappa f}{2}\right)} - 2\right\} \tag{12}$$

was recently used to calculate the dependence of adsorbed film thicknesses on Π_{el}, then combined with Π_{vdW} to predict DLVO-based film thicknesses for silica and smectite surfaces under geologic C sequestration conditions (Tokunaga 2012). Although the CA closely matches numerical solutions for surfaces with constant charge, interfaces more generally vary with respect to both their charge and ψ_{ei} during compression and expansion of the electric double layer (Israelachvili 1991). This charge regulation results in $\Pi_{el}(f)$ behavior that is intermediate between the two limits of constant surface charge and constant ψ_{ei}, such that the linear superposition approximation (LSA) to the Poisson-Boltzmann equation can give better results than the CA (Gregory 1975). The LSA treats the opposing double layers additively (Verwey and Overbeek 1948; Gregory 1975), resulting in

$$\Pi_{el}(f) = 64 n_{\infty} k_B T \tanh\left(\frac{Y_{e,1}}{4}\right)\tanh\left(\frac{Y_{e,2}}{4}\right)\exp(-\kappa f) \tag{13}$$

Example predictions of film thicknesses on silica and smectite under reservoir conditions are shown in Figure 7. This graph shows predicted film thicknesses on these common minerals for *P* and *T* typical of 1 km depth, for a 100 mM brine, and for negligible electrostatic potential at the $scCO_2$-brine interface ($\psi_{e,2} = 0$). Silica was selected because of its common occurrence, and because its low, pH-dependent charge is expected to support only very thin films under confinement by $scCO_2$. Smectite on the other hand is expected to maintain a higher $\psi_{e,1}$ because of its high surface charge. Assigning mineral surface electrostatic potentials of −5 mV for silica and −50 mV for smectite allowed inspection of the impacts of hypothetical $\psi_{e,1}$ on film thicknesses. As shown in Figure 7, the electrostatic contribution to film thickness is clearly greater for the higher magnitude $\psi_{e,1}$, but both cases involve fairly compressed (< 5 nm) films because of the moderately high ionic strength (100 mM). In both of these examples, the inclusion of the dispersion (van der Waals) contribution leads to substantially thicker films. The influence of Π on film thickness is clearly strong, compressing adsorbed films to nm thicknesses at Π > 100 kPa, and allowing film expansion as Π approaches low magnitudes. However, it should be noted that the lower magnitude of Π in porous media is finite, and dependent on pore size because brine saturation occurs at sufficiently low $P_c = \Pi$. The pore size-dependence for capillary drainage of different pore sizes, estimated from Equation (1) (assuming θ = 0), is plotted along the upper *x*-axis of Figure 7. This upper scale is only a rough indication of the accessible Π range, because hysteresis in the $P_c(S)$ relation and finite θ values expand the Π range over which films can occur (discussed later). Nevertheless, the capillary entry P_c values indicate that for typical reservoirs with pore diameters greater than 10 μm, adsorbed brine film thicknesses are expected to range from about 2 to 20 nm. A final observation to make on the LSA

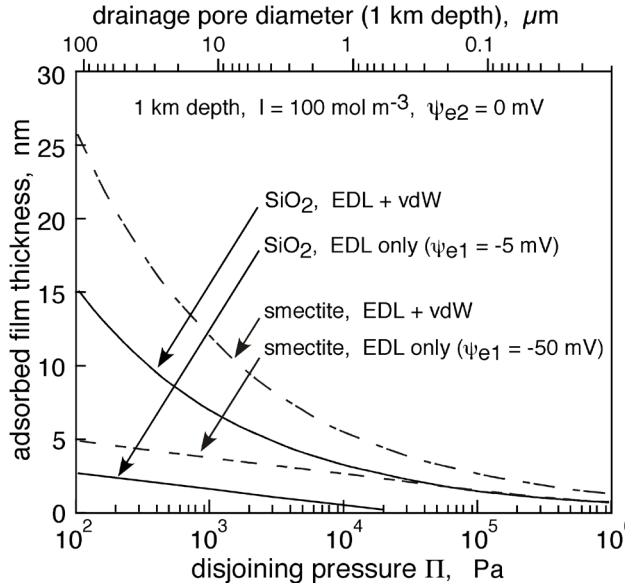

Figure 7. LSA-based comparisons of electrostatic only (EDL), and DLVO (EDL + vdW) predictions of aqueous film thicknesses for SiO_2 and smectite under CO_2 confinement at 1 km depth (323 K, 10.6 MPa) (Tokunaga 2012).

results shown in Figure 7 is that they are practically identical to predictions based on the CA for the same conditions, which were presented in Tokunaga (2012).

Experimental measurements of film thicknesses under controlled P_c

As noted above, in addition to adsorption, capillarity is an important contributor to retention of brine films under $scCO_2$ confinement. It is therefore desirable to develop the capability to measure aqueous film thicknesses on both smooth and rough mineral surfaces under reservoir conditions, at controlled P_c. A pressure/suction plate method used for investigating water films at atmospheric P through synchrotron X-ray fluorescence of tracer ions in the film phase (Tokunaga et al. 2000) was recently modified to permit measurements with $scCO_2$ as the nonwetting phase (Kim et al. 2012a). In brief, the key components of the system consist of a stationary high-P chamber in which the brine film is generated and measured by synchrotron X-ray fluorescence, and a variable elevation high-P reservoir for controlling P_c (Fig. 8). These components are linked in a closed loop via a lower brine line and an upper $scCO_2$ line, with both phases in the reservoir, $scCO_2$ in the main body of the measurement chamber, and the wetting brine film coating the substrate surface attached to the inward facing side of a high-P sapphire window. While the whole system is maintained at a constant total P of 7.8 MPa with a high pressure pump and at constant T of 40 °C, the P_c is varied by raising or lowering the reservoir height. A 1.0 M $KCsI_2$ solution was used as the brine to allow synchrotron X-ray fluorescence measurements of the Cs^+ and I^- in the films. Unlike several other surface methods (reflectivity, ellipsometry), the X-ray fluorescence-based approach allows measurements on smooth as well as rough surfaces (up to several μm in root mean square roughness, R_{rmsr}). To date, this system has been used to measure brine films on silica at the Advanced Photon Source, Argonne National Laboratory (Kim et al. 2012a), and on mica at the Stanford Synchrotron Radiation Lightsource (Kim et al. 2013).

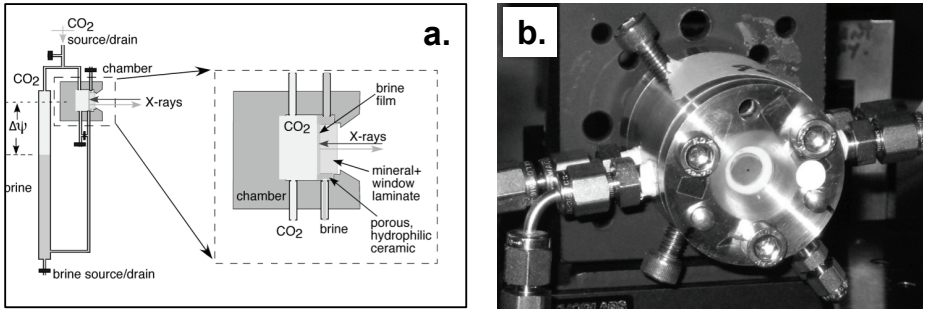

Figure 8. Experimental system for measuring brine film thicknesses. (**a**) Side view schematics of the configuration for the measurement chamber and P_c-controlling reservoir. (**b**) Photograph of brine film chamber, viewed from front.

Measurements at 7.8 MPa and 40 °C (representative of conditions at about 0.8 km below land surface) of brine film thicknesses on SiO_2 were obtained on samples with smooth (1.6 nm R_{rmsr}) and rough surfaces (330 nm R_{rmsr}), under confinement with supercritical (sc) CO_2 (Fig. 9). Over a P_c range of 0.18 to 3.7 kPa, measured area-averaged film thicknesses on the rough silica surface ranged from 265 nm to 249 nm. Over this same range of P_c, film thicknesses measured on the smooth silica surface were about 2 nm, although equilibrium may not have been achieved. Measurements obtained on the smooth surface were lower than predicted based on the combined effects of electrostatic and van der Waals interactions (DLVO model), but higher than that predicted from electrostatic interactions alone (Fig. 9). This

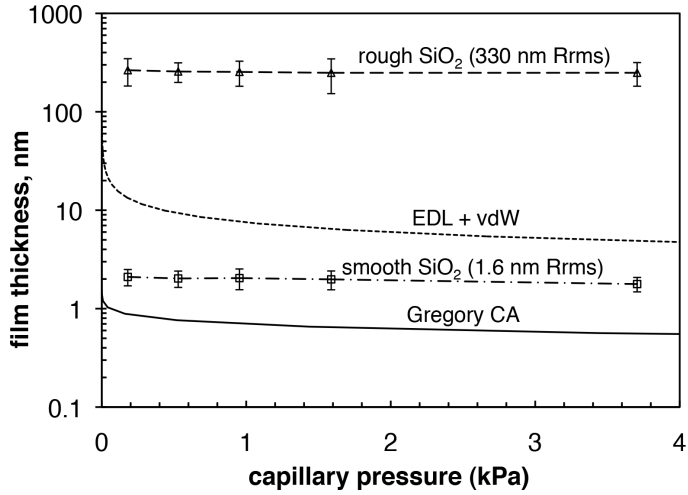

Figure 9. Variations in film thicknesses on silica surfaces, over a range of P_c, under $scCO_2$ confinement (7.8 MPa and 40 °C) from Kim et al. (2012a). Measurements were obtained on roughened (330 nm R_{rmsr}) and smooth (1.6 nm R_{rmsr}) surfaces. The measurements on the smooth SiO_2 sample were compared to model predictions based on estimated electric double layer compression (Gregory CA) and the combined electrostatic and dispersion forces (DLVO).

suggests that the magnitude of the composite Hamaker constant assumed in the calculation (-8×10^{-21} J) may be too large. In summary (1) a novel device for measuring film thicknesses under $scCO_2$ confinement and controlled P_c was recently developed, (2) the stability of wetting brine films on silica has been demonstrated, (3) the measured average brine film thicknesses were strongly controlled by surface roughness, with very weak variation over the fairly narrow range of tested P_c, and (4) discrepancies between measured and modeled film thicknesses on smooth surfaces may reflect slow approach to hydrostatic equilibrium in thin films and/or incorrect parameters assumed in the DLVO calculation.

CAPILLARY PRESSURE-SATURATION RELATIONS

Background

Capillary pressure-saturation relations for $scCO_2$-brine reflect the integrated influences of the previously discussed phenomena; capillary pressure, interfacial tension, contact angles, and wetting films. Understanding the dependence of capillary pressure (P_c) on water saturation (S_w) is needed to predict CO_2 flow and initial storage in reservoirs, and to predict later stage mobility and the key storage process of capillary trapping (residual trapping) (IPCC 2005; Bachu et al. 2007; Benson and Cole 2008). The capillary trapping capacity of reservoir materials has complex dependence on a number of factors including porosity, pore size distribution, pore body:throat aspect ratio, nonwetting phase displacement extent, and the rewetting process (Iglauer et al. 2011b; Tanino and Blunt 2012).

Despite the critical need to understand $P_c(S_w)$ relations and capillary trapping of CO_2 at its residual saturation, few investigations have directly measured these basic relations with CO_2/H_2O at reservoir pressures and temperatures (Plug and Bruining 2007; Krevor et al. 2011; Pentland et al. 2011; Pini et al. 2012; Pini and Benson 2013). Plug and Bruining (2007) reported drainage and imbibition measurements with distilled water-CO_2(gas), CO_2(liquid), and $scCO_2$ on quartz sand ($360 < D_{50} < 410$ μm) packs. Although their experiments conformed

to typical drainage and imbibition behavior when conducted with CO_2 in gas and liquid phases, their $scCO_2$ drainage curve exhibited instabilities in P_c, and their imbibition curves exhibited a shift to unusually low P_c. They interpreted their lower magnitude, and even negative P_c values as indications that the quartz surface became intermediate wettable. Silica surface wettability changes of varying extents have been reported in other studies conducted under reservoir-relevant $scCO_2$ conditions (McCool and Tripp 2005; Chiquet et al. 2007a; Bikkina 2011; Jung and Wan 2012; Kim et al. 2012b; Saraji et al. 2013). Pentland et al. (2011) recently showed general agreement among drainage $P_c(S_w)$ relations for brine-$scCO_2$, brine-decane, and air-mercury (Hg injection porosimetry) on Berea sandstone cores when capillary-scaled with respect to the Leverett-J function. Pini et al. (2012) obtained much closer agreement among Leverett-scaled $P_c(S_w)$ results for drainage $P_c(S_w)$ relations with water-$scCO_2$ and air-mercury (Hg injection porosimetry) on Berea and Arqov sandstone cores. Pini and Benson (2013) more recently found good agreement in the scaled capillary behavior for relative permeabilities and $P_c(S_w)$ of $scCO_2$-brine, brine displaced by gas phase CO_2, as well as brine displaced by gas phase N_2. New experimental methods coupling CO_2-water flow with X-ray computed tomography are providing insights into CO_2 trapping associated with finer-scale (sub-core, down to ~ 10^{-3} m) heterogeneity (Perrin and Benson 2010; Pini et al. 2012). Still higher resolution (~14 μm) X-ray computed micro-tomography images have yielded images of capillary-trapped $scCO_2$ blobs in reservoir cores (Iglauer et al. 2011a).

Given the vast variety in sizes, shapes, and connectivity of pores occurring in geological media, procedures are needed to generalize measurements of hydraulic properties in order to extend their value beyond sample-specific properties. Capillary scaling (Leverett 1941; Miller and Miller 1956) has been employed in many of the recent studies to facilitate comparisons among diverse experimental systems. The scaled capillary pressure Π_c can be defined by multiplying P_c by a characteristic capillary length scale λ (either a characteristic pore size or characteristic grain size) for the porous medium, and dividing by γ

$$\Pi_c = \frac{\lambda P_c}{\gamma} \tag{14}$$

Geometrically similar porous media are predicted to share a common universal drainage $\Pi_c(S_w)$ and a separate universal wetting $\Pi_c(S_w)$ curve (Haines 1930; Miller and Miller 1956; Klute and Wilkinson 1958; Schroth et al. 1996; Tokunaga et al. 2004). Miller-Miller similitude describes sets of media that are geometrically effectively equivalent in pore network structure and fluid-fluid interfacial shape when enlarged or reduced in size (Miller and Miller 1956). Geometrically similar media have only one value of porosity n because it is invariant under such scaling transformations. Prior to the analysis by Miller and Miller (1956), Leverett scaled a set of measured unsaturated hydraulic relations with

$$J(S_w) = \sqrt{\frac{k}{n}}\frac{P_c}{\gamma} \tag{15}$$

where k is the permeability (Leverett 1941; Leverett et al. 1942). The term $(k/n)^{1/2}$ has been regarded as proportional to the porous medium's average pore radius (Rose and Bruce 1949), although the reliability of this scaling factor has not been tested over very wide ranges in k and n. Subsequent modifications to the J function have been developed to account for differences in contact angle θ (Rose and Bruce 1949; Demond and Roberts 1991; Moseley and Dhir 1996) through

$$\frac{\Pi_c}{\cos\theta} = \sqrt{\frac{k}{n}}\frac{P_c}{\gamma\cos\theta} \tag{16}$$

However, wettability phenomena for porous media are considerably more complex than for droplets on flat surfaces (Morrow 1975; Anderson 1986). Receding θ operative during drainage remain very low and fairly insensitive to intrinsic (equilibrium, flat surface) θ, whereas advancing θ operative during rewetting progressively exceed their intrinsic values above θ ≈ 45° (Morrow 1975). Philip (1969, 1971) noted that even under ideal conditions, basic inconsistencies are inherent in contact angle scaling; although Parlange (1974) showed that the result errors are commonly small. In view of these sources of uncertainty, including θ in capillary scaling models appears to improve fits only over a moderate range of conditions. A further problematic aspect of scaling with θ is that unique values may not be available to apply, evident from reviewing the recent literature.

Although the water (brine)-scCO_2 behavior in these recent studies generally appear to comply with expectations based on capillary scaling, it is important to note that assumptions or adjustments with respect to contact angles and/or interfacial tensions were sometimes involved. Furthermore, most experimental studies have determined only the aqueous phase drainage curves, yet hysteresis in $P_c(S_w)$ relations is important for predicting capillary trapping and the long-term CO_2 footprint in reservoirs (Doughty 2007; Juanes et al. 2010; Iglauer et al. 2011b). Only Plug and Bruining (2007) appear to have measured capillary-trapped scCO_2 saturation in a manner representative of expected reservoir processes where P_c would gradually approach zero.

Given the limited number of measurements of the capillary behavior of CO_2, simulations of CO_2 sequestration in reservoirs commonly rely on modifying more familiar air/H_2O and oil/H_2O $P_c(S_w)$ relations obtained at atmospheric P and T (Doughty 2007; Ide et al. 2007; Alkan et al. 2010; Zhou et al. 2010; Oldenburg and Doughty 2011), adjusted to account for differences in fluid densities, interfacial tension, and sometimes wettability. However, supercritical (sc) CO_2 drives geochemical reactions in reservoirs (Kaszuba et al. 2003; Kharaka et al. 2006; Shao et al. 2011), including wettability alterations (Dickson et al. 2006; Chiquet et al. 2007b; Bikkina 2011; Jung and Wan 2012; Kim et al. 2012b). Thus, the capillary behavior of scCO_2 with brine may not be reliably inferred through extrapolation of nonreactive immiscible fluids such as air, certain oils, or mercury. The few available experimental determinations of $P_c(S_w)$ relations for scCO_2/H_2O appear less complete in view of the fact that reservoir conditions span a very broad range of P, T, and chemistry; over which large variations occur in scCO_2 properties (Span and Wagner 1996), scCO_2/H_2O interfacial tension (Bachu and Bennion 2009b; Chalbaud et al. 2010; Li et al. 2012), and mineral wettability (Chiquet et al. 2007a; Bikkina 2011; Jung and Wan 2012; Saraji et al. 2013; Wang et al. 2013).

Recent capillary scaling tests of brine-scCO_2 drainage and rewetting in quartz sand

A series of drainage-imbibition experiments were recently completed for brine-air and brine-scCO_2 in order to detect possible deviations from predictable capillary behavior (Tokunaga et al. 2013). The brine consisted of 1.00 M NaCl, and experiments involving scCO_2 included pre-equilibration of the two immiscible phases. The P_c control system used for these experiments was essentially the same as that shown in Figure 8 for the film thickness studies. However, for the $P_c(S_w)$ experiments, the sight glass reservoir also served as an outflow/inflow meter. A high-P reactor was modified to operate as a pressure plate chamber similar to that described in Plug and Bruining (2007). The drainage and imbibition (rewetting) processes were determined on a 300 μm quartz sand pack with scCO_2-brine at pressures of 8.5 and 12.0 MPa (45 °C), and air-brine at 21 °C and 0.1 MPa.

The measured drainage and rewetting relations are shown in Figures 10a and 10b, respectively. Three main trends were observed in the $P_c(S_w)$ results going from air-brine, to 8.5 MPa scCO_2-brine, to 12.0 MPa scCO_2-brine; (1) shifts to smaller P_c values associated with any given S_w value, (2) shifts to smaller S_r, and (3) greater nonwetting phase trapping upon

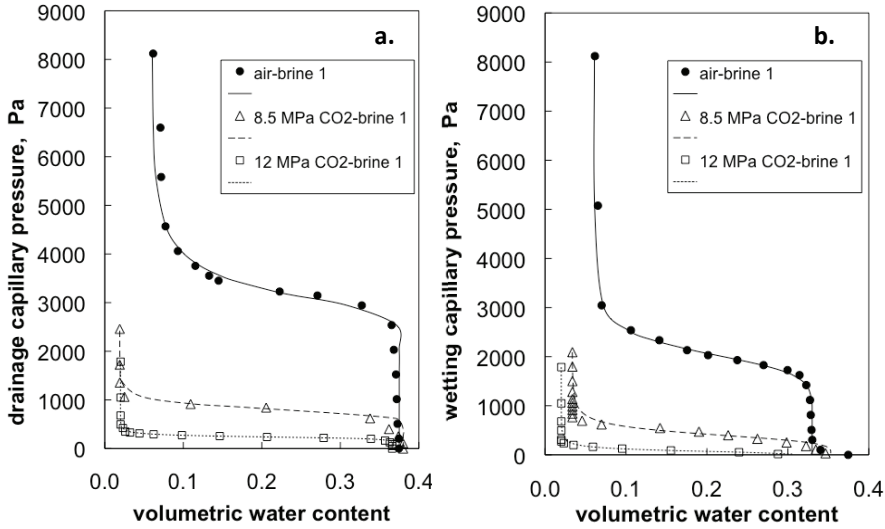

Figure 10. P_c dependence on brine (1 M NaCl) volumetric fraction (saturation times porosity) during (**a**) drainage, and (**b**) rewetting (Tokunaga et al. 2013). Complete saturation is equivalent to a volumetric water content of 0.381. The experimental sequence involved duplicate drainage-rewetting cycles for air-brine, followed by duplicate cycles with $scCO_2$ at 8.5 MPa, and finally duplicate cycles with $scCO_2$ at 12 MPa. Only the first run from each closely replicated duplicate cycle is shown for simplicity.

rewetting to $P_c = 0$. The lower P_c values measured at intermediate stages of wetting (Fig. 10b) relative to corresponding draining under the same conditions (Fig. 10a) reflect the expected hysteresis in $P_c(S_w)$ curves. Shifts to lower P_c are also qualitatively consistent with decreased interfacial tension in going from air-brine (0.1 MPa) to $scCO_2$-brine (8.5 MPa), to $scCO_2$-brine (12 MPa).

Capillary scaling results. If the shifts in these drainage and wetting curves were attributable only to differences in γ, then Miller-Miller scaling (Eqn. 14) of the data would condense all results onto one universal drainage curve and a separate universal wetting curve. The γ-scaled results remain clearly separated (Fig. 11), and demonstrate that interfacial tension alone cannot account for observed shifts in $P_c(S_w)$ relations. Only the air-brine experiments have inflection points in $\Pi_c(S_w)$ relations within the expected range (marked on each graph).

For experiments involving $scCO_2$, drainage and rewetting at intermediate S_w levels shifted to Π_c values that were from 30% to 90% lower than predicted, demonstrating that factors other than interfacial tension are affecting the $P_c(S_w)$ relations. When these interfacial tension-based predictions are further scaled using independently measured θ (Jung and Wan 2012), slightly more consistent curves are obtained (Fig. 12). Recall that a wide range of θ values has been reported for silica surfaces, further indicating that scaling-based predictions will have large uncertainties.

Capillary trapping of $scCO_2$. Amounts of $scCO_2$ trapped within formation pores after cessation of injection and reentry of native brine are important to know for predicting long-term storage capacities of reservoirs. Because of experimental challenges in measuring capillary-trapped $scCO_2$, current understanding is largely inferred from experiments conducted at or near atmospheric pressure and room temperature, using other nonwetting fluids such as gas, octane, and mineral oil, (Delclaud 1991; Pentland et al. 2008; Gittins et al. 2010; Iglauer et al. 2011b). In general, greater displacement of water by the nonwetting fluid phase leads to

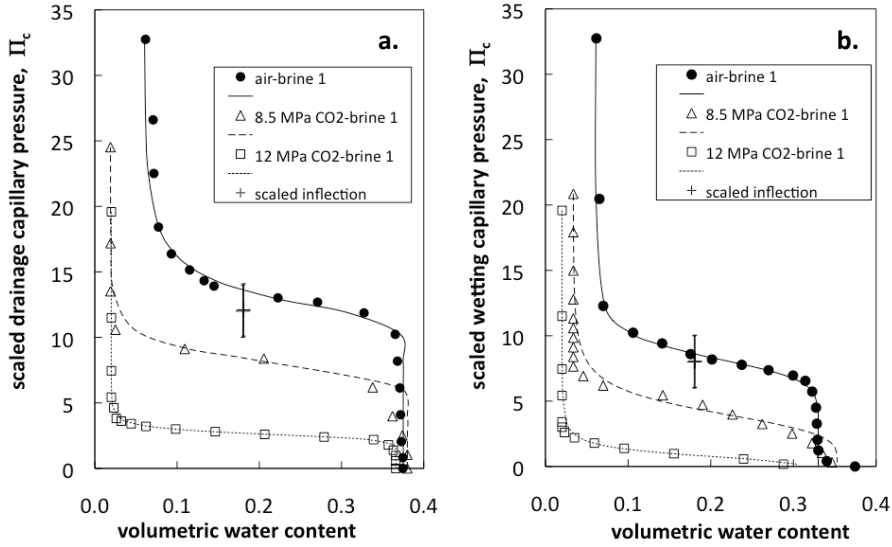

Figure 11. Scaled capillary pressure, $\Pi_c = \lambda P_c/\gamma$, dependence on volumetric brine content (**a**) drainage, and (**b**) wetting curves. Typical values of inflection point Π_c observed in other homogeneous sands are included for comparisons. Values of γ are 74.4 mN m^{-1} (air-brine), 33.1 mN m^{-1} (8.5 MPa $scCO_2$-brine), and 30.1 mN m^{-1} (12.0 MPa $scCO_2$-brine).

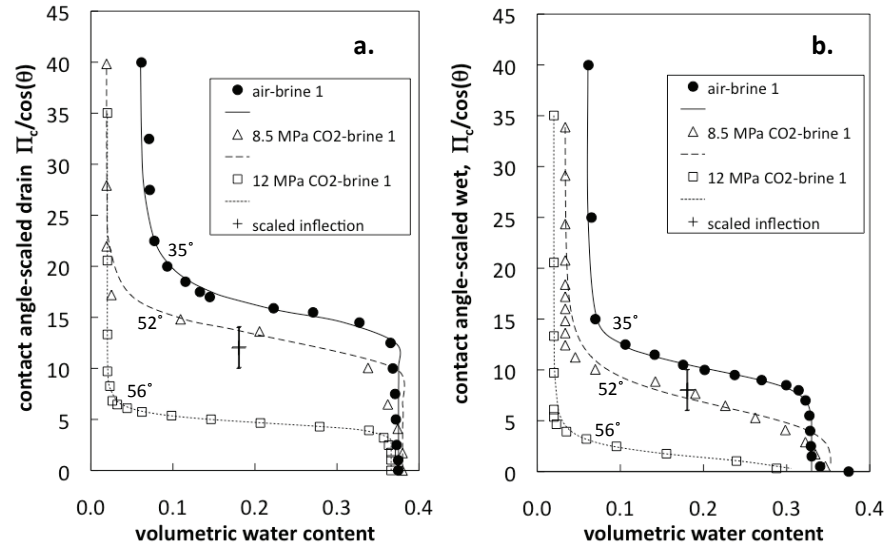

Figure 12. Contact angle-scaled capillary pressure, $\Pi_c/\cos(\theta)$ relations to volumetric brine content for (**a**) drainage, and (**b**) rewetting curves. The assigned θ values for brine on smooth silica with air, 8.5 MPa CO_2, and 12 MPa CO_2 are 35°, 52°, and 56°, respectively, as reported by Jung and Wan (2012).

higher residual nonwetting phase saturation, S_{nr}, upon subsequent imbibition of the aqueous phase (Land 1968). The studies of S_{nr} using nonaqueous fluids other than CO_2 have yielded fairly low values of capillary trapping in homogeneous sand packs, with S_{nr} typically less than 0.13. Relative to sand packs, S_{nr} obtained from experiments on cores commonly are higher, reaching up to ~0.5, although (Bennion and Bachu 2010; Pentland et al. 2011). S_{nr} for $scCO_2$ in cores have been found to be less than values obtained with decane (Pentland et al. 2011), and even with gas phase CO_2 (Akbarabadi and Piri 2013). When $scCO_2$ was used as the nonwetting phase in $P_c(S_w)$ measurements in a sand pack by Plug and Bruining (2007), much greater capillary trapping was achieved relative to other nonwetting phases, with $S_{nr} \sim 0.5$ obtained at $P_c \sim 0$. Thus, the one previously published measurement of $scCO_2$ S_{nr} in a sand pack indicated that trapping is much greater than observed with other nonwetting phase fluids.

Our experimental system and procedure yielded measurements of S_{nr} during the sequence of air-brine, 8.5 MPa $scCO_2$-brine, and 12.0 MPa $scCO_2$-brine imbibition cycles. The behavior of all rewetting curves (a subset of the range previously shown in Fig. 10b) in the vicinity of $P_c = 0$ is presented in Figure 13a. The S_{nr} were calculated as $1 - S_w$, at $P_c = 0$, and plotted as a histogram in Figure 13b to facilitate comparisons. The collective results indicate that capillary trapping of $scCO_2$ in silica sands is significantly greater than trapping of air, and that the trapped amounts increase with increased pressure (corresponding to increased reservoir depth). These results are consistent with findings of Plug and Bruining (2007), and suggest that reservoir CO_2 storage capacities may be larger than currently estimated. It should be noted that the increased capillary-trapped $scCO_2$ saturations attributed to decreased wettability in these studies (Plug and Bruining 2007; Jung and Wan 2012; Tokunaga et al. 2013) are contrary to predictions of the model developed by Spiteri et al. (2008), which predicts decreased S_{nr} with decreased wettability . Reconciliation of this difference between these measurements involving $scCO_2$ and existing trapping models will require further investigation. It should also be noted that the sequence of air-brine, 8.5 MPa $scCO_2$-brine, and 12.0 MPa $scCO_2$-brine tests also represents the

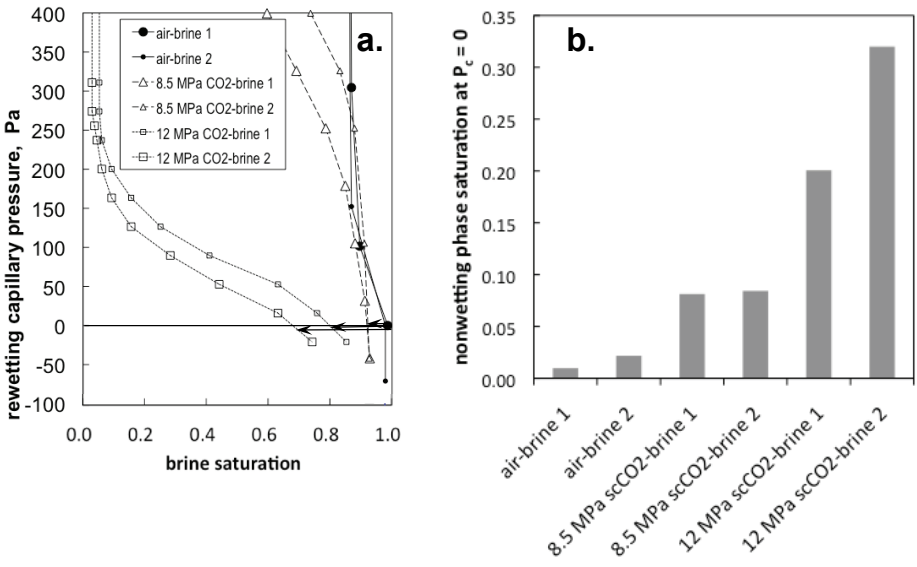

Figure 13. Measured saturation of the nonwetting phase (air or $scCO_2$) obtained upon rewetting to $P_c = 0$. (**a**) Close-up view of imbibition curves, highlighting departures from rewetting to complete brine saturation (volumetric water content = 0.38). (**b**) Saturations of nonwetting phases at $P_c = 0$, shown sequentially over the course of measurements.

time course of this experiment. Thus, the effects of $scCO_2$ exposure time may also be important; a possibility reinforced by the fact that the second test cycle at 12.0 MPa $scCO_2$ resulted in the highest capillary-trapped $scCO_2$ saturation (0.32, versus 0.20 in the first 12.0 MPa cycle). Given the very long time scales expected of geologic CO_2 sequestration, and the influence of time-dependent wettability changes on capillary trapping could be very important.

SUMMARY AND RESEARCH NEEDS

Wettability and capillary phenomena are critical to understand for predicting reservoir and caprock performance. Investigations on wetting and capillary behavior of brine-$scCO_2$ are clearly very complex, and require measurements over widely varying conditions. Studies to date have yielded diverse and sometimes inconsistent results, warranting further systematic testing. Overall, our results are showing that $scCO_2$ will enter silica-rich reservoirs more easily than expected because of decreased wettability, and will later be stored through capillary trapping at fairly high S_{nr}. More experimental investigations of this type are required, conducted with $scCO_2$ as well as with H_2S acid gases and different brines, in dominant types of reservoir materials, in order to improve predictions of $scCO_2$ behavior in geologic carbon sequestration. Much longer-term experiments conducted on the stability of capillary-trapped $scCO_2$ would clearly be valuable, given its currently assumed large contribution in geologic carbon sequestration. In each of these identified research areas, investigations into changes at interfaces are needed in order to determine underlying mechanisms for changes in wettability and capillary behavior.

ACKNOWLEDGMENTS

This material is based upon work supported as part of the Center for Nanoscale Control of Geologic CO_2, an Energy Frontier Research Center, funded by the U.S. Department of Energy, Office of Science, Office of Basic Energy Sciences under Award Number DE-AC02-05CH11231, and as part of the core program of the Chemical Sciences, Geosciences and Biosciences Division, Office of Science, Office of Basic Energy Sciences, of the US Department of Energy under Contract No. DE-AC02-05CH11231. Additional support for equipment was provided by ZERT and NRAP. The ZERT project was funded by the Assistant Secretary for Fossil Energy, Office of Sequestration, Hydrogen, and Clean Coal Fuels, through the National Energy Technology Laboratory (NETL), U.S. Department of Energy under Contract No. DE-AC02-05CH11231. Portions of this work were completed as part of National Risk Assessment Partnership (NRAP) project. Support for this project came from the DOE Office of Fossil Energy's Cross Cutting Research program. The authors wish to acknowledge Robert Romanosky (NETL Strategic Center for Coal) and Regis Conrad (DOE Office of Fossil Energy) for programmatic guidance, direction, and support. NRAP is a multi-lab effort that leverages broad technical capabilities across the DOE complex. NRAP involves five DOE national laboratories: NETL, Lawrence Berkeley National Laboratory, Lawrence Livermore National Laboratory, Los Alamos National Laboratory, and Pacific Northwest National Laboratory. This team is working together to develop a science-based method for quantifying the likelihood of risks (and associated potential liabilities) for CO_2 storage sites. The work in this paper was reviewed by members of the NRAP Technical Leadership Team, including Jens Birkholzer. NRAP funding was provided to Lawrence Berkeley National Laboratory under U.S. Department of Energy Contract No. DE-AC02-05CH11231. Portions of this work were performed at GeoSoilEnviroCARS (Sector 13), Advanced Photon Source (APS), Argonne National Laboratory. GeoSoilEnviroCARS is supported by the National Science Foundation - Earth Sciences (EAR-1128799) and Department of Energy - Geosciences (DE-FG02-94ER14466). Use of the Advanced Photon Source was supported by the U. S. Department of Energy, Office of Science, Office of Basic Energy

Sciences, under Contract No. DE-AC02-06CH11357. We thank Sam Krevor and Edo Boek (both at Imperial College London), and Alex Navrotsky (University of California, Davis) for helpful review comments.

REFERENCES

Akbarabadi M, Piri M (2013) Relative permeability hysteresis and capillary trapping characteristics of supercritical CO_2/brine systems: An experimental study at reservoir conditions. Adv Water Resour 52:190-206

Alkan H, Cinar Y, Ulker EB (2010) Impact of capillary pressure, salinity and in situ conditions on CO_2 injection into saline aquifers. Transport Porous Media 84:799-819

Amirfazli A (2004) On thermodynamics of thin films: The mechanical equilibrium condition and contact angles. J Adhesion 80:1003-1016

Anderson WG (1986) Wettability literature survey. Part 2: Wettability measurement. J Pet Technol 38:1246-1262

Anderson WG (1987) Wettability literature survey- Part 4: Effects of wettability on capillary pressure. J Pet Technol 39:1283-1300

Angeli M, Soldal M, Skurtveit E, Aker E (2009) Experimental percolation of supercritical CO_2 through a caprock. Energy Procedia 1:3351-3358

Bachu S, Bonijoly D, Bradshaw J, Burruss R, Holloway S, Christensen NP, Mathiassen OM (2007) CO_2 storage capacity estimation: Methods and gaps. Int J Greenhouse Gas Control 1:430-443

Bachu S, Bennion DB (2009) Interfacial tension between CO_2, freshwater, and brine in the range of pressure from (2 to 27) MPa, temperature from (20 to 125) °C, and water salinity from (0 to 334 000)mg·L^{-1}. J Chemical Engineering Data 54:765-775

Bennion DB, Bachu S (2010) Drainage and imbibition CO_2/brine relative permeability curves at reservoir conditions for carbonate formations. *In:* SPE Annual Technical Conference and Exhibition, p. 18, Society of Petroleum Engineers, Florence, Italy

Benson SM, Cole DR (2008) CO_2 sequestration in deep sedimentary formations. Elements 4:325-331

Bergstrom L (1997) Hamaker constants of inorganic materials. Adv Colloid Interface Sci 70:125-169

Bijeljic BA, Muggeridge H, Blunt MJ (2003) Multicomponent mass transfer across water films during hydrocarbon gas injection. Chem Eng Sci 58:2377-2388

Bikkina PK (2011) Contact angle measurements of CO_2-water-quartz/calcite systems in the perspective of carbon sequestration. Int J Greenhouse Gas Control 5:1259-1271

Bikkina PK, Shoham O, Uppaluri R (2011) Equilibrated interfacial tension data of the CO_2-water system at high pressures and moderate temperatures. Chem Engineering Data 56:3725-3733

Broseta D, Tonnet N, Shah V (2012) Are rocks still water-wet in the presence of dense CO_2 or H_2S? Geofluids12:280-294

Celia MA (2008) Geological storage as a carbon mitigation option. Henry Darcy Distinguished Lecture Series in Ground Water Science, figure from Robert Bruant. National Ground Water Research and Education Foundation

Chalbaud C, Robin M, Lombard JM, Martin F, Egermann P, Bertin H (2009) Interfacial tension measurements and wettability evaluation for geological CO_2 storage. Adv Water Resources 32:98-109

Chiquet P, Broseta D, Thibeau S (2007a) Wettability alteration of caprock minerals by carbon dioxide. Geofluids 7:112-122

Chiquet P, Daridon JL, Broseta D, Thibeau S (2007b), CO_2/water interfacial tensions under pressure and temperature conditions of CO_2 geological storage. Energy Convers Manage 48:736-744

Decker EL, Frank B, Suo Y, Garoff S (1999), Physics of contact angle measurement. Colloids Surfaces A: 156:177-189

Delclaud J (1991) Laboratory measurement of residual gas saturation. *In:* Second European Core Analysis Symposium, pp. 431-451, London

Demond AH, Roberts PV (1991) Effect of interfacial forces on two-phase capillary pressure-saturation relations. Water Resour Res 27: 423-437

Derjaguin BV, Churaev NV, Muller VM (1987) Surface Force. Consultants Bureau, New York

Dickson JL, Gupta G, Horozov TS, Binks BP, Johnston KP (2006) Wetting phenomena at the CO_2/water/glass interface. Langmuir 22:2161-2170

Doughty C (2007) Modeling geologic storage of carbon dioxide: Comparison of non-hysteretic and hysteretic characteristic curves. Energy Convers Manage 48:1768-1781

Duchateau C, Broseta D (2012) A simple method for determining brine-gas interfacial tensions. Adv Water Resour 42:30-36

Dullien FAL (1992) Porous Media Fluid Transport and Pore Structure, 2nd ed. Academic Press, San Diego

Espinoza DN, Santamarina JC (2010) Water-CO_2-mineral systems: Interfacial tension, contact angle, and diffusion-Implications to CO_2 geological storage. Water Resour Res 46:W07537

Farokhpoor R, Bjorkvik BJA, Lindeberg E, Torsaeter O (2013) Wettability behaviour of CO_2 at storage conditions. Int J Greenhouse Gas Control 12:18-25

Fleury M, Pironon J, Le Nindre YM, Bildstein O, Berne P, Lagneau V, Broseta D, Pichery T, Fillacier S, Lescanne M, Vidal O (2010) Evaluating sealing efficiency of caprocks for CO_2 storage: an overview of the Geocarbone-Integrity Program and results. Oil Gas Science Technol 65:435-444

Gittins P, Iglauer S, Pentland CH, Al-Mansoori S, Al-Sayari S, Bijeljic B, Blunt MJ (2010) Nonwetting phase residual saturation in sand packs. J Porous Media 13:591-599

Gregory J (1975) Interaction of unequal double layers at constant charge. J Colloid Interface Sci 51:44-51

Haines WB (1930) Studies in the physical properties of soil, V. The hysteresis effect in capillary properties, and the modes of moisture distribution associated therewith. J Agricultural Sci 20:97-116

Hamm LM, Bourg IC, Wallace AF, Rotenberg B (2013) Molecular simulation of CO_2- and CO_3-brine-mineral systems. Rev Mineral Geochem 77:189-228

Hiemenz PC, Rajagopalan R (1997) Principles of Colloid and Surface Chemistry. Third Edition, Revised and Expanded. Marcel Dekker, Inc., New York

Hirasaki GJ (1991a) Thermodynamics of thin films and three-phase contact regions. *In:* Interfacial Phenomena in Petroleum Recovery. Morrow NR (ed) Marcel Dekker, Inc., New York, p 23-76

Hirasaki GJ (1991b) Wettability: Fundamentals and surface forces. SPE Formation Evaluation 6:217-226

Hough DB, White LR (1980) The calculation of Hamaker constants from Lifshitz theory with applications to wetting phenomena. Adv Colloid Interface Sci 14:3-41

Ide ST, Jessen K, Orr FMJ (2007) Storage of CO_2 in saline aquifers: Effects of gravity, viscous, and capillary forces on amount and timing of trapping. Int J Greenhouse Gas Control 1:481-491

Iglauer S, Paluszny A, Pentland CH, Blunt MJ (2011a) Residual CO_2 imaged with X-ray micro-tomography. Geophys Res Lett 38:(L21403)

Iglauer S, Wulling W, Pentland CH, Al-Mansoori SK, Blunt MJ (2011b) Capillary-trapping capacity of sandstones and sandpacks. SPE J 16:778-783

Iglauer S, Mathew MS, Bresme F (2012) Molecular dynamics computations of brine-CO_2 interfacial tensions and brine-CO_2-quartz contact angles and their effects on structural and residual trapping mechanisms in carbon geo-sequestration. J Colloid Interface Sci 386:405-414

IPCC (2005) Underground geological storage. *In:* IPCC Special Report on Carbon Dioxide Capture and Storage. Cambridge University Press, Cambridge, p 195-276

Israelachvili JN (1991) Intermolecular and Surfaces Forces, 2nd edition. Academic Press, London

Juanes R, MacMinn CW, Szulczewski ML (2010) The footprint of the CO_2 plume during carbon dioxide storage in saline aquifers: Storage efficiency for capillary trapping at the basin scale. Transport Porous Media 82:19-30

Jung JW, Wan J (2012) Supercritical CO_2 and ionic strength effects on wettability of silica surfaces: Equilibrium contact angle measurements. Energy Fuels 26:6053-6059

Kaszuba JP, Janecky DR, Snow MG (2003) Carbon dioxide reaction processes in a model brine aquifer at 200 degrees C and 200 bars: implications for geologic sequestration of carbon. Appl Geochem 18:1065-1080

Kharaka YK, Cole DR, Hovorka SD, Gunter WD, Knauss KG, Freifeld BM (2006) Gas-water-rock interactions in Frio Formation following CO_2 injection: Implications for the storage of greenhouse gases in sedimentary basins. Geology 34:577-580

Kim TW, Tokunaga TK, Shuman DB, Sutton SR, Newville M, Lanzirotti A (2012a) Thickness measurements of nanoscale brine films on silica surfaces under geologic CO_2 sequestration conditions using synchrotron X-ray fluorescence. Water Resour Res 48:W09558

Kim Y, Wan J, Kneafsey TJ, Tokunaga TK (2012b) Dewetting of silica surfaces upon reactions with supercritical CO_2 and brine: Pore-scale studies in micromodels. Environ Sci Technol 46:4228-4235

Kim TW, Tokunaga TK, Bargar JR, Latimer MJ, Webb SM (2013) Brine film thicknesses on mica surfaces under geologic CO_2 sequestration conditions and controlled capillary pressures. Water Resour Res 49, doi:10.1002/wrcr.20404

Klute A, Wilkinson GE (1958) Some tests of the similar media concept of capillary flow: 1. Reduced capillary conductivity and moisture characteristic data. Soil Sci Soc Proc 22:278-281

Krevor SCM, Pini R, Li BX, Benson SM (2011) Capillary heterogeneity trapping of CO_2 in a sandstone rock at reservoir conditions. Geophys Res Lett 38:L15401

Land CS (1968) Calculation of imbibition relative permeability for two- and three-phase flow from rock properties. SPE J 8:149-156

Lefevre G, Jolivet A (2009) Calculation of Hamaker constants applied to the deposition of metallic oxide particles at high temperature. *In:* Proceedings of International Conference on Heat Exchanger Fouling and Cleaning VIII, Schladming, Austria, June 14-19, 2009. Muller-Steinhagen H, Malayerl MR, Watkinson AP (eds) Published online: *http://www.heatexchanger-fouling.com/papers/papers2009/16_Lefevre_Hamaker_F.pdf*

Leverett MC (1941) Capillary behavior in porous solids. Trans Am Inst Min Metall 142:152-169
Leverett MC, Lewis WB, True ME (1942) Dimensional-model studies of oil-field behavior. Trans Am Inst Mining Metall 146:175-193
Li D, Neumann AW (1991) Thermodynamics of contact angle phenomena in the presence of a thin liquid film. Adv Colloid Interface Sci 36:125-151
Li SW, Dong M, Li Z, Huang S, Qing H, Nickel E (2005) Gas breakthrough pressure for hydrocarbon reservoir seal rocks: implications for the security of long-term CO_2 storage in the Weyburn field. Geofluids 5:326-334
Li ZW, Dong MZ, Li SL, Huang S (2006) CO_2 sequestration in depleted oil and gas reservoirs - caprock characterization and storage capacity. Energy Convers Manage 47:1372-1382
Li X, Boek E, Maitland GC, Trusler JPM (2012) Interfacial tension of (brine + CO_2): (0.864 NaCl + 0.136 KCl) at temperatures between (298 and 448) K, pressures between (2 and 50) MPa, and total molalities of (1 to 5) mol·kg-1. J Chem Eng Data 57:1078-1088
Li X, Ross DA, Trusler JPM, Maitland GC, Boek ES (2013), Molecular dynamics simulations of CO_2 and brine interfacial tension at high temperatures and pressures. J Phys Chem B 117:5647-5652
Loring JS, Thompson CJ, Wang Z, Joly AG, Sklarew DS, Schaef HT, Ilton ES, Rosso KM, Felmy AR (2011) In situ infrared spectroscopic study of forsterite carbonation in wet supercritical CO_2. Environ Sci Technol 45:6204-6210
Mazzoco RR, Wayner PC (1999) Aqueous wetting films on fused quartz. J Colloid Interface Sci 214:156-169
McCool B, Tripp CP (2005) Inaccessible hydroxyl groups on silica are accessible in supercritical CO_2. J Phys Chem B 109:8914-8919
McGrail BP, Schaef HT, Glezakou VA, Dang LX, Owen AT (2009) Water reactivity in the liquid and supercritical CO_2 phase: Has half the story been neglected? Energy Procedia 1:3415-3419
Miller EE, Miller RD (1956) Physical theory for capillary flow phenomena. J Appl Phys 4:324-332
Mills J, Riazi M, Sohrabi M (2011) Wettability of common rock-forming minerals in a CO_2-brine system at reservoir conditions. Paper presented at International Symposium of the Society of Core Analysts, Austin, United States, p 1-12
Morrow NR (1975) The effects of surface roughness on contact angle with special reference to petroleum recovery. J Can Pet Technol 14:42-53
Morrow NR (1990) Wettability and its effect on oil recovery. J Pet Technol 42:1476-1484
Moseley WA, Dhir VK (1996) Capillary pressure-saturation relations in porous media including the effect of wettability. J Hydrology 178:33-53
Nielsen LC, Bourg IC, Sposito G (2012) Predicting CO_2-water interfacial tension under pressure and temperature conditions of geologic CO_2 storage. Geochim Cosmochim Acta 81:28-38
Novy RA, Toledo PG, Davis HT, Scriven LE (1989) Capillary dispersion in porous media at low wetting phase saturations. Chem Eng Sci 44:1785-1797
Oldenburg CM, Doughty C (2011) Injection, flow, and mixing of CO_2 in porous media with residual gas. Transport Porous Media 90:201-218
Parlange JY (1974) Scaling by contact angle. Soil Sci Soc Am Proc 38:161-162
Parsegian VA (2006) Van der Waals Forces. Cambridge University Press, Cambridge
Pentland CH, Al-Mansoori S, Iglauer S, Bijeljic B, Blunt MJ (2008) Measurement of non-wetting phase trapping in sand packs. *In:* SPE Annual Technical Conference and Exhibition, SPE, Denver, CO, p. 11,
Pentland CH, El-Maghraby R, Iglauer S, Blunt MJ (2011) Measurements of the capillary trapping of supercritical carbon dioxide in Berea sandstone. Geophys Res Lett 38:L06401
Perrin JC, Benson SM (2010) An experimental study on the influence of sub-core scale heterogeneities on CO_2 distribution in reservoir rocks. Transport Porous Media 82:93-109
Philip JR (1969) Theory of infiltration. Adv Hydrosci 5:215-296
Philip JR (1971) Limitations on scaling by contact angle. Soil Sci Soc Am Proc 35:507-509
Pini R, Krevor SCM, Benson SM (2012) Capillary pressure and heterogeneity for the CO_2/water system in sandstone rocks at reservoir conditions. Adv Water Resour 38:48-59
Pini R, Benson SM (2013) Simultaneous determination of capillary pressure and relative permeability curves from core-flooding experiments with various fluid pairs. Water Resour Res 49:3516-3530, doi: 10.1002/wrcr.20274
Plug WJ, Bruining J (2007), Capillary pressure for the sand-CO_2-water system under various pressure conditions. Application to CO_2 sequestration. Adv Water Resour 30:2339-2353
Rose W, Bruce WA (1949) Evaluation of capillary character in petroleum reservoir rock. Trans Am Inst Min Metall Eng 186:127-142
Saraji S, Goual L, Piri M, Planchar H (2013) Wettability of supercritical carbon dioxide/water/quartz systems: Simultaneous measurement of contact angle and interfacial tension at reservoir conditions. Langmuir 29:6856-6866

Schaef HT, McGrail BP, Loring JL, Bowden ME, Arey BW (2013) Forserite [Mg_2SiO_4] carbonation in wet supercritical CO_2: An in situ high-pressure X-ray diffraction study. Environ Sci Technol 47:174-181

Schroth MH, Ahearn SJ, Selker JS, Istok JD (1996) Characterization of Miller-similar silica sands for laboratory hydrologic studies, Soil Sci Soc Am J 60:1331-1339

Shao H, Ray JR, Jun YS (2011) Effects of salinity and the extent of water on supercritical CO_2-induced phlogopite dissolution and secondary mineral formation. Environ Sci Technol 45:1737-1743

Sharma A (1993) Equilibrium contact angles and film thicknesses in the apolar and polar systems: Role of intermolecular interactions in coexistence of drops with thin films. Langmuir 9:3580-3586

Siemons N, Bruining H, Castelijns H, Wolf KH (2006) Pressure dependence of the contact angle in a CO_2-H_2O-coal system. J Colloid Interface Sci 297:755-761

Span R, Wagner W (1996) A new equation of state for carbon dioxide covering the fluid region from the triple-point temperature to 1100 K at pressures up to 800 MPa. J Phys Chem Ref Data 25:1509-1596

Spiteri EJ, Juanes R, Blunt MJ, Orr FMJ (2008) A new model of trapping and relative permeability hysteresis for all wettability characteristics. SPE J 13:277-288

Suekane T, Soukawa S, Iwatani S, Tsushima S, Hirai S (2005) Behavior of supercritical CO_2 injected into porous media containing water. Energy 30:2370-2382

Tanino Y, Blunt MJ (2012) Capillary trapping in sandstones and carbonates: Dependence of pore structure. Water Resour Res 48:W08525

Tokunaga TK, Wan J, Sutton SR (2000) Transient film flow on rough fracture surfaces. Water Resour Res 36:1737-1746

Tokunaga TK, Olson KR, Wan J (2004) Conditions necessary for capillary hysteresis in porous media: Tests of grain size and surface tension influences. Water Resour Res 40:WO5111

Tokunaga TK (2011) Physicochemical controls on adsorbed water film thickness in unsaturated geological media. Water Resour Res 47:W08514

Tokunaga TK (2012) DLVO-based estimates of adsorbed water film thicknesses in geologic CO_2 reservoirs. Langmuir 28:8001-8009

Tokunaga TK, Wan J, Jung JW, Kim TW, Kim Y, Dong W (2013) Capillary pressure and saturation relations for supercritical CO_2 and brine in sand: High-pressure $P_c(S_w)$ controller/meter measurements, and capillary scaling predictions. Water Resour Res 49, doi: 10.1002/wrcr.20316

Tonnet N, Shah V, Chiquet P, Diaz J, Mouronval G, Broseta D (2008) Wettability alteration of caprock minerals by acid gases. Proceedings of the 10th International Symposium on Reservoir Wettability, Abu Dhabi, 26-28 October, 2008

Verwey EJW, Overbeek JTG (1948) Theory of the Stability of Lyophobic Colloids. Dover Publications, Mineola, NY

Wang S, Edwards IM, Clarens AF (2013) Wettability phenomena at the CO_2-brine-mineral interface: Implications for geologic carbon sequestration. Environ Sci Technol 47:234-241

Wollenweber J, Alles S, Kronimus A, Busch A, Stanjek H, Krooss BM (2009) Caprock and overburden processes in geological CO_2 storage: An experimental study on sealing efficiency and mineral alterations. Energy Procedia 1:3469-3476

Wollenweber J, Alles S, Busch A, Krooss BM, Stanjek H, Littke R (2010) Experimental investigation of the CO_2 sealing efficiency of caprocks. Int J Greenhouse Gas Control 4:231-241

Xu JQ (2008) Modeling unsteady-state gravity-driven flow in porous media. J Petroleum Sci Eng 62:80-86

Yang DY, Gu YG, Tontiwachwuthikul P (2008) Wettability determination of the reservoir brine-reservoir rock system with dissolution of CO_2 at high pressures and elevated temperatures. Energy Fuels 22:504-509

Zhou QL, Birkholzer JT, Mehnert E, Lin YF, Zhang K (2010) Modeling basin- and plume-scale processes of CO_2 storage for full-scale deployment. Ground Water 48:494-514

Reviews in Mineralogy & Geochemistry
Vol. 77 pp. 505-539, 2013
Copyright © Mineralogical Society of America

Geochemistry of Wellbore Integrity in CO_2 Sequestration: Portland Cement-Steel-Brine-CO_2 Interactions

J. William Carey

Earth and Environmental Sciences Division
Los Alamos National Laboratory
Los Alamos, New Mexico 87545, U.S.A.

bcarey@lanl.gov

INTRODUCTION

Geochemistry and wellbore integrity in CO_2 sequestration

Effective geologic sequestration of CO_2 requires long-term storage with very low leak rates. Injection wells are an obvious leakage pathway for CO_2 because they perforate the confining caprock. In addition, sequestration sites are likely to use monitoring wells to assess performance and, in the case of depleted oil and gas fields, may contain 10s to 1000s of older operating and abandoned wells.

All wells may have leakage pathways due to faulty construction or other defects. However, it is the subject of this chapter to consider whether geochemical reactions induced by CO_2 could result in damage to wells and the development of leaks. This concern is based on the thermodynamic incompatibility of CO_2-saturated fluids with the Portland cement and steel used to prevent fluid migration to the surface. Portland cement is an alkaline substance with pH > 12.5 and is not in equilibrium with CO_2-bearing fluids (pH < 6). Low-carbon steel used as well casing is subject to aggressive corrosion by carbonic acid. As a result, well integrity has been a central issue in risk analysis of sequestration sites (Gasda et al. 2004; IPCC 2005; Viswanathan et al. 2008; Nordbotten et al. 2009).

At the outset, it is important to bear in mind that geochemical reactions alone do not yield insight into wellbore integrity, which is governed primarily by the effective permeability of the Portland cement seal and the mechanical integrity of the system. Thus the significance of chemical reactions must be considered with respect to their impact to changes in permeability or in strength. There is an unfortunate tendency in the literature to not distinguish between reaction and impact. Often CO_2 reactions are described as "degradation of cement" or "corrosion of cement" without adequately defining what these terms encompass. They certainly suggest a deterioration in performance, but often such studies show only that materials have reacted and do not address the impact or significance of reactions on integrity (also see Zhang and Bachu 2011).

The CO_2-specific literature on carbonation of cement and the corrosion of steel is quite recent and necessarily of somewhat limited extent. However, there is earlier work on CO_2-cement interactions in relation to CO_2-enhanced oil recovery (CO_2-EOR) and geothermal systems (Onan 1984; Bruckdorfer 1986; Milestone et al. 1986; Shen and Pye 1989). There is also a very substantial body of work on carbonation of Portland cement and corrosion of reinforcing steel and pipelines in the building materials literature (e.g., Papadakis et al. 1991; Cabrera 1996). While this earlier work for construction applications provides useful

1529-6466/13/0077-0015$05.00 http://dx.doi.org/10.2138/rmg.2013.77.15

insights, the results must be qualified by the different environmental conditions for building materials and wells in the deep subsurface. Portland cement in wells is subject to CO_2-induced reactions at supercritical conditions rather than at a thousandth of an atmosphere and, perhaps more critically, occur under water-saturated conditions. In contrast, relative humidity is a key variable controlling the rate of CO_2 penetration in building materials (e.g., Bary and Sellier 2004; Glasser et al. 2008). CO_2-induced corrosion has been studied at high pressures that exist in pipelines (35-70 bar; e.g., Nešić 2007). However, sequestration involves a distinct geochemical environment. For both cement and steel, a critical variable is the rate of flow of reactive fluids, which in some geologic environments may be highly restricted.

This review considers field, experimental and numerical studies of the geochemical impact of CO_2 on Portland cement and steel in relation to wellbore integrity. The focus is on water-mediated reactions. Several studies have considered direct reaction of supercritical CO_2 with cement or steel (Kutchko et al. 2007, 2009; Rimmelé et al. 2008; McGrail et al. 2009), but these results are not reviewed here. Water is ubiquitous in the wellbore environment, whether as free phase, residual phase, surface films or mineral hydrates. There may be true dry-out zones adjacent to CO_2 injection perforations, but in the wellbore-caprock region, CO_2 is unlikely to completely desiccate or displace the water. Previous reviews of the wellbore integrity problem in CO_2 sequestration include Zhang and Bachu (2011).

Leakage in wells

Leakage in wells can be defined as any unwanted migration of fluids from any component of the well system. This is critical in the injection well, which must handle high-pressure CO_2. The injection well is likely to be purpose-built for the sequestration project and subject to regulations governing construction methods and materials and will be subject to monitoring. As such, there is less concern about leakage from injection wells than leakage from wells not specifically designed for CO_2 that already exist and penetrate the CO_2 storage reservoir. These wells may be operational or plugged, and the primary leakage pathways involve CO_2 migrating along the external annulus between the external casing and the rock formation (Fig. 1).

Gasda et al. (2004) outlined the key mechanisms of CO_2 leakage for non-injection wells (Fig. 1). The conceptual model is that CO_2 migrates through the storage reservoir, encounters a monitoring well or an old, perhaps abandoned well, and has the potential to leak toward the surface via:

1. Interfaces between cement and rock
2. Cement matrix permeability
3. Fractures/defects in the cement
4. Interfaces between cement and steel casing
5. Holes within the steel casing

The key geochemical questions are twofold. Can CO_2 create these pathways by dissolution of cement or corrosion of steel? Once these pathways exist, do CO_2-induced reactions result in enhanced permeability due to dissolution or reduced permeability due to precipitation? I argue that in most cases reactions alone are insufficient to create leakage pathways because of the length of the protective Portland cement (10s-100s m).

As reflected by Figure 1, the type of leakage considered here is the relatively slow migration of CO_2 ± brine from the storage reservoir toward the surface. The primary risks are damage to drinking water aquifers, the potential for accumulations of CO_2 at the surface that harm the environment or human health, and the defeat of the very purpose of sequestration, permanent storage of CO_2 (e.g., IPCC 2005). These leakage concerns are closely related to wellbore integrity problems known as sustained casing pressure (SCP). Causes of SCP

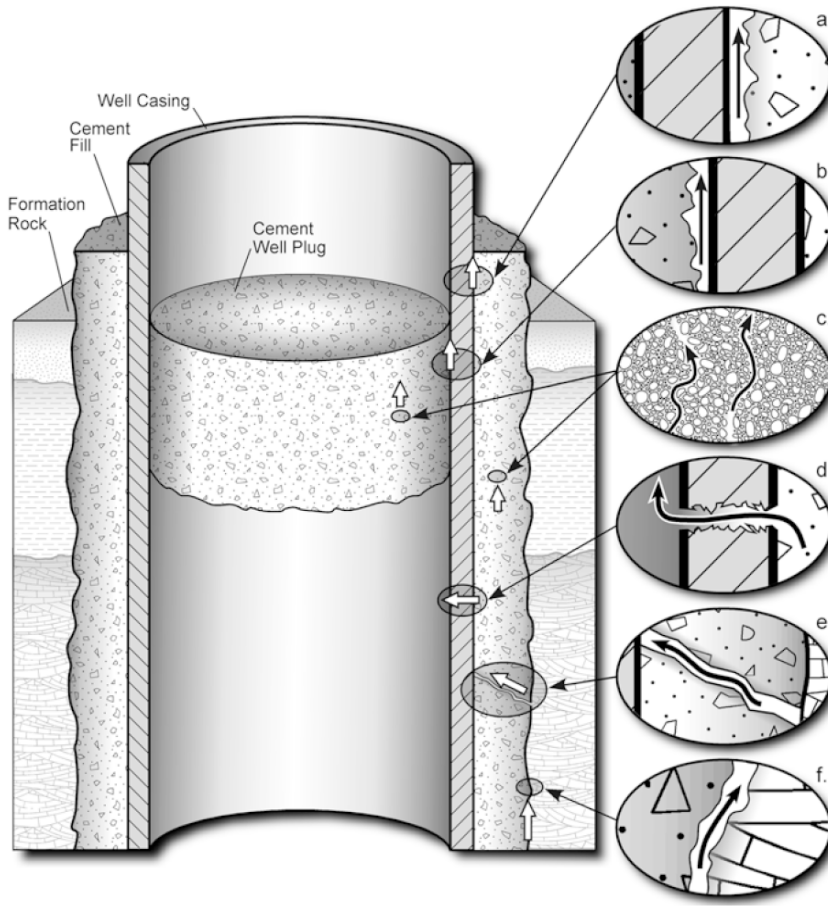

Figure 1. Wellbore leakage mechanisms in a plugged and abandoned well. Migration pathways could occur along the casing-cement interface (a,b), through cement matrix permeability (c), via corrosion of the steel casing (d), through fractures in the cement , and along the cement-rock interface. [With kind permission of Springer Science and Business Media, from Gasda et al. (2004), *Environmental Geology,* Vol. 46, Fig. 1, p.709.]

were reviewed by Wotjanowicz (2008) and include failure of cement to isolate fluids in the subsurface. Watson and Bachu (2007, 2008) review well-construction risk factors in the development of SCP. The appearance of a typical SCP problem is shown in Figure 2.

Other research areas relevant to geochemistry and wellbore integrity

The geochemistry of wellbore integrity has several applications outside of CO_2 sequestration. Well integrity is a central concern of all oil and gas operations including CO_2-enhanced oil recovery. Well integrity plays a key role in the controversy over the use of hydrofracking for shale gas as leaking wells are one of the most plausible modes of methane migration to the surface (Osborn et al. 2011). Other applications include acid gas disposal (injection of $H_2S \pm CO_2$) and other waste disposal operations involving injection into the subsurface.

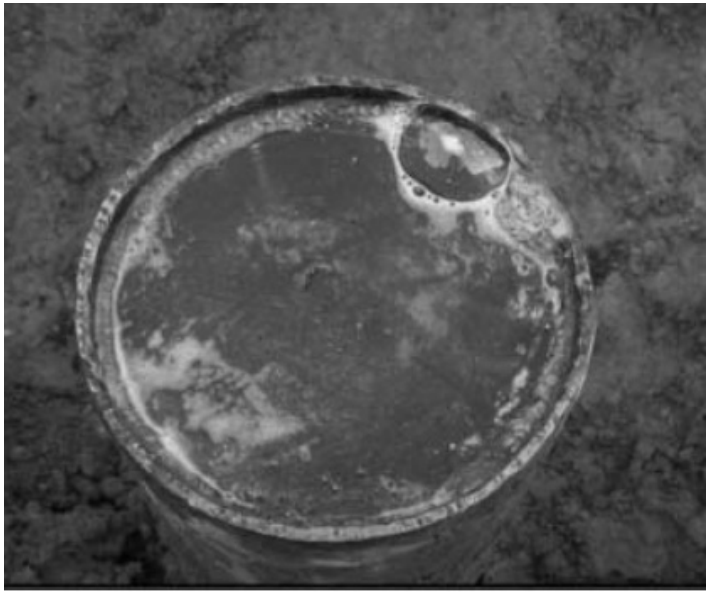

Figure 2. Methane gas bubbles leaking from an abandoned well due to sustained casing pressure: an analog for CO_2 leakage. [Copyright 2007, E&P Environment and Safety Conference. Reproduced with permission of SPE. From Watson and Bachu (2007), Fig. 11.]

CHARACTER OF THE WELLBORE ENVIRONMENT

Construction and physical features

Well construction consists of drilling the borehole, setting steel casing and cementing the pipe with Portland cement (Fig. 3). Drilling involves circulating drilling mud down the hole to cool the bit and to carry cuttings back to the surface. Drilling proceeds in stages with a series of decreasing borehole diameters. At each stage, steel casing is lowered into the hole and is cemented into place by first circulating fluid to remove the drilling mud and then injecting a Portland cement slurry down the drill pipe and back toward the surface along the outside of the casing. Cleaning the hole of drilling mud is essential to allowing a good bond to develop between the Portland cement and the steel and rock surfaces. The Portland cement prevents fluids from migrating between the casing and rock formation, which is known as creating zonal isolation.

The first drilling stage sets a conductor casing, which is used to stabilize unconsolidated surface sediments. By regulation, actual or potential drinking water sources are protected with a surface casing that is set below any such aquifers and which is cemented to the surface. Depending on depth and many other factors, one or more casings are set to reach total depth of the well. Note that these subsequent casings (e.g., the production casing) may or may not be cemented back to the surface. They are generally cemented across the reservoir and up into the impermeable caprock that traps the reservoir fluids.

Well integrity involves the successful production (or injection) of fluids from the reservoir and the isolation of fluids in the reservoir and overlying units to prevent their communication or migration to the near surface.

Problems due to migration of fluids can be divided into operational failures, faulty construction and subsequent well-material degradation (e.g., Wojtanowicz 2008). Operational

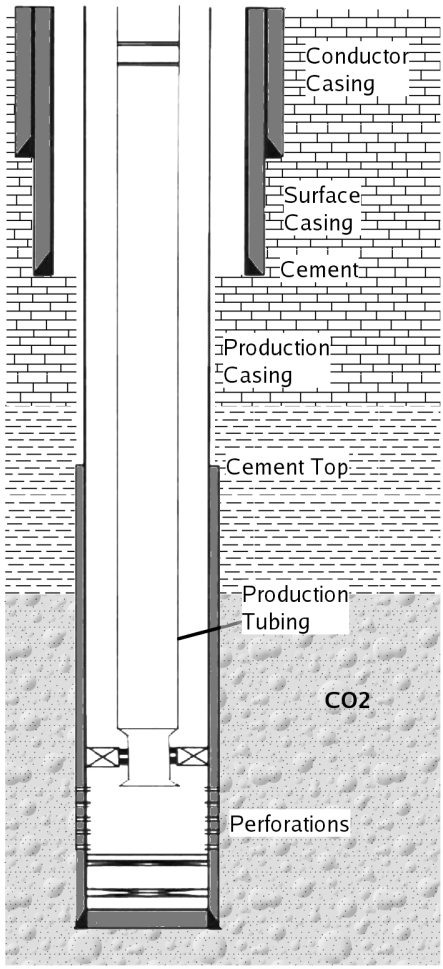

Figure 3. Schematic diagram illustrating the primary features of the wellbore including a nested set of steel casing and Portland cement used to create zonal isolation. Not to scale: borehole diameters at depths of 0.5-3 km are about 20 cm.

issues are focused on prevention of the loss of drilling fluids to rock formations and the influx of formation fluids into the borehole that can result in blowouts and are mitigated by the use of proper weighting of drilling mud, placement of cement and use of blowout preventers. Construction issues have to do with failures to place well-bonded cement uniformly around the steel casing and arise from poor centralization of casing, formation damage (caving or flow of cement into the formations), failure to clear drilling mud (contamination of cement with mud), formation of gas channels within the cement, inadequate bonding of cement to steel or formation, insufficient cement coverage, or shrinkage of cement during curing. These problems can be minimized by following best practices (e.g., API 2010) and by post-cementing logging to evaluate cement quality.

Following completion of the well, integrity problems can arise from well-material degradation induced by mechanical, thermal and chemical stresses. Mechanical and thermal stresses arise from changes in the formation pressure (due to depletion or injection of fluids), production/injection of relatively hot/cold fluids that expand/contract the steel casing, changes in the internal pressure of the casing due to well operations. Any of these processes can create a microannulus at the cement-steel or cement-rock interface or fracture the cement (see Fig. 1).

This review focuses on the geochemical stresses induced by incompatibilities between CO_2-bearing fluids migrating through the external annulus of the well and the Portland cement and steel providing zonal isolation. Dissolution and precipitation reactions in cement can alter the hydrologic and/or mechanical properties of the cement resulting in loss of zonal isolation. This can happen due to loss of material (erosion) at interfaces or due to increased permeability allowing fluids to migrate through the cement matrix. In contrast, corrosion of steel allows fluids to communicate between inside and outside of the pipe potentially allowing fast paths for fluid migration to the surface (Figs. 1 and 3).

In a properly constructed well, there is little potential for CO_2-bearing fluids in the reservoir to chemically impact well integrity because the fluids would have to eat their way vertically through 10s to 100s of meters of cement and steel (Fig. 3). There is potential for fluids in formations to attack cement (e.g., sulfate attack) or corrode exposed steel, but the rate of fluid movement migrating through the formation toward the wells is likely to be small and so these reactions are diffusion limited and likely to be small.

The most important role of geochemical reactions is in acting on pathways created by mechanical stresses (e.g., a microannulus at the cement-steel interface) or created by construction problems that provide avenues for fluid migration. Once fluids have access to the well and can flow at significant volumes in response to pressure gradients between permeable formations, then chemical reactions have the potential to either worsen the situation by eroding cement or corroding steel or actually healing the breach by precipitation of migrating cement phases or secondary phases such as carbonate.

Physical and chemical conditions at the wellbore

The most likely sequestration targets are sedimentary basins at depths > 1 km (to ensure supercritical or dense phase CO_2) to depths of 4 km (a maximum limited by costs and decreasing permeability with depth). The associated (hydrostatic) pressures are on the order of 100 to 400 bars. As sedimentary basins, these are relatively cool with temperatures ranging from 40 to perhaps 120 °C. The primary targets are depleted oil and gas reservoirs or non-potable (> 10,000 ppm) saline aquifers. In many cases, the targets will have very high salinity brines ranging from 100-300 ppt dissolved solids, requiring Pitzer-type aqueous speciation models in reactive transport calculations. These environments may also include appreciable gas such as H_2S, CH_4, and/or CO_2 but will generally lack O_2 (Berner 1981; Kharaka and Hanor 2003).

There has been considerable variation in conceptual models of the nature of fluids produced by CO_2 sequestration and their interaction with wellbore materials. Some studies have emphasized the potential for pure (i.e., without alkalinity) CO_2-brines encountering well cement or steel (e.g., Duguid and Scherer 2010). These have the minimum possible pH (between 3.0 and 3.25), and thus are at greatest disequilibrium with the well. Other studies have argued that although a local region adjacent to injection perforations may see such fluids, any migration of the CO_2+brine will result in buffering reactions (particularly with carbonates) such that CO_2-brine fluids are effectively in equilibrium with calcite at pH of about 4.5-5.0 (e.g., Carey et al. 2010; Zhang and Bachu 2011). This distinction carries through to considerations of injection of CO_2 into sandstone as compared with carbonates (e.g., Duguid et al. 2011). However, most sandstone contains some carbonate and other reactive minerals such that the existence of unbuffered fluids seems unlikely.

The potential role of "dry" supercritical CO_2 has been discussed by McGrail et al. (2009) and further developed in studies such as Springer et al. (2012). Several experimental studies have examined reactions with supercritical CO_2 (e.g., Kutchko et al. 2007; Barlet-Gouédard et al. 2009; Felmy et al. 2012) and demonstrated differences in behavior relative to CO_2-saturated brine. However, it appears that water must be present for chemical reactivity and consideration of the wellbore environment suggests that except immediately adjacent to injection perforations in the well, water will always be present. In addition, some systems, including cement and shale, always have interstitial water available for reaction and produce additional water during carbonation reactions. In this review, consideration is given only to reactions with CO_2-saturated brines as these appear to be predominant, and in any case, water is necessary for significant mass transfer.

Role of coupled processes

This review emphasizes geochemistry, but, in terms of well integrity, chemical reactions cannot be isolated from fluid flow and geomechanical processes. As discussed above, in order to have significant impact in the wellbore environment, chemical reactions require fluid flow along either existing defects or mechanically induced damage zones. In addition, since the measure of well integrity is zonal isolation, chemical reactions must be considered in terms of their impact on hydrologic and mechanical properties. While the impact of CO_2 on cement properties has been studied, little is known about the behavior of defects and other interfaces of importance in the wellbore system. Thus the analysis of chemical reactions must bear in mind

what processes exist that allow fluids to migrate and should judge the impact of reactions not on whether reactions have occurred but as to whether the reactions have degraded or perhaps enhanced the hydrologic or mechanical integrity of the system.

CEMENT

Background on Portland cement

Portland cement is a hydraulic cement, which means that it sets (hardens) when combined with water creating a product that is impervious to water. The setting process does not involve drying but involves the chemical reaction of water with cement powder to produce new mineral phases that give cement its structural properties. Portland cement is manufactured by heating limestone with some clay and quartz-bearing clastic material in a kiln to temperatures in excess of 1,400 °C. The resulting mixture (clinker) consists predominantly of four compounds: Ca_2SiO_4, Ca_3SiO_5, $Ca_3Al_2O_6$ and $Ca_4Al_2Fe_2O_{10}$. These are ground together with gypsum to produce a fine Portland cement powder. (See, e.g., Taylor 1990 for more details.)

The addition of water to Portland cement powder results in exothermic hydration reactions that produce four primary phases: in a typical Portland cement 93% of the hydration products are composed of calcium silica hydrate (C-S-H), portlandite, monosulfate-type phases and ettringite phases (Table 1; Taylor 1990).

The primary binding agent in hydrated cement is the C-S-H phase, which is fibrous in nature. A note on terminology: strictly speaking, cement is the dry powder and the mixture with water is a hydrated cement. Concrete is a mixture of Portland cement and aggregate consisting of coarse pebbles and fine sand. Mortar and grout are both mixtures of Portland cement and fine aggregate (sand); mortar is used as a structural element bonding together, for example, bricks; grout is used to fill spaces or gaps and is commonly used to describe oilwell cement.

A large variety of additives are used in oilwell cement that include materials to accelerate or retard setting, to modify density (e.g., barite or bentonite), to control fluid-loss and to disperse cement particles. Fly ash is commonly used to extend the cement (as a low-cost supplement to Portland cement) and/or to reduce the density of the cement. Additional details on Portland cement manufacture and chemistry can be found in many references including Taylor (1990). Portland cement is also the subject of Volume 74 of the Reviews in Mineralogy and Geochemistry series (Broekmans and Pöllman 2012).

Thermodynamic properties of cement and model cement systems

The cement chemical system is comprised of CaO-SiO_2-H_2O-Al_2O_3-Fe_2O_3-SO_3-Na_2O-K_2O-CO_2. Because of the calcining process in the manufacture of cement clinker, the system contains negligible ferrous iron. Solid solution is important in all of the hydrated cement phases except portlandite, with common substitutions including ferric iron for aluminum; a

Table 1. Primary cement phases in ordinary Portland cement (from Taylor 1990). AFm and AFt in cements refers to groups of calcium-alumino-ferric phases with either one (mono) or three (tri) sulfates per formula unit.

Phase	Formula	Volume %	Notes
Portlandite	$Ca(OH)_2$	19%	
Calcium-silica-hydrate (C-S-H)	$Ca_rSiO_{2+r}\cdot r\ H_2O$	48%	Idealized formula, r = 1.7
Monosulfate	$Ca_4Al_2(OH)_{12}SO_4\cdot 6H_2O$	18%	AFm phases
Ettringite	$Ca_6Al_2(OH)_{12}(SO_4)_3\cdot 26H_2O$	9%	AFt phases

calcium hydroxide-silica exchange; substitutions among hydroxyl, carbonate, chloride, and sulfate; and variable hydration states. Many of these substitutions form distinct crystalline entities making the number of potential phases in the system quite large (see Taylor 1990). Because of the poorly defined chemistry and thermodynamic properties of C-S-H, some studies use jennite ($Ca_9Si_6O_{18}(OH)_6{\cdot}8(H_2O)$) and/or tobermorite ($Ca_{4.3}Si_{5.5}Al_{0.5}O_{16}(OH)_2{\cdot}4(H_2O)$) as better crystalized analog phases to C-S-H. These phases are known to have structural elements in common with the mostly amorphous C-S-H (Richardson 2004).

There are many other minor phases that occur in ordinary Portland cement, as higher temperature reaction products, or as reaction products due to infiltration of fluids. These include calcium carbonate, brucite ($Mg(OH)_2$), hydrotalcite-type minerals ($Mg_6Al_2(CO_3)(OH)_{16}{\cdot}4(H_2O)$ with ferric iron), and hydrogarnets ($Ca_3Al_2(OH)_{12}$ with ferric iron and silica substitutions).

In reaction of cement with CO_2 and brine, three polymorphs of calcium carbonate occur: calcite, aragonite and vaterite. The metastable polymorphs are common because of the very high degree of disequilibrium between Portland cement and CO_2-saturated fluids. However, the relative abundance and temporal evolution of the polymorphs is not understood. In addition, the potential exists for differences in polymorphs in reactions with CO_2-saturated brine versus the supercritical CO_2 phase. An example of the spatial distribution of polymorphs in the field is given in Crow et al. (2010), who showed a preponderance of aragonite in the CO_2 reservoir, calcite just above the reservoir, and vaterite at 20 m into the caprock.

The thermodynamic end-state of CO_2-reacted Portland cement is an assemblage of calcium carbonate and oxide/hydroxides of silica, alumina and iron (Table 2; Taylor 1990). Several intermediate phases in this process may appear such as decalcified C-S-H or carbonated alumino-silicate hydrates.

Thermodynamic data for cement phases exist from a variety of sources (e.g., the Lawrence Livermore National Laboratory database, slop98.dat and its implementation in PHREEQC and Geochemist's Workbench; Marty et al. 2009). However, thermodynamic analysis of cement is limited by the poor crystallinity of most phases, including C-S-H, monosulfate, and several of the reaction products. For end-member compositions, one of the more complete and cement-specific collections is available from experimental and modeling work developed by a group from the University of Aberdeen and the Federal Materials Laboratory (ETH) in Switzerland

Table 2. Secondary minerals precipitating in CO_2-reacted Portland cement. The value of r in the formula for C-S-H is approximately 1.8 and y increases from 0 to about 1.65 in progressively decalcified C-S-H (Chen et al. 2004).

Phase	Formula
Calcium carbonate (calcite, aragonite, vaterite)	$CaCO_3$
Decalcified C-S-H	$Ca_{r-y}SiO_{2+r-y}{\cdot}(r-y)\ H_2O$
Friedel's salt	$Ca_4Al_2(OH)_{12}Cl_2{\cdot}6H_2O$
Amorphous silica	SiO_2
Amorphous alumina	$Al(OH)_3$
Amorphous iron hydroxide	$Fe(OH)_3$
Brucite	$Mg(OH)_2$
Thaumasite	$Ca_3Si(CO_3)(SO_4)(OH)_6{\cdot}12(H_2O)$
Carboaluminate	$3CaO{\cdot}Al_2O_3{\cdot}CaCO_3{\cdot}12(H_2O)$

(see especially Matschei et al. 2007 and Lothenbach et al. 2008) available through the EMPA group at the Federal Materials Lab via *http://www.empa.ch/cemdata*. It includes approximately 33 phases and was developed in conjunction with the reaction code GEM-SELEKTOR at the Paul Scherer Institute in Switzerland (Kulik et al. 2003).

Unfortunately, the cement database is not readily used in typical geochemical reaction codes as mineral properties are given in terms of the Gibbs free energy rather than the solubility products that are used in many codes. An implementation of the database suitable for use in PHREEQC or Geochemist's Workbench is available from the author (Carey 2010).

Solid solution in C-S-H crystal chemistry

As mentioned earlier, many of the phases show solid solution. None are as important as C-S-H, the main binding phase in cement. In response to changing chemical environments, C-S-H varies between Ca-rich and Si-rich compositions:

$$Ca_rSiO_{2+r}{\cdot}r\ H_2O = Ca_{r-y}SiO_{2+r-x}{\cdot}(r-y)\ H_2O + yCa^{2+} + 2y\ OH^- \quad (1)$$

(Note that the chemical formula used in Eqn. 1 is idealized; cf. Richardson 2004.) As reflected in the chemical reaction, C-S-H composition is sensitive to pH and is decalcified in acidic environments, including CO_2-saturated water. The C-S-H phase is complex and does not appear to represent a single structural type having a crystal chemistry-controlled chemical substitution (Chen et al. 2004). However, taking an empirical approach, Gartner and Jennings (1987) suggested a simplified solid solution model for C-S-H spanning fictional calcium hydroxide and silica end-members:

$$Ca_rSiO_{2+r}{\cdot}r\ H_2O = (1+r)[(1-x)Ca(OH)_2 + xSiO_2] \quad (2)$$

where x is the mole fraction silica in the C-S-H phase. Carey and Lichtner used this end-member model and the solubility of Chen et al. (2004) to develop a solid solution model for C-S-H (Fig. 4). The non-ideal, asymmetric model correctly predicts an alyotropic minimum

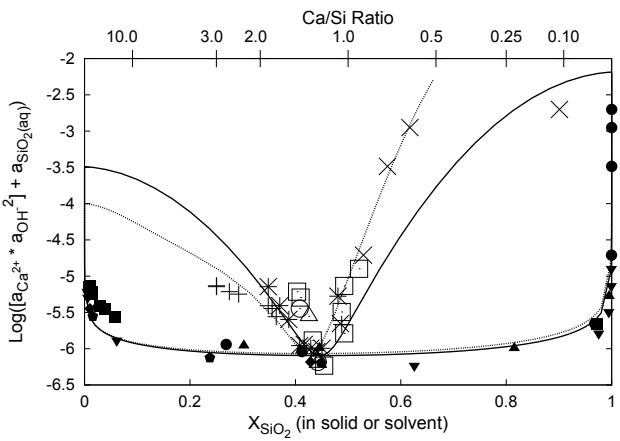

Figure 4. Experimental data (Chen et al. 2004) for the solubility of C-S-H phases of varying Ca/Si ratio expressed as mol-fraction SiO_2 versus aqueous concentration in a Lippmann diagram. Solid symbols are liquid compositions; open symbols, crosses and Xs are solid compositions. The curves represent two thermodynamic model fits to the data. The solid curve represents complete solubility between the $Ca(OH)_2$ and SiO_2 endmembers; the dotted curve shows more limited solubility of the silica-rich endmember. [This material is reproduced with permission of John Wiley & Sons, Inc, from Carey and Lichtner (2007), *Transport Properties and Concrete Quality*, Fig. 2, p. 75.]

point where the solid dissolves congruently to a liquid of its own composition (X_{SiO2} = 0.44). C-S-H phases richer in SiO_2 dissolve to Si-enriched liquids, while C-S-H phases richer in $Ca(OH)_2$ dissolve to Ca-enriched liquids.

Carey and Lichtner (2007) implemented the solid solution model in a reactive transport code using the methodology of Lichtner and Carey (2006). This involves discretizing the composition of the C-S-H phase into an arbitrary number of discrete phases (they used 100). The method does not require explicit formulation of the solid solution model as this is embodied in the chemical potential of each of the discrete, stoichiometric phases. All of the discrete phases are potentially reactive and the method uses saturation-dependent reaction kinetics that results in the system evolving to equilibrium compositions with time. The method reproduces complex phase diagrams as in Figure 4. For example, Figure 5 shows calculations of precipitation from supersaturated solutions (left) and incongruent dissolution (right). On the left, a supersaturated solution that is initially X_{SiO2} = 0.5 precipitates the full range of C-S-H compositions (as they are all supersaturated) but with an average composition that is slightly Ca-enriched; the system equilibrates as it descends the diagram to the stable composition of C-S-H with X_{SiO2}= 0.5. On the right, the system starts with a C-S-H phase of composition X_{SiO2} = 0.36 in pure water. The calculation shows only secondary precipitates, which are initially absent. Dissolution enriches the aqueous solution and at a Lippman variable of approximately −5 forms a Ca-depleted C-S-H that can be interpreted as a leached layer on the original C-S-H phase. With time, the solution and the secondary precipitates evolve toward the equilibrium composition of X_{SiO2} = 0.36 phase. The method also allows for flexible interpretation of the system behavior. The average composition of all of the discrete C-S-H phases can be used to represent the equilibrium composition. The system can also be allowed to react irreversibly, effectively creating leached layers or armored precipitates.

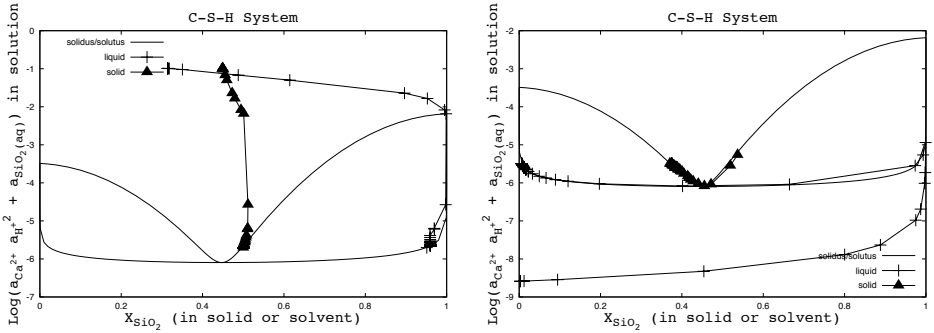

Figure 5. A: Precipitation (left) and B: dissolution (right) reactive transport calculation for C-S-H using the solid solution model of Carey and Lichtner (2007). The evolution of fluid and solid compositions represents the kinetic behavior of the system as the systems move toward equilibrium. Solid triangles are solid compositions; crosses are liquid compositions. The lower continuous curve is the solidus (solid composition) and the upper continuous curve is the liquid composition based on the thermodynamic model for C-S-H of Carey and Lichtner (2007).

Chemical reactions of cement-CO_2

Portland cement is highly alkaline and not in chemical equilibrium with naturally occurring and CO_2-bearing brines. The pH of Portland cement is governed primarily by the solubility of portlandite, which provides a minimum pH of about 12.5. In addition, Portland cement contains a significant quantity of sodium and potassium hydroxides so that typical pH values of Portland cement pore fluids are between 13 and 14 (Taylor 1990).

Reaction of CO_2 with cement proceeds by destruction of portlandite to produce calcium carbonate (as calcite, aragonite and/or vaterite):

$$Ca(OH)_2 + H_2CO_3 = CaCO_3 + 2\ H_2O \quad (3)$$

This lowers the pH of the cement pore fluid below 12 at which point the C-S-H phase begins to dissolve incongruently (Chen et al. 2004):

$$Ca_rSiO_{2+r}{\cdot}r\ H_2O + y\ H_2CO_3 = Ca_{r-y}SiO_{2+r-y}{\cdot}r{-}yH_2O + y\ CaCO_3 + 2y\ H_2O \quad (4)$$

C-S-H with an initial Ca/Si ratio of r is progressively decalcified to ratios of $(r–y)$. At complete reaction ($y = r$), C-S-H decomposes completely to amorphous silica and calcium carbonate.

Other hydrated cement phases such as ettringite, katoite, and AFm are similarly attacked by CO_2 to create calcium carbonate and a (amorphous) residue of aluminum, iron and/or silica hydroxides.

Field and experimental observations of cement-CO_2 reactions

Field and experimental observations show two different types of carbonation behavior. Portland cements without fly ash or other pozzolans generally show a distinct reaction front between carbonated and unreacted cement. In Figure 6, a sample of Portland cement was recovered from a 55 year-old well with 35 years of CO_2 operation at the SACROC CO_2-enhanced oil recovery field in west Texas. CO_2 diffused into the cement creating a completely altered "orange" zone containing calcite, aragonite and vaterite as crystalline phases and everything else as amorphous (Carey et al. 2007). The unaltered region of Portland cement contains portlandite (a key indicator that this region has not seen CO_2), katoite and a few other typical cement phases. A dense zone of carbonate precipitation occurs between the carbonated cement and the unaltered cement. This zone appears to act as a diffusion barrier to further diffusion and reaction of CO_2 into the cement interior.

Experimental studies on pozzolan-free cements show a similar picture as found in field samples at SACROC including the association of an orange color with carbonation (Kutchko et al. 2007, 2008; Rimmelé et al. 2008; Fabbri et al. 2009; Wigand et al. 2009; Duguid and Scherer

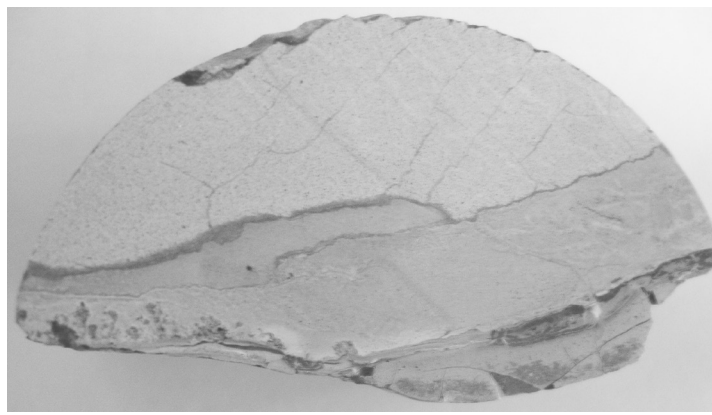

Figure 6. A sample of Portland cement collected from outside the casing of a 55-year old well with 35 years of potential CO_2 exposure. The image is rotated 90° from the cement's original orientation. CO_2 migrated along the cement-rock interface (bottom of image) and diffused into the Portland cement creating a distinct orange reaction zone (lower half of sample). A band of dense carbonate deposition (dark gray) separates unaltered (above) and carbonated cement (below). Healed conjugate fractures occur in the unaltered gray cement. The sample is 5 cm in length. [Reprinted from *International Journal of Greenhouse Gas Control*, Carey et al. (2007), Vol. 1, Fig. 2, p. 79 with permission from Elsevier.]

2010; Laudet et al. 2011; Matteo and Scherer 2012; Rochelle and Milodowski 2013; Jung and Um 2013; Jung et al. 2013; Mason et al. 2013). Kutchko et al. (2007) reacted supercritical CO_2-saturated brine with Class H (oilwell) Portland cement at 50 °C and observed three distinct reaction zones (Figs. 7 and 8). Zone 1 is a region depleted in portlandite adjacent to the unaltered interior of the cement. Zone 2 corresponds to the "orange" carbonated zone observed by Carey et al. (2007) with crystalline phases dominated by calcium carbonate polymorphs. Kutchko et al. found a precipitation front between zones 1 and 2, similar to that observed by Carey et al. Zone 3 was not observed in the field sample and consists of outer leached region free of calcium carbonate and consisting primarily of amorphous silica.

Rimmelé et al. (2008) conducted experiments at substantially higher temperature (90 °C), conditions likely to alter cement mineralogy to more crystalline phases such as tobermorite.

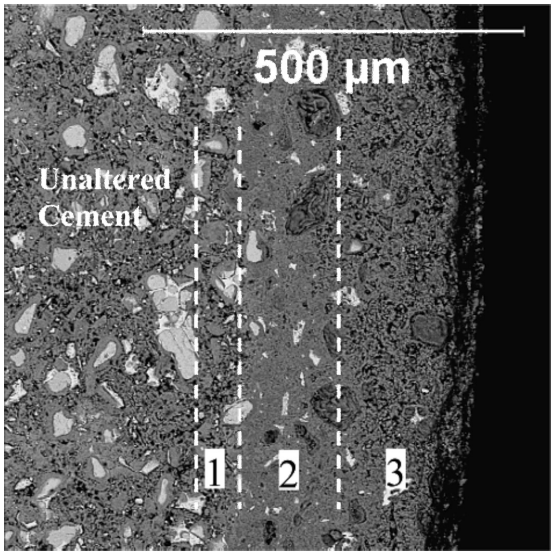

Figure 7. Backscattered electron image of Portland cement reacted with supercritical CO_2-saturated brine showing three distinct reaction zones (compare Fig. 8). [Reprinted with permission from Kutchko et al. (2007), *Environmental Science & Technology,* Vol. 41, Fig. 2, p. 4789. Copyright 2007 American Chemical Society.]

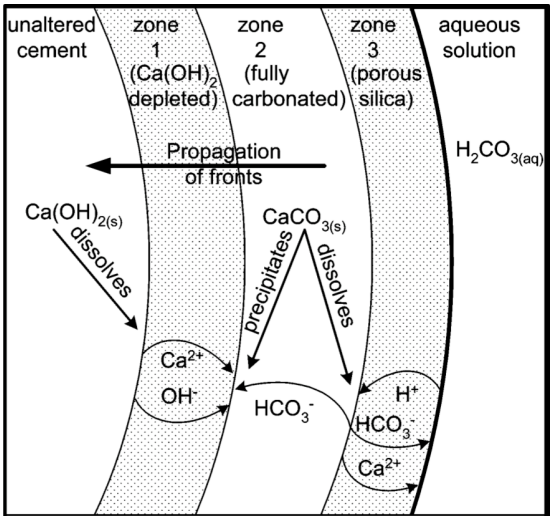

Figure 8. Interpretation of experimental study of reaction of CO_2 with cement (compare Fig. 7). Three distinct zones occur plus a precipitation front between zones 1 and 2. [Reprinted with permission from Kutchko et al. (2007), *Environmental Science & Technology,* Vol. 41, Fig. 3, p. 4789. Copyright 2007 American Chemical Society.]

However, they also found a carbonation zone (2) separated from a dissolution zone (1) by a precipitation-rich front. They report elevated porosity in zone 1 and suggest that dissolution products flow toward the carbonation front (i.e., toward the interface with CO_2-rich fluids). Fabbri et al. (2009) were able to show that the precipitation front depends on water saturation and was absent when dehydrated samples were used. This shows the importance of the interplay between diffusion, water saturation and reaction kinetics in the penetration of CO_2 into cement.

The character of the cement carbonation reactions is critically dependent on water-rock ratios. This was shown clearly by Duguid and Scherer (2010) in which they exposed cement to continuously refreshed CO_2- and acid-bearing fluids. In this very aggressive environment, the outer region of cement (zone 3) was completely devoid of calcium and was mechanically incompetent amorphous silica. Nonetheless, a zone of carbonate precipitation persisted at the interface with relatively unaltered cement. At the other end of the spectrum, Jacquemet et al. (2012) found that at low water/rock ratios the calcium carbonate deposition layer moved to the interface between brine and cement and effectively blocked further migration of CO_2 into the cement.

Cement reactions involving phases other than portlandite occurring in zones 1-3 of Kutchko et al. (2007) are difficult to determine because the phases are X-ray amorphous and often indistinct in microscopy. The fate of C-S-H in these zones is of particular importance, as it is the main structural component of cement. Kutchko et al. argue that C-S-H is stable until portlandite is consumed and pH drops. Consideration of the thermodynamics of C-S-H, as discussed below, shows that this is sensible and is consistent with much of the cement literature (e.g., Taylor 1990). However, Mason et al. (2013) used nuclear magnetic resonance (NMR) to examine cement alteration zones and found that decomposition of C-S-H was concurrent with portlandite dissolution. Using the same technique, they also argue that the final product of C-S-H decomposition is not amorphous silica, but an amorphous zeolite-like phase. In any case, it appears that the C-S-H phase does not coexist with calcium carbonate, which leaves open the question of how carbonated cement derives its structural integrity.

Orange color of cement. The orange color of carbonated neat cement suggests a redox reaction involving iron (Fig. 6). However, Portland cement consists almost entirely of ferric iron (a consequence of high-temperature heating in air) and so reaction with CO_2 cannot induce oxidation of iron. The color would therefore appear to be a result of a change in phase of the ferric iron from hydrated cement to perhaps an amorphous iron hydroxide. The nature of this reaction and the cause of the orange color remain unclear.

Role of fly ash. The addition of fly ash to cement decreases the calcium hydroxide content, increases porosity and with sufficient time will result in stronger, less permeable cement (Taylor 1990). Kutchko et al. (2009) demonstrated that the rate of CO_2 penetration into fly ash cements is much more rapid than with neat Portland cement. In addition, the reaction passed through the cement without the development of distinct fronts as in Figure 7. Interestingly carbonated fly ash cements do not appear to develop orange alteration zones. These results are consistent with field observations of Crow et al. (2010) in which they observed uniform carbonation of fly ash cements obtained from a well in a natural CO_2 production field. The more rapid penetration of CO_2 into fly ash-bearing cement appears to be a consequence of greater porosity (resulting in higher effective diffusion rates) and reduced calcium hydroxide content (resulting in less or less-rapid carbonate precipitation retarding diffusion and/or reducing effective diffusivity).

Impact of carbonation on hydrologic properties of cement. There has been rather limited work specific to CO_2 sequestration that addresses key hydrologic and mechanical properties of carbonated cement. There has been significant work on carbonation of cement in relation to building materials. These generally find that carbonation of cement at atmospheric conditions

leads to a decrease in porosity, a reduction in permeability and an increase in strength (e.g., Taylor 1990; Groves et al. 1990). It is clear from this literature that carbonation of cement is not necessarily detrimental to performance and can enhance integrity.

The properties of Portland cement are variable based on the cement type, curing time, additives, etc., with perhaps the most important factor being the water/cement (w/c) ratio. Higher values of w/c lead directly to higher porosity, higher permeability and reduced strength. Nonetheless, as a general guideline, Portland cement is a highly porous material (30-40%) with a very low permeability (of micro- to nano-Darcy). In the wellbore environment, the strength of Portland cement is more than adequate to the task of holding the steel casing. Thus strength, per se, is not a critical variable. However, the mechanical behavior (the mechanical moduli, swelling/shrinking during curing, and brittleness/ductility) plays a key role in the ability of cement to maintain zonal isolation.

Field studies provide a useful baseline for the potential impacts of carbonation on hydrologic properties. In a Portland cement from a CO_2-EOR field, Carey et al. (2007) found no substantial difference in permeability between carbonated and uncarbonated cement, although the permeability of the 55 year-old cement was elevated (0.1 mD) relative to freshly prepared cement. However, in fly ash-bearing cement, Crow et al. (2010) found that increasing degrees of carbonation resulted in an increase of permeability and porosity from 1 to 30 μD and 25-40% (they did not recover uncarbonated cement from the field but observed that freshly prepared cement using a similar formulation had permeability and porosity of 0.1 μD and 14%). Note that in all these cases, permeability of approximately 1 mD or less may not lead to significant (i.e., detectable) leakage of CO_2.

One complication in the field studies is that there is an as yet an unquantified impact of aging and interaction with typical formation fluids on cement properties. For example, Scherer et al. (2011) observed sulfate-attack (formation of ettringite) and decalcification reactions in a 19-year-old cement that had not been exposed to CO_2.

Determination of the impact of carbonation in laboratory studies is limited in part because of the difficulty of characterizing zones or narrow regions of carbonation within a core (e.g., Fig. 7). Using electron microscopy, Kutchko et al. (2007) found a slight increase in porosity in zone 1, a slight decrease in zone 2, and a significant increase in zone 3 (Fig. 8). Similarly, Rimmelé et al. (2009) used both electron microscopy and mercury porosimetry and found a reduced porosity associated with calcium carbonate deposition and an increase in porosity in the equivalent of zone 3. Kutchko et al. (2009) also found a porosity decrease in fly ash-cement.

Laboratory studies of the impact of carbonation are mixed but no studies show permeability enhanced to levels that would suggest compromised hydrologic properties. Fabbri et al. (2009) and Jung and Um (2013) found that permeability *decreases* with carbonation. Rimmelé et al. (2008) found that permeability of carbonated cement remained less than 8 μD. However, Kutchko et al. (2009) found a permeability increase of 10-20× in fly ash-cements, however their interpretation is complicated by the existence of microcracks following decompression and non-uniform carbonation.

Impact of carbonation on mechanical properties of cement. There are few studies of the mechanical properties of carbonated cement. Crow et al. (2010) obtained elastic moduli for carbonated field samples of fly ash-cement and found softening of the moduli by a factor of 2 compared to freshly prepared fly ash-cement. In laboratory studies, Duguid and Scherer (2011) demonstrated the complete loss of mechanical integrity of the leached layer of cement (zone 3 of Fig. 8) by using very high water/rock ratios (a flowing boundary condition). Kutchko et al. (2007, 2009) used nanoindentation methods to show that carbonation increases hardness, which has been correlated with strength. Using similar methods, Mason et al. (2013) and Walsh et al. (2013) observed softening (decrease in the Young's modulus) of carbonated

cement. Liteanu et al. (2009) conducted triaxial tests on the mechanical properties of cement and compared dried cement with water-saturated and water+CO_2-saturated cement. The addition of CO_2 did not markedly change the mechanical response of water-saturated cement. Under confining pressure, Portland cement does not show brittle failure but rather undergoes strain hardening (i.e., extended plastic deformation) before failing (Fig. 9). This has important implications with regard to the role of interface behavior as Figure 9 shows that cements will creep under significant load and collapse interfaces.

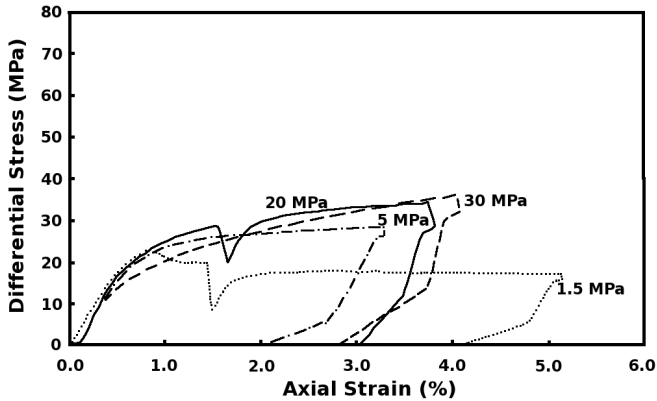

Figure 9. Triaxial experiments conducted on Portland cement exposed to CO_2-saturated water showing plastic deformation before failure as a function of confining pressure. [Reprinted from *Energy Procedia*, Liteanu et al. (2009), Vol. 1, Fig. 3, p. 3557 with permission from Elsevier.]

Ultimate state of cement. It is clear from thermodynamic considerations that Portland cement cannot survive in pure solutions of water and CO_2 (pH < 4.5). At these conditions, cement will decompose yielding a solution rich in calcium bicarbonate with residual amorphous silica, alumina, and ferrous hydroxide compounds (e.g., Taylor 1990). However, in situations where excess water is not present, cement and CO_2-saturated water will equilibrate to calcium-carbonate-saturated conditions and the solid will include abundant calcium carbonate.

Duguid and Scherer (2010) and then Matteo and Scherer (2012) studied the more extreme forms of acid attack on cement with and without CO_2. In these studies, a continually refreshed solution of pH 0-3 was passed across the cement. A silica-rich residue formed in these aggressive environments and with sufficient flow the residue was removed resulting in the slow erosion of the cement. Matteo and Scherer (2012) were able to quantify the rate of cement erosion as a function of temperature and pH. They conclude that the rate is sufficiently slow that 10 m of cement provides 2 million years of protection. They, as do earlier workers, conclude that the primary geochemical threat to cement is by flow along interfaces.

Role of CO_2 pressure. The impact of supercritical CO_2 conditions on the aqueous carbonation of cement is primarily a function of pressure. The CO_2 concentration increases and the pH decreases as a monotonic function of pressure, although there is a sharp reduction of the rate of change at pressures above the critical point (74 bars; Fig. 10). However, even 1-bar CO_2-saturated water has a pH of < 4.5 and is strongly out of equilibrium with cement (pH > 12.5). Perhaps the most important impact of pressure is that the amount of cement that must react to neutralize the solution is much greater than at low pressures because of increasing CO_2 solubility.

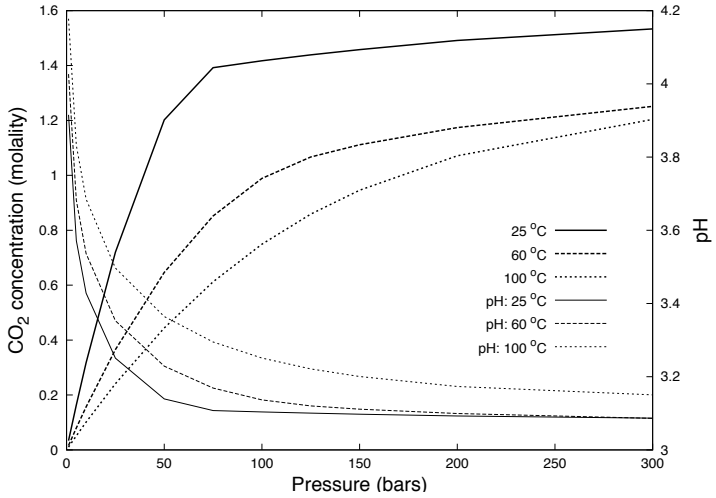

Figure 10. Calculated solubility and pH of pure CO_2-water system as a function of temperature and pressure (after Carey 2006).

Reactive transport calculations of cement carbonation

Reactive transport studies are useful for analysis of the mineralogical evolution of cement in reactions with supercritical CO_2-saturated water. These studies require a thermodynamic database for cement phases and for CO_2. Although most research reactive transport codes contain accurate equations of state for CO_2, it is important to recognize that commonly used programs such as PHREEQC and Geochemist's Workbench cannot be used accurately at elevated CO_2 pressures These codes calculate CO_2 concentrations with a Henry's law constant that is not a function of pressure, resulting in linearly increasing concentration of aqueous CO_2 with fugacity of CO_2 in contrast to the sharp change in the growth of solubility above about 75 bars (Fig. 10). In addition, these programs are based on fugacity and do not include a mechanism for converting to pressure. There are approaches to overcoming these limitations by modifying the databases for these programs as described by Carey (2006) that allow a more accurate representation of CO_2 concentration, pH and pressure.

Reactive transport studies of Portland cement have significant limitations because of the poorly crystalline nature of cement phases. This makes thermodynamic properties uncertain but there is equally significant uncertainty associated with the composition of the phases. Thermodynamic data for the major cement phases exist (hydrated and clinker phases; see section above), however, there are little to no kinetic data for reaction rates.

In terms of geochemistry, portlandite is perhaps the most important component in cement as its solubility provides a direct control of pH (about 12.5 at room conditions). As such, simple geochemical models of cement can be constructed using portlandite as the reactive phase. In general, however, most models have examined a more complete representation of cement mineralogy (e.g., Tables 1 and 2) including the studies of Carey and Lichtner (2007), Carey et al. (2007), Huet et al. (2010), Corvisier et al. (2010), McNab and Carroll (2011), Deremble et al. (2011), Wilson et al. (2011), Gherardi et al. (2012), Fabbri et al. (2012), Raoof et al. (2012), Jacquemet et al. (2012), Brunet et al. (2013) and Wertz et al. (2013).

In general terms, these studies are successful at reproducing the basic reaction features in CO_2-cement systems. At SACROC, Carey et al. (2007) were able to reproduce the mineralogy,

porosity, and chemical evolution of a carbonated sample from a CO_2-EOR field using a model of diffusion of CO_2 into the cement (Fig. 11; cf. Fig. 6). As discussed more fully in Carey and Lichtner (2007), notable features of their model included the use of complete solid solution for C-S-H (see above) with a cement mineralogy that also included portlandite, monosulfate, and hydrogarnet. As brine equilibrated with 180 bar CO_2 infiltrated the cement by diffusion, reactions produced calcite, amorphous silica, gibbsite (representing amorphous alumina), ettringite, Friedel's salt (Cl-substituted ettringite). By tuning model parameters discussed below, Carey and Lichtner were able to reproduce the width and character of the carbonation zone in the cement after 30 years of reaction (Fig. 11). In particular, the model reproduces an unaltered interior, a completely carbonated region between the shale and unaltered cement (zone 2 of Kutchko et al. 2007; the orange zone in Fig. 6); and lower porosity zones of carbonate deposition.

Huet et al. (2010) applied their reactive transport code to Duguid and Scherer's (2010) experimental data on exposure of cement to flowing acidic (including CO_2-bearing) solutions. Their model used jennite as a distinct phase representing C-S-H along with portlandite, monosulfate and ettringite as primary phases. They reproduced the experimental features of an unreacted internal zone, a portlandite depleted region (zone 1 in Fig. 8), the carbonate deposition zone (zone 2) and a region of amorphous silica (zone 3). In agreement with Carey and Lichtner (2007), they find that AFm and ettringite are not stable in the presence of CO_2 saturated solutions (or as a stable assemblage with calcium carbonate). They calculate a porosity increase in zone 2, a decrease in zone 3, and then a very large increase in porosity in zone 3, but found that simple power laws relating porosity to diffusivity were inadequate for explaining the observed zone widths and the migration rate of CO_2.

In one other example, Gherardi et al. (2012) studied a more complete representation of the borehole system in a 2D slice including reservoir, caprock and wellbore without the

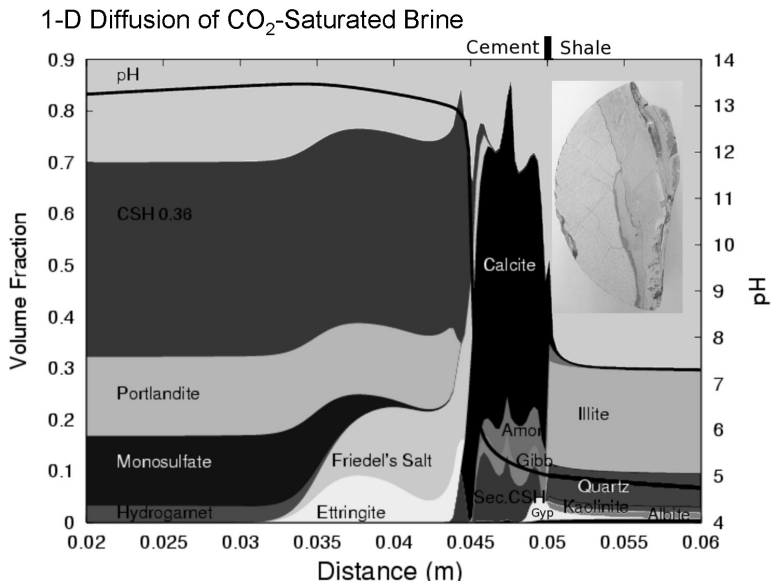

Figure 11. A 1D diffusion model of the carbonation of cement at SACROC, west Texas. CO_2-saturated brine diffuses from shale on the right into Portland cement on the left over 30 years. At the interface, the cement is replaced by an assemblage of calcium carbonate, amorphous silica and amorphous alumina. The model reproduces the basic features of a sample recovered from SACROC (inset). (Derived from Carey et al. 2007).

benefit of experimental or field constraints for their particular field site. They modeled cement interactions with caprock and reservoir over a 1,000-year period. They found, consistent with experimental and field observations, that the extent of cement alteration induced by migration of CO_2-bearing fluids from the reservoir was limited to less than 1 meter. However, they did find enhanced porosity developed at the caprock-cement interface after several hundred years.

The reactive transport models are subject to considerable uncertainty because of a significant number of assumptions required to represent the cement-CO_2 system. These include the following:

1. Porosity (especially contrasts between the cement, interfaces or rock)
2. Diffusivity (tortuosity limits the effective diffusion rate)
3. Changes in diffusivity induced by mineral precipitation/dissolution (i.e., porosity changes)
4. Kinetics of reactions including reactive surface areas
5. Solid solution models, particularly for C-S-H
6. Species-dependent diffusion,
7. Formation fluid composition (particularly whether these fluids are calcite-saturated)
8. Cement initial mineralogy and relative abundances
9. Secondary mineralogy considered
10. Ionic activity model
11. Water content of the hydrated phases in relation to reaction-induced flow

Sensitivity to many of these factors was investigated by Carey and Lichtner (2007), Huet et al. (2010), and Gherardi et al. (2012) among others. Fortunately, observations of cement behavior in experiment and field environments provide effective constraints to at least approximate values for these parameters. For example, Carey and Lichtner (2007) used the depth of the carbonation and the width of the reaction front to constrain diffusivity and reaction rates. They also found that porosity and bulk compositional profiles yielded important checks to parameter values.

Carey and Lichtner (2007) examined the impact of using a solid solution representation of C-S-H (also see Wilson et al. 2011). They employed the method of Lichtner and Carey (2006) to incorporate solid solution behavior of C-S-H in a multiphase flow and reactive transport code (FLOTRAN). They showed that starting with a typical C-S-H composition of $X_{SiO2} = 0.36$, reaction with CO_2 progressively decalcified the C-S-H until it reached $X_{SiO2} = 0.44$, the alyotropic minimum. At that point, the code predicted a discontinuity in secondary C-S-H phases with highly SiO_2-enriched C-S-H precipitating ($X_{SiO2} > 0.9$). (These may be artifacts of the solid solution model, although there is one experimental point suggesting such compositions are possible). In any case, the model predicts the progressive decalcification of C-S-H until essentially amorphous silica forms. However, the very strong disequilibrium between Portland cement and CO_2-saturated brine produced rather narrow zones in which the effects of solid solution could be observed, and Carey and Lichtner concluded that these effects did not have a profound significance given the limited size of the compositional transition zone and the extent of other uncertainties in the model.

The available CO_2 sequestration modeling studies have not examined the impact of fly ash. Experiments of Kutchko et al. (2009) and field studies of Crow et al. (2010) show that CO_2 reactions with fly ash cements do not produce distinct reaction fronts and show much greater rates of CO_2 penetration.

STEEL AND STEEL-CEMENT INTERACTIONS

Steel casing in wells is generally a low-carbon (mild) steel, which is relatively inexpensive but is susceptible to corrosion. In specialty environments, stainless steel or plastics may be used. For example, some of DOE's Regional Partnerships have used corrosion resistant steel for injection tubulars and for production casing. However, almost all well construction uses mild carbon steel.

Corrosion reactions

Corrosion of steel can be a serious problem that can damage wells rapidly on time scales as short as months. There is a great deal of literature on corrosion of steel because of its significance in construction and pipelines. In particular, there is abundant literature on CO_2-induced corrosion of steel (e.g., Kermani and Morshed 2003; Nešić 2007) because of CO_2 pipelines used, for example, to transport CO_2 from natural CO_2 reservoirs in New Mexico and Colorado to the Permian Basin in west Texas. CO_2 partial pressures > 2 bar in the presence of water are considered to be highly aggressive to low carbon steel (Kermani and Morshed 2003).

Corrosion issues related to wellbore integrity have been reviewed recently by Choi et al. (2013). They emphasize the key role that cement plays in protecting steel from corrosion impacts.

Corrosion of steel in CO_2-systems occurs by the following reaction pathways (Nešić 2007; Han et al. 2011a). The key anode half-cell reactions are

$$2H_2CO_{3(aq)} + 2e^- = H_{2(g)} + 2HCO_3^- \quad (5)$$

$$2H^+_{(aq)} + 2e^- = H_{2(g)} \quad (6)$$

$$2H_2O_{(aq)} + 2e^- = H_{2(g)} + 2OH^- \quad (7)$$

In addition, some workers have suggested that bicarbonate-induced corrosion can be important at higher pH (e.g., Han et al. 2011b):

$$2HCO_3^- + 2e^- = H_2(g) + 2CO_3^{2-} \quad (8)$$

although some workers find that the effect of bicarbonate is difficult to distinguish from Reaction 6 (Nešić 2007).

The anodic reactions are balanced by a simple cathode half-cell reaction that releases iron:

$$Fe(s) + 2e^- = Fe^{2+} \quad (9)$$

Note that oxygen does not play a significant role in the anoxic wellbore (or pipeline) environment. However, co-injection of O_2 as a contaminant of a CO_2 stream would create additional potential for corrosion and increase corrosion rates according to Choi et al. (2010).

The rate of corrosion is given by the sum of the activity of each of the pathways. The relative importance of the three anodic reactions depends, in part, on the concentrations of species. In the CO_2-H_2O system at elevated pressure, the carbonic acid concentration is much greater than the hydrogen ion concentration and corrosion rates are determined primarily by carbonic acid.

CO_2-induced corrosion of low carbon steel can occur as a uniform process wearing steel thin or as a localized phenomenon that results in pits or mesa structures (Kermani and Morshed 2003). Prediction of uniform corrosion rates is much better understood and is the primary focus of this review. Localized corrosion can be much more serious because rates are significantly enhanced over uniform rates. The causes of localized corrosion may include stress-induced defects in steel, incomplete scale coverage, and mechanical damage to protective scale, all of

which create a galvanic effect between the protected and unprotected steel, and the presence of particular chemical components such as acetic acid or H_2S (Kermani and Morshed 2003).

Uniform corrosion rates of bare steel in supercritical CO_2 solutions can be very rapid. Experimental studies by Choi and Nešić (2011) show relatively constant rates at 50 °C and pressures from 40 to 80 bars CO_2 of about 20 mm/year. They also found that corrosion rates of steel in water-bearing supercritical CO_2 were much lower, although still significant, around 0.2-0.4 mm/year. Clearly, unprotected steel does not survive long in the presence of CO_2-bearing water.

These rates represent worst-case scenarios. Depending on conditions, and particularly where fluids are buffered to equilibrium with carbonate, CO_2-induced corrosion produces iron carbonate scale that can have protective qualities, depending on the porosity and thickness of the scale (Nešić 2007). For example, Han et al. (2011c) found a reduction in corrosion rate from 9 to about 0.5 mm/year after formation of an iron carbonate scale. They also show that Fe-carbonate scale can, under the right conditions, form dense precipitates with minor porosity (Fig. 12). Scale formation requires supersaturation with iron carbonate, a condition that is favored by higher pH (e.g., > 5). The quality of the scale depends on supersaturation level, temperature, and minor chemicals, but the prediction of scale properties is not yet well developed (Kermani and Morshed 2003).

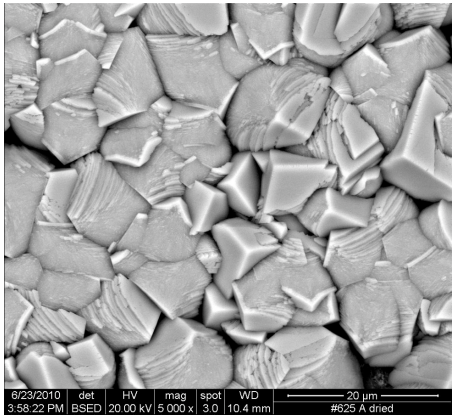

Figure 12. Scanning electron microscopy image of Fe-carbonate scale formed on low-carbon steel immersed in CO_2-saturated brine at 100 bars and 50 °C. The scale formed within a 100-µm gap between the steel and an impervious barrier. [Used by permission of NACE International, from Han et al. (2011c), *NACE Corrosion Conference and Expo 2011* Fig. 4, p. 7. © NACE International 2011.]

Role of Portland cement in corrosion

Good quality Portland cement provides a highly alkaline environment (pH > 12.5) that passivates the surface of steel, resulting in negligible corrosion rates (e.g., Taylor 1990). Thus the first line of defense in protecting steel in the wellbore environment is well-placed and bonded cement. Injection wells or monitoring wells at a CO_2 sequestration site will be designed for CO_2 and will certainly have Portland cement protecting the casing in the reservoir and the overlying caprock. However, as shown in Figure 3, the Portland cement may not cover the entire length of the production casing. If CO_2 is able to migrate above the cement-protected region, then this portion of the casing would be vulnerable. Similarly, for old wells that may be intersected by the CO_2 plume, it is essential that Portland cement protects casing in the CO_2 reservoir and overlying caprock.

Several processes can allow CO_2 to potentially induce corrosion of steel despite the presence of cement. As discussed above, a microannulus can form between the steel and cement that could allow migration of CO_2 brines. For example, Carey et al. (2007) observed

carbonate deposits at the interface between steel and cement in a CO_2-EOR well. Han et al. (2011c) conducted experiments to investigate the effect of varying gaps on the rate of corrosion in CO_2-saturated brine. They compared a steel-epoxy composite having a tight bond, a 20-μm gap, a 100-μm gap and an open face to a 1% NaCl solution. They found that corrosion rates were similar for the 100 μm and open faces, but that the rates decreased for the 20-μm gap. Thus there is some indication that corrosion rates are moderated with tight interfaces.

The other processes that may enhance corrosion of steel through cement are carbonation of the cement and fractures or defects in the cement that allow CO_2-saturated brine to penetrate to the steel interface. Carbonation of cement lowers the pH of the cement pore fluid below 10, which could de-passivate the steel and accelerate corrosion (Taylor 1990). CO_2-bearing fluids penetrating through fractures in the cement are likely to be buffered toward calcium carbonate equilibrium by reaction with cement pore fluids. Nonetheless, these will be strongly out of equilibrium with steel and may have sufficient CO_2 to accelerate corrosion.

Han et al. (2012) conducted experiments on steel-cement composites to investigate the extent of protection that carbonated, defect-bearing cement provides to steel. They covered steel with thin layers of Portland cement (1 mm and 5 mm thick) and immersed the composites in 1% NaCl brine at 50 °C and 100 bar CO_2. They compared corrosion rates of samples immersed in a calcium carbonate-buffered solution with a sample in which the cement was leached of calcium carbonate. The corrosion rates showed that carbonated cement, even with defects, reduced corrosion rates by two orders of magnitude below unprotected steel (Fig. 13). However, if the cement was leached of calcium carbonate (by exposure to large quantities of pure CO_2-brine), then the corrosion rates were similar to that observed for the cement-free sample.

In the Han et al. (2012) experiments, a 425-μm gap existed between the steel and cement, and cracks in the cement coating allowed migration of CO_2-bearing fluids into the interface

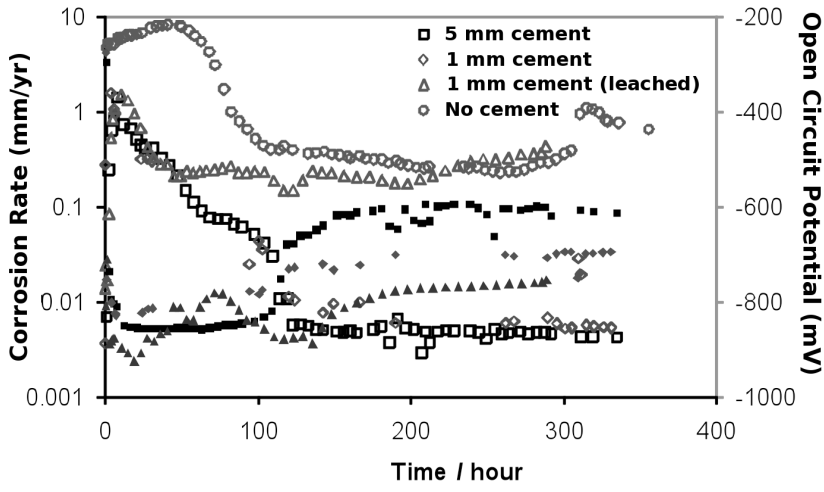

Figure 13. Experimental measurement of corrosion rates (open symbols) and open circuit potential (closed symbols) for low-carbon steel covered with varying thickness of cement and exposed to 100 bar CO_2 at 50 °C. The 5 mm and 1 mm cement samples were immersed in a solution with excess cement and buffered to calcium carbonate equilibrium. The leached sample had insufficient cement to prevent the dissolution of calcium carbonate in the cement. The sample without cement corrodes first as a bare metal (rate almost 10 mm/yr) and then scale forms reducing the rate by a factor of 20. [Used by permission of NACE International, from Han et al. (2012), *NACE Corrosion Conference and Expo 2012*, Fig. 4, p. 10. © NACE International 2012.]

region (Fig. 14). Nonetheless, the steel in the interface region has very little evidence of corrosion, consistent with the measurements in Figure 13. Instead, abundant calcium carbonate precipitation occurred that coated the steel and which appeared to be in the process of filling and sealing the interface region. Thus the steel-cement system showed evidence of self-healing process where CO_2-fluids were buffered to calcium carbonate saturation.

The scale formed during corrosion of steel in the presence of cement is not a pure iron carbonate but consists of a Ca-Fe carbonate mixture (Fig. 15; Carey et al. 2010). In electron microscopy, the distributions of Ca and Fe are heterogeneous and do not appear to be stoichiometric. Liesegang-like rings of varying Fe/Ca ratio occur, perhaps reflecting rapid precipitation from supersaturated solutions. Attempts to obtain crystal structure information on these precipitates were not successful.

Modeling of corrosion reactions

Computational models of CO_2-induced, uniform corrosion have been developed (see Nešić 2007 for a discussion). For example, Han et al. (2011a) developed an electrochemical model for corrosion that is applicable to high salinity environments encountered in saline aquifers. Corrosion rates in the model are limited by the kinetics of electrochemical reactions and by mass transfer from solution to the steel interface. The kinetics of electrochemical reactions are determined by the product of the chemical and electrical rate equations:

$$r_c = k_c \prod a_i \tag{10}$$

$$r_e = k_e e^{-\alpha F \Delta\phi / RT} \tag{11}$$

where k_c and k_e are the chemical and electrical rate constants, a_i are the activity of species in the corrosion reactions (Eqns. 5-9), α is a symmetry factor that is 0.5 for most metals, F is

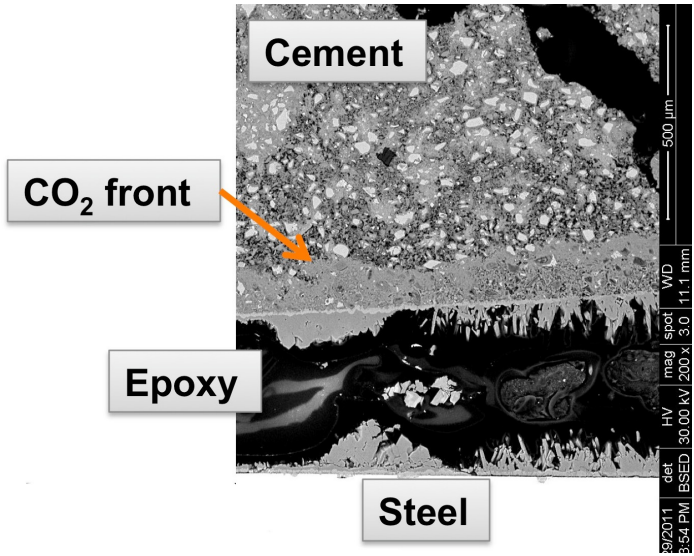

Figure 14. Scanning electron microscopy image of a cross-section through a cement-steel composite exposed to supercritical CO_2 (the 1 mm-thick cement sample from Fig. 13). A CO_2 carbonation front is observed in the cement and calcium carbonate crystals grow into the interface region. The interface is 425 µm in width. Note the lack of visible corrosion of the steel. [Used by permission of NACE International, from Han et al. (2012), *NACE Corrosion Conference and Expo 2012*, Fig. 4, p. 10. © NACE International 2012.]

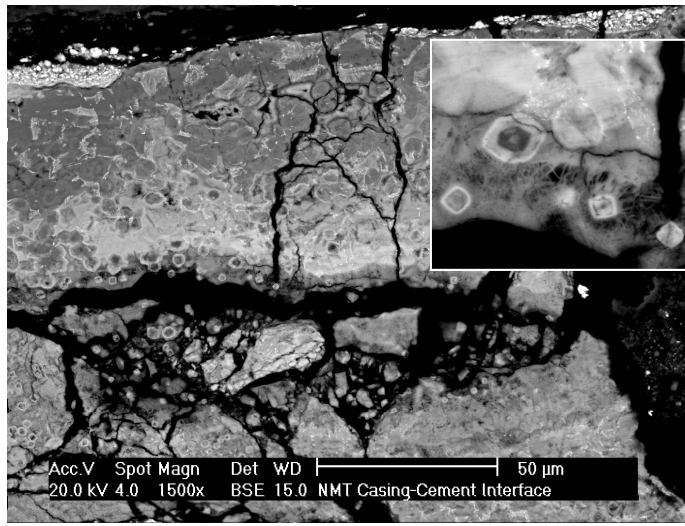

Figure 15. Back-scattered electron image of Fe-Ca scale formed between cement (above, not shown) and steel (below, not shown). The scale shows brighter (Fe-rich) and darker (Ca-rich) regions, including interesting "eye" structures representing, perhaps, kinetically controlled precipitation (see inset in upper right). Unpublished photo from experiments described in Carey et al. (2010).

Faraday's constant, $\Delta\phi$ is the difference in potential across the metal-solution interface, and *RT* is the product of the gas constant and temperature. Equation (10) is a typical transition-state theory kinetic expression for a chemical reaction, and Equation (11) is the analogous equation for electron transfer kinetics. In Han et al.'s study, they use Pitzer activity coefficients to calculate the chemical kinetics. The mass transfer kinetics are governed by advection and diffusion of chemical species in the system.

Han et al. (2011a) use their model to predict bare steel corrosion rates as a function of temperature, CO_2 pressure and salinity (Fig. 16). These show the rapid rise in corrosion rates with temperature and with pressure (particularly between 1 and 50 bar). The predicted rates are very high and reflect worst-case scenarios in which the steel does not develop protective corrosion scale. Salt lowers corrosion rates because it reduces the solubility of CO_2 (Eqn. 1). (In the case of uniform corrosion of bare metal, salt does not have its well-known effect of destabilizing protective scale that enhances corrosion rates.)

COUPLED PROCESSES

Understanding the significance of geochemical processes in the wellbore environment requires considering the coupled processes that allow reactants to reach Portland cement and steel. These processes may be as simple as diffusion from adjacent rock formations to as complex as the interaction of mechanical stresses with fracture formation, subsequent fluid flow and precipitation/dissolution reactions that modify the fracture permeability. As discussed in the introduction, Portland cement provides isolation from fluid migration and protects the steel from corrosion. It is only through either defects in the construction or subsequent geomechanical damage that CO_2 and CO_2-saturated brine can migrate and initiate potentially damaging chemical reactions

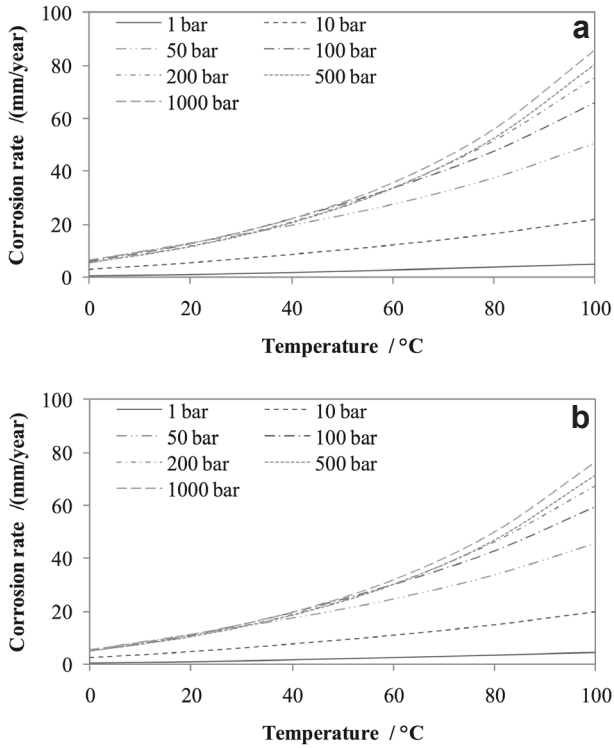

Figure 16. Calculated corrosion rates of bare low-carbon steel in aqueous solutions of (a) 1 wt% NaCl and (b) 20 wt% NaCl as a function of temperature and CO_2 pressure. NaCl has the effect of reducing corrosion rates, primarily through the reduced solubility of CO_2. [Reprinted from *International Journal of Greenhouse Gas Control*, Han et al. (2011a), Vol. 5, Fig. 9, p. 783 with permission of Elsevier.]

Flow processes and multiphase behavior

Fluid flow external to well casing can occur via matrix flow through the Portland cement or via micro-annuli, cracks, or void spaces (e.g., gas channels or uncemented regions of the well). Matrix flow in properly made Portland cement is negligible over the 10s to 100s of meters of cement protection in a well given the very low intrinsic permeability of cement (micro- to nano-Darcy; Taylor 1990).

Cement possesses capillary pressure barriers to the entry of gas or supercritical CO_2 that limit the possibility of separate phase migration of supercritical CO_2 through cement (e.g., Monlouis-Bonnaire et al. 2004). Carey and Lichtner (2011) conducted multiphase flow calculations to explore capillary properties of cement. Beginning with the assumption that supercritical CO_2 reaches cement via relatively permeable material (reservoir rock or defects), they showed that penetration of $scCO_2$ was minimal in Portland cement and flow was likely confined to interfaces and other defects. In the unlikely situation that $scCO_2$ was present in rock (e.g., shale) with similar capillary properties to cement and in perfect hydrologic contact with cement, then penetration of CO_2 into cement was more significant.

These results are supported by coreflood studies in which $scCO_2 \pm$ brine are injected into cement, cement-steel or cement-rock composites (Wigand et al. 2009; Carey et al. 2010; Newell and Carey 2013). All of these studies show that $scCO_2$ is confined to interfaces and

does not flow through cement (Fig. 17). Instead, reaction of cement and CO_2 occurs only via diffusion from interfaces or permeable material into the cement. In addition, the field study of Carey et al. (2007) shows clear evidence for diffusion-based penetration of CO_2 into cement (Fig. 6). However, these observations do not address the potential for $scCO_2$ flow through poor-quality cement, contaminated cement, or more generally the impact of the large variety of additives that are put into cement.

These results show that diffusion of CO_2 through the aqueous phase is the key transport process that brings CO_2 into contact with cement.

Reactive transport in well integrity

Reactive transport modeling studies of CO_2 with Portland cement are discussed in the section Chemical Reactions in Cement-CO_2. These studies and the related experimental work all involve the assumption that diffusion is the predominant mechanism bringing CO_2 into cement for reactions. There has been relatively little work on the topic of the capillary pressure behavior of carbonated cement discussed above. Crow et al. (2010) studied the change in capillary pressure properties on carbonation of fly ash-amended cement and found that the capillary pressure resistance was reduced by carbonation. Thus a process in which cement is carbonated via diffusion could lead to greater possibility of separate phase CO_2 flow through cement. Although Crow et al. note that the carbonated cement still has capillary resistance. This important topic needs further study.

Direct experimental studies of hydrologic changes in cement due to CO_2 reaction are uncommon. Bachu and Bennion (2009) injected $scCO_2$-saturated brine through good quality Portland cement in a coreflood study. They found a *reduction* of permeability from about 0.1 to 0.01 mD during the experiment. However, as noted by Bachu and Bennion (2009), the experiments are difficult to interpret because of the potential for exsolution of CO_2 from the solution due to the pressure drop across the core. This would result in multiphase flow and

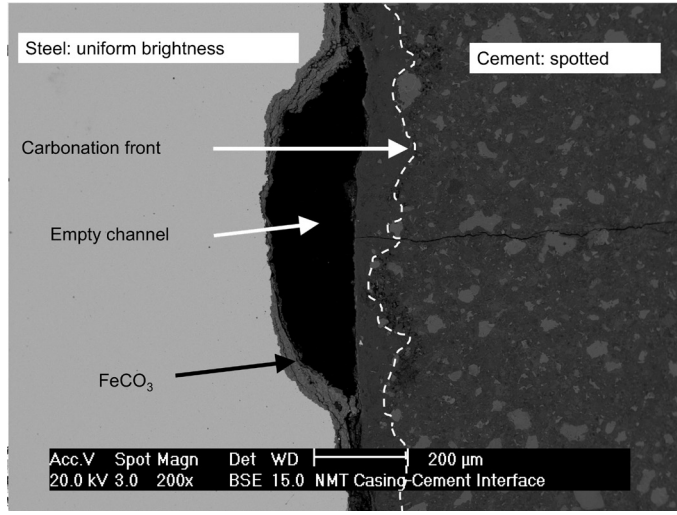

Figure 17. Backscattered electron image of a coreflood experiment in which $scCO_2$+brine was injected into a steel-cement composite (perpendicular to image). Flow of $scCO_2$ and CO_2-saturated brine was limited to defects (illustrated in this cross-section through a channel). Carbonation of cement occurred only by diffusion of CO_2 from the steel-cement interface, penetrating only a small distance. Steel corrosion occurred resulting in precipitation of iron carbonate at the steel surface. [Reprinted from *International Journal of Greenhouse Gas Control*, Carey et al. (2010), Vol. 4, Fig. 7, p. 276 with permission from Elsevier.]

relative permeability effects that could account for the reduction in permeability. Nonetheless, they found that they were not able to restore permeability by subsequent flow of pure brine (which should dissolve residual CO_2) suggesting that they had observed carbonation-induced changes in permeability. They conclude that they do not expect that flow of CO_2-saturated brine through cement would result in degraded cement hydrologic properties.

Although there are models for corrosion of steel (discussed above), there have been no reactive transport studies of steel that couple corrosion with flow of $scCO_2$-brine through cement and rock in the wellbore environment. The mechanism for doing this should be straightforward given the similarity in the kinetic approach between chemical and corrosion reactions embodied in Equations (10) and (11) and as described in Han et al. (2011a).

Flow and reaction in defects. Because of the low permeability of the cement-steel system, experimental flow and reaction studies have focused on flow through defects. Several studies have examined the behavior of fractured cement including Bachu and Bennion (2009), Wigand et al. (2009), Yalcinkaya et al. (2011), Liteanu and Spiers (2011), Huerta et al. (2013), Mason et al. (2013), Walsh et al. (2013) and Luquot et al. (2013). These have all used manufactured fractures and involved flow of CO_2-saturated fluids, acidic fluids or supercritical CO_2 designed to understand the impact of acid dissolution processes on fracture behavior.

Bachu and Bennion (2009) considered multiphase flow through fractured cement using water-supercritical ethane as an analog to the $scCO_2$-brine system. By alternating water with ethane in a coreflood device, they found little evidence of relative permeability effects. Their results suggest that migration of single-phase $scCO_2$ into fractures would drain the brine, creating CO_2-rich conditions.

Wigand et al. (2009) flowed pure $scCO_2$ through a hairline fracture in cement. The initial permeability of the fracture to brine was below detection, which they attributed to the effect of confining pressure on closing the fracture. They observed precipitation of calcium carbonate in the fractures, suggesting a healing process, but also inferred (did not directly measure) an increase in effective permeability, which they attributed to the force of carbonate crystallization widening the fractures.

Yalcinkaya et al. (2011) describe coreflood experiments at sub-critical conditions of CO_2-saturated brine using epoxy to separate two cement halves. They used X-ray tomography to observe increases in porosity in CO_2-altered regions adjacent to the fracture and had some evidence for widening of the fracture apertures.

Liteanu and Spiers (2011) examined the behavior of wet fractured cement samples after immersion in $scCO_2$. Their experiments were static (not flow-through), and thus they studied the impact of long residence times of CO_2-bearing fluids on fracture behavior. They observed carbonate precipitation and bonding of the fractured surfaces. In post-experiment permeability measurements, they found a reduction from 40 to 10 mD of fractured samples.

Huerta et al. (2013) conducted coreflood experiments using HCl-bearing brine as a surrogate for CO_2-saturated brine in cores with fractures created by the Brazilian method. Despite the use of more aggressive solutions, they observed increases in pressure with flow, distinct channeling of fluids along the fracture interface, and precipitation/mobilization of material in addition to dissolution reactions. They conclude that their results indicate self-sealing properties of cement systems, provided fracture apertures are sufficiently small and fluids have sufficiently long residence times.

Luquot et al. (2013) studied three different fractured cement cores using CO_2-saturated brine and investigated the relationship between permeability, flow rate and initial fracture aperture. They found that small fracture apertures were healed by carbonate precipitation with a corresponding reduction in permeability. On the other hand, larger initial fracture apertures

allowed the development of residual amorphous silica on the fracture surface that the authors believe maintained the fracture aperture and allowed permeability to increase with time.

Several studies have used composite samples in coreflood systems to study brine±scCO_2 along cement-rock interfaces (Newell and Carey 2013; Mason et al. 2013; Walsh et al. 2013) and cement-casing (Carey et al. 2010). All three cement-rock studies found either a decrease or no change in permeability with fluid flow. Newell and Carey (2013) created an interface between cement and siltstone made of ground cement and rock representing a permeable zone created by disturbed rock and cement filter cake. They found that flow of scCO_2+brine through the interface did not damage the adjacent cement, which was carbonated only by diffusion of CO_2 into the matrix. They also found that the siltstone had no evidence for CO_2-induced reactions. Cement in the interface, however, had dissolved and appeared to have re-precipitated downstream. Although the interface had no carbonate and the effluent was undersaturated with calcium carbonate, a reduction of permeability was observed probably because of clogging by migrating/reprecipitating cement phases.

In tandem studies, Mason et al. (2013) and Walsh et al. (2013) used a different method to examine flow of CO_2-saturated brine along an interface between cement and dense sandstone. They created a textured interface by sandblasting with beads (Mason et al. 2013) or used a mask+sandblasting to create a designed pattern of fracture asperities. Mason et al. focused on mineralogical changes in the adjacent cement, while Walsh et al. used tomography to characterize interface behavior. Both studies found a reduction in permeability of the interface, with Walsh et al. reporting a 2 order of magnitude change from 10 to 0.1 mD. The two studies attributed the reduced permeability to a combination of swelling of amorphous dissolution products and/or a mechanical softening of the reacted cement that allowed the interface to close (Fig. 18).

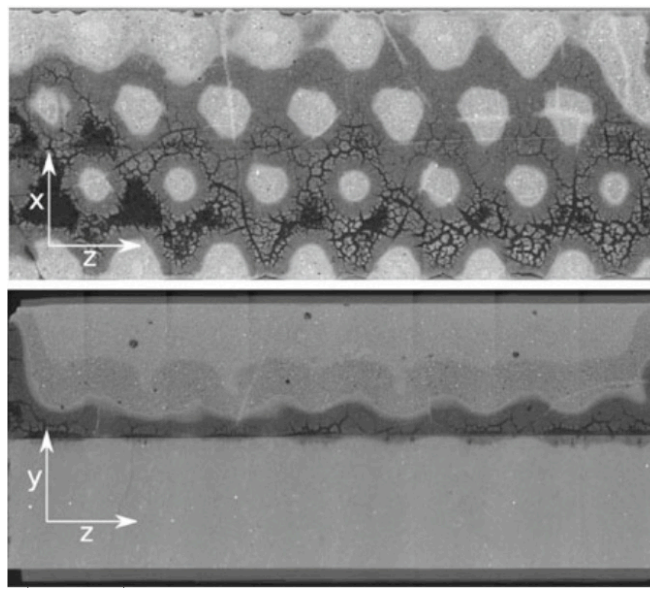

Figure 18. Two X-ray tomography slices of a coreflood experiment involving flow of CO_2-saturated brine through an interface between dense sandstone and cement. The upper figure is in the plane of the interface and shows dessication cracks in the leached cement phase surrounding pillars of cement that support the interface. The lower figure shows a cross-section through the interface (sandstone below) with dark, leached cement (zone 3) grading into carbonated cement (zone 2) and unaltered cement above. [With kind permission of Springer Science and Business Media, from Walsh et al. (2013), Vol. 46, Fig. 4, p. 459.]

Carey et al. (2010) studied a defective steel casing-cement interface created by cutting grooves into the steel. They injected a mix of $scCO_2$ and brine at high rates, expecting to observe substantial erosion of Portland cement. Despite injection of approximately 59,000 pore volumes over the course of sixteen days, they found essentially no change in permeability of the system. Electron microscopy analysis of the interface showed that the cement interface remained flat and had not been eroded by flow of CO_2 (Fig. 17). However, abundant corrosion products (Fe-Ca carbonates in Figs. 15 and 17) had formed and, in some places, had almost completely blocked the original defect in the steel.

At this time, there are no reactive transport studies of CO_2 and brine flow through defects or interfaces in the wellbore system. This is likely because of the difficulty in representing dissolution and precipitation processes at the interface wall and their impact on the evolution of porosity and permeability of the interface region.

Coupled geomechanics, flow and reaction

Stresses in the wellbore environment arise from tectonic forces and thermal and fluid pressure changes both inside operating wells and outside the well within the storage reservoir. These can damage the well, generating fluid pathways, by separating the steel-cement or cement-rock interface (micro-annulus formation) and by fracturing the cement. Tectonic stresses are particularly significant in deformable rock types such as salt and some shale that readily transmit these stresses to the well system. Injection of CO_2 will change temperatures and pressures within the injection well and create differential movement of materials due to mismatch in thermal expansion coefficient and elastic moduli among steel, cement and rock. Other well operations including mechanical integrity tests and wireline logging operations generate stresses that can be damaging. Finally, pressure and temperature changes in the reservoir due to injection/withdrawal of fluids can act on all of the wells in the field.

Experimental studies of coupled mechanical processes (i.e., triaxial coreflood studies) on wellbore materials involving CO_2 are rare but include Takla et al. (2011) and Laudet et al. (2011). Takla et al. (2011) studied the effects of confining pressure and degree of carbonation on permeability and mechanical strength (Fig. 19). They carbonated cement cylinders to varying degrees ranging to complete penetration and measured permeability and strength in a triaxial device as a function of confining pressure. Permeability drops an order of magnitude and strength increases by a factor of 2 with complete carbonation.

In a staged triaxial experiment, Laudet et al. (2011) first injected water equilibrated with cement to establish permeability, then applied an axial (deviatoric) load, and finally injected CO_2-saturated brine. They found a small decrease in permeability of the cement in response to the deviatoric stress and resulting cement deformation. Upon flow of CO_2-saturated water, permeability decreased (below detection limits), although they found no change in the strain rate of the carbonated cement.

Although not a coupled process measurement, Liteanu et al. (2009) conducted triaxial deformation studies of cement, comparing dry, wet, and $scCO_2$-reacted cement samples. These results showed the importance of confining pressure in the mechanical failure of cement samples. At higher confining pressures, cement does not undergo brittle failure but deforms plastically. The addition of CO_2 did not measurably change the mechanical properties of the cement. This is in contrast to the results of Takla et al. (2011; above) and to unconfined tests that show an increase in cement strength following carbonation (e.g., Taylor 1990).

It should be noted that coreflood studies without a triaxial component, nonetheless have a mechanical component in the effect of confining pressure on permeability (Fig. 19). For example, in creating a steel casing-cement composite, Carey et al. (2010) found it necessary to introduce grooved defects into the steel to permit measurable flow at the cement-steel interface. In addition, Mason et al. (2013) and Walsh et al. (2013) interpret the observed reduction in

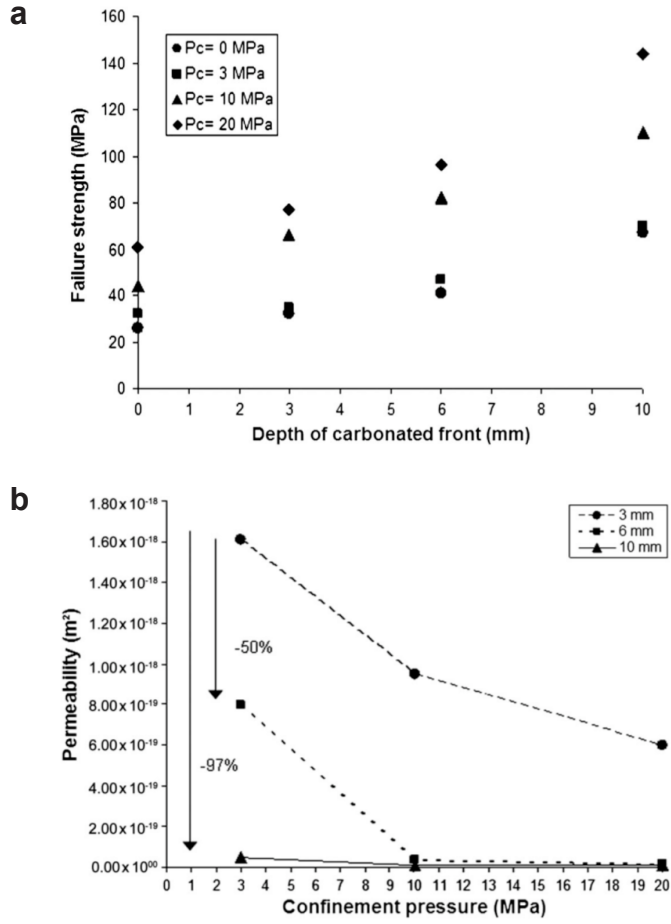

Figure 19. Effect of cement carbonation as a function of the fraction of the depth of carbonation (in a 20 mm diameter cylinder): (a) strength as a function of confining pressure and (b) permeability versus confining pressure. Carbonation improves the hydrologic and mechanical properties of cement. [With permission of the American Society of Civil Engineers, from Takla et al. (2011), *Journal of Materials in Civil Engineering,* Vol. 23, Figs. 6 and 7, p. 745.]

permeability of their coreflood data as involving deformation of mechanically softened CO_2-reacted cement in response to confining pressure.

Self healing and well integrity

The evolution of defects in the wellbore is one of the most important geochemical problems. Predicting this behavior is essential to evaluating whether leakage of CO_2 in wells becomes worse with time because of dissolution or whether leakage is self-limiting because of CO_2-induced reactions. Most of the direct measurements described in this section provide evidence that at least in some circumstances chemical reactions lead to self-healing of defects either due to precipitation, swelling/volume changes of reaction products, or to mechanical softening of reaction products. The results show that it is not necessary to have carbonate precipitation to create reduced permeability, as flow of acidic solutions or carbonate-undersaturated solutions has shown.

Experimental studies have long shown that simple carbonation of Portland cement reduces permeability and increases strength. However, our understanding of the impacts of CO_2 flow on permeability, particularly in interfaces, is incomplete. Simple conceptual models of flow in interfaces suggest a limiting flow rate, below which carbonate precipitation seals the defect and above which dissolution dominates and permeability increases. Recent work by Huerta et al. (2013), Walsh et al. (2013), Mason et al. (2013) and Luquot et al. (2013) shows that the situation is more complex as the behavior of amorphous silica, derived by leaching of cement phases, can act to either limit fracture permeability or maintain and even expand fracture apertures. We do not yet have a sufficient understanding of cement-defect behavior to determine the relationship between flow rates and permeability that would improve confidence in predictive models. Such an understanding would be similar to that found by Luquot and Gouze (2009), who determined experimentally the coupling between flow rates and dissolution/precipitation rates for CO_2-brine mixtures in carbonate rocks.

Evidence for self-healing can also be found in field studies at SACROC that show precipitation of calcium carbonate at the shale-cement interface that fills a 1-mm wide gap (Fig. 20) and carbonate deposition at the cement-casing interface (Carey et al. 2007).

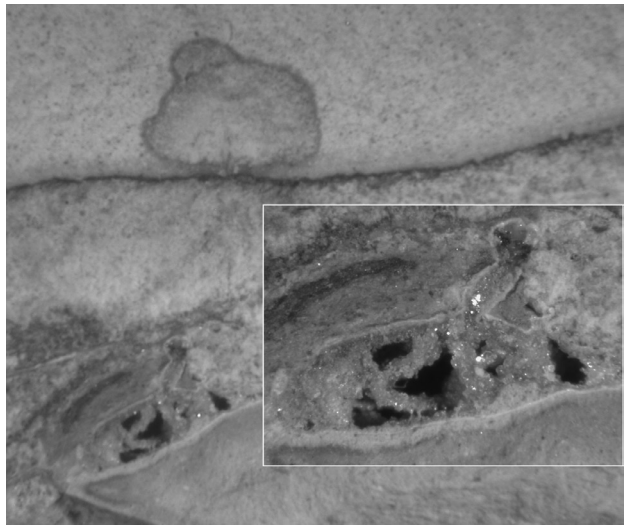

Figure 20. Photograph of the interface between cement and shale of a wellbore sample from the SACROC CO_2-EOR field in west Texas. The image shows a triangular wedge of shale (below) with a crystal-filled cavity separating it from cement (above). Calcium carbonate crystals are filling and perhaps healing this interface defect (inset at right). A dense carbonate deposition zone appears as a dark line in the upper part of the image. The carbonate front is pierced by a balloon of CO_2-reacted cement that formed by diffusion from the interface through a break in the carbonate precipitation front. [Reprinted from *International Journal of Greenhouse Gas Control*, Carey et al. (2007), Vol. 1, Fig. 4, p. 80 with permission from Elsevier.]

CONCLUSIONS AND FUTURE RESEARCH

The common materials of oil and gas wells, Portland cement and low-carbon steel, are unstable in CO_2-saturated brines and react relatively rapidly to form, principally, calcium carbonate and iron carbonate. Despite this thermodynamic fate, wellbore materials perform and maintain zonal isolation in field and experimental observations. This is understood as a consequence of coupled behavior between flow of reactants (CO_2-water) and the rate of dissolution and precipitation of cement or corrosion of steel. In the restricted flow environments found in well-

bore systems, cements are carbonated but do not suffer significant deterioration of hydrologic or mechanical properties. In fact, cement carbonation often results in reduced permeability and enhanced mechanical strength. While steel is susceptible to corrosion, wellbore environments allow development of protective iron carbonate scale. In addition, the presence of Portland cement, even carbonated cement, provides protection against significant rates of corrosion.

The impact of geochemical reactions in the wellbore environment cannot be separated from coupled flow, thermal and mechanical processes. CO_2-induced chemical reactions migrating upward from a storage reservoir will not result in the creation of defects or the wholesale dissolution of cement or steel. Defects must exist that allow CO_2±brine to flow and to come in contact with well materials. These defects may originate in faulty construction or arise from thermal and mechanical stresses that crack cement or separate cement-casing and cement-formation interfaces. Once flow along defects occurs, CO_2-induced reactions may aggravate or ameliorate the condition through dissolution or precipitation.

Several experimental and field studies show that cement and steel have substantial self-healing tendencies. These arise from the precipitation of calcium and iron carbonates, but also appear to originate from swelling of Ca-depleted, residual C-S-H phases and/or migration and reprecipitation of cement phases. The mechanical behavior of the cement system is of particular importance as plastic deformation of reacted and unreacted cement appears to provide limits to the aperture of defects and thus limits to the effective permeability of wellbore leaks.

Future research directions

Self-healing in wellbore systems is still an uncertain prospect. Until we can define the outer limits at which chemical reactions deteriorate wellbore integrity, we cannot be confident of the self-mitigation of CO_2 leakage. This will require systematic experimental studies, complemented by field observations that show transitions between self-sealing and self-opening flow environments. With these data, it may then be possible to develop computational models for flow and reaction in defects that would provide predictive tools for well performance.

Experiments are just now hinting at the complexities of coupled geomechanics, flow and reaction. The cement-CO_2-brine system appears to have properties that make it sensitive and reactive to all of these processes and offers an ideal test bed for developing coupled experimental and computational models. Much work is needed to show how cement deformation interacts with reactions to restrict or enhance flow.

Work on corrosion suffers because it lies between engineering disciplines that are very good at processes in pipelines but lack insight into the character of geologic environments and geochemistry where knowledge of corrosion processes is limited. Thus there is much to learn from experimental and modeling studies that couple corrosion of steel with geochemical reactions of cement. This is to say nothing of the large uncertainties related to localized corrosion and its relation to iron carbonate scale heterogeneity and carbonated cement.

ACKNOWLEDGMENTS

Funding from the Department of Energy's Fossil Energy Program (Joshua Hull, program manager) to Los Alamos National Laboratory for research on the hydrodynamic integrity of wellbore and caprock systems is gratefully acknowledged. Thanks are also given for support of research on well integrity and access to unique field studies provided by the CO_2 Capture Project (Walter Crow program manager). I also wish to thank the many colleagues who have contributed their insights and scientific results to the development of the ideas in this review (see the references), but particular thanks to Dennis Newell, Jiabin Han, Peter Lichtner, Marcus Wigand, George Guthrie, Rajesh Pawar, Stefan Bachu, Theresa Watson, Barbara Kutchko, Brian Strazisar, and Walter Crow.

REFERENCES

API (2010) Isolating potential flow zones during well construction. Technical Report API Standard 65–Part 2, 2nd edition, American Petroleum Institute

Bachu S, Bennion DB (2009) Experimental assessment of brine and/or CO_2 leakage through well cements at reservoir conditions. Int J Greenhouse Gas Control 3:494-501

Barlet-Gouédard V, Rimmelé G, Porcherie O, Quisel N, Desroches J (2009) A solution against well cement degradation under CO_2 geological storage environment. Int J Greenhouse Gas Control 3:206-216

Bary B, Sellier A (2004) Coupled moisture-carbon dioxide-calcium transfer model for carbonation of concrete. Cem Concr Res 34:1859-1872

Berner RA (1981) A new geochemical classification of sedimentary environments. J Sediment Petrol 51:359-365

Broekmans MATM, Pöllman H (eds) (2012) Applied Mineralogy of Cement & Concrete. Reviews in Mineralogy and Geochemistry. Vol 74. Mineralogical Society of America

Bruckdorfer RA (1986) Carbon dioxide corrosion in oilwell cements. *In*: SPE Rocky Mountain Meeting, Billings, MT, 19-21 May 1986 SPE 15176

Brunet J-PL, Li L, Karpyn ZT, Kutchko BG, Strazisar B, Bromhal G (2013) Dynamic evolution of cement compositional and transport properties under conditions relevant to geological carbon sequestration. Energy Fuels 27(8):4208-4220

Cabrera JG (1996) Deterioration of concrete due to reinforcement steel corrosion. Cem Concr Compos 18:47-59

Carey JW (2006) Modifying the PHREEQC and Geochemist's Workbench databases for a more accurate CO_2 solubility. Technical Report LA-UR-06-4676, Los Alamos National Laboratory

Carey JW (2010) Development of a cement phase database from CEMDATA for elevated temperature calculations in PHREEQC. Technical Report LA-UR, Los Alamos National Laboratory

Carey JW, Lichtner PC (2007) Calcium silicate hydrate (C-S-H) solid solution model applied to cement degradation using the continuum reactive transport model FLOTRAN. *In:* Transport Properties and Concrete Quality: Materials Science of Concrete. Mobasher, B, Skalny, J (eds) American Ceramic Society; John Wiley & Sons, Inc, p 73-106

Carey JW, Lichtner PC (2011) Computational studies of two-phase cement-CO_2-brine interaction in wellbore environments. SPE J 16:940-948

Carey JW, Svec R, Grigg R, Zhang J, Crow W (2010) Experimental investigation of wellbore integrity and CO_2-brine flow along the casing-cement microannulus. Int J Greenhouse Gas Control 4:272-282

Carey JW, Wigand M, Chipera S, WoldeGabriel G, Pawar R, Lichtner P, Wehner S, Raines M, Guthrie GD Jr (2007) Analysis and performance of oil well cement with 30 years of CO_2 exposure from the SACROC Unit, West Texas, USA. Int J Greenhouse Gas Control 1:75-85

Chen JJ, Thomas JJ, Taylor HFW, Jennings HM (2004) Solubility and structure of calcium silicate hydrate. Cem Concr Res 34:1499-1519

Choi Y-S, Nešić S (2011) Determining the corrosive potential of CO_2 transport pipeline in high pCO_2–water environments. Int J Greenhouse Gas Control 5:788-797

Choi Y-S, Nešić S, Young D (2010) Effect of impurities on the corrosion behavior of CO_2 transmission pipeline steel in supercritical CO_2-water environments. Environ Sci Technol 44:9233–9238

Choi Y-S, Young D, Nešić S, Gray LGS (2013) Wellbore integrity and corrosion of carbon steel in CO_2 geologic storage environments: A literature review. Int J Greenhouse Gas Control 16S:S70-S77

Corvisier J, Brunet F, Fabbri A, Bernard S, Findling N, Rimmelé G, Barlet-Gouédard V, Beyssac O, Goffé B (2010) Raman mapping and numerical simulation of calcium carbonates distribution in experimentally carbonated Portland-cement cores. Eur J Mineral 22:63-74

Crow W, Carey JW, Gasda S, Williams DB, Celia M (2010) Wellbore integrity analysis of a natural CO_2 producer. Int J Greenhouse Gas Control 4:186-197

Deremble L, Loizzo M, Huet B, Lecampion B, Quesada D (2011) Stability of a leakage pathway in a cemented annulus. Energy Procedia 4:5283-5290

Duguid A, Butsch R, Carey JW, Celia M, Wang J, Chuganov N, Stabinski E, Ramakrishnan TS, Stamp V (2011) Collection and analysis of baseline wellbore leakage risk data in multiple wells from the same field. 10th Carb Capt Sequ, May 2011, Pittsburgh, PA

Duguid A, Scherer GW (2010) Degradation of oilwell cement due to exposure to carbonated brine. Greenhouse Gases Sci Technol 4:546–560

Fabbri A, Corvisier J, SchubnelA, Brunet F, Goffé B, Rimmele G, Barlet-Gouédard V (2009) Effect of carbonation on the hydro-mechanical properties of Portland cements. Cem Concr Res 39:1156-1163

Fabbri A, Jacquemet N, Seyedi DM (2012) A chemo-poromechanical model of oilwell cement carbonation under CO_2 geological storage conditions. Cem Concr Res 42:8–19

Felmy AR, Qafoku O, Arey BW, Hu JZ, Hu M, Schaef TH, Ilton ES, Hess NJ, Pearce CI, Feng J (2012) Reaction of water-saturated supercritical CO_2 with forsterite: Evidence for magnesite formation at low temperatures. Geochim Cosmochim Acta 91:271-282

Gartner EM, Jennings HM (1987) Thermodynamics of calcium silicate hydrates and their solutions. J Am Ceram Soc 70:743-749

Gasda SE, Bachu S, Celia MA (2004) Spatial characterization of the location of potentially leaky wells penetrating a deep saline aquifer in a mature sedimentary basin. Environ Geol 46:707-720

Gherardi F, Audigane P, Gaucher EC (2012) Predicting long-term geochemical alteration of wellbore cement in a generic geological CO_2 confinement site: Tackling a difficult reactive transport modeling challenge. J Hydrol 420-421:340359

Glasser F, Marchand J, Samson E (2008) Durability of concrete - degradation phenomena involving detrimental chemical reactions. Cem Concr Res 38:226-246

Groves GW, Rodway DI, Richardson IG (1990) The carbonation of hardened cement pastes. Adv Cem Res 3:117-125

Han J, Carey JW, Zhang J (2011a) A coupled electrochemical-geochemical model of corrosion for mild steel in high-pressure CO_2-saline environments. Int J Greenhouse Gas Control 5:777-787

Han J, Carey JW, Zhang J (2011b) Effect of bicarbonate on corrosion of carbon steel in CO_2 saturated brines. Int J Greenhouse Gas Control 5:1680-1683

Han J, Carey JW, Zhang J (2011c) Effect of debonded interfaces on corrosion of mild steel composites in supercritical CO_2-saturated brines. NACE Ann Conf, May 31-June 3, Dallas Texas, pp 14

Han J, Carey JW, Zhang J (2012) Degradation of cement-steel composite at bonded steel-cement interfaces in supercritical CO_2 saturated brines simulating wellbore systems. NACE Int—Corr Conf Expo 2012, 1:151-179

Huerta NJ, Hesse MA, Bryant SL, Strazisar BR, Lopano CL (2013) Experimental evidence for self-limiting reactive flow through a fractured cement core: Implications for time-dependent wellbore leakage. Environ Sci Technol 47:269-275

Huet BM, Prevost JH, Scherer GW (2010) Quantitative reactive transport modeling of Portland cement in CO_2-saturated water. Int J Greenhouse Gas Control 4:561-574

IPCC (2005) IPCC Special Report on Carbon Dioxide Capture and Storage. Metz B, Davidson O, de Coninck H, Loos M, Meyer L (eds) Intergovernmental Panel on Climate Change. *http://www.ipcc.ch/activity/srccs/index.htm*

Jacquemet N, Pironon J, Lagneau V, Saint-Marc J (2012) Armouring of well cement in H_2S-CO_2 saturated brine by calcite coating – experiments and numerical modelling. App Geochem 27:782-795

Jung HB, Jansik D, Um W (2013) Imaging wellbore cement degradation by carbon dioxide under geologic sequestration conditions using X-ray computed microtomography. Environ Sci Technol 47:283-289

Jung HB, Um W (2013) Experimental study of potential wellbore cement carbonation by various phases of carbon dioxide during geologic carbon sequestration. App Geochem 35:161-172

Kermani MB, Morshed A (2003) Carbon dioxide corrosion in oil and gas production — a compendium. Corr 59:659-683

Kharaka YK, Hanor JS (2003) Deep fluids in the continents: I. sedimentary basins. *In:* Treatise in Geochemistry. Vol 5. Drever, JI (ed) Elsevier Ltd, p 499-540

Kulik D, Berner U, Curti E (2003) Modelling chemical equilibrium partitioning with the GEMS-PSI code. Technical Report PSI Scientific Report IV, Paul Scherer Institute. *http://gems.web.psi.ch/*

Kutchko B, Strazisar B, Dzombak D, Lowry G, Thaulow N (2007) Degradation of well cement by CO_2 under geologic sequestration conditions. Environ Sci Technol 41:4787-4792

Kutchko B, Strazisar B, Dzombak D, Lowry G, Thaulow N (2008) Rate of CO_2 attack on Class H well cement under geologic sequestration conditions. Environ Sci Technol 42:6237–6242

Kutchko BG, Strazisar BR, Huerta N, Lowry GV, Dzombak DA, Thaulow N (2009) CO_2 reaction with hydrated class H well cement under geologic sequestration conditions: Effects of fly ash admixtures. Environ Sci Technol 43:3947-3952

Laudet J-B, Garnier A, Neuville N, Guen YL, Fourmaintraux D, Rafai N, Burlion N, Shao J-F (2011) The behavior of oil well cement at downhole CO_2 storage conditions: Static and dynamic laboratory experiments. Energy Procedia 4:5251-5258

Lichtner PC, Carey JW (2006) Incorporating solid solutions in geochemical reactive transport equations using a kinetic discrete-composition approach. Geochim Cosmochim Acta 70:1356-1378

Liteanu E, Spiers C (2011) Fracture healing and transport properties of wellbore cement in the presence of supercritical CO_2. Chem Geol 281:195-210

Liteanu E, Spiers CJ, Peach CJ (2009) Failure behavior of wellbore cement in the presence of water and supercritical CO_2. Energy Procedia 1:3553-3560

Lothenbach B, Matschei T, Moschner G, Glasser FP (2008) Thermodynamic modelling of the effect of temperature on the hydration and porosity of Portland cement. Cem Concr Res 38:1-18

Luquot L, Gouze P (2009) Experimental determination of porosity and permeability changes induced by injection of CO_2 into carbonate rocks. Chem Geol 265:148-159

Luquot L, Abdoulghafour H, Gouze P (2013) Hydro-dynamically controlled alteration of fractured portland cements flowed by CO_2-rich brine. Int J Greenhouse Gas Control 16:167-179
Marty NC, Tournassat C, Burnol A, Giffaut E, Gauchera EC (2009) Influence of reaction kinetics and mesh refinement on the numerical modelling of concrete/clay interactions. J Hydrol 364:58-72
Mason HE, Du Frane WL, Walsh SD, Dai Z, Charnvanichborikarn S, Carroll SA (2013) Chemical and mechanical properties of wellbore cement altered by CO_2-rich brine using a multianalytical approach. Environ Sci Technol 47:1745-1752
Matschei T, Lothenbach B, Glasser FP (2007) Thermodynamic properties of Portland cement hydrates in the system CaO-Al_2O_3-SiO_2-$CaSO_4$-$CaCO_3$-H_2O. Cem Concr Res 37:1379-1410
Matteo EN, Scherer GW (2012) Experimental study of the diffusion-controlled acid degradation of Class H Portland cement. Int J Greenhouse Gas Control 7:181-191
McGrail BP, Schaef HT, Glezakou VA, Dang LX, Owen AT (2009) Water reactivity in the liquid and supercritical CO_2 phase: Has half the story been neglected? *In:* Greenhouse Gas Control Technologies 9. Vol 1. Gale, J, Herzog, H, Braitsch, J, (eds) p 3415-3419
McNab WW, Carroll SA (2011) Wellbore integrity at the Krechba carbon storage site, In Salah, Algeria: 2. Reactive transport modeling of geochemical interactions near the cement-formation interface. Energy Procedia 4:5195-5202
Milestone NB, Sugama T, Kukacka LE, Carciello N (1986) Carbonation of geothermal grouts – part 1: CO_2 attack at 150 °C. Cem Concr Res 16:941-950
Monlouis-Bonnaire JP, Verdier J, Perrin B (2004) Prediction of the relative permeability to gas flow of cement-based materials. Cem Concr Res 34:737-744
Nešić S (2007) Key issues related to modelling of internal corrosion of oil and gas pipelines — A review. Corros Sci 49:4308-4338
Newell DL, Carey JW (2013) Experimental evaluation of wellbore integrity along the cement-rock boundary. Environ Sci Technol 47:276-282
Nordbotten JM, Kavetski D, Celia MA, Bachu S (2009) Model for CO_2 leakage including multiple geological layers and multiple leaky wells. Environ Sci Technol 43:743-749
Onan DD (1984) Effects of supercritical carbon dioxide on well cements. SPE AIME, p 161-172, doi: 10.2118/12593-MS
Osborn SG, Vengosh A, Warner NR, Jackson RB (2011) Methane contamination of drinking water accompanying gas-well drilling and hydraulic fracturing. Proc Natl Acad Sci 108:8172-8176
Papadakis VG, Vayenas CG, Fardis MN (1991) Experimental investigation and mathematical modeling of the concrete carbonation problem. Chem Eng Sci 46:1333-1338
Raoof A, Nick H, Wolterbeek T, Spiers C (2012) Pore-scale modeling of reactive transport in wellbore cement under CO_2 storage conditions. Int J Greenhouse Gas Control 11:67-77
Richardson IG (2004) Tobermorite/jennite- and tobermorite/calcium hydroxide-based models for the structure of C-S-H: applicability to hardened pastes of tricalcium silicate, β-dicalcium silicate, Portland cement, and blends of Portland cement with blast-furnace slag, metakaolin, or silica fume. Cem Concr Res 34:1733-1777
Rimmelé G, Barlet-Gouédard V, Porcherie O, Goffé B, Brunet F (2008) Heterogeneous porosity distribution in portland cement exposed to CO_2-rich fluids. Cem Concr Res 38:1038-1048
Rochelle CA, Milodowski AE (2013) Carbonation of borehole seals: Comparing evidence from short-term laboratory experiments and long-term natural analogues. App Geochem 30:161-177
Scherer GW, Kutchko B, Thaulow N, Duguid A, Mook B (2011) Characterization of cement from a well at Teapot Dome Oil Field: Implications for geological sequestration. Int J Greenhouse Gas Control 5:115-124
Shen JC, Pye DS (1989) Effects of CO_2 attack on cement in high-temperature applications. SPE/IADC 1989 Drilling Conference; Feb 28-Mar 3 1989; New Orleans, LA, USA
Springer RD, Wang Z, Anderko A, Wang P, Felmy AR (2012) A thermodynamic model for predicting mineral reactivity in supercritical carbon dioxide: I. phase behavior of carbon dioxide–water–chloride salt systems across the H_2O-rich to the CO_2-rich regions. Chem Geol 322-323:151-171
Takla I, Burlion N, Shao JF, Saint-Marc J, Garnier A (2011) Effects of the storage of CO_2 on multiaxial mechanical and hydraulic behaviors of oil-well cement. J Mater Civil Eng, 23:741-746
Taylor HFW (1990) Cement Chemistry. Academic Press, London
Viswanathan HS, Pawar RJ, Stauffer PH, Kaszuba JP, Carey JW, Olsen SC, Keating GN, Kavetski D, Guthrie GD Jr (2008) Development of a hybrid process and system model for the assessment of wellbore leakage at a geologic CO_2 sequestration site. Environ Sci Technol 42:7280-7286
Walsh SD, Du Frane WL, Mason HE, Carroll SA (2013) Permeability of wellbore-cement fractures following degradation by carbonated brine. Rock Mech Rock Eng 46:455-464
Watson TL, Bachu S (2007) Evaluation of the potential for gas and CO_2 leakage along wellbores. SPE E&P Environmental and Safety Conference, 5-7 March, 2007

Watson TL, Bachu S (2008) Identification of wells with high CO_2-leakage potential in mature oil fields developed for CO_2-enhanced oil recovery. 16th SPE/DOE Improved Oil Recovery Symposium 2008 - "IOR: Now More Than Ever." 1:234-243

Wertz F, Gherardi F, Blanc P, Bader A-G, Fabbri A (2013) Cement CO_2-alteration propagation at the well-caprock-reservoir interface and influence of diffusion. Int J Greenhouse Gas Control 12:9-17

Wigand M, Kaszuba JP, Carey JW, Hollis WK (2009) Geochemical effects of CO_2 sequestration on fractured wellbore cement at the cement/caprock interface. Chem Geol 265:122-133

Wilson JC, Benbow SJ, Metcalfe R, Savage D, Walker CS, Chittenden N (2011) Fully coupled modeling of long term cement well seal stability in the presence of CO_2. Energy Procedia 4:5162-5169

Wojtanowicz AK (2008) Environmental control of well integrity. *In:* Environmental Technology in the Oil Industry. Orszulik, ST (ed) Springer, Netherlands, p 53-75

Yalcinkaya T, Radonjic M, Willson CS, Bachu S (2011) Experimental study on a single cement-fracture using CO_2 rich brine. Energy Procedia 4:533505342

Zhang M, Bachu S (2011) Review of integrity of existing wells in relation to CO_2 geological storage: What do we know? Int J Greenhouse Gas Control 5:826-840